

B. Eckhardt
Editor

SPRINGER PROCEEDINGS IN PHYSICS 132

Advances in Turbulence XII

Proceedings of the 12th EUROMECH
European Turbulence Conference,
September 7-10, 2009, Marburg, Germany

 Springer

Bruno Eckhardt

Editor

Advances in Turbulence

XII

Proceedings of the 12th EUROMECH
European Turbulence Conference,
September 7–10, 2009, Marburg, Germany

With 594 Figures

 Springer

Professor Dr. Bruno Eckhardt
Philipps-Universität Marburg
Fachbereich Physik
Renthof 6
35032 Marburg, Germany
E-mail: bruno.eckhardt@physik.uni-marburg.de

ISSN 0930-8989 e-ISSN 1867-4941
ISBN 978-3-642-03084-0 e-ISBN 978-3-642-03085-7
DOI 10.1007/978-3-642-03085-7
Springer Dordrecht Heidelberg London New York

Library of Congress Control Number: 2009931716

© Springer-Verlag Berlin Heidelberg 2009

This work is subject to copyright. All rights are reserved, whether the whole or part of the material is concerned, specifically the rights of translation, reprinting, reuse of illustrations, recitation, broadcasting, reproduction on microfilm or in any other way, and storage in data banks. Duplication of this publication or parts thereof is permitted only under the provisions of the German Copyright Law of September 9, 1965, in its current version, and permission for use must always be obtained from Springer-Verlag. Violations are liable to prosecution under the German Copyright Law.

The use of general descriptive names, registered names, trademarks, etc. in this publication does not imply, even in the absence of a specific statement, that such names are exempt from the relevant protective laws and regulations and therefore free for general use.

Cover design: SPi Publisher Services

Printed on acid-free paper

Springer is part of Springer Science+Business Media (www.springer.com)

Preface

Since the first meeting in Lyon in 1986, the biannual European Turbulence Conferences have provided an informative survey of the international efforts in understanding turbulence in its fundamental and applied aspects. Now integrated into the conference cycles coordinated by the European Mechanics Society the meetings provide a regular forum for the exchange of ideas and the discussion of the latest developments. The more recent conferences in Barcelona (2000), Southampton (2002), Trondheim (2004), and Porto (2007) have attracted several hundred participants from 30 and more countries. The 12th meeting in this series, ETC 12, which was held in Marburg September 7-10, 2009, continues this tradition. Researchers from 34 countries submitted 336 abstracts to the conference. The number of submissions is somewhat lower than for the Porto or Barcelona meetings, but in line with the previous ones in Northern Europe.

The contributions that were presented in Marburg were selected by the international advisory board for the European Turbulence Conferences. The committee was chaired by Professor Arne V. Johansson (Stockholm) and consisted of Professors Helge I. Andersson (Trondheim), Konrad Bajer (Warsaw), Luca Biferale (Rome), Claude Cambon (Lyon), Hans-Hermann Fernholz (Berlin), Peter Davidson (Cambridge, UK), Yuri Kachanov (Novosibirsk), Detlef Lohse (Twente), Jose L. Palma (Porto), Jean-Francois Pinton (Lyon) and the local organizer.

Impressed by the high quality of the abstracts the committee selected 250 for oral presentation, corresponding to a record number of almost 75% of the submissions. In addition, 70 papers were selected for presentation in a poster and seminar session. These numbers attest to the healthy state of the field and the reputation the conferences have achieved.

As in previous years, the papers are grouped by the subfields as reflected in the sections given in the table of contents. Naturally, the level of activity in the subareas varies from conference to conference. For ETC12, the largest numbers of submissions were recorded for the areas of instability and transition, and wall bounded flows. These were closely followed by intermittency

and scaling, transport and mixing, vortex dynamics and structure formation, and geophysical and astrophysical turbulence, which received similar numbers of submissions. Further topics presented at the meeting include turbulence in multiphase and non-Newtonian flows, Lagrangian aspects, Large Eddy Simulations and related techniques, Magnetohydrodynamic Turbulence, control of turbulent flows, reacting and compressible flows as well as acoustics of turbulent flows.

The program of the meeting had the invited talks and the seminar session during which the posters were presented as plenary sessions, and the other contributed talks arranged in four parallel session of up to six talks per group. These proceedings are the written record of six invited talks, 211 contributed talks and 35 posters. They are grouped by the main topics and arranged in the order in which they were presented within the sessions.

The meeting would not have been possible without the unselfish support of the staff of the various departments of the Philipps-Universität Marburg, the assistance of Marburg Tourist and Marketing, and the Springer Verlag who publishes these proceedings. Several exhibitors and organizations contributed to the budget of the meeting. Among them, I would like to mention the European Community, who within its program to support Cooperation in Science and Technology (COST) finances an activity on Particles in Turbulence. The opening meeting of this COST Action was held as part of the meeting. They all are to be thanked for their help in making this meeting possible and for promoting turbulence research in Europe.

Marburg,
May 2009

Bruno Eckhardt
Local Organizer

Contents

Preface	v
---------------	---

Part I Lagrangian aspects

1 Lagrangian modeling and properties of particles with inertia <i>F. Toschi, L. Biferale, E. Calzavarini, E. L�ev�eque and A. Scagliarini</i> ..	3
2 Effect of Fax�en forces on acceleration statistics of material particles in turbulent flow <i>E. Calzavarini, R. Volk, M. Bourgoin, E. L�ev�eque, J.-F. Pinton and F. Toschi</i>	11
3 Lagrangian analysis of turbulent convection <i>J. Schumacher and M. S. Emran</i>	15
4 Linear and angular dynamics of an inertial particle in turbulence <i>Y. Gasteuil and J.-F. Pinton</i>	19
5 Collision rate between heavy particles in a model turbulent flow <i>L. Ducasse and A. Pumir</i>	23
6 From cloud condensation nuclei to cloud droplets: a turbulent model <i>A. Celani, A. Mazzino, and M. Tizzi</i>	27
7 Lagrangian statistics of inertial particles in turbulent flow <i>M. Bourgoin, N. Qureshi, C. Baudet, A. Cartellier, and Y. Gagne</i>	31
8 Lagrangian statistics of two-dimensional turbulence in a square container <i>B. Kadoch, W.J.T. Bos, and K. Schneider</i>	35

9 Measurement of Lagrangian particle trajectories by digital in-line holography	
<i>G. Gülker, T. Homeyer and J. Peinke</i>	39
10 3-D Particle Tracking Velocimetry (PTV) in gas flows using coloured tracer particles	
<i>D. Tarlet, C. Bendicks, R. Bordás, B. Wunderlich, D. Thévenin, and B. Michaelis</i>	43
11 Two-particle dispersion in 2D inverse cascade turbulence and its telegraph equation model	
<i>A. Mizuta, S. Toh, and T. Matsumoto</i>	47
12 Numerical simulations of particle dispersion in stratified flows	
<i>G. Brethouwer and E. Lindborg</i>	51
<hr/>	
Part II Instability and Transition	
<hr/>	
13 Experimental study of the von Kármán flow from $Re = 10^2$ to 10^6: spontaneous symmetry breaking and turbulent bifurcations	
<i>P.-P. Cortet, S. Atis, A. Chiffaudel, F. Daviaud, B. Dubrulle, and F. Ravelet</i>	59
14 Flow reversals in a vertical channel	
<i>J.-C. Tisserand, M. Creyssels, M. Gibert, B. Castaing, and F. Chilla</i>	63
15 Linear instability of streamwise corner flow	
<i>F. Alizard, U. Rist, J.-C. Robinet</i>	67
16 DNS of turbulent plane Couette flow with emphasis on turbulent stripe	
<i>T. Tsukahara, Y. Kawaguchi, and H. Kawamura</i>	71
17 Geometry of state space in plane Couette flow	
<i>P. Cvitanović and J.F. Gibson</i>	75
18 Linear and nonlinear instabilities of sliding Couette flow	
<i>K. Deguchi and M. Nagata</i>	79
19 Localization in plane Couette edge dynamics	
<i>T.M. Schneider, D. Marinic, and B. Eckhardt</i>	83
20 Nonlinear optimal perturbations in plane Couette flow	
<i>L. Brandt, Y. Duguet, and R. Larsson</i>	85

21 Order parameter in laminar-turbulent patterns
L.S. Tuckerman, D. Barkley, D. Moxey, and O. Dauchot 89

22 Pattern formation in low Reynolds number plane Couette flow
Y. Duguet, P. Schlatter, and D.S. Henningson 93

23 Quasi-stationary and chaotic convection in low rotating spherical shells
B. Fütterer and C. Egbers 97

24 Linear stability of 2D rough channels
F. Fabiani, P. Orlandi, and S. Leonardi 103

25 Transient turbulent bursting in enclosed flows
K. Hochstrate, M. Avila, J. Abshagen, and G. Pfister 107

26 On new localized vortex solutions in the Couette-Ekman layer
M. Withalm and N.P. Hoffmann 111

27 Shear instabilities in Taylor-Couette flow
A. Meseguer, F. Mellibovsky, F. Marques, and M. Avila 115

28 Particle Tracking Velocimetry in transitional plane Couette flow
B. Lüthi, M. Holzner, M. Kinzel, A. Liberzon, and A. Tsinober 119

29 Experimental study of coherent structures in turbulent pipe flow
A. de Lozar and B. Hof 123

30 Forced localized turbulence in pipe flows
M. Avila and B. Hof 125

31 From localized to expanding turbulence
B. Hof and A. de Lozar 129

32 Influence of test-rigs on the laminar-to-turbulent transition of pipe flows
F. Durst, K. Haddad, and Ö. Ertunç 131

33 Interaction of turbulent spots in pipe flow
D. Samanta, A. de Lozar, and B. Hof 135

34 Large-scale transitional dynamics in pipe flow
F. Mellibovsky, A. Meseguer, T.M. Schneider, and B. Eckhardt 137

35 Nonlinear coherent structures in a square duct <i>H. Wedin, A. Bottaro, and M. Nagata</i>	141
36 Quantitative measurement of the life time of turbulence in pipe flow <i>D.J. Kuik, C. Poelma, B. Hof, and J. Westerweel</i>	145
37 Experimental investigation of turbulent patch evolution in spatially steady boundary layers <i>J.H.M. Fransson</i>	149
38 Interaction of noise disturbances and streamwise streaks <i>P. Schlatter, L. Brandt, and R. de Lange</i>	151
39 Linear generation of multiple time scales by 3D unstable perturbations <i>S. Scarsoglio, D. Tordella, and W.O. Criminale</i>	155
40 Convection at very high Rayleigh number: signature of transition from a micro-thermometer inside the flow <i>J. Salort, F. Gauthier, B. Chabaud, O. Bourgeois, J.-L. Garden, R. du Puits, A. Thess, and P.-E. Roche</i>	159
41 Estimating local instabilities for irregular flows in the differentially heated rotating annulus <i>U. Harlander, R. Faulwetter, K. Alexandrov, and C. Egbers</i>	163
42 Search for the ultimate state in turbulent Rayleigh-Bénard convection <i>E. Bodenschatz, D. Funfschilling, and G. Ahlers</i>	167
43 Rayleigh-Taylor instability in two dimensions and phase-field method <i>A. Celani, A. Mazzino, P. Muratore-Ginanneschi, and L. Vozella</i>	169
44 Split energy cascade in quasi-2D turbulence <i>G. Boffetta, A. Celani, and S. Musacchio</i>	173
45 Stability and laminarisation of turbulent rotating channel flow <i>S. Wallin, O. Grundestam, and A.V. Johansson</i>	177
46 The vortical flow pattern exhibited by the channel flow on a rotating system just past transition under the influence of the Coriolis force <i>V. I. Vasanta Ram, B. Müller, and F. Azhari</i>	179

47 Transient evolution and high stratification scaling in horizontal mixing layers
C. Arratia, S. Ortiz, and J.-M. Chomaz 183

Part III Control of turbulent flows

48 Toward cost-effective control of wall turbulence for skin friction drag reduction
N. Kasagi, Y. Hasegawa, and K. Fukagata 189

49 Active control of turbulent boundary layer using an array of piezo-ceramic actuators
HL Bai, and Y. Zhou 201

50 Flat plate turbulent boundary-layer control using vertical LEBUs
V.I. Kornilov and A.V. Boiko 205

51 Estimation of the spanwise wall shear stress based on upstream information for wall turbulence control
B. Frohnäpfel, Y. Hasegawa, N. Kasagi, and S. Große 209

52 Interactions between vortex generators and a flat plate boundary layers. Application to the control of separated flows.
T. Duriez, B. Thiria, T. Cambonie, J.E. Wesfreid and J.L. Aider 213

53 Modulated global mode of a controlled wake
V. Parezanović, and O. Cadot 217

54 Swirl effects in turbulent pipe flow
F. Nygård and H.I. Andersson 221

55 Control of an axisymmetric turbulent wake by a pulsed jet
J.F. Morrison and A. Qubain 225

56 Direct Numerical Simulations of turbulent mixed convection in enclosures with heated obstacles
O. Shishkina, and C. Wagner 229

57 On drag reduction in turbulent channel flow over a superhydrophobic surfaces
C. Peguero and K. Breuer 233

58 Response of periodically modulated turbulence
H.E. Cekli and W. van de Water 237

59 Turbulent drag reduction by feedback: a Wiener-filtering approach	
<i>F. Martinelli, M. Quadrio, and P. Luchini</i>	241

Part IV Vortex dynamics and structure formation

60 A driving mechanism of turbulent puff in pipe flow	
<i>M. Shimizu and S. Kida</i>	249
61 Wavelet tools to study vortex bursting and turbulence production	
<i>M. Farge, J. Ruppert-Felsot, and P. Petitjeans</i>	253
62 The minimum-entropy principle for decaying 2D turbulence in circular domains	
<i>G.H. Keetels, H.J.H. Clercx, G.J.F. van Heijst</i>	257
63 Direct numerical simulation of a turbulent vortex ring	
<i>P.J. Archer, T.G. Thomas, and G.N. Coleman</i>	261
64 Reconnection of vortex bundles	
<i>S. Alamri, A.J. Youd, and C. F. Barenghi</i>	265
65 Turbulent energy cascade caused by vortex stretching	
<i>S. Goto</i>	269
66 Instabilities and transient growth of trailing vortices in stratified fluid	
<i>C. Donnadieu, J.-M. Chomaz, and S. Ortiz</i>	273
67 Implementation of vortex stretching into the two-dimensional Navier-Stokes Equations via arbitrary external straining	
<i>F. Sabetghadam, S.A. Ghaffari, and M. Dadashi</i>	277
68 Turbulent cascade of quantum fluid at finite temperature	
<i>E. Lévêque, C.F. Barenghi, P. Diribarne, and P.-E. Roche</i>	281
69 Visualization of quantum turbulence in $^3\text{He-B}$ by thermal excitations	
<i>Y.A. Sergeev, C.F. Barenghi, and N. Suramlishvili</i>	285
70 The 3D structure of a dipole in a shallow two-layer fluid	
<i>R.A.D. Akkermans, L.P.J. Kamp, H.J.H. Clercx, and G.J.F. van Heijst</i>	289

71 The 3D character of decaying turbulence in a shallow fluid layer
A.R. Cieslik, L.P.J. Kamp, H.J.H. Clercx, and G.J.F. van Heijst 293

72 Vortex dynamics in a Karman street behind a heated cylinder: defects and potentialities of acoustic diagnostics
V.V. Chernov, P.L. Soustov, P.R. Gromov, A.B. Ezersky, and P. Paranthoen 297

73 Asymmetric vortex shedding in the turbulent wake of a flat plate in a rotating fluid
H.A. Khaledi, M. Barri, and H.I Andersson 301

74 Stability of steady vortices and new equilibrium flows from Imperfect-Velocity-Impulse diagrams
P. Luzzatto-Fegiz and C.H.K. Williamson 305

75 The effect of freestream turbulence on far axisymmetric wakes
E. Rind, and I.P. Castro 309

76 Application of the deterministic turbulence method to study of LEBU-device mechanism
V.I. Borodulin, Y.S. Kachanov, and A.P. Roschektayev 313

77 The role of the intense vorticity structures in the turbulent structure of the jet edge
R.J.N. Reis, C.B. da Silva, J.C.F. Pereira 317

78 Large scale dynamics of a jet in a counter flow
C. Duwig and J. Revstedt 321

79 Dynamics of vortex filaments in turbulent flows and their impact on particle dispersion
A. Scagliarini, L. Biferale, and F. Toschi 325

80 The effect of coherent structures on the secondary flow in a square duct
A. Sekimoto, A. Pinelli, M. Uhlmann, and G. Kawahara 329

Part V Multiphase and non-Newtonian flows

81 How to discriminate between light and heavy particles in turbulence
H.I. Andersson, P.H. Mortensen, J.J.J. Gillissen, L.H. Zhao, and B.J. Boersma 335

82 Anisotropic clustering and particles velocity statistics in shear turbulence
P. Gualtieri, F. Picano, G. Sardina, and C.M. Casciola 339

83 Direct numerical simulation of inertial particle accelerations in near-wall turbulence: effect of gravity
V. Lavezzo, S. Gerashchenko, Z. Warhaft, L. Collins and A. Soldati .. 343

84 Simulating fibre suspensions: Lagrangian versus statistical approach
L.H. Zhao, H.I. Andersson, J.J.J. Gillissen, and B.J. Boersma 347

85 Inertial particles in a turbulent pipe flow: spatial evolution
F. Picano, G. Sardina, and C.M. Casciola 351

86 Heat transfer mechanisms in bubbly Rayleigh-Benard convection
P. Oresta, R. Verzicco, D. Lohse and A. Prosperetti 355

87 Scaling of polymer drag reduction with polymer and flow parameters in turbulent channel flow
D. H. Lee and R. Akhavan 359

88 DNS study on diameter effect of drag reduction in viscoelastic-fluid flow
T. Ishigami, T. Tsukahara, and Y. Kawaguchi 363

89 Modifications of turbulent structure in a bubbly boundary layer
B. Jacob, M. Miozzi, A. Olivieri, E-F. Campana and R. Piva 367

90 Budgets of polymer free energy in homogeneous turbulence
E. de Angelis, C.M. Casciola, and R. Piva 371

91 Shear-induced self-diffusion in a Couette flow of a dilute suspension
E.S. Asmolov 375

Part VI Atmospheric turbulence

92 Turbulent flow over rough walls
I.P. Castro 381

93 Top-down and bottom-up eddy motion in wall bounded turbulence
P. Carlotti and F. Laddhari 389

94 A study of turbulent Poiseuille-Ekman flow at different rotation rates using DNS
A. Mehdizadeh, and M. Oberlack 393

95 Experimental study of forced stratified turbulence
P. Augier, P. Billant, E. Negretti, and J.-M. Chomaz 397

96 DNS of the turbulent cloud-top mixing layer
J.P. Mellado, H. Schmidt, B. Stevens, and N. Peters 401

97 Modelling and simulation of momentum and heat transfer in the atmospheric boundary layer over rough surface: study with improved turbulence model
A.F. Kurbatskiy and L.I. Kurbatskaya 405

98 Wind direction effects on urban like roughness: an LES Study
J.M. Claus, I.P. Castro, and Z.-T. Xie 409

Part VII Geophysical and astrophysical turbulence

99 Anisotropy in turbulent rotating convection
R.P.J. Kunnen, H.J.H. Clercx, and B.J. Geurts 415

100 Nonlocal interactions and condensation in forced rotating turbulence
L. Bourouiba, and D. Straub 419

101 Structural features of rotating sheared turbulence
F. Jacobitz, W.J.T. Bos, K. Schneider, and M. Farge 423

102 Structure functions and energy transfers in a decaying rotating turbulence experiment
F. Moisy, L. Agostini, and G. Tan 427

103 Table-top rotating turbulence: an experimental insight through particle tracking
L. Del Castello, H.J.H. Clercx, R.R. Trieling, A. Tsinober, 431

104 On the structure of rapidly-rotating, decaying turbulence
P.A. Davidson and P.J. Staplehurst 435

105 Large-eddy simulations of gravity current flows past submerged cylinders
E. Gonzalez-Juez, E. Meiburg, G. Constantinescu, and T. Tokyay 439

106 Large scale quasi-2D structures and the problem of nonlinear bottom friction
A.A. Khapaev, S.V. Kostrykin, and I.G. Yakushkin 443

107 Double-period oscillation of passive scalar flux in stratified turbulence
H. Hanazaki, T. Miyao, and T. Okamura 447

108 Energy spectra of stably stratified turbulence
Y. Kimura, and J.R. Herring 449

109 The wind-driven turbulent oscillating channel flow subjected to a stable stratification
W. Kramer, V. Armenio, and H.J.H. Clercx 453

110 Numerical studies of turbulence in breaking internal waves
S.N. Yakovenko, T.G. Thomas, and I.P. Castro 457

111 Vortex self-similarity and the evolution of unforced inviscid two-dimensional turbulence
D.G. Dritschel, R.K. Scott, C. Macaskill, G.A. Gottwald, and C.V. Tran 461

112 Large Eddy Simulation of compressible magnetohydrodynamic turbulence in the local interstellar medium
A.A. Chernyshov, K.V. Karelsky and A.S. Petrosyan 465

Part VIII Transport and mixing

113 Experimental studies of turbulent Rayleigh-Bénard convection
K.-Q. Xia 471

114 Various flow amplitudes in 2D non-Oberbeck-Boussinesq Rayleigh-Bénard convection in water
E. Calzavarini, S. Grossmann, D. Lohse, K. Sugiyama 479

115 A comparison of turbulent thermal convection between conditions of constant temperature and constant heat flux boundaries
H. Johnston and C.R. Doering 483

116 Diffusion of heavy particles in turbulent flows
A.S. Lanotte, J. Bec, L. Biferale, M. Cencini, A. Scagliarini, and F. Toschi 485

117 Quantification of heavy particle segregation in turbulent flows: a Lagrangian approach
E. Meneguz, M.W. Reeks, and A. Soldati 489

118 The dispersion of lines written in a turbulent jet flow
M. Mirzaei, N.J. Dam, J.J. ter Meulen, and W. van de Water 493

119 PDF modeling of vapour micromixing in turbulent evaporating sprays
G. Anand and P. Jenny 497

120 Forces on light particles in stratified turbulence
M. van Aartrijk, and H.J.H. Clercx 501

121 Renormalized transport of inertial particles
M. Martins Afonso, A. Celani, A. Mazzino, and P. Olla 505

122 Turbulence modification in the vicinity of a solid particle
A. Naso and A. Prosperetti 509

123 Particle transport in turbulent wakes behind spherical caps
N.G.W. Warncke, R. Delfos, and J. Westerweel 513

124 Turbulent heat transfer and large-scale flow in convection cells with aspect ratio $\Gamma > 1$
M.S. Emran, J. Bailon-Cuba, and J. Schumacher 517

125 Shot noise of thermal plumes : Evidence of a boundary layer instability consistent with the onset of Kraichnan’s regime of convection
F. Gauthier, and P.-E. Roche 521

126 Scalar mixing in turbulent confined flow
D. Kolomensky, B. Kadoch, W.J.T. Bos, K. Schneider, and P. Angot . 525

127 Prandtl-, Rayleigh-, and Rossby-number dependence of heat transport in turbulent rotating Rayleigh-Bénard convection
R.J.A.M. Stevens, J.-Q. Zhong, H.J.H. Clercx, R. Verzicco, D. Lohse and G. Ahlers 529

128 Oscillations of large-scale structures in turbulent mixed convection in a rectangular enclosure
A. Westhoff, D. Schmeling, J. Bosbach, and C. Wagner 533

129 Interaction between slope flows and an urban heat island
M. Giorgilli, M. Moroni, P. Monti, and A. Cenedese 537

130 Origin of the small-scale anisotropy of the passive scalar fluctuations
J. Kalda and A. Morozenko 541

131 Mixing asymmetry in variable density turbulence
D. Livescu and J.R. Ristorcelli 545

132 Turbulent transport close to a wall
G. Boffetta, F. de Lillo, and A. Mazzino 549

133 Persistence of inhomogeneity of the turbulence generated by the static grid structures
Ö. Ertunç, N. Özyilmaz, H. Lienhart, and F. Durst 553

134 On the energy decay of grid generated turbulence
P.-A. Krogstad and P.A. Davidson 557

135 Turbulent entrainment in jets: the role of the kinetic energy
R.M.R. Taveira, C.B. da Silva, and J.C.F. Pereira 561

136 Fast and slow changes of the length of gradient trajectories in homogeneous shear turbulence
P. Schäfer, M. Gampert, L. Wang and N. Peters 565

Part IX Wall bounded flows

137 Coherent streaky structures and optimal perturbations of turbulent boundary layers
C. Cossu, G. Pujals, and S. Depardon 573

138 Time-mean description of turbulent bluff-body separation in the high-Reynolds-number limit
B. Scheichl, A. Klumick, and F.T. Smith 577

139 Isotropic free-stream turbulence promotes anisotropy in a turbulent boundary layer
S. Torres-Nieves, B. Brzek, J. Lebrón, R.B. Cal, H.S. Kang, C. Meneveau, and L. Castillo 581

140 Travelling waves in a straight square duct
M. Uhlmann, G. Kawahara, and A. Pinelli 585

141 Thermal boundary layers in turbulent Rayleigh-Bénard convection
R. du Puits, C. Resagk, and A. Thess 589

142 DNS of turbulent transport of scalar concentration in various thermally stratified boundary layers
H. Hattori, S. Yamazaki and Y. Nagano 593

143 Wall turbulence without walls
Y. Mizuno, and J. Jiménez 597

144 Turbulent flow and heat transfer in eccentric annulus
N.V. Nikitin, S.I. Chernyshenko, and H.L. Wang 601

145 On imperfect hot-wire resolution issues and their effect on mean quantities
R. Örlü, J.H.M. Fransson, and P.H. Alfredsson 605

146 The diagnostic plot - a new way to appraise turbulent boundary layer data
P.H. Alfredsson, R. Örlü, T. Kurian, J.H.M. Fransson, A. Segalini, J.-D. Ruedi, and A. Talamelli 609

147 DHMPIV and Tomo-PIV measurements of three-dimensional structures in a turbulent boundary layer
O. Amili, C. Atkinson, and J. Soria 613

148 LDA measurements of Reynolds stresses in a swirling turbulent pipe flow
B.Z. Genç, Ö Ertunç, J. Jovanović, and A. Delgado 617

149 Time-resolved stereoscopic PIV of the log-layer in fully developed turbulent pipe flow
S. Große, D.J. Kuik, and J. Westerweel 621

150 Massive separation in rotating turbulent flows
M. Barri, G.K. El Khoury, H.I. Andersson and B. Pettersen 625

151 Scaling of torque in turbulent Taylor-Couette flow with background rotation
R. Delfos, F. Ravelet, and J. Westerweel 629

152 Velocity gradient statistics in a turbulent channel flow
D. Krasnov, T. Boeck, and J. Schumacher 633

153 Channel flow LES with stochastic modeling of the sub-grid acceleration
R. Zamansky, I. Vinkovic, and M. Gorokhovski 637

154 DNS of three-dimensional separation in turbulent diffuser flows	
<i>J. Ohlsson, P. Schlatter, P.F. Fischer, and D.S. Henningson</i>	641
155 Optimal amplification of large-scale streaks structures in the turbulent Couette flow	
<i>Y. Hwang, and C. Cossu</i>	645
156 Symmetry of coherent vortices in plane Couette flow	
<i>T. Itano, S.C. Generalis, S. Toh, and J.P. Fletcher</i>	649
157 Universal character of perturbation growth in near-wall turbulence	
<i>N. Nikitin</i>	653
158 Experimental assessment of turbulent drag reduction by wall traveling waves	
<i>M. Quadrio, F. Auteri, A. Baron, M. Belan, and A. Bertolucci</i>	657
159 Effects of very-large roughness in turbulent channel flow	
<i>D.M. Birch, and J.F. Morrison</i>	661
160 Roughness effects in a rotating turbulent channel	
<i>V.D. Narasimhamurthy and H.I. Andersson</i>	665
161 Mean flow and turbulence over rough surfaces	
<i>M. Amir and I.P. Castro</i>	669
<hr/>	
Part X Intermittency and scaling	
<hr/>	
162 DNS of vibrating grid turbulence	
<i>G. Khujadze and M. Oberlack</i>	675
163 Step onset from an initial uniform distribution of turbulent kinetic energy	
<i>D. Tordella and M. Iovieno</i>	677
164 Fractal-generated turbulent scaling laws from a new scaling group of the multi-point correlation equation	
<i>M. Oberlack and G. Khujadze</i>	681
165 Casimir Cascades in two-dimensional turbulence	
<i>J.C. Bowman</i>	685
166 The development of truncated inviscid turbulence and the FPU-problem	
<i>G. Ooms, and B.J. Boersma</i>	689

167 The renormalized eddy-fragmentation equation and its exact solutions
V.L. Saveliev and M. Gorokhovski 693

168 Determination of the statistics of the velocity gradient tensor as a function of scale: solution of the tetrad model
A. Naso and A. Pumir 697

169 TSF Experiment for comparison of high Reynold’s number turbulence in HeI and He II: first results
P. Diribarne, J. Salort, C. Baudet, B. Belier, B. Castaing, L. Chevillard, F. Daviaud, S. David, B. Dubrulle, Y. Gagne, A. Girard, B. Rousset, P. Tabeling, P. Thibault, H. Willaime, and P.-E. Roche ... 701

170 Extraction of the non-equilibrium energy spectrum in high Reynolds number turbulence
K. Horiuti, Y. Tsuji, and K. Saitou 705

171 Universality of Kolmogorov law in spectrally condensed turbulence in thin layers
H. Xia, M.G. Shats, and H. Punzmann 709

172 Multi-scale correlations in regular and fractal-generated turbulence
R. Stresing, J. Peinke, R.E. Seoud, and J.C. Vassilicos 711

173 On an alternative explanation of anomalous scaling and how inertial is the inertial range
M. Kholmyansky, and A. Tsinober 715

174 Phenomenological relation between the Kolmogorov constant and the skewness in turbulence
L. Chevillard, B. Castaing, E. L ev eque and A. Arneodo 719

175 Kolmogorov scaling and intermittency in Rayleigh-Taylor turbulence
G. Boffetta, S. Musacchio, A. Mazzino, and L. Vozella 721

176 Observation of weak turbulence spectra of capillary waves
H. Punzmann, M.G. Shats, and H. Xia 725

177 A new numerical methodology to follow the time-decay of turbulence
G. Sardina, P. Gualtieri, and C.M. Casciola 729

178 Velocity kinematic relations in decaying turbulent flow past a grid	
<i>R. Gurka, G. Kopp, A. Liberzon, P. Sarathi, and A. Tsinober</i>	733
179 Lagrangian intermittency and time-correlations in two-dimensional turbulence	
<i>K. Schneider, S. Neffaa, B. Kadoch, and W.J.T. Bos</i>	737
<hr/>	
Part XI Large eddy simulation	
<hr/>	
180 Implicit Large-Eddy Simulation: Theory and Application	
<i>N.A. Adams and S. Hickel</i>	743
181 A challenging new problem for LES: the flow near the turbulent/nonturbulent interface	
<i>C.B. da Silva</i>	751
182 Towards practical large-eddy simulation of complex turbulent flows	
<i>J. Boudet, A. Cahuzac, P. Borgnat, E. L��v��que and F. Toschi</i>	755
183 Coherent vortex simulation: application to 3D homogeneous isotropic turbulence	
<i>N. Okamoto, K. Yoshimatsu, K. Schneider, M. Farge and Y. Kaneda</i>	759
184 LES of a non-premixed flame with an assumed tophat FDF	
<i>A. Kempf and A. Kronenburg</i>	763
185 Closure models for inhomogeneous turbulence	
<i>R. Rubinstein, W.J.T. Bos, D. Livescu, and S.L. Woodruff</i>	767
186 Statistical Mechanics of Fluid Turbulence based on the Cross-Independence Closure Hypothesis	
<i>T. Tatsumi</i>	771
187 Large-Eddy Simulation of two-phase plane mixing layer	
<i>M. Dianat, Z Yang, and J J McGuirk</i>	775
188 Subgrid particle resolution for the turbulent transport of a passive scalar	
<i>G.-H. Cottet, G. Balarac, and M.Coquerelle</i>	779
189 An adaptive local deconvolution method for general curvilinear coordinate systems	
<i>S. Hickel, D. von Terzi, and J. Fr��hlich</i>	783

190 On under-resolved simulation of atmospheric convection
Z. Piotrowski, P.K. Smolarkiewicz, S.P. Malinowski,
and A.A. Wyszogrodzki 787

191 The multispectral method: progress and prospects
M. Roberts, J.C. Bowman, and B. Eckhardt 791

**192 Discretization errors and subgrid scale implementations
in Large Eddy Simulations**
A. Viré and B. Knaepen 795

Part XII Magnetohydrodynamical turbulence

**193 Reversals of the magnetic field generated by a turbulent
flow**
S. Fauve, E. Dormy, C. Grissinger and F. Pétrélis 801

**194 Direct measurement of turbulent magnetic diffusivity in
liquid metal flow**
P. Frick, S. Denisov, V. Noskov, and R. Stepanov 809

195 Shell models for MHD turbulence
T. Lessinnes, D. Carati, M.K. Verma, and F. Plunian 813

196 Turbulence induced by magnetic fields
K. Bajer and K.A. Mizerski 817

197 Spin-up in MHD turbulence
S. Neffaa, W.J.T. Bos, and K. Schneider 821

**198 Influence of helicities on statistical properties of MHD
turbulence**
P. Frick, I. Mizewa, and R. Stepanov 825

199 Transient growth in MHD duct flow
T. Boeck, D. Krasnov, M. Rossi, and O. Zikanov 829

**200 Optical visualisation of the flow around a cylinder in
electrolyte under strong axial magnetic field**
O. Andreev, A. Kobzev, Yu. Kolesnikov, and A. Thess 833

**201 Synthetic turbulence model and DNS for
magnetohydrodynamics with rotation**
B. Favier, F.S. Godeferd, and C. Cambon 837

202 Spectral analysis of energy transfers in anisotropic MHD turbulence	
<i>B. Teaca, D. Carati, B. Knaepen, and M.K. Verma</i>	841

Part XIII Acoustics of turbulence flows

203 Boundary layer influence on cavity noise generation	
<i>V. Koschitzky, R. Delfos, B.J. Boersma, and J. Westerweel</i>	847
204 Instability waves as a source of subsonic jet noise	
<i>V. Sponitsky, and N.D. Sandham</i>	851
205 Experimental study of sound production for constricted channels: application to simplified vocal tract geometries	
<i>O. Estienne, A. van Hirtum, H. Bailliet, and X. Pelorson</i>	855
206 Turbulent pressure statistics in an underwater boundary-layer experiment	
<i>J. Abshagen</i>	859
207 Spectral reconstruction of sound radiated by an organ pipe	
<i>M. Abel and K. Ahnert</i>	863
208 Aerodynamic sound generation by turbulence in shear flows	
<i>G. Khujadze, G. Chagelishvili, M. Oberlack, A. Tevzadze, and G. Bodo</i>	867

Part XIV Reacting and compressible turbulence

209 On implicit turbulence modeling for LES of compressible flows	
<i>S. Hickel, and J. Larsson</i>	873
210 Injection of a plane reacting jet into a supersonic turbulent channel flow	
<i>C. Schaupp and R. Friedrich</i>	877
211 Turbulent premixed flame fronts: fractal scaling and implications for LES modeling	
<i>G. Troiani, F. Picano, and C.M. Casciola</i>	881
212 Large eddy simulation of a lean premixed swirl flame in complex geometry - comparison of two turbulent combustion models	
<i>P. Wang, J. Fröhlich and U. Maas</i>	885

Part XV Posters

213 KS inertial range and validity of Richardson’s law
F. C. G. A. Nicolleau 891

214 Lagrangian vortex methods in turbulent channel flows
R. Yokota, K. Fukagata, and S. Obi 893

215 Unstable and turbulent flows simulated by means of the Boltzmann kinetic equation
V.V. Aristov, A.A. Frolova, O.I. Rovenskaya, and S.A. Zabelok 895

216 Natural transition in plane Poiseuille flow
H.G. Silva, R.A.C. Germanos, and M.A.F. Medeiros 897

217 Stabilization of the turbulent flows in anisotropic viscoelastic tubes
N. Kizilova and M. Hamadiche 899

218 Simulation of induced transition in hypersonic regime: Validation of foot print of the vortical structures
F. Pinna, S. Tirtay, O. Chazot, and P. Rambaud 901

219 Active grid generated turbulence
P. Knebel, and J. Peinke 903

220 Velocity characterisation of axisymmetric jets from human-sized channels
X. Grandchamp, A. Van Hirtum, X. Pelorson 905

221 The role of nonlocality in unsteady turbulence
W.J.T. Bos, and R. Rubinstein 907

222 Coherent enstrophy production and dissipation in 2D turbulence with and without walls
R. Nguyen van yen, M. Farge, and K. Schneider 909

223 Space-scale analysis of enstrophy transfers in two-dimensional turbulence
P. Fischer and Ch. H. Bruneau 911

224 Hydrodynamic stability of a stratified suspension flow in a plane channel
S.A. Boronin 913

225 Localization of compact invariant sets of the Lorenz’ 1984 model
K.E. Starkov 915

226 Large-scale energy dissipation and equatorial superrotation in shallow water turbulence <i>R.K. Scott</i>	917
227 The effects of rain on wind-driven turbulent flow <i>N. Takagaki, I. Iwano, S. Komori</i>	919
228 New results on grid-generated turbulence <i>Thomas Kurian and J.H.M. Fransson</i>	921
229 Gas-liquid interaction under vibration field effect <i>V. Kholmer and L. Grinis</i>	923
230 An Invariant Nonlinear Eddy Viscosity Model based on a 4D Modelling Approach <i>M. Frewer</i>	925
231 Projection of the turbulence closure problem on the invariant triangle as the basis for improved predictions of complex flows <i>J. Jovanović, B. Frohnäpfel, and M. Breuer</i>	927
232 A computational study of the hydrodynamic forces on a rough wall <i>C. Braun, M. García-Villalba, and M. Uhlmann</i>	929
233 Turbulent flow structure investigation within target fluidic flowmeter <i>F.H. Hannemann, A.F. Nowakowski, F.C.G.A. Nicolleau, and H. Zheng</i>	931
234 The wake of a single 2D roughness element immersed in a turbulent boundary layer <i>B.T. Tee, L.K.B. Li, and T.B. Nickels</i>	933
235 High spanwise wall-shear stress events in turbulent duct flow <i>S. Große, and W. Schröder</i>	935
236 A POD-based reconstruction method for the flow in the near-wall region <i>B. Podvin, Y. Fraigneau, J. Jouanguy, and J.P. Laval</i>	937
237 Near-wall velocity and wall shear stress correlations in a separating boundary layer <i>P. Nathan and P.E. Hancock</i>	939

238 Lifetimes of flow topology in a turbulent boundary layer
G.E. Elsinga and I. Marusic 941

239 RDT or low wavenumber modes' dynamics ?
S.R. Bogdanov 943

240 Intermittency in high resolution direct numerical simulation of turbulence in a periodic box: a wavelet viewpoint
K. Yoshimatsu, N. Okamoto, K. Schneider, Y. Kaneda, and M. Farge . 945

241 Detached eddy simulation of turbulence flows in a pipe with fractal shape orifices
H.W. Zheng, F.C.G.A. Nicolleau, and N. Qin 947

242 Recovery of subgrid-scale turbulence kinetic energy in LES of channel flow
Y. Tang, and R. Akhavan 949

243 Beyond Reynolds stress analysis of quasilaminar flows
J. Araya, R.B. Cal, C. Meneveau and L. Castillo 951

244 Anisotropic organised eddy simulation for statistical and hybrid modelling of turbulent flows around bodies
R. Bourguet, M. Braza, R. El Akoury and G. Harran 953

245 Experimental vortex generation and instabilities at flow around a magnetic obstacle
Yu. Kolesnikov and A. Thess 955

246 A dynamic multiscale subgrid model for MHD turbulence based on Kolmogorov's equation
L. Fang, W.J.T. Bos, L. Shao, and J.P. Bertoglio 957

247 Low-Prandtl number MHD cooling in a vertical cylindrical container
I.E. Sarris, A.I. Iatridis, C. Dritselis, and N. Vlachos 959

248 Anomalous scaling of passively advected magnetic field in the kinematic MHD Kazantsev-Kraichnan model
E. Jurčišínova, M. Jurčišín, and R. Remecky 961

249 A new compressible turbulence model for free and wall-bounded shear layers
J.Y. Kim and S.O. Park 963

250 Modelling of turbulent flow in a gas burner
K. Kwiatkowski and K. Bajer 965

Contributors **967**

Part I Lagrangian aspects

Lagrangian modeling and properties of particles with inertia

F. Toschi¹, L. Biferale², E. Calzavarini³, E. Lévêque³, A. Scagliarini²

¹ Department of Physics and Department of Mathematics and Computer Science, Eindhoven University of Technology P.O. Box 513, 5600 MB Eindhoven, The Netherlands

² Dept. Physics and INFN, University of Rome, Tor Vergata, Via della Ricerca Scientifica 1, 00133 Rome, Italy

³ Laboratoire de Physique, École Normale Supérieure de Lyon, CNRS UMR5672, 46 Allée d'Italie, 69007 Lyon, France.

`federico.toschi at tue.nl`

Summary. Recently many efforts has been devoted to the experimental investigations of the Lagrangian properties of particles in turbulence. Different experimental techniques allow to investigate particles with different physical properties, e.g. values of size and density, within some specific range. No experimental studies have been able to cover large range of parameters space. We have recently performed a set of Direct Numerical Simulation (DNS) with the precise goal to cover systematically particle's from heavy ones to very light ones. We also performed numerical simulations of particles with the same physical properties at different Reynolds numbers and with different physical modeling. We discuss briefly the limitations of the point particle model and suggest a simple but effective way to extend it.

The transport of particulate by means of turbulent flows is an ubiquitous phenomenon in nature and in industrial applications alike. Turbulent flows are characterised by strong fluctuations both in space and in time of the energy dissipation field, a phenomenon know as intermittency [1].

Here we present results from recent Direct Numerical Simulation (DNS) devoted at investigating the statistical properties of particles in homogeneous and isotropic turbulence. The incompressible fluid velocity \mathbf{u} are evolved according to the Navier-Stokes equations:

$$\frac{D\mathbf{u}}{Dt} \equiv \frac{\partial\mathbf{u}}{\partial t} + \mathbf{u} \cdot \nabla\mathbf{u} = -\nabla p + \nu\Delta\mathbf{u} + \mathbf{f}. \quad (1)$$

where p is the pressure and \mathbf{f} an external forcing injecting energy at a rate $\epsilon = \langle \mathbf{u} \cdot \mathbf{f} \rangle$. Equation (1) is integrated numerically by means of a pseudo-spectral code with a second order Adams-Bashforth scheme. The same scheme was also used for the particles evolving according to the dynamic given by

equation (2), where we used tri-linear interpolation to obtain the Eulerian values of the velocity field at the particle's positions (see [2, 3] for details). The forcing applied to the system was chosen to maintain constant the spectral energy content of the first two shells in Fourier space.

The main aim of this set of numerical investigations was to systematically explore the properties of particles at changing the inertia properties. To this end we decided to compromise space (Eulerian) resolution in favour of a larger number of particles classes.

Along with the Eulerian field, the Lagrangian evolution of particles was integrated by means of one of the simplest, yet nontrivial, model for passively advected particles as derived in Refs. [4, 15] which is valid for dilute suspensions of small spherical particles:

$$\frac{d\mathbf{x}}{dt} = \mathbf{v}, \quad \frac{d\mathbf{v}}{dt} = \beta \frac{D\mathbf{u}}{Dt} + \frac{1}{\tau_p}(\mathbf{u} - \mathbf{v}), \quad (2)$$

In the above equations $\mathbf{x}(t)$ and $\mathbf{v}(t)$ denote the particle position and velocity, respectively. The parameters in equation (2) are the particle's response time $\tau_p = a^2/3\beta\nu$ (where a is the particle radius and ν is the viscosity) and β which is related to the density contrast between the density of the particle, ρ_p , and the one of the fluid, ρ_f : $\beta = 3\rho_f/(\rho_f + 2\rho_p)$. The dimensionless ratio between the response time of particles and the smallest time scale in turbulence (dissipative time scale) is the Stokes number $St = \tau_p/\tau_\eta$.

The physical parameters St and β characterize the particle's properties and it has to be noted that they implicitly carry a dependence from the particle's radius. In the case of particles much smaller than the dissipative scale of turbulence one can treat them as pointwise. The Eulerian flow is characterized by the Reynolds number Re . The ratio between the particle diameter D and the dissipative scale of the Eulerian flow may or may not be small, according to the particular value of the parameter β , St and Re . In the case that the ratio D/η is order unity or larger, the physical description in terms of pointwise particles clearly cannot be correct. It is however very difficult to estimate quantitatively the error committed by using the point particle (PP) description as a function of the position in the parameter space. To quantify the importance of the full description of the particle size, we performed recently some numerical simulations where the finite particle size was implemented by means of a coarse graining of the Eulerian velocity field.

We performed four numerical simulations, at resolutions 128^3 and 512^3 (corresponding to $Re_\lambda \simeq 75$ and $Re_\lambda \simeq 180$) with point particle model (PP) [6] and with Faxén corrections (FC, see Section 2). The different classes of particles in the β, St parameter space that we studied are reported pictorially in Figure 1. We proceed now to briefly discuss the changes in the phenomenology when one moves from the heavy pointwise particle model, to inertial particles with generic densities and then to particles with finite size.

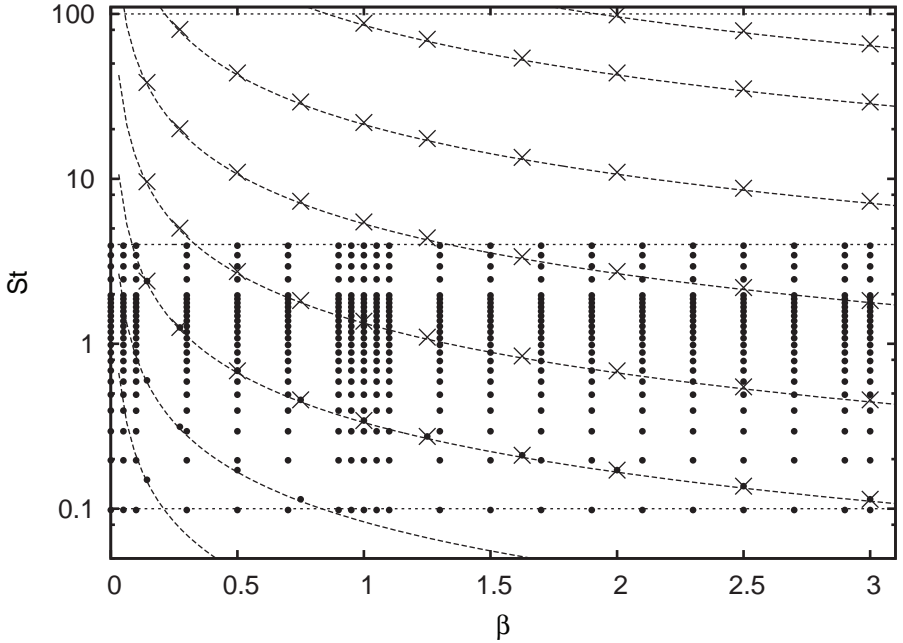


Fig. 1. Different class of particles studied in the parameter space, (β, St) . Black dots corresponds to the particles classes integrated at a resolution 128^3 with $Re_\lambda = 75$ and Point Particle model (PP). Crosses corresponds to 128^3 ($Re_\lambda = 75$) and 512^3 ($Re_\lambda = 180$) for the Faxén corrected (FC) model, see Section 2.

1 Lagrangian structure functions

Recently temporal correlations of Lagrangian velocities have been studied by means of Lagrangian Velocity Structure Functions (LVSF) of the particle velocities, $S^{(p)}(\tau)$:

$$S^{(p)}(\tau) = \langle |v(t + \tau) - v(t)|^p \rangle \quad (3)$$

where v denotes one particular component of the particle velocity.

From the structure functions one can readily define what has been dubbed as local slopes, or local scaling exponents:

$$\zeta(p, \tau) = \frac{d \log S^{(p)}(\tau)}{d \log S^{(2)}(\tau)}$$

probably the most sensitive tool to study the presence of eventual homogeneous scaling in the inertial range and to quantify associated uncertainties. It was shown that the local slopes of the LVSF do present a strong dip at scales intermediate between the dissipative scales and the inertial range [8, 9]. The dip is present in all currently available datasets (both experimental and

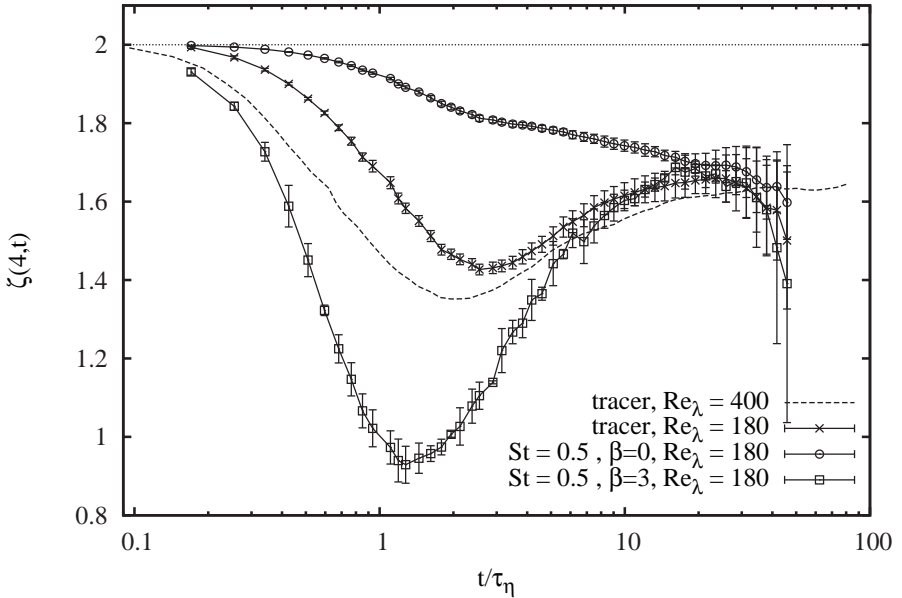


Fig. 2. Relative local slopes of $\zeta(4, \tau)$ vs. $\zeta(2, \tau)$ of LVSF for: tracers at $Re_\lambda = 400$ (solid line); tracers at $Re_\lambda = 200$ (red squared); heavy particles with ($St = 0.5$, $\beta = 0$) (green circles) and light particles with ($St = 0.5$, $\beta = 3$) (blue triangles). Notice the small enhancement on the dip for tracers at increasing Reynolds and the big enhancement/depletion for light/heavy particles respectively. Both trends confirm the importance of velocity statistics associated to small scale vortical filamentary structures in the dip region.

numerical ones) [10]. It has also been shown that the dip can be explained in terms of a multifractal modeling [10] of Lagrangian velocity increments and that it is suppressed either by filtering the velocity signal or by observing heavy particles instead of passive tracers [11]. This last observation leads to the conclusion that the dip is mainly sensitive to the statistics of small scale vortex filaments.

Here we show for the first time the behaviour of the local slopes for tracers, heavy and light particles evolving in the same turbulent flow. As it can be seen from Figure 2 the dip in the case of light particles is even more strongly pronounced. It is well known that light particles tends to accumulate in small scale vortex filaments [12], this is another strong evidence of the fact that the dip is strongly sensitive to the statistical fluctuations of the velocity field around small scales vortex filaments. In Figure 2 one may also notice a small enhancement of intermittency (i.e. on the dip excursion) at

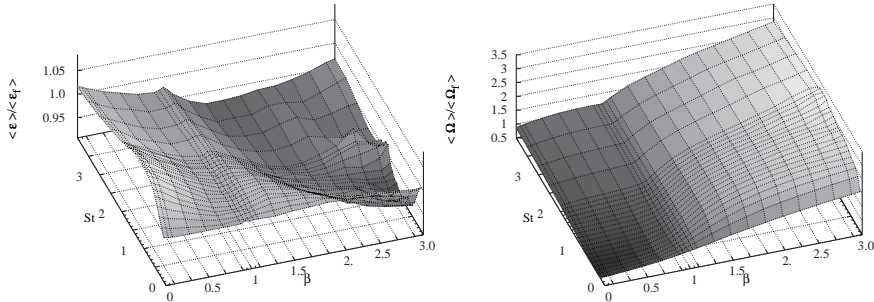


Fig. 3. The average energy dissipation of the fluid (left) and mean enstrophy (right) at the position of the particles normalized by the averaged values for fluid tracers, as a function of different particles properties (β , St).

increasing Reynolds for the tracers statistics, indicating a possible non trivial dependency of the vortex filament statistics on Reynolds number.

Another statistical quantity useful to quantitatively measure the preferential concentration for light particles in high vorticity regions is visible in Figure 3, where it is shown the energy dissipation field, $\varepsilon = \sum_{i,j} (\partial_i u_j + \partial_j u_i)^2$, and the enstrophy (squared vorticity) magnitude, $\Omega = \sum_{i,j} (\partial_i u_j - \partial_j u_i)^2$, calculated at the particle positions for all β and St . As one can see, light particles have a pretty larger total vorticity when normalized with the corresponding value measured on the tracers (up to a factor 3).

2 Finite particle size

The point particle model is computationally efficient, theoretically simple and often an excellent approximation of physical reality. On the other hand, is to be expected that larger particles can behave in a considerable different way from material points and that to describe them the PP model cannot be employed.

In [13] it is described how to model finite size particles by adding to the equation for the particles motion the Faxén terms which account for the non-uniformity of the flow at the particle-scale. Faxén forces represent corrections for particles in turbulence with dimension $D > \eta$. We chose to model finite size particles in this way, in order to maintain a good computational efficiency. Indeed the finite size correction only implies some extra Fourier Transform and, once implemented, many particles can be integrated with essentially no additional computational costs. Adding an extra class of particle (diameter) do instead imply an additional computational cost. The Faxén theorem for the drag force on a moving sphere states that:

$$\mathbf{f}_D = 6\pi\nu\rho_f a \left(\frac{1}{4\pi a^2} \int_{S_a} \mathbf{u}(\mathbf{x}) dS - \mathbf{v} \right) = 6\pi\nu\rho_f a (\langle \mathbf{u} \rangle_{S_a} - \mathbf{v}), \quad (4)$$

with the integral evaluated over the surface of the sphere and where $\mathbf{u}(\mathbf{x})$ is the non homogeneous velocity of the fluid in the absence of the sphere. As shown in [15] also Faxén forces via sphere volume average must be included. The expression for the fluid acceleration and added mass force is:

$$\mathbf{f}_A = \frac{4}{3}\pi a^3 \rho_f \left(\left\langle \frac{D\mathbf{u}}{Dt} \right\rangle_{V_a} + \frac{1}{2} \left(\left\langle \frac{d\mathbf{u}}{dt} \right\rangle_{V_a} - \frac{d\mathbf{v}}{dt} \right) \right) \quad (5)$$

where the above $\langle \dots \rangle_{V_a}$ denotes the volume average over the spherical particle. Putting together the two contributions, given by Equations (4) and (5), to the total force one obtain the equation of motion for a sphere, $(4/3)\pi a^3 \rho_p d\mathbf{v}/dt = \mathbf{f}_D + \mathbf{f}_A$, and keeping into account the Auton added mass correction for finite particle Reynolds numbers, i.e., $d\mathbf{u}/dt \rightarrow D\mathbf{u}/Dt$ [7], one obtain the phenomenological Faxén-corrected equation of motion:

$$\frac{d\mathbf{v}}{dt} = \frac{3 \rho_f}{\rho_f + 2 \rho_p} \left(\left\langle \frac{D\mathbf{u}}{Dt} \right\rangle_{V_a} + \frac{3\nu}{a^2} (\langle \mathbf{u} \rangle_{S_a} - \mathbf{v}) \right). \quad (6)$$

The above equation can be considered a generalization of Equation (2) and reduces to that equation in the limit $D/\eta \rightarrow 0$.

In [13] some first results obtained by numerical integration of Equation (6) are presented, along with preliminary comparison to experimental data. Here we show the behaviour of the Kaplan-Yorke dimension for the FC model. The Kaplan-Yorke dimension for the PP model was already discussed in [5, 16]. We recall that the phase space for the particle dynamics is (\mathbf{x}, \mathbf{v}) thus we have 6 Lyapunov exponents. Due to the dissipative and chaotic nature of the dynamics, the phase-space distribution of particles evolves toward a dynamical (multi)fractal set. Fractal dimension of particle distribution can be measured by means of Kaplan-Yorke dimension [17] as $d_\lambda = j + \sum_{i=1}^j \lambda_i / |\lambda_{j+1}|$ where j is the largest integer such that $\sum_{i=1}^j \lambda_i > 0$.

In Figure 4 it is shown the Kaplan-Yorke dimension as a function of β and St for the PP model (left panel) and the difference of D_{KY} for the FC and PP model (right panel). The present measurement is an useful quantitative indicator of where the finiteness of the particle play a larger role in the phase space dynamics. In [14] other quantitative results regarding the acceleration variance are presented and discussed.

3 Conclusions

In conclusion, we have shown that light/heavy point particles and light/heavy finite-size particles show highly non trivial statistics which is strongly affected by preferential concentration. In particular, we stress the importance for light

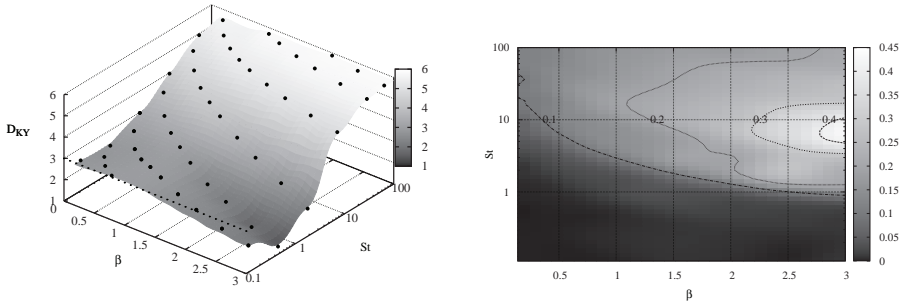


Fig. 4. The Kaplan-Yorke dimension D_{KY} vs. (β, St) for the PP model (left). The difference between the Kaplan-Yorke dimension as measured from the FC and the PP models, $D_{KY}^{FC} - D_{KY}^{PP}$ (right). The phase space dynamics measured by KY dimension is not highly sensitive to the finiteness of the particle size.

particles to be concentrated inside vortex filaments, with strong consequent enhancement of the velocity intermittency along particle' trajectories. Such phenomenon may be of key importance for a proper stochastic modeling of light particle dispersion in turbulent fields. Experimental investigations of the Lagrangian properties of light particles would be of great value.

Acknowledgments We wish to acknowledge M. Bourgoïn, M. Cencini, A. Lanotte, J.-F. Pinton and R.Volk, for their contributions in former studies on numerical and experimental investigation of inertial particles.

References

1. Frisch, U. *Turbulence: the legacy of A.N. Kolmogorov* (Cambridge University Press, Cambridge UK, 1995).
2. Mazzitelli, I.M., Lohse, D. and Toschi, F. "The effect of microbubbles on developed turbulence", *Phys Fluids* **15**, L5-L8 (2003).
3. Biferale, L., Boffetta, G., Celani, A., Devenish, B.J., Lanotte, A. and Toschi F., "Multifractal statistics of Lagrangian velocity and acceleration in turbulence", *Phys Rev Lett* **93** 064502 (2004).
4. Maxey, M.R. and Riley, J.J., "Equation of motion for a small rigid sphere in a nonuniform flow", *Phys. Fluids* **26** 883-889 (1983).
5. Calzavarini, E., Kerscher, M., Lohse, D. & Toschi, F., "Minkowski functionals: Characterizing particle and bubble clusters in turbulent flow", *J. Fluid Mech.* **607**, 13-24 (2008).
6. Calzavarini, E., Cencini, M., Lohse, D. & Toschi, F., "Quantifying turbulence-induced segregation of inertial particles" *Phys. Rev. Lett.* **101**, 084504 (2008).
7. Auton, T., Hunt, J. & Prud'homme, M. "The force exerted on a body in inviscid unsteady non-uniform rotational flow", *J. Fluid Mech.* **197**, 241-257 (1988).
8. Biferale, L., Boffetta, G., Celani, A., Lanotte, A., Toschi, F., "Particle trapping in three-dimensional fully developed turbulence" *Phys. Fluids* **17**, 021701 (2005).

9. Biferale, L. , Bodenschatz, E., Cencini, M., Lanotte, A., Ouellette, N., Toschi, F. and Xu, H., “Lagrangian structure functions in turbulence: A quantitative comparison between experiment and direct numerical simulation”, *Phys. Fluids* **20**, 065103 (2008).
10. Arneodo, A., Benzi, R. Berg, J., Biferale, L., Bodenschatz, E., Busse, A., Calzavarini, E., Castaing, B., Cencini, M. Chevillard, L., Fisher, R.T., Grauer, R. Homann, H., Lamb, D., Lanotte, A.S., Leveque, E., Luethi, B., Mann, J., Mordant, N., Mueller, W.-C., Ott, S., Ouellette, N.T., Pinton, J.-F., Pope, S.B., Roux, S.G., Toschi, F., Xu, H.,Yeung, P.K., “Universal intermittent properties of particle trajectories in highly turbulent flows”, *Phys. Rev. Lett* **100**, 254504 (2008).
11. Bec, J., Biferale, L., Cencini, M., Lanotte, A.S., Toschi, F., “Effects of vortex filaments on the velocity of tracers and heavy particles in turbulence” *Phys. Fluids* **18**, 081702 (2006).
12. Douady, S., Couder, Y., Brachet, M.E., “Direct observation of the intermittency of intense vorticity filaments in turbulence” *Phys. Rev. Lett.* **67** 983-986 (1991).
13. Calzavarini, E., Volk, R., Bourgoïn, M., L ev eque, E., Pinton, J.-F., Toschi, F., “Acceleration statistics of finite-sized particles in turbulent flow: the role of Fax en corrections”, **JFM in press**.
14. Calzavarini, E., Volk, R., Bourgoïn, M., L ev eque, E., Pinton, J.-F. and Toschi, F., “Effect of Fax en forces on acceleration statistics of material particles in turbulent flow”, proceeding of ETC12 in this same volume.
15. Gatignol, R. “The fax en formulae for a rigid particle in an unsteady non-uniform stokes flow” *J. Mecanique Theorique et Appliqu e* **1**, 143–160 (1983).
16. Toschi F. and Bodenschatz E. “Lagrangian properties of particles in Turbulence” **Ann. Rev. Fluid Mech.** **41** 375-404 (2009).
17. Kaplan, J. L. and Yorke, J. A.in Chaotic Behavior of Multidimensional Difference Equations, Lecture Notes in Mathematics, eds. Peitgen, H.-O. and Walther, H.-O. (Springer, Berlin), **730**, 204227 (1979).

Effect of Faxén forces on acceleration statistics of material particles in turbulent flow

E. Calzavarini^{1,*}, R. Volk¹, M. Bourgoïn², E. Lévêque¹, J.-F. Pinton¹ and F. Toschi³

¹Laboratoire de Physique, École Normale Supérieure de Lyon, Lyon (F).

²Laboratoire des Écoulements Géophysiques et Industriels, Grenoble (F).

³Eindhoven University of Technology, Eindhoven (NL).

* enrico.calzavarini@ens-lyon.fr

The statistical description of particle dispersion in turbulent flow constitutes nowadays an active research area. Such a field is linked to the Lagrangian description of fluid turbulence and poses long standing questions on modeling of hydrodynamical forces on objects in unsteady nonuniform flows [1]. Even in the simplest conditions of highly diluted suspensions of particles whose sizes are smaller than the dissipative scale of the carrier flow, the presently available models are highly idealized. Therefore, theoretical results and predictions need systematic verifications with experimental measures. Particle tracking experiments are technically challenging for the high time and space resolution demanded and for the need to precisely estimate and control the intensity of turbulent flow. Our recent works have been devoted to comparisons between experiments and numerical simulations of simple dynamical particle models [2, 3]. We have widely investigated Lagrangian particle models evolving in a turbulent environment which is described from an Eulerian point of view. In this abstract we shortly review the methods employed: the models for particle dynamics together with the numerical methodology, and we detail on some recent progresses and results.

Lagrangian models for particle dynamics

Lagrangian models for particle dynamics build-up on the equation of motion for a parcel of fluid (fluid tracer) in a flow. The trajectory of such an ideal particle can be described by the equation $d\mathbf{x}/dt = \mathbf{u}(\mathbf{x}(t), t)$, where $\mathbf{x}(t)$ denotes tracer's position at time t and \mathbf{u} the velocity of the fluid at that location. When a spherical massive particle (with diameter d much smaller than the dissipative scale η) is considered, the so called point-particle (PP) model can be employed:

$$\frac{d\mathbf{x}}{dt} = \mathbf{v}; \quad \frac{d\mathbf{v}}{dt} = \frac{3}{\rho_f + 2\rho_p} \left(\frac{D\mathbf{u}}{Dt} + \frac{12\nu}{d^2} (\mathbf{u} - \mathbf{v}) \right), \quad (1)$$

ρ_f and ρ_p denote respectively the fluid and the particle density, ν the fluid kinematic viscosity and \mathbf{v} is the particle velocity. While \mathbf{u} and $D\mathbf{u}/Dt$ are the fluid velocity and acceleration evaluated at the particle center position. The above dynamical model, when coupled to Navier-Stokes equations to describe the evolution of \mathbf{u} , may be characterized by two dimensionless parameters, the modified density ratio $\beta = 3\rho_f/(\rho_f + 2\rho_p)$ and the Stokes number $St = \tau_p/\tau_\eta$, where $\tau_p = d^2/(12\beta\nu)$ is the particle response time and τ_η is dissipative time-scale of turbulence. Despite its simplicity - only Stokes drag force and inertial added-mass effects are accounted for - eq.(1) produces non trivial effects on particle concentrations, velocity and acceleration statistics [4]. When the particle size is larger than η - but still the slip velocity of the particle is much smaller than the mean fluid velocity - we have recently proposed that Faxén forces become relevant and must be included [3]:

$$\frac{d\mathbf{x}}{dt} = \mathbf{v}; \quad \frac{d\mathbf{v}}{dt} = \frac{3\rho_f}{\rho_f + 2\rho_p} \left(\left\langle \frac{D\mathbf{u}}{dt} \right\rangle_{V_p} + \frac{12\nu}{d^2} (\langle \mathbf{u} \rangle_{S_p} - \mathbf{v}) \right), \quad (2)$$

where $\langle \dots \rangle_{V_p}$ and $\langle \dots \rangle_{S_p}$ denote volume and surface average over the (spherical) particle. These averages constitute the Faxén correction (FC) terms, which account for the non-uniformity of the flow at the particle-scale. Finally, we note that this modeling approach assumes the particles' induced perturbation on the fluid flow negligible, and also inter-particle collisions and gravity are neglected.

Eulerian-Lagrangian Numerical simulations

The Lagrangian particle models (1),(2) are evolved in a statistically stationary, homogeneous and isotropic turbulent flow. Turbulence is simulated on a periodic cubic domain by integrating Navier-Stokes (NS) equations forced by a large-scale volume term. In our numerical implementation NS is discretized on a regular grid, integrated using pseudo-spectral algorithm and second-order time marching scheme. The idea sustaining this approach is that small-scale Eulerian as well as Lagrangian statistics is universal, i.e., independent of the type of forcing applied at large scale, this has been recently tested in [5]. In order to validate and benchmarking our simulations we have performed a test on acceleration statistics of fluid tracers. We have run two independently developed codes which implements slightly different algorithms: i) Verlet time-stepping algorithm vs. second order Adams-Bashfort, ii) tri-cubic vs. tri-linear interpolation, iii) forcing term at constant energy input vs. constant energy at large-scales. We obtain an excellent level of universality for comparable turbulence levels (see fig. 1).

Results

Recent experimental studies on the acceleration of neutrally buoyant particles ($\rho_p = \rho_f$) have highlighted statistical effects linked to the particle size (d),

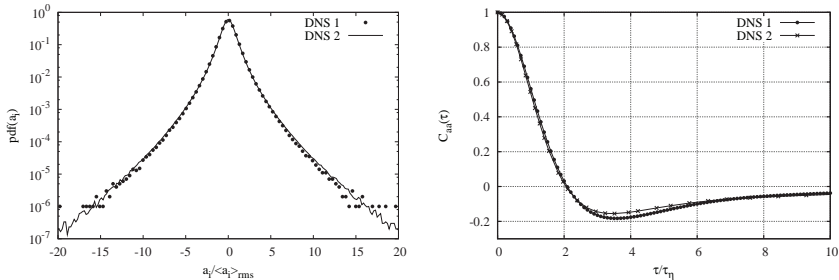


Fig. 1. Single-component acceleration p.d.f. (left) and time correlation function (right) for lagrangian fluid tracers. Results from two different simulations, with different large-scale forcing but comparable level of turbulence ($Re_\lambda = 50$ and 75).

namely a decrease of acceleration variance and increase of correlation times at increasing d , and independence on d of the probability density function of the acceleration once normalized by its variance [2, 6]. We showed that these effects are not captured by PP model (1), [2], while the FC one adds important and necessary physical corrections (see [3] for a detailed comparison with experimental data). The differences between PP and FC on the single-component acceleration r.m.s. value as a function of d/η - also when $\rho_p \neq \rho_f$ - are shown in fig. 2. Faxén terms always reduce the acceleration amplitude for particles larger than about 10η . Alternatively, one can look at the behavior of acceleration r.m.s. in the β - St parameter space. Fig. 3 shows the different behavior of $\langle a_i \rangle_{rms}$ values measured in PP and FC simulations for the same flow conditions. FC significantly reduce the acceleration values for particles lighter than the fluid, such as air bubbles in water. In fig. 4 we report the value of acceleration flatness, $F(a_i) = \langle a_i^4 \rangle / \langle a_i^2 \rangle^2$, showing that light particles ($\beta > 3$), which can have a highly intermittent statistics at small St both in PP and FC model, in the large St limit become gradually less intermittent only if Faxén corrections are included. However, the PP vs. FC acceleration scenario changes much less for heavier particles ($\beta < 1$). We wish these predictions to be tested against experimental measurements in the near future.

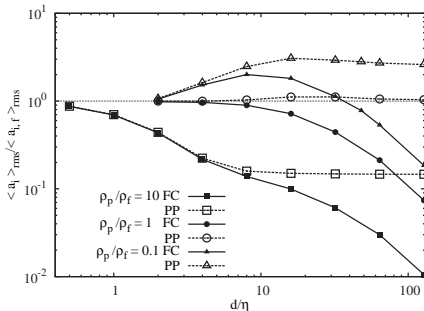


Fig. 2. Particle acceleration r.m.s. normalized by the fluid one, $\langle a_i \rangle_{rms} / \langle a_{i,f} \rangle_{rms}$, vs. d/η for particle types with densities $\rho_p / \rho_f = 0.1, 1, 10$, at $Re_\lambda = 75$.

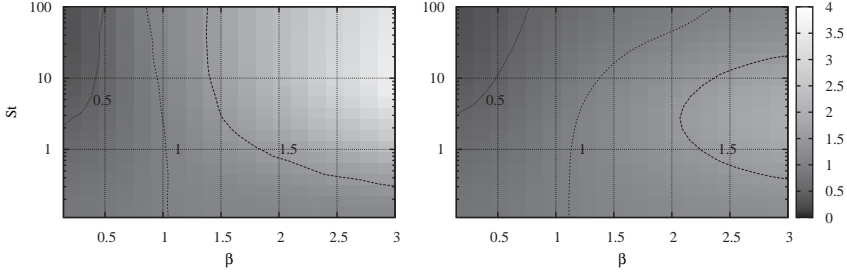


Fig. 3. $\langle a_i \rangle_{rms} / \langle a_{i,f} \rangle_{rms}$, in the β - St plane for PP (left) and FC (right) model. Isolines are traced at 0.5,1,1.5 values.

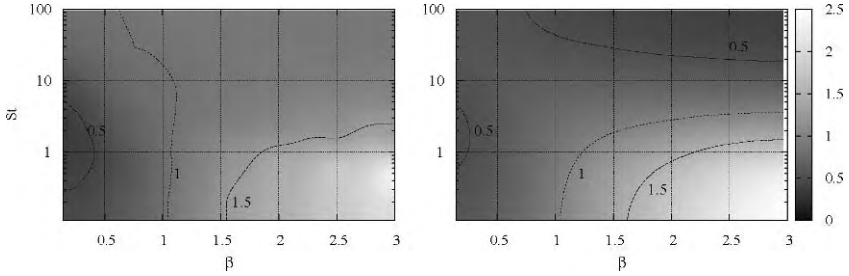


Fig. 4. Ratio of particles' to fluid acceleration flatness, $F(a_i) / F(a_{i,f})$, in the β - St plane for PP model (left) and FC (right). Isolines are traced at 0.5,1,1.5 values.

References

1. Toschi, F. & Bodenschatz, E. *Ann. Rev. Fluid Mech.* **41**, 375–404 (2009).
2. Volk, R., Calzavarini, E., Verhille, G., Lohse, D., Mordant, N., Pinton, J. F. & Toschi, F. *Physica D* **237** (14-17), 2084–2089 (2008).
3. Calzavarini, E., Volk, R., Bourgoïn, M., Leveque, E., Pinton, J. F. & Toschi, F. *J. Fluid Mech.* in press (2009).
4. Calzavarini, E., Kerscher, M., Lohse, D. & Toschi, F. *J. Fluid Mech.* **607**, 13–24 (2008).
5. Arneodo, A. *et al.*, *Phys. Rev. Lett.* **100** (25), 254504–5 (2008).
6. Qureshi, N. M., Bourgoïn, M., Baudet, C., Cartellier, A. & Gagne, Y. *Phys. Rev. Lett.* **99** (18), 184502 (2007).

Lagrangian analysis of turbulent convection

Jörg Schumacher and Mohammad S. Emran

Institut für Thermo- und Fluidodynamik, Technische Universität Ilmenau, D-98693
Ilmenau, Germany
joerg.schumacher@tu-ilmenau.de

1 Introduction

Turbulent convection is one of the best studied flows in experimental and numerical fluid dynamics [1]. One reason is the existence of a wide range of natural phenomena and industrial applications in which turbulent motion is initiated and sustained by heating a fluid from below and cooling from above. In this paper, we present direct numerical simulations of three-dimensional turbulent convection with the focus on the Lagrangian properties of the flow. Two different systems are studied for this purpose. The first one is a Cartesian slab with an aspect ratio of four, bounded by free-slip planes at the top and bottom and periodic side walls [2, 3]. The second configuration is a closed cylindrical cell with an adiabatic side wall and isothermal top and bottom plates with an aspect ratio of one [4]. Turbulent Rayleigh-Bénard convection is discussed in the Boussinesq approximation in both cases. We apply a pseudospectral method for the Cartesian case and a second-order finite difference method for the cylindrical one. The Prandtl number is $Pr = 0.7$ for all cases. The Rayleigh numbers Ra vary between 10^7 and 10^9 . Figure 1 shows a snapshot of the temperature field in the Cartesian cell. Clearly visible skeleton-like structures of thermal plumes close to the top and bottom planes are present in the contour plots of temperature.

2 Lagrangian particle dispersion

Convective turbulence is inhomogeneous in general. In the case of Cartesian slab, the inhomogeneity is with respect to the vertical direction, however, in the cylindrical cell, it is present in all spatial directions. This affects the dispersion properties of the Lagrangian tracers which are manifested by different strength of lateral and vertical two-particle dispersion. Similar to isotropic turbulence, we find that the pair dispersion properties depend sensitively on the initial separation of tracers and yield a short-range Richardson-like scaling

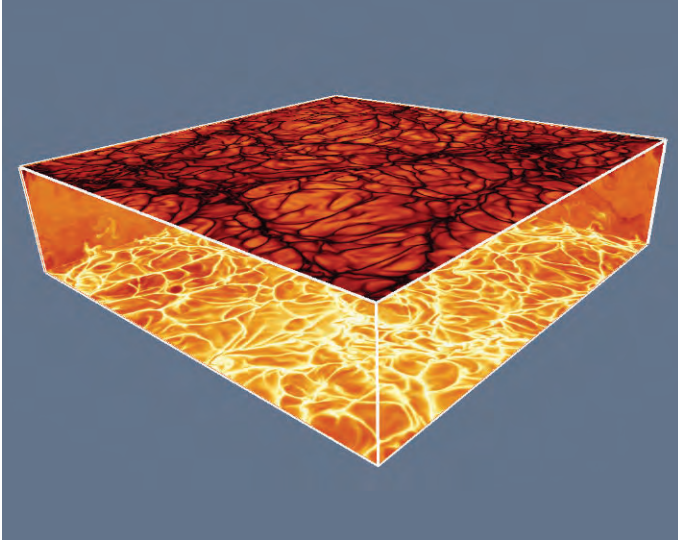


Fig. 1. Contours of the total temperature field close to the top and bottom plates in a Cartesian cell with aspect ratio of four.

regime with a smaller Richardson constant [2]. Furthermore, different initial seeding positions of the tracer pairs in the convection cell cause differences in the lateral and vertical dispersion at initial and intermediate times. For example, pairs which are seeded initially in the thermal boundary layer will pass the mixing zone where detached thermal plumes move into the bulk region. Frequently, this detachment process is associated with local maxima of the vorticity which affect the lateral accelerations and thus relative lateral pair motion.

Interestingly, we observe that the four-particle motion and statistics in the Cartesian slab is quantitatively similar to homogeneous isotropic turbulence in the long-time limit. The clouds of four tracers show a clear trend to form flat objects, as reported in [5]. In Figure 2, we display the time evolution of the normalized eigenvalues of the moment-of-inertia tensor, $\langle I_i(t) \rangle_L$. It holds $\sum_{i=1}^3 \langle I_i \rangle_L = 1$ with $\langle \cdot \rangle_L$ the average over the Lagrangian tracer ensemble. The long-time limit of $\langle I_3 \rangle_L$ is 0.01, which reflects the dominance of flat objects and agrees with the isotropic case. This indicates that the large-scale geometry of the cluster is almost independent of particular aspects of the turbulence, such as plumes in convection.

3 Heat transport and acceleration

We also analyse the statistics of the acceleration components. Significant efforts are necessary to resolve the acceleration statistics accurately: in order to

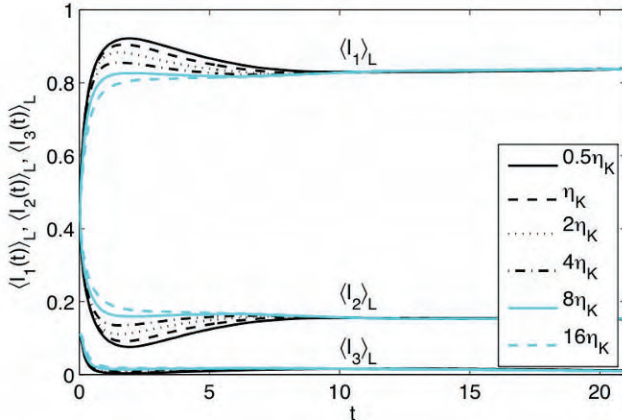


Fig. 2. Time evolution of the ensemble-averaged and normalized eigenvalues of the moment-of-inertia tensor of four-particle clusters. The initial separation of the tracers is indicated in the legend. The four-particle cluster were seeded across the whole Cartesian slab at the beginning of the run.

resolve the tails of the distributions we included more than 10^8 data points in the statistical analysis [3]. We find that the vertical acceleration component is less intermittent than the lateral ones which is indicated by the sparser tails of the probability density function. We also discuss the joint statistics of the vertical acceleration with respect to the local convective and conductive heat fluxes. It is found that rising and falling thermal plumes are not connected with the largest vertical acceleration magnitudes.

In the Lagrangian frame, the Nusselt number can be defined as

$$Nu_L = 1 + \frac{H}{\kappa \Delta T} \langle u_z T \rangle_L. \quad (1)$$

Here H is the height of the cell, κ the thermal diffusivity, ΔT the total temperature drop, u_z the vertical velocity component and T the temperature field. Interestingly, it is observed that Nu_L needs a significant duration of time to relax to the Eulerian value Nu_E for which $\langle u_z T \rangle_L$ in Eq. (1) has to be substituted by the volume-time average $\langle u_z T \rangle_{V,t}$. Our result differs from a recently reported experimental finding with a smart particle [6]. In this experiment, $Nu_L > Nu_E$ which can be attributed to the finite size of the smart particle. Our studies suggest that the tracer ensemble takes a certain time to “thermalize” in the convective flow. We conclude that this is due to the fact that velocity *and* temperature are sampled along the Lagrangian tracks in the present case. After this period, the majority of particles follows the large-scale circulation and $Nu_L \rightarrow Nu_E$.

Figure 3 shows five representative Lagrangian tracer tracks in the cylindrical cell. Similar to the findings by Gasteuil *et al.* [6], the particles follow on

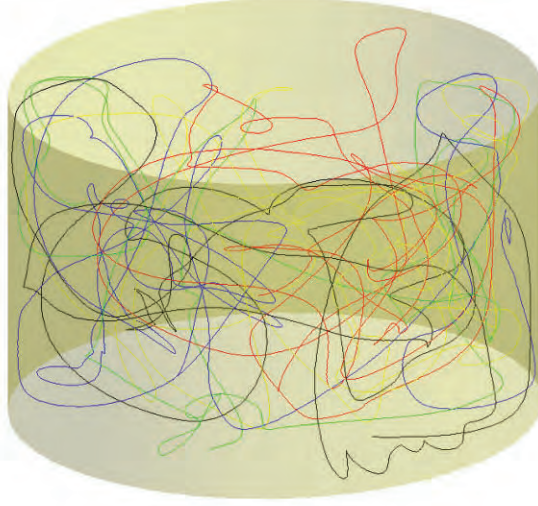


Fig. 3. Time evolution of five Lagrangian tracers in the cylindrical cell. The tracks are monitored for one hundred turnover times. The Rayleigh number for this run is 10^7 and the aspect ratio $\Gamma = 1$.

average the large-scale circulation of the flow. It is also observed that the (central) bulk is less frequently visited by the tracers than the regions near the walls, in particular the side walls. In the closed vessel, the long-time particle pair dispersion does not cross over into the Taylor diffusion limit, but levels off to a constant value. An interesting aspect which we want to address in future work is the dependence of the Lagrangian statistics on the aspect ratio. For larger values, the effects of the side walls should become sub-dominant.

This work is supported by the Deutsche Forschungsgemeinschaft under grants SCHU 1410/2-1 and SCHU 1410/5-1 and by the Jülich Supercomputing Centre (Germany) under grants HMR09 and HIL02.

References

1. G. Ahlers, S. Grossmann, and D. Lohse, *Rev. Mod. Phys.* **81**, in press (2009).
2. J. Schumacher, *Phys. Rev. Lett.* **100**, 134502 (2008).
3. J. Schumacher, *Phys. Rev. E*, in press (2009).
4. M. S. Emran and J. Schumacher, *J. Fluid Mech.* **611**, 13 (2008).
5. L. Biferale, G. Boffetta, A. Celani, B. J. Devinish, A. Lanotte, and F. Toschi, *Phys. Fluids* **17**, 115101 (2005).
6. Y. Gasteuil, W. L. Shew, M. Gibert, F. Chillá, B. Castaing, and J.-F. Pinton, *Phys. Rev. Lett.* **93**, 234302 (2007).

Linear and angular dynamics of an inertial particle in turbulence

Yoann Gasteuil and Jean-François Pinton

Laboratoire de Physique de l'École Normale Supérieure de Lyon,
CNRS & Université de Lyon, 46 Allée d'Italie, 69007 Lyon, France
pinton@ens-lyon.fr

Lots of attention has been recently given to the dynamics of inertial particles in turbulence [1, 2, 3]. This knowledge is relevant for many practical situations where objects are being advected by an underlying turbulent flow. One central question concerns the modelling of the forces which act on inertial particles. For objects smaller than the Kolmogorov dissipation length, a point-wise model (PP) including added mass and Stokes drag term has proven quite successful. For larger particle there are noticeable discrepancies compared to experimental observations [4, 5]. This has motivated to include corrections, in particular the inclusion of size effects. Taking into account the non-uniformity of the flow at the particle scale has improved the models [6], but some effects remain, like those associated with the eventual rotation of the particle. We report here an experimental investigation of the 6-dimensional motion (3 space and 3 angle coordinates) of an inertial size particle in a fully turbulent flow.

Experimental setup and method

The experiment uses a von Kármán flow in water, driven by the counter-rotation of impellers with a 10 cm radius R , fitted with straight blades 1 cm in height. The flow domain in between the impeller has characteristic lengths $H = 2R = 20$ cm. At the nominal rotation rate of 3 rpms of the measurements reported here, the flow has a Reynolds number, based on the Taylor microscale, of $R_\lambda \sim 250$. The 'particle' size is $D = 1.75$ cm. It is very large compared to the dissipation length ($D/\eta \sim 280$!), smaller than the flow integral scale $L \sim 4$ cm. The particle is neutrally buoyant: its velocity of sedimentation in the fluid at rest is of the order of a millimeter per second, corresponding to a density matching better than 0.1 percent.

The particle is tracked optically using a Phantom 7.3 camera; it is painted with a texture that allows to find its orientation with a pattern-recognition algorithm. Calibration and consistency checks show that the precision of the

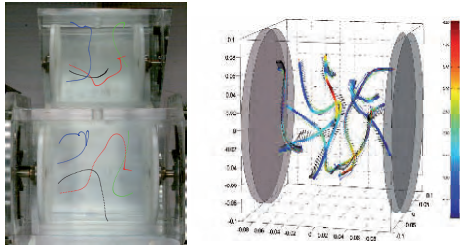


Fig. 1. (a) Experimental setup: the ‘washing machine flow’, imaged by the fast camera; (b) Examples of a trajectories, showing the local particle orientation.

measurement is ± 1 mm for its position and ± 1 degree for its angular orientation. With typical linear velocities of the order of 0.5 m/s and a frame rate of 100 Hz, a particle motion is resolved over a fraction of its diameter so that derivatives can be computed accurately to estimate the particle’s velocity and acceleration, and similarly for its angular motion. Segments of particle motions analyzed here have durations between 800 and 4800 ms, corresponding to time lengths between 1 and 6 Lagrangian integral time scales T_L . Analysis of probability density functions of the particle linear and angular coordinates show that it samples uniformly the flow; orientations have a very small bias, probably tracing back to the assembly of the particle from 2 hemispheres.

Linear motion

The particle velocity has a Gaussian distribution, with zero mean and variance equal to 0.15 m/s. Hence the particle’s Reynolds number is about 2500, but with its variations in time are of the same order of magnitude. The slip-velocity is therefore large and one may expect that interactions between flow and wake influence the particle’s dynamics.

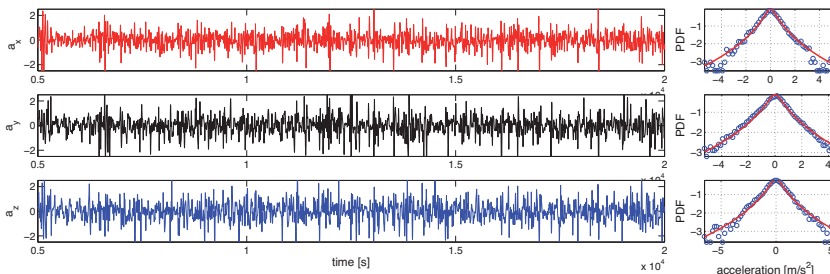


Fig. 2. Linear acceleration. (left): time traces of the particle’s acceleration – segments are concatenated; (right): corresponding probability density functions (PDFs) – the solid red line is the lognormal functional form of Eq.1, with $s = 0.70$.

The autocorrelation functions of the velocity components decrease in a characteristic time of order T_L , and the cross-correlations between components are essentially null. The particle acceleration is strongly non Gaussian. As shown in Fig.2, the statistics of its components is well modeled by a lognormal form[7],

$$P(a_i) = \frac{\exp(s^2)}{4m} \left(1 - \operatorname{erf} \left(\frac{s^2 + \ln \frac{|a_i|}{m}}{\sqrt{2}s} \right) \right), \quad (1)$$

where $m = \sqrt{2/e^{2s^2}}$ for a centered variable with zero mean, and s is a free fitting parameter. For Lagrangian tracers, a value $s = 1$ has been reported [7] in a von Kármán flow, while $s = 0.62$ has been found for both tracers and inertial particles in grid turbulence [8]. Note the distribution flatness is related to the s -parameter by $F = (9/5) \exp 4s^2$. Here we find $s = 0.70 \pm 0.04$, i.e. the statistics of the acceleration of the particle is still as non-Gaussian as that of the tracers, despite its size being 280 times the Kolmogorov's length. For the acceleration variance, if one assumes a functional form $\langle a_i^2 \rangle = a'_0 \epsilon^{4/3} D^{-2/3}$, one gets $a'_0 \sim 1.4$ instead of 18 as proposed originally in [8].

From the particle trajectory, one can compute geometrical features (longitudinal and transverse accelerations, curvature, etc.) as introduced in [9]. The results for this large inertia particle reproduce the feature for the tracers, as reported in [10].

Angular dynamics

One surprising results of our measurements, the very strong non-Gaussianity of the particle's angular velocity, is shown in figure 3. Using the lognormal expression in equation 1, one obtains $s = 0.71 \pm 0.03$, very similar to the value obtained for the linear acceleration. The variance of the angular velocity components is vary accurately given by $(d\theta_i/dt)_{\text{rms}} \sim u_{\text{rms}}/D = 7.6 \text{ rd/s}$.

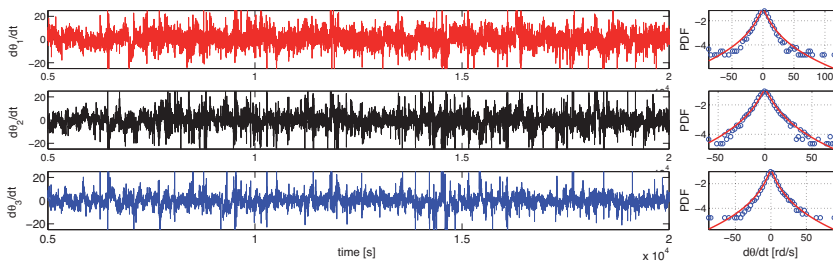


Fig. 3. Angular velocity. (left): time traces; (right): corresponding probability density functions – solid red line corresponds to $s = 0.71$ in Eq.1.

There is thus no simple connexion between the particle angular velocity statistics and that of the vorticity of the flow at a scale equal to the particle

size (it would be almost Gaussian at $D \sim L/2$). The analysis of the statistics of the angular rotation projected onto the Frenet coordinates has shown weak correlations, *i.e.* angular motion and the geometry of the trajectory are not simply connected – as they would be if strong lift forces were at work.

The angular acceleration of the particle is also quite non Gaussian, with distributions again well accounted for by equation 1, with $s = 0.97 \pm 0.04$. The value of the variance of angular acceleration is accurately estimated as $(d^2\theta_i/dt^2)_{\text{rms}} \sim (u_{\text{rms}}/D)^2 = 58 \text{ rd/s}^2$. The angular acceleration is *more* intermittent than the linear part ($s \sim 1$ corresponds a flatness factor of nearly 100). Note that rotation is associated to transverse velocity variations, which are known to be more intermittent than longitudinal ones.

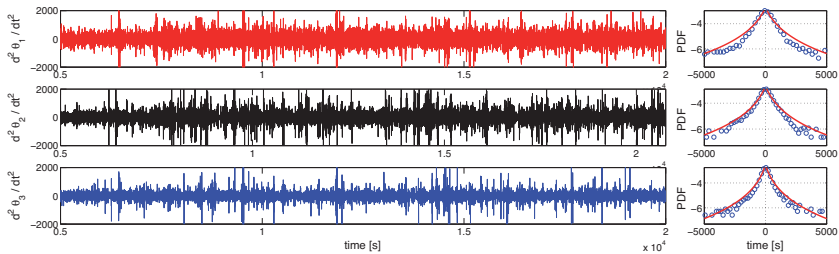


Fig. 4. Angular acceleration. (left): time traces; (right): corresponding probability density functions – solid red line corresponds to $s = 0.97$ in Eq.1.

Many other features, such as energy budgets are under investigations and will be reported in the near future. One notes, for instance, that the kinetic energy of the particle associated with rotational motion is almost an order of magnitude *less* than the one associated to translational motion. This is what is expected if one assumes that the particle moves on average with velocity u_{rms} , and rotates with characteristic speed u_{rms}/D .

References

1. G.A. Voth et al. *J. Fluid Mech.* **469**, pp.121-160 (2002)
2. N. Mordant et al. *Phys. Rev. Lett.*, **87**(21), 214501, (2001)
3. Xu HT et al., *Phys. Rev. Lett.*, **98**(5), 050201, (2007)
4. Mazzitelli IM et al., *J. Fluid Mech.* **488**, pp.283-313 (2003)
5. Volk R. et al. *Physica D* **237**(14), 2084-2089 (2008)
6. E. Calzavarini et al. *J. Fluid Mech.* (2009), in press.
7. N. Mordant et al. *Phys. Rev. Lett.* **94**, 024501 (2004)
8. N.M. Qureshi et al., *Euro. Phys. J.B* **66**(4), 531 (2008)
9. Braun W, De Lillo F, Eckhardt B, *J. Turbulence* **7**(62), 1 (2006)
10. Xu HT, Ouellette NT, Bodenschatz E, *Phys. Rev. Lett.* **98**(5), 05201 (2007)

Collision rate between heavy particles in a model turbulent flow

L. Ducasse¹ and A. Pumir²

¹ Institut Non Linéaire de Nice, 1361, route des Lucioles, F-06560, Valbonne, France

² Laboratoire de Physique, Ecole Normale Supérieure de Lyon, 46, Allée d'Italie, F-69007, Lyon, France
alain.pumir@ens-lyon.fr

1 Introduction

Understanding and predicting the collision rate of small inertial particles in turbulent flows is of importance in many meteorological and industrial processes. For instance, predicting the time of rain initiation of warm clouds, which are known to be turbulent in their core, is still an open problem. Droplets in such clouds, which can be treated as inertial particles, are believed to grow to rain drop by coalescence due to collisions.

As shown in [1], the collision rate N_c per unit of volume of equal size particles of diameter a and mean density n_0 can be written :

$$N_c = \pi n_0^2 a^2 \langle |w_r| \rangle g(a) \quad (1)$$

where w_r is the radial relative velocity between particles and $g(a)$ the radial distribution function at contact. Numerical simulations have shown that this collision rate is larger for inertial particles than in the case of simple tracers [2]. This observation can be explained by two effects. On one side, the concentration around particles is locally larger than the mean density ($g(a) > 1$), a result of the effect of preferential concentration [3]. On the other hand, the relative velocity between two colliding particles can be significantly larger than expected based on the typical rate of strain tensor, as described by the Saffman-Turner formula [4] for the case of inertialess particles.

For a fixed value of the Reynolds number, two dimensionless parameters are relevant in this problem : the Stokes number $St = \tau/\tau_K$ and the Froude number $Fr = u_K/g\tau$ which measure the inertia of the particles and the influence of the gravity respectively. In this formulation τ is the response (Stokes) time of the particles, τ_K and u_K the time and velocity at the Kolmogorov scale and g the acceleration of gravity. As shown in [3] the dimensionless (simplified) equation of motion of a particle in this context can be written :

$$d\mathbf{v}/dt = (\mathbf{u} - \mathbf{v})/St - \hat{\mathbf{z}}/\epsilon_0 \quad (2)$$

where $\epsilon_0 = St \times Fr$, \mathbf{v} is the velocity of the particles and \mathbf{u} the velocity of the fluid. Differentiating Eq.(2), one can obtain the equation of evolution of the gradient velocity tensor in the Lagrangian frame [5]:

$$d\sigma_{ij}/dt = (h_{ij} - \sigma_{ij})/St - \sigma_{ik}\sigma_{kj} \quad (3)$$

where $\sigma_{ij} = \partial_j v_i$ and $h_{ij} = \partial_j u_i$. The nonlinear term in (3), leads to the possibility of a divergence in finite time for σ . This can happen when particles going through a region of large gradient ($|\mathbf{h}| \gg 1/St$) are sufficiently accelerated to acquire a velocity, which differs strongly from the fluid velocity. Particles experiencing such a sling shot [5] are prone to collide with other particles having very different histories and velocities. As a result, the sling effect enhances the relative velocity between particles, hence the term $\langle |w_r| \rangle$ in eq.(1), and ultimately the collision rate N_c . When a sling effect occurs on a trajectory, the velocity field of the particles \mathbf{v} becomes multi-valued (particles at the same point have different velocities), corresponding to the formation of caustics of particle rays [6]. In this situation, colliding particles can come from very different regions of the fluid so their relative velocities is not assessable from σ .

The main idea of this work is to distinguish two different type of collisions, these for which the relative velocity can be evaluated from σ referred to as the continuous collisions and those for which this assessment is impossible referred to as the sling collisions.

A method to evaluate separately these two contributions has been proposed in [7]. It is based on a direct integration of the equations of the Lagrangian evolution of heavy particles, and involves a phenomenological parametrisation of the sling contribution to the collision term.

In this work, we compare systematically the collision rates measured in a synthetic turbulent flow (kinematic simulation, [8]) and the prediction of the simplified Lagrangian parametrisation. Our results suggest several crucial improvements to the parametrisation proposed by [7] and show a strong dependence of the sling contribution on the gravity.

2 Direct measurements

We considered very small particles in a periodic simulation domain. The system is supposed to be diluted enough to neglect particles interactions and all feedback due to their movements on the surrounding fluid. For a continuous collision, the radial relative velocity at contact between the two particles, should be given by : $w_r = a \times \hat{\mathbf{r}} \cdot \sigma \cdot \hat{\mathbf{r}}$. In order to distinguish the continuous component from the sling one, we compare for each collision the real radial relative velocity and the quantity : $a \times \hat{\mathbf{r}} \cdot (\sigma_1 + \sigma_2) \cdot \hat{\mathbf{r}}$. Where σ_1 and σ_2 are the values of σ measured at the positions of the particle 1 and 2. The PDF of

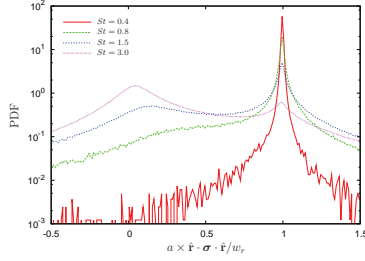


Fig. 1. PDF of the ratio between the supposed radial relative velocity estimated by $a \times \hat{\mathbf{r}} \cdot (\boldsymbol{\sigma}_1 + \boldsymbol{\sigma}_2) \cdot \hat{\mathbf{r}}$ and the real one w_r at the moment of the collision.

the ratio of these two quantities, measured at the moment of each collision, is shown on Fig.1. The PDF of the ratio of these two quantities, measured at the time step preceding each collision, is shown on Fig.1. One can see clearly on this figure a quite narrow peak at $a \times \hat{\mathbf{r}} \cdot (\boldsymbol{\sigma}_1 + \boldsymbol{\sigma}_2) \cdot \hat{\mathbf{r}}/w_r = 1$. This peak corresponds to the continuous contribution to the collision rate. In this case, the radial relative velocity can be greatly evaluated from the gradient velocity tensor. This contribution decreases with St , and the Fig.1 lets appear a broader peak around $a \times \hat{\mathbf{r}} \cdot (\boldsymbol{\sigma}_1 + \boldsymbol{\sigma}_2) \cdot \hat{\mathbf{r}}/w_r = 0$, corresponding to the sling collisions. In most of cases a sling collision is characterised by a radial relative velocity larger than it should be in the continuous case. In order to evaluate the two contribution to the collision rate, we simply condition the origin of a collision with the value of the ratio $a \times \hat{\mathbf{r}} \cdot (\boldsymbol{\sigma}_1 + \boldsymbol{\sigma}_2) \cdot \hat{\mathbf{r}}/w_r$.

3 Indirect estimation

We use here the method proposed in [7] to estimate the collision rate and compare it with the results obtained with the direct measurements. The continuous contribution is directly evaluated from a Lagrangian measurement of the velocity gradient tensor :

$$N_c^{cont} = \frac{n_0 a^3}{2} \left\langle \frac{1}{T} \int_0^T n(t) \int_{\hat{\mathbf{r}} \cdot \boldsymbol{\sigma} \cdot \hat{\mathbf{r}} < 0} \hat{\mathbf{r}} \cdot \boldsymbol{\sigma} \cdot \hat{\mathbf{r}} d\Omega dt \right\rangle \quad (4)$$

The bracket designate an average on the trajectories. This approach is similar to the Saffman-Turner one (ST), in the case of inertialess particles. The time T correspond to the time needed for the contraction rate along a trajectory to grow by a factor (η/a) . Indeed, all the contribution of the coarse grained density until the scale $r = a$ are expected to contribute to continuous part of the collision rate.

The evaluation of the sling contribution is more phenomenological. A sling event is characterised by the fact that two particles can hit frontally. In a continuous description of the velocity field of the particles \mathbf{v} , this means that

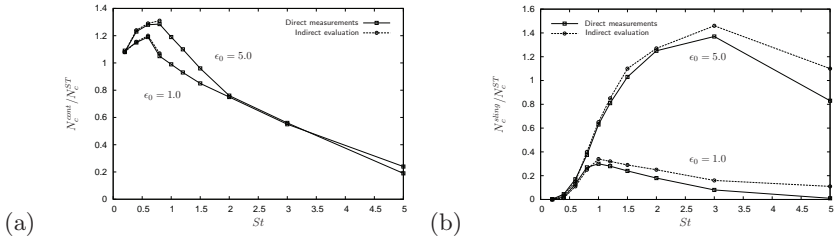


Fig. 2. Comparison between direct measurements and the indirect evaluation of the different contributions to the collision rate normalized by the ST case for two different intensity of the gravity. (a) Continuous contribution. (b) Sling contribution.

this latter becomes multi-valued resulting in a divergence for σ . Thus, the sling contribution will be proportional to the average frequency of the sling events f_{bu} (blowup frequency) on a Lagrangian trajectory. This quantity is directly accessible integrating eq.(3) on many trajectories. The main challenge of our parametrisation is to estimate the mean number of collisions \mathcal{N}_{sling} occurring in the wake of a sling event. Then, the blowup frequency will be given by :

$$N_c^{sling} = \frac{n_0}{2} \times \mathcal{N}_{sling} \times f_{bu} \quad (5)$$

In practice, \mathcal{N}_{sling} is estimated as the mean flux of particles during the typical duration of a sling event which is supposed to be of order τ .

Both contributions to the collision rate, continuous and sling normalized by the ST case N_c^{ST} , are shown on Fig.(2). This figure reveals that the sling contribution is essentially zero for $St < 0.2$ and start to grow fast after this value as a consequence of the dependence $f_{bu} \sim \exp(-A/St)$ for small St [9]. One can see also that the gravity tends to reduce strongly the sling contribution. On the other hand the continuous component is larger than the ST case for $St \lesssim 1$ as a consequence of the preferential concentration. This latter contribution seems to be weakly affected by the gravity in comparison to the sling one.

References

1. LP. Wang, A. S. Wexler and Y. Zhou, Phys. Fluids. **10**, 266-276 (1998a).
2. S. Sundaram and L. R. Collins, J. Fluid Mech. **335**, 75-109 (1997).
3. R. Shaw, Ann. Rev. Fluid Mech. **35**, 183-227 (2003).
4. P. G. Saffman and J. S. Turner, J. Fluid Mech. **1**, 16-30 (1956).
5. G. Falkovich, A. Fouxon and M. G. Stepanov, Nature **419**, 151 (2002).
6. M. Wilkinson, B. Mehlig and V. Bezuglyy, Phys. Rev. Lett. **97**, 048501 (2006).
7. G. Falkovich and A. Pumir, J. Atmos. Sci. **64**, 4497 (2007).
8. J. C. H. Fung et al., J. Fluid Mech. **236**, 281 (1992).
9. M. Wilkinson and B. Mehlig, Europhys. Lett. **72**, 186-192 (2005).

From cloud condensation nuclei to cloud droplets: a turbulent model

A. Celani¹, A. Mazzino², and M. Tizzi²

¹ Centre National de la Recherche Scientifique, Unité de Recherche Associée 2171, Institut Pasteur, 75015 Paris, France

² Università di Genova, Dipartimento di Fisica and Istituto Nazionale di Fisica Nucleare, sezione di Genova, 16146 Genoa, Italy
`tizzi at fisica.unige.it`

Introduction

The formation of a warm vertical cloud is classically described by the evolution of microscopic droplets [1]. Droplets start to nucleate around solid particles in a favourable environment (i.e. for positive supersaturation in the absence of solute effect). Then, if the available vapour is sufficient, they grow by condensation. Once their size is large enough, their terminal velocity is no more negligible and they start to collide with both slower and faster droplets. The resulting growth by coalescence is explosive and eventually a precipitation can occur. This simple description is able to capture the basic mechanisms behind the first development of the cloud.

Nevertheless, the classical description leaves some problems open and also leads to a serious inconsistency. Indeed, the prediction for the condensational growth states that smaller droplets grow faster than larger droplets. As a result, during the condensation stage the droplet population becomes more and more homogeneous, while the growth slows down. On the one hand, this slowing process cannot lead to a precipitation in reasonable times; on the other hand, the explosive process ensured by collisions cannot occur, if all the droplets share the same size (i.e. the same terminal velocity). Therefore, the size distribution (known as *size spectrum*) during the condensation stage must broaden in some way. Such a contradiction with the classical prediction is confirmed by experimental observations in clouds, where a broader size spectrum is detected [2, 3].

To solve this problem, sometimes referred to as the *bottleneck of condensation*, many different models have been proposed, either improving the classical model with the inclusion of neglected effects or rephrasing it with a different approach. For the time being, no univocal explanation has been provided. Partial justifications are based on entrainment with dry air [4], on the role of giant condensation nuclei [5, 6, 7] or on the local effects of turbulence on

the collection kernel [8, 9] and on the preferential concentration of inertial particles [10, 11]. However, considering turbulent fluctuations in an ascending air parcel does not result in an appreciable spectrum broadening [12, 13].

A different approach is adopted in a series of recent works [14, 15, 16, 17], where a basic ingredient, previously not taken into account, is added, i.e. turbulence in the whole cloud. Rather than following the evolution of a small air parcel and the fluctuations inside it, the focus is on a large part of the cloud. The effects of global turbulent motions are considered. The idea is that droplets get to know very different environmental conditions in short times, so that very different sizes are present in droplet population. As a result, a strong spectrum broadening is observed during the condensation stage. Moreover, turbulence acts as an effective cloud condensation nucleus (CCN), allowing droplets to nucleate around smaller CCN than in a classical picture [16].

Here, we generalize these turbulent models by describing both the nucleation and the condensation stages, without neglecting vapour absorption by growing cloud droplets. This latter effect plays to reduce the broadening of size spectra and thus to produce results in closer agreement with observations.

Model

Our model is inspired by those presented in [15, 16]: instead of focusing on the evolution of an ascending air parcel (where droplets cannot experience large vapour fluctuations and, hence, broaden their size spectrum considerably), our attention is directed on turbulent fluctuations in a large part of the cloud. From a classical viewpoint we can imagine the cloud as formed by a high number of air parcels moving inside it, some in updrafts, others in downdrafts. Each parcel knows a supersaturation s depending on its vertical velocity w , classically assumed as constant. The basic idea is to consider w as the vertical component of the turbulent velocity field \mathbf{u} and to leave the Lagrangian approach given by parcels evolution, following the Eulerian behaviour of two turbulent fields in the whole cloud.

Moreover, both droplet nucleation from CCN (not considered in [15]) and droplet feedback on vapour (neglected in [16]) are taken into account here. If we consider N passive non-inertial particles, the complete model is given by the following equations:

$$\begin{cases} \partial_t \mathbf{u} + \mathbf{u} \cdot \partial \mathbf{u} = -\frac{1}{\rho_a} \partial p + \mathbf{f} + \nu \partial^2 \mathbf{u} \\ \partial_t s + \mathbf{u} \cdot \partial s = G_s w (1 + s) - C_s \lambda (b_s + s) + D \partial^2 s \end{cases}$$

for the two Eulerian fields $\mathbf{u}(\mathbf{x}, t)$ and $s(\mathbf{x}, t)$ and

$$\begin{cases} \frac{d}{dt} \mathbf{X}_i(t) = \mathbf{u}(\mathbf{X}_i(t), t) + \sqrt{2D} \boldsymbol{\eta}_i(t) & i = 1, N \\ \frac{d}{dt} R_i^2(t) = 2C_R \left(1 + s(\mathbf{X}_i(t), t) - e^{\frac{c}{R_i(t)} - \frac{h_i}{R_i^3(t)}} \right) & R_i(t) \geq R_i(0) \end{cases}$$

for the Lagrangian evolution of particle trajectories $\mathbf{X}_i(t)$ and radii $R_i(t)$. Here ρ_a is the air density, p represents the pressure field, \mathbf{f} is a forcing term, ν is the kinematic viscosity, G_s , C_s , b_s , C_R and c can be regarded as constants, D is the vapour diffusivity, $\boldsymbol{\eta}_i$ are independent white noises, h_i is proportional to the i -th CCN mass. Furthermore, λ is a *condensation density* field representing the (Lagrangian) droplet feedback on the (Eulerian) supersaturation field and its expression is

$$\lambda(\mathbf{x}, t) = \frac{1}{\delta V} \sum_{i=1}^{\delta N(\mathbf{x}, t)} R_i(t) \left(1 + s(\mathbf{X}_i(t), t) - e^{\frac{c}{R_i(t)} - \frac{h_i}{R_i^3(t)}} \right)$$

where $\delta N(\mathbf{x})$ is the total number of droplets present at time t in a little volume δV surrounding \mathbf{x} . Notice that both curvature and solute effects are included via the terms proportional to c and h_i , respectively.

Results

We performed a series of two-dimensional DNS of resolution 1024^2 of model equations, putting $5 \cdot 10^6$ CCN randomly in space once the Eulerian fields has reached a stationary state. To mimic different cloud conditions, we simulated different set-ups by varying the turbulent intensity ε , the CCN mass m_s and droplet density n .

As expected, results indicate that droplet feedback on vapour plays an important role, slowing down droplet growth and reducing spectrum broadening compared to the situation observed when feedback is neglected. Nevertheless, although the environment becomes more and more undersaturated as droplets subtract vapour to it, a considerable percentage of droplets is still able to nucleate and grow fast by condensation up to radii comparable to those needed to start up collection (see Fig. 1). Moreover, droplet-size spectra still broaden in time strongly (see Fig. 2). It is worth noticing that the larger turbulent fluctuations, the stronger effects are observed.

References

1. H. R. Pruppacher and J. D. Klett, *Microphysics of Clouds and Precipitation*, Kluwer Academic Publishers, Boston MA 1996.
2. I. J. Lee and H. R. Pruppacher, *Pure Appl. Geophys.*, **115**, 523 (1977).
3. J. L. Brenguier and L. Chaumat, *J. Atmos. Sci.*, **58**, 628 (2001).
4. J. W. Telford, *Atmos. Res.*, **40**, 261 (1996).
5. D. B. Johnson, *J. Atmos. Sci.*, **39**, 448 (1982).
6. A. M. Blyth, S. G. Lasher-Trapp, W. A. Cooper, C. A. Knight and J. Latham, *J. Atmos. Sc.*, **60**, 21 (2001).
7. Y. Segal, A. Khain, M. B. Pinsky and D. Rosenfeld, *Atmos. Res.*, **71**, 3 (2004).

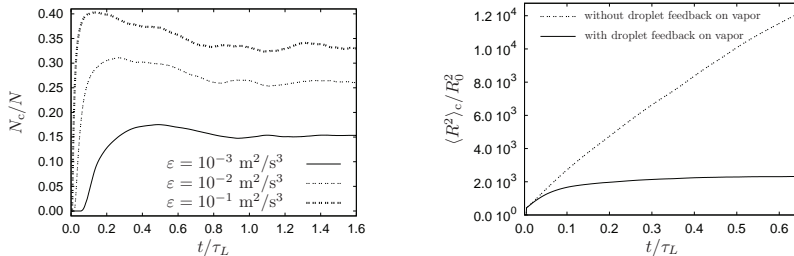


Fig. 1. First, the number of cloud droplets N_c grows quickly at a rate increasing with the turbulent dissipation rate ε (left). Then, N_c reaches a stationary level, which still depends on ε . This stationarity is a fingerprint of the separation between the populations of haze and cloud droplets and is due to the progressive erosion of large positive fluctuations of s . As expected, cloud-droplet growth is slower when the feedback term is taken into account (right). Clearly, in this case cloud droplets absorb the surrounding vapour, so eroding their sustenance and slowing down their growth.

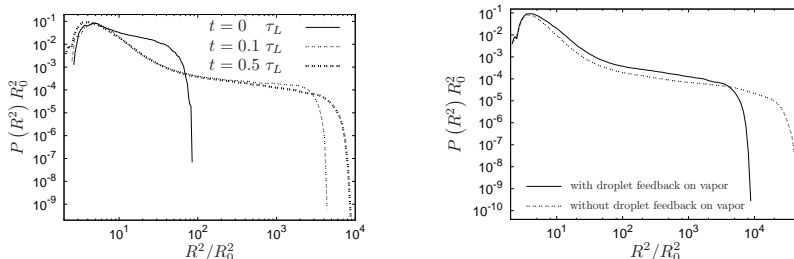


Fig. 2. Droplet-size spectra strongly broaden in time (left). At lower dissipation rates spectra broaden less. The left panel refers to the case with feedback. A comparison between the cases with and without feedback is presented on the right. Although vapour absorption slows down droplet growth by condensation, a strong spectrum broadening is still evident.

-
8. G. Falkovich, A. Fouxon and G. Stepanov, *Nature*, **419**, 151 (2002).
 9. S. Ghosh, J. Davila, J. C. R. Hunt, A. Srdic, H. J. S. Fernando and P. R. Jonas, *Proc. Royal Soc.*, **461**, 3059 (2005).
 10. S. Sundaram and L. R. Collins, *J. Fluid Mech.*, **335**, 75 (1997).
 11. K. Lehmann, H. Siebert, M. Wendish and R. A. Shaw, *Tellus B*, **59**, 1 (2007).
 12. P. A. Vaillancourt, M. K. Yau and W. W. Grabowski, *J. Atmos. Sci.*, **58**, 1945 (2001).
 13. P. A. Vaillancourt, M. K. Yau, P. Bartello and W. W. Grabowski, *J. Atmos. Sci.*, **59**, 3421 (2002).
 14. A. Celani, G. Falkovich, A. Mazzino and A. Seminara, *Europhys. Lett.*, **70** 6, 775 (2005).
 15. A. Celani, A. Mazzino, A. Seminara and M. Tizzi, *J. Turbul.*, **8**, 17 (2007).
 16. A. Celani, A. Mazzino and M. Tizzi, *N. J. Phys.*, **10**, 075021 (2008).
 17. A. S. Lanotte, A. Seminara and F. Toschi, *J. Atmos. Sci.*, preprint.

Lagrangian statistics of inertial particles in turbulent flow

Mickaël Bourgoïn, Nauman Qureshi, Christophe Baudet, Alain Cartellier, and Yves Gagne

L.E.G.I. - U.M.R. 5519 C.N.R.S./I.N.P.G./U.J.F.,
1025 rue de la Piscine, 38041 - Grenoble, France ; mickael.bourgoïn@hmg.inpg.fr

Turbulent transport of material inclusions plays an important role in many natural and industrial situations. Being able to accurately model and predict the dynamics of dispersed particles transported by a turbulent carrier flow, remains a challenge. When the particles are neutrally buoyant and small (typically comparable in size with the dissipation scale of the surrounding turbulence) they are known to behave as tracers for fluid particles. However, in many practical situations, the particles are denser than the carrier fluid and/or larger than the dissipation scale. Their dynamics, which is then affected by so called inertial effects, deviates from that of fluid particles[1, 2, 3]. One critical and difficult point is to develop models which correctly describe the dynamics of particles over a wide range of sizes and density.

In the present study, we report an exhaustive experimental investigation of material particles acceleration in a turbulent air flow, over a wide range of sizes and densities. With respect to previous existing studies, we particularly focus on the so far unexplored regime of finite size (particles diameter D being larger than the turbulent dissipation scale η) and highly inertial particles (much denser than the carrier fluid) [4] (see figure 1a). As particles we use adjustable soap bubbles which can be considered as rigid spheres. They are characterized by their diameter D and density ρ_p . In the following we use the dimensionless parameters $\phi = D/\eta$ and $\Gamma = \rho_p/\rho_f$ where ρ_f is the density of the carrier fluid. We consider a turbulent carrier flow generated downstream a grid in a wind tunnel experiment with a Reynolds number (based on Taylor microscale) of $R_\lambda \sim 160$. The dissipation scale η is $240 \mu\text{m}$ and the energy injection scale L is 6 cm . Particles velocity is measured along their trajectories by Lagrangian acoustical tracking [5, 6, 4] from which acceleration is calculated.

For fixed carrier flow conditions, we find that acceleration statistics of finite size inertial particles are very robust to size and density variations, the influence of which is mostly carried by acceleration variance only. In particular the shape of acceleration probability density function (normalized to variance one) remains unchanged, within statistical errorbars, over the whole range of

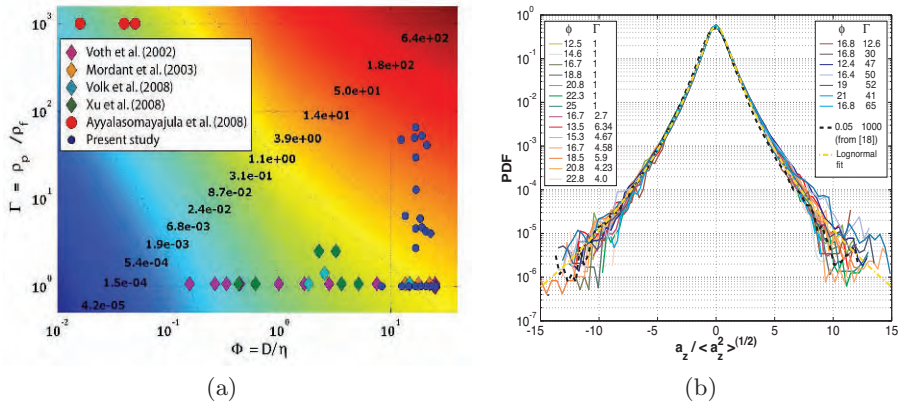


Fig. 1. (a) Particles classes considered in previous studies and in the present work, described in the (ϕ, Γ) phase space. The contour lines indicate an estimation of the particles Stokes number $St = \tau_p/\tau_D$, where the response time τ_p of the particle has been corrected for added mass and for finite Reynolds number effects according to Schiller and Nauman [7, 8] and τ_D is the flow eddy turnover time at the scale of the particle diameter D . (b) Normalized component acceleration probability density function (PDF) of material particles transported in a turbulent air flow (ϕ is the ratio of particles diameter D to the carrier flow dissipation scale η and Γ is the particle to fluid density ratio). Dashed line corresponds to the measurement by Ayyalasomayajula et al. [3] for water droplets (with size $\phi \sim 5 \times 10^{-2}$ and $\Gamma \sim 1000$). To help the comparison with previous and future studies the dot-dashed line shows a fit associated to a lognormal distribution of the acceleration amplitude.

sizes and densities explored (figure 1b). This is in contrast with predictions based on point particles models which predict a monotonic decrease of acceleration flatness as particles inertia is increased [9]. Interestingly we also find our acceleration PDF to be almost identical to that measured at Cornell University by Ayyalasomayajula et al. [3] for subkolmogorov ($\phi \sim 5 \times 10^{-5}$) water droplets ($\Gamma \sim 10^3$) in a similar turbulent wind tunnel experiment. This indicates that point particle models might apply only to even smaller particles, as also suggested by recent experiments by the Cornell group [10]. We also find our acceleration PDF to be much narrower than that measured for similar particles in von Kármán flows. This suggests a possible influence of large scale properties of the carrier flow, as von Kármán flows are closed and highly anisotropic while wind tunnel experiments are open flows with higher isotropy level. This point is being studied in forthcoming work.

While acceleration statistics normalized to variance one do not exhibit any specific size and density dependence, we find a non-trivial, and so far unpredicted, dependence with size and density (figure 2a) for acceleration variance. When density is increased at fixed particle size, acceleration variance is found to decrease and saturate to a size dependent finite limit $a_0^\infty(\phi)$; when size is

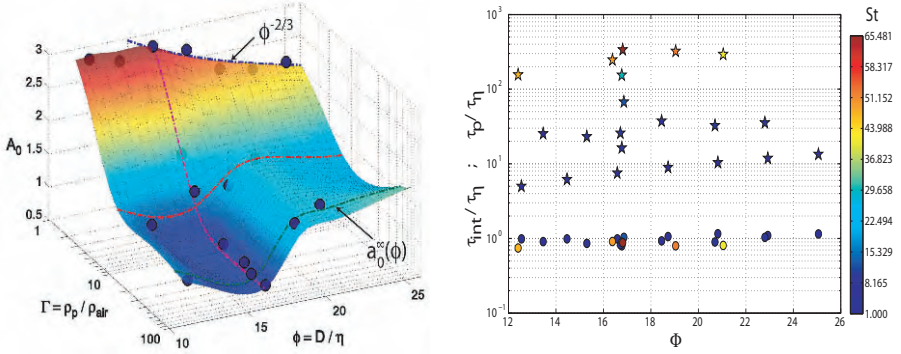


Fig. 2. (a) Acceleration variance for all particles studied in the (ϕ, Γ) parameter space (dots). The surface represents a rough interpolation based on the available measurements. (b) circles : particles forcing time τ_{int} determined experimentally from acceleration autocorrelation functions ; stars : particles Stokes time τ_p . Symbols are color coded according to the corresponding particles Stokes number (St).

increased at fixed density the trend of acceleration variance depends on particles density : for close to neutrally buoyant particles, acceleration decreases with increasing size (as already shown by [11, 6]), but for heavy particles an increase of $a_0^\infty(\phi)$ with ϕ is observed for particles size around $\phi \sim 18$. In particular, this indicates that for heavy particles, finite size effects can be trivially extrapolated neither from the heavy point particle limit nor from the finite size neutrally buoyant case as both of these limits predict a monotonic decrease of acceleration variance with increasing inertia, contradictory with the trends measured for finite size heavy particles. Observed finite size and density effects cannot be accounted by simple filtering arguments only based on Stokes number effects as in the point particle case. A sampling scenario, in the spirit of *sweep-stick* mechanisms [12] seems more adequate to possibly describe the simultaneous influence of density and size. Heavy particles tend to explore preferentially the quietest regions of the flow (low vorticity and/or low acceleration regions) what causes their acceleration variance to decrease. As particles become larger they have less available space in these quiet regions so that they start experiencing the more active regions of the turbulent carrier flow, what may cause an increase of acceleration variance. Such a scenario is also consistent with measurements of preferential concentration which have shown a typical size of clusters (which can be considered as an estimate of the typical size of the quietest sticking regions of the carrier flow) of the order of $10 - 20\eta$, consistent with the typical size ($\phi_c = 18$) for which the increase of $a_0^\infty(\phi)$ is observed.

Finally, we study Lagrangian acceleration auto-correlation functions $R_{aa}(\tau)$ from which we define a characteristic forcing time $\tau_{int} = \int_0^{\tau_0} R_{aa}(\tau) d\tau$ as in [13], where τ_0 is the first zero crossing time ($R_{aa}(\tau_0) = 0$). Figure 2b shows

that for all particles classes the characteristic forcing time τ_{int} remains of the order of the Kolmogorov dissipation time τ_η of the carrier flow. In particular this characteristic time has nothing to do with the Stokes time of the particles which in the present case is expected to change by several order of magnitudes from the smallest neutrally buoyant particles to the largest and heaviest particles. This observation suggests that for all particles classes of finite size particles considered in the present study the dominant small scale forcing term acting on the particles is the pressure gradient and that Stokes number effects cannot be considered alone to properly characterize and model such inertial particles.

References

1. M. R. MAXEY AND J. J. RILEY. *Physics of Fluids* **26**(4), 883–889 (1983).
2. A. ALISEDA, A. CARTELLIER, F. HAINAUX, AND J. LASHERAS. *Journal of Fluid Mechanics* **468**, 77–105 (2002).
3. S. AYYALASOMAYAJULA, A. GYLFASON, L. COLLINS, E. BODENSCHATZ, AND Z. WARHAFT. *Physical Review Letters* **97**, 144507 (2006).
4. N. M. QURESHI, U. ARRIETA, C. BAUDET, Y. GAGNE, AND M. BOURGOIN. *European Physical Journal B* **66**, 531–536 (2008).
5. N. MORDANT, P. METZ, J. F. PINTON, AND O. MICHEL. *Review of Scientific Instruments* **76**(2), 025105 (Feb 2005).
6. N. M. QURESHI, M. BOURGOIN, C. BAUDET, A. CARTELLIER, AND Y. GAGNE. *Physical Review Letters* **99**, 184502 (2007).
7. R. CLIFT, J. R. GRACE, AND M. E. WEBER. “Bubbles, drops and particles”. Academic Press, New York (1978).
8. H. XU AND E. BODENSCHATZ. *Physica D* **237**, 2095–2100 (2008).
9. J. BEC, L. BIFERALE, G. BOFFETTA, A. CELANI, M. CENCINI, A. LANOTTE, S. MUSACCHIO, AND F. TOSCHI. *Journal of Fluid Mechanics* **550**, 349–358 (2006).
10. S. AYYALASOMAYAJULA, A. GYLFASON, AND Z. WARHAFT. In Y. KANEDA, editor, “IUTAM Symposium on Computational Physics and New Perspectives in Turbulence”, vol. 4, pp. 171–175, Nagoya, Japan (September, 11-14 2006). Nagoya University, Springer.
11. G. A. VOTH, A. LAPORTA, A. M. CRAWFORD, J. ALEXANDER, AND E. BODENSCHATZ. *Journal of Fluid Mechanics* **469**, 121–160 (2002).
12. S. GOTO AND J. C. VASSILICOS. *Physical Review Letters* **100**(5), 054503 (2008).
13. E. CALZAVARINI, R. VOLK, M. BOURGOIN, E. LÉVÊQUE, J.-F. PINTON, AND F. TOSCHI. *Journal of Fluid Mechanics* **in press** (2009).

Lagrangian statistics of two-dimensional turbulence in a square container

B. Kadoch¹, W.J.T. Bos² and K. Schneider¹

¹ M2P2-UMR 6181 CNRS CMI, Aix-Marseille Université, Marseille, France

² LMFA-UMR 5509 CNRS, Ecole Centrale de Lyon-Université Claude Bernard
Lyon 1-INSA de Lyon, Ecully, France
kadoch@L3M.univ-mrs.fr

Two-dimensional decaying turbulence is studied in a square domain to investigate the influence of solid boundaries on the Lagrangian dynamics. It was shown in [1] for a circular geometry, that the vorticity generation at the walls and subsequent detachment strongly influence the velocity increment and acceleration statistics. In the present work we assess the influence of the geometry by considering a square domain. The recirculation zones in the corners and the generation of a large-scale swirling flow [2, 3] could influence the statistics. Therefore we compare the Lagrangian statistics of decaying flows in a square and in a circular domain. The numerical set-up is described in [1, 4] and the Lagrangian statistics are averaged over 10^4 trajectories. The numerical resolution is $N = 1024^2$. The initial eddy turn over time is $T_e = 1/\sqrt{2Z} = 0.12$ and the initial Reynolds number is $Re = L\sqrt{E}/\nu = 3 \cdot 10^4$, where E is the initial kinetic energy and $L = 2\pi * 10/11$ is the size of the square.

The visualization of the vorticity field at $85T_e$ in Fig. 1 (left) reveals that vortices are created near the wall. Three typical trajectories are plotted in Fig. 1 (right). The particles can proceed in almost straight lines, spiraling motion and are accelerated or slowed down near the wall.

In Fig. 2 (left) the PDFs of the time-averaged Lagrangian velocity increments, defined by

$$\Delta u_L(\tau) = \langle u_L(t + \tau) - u_L(t) \rangle_t, \quad (1)$$

are shown ($\langle \cdot \rangle_t$ denotes the time average) for the square and circular domain. For small τ , the PDF of the Lagrangian velocity increments tends to the Lagrangian acceleration PDF and for large τ it tends to the PDF of the Lagrangian velocity. The behavior for small τ is clearly different for both geometries. The PDFs of Lagrangian acceleration present extreme values for both cases compared to the PDFs obtained in the double periodic case [1]. Furthermore, all the PDFs nearly collapse in the center. However, heavy tails are observed in the circle. This is confirmed by Fig. 3 (left) which shows the

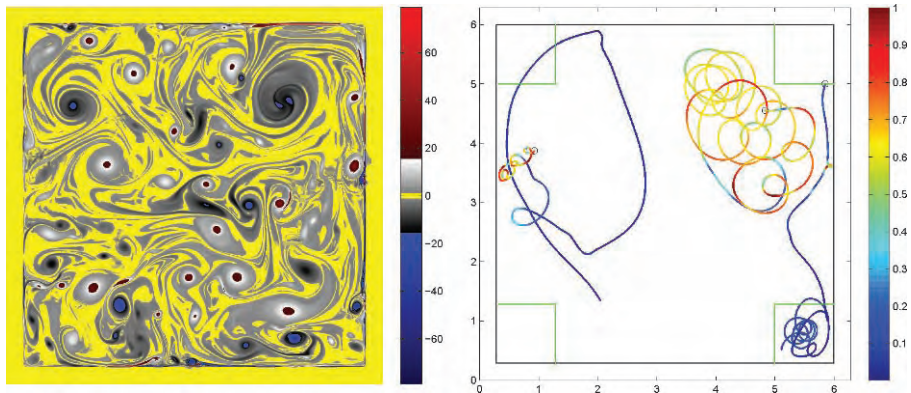


Fig. 1. Left: Vorticity field at $\tau = 85 T_e$. Right: Three typical trajectories in the square geometry. Each trajectory is colored with the modulus of Lagrangian acceleration normalized by its maximum value: $|\mathbf{a}_L(t)|/\max(|\mathbf{a}_L(t)|)$, where $\max|\mathbf{a}_1| = 10.36$, $\max|\mathbf{a}_2| = 7.93$ and $\max|\mathbf{a}_3| = 14.89$ for the particles 1, 2 and 3 from left to right, respectively. The circles indicate the initial position of the particles.

PDFs of Lagrangian acceleration and velocity for the two geometries. The PDFs of Lagrangian velocities are qualitatively very similar to the ones obtained for the circular case [1]. Indeed a small cusp around zero is observed which corresponds to a large probability to get almost zero velocity due to the no-slip condition. Moreover, Fig. 3 (right) presents the flatness of the Lagrangian velocity increments for both geometries. At small τ the flatness tends to a value of 18 for the square geometry which is stronger than for the circular geometry where the maximum flatness is 11. This indicates that the flow in the square from a Lagrangian viewpoint is more intermittent. At large τ , the flatness for the two cases collapses with a value close to 3 which corresponds to a Gaussian distribution.

In the following we investigate the role of the corners with the aim to understand which part of the flow domain is responsible for the increased flatness for small τ . This influence is investigated by considering four squares attached to the four corners of the main square, as illustrated in Fig. 1 (right). First, we choose an arbitrary size $r_c \leq S$ (S is the half side length of the square) which defines the squares in the fluid domain. Then we separate the statistics into two parts, inside (denoted by $a_{L_{r < r_c}}$) and outside ($a_{L_{r > r_c}}$) the selected subdomain. The flatness of the conditional Lagrangian acceleration $a_{L_{r < r_c}}$ is defined as

$$F_{a_L}(r_c) = \frac{\langle a_{L_{r < r_c}}^4 \rangle}{\langle a_{L_{r < r_c}}^2 \rangle^2}, \quad (2)$$

where $\langle \cdot \rangle$ denotes the ensemble average for the particles confined to subdomains defined by the size r_c . Thus, a single trajectory can contribute to both

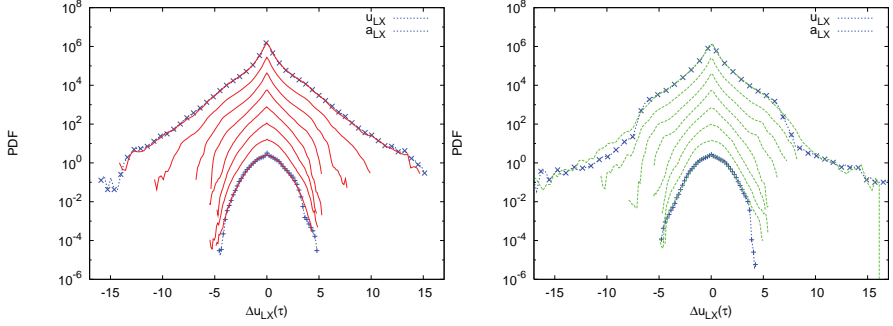


Fig. 2. PDFs of normalized Lagrangian velocity increments $\Delta u_L(\tau)/\sigma(\tau)$ where $\sigma(\tau) = \langle (\Delta u_L(\tau))^2 \rangle^{1/2}$, in the square (left) and the circle (right). The curves are shifted vertically for clarity. From top to bottom: $\tau = 0.2, 0.4, 0.8, 1.6, 3.2, 6.4, 12.8$ and 25.6 .

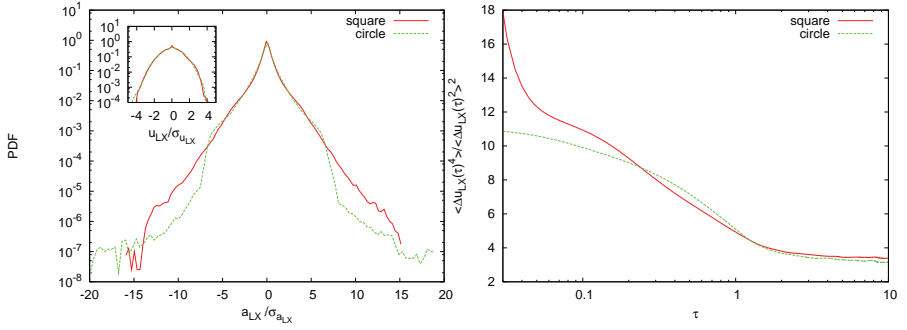


Fig. 3. Left: PDFs of normalized Lagrangian acceleration a_L/σ_{a_L} where $\sigma_{a_L} = \langle a_L^2 \rangle^{1/2}$ ($\langle \cdot \rangle$ denotes the ensemble average) for the square and the circle; inset PDFs of normalized Lagrangian velocity u_L/σ_{u_L} where $\sigma_{u_L} = \langle u_L^2 \rangle^{1/2}$. Right: Flatness of the Lagrangian velocity increments as a function of τ for both geometries.

regions.

The conditional flatness, in Fig. 4, enables us to see the influence of the corners in square geometry. For increasing size r_c , the surface of the four squares becomes larger. Note that $r_c/S = 0.5$ corresponds to the full domain. The highest values of the flatness are found for $r_c/S < 0.2$, which means that the corners are responsible for a strong increase of intermittency. Indeed, the generation of vortices with high intensity by the walls combined with the recirculation zone in the corners could explain this result.

In conclusion, we compared the influence of walls in a square and a circular geometry. The presence of no-slip conditions at the wall creates extreme values in the Lagrangian acceleration, while the Lagrangian velocity exhibits

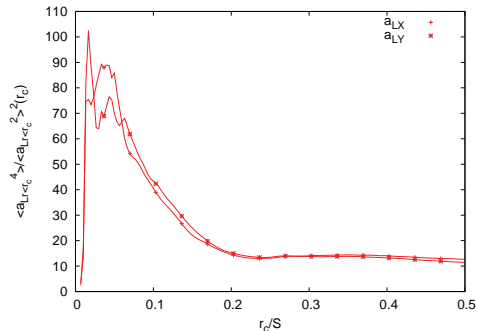


Fig. 4. Conditional flatness of the Lagrangian acceleration as a function of size r_c/S . r_c is the size of four squares drawn from the corners. Note that for the smallest values of r_c/S the statistics have not completely converged.

a Gaussian distribution with a small cusp around zero. In the square, the intermittency is stronger due to the presence of the corners which is revealed by the conditional statistics. This study was performed for decaying flows, the next step will be to investigate the influence of the walls in statistically stationary flows.

References

1. B. Kadoch, W. J. T. Bos and K. Schneider; Extreme Lagrangian acceleration in confined turbulent flow. *Phys. Rev. Lett.*, **100**, 184503, 2008.
2. H. J. H. Clercx, S. R. Maassen and G. J. F. van Heijst; Spontaneous Spin-Up during the Decay of 2D Turbulence in a Square Container with Rigid Boundaries. *Phys. Rev. Lett.*, **80**, 5129, 1998.
3. G. J. F. van Heijst and H. J. H. Clercx; Laboratory Modeling of Geophysical Vortices. *Annu. Rev. Fluid Mech.*, **41**, 143, 2009.
4. K. Schneider, M. Farge; Decaying two-dimensional turbulence in a circular container. *Phys. Rev. Lett.* **95**, 244502, 2005.

Measurement of Lagrangian Particle Trajectories by Digital in-line Holography

G. Gülker, T. Homeyer and J. Peinke

Hydrodynamics and Wind Energy & ForWind, Institute of Physics, Carl von Ossietzky University Oldenburg, D-26111 Oldenburg, Germany
tim.homeyer@uni-oldenburg.de

Summary. A digital holographic in-line setup was used to track particles in a small turbulence chamber. Different particle validation methods have been tested to filter out speckles and to enhance accuracy of the longitudinal particle coordinates. In first measurements particle trajectories were measured and visualized together with fitted spline curves. A pronounced decrease of the standard deviation of the particle coordinates with respect to their spline curves was achieved.

1 Introduction

It is well-known for a long time that most turbulent flows show a highly three dimensional topology. For their investigation some optical methods were developed which are able to measure the complete velocity field within a three dimensional volume of a flow field (3C-3D). Two candidates are Tomographic PIV/PTV with multi-camera arrangements or Holographic PIV, latter traditionally recorded on a high-resolution silver-halide film on a glass plate. The basics of all these techniques are the registration of light reflected from tracer particles which are added to the flow and which are illuminated by short laser pulses. Consecutive recordings of the illuminated volume were taken and evaluated resulting in a complete vector field of the flow velocity. More recently, digital holographic recording on CCD-cameras combined with PIV or PTV analysis techniques has been used.

Digital Holographic PTV techniques can be used to track particles in a turbulent flow. The goal is to measure Lagrangian trajectories to analyze their velocity and acceleration distributions, what is of actual interest for the understanding of fully developed turbulence [1]. Therefore the detection of particle positions, especially their longitudinal or depth positions, has to be optimized. We found that a pronounced improvement can be achieved using particle validation routines.

2 Hologram recording and reconstruction

To determine the characteristics of a turbulent flow we have used in our investigations a digital holographic in-line arrangement with a single camera (Fig. 1). This setup has the main advantage, that it is very compact and simple.

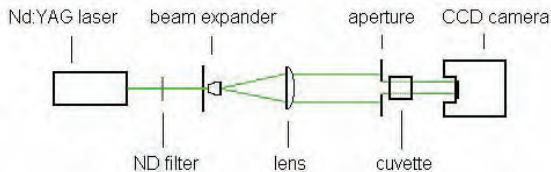


Fig. 1. Digital holographic in-line setup used to record particles in a small cuvette.

The collimated beam of a Nd:YAG laser is used to illuminate the object, e.g. a small turbulence chamber consisting of a glass cube filled with pure water and seeded with $10 \mu\text{m}$ monodisperse polystyrene microspheres. The bottom of the cube can be heated just to produce particle motion. The laser light which is scattered by the particles forms the object light, while the unobstructed light propagates to the CCD sensor and acts as the reference light, thus forming a digital hologram. Since the mainly forward-scattered light is recorded the laser light is used very economically, which is another important advantage of the method. In our experiments we used a Kodak Megaplug ES4.0 camera with $7,4 \mu\text{m}$ square pixels. For performance reasons we only used the inner 1024×1024 pixels.

Before reconstructing the recorded volume the digital holograms are preprocessed to improve their quality. The disturbing interference pattern of stationary objects and reflections are filtered out by respectively subtracting the time average of all holograms.

The reconstruction of the digital holograms is directly performed in the computer. If a hologram $h(x, y)$ is illuminated with the plane reference wave $R(x, y)$ of the wavelength λ , the diffraction image $\Gamma(\xi, \eta)$ in the distance d is described by the Fresnel-Kirchhoff integral [2]:

$$\Gamma(\xi, \eta) = \frac{i}{\lambda} \int_{-\infty}^{\infty} \int_{-\infty}^{\infty} h(x, y) R(x, y) \frac{\exp(-i \frac{2\pi}{\lambda} \rho)}{\rho} dx dy \quad (1)$$

with

$$\rho = \sqrt{(x - \xi)^2 + (y - \eta)^2 + d^2} \quad (2)$$

This reconstruction of the real particle image fields can effectively be realized with different algorithms. We used the Fresnel approximation where ρ is approximated by a Taylor expansion. The whole volume is composed of reconstructed planes of $10 \mu\text{m}$ distance each, allowing the extraction of particle positions.

3 Particle detection, validation and tracking

First of all the well known intensity method is used to extract particle positions. In this method bright spots in the reconstructed planes are determined to get the transversal positions. Their intensity maxima in depth are defined as their longitudinal positions. Main problems of this method are the inaccuracy of the depth position and speckles that are erroneously detected as particles.

To filter out the speckles, different particle validation methods have been presented. Due to the availability of the complete complex wave in the reconstruction planes, one can distinguish between speckles and particles by analyzing the phase signature in the region of the detected particles [3] or look for other particle signatures in the complex wave field [4, 5]. With these validation methods, it is also possible to get more accurate values for the depth position of the particles.

The reconstructed particle fields of subsequently recorded holograms were then processed using a free particle-tracking algorithm [6]. The resulting traces show physical reasonable trajectories in the transversal two-dimensional coordinate view, but in the depth coordinates there are sudden and probably defective jumps in the particle traces due to the limited depth resolution. Thus, the traces in this dimension are fitted with spline functions. The results are three-dimensional trajectories of validated particles in a reconstructed volume of $7,6 \times 7,6 \times 20 \text{ mm}^3$ (Fig.2). They indicate the onset of a slow convective flow in which most of the particles move upwards caused by slightly heating the bottom of the cuvette.

To compare the different particle validation methods the spline curves for the reconstructed particle fields validated with the different methods are assumed to be the true trajectories. The comparison of the standard deviations of the particles to their spline curves indicates, that the *complex amplitude method* [4] seems to be most suitable to enhance the longitudinal accuracy of the particle positions. For our experimental realization we reached an enhancement of the standard deviation from $102,4 \mu\text{m}$ for the intensity method to $76,2 \mu\text{m}$ for the complex amplitude method.

4 Conclusions

Trajectories of particles following a slow convection flow have been tracked with a digital in-line holography approach. To enhance the depth position of particles different particle validation routines were compared. The uncertainty could thus be reduced by about 26%.

Prospectively, cameras with frame rates higher than the Kolmogorov time scale [7] can be utilized to measure Lagrangian particle trajectories in three spatial dimensions and to obtain e.g. Lagrangian velocity and acceleration

distributions in a convenient turbulent flow. The next steps are further improvements of particle positions and particle tracking for longer time periods.

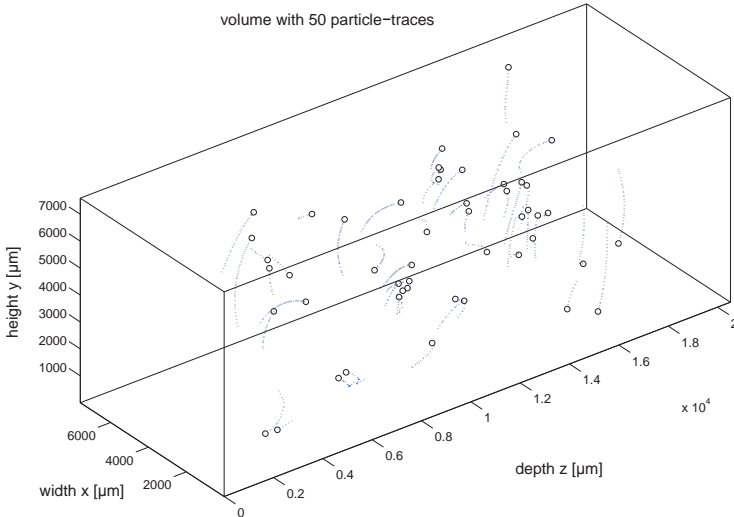


Fig. 2. 3D particle trajectories in a small water-filled glass cube. The particles have been tracked over 50 reconstructed volumes with a framerate of 7,5 *fps*.

References

1. A. La Porta, G. A. Voth, A. Crawford, J. Alexander, and E. Bodenschatz, "Fluid particle accelerations in fully developed turbulence", *Nature* 409, 1017-19 (2001)
2. U. Schnars and W. P. O. Jüptner, "Digital recording and numerical reconstruction of holograms", *Measurement Science and Technology* 13, R85-R101 (2002)
3. W. Yang, A. B. Kostinski, and R. A. Shaw, "Phase signature for particle detection with digital in-line holography", *Opt. Lett.* 31, 1399-1401 (2006)
4. G. Pan and H. Meng, "Digital Holography of Particle Fields: Reconstruction by Use of Complex Amplitude", *Appl. Opt.* 42, 827-833 (2003)
5. J. de Jong and H. Meng, "Digital holographic particle validation via complex wave", *Appl. Opt.* 46, 7652-7661 (2007)
6. J. C. Crocker and D. G. Grier, "Methods of Digital Video Microscopy for Colloidal Studies", *Journal of Colloid and Interface Science* 179, 298-310 (1996)
7. N. T. Ouellette, H. Xu, E. Bodenschatz "A quantitative study of 3D Lagrangian particle tracking algorithms", *Exp. in Fluids*, Vol. 40, I. 2, 301-313 (2005)
8. J. Lu, J. P. Fugal, H. Nordsiek, E. W. Saw, R. A. Shaw, W. Yang, "Lagrangian particle tracking in three dimensions via single-camera in-line digital holography", *New J. Phys.* 10, 125013, 24pp (2008)

3-D Particle Tracking Velocimetry (PTV) in gas flows using coloured tracer particles

Dominique Tarlet¹, Christian Bendicks², Robert Bordás,¹
Bernd Wunderlich¹, Dominique Thévenin¹, and Bernd Michaelis²

(1) Inst. für Strömungstechnik und Thermodynamik (ISUT)

(2) Inst. für Elektronik, Signalverarbeitung und Kommunikationstechnik (IESK)
Otto-von-Guericke-Universität, Universitätsplatz 2, 39106 Magdeburg, Germany
dominique.thevenin@ovgu.de

Although relatively often used for liquid flows, Particle Tracking Velocimetry (PTV) is still considered as a major challenge in gaseous flows. One of the main objections is the higher tracer density necessary for gaseous measurements [1, 2], resulting from higher characteristic speeds and smaller space- and time-scales of the important flow structures. Nevertheless, the widely recognized interest of Lagrange-based measurements (such as PTV) for the investigation of turbulence and vortical structures in real flows [3] is a sufficient reason to face all these challenges. The solution proposed in this work is to employ coloured particles and use the associated separation into different colour classes. Considering separately each resulting colour class, the apparent particle density is decreased without restrictions in the measurement accuracy.

Colour recognition of tracer particles is realised by means of an Artificial Neural Network (ANN), treating the raw information out of the Bayer-Pattern (G-R/B-G) sensors of the cameras. As a consequence, the 3-D correspondence problem becomes immediately easier to solve concerning two neighbour tracer particles of different colours. Furthermore, considering a single colour class for the lagrangian reconstruction of trajectories makes it cheaper in terms of computations. The technique described in this paper for particle colouring is easily reproducible by other researchers, and a new training of the ANN would enable the recognition of different colour shades produced by different pigments. The applied PTV technique (500 Hz, exposure time : 1 ms) is used to locate the particles in 3-D in a small Eiffel wind tunnel. The test section contains 3 winglets, employed to create locally various flow conditions (recirculation, streamline curvature, acceleration) as documented in companion CFD simulations. Using these simulations, the ability of coloured tracer particles to respond to a steep change in the velocity of a gaseous flow is quantified through the Stokes number, Eq. 1. This is done by assuming a Stokes flow around the tracer particles [4], while τ_f is the characteristic time-scale of the

gaseous flow, obtained by dividing a characteristic scale by a characteristic velocity, both issued of companion simulations.

$$\tau_p = \frac{1}{18} \frac{\rho_p d^2}{\rho_f \nu}, \quad \tau_f = \frac{l_{char}}{V_{char}}, \quad Stk = \frac{\tau_p}{\tau_f} \quad (1)$$

Monochrome indexed images are used, with raw information from a G-R/B-G Bayer Pattern ("input data", see Fig.1) delivered to the entry layer of the ANN as a feature vector of 12 elements [5]: The 9 values of the pixels around the next green one, plus the 2-D coordinates on the image and one integer function of the location of the next green pixel on the Bayer pattern (0: there, 1: right, 2: left, 3: below, 4: above).

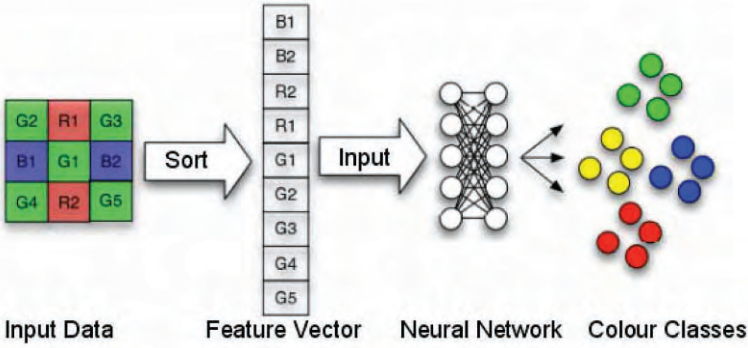


Fig. 1. ANN principle for colour classification

In order to train the ANN, the wind tunnel is first seeded exclusively with red or green or blue Expanded Micro Spheres (EMS®) particles of 70 μm diameter, leading to a training file composed of 5000 feature vectors for each colour. The training algorithm is based on back-propagation, activated through 5000 steps. The resulting ANN is then tested against a set of 100 feature vectors of each colour, randomly sampled among non-training data. For each colour, the percentage of effectively recognized vectors is called "Recognition rate". Excellent results are obtained, with a typical recognition rate exceeding 90% : 97% for red, 91% for green, 85% for blue.

Besides solving the 3-D correspondence problem, calibration of each camera is required to compute 3-D coordinates. Calibration means determining the extrinsic and intrinsic parameters of the used camera model. Extrinsic parameters define the location and orientation of the camera reference frame with respect to a known world frame. The intrinsic parameters characterize the optical, geometric, and digital properties of the camera. The mathematical formulation of the camera model is expressed by the collinearity equations,

which describe the transformation of 3-D world coordinates to 2-D image coordinates [6]. To compute the unknown camera parameters a set of well-known 3-D coordinates is needed, which can be mapped to their corresponding positions in camera images. For this purpose the image of a calibration target (Fig.2, left) is captured for each camera. For each mark two colinearity equations are set up (one for each image coordinate). This leads to an over-determined equation system, solved by the least-squares method. To search for tracer correspondences in camera image triples the epipolar geometry is utilized as described by Maas [1]. Indeed, the number of candidates is now limited to tracer positions near to intersections of epipolar lines (Fig.2, right). For a further reduction of ambiguities, the colour information can now be used.

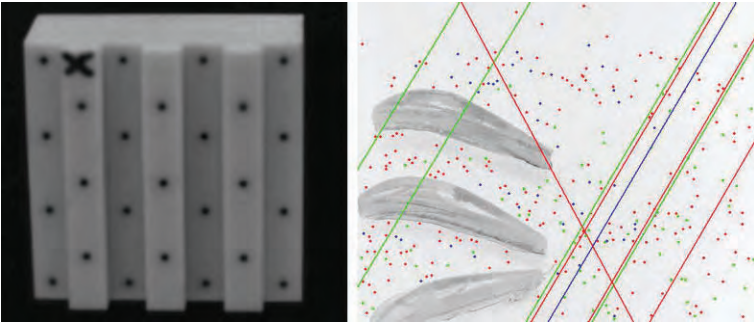


Fig. 2. Calibration target (left) and example of correspondence search using epipolar geometry and considering colour (right)

Finally, the 3-D coordinates are treated by a Tracking algorithm, as it is done by different authors [7, 8]. The presently employed PTV method uses the specific algorithm of Crocker and Grier [9] to link locations of the N particles present at a given step of time. Colour information is also taken into account. The principle of this algorithm relies on the squared displacement δ_i^2 between the point of ID i and its corresponding candidate at the next step of time. This algorithm actually minimizes the *sum* of these squared displacements, $\sum_{i=1}^N \delta_i^2$. More efficient algorithms taking into account a criterion of minimum acceleration [3] are presently being tested.

The obtained results (Fig. 3) demonstrate that the complete 3-D PTV procedure is working very well in the considered flow, involving organized structures, and is able to reveal small-scale recirculating flow (millimeter size) and simultaneously long, uninterrupted and curved trajectories. This constitutes an ideal complement to other measuring techniques such as Particle-Image Velocimetry. Present tests show the possibility of extending this method for later investigations involving a higher number of colours, higher velocities and small-scale turbulent structures.

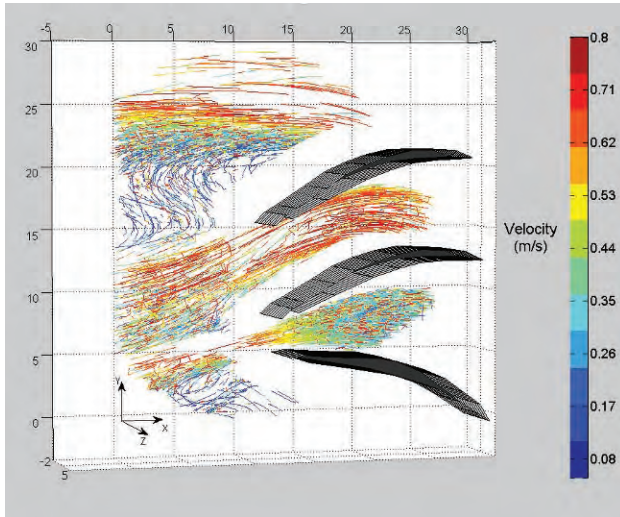


Fig. 3. 3-D PTV results of velocity magnitude around the three winglets, using three different tracer particle colours (scale in mm)

References

1. H.G. Maas, *International Archives on Photogrammetry and Remote Sensing*, **XXIX**, 102-107 (1992).
2. T. Netzsch and B. Jähne, Ein schnelles Verfahren zur Lösung des Stereokorrespondenz-Problems bei der 3D-Particle Tracking Velocimetry, Eds. J. Pöpl and H. Handels, Springer Verlag (1993).
3. N.T. Ouelette, H. Xu and E. Bodenschatz, *Experiments in Fluids*, **40**, 301-303 (2006).
4. C.T. Crowe, *Multiphase flow handbook*, Eds. Taylor & Francis (2006).
5. R. Kuhn, R. Bordás, B. Wunderlich, B. Michaelis and D. Thévenin, 10th International Conference on Engineering Applications of Neural Networks, Thessaloniki, Greece, 387-394 (2007).
6. T. Luhmann, *Nahbereichsphotogrammetrie*, Wichmann-Verlag, Heidelberg (2000).
7. D. Papantoniou and T. Dracos, *Advances in turbulence*, Ed. Hernholz and Fiedler, Springer Verlag **2** (1989).
8. N. Kasagi and Y. Sata, *Sixth International Symposium on Flow Visualization*, 832-837 (1992).
9. J.C. Crocker, D.G. Grier, *Journal of Colloid and Interface Science* **179**, 298 (1996).

Two-particle dispersion in 2D inverse cascade turbulence and its telegraph equation model

Atsushi MIZUTA, Sadayoshi TOH and Takeshi MATSUMOTO

Division of Physics and Astronomy, Graduate School of Science, Kyoto University
Kitashirakawa Oiwakecho Sakyo-ku, Kyoto 606-8502, Japan
atsushi at kyoryu.scphys.kyoto-u.ac.jp

1 Introduction

How the distance between two fluid particles advected by a turbulent flow evolves in time is one of the fundamental questions in turbulence research. The final goal of this two-particle dispersion problem is to describe the probability density function (PDF) of the dispersion $P(r, t)$, which gives probability to have a pair of particles whose relative distance is r at time t . L.F. Richardson made the first attempt to phenomenologically derive an equation of $P(r, t)$

$$\partial_t P = \partial_r [r^{d-1} K(r) \partial_r (P/r^{d-1})] \quad (1)$$

where d is the spatial dimension and the diffusion coefficient is given by the inertial range scaling as $K(r) \propto \epsilon^{1/3} r^{4/3}$ with the energy dissipation rate ϵ .

Since then a number of models have been proposed by extending this type of the diffusion equation of $P(r, t)$ (see e.g. [1]). Here we consider the recently proposed equation in Ref.[2]:

$$(T_c(r)/\lambda) \partial_t^2 P + \partial_t P = \partial_r [K(r) r^{d-1} \partial_r (P/r^{d-1})] + \sigma \partial_r (v(r)P), \quad (2)$$

which is called self-similar telegraph model. The characteristic time and velocity $T_c(r), v(r)$ are determined by the Kolmogorov scaling, namely $T_c(r) \propto \epsilon^{-1/3} r^{2/3}$, $v(r) \propto \epsilon^{1/3} r^{1/3}$. The importance of this telegraph model lies in the parameters λ, σ : λ measures strength of persistency (persistency here means that the sign of dr/dt stays the same); σ gives strength of drift, which measures difference in the transition rate between compression $dr/dt < 0$ and expansion $dr/dt > 0$ states. Obviously the parameters λ, σ reflect coherence of the turbulent flow. Another feature of this model is finiteness of the diffusion speed.

The aim of our study is to check whether or not the telegraph model provides a better description of $P(r, t)$ for 2D inverse cascade turbulence. In Refs.[2] such test is made for 2D Boussinesq convection turbulence where the nonlinearity generates successively smaller scale structures (direct cascade of

the temperature variance occurs). Qualitative difference of the advecting turbulences, namely difference between smaller-scale generating and larger-scale generating (inverse cascade) turbulences, is likely to influence the dispersion. Such difference can be captured by the telegraph model since it contains certain information about coherence of the flow, as we shall see.

2 Results and Discussion

In practice the check of the telegraph model may consist of three steps: (i) estimation of the parameters λ and σ from a direct numerical simulation (DNS) of two-particle dispersion in the 2D inverse cascade turbulence; (ii) numerical simulation of the telegraph model with the parameters determined by the step (i); (iii) comparison of $P(r, t)$ or other mean values obtained from the telegraph model (result of the step (ii)) and those obtained from DNS.

So far we are in the middle of the step (ii). We here report the result of the step (i). It is known that the parameters λ, σ can be estimated from PDF of the exit time [2]. As shown in Fig.2, the PDF has a peak around the origin and decreases exponentially at large exit times. From the width of the peak and the exponential decrease, the parameters are estimated as $\lambda = 11$, $\sigma = -0.067$ for the 2D inverse cascade turbulence. For the 2D Boussinesq convection turbulence, the values are obtained as $\lambda = 5.2$, $\sigma = 0.083$ [2]. The sign of the drift coefficient σ is opposite, which has important consequences.

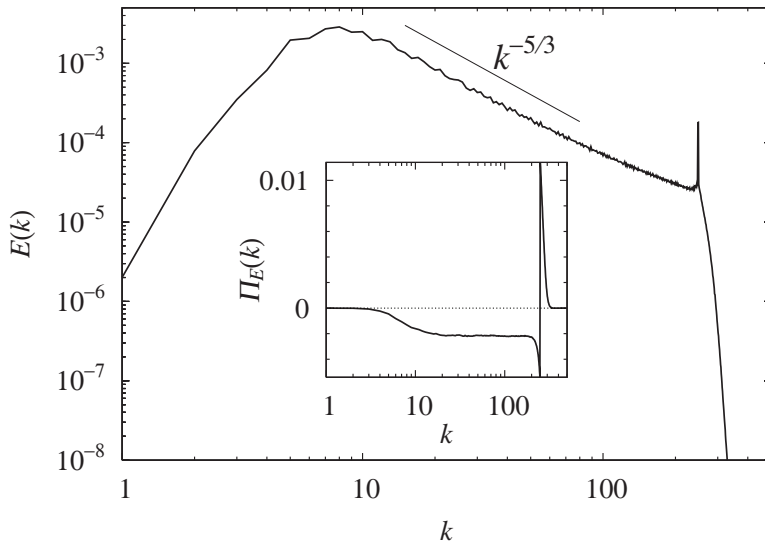


Fig. 1. Energy spectrum and energy flux (inset) of the 2D inverse cascade turbulence (resolution 1024^2 with hyperviscosity and a large-scale friction).

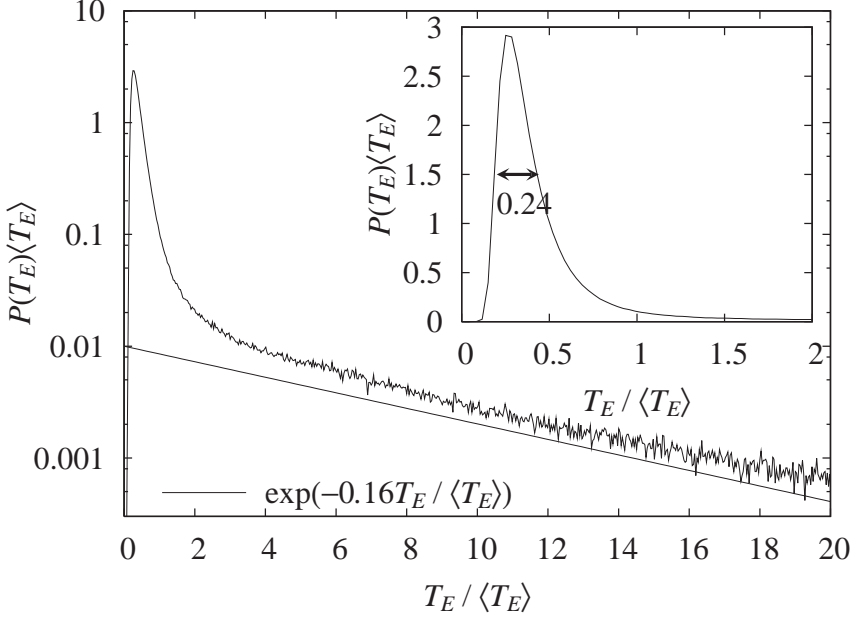


Fig. 2. PDF of the exit time in lin-log and lin-lin (inset) scales. The exit time is defined here as the time needed for the separation r to become $1.1r$.

A way to appreciate this sign difference may be to compare influence of turbulent flow structures on particle pairs. Coherent structures in the 2D Boussinesq convection turbulence are clearly visible in terms of the gradient of temperature $|\nabla T|$ as shown in the left of Fig.3. It is known that around high- $|\nabla T|$ regions, strain rate is also intense [2]. Most of the rapidly expanding particle pairs are clustered around these regions. On the contrary, in the 2D inverse cascade turbulence, no such clustering is observed. Correspondence between the rapidly expanding particle pairs and the flow structures (vorticity, strain field, and stream lines) is not seen as clear as the convection though stagnation points are known to play a major role in Ref.[3]. This kind of impression of the difference out of the rough observation can be quantified by means of the coefficient λ, σ in the telegraph model.

In other words, the telegraph model may offer a new way of quantifying turbulent flows. Until the conference we shall complete our research steps (ii) and (iii) mentioned above with higher resolution DNS.

Acknowledgments:

The numerical calculations were carried out on SX8 at YITP in Kyoto University. This work was supported by the Grant-in-Aid for the Global COE Program "The Next Generation of Physics, Spun from Universality and Emergence" from the Ministry of Education, Culture, Sports, Science and Technology (MEXT) of Japan.

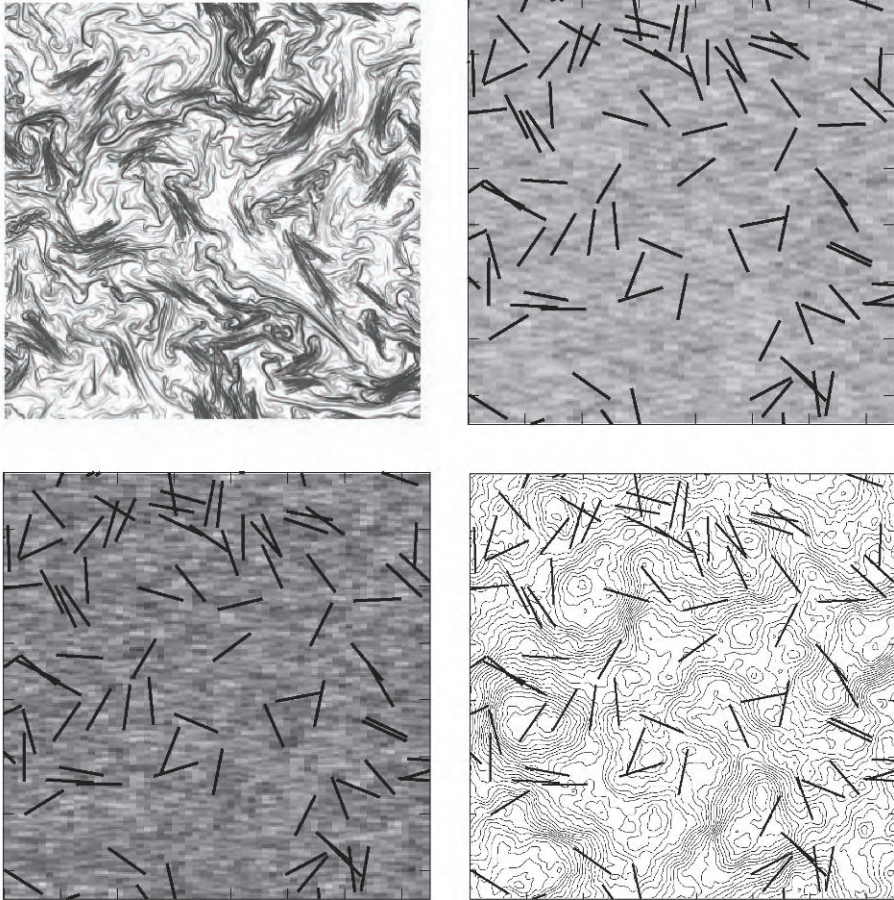


Fig. 3. Snapshot of the rapidly expanding pairs of particle (connected with short lines) and flow structure. Top left: 2D Boussinesq convection turbulence ($|\nabla T|$) [2]. Top right: 2D inverse cascade turbulence (vorticity). Bottom left: 2D inverse cascade turbulence (rate of strain). Bottom right: 2D inverse cascade turbulence (stream lines).

References

1. J.P.L.C. Salazar and L.R.Collins, *Annu. Rev. Fluid Mech.* **41** 405-32 (2009)
2. T.Ogasawara and S.Toth, *J. Phys. Soc. Japan* **75** 083401 (2006); *J. Phys. Soc. Japan* **75** 104402 (2006).
3. S.Goto and J.C.Vassilicos, *New J. Phys.* **6** 65 (2004)

Numerical simulations of particle dispersion in stratified flows

G. Brethouwer and E. Lindborg

Linné Flow Centre, KTH Mechanics, KTH, SE-100 44 Stockholm, Sweden
geert@mech.kth.se

1 introduction

Several researchers have examined the vertical dispersion of fluid particles in stratified flows to obtain a better understanding of mixing in geophysical flows. Pearson *et al.* [5] used a Langevin model to predict that the mean square of vertical fluid particle displacements reaches a plateau with $\langle \delta z^2 \rangle \sim \langle w^2 \rangle / N^2$ at $t \sim N^{-1}$ in stationary stratified flows. Here, w is the vertical velocity fluctuation and N is the Brunt-Väisälä frequency. At long times, they predict that $\langle \delta z^2 \rangle \sim \langle w^2 \rangle t / N$, when molecular diffusion alters the particle density. Venayagamoorthy and Stretch [6] examined the role of the changing particle density on vertical dispersion in DNS of decaying stratified turbulence and observed that after one eddy turnover time diabatic dispersion dominated. Van Aartrijk *et al.* [1] studied particle dispersion in DNS of stationary stratified turbulence and observed a plateau with $\langle \delta z^2 \rangle \sim \langle w^2 \rangle / N^2$ at $t \sim N^{-1}$. However, some of the DNS showed that $\langle \delta z^2 \rangle \sim t$ at long times caused by density changes of fluid particles by molecular diffusion.

In a recent paper we have analysed and derived relations for the vertical dispersion of fluid particles in stratified turbulence [4]. Assuming a statistically stationary and stratified homogeneous turbulent flow and integrating the Boussinesq equations along a fluid particle trajectory, we derived

$$\langle \delta z^2 \rangle = \frac{2}{N^2} \left[\varepsilon_P t \left(1 - \mathcal{O}(\mathcal{R}^{-1/2}) \right) + 2E_P \right] \quad (1)$$

for $t \gg E_P / \varepsilon_P$. Here, ε_P is the dissipation of potential energy, E_P is the potential energy, $\mathcal{R} = \varepsilon_K / \nu N^2$ is the buoyancy Reynolds number, ε_K is the turbulent kinetic energy dissipation and ν is the viscosity. Adiabatic displacements of fluid particles leads to the last term in (1) and gives a finite contribution to long time dispersion. The diabatic dispersion contribution due to the changing particle density is represented by the first term on the right-hand-side of (1) and leads to $\langle \delta z^2 \rangle \sim t$ for $t \rightarrow \infty$. In laboratory experiments or numerical simulations \mathcal{R} is not always large, therefore, the $\mathcal{O}(\mathcal{R}^{-1/2})$ -term

in (1) can give a significant contribution. Relation (1) is expected to be valid when $t \gg T$ where T is an eddy turnover time. Assuming an inertial range at scales larger than the Ozmidov length scale as found in [3] we also derived

$$\langle \delta z^2 \rangle = \frac{2}{N^2} \varepsilon_P t \left[1 + \pi C_{PL} - \mathcal{O}(\mathcal{R}^{-1/2}) \right], \quad (2)$$

for $N^{-1} \ll t \ll E_P/\varepsilon_P$. We estimated that the constant $C_{PL} \approx 3$.

More background on the analysis and relations for vertical dispersion in decaying stratified turbulence can be found in [4]. The aim of this study is to test relations (1) and (2) for the vertical dispersion of fluid particles by numerical simulations.

2 Numerical simulations and results

We have carried out a series of DNS of homogeneous stratified turbulence. Forcing is applied to obtain statistically stationary turbulence. Numerical and physical parameters of the DNS are presented in table 1.

Four sets of simulations are carried out where the buoyancy Reynolds number \mathcal{R} is varied between the sets but is approximately equal for all simulations within each set, while the Froude number $F_h = \varepsilon_K/(NE_K)$, where E_K is the mean turbulent kinetic energy, is varied. The four sets are designated *A*, *B*, *C* and *D*. The Prandtl number, $Pr = \nu/\kappa = 0.7$ in all these simulations. More details on the numerical approach and forcing can be found in [3][2].

Table 1. Numerical and physical parameters of the DNS. L_h/L_v is the aspect ratio of the horizontal to vertical domain size and N_h , N_v are the number of nodes in the horizontal and vertical direction, respectively.

run	F_h	\mathcal{R}	$\frac{L_h}{L_v}$	$N_h \times N_v$
A1	0.03	0.9	2.0	128×80
A2	0.02	0.9	3.3	256×96
A3	0.01	0.9	5.0	512×128
B1	0.1	9.3	2.0	128×80
B2	0.06	9.3	3.3	256×96
B3	0.04	9.5	5.0	512×128
B4	0.03	9.9	6.0	1024×256
C	0.07	38	1.0	512×512
D1	2.2	6200	1.0	128×128
D2	1.6	6200	1.0	256×256
D3	0.8	5900	1.0	512×512

If $\mathcal{R} \gg 1$ the relations (1) and (2) can be written as

$$\langle \delta z^2 \rangle^* = 1 + \frac{1}{2} t^*, \quad t^* \gtrsim 1, \quad (3)$$

$$\langle \delta z^2 \rangle^* = \frac{1}{2} t^* (1 + \pi C_{PL}), \quad F_h \ll t^* \ll 1. \quad (4)$$

Here, $\langle \delta z^2 \rangle^* = \langle \delta z^2 \rangle N^2 / 4E_P$ and $t^* = t/T$ are the nondimensional mean square of the vertical particle displacements and time respectively. The eddy turnover time is defined by $T = E_P / \varepsilon_P$.

Figure 1 shows the time development of $\langle \delta z^2 \rangle^*$ in the DNS together with relations (3) and (4). The initial period shows ballistic dispersion with $\langle \delta z^2 \rangle^* \sim$

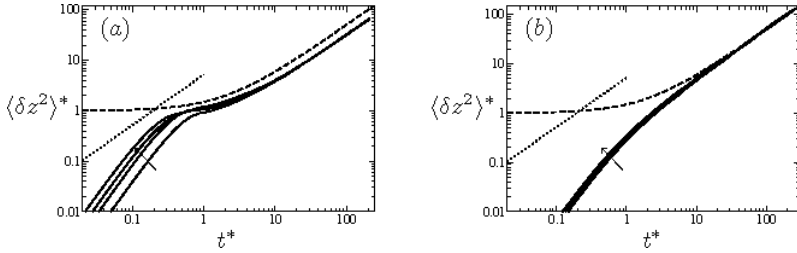


Fig. 1. Time development of $\langle \delta z^2 \rangle^*$ vs. t^* . The dashed and dotted lines show (3) and (4) respectively, and the solid lines DNS results. The arrow indicates the direction of decreasing F_h or increasing Re . (a) B-runs ($\mathcal{R} \simeq 9$) and (b) D-runs ($\mathcal{R} \simeq 6000$).

t^2 . Thereafter, the growth of $\langle \delta z^2 \rangle^*$ slows down. The evolution of $\langle \delta z^2 \rangle^*$ should become independent of F_h when $R \gg 1$ and $F_h \ll 1$ according to our analysis. However, the curves in figure 1(a) still show a clear dependence on F_h for $t^* < 1$. The mean square displacement, $\langle \delta z^2 \rangle^*$, moves closer to the straight line representing (4) as F_h decreases, but no linear range is visible. We must conclude that we have to perform simulations with considerably lower F_h to test relation (4). We also see the onset of a plateau at $t^* \sim 1$ in figure 1(a). Such a plateau has also been observed [1] and indicates that the adiabatic mean square displacement has approached its upper bound $\langle \delta z^2 \rangle^* = 4E_P / N^2$, i.e. $\langle \delta z^2 \rangle^* = 1$. The adiabatic dispersion regime or the onset of a plateau cannot be seen in DNS results with $F_h \gtrsim 1$ displayed in figure 1(b).

After the slow down of vertical dispersion seen in figure 1(a), $\langle \delta z^2 \rangle^*$ grows faster again and approaches the asymptotic diabatic dispersion limit (3) with $\langle \delta z^2 \rangle^* \sim t^*$. Noticeable is that the asymptotic diabatic dispersion limit is seen in DNS with strong as well as weak stratification. Furthermore, the plots show the collapse of $\langle \delta z^2 \rangle^*$ for $t^* > 1$ in DNS with approximately equal \mathcal{R} . The relation (1) predicts that $\langle \delta z^2 \rangle^* \rightarrow t^*/2$ for long times, as \mathcal{R} is increased. We see that the simulation results are consistent with this prediction. Note that the linear growth at late times only can be observed in stationary flows. In decaying stratified turbulence, $\langle \delta z^2 \rangle^*$ goes to a constant [4].

In figure 2(a) most of the runs are collected. All runs initially display ballistic dispersion with $\langle \delta z^2 \rangle \approx \langle w^2 \rangle t^2$. Pearson *et al.* [5] suggested that adi-

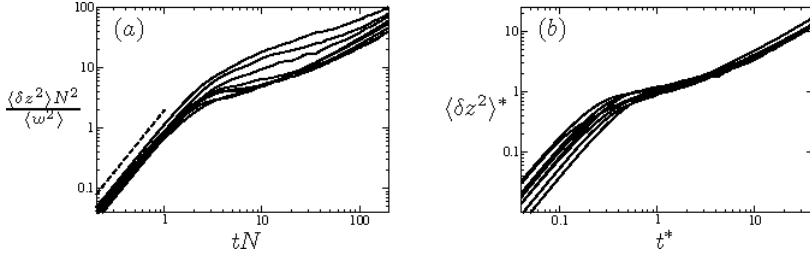


Fig. 2. (a) Time development of $\langle \delta z^2 \rangle N^2 / \langle w^2 \rangle$ and (b) $\langle \delta z^2 \rangle^*$. The solid lines are the results of all A, B and C runs. The dashed line in (a) indicates $\langle \delta z^2 \rangle \sim t^2$.

abatic dispersion should be bounded by $\langle \delta z^2 \rangle \simeq \langle w^2 \rangle / N^2$ and reach this limit at $t \simeq N^{-1}$. This behaviour was observed by [1] in their DNS. In our DNS, scaling of $\langle \delta z^2 \rangle$ and t by $\langle w^2 \rangle / N^2$ and N^{-1} respectively does not lead to a collapse of the adiabatic dispersion plateau in the many DNS. The reason why we do not observe this scaling is that our DNS covers the regime $\mathcal{R} \gtrsim 1$ while [1] considered the regime $\mathcal{R} \lesssim 1$. Figure 2(b) shows the time development of $\langle \delta z^2 \rangle^*$ for the same runs. In accordance with (3) the onset of the adiabatic dispersion plateau appears when $\langle \delta z^2 \rangle \simeq 4E_P / N^2$. However, the range of F_h is too limited to firmly determine whether the onset appears when $t \sim E_P / \varepsilon_P$ ($t^* \sim 1$) or when $t \propto N^{-1}$. Nevertheless, it seems that the DNS data are in better agreement with the prediction by [4]. Venayagamoorthy and Stretch [6] also found that T is the relevant dispersion time scale.

Since the DNS do not reveal a clear inertial stratified turbulence range, we have carried out additional hyperviscosity simulations. Figure 3 shows the time development of $\langle \delta z^2 \rangle^*$ in the hyperviscosity simulations together with relations (3) and (4). For increasing stratification, $\langle \delta z^2 \rangle$ moves closer to expression (4) for the adiabatic dispersion in the inertial range of stratified turbulence with $C_{PL} = 3$ for $N^{-1} \ll t \ll T$, but there is no extended range where it matches the relation.

3 Conclusions

We have used DNS and numerical simulations with hyperviscosity to examine vertical fluid particle dispersion in stationary stratified homogeneous turbulent flows [2]. The DNS are in good agreement with relation (1) for the mean square of the vertical fluid displacements $\langle \delta z^2 \rangle$ derived by [4]. In all DNS,

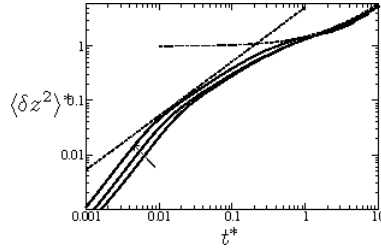


Fig. 3. Time development of $\langle \delta z^2 \rangle^*$. The straight and bent thin dashed lines show relations (4) and (3) respectively. In both plots the solid lines show the result of the hyperviscosity simulations. The arrow indicates the direction of decreasing F_h .

spanning a quite extended range of Froude and Reynolds numbers, $\langle \delta z^2 \rangle$ approaches $2\varepsilon pt/N^2$ in the long time limit. For increasing stratification the adiabatic dispersion contribution moves closer to $2\pi C_{PL}\varepsilon pt/N^2$ with $C_{PL} \sim 3$ for $N^{-1} \ll t \ll T$, according to the simulations with hyperviscosity. However, the growth of $\langle \delta z^2 \rangle$ is somewhat slower than linear even in the simulation with the strongest stratification. We can only speculate that it may require very extended inertial ranges as in geophysical flows to observe the behaviour expressed by (4). At about $t \approx T$ we see the onset of a plateau since the adiabatic dispersion reaches its upper bound $4E_P/N^2$.

References

1. AARTRIJK M. VAN, CLERCX H.J.H. AND WINTERS K.B. 2008 Single-particle, particle-pair, and multiparticle dispersion of fluid particles in forced stably stratified turbulence. *Phys. Fluids* **20**, 025104
2. BRETHOUWER G., AND LINDBORG, E. 2009 Numerical study of vertical dispersion by stratified turbulence. *J. Fluid Mech.*, in press.
3. LINDBORG, E., AND BRETHOUWER, G. 2007 Stratified turbulence forced in rotational and divergent modes. *J. Fluid Mech.* **586**, 83–108.
4. LINDBORG, E., AND BRETHOUWER G. 2008 Vertical dispersion by stratified turbulence. *J. Fluid Mech.* **614**, 303–314.
5. PEARSON, H.J., PUTTOCK, J.S., AND HUNT, J.C.R. 1983 A statistical model of fluid-element motions and vertical diffusion in a homogeneous stratified turbulent flow. *J. Fluid Mech.* **129**, 219–249.
6. VENAYAGAMOORTHY, S.K., AND STRETCH, D.D. 2006 Lagrangian mixing in decaying stably stratified turbulence. *J. Fluid Mech.* **564**, 197–226.

Part II Instability and Transition

Experimental study of the von Kármán flow from $Re = 10^2$ to 10^6 : spontaneous symmetry breaking and turbulent bifurcations

P.-P. Cortet, S. Atis, A. Chiffaudel, F. Daviaud, B. Dubrulle and F. Ravelet

CEA Saclay, IRAMIS, SPEC, CNRS URA 2464, 91191 Gif-sur-Yvette, France
pierre-philippe.cortet@cea.fr

Spontaneous symmetry breaking and bifurcations can be observed in highly turbulent flows. Such phenomena are particularly interesting because they may be considered as laboratory models for changes of states in far-from-equilibrium complex and/or large natural systems.

The von Kármán flow is a closed swirling shear flow produced by two counterrotating impellers in a cylindrical vessel which allows to easily access high Reynolds numbers Re up to 10^6 . In this study, we have used water-glycerol mixtures to scan a wide range of Re from 10^2 to 10^6 . Using stereoscopic PIV, we have been able to measure the three components of the velocity field in a meridian plane of the flow. Our acquisition frequency is moderate, around 10 Hz, but our system is able to record up to 32 000 velocity fields providing a large statistics and highly converged averages.

With exact counterrotation of the impellers ($F_1 = F_2$), the system (cf. fig. 1(a)) is symmetric with respect to any \mathcal{R}_π -rotation exchanging the two impellers (like rotating a sandglass). At low Re , the laminar flow consists of two toric recirculation cells separated by an azimuthal shear layer (cf. fig.

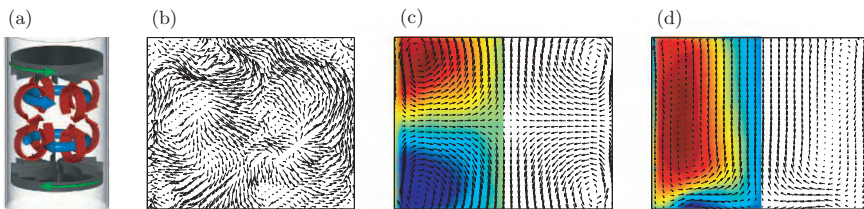


Fig. 1. (a) Schematic view of the von Kármán experiment. We define the Reynolds number as $Re = \pi(F_1 + F_2)R_c^2/\nu$, where F_1 and F_2 are the impellers frequencies, ν the viscosity and $R_c = 10\text{cm}$ the vessel radius. (b-d) Examples of velocity fields in the meridian plane of the von Kármán flow: (b) instantaneous flow, (c) symmetric and (d) bifurcated mean flows.

1(a) and (c)) and reflects the symmetry of the system. At higher Re , as the transition to turbulence occurs, the \mathcal{R}_π -symmetry is only conserved by the time-averaged flow.

When both frequencies differ ($\theta = (F_1 - F_2)/(F_1 + F_2) \neq 0$), the shear layer moves towards the slowest impeller, breaking the \mathcal{R}_π -symmetry, but keeping the two-cells topology (cf. fig. 1(c)) if θ is small. For θ above typically 0.1 to 0.2 depending of the impellers design, the flow switches to a one-cell topology *i.e.* there is only one toric recirculation cell left as illustrated in fig. 1(d).

Furthermore, when the flow is turbulent enough—in the inertial regime—, *i.e.* for $Re \gtrsim 10^4$, we observe the same kind of symmetry breaking occurring spontaneously at exact counterrotation $\theta = 0$. We call such transition between time-averaged flows with different symmetries “turbulent bifurcations”. Of course, such a turbulent bifurcation can be associated—or not associated—with a topological change as in fig. 1(c) and (d). This will be illustrated below with the curved-blades-impellers flow described in ref. [1], rotated in either positive (+) or negative (−) sense, *i.e.* pushing the fluid with the convex or concave faces of the blades.

1 Effect of the Reynolds number: onset of multistability

We use a global quantity—*e.g.* the torque number $K_p = (\Gamma_1 + \Gamma_2)/2$, where $\Gamma_{1,2}$ are the non-dimensional torques—to monitor the flow regimes across the full Reynolds number range (cf. fig. 2). The two lowest curves corresponds to the \mathcal{R}_π -symmetric (*s*) two-cells flows (cf. fig. 1(c)) obtained when both motors are running at the same frequency for both (+) and (−) rotation sense. We observe successively a viscous regime at low Re , the transition to turbulence at intermediate Re and an inertial plateau at high Re [2].

In the (−) sense, this curve is obtained if and only if the two motors are started together and carefully kept at the same frequency at any time. If, above $Re = Re_m \sim 10^4$, one impeller is started first, it pumps the fluid in a one-cell flow and then we observe that running the second impeller does not change the one-cell flow topology. This methods produces two bifurcated regimes (b_1) and (b_2) (cf. fig. 1(d)) which are each other symmetric through \mathcal{R}_π -rotation. These regime give the upper branch (★) in fig. 2, with 3 time more torque.

Finally, one should notice that the three regimes (*s*), (b_1) and (b_2) co-exist for $Re \gtrsim Re_m = 10^4$. This is an example of multistability in turbulence. Bifurcated flows appear stable, *i.e.* once they are created, the way to recover the \mathcal{R}_π -symmetric flow is to stop the motors or at least to decrease Re below Re_m . Ravelet *et al.* have shown that the symmetric state (*s*) is metastable or marginally stable [1]. Therefore, there is a large hysteresis and we consider this turbulent bifurcation as a subcritical bifurcation in Re .

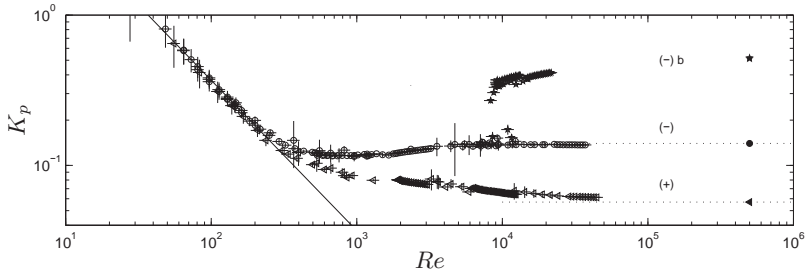


Fig. 2. Non-dimensional torque $K_p(Re)$ for sense (+) (\triangleleft), and sense (-) with symmetric flow (\circ) and bifurcated flow (\star).

For the (+) rotation sense, no such strongly subcritical bifurcation is observed and there is only one branch for K_p at $\theta = 0$. However, the question of \mathcal{R}_π -symmetry breaking occurs in the same Reynolds number range.

Careful PIV measurements shows that, at $\theta = 0$, the shear layer position z_s remains permanently in the equatorial plane $z = 0$ for low Reynolds numbers — $Re \lesssim 10^4$ — only. For higher Re , we observe two effects. In a very narrow range around $\theta = 0$, *i.e.* for $|\theta| \lesssim 0.005$, we observe fluctuations of the mean position $\langle z_s \rangle$ within $\pm 0.2R_c$ with frequent reversals between positive and negative values [3]. So there is an intermediate time scale on which symmetry breaking can be detected but, on very long time scales the mean position is $\langle z_s \rangle = 0$ for $\theta = 0$. This regime recalls the magnetic reversal regime of the geodynamo of the von Karman Sodium (VKS) experiment [4]. In a wider range of θ —for typically $|\theta| \lesssim 0.1$ —, we observe that sensitivity to the asymmetry of the system $\partial \langle z_s \rangle / \partial \theta$ increases with the Reynolds number and seems to saturate above $Re \sim 6 \times 10^4$. These behaviors may be interpreted as a turbulent bifurcation conserving the flow topology. In this case, the bifurcation appears typically of supercritical nature. However, precise and continuous measurements of the amplitude of these two effects —(i) time intermittency between multiple symmetry breaking states and (ii) increase of susceptibility $\partial \langle z_s \rangle / \partial \theta$ — is still an experimental challenge.

2 Controlled \mathcal{R}_π -symmetry breaking

In the previous section, we focused on the turbulent bifurcations observed at —or near— $\theta = 0$ with Reynolds number for control parameter and the absolute torque or the mean shear layer position as order parameter. To understand the global dynamics, it is also necessary to vary the other control parameter, θ , which continuously controls the symmetry of the system itself.

At a given Reynolds number, we perform cycles in θ between $\theta = +1$ and $\theta = -1$, *i.e.* between the two regimes where one impeller is at rest. Such cycles are displayed in fig. 3. The order parameter we present in this paper is

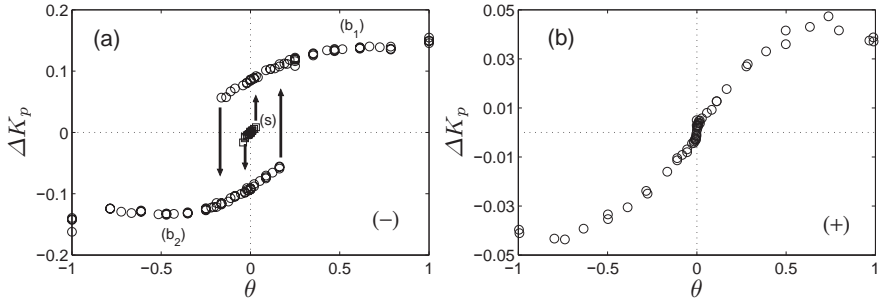


Fig. 3. $\Delta K_p(\theta)$ for both (-) and (+) rotation sense.

the reduced torque difference between both impellers $\Delta K_p = \Gamma_1 - \Gamma_2$. This parameter directly traces back the symmetry of the flow in any flow regime while $\langle z_s \rangle$ is defined only in the two-cell regimes.

For negative (-) rotation sense (cf. fig. 3(a)), the subcriticality in θ is obvious with a large hysteresis cycle between the two symmetric one-cell branches (b_1) and (b_2) surrounding the tiny metastable two-cells branch (s) in the center of the plot. However, for positive (+) rotation sense (cf. fig. 3(b)), we observe a single almost continuous curve. The topological transition between the non-symmetric two-cells flow and the one-cell flow, near $|\theta| \sim 0.1$, is a continuous transition. However, very close to $\theta = 0$, the curve shows a small but sharp transition from negative to positive torque difference between $\theta = -0.005$ and $\theta = +0.005$, *i.e.* in the region of the fluctuations and reversals of the shear layer position. Such behavior is characteristic of a noisy subcritical transition where the hysteresis region is replaced by a region where the different regimes are explored successively along time.

3 Conclusion

We observed two very different examples of turbulent bifurcations occurring above $Re \sim 10^4$. These bifurcations seem really specific of fully developed turbulent flows and correspond to new transitions with spontaneous symmetry breakings—at least on certain intermediate time scales—in the fully turbulent regime at high Reynolds number.

References

1. F. Ravelet *et al.*, Phys. Rev. Lett., **93**, 164501, (2004).
2. F. Ravelet, A. Chiffaudel and F. Daviaud, J. Fluid Mech. **601**, 339 (2008).
3. A. de la Torre and J. Burguete, Phys. Rev. Lett., **99**, 054101 (2007).
4. M. Berhanu *et al.*, Europhys. Lett. **77**, 59007 (2007).

Flow reversals in a vertical channel

J.-C. Tisserand, M. Creyssels, M. Gibert, B. Castaing, and F. Chilla

Ecole Normale Supérieure - Université de Lyon, 69007 Lyon, France
jean-christophe.tisserand at ens-lyon.fr

Convection is one of the most relevant heat transport mechanism and we can find it in many situations as for example geophysics or astrophysics. We study it in a vertical channel which links two chambers, the cold one at the upper end and the hot one at the lower end. In the channel, the flow is either globally ascending in the right part, and descending in the left one, or the opposite. Thus, we can see flow reversals and they can be characterized by a time τ . It is worth noticing that reversals can be found in other situations such as for example with earth magnetic field or in the recent magnetic turbulent dynamo experiment [1]. Here, we study the variation of τ with the difference of temperature δT between the hot plate and the cold plate.

For the experiments, the cell, filled with water, is constituted of a Rayleigh-Benard's cell with two horizontal plates : the upper is cold and the bottom one is hot. The section of the cell is $40 \times 10 \text{ cm}^2$ and its height is 40 cm. The thickness of the walls, made with PMMA, is 2 cm. Furthermore, two honeycomb structures allow to prevent convection from appearing in about 50% of the cell and, as we can see on Fig. 1, between these structures, the channel, which is the zone of interest, has a cross section of $10 \times 10 \text{ cm}^2$ and its height is 20 cm. Besides, the temperature of the upper plate is regulated by water bath and thanks to resistors, Joule effect heats the bottom plate.

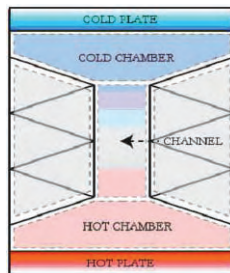


Fig. 1. Picture of the cell.

To measure the difference of temperature, we use thermistors inserted into the plates. Moreover, we record images of the channel, obtained by shadow-graph, thanks to a camera with a frequency of 1 Hz. Each measurement lasts three weeks and it allows to have several thousands of flow reversals. Looking at the correlation between two successive images, we can deduce in real time if the flow in the channel is globally descending in the left part, and ascending in the right one ($\epsilon = 1$), or the opposite ($\epsilon = -1$). We thus define the function $\epsilon(t)$, whose auto correlation:

$$C(t) = \langle \epsilon(t' + t)\epsilon(t') \rangle \quad (1)$$

characterizes the dynamics of these reversals. As a first step, we can try to extract a characteristic time for the reversals from $C(t)$. With a simple model, where the probability of a reversal during the time interval dt is dt/τ , with a constant τ , it can easily be shown that $C(t) = e^{-2t/\tau}$. An exponential fit of $C(t)$ gives τ , which is shown on Fig. 2, versus the difference of temperature δT .

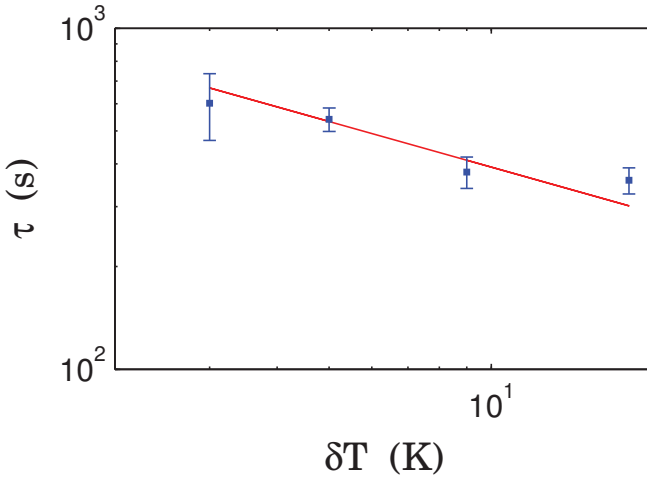


Fig. 2. Characteristic time versus the difference of temperature.

In [2] and [3], it is shown that the driving power Q scales as $(\delta T)^{4/3}$, and that $Q \propto U^3$, where U is the velocity of thermal plumes. Then we can expect $U \propto (\delta T)^{4/9}$, and $\tau \propto (\delta T)^{-4/9}$. Within the large uncertainty, our results are coherent with this scaling. In a second step, we can remark that $C(t)$ do not fit perfectly with an exponential, but rather better with a stretched exponential (see figure 3):

$$C(t) = \exp(-(t/\tau_o)^\beta) \quad (2)$$

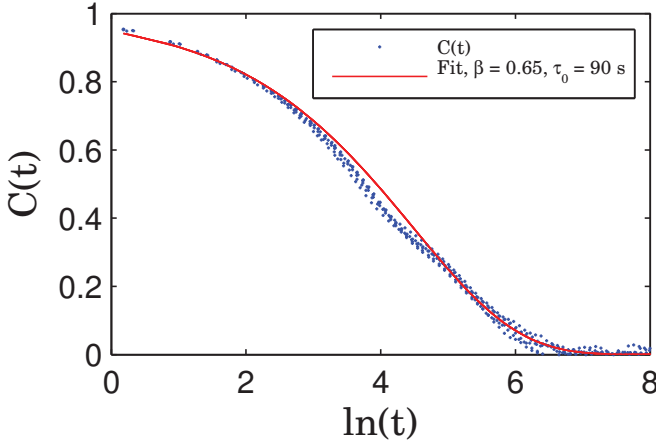


Fig. 3. $C(t)$ versus $\ln(t)$. The slope at the inflexion point gives β .

In the article [4], such a behavior is related to a random distribution of the relaxation times τ . The width of the distribution of $\ln(\tau)$, w , is well estimated by:

$$w^2 = \langle \ln(\tau)^2 \rangle - \langle \ln(\tau) \rangle^2 \simeq \frac{1}{\beta^2} - 1 \tag{3}$$

Such a distribution could reflect the complexity of the flow in the chambers giving rise to the reversals. The same behavior for other reversals phenomena (as earth magnetic field reversals) could also reflect the complexity of the sublying flow.

References

1. Berhanu and al., Magnetic field reversals in an experimental turbulent dynamo, *Europhys. Lett.*, **77**, 59001 (2007).
2. M. Gibert, H. Pabiou, F. Chilla and B. Castaing, High-Rayleigh-Number Convection in a Vertical Channel, *Phys.Rev. Letters*, **96**, 084501 (2006).
3. M. Gibert, H. Pabiou, J.-C. Tisserand, B. Gertjerenken, B. Castaing, and F. Chilla, Heat convection in a vertical channel: Plumes versus turbulent diffusion, *Phys. Fluids*, **21** 035109 (2009)
4. B. Castaing, J. Souletie, Dynamic scaling and non exponential relaxations in the presence of disorder - Application to spin-glasses. *J. Phys. I (Paris)*, **1**, 403-414, (1991).

Linear Instability of Streamwise Corner Flow

F. Alizard^{1,2}, U. Rist², and J.-C. Robinet¹

¹SINUMEF, ENSAM Paris, France; ²IAG, Universität Stuttgart, Germany
rist@iag.uni-stuttgart.de

A streamwise corner is obtained when two flat plates meet at an angle to form a corner parallel to the free-stream flow direction. The interaction of the two boundary layers creates a secondary flow that makes the flow susceptible to separation and early laminar-turbulent transition, which is unwanted. Despite its simplicity, there are not many studies of this flow and current understanding of instability, laminar-turbulent transition, and turbulence is very incomplete. As such, existing computations cannot yet describe premature transition or separation observed in experiments.

On the long term the present work is intended to fill an obvious gap in predicting, understanding, and controlling laminar-turbulent transition in streamwise corners. The laminar base flow for a 90° right-angled corner is considered. Linear stability computations have been performed using a two-dimensional local linear stability theory to compute temporal growth rates and a parabolized stability equations (PSE) approach for spatial growth. These methods have been developed out of previous work by Alizard & Robinet for two-dimensional flows [1].

Typical eigenvalue spectra for both approaches are compared in Fig. 1. The temporal amplification is for $Re = 707$ ($Re_x = 2.5 \times 10^5$) and $\alpha = 0.2$ for comparison with Parker & Balachandar [2]. The spatial case is for the frequency $\Omega = 0.08$ at $Re = 450$ based on the initial position $x_0 = 225$. All data are normalized with respect to the length scale $\delta = \sqrt{2\nu x/U_\infty}$. Different symmetries of the disturbance profiles are possible with respect to the corner bisector: “even modes” whose streamwise velocity is symmetric, and “odd modes” which are antisymmetric with respect to the bisector. On one hand this information was used to reduce the number of unknowns by a factor of 2 (by computing each class of disturbances separately) and on the other hand it was used to verify the code by solving the full problem without symmetry conditions, see Fig. 1. A grid refinement study was performed at the same time to assure the grid independence of the results.

All eigenvalue spectra exhibit a branch of eigenvalues which can be attributed to Tollmien-Schlichting (TS-) modes and an isolated corner mode.

Further insight into these is obtained from their corresponding eigenfunctions, see figures 2-4. The two most unstable eigenvalues are odd and even. They correspond to two-dimensional TS-waves of the flat-plate boundary layer. This can be seen in the eigenmodes of Fig. 2 where the amplitudes develop the shape of a TS-wave far away from the corner, both in y and z direction. Accordingly, the other TS-modes correspond to pairs of oblique waves with increasingly smaller transverse wave lengths, as illustrated by the local maxima in Fig. 3. The even-symmetric modes have a local maximum in the corner. Compared to the odd symmetries where this maximum is absent (see Fig. 2, left) they are more unstable than the odd ones, see Fig. 1.

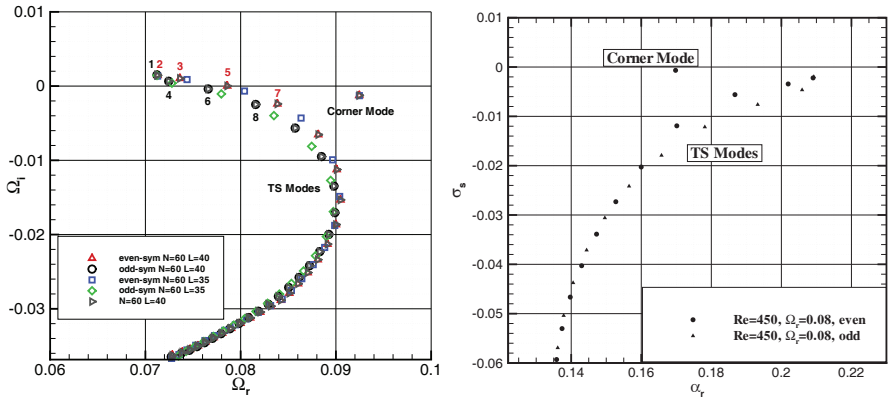


Fig. 1. Comparison of temporal (left) and spatial spectra (right)

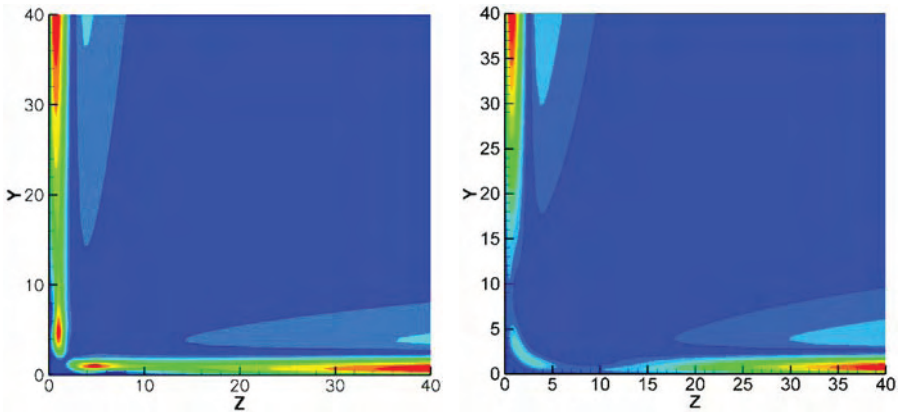


Fig. 2. Streamwise velocity component of the most unstable odd (left) and even (right) temporal TS modes at $Re = 707$ ($Re_x = 2.5 \times 10^5$) $\alpha = 0.2$

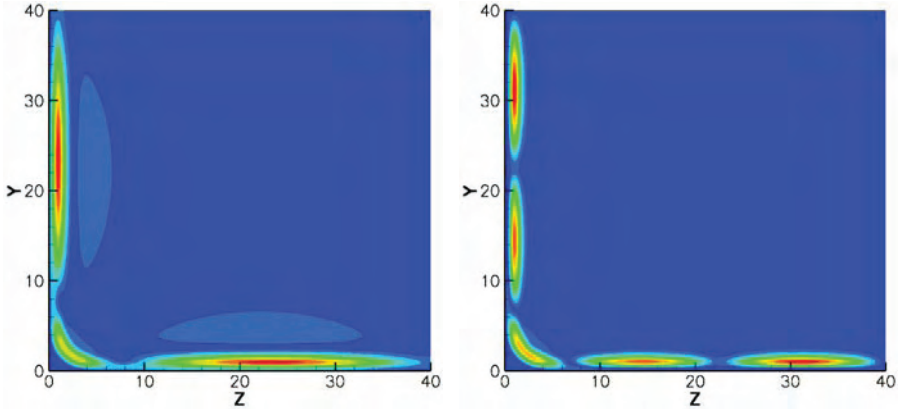


Fig. 3. Streamwise velocity contours of higher (even) TS-modes. Mode 3 (left), mode 5 (right)

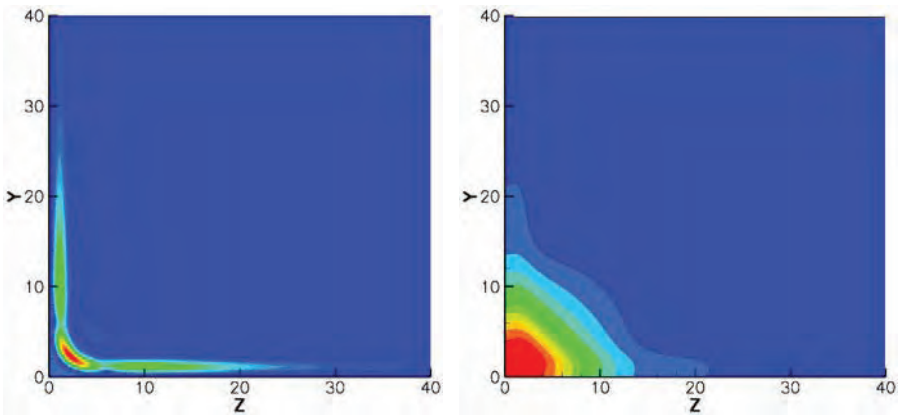


Fig. 4. Spatial structure of the temporal corner mode at $Re = 707$ ($Re_x = 2.5 \times 10^5$) $\alpha = 0.2$. Streamwise velocity component (left) and pressure (right).

The eigenfunctions are essential to classify the eigenvalues. As such, the corner mode shown in Fig. 4 is clearly distinguished by a velocity maximum which rides on the inflection point of the base-flow velocity profile in the corner bisector. Because of this it is supposed to be related to an inviscid instability. Away from the corner and along the plates the corner mode decays. Its relation to the corner is best illustrated in a plot of its pressure eigenfunction in Fig. 4, right.

Even if the corner mode is very close to the border between stable and unstable disturbances, it is never unstable in the present local stability analysis. It seems that the local theory cannot explain why experimentalists ob-

serve a premature laminar-turbulent transition of the corner flow compared to the flat-plate boundary layer. Our comparison with Parker & Balachandar [2] shows close but not identical agreement. The latter can be attributed to slight differences in the computed base flow, which is very sensitive, cf. Ridha [3]. This aspect is now further investigated in the work of Alizard *et al.* [4].

However, extending our computations to a full PSE that follows a given frequency in downstream direction such that non-parallel growth of the flow is no longer neglected, we made an unexpected observation, shown in Fig. 5. Non-parallel effects are irrelevant for the TS modes as in the case of the Blasius boundary layer, but the corner mode which was stable before now becomes unstable as well. Different non-parallel criteria will be studied in order to determine precisely the critical Reynolds number associated with the corner mode. This discovery could help to explain experimental results.

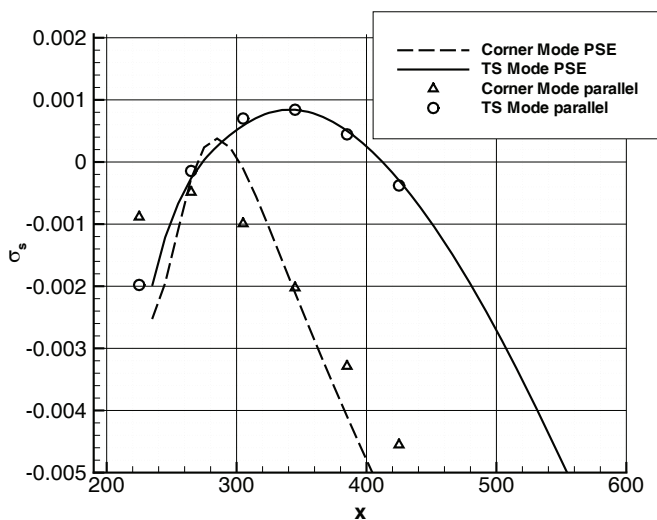


Fig. 5. Comparison of parallel theory with PSE analysis for $\Omega = 0.08$

References

1. F. Alizard, J.-C. Robinet: Spatially convective global modes in a boundary layer, *Phys. Fluids.*, **19**: 114105, 2007.
2. S.J. Parker and S. Balachandar: Viscous and inviscid instabilities of flow along a streamwise corner, *Theoret. Comput. Fluid Dynamics*, **13**, 231–270, 1999.
3. A. Ridha: Flow along streamwise corners revisited, *J. Fluid Mech.* **476**, 223–265, 2003.
4. F. Alizard, J.-C. Robinet, U. Rist: Sensitivity to base flow variation of a streamwise corner flow, Proc. IUTAM Symposium on Laminar-Turbulent Transition, June 23–26 2009, Stockholm, Sweden, 2009.

DNS of turbulent plane Couette flow with emphasis on turbulent stripe

T. Tsukahara, Y. Kawaguchi, and H. Kawamura

Department of Mechanical Engineering, Tokyo University of Science,
2641 Yamazaki, Noda, Chiba 278-8510, Japan
tsuka@rs.noda.tus.ac.jp

1 Introduction

Reverse transition of ‘turbulence \rightarrow laminar’ in wall-bounded shear flows remains poorly understood and few studies have been reported. A plane Couette flow (CF) is conceptually one of the simplest non-trivial fluid dynamics systems, where the flow is solely driven by the shear. This flow is linearly stable for all Reynolds numbers, but experiences direct transition to turbulence through the development of localized perturbations (cf. [1] for a discussion). Above some threshold, turbulence is sustained with a complex behavior characterized by laminar-turbulent co-existence in the form of ‘turbulent stripe’. The transition, though well-described experimentally [2], is far from being completely elucidated. On the other hand, a direct numerical simulation (DNS) of intermittently turbulent flows is challenging and requires a huge computational domain so that another strategy has been necessary. For instance, existing numerical studies are limited within frameworks of a semi-realistic model [3] or of a tilted geometry with a minimal domain [4]. However, owing to the recent development of computers, DNS of the subcritical CF is now possible to be performed.

In this study, a series of DNS on CF for the transitional Reynolds-number regime are carried out with the use of a large enough domain compared to a prospective size of the inherent structures. In particular, we focus on how large the turbulent stripe is and on its Reynolds-number dependency. The present Reynolds number is decreased in steps from the fully turbulent regime to an aimed Reynolds number in the transitional regime.

2 Numerical conditions

The flow considered here is bounded by two infinite parallel walls moving at speeds $\pm U_w$ with a distance of 2δ apart. The Reynolds number $Re = U_w\delta/\nu$ (ν the kinetic viscosity) ranges from 500 to 350, while the Reynolds number

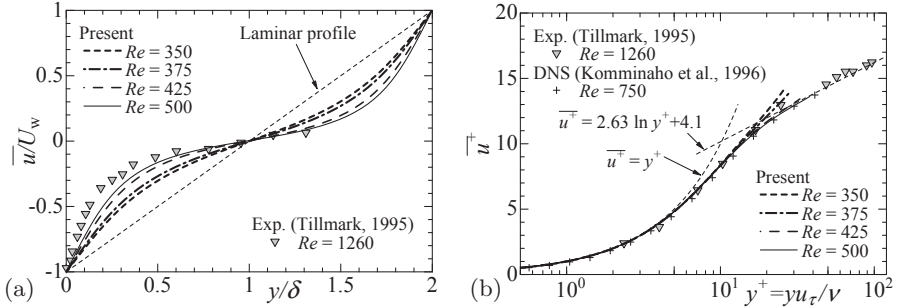


Fig. 1. Mean velocity profile scaled with (a) outer and (b) inner variables.

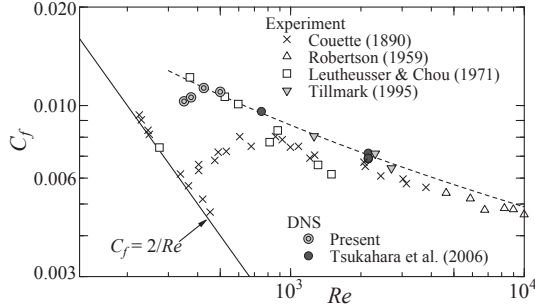


Fig. 2. Skin-friction coefficient as a function of Reynolds number: ---, empirical correlation of Eq. (2) with $G = 0.198$; \times , the data for circular Couette flow [8].

Re_τ based on the friction velocity is 37–21. A cyclic domain size and number of grid points are $L_x \times L_y \times L_z = 409.6\delta \times 2\delta \times 204.8\delta$ and $N_x \times N_y \times N_z = 4096 \times 96 \times 2048$ (x , y , and z are respectively the streamwise, wall-normal, and spanwise coordinates). See [5] for some details of the numerical method. The initial fields were constructed from a featureless turbulent CF (at $Re = 750$) obtained by the earlier work [5]. Note that statistical data and visualized fields are obtained after a flow field has reached statistical-steady state.

3 Results and discussion

The mean velocity profile in Fig. 1 together with DNS data of Komminaho et al. [6] and experimental data of Tillmark [7]. The profiles in Fig. 1(a) exhibit typical S-shape distributions with a distinct trend toward the laminar profile as Re decreased. As given in Fig. 1(b), the universal law of the wall accurately represents, and the logarithmic regions extend right to the channel center, i.e., $y^+ = Re_\tau$. However, a significant deviation from the log law is observed in the cases of $Re = 350$ and 375 , where the turbulent stripe occurs (as shown later). A well-defined demarcation between the fully turbulent regime and the transitional regime with the turbulent stripe may be

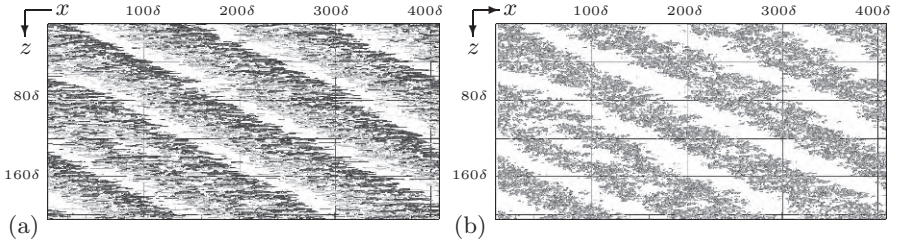


Fig. 3. Top view of the turbulent stripe for $Re = 375$. (a) Light-gray iso-surface represents positive streamwise velocity fluctuation ($u'/U_w > 0.2$), while darker one negative region ($u'/U_w < -0.2$). (b) Iso-surface represents second invariant of deformation tensor, $II'^+ < -0.014$, which is equivalent to the vortical position.

illustrated by Fig. 2, which shows the Reynolds-number dependence of skin friction coefficient. For CF, the friction coefficient is usually defined as

$$C_f = \frac{2u_\tau^2}{U_w^2} \quad (1)$$

Robertson [9] suggested that C_f for the turbulent regime could be predicted from the following expression:

$$\sqrt{\frac{C_f}{2}} = \frac{G}{\log Re} \quad (2)$$

where G is an empirical constant. The present turbulent-friction results including the previous DNS [5] are well fitted by Eq. (2) and in good agreement with existing experimental data [7]–[10], if we take $G = 0.198$. It is of interest that the values for $Re = 350$ and 375 deviate from the empirical correlation.

Figure 3 depicts a typical flow field, which is accompanied by a unique pattern emerging spontaneously from featureless turbulence (at $Re = 500$) as the Reynolds number is decreased down to 375 . Shown in (a) and (b) are the streamwise velocity fluctuation, u' , and the vortical structure in the whole domain, respectively. As seen from the figures, quasi-streamwise streaks and vortices are unevenly distributed. Hence, spatially periodic pattern composed of distinct regions of turbulent and laminar flows can be clearly observed.

In order to examine the scale of the turbulent stripe and its self-contained energy, the pre-multiplied energy spectra $k_i E_{uu}(k_i)$ are given in Fig. 4 as a function of wavelength, $\lambda_i = 2\pi/k_i$. Note that its peak position corresponds to a mean spacing of the most energetic structure. For all of the present Re , the peak in the spanwise component is located at around 4δ (≈ 120 in wall units), which is approximately the same size with well-known spanwise periodicity of the streaks. The streamwise streaks with spanwise separation approximately 4δ are indeed visible at the edge of the turbulent regions. If emphasis is placed on longer wavelengths, an additional peak is detected at $\lambda_x = 137\delta$ and $\lambda_z = 68\delta$ (see Figs. 4(a) and (b)) for $Re \leq 375$, and its peak

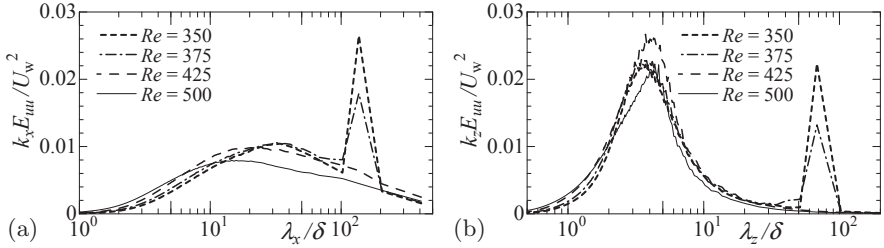


Fig. 4. Pre-multiplied energy spectra for u' at the channel center, $y = \delta$, as a function of (a) streamwise and (b) spanwise wavelengths for various Reynolds number.

value tends to increase with decreasing Re . The angle and total wavelength of the stripe pattern can be dictated by the streamwise wavelength and spanwise one as $\theta = \tan^{-1}(\lambda_z/\lambda_x) = 27^\circ$ and $\lambda = \lambda_z \cos(\theta) = 61\delta$. They are consistent with the visualization shown in Fig. 3, and compare well with the experimentally observations [1, 2]. The fraction of the streamwise kinetic energy can be estimated from the spanwise spectra. For $Re = 350$, about 20% of the energy is associated with long wavelengths ($\lambda_z \geq 51\delta$), namely the turbulent stripe.

4 Conclusion

Results from DNS on a plane Couette flow using a large-scale computational domain show encouraging agreement with experiments [2] and minimal-flow-unit simulations [4], with respect to the turbulent stripe in the transitional regime. The tilt angle to the streamwise direction and the total wavelength of the stripe are 27° and 61δ , irrespective of the Reynolds number.

Acknowledgements: The first author has received support of the Grand-in-Aid for Young Scientist: KAKENHI (#20860070). The present computations were performed with the use of SX-9 at Cyberscience Center, Tohoku University.

References

1. T. Mullin and R. Kerswell, eds., IUTAM Symp. on Laminar-Turbulent Transition and Finite Amplitude Solutions, Springer (2005).
2. A. Prigent *et al.*, Phys. Rev. Lett., **89**, 014501 (2002).
3. M. Lagha and P. Manneville, Advances in Turbulence X, 463 (2004); P. Manneville and M. Lagha, Advances in Turbulence XI, 130 (2007).
4. D. Barkley and L. S. Tuckerman, J. Fluid Mech., **576**, 109 (2007).
5. T. Tsukahara *et al.*, J. Turbulence, **7**(19), 1 (2006).
6. J. Komminaho *et al.*, J. Fluid Mech., **320**, 259 (1996).
7. N. Tillmark, Ph. D. Thesis, Royal Inst. of Tech., Stockholm (1995).
8. M. Couette, Ann. Chem. Phys., **21**, 433 (1890).
9. J. M. Robertson, Proc. 6th Ann. Conf. Fluid Mech., Univ. of Texas, 169 (1959).
10. H. J. Leutheusser and V. H. Chu, J. Hydr. Div., ASCE, **97**, 1269 (1971).

Geometry of state space in plane Couette flow

P. Cvitanović and J. F. Gibson

Center for Nonlinear Science, Georgia Institute of Technology
Atlanta, GA 30332-0430, USA predrag.cvitanovic@physics.gatech.edu

Summary. A large conceptual gap separates the theory of low-dimensional chaotic dynamics from the infinite-dimensional nonlinear dynamics of turbulence. Recent advances in experimental imaging, computational methods, and dynamical systems theory suggest a way to bridge this gap in our understanding of turbulence. Recent discoveries show that recurrent coherent structures observed in wall-bounded shear flows (such as pipes and plane Couette flow) result from close passes to weakly unstable invariant solutions of the Navier-Stokes equations. These 3D, fully nonlinear solutions (equilibria, traveling waves, and periodic orbits) structure the state space of turbulent flows and provide a skeleton for analyzing their dynamics. We calculate a hierarchy of invariant solutions for plane Couette, a canonical wall-bounded shear flow. These solutions reveal organization in the flow's turbulent dynamics and can be used to predict directly from the fundamental equations physical quantities such as bulk flow rate and mean wall drag. All results and the code that generates them are disseminated through our group's open-source CFD software and solution database Channelflow.org and the collaborative e-book ChaosBook.org.

In a seminal paper, Hopf [1] envisioned the function space of Navier-Stokes velocity fields as an infinite-dimensional state space, parameterized by viscosity, boundary conditions, and external forces, in which each 3D fluid velocity field is represented as a single point. As the viscosity decreases, turbulence sets in, represented by chaotic state-space trajectories. Hopf's observation that viscosity causes state-space volumes to contract under the action of dynamics led to his key conjecture: that long-term, typically observed solutions of the Navier-Stokes equations lie on finite-dimensional manifolds embedded in the infinite-dimensional state space of allowed velocity fields.

Recent experimental and theoretical advances [2] support Hopf's dynamical vision of turbulence. Space limitations prevent us from doing justice here to the fundamental 'pipes and planes' work on shear flows by Nagata, Busse, Clever, Waleffe, Holmes, Moin, Moser, Kim, Lumley, Mullin, Jiménez, Kawahara, Eckhardt, Kerswell, Tuckerman, Schmiegel, Barkley, Hof, Viswanath, and others that we build upon; we refer the reader to Refs. [3, 4, 5, 6] for an overview. The preponderance of recurrent, coherent states in wall-bounded

shear flows suggests that their long-time dynamics lie on low-dimensional attractors and might thus be amenable to dynamical systems modeling. The qualitative success and quantitative shortcomings of low-dimensional ‘Proper Orthogonal Decomposition’ models [3] motivate our work [6, 7, 8, 9]: We seek to understand the dynamics of turbulence not through a low- d ODE *model*, but through a hierarchy of *exact invariant solutions* of the *fully-resolved* Navier-Stokes equations. These exact solutions turn out to be remarkably similar in appearance to coherent structures observed in both numerical simulations and experiments.

The correspondence between coherent structures and invariant solutions can be understood in terms of dynamical theory. Invariant sets (equilibria, traveling waves, periodic solutions, relative periodic solutions, their stable and unstable manifolds) *partition* state space. A trajectory within an invariant set stays within it forever, whereas a trajectory that starts outside an invariant set cannot traverse it. Thus the union of invariant sets can explain a good deal of the dynamics, and the structure imposed by invariant solutions enables systematic exploration and characterization of dynamical behaviors.

While the equilibria of a dynamical system (steady states of Navier-Stokes) do not participate in dynamics directly, their stable / unstable manifolds do shape the flow in their vicinity. The simplest time-dependent invariant solutions are periodic orbits (spatiotemporally periodic solutions of Navier-Stokes). Periodic orbits are densely embedded in the natural measure of a chaotic system. Most periodic orbits found in [9] individually capture the mean flow and Reynolds stresses of plane Couette turbulence to within a few percent. Given a hierarchical set of longer and longer such solutions, the ‘trace formulas’ of *periodic orbit theory* [10] should provide a systematic framework for calculating system’s statistical properties (this claim is as yet untested in the context of turbulent fluid flows). Empirically, the geometry and dynamics of attractors are dominated by the *least unstable* periodic orbits. A coarse global description of dynamics is then provided by specifying the sequence of invariant solutions whose neighborhoods are visited by a chaotic trajectory, while linearization about these solutions provides highly accurate local descriptions.

In the following series of papers and our web repository, we take several steps towards realizing these goals for the case of small aspect-ratio plane Couette flow. Ref. [6] describes numerical methods for determining invariant solutions of Navier-Stokes (equilibria, periodic orbits, and their relatives; linearized stability, invariant manifolds) and a method for constructing state-space portraits of the infinite-dimensional Navier-Stokes state space. We find that projections such as Fig. 1.1 onto low- d subspaces spanned by exact equilibrium solutions reveal much about the spatiotemporal structure of turbulent dynamics. The resulting state-space portraits are dynamically invariant, intrinsic, and representation independent, and can be applied to experimental as well as numerical data.

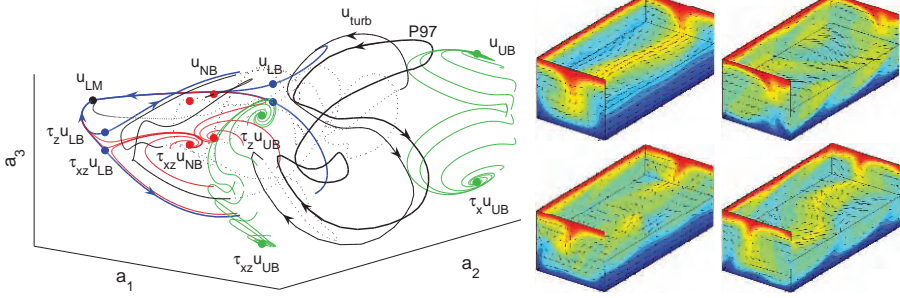


Fig. 1.1. A turbulent trajectory tracking a periodic orbit. (left panel) A turbulent trajectory (dotted line) is shown against the backdrop of unstable invariant structures, projected from 10^5 dimensions to 3. Solid dots and lines indicate equilibria and their unstable manifolds (\mathbf{u}_{LM} is laminar equilibrium). Key portions of the turbulent trajectory are highlighted with solid lines: close passes to a periodic orbit (thick black line) and to the unstable manifolds of several equilibria. A shorter periodic orbit –not labeled here– is also shown. (right panel) Snapshots along the periodic orbit at intervals $\Delta t = 15$, marked by open circles in the left panel, starting at the point labeled $P97$. See [6] for nomenclature and details of the state-space projection. Side-by-side animations of state-space projections and 3D fluid velocity fields given in ChaosBook.org/tutorials are particularly revealing.

Ref. [7] describes eleven equilibrium and five traveling wave solutions of plane Couette flow, most of them new, and demonstrates the robustness of these solutions under variations of Re and aspect ratios. We provide a partial classification of the isotropy subgroups of plane Couette flow and show which subgroups admit of which types of solution. Solutions are found by a novel method of generating initial guesses; namely, we start our searches from the turbulent simulation data, in contrast to more traditional continuations from / bifurcations off the known solutions.

Ref. [8] reports several heteroclinic connections amongst the equilibria solutions and shows that these connections form the backbone of transitions from multiple to single-roll states. Ref. [9] presents twenty new periodic orbit solutions to plane Couette flow and investigates how well they probe the natural measure. Lastly, our online, user-editable database of solutions at www.channelflow.org, aims to promote the rapid dissemination of research results within the community. The website also hosts our public domain high-level software system for plane Couette and channel flows, designed to lower the barrier to entry to research in dynamical systems and turbulence.

Together, these steps lead to a new way of thinking about coherent structures and turbulence: (a) that coherent structures are the physical images of the flow’s least unstable invariant solutions, (b) that turbulent dynamics consists of walk among the set of these unstable solutions.

The long-term goals of this research program are to develop this vision into quantitative, predictive description of moderate- Re turbulence, and to use this

description to control flows and explain their statistics. Open research topics include (a) Symmetry reduction of plane Couette and pipe-flow state space. (b) Construction of Poincaré sections, Poincaré maps, symbolic dynamics, and transition (Markov) graphs. (c) Extension to large and infinite aspect-ratio systems. (d) Predicting turbulent statistics from expansions over periodic orbits.

Acknowledgement. We are indebted to F. Waleffe, D. Viswanath, J. Halcrow, G. Kawahara, L.S. Tuckerman, B. Eckhardt, and D. Barkley for inspiring collaborations and/or discussions. P.C. and J.F.G. thank G. Robinson, Jr. for support. J.F.G. was partly supported by NSF grant DMS-0807574. Special thanks to the Georgia Tech Student Union which generously funded our access to the Georgia Tech Public Access Cluster Environment (GT-PACE).

References

1. Hopf, E.: A mathematical example displaying features of turbulence. *Comm. Pure Appl. Math.* **1** (1948) 303–322
2. Hof, B., van Doorne, C.W.H., Westerweel, J., Nieuwstadt, F.T.M., Faisst, H., Eckhardt, B., Wedin, H., Kerswell, R.R., Waleffe, F.: Experimental observation of nonlinear traveling waves in turbulent pipe flow. *Science* **305**(5690) (2004) 1594–1598
3. Holmes, P., Lumley, J.L., Berkooz, G.: *Turbulence, coherent structures, dynamical systems and symmetry.* Cambridge University Press, Cambridge (1996)
4. Panton, R.L., ed.: *Self-sustaining mechanisms of wall turbulence.* Computational Mechanics Publications, Southampton (1997)
5. Robinson, S.K.: Coherent motions in the turbulent boundary layer. *Annual Review of Fluid Mechanics* **23** (1991) 601–639
6. Gibson, J.F., Halcrow, J., Cvitanović, P.: Visualizing the geometry of state-space in plane Couette flow. *J. Fluid Mech.* **611** (2008) 107–130 [arXiv:0705.3957](#).
7. Halcrow, J., Gibson, J.F., Cvitanović, P.: Equilibrium and traveling-wave solutions of plane Couette flow. [arXiv:0808.3375](#), *J. Fluid Mech.*, to appear (2009)
8. Halcrow, J., Gibson, J.F., Cvitanović, P., Viswanath, D.: Heteroclinic connections in plane Couette flow. *J. Fluid Mech.* **621** (2009) 365–376 [arXiv:0808.1865](#).
9. Gibson, J.F., Cvitanović, P.: Periodic orbits of plane Couette flow. In preparation (2009)
10. Cvitanović, P., Artuso, R., Mainieri, R., Tanner, G., Vattay, G.: *Chaos: Classical and quantum.* Niels Bohr Institute, Copenhagen (2009) [ChaosBook.org](#).

Linear and nonlinear instabilities of sliding Couette flow

K. Deguchi, and M. Nagata

Department of Aeronautics and Astronautics,
Graduate School of Engineering, Kyoto University, JAPAN
nagata@kuaero.kyoto-u.ac.jp

1 Introduction

We consider an incompressible viscous fluid with the kinematic viscosity ν between two infinitely long concentric cylinders with radii a and b ($b > a$). The fluid experiences a shear motion produced by pulling the inner cylinder with the axial speed U while keeping the outer cylinder at rest (see Fig.1). The axial basis flow at the radius r ,

$$U_B(r) = R \frac{\ln(r(1-\eta)/2)}{\ln(\eta)}, \quad (1)$$

can be obtained as an exact solution of the Navier-Stokes equation, where $R = U(b-a)/2\nu$ is the Reynolds number and $\eta = a/b$ is the radius ratio.

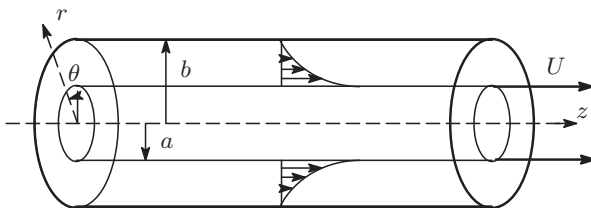


Fig. 1. The configuration of sliding Couette flow.

This flow is classified as sliding Couette flow by [1]. It is known that when the radius ratio is greater than 0.14 the linear critical Reynolds number is infinite [2], so that secondary flows, if they exist, must emerge abruptly from the laminar state. The absence of linear critical states similarly occurs in other problems, such as plane Couette flow [3], pipe Poiseuille flow [4] and flow in a square duct [5]. These flows have been extensively explored with success in recent years. In contrast, sliding Couette flow has attracted much less attention with its finite amplitude solutions still unexplored.

2 Formulation and Numerical Methods

The equations governing the development of disturbances which are superimposed on the basis state (1) are derived and solved numerically. We express disturbances by Fourier series in the axial and the azimuthal directions and Chebyshev polynomials in the radial direction. For a linear stability analysis the eigenvalue problem with the disturbance growth rate as the eigenvalue is solved. For a nonlinear analysis Newton-Raphson iterative scheme is used to obtain non-trivial disturbance amplitudes.

3 Results and Discussion

3.1 Linear Analysis

Our linear stability analysis confirms the results by [2]. Fig. 2 shows that as η is decreased from the narrow gap limit ($\eta = 1$) the neutral curve appears from infinity at $\eta \approx 0.14$, drops sharply taking the minimum at $\eta \approx 1.0$ and ascends sharply toward infinity as η approaches zero. We find that growing non-axisymmetric disturbances are either absent ($0.14 \leq \eta \leq 1.0$) or occur above the neutral curve determined by axisymmetric disturbances.

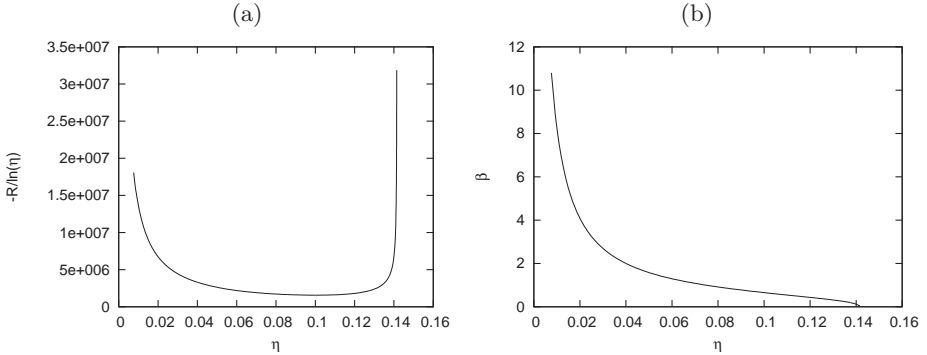


Fig. 2. The neutral curve determined by axisymmetric disturbances for the radius ratio η . (a): the critical Reynolds number; (b): the critical axial wavenumber β .

3.2 Nonlinear analysis

When $\eta = 0.1$ the critical Reynolds number R_c takes the value 0.361×10^7 with $\beta = 0.6546$. Fig. 3 shows the subcritical bifurcation of an axisymmetric nonlinear solution from this critical point with a saddle-node at $R = 0.401 \times 10^5$.

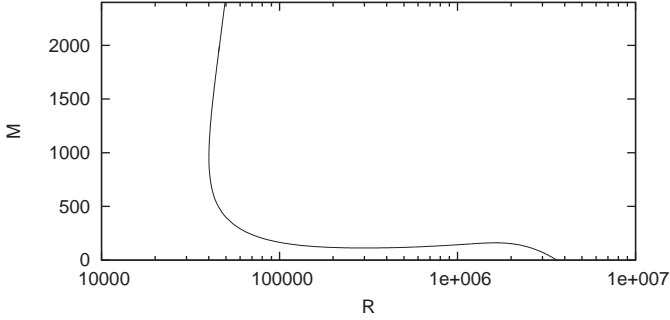


Fig. 3. The bifurcation of the axisymmetric solution for $\eta = 0.1$. The measure of the nonlinearity is represented by the momentum transport M on the inner cylinder.

It is unlikely that the basis state physically keeps its stability up to such a high critical Reynolds number as obtained by the linear and nonlinear analyses with respect to axisymmetric disturbances.

We anticipate that the three-dimensional solutions of plane Couette flow [3] as our narrow gap limit ($\eta \rightarrow 1$) still exist in wide gap cases ($\eta < 1$). In the case of $\eta = 0.5$, where the linear critical state is absent, the saddle-node bifurcations are detected for various wavenumber pairs (see Fig. 4). The minimum Reynolds number at the saddle-node bifurcation takes place at 253.1 with the azimuthal wavenumber $\alpha = 3$ and the axial wavenumber $\beta = 0.51$. The solution seems to bifurcate from infinity (see Fig. 5 (a)) and travelling in the axial direction with the phase velocity c_z (see Fig. 5 (b)).

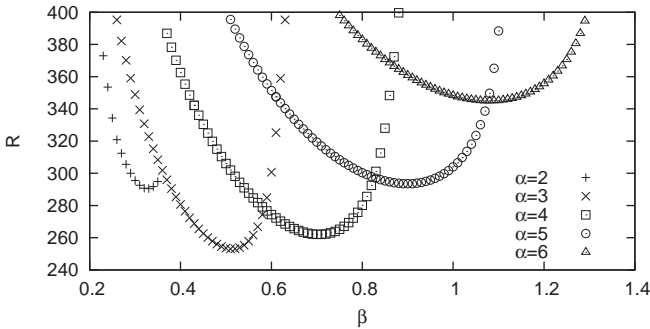


Fig. 4. The Reynolds number at the saddle-node bifurcation point for the non-axisymmetric solutions with various wavenumber pairs (α, β) .

The flow field of the non-axisymmetric solution for $\eta = 0.5$ is shown in Fig. 6. The figure shows only a fluctuation part. This solution satisfies $\mathbf{u}(r, \theta, z) = \mathbf{u}(r, -\theta, z + \pi/\beta)$, and so it inherits the symmetry of plane Couette solution [3].

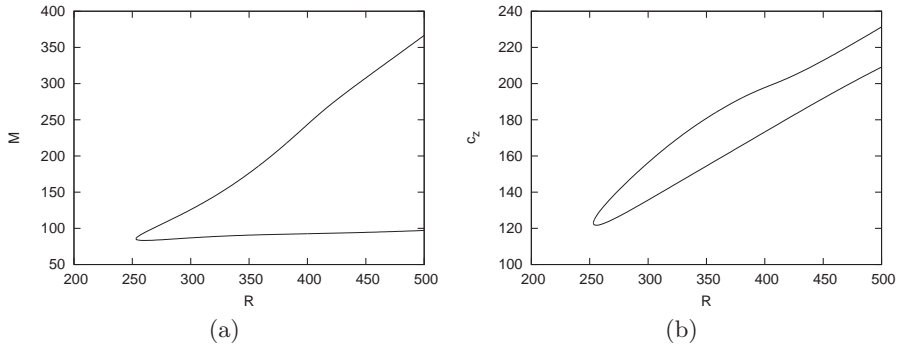


Fig. 5. The bifurcation diagram for $(\eta, \alpha, \beta) = (0.5, 3, 0.51)$. (a): the momentum transport M on the inner cylinder; (b) the phase velocity c_z .

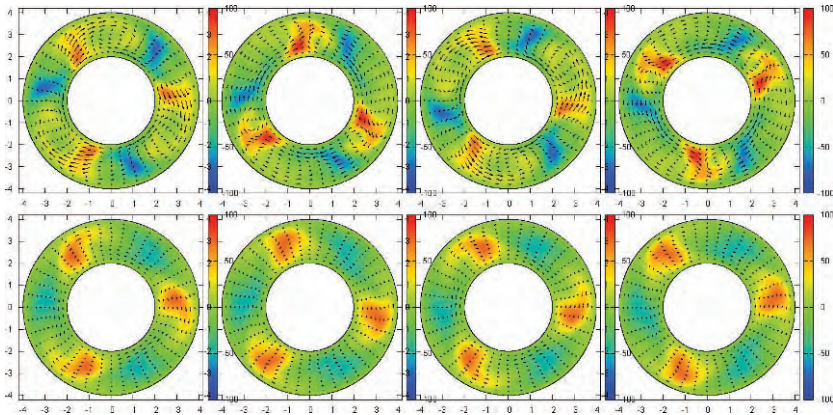


Fig. 6. The flow field of the non-axisymmetric solution for $(\eta, \alpha, \beta, R) = (0.5, 3, 0.51, 400)$ at each quarter axial wavelength position. Arrows represent the projection of the velocity and the colour code represents the axial component of the velocity. Upper/lower four figures correspond to the upper/lower branch.

References

1. D. D. Joseph, *Stability of Fluid Motions I*. Springer-Verlag, 1976.
2. P. Gittler, Stability of Poiseuille-Couette flow between concentric cylinders. *Acta Mechanica.*, 101:1–13, 1993.
3. M. Nagata, Three-dimensional finite amplitude solutions in plane Couette flow: bifurcation from infinity. *J. Fluid Mech.*, 217:519–527, 1990.
4. B. Hof, C. W. H. van Doorne, J. Westerweel, F. T. M. Nieuwstadt, H. Faisst, B. Eckhardt, H. Wedin, R. R. Kerswell, and F. Waleffe. Experimental observation of nonlinear traveling waves in turbulent pipe flow. *Science.*, 305:1594–1598, 2004.
5. H. Wedin, A. Bottaro, M. Nagata, Three-dimensional traveling waves in a square duct, submitted to *Phys. Rev. E.*, 2009.

Localization in plane Couette edge dynamics

Tobias M. Schneider, Daniel Marinic and Bruno Eckhardt

School of Engineering and Applied Sciences, Harvard University, Cambridge 02138 MA, USA

Fachbereich Physik, Philipps-Universität Marburg, 35032 Marburg, Germany
tschneid at seas.harvard.edu

In linearly stable shear flows including pipe and plane Couette flow finite amplitude perturbations are required to trigger turbulence [1]. Studying lifetimes of perturbations and locating the transition between smooth variations and sensitive dependence on initial conditions we identify the boundary in between laminar and turbulent dynamics [2, 3]. States within this *edge of chaos* evolve towards a relative attractor, the *edge state* whose stable set forms the edge.

In numerical studies of small domains, spatially periodic edge states have been identified. However, transitional turbulence in spatially extended systems is observed in localized patterns such as slugs and puffs in pipe flow or striped turbulence in Taylor-Couette and plane Couette flow [5, 6] suggesting the existence of localized edge states.

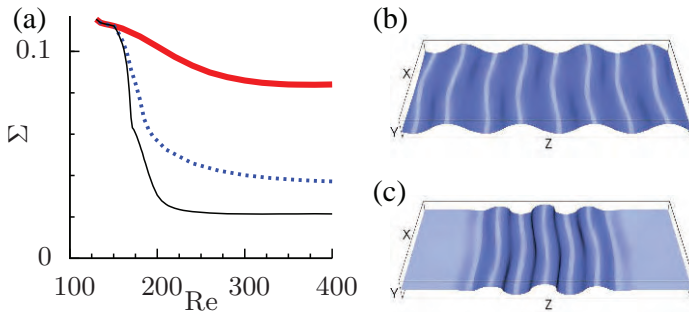


Fig. 1. Localized edge state in a plane Couette cell of 4π streamwise (x) and 8π spanwise (z) extension (in units of half the gap width). (a) Bifurcation diagram: Periodic lower branch equilibrium (thick red solid line), localized edge state traveling wave (dashed line) and localized equilibrium (thin solid line). (b)/(c): Isosurfaces of vanishing downstream velocity ($u_x \equiv 0$) for the periodic equilibrium (b) and the localized edge state (c). The Reynolds number is 400.

Here we focus on plane Couette geometry where the flow is driven by two parallel plates moving in opposite direction. Introducing discrete translational symmetry in the spatially homogeneous downstream and spanwise direction i.e. considering a small periodic domain, a known lower branch equilibrium solution has been identified as the edge state [4]. When extending the domain in spanwise direction, while keeping the downstream length of 4π , the edge tracking algorithm converges to states that are localized in the spanwise direction, see Fig. 1(c). The localized edge state is a traveling wave with a single unstable eigenvalue so that its stable manifold is of codimension 1 and separates laminar from turbulent dynamics. The localized traveling wave coexists with a known lower branch fixed point solution (Fig. 1(b)) from which it bifurcates in a ‘pattern-forming’ bifurcation. Together with the localized traveling wave also a localized equilibrium appears (Fig. 1(a)) whose stable manifold is of higher codimension so that it does not act as the relevant edge state. Relating the observed bifurcation scenario to other pattern-forming systems we discuss possible mechanisms underlying localization in homogeneously driven extended hydrodynamical systems.

Increasing both the length and the width of the domain an edge state localized both in stream- and spanwise direction is identified. The fully localized edge state differs from a turbulent spot in that it does not invade laminar flow and shows a very simple internal dynamics. The evolution towards turbulence proceeds by a local transition of the spot followed by its spatial spreading. Thus, the localized edge state forms the minimal turbulent *seed* for turbulence transition in spatially extended plane Couette flow. We will relate our findings to observations in spatio-temporal chaos and percolation models as well as discuss implications on turbulence studies in finite domains.

References

1. Eckhardt, B., Schneider, T. M., Hof, B., and Westerweel, J. (2007). *Annu. Rev. Fluid Mech.*, 39:447.
2. Skufca, J., Yorke, J., and Eckhardt, B. (2006). *Phys. Rev. Lett.*, 96:174101.
3. Schneider, T. M., Eckhardt, B., and Yorke, J. A. (2007). *Phys. Rev. Lett.*, 99:034502.
4. Schneider, T.M., Gibson, J.F., Lagha, M., De Lillo F., and Eckhardt, B. (2008), *Phys. Rev. E*, 78:037301.
5. Bottin, S., Daviaud, F., Manneville, P., and Dauchot, O. (1998), *Europhys. Lett.*, 43:171.
6. Barkley, D., and Tuckermann, L.S. (2005), *Phys. Rev. Lett.*, 94:014502.

Nonlinear optimal perturbations in plane Couette flow

Luca Brandt, Yohann Duguet and Robin Larsson

Linné FLOW Centre, KTH Mechanics, SE-10044 Stockholm, Sweden

luca@mech.kth.se

Subcritical transition to turbulence can occur in a variety of wall-bounded shear flows when the laminar base state is not subject to linear instability. In this case, perturbations to the base state with a finite but very small amplitude can be amplified by non-normal effects, up to a level where nonlinear interactions come into play. Since transition is often undesired, leading to a dramatic increase in wall drag, it is important to know which kind of (weak) perturbations are susceptible to trigger it if we wish to delay it. A vast amount of literature has described the linear mechanisms responsible for disturbance amplification. Optimisation methods have yielded *linear optimal disturbances* [1, 2], the disturbances which exhibit the largest linear growth. Yet the focus has been on linear amplification rather than on actual transition, which requires full nonlinearity to be taken into account. In this study, we go back to the original question of which perturbation is most likely to trigger transition to turbulence. We are hence investigating *nonlinear optimal disturbances*, those with smallest initial energy which effectively lead to a highly disordered flow. In the recent years, progress in the understanding of subcritical transition was made using the concept of 'edge states', originating from dynamical systems theory. 'Edge state' refers to the flow regime reached asymptotically by critical trajectories at the exact onset of transition. It is an unstable flow state and cannot be observed in experiments, but its stable manifold determines the basin of attraction of the base state. Direct numerical simulation in minimal domains of plane Couette flow has shown that the flow at the onset of transition asymptotically approaches an unstable finite-amplitude steady state solution, characterised by wavy streaks and streamwise rolls [3]. Using a shooting method, approach to such steady states is the way to characterise whether a transitional trajectory in phase space is actually an 'edge' trajectory.

In our investigation, we also focus on plane Couette flow in a computational box of size $4\pi h \times 2h \times 2\pi h$. The Reynolds number (based on the half-gap h) used for most of the computations presented here is 400. The numerical simulations are performed with a pseudospectral code using $48 \times 33 \times 48$ grid points in

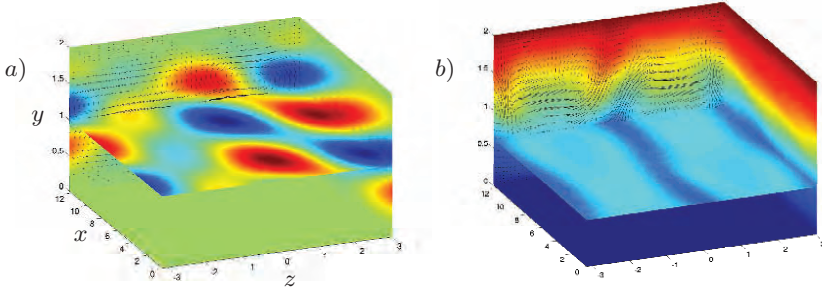


Fig. 1. *a)* Nonlinear optimal initial condition and *b)* corresponding symmetric edge state. The color indicates wall-normal velocity in *a)* and streamwise velocity in *b)*. Velocity vectors represent in-plane velocities. The edge state has about 90 times more kinetic energy than the initial perturbation.

the streamwise, wall-normal and spanwise direction respectively. The method is though generalisable to all parallel shear flows. We use a finite-dimensional basis of linear optimal disturbances to generate candidates for the nonlinear optimal disturbances. Those linear optimal modes (and as well all linear combinations of them), satisfy two necessary conditions for nonlinear optimality: at time $t = 0$, the first time derivative of the perturbation energy is zero while the second derivative is positive [4]. Only the linear optimal modes with lowest wavenumbers, i.e. those exhibiting the largest transient growth, are considered in the optimisation. We focus on two different transition scenarios involving departure from either oblique waves -with wavenumbers $(1, \pm 1)$ - or streamwise vortices with wavenumber $(0, 2)$ -, see also [5]. (The integers refers to multiples of the fundamental streamwise and spanwise wavenumbers, respectively)

For the range of parameters tested, the oblique wave scenario seems to be optimal, consistently with threshold studies in other shear flows [2]. The nonlinear interaction of two initial oblique waves of opposite angle and equal initial energy forces streamwise vortices. The lift-up effect then generates streaks and the whole structure approaches transiently the edge state. As a result of the optimisation, the nonlinear optimal initial condition is a symmetric pair of oblique waves, $(1, \pm 1)$, slightly perturbed by the mode $(1, 2)$ with a phase departure of 0.6π . The distortion induced by the mode $(1, 2)$ is small and corresponds to 9% of the energy of the total perturbation. The corresponding flow structure is shown in Fig. 1*a)*: the symmetric checkerboard patterns usually encountered in oblique transition is here distorted by the oblique mode $(1, 2)$.

In the general case we find that not one, but three different steady state solutions can be transiently approached, depending on the exact shape and symmetries of the initial perturbations. Some of these steady states are new; one of them (denoted here 'Edge I') has lower energy than those previously found,

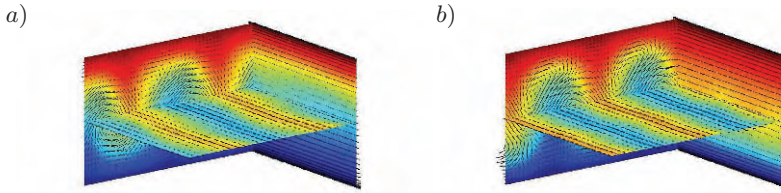


Fig. 2. *a)* Edge state II and *b)* edge state III. The color indicates streamwise velocity while velocity vectors represent in-plane velocities. Table 1 reports the energy of these steady solutions.

and displays low-speed streaks with a varicose structure, see Fig. 1*b*). It is the state transiently approached by optimal initial perturbations close to oblique waves. The two other edge states are approached transiently when perturbing linearly optimal streamwise vortices. They are displayed in Fig. 2. They are here refined down to machine accuracy using a Newton-Krylov solver. The steady solution denoted as edge state II has two wavy streamwise streaks with one sinuous oscillation within our computational box. It corresponds to the state observed in [3]. Edge state III, the most energetic among those found in our configuration, also has two streamwise streaks but with two streamwise oscillations.

The energy associated to the different edge states observed is reported in Table 1. The minimal energy required by the simplest possible initial conditions approaching these is also compiled in the table. Edge II is reached by initial conditions consisting of streamwise rolls and a small amount of perturbation in the Fourier component (1, 2), of the order of few percents of the total energy. Conversely, the solution denoted by III is approached by a perturbation where the energy in the oblique mode (1, 1) is about half of that of the streamwise rolls.

	Energy	Initial energy	Perturbation
Edge I	2.84×10^{-3}	3.34×10^{-5}	$E_{(1,1)} = E_{(1,-1)}$
Edge II	1.82×10^{-2}	1.98×10^{-4}	$E_{(1,2)} = 0.0965E_{(0,2)}$
Edge III	2.61×10^{-2}	1.72×10^{-4}	$E_{(1,1)} = 0.48E_{(0,2)}$

Table 1. Energy of the edge states identified with corresponding energy of the simplest initial conditions (only two Fourier modes) approaching them.

Finally, we investigate the Reynolds number behavior of the threshold energy associated to the oblique scenario and of the corresponding symmetric edge states. The energy thresholds are obtained by running the bisection algorithm using only the modes (1, ±1) with equal energy while the steady solutions are computed by continuation starting from the solution at $Re = 400$

in Fig. 1b). The perturbation energy associated to the symmetric edge state decreases asymptotically like $Re^{-0.5}$, whereas the initial energy required to approach these states decreases like $Re^{-1.9}$. The scaling of this optimal perturbation is very close to the optimal theoretical bound in $O(Re^{-2})$ derived by Chapman [6].

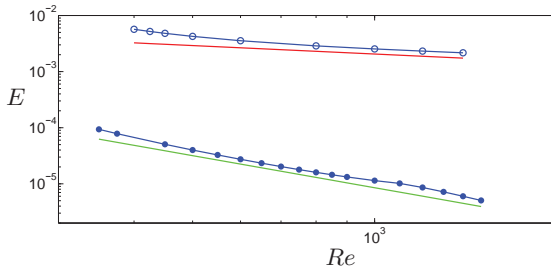


Fig. 3. Energy of the symmetric edge state I (open symbols) and of the symmetric initial condition with lowest energy lying on the laminar-turbulent boundary (filled symbol) versus the Reynolds number Re . The red and green lines represent best fitting power laws, $Re^{-0.5}$ and $Re^{-1.9}$ for the energy pertaining to the steady solutions and to the symmetric initial condition respectively.

The approach presented allows us to reconstruct the whole nonlinear transition process for critical optimal trajectories, starting from the linear regime. It also improves our understanding of the topology of the laminar-turbulent boundary in phase-space as Re increases.

References

1. K. Butler and B. F. Farrell, Three-dimensional optimal perturbations in viscous shear flow, *Physics of Fluids, A* **4**, 1637 (1992).
2. P. J. Schmid and D. S. Henningson, *Stability and transition in shear flows*, Springer, 2001.
3. T. M. Schneider, J. F. Gibson, M. Lagha, F. De Lillo and B. Eckhardt, Laminar-turbulent boundary in plane Couette flow, *Phys Rev E*, 037301 (2008).
4. C. Cossu, An optimality condition on the minimum energy threshold in subcritical instabilities, *Comptes Rendus Mecanique*, **333**, 4, 331 (2005)
5. S. C. Reddy, P. J. Schmid, J. S. Baggett and D. S. Henningson, On the stability of streamwise streaks and transition thresholds in plane channel flows, *Journal of Fluid Mechanics*, **365**, 269 (1998).
6. J.S. Chapman, Subcritical transition in channel flows, *Journal of Fluid Mechanics*, **451**, 35 (2002)

Order parameter in laminar-turbulent patterns

L.S. Tuckerman¹, D. Barkley², D. Moxey², O. Dauchot³

¹PMMH-ESPCI (France), ²Univ. of Warwick (U.K.), ³CEA-Saclay (France)
laurette at pmmh.espci.fr

Over a century, and thousands of articles, after Reynolds' description of the transition to turbulence in pipe flow, a predictive theory of transition is still unavailable. One of the most intriguing phenomena observed near transition is the coexistence of well-defined and long-lived laminar and turbulent regions, first observed in counter-rotating Taylor-Couette flow in the 1960s [1]. In the 2000s, Prigent & Dauchot [2] showed that these coexisting regions were part of a regular pattern of stripes, whose wavelength and orientation are Reynolds-number-dependent and reproducible. Analogous phenomena have been observed experimentally [2] and numerically [3] in plane Couette flow, in stator-rotor experiments (the flow between a stationary and a rotating disk) [4], in plane Poiseuille simulations [5], and, most recently, in simulations of pipe flow [6].

We analyze these flows as wave patterns, measuring their strength by the instantaneous 1D Fourier component a corresponding to their wavenumber and phase. Since the flows are stationary only in a statistical sense, we treat a as a random variable and construct its probability distribution function (pdf). Timeseries and pdfs for a from simulations of plane Couette flow are shown below. Three regimes can be distinguished. For $Re \gtrsim 420$, the turbulence is *uniform*, extending over the entire domain; the corresponding pdf has its maximum at $a = 0$. For $400 \lesssim Re \lesssim 420$, the pattern is *intermittent*, appearing and disappearing erratically; the corresponding pdf is neither maximal nor zero at $a = 0$. For $290 \lesssim Re \lesssim 400$, a statistically steady *turbulent-laminar pattern* is present; the corresponding pdf is zero at $a = 0$.

References

1. D. Coles, *J. Fluid Mech.* **21**, 385–425 (1965); C. W. van Atta, *J. Fluid Mech.* **25**, 495–512 (1966); D. Coles, & C. W. van Atta, *AIAA J.* **4**, 1969–1971 (1966).
2. A. Prigent, G. Grégoire, H. Chaté, O. Dauchot & W. van Saarloos, *Phys. Rev. Lett.* **89**, 014501 (2002); A. Prigent, G. Grégoire, H. Chaté & O. Dauchot, *Physica D* **174**, 100 (2003).
3. D. Barkley & L.S. Tuckerman, *Phys. Rev. Lett.* **94**, 014502 (2005); D. Barkley & L.S. Tuckerman, *J. Fluid Mech.* **576**, 109–137 (2007)
4. A. Cros & P. Le Gal, *Phys. Fluids* **14**, 3755–3765 (2002).
5. T. Tsukahara, Y. Seki, H. Kawamura & D. Tochio, D., in *Proc. 4th Int. Symp. on Turbulence and Shear Flow Phenomena*, pp. 935–940 (2005).
6. D. Moxey & D. Barkley, to be published.

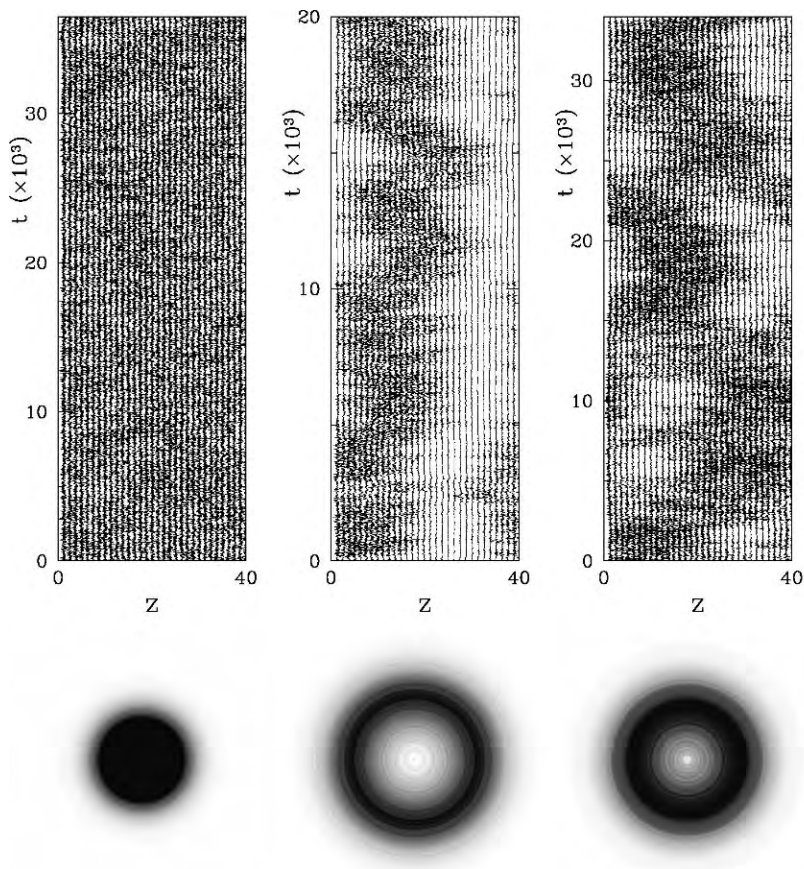


Fig. 1. Above: timeseries at $Re = 500$ (uniform turbulence), 410 (intermittent), 350 (turbulent-laminar pattern). Below: pdfs of Fourier component a .

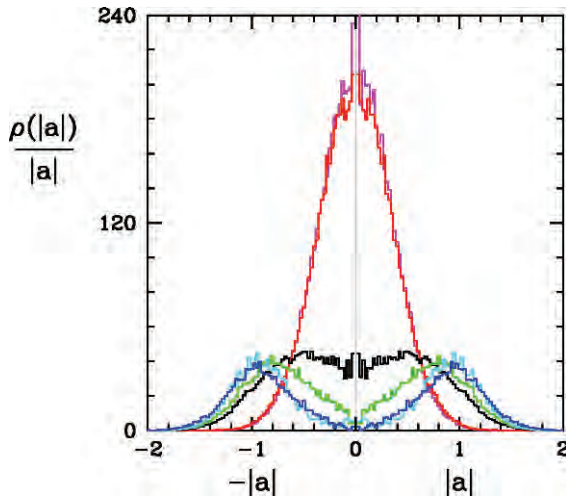


Fig. 2. Probability distribution function for $|a|$ for $Re = 580, 520, 420, 400, 350, 330$, in order of decreasing value at $|a| = 0$.

Pattern formation in low Reynolds number plane Couette flow

Y. Duguet, P. Schlatter, and D.S. Henningson

Linné Flow Centre, KTH Mechanics, SE-10044 Stockholm, Sweden
duguet@mech.kth.se

Plane Couette flow is the flow between two counter-sliding plates of velocity U separated by a gap $2h$. It has a simple laminar solution with constant shear which is stable for all values of the Reynolds number $Re = \frac{Uh}{\nu}$ (ν is the kinematic viscosity of the fluid). However, transition to turbulence is observed experimentally above a threshold value of Re between 300 and 400. Whereas featureless turbulence is seen for $Re \geq 400$, lower- Re experiments have shown a turbulent regime displaying spatio-temporal intermittency effects, notably the appearance of turbulent stripes, inclined with respect to the direction of the base flow, interspersed with quiescent, nearly laminar regions [1], see Figure 1. It is the 'spiral turbulence' regime, so-called because it has also been identified in Taylor-Couette experiments. Similar patterns have also been numerically reproduced in a minimal-like computational domain (of size $10h$ in length and $40h$ in width), oriented against the inclination of one stripe [2]. This reduced computational box allows to understand locally the appearance and the stability of these localised structures.

The aim of the present *numerical* experiment is to reproduce such patterns using direct numerical simulation. We use a parallel spectral code [3] in an unusually large computational domain ($800h$ in length and $356h$ in width with periodic boundary conditions) in order to highlight the large-scale self-organisation of the flow, out-of-reach in former simulations. The numerical resolution is $2048 \times 33 \times 1024$. The use of both a large domain and good numerical resolution allows to overcome the limitations in the models used by Manneville [4] (simplification of the wall-normal structure of the flow) or by Tuckerman & Barkley [2] (strong constraints by narrow spatial periodicity). The values of Re range from 300 to 400, and we choose a noisy non-localised initial velocity field. For $Re \leq 320$, the initial condition rapidly develops streamwise streaks which undergo viscous decay, except at a few random and isolated locations where the streaks locally break down. A network of isolated localised structures ('spots') form naturally and start to grow, but they all eventually decay. Sustained turbulence appears somewhere between $Re = 320$ and $Re = 330$

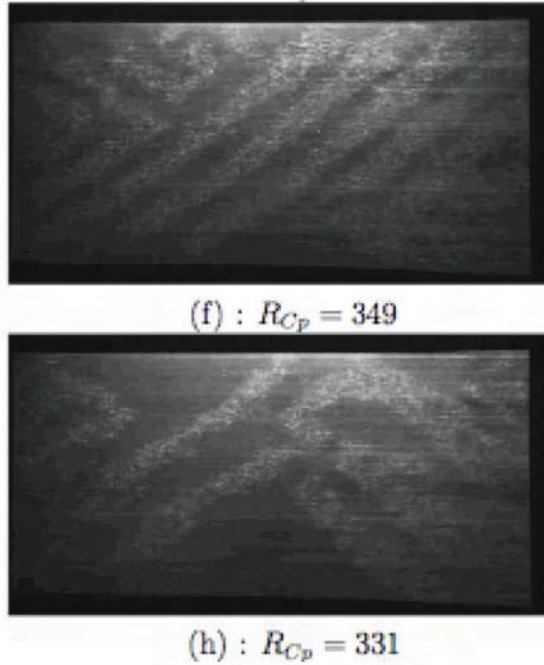


Fig. 1. Experimental evidence for the turbulent banded patterns in the experiment by Prigent et al. (2001) at low values of $Re = 349$ and $Re = 331$. The domain has a size $770h \times 2h \times 340h$. The value of Re is here progressively decreased starting from an uniform turbulent state.

(see Fig. 3), which is in excellent agreement with the experiments by Prigent [1]. For $330 \leq Re \leq 380$, similar spots also form and then grow spatially in the plane in a very disordered way. When neighbouring growing spots are close to each other, they undergo distortion and merging, and turbulent stripes arise, interspersed with quiescent, nearly laminar regions. The spatial organisation of these banded patterns is investigated, depending on the values of Re . The system evolves asymptotically towards a stable fragmented large-scale pattern (see Fig. 3 and 4), where two opposite inclinations can coexist. As Re is increased towards 400, the banded pattern progressively invades the whole domain, and the turbulent fraction of the domain approaches unity. Above $Re = 400$, the flow does not show any sign of large-scale structure, and is only dominated by streaks, where transient laminar regions appear but cannot sustain due to contamination.

This study highlights the role of spots in the transition process and their dynamics during expansion. Further numerical simulations using a localised initial condition were performed at $Re = 350$ and $Re = 500$ in the same large domain, in order to reduce the influence of periodic boundary conditions.

There is a fundamental difference in the spot expansion mechanisms between the two cases. For $Re = 500$, spots expand while keeping their shape, as in the simulations by Lundbladh and Johansson [5]. For $Re = 350$ however, the use of a larger spatial domain reveals that the expansion of the spot is very anisotropic in the in-plane directions, though initially no angle seems clearly favoured. Eventually turbulent bands also form through a sequence of splitting and merging events (see figure 2).



Fig. 2. Growth of a spot in a direct numerical simulation of plane Couette flow, $Re = 350$. Half-gap slice of the axial velocity field, in a large periodic box of dimension $800h \times 2h \times 356h$.

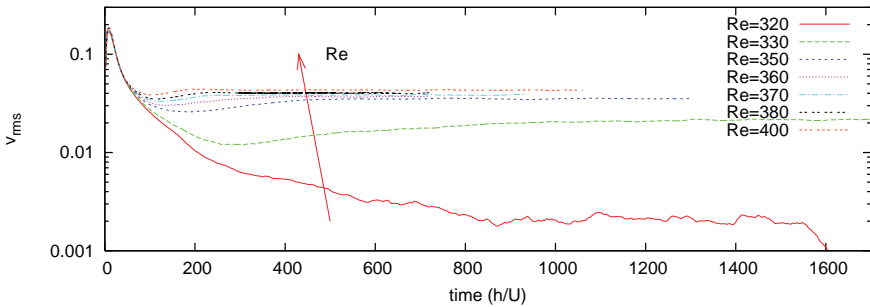


Fig. 3. Time evolution of the averaged wall-normal velocity parametrised by Re , in a large periodic box of dimension $800h \times 2h \times 356h$. The initial condition corresponds every time to the same featureless noise.

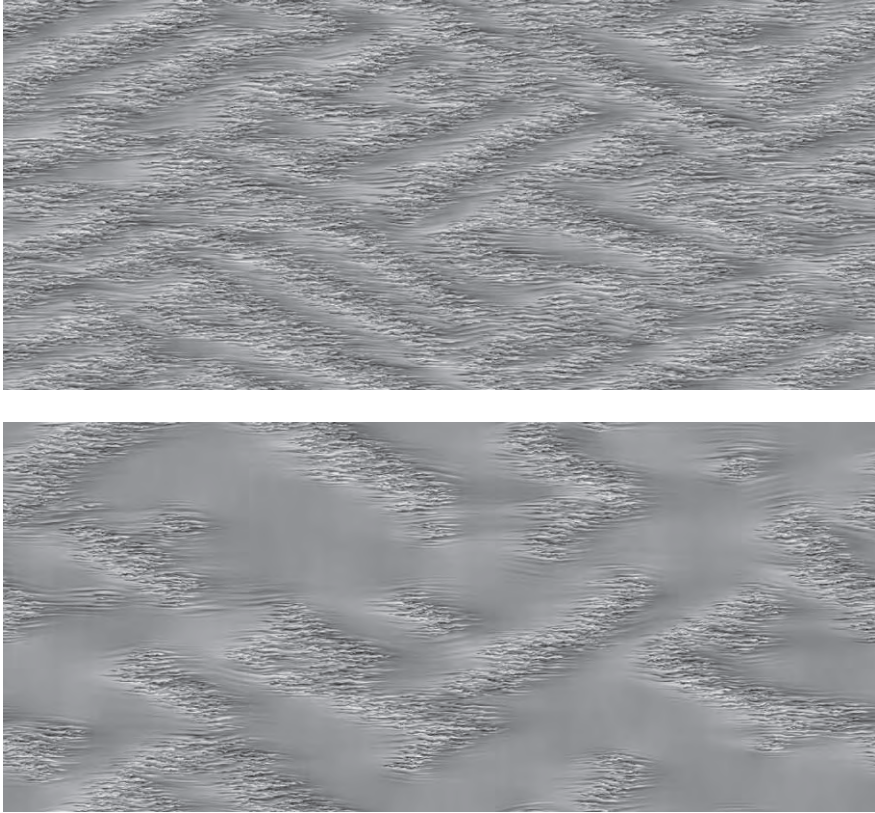


Fig. 4. Pattern formation in a direct numerical simulation of plane Couette flow, $Re = 350$ (top) and $Re = 330$ (bottom). Same visualisation as in Figure 1. The initial condition corresponds here to featureless noise.

References

1. A. Prigent, G. Grégoire, H. Chaté, O. Dauchot, W. van Saarloos, Large-Scale Finite-Wavelength Modulation within Turbulent Shear Flows. *Physical Review Letters*, 89:014501, 2001.
2. D. Barkley, L. Tuckerman, Computational Study of Turbulent Laminar Patterns in Couette Flow. *Physical Review Letters*, 94:014502, 2005.
3. M. Chevalier, P. Schlatter, A. Lundbladh, D.S. Henningson SIMSON A pseudo-spectral solver for incompressible boundary layer flows. *Technical Report TRITA-MEK 2007:07*, KTH Mechanics, Stockholm, Sweden.
4. M. Lagha, P. Manneville Modeling transitional plane Couette flow. *European Physical Journal B*, 58 (4), 433, 2007.
5. A. Lundbladh, A.V. Johansson, Direct simulation of turbulent spots in plane Couette flow. *Journal of Fluid Mechanics*, 229, 499, 1991.

Quasi-stationary and chaotic convection in low rotating spherical shells

B. Futterer and C. Egbers

Dept. Aerodynamics and Fluid Mechanics, Brandenburg University of Technology,
Siemens-Halske-Ring 14, 03046 Cottbus, Germany

`birgit.futterer at tu-cottbus.de`

Summary. The geophysical flow simulation experiment ‘GeoFlow’ studies convection phenomena in rotating spherical shells under influence of a spherical symmetric buoyancy field. It is a space station experiment, that is backed by three-dimensional numerical simulation done with a spectral code. Here we present simulated dynamics in the low rotational regime. Flow patterns are characterized by solutions of axisymmetric, cubic and pentagonal symmetry with adjustment to rotating axes. For the example of a cubic pattern in supercritical convection regime, the evolution of heat transfer and kinetic energy is discussed, if the rotational influence increases. While these global variables point out that the flow is stationary in the rotating reference frame, it is the local variable of spherical harmonics in azimuthal direction which shows a periodic drift, i.e. the pattern is counter rotating to the sphere. Transition to chaos is in form of a sudden onset.

Studies of convection phenomena in an astro- and geophysical framework has a long tradition [1]. Besides a rich variety of theoretical and numerical work on convection in rotating, self-gravitating spherical shells, there are only minor experiments in these shell models, with concentric spheres that are maintained at different temperatures and rotatable about their common axes. From experimental point of view the experiment ‘GeoFlow’ (Geophysical Flow Simulation) generates the necessary buoyancy field by means of a spherical symmetric electric field acting in a dielectric insulating fluid. In order to avoid interference with axial gravity in laboratory the experiment is carried out in space, here it is the International Space Station ISS with its European platform COLUMBUS. Special goal of ‘GeoFlow’ is to capture the large-scale convective motion without rotation as well as the superposition of rotation up to stabilizing effects due to centrifugally driven convection. For this spherical Rayleigh-Bénard convection we present the numerically simulated dynamics of the rotating cases with focus on low rotation regime. This is part of preparation as well as backing of the experiment which is actually running on orbit.

Non-dimensional Boussinesq equations for thermal convection in rotating reference frame under influence of a dielectrophoretic acting force field are

given by

$$\nabla \cdot \mathbf{U} = 0, \quad (1)$$

$$Pr^{-1} \cdot \left[\frac{\partial \mathbf{U}}{\partial t} + (\mathbf{U} \cdot \nabla) \mathbf{U} \right] = -Pr^{-1} \nabla p + \nabla^2 \mathbf{U} + Ra_{centr} \cdot \frac{\eta^2}{(1-\eta)^2} \cdot \frac{1}{r^5} T \hat{\mathbf{e}}_r \\ - \sqrt{Ta} \hat{\mathbf{e}}_z \times \mathbf{U} + \widetilde{Ra} T r \sin \theta \hat{\mathbf{e}}_{eq}, \quad (2)$$

$$\frac{\partial T}{\partial t} + (\mathbf{U} \cdot \nabla) T = \nabla^2 T. \quad (3)$$

Equations are scaled with outer spherical radius r_o for length, thermal diffusive time r_o^2/κ for time, $\rho_0 \kappa^2/r_o^2$ for pressure and temperature difference $\Delta T = T_i - T_o$ for temperature, where κ is the thermal diffusivity and ρ_0 is the reference density. Boundary conditions are no-slip for velocity \mathbf{U} , and for temperature T values are set to $T(\mu) = 1$ and $T(1) = 0$. Herewith dynamics of ‘GeoFlow’ is described with:

$$\text{radius ratio} \quad \eta = \frac{r_i}{r_o}, \quad (4)$$

$$\text{Prandtl number} \quad Pr = \frac{\nu}{\kappa}, \quad (5)$$

$$\text{Rayleigh number } Ra_{centr} = \frac{2\epsilon_0 \epsilon_r \gamma}{\rho \nu \kappa} V_{rms}^2 \Delta T, \quad (6)$$

$$\text{Taylor number} \quad Ta = \left(\frac{2\Omega r_o^2}{\nu} \right)^2. \quad (7)$$

Geometrical and physical properties, discussed with η and Pr , respectively, are fixed with $\eta = 0.5$ and $Pr = 64.64$. The Rayleigh number Ra_{centr} measures the imposed thermal forcing with $Ra_{centr} \sim \Delta T$. Coriolis force is treated by the Taylor number \widetilde{Ta} , with $Ta \sim n$ as the rotation rate of the sphere. The additional factor $\widetilde{Ra} = \alpha \Delta T/4 \cdot Pr \cdot Ta$ directs attention to centrifugal effects. Refer to [2] for detailed listing of experiment parameters including geometric dimensions and physical properties of the working fluid, which is a silicone oil (viscosity ν , relative permittivity ϵ_r , coefficient of expansion α), resulting in achievable magnitudes for $Ra_{centr} \leq 1.4 \cdot 10^5$ and $Ta \leq 1.3 \cdot 10^7$. Additional factor of \widetilde{Ra} is in the order of 10^6 .

Numerical simulation calculates solutions for equation (1)-(3) at parameter sets of Ra_{centr} and Ta . Proceeding is to set Ra_{centr} and to increase Ta . By highlighting the low rotation regime the parameter domain is spanned by Ra_{centr} up to $2 \cdot 10^4$ and $2 \cdot 10^2 \leq Ta \leq 2 \cdot 10^4$. Here we used the numerical code from Hollerbach as it is described in [3]. Truncations of serial expansion in spherical harmonics for both fields \mathbf{U} and T in all directions were (radial, meridional, azimuthal)=(30,60,20). Time-stepping was set to $1 \cdot 10^{-5}$. Iteration was observed with logging of spectral coefficients at arbitrarily chosen limbs of the serial expansion. These coefficients are simply part of the whole solution decomposed in spherical harmonics and act as local variables in all directions.

Overall time-dependency is identified with the kinetic energy and the Nusselt number at the inner and outer spherical shell. Steady states show constant

kinetic energy with $E_{kin} = const.$ and furthermore $Nu_i = Nu_o$. Periodic fluid flow shows periodic time series for these global variables of E_{kin} , Nu_i and Nu_o , which are no longer equal then. Irregular fluctuating time-series mark chaotic solutions. Local variables follow this classification.

By means of regarding evolution of time-series for global and local variables quasi-stationary and chaotic convection is identified (Fig. 1 and Fig. 2, resp.). As transition in between those two temporal identified flow states no pure periodicity is found. Evolution of the global variables is obvious, the periodogram proves the stationary property of the solution with vanishing noise in the order of 10^{-19} for E_{kin} and 10^{-24} for Nu . For chaotic solutions remarkable magnitudes in the order of 10^4 are achieved for frequencies below 40. Amplitude distribution over the frequencies is sloping to higher frequencies. Regarding the evolution of time-series for spectral coefficients these local variables follow this procedure in principal, except the one marking the azimuthal component of the solution. Here a longterm periodicity is visible and will be discussed in the following by describing pattern of convection.

The cubic pattern of convection shows no stretching or compressing by rotation. Rotation of the sphere just leads to lift the convective cells, i.e. the Nusselt number is constant as well as the kinetic energy. But the azimuthal component shows that the pattern has a periodic drift, indeed that is why we name it a quasi-stationary solution. While the sphere is rotating counter-clockwise, the pattern is rotating clockwise, i.e. the drift is retrograde. For the chaotic fluid flow pattern no specific symmetry gets visible.

While the Nusselt number gives information on the effective heat transfer in the system, it is the kinetic energy, with which we track the rotational influence. For the two presented parameter sets of Ra_{centr} and Ta , we observe a decrease of Nu , if Ta is increasing. Hence the rotational driven flow suppresses the convection driven flow. Furthermore it is also E_{kin} , that is decreasing. Chaotic convection seems to have a more efficient energy conversion.

This low rotation regime captures properties of the GeoFlow's non-rotating case as described in [4] and [5], with a transition from steady state to chaotic fluid flow in form of a sudden onset. In this paper we presented only the cubic solution and its drift in the rotating sphere, but as in the non-rotating case, axisymmetric as well as pentagonal convective pattern were found with a drift, which still has to be classified.

References

1. F.H. Busse, Phys. Fluids, **14**, 4 (2002).
2. Th. von Larcher, B. Futterer, C. Egbers, R. Hollerbach, P. Chossat, P. Beltrame, L. Tuckerman, F. Feudel, J. Jpn. Soc. Microgravity Appl., **25**, (2008).
3. R. Hollerbach, Int. J. Num. Meth. Fluids, **32**, (2000).
4. K. Bergemann, F. Feudel, and L.S. Tuckerman, J. Phys.: Conf. Ser., **137**, (2008).
5. B. Futterer, R. Hollerbach, C. Egbers, J. Phys.: Conf. Ser., **137**, (2008).

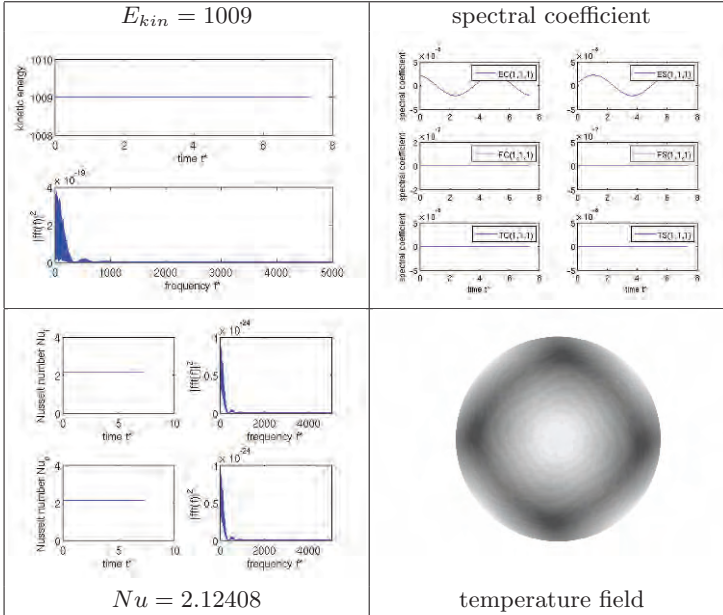


Fig. 1. Steady convection in low rotating spherical shells at $Ra_{centr} = 8 \cdot 10^3$, $Ta = 2 \cdot 10^2$: Evolution of time series and pattern of convection. Time series and periodogram for kinetic energy E_{kin} (top left), Nusselt number at inner and outer spherical shells Nu_i resp. Nu_o (bottom left); arbitrarily chosen spectral coefficients for velocity EC , ES , FC , FS and for temperature TC and TS (top right). Top view of temperature field plotted on spherical surface in the shell (bottom right) with dark color marking hot regions with warm up flow and bright color marking cold regions with discharge flow.

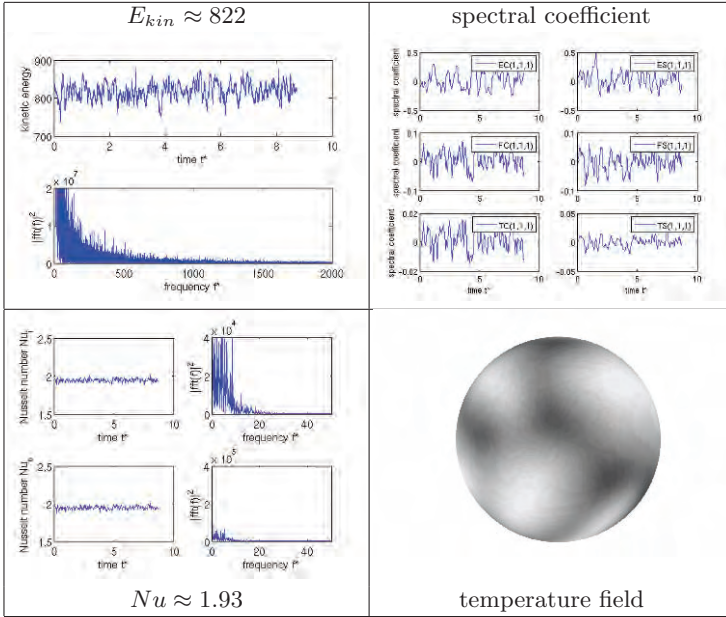


Fig. 2. Chaotic convection in low rotating spherical shells at $Ra_{centr} = 8 \cdot 10^3$, $Ta = 1 \cdot 10^4$: Evolution of time series and pattern of convection, following the display of Fig.1.

Linear stability of 2D rough channels

F. Fabiani¹, P. Orlandi¹ and S. Leonardi²

¹Dipartimento di Meccanica e Aeronautica Università La Sapienza, Via Eudossiana 18, 00184, Roma, Italy

²Department of Mechanical Engineering, University of Puerto Rico at Mayaguez, Mayaguez 00680-9045 Puerto Rico. fabiani@kolmogorov.ing.uniroma1.it

1 Introduction

Flow past rough walls have been deeply studied in the past, initially in laboratory experiments and recently by numerical simulations. In practical applications as for instance for flow over urban settlements or past wings, the flows are turbulent and the drag largely depends on the shape of the surfaces. In general the roughness produces a drag increase. However in particular conditions, for instance riblets, the drag may decrease. The comprehension of the flow physics near the roughness and their dependence on the shape of the surfaces can be understood by the numerical simulations also for the experimental evidence that the friction coefficient do not strongly depend on the Reynolds number.

In laboratory experiments difficulties are encountered to perform measurements near the rough elements (Burattini *et al.* 2008), that are absent in numerical simulations. The simulations, starting from that by Leonardi *et al.* 2003, in the last years increased the knowledge of the flow physics of fully turbulent flows. On the other hand, simulations of stability and transition regimes are lacking. The present work is devoted to analyse the variations of the critical Reynolds in channels with different kind of rough surfaces on a wall.

The three-dimensional analysis of the stability in smooth channels can be reduced to an equivalent two-dimensional problem by the Squires transformation. In order to apply this technique to rough surfaces, the study is limited to the stability of channels with obstacles spanning in the whole axial direction. The resulting eigenvalue problem, for smooth walls, often has been resolved analytically by giving the basic parabolic velocity profile and by observing that, at a critical Reynolds number (Re_{cr}) and at a certain wave number (α), the eigenvalue has a positive real part. This procedure is more complicated in presence of complex geometries, then the strategy consists in solving the Navier-Stokes equation in physical space. The equations are discretized by a second order accurate staggered finite difference scheme together

with an efficient immersed boundary technique (Leonardi & Orlandi 2004). This method is not restricted to linear stability but it can treat any kind of realistic disturbances as those produced by the rough surfaces.

2 Results

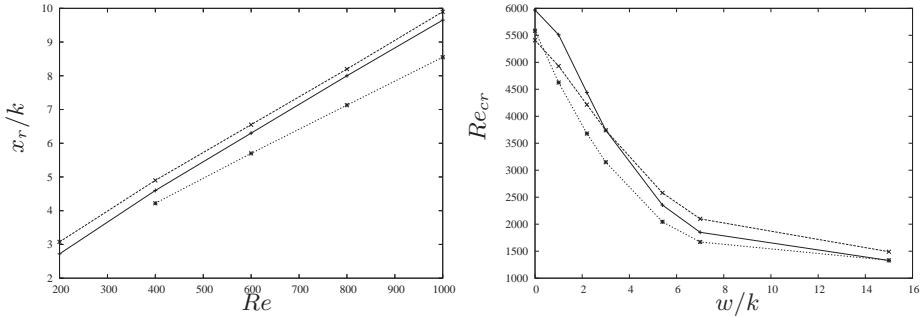


Fig. 1. a) Reattachment length versus Re , b) Re_{cr} vs. w/k : — squares; ---- triangles, circles

The Navier-Stokes equations are not given, these, together with a brief description of the numerical method can be found in Leonardi & Orlandi (2004). A validation for the fully turbulent regime was presented by Orlandi *et al.* (2006). In the present study the numerical method has been validated by reproducing the formation and propagation of the Tollmienn-Schlichting (T-S waves) in a smooth channel, and by comparing the Re_{cr} with that found in semi-analytical studies. The chart $Re_{cr}(\alpha)$, in very good agreement with that in Drazin & Reid (1981), is not reported for lack of space. The same small disturbances have been applied to the parabolic velocity profile in presence of the rough elements; these disturbances are amplified by the roughness and their amplification depends on the shape of the roughness. Several two-dimensional geometries (squares, triangles and rods) have been considered to find the relation (if it exists) between the critical Reynolds (Re_{cr}) and the shape and the distributions of the obstacles. The number of the obstacles is related to the ratio w/k , where k is the height of the obstacle and w the separation distance. The simulations with $k = 0.2h$ have shown that even in presence of roughness, and independently on the shape, the T-S waves form and their form depends on the distance $2h$ between the walls. On the other hand, it has been observed a strong effect of the roughness on the Re_{cr} , which can be related to the variations of the normal velocity fluctuations which interact with the main flow over the obstacles. This interaction leads to a decrease of the Re_{cr} . The simulations have shown a strong dependence of the Re_{cr} on w/k rather than on the shape of the obstacle, in particular at high values of w/k . This can be explained by the numerical results showing that, in two-dimensions, the recirculating region behind a body is weakly affected by the shape of the obstacle

(Fig.1a). Fig.1a was obtained with only two obstacles separated by a distance $w/k = 20$ to let the bubble to be free to increase; different is the growth when the following obstacle limits the size of the bubble. If the obstacles are close the bubbles reattach on the successive obstacles producing a greater shape dependence (Fig.1b). A weak recirculating region leads to a reduction of the amplitude of the disturbances emanating from the roughness. Fig.1b shows a strong decrease of the Re_{cr} with w/k , which does not largely differ for the three geometries. It is worth to recall that for the squares $w/k = 0$ gives a smooth wall, and the corresponding values Re_{cr} agrees with the theoretical value obtained for $\alpha = 6.4/2\pi$. For $w/k = 0$ the small reduction of Re_{cr} for the circles and for the triangles is due to the small empty area between the two contiguous elements. The area is slightly bigger for the triangles and this explain why Re_{cr} is the smallest. The reduction for $1 < w/k < 3$ for the circles is greater for the unsteadiness of the separation point. The interesting feature of Fig. 1b is that the reduction is significant up to $w/k = 7$ and that a further increase of w/k leads to an almost constant value of Re_{cr} for all the three geometries.

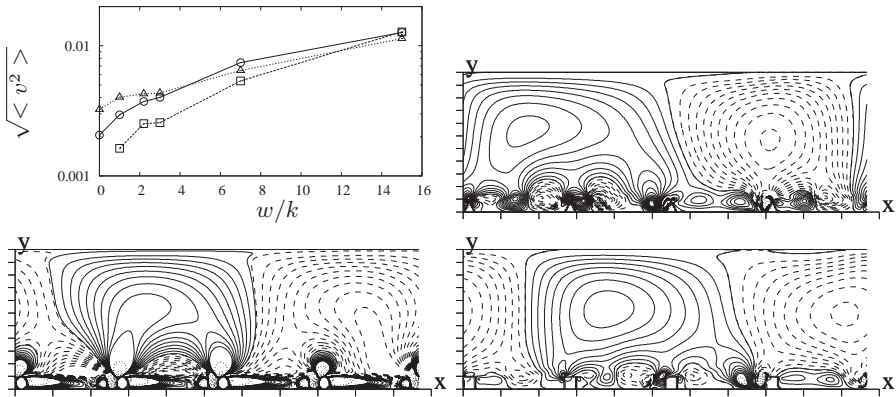


Fig. 2. a) Velocity disturbance $\sqrt{\langle v^2 \rangle}$ versus w/k : — squares, ---- triangles, circles; Normal velocity V isolines for $w/k = 7$ at $Re = 5600$, (b) triangles, (c) circles, (d) squares.

Leonardi *et al.* (2003) found that for the fully turbulent regime the maximum resistance was obtained for the square bars at $w/k = 7$ and Orlandi *et al.* (2006) observed that the same occurred for the rod bars. Also for the fully turbulent regime this was explained by analysing the shape of the mean separation bubble that was found to reattach at $x_R/k \approx 5$. From the results here presented for the transition it seems that the same phenomenon occurs. A more quantitative comprehension why the strong decrease ends at $w/k = 7$ can be obtained by the variation of $\sqrt{\langle v^2 \rangle}$, at the plane of the crests, in function of w/k shown in Fig.2a. This figure shows that the $\sqrt{\langle v^2 \rangle}$ for the squares is smaller than that for the other two geometries and this explain

why for $w/k < 3$ the Re_{cr} for the squares is greater. For $w/k > 3$ there is an effect of the other small separation region ahead of the obstacles that can be understood by flow visualisations.

Contour plots of normal velocity allow to see whether the disturbances generated by the roughness have the strength to completely destroy the external field and hence to generate T-S waves different from those in a channel with smooth walls. The vertical profiles of the v rms indicate that for the three geometries the peak value decays by increasing the distance from the plane of the crests, and that in large part of the channel is small, then it is expected that the T-S waves should not be largely affected. Fig.2, indeed, shows that for the three geometries at $w/k = 7$ the shape of the waves is mainly dictated by the size of the channel; the waves are disturbed near the obstacles but this disturbance is only localised near the solid element.

3 Conclusions

In the present study two-dimensional simulations were performed to investigate the effect of the roughness on the critical Reynolds number. A large influence of the distance between the elements on the Re_{cr} has been observed. In agreement with the fully rough turbulent simulations it has been found that the major effects occur at $w/k = 7$. The two-dimensional geometries here considered are ideal and rather different from those in real applications that are three-dimensional. A large number of three-dimensional simulations are necessary to create a database which will contribute to understand the transitional regime of rough flows.

4 References

- Burattini, P., Leonardi, S., Orlandi, & Antonia, R.A., 2008, "Comparison between experiments and direct numerical simulations in a channel ow with roughness on one wall" *J.Fluid Mech.* Vol. 600 pp.403 –426 .
- Leonardi, S., Orlandi, P., Smalley R.J., Djenidi, L. & Antonia, R. A., 2003, "Direct numerical simulations of turbulent channel flow with transverse square bars on the wall" *J. Fluid Mech.* Vol. 491 , 229 - 238.
- Leonardi S. & Orlandi P., 2004, "A numerical method for turbulent flows over complex geometries" *ERCFTAC bulletin* Vol. 62, 41-46.
- Orlandi P., Leonardi S., & Antonia R.A., 2006, "Turbulent channel flow with either transverse or longitudinal roughness elements on one wall" *J. Fluid Mech.* Vol. 561, pp. 279-305.
- Drazin, P.G., & Reid W.H., 1981, *Hydrodynamic Stability*, Cambridge University Press

Transient turbulent bursting in enclosed flows

K. Hochstrate¹, M. Avila², J. Abshagen¹, and G. Pfister¹

¹Institute of Experimental and Applied Physics, University of Kiel, 24118 Kiel, Germany

²Max Planck Institute for Dynamics and Self Organization, 37073 Göttingen, Germany

hochstrate@physik.uni-kiel.de

1 Introduction

The origin and the transition to turbulence in wall-bounded shear flows is one of the outstanding problems of classical physics. In order to shed light on this transition, recent investigations have analyzed the decay of localized turbulent structures. At low Reynolds numbers, an exponential distribution of survival times has been observed in pipe and plane Couette flows [1, 2, 3, 4]. In phase space this is related to the decay from a chaotic saddle. However, pipe flow is an open flow, posing many experimental and numerical challenges for the study of bifurcation events. In a closed system we have found a flow state that shows transient turbulent behavior also at low Reynolds numbers. It appears as turbulent bursting in the Taylor-Couette system without an external forcing for counter-rotating cylinders above the centrifugal instability. Therefore it competes with coherent states of the system. Here we present spatiotemporal properties and lifetime behavior of this flow.

2 Experimental setup

The Taylor-Couette system consists of fluid of kinematic viscosity ν confined between two concentric rotating cylinders. The inner cylinder is machined of stainless steel with a radius of $r_i = (12.50 \pm 0.01)$ mm, the outer one is made of optically polished glass with a radius of $r_o = (25.00 \pm 0.01)$ mm. The axial length of the system L is determined by the position of two solid end plates. In this investigations the radius ratio is constant at $\eta = r_o/r_i = 0.5$, while the aspect ratio $\Gamma = L/(r_o - r_i)$ varies from 4 to 8. The system is non-dimensionalized with the gap width $d = r_o - r_i$ (length) and diffusion time $\tau = d^2/\nu$. The Reynolds numbers of the cylinders are defined as $Re_{i,o} = r_{i,o}d\Omega_{i,o}/\nu$ (where $\Omega_{i,o}$ are the angular speeds of inner and outer cylinders). In this investigation two different experiments are used, one for flow visualization

monitored with a HDD-camera, another one for high-precision measurements with Laser-Doppler-Velocimetry.

3 Results

The turbulent bursting is transient and appears without an external forcing in the system at a certain Reynolds number of the inner cylinder Re_t , which is well above the centrifugal instability. In particular, the bursting emerges as an instability of a rotating wave, a so-called wavy mode.

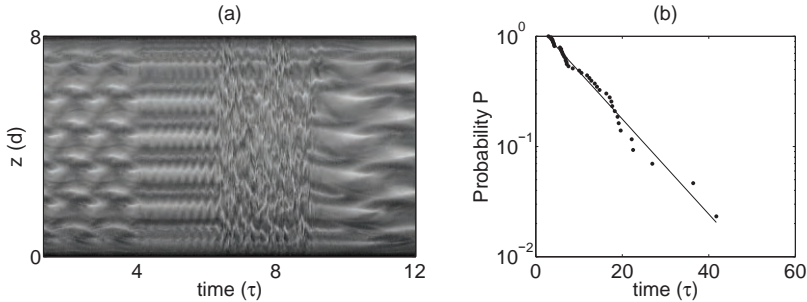


Fig. 1. Sudden increase of Re_i from 250, where the wavy mode is stable, to 280 ($Re_o = -180$, $\Gamma = 8$)

- (a) experimentally observed bursting in a space-time diagram
- (b) probability of lifetimes

Fig. 1 (a) shows a space-time diagram of the bursting obtained by flow visualization. Four different sequences can be distinguished. In the first sequence, the wavy mode is a global flow state with a constant frequency and shows no turbulent behavior at all. Later, the wavy-mode becomes modulated, so that vortices start to oscillate in the axial direction (after about 4 diffusion times τ), until turbulent bursts appear abruptly ($\tau \approx 7$). Within this last period the turbulent bursting is localized and randomly distributed over the whole length of the system and has a complex structure. After some time the turbulent behavior disappears and we observe a new wavy mode with a slower oscillation ($\tau \approx 9$) which remains stable in time. The flow visualization is recorded at $\Gamma = 8$ and a constant outer Reynolds number of $Re_o = -180$. The Reynolds number of the inner cylinder Re_i is increased instantaneously at $\tau = 0$ from 250 to 280, which is slightly above Re_t .

At the same parameters we have obtained distributions of lifetimes of the turbulent bursting, measuring the time from the change in Re_i until the turbulent bursts disappear and the slow wavy mode sets in. We observe an exponential probability distribution, shown in Fig. 1(b). Therefore, the decay is a memoryless process, i.e. it is independent of the age of the bursting. In

phase space, an exponential probability distribution of lifetimes is typical for the decay from a chaotic saddle [5].

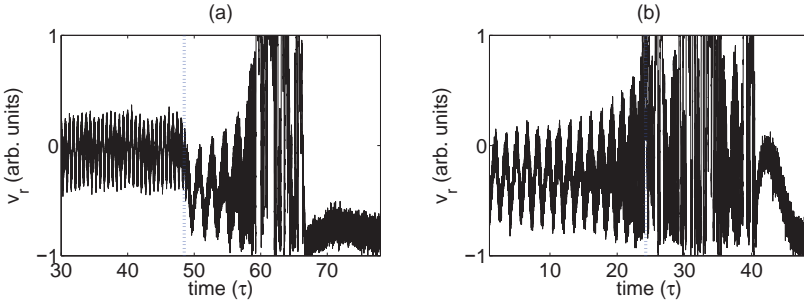


Fig. 2. Radial velocity of the bursting, measured by LDV ($Re_o = -180, \Gamma = 8$)
 (a) Instantaneously increasing of Re_i from 250 to 280
 (b) Quasi stationary increasing from $Re_i = 279$ to $Re_i = 280$
 the gray dotted line indicates the changes in Re_i , the signal saturates during the bursts with the chosen electronic amplification

In Fig. 2 Laser-Doppler-Velocimetry (LDV) measurements of the radial velocity v_r of the wavy modes and the transient bursting are plotted. The gray dotted line in (a) (at $\tau \approx 48$) indicates the change in Re_i from 250 to 280. On the left side of this line the regular wavy mode with a frequency of 0.06 can be seen. By changing the Reynolds number rapidly, the oscillation slows down and turbulent bursts appear. The bursts show high velocities compared to the wavy mode, so that the chosen electronic amplification reaches its maximum and the signal saturates. After a lifetime of about $\Delta\tau \approx 20$ (counting from the jump in Re_i) the turbulent bursting disappears and the oscillation of the slow wavy mode starts.

The bursting of the wavy mode does not require a jump in the Reynolds number. It also appears for quasi-stationary increases of Re_i . Therefore we increased Re_i from 250 to 280 in steps of $\Delta Re_i = 1$, measuring the velocity at each step for $\Delta\tau = 24$. In Fig. 2 (b) the time series at $Re_i = 279$ (left of the dotted gray line at $\Delta\tau = 24$) and $Re_i = 280$ (right of the dotted gray line) are shown. Comparing these measurements with the one after the jump in Re_i in (a), we observe the same flow behavior consisting of a regular oscillation, the bursting and a slow oscillation afterwards.

A closer look at the time series during the bursting in Fig. 2 (b) reveals periods of regular oscillation, interrupted by single bursts. This behavior can also be seen in the space-time diagram in Fig. 3 from numerical simulations (see [6] for details on the method). Radial velocity during the turbulent bursting is shown for 4τ after jumping from $Re_i = 250$ to 300 at $Re_o = 110, \Gamma = 4$.

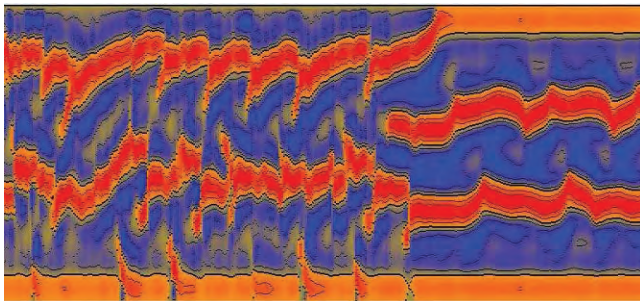


Fig. 3. Space-time diagram of the bursting from numerical simulations. Radial velocity at mid-gap is plotted over system length (Y axis) and time (X axis). The parameters are $Re_o = 110$, $\Gamma = 4$ and $Re_i = 300$, after increasing from 250.

4 Conclusion and outlook

We have found a flow state in the counter-rotating Taylor-Couette system which shows transient turbulent bursting at low Reynolds numbers. It appears above the centrifugal instability without an external forcing and therefore it competes with coherent states of the system. We observe the same spatio-temporal characteristics of the turbulent bursting for quasi-static increases of the Reynolds number, as well as for sudden jumps in Re_i . An analysis of lifetimes for the second case shows an exponential distribution, which is often related to the existence of a chaotic saddle.

Since Taylor-Couette flow is a closed system and considered as one of the best controllable experiments in hydrodynamics, it is ideally suited to investigate the asymptotic stability of a flow state. On the other hand, stable and even unstable solutions can be determined via calculations of the Navier-Stokes equations in quantitative agreement with experiments [7]. The purpose of our combined experimental and numerical study is to understand the dynamical reasons underlying this type of turbulence.

References

1. J. Peixinho, and T. Mullin. Phys. Rev. Lett., **96**, 094501 (2006).
2. A. P. Willis, and R. R. Kerswell. Phys. Rev. Lett., **98**, 014501 (2007).
3. T. M. Schneider, and B. Eckhardt. Phys. Rev. E, **78**, 046310 (2008).
4. B. Hof, A. Lozar, D. J. Kuik, and J. Westerweel. Phys. Rev. Lett., **101**, 214501 (2008).
5. T. Tél, and Y.-C. Lai. Phys. Rep., **460**, 245–275 (2008).
6. M. Avila, M. Grimes, J. M. Lopez and F. Marques. Phys. Fluids, **20**, 104104 (2008).
7. J. Abshagen, J. M. Lopez, F. Marques, and G. Pfister. J. Fluid Mech., **613**, 357–384 (2008).

On New Localized Vortex Solutions in the Couette-Ekman Layer

M. Withalm and N. P. Hoffmann

Institute of Mechanics and Ocean Engineering
Hamburg University of Technology
Eißendorfer Straße 42, 21073 Hamburg, Germany

`martin.withalm@tuhh.de`, `norbert.hoffmann@tuhh.de` corresponding author

Transition to turbulence can often be understood through analysis of instabilities and bifurcations. Plane Couette-flow and Hagen-Poiseuille flow, however, are well known to be linearly stable for all Reynolds numbers. Rather recently finite-amplitude states not bifurcating from the laminar base flow have been found [1, 2] and are now being discussed as possibly forming decisive structures in the high-dimensional phase space in which the transition to turbulence actually takes place [3, 4, 5]. It is noteworthy that most of the recently investigated finite-amplitude states in plane Couette and Hagen-Poiseuille flow are periodic and infinitely extended in the spatial directions in which the underlying system is homogeneous. One of the remaining questions seems to be, however, how the spatial localization of turbulence structures like puffs and patches can be explained in terms of a dynamical systems perspective. The existence of localized finite-amplitude states in the style of strongly nonlinear dissipative solitons is an attractive hypothesis in that context: The complex spatially localized turbulence could then be affected in one way or another by the phase-space properties and the phase space neighborhood of such localized solutions. The existence of these localized, solitary solutions in plane Couette flow is still being debated [6, 7, 8, 9]. In other pattern forming systems solitary solutions have, however, been found: in magnetohydrodynamics so-called 'convectons' have recently been detected [10, 11]; in Ekman type flows localized vortex solutions have been reported [12]; and also in granular materials spatially strongly localized patterns have been observed [13].

The present work forms an extension of earlier studies on localized solitary vortex solutions in the Couette-Ekman system, see figure 1. In this system, which consists of a plane Couette configuration in a reference system rotating with constant angular velocity normal to the plates [14], the existence of stationary localized solitary vortex solutions had previously been detected numerically [12]. In this previous study the solitary solutions appeared through saddle-node type bifurcations and could not be linked to secondary states

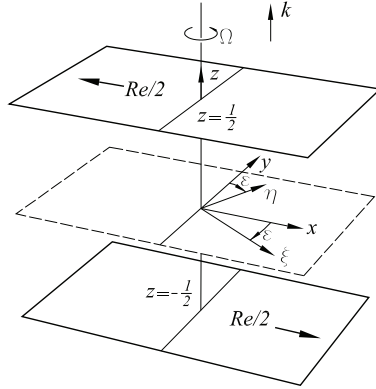


Fig. 1. Graphical visualization of the Ekman-Couette system.

of the flow, which all seemed to bifurcate supercritically from the base flow. Moreover, the solitary roll-like vortex structures turned out to be linearly unstable in all cases under investigation. In the limit of vanishing system rotation, i.e. in the standard non-rotating plane Couette flow configuration, the solutions did, however, not exist.

The present work describes new localized solutions related to the previously determined ones and describes some additional features of the newly found solutions. These new solutions are characterized by a finite number of neighboring rolls within the unperturbed base flow. Solutions with different numbers of rolls seem to emerge from the single-roll structures through saddle-node bifurcations in which at the turning point an additional pair of vortex rolls attached to the original roll is generated or destroyed, respectively.

The phenomenon seems to be sort of analogous to what has recently been called 'snaking' in the context of binary fluid convection (e.g. [15]), where several saddle-node bifurcations are linked when there is a subcritical bifurcation. It then is of course plausible that there should be finite-amplitude solutions representing domain-like solutions. In the present case of Ekman-Couette flow all bifurcations close to the critical points of the neutral surface had been found to be supercritical, such that domain-type solutions would not

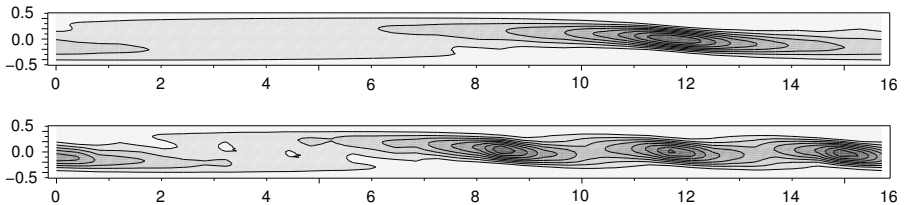


Fig. 2. Typical streamlines of the localized solutions in the form of single and triple rolls.

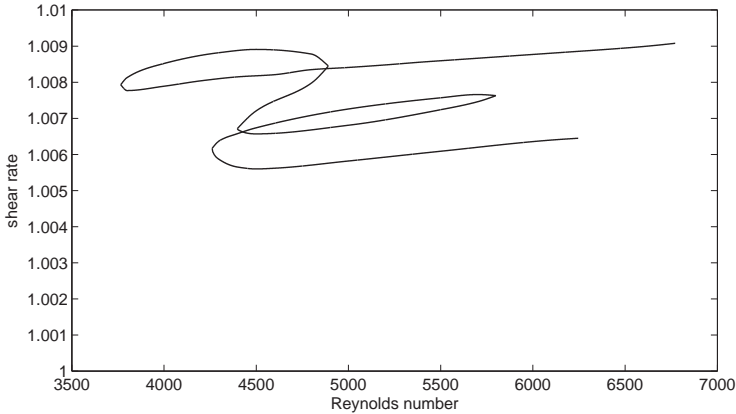


Fig. 3. Typical bifurcation structures for two different parameter regimes.

have been expected. The system does, however, have a rather twisted neutral surface that for some parameter combinations folds back, such that the basic flow remains linearly unstable only in a finite Reynolds number interval [16]. Taking this into account one could imagine that domain-type solutions are sort of generated in those parameter regimes and can then - possibly for higher Reynolds numbers - be followed into other parameter regimes, where the underlying bifurcation structure has turned supercritical.

Figure 4 shows some results for shear rates when the box size is changed. First of all it can be seen in the graph that the numerical resolution chosen turns out to be adequate for the structures under investigation. In addition one may note that in many cases the shear rates vary linearly with the wavenumber derived from the box size. This is the behavior that truly localized structures should show. In other cases, however, there are deviations from that behavior that do not seem to originate in insufficient numerical resolution; possibly the states determined are not truly localized, but are rather related to a solution class linking the solitary and the periodic states, just like the cnoidal waves in the Korteweg-de-Vries equation. The issue does require further study.

Looking for experimental evidence of localized solutions, roll-like vortices have been reported experimentally in rotating disc boundary layers (e.g. [17]); one might conjecture that the observed localized structures (then called 'spots' and 'rollers') could be related to the solutions found presently. First linear stability calculations for the present solutions do suggest, however, that also the new solutions are linearly unstable. Among the instabilities appearing, there are both modes that could lead to three-dimensional structures, as well as modes of modulational character. Further numerical analysis will therefore be required to assess the role of the described solutions in the possibly more complex high-dimensional, and even time-dependent, dynamics actually taking place. Another interesting point remains the quest for localized finite-

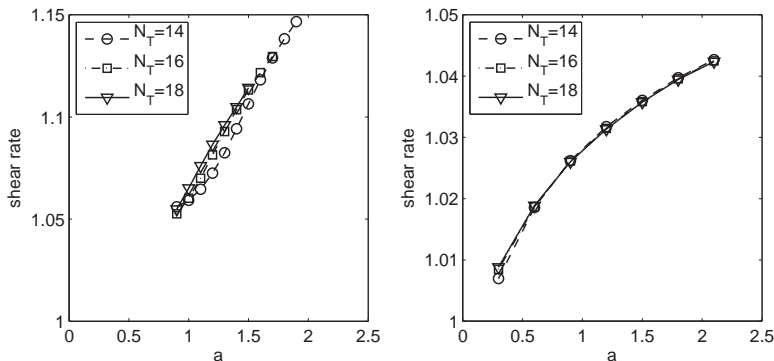


Fig. 4. Variation of shear rate vs. box size. The box wavenumber a is here defined as $a = 2\pi/L$ with L being the length of the computational box. N_T is the numerical resolution.

amplitude states in non-rotating plane Couette flow [18, 19]: the presently described solutions could not be followed into configurations with vanishing rotation. It does, however, seem plausible that there should be three-dimensional solutions bifurcating from the present two-dimensional ones. If such three-dimensional solutions, localized at least in one spatial direction, could then be followed to zero rotation, is still to be answered.

References

1. M. Nagata and F. H. Busse, *J. Fluid Mech.*, **135**, 1 (1983).
2. H. Wedin and R. R. Kerswell, *J. Fluid Mech.*, **508**, 333 (2004).
3. R. M. Clever and F. H. Busse, *J. Fluid Mech.*, **243**, 511 (1992).
4. R. R. Kerswell, *Nonlinearity*, **18**, R17 (2005).
5. B. Hof, J. Westerweel, T. M. Schneider and B. Eckhardt, *Nature*, **443**, 59 (2006).
6. A. Cherhabili and U. Ehrenstein, *Eur. J. Mechanics B / Fluids*, **14**, 677 (1997).
7. A. Cherhabili and U. Ehrenstein, *J. Fluid Mech.*, **342**, 159 (1997).
8. F. Rincon, *Phys. Fluids*, **19**, 074105 (2007).
9. U. Ehrenstein, M. Nagata and F. Rincon, *Phys. Fluids*, **20**, 064103 (2008).
10. S. Blanchflower, *Phys. Lett. A*, **261**, 74 (1999).
11. S. Blanchflower and N. Weiss, *Phys. Lett. A*, **294**, 297 (2002).
12. N. P. Hoffmann and F. H. Busse, *Eur. J. Mech. B - Fluids*, **19**, 391 (2000).
13. P. B. Umbanhowar, F. Melo and H. L. Swinney, *Nature*, **382**, 793 (1996).
14. N. Hoffmann, F.H. Busse and W.-L. Chen, *J. Fluid Mech.*, **366**, 311 (1998).
15. O. Batiste, E. Knobloch, A. Alonso and I. Mercader, *J. Fluid Mech.*, **560**, 149 (2006).
16. N. P. Hoffmann, *Beiträge zur Theorie der Ekman-schicht*, Bayreuth 1997.
17. P. I. Sankov and E. M. Smirnov, *Fluid Dyn.*, **19**, 695 (1985).
18. F. Rincon, *Phys. Fluids*, **19**, 074105 (2007).
19. U. Ehrenstein, *Phys. Fluids*, **20**, 064103 (2008).

Shear instabilities in Taylor-Couette flow

A. Meseguer⁽¹⁾, F. Mellibovsky⁽¹⁾, F. Marques⁽¹⁾ and M. Avila⁽²⁾

(1) Dept. Applied Physics, Universitat Politecnica de Catalunya, Barcelona, Spain

(2) Max Planck Inst. for Dynamics and Self-Organization, Göttingen, Germany

alvar@fa.upc.edu

Summary. Subcritical instabilities in small gap Taylor-Couette (TCF) problem are studied numerically when both cylinders rotate in opposite directions. The computations are carried out for a radius ratio $\eta = r_i/r_o = 0.883$. A first exploration is focused on the study of spiral flows originated from subcritical Hopf bifurcations of the basic circular Couette solution. The second exploration addresses the transition from laminar flow to the usually termed as *spiral turbulence* regime characterized by alternating laminar and turbulent spiral bands which co-exist even in regions of the parameter space where the circular Couette flow is linearly stable.

1 Formulation

In TCF, an incompressible fluid of kinematic viscosity ν and density ρ is contained between two concentric rotating cylinders whose inner and outer radii and angular velocities are r_i^* , r_o^* and Ω_i , Ω_o respectively. The dimensionless parameters are the radius ratio $\eta = r_i^*/r_o^*$ and the inner and outer Reynolds numbers $R_i = dr_i^*\Omega_i/\nu$ and $R_o = dr_o^*\Omega_o/\nu$ of the cylinders. All variables are rendered dimensionless using the gap $d = r_o^* - r_i^*$ and viscous time d^2/ν as units for space and time, respectively. The dynamics of the flow is controlled by the incompressible Navier–Stokes equations

$$\partial_t \mathbf{v} + (\mathbf{v} \cdot \nabla) \mathbf{v} = -\nabla p + \Delta \mathbf{v}, \quad \nabla \cdot \mathbf{v} = 0. \quad (1)$$

In nondimensional cylindrical coordinates (r, θ, z) , the basic circular Couette flow (CCF) is $\mathbf{v}_B = (u_B, v_B, w_B) = (0, Ar + B/r, 0)$, with $A = (R_o - \eta R_i)/(1 + \eta)$ and $B = \eta(R_i - \eta R_o)/(1 - \eta)(1 - \eta^2)$. The flow is assumed to be L^* -periodic in the axial direction so that the dimensionless domain is $(r, \theta, z) \in \mathfrak{D} = [r_i, r_o] \times [0, 2\pi) \times [0, \Lambda)$, where $\Lambda = L^*/d$ is the *aspect ratio* of the computational box. Arbitrary perturbations \mathbf{u} of the base flow, $\mathbf{v} = \mathbf{v}_B + \mathbf{u}$, are expanded in a solenoidal spectral Fourier-Galerkin basis

$$\mathbf{u}(r, \theta, z, t) = \sum_{l, n, m} a_{lnm}(t) e^{i(lk_0 z + n\theta)} \mathbf{v}_{lnm}(r), \quad (2)$$

for $(l, n, m) \in [-L, L] \times [-N, N] \times [0, M]$ and $k_0 = 2\pi/\Lambda$. The time integration is carried out with a 4th order linearly implicit time marching method [3]. Following former experimental works [1], the computations presented here were obtained for $\eta = 0.883$, i.e., $r_i = 7.547$ and $r_o = 8.547$, with $(R_o, R_i) \in [-3000, -1200] \times [0, 1000]$ and $\Lambda = 2\pi/k_0 \in [1.23, 29.9]$. The spectral resolution used for the computation of secondary laminar regimes lies within the intervals $(N_r, N_\theta, N_z) \in [28, 48] \times [28, 48] \times [16, 32]$ radial \times azimuthal \times axial grid points, resulting in spectrally converged solutions. For the laminar-turbulent spiral patterns, a resolution within $(N_r, N_\theta, N_z) \in 20 \times [100, 220] \times [100, 220]$ was used, resulting in a dynamical system with up to $\mathcal{O}(10^6)$ degrees of freedom.

2 Subcritical equilibria from modal instabilities of Couette flow

The first exploration has consisted of a comprehensive numerical exploration of secondary finite amplitude solutions using Newton-Krylov methods embedded within arclength continuation schemes. Two different families of rotating waves have been identified: short axial wavelength subcritical spirals ascribed to centrifugal mechanisms and large axial scale supercritical spirals and ribbons associated with shear dynamics in the outer linearly stable radial region.

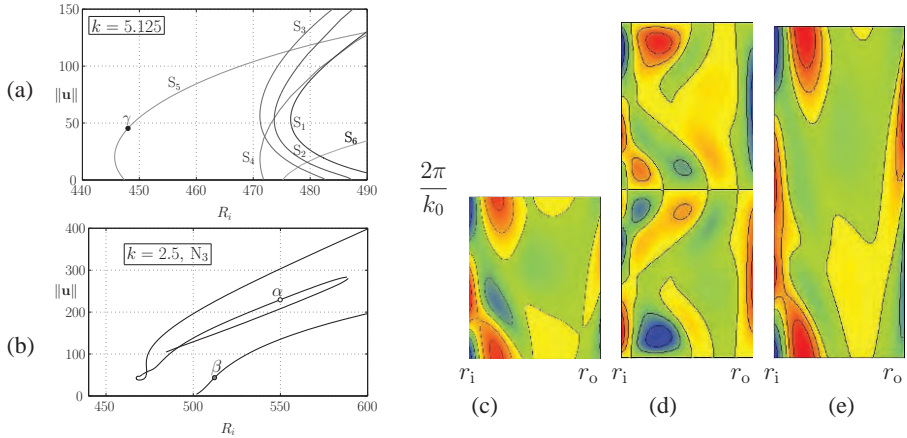


Fig. 1. (a) Norm of bifurcating spiral solutions of azimuthal wavenumbers $n \in [1, 6]$ as a function of R_i for $R_o = -1200$ and axial wavenumber $k = 5.125$. (b) Same as (a) showing a disconnected ribbon solution branch (α) and a supercritical spiral branch (β) for $k = 2.5$. (c), (d) and (e) show azimuthal vorticity distributions on a $\theta = \text{const.}$ section of regimes γ , α and β shown in (a) and (b), respectively.

As shown in Fig. 1a, all the spiral regimes originate from the circular Couette flow at Hopf bifurcations, some of them of subcritical nature. Their instability is clearly related to centrifugal mechanisms and their axial wavelength is consistent

with the characteristic width of the inner centrifugally unstable region. Spiral flows with higher azimuthal and axial wave numbers tend to be less subcritical whereas spirals with lower azimuthal and axial wavenumbers, although not dominant at transition, clearly show more pronounced subcriticality. This motivated further exploration for lower values of k_0 in order to find the large-scale axial dynamics typical of spiral turbulence. However, straightforward continuation of the spirals for lower values of k_0 was unsuccessful, exhibiting turning points before k reaches lower values. The computation of these new spiral shear modes required two different techniques, based on artificially cutting off high axial modes in the time evolution and quasistatic *homotopy* transformation in η , combined with an axial forcing. By including axial advection and reducing η it was possible to find new spirals of larger wavelength. A very careful variation of these two combined effects sometimes succeeded in recovering low axial wavenumber rotating waves for our original problem. However, the described procedures have only been successful for $n_0 = 2$ and $n_0 = 3$ cases. Two families of new solutions have been found; one of them are spirals that bifurcate supercritically from the Couette flow. The other family consists of *ribbons*, apparently disconnected from the basic flow. Figure 1b shows both families for $k_0 = 2.5$. The inner structures of the aforementioned equilibria are shown in Fig. 1c-f.

3 Intermittent regimes from nonmodal instabilities

The second exploration has consisted in triggering transition within the linearly stable region of the parameter space. This has been done for values of R_i and R_o for which experiments reported laminar-turbulent spiral coherence, also termed as *spiral turbulence* [2, 5, 4]. Numerical simulation with moderate resolution have managed to reproduce such a flow (see Fig. 2) within an axially periodic domain, thus confirming that this pattern is not necessarily induced by top or bottom lid effects. Figures 2a and 2b show typical snapshots of computed SPT, conspicuously resembling the experimental results. The exploration reported here is summarized in Fig. 2c, where two parametric paths for $R_o = -3000$ and $R_o = -1200$ (labelled as Γ_1 and Γ_2 , respectively) were followed. Both paths start within the shadowed region of Fig. 2c, where experiments [1] reported supercritical SPT regimes when increasing R_i from below. Starting with a random perturbation at $(R_o, R_i) = (-3000, 900)$ in Γ_1 and $(R_o, R_i) = (-1200, 640)$ in Γ_2 , the time integrations drove the flow towards SPT patterns in less than one viscous time unit. From those starting points, R_i was quasistatically decreased and the time evolution of the flow was monitored for more than 6 viscous time units afterwards. Over Γ_2 , SPT regimes followed exactly the same supercritical behaviour as the one observed in the experiments [1], where smooth decreasing of R_i led to *intermittency* regimes (INT, characterized by localized turbulent spots), *interpenetrating spirals* (ISP) and relaminarization to the basic CCF profile. However, over Γ_1 , the SPT flow was found to be sustained even below the linear stability boundary of the CCF, labelled as LSB in Fig. 2c. The H_1 and H_2 bulleted curves shown in Fig. 2c correspond to experimental hysteretic SPT boundaries when decreasing R_i from above in [2] and [1], respectively. In particular, we found

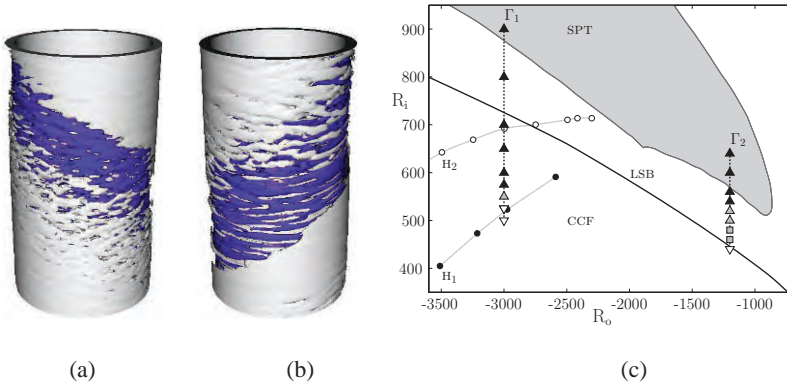


Fig. 2. Angular momentum $L = rv$ isosurfaces of typical SPT flows ($L > 0$ and $L < 0$ in white and blue, respectively). (a) Subcritical SPT at $(R_o, R_i) = (-3000, 650)$ showing $L = \pm 1900$. (b) Supercritical SPT at $(R_o, R_i) = (-1200, 600)$ showing $L = \pm 950$. (c) Explored regions in (R_o, R_i) -parameter space. Black triangles, gray triangles, gray squares and white triangles correspond to SPT, INT, ISP and CCF flows, respectively.

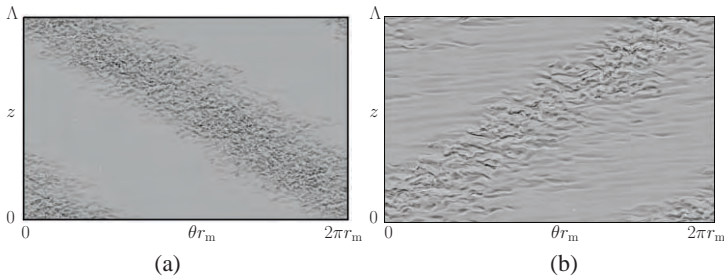


Fig. 3. Radial vorticity $(\nabla \times \mathbf{u})_r$ of SPT flows on the intermediate radial surface $r_m = 8.21$. (a) $(R_o, R_i) = (-3000, 650)$, with $(\nabla \times \mathbf{u})_r \in [-1.3 \times 10^4, 1.4 \times 10^4]$, and (b) $(R_o, R_i) = (-1200, 600)$, with $(\nabla \times \mathbf{u})_r \in [-6.6 \times 10^3, 6.1 \times 10^3]$. Dark and light regions represent negative and positive radial vorticity, respectively.

our computations to agree with the H_1 boundary found by Coles. This work was supported by the Spanish Government grants FIS2007-61585 & AP-2004-2235, and the Catalan Government grant SGR-00024.

References

1. C. Andereck, *et al.*, J. Fluid Mech., **164**, 155 (1986).
2. D. Coles, J. Fluid Mech., **21**, 385 (1965).
3. A. Meseguer, *et al.*, Eur. Phys. J. Special Topics, **146** 249 (2007).
4. A. Prigent, *et al.*, Phys. Rev. Lett., **89**(1) 014501 (2002).
5. C. Van Atta, J. Fluid Mech., **25**, 495 (1966).

Particle Tracking Velocimetry in Transitional Plane Couette Flow

B. Lüthi, M. Holzner, M. Kinzel, A. Liberzon, and A. Tsinober

Institute of Environmental Engineering, ETH Zürich, 8093 Zürich, Switzerland
luethi at ifu.baug.ethz.ch

Plane Couette flow has the peculiar property that transition to turbulence occurs despite the fact that its laminar profile is linearly stable. For high enough Reynolds numbers small amplitude perturbations are enough to initiate the growth of turbulent spots. Such spots have been subject to investigation for a few decades, see e.g. [1, 2]. In addition, it has been observed that around transitional Reynolds numbers laminar and turbulent regions can co-exist if this Reynolds number is approached from the turbulent side, e.g., [3, 4]. For both cases, distinct interfaces divide the regimes between turbulent and non turbulent flow. It is our main interest to study the evolution of such interfaces similar to the work of [5] where the shear free case with inhomogeneous forcing by an oscillating grid has been investigated in detail.

In this work we present the design and implementation of a plane Couette facility that has a large aspect ratio of $100 \times 100 \times 1$ (height, width and half-gap, respectively) and that is accessible for the three dimensional particle tracking velocimetry (3D-PTV) technique, see figure 1. Our setup will allow for the first time to access experimentally the full range of scales in a plane Couette flow. Ultimately, our aim is to explore the transitional flow regime of $325 < Re < 415$. In particular the field of velocity gradients close to the turbulent non-turbulent interface is at the center of our attention.

The flow domain is between a moving belt and a glass plate separated by a distance of 0.031 m. At the entrance of the domain the flow is becalmed by a honey-comb with tube diameters and lengths of 3 mm and 30 mm, respectively. In the hone-comb and along the return flow, in the 0.055 m gap between the glass plate and the glass tank wall, pressure losses occur, which will have to be compensated with a sucking and blowing device. Currently, this is still under construction.

The presented results stem from 3D-PTV measurements in a domain of $0.3 \times 0.21 \times 0.03 \text{ m}^3$ at maximum belt speed $u_b = 0.062 \text{ m/s}$, i.e. $Re = 560$, based on half gap and half belt velocity. For each frame, the positions of 7000 tracer particles of diameter $100 \mu\text{m}$ are determined and linked. The pressure losses are reflected in a significant counter flow along the glass wall, 0.01



Fig. 1. Plane Couette facility setup. Inside a $2 \times 2 \times 0.25 \text{ m}^3$ water tank an endless belt of 1.6 m width is controlled by two large driving drums that measure 219 mm in diameter. The optically accessible measuring domain with sheared flow is $1.6 \times 1.6 \times 0.03 \text{ m}^3$.

$m < z_c < 0.03 \text{ m}$, as can be seen for all streamwise velocity profiles shown in figure 2(a). In the middle of the domain a 2 mm diameter hole in the glass plate allows for cross-jet perturbations. For the time being, we perturb the flow - in a rather crude way - for the duration of 1 sec with an initial pressure head of 0.6 m. The resulting ‘spot’, as seen after 10 sec, is shown in figure 2(b), where tracer particles are recorded with 1 sec exposure time.

An analysis of the corresponding tracer trajectories, figure 3(a), reveals that inside the spot region significant wall normal velocities are present. This is consistent with the velocity profiles becoming ‘flatter’ with time, figure 2(a), due to the momentum transport by the vertical velocity fluctuations across the gap. Using a reference profile from the unperturbed flow state, the kinetic energy due to the perturbation is measured. As can be seen qualitatively from figure 2(b) and quantitatively from figure 3(b) the perturbation energy is organized in ‘high-speed’ streaks. For the current setting, we observe visually that these streaks have a life-time of approximately 30 sec.

The preliminary results show that we have managed to produce a quasi-laminar shear flow. We demonstrated the feasibility of high quality 3D-PTV

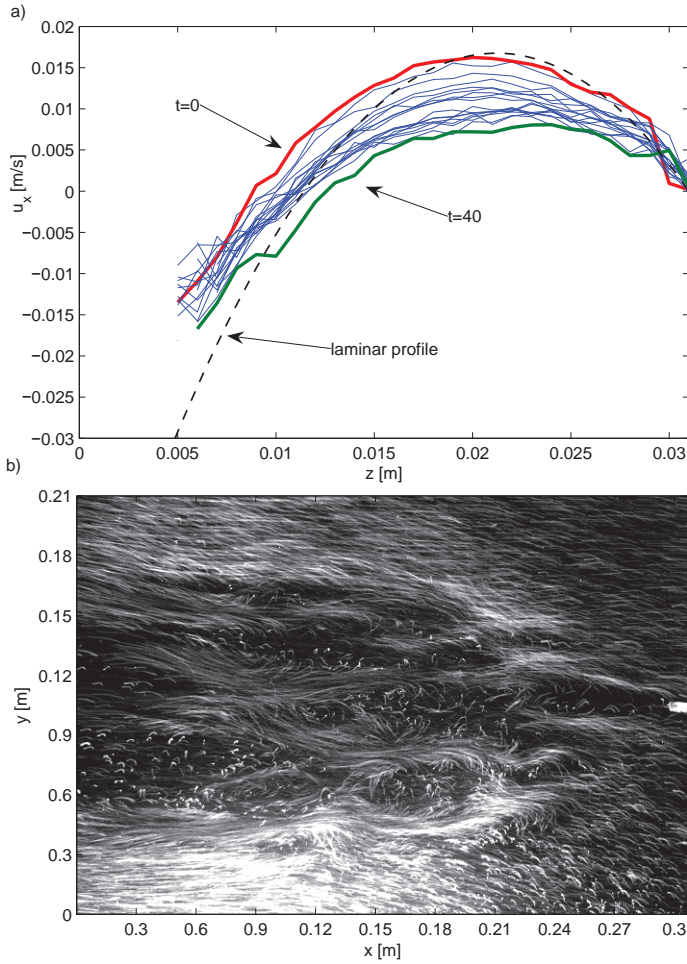


Fig. 2. a) The $u_x(z, t)$ velocity component averaged over the $\{x, y\}$ plane is shown for $0 \text{ sec} < t < 40 \text{ sec}$. The dashed line is the best fit of the corresponding laminar shear profile with $dp/dx = 370 \text{ Pa}$. b) Overlay of 50 frames (1 sec) of particle images 10 seconds after perturbation. The perturbation is applied at position $\{0.3, 0.11\}$, the belt is moving in negative x direction with $u_b = 0.062 \text{ m/s}$.

measurements in this setup. With the pressure loss of 370 Pa we found the flow to be stable up to $Re = 560$. In order to reach a symmetric flow and to explore the transitional Re regimes, a sucking and blowing device needs to be implemented. From results shown in figure 2(a) we estimate the missing flux as $Q_m \sim 1 \text{ l/sec}$. Once the symmetric flow profile is established, 3D-PTV measurements at large and at small scales will be performed, within the turbulent spots, but also at the turbulent non-turbulent interface.

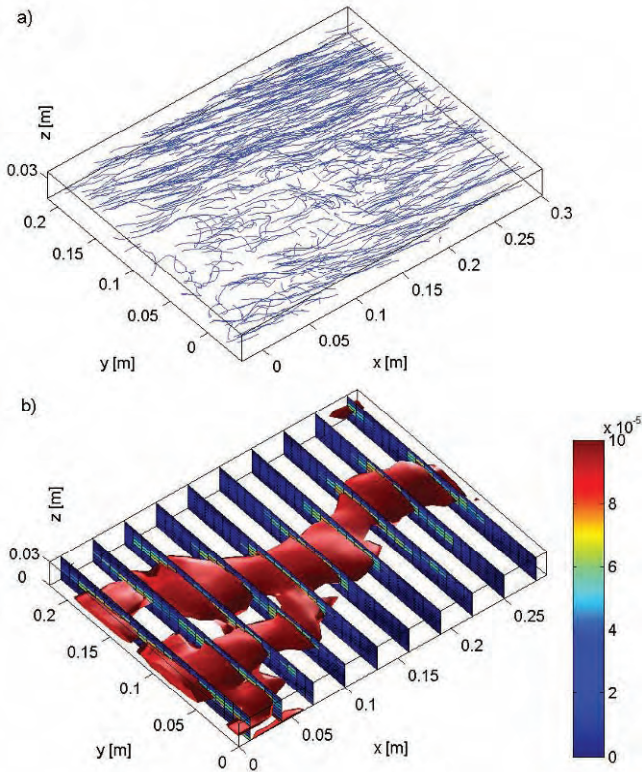


Fig. 3. a) Particle trajectories within $10 \text{ sec} < t < 13 \text{ sec}$ after the perturbation. b) The difference of kinetic energy, u_i^2 to the unperturbed velocity profile is rendered with slices and with an iso-surface for values of $u_i^2 > 6 \cdot 10^{-5} \text{ m}^2/\text{s}^2$.

References

1. Mohamed Gad el Hak, Ron F. Blackwelder, and James J. Riley. On the growth of turbulent regions in laminar boundary layers. *J. Fluid Mech.*, 110:73–95, 1981.
2. Bruno Eckhardt, Holger Faisst Armin Schmiegell, and Tobias M. Schneider. Dynamical systems and the transition to turbulence in linearly stable shear flows. *Phil. Trans. R. Soc. A*, 366:1297–1315, 2008.
3. Paul Manneville. Spots and turbulent domains in a model of transitional plane couette flow. *Theoret. Comput. Fluid Dynamics*, 18:169–181, 2004.
4. Dwight Barkley and Laurette S. Tuckerman. Mean flow of turbulent-laminar patterns in plane Couette flow. *J. Fluid Mech.*, 576:109–137, 2007.
5. M. Holzner, A. Liberzon, N. Nikitin, B. Lüthi, W. Kinzelbach, and A. Tsinober. A Lagrangian investigation of the small-scale features of turbulent entrainment through particle tracking and direct numerical simulation. *J. Fluid Mech.*, 598:465–475, 2008.

Experimental study of coherent structures in turbulent pipe flow

A. de Lozar, and B. Hof

Max Planck Institute for Dynamics and Self-Organization at Göttingen, Germany
adelozar at gmail.com

Coherent structures seem to play an important role in turbulent shear flows. In the last years, unstable solutions with the form of traveling waves have been identified in numerical simulations in plane Couette and pipe flow. It is believed that these solutions form a strange saddle in the phase space, so that the flow state transiently visits these unstable solutions before eventually returning to the laminar state and indeed, these structures were observed in experiments in the form of transients [1]. Furthermore, coherent structures which live between the laminar and the turbulent state have been numerically found, suggesting the existence of a separatrix in the phase space between the laminar and turbulent profile [2]. The main aim of our study is to extend the previous observations of coherent structures, characterize and quantify the occurrence of such periodic states and to rationalize their role in turbulent puffs and slugs.

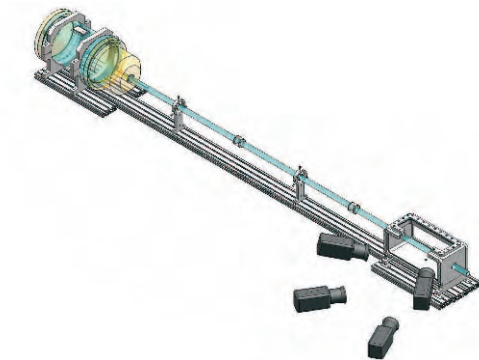


Fig. 1. Experimental setup. Water enters the pipe through a specially designed inflow section. Turbulence can be triggered at injection points along the pipe. Volume resolved velocity measurements are carried out using two high speed (480Hz) LaVision Stereo PIV systems.

Turbulent pipe flow is studied in the transitional regime for $1500 < Re < 4000$. The working fluid is water and the pipe has a diameter of $D = 30$ mm. Two parallel stereo PIV systems have been mounted looking at two planes perpendicular to the flow (see Fig. 1). The distance between the two planes is about $4D$. With this setup the full 3D velocity profile can be obtained in both planes. This new setup allows a better characterization of the coherent structures. For example, the phase velocities of traveling waves can be obtained from the correlation between the velocities at both planes.

References

1. B. Hof, C.W.H. Doorne, J. Westerweel, F.T.M. Nieuwstadt, H. Faisst, B. Eckhardt, H. Wedin, R.R. Kerswell and F. Waleffe, *Science*, **305**, 1594 (2004)
2. T.M. Schneider, B. Eckhardt, and J.A. Yorke, *Phys. Rev. Lett.* **99**, 034502 (2007).

Forced localized turbulence in pipe flows

M. Avila and B. Hof

Max Planck Institute for Dynamics and Self-Organization, Göttingen, Germany
mavila@ds.mpg.de corresponding author

Summary. Low Reynolds number turbulence is manifested in shear flows in the form of disordered patches of fluid motion embedded in laminar flow. Here, we investigate the mean properties of these patches in pipe flow and present a new method to influence their physical mechanisms.

1 Introduction

Transitional shear flows are characterized by the presence of localized turbulent structures which are bounded by laminar regions. This has been observed in different canonical shear flow geometries: Taylor–Couette, plane Couette and pipe flows [1, 2, 3]. In the latter, these localized turbulent patches are known as ‘puffs’ and travel in the downstream direction at approximately the mean advection speed [3, 4]. Experiments and numerical simulations show that at low Reynolds number puffs are transient and their lifetime distribution follows an exponential law. However, it is currently debated whether there exists a critical Reynolds number above which puff turbulence is sustained [5, 6, 7, 8].

In this paper we present a new method that may be used to influence the lifetime and dynamical behavior of ‘puff’ turbulence and aid in understanding the underlying physical mechanisms. In particular, a volume force is applied to the Navier–Stokes equations to modify the parabolic axial velocity profile. Global and spatially localized deviations are considered in a long periodic pipe.

2 Formulation

The Navier–Stokes equations with an additional volume force F

$$\partial_t \mathbf{v} + (\mathbf{v} \cdot \nabla) \mathbf{v} = -\nabla p + \frac{1}{\text{Re}} \Delta \mathbf{v} + \mathbf{F}, \quad \nabla \cdot \mathbf{v} = 0, \quad (1)$$

are solved with a Petrov–Galerkin spectral method [9]. Chebyshev polynomials in the radial direction are combined with Fourier expansions in the azimuthal and axial directions. The Reynolds number is defined as $Re = UD/\nu$, where U is the mean flow speed, D the pipe diameter and ν the kinematic viscosity of the fluid. The mass-flux is kept constant, and thus the mean pressure gradient in the axial direction is time-dependent. The results reported here have been obtained in a long periodic pipe of $50D$ in a grid of about 4×10^6 points.

3 The turbulent puff: mean flow



Fig. 1. (a) Stream-wise vorticity (averaged in the azimuthal direction) of a turbulent puff snapshot at $Re = 1900$. Note that the image has been compressed by a factor of 5 in the axial direction. The flow is from left ($z = 0$) to right ($z = 50$) in a periodic pipe of 50 diameters.

Figure 1 shows an instantaneous snapshot of stream-wise vorticity of a turbulent puff at $Re = 1900$ (note that an average over the azimuthal direction has been performed). At the trailing edge of the puff, vorticity decays sharply and laminar flow is quickly recovered. The turbulent fluctuations within a puff are much faster than its down-stream propagation speed, thus it is difficult to compute instantaneous propagation speeds. We define the puff speed in the interval $[t, t + \Delta t]$ as

$$c = \frac{\Delta z}{\Delta t} : \quad \min_{\Delta z} \|v(r, \theta, z - \Delta z, t + \Delta t) - v(r, \theta, z, t)\|_2 \quad (2)$$

where Δz is the spatial shift that minimizes the norm of the velocity fields difference between two snapshots. It is worth noting that correlations between the turbulent motions may produce a drift in the computed speed. Our results show that a time of $\Delta t \sim 20D/U$ between snapshots is appropriate to eliminate these effects. Using this method, time averaged quantities can be computed to characterize the stationary statistical puff by collecting data in a co-moving frame.

Figure 2 shows the time-averaged stream-wise velocity distribution of a turbulent puff at $Re = 1900$. Note that the basic Poiseuille profile has been subtracted to aid visualization. Fluid is accelerated close to the pipe wall and decelerated in the center, thus creating a large-scale circulation, with radially outward flow at the trailing edge, that is apparent in the corresponding stream-function of Fig.2(b).

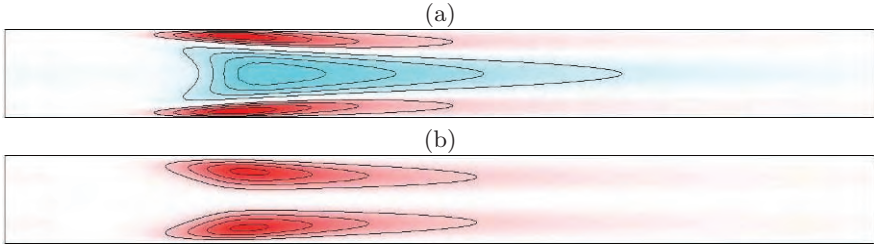


Fig. 2. (a) Time average of stream-wise velocity of a turbulent puff at $Re = 1900$. (b) Associated azimuthal stream-function.

4 Localized forcing

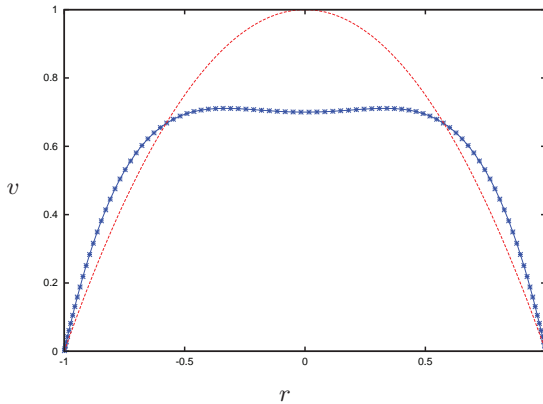


Fig. 3. Laminar Poiseuille profile (dashed line) and forced pluck-like profile, with $\alpha = 0.3$, i.e with a centerline velocity drop of about 30%.

A volume force F is applied to the Navier–Stokes equations (1) to modify the basic profile and verify how the mean properties of the puff are influenced. Figure 3 shows the parabolic Poiseuille profile (dashed line) and the resulting profile (solid line with crosses) when F is applied. The latter is similar to the mean profile of a turbulent puff close to the leading edge (see Fig. 2(a)).

The forcing is defined with a single parameter α , which defines the drop in centerline velocity with respect to the Poiseuille profile (the mass-flux is kept constant). In the case of a globally modified profile, the incompressibility condition is automatically satisfied, as $v = v(r)$. However, when the forcing is localized in the axial direction, $v = v_1(r)v_2(z)$, and incompressibility enforces a secondary weak radial flow (of an order of magnitude less than the modification in stream-wise velocity). The localization is accomplished with

a Gaussian function, $v_2(z) = \exp[-(z/L)^2]$, where L controls the axial extent of the forcing.

Current and future work is focused on the effect of the forcing on the localisation mechanism and lifetimes of low Re turbulence.

References

1. D. Coles, *J. Fluid Mech.*, **21**, 385–425 (1965).
2. A. Prigent, and G. Grégoire, and H. Chaté, and O. Dauchot, and W. van Saarloos, *Phys. Rev. Lett.*, **89**, 014501 (2002).
3. I. J. Wygnanski, and F. H. Champagne, **59**, 281-335 (1973).
4. A. de Lozar, and B. Hof, *Phyl. Trans. R. Soc. London A*, **367** (2008).
5. J. Peixinho, and T. Mullin, *Phys. Rev. Lett.*, **96**, 094501 (2006).
6. A. P. Willis, and R. R. Kerswell, *Phys. Rev. Lett.*, **98**, 014501 (2007).
7. T. M. Schneider, and B. Eckhardt, *Phys. Rev. E*, **78**, 046310 (2008).
8. B. Hof, A. de Lozar, D. J. Kuik, and J. Westerweel, *Phys. Rev. Lett.*, **101**, 214501 (2008).
9. A. Meseguer, and F. Mellibovsky, *Appl. Num. Math.*, **57**, 920-938 (2007).

From localized to expanding turbulence

B. Hof and A. de Lozar

Max Planck Institute for Dynamics and Self-Organization, 37073 Göttingen,
Germany
bhof@gwdg.de

In the transitional regime turbulence in pipe, channel and Couette flow appears in localized patches, sometimes called spots or puffs. These have a fixed length and a propagation speed which depends on the Reynolds number. It has been demonstrated in recent studies of pipe flow that such turbulent puffs have a finite lifetime and that their decay is a memoryless process [1, 2]. Generally this behaviour is consistent with the assumption that the turbulent state forms a chaotic saddle in phase space.

For somewhat larger Reynolds numbers ($Re > 2500$ in pipes or $Re > 400$ in Couette flow) turbulent structures begin to grow in size. In the case of pipe flow localized spots are commonly referred to as puffs and spatially growing structures as slugs. Puffs and slugs can be distinguished ([3]) by the characteristic change of the centreline velocity during the passage of the respective structure (Fig. 1.). While qualitative differences have been pointed out in a

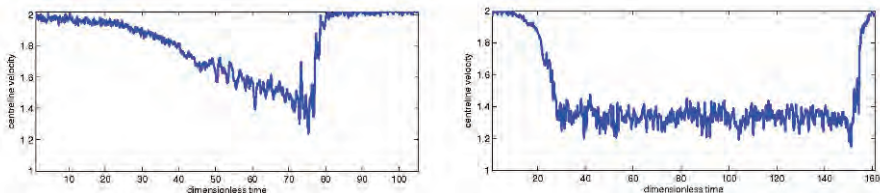


Fig. 1. a) centreline velocity during the passage of a turbulent puff at $Re = 2300$. The decay of the velocity at the downstream interface is slow while that at the upstream interface is sharp. b) During the passage of a turbulent slug ($Re = 4000$) a sharp change of the centre line velocity is observed at both interfaces.

number of earlier studies (e.g. [3, 4, 5]) it has not been clarified if growing spots (or slugs) gradually evolve from localized ones and essentially correspond to the same state or if they emerge as a distinct state at a well defined bifurcation point. We here present evidence for the occurrence of a bifurcation, marking

the transition from localized turbulent spots to growing ones. In particular we present data for pipe, duct and channel flow. The consequences for the global dynamics of the turbulent state, e.g. a possible transition from a chaotic repeller (characterized by a finite lifetime of turbulence) to an attractor are discussed.

References

1. B.Hof, J. Westerweel, T. Schneider, and B. Eckhardt, *Nature* **443**, 55 (2006).
2. Hof, B., de Lozar, A., van Kuik, D. J. and Westerweel, J., *Phys. Rev. Lett.* **101**, 214501 (2008).
3. I. Wygnansky and F. Champagne, *J. Fluid Mech.* **59**, 281 (1973).
4. M. Nishi, B. Ünsal, F Durst and G. Biswas *J. Fluid Mech.*, **614**, 425446 (2008).
5. A. Willis and R.R. Kerswell, *Phys. Rev. Lett.* **100**, 124501 (2008)

Influence of test-rigs on the laminar-to-turbulent transition of pipe flows

F. Durst*, K. Haddad*^{***}, Ö. Ertuğ**

* Centre of Advanced Fluid Mechanics, FMP Technology GmbH, D-91058 Erlangen, Germany

** Lehrstuhl für Strömungsmechanik Erlangen, Friedrich-Alexander-Universität Erlangen-Nürnberg, D-91058, Germany
f.durst@fmp-technology.com

Abstract

Theoretical studies of the laminar-to-turbulent transition of pipe flow, based on linear instability considerations, suggest an inherent stability of the flow to small disturbances. Different to this finding, even in most carefully carried out experiments, transition of pipe flows occurs at finite Reynolds numbers. However, the reported critical Reynolds number range differs by nearly two orders of magnitude ($1.9 * 10^3 \leq Re_{cr} \leq 1 * 10^5$). No reason for this extended range is given in the literature. A closer look at the existing data shows, however, that there is a clear dependence of the critical Reynolds number on the employed pipe diameter. The authors work aimed at a closer understanding of the dependence of Re_{cr} on the pipe diameter of the employed test rig. It is shown that the existing data show an increase of the critical Reynolds number with increasing pipe diameter. With this understanding a new pipe flow test facility was designed, manufactured and employed for experiments to achieve an increase of the critical Reynolds number with decreasing pipe diameter. New test facility yielded much higher critical Reynolds numbers for pipe flows than those reported in literature up to date for the investigated pipe diameters. The paper also suggests that the developments of turbulent velocity fluctuations in nozzles, i.e. the decrease of longitudinal velocity fluctuations and the increase of the cross flow fluctuations, is one of the mechanisms that cause transition in pipe flows.

1 Introduction and Aim of Work

An extensive literature survey, with particular attention being paid to the pipe diameter employed in the reported investigations, reveals a clear dependence of the critical Reynolds number on the pipe diameter d , as can be seen

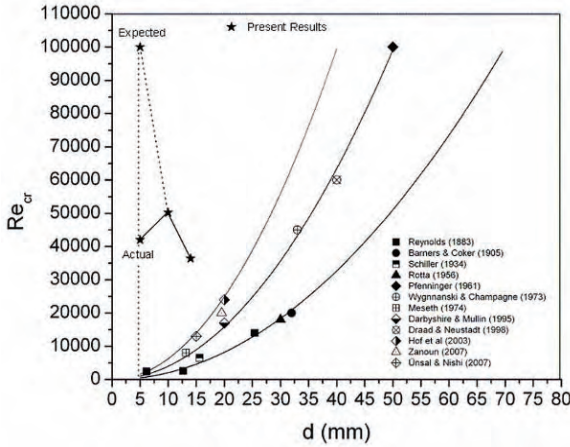


Fig. 1. The dependence of critical Reynolds number on the pipe diameter deduced from the experiments reported in the literature [1, 2, 3, 4, 5, 6, 7, 8, 9, 10, 11, 12, 13, 14].

in Fig. 1. These embrace Re_{cr} data varying over nearly two orders of magnitude and corresponding pipe diameters that change over nearly one order of magnitude.

One of the earlier investigations on laminar-to-turbulent transition of pipe flows was carried out by Rotta [4]. The main parts of the test rig consisted of a pipe of 30 mm diameter and a total length of 9.66 m about corresponding to $L/d = 322$. In order to keep the air flow rate constant regardless of the pressure variations, Rotta used a specially designed air supply valve. The air was sucked from his laboratory and then forwarded to a settling chamber where it passed flow straighteners and then entered the pipe through a contracting nozzle. Hence the test rig embraced all the parts that are typical for all test rigs employed in pipe flow investigations.

There are more test rigs described in the literature that were employed to study laminar-to-turbulent flow transition in pipes and they were all set up to avoid disturbances of the flow to enter the inlet of the actual pipe. All test rigs used nozzles to guide the flow from the plenum chamber to the pipe inlet. However no fluid mechanics considerations were employed to lay out the inlet parts of the pipe flow test rigs. Therefore, the question arises whether improved inlet-sections are feasible to yield higher critical Re-numbers than those achieved by test rigs used so far for experimental studies of laminar-to-turbulent flow transition of pipe flows.

In a first step, the performance of existing test rigs is considered that are usually built to embrace a plenum chamber. This provides a conditioned flow prior to passing it through a contraction nozzle to the entrance of the pipe. From there it develops downstream and in its initial part, it develops a velocity profile containing an inflection point. It is well known that inflection of the velocity profile acts as an amplifier of disturbances. As the section below shows, these disturbances are produced by the nozzles usually placed before the pipe flow test section.

2 Effects of Nozzle on Pipe Inlet Turbulence

Ertuğ and Durst [15] showed through detailed experiments that homogeneous turbulence strained through axisymmetric contractions with high contraction ratios $c = A_{inlet}/A_{outlet} \geq 9$ develops according to derivation with the help of the Rapid Distortion Theory (RDT). This theory clearly shows that the mean square of the longitudinal velocity fluctuations \overline{uu} decreases and that of the transverse fluctuations \overline{vv} increases along the nozzle-axis. The rate of decrease for \overline{uu} and the increase for \overline{vv} are functions of the local contraction ratio c provided by the nozzle. The effect of the nozzles with high-contraction ratio can be illustrated simply using the Vortex Stretching Theory (VST),

$$\overline{uu}_{outlet} = \frac{1}{c^2} \overline{uu}_{inlet} \text{ and } \overline{vv}_{outlet} = c \overline{vv}_{inlet}, \tag{1}$$

which delivers the similar trends of velocity fluctuations as RDT. Note that due to the axisymmetry of grid generated turbulence, the two transverse components should be equal, i.e. $\overline{vv} = \overline{ww}$.

In a RDT- based analysis, we consider two test-rigs with the same inlet diameters of nozzles D_{inlet} but different pipe diameters d^A and d^B , such that $d^B < d^A$. Assuming that at the same mass flow rate, both test rigs have the same relative turbulence intensity at their nozzle inlet, the ratios of the mean square of the velocity fluctuations can be found to be:

$$\overline{uu}_{outlet}^A / \overline{uu}_{outlet}^B = (d^A/d^B)^4 \text{ and } \overline{vv}_{outlet}^A / \overline{vv}_{outlet}^B = (d^B/d^A)^2. \tag{2}$$

In other words, $\overline{uu}_{outlet}^B < \overline{uu}_{outlet}^A$ and $\overline{vv}_{outlet}^B > \overline{vv}_{outlet}^A$. According to linear stability analysis, it is the turbulence intensity which influences the transitional Reynolds number. Comparison of the relative turbulence energy of the transverse velocity fluctuations

$$\overline{vv}/\overline{U^2}^A_{outlet} / \overline{vv}/\overline{U^2}^B_{outlet} = (d^A/d^B)^2 \tag{3}$$

reveals that the relative turbulent energy drops with the reduction in pipe diameter at the same mass flow rate, . However decreasing the pipe diameter means also an increase in Reynolds number for the same mass flow rate $Re = 4\dot{m}/(\mu\pi d)$ and the flow becomes more sensitive to disturbances. Hence, increase in transitional Reynolds number has to be expected with decreasing the pipe diameter.

3 Design Strategy for New Test Rig and Experiments

To verify that the dependence of critical Reynolds number on d^2 can be overcome by a different a different test section design, utilizing the understanding of transition in conventional test rigs, a test rig with a pipe plenum

chamber was set up. The diameter of the plenum chamber was chosen to be $Re = 4\dot{m}/(\mu\pi d) \leq 1940$. Hence as shown by Nishi et al. [14], all disturbances would decay. Adding a specially designed nozzle at the inlet of the pipe, that would not produce inflection points in the inlet velocity profiles, see Fig. 2, yielded a test rig that provided $Re_{cr} \propto 1/d$.

Transition in the new test rig was not caused by amplifications of disturbances in the inlet of the test rig, but by Helmholtz-resonator effects, introduced by the plenum chamber pipe flow assembly, having a volume of V_0 and a length of L . The turbulent slug moving with the streamwise velocity U_{slug} disturbs the flow as it leaves the pipe and cause the formation of the next slug. This yielded $(V_0/\dot{V}) = (L/U_{slug})$ and hence, transition happened at constant volume flow rate \dot{V} resulting in $Re_{cr} \propto 1/d$.

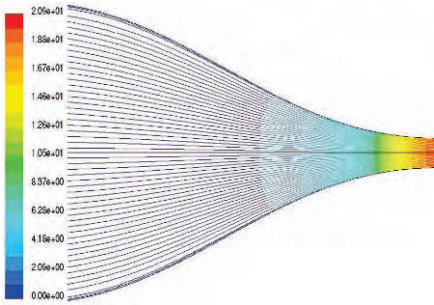


Fig. 2. Nozzle designed for laminar-to-turbulent flow studies yielding $Re_{cr} \propto 1/d$. Computed streamlines shows no separation.

References

1. O. Reynolds, Philos. Trans. R. Soc. London, **Ser. A 174**, 935 (1883).
2. H. T Barnes and E. G Coker, Proc. Roy. Soc. London, **74**, (1905).
3. L. Schiller, ZAMM, **14** 36 (1934).
4. J. Rotta, Ingenieur-Archiv, **24** (4) 258 (1956).
5. W. Pfenninger, Boundary Layer and Flow Control, ed. by G. V. Lachman, Pergamon Press, Oxford **961** (1961).
6. J. Wagnanski and F.H. Champagne, J. Fluid Mech., **59** 281 (1973).
7. J. Wagnanski, M. Sokolov and D. Friedman, J. Fluid Mech., **69** 283 (1975).
8. J. Meseth, Mitteilungen aus dem Max-Planck-Institut für Strömungsforschung und der Aerodynamischen Versuchsanstalt **58**, (1974).
9. G. Darbyshire and T. Mullin, J. Fluid Mech., **289** 83 (1995).
10. A.A. Draad, G.D.C. Kuiken and F.T.M. Nieuwstadt, J. Fluid Mech., **377** 267 (1998).
11. B. Hof, A. Juel, A. and T. Mullin, , Phys. Rev. Lett., **91** 244502 (2003).
12. E. M. Zanoun, personal communication, (2007).
13. F. Durst and B. Ünsal, J. Fluid Mech., **560** 449 (2006).
14. M. Nishi, B. nsal, F. Durst and G. Biswas, J. Fluid Mech., **614** 425 (2008).
15. Ö. Ertunç and F. Durst: Phys. Fluids, **20** 025103 (2008).

Interaction of turbulent spots in pipe flow

Devranjan Samanta, Alberto de Lozar, Bjoern Hof

Dep. of 'Onset of turbulence and Complexity', MPIDS Goettingen, 37073 ,
Germany
devranjansamanta@gmail.com

The process of transition from laminar to turbulent regime in shear driven flows is still an unresolved issue. Localized turbulent regions or spots occur in pipe flow for Reynolds numbers around 2000. Typically in this regime an intermittent change between laminar and turbulent flow is observed (Wygnanski). Indeed, even if a large section of the laminar flow is uniformly perturbed localized turbulent spots emerge rather than an extended region of turbulence. A good understanding of this localization process is crucial for the comprehension of the transition to turbulence. We investigate the interaction of such turbulent spots in pipe flow for Reynolds numbers from 1900 to 2500. Turbulence is created locally by injecting a jet of water through a small hole in the pipe wall. For small perturbation frequencies the spacing of the turbulent spots downstream is inversely proportional to the frequency. It is observed that for distances less than approximately 20 pipe diameters turbulent spots start to interact and annihilate each other. The interaction distance is measured as a function of Reynolds number. We are also studying the effect of amplitude of the perturbations on the mutual interaction of the puffs. This investigation is closely related to spatially turbulent laminar periodic patterns which were earlier observed in other shear driven flows like Taylor-Couette or plane Couette (Prigent et al), (D. Barkley and L. Tuckerman).

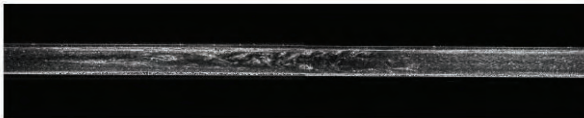


Fig. 1. Snapshot of turbulent puff in pipe flow at Reynolds number 2000.

References

1. I. J. Wygnanski, F.H. Champagne, *J. Fluid Mech.* (1973), vol. 59
2. A. Prigent, G. Grgoire, H. Chat , O. Dauchot and W.V. Sarloos, *Phys. Rev. Lett.* (2002), vol. 89
3. D. Barkley and L.Tuckerman *Phys. Rev. Lett.* (2005), vol. 94

Large-scale transitional dynamics in pipe flow

F. Mellibovsky¹, A. Meseguer^{1†}, T.M. Schneider^{2,3} and B. Eckhardt²

¹Departament de Física Aplicada, Universitat Politècnica de Catalunya, 08034, Barcelona, Spain

²Fachbereich Physik, Philipps-Universität Marburg, D-35032 Marburg, Germany

³School of Engineering and Applied Sciences, Harvard University, Cambridge, MA 02138, USA

fmellibovsky@fa.upc.edu

Summary. Direct numerical simulation of transitional pipe flow is carried out in a long computational domain in order to characterize the dynamics within the saddle region of phase space that separates laminar flow from turbulent intermittency. A shoot & bisection method is used to compute critical trajectories. The chaotic saddle or edge state approached by these trajectories is studied in detail. For $Re \leq 2000$ the edge state and the corresponding intermittent puff are shown to share similar averaged global properties. For $Re \geq 2200$, the puff length grows unboundedly whereas the edge state varies but mildly with Re . In this regime, transition is shown to proceed in two steps: first the energy grows to produce a localized turbulent patch, which then, during the second stage, spreads out to fill the whole pipe.

Transition to turbulence in pipe flow (fluid flow through an infinitely long pipe of circular cross-section) still remains an open problem of hydrodynamic stability theory. The basic parabolic solution is believed to be always stable with respect to infinitesimal perturbations [1] but becomes turbulent in practice [2, 3, 4], constituting one of the most fundamental examples of *sub-critical* transition to turbulence in fluid dynamics (see [5, 6] and references therein). Instability of pipe flow typically occurs for Reynolds numbers above $Re = D\bar{U}/\nu \simeq 1750$ [3] (D is the pipe diameter, \bar{U} is the mean streamwise flow speed and ν is the kinematic viscosity of the fluid). For Reynolds numbers within the range $Re \in [1750, 2700]$, perturbations can trigger transition to intermittent turbulent spots usually named *puffs*, which coexist with the laminar flow [2, 4]. Around $Re \simeq 2200$ -2700, puff structures destabilize, either experiencing a splitting process that leads to a higher number of puffs or, eventually, growing in size and leading to much longer intermittent structures (*slugs*), which are the predecessors of global pipe turbulence.

The problem is formulated using the Navier-Stokes equations in a periodic cylindrical domain of length $L = 100$ -radii with an imposed mass-flux. The discretization is accomplished with a solenoidal Petrov-Galerkin spectral

scheme with $M_r \times N_\theta \times L_z = 25 \times 33 \times 193$ radial \times azimuthal \times axial grid points. The solution is evolved in time using a 4th order linearly implicit method [10].

Starting from a localized pair of rolls filling a few radii length of the pipe, a refinement in the critical amplitude is carried out via an iterative bisection method, allowing to transiently land on the stable manifold of the critical *edge state* [11]. This is illustrated in Fig. 1a, where the resulting edge trajectory and some of the corresponding relaminarizing and turbulent bounding orbits are represented. The results for $Re \in [1800, 2800]$ are shown in Fig. 1b, where

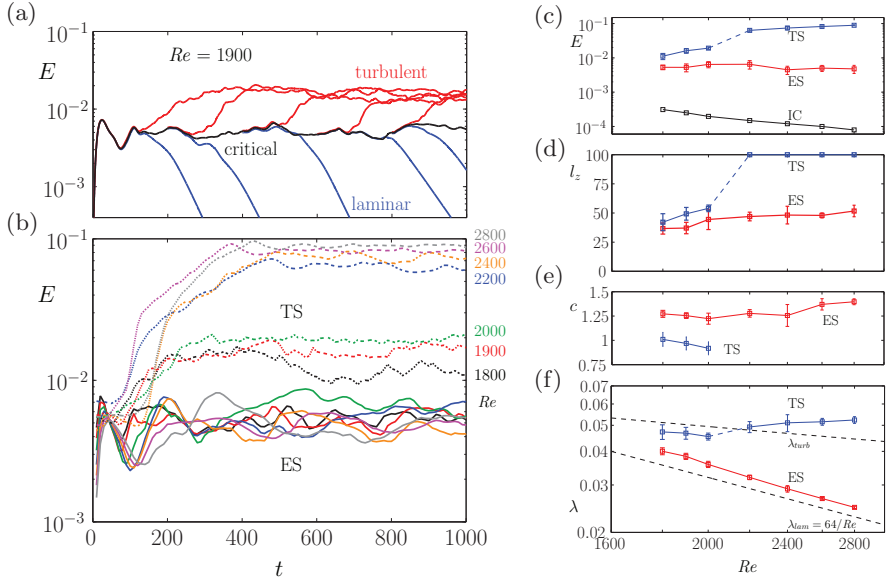


Fig. 1. (a) Energy of turbulent (red) and relaminarizing (blue) trajectories which bracket the edge state (black). (b) Energies of the critical (solid) and turbulent (dashed) trajectories for different Re . (c,d,e,f) Statistical properties of the turbulent states (blue, TS, puffs and slugs) and the edge states (red, ES) as a function of Re . (c) Energy. (d) Structure length. (e) Mean axial speed in \bar{U} units. (f) Friction factor.

the total perturbation energy associated to trajectories that remain on the edge for arbitrarily long times has been represented as a function of time in $D/4\bar{U}$ units (dubbed ES, solid curves). Also represented are the energies of trajectories that lead to a turbulent 'state' (labelled TS, dashed curves).

Since the states analyzed are chaotic, we report statistical properties, averaged over long time series, rather than properties at given time instants. In Fig. 1c we represent time-averaged energies corresponding to edge and turbulent states, asymptotically approached by the critical and turbulent trajectories shown in Fig. 1b, respectively, for all the Reynolds numbers explored. The error bars correspond to $\pm 2\sigma$. The edge state energy does not change noticeably within the explored Re -range while the energy of the turbulent regime

experiences a noticeable jump for $Re \geq 2200$. To better understand this discontinuity, Fig. 1d, shows the axial length l_z of the structures, as a function of Re . These curves clearly show that the turbulent energy surge observed at $2000 \leq Re \leq 2200$ is associated with the unbounded growth of the turbulent structures, which end up filling the whole domain. In contrast to turbulence, which starts to expand at about $Re \sim 2200$, there is no such transition in the edge states branch. The flow structure's length slightly increases with Re but remains bounded, the edge being localized regardless of the dominant turbulent state (puff or slug) to which transition is experienced. Fig. 1e shows the mean streamwise speed c of the localized states. The advection speed of the edge states does not remarkably change with Re and they always move faster than the mean flow and than the puffs. Finally, Fig. 1f depicts the friction factor λ , computed over the structure length l_z , corresponding to both edge and turbulent states. This last plot clearly reveals that the former preserve strong laminar properties, whereas the latter (especially in the puff regime) follow a law which is closer to the one describing fully developed turbulent flow.

The structure of puffs and edge states is compared at $Re = 1900$ in Fig. 2. The puff is characterized by an extended leading edge (front) and a sharp trailing edge (rear). In contrast, the edge state, is slightly shorter and characterized by extended interfaces in both the front and rear regions. The edge state flow field appears as much less complex and preserves higher spatial coherence than the turbulent puff.

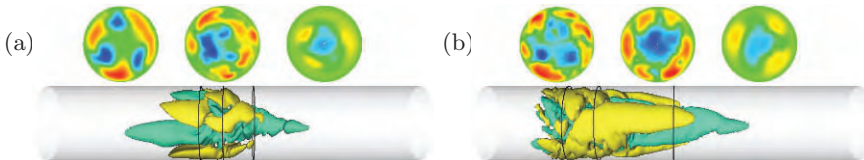


Fig. 2. Cross-sectional distributions of u_z and $u_z = \pm 0.07$ isosurfaces of the edge and the turbulent state at $Re = 1900$. The axial positions of the visualized cross-sections are represented with rings below. Red, green and blue regions correspond to high, quiescent and low streamwise flow speed. (a) Edge state. (b) Turbulent state (developed puff).

The simple structure and smoothness of the edge state is preserved and even smoothed as Re is increased and this is clearly evidenced in Fig. 3a, for a localized edge state at $Re = 2800$. Clear traces of the travelling wave [9] underlying the edge in a short $5D$ pipe [12] can be recurrently found at the rear of the structure.

The nature of transition to global turbulence is clarified in Fig. 3b, where the energy (E) and axial perturbation length (l_z) have been represented for a destabilizing edge state at $Re = 2800$. It becomes apparent that transition

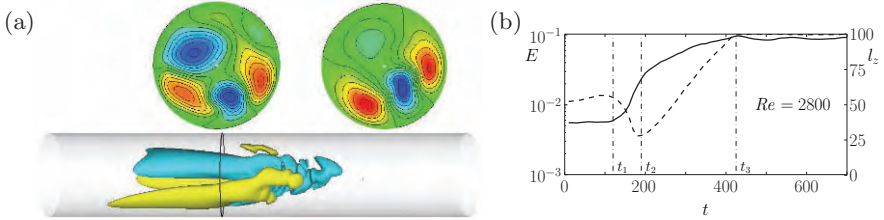


Fig. 3. (a) $u_z = \pm 0.07$ isosurfaces of the edge state at $Re = 2800$. Also shown u_z cross-sectional contours at the indicated axial location (top left), to be compared with the travelling wave underlying the short pipe edge state at $Re = 2875$ (top right). (b) Time evolution of a destabilizing edge state at $Re = 2800$: total energy (E , bold line) and structure length (l_z , dashed line). t_1 , t_2 and t_3 indicate the beginning of the exponential energy growth, the beginning of the linear growth of axial extent and the saturation to fully developed turbulence, respectively.

follows two stages. In a first stage ($t_1 < t < t_2$), a linear instability nucleates in a very short axial region of the edge state, and starts growing exponentially in energy but remains narrowly localized in space producing an axial concentration of total energy. The result is a turbulent spot that, in a second stage ($t_2 < t < t_3$), starts a linear unbounded axial expansion. The two stages of the transition process suggest that two distinct instability mechanisms are at work: a first one responsible for the energy increase and a second one causing the spreading in space. While the first one can be understood through an instability of a rather simple structure of travelling wave type, the second one is perhaps related to the mechanisms at work in other examples of structured turbulence [13].

References

1. A. Meseguer and L. N. Trefethen, *J. Comput. Phys.* **186**, 178 (2003).
2. O. Reynolds, *Phil. Trans. Roy. Soc. Lond. A* **174**, 935 (1883).
3. B. Hof, A. Juel, and T. Mullin, *Phys. Rev. Lett.* **91**(24), 244502 (2003).
4. I. J. Wygnanski and F. H. Champagne, *J. Fluid Mech.* **59**, 281 (1973).
5. R. Kerswell, *Nonlinearity* **18**, R17 (2005).
6. B. Eckhardt, T. Schneider, B. Hof, and J. Westerweel, *Ann. Rev. Fluid Mech.* **39**, 447 (2007).
7. H. Faisst and B. Eckhardt, *Phys. Rev. Lett.* **91**, 224502 (2003).
8. C. Pringle and R. R. Kerswell, *Phys. Rev. Lett.* **99**, 074502 (2007).
9. F. Mellibovsky and A. Meseguer, *Phil. Trans. Roy. Soc. Lond. A* **367**, 545 (2009).
10. A. Meseguer and F. Mellibovsky, *Appl. Num. Math.* **57**, 920 (2007).
11. D. Skufca, J. A. Yorke, and B. Eckhardt, *Phys. Rev. Lett.* **96**, 174101 (2006).
12. T. M. Schneider, B. Eckhardt, and J. A. Yorke, *Physical Review Letters* **99**, 034502 (2007).
13. A. Prigent, G. Gregoire, H. Chate, O. Dauchot, and W. van Saarloos, *Phys. Rev. Lett.* **89**, 014501 (2002).

Nonlinear coherent structures in a square duct

Håkan Wedin¹, Alessandro Bottaro¹, and Masato Nagata²

¹DICAT, University of Genova, Via Montallegro 1, 16145 Genova, Italy;

²Graduate School of Engineering, Kyoto University, Yoshida- Honmachi, Sakyo-ku, Kyoto 606-8501, Japan

wedin@dicat.unige.it

Introduction

The transition to turbulence in a square duct is an intriguing problem of hydrodynamics and has been studied since the work by Nikuradse [5]. The mean secondary flow of the turbulent state is made up by 8 vortices in the cross-sectional plane with 2 vortices in each corner, symmetric about the diagonals [2, 3, 5, 6, 7, 8]. The underlying mechanism causing this flow has been related to anisotropic turbulent fluctuations. Recently it has been shown through numerical simulations that the flow at transitional Reynolds numbers ($Re_b = \hat{U}_b \hat{b} / \hat{\nu}$, where \hat{U}_b is the bulk speed, $\hat{\nu}$ the kinematic viscosity and \hat{b} the half duct height) can feature instantaneous 4-vortex states (Biau & Bottaro [1] and Uhlmann *et al* [7]). The lower limit for transition in Re_b is between 865 and 1077 [1, 7].

The laminar flow is linearly stable at all flow velocities [4], hence it is conjectured that the transition is caused by the emergence of nonlinear exact coherent structures (ECS) to the Navier-Stokes equations. The ECS are unstable fixed points in phase space and are thought to provide a skeleton around which the flow dynamics is organised. This has recently been observed in numerical and experimental pipe flow [9, 11, 13]. Since the ECS are generally unstable a flow can never settle onto such states, but it can remain in their vicinities for a long time. The very first nonlinear ECS were discovered numerically by Nagata [14] in 1990 for plane Couette flow. Later additional coherent states were discovered [15, 19, 17] and relative periodic orbits [18].

Definitions

A nonlinear study of the isothermal flow through a square duct confined by four walls is presented. The cartesian coordinates \hat{x} , \hat{y} , and \hat{z} define the stream-wise, vertical and spanwise coordinate. The unit vectors are \mathbf{i} , \mathbf{j} and \mathbf{k} , the

velocity vector is defined as $\hat{\mathbf{u}} = \hat{u}\mathbf{i} + \hat{v}\mathbf{j} + \hat{w}\mathbf{k}$, the pressure as \hat{p} . Denoting the base flow by capital letters, a constant pressure gradient \overline{P}_x sets the fluid in motion. The Reynolds number and the bulk Reynolds number are defined as $Re = \overline{U}_{max}\hat{b}/\hat{\nu}$ and $Re_b = \hat{U}_b\hat{b}/\hat{\nu}$, where \overline{U}_{max} is the laminar centreline velocity and \hat{U}_b the bulk speed. We impose a perturbation $\mathbf{u}' = (u', v', w')$ and p' on the steady laminar flow $\overline{U}(y, z)$ and $\overline{P}(x)$. The laminar flow is governed by $\nabla^2\overline{U} = Re\overline{P}_x$ with no-slip conditions at the four walls and $\overline{U}(0, 0) = 1$ for a given \overline{P}_x . The non-dimensional governing equations for the perturbation are thus:

$$\frac{\partial \mathbf{u}'}{\partial t} + \overline{U} \frac{\partial \mathbf{u}'}{\partial x} + (v' \frac{\partial \overline{U}}{\partial y} + w' \frac{\partial \overline{U}}{\partial z}) \mathbf{i} - \frac{1}{Re} \nabla^2 \mathbf{u}' + \mathbf{u}' \cdot \nabla \mathbf{u}' + \nabla p' = \mathbf{0} \quad (1)$$

and $\nabla \cdot \mathbf{u}' = 0$, with no-slip conditions $\mathbf{u}'(t, x, y = \pm 1, z) = \mathbf{u}'(t, x, y, z = \pm 1) = \mathbf{0}$ and periodicity in x or $\mathbf{u}'(t, x, y, z) = \mathbf{u}'(t, x + L_x, y, z)$. The disturbance is expressed as a travelling wave, periodic in x and t according to equation 2.

$$\mathbf{u}' = \sum_{b=-N_x}^{N_x} \tilde{\mathbf{u}}^{(b)}(y, z) e^{Ib\alpha(x-ct)} = \sum_{b=-N_x}^{N_x} \sum_{i=0}^{N_y} \sum_{j=0}^{N_z} \hat{\mathbf{u}}_{bij} \phi_i(y) \phi_j(z) e^{Ib\alpha(x-ct)}, \quad (2)$$

where $I = \sqrt{-1}$.

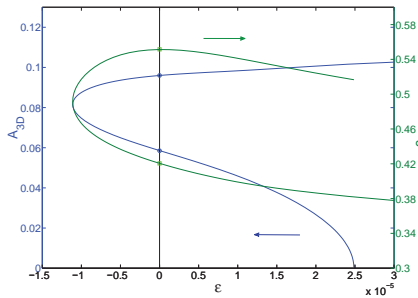


Fig. 1. A homotopy approach for $Re=3000$ and $\alpha=1.5$. The amplitude of the nonlinear solution is defined as $A_{3D} = \sqrt{\sum_{j=0}^{NZ} |\hat{u}_{10j}|^2 + |\hat{v}_{10j}|^2 + |\hat{w}_{10j}|^2}$, the $\hat{\mathbf{u}}_{10j}$ are the solution coefficients shown in equation 2 and c is the speed of the wave. Two relevant nonlinear solutions are located at a forcing amplitude $\epsilon = 0$.

Results

The discovery of the nonlinear solutions is based on the recent study by Wedin *et al* [10]. The solutions are found by a homotopy approach [11, 12, 13] by

adding a forcing function $f(y, z)$ to the governing equations hence causing in return an artificial flow situation. At a certain amplitude ϵ of f the forced system is neutrally stable, which corresponds to a point from where the search for steady nonlinear solutions can start. Figure 1 shows an example on how the amplitude of the forcing function can be brought to zero at fixed value of the Reynolds number and wavelength. Then, the point in $Re_b(\alpha)$ where the travelling wave emerges is found by a search over α . Three types of solutions of different symmetries are shown in figure 2 where the two top ones resemble observations in transitional [7] (top left) and turbulent conditions [6] (top right). The bottom figure shows an additional 8-vortex structure which has not yet been observed in either transitional or turbulent conditions.

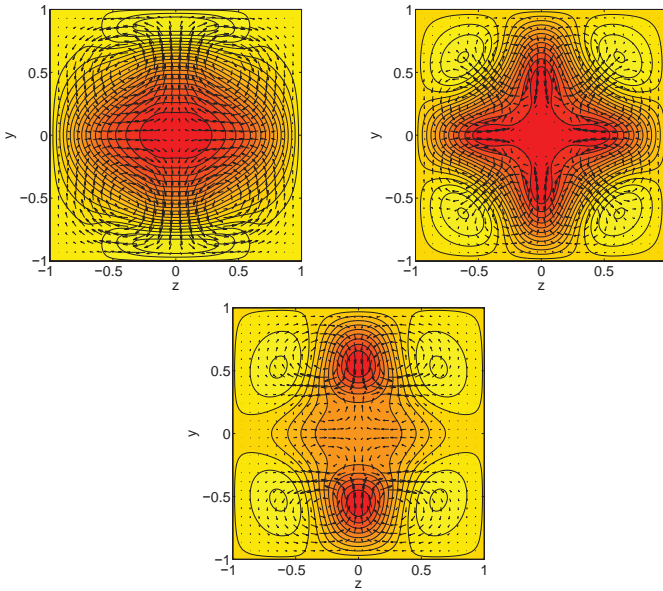


Fig. 2. A selection of the ECS found. *Top left:* the mean 4-vortex state, observed also in transitional conditions [7]. *Top right:* the mean 8-vortex structure that also has been observed in turbulence [6]. *Bottom* figure shows an additional structure whose pertinence is not still known. The contour levels correspond to the streamwise flow away from $\bar{U}(y, z)$ (light positive and dark negative contours) and the arrows denote cross-stream velocity vectors.

Conclusions

Three types of nonlinear coherent structures are found for a square duct flow. The discovery is based on the preliminary results of Wedin *et al* [10]. With

a homotopy approach the nonlinear solutions are identified. A mean 4-vortex structure is identified and resembles the instantaneous structures observed in numerical simulations in [7]. Furthermore a mean 8-vortex structure is found similar to that observed in turbulent conditions [6]. The third solution has a different 8-vortex structure, which resembles that found recently by Pringle *et al* [19] for the flow in a cylindrical pipe.

References

1. D. Biau and Alessandro Bottaro, "An optimal path to transition in a duct," *Phil. Trans. Roy. Soc. A*, **367**, 529, (2009).
2. A. Huser and S. Biringen, "Direct numerical simulation of turbulent flow in a square duct," *J. Fluid Mech.* **257**, 65 (1993).
3. F.B. Gessner, "The origin of secondary flow in turbulent flow along a corner," *J. Fluid Mech.* **58**, 1 (1973).
4. T. Tatsumi and T. Yoshimura, "Stability of the laminar flow in a rectangular duct," *J. Fluid Mech.* **212**, 437 (1990).
5. J. Nikuradse, "Untersuchungen uber die Geschwindigkeitsverteilung in turbulenten Stromungen," PhD Thesis, Göttingen, 1926.
6. S. Gavrilakis, "Numerical simulation of low-Reynolds-number turbulent flow through a straight square duct," *J. Fluid Mech.*, **244**, 101 (1992).
7. M. Uhlmann, A. Pinelli, G. Kawahara and A. Sekimoto, "Marginally turbulent flow in a square duct," *J. Fluid Mech.*, **588**, 153 (2007).
8. D. Biau, H. Soueid and A. Bottaro, "Transition to turbulence in duct flow," *J. Fluid Mech.*, **596**, 133 (2008).
9. B. Hof, C.W.H. van Doorne, J. Westerweel, F.T.M. Nieuwstadt, H. Faisst, B. Eckhardt, H. Wedin, R.R. Kerswell and F. Waleffe, "Experimental observation of nonlinear travelling waves in turbulent pipe flow," *Science*, **305**, 1594 (2004).
10. H. Wedin, D. Biau A. Bottaro and M. Nagata, "Coherent Flow States in a Square Duct," *Phys. Fluids.*, **20**, 094105 (2008).
11. H. Wedin and R.R. Kerswell, "Exact coherent structures in pipe flow: travelling wave solutions," *J. Fluid Mech.*, **508**, 333 (2004).
12. F. Waleffe, "Homotopy of exact coherent structures in plane shear flows," *Phys. Fluids.*, **15**, 1517 (2003).
13. H. Faisst and B. Eckhardt, "Travelling waves in pipe flow," *Phys. Rev. Lett.*, **91**, 224502 (2003).
14. M. Nagata, "Three-dimensional finite amplitude solutions in plane Couette flow: bifurcation from infinity," *J. Fluid Mech.*, **217**, 519 (1990).
15. Y. Duguet, A.P. Willis and R.R. Kerswell, "Transition in pipe flow: the saddle structure on the boundary of turbulence," *J. Fluid Mech.*, **613**, 255 (2008).
16. C.C.T. Pringle, Y. Duguet and R.R. Kerswell, "Highly symmetric travelling waves in pipe flow," *Phil. Trans. Roy. Soc. A*, **367**, 457 (2009).
17. C. Pringle and R.R. Kerswell, "Asymmetric, helical and mirror-symmetric travelling waves in pipe flow," *Phys. Rev. Lett.*, **99**, 074502 (2007).
18. Y. Duguet, C.C.T. Pringle and R.R. Kerswell, "Relative periodic orbits in transitional pipe flow," *Phys. Fluids*, **20**, 114102 (2008).
19. C.C.T. Pringle, Y. Duguet and R.R. Kerswell, "Highly symmetric travelling waves in pipe flow," *Phil. Trans. Roy. Soc. A*, **367**, 457 (2009).

Quantitative measurement of the life time of turbulence in pipe flow

D.J. Kuik¹, Christian Poelma¹, Bjorn Hof², and J. Westerweel³

¹ Laboratory for Aero- & Hydrodynamics, Delft University of Technology, Delft, The Netherlands

d.j.kuik@tudelft.nl

² Max-Planck-Institut für Dynamik und Selbstorganisation, Göttingen, Germany.

Summary. In pipe flow at low Reynolds number, decay of localized disturbances is observed. As the Reynolds number is increased, the question emerges whether the life time of these disturbances diverges at a finite Reynolds number or remains transient. In the current investigation we determine their life *time* quantitatively from pressure measurements, while in previous investigations the *distance* over which a structure survives has been determined. The obtained results confirm that the life time of localized disturbances does not diverge in the range of Reynolds numbers covered in the current experiment.

Recent simulations and measurements have shown that localized turbulence in pipe flow, in the form of 'puffs', decay exponentially [1, 2, 3, 4]. The life time of these disturbances increases with Reynolds number. The principal question has been whether the life time diverges to infinity at a given critical Reynolds number Re_c . Initial experiments [2] and numerical simulations [3] appeared to indicate that the life time increases proportional to $T \sim (Re - Re_c)^{-1}$, although no agreement was found on the value of Re_c . Later numerical simulations and measurements in very long pipes showed that far above the previously identified Re_c turbulent puffs still decay [5]. It was found that the life time increases exponentially, $T \sim \exp(-Re)$. The life times were determined by observing puffs that emerged at the end of a very long pipe (with a length of 7,500 times its diameter), and considering the probability as a function of pipe length and Reynolds number, which shows a characteristic S-shape in the case of an exponential scaling for T . Later the life time measurements were improved [6], which showed a super-exponential scaling, i.e. $T \sim \exp(-\exp(c_1 Re + c_2))$ covering more than 8 decades in life time.

To further substantiate these findings, additional measurements were performed that are reported here. Since all previous measurements were either based on flow visualization [2] or the observation of a flow disturbance at the pipe exit [5, 6], additional measurements were performed to provide more

quantitative results. The measurements were carried out in a $2030D$ long pipe with an inner diameter of 10 ± 0.01 mm (this is a setup similar to those described by [6]). First of all, LDA measurements were carried out near the pipe exit, in order to validate quantitatively that the flow disturbances were indeed puffs. Secondly, pressure difference measurements were carried out over two pipe sections. Given the high accuracy of the pressure measurements, it was possible to determine whether or not a given pipe section would contain a turbulent puff. We thus could determine in each section the average puff velocity (from the time it passes from one pressure tap to the next one). Since the disturbance mechanism was placed well before the first section where we measured the pressure drop, we could validate whether the injection had indeed generated a puff. It also was possible to observe the decay of a puff from the pressure measurements, which enabled us to determine directly the life time of these puffs; in previous measurements the life time was deduced from the survival probability and the pipe length divided by the (estimated) mean puff speed.

The $2030D$ pipe consists of 16 sections of $120D$ to $130D$ long precision bored glass, which were connected using PMMA push fittings. Each connector was equipped with one up to six 0.5 mm diameter ports, either used to introduce the disturbance or to attach the Validyne DP45 differential pressure transducers. The pressure transducers were placed between $125D$ and $250D$ after the point where the disturbance was introduced and one between $250D$ and $496D$.

The flow is driven by a constant pressure head. Before the fluid enters the pipe, it passes a large restriction and then enters a settling chamber containing several meshes with reducing grid size to get rid of remaining fluctuations present in the entering fluid, followed by a contraction (contraction ratio ten to one). The additional restriction ensured that the flow rate in the pipe was independent of the flow state. The base flow was checked by pressure drop and flow rate measurement, showing that the flow remained laminar beyond $Re = 9 \cdot 10^3$.

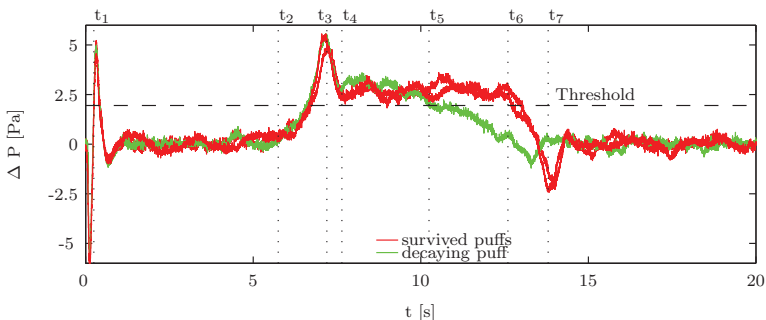


Fig. 1. Pressure increase due to the presence of a puff, shown are two survived puffs and one decaying puff.

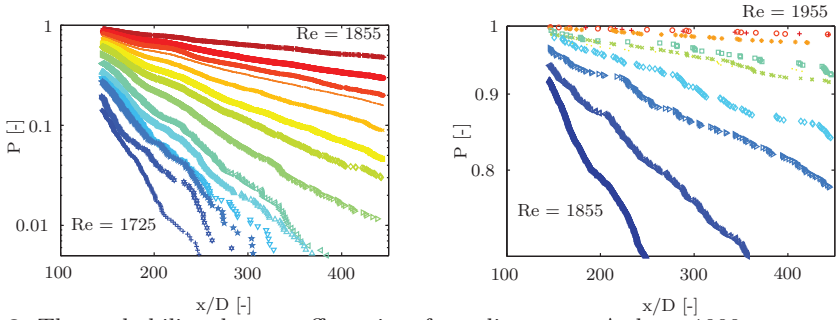


Fig. 2. The probability that a puff survives for a distance x . At least 1000 measurements were performed for each Reynolds number *left* for Reynoldsnumbers between 1755 ± 5 to 1855 ± 5 *right* between 1855 and 1955 in steps of 10

In figure 1 a typical pressure drop measurement for the first pressure transducer is shown. For clarity only the additional pressure drop is given. In this figure two puffs are visible (red) that survived for at least $250D$ after they have been created. The decaying puff (green) can clearly be distinguished: the additional pressure drop due to the presence of the puff relaxes to zero already around t_5 .

For each measurement the life time of the disturbance was determined by the time at which the additional pressure falls below the prescribed threshold, given by the dashed line. All measurements were sorted based on their Reynolds number, resulting in at least 1000 measurements per Reynolds number. Using the mean advection velocity of a disturbance, the position at which the disturbance decayed was obtained. As a result the probability a disturbance survived up to a certain distance could be derived. This probability is presented in figures 2.

The distributions given in figures 2 show clearly that the tails of the decay are of exponential nature and thereby confirming that an appropriate description of the decay is:

$$P(t - t_0, Re) = \exp((t - t_0) \tau^{-1} (Re)) \quad (1)$$

By fitting a straight line through the curves given in figures 2 both the initial formation time t_0 and the inverse of the characteristic life time τ^{-1} can be determined.

The inverse of the characteristic life time is presented in figure 3 together with the recent results obtained by Hof et al. [6]. An excellent agreement is observed, and therefore these results support their claim that the correct dynamical model of linear stable shear flows is that of a strange repeller.

To show the robustness of the current method, the inverse characteristic life time is given in figure 3 for different detection thresholds. Only for low Reynolds numbers and high threshold values a larger variation is observed.

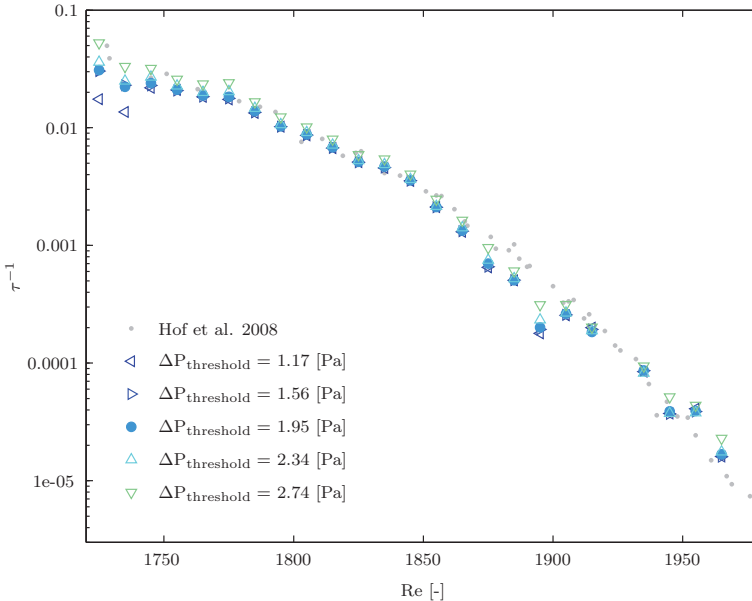


Fig. 3. Escape rate of a puff for different Reynolds number in a log-lin scale

However, for almost all Reynolds numbers the characteristic life time is found to be independent of the threshold used.

In the present paper we showed the direct measurements of the life *time* of turbulent structures by pressure measurements. To our knowledge this is the first time the life *time* of puffs is measured *quantitatively*, because in previous investigation the *distance* over which a turbulent structure survives has been determined by visual inspection. The results show excellent agreement with the results of Hof et al. [6] and therefore support that the life time of puffs does not diverge for a finite Reynolds number, but remains transient.

References

1. H. Faisst and B. Eckhardt, Physical Review Letters, **91**, 224502, 2003.
2. J. Peixinho and T. Mullin, Physical Review Letters, **96**, 094501, 2006.
3. A. P. Willis and R. R. Kerswell, Physical Review Letters, **98**, 014501, 2007.
4. B. Eckhardt et al., Annual review of fluid mechanics, **39**, 447–468, 2007.
5. B. Hof et al., Nature, **443**, 59–62, 2006.
6. B. Hof et al., Physical Review Letters, **101**, 214501, 2008.

Experimental investigation of turbulent patch evolution in spatially steady boundary layers

Jens H.M. Fransson

Linné Flow Centre, KTH Mechanics, SE-100 44 Stockholm, Sweden
jens.fransson@mech.kth.se

Turbulent patches and their streamwise evolution play a major rôle in the late stage of any transition scenario. The appearance of turbulent patches in laminar boundary layers was first noted by Emmons [1], who proposed a turbulent spot probability appearance model, which recently [2] has proven to work well for the free stream turbulence (FST) induced transition scenario. However, there are many fundamental questions still remaining unanswered, which are important in the striving after new transition prediction models.

In the present experimental study the effects of initial condition, Reynolds number (Re) and FST on turbulent patch evolution have been studied while keeping the boundary layer thickness constant. This type of study can only be performed in the asymptotic suction boundary layer (ASBL), where continuous suction through the wall gives rise to a boundary layer which does not develop in space, i.e. a spatially steady boundary layer. The wall-normal streamwise velocity profile $u(y)$ in the ASBL can readily be derived from the Navier-Stokes and the continuity equations as,

$$u(y) = U_\infty \left\{ 1 - e^{yV_w/\nu} \right\}, \quad (1)$$

where U_∞ , V_w , and ν are the free stream velocity, the suction velocity (< 0), and the kinematic viscosity, respectively. With the access of an analytic solution (1) to the Navier–Stokes equation for the ASBL case it is straight forward to calculate the displacement and the momentum thicknesses as $\delta_1 = -\nu/V_w$ and $\delta_2 = \delta_1/2$, respectively, giving a constant shape factor, $H_{12} = \delta_1/\delta_2 = 2$, independent of the suction velocity. The Reynolds number based on the displacement thickness, thus, becomes $Re = -U_\infty/V_w$ allowing for Re -changes without necessarily changing the boundary layer thickness, $\delta_{99} = \delta_1 \ln(100)$, here defined as the wall-normal position where the streamwise velocity reaches 99% of U_∞ . Finally, the friction velocity u_τ and the viscous length scale ℓ^* become $\sqrt{U_\infty V_w}$ and $\delta_1 Re^{-1}$, respectively, in the ASBL.

In the past very few experiments have been performed in ASBLs [3] due to the inherent difficulties in setting up this type of boundary layer experiment. These experiments were carried out in the MTL wind tunnel at KTH

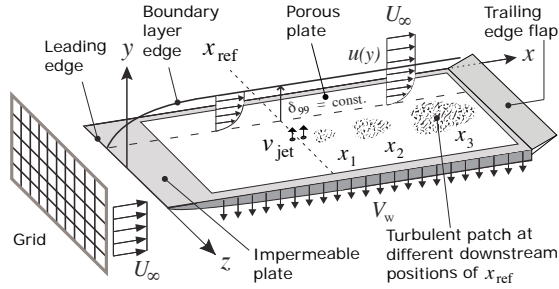


Fig. 1. Schematic of the flow field over a flat plate subjected to constant suction. Note that this sketch is not according to scale.

Mechanics. A porous plate ($2250 \times 1000 \text{ mm}^2$) made of a sintered plastic material, with an averaged pore size of $16 \mu\text{m}$, was used in order to allow for uniform surface suction. See Fig. 1 for a sketch of the experimental setup. In a pre-study the material permeability was determined, which through Darcy's law relates the pressure difference (Δp) across the plate to the velocity through the porous material. In this way the suction velocity can be calculated simply by measuring Δp during the actual experiments. Turbulent patches were generated at the reference position, $x_{\text{ref}} = 1.85 \text{ m}$ from the leading edge, by means of short pulsed wall-jets through one or two streamwise located holes in the porous plate. The ceiling was adjusted for zero pressure gradient at $\Delta p = 18 - 19 \text{ Pa}$, giving a displacement thickness of $\delta_1 = 1.45 \pm 0.03 \text{ mm}$ over a streamwise distance of $(x - x_{\text{ref}})/\delta_1 = 13 - 454$. The wall-jet pulse was computer generated through a D/A board to an audio amplifier driving a sealed loud speaker, which was connected to the hole(s) through vinyl hosing. The pulse height of the signal to the loud speaker was quantified by measuring the AC output voltage from the amplifier with a voltage meter. The measurements were performed with hot-wire anemometry triggered by the pulse with a suitable time delay, and the probe was traversed in the spanwise direction (91 positions), at $y = \delta_1$, in the wall-normal direction (30 positions), at the mid-plane $z = 0$, and in the streamwise direction (6 positions), $(x - x_{\text{ref}})/\delta_1 = (102, 135, 169, 202, 235, 269)$. At each position the turbulent patch measurement was repeated 80 times giving a total number of generated patches of over 387 000 pcs. considering all experiments performed. This gives a good spatial resolution of the spots which in turn allows for detailed data analyses to be presented.

References

1. H. W. Emmons, *J. Aero. Sci.* **18**, 490 (1951).
2. J. H. M. Fransson, M. Matsubara and P. H. Alfredsson, *J. Fluid Mech.* **527**, 1 (2005).
3. J. H. M. Fransson and P. H. Alfredsson, *J. Fluid Mech.* **482**, 51 (2003).

Interaction of noise disturbances and streamwise streaks

Philipp Schlatter¹, Luca Brandt¹ and Rick de Lange²

¹ Linné Flow Centre, KTH Mechanics, Stockholm, Sweden

² TUE Mechanical Engineering, Eindhoven, The Netherlands

pschlatt at mech.kth.se

Disturbance evolution in a boundary layer with streamwise streaks and random two- and three-dimensional noise of various amplitudes is studied via numerical simulations. The aim of the present work is to determine the impact of the interaction on the arising flow structures and, eventually, on the location and details of the breakdown to turbulence. It is shown that large-scale 2D noise can be controlled via streaks, whereas the more general 3D noise configuration is prone to premature transition due to increased instability of the introduced streaks. It is interesting to note that the latter transition scenario closely resembles the flow structures found in bypass transition.

A recent theoretical and numerical study by Cossu and Brandt [2] has shown that a substantial stabilisation of a boundary layer subject to essentially two-dimensional disturbances (*i.e.* Tollmien-Schlichting (TS) waves) can be achieved by a spanwise modulation of the mean flow, *i.e.* via superimposed streamwise streaks on the laminar Blasius flow. In particular, it has been shown both experimentally via finite-amplitude roughness [3] and later via large-eddy simulation (LES, [5]) that transition to turbulence can effectively be moved to a more downstream position via this essentially passive control mechanism. However, the disturbances considered in the mentioned studies have all had their maximum energy in two-dimensional (spanwise invariant) modes. It is therefore interesting to examine the interaction of streamwise streaks with disturbances of a more general nature, *i.e.* 2D and 3D random noise at various frequencies and (spanwise) wavenumbers.

The present study uses a spectral numerical method [1] together with LES based on high-order filtering (ADM-RT model [6]), in a similar setup as presented in Ref. [5]. In particular, the computational domain starts at $Re_x = 32000$ extending up to $Re_x = 590000$. The streaks are introduced at the inlet as optimal disturbances computed from PSE (parabolised stability equations), subsequently evolving nonlinearly inside the domain. Conversely, the noise is forced within the computational domain at $Re_x = 60000$ by a volume force close to the wall. Two frequency spectra of the noise are shown in Fig.

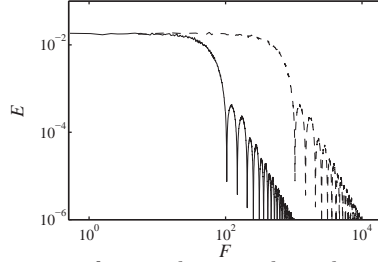


Fig. 1. Frequency spectrum of — large-scale and - - - small-scale noise. The maximum spanwise scale based on the local boundary-layer thickness δ_{99} at the position of forcing ($Re_x = 60000$) for the 3D noise cases is chosen as $\lambda_{z,\max} = 2.25\delta_{99}$ and $\lambda_{z,\max} = 0.75\delta_{99}$ for the large and small-scale noise, respectively.

1, specifying the frequencies and spanwise scales denoted “large-scale” and “small-scale” in the following. Note that for all simulations small-amplitude three-dimensional noise is included to enable transition to turbulence.

The amplitude of the noise is determined in such a way that transition to turbulence, *i.e.* the appearance of a turbulent patch, could be observed in the computational box ($Re_x < 590000$) for the uncontrolled setup (no streaks). The same noise was then used to investigate the interaction of the noise with the streamwise streaks. Depending on the nature of the noise (dimensionality and scales), different amplitudes had to be chosen: two-dimensional, fine-scale noise proved to be more efficient for reaching transition, requiring $u_{\text{rms,noise}} \approx 2.6\%$. On the other hand, 2D large-scale noise lead to transition only with the significantly larger amplitude of 18.3%. The three-dimensional noise cases lie in between these values.

Directly connected to the different amplitudes required for the noise disturbances in the uncontrolled cases is the predominant transition scenario observed in the flow. Sample visualisations are shown in Figs. 2a) and 3a). It becomes clear that two-dimensional small-scale noise in fact leads to the appearance of spanwise uniform waves, similar to TS-waves, see Fig. 2a). The growth associated to the TS-waves is sufficient to lead to non-linear breakdown within the computational box even for the mentioned low amplitudes. On the other hand, large-scale 2D noise does not excite any growing instability in the boundary layer at the considered Reynolds numbers due to the low frequency $F < 80$ and the two-dimensionality of the disturbances (*i.e.* no lift-up mechanism). Therefore, intermittent turbulent spots are directly triggered at the forcing position, which then grow downstream (not shown).

For the cases with three-dimensional noise, the dominant instability mechanism is non-modal growth based on the lift-up mechanism, generating to streamwise streaks. Again, a dependence of the arising flow structures on the scales of the disturbances is observed: Fine scales tend to decay quickly, whereas larger scales lead to a flow with significant streamwise streaks, which then might get unstable developing a growing wave packet [4] and finally

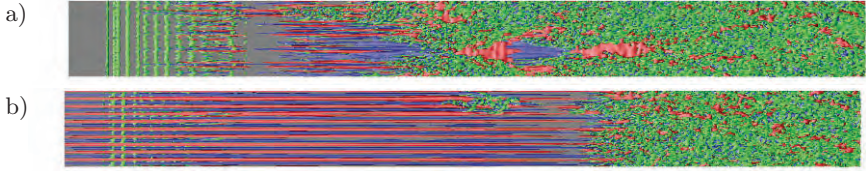


Fig. 2. Top view of the three-dimensional flow structures for cases with 2D, fine-scale noise. *a)* no streaks. *b)* Streaks with amplitude 19%. Light isocontours represent the λ_2 vortex-identification criterion, dark and light grey isocontours are positive and negative disturbance velocity. Flow from left to right.

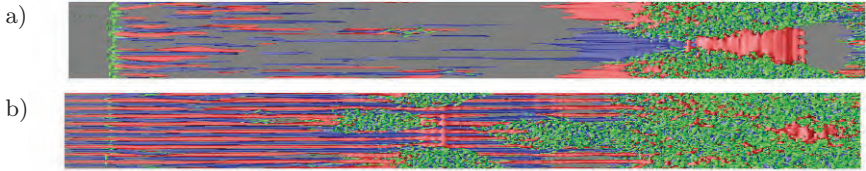


Fig. 3. Top view of the three-dimensional flow structures for cases with 3D large-scale noise, same isocontour levels and colours as in Fig. 2. *a)* no streaks. *b)* streaks with amplitude 19%.

break down into triangle-shaped turbulent spots as seen in Fig. 3a). The flow structures appearing in these cases are similar to observations in bypass transition induced by ambient free-stream turbulence. Note that in the presence of strong streaks – irrespective of whether they are actively introduced in the flow or naturally arise due to *e.g.* free-stream turbulence, the turbulent spots do not feature a clear triangular shape.

The efficiency of the imposed streamwise streaks to damp the amplification of disturbances in the boundary layer is naturally strongly dependent on the nature of these disturbances and the respective transition scenario. The damping abilities of streaks has been demonstrated for cases with dominant two-dimensional waves, see the references mentioned above [2, 3, 5]. Consequently, for the case which leads to TS-wave dominated transition (2D small-scale noise), transition delay can be observed, see Fig. 2b). Quantitative data is given in Fig. 4a) showing the disturbance growth inside the boundary layer. However, as opposed to cases with clean TS-waves (for example $F = 120$ as in Ref. [5]) no complete stabilisation of the boundary layer can be achieved; intermittent turbulent spots are appearing further downstream as an instability of the strong streaks.

On the other hand, three-dimensional noise produces a change of the disturbance growth mechanism in the boundary layer from modal (TS-waves) to non-modal (lift-up, streaks). The spanwise periodic base flow created by forcing large-amplitude streaks does not lead to any transition delay. To the contrary, turbulent spots can be observed more frequently and further upstream, see Fig. 3b). As for the uncontrolled case, the transition scenario is a secondary instability of the streak, characterised by a growing wave packet

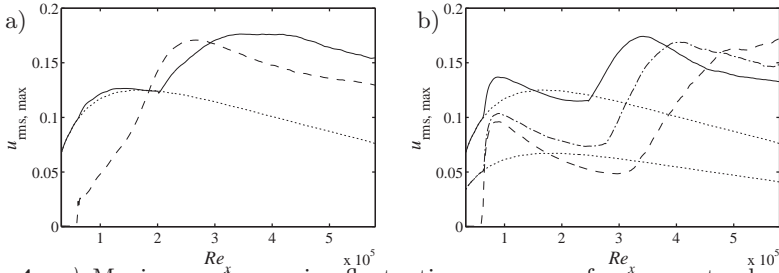


Fig. 4. *a)* Maximum streamwise fluctuations $u_{\text{rms,max}}$ for --- streaks (19%) and small-scale 2D noise (amplitude 0.3%), - - - only noise, no streaks, \cdots\cdots undisturbed streaks. *b)* $u_{\text{rms,max}}$ for streaks (--- 19%, - - - 10%) and large-scale 3D noise, - - - only noise (amplitude 0.9%), no streaks, \cdots\cdots undisturbed streaks.

riding on the streak [4]. However, due to the larger amplitude of the streaks, this breakdown occurs further upstream. In Fig. 4b) the growth of u_{rms} inside the boundary layer is shown; the breakdown location is clearly moving upstream for larger amplitudes of the introduced streaks.

It can therefore be concluded that the passive control mechanism based on a spanwise modulated base flow and the subsequent damping of the growth of TS-waves [2] is very efficient for transition scenarios based on the modal growth of essentially two-dimensional disturbances. On the other hand, if transition is induced by (non-modal) growth related to bypass transition, then the addition of a strong base-flow modulation might lead to premature transition. Similar results have been obtained for transition induced by free-stream turbulence (not shown), for which as expected no transition delay could be observed.

References

1. M. Chevalier, P. Schlatter, A. Lundbladh and D. S. Henningson. SIMSON - A Pseudo-Spectral Solver for Incompressible Boundary Layer Flows. *Tech. Rep.*, TRITA-MEK 2007:07, KTH Mechanics, Stockholm, Sweden, 2007.
2. C. Cossu and L. Brandt. Stabilization of Tollmien-Schlichting waves by finite amplitude optimal streaks in the Blasius boundary layer. *Phys. Fluids*, 14(8):L57–L60, 2002.
3. J. H. M. Fransson, A. Talamelli, L. Brandt and C. Cossu. Delaying transition to turbulence by a passive mechanism. *Phys. Rev. Lett.*, 96(064501):1–4, 2006.
4. P. Schlatter, L. Brandt, H. C. de Lange and D. S. Henningson. On streak breakdown in bypass transition. *Phys. Fluids*, 20(101505):1–15, 2008.
5. P. Schlatter, H. C. de Lange and L. Brandt. Numerical study of the stabilisation of Tollmien-Schlichting waves by finite amplitude streaks. In *Turbulence and Shear Flow Phenomena 5*, edited by R. Friedrich *et al.*, 849–854, 2007.
6. P. Schlatter, S. Stolz and L. Kleiser. LES of transitional flows using the approximate deconvolution model. *Int. J. Heat Fluid Flow*, 25(3):549–558, 2004.

Linear generation of multiple time scales by 3D unstable perturbations

S. Scarsoglio*, D. Tordella*, and W. O. Criminale^b

*Dipartimento di Ingegneria Aeronautica e Spaziale, Politecnico di Torino, 10129 Torino, Italy, **corresponding author: daniela.tordella@polito.it**

^bDepartment of Applied Mathematics, University of Washington, Seattle, WA 98195-2420, USA

In this paper we present few observations concerning the appearance of different time scales during the transient growth of small three-dimensional perturbations superposed to a sheared flow, the bluff-body wake. The interesting point is that these phenomena are developing in the context of the linear dynamics. Before to comment these results let us shortly describe the method of study.

The early transient and long asymptotic behaviour is studied using the initial-value problem formulation. The base flow is approximated through an analytical expansion solution [1] of the Navier-Stokes equations. The viscous perturbative equations are written in terms of the vorticity and the transversal velocity [2] and then transformed through a Laplace-Fourier decomposition [3] in the plane (x, z) which is normal to the base flow plane (x, y) ,

$$\frac{\partial^2 \hat{v}}{\partial y^2} - (k^2 - \alpha_i^2 + 2i\alpha_r\alpha_i)\hat{v} = \hat{\Gamma} \quad (1)$$

$$\frac{\partial \hat{\Gamma}}{\partial t} = (i\alpha_r - \alpha_i)\left(\frac{d^2 U}{dy^2}\hat{v} - U\hat{\Gamma}\right) + \frac{1}{Re}\left[\frac{\partial^2 \hat{\Gamma}}{\partial y^2} - (k^2 - \alpha_i^2 + 2i\alpha_r\alpha_i)\hat{\Gamma}\right] \quad (2)$$

$$\frac{\partial \hat{\omega}_y}{\partial t} = -(i\alpha_r - \alpha_i)U\hat{\omega}_y - i\gamma\frac{dU}{dy}\hat{v} + \frac{1}{Re}\left[\frac{\partial^2 \hat{\omega}_y}{\partial y^2} - (k^2 - \alpha_i^2 + 2i\alpha_r\alpha_i)\hat{\omega}_y\right] \quad (3)$$

The transversal velocity and vorticity components are indicated as \hat{v} and $\hat{\omega}_y$ respectively, while $\hat{\Gamma}$ is defined through the kinematic relation $\tilde{\Gamma} = \partial_x \tilde{\omega}_z - \partial_z \tilde{\omega}_x$ that in the physical plane links together the perturbation vorticity components in the x and z directions ($\tilde{\omega}_x$ and $\tilde{\omega}_z$) and the perturbed velocity field. Equations (2) and (3) are the Orr-Sommerfeld and Squire equations respectively, from the classical linear stability analysis for three-dimensional disturbances in the phase space. We define k as the polar wavenumber, $\alpha_r = k\cos(\phi)$ as the wavenumber in x direction, $\gamma = k\sin(\phi)$ as the wavenumber in z direction, ϕ as the angle of obliquity with respect to the physical plane, and α_i as

the spatial damping rate in x direction. We introduce the amplification factor $G(t)$ as the disturbance kinetic energy density $E(t)$, the temporal growth rate $r(t) = \log|E(t)|/2t$ and the frequency $\omega(t)$ as the time derivative of the perturbation phase.

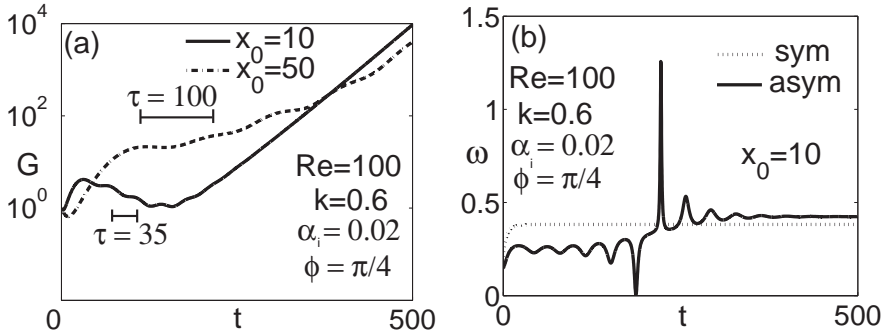


Fig. 1. $Re = 100$, $k = 0.6$, $\alpha_i = 0.02$, $\phi = \pi/4$. (a): Asymmetric case. Amplification factor $G(t)$ for intermediate ($x_0 = 10$) and far ($x_0 = 50$) wake sections. (b): Intermediate section $x_0 = 10$. Pulsation $\omega(t)$ for asymmetric and symmetric cases.

The results on the onset of multiple time scales – obtained by observing the amplification factor $G(t)$ and the pulsation $\omega(t)$ – are presented in Fig. 1 (a, b). In Fig. (1a) the amplification factor $G(t)$ is shown for two typical intermediate ($x_0 = 10$) and far ($x_0 = 50$) wake sections. The perturbations are asymmetric. For $x_0 = 10$ a local maximum, followed by a minimum, is visible in the energy density, then the perturbation is slowly amplifying and the transient is extinguished only after hundreds of time scales. For $x_0 = 50$ these features are less marked. It can be noted that the far field configuration ($x_0 = 50$) has a faster growth than the intermediate field configuration ($x_0 = 10$) up to $t = 400$. Beyond this instant the growth related to the intermediate configuration will prevail on that of the far field configuration. For $x_0 = 10$ the amplification factor $G(t)$ shows a modulation which is very evident in the first part of the transient (see [4]), and which corresponds to a modulation in amplitude of the pulsation of the instability wave depicted in Fig. (1b). Here, the frequency $\omega(t)$ for symmetric and asymmetric perturbations at $x_0 = 10$ is shown. The modulation is only present for the asymmetric wave (for the symmetric case the amplitude is constant after few time scales). This behaviour is in general found for asymmetric longitudinal or oblique waves. In these instances two time scales are simultaneously observed in the transient and long term behaviour: the periodicity associated to the average value of the pulsation in the early transient ($\omega \approx 0.3$) and the asymptotic pulsation ($\omega \approx 0.45$). Moreover, the oscillation of this pulsation $\omega(t)$ in the early transient introduces another time scale τ , which in terms of pulsation is about 0.17.

The frequency determination is validated through the comparison of the temporal asymptotic behaviour ($t \rightarrow \infty$) of the initial-value analysis with a recent normal mode analysis [5] and experimental data of nearly supercritical oscillations [6] for different Reynolds numbers ($Re = 50, 70, 100$) (see Fig. 2).

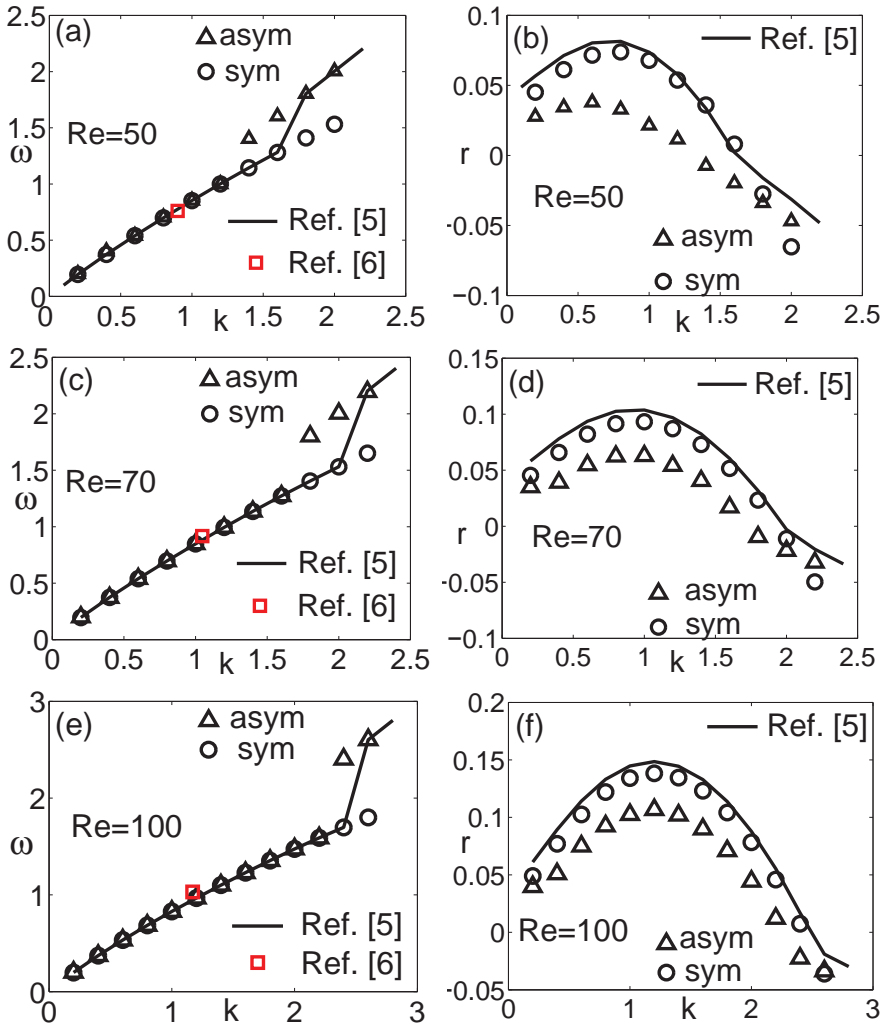


Fig. 2. (a, c, e) pulsation $\omega(t)$ and (b, d, f) temporal growth rate $r(t)$ for present results (asymmetric case: black triangles, symmetric case: black circles), modal analysis [5] (solid curves) and experimental data [6] (red squares). $\alpha_i = 0.05$, $\phi = 0$, $x_0 = 10$, $Re = 50, 70, 100$.

The comparison is quantitatively good for all the Reynolds numbers considered, because it shows that a wavenumber close to the wavenumber that theoretically has the maximum growth rate has a - theoretically deduced - frequency which is very close to the frequency measured in the laboratory. The noticeable point of this analysis is the variety of temporal scales revealed by the transient, which are associated to a given specific value of the instability wavelength. In particular, if the perturbation is asymmetric and oblique it is possible to count up to five different time scales for the system: (i) the temporal scale $D/U \sim 1$ related to the base flow (where D is the cylinder diameter and U is the free stream velocity), (ii) the length of the transient (200-300 time units), (iii and iv) the scales associated to the instability frequency in the early transient (about 21 time units) and in the asymptotic state (about 14 time units), and (v) the modulation of the pulsation in the early transient (about 35-40 time units). Another interesting point is that these scales are different each other and are also different from the asymptotic value predicted either by the initial-value problem or the modal theory.

References

1. D. Tordella and M. Belan, *Phys. Fluids*, **15** (2003).
2. W. O. Criminale and P. G. Drazin, *Stud. Appl. Math*, **83** (1990).
3. S. Scarsoglio, D. Tordella, W. O. Criminale, to appear in *Stud. Appl. Math*, 2009.
4. G. Coppola and L. De Luca. *Phys. Fluids*. **18**: **078104** (2006).
5. D. Tordella, S. Scarsoglio and M. Belan, *Phys. Fluids*, **18**: **054105** (2006).
6. C. H. K. Williamson, *J. Fluid Mech* **206** (1989).

Convection at very high Rayleigh number: signature of transition from a micro-thermometer inside the flow

J. Salort¹, F. Gauthier¹, B. Chabaud¹, O. Bourgeois¹, J.-L. Garden¹, R. du Puits², A. Thess² and P.-E. Roche¹

¹ Institut Néel, CNRS / UJF, BP166, 38042 Grenoble CEDEX 9, France

² Department of Mechanical Engineering, Ilmenau University of Technology, P.O. Box 100565, 98684 Ilmenau, Germany
julien.salort@grenoble.cnrs.fr

1 Introduction

In 2001, a change in the statistics of temperature fluctuations in Rayleigh-Bénard convection was reported at very high Rayleigh number ($Ra \sim 10^{12}$) [1]. This change was concomitant with an enhancement of the heat transfer which had been interpreted [2] as the triggering of Kraichnan Convection Regime [3]. But a systematic study of finite probe size effect showed that the 200 μm probe used in the 2001 study was about three times too large to be free from finite size correction [4], calling for a confirmation of these results. We report new measurements of temperature fluctuations performed with a probe ten times smaller than the one used in 2001.

In this proceeding, we discuss experimental aspects of this experiment and complementary measurements made in the “Barrel of Ilmenau”. The first experiment was conducted with cryogenic helium and the second with air. Once combined, those two experiments lead to evidence of a signature of a transition in the local temperature fluctuations, supporting the conclusion of the 2001 study.

2 Micron-size thermometer

The temperature probe is a 17- μm glass fiber, on which a 1 μm layer of NbN [5] was deposited and annealed. The fiber and its stainless steel frame was glued on a wooden tripod. The fiber is placed two millimeters above the bottom plate of a 43-cm-high 10-cm diameter convection cell (see figure 1). It is connected to two pairs of copper wires for the 4-wire-measurement. We were careful not to over-heat the fiber with the measuring current to avoid hot-wire

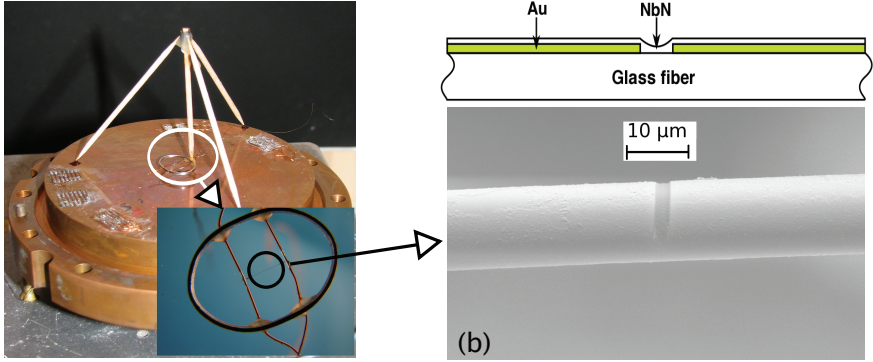


Fig. 1. (a) Temperature probe on its tripod above the bottom plate of the 43-cm-high cryogenic Rayleigh-Bénard cell. Inset: detail on the web-like fiber support. (b) Drawing and electronic microscope picture of the sensitive element

artefact. As can be seen on figure 2, the fiber starts to self-heat meaningfully for input current of order of $1 \mu\text{A}$. All subsequent measurements were done with an input current of $0.5 \mu\text{A}$.

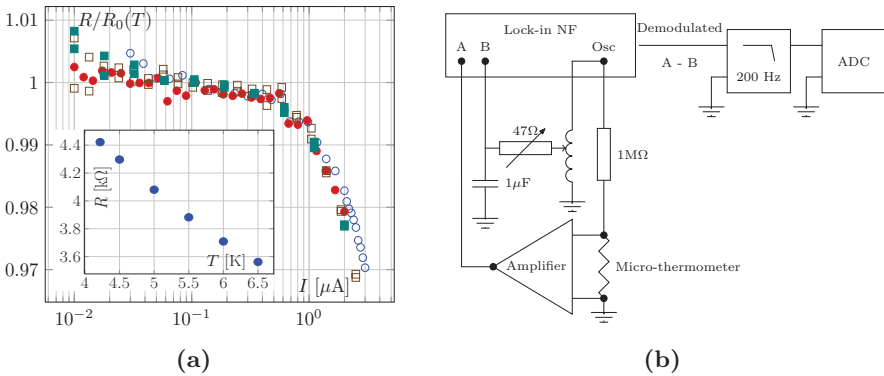


Fig. 2. (a) Self-heating of the micro-thermometer for various experimental conditions. $\rho = 1.6 \text{ kg/m}^3$, $T \approx 6.5 \text{ K}$ (\circ); $\rho = 6.5 \text{ kg/m}^3$, $T \approx 6.0 \text{ K}$ (\bullet); $\rho = 19 \text{ kg/m}^3$, $T \approx 6.0 \text{ K}$ (\square); $\rho = 40 \text{ kg/m}^3$, $T \approx 6.0 \text{ K}$ (\blacksquare). Inset : Resistance of the fiber versus temperature. (b) Electronic diagram of the acquisition system.

The temperature response of the probe is calibrated versus Ge thermometers in homogeneous temperature conditions. We find a temperature sensitivity $\partial \ln R / \partial \ln T \simeq 0.7$ at 5 K (see inset in figure 2). The performance is limited by a resistance noise with spectral density $1.5 \times 10^{-6} / f$, where f is the frequency in Hertz, corresponding to a rms noise of order 1 mK over the bandwidth

of interest. This noise prevented operation above $Ra = 5 \times 10^{13}$ in order to maintain Boussinesq conditions.

The fluctuation data was acquired using the electronic setup shown on figure 2 : the input current is provided by the generator of a *NF* Lock-In Amplifier LI-5640 ($V = 500$ mV, $f = 7825$ Hz). The voltage drop across the fiber is pre-amplified (JFET, Gain 10^4 , typical noise input voltage 700 pV/ $\sqrt{\text{Hz}}$). We subtract the mean-value of the temperature signal using a *Singer* inductor bridge and an adjustable *RC* filter to compensate for the phase shift, in order to use all the dynamics of the Lock-in. The demodulated signal is filtered by a General Purpose *Kemo* 1208/20/41LP low-pass filter (8 pole Elliptic filter with a flat passband, frequency cutoff 200 Hz) to avoid aliasing and then acquired by a *NI* Analog-Digital Converter NI6289 (18 bits).

3 Results and interpretation

Following Chavanne *et al.* [1], we consider the exponent ξ_2 of the 2nd order structure function of the temperature fluctuations $T(t)$:

$$\xi_2 = \frac{d \log \langle (T(t + \tau) - T(t))^2 \rangle_t}{d \log \tau} \tag{1}$$

where the brackets represent time averaging. The dependence of ξ_2 versus the time increment τ holds the same information as a temperature spectrum.

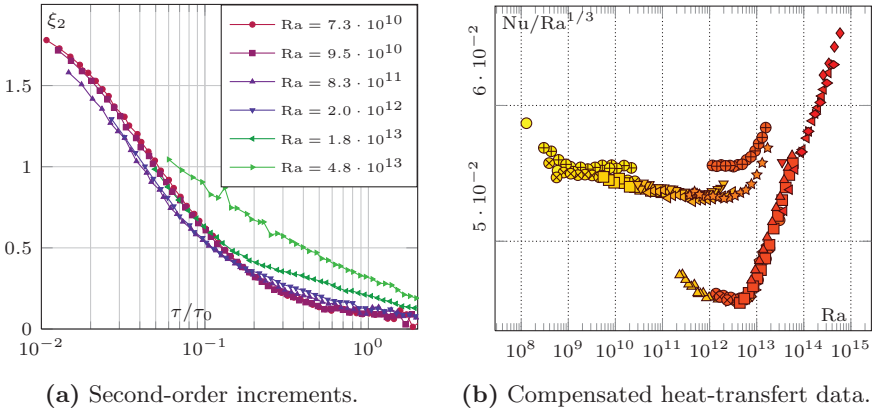


Fig. 3. Data measured in the 43-cm Rayleigh-Bénard cell.

Fig. 3-a shows ξ_2 versus the dimensionless increment τ/τ_0 where $\tau_0 = (h/2Nu)^2/\kappa$ is a characteristic time scale of the flow. A change of shape occurs above $Ra \approx 10^{13}$, which is also the threshold Ra for which a heat transfer transition is measured in this cell, as shown on fig. 3-b. The observed jumps of

$Nu(Ra)$ are characteristic of the multiple possible configurations of the mean large scale circulation in elongated cells. They are known to hardly affect the temperature spectra, and therefore ξ_2 , although they can be responsible for a few tens of % offset of the x-axis of fig.3-a through the Nu dependence of τ_0 .

For $Ra \geq 10^{12}$, $h/2Nu \leq 400 \mu\text{m} < 2 \text{ mm}$: the probe is clearly outside the thermal boundary layer. We also studied the systematic dependance of $\xi_2(\tau)$ versus the probe-plate distance below the transition ($Ra = 3.2 \times 10^{11}$) in the “Barrel of Ilmenau” in the range $0.1 < z/(h/2Nu) < 20.3$. This study reported in [4] showed that the variation of this effective plate-probe distance cannot explain the transition observed on the temperature statistics.

The observed change in shape of ξ_2 is consistent with Chavanne *et al.*'s qualitative observations, confirming *a posteriori* that their observation was not an artefact although it was partly altered by a finite size effect [1].

4 Conclusion

The regime observed (and named “Ultimate Regime”) in [1] is thus characterised by 3 specific signatures : an integral one (heat transfer enhancement) and localized ones on the thermal boundary layer [6] and inside the flow as shown in this paper (see also [4]). These signatures are compatible with Kraichnan's prediction [3] but more work is certainly needed to understand the basic mechanism of the flow instability at very high Ra .

Acknowledgements : We thank B. Hébral, F. Chillà and more especially B. Castaing for numerous discussions. The assistance of T. Fournier, P. Diribarne and P. Lachkar in instrumentation is gratefully acknowledged. A Procope collaboration was made possible thanks to Deutscher Akademischer Austauschdienst (D/0707571) and Ministère des Affaires Etrangères (17858YD)

References

1. Turbulent Rayleigh-Bénard convection in gaseous and liquid He, X. CHAVANNE *et al.*, *Phys. Fluids*, **13**:1300, 2001
2. Observation of the ultimate regime in Rayleigh-Bénard convection, X. CHAVANNE *et al.*, *Phys. Rev. Lett.*, **79**:3648, 1997
3. Turbulent thermal convection at arbitrary Prandtl numbers, R. KRAICHNAN, *Phys. Fluids*, **5**:1374, 1962
4. Temperature fluctuations in the Ultimate Regime of Convection, F. GAUTHIER *et al.*, *to be submitted in 2009*
5. Liquid nitrogen to room-temperature thermometry using niobium nitride thin films, O. BOURGEOIS *et al.*, *Rev. Sci. Instruments*, **77**:126108, 2006
6. Evidence of a boundary layer instability at very high Rayleigh number, F. GAUTHIER and P.-E. ROCHE, *EPL*, **83**:24005, 2008

Estimating local instabilities for irregular flows in the differentially heated rotating annulus

U. Harlander¹, R. Faulwetter², K. Alexandrov¹, and C. Egbers¹

[1]Dept. of Aerodynamics and Fluid Mechanics, BTU Cottbus, 03046 Cottbus, Germany;

[2]Dept. of Theoretical Meteorology, University of Leipzig, 04103 Leipzig, Germany

haruwe at tu-cottbus.de

1 Introduction

In stable flows, transient growth of 'non-normal' modes can lead to turbulence. Usually, non-normal modes are computed from linearized model equations [1]. However, for some problems the proper set of equations is unknown, or unhandy for the purpose of finding non-normal modes. Therefore it is proposed to estimate non-normal modes from data alone, without using the model equations. Crucial for such an estimation is a good guess of the linear system matrix for the flow under consideration. Such a guess can be obtained following the approach by [2] discussed in the context of climate analysis.

In the present paper a simple test case will be presented that demonstrates the suitability of the approach. Subsequently, the method is applied to temperature data from a differentially heated rotating annulus, a laboratory model that covers features of the large-scale atmospheric circulation [3]. The method proposed might help to gain insight into the spatial structures of local instability in annulus flows.

2 Motivation and test case

2.1 Growing modes in stable systems

To motivate 'non-classical' hydrodynamic instability, [4] used the simple two-dimensional model:

$$\frac{d}{dt} \begin{pmatrix} u \\ v \end{pmatrix} = \begin{pmatrix} -R^{-1} & 1 \\ 0 & -2R^{-1} \end{pmatrix} \begin{pmatrix} u \\ v \end{pmatrix} = \mathbf{A}\mathbf{u}. \quad (1)$$

The matrix \mathbf{A} is called the system matrix. For symmetric system matrices it can be shown that for any given period of time, the largest growth of $u^2 + v^2$ is determined by the most unstable eigenvector (or normal mode) of \mathbf{A} . If there is no unstable eigenvector, the system cannot grow. The situation becomes different when \mathbf{A} is

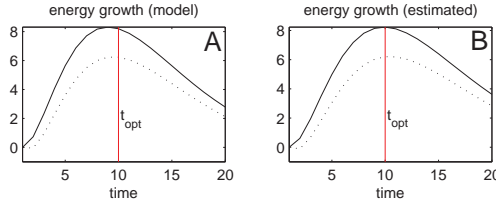


Figure 1: A) Time development of $u^2 + v^2$ for the first singular vector (solid line) and an arbitrary other initial vector (dashed line). B) As A but computed by using the estimated propagator \mathcal{P} . We used $R = 12, t_0 = 0, t_{opt} = 10$.

non-symmetric as in (1). Then for any predefined period $0 < t < t_{opt}$, where t_{opt} is the so called 'optimization time', a complete set of growing 'non-normal' modes (called singular vectors, or SVs) can be found. In contrast to unstable eigenmodes, SVs change their shape in time. Most interesting is the SV with the largest growth rate. For $t = 0$ it defines the initial field that shows the largest growth in the period $0 < t < t_{opt}$.

The formal solution of the linear system (1) reads

$$\mathbf{u}(t) = \mathbf{P} \mathbf{u}(t_0), \quad \mathbf{P} = e^{(t-t_0)\mathbf{A}}. \quad (2)$$

The matrix \mathbf{P} is called the propagator of the linear system. The singular vectors are the eigenvectors of $\mathbf{M}\mathbf{v} = \lambda\mathbf{v}$, where $\mathbf{M} = \mathbf{D}^{-1}\mathbf{P}'\mathbf{D}\mathbf{P}$, \mathbf{D} is the identity matrix and \mathbf{P}' is the transpose of \mathbf{P} [5].

Figure 1A shows the energy growth of SV1 (solid line) and an arbitrarily chosen initial vector (dashed line). The growth of the singular vector is larger (and it is in fact larger than the growth of any other initial vector).

2.2 Estimating the propagator from data

Let us assume that we do not know (1) but instead that we have just data $\mathbf{u}(i)$. In fact, this is the situation that is frequently encountered in practice. We propose that the data are consistent with the linear process $\mathbf{u}(i+1) = \mathcal{P}\mathbf{u}(i)$. Then, by following [2], the propagator is estimated as

$$\mathcal{P} = \Sigma_1 \Sigma_0^{-1} \approx \mathbf{P}, \quad (3)$$

where

$$\Sigma_j = \frac{1}{N} \sum_i^N (\mathbf{u}(i+j) - \bar{\mathbf{u}})(\mathbf{u}(i) - \bar{\mathbf{u}})'. \quad (4)$$

Here $j = 0, 1$, $\bar{\mathbf{u}}$ is the time mean and the prime denotes the transpose. Figure 1B is equal to A except that the energy growth is computed from \mathcal{P} and not from \mathbf{P} .

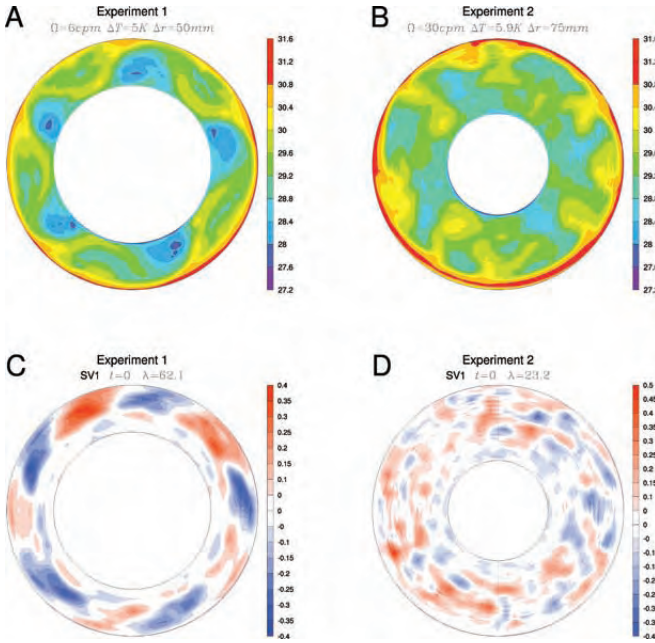


Figure 2: Snapshot of the temperature field of the two experiments discussed. A) **exp1**, $\Omega = 6cpm$, $\Delta T = 5K$, $\Delta r = 50mm$. B) **exp2**, $\Omega = 30cpm$, $\Delta T = 5.9K$, $\Delta r = 75mm$. C) SV1 at $t = 0$ for exp1. D) SV1 at $t = 0$ for exp2.

The data used come from (1) with a sampling rate of $\Delta t = 1$, and $0 < t < 100$. Obviously, \mathcal{P} is estimated very well. Nevertheless, its quality depends on the length of the data time series, the sampling rate and the data noise level (that was zero in the example considered).

3 Thermally driven rotating annulus

At the BTU Cottbus a rotating annulus experiment is conducted as one of the reference experiments in the 'SPP 1276 MetStröm' priority program of the German Science Foundation (DFG). The experiment is described in detail in [6] and [7]. Here we discuss two experiments, one in a stable wave regime (exp1), and the other one in an irregular regime (exp2) (see Figure 2A,B). Data were collected once per cycle over several hours. The Figure shows snapshots of the surface temperature for both experiments. It is obvious that for slow rotation, the flow settles down in a rather stable wave state (A). In contrast, no simple flow pattern can be found for the faster rotation (B)[3,6].

3.1 Estimating growing patterns of the rotating annulus flow

The surface temperature data were used to find \mathcal{P} from (3). The data were first subjected to a truncated EOF expansion [8] to reduce the number of spatial degrees of freedom. \mathcal{P} results then from the vector of the leading EOFs. Byproducts of this procedure is that noisy components can be filtered out and that Σ_0 becomes diagonal.

SV1 computed from \mathcal{P} is shown in Figure 2C. SV1 of exp1 looks like a wave with zonal wave number 5. Thus qualitatively, SV1 corresponds with the most unstable baroclinic mode of exp1. Typically, the pattern shows a tilt with respect to the radial direction. During the energy uptake this tilt is reduced and it approaches zero for $t = t_{opt}$. SV3 (not shown) corresponds well with the growing neutral waves in shear currents discussed by [9]. For exp2, the patterns of optimal growth are governed by patchy small scale features (Figure 2D). Such SVs are hard to interpret and future work is necessary to test these structures for physical relevance. What can be said so far is that the patterns become focused near the inner cylinder for $t \rightarrow t_{opt}$. This behavior has also be observed for exp1.

4 Conclusion and future work

We demonstrated that singular vectors can be estimated from data alone. For exp1, the patterns of optimal growth have a straightforward physical interpretation. For the quasi-turbulent flow of exp2 it appears that the noise level is too large. For future analysis the noise has to be filtered out. Moreover, other optimization intervals and other norms have to be tested for an empirical computation of singular vectors.

References

1. A. Will, U. Harlander, and W. Metz Meteorolog. Zeitschrift, **15**, 463- (2006).
2. K.F. Hasselmann, J. Geophys. Res. **93**, 11015-11021 (1988).
3. W.-G. Fröh and P. Read, Phil. Trans. R. Soc. Lond. A, **355**, 101-153 (1997).
4. L.N. Trefethen, A.E. Trefethen, S.C. Reddy and T.A. Driscoll, Science, **261**, 578-584 (1993).
5. H. Heinrich, Wiss. Mitt. LIM Univ. Leipzig **33**, 105pp (2004).
6. Th. v. Larcher and C. Egbers, Non. Proc. Geophys., **12**, 1033- (2005).
7. U. Harlander, Th. v. Larcher, Y. Wang and C. Egbers, subm. to Exp. in Fluids (2008).
8. H. v. Storch and Zwiers, Cambridge, 484pp, (1999).
9. B.F. Farrell, J. Atmos. Sci., **46**, 1193-1206 (1989).

Search for the “ultimate state” in turbulent Rayleigh-Bénard convection

E. Bodenschatz¹, D. Funfschilling², and G. Ahlers³

¹Max Planck Institute for Dynamics and Self-Organization, Am Fassberg 17, D-37077 Goettingen, Germany

²LSGC CNRS - GROUPE ENSIC, BP 451, 54001 Nancy Cedex, France

³Department of Physics, University of California, Santa Barbara, CA 93106, USA
eberhard.bodenschatz@ds.mpg.de

Turbulent convection in a fluid heated from below and cooled from above is an important process in many geo- and astro-physical processes with typical Rayleigh numbers $Ra \approx 10^{20}$. It has been anticipated that the convective heat transport changes fundamentally for $Ra = Ra^*$, where Ra^* is a function of Prandtl number Pr . Below Ra^* heat transport is expected to be determined by thermal boundary layers and above, in the “ultimate regime”, by the bulk fluid [1]. Unfortunately these Ra ranges are not readily accessible in laboratory experiments. Most measurements are limited to $Ra < 10^{12}$. A decade ago

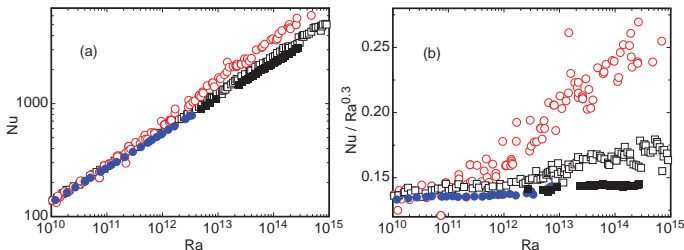


Fig. 1. (a): Nusselt number Nu as a function of the Rayleigh number Ra . (b): Reduced Nusselt number $Nu/Ra^{0.3}$ as a function of Ra . Open circles: Ref. [2]. Open squares: from Ref. [3]. Solid circles: This work using N₂. Solid squares: This work using SF₆.

Chavanne *et al.* [2] obtained the measurements shown in Fig. 1 of the Nusselt number Nu (the normalized thermal conductivity) using helium near 5 K for Ra up to 10^{15} . They observed a transition in $Nu(Ra)$ near $Ra = 10^{11}$, which they interpreted to be the transition to the ultimate regime. Soon thereafter Niemela *et al.* [3] made similar measurements using low-temperature helium

up to $Ra \simeq 10^{17}$ (see Fig. 1) and did not find such a transition. As shown in Fig. 2 in both experiments at the larger Ra the Pr varied significantly.

Here we report measurements of $Nu(Ra)$ in Rayleigh-Bénard convection (RBC) conducted at the “High Pressure Convection Facility” in Goettingen in a cylindrical pressure vessel of diameter 2.5 m and length 5.5 m, with its axis horizontal, and with a turret above it that extends the height to 4 m over a diameter of 1.5 m. It can be filled with various gases to pressures ranging from 1 mbar to 15bar. Here we used Nitrogen N_2 or Sulfurhexafluoride SF_6 gas, which give $0.73 \leq Pr \leq 0.84$. In the section containing the turret we placed a RBC sample-cell of interior height 2.24 m and interior diameter 1.12 m which yielded $10^{10} \leq Ra \leq 10^{15}$.

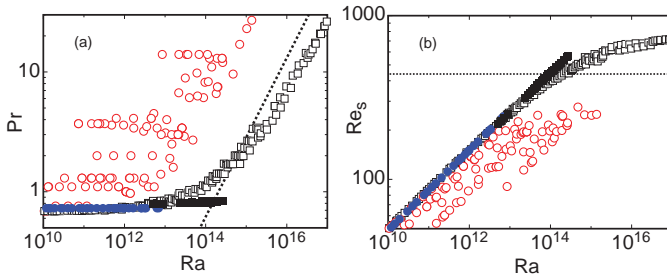


Fig. 2. (a): Prandtl number Pr as a function of the Rayleigh number Ra . (b): Shear Reynolds number Re_s as a function of Ra . The symbols are as in Fig. 1.

Our data are shown in Fig. 1 as solid symbols. They reveal no transition and over their entire range can be described well by a power law with $\gamma_{eff} = 0.31$. In Fig. 2a we show the $Pr(Ra)$ range covered by all three data sets. The dotted line is an estimate of $Ra^*(Pr)$. Figure 2b gives an estimate of the shear Reynolds numbers Re_s of the viscous boundary layers near the top and bottom plates, based on bulk Re measurements of Ref. [2]. Ra^* is expected to be reached when $Re_s = Re_s^* \simeq 400$ (dotted line). The data of Ref. [2] never came close to Ra^* or Re_s^* ; thus it seems unlikely that their transition is related to the transition to the “ultimate” or bulk regime. The data of Ref. [3], as well as ours, extend about equally far and slightly above Ra^* or Re_s^* .

References

1. R. H. Kraichnan, Phys. Fluids **5**, 1374 (1962).
2. X. Chavanne, F. Chillà, B. Castaing, B. Hébral, B. Chabaud, and J. Chaussy, Phys. Rev. Lett. **79**, 3648 (1997); X. Chavanne, F. Chillà, B. Chabaud, B. Castaing, and B. Hébral, Phys. Fluids **13**, 1300 (2001).
3. J. Niemela, L. Skrbek, K. R. Sreenivasan, and R.J. Donnelly, Nature **404**, 837 (2000); J. Niemela and K. R. Sreenivasan, J. Low Temp. Phys. **143**, 163 (2006).

Rayleigh–Taylor instability in two dimensions and phase-field method

A. Celani¹, A. Mazzino², P. Muratore-Ginanneschi³ and L. Vozella²

¹ Institut Pasteur, CNRS, URA 2171, 25 Rue du docteur Roux, 75015 Paris, France

² Dipartimento di Fisica, Università di Genova and INFN-Sezione di Genova, Via Dodecaneso 33, I-16146 Genova, Italy

³ Department of Mathematics and Statistics, University of Helsinki, P.O. Box 4, 00014 Helsinki, Finland
vozella at fisica.unige.it

The Rayleigh–Taylor (RT) instability [1, 2] is a fluid-mixing mechanism occurring at the interface of two fluids of different densities, subjected to an external acceleration. The relevance of this mixing mechanism embraces many different phenomena occurring in completely different contexts (e.g., supernovae explosions [3] and solar flare formation [4]). In many of these situations the two fluids are immiscible owing to a non negligible surface tension. By means of Direct Numerical Simulations we investigate the immiscible two-dimensional setting in the limit of small Atwood numbers. The surface tension introduces serious problems in numerical description: the interface is sharp and subject to morphological changes such as breakup, coalescence and reconnections (see Fig. 1).

These obstacles can be overcome by using a phase-field description [5, 6]. We present an accurate numerical study that validates the phase-field method by testing known results of immiscible RT instability both at level of linear and weakly nonlinear analysis.

1 System configuration and phase-field description

The system consists of two immiscible, incompressible fluids (labelled by 1 and 2) having different densities, ρ_1 and ρ_2 ($> \rho_1$), with denser placed above the less one.

The idea of the phase-field description is to replace the sharp interface with a thin, yet finite, transition region where the fluids, nominally immiscible, can mix. More quantitatively, this amounts to assigning to the system a Ginzburg–Landau free-energy, \mathcal{F} , expressed in term of the order parameter $\phi(\mathbf{x})$ as [6]:



Fig. 1. Two-color snapshots of density field at different times. White (black) corresponds to a light (heavy) fluid. Our system consists of two immiscible, incompressible fluids having different densities in the presence of gravity. At initial time, the system is at rest in unstable configuration. If a disturbance is imposed on the interface separating the two fluids, the instability develops.

$$\mathcal{F}[\phi] = \int_{\Omega} \frac{\Lambda}{2} |\nabla \phi(\mathbf{x})|^2 + \frac{\Lambda}{4\epsilon^2} (\phi^2 - 1)^2 d\mathbf{x} \quad (1)$$

where Ω is the region of space occupied by the system, ϵ is the capillary width, representative of the interface thickness and Λ is the magnitude of the free-energy. The order parameter ϕ serves to identify fluid 1 and 2. We assume $\phi = 1$ in the region occupied by fluid 1 and $\phi = -1$ in those where fluid 2 is present.

The equilibrium state is the minimiser of the free-energy functional \mathcal{F} respect to variations of the function ϕ . If one considers an one-dimensional interface, varying along the gravitational direction z , one easily obtain the equilibrium profile for the phase field [6]:

$$\phi(z) = \pm \tanh\left(\frac{z}{\sqrt{2}\epsilon}\right) \quad (2)$$

Moreover, for a plane interface, we can relate the surface tension σ to the free-energy parameters as follows [6]:

$$\sigma = \frac{2\sqrt{2}}{3} \frac{\Lambda}{\epsilon} \quad (3)$$

From the previous relations it is easy to realize that the classical sharp interface limit is obtained for $\epsilon, \Lambda \rightarrow 0$.

Let us suppose to introduce a small disturbance on the interface separating the two fluids. Such perturbation will displace the phase field from the previous equilibrium configuration to a new configuration for which in general, the free-energy minimization is not longer verified. The system will react so as to try to reach again an equilibrium configuration. In formulae, the so-called Cahn-Hilliard equation rules the phase-field evolution [5, 6]:

$$\partial_t \phi + \mathbf{v} \cdot \nabla \phi = \gamma \Lambda \Delta \left[-\Delta \phi + \frac{(\phi^3 - \phi)}{\epsilon^2} \right] \quad (4)$$

where γ is the so-called mobility.

The dynamics of the velocity field \mathbf{v} is governed by the usual Boussinesq Navier–Stokes equation plus an additional stress contribution arising at the interface where the effect of surface tension enters into play [6, 7]:

$$\partial_t \mathbf{v} + \mathbf{v} \cdot \nabla \mathbf{v} = -\frac{\nabla p}{\rho_o} + \nu \Delta \mathbf{v} - \frac{\Lambda}{\rho_o} \Delta \phi \nabla \phi - \mathcal{A} \mathbf{g} \phi \quad (5)$$

$$\nabla \cdot \mathbf{v} = 0 \quad (6)$$

where $\rho_o = (\rho_1 + \rho_2)/2$, ν the kinematic viscosity, $\mathcal{A} = (\rho_2 - \rho_1)/(\rho_2 + \rho_1)$ the Atwood number, and \mathbf{g} the gravity selected along the z axis.

2 Numerical investigation

By means of Direct Numerical Simulations we consider the model (4)-(5)-(6) in two-dimensional setting. We focus both on the linear and weakly nonlinear regimes (for $\mathcal{A} \ll 1$) in order to properly test the phase-field approach against known results for both of these regimes. All simulations presented start from an initial condition corresponding to an equilibrium configuration: zero velocity and hyperbolic tangent profile for the phase field, expressed as $\tanh((z - h(x, t = 0))/\sqrt{2}\epsilon)$ with $\eta(x, t = 0) = \eta_0 \sin(x)$. The initial disturbance amplitude is selected in a way to satisfy both limits of small disturbance and infinitesimal capillary width.

Under the hypothesis of small disturbance the initial evolution can be described by a linear theory [8]. In the limit of sharp interface, we can redivered (details are not reported here) the following expression for the time evolution of the amplitude disturbance:

$$\eta(t) = \eta_0 \cosh(\alpha t) \quad \text{with} \quad \alpha = \sqrt{\mathcal{A} g k - \frac{\sigma}{\rho_1 + \rho_2} k^3} \quad (7)$$

Our aim is to verify the expression for the linear growth rate α . Our results are summarized in Fig. 2a.

When the amplitude disturbance becomes large enough [9], deviations from the linear predictions are observed. The disturbance grows nonlinearly and interface starts deforming in the shape of thermal plumes. There is a general consensus on the dynamics in this stage: the exponential growth of the amplitude disturbance is replaced by a linear-in-time behavior (see [10] and references therein). Indeed the thermal plumes reach a constant terminal velocity [11]:

$$U = \sqrt{\frac{2}{3} \mathcal{A} \frac{g}{k} - \frac{2}{9} \frac{\sigma}{\rho_1 + \rho_2} k} \quad (8)$$

Our results, shown in Fig. 2b reproduce this behavior.

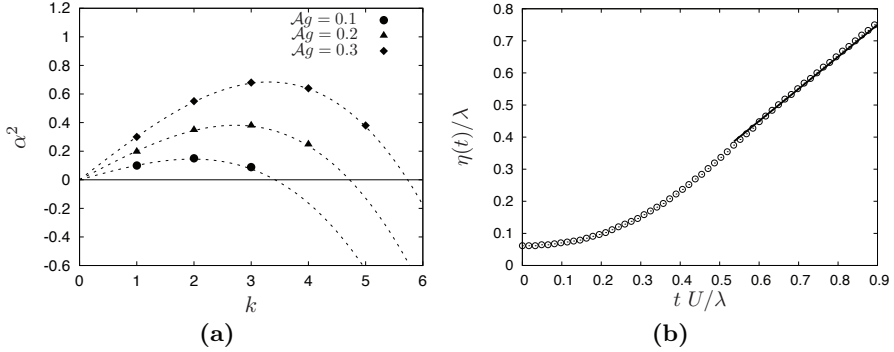


Fig. 2. (a) Squared linear growth rate α^2 for three different values of Ag and the same value of σ . The dashed lines are the corresponding linear-theory predictions. (b) Time evolution of amplitude perturbation $\eta(t)$ ($\lambda = 2\pi/k$). The dashed line is a slope given in (8). A good agreement is found between numerics and theory in the range $0.5 < tU/\lambda < 0.9$. At larger times, neighbouring plumes start to interact and the arguments leading to the velocity expression (8) do not longer apply.

3 Conclusions

From our numerical results, it turns out that the phase-field strategy provides a valuable numerical instrument for the study of immiscible RT instability. Numerical results compare well with known analytical results both for the linear and weakly nonlinear stages. All these results are therefore encouraging in a view of the next step, that is a quantitative treatment of the turbulent regime, the final regime of the instability, characterized by the interplay between hydrodynamics and interface degrees of freedom [12].

References

1. Lord Rayleigh, Proc. London Math. Soc., **14**, 170 (1883).
2. G. T. Taylor, Proc. R. London Ser. A, **201**, 192 (1950).
3. W. H. Cabot and A. W. Cook, Nature Physics, **2**, 5621 (2006).
4. H. Isobe, T. Miyagoshi, K. Shibata and T. Yokoyama, Nature, **434**, 478 (2005).
5. J. W. Cahn and J. E. Hilliard, J. Chem. Phys., **28**, 258 (1958).
6. A. J. Bray, Advances in Physics, **51**, 481 (2002).
7. C. Liu, J. Shen, Physica D, **179**, 211 (2003).
8. S. Chandrasekhar, Hydrodynamic and Hydromagnetic Stability, Clarendon Press, Oxford (1961).
9. D. H. Sharp, Physica D, **12**, 3 (1984).
10. J. T. Waddell, C. E. Niederhaus, J. W. Jacobs, Phys. Fluids, **13**, 1263 (2001).
11. Y. N. Young, F. E. Ham, J. Turbul., **71**, 1 (2006).
12. M. Chertkov, I. Kolokolov, V. Lebedev, Phys. Rev. E, **71**, 055301 (2005).

Split energy cascade in quasi-2D turbulence

G. Boffetta¹, A. Celani² and S. Musacchio¹

¹ Dipartimento di Fisica Generale, INFN and CNISM, Via Pietro Giuria 1, 10125, Torino, Italy,

² CNRS URA 2171, Institut Pasteur, 75724 Paris Cedex 15, France
smusacch@to.infn.it

Summary. By means of numerical simulations we investigate the transition from two-dimensional to three-dimensional turbulence which occurs in the turbulent flow of a thin layer of incompressible fluid as the thickness of the layer is increased. Coexistence of 2D and 3D turbulence is observed when the thickness is larger than viscous scale, but smaller than the forcing correlation length.

Two-dimensional Navier-Stokes equation is a prototype model for geophysical flow, in which the combined effects of rotation and stratification suppress vertical motions and allows to describe mesoscale dynamics in terms of two-dimensional equations.[1, 2, 3] In these applications the two-dimensional flow is thought as the limit of vanishing ratio between the thickness of the fluid layer and the horizontal scales of interest.

The phenomenology of two-dimensional turbulent flows remarkably differs from the behavior of three-dimensional turbulence. In the classical picture of the Richardson cascade kinetic energy injected at large scale by an external forcing is transferred to smaller and smaller eddies until it reaches the viscous scale where it is dissipated by the viscosity. Conversely, in two dimensions, the simultaneous conservation of kinetic energy and enstrophy results in an inverse energy cascade, i.e. the power injected by the forcing feeds large-scale structures in the flow.[4]

In thin layers of fluid one expects to observe a transition from two-dimensional to three-dimensional turbulence characterized by an inversion of the direction of the energy cascade, as the thickness of the layer is increased. In this paper we investigate this transition by means of numerical simulations. Three-dimensional Navier-Stokes equations

$$\partial_t \mathbf{u} + \mathbf{u} \cdot \nabla \mathbf{u} = -\nabla P / \rho - \nu \nabla^2 \mathbf{u} + \mathbf{f} \quad (1)$$

with the incompressibility constraint $\nabla \cdot \mathbf{u} = 0$, are solved in a periodic box of sizes $L_x = L_y = 2\pi$, $L_z = rL_x$ at resolution $N_x = N_y = 512$, 1024 , $N_z = rN_x$ for various aspect ratio r . The flow is sustained by a two-dimensional random

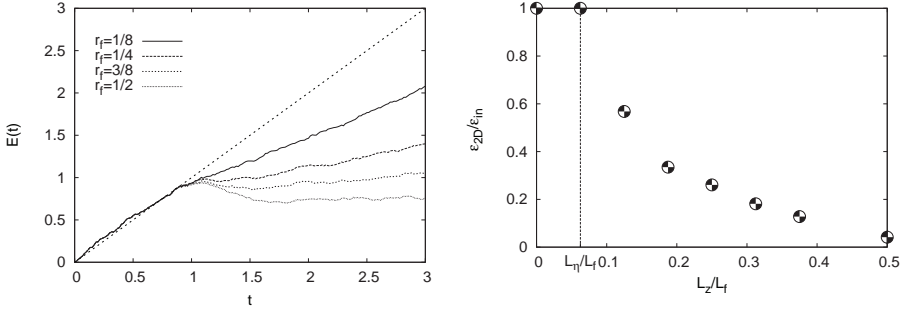


Fig. 1. *Left panel:* Growth of kinetic energy for various values of $r_f = L_z/L_f$. *Right panel:* Kinetic energy growth rate ϵ_{2D} normalized with the power injected as a function of r_f .

force which excites only the horizontal components of the velocity field. The forcing is active on wavenumbers $|\mathbf{k}| \sim k_f$ with $k_z = 0$, and has correlation length $L_f = 2\pi/k_f$. The behavior of the resulting turbulent flow is strongly dependent on the thickness of the layer L_z .

When the thickness of the fluid is smaller than the viscous lengthscale L_η , vertical motions are suppressed by the viscosity. In this regime the fluid recovers the two-dimensional behavior, characterized by an inverse energy cascade with a constant flux of kinetic energy toward large scales $\ell > L_f$. In absence of large-scale dissipations the kinetic energy grows linearly in time, with a growth rate equal to the power injected by the forcing.

Conversely, when $L_z > L_\eta$, small three-dimensional perturbations can be amplified by the vortex stretching mechanism. The amount of small-scale vorticity produced is able to dissipate a substantial part of the energy injected. As a consequence the fraction of the energy that is transferred toward large scale reduces, and the energy growth rate decreases, as shown in Figure 1. The ratio between the energy growth rate and the power injected is dependent on the aspect ratio $r_f = L_z/L_f$ between the thickness and the forcing correlation length (see Fig. 1, right panel).

When the thickness of the fluid is much larger than viscous scale, but smaller than the forcing correlation length L_f , 2D and 3D turbulence can coexist. In this regime we observe a splitting of the energy cascade. Part of the energy is still transferred toward large scale, feeding the inverse cascade. The remnant energy gives rise to a direct energy cascade with constant flux toward small scale (see Figure 2).

Coexistence of 2D and 3D turbulence is clearly visible in the energy spectra (see Figure 3). At small wavenumbers $k < k_f$ the energy spectrum of horizontal velocities has a scaling region $E(k) \sim \epsilon_{2D}^{2/3} k^{-5/3}$ which is the signature of the two dimensional inverse energy cascade. At high wavenumbers $k > k_z$

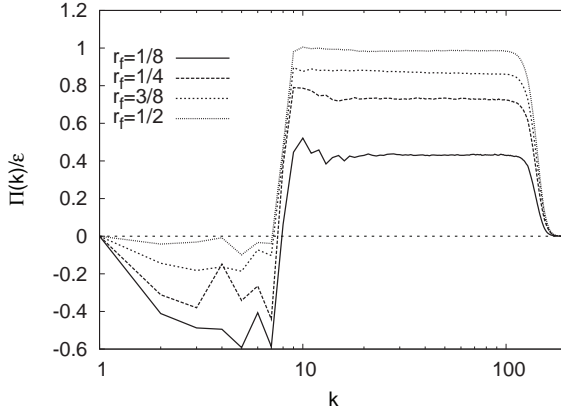


Fig. 2. Spectral flux of kinetic energy for various values of $r_f = L_z/L_f$.

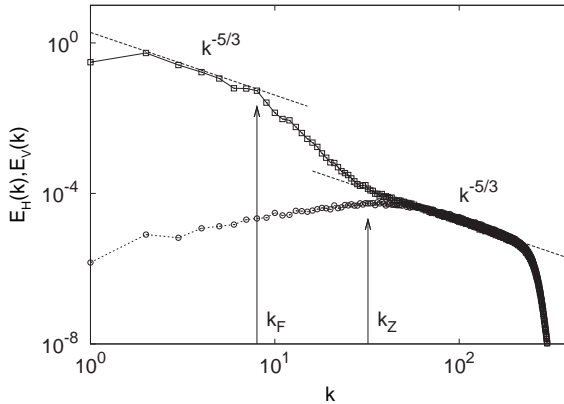


Fig. 3. Kinetic energy spectrum of horizontal (squares) and vertical (circles) velocities. Here $r_f = 1/4$

Kolmogorov spectra are observed both for horizontal and vertical velocities, signaling the presence of 3D turbulence at small scales.

References

1. P. Bartello, *J. Atmos. Sci.* **40**, 4410 (1995).
2. L. M. Smith, J. R. Chasnov, F. Waleffe, *Phys. Rev. Lett.* **77**, 2467 (1996).
3. K. Ngan, D. N. Staub, P. Bartello, *Phys. Fluids* **17**, 125102 (2005).
4. R. H. Kraichnan, *Phys. Fluids* **10**, 1417 (1967).

Stabililty and laminarisation of turbulent rotating channel flow

S. Wallin, O. Grundestam, and A.V. Johansson

Linné FLOW Centre, Dept. of Mechanics, KTH, SE-10044 Stockholm, Sweden
stefan.wallin@foi.se

The influence of moderate rotation rate on turbulent channel flow is that the turbulence is suppressed on the stable side and augmented on the unstable side because of the Coriolis force. With increasing rotation rate the turbulent region becomes restricted to a decreasing zone near the unstable wall. For the rotation number, $Ro > 3$ (normalized by bulk velocity and channel height) inviscid linear theory yields a stable laminar flow [1] and a recent DNS study [2] indicates that the turbulent flow laminarizes for Ro below 3.

The critical Ro has been identified by a standard text-book linear stability analysis of rotating laminar channel flow including the viscous effects. The Reynolds number, $Re = 10800$ based on the bulk velocity and channel half height, is the same as in the recent DNS [2]. The most unstable mode consists of tilted slightly oblique streamwise vortices with a critical rotation number of $Ro_c = 2.805$ and streamwise and spanwise wave numbers of $\alpha = 2.7$ and $\beta = 19$ respectively. Steady streamwise roll-cells are slightly more stable.

In order to verify Ro_c , the DNS study [2] was complemented with three additional rotation numbers. The level of turbulence is illustrated by the bulk velocity where a completely laminar flow corresponds to the highest bulk velocity of $U_b^+ = 60.0$. In the DNS study we managed to pinpoint the critical rotation number to be in between $Ro = 2.800$ and $Ro = 2.810$ with the theoretical Ro_c in between, see figure 1. Also, the linear modes are clearly visible in the DNS for a lower $Ro = 2.49$ which is fully turbulent. For this rotation number the modes are extremely amplified with an amplification factor around 0.5.

The Reynolds number dependency was derived for Re ranging from 10^3 to 10^6 . The deviation from $Ro = 3$ is plotted in figure (2) in terms of $1/(3 - Ro_c)$ and follows remarkable close to a power law for all but the lowest Reynolds number. A linear least-square fit, excluding $Re = 10^3$, gives $Ro_{crit} = 3 - 8.4Re^{-0.4}$. The corresponding critical wave numbers, α and β , increases with increasing Reynolds number and a linear fit gives $\alpha_{crit} = 0.48Re^{0.18}$ and $\beta_{crit} = 0.46Re^{0.4}$.

Tollmien-Schlichting (TS) waves are unaffected by rotation and are always unstable for supercritical Re . The secondary instabilities are, however, damped by rotation and, thus, the TS waves might grow strongly before interacting with the other modes. In the DNS we have seen a sudden very strong burst of turbulence in these situations. The streamwise TS wave length is large and interacts with the typical box length used in DNS which has to be chosen with care.

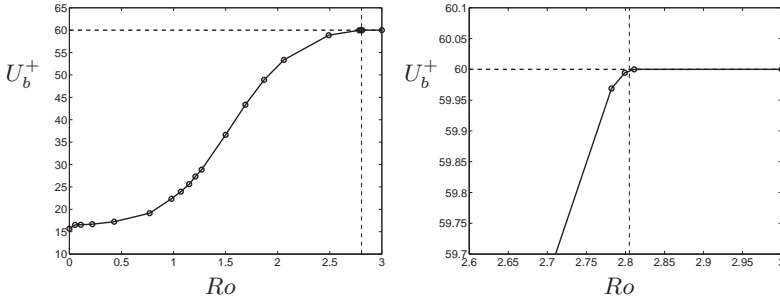


Fig. 1. Normalized bulk velocity, U_b^+ , for different rotation numbers. Laminar $U_b^+ = 60$ and critical $Ro = 2.805$ are marked as dashed lines in right figure.

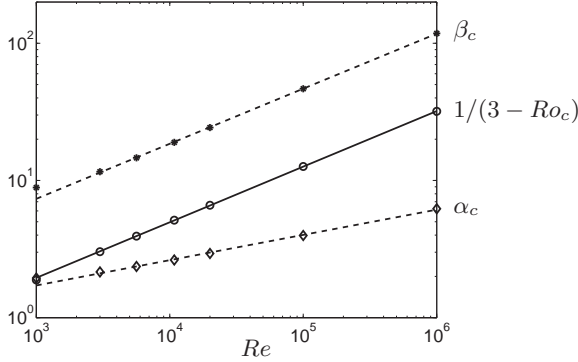


Fig. 2. Reynolds number dependency of critical Ro_c (— and \circ) plotted as $1/(3 - Ro_c)$ and critical stream- and spanwise wave numbers α_c (- - and $*$) and β_c (- - and \diamond).

References

1. P. Bradshaw, *J. Fluid Mech.*, **36**, 177 (1969)
2. O. Grundestam, S. Wallin & A.V. Johansson, *J. Fluid Mech.*, **598**, 177 (2008)

The vortical flow pattern exhibited by the channel flow on a rotating system just past transition under the influence of the Coriolis force

Venkatesa I. Vasanta Ram, Burkhard Müller and Fantri Azhari

Institut für Thermo und Fluidodynamik, Fakultät Maschinenbau, Ruhr Universität Bochum, 44780 Bochum, Germany
vvr@lstm.rub.de

1 Introduction and scope of the work

The subject of our paper is the post-transition flow pattern formed in the plane channel flow on a rotating system when transition is induced by the Coriolis force acting when the rotation vector is aligned with the spanwise direction of the channel. It is known from previous work, see eg. [5] [6], that, when transition sets in in this flow, it does so at rather low Reynolds numbers of only around 50 and the flow in the post-transition stage exhibits stationary longitudinal vortices, an observation standing in sharp contrast to the case of no rotation. The object of our present work is to try to extract this salient flow feature in quantitative terms through studying the bifurcation characteristics of this flow on the verge of transition. The focus of our attention is on the spatial periodicity of the longitudinal vortices, for which the relevant properties of the *bifurcating solution* of the nonlinear equations of motion for disturbances to the basic flow are examined. The velocity profile of the basic flow here is simply the parabola itself. The parameters influencing transition in this flow are, in conventional notation, the Reynolds number $Re = \frac{U_{ref}H}{\nu}$ and the rotation number $Ro = \frac{\Omega H}{U_{ref}}$, where $2H$ is the channel-height.

2 The equations, the ansatz and the procedure for their solution

The starting point for our work ist the set of nonlinear equations of motion for fluid flow in which Coriolis force effects are included and from which pressure is eliminated as an unknown through the same two procedures as in the derivation of the Orr-Sommerfeld and Squire equations in transition studies

in fluid flows, see eg. [1]. We refer to these as the *extended Orr-Sommerfeld* and *Squire* equations respectively. With $\Delta = \left(\frac{\partial^2}{\partial x^2} + \frac{\partial^2}{\partial y^2} + \frac{\partial^2}{\partial z^2} \right)$, the *extended Orr-Sommerfeld equation* is as follows:

$$-\frac{\partial}{\partial t} (\Delta v_y) - (1 - y^2) \frac{\partial}{\partial x} (\Delta v_y) - 2 \frac{\partial v_y}{\partial x} + \frac{1}{Re} (\Delta^2 v_y) - 2Ro \left(\frac{\partial^2 v_y}{\partial x \partial y} + \frac{\partial^2 v_x}{\partial x^2} + \frac{\partial^2 v_x}{\partial z^2} \right) = \frac{\partial}{\partial y} \left(\frac{\partial}{\partial x} \left(\frac{\partial}{\partial x} (v_x^2) + \frac{\partial}{\partial y} (v_x v_y) + \frac{\partial}{\partial z} (v_x v_z) \right) + \frac{\partial}{\partial z} \left(\frac{\partial}{\partial x} (v_x v_z) + \frac{\partial}{\partial y} (v_y v_z) + \frac{\partial}{\partial z} (v_z^2) \right) \right) + \left(\frac{\partial^2}{\partial x^2} + \frac{\partial^2}{\partial z^2} \right) \left(\frac{\partial}{\partial x} (v_x v_y) + \frac{\partial}{\partial y} (v_y^2) + \frac{\partial}{\partial z} (v_y v_z) \right). \quad (1)$$

The *extended Squire equation* is as follows where $\omega_y = \frac{\partial v_x}{\partial z} - \frac{\partial v_z}{\partial x}$ is the wall-normal vorticity:

$$\frac{\partial \omega_y}{\partial t} + (1 - y^2) \frac{\partial \omega_y}{\partial x} - 2y \frac{\partial v_y}{\partial z} + \frac{1}{Re} (\Delta \omega_y) - 2Ro \frac{\partial v_y}{\partial z} = -\frac{\partial}{\partial z} \left(\frac{\partial}{\partial x} (v_x^2) + \frac{\partial}{\partial y} (v_x v_y) + \frac{\partial}{\partial z} (v_x v_z) \right) + \frac{\partial}{\partial x} \left(\frac{\partial}{\partial x} (v_x v_z) + \frac{\partial}{\partial y} (v_y v_z) + \frac{\partial}{\partial z} (v_z^2) \right). \quad (2)$$

The above two equations are to be supplemented by the continuity equation for the flow of a constant density fluid which is as follows:

$$\frac{\partial v_x}{\partial x} + \frac{\partial v_y}{\partial y} + \frac{\partial v_z}{\partial z} = 0. \quad (3)$$

For convenience of presentation later in this short paper, we write the equations (1,2,3) in a matrix-vector notation $\mathcal{D}\mathbf{v} = \mathbf{N}$ as follows:

$$\mathcal{D} = \begin{pmatrix} D_{OSy} & D_{OSz} & D_{OSx} \\ D_{Sqy} & D_{Sqz} & D_{Sqx} \\ D_{Coy} & D_{Coz} & D_{Cox} \end{pmatrix}, \quad \mathbf{v} = \begin{pmatrix} v_y \\ v_z \\ v_x \end{pmatrix}, \quad \mathcal{N} = \begin{pmatrix} N_{OS} \\ N_{Sq} \\ N_{Co} \end{pmatrix}, \quad (4)$$

where the meaning of the various symbols follows from a comparison of (4) with (1,2,3).

In the perturbation approach followed in our present work, the vector of the unknown variable $\mathbf{v} = (\mathbf{v}_y, \mathbf{v}_z, \mathbf{v}_x)^T$ is asymptotically expanded in terms of an **amplitude parameter** ϵ_A as follows:

$$\mathbf{v} \simeq \epsilon_A \mathbf{v}_1 + \epsilon_A^2 \mathbf{v}_2 + \epsilon_A^3 \mathbf{v}_3 + o(\epsilon_A^3), \quad (5)$$

where the vectorial unknowns $\mathbf{v}_1, \mathbf{v}_2, \mathbf{v}_3$ are regarded as functions of both the *fast/short* and *slow/long* scale variables. These are, when the flow exhibits the form of strictly longitudinal rolls, (t, y, z) and (T_1, T_2, Z_1, Z_2) respectively.

The equation for the terms in (5) then follow by its substitution in the governing equations, (1, 2, 3) or (4). In the compact matrix-operator notation these may be written as follows:

$$\begin{aligned}
 O(\epsilon_A) : \quad \mathcal{D}\mathbf{v}_1 &= (\mathbf{RHS})_1 = \mathbf{0} \\
 O(\epsilon_A^2) : \quad \mathcal{D}\mathbf{v}_2 &= (\mathbf{RHS})_2 \\
 O(\epsilon_A^3) : \quad \mathcal{D}\mathbf{v}_3 &= (\mathbf{RHS})_3
 \end{aligned} \tag{6}$$

The solution for \mathbf{v}_1 is sought in a product form as follows:

$$\begin{aligned}
 v_{1y} &= B_y(T_1, T_2, Z_1, Z_2)\tilde{v}_y(t, y, z) \\
 v_{1z} &= B_z(T_1, T_2, Z_1, Z_2)\tilde{v}_z(t, y, z) \\
 v_{1x} &= B_x(T_1, T_2, Z_1, Z_2)\tilde{v}_x(t, y, z),
 \end{aligned} \tag{7}$$

where $(\tilde{v}_y, \tilde{v}_z, \tilde{v}_x)$ are set as an additive superposition of waves of wavelength $\lambda_{zn} = n\lambda_z, n = 1, 2, \dots$, and frequency ω_n as follows:

$$(\tilde{v}_y, \tilde{v}_z, \tilde{v}_x)^T = \sum_{n=1}^N (A_{ny}, A_{nz}, A_{nx})^T e^{i(n\lambda_z z - \omega_n t)} + c.c., \tag{8}$$

(A_{ny}, A_{nz}, A_{nx}) being functions of y .

Substitution of (5) into (1, 2, 3), together with (8) then leads to the classical eigenvalue problem in hydrodynamic stability which answers the question of the response of the basic flow in question to infinitesimally small disturbances, see eg. [5] [6]. Results of this linear theory, which form the starting point for the bifurcation studies in the present work, were obtained by casting the differential eigenvalue problem into a matrix eigenvalue problem by the spectral collocation method, and using MATLAB subroutines for a solution of the same. The results are summarised in Fig.1 which shows neutral stability curves for this flow for a cross section of Reynolds numbers, Re , over a range of the rotation number Ro . It is worthy of note that the neutral stability curves exhibit forms of closed loops in a certain region, with the presence of maxima and minima with respect to rotation numbers. The wave-number domain within the closed loop constitutes the band of amplification of infinitesimally small disturbances. Within the framework of the linear theory the amplification is exponential, rendering the linear theory invalid.

The next step in the investigation of the bifurcation characteristics is the formulation and computation of the *adjoint problem*, necessary to handle the effect of the nonlinearities. For details of the procedure for this step we refer to [1], restricting ourselves here to sketching its outlines for reasons of availability of space. It is scalar multiplication of the *extended* Orr-sommerfeld, Squire and continuity equations for the problem with the conjugate complex of the adjoint of the unknown, $(A_y^{+*}, A_z^{+*}, A_x^{+*})^T$, followed by integration across the domain $-1 \leq y \leq 1$ and subsequent regrouping.

The further step in obtaining the bifurcation characteristics of the flow problem is a proper accounting of the nonlinearities that were neglected in the linear theory. Since a treatment of the effect of nonlinearities in general

terms is beyond reach at present, we pursue the method of Stewartson and Stuart [3], which focusses attention on the effect of the nonlinearities in the neighbourhood of the critical point. For this purpose, the interaction of only two waves around the critical point is considered, i.e. $n = 2$ in (8). The dispersive nature of the wave motion, i.e. the dependence of the phase velocity $\frac{\omega_n}{\lambda_{zn}}$ upon the wavenumber λ_{zn} is however accounted for in the following manner:

$$\omega_2 = \omega_1 + \frac{\partial\omega}{\partial\lambda_z}\Big|_1(\lambda_{z2} - \lambda_{z1}) = \omega_c + \frac{\partial\omega}{\partial\lambda}\Big|_c\lambda_c \quad (9)$$

Formulating the solvability condition for the equations to the orders $O(\epsilon_A^2)$ and $O(\epsilon_A^3)$ in (6), which involves the solution of the adjoint problem paying due regard to (9), then leads to the amplitude evolution equations for (B_y, B_z, B_x) in (7) which is an expression of the bifurcation characteristics of flow problem.

Fig. 1. Neutral Stability Plots according to Linear Theory for Channel Flow subject to Transition by Coriolis force. The four curves are, starting from the innermost loop in the order, for Reynolds numbers $Re = 80, 100, 120$ and 130 respectively.

References

1. P. J. Schmid and D. S. Henningson *Stability and Transition in Shear Flows*. Applied Mathematical Sciences **142**, Springer, Berlin, 1990.
2. P. Huerre and M. Rossi Hydrodynamic Instabilities of Open Flows, in Godreche and Mannville (Eds.) *Hydrodynamic and Nonlinear Instabilities*. Cambridge University Press, Cambridge, UK, 1998.
3. K. Stewartson and J. T. Stuart A nonlinear instability theory for a wave system in plane Poiseuille flow, *J. Fluid Mech.* **48**, 1971, 529-545.
4. D. P. Wall and M. Nagata Nonlinear secondary flow through a rotating channel, *J. Fluid Mech.* **564**, 2006, 25-55.
5. P. H. Alfredsson and H. Persson Instabilities in channel flow with system rotation, *J. Fluid Mech.* **202**, 1989, 543-557.
6. G. Marliani, M. Matzkeit and V. I. Vasanta Ram Visualisation studies of the transition regime flow in a channel of varying cross section under the influence of Coriolis force, *Exp. in Fluids.* **23**, 1997, 64-75.

Transient evolution and high stratification scaling in horizontal mixing layers

C. Arratia^a, S. Ortiz^{a,b} and J. M. Chomaz^a

^a Laboratoire d'Hydrodynamique (LadHyX), École Polytechnique-CNRS, 91128 Palaiseau Cedex, France

^b UME/DFA, ENSTA, chemin de la Hunière, 91761 Palaiseau Cedex, France
cristobal.arratia at ladhyx.polytechnique.fr

1 Introduction

Mixing layers (sheared flows in homogeneous or stratified fluid) are present in many geophysical contexts and may lead to turbulence and mixing. In several cases, mixing layers are known to exhibit the Kelvin-Helmholtz instability leading to the roll-up of spanwise vortices, the Kelvin-Helmholtz (KH) billows. This is an essentially two-dimensional (2D) process. In fact, in the homogeneous cases the Squire's theorem implies that the most unstable mode is 2D. However, Squire's theorem applies only for the exponentially growing perturbations that control the large time dynamics and is not valid for the transient dynamics at short time. Indeed, Iams et al.[1] have shown that, in the non-stratified case, the most amplified optimal perturbations for short times are three-dimensional (3D) and result from a cooperation between the lift-up and Orr mechanisms[2]. This provides a finite time mechanism for spanwise scale selection, scale that may persist at later times if nonlinearities are strong enough.

In the present contribution, we extend the computation of 3D, finite time optimal perturbations to the case of an horizontal mixing layer with vertical linear stratification. As discussed by Deloncle *et al.*[4], the Squire's theorem does not apply to this horizontal shear layer when the fluid is stratified, but the inviscid stability analysis of [4] shows that the most unstable mode is still 2D. The nonlinear dynamics of such an horizontal shear vertically stratified has been numerically simulated by Basak & Sarkar[3]. They observed the development of a disordered 3D structure made of a pilling up of horizontal layers where the velocity is mainly horizontal and decorrelated from one layer to the next. The evolution equations, being homogeneous in z , impose no vertical scale in the flow evolution and the mechanism selecting this scale has yet to be understood. Extrapolating from the homogeneous case, transient growth is a possible linear mechanism that might explain the vertical scale selection.

In the present paper, optimal transient growth are therefore computed for an horizontal shear flow vertically stratified.

2 Formulation and Methods

Using cartesian coordinates $\mathbf{x} = (x, y, z)$ with z increasing upwards, and time coordinate t , we consider the evolution of the perturbative velocity $\mathbf{u}(\mathbf{x}, t)$ and density $\rho(\mathbf{x}, t)$ fields according to the linearized incompressible Navier-Stokes equations in the Boussinesq approximation. Our base state is $\mathbf{U}_B = U_0 \tanh(y/L)\hat{x}$ with a stable linear density stratification $\rho_B(z) = \rho_0(1 - N^2 z/g)$, where ρ_0 is a reference density, g is the acceleration of gravity and $N = \sqrt{-g/\rho_0 d\rho_B/dz}$ is the Brunt-Väisälä frequency. The adimensionalization is such that $L = U_0 = 1$, so that the value of the Brunt-Väisälä frequency N measures the buoyancy strength as the ratio between the advective and the buoyancy time scales: the stronger the stratification, the faster it affects the dynamics. The corresponding adimensional parameter is the horizontal Froude number $F_h \equiv U_0/LN = N^{-1}$, which goes to zero in the high stratification limit. The other adimensional parameters of the problem, coming from viscosity ν and molecular diffusivity D , correspond to the Reynolds $Re = U_0 L/\nu$ and the Schmidt $Sc = \nu/D$ numbers. Throughout the paper their values will be $Re = 1000$ and $Sc = 1$.

The homogeneity in x and z of the evolution equations allows us to rewrite the fields as $[\mathbf{u}, \rho](x, y, z, t) \rightarrow [\mathbf{u}, \rho](y, t)e^{i(k_x x + k_z z)}$ and consider independently the linear evolution of the different streamwise-spanwise wavenumbers. Because of the latter, for each point in the (k_x, k_z) -plane we can define the optimal gain as

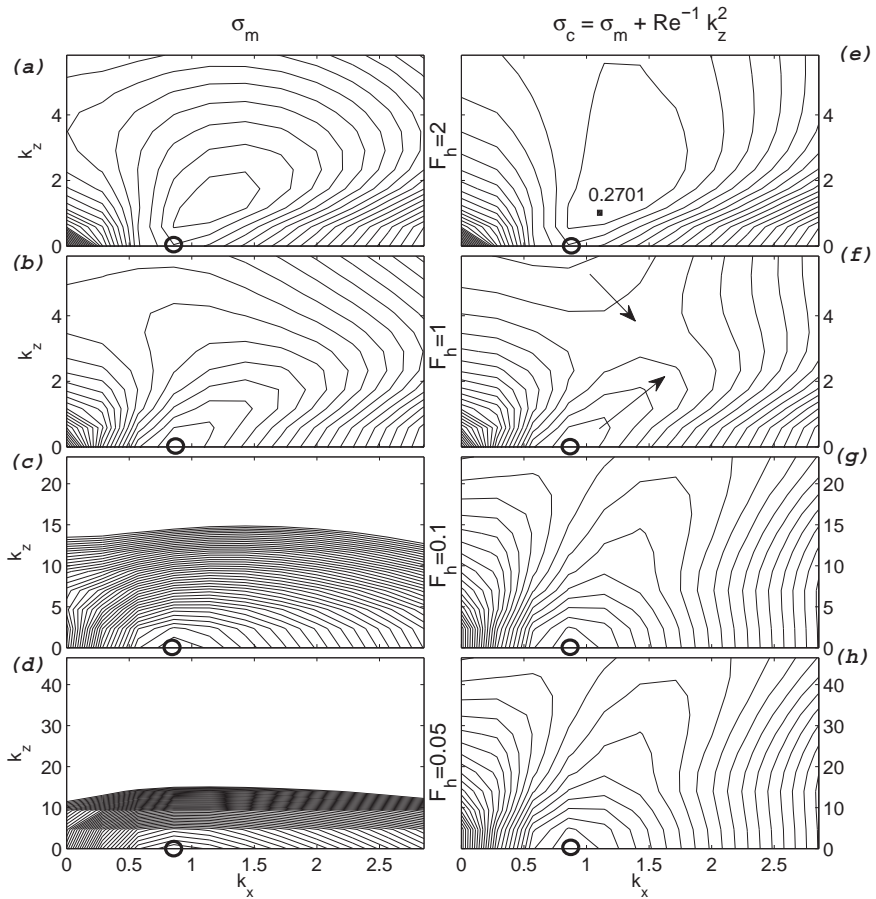
$$G(T) \equiv \max_{[\mathbf{u}, \rho](y, 0)} \left(\frac{\int \mathbf{u}^2(T) + N^2 \rho^2(T) dy}{\int \mathbf{u}^2(0) + N^2 \rho^2(0) dy} \right), \quad (1)$$

i.e., the maximum attainable increase in energy up to time T . We span the (k_x, k_z) -plane for each time T at which we compute the optimal perturbation, that is, the initial condition $[\mathbf{u}, \rho](y, 0)$ that attains the optimal gain G . These optimal perturbations are computed by the iterative procedure proposed by Corbett & Bottaro[5], whereby the successive numerical integration of the direct and the time reversed adjoint equations is performed until convergence is achieved. For the computations we use a pseudo-spectral method with an Adams-Bashfort time scheme.

In the following, we characterize our results by the optimal mean growthrate of the perturbation

$$\sigma_m(k_x, k_z, T) \equiv \frac{\ln(G(k_x, k_z, T))}{2T} \quad (2)$$

which allows an easier comparison with the maximum growthrate of the most unstable KH mode, $\sigma_{KH} \approx 0.18$ as a reference.



[b]

Fig. 1. Amplification of the optimal perturbations for $T=7$.

On the left column we show the positive isolines of the optimal mean growthrate (the right column shows the same values corrected to compensate the viscous dissipation of perturbations, see text) for 4 different F_h numbers as indicated on each row. The values of the isolines are defined equally in all figures, decreasing in steps of 0.006 from the overall maximum value $\simeq 0.2701$ (marked by the \blacksquare in *e*). The arrows in (*f*) represent the decreasing directions of the contours and the (\circ) on each plot represents the maximum gain for 2D perturbations, which has the same value of $\simeq 0.26$ in all figures. The horizontal (resp. vertical) axes are equal on each column (resp. row). Note the change in the vertical axis in the last 2 rows.

3 Results and Discussion

In the figure 1(**a-d**), we show contours of $\sigma_m(k_x, k_z) > 0$ for $T = 7$ and for different levels of stratification. For moderate stratifications ($F_h = 2$, figure 1(**a**)), the most amplified optimal perturbations are 3D. In this case there is essentially no difference with the homogeneous case of [1], the largest optimal gain being associated with the combination of the lift-up and Orr mechanisms. When stratification is increased (figures 1(**b, c, d**)), the optimal perturbations with the largest gain becomes 2D ($k_z = 0$).

In order to take into account the viscous diffusion, we plot the corrected optimal mean growthrate $\sigma_c(k_x, k_z) = \sigma_m(k_x, k_z) + Re^{-1}k_z^2$ (right column of fig. 1 **e - h**), where only the diffusion in z is compensated since for small F_h , large k_z are destabilized. In the $F_h = 1$ case (fig. 1 (**f**)), we observe that the most amplified perturbation is 2D and due to the Orr mechanism alone, as confirmed by looking at the perturbation field data (not shown).

In the strongly stratified cases ($F_h = 0.1, 0.05$), we note that the dependence on the vertical wavenumber scales as F_h^{-1} , as it is evident from the almost perfect invariance with the Froude number of the contours when plotted in the scaled range of vertical wavenumbers. This scaling law corresponds to the inviscid self similarity proposed by Billant & Chomaz[6], which extends the analyses of Riley *et al.* [7] and Lilly [8]. Here we generalize this scaling for finite viscosity and capture the F_h dependence in the high stratification limit as

$$\sigma_m(k_x, k_z, T, F_h, Re) \approx \sigma_c(k_x, k_z F_h, T) - Re^{-1}k_z^2. \quad (3)$$

This shows that the inviscid scaling of the high stratification limit is indeed valid for the linear transient growth of perturbations, viscosity being easily accounted for by adding the corresponding damping term.

Despite transient growth does not select a particular vertical length-scale, the scaling found affects the receptivity by increasing the range of vertical scales sensitive to noise and decreasing the selectivity for 2D structures. Current research is on how this selectivity is affected by nonlinearities.

References

1. S. Iams, C. Arratia, C. Caulfield and J. M. Chomaz, In preparation (2009).
2. B. Farrel and P. J. Ioannou, *Phys. Fluids A* **5**, 2298 (1993).
3. S. Basak and S. Sarkar, *J. Fluid. Mech.* **568**, 19 (2006).
4. A. Deloncle, J. M. Chomaz and P. Billant, *J. Fluid. Mech.* **570**, 297 (2007).
5. P. Corbett and A. Bottaro *J. Fluid. Mech.* **435**, 1 (2001).
6. P. Billant and J. M. Chomaz, *Phys. Fluids* **13**, 1645 (2001).
7. J. J. Riley, R. W. Metcalfe and M. A. Weissman in *Nonlinear Properties of Internal Waves*, edited by B. J. West, AIP Conf. Proc. **76**, 79 (1981).
8. D. K. Lilly *J. Atmos. Sci.* **40**, 749 (1983).

Part III Control of turbulent flows

Toward Cost-effective Control of Wall Turbulence for Skin Friction Drag Reduction

¹Nobuhide Kasagi, ¹Yosuke Hasegawa, and ²Koji Fukagata

¹Department of Mechanical Engineering, The University of Tokyo, Hongo 7-3-1, Bunkyo-ku, Tokyo 113-8656, Japan

²Department of Mechanical Engineering, Faculty of Science and Technology, Keio University, Hiyoshi 3-14-1, Kohoku-ku, Yokohama 223-8522, Japan
kasagi@tthtlab.t.u-tokyo.ac.jp

Abstract

This paper discusses the active control of turbulence for skin friction reduction with an emphasis on cost effectiveness. By introducing performance indices such as the net energy saving rate and the control gain, we assess existing control algorithms for true energy saving. We review recent attempts to reduce costs accompanying practical applications, and discuss remaining issues in developing more practically applicable control algorithms.

1 Introduction

Facing the global issues such as depletion of energy resources and environmental deterioration, highly advanced technology of turbulence control is ever more needed. Turbulence control opens up new possibilities to achieve far greater efficiency and least environmental impact of various thermal-fluid systems supporting the human society through the manipulation and modification of momentum/heat/mass transfer, noise as well as chemical reaction.

In this paper, we focus on the turbulent flow control for skin friction drag reduction. During the past several decades, an enormous amount of time and effort of the turbulence research community has been devoted to advance the understanding of dynamical mechanism of the near-wall coherent structures, and this has been accomplished by exploiting modern measurement techniques and computational fluid dynamics. For example, it is now well known that large skin frictional drag in turbulent flow is attributed to the existence of near-wall vortical structures and associated ejection/sweep events (Robinson, 1991; Hamilton et al., 1995). Based on this knowledge, various flow control strategies have been proposed, although most of them are tested and evaluated simply in terms of the drag reduction rate. However, the time has come for

us to make assessment of any new control method by taking into account the total cost of manufacturing, installation, operation and maintenance, and we should aim at developing such control as to achieve high cost-effectiveness even in fundamental research work.

Existing control schemes are roughly classified into two categories, i.e., active and passive controls. Passive control as typified by a riblet surface has an advantage that it does not need continuous power supply to sustain the flow control. However, the control performance achieved is generally worse if compared to active control. In addition, the effectiveness of passive control is often limited under flow conditions close to a design point. Development of robust and effective passive control schemes is still a challenging issue.

Active control is further classified into predetermined and feedback controls. In the former, its control input is specified *a priori* as in spanwise wall-oscillation (Jung et al., 1992; Quadrio and Ricco, 2004), streamwise/spanwise traveling waves (Min et al., 2006; Du et al., 2002), and steady streamwise forcing (Xu et al., 2007) without knowing a turbulence state at each instant. Existing predetermined controls commonly suffer from a disadvantage of large power consumption as will be discussed later. On the contrary, in a feedback control its input is always determined from sensor signals by a control law, so that it can be more robust and flexible.

The feedback control generally offers better control performance with smaller power consumption than the predetermined control. The former, however, has a disadvantage of requiring numerous sensors to detect an instantaneous flow state, of which signals are used to trigger actuators. In addition, measurable flow quantities are likely to be limited to those at the wall, where sensors can be implemented without changing the system design drastically. Most feedback control algorithms so far proposed assume that massively arrayed sensors and actuators are provided on a wall surface. Considering a fact that physical dimensions and response times of these hardware components should be very small, i.e., less than millimeter and millisecond (Kasagi et al., 2009), fabrication and maintenance of these devices would impose an unbearable cost even with rapidly developing MEMS technology. Thus, the predetermined control is superior in a sense that it employs a much simpler hardware system than the feedback control.

In the following, we will discuss several control schemes that are deemed to reduce incurring costs associated with predetermined and feedback controls. First, we introduce three kinds of indices to be considered in assessing the control and some fundamental theories on drag reduction. Then, we will review recent attempts to reduce various costs accompanying practical applications with a particular focus on control algorithm. For the recent progress of hardware components, refer to a review paper by Kasagi et al. (2009) and references therein.

2 Fundamental Concepts

2.1 Control Performance Indices

Consider a constant-rate flow driven by a pressure gradient in a straight duct, where the form drag is zero. Then, the pressure gradient must be balanced with the total skin friction at the wall. Obviously, the drag reduction rate R is equivalent to the reduction of pumping power P :

$$R = (P_0 - P)/P_0 \quad (1)$$

where the subscript of 0 represents a quantity in the original uncontrolled flow. By taking into account the power consumption P_{in} to manipulate the flow, the net energy saving rate S is defined as:

$$S = \{P_0 - (P + P_{in})\}/P_0. \quad (2)$$

Another important parameter is the effectiveness of a control algorithm, i.e., the gain G defined as:

$$G = (P_0 - P)/P_{in}, \quad (3)$$

which is the reduction of pumping power divided by the control power input.

The above three parameters are related as follows.

$$S = R/(1 - G^{-1}). \quad (4)$$

Presently, we choose S and G as performance indices for evaluating a control algorithm, although there are also the practical cases where only direct control effect is of interest from a viewpoint of merits such as utmost speed of cruising, least level of noise and/or extremely high rates of heat transfer and combustion. The index of S represents the maximum energy saving rate achieved when neglecting all possible energy losses in driving hardware components. Obviously, in order to obtain a net energy saving, i.e., $S > 0$, G need to be larger than 1. In a real system, however, there always exist such energy losses associated with actuators, sensors, control circuits and so forth. Hence, in order to achieve a true energy saving in a real system, G should be sufficiently large regardless of R . For instance, when G is 10, the overall hardware efficiency should be much higher than 10 % in order to have $S \gg 0$.

In Fig. 1, typical data of S and G obtained by active control schemes are plotted. Here, all results are obtained in fully developed turbulent channel flow at relatively low friction-based Reynolds numbers from $Re_\tau = 110$ to 640. Since S and G strongly depend on parameters in each control scheme, we select only favorable results in this figure. These include: feedback controls such as V-control (Choi et al., 1994) and suboptimal control (Lee et al., 1998) assessed at different Reynolds numbers by Iwamoto et al. (2002), temporally-periodic spanwise wall-oscillation control (Quadrio and Ricco, 2004), streamwise traveling wave control (Min et al., 2006), steady streamwise forcing control (Xu et

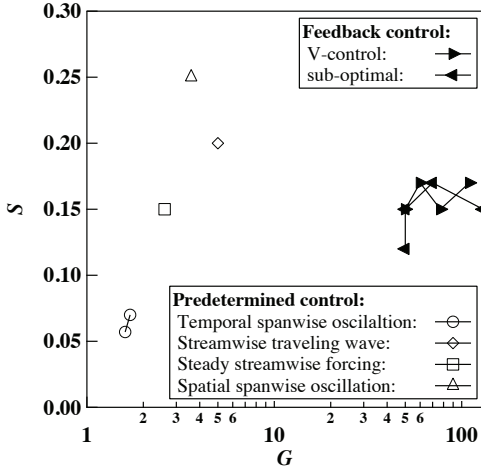


Fig. 1. Net energy saving rate achieved by different active control schemes: V-control and suboptimal control (Iwamoto et al., 2002), temporally-periodic spanwise wall-oscillation control (Quadrio and Ricco, 2004), streamwise traveling wave control (Min et al., 2006), steady streamwise forcing control (Xu et al., 2007), and spatially-periodic spanwise oscillation control (Yakeno et al., 2009).

al., 2007) and spatially-periodic spanwise oscillation control (Yakeno, et al., 2009). Other predetermined controls such as spanwise traveling wave control (Du et al., 2002) and large-scale streamwise vortex excitation control (Schoppa and Hussain, 1998) are not included since their control power inputs are not known.

It is found that the net energy saving rate S achieved by the predetermined controls can be comparable or even better compared to the feedback controls. Once G is considered, however, one can see that the values of the predetermined controls are at most $G \sim 5$ and generally much smaller, say, by one or two orders of magnitude, than those achieved by the feedback controls. For example, the maximum gain $G = 1.7$ achieved by the temporally periodic spanwise wall-oscillation makes S reach its maximum of 7 %. In this case, the actuator efficiency must be larger than $1/G \sim 60\%$ in order to obtain net energy saving. This is not easy generally, and should impose a severe constraint in practical applications.

2.2 Theoretical Constraint

Drag reduction rate

Fukagata et al. (2002) derived a simple mathematical relationship between the skin friction coefficient and the Reynolds stress distribution from the streamwise momentum equation. In the case of a fully developed channel flow, the result leads to:

$$C_f = \frac{12}{Re_b} + 12 \int_0^1 2(1-y)(-\overline{u'v'})dy, \tag{5}$$

where $y = 0$ and 1 correspond to the wall and the channel center, respectively, and the overbar denotes the average in homogeneous directions. All the variables are made dimensionless by using the channel half-width and twice the bulk mean velocity, and Re_b denotes the bulk Reynolds number. The above identity indicates that the skin friction coefficient is decomposed into the laminar contribution, $12/Re_b$, which is identical to the well-known laminar solution, and the turbulent contribution, which is proportional to the weighted spatial average of Reynolds stress. Note that the weight linearly decreases with the distance from the wall.

The identity suggests that sublaminal friction drag, which is smaller than that of the laminar flow at the same flow rate, is attained if the second term on the RHS of Eq. (5) becomes negative. Actually, Fukagata et al. (2005) and Min et al. (2006) have achieved sublaminal drag by applying a virtual body force in the wall-normal direction and a traveling wave-like blowing/suction, respectively. This is only possible with a penalty of $S < 0$ as described below.

Lower-bound for minimum energy consumption

It is mathematically proved that there exists a lower bound for the minimum energy consumption in any skin friction control (Fukagata et al., 2009; Bewley, 2009). In a fully developed channel flow, the sum of pumping and control work should be eventually dissipated by viscosity. Hence, minimizing the total power is equivalent to minimizing the volume integral of the viscous dissipation over the whole flow domain. Under a constant mass flow rate and a no-slip condition at top and bottom walls, it can be proved that the laminar velocity profile gives the minimum viscous dissipation, and therefore the minimum power input. This fact indicates that the ultimate goal of skin friction drag reduction control for energy saving is to lead the turbulent flow toward a relaminarized state.

2.3 Toward Control of High Reynolds Number Flows

In real applications, the Reynolds number is far beyond the values that DNS can reach, whilst various flow control strategies have been tested in relatively simple canonical flows at low Reynolds numbers. Assessment of V-control and suboptimal control in fully developed channel flow by Iwamoto et al. (2002) demonstrated that the degree of drag reduction gradually decreases with increasing the Reynolds number from $Re_\tau = 110$ to 640. A similar trend is also observed for spanwise wall-oscillation control (Choi et al., 2002; Ricco and Quadrio, 2008).

Figure 2 shows the weighted Reynolds shear stress, $(1 - y)(-\overline{u'v'})$, i.e., the integrand of the second term in Eq. (5), in uncontrolled flows at different Reynolds numbers. At higher Reynolds numbers, the relative contribution of the near-wall Reynolds shear stress to the friction drag drastically decreases, whereas that of the outer layer becomes dominant. Therefore, a

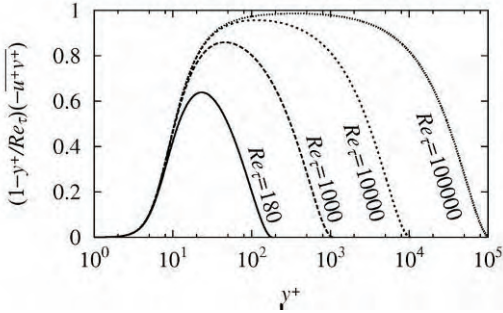


Fig. 2. Weighted Reynolds shear stress at different Reynolds numbers calculated from the eddy viscosity model with the van Driest damping function (Kasagi et al., 2009).

question arises whether the conventional near-wall manipulation is effective even at high Reynolds numbers.

Iwamoto et al. (2005) numerically simulated a fully developed turbulent channel flow with damping of velocity fluctuations in the near-wall layer and derived a theoretical relationship among the Reynolds number Re_τ of uncontrolled flow, the damping layer thickness y_d/δ non-dimensionalized by the channel half width δ and the drag reduction rate R . As a result, they found that the dependency of R on Re_τ is moderate. For instance, when the fluctuation at $y_d^+ < 10$ is damped, R is about 43 % at $Re_\tau = 10^3$, while 35 % even at $Re_\tau = 10^5$, where the damping layer is extremely thin compared to the channel half-width, i.e., $y_d/\delta = 10^{-4}$.

The reason for the success of near-wall manipulation is explained as follows. The velocity inside the thin damping layer, which is increased as a result of turbulence damping by the control, results in the decreased velocity difference between the outer edge of the damping layer and the channel center. Therefore, the effective Reynolds number of the bulk flow is much reduced. This example suggests that the basic strategy of attenuating only near-wall turbulence can be considered valid even when the Reynolds number is considerably increased.

3 Feedback Control

3.1 Control Algorithms with Wall Sensors

In real systems, the available state information is considered to be practically limited to the following quantities: (1) the streamwise wall-shear stress, $\tau_{wx} = (\mu \partial u / \partial y)_w$; (2) the wall pressure, p_w ; and (3) the spanwise wall-shear stress, $\tau_{wz} = (\mu \partial w / \partial y)_w$. According to DNS studies, the control algorithms using τ_{wz} or p_w are very effective (Lee et al., 1997; Lee et al., 1998; Koumoutsakos, 1999). These quantities, however, are in most cases difficult to measure by using small sensors distributed on the wall (Kasagi et al., 2009).

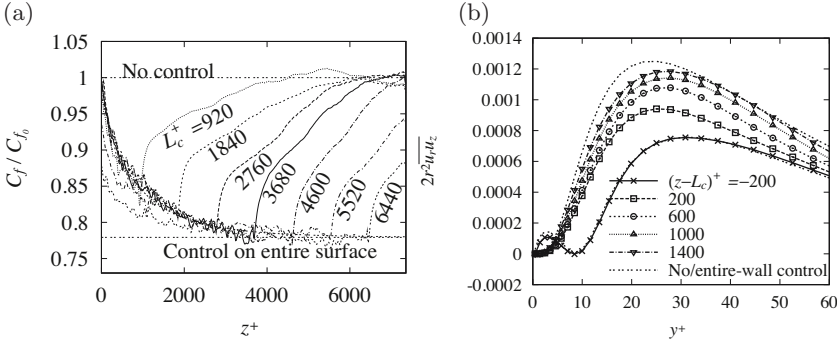


Fig. 3. DNS results of turbulent pipe flow with the opposition control applied to a partial area (Fukagata and Kasagi, 2003): (a) Normalized local skin friction coefficient as a function of streamwise location, for different control lengths, L_c , (b) Profiles of Reynolds shear stress weighted by $2r^2$ (in accordance with the FIK identity for pipe flows) around the termination point of control.

Development of effective control algorithms based on τ_{wx} was initially judged difficult. For example, Lee et al. (1998) succeeded in τ_{wz} - and p_w -based suboptimal schemes, but they failed to reduce the drag by sensing only τ_{wx} . A reason for this failure may be attributed to their cost function based on the fluctuating wall shear stress $(\tau'_{wx})^2$, of which relationship to the mean shear is not always clear. In fact, Fukagata and Kasagi (2004) redefined the cost function based on the near-wall Reynolds shear stress, which is directly related to the friction drag like in Eq. (5). They successfully attained 11% drag reduction in their DNS of turbulent pipe flow.

Control algorithms using τ_{wx} has also been developed by the physical argument or by adopting evolutionary optimization techniques. Based on the correlation between the near-wall structure and wall variables, Endo et al. (2000) proposed an algorithm to attenuate the meandering of low-speed streaks. Morimoto et al. (2002) used a genetic algorithm (GA) to optimize weights in a prescribed function, which determined actuator’s movement from sensor signals. About 10% drag reduction was attained in both cases. Yoshino et al. (2008) also used a GA in their MEMS-based feedback control system in a wind-tunnel experiment and obtained about 6% drag reduction. Recently, Frohnepfel et al. (2009) proposed a new feedback control of attenuating the spanwise velocity fluctuation based on τ_{wx} measured upstream, and obtained almost 20 % drag reduction, which is the highest value achieved by sensing τ_{wx} only.

3.2 Power Saving with Selective Space/Scale Control

Early studies of feedback control always assumed control inputs ideally applied on the entire wall surface. From both technologically and economical

viewpoints, however, such design of a broad surface covered with an array of feedback control units is not feasible. Therefore, one may envision a control, of which effect would last over a long downstream distance, so that the cost can be reduced with simplified design and implementation.

Fukagata and Kasagi (2003) applied, in their DNS of pipe flow, the opposition control of Choi et al. (1994) only in the region of $0 < z < L_c$, while uncontrolling the rest of the region, $L_c < z < L$, where L is the computational domain length. Their results reveal that the drag reduction rate is nearly proportional to the ratio of controlled to total areas. This is attributed to the relatively fast recovery of the skin friction coefficient after the termination of control, as shown in Fig. 3(a). Similar results are reported by Pamiès et al. (2007) for a spatially-developing boundary layer under opposition control. As shown in Fig. 3(b), the quick recovery of local friction is caused by the quick response of Reynolds shear stress near the wall.

One may be able to save the control cost by limiting the scales of turbulence or number of modes. Suppose we can design a friction drag reduction technique to only manipulate large structures, it would be tremendously beneficial in terms of hardware development, particularly in higher Reynolds number flows; it would certainly relax various requirements for the size, dynamic range and frequency response of sensors and actuators.

Fukagata et al. (2008) explored such a possibility by means of DNS at $Re_\tau = 640$. As an idealized feedback control, they selectively damp either the small-scale wall-normal velocity fluctuations (defined as those with spanwise wavelengths smaller than 300 wall units) or the large-scale fluctuations (spanwise wavelengths larger than 300 wall units). They report that the damping of small-scale fluctuations is more efficient than that of large-scale ones as shown in Fig. 4, where the contributions of laminar and two different-scale Reynolds stress components to the skin friction under the selective scale controls are compared. When only the small ones are damped, the friction drag diminishes simply because of the absence of small-scale fluctuations near the wall. On the other hand, with the large-scale damping, the small-scale fluctuations are drastically increased and this results in the friction drag larger than expected from the absence of large-scale contributions.

From the studies above, it is conjectured that saving of control effort in space or scales is, in principle, difficult as far as the drag reduction relies on the suppression of fine-scale turbulence in the vicinity of the wall, although further study is needed for inventing new types of control.

4 Predetermined Control

Most predetermined controls employ a wall velocity, which has a spatial or temporal periodicity. These control inputs can be generally represented as:

$$u_i(x, 0, z, t) = \hat{u}_i \cdot \text{Real}[\exp\{i(\omega t + k_x x + k_z z)\}] \quad (6)$$

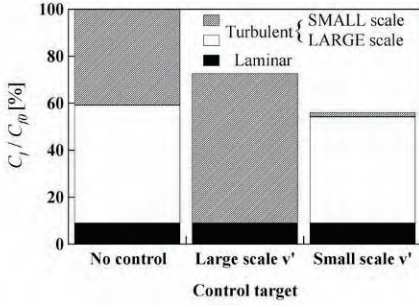


Fig. 4. Integral contributions to friction drag from different scales in DNS of channel flow at $Re_\tau = 640$ under idealized damping of wall-normal velocity fluctuations (Fukagata et al., 2008): Comparison between no-control, damping of large-scale only, and damping of small-scale only.

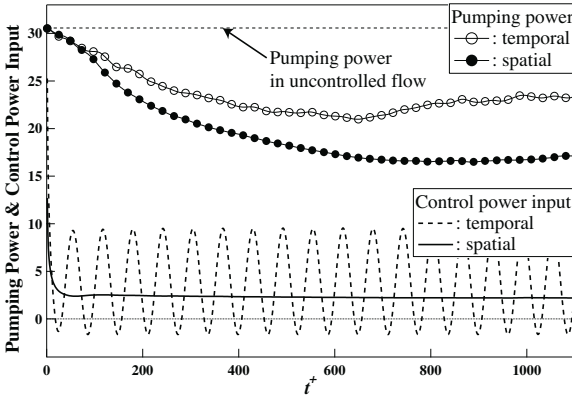


Fig. 5. Time traces of pumping and control power inputs under temporally- and spatially-periodic spanwise oscillation controls (Yakeno et al., 2009).

For example, the temporally-periodic spanwise (wall) oscillation control proposed by Jung et al. (1992) corresponds to $(\omega \neq 0, k_x = k_z = 0)$, while the traveling-wave controls such as Du et al. (2002) and Min et al. (2006) are defined as $(\omega \neq 0, k_z \neq 0)$ and $(\omega \neq 0, k_x \neq 0)$, respectively. Recently, stationary, but longitudinally-periodic controls, i.e., $(k_x \neq 0, \omega = k_z = 0)$, have been proposed by Quadrio et al. (2007) and Yakeno et al. (2009).

When such periodic wall velocity is assumed, the resultant velocity field would be a superposition of periodic and irregular components. Hence, by decomposing an instantaneous velocity u_i into a spatio-temporal mean component \bar{u}_i , a phase-fluctuating component \tilde{u}_i and a random incoherent component u_i'' , the Reynolds stress in the integrand of Eq. (5) can be rewritten as:

$$-\overline{u'v'} = -(\overline{\tilde{u}\tilde{v}} + \overline{u''v''}). \tag{7}$$

According to Eqs. (5) and (7), there are two possibilities to obtain drag reduction. The first strategy is to make the first coherent term negative, which is otherwise very small or almost zero. This strategy was successfully adopted by a traveling wave-type control by Min et al. (2006). The steady streamwise forcing by Xu et al. (2007) also applies a body force so as to directly reduce the

drag, namely, decelerating the flow in the near-wall layer, while accelerating further away from the wall.

The second strategy is to suppress the second incoherent term of Eq. (7), which is a major factor for skin friction drag in uncontrolled flow. For example, Yakeno et al. (2009) investigate the effects of two different spanwise wall velocities, which are temporally and spatially periodic, on the coherent structures and the resultant drag reduction. The temporally-periodic control is essentially the same as that proposed by Jung et al. (1992). In the spatially-periodic control, stationary, but longitudinally-periodic spanwise control input is applied at the wall. They show that there exist the optimal conditions for the period of $T^+ \sim 100$ and the streamwise wavelength $\lambda_x^+ \sim 1000$ for drag reduction. Time traces of the pumping and control power inputs under these conditions are shown in Fig. 5. The spatially-periodic control achieves larger drag reduction rate with less control power input, and gives larger net energy saving. In these cases, a drastic decrease in $-\overline{u''v''}$ accounts for the drag reduction.

Since the first term in Eq. (7) is a direct result of the introduced control input, so that it is easier to modify, the former strategy seems more feasible. However, the results of Min et al. (2006) and Xu et al. (2007) indicate that the second term in Eq. (7) is also decreased with their controls. Recently, the authors have tested control inputs, which force the first term to be negative at least in the very vicinity of the wall. In most cases, however, the drag increases against our expectation because of marked enhancement of the second term further away from the wall. These results suggest that modifying the random component $-\overline{u''v''}$ is primarily important for drag reduction.

The mechanism of turbulence suppression in the predetermined control has not been fully understood despite its simplicity. In contrast to the feedback control, where a control input is given so as to locally diminish a coherent streamwise vortex, the predetermined control is likely to prevent vortex generation by interfering the regeneration cycle near the wall (Hamilton et al., 1995). For example, the phase-averaged flow field around a streamwise vortex shown by Choi et al. (2002) clearly shows that the spanwise wall-oscillation control disrupts phase-locking of the streaks and streamwise vortices near the wall. Recently, Jovanović (2008) showed that the turbulence suppression due to spanwise wall-oscillation can be predicted by the receptivity analysis of the linearized Navier-Stokes equation. In contrast, Lee et al. (2008) conclude that a linear stability analysis of a channel flow subject to traveling wave-like blowing/suction from the wall cannot explain turbulence suppression observed in the corresponding DNS of Min et al. (2006). At this moment, it is not clear whether such stability analyses provide a unified explanation to turbulence suppression observed in various predetermined controls.

5 Conclusions and Challenges for the Future

We have briefly reviewed the recent advances in active turbulence control algorithms, particularly for skin friction drag reduction. With deepening understanding of the dynamical mechanism of near-wall coherent structures, various control strategies have been proposed by exploiting modern control theory, physical arguments, adaptive methods and so forth. Although most of them are validated under idealistic conditions, it is of great importance to assess any control method by taking into account the total cost of manufacturing, installation, operation and maintenance. Namely, we should pay much attention upon cost effectiveness even when developing a fundamental control law. From this viewpoint, the control gain should be much larger than unity to compensate possible energy losses in hardware components.

Feedback control generally works better than predetermined control in terms of the gain, since the former determines best control input by sensing the flow state at each time instant. In order to avoid a heavy burden associated with hardware requirements, however, it is desirable to develop a control algorithm that demands a reduced number of sensors and actuators. So far, reducing the surface control area has simply led to deteriorated overall control effectiveness, but selective wavenumber control should be worth further studying, particularly from a viewpoint of receptivity of the near-wall layer.

Predetermined control methods achieve considerable drag reduction with an advantage of easier implementation, but they are likely to suffer from large power consumption. This is a major problem in existing predetermined controls. Thus, it is strongly desired to minimize the control input while keeping its high control effectiveness. For this, understanding the mechanism of turbulence suppression due to a prescribed forcing mode should be indispensable.

So far, the control performance has been assessed at low Reynolds numbers. A few previous studies show that the drag reduction rate in both feedback and predetermined controls commonly tends to decrease gradually, although moderate, with increasing the Reynolds number. Applicability of these control strategies to practically high Reynolds number flows need to be further studied theoretically, numerically and experimentally.

With all above said, for real application of turbulence control technology, a breakthrough should be indispensable in design, fabrication and implementation of hardware components such as durable high-performance sensors, actuators and controllers (Kasagi et al., 2009).

Acknowledgements

This work was financially supported through the Grant-in-Aid for Scientific Research (A) (No. 20246036) by the Ministry of Education, Culture, Sports, Science and Technology (MEXT).

References

1. T. R. Bewley, *J. Fluid Mech.*, in press
2. H. Choi, P. Moin and J. Kim, *J. Fluid Mech.*, **262**, 75 (1994)
3. J. I. Choi, C. W. Xu and H. J. Sung, *AIAA Journal*, **40**, 842 (2002)
4. Y. Du, V. Symeonidis and G. E. Karniadakis, *J. Fluid Mech.*, **457**, 1 (2002)
5. T. Endo, N. Kasagi and Y. Suzuki, *Int. J. Heat Fluid Flow*, **21**, 568 (2000)
6. B. Frohnäpfel, Y. Hasegawa and N. Kasagi, Proc. 6th Int. Symp. on Turbulence and Shear Flow Phenomena (TSFP6), Seoul, to be presented (2009)
7. K. Fukagata, K. Iwamoto and N. Kasagi, *Phys. Fluids*, **14**, L73 (2002)
8. K. Fukagata and N. Kasagi, *Int. J. Heat Fluid Flow*, **24**, 480 (2003)
9. K. Fukagata and N. Kasagi, *Int. J. Heat Fluid Flow*, **25**, 341 (2004)
10. K. Fukagata, N. Kasagi and K. Sugiyama, Proc. 6th Symp. Smart Control of Turbulence, Tokyo, 143 (2005)
11. K. Fukagata, M. Kobayashi, N. Kasagi, Proc. 7th Int. Symp. on Engineering Turbulence Modelling and Measurement (ETMM7), Cyprus, 131 (2008)
12. K. Fukagata, K. Sugiyama and N. Kasagi, *Physica D*, in press
13. J. M. Hamilton, J. Kim and F. Waleffe, *J. Fluid Mech.*, **287**, 317 (1995)
14. K. Iwamoto, Y. Suzuki and N. Kasagi, *Int. J. Heat Fluid Flow*, **23**, 678 (2002)
15. K. Iwamoto, K. Fukagata, N. Kasagi and Y. Suzuki, *Phys. Fluids*, **17**, 011702 (2005)
16. M. R. Jovanović, *Phys. Fluids*, **20**, 014101 (2008)
17. W. J. Jung, N. Mangiavacchi and R. Akhavan, *Phys. Fluids*, **4**, 1605 (1992)
18. N. Kasagi, Y. Suzuki and K. Fukagata, *Annu. Rev. Fluid Mech.*, **41**, 231 (2009)
19. P. Koumoutsakos, *Phys. Fluids*, **11**, 248 (1999)
20. C. Lee, J. Kim, D. Babcock and R. Goodman, *Phys. Fluids*, **9**, 1740 (1997)
21. C. Lee, J. Kim and H. Choi, *J. Fluid Mech.*, **358**, 245 (1998)
22. C. Lee, T. Min and J. Kim, *Phys. Fluids*, **20**, 101513 (2008)
23. T. Min, S. M. Kang, J. L. Speyer and J. Kim, *J. Fluid Mech.* **558**, 309 (2006)
24. K. Morimoto, K. Iwamoto, Y. Suzuki and N. Kasagi, Proc. 3rd Symp. Smart Control of Turbulence, Tokyo, 107 (2002)
25. M. Pamiès, E. Garnier, A. Merlenm and P. Sagaut, *Phys. Fluids* **19**, 108102 (2007)
26. M. Quadrio and P. Ricco, *J. Fluid Mech.*, **521**, 251 (2004)
27. M. Quadrio, J. M. Floryan and P. Luchini, *J. Fluid Mech.*, **576**, 425 (2007)
28. P. Ricco and M. Quadrio, *Int. J. Heat Fluid Flow*, **29**, 891 (2008)
29. S. K. Robinson, *Annu. Rev. Fluid Mech.*, **23**, 601 (1991)
30. W. Schoppa and F. Hussain, *Phys. Fluids*, **10**, 1049 (1998)
31. J. Xu, S. Dong, M. Maxey and G. E. Karniadakis, *J. Fluid Mech.*, **582**, 79 (2007)
32. A. Yakeno, Y. Hasegawa and N. Kasagi, Proc. 6th Int. Symp. on Turbulence and Shear Flow Phenomena (TSFP6), Seoul, to be presented (2009)
33. T. Yoshino, Y. Suzuki and N. Kasagi, *J. Fluid Sci. Tech.*, **3**, 137 (2008)

Active control of turbulent boundary layer using an array of piezo-ceramic actuators

H.L. Bai, Y. Zhou

Department of Mechanical Engineering, The Hong Kong Polytechnic University,
Hung Hom, Kowloon, Hong Kong
myzhou at polyu.edu.hk

This paper presents preliminary results from an experimental exploration on drag reduction in a turbulent boundary layer using an array of piezo-ceramic actuators. The actuator array consisting of 16 actuators can generate wall-normal oscillations and, given a phase shift between two adjacent actuators, a spanwise travelling wave. A sinusoidal waveform with four different amplitudes was investigated while oscillating in a wide range of frequencies. The preliminary results showed that about 5% reduction in drag could be obtained based on the measurement of a hot-film flush-mounted on the wall. A drag increase up to 20% was also observed when the actuator array worked in large amplitudes and high oscillation frequencies. Investigations are ongoing to use different control strategies such as different actuation signals, spanwise travelling wavelengths and speeds, etc. in order to achieve better results in terms of drag reduction.

1 Introduction

Active control of a fully developed turbulent boundary layer for drag reduction has recently attracted a great deal of attention. It has been demonstrated numerically and experimentally that the high wall shear stress is associated with the quasi-streamwise vortices (QSV), in particular the sweep events in the near-wall region, and inhibiting or annihilating these QSV can mitigate the turbulence production and reduce the skin friction (e.g. [1, 2]). Based on their DNS data, Du and Karniadakis [3] showed that a transverse wave induced by a spatial force travelling in the viscous sublayer could suppress dramatically the coherent structures in the near-wall region, resulting in a drag reduction exceeding 50%. Their preliminary experiment with Lorentz actuators produced results consistent with the DNS data [4]. Nevertheless, this technique has yet to be demonstrated experimentally [5]. The present work aims to investigate experimentally the drag reduction in a turbulent boundary layer using an actuator array. An array of 16 piezo-ceramic actuators, flush mounted with the wall surface and aligned in the spanwise, was used to generate the wall-normal oscillation and a transverse travelling wave given a phase shift between two adjacent actuators. Three

distinct waveforms with four different amplitudes were tested while oscillating in a wide range of frequencies.

2 Experimental Details

Experiments were conducted in a closed-circuit wind tunnel which has a 2.4-m-long test section of 0.6 m × 0.6 m. Tripped at the leading edge, a boundary layer was produced by a 2.2-m-long Perspex flat plate. The plate was slightly inclined to ensure a nearly zero-pressure gradient along the test section. The oncoming velocity of the free stream is $U_o = 4.0$ m/s. The actuation location is $L = 1.5$ m downstream of the leading edge. At this location, the Reynolds number Re_L is 4×10^5 , based on L and U_o . Fig. 1 shows schematically the arrangement of actuators, each having a dimension of 22 mm × 2 mm × 0.33 mm (length × width × thickness). The gap between the sides of the actuator and the wall edge around it is about 0.05 mm. The spacing between two adjacent actuators is 1 mm. As such, the entire actuator array covers 450 and 200 wall units along the spanwise and streamwise directions, respectively. The origin of the coordinate system is defined at the actuator tip, with x , y , and z along the streamwise, normal (to the wall) and spanwise (or transverse) directions, respectively.

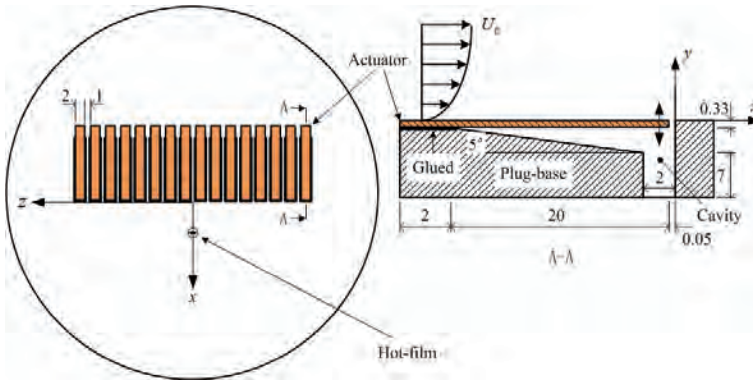


Fig. 1. The schematic of the spanwise-arranged actuator array (not in scale, units in mm).

The piezo-ceramic actuator used currently can work in a wide range of oscillation-frequencies (f), with the peak-to-peak amplitude (A) of the free tip about 0.5 mm, or 5 wall units. Every actuator was driven by an individual voltage amplifier and guaranteed to have identical A by offsetting their driving voltages at each working frequency. In preliminary tests, three different phase shift ($\phi_{i,i+1}$, $i = 1, 2, \dots, 15$), i.e. $\phi_{i,i+1} = 0^\circ, 24^\circ, \text{ or } 180^\circ$ and four different A , viz. 80 μm , 160 μm , 240 μm and 320 μm (or $A^+ = 0.8, 1.6, 2.4$ and 3.2 , where the superscript “+” denotes normalization by wall variables), were examined, while the actuators oscillated at a frequency range of 50 Hz ~ 500 Hz.

A miniature single-wire probe (55P15, Dantec) was used to measure the stream-wise velocity profile at the actuation location. A hot-film (55R45, Dantec) located at $x = 5$ mm or $x^+ = 50$ downstream of the actuator tip was used to determine the change in wall shear stress. The hot-film was calibrated in situ based on the mean of wall shear stress from the hotwire measurement. The mean velocity profile, close to the wall ($y^+ < 12$), was adopted to estimate the mean of wall shear stress at a free stream velocity ranging from 2 m/s to 6 m/s. The measuring uncertainty of the hot-film was estimated to be within $\pm 1\%$.

3 Results and Discussion

In this section we will present and discuss preliminary results. The averaged change of wall shear stress is defined as $\Delta D^* = (D - D_o)/D_o(\%)$, where D and D_o are time-averaged drags measured with and without control, respectively.

In the current study, given $\phi_{i,i+1} = 24^\circ$, the 16 actuators formed one discrete sinusoidal wave travelling in the spanwise direction. These discrete actuators oscillating in the wall-normal direction may also interact directly with the coherent structures. Fig. 2a shows the dependence of ΔD^* (%) on f^+ for four different A^+ . It can be seen that ΔD^* is appreciable for the whole range of f^+ when A^+ is relatively small, i.e. $A^+ = 0.8$ and 1.6. As A^+ increases to 2.4, drag increase is observed at $f^+ > 0.228$. For the largest $A^+ = 3.2$, only can drag reduction be obtained at $f^+ < 0.114$; in contrary, more than 15% drag increase results at $f^+ \geq 0.2565$. The valley for $A^+ = 2.4$ and 3.2, witnessed at $f^+ = 0.228$, may result from the resonance (around 400 Hz) of the actuators. The results seem to be consistent with Du et al.'s [4] suggestion that the drag reduction strongly depended on energy input (or disturbance strength) through actuation into the flow. Large drag reduction would be achieved only when energy input was close to a threshold; otherwise, the near-wall streaks were unaffected or drag increase was observed.

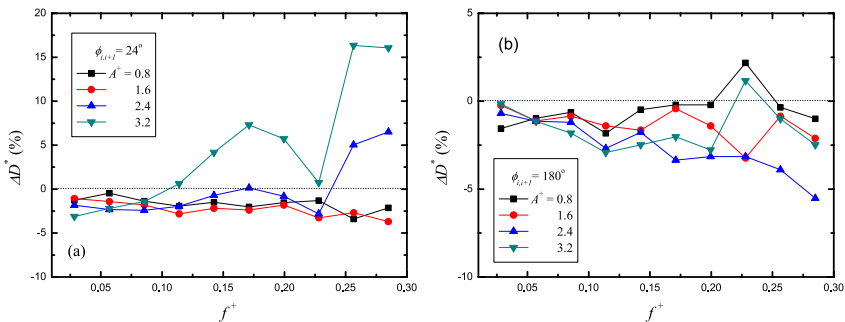


Fig. 2. The dependence of ΔD^* on f^+ for (a) $\phi_{i,i+1} = 24^\circ$ and (b) $\phi_{i,i+1} = 180^\circ$.

As $\phi_{i,i+1} = 0^\circ$, the entire array of actuators oscillated in phase, resembling a waveform with ‘infinite’ wavelength. In this case, the maximum of drag reduction (about 4.5%) is observed at $f^+ = 0.0855$ for $A^+ = 1.6$. On the other hand, the drag increase of near 20% was observed at $f^+ > 0.2565$ for the largest $A^+ = 3.2$.

As $\phi_{i,i+1} = 180^\circ$, two adjacent actuators in the array oscillated in an anti-phase fashion, corresponding to no travelling wave. The dependence of ΔD^* on f^+ is shown in Fig. 2b. In this case, no profound drag increase was observed except at $f^+ = 0.228$, at which the actuators worked resonantly. The largest drag reduction (about 5%) was obtained for $A^+ = 2.4$ at $f^+ = 0.285$.

4 Conclusion

Drag reduction in a turbulent boundary layer based on a spanwise array of actuators was experimentally investigated. Three waveforms with four different amplitudes were formed by these actuators working in a wide range of the oscillation frequencies. Though preliminary, experimental results show a drag reduction of up to 5% when the wave was in a caniniform ($A^+ = 2.4$) and worked at $f^+ = 0.285$. Investigations are on-going to use different control strategies such as different actuation signals, spanwise travelling wavelengths and speeds, etc. in order to achieve better results in terms of drag reduction.

Acknowledgement

YZ wishes to acknowledge support given to him by the Research Grants Council of the Government of the HKSAR through Grant PolyU 5334/06E.

References

1. A. G. Kravchenko, H. Choi and P. Moin, On the relation of near-wall streamwise vortices to wall skin friction in turbulent boundary layers, *Phys. Fluids A*, **5**(12), 3307 (1993).
2. H. Choi, P. Moin and J. Kim, Active turbulence control for drag reduction in wall-bounded flows, *J. Fluid Mech.*, **262**, 75 (1994).
3. Y. Du and G. E. Karniadakis, Suppressing wall turbulence by means of a transverse travelling wave, *Science*, **288**, 1230 (2000).
4. Y. Du, V. Symeonidis and G. E. Karniadakis, Drag reduction in wall-bounded turbulence via a transverse travelling wave, *J. Fluid Mech.*, **457**, 1 (2002).
5. G. E. Karniadakis and K.-S. Choi, Mechanism on transverse motions in turbulent wall flows, *Annu. Rev. Fluid Mech.*, **35**, 45 (2003).
6. J. Kim, P. Moin and R. Moser, Turbulence statistics in fully developed channel flow at low Reynolds number, *J. Fluid Mech.*, **177**, 133 (1987).

Flat plate turbulent boundary-layer control using vertical LEBUs

V.I. Kornilov and A.V. Boiko

Khristianovich Institute of Theoretical and Applied Mechanics, SB RAS,
Novosibirsk 630090, Russia
kornilov at itam.nsc.ru

Necessity of aerodynamic drag reduction of aircrafts and other moving objects stimulates researchers for finding out new means of the near-wall turbulence control. In [1] it has been found that the vertical positioning of the LEBUs in boundary layer can be much more efficient compared to the conventional horizontal one, although, according to the same authors, the devices were far from being optimized. Present work is focused upon the study of possibility of turbulent skin-friction reduction using flow-aligned vertical LEBUs, the LEBUs being mounted perpendicular to the flat plate surface in nominally gradient-free incompressible turbulent boundary layer. The Reynolds number based on the momentum thickness of the boundary layer at the LEBUs' position was 1099. All measurements were performed using a computer-controlled automated system of space/time hot wire visualization of mean and fluctuating components of the velocity field. The system provided accuracy not worse than approximately $\pm 2 \mu\text{m}$ along x , y , and z coordinates. Local skin friction coefficient C_f in the regular (unmodified) shear flow was determined from the condition of the best correspondence between measured and classic velocity profiles in the region of the law of the wall functionality $U^+ = A \log y^+ + B$ with known coefficients A and B . In the modified boundary layer C_f was determined by the mean velocity gradient at the wall $(\partial U / \partial y)_{y=0}$. The measurement technique is given in more detail in [2].

A fragment of the flat plate surface with the mounted vertical LEBUs and the coordinate system are shown in Fig. 1. The typical LEBUs' sizes in wall units are as follows: the blade height is $h^+ = 194$ that is equal to about one half of the local boundary-layer thickness and the chord length $c^+ = 99$; the spanwise spacing between the blades $\lambda^+ = 69$.

Analysis of boundary-layer mean velocity profiles, instantaneous values of streamwise velocity fluctuations, and the Clauser equilibrium parameter, as well as skin friction in 13 spanwise sections along the model show that the characteristics of the regular shear flow perfectly correspond to the physical

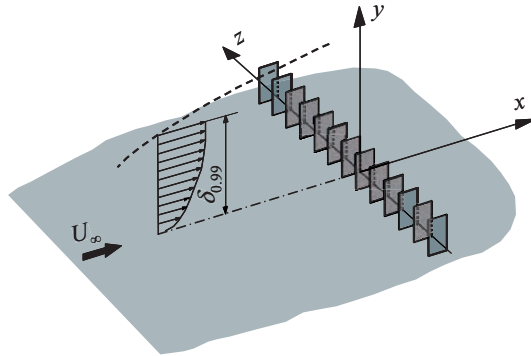


Fig. 1.

concepts on the properties of turbulent boundary layer formed on a flat plate at nominally gradientless flow.

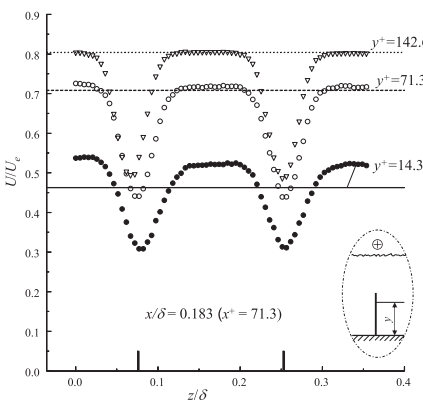


Fig. 2.

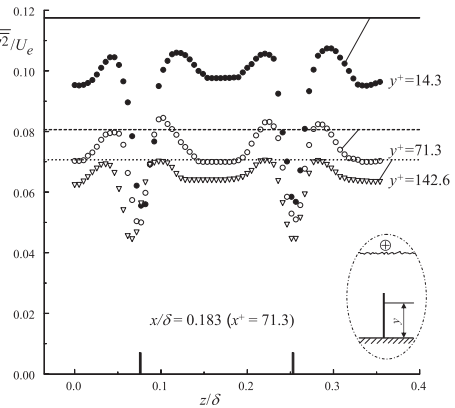


Fig. 3.

Distinctive features of the modified flow can be clearly seen in mean velocity distributions U/U_e and streamwise velocity fluctuations $\sqrt{u'^2}/U_e$. Such examples of the mean velocity distributions in spanwise direction $U/U_e = f(z/\delta)$ at $x = 0.183\delta$ ($x^+ = 5$) are given in Fig. 2 at characteristic values of wall-normal coordinate y^+ . Corresponding values of U/U_e in the regular flow are shown by the horizontal lines. Location of neighbouring vertical elements is indicated by the vertical segments on x -axis. Quite naturally that due to the loss of kinetic energy by the mean flow to overcome the local drag caused by the element, the flow is retarded directly downstream of it ($z/\delta = 0.076$ and 0.255), hereupon there appears a pronounced velocity defect in this region. On the contrary, the flow is accelerated between the elements; hence, a flow

with relatively high velocity is formed in this region. It is significant that the velocity excess decreases as coordinate y^+ grows. This is stipulated by the decrease of the kinetic energy loss to overcome the local drag as the element tip is approached. Similar effect is observed further downstream where the velocity defect is formed even in the flow region between the elements. Meanwhile, velocity distribution in the spanwise direction becomes substantially smoothed. In whole, the dynamics of the process is such that as the streamwise coordinate x grows, spanwise mean velocity distribution in the boundary layer gradually relaxes to the distribution typical for the equilibrium state.

Reduction of the level of turbulent fluctuations $\sqrt{u'^2}/U_e$ compared to the regular flow not only directly downstream of the elements ($z/\delta = 0.076$ and 0.255), but also between them is a characteristic feature of the root-mean-square velocity distribution (Fig. 3). Note that this effect is observed also further downstream up to the last measured section. The only exclusion is a narrow region directly behind the vertical element (mainly at the flow near its tip), where the disturbance level is increased compared to the regular flow at the same y -coordinates. It can be supposed that a vortex was shed from the element tip.

Comparison of disturbance spectra in the modified and regular flows clearly indicates the decrease of disturbance energy directly behind the elements, the decrease being multifold at low-frequencies. Meanwhile, the frequency band in the modified flow is about two times narrower than in the regular flow. Hence, the efficiency of the vertical LEBUs to suppress the field of the turbulent velocity disturbances is substantial.

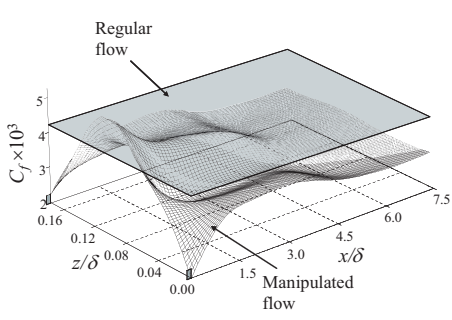


Fig. 4.

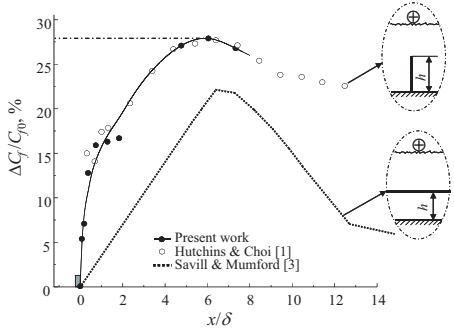


Fig. 5.

The results show that the LEBUs with given geometry are quite effective means for turbulent boundary-layer modification. They provide a substantial benefit in the local skin friction as compared to the appropriate values for the regular flow (Fig. 4).

Beginning from x -coordinate of several tenth of the boundary-layer thickness δ downstream of the LEBUs and further downstream up to $(7-8)\delta$, a

persistent skin-friction reduction, whose maximum value reaches 27–28% at $x/\delta \approx 6$, can be observed.

Data on skin friction coefficient C_f modification characterizing percentage benefit compared to the corresponding values in the regular flow are shown in Fig. 5 as function $\Delta C_f/C_{f0} = f(x/\delta)$. Here $\Delta C_f = (C_{fm} - C_{f0})$, where subscripts "m" and "0" mean modified and regular boundary layers, respectively. Values C_{fm} for each section x were obtained by integrating the distribution of this value in the spanwise direction. The results extracted from [1] are also shown for comparison. In general, the results of both experiments are in a good accordance. Maximum benefit in the local drag is about 27–28%. Generally, this supports the statement in [1] that the vertical elements are more effective compared to the elements directed parallel to the wall, results for which were extracted from [3]. In fact, in the literature available to us such a pronounced effect was never recorded. However, one has to take into account that the total wetted area of the vertical elements, when their heights are larger than the spacing between them, is larger than that of an isolated conventional LEBU directed parallel to the surface. Consequently, such devices can appear not too effective, if to account for their own drag. This, however, requires additional studies.

Final conclusions about effectiveness of such devices and expected tendency at the flow velocity increase can be drawn using a technique which accounts also the LEBU-induced drag.

References

1. N. Hutchins and K.-S. Choi, Proc. of the 12th European Drag Reduction Meeting, Denmark (2002).
2. A.V. Boiko and V.I. Kornilov, Thermophysics and Aerodynamics. 2009, Vol.16, No.2 (in press).
3. A.M. Savill and J.C. Mumford, J. Fluid Mech., 1988, Vol.191.

Estimation of the spanwise wall shear stress based on upstream information for wall turbulence control

B. Frohnafel*, Y. Hasegawa⁺, N. Kasagi⁺, S. Große^o

* Center of Smart Interfaces, TU Darmstadt, Germany

⁺ Dept. of Mechanical Engineering, The University of Tokyo, Japan

^o Lab. Aero- and Hydrodynamics, Delft Univ. of Technology, The Netherlands
frohnafel at csi.tu-darmstadt.de

In the last decade many research efforts in flow control were directed to feedback control schemes due to the fact that large energy gain was anticipated. To achieve practically realizable control, the footprints of near wall turbulence need to be detected through sensors that are mounted on the wall. In this respect, sensing wall shear stresses is considered most feasible. Especially the instantaneous spanwise wall shear stress, $\tau_z = (\partial w / \partial y)_{wall}$, is known to be useful for the state estimation of wall turbulence and it has been shown that control laws based only on the time trace of this component work well [1, 2].

Up to now, most of the research on feedback control have been done in direct numerical simulation (DNS) with idealized systems in which continuous sensing and actuation are assumed at the same location. Since this assumption is unrealistic, we investigate whether the local instantaneous spanwise wall shear stress can be obtained based on upstream information.

It is well known that quasi streamwise vortices (QSV) as well as high and low speed streaks are a part of the regeneration cycle of wall turbulence [3]. Endo et al. [4] showed that the QSV located at the downstream side of a meandering low speed streak can be captured by measuring the spatial gradients of both wall shear stresses, $\tau_x = (\partial u / \partial y)_{wall}$ and $\tau_z = (\partial w / \partial y)_{wall}$, about 50 viscous length units upstream. In general, the experimental assessment of τ_z and its spatial gradients needs significantly more effort than the measurement of τ_x [5]. With the goal of providing an easily accessible input information that replaces the knowledge of τ_z at the actuation location, we investigate the correlation between the spanwise gradient of the streamwise wall shear stress, $\partial \tau_x / \partial z = \frac{\partial}{\partial z} (\partial u / \partial y)_{wall}$, and τ_z .

In general, the correlation function has a form of $R(\Delta x, \Delta z, \Delta t)$. The present work is limited to the case where the time lag, Δt , and the spanwise displacement, Δz , are zero.

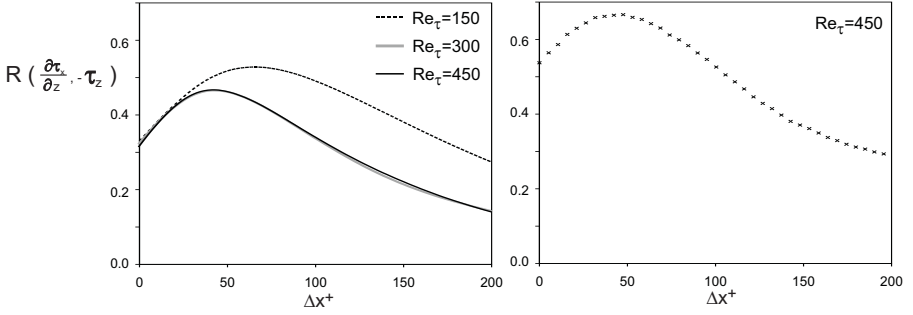


Fig. 1. Spatial correlation between the spanwise gradient of the streamwise wall shear stress and the negative wall shear stress in a turbulent channel flow (left, DNS) and a duct flow (right, experiment).

We carry out DNS of a fully developed channel flow with a constant flow rate. The bulk Reynolds number based on the channel height is changed as $Re_b = U_b H / \nu \simeq 4600, 10100$ and 16100 , which corresponds to friction Reynolds numbers for the uncontrolled case, $Re_\tau = u_\tau \delta / \nu = 150, 300$ and 450 , respectively.

The obtained spatial correlations, $R(\frac{\partial \tau_x}{\partial z}(x), -\tau_z(x + \Delta x^+))$, for the three Reynolds numbers are depicted in Fig. 1, left. For $Re_\tau = 150$ the highest correlation is slightly above 50% and is located at a streamwise distance of $\Delta x^+ \approx 65$. For $Re_\tau = 300$ and 450 the maximum value is reduced to 47% and shifted to smaller streamwise distances such that the maximum correlation is located at $\Delta x^+ \approx 43$. The good agreement between the two correlations at the higher Reynolds numbers suggests that the Reynolds number dependence at $Re_\tau > 300$ would be small.

In addition to the numerical simulation, we consider experimental data obtained in a duct flow at $Re_b \simeq 15400$. The corresponding friction Reynolds number is given by $Re_\tau = u_\tau \delta / \nu = 450$. A spanwise row of micro-pillar shear-stress sensors MPS³ [6], shown in Fig. 2, is placed in the duct flow to simultaneously measure the instantaneous streamwise and spanwise wall shear stresses. The sensors do not emerge out of the viscous sublayer and measure the temporal evolution of the wall shear stresses such that a temporal correlation between $\partial \tau_x / \partial z$ and τ_z can be obtained in the center of the duct where the flow was shown to be two-dimensional based on PIV data. In the present investigation the spanwise spacing of the sensors is given by $\Delta z^+ = 10$. Employing Taylor's Hypothesis the temporal correlation is transformed to the spatial correlation.

The resulting correlation is plotted in Fig. 1, right. It can be seen that the correlation for the duct flow shows the same qualitative trend as the correlations obtained for channel flows at $Re_\tau = 300$ and 450 , suggesting that the convection velocity was chosen appropriately. However, the correlation values are much higher than in the channel flow simulation. The difference between



Fig. 2. A row of micro-pillar shear-stress sensors. If the sensors are aligned in spanwise direction (z) it is possible to obtain a temporal correlation between $\partial\tau_x/\partial z$ and τ_z . Note that in the present investigation the sensors are placed further apart than in the picture. Their spacing roughly corresponds to twice the pillar height.

the obtained correlations cannot solely be attributed to the statistical uncertainty in the available data. Since the evaluation of $\partial\tau_x/\partial z$ in the experimental investigation is based on the spanwise distance between the pillars, we have performed numerical reference computations in which the spanwise distance of the τ_x -sensing locations is increased up to two pillar spacings. We found that this increased "sensor spacing" does not significantly influence the correlation value. At this moment we can not explain the observed difference, although it seems that the temporal correlation is higher than the spatial one.

In order to test the feasibility of the suggested τ_z -estimation, we investigate the influence of replacing τ_z with the upstream information of $\partial\tau_x/\partial z$ in a control loop similar to the one suggested in [2]. We employ a spanwise body force within a forcing layer $y_f^+ = 10$ on the top and bottom walls of the channel flow and carry out simulations at $Re_\tau = 150$ in which the body force is given by either

$$bf(x, y, z) = \frac{1}{\Phi}(y_f - y) \underbrace{\tau_z(x, z)}_{\text{measured quantity}} \quad (1)$$

or

$$bf(x, y, z) = \frac{1}{\Phi}(y_f - y) \underbrace{\frac{\partial\tau_x(x - \Delta x, z)}{\partial z}}_{\text{measured quantity}}. \quad (2)$$

Note that Δx corresponds to the streamwise distance between sensor and actuator locations and that Φ is the forcing time constant which, in combination with the sensor value, determines the strength of the forcing and thus the required control power input.

Based on the body force formulation given by equation (1) drag reduction of $DR = 25.3\%$ can be achieved. With the body force formulation given by equation (2) and $\Delta x^+ = 65$ (location of the highest correlation) a similar control power input leads to $DR = 17.2\%$.

Fig. 3 shows the obtained Reynolds stresses in comparison to the uncontrolled flow. It can be seen that the two control schemes have a very similar influence on $\overline{u_2^2}$, $\overline{u_3^2}$ and $\overline{u_1 u_2}$. The suppression of these components is stronger for higher drag reduction as expected. For $\overline{u_1^2}$ this is not the case, and this

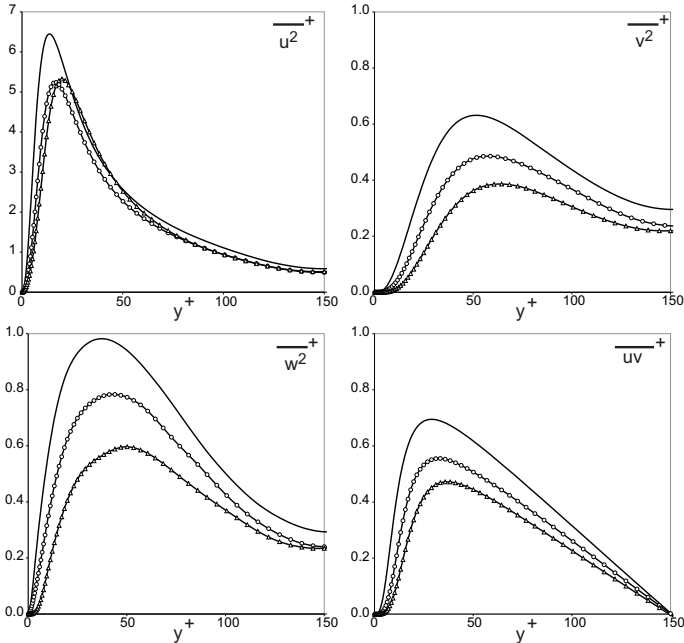


Fig. 3. Reynolds stress distribution for the control based on equation (1) (triangles, DR=25.3%) and on equation (2) (circles, DR=17.2%) in comparison to the uncontrolled channel flow (straight line). The normalization is based on the inner variables of the uncontrolled channel flow.

fact suggests that the suppression of $\overline{u_1^2}$ is an effect that consumes energy but is not necessarily required for drag reduction. If the sensor is placed at $\Delta x^+ = 47$, DR = 16.3% is achieved.

The present results demonstrate that the upstream spanwise gradient of the streamwise wall shear stress, $\partial\tau_x/\partial z$, can be used to predict the spanwise wall shear stress which is known to be a good candidate for state estimation of near-wall turbulence. It was shown that this correlation does not only exist in uncontrolled flows but that it can also be successfully used for the design of flow control loops, at least at low Reynolds numbers. Whether this also holds at higher Reynolds numbers remains to be clarified in future work.

References

1. C. Lee, J. Kim, H. Choi, *J. Fluid Mechanics*, **358**, 245 (1998).
2. C. Lee, J. Kim, *Physics of Fluids*, **14(7)**, 2523 (2002).
3. J.M. Hamilton, J. Kim, F. Waleffe, *J. Fluid Mechanics*, **287**, 317 (1995).
4. T. Endo, N. Kasagi, Y. Suzuki, *Int. J. Heat Fluid Flow*, **21**, 568 (2000).
5. Y. Suzuki, N. Kasagi, *Experimental Thermal and Fluid Science*, **5**, 69 (1992).
6. S. Große, W. Schröder, *AIAA Journal*, **47(2)**, 314 (2009).

Interactions between vortex generators and a flat plate boundary layer. Application to the control of separated flows.

T. Duriez, B. Thiria, T. Cambonie, J.E. Wesfreid and J.L. Aider,

Laboratoire PMMH, CNRS UMR 7636, ESPCI, 10 rue Vauquelin, Paris, 75005, France

aider@pmmh.espci.fr, wesfreid@pmmh.espci.fr

Vortex generators (VG) are among the most popular actuators for flow control. They all are prone to produce counter-rotating streamwise vortices which will more or less interact with each other depending on many parameters like the size of the VGs or the spacing between each VG (Betterton *et al.* (2000); Godard & Stanislas (2006)). From a general point of view, the 3D steady (or unsteady) perturbations induced by the VG are used to modify a boundary layer in order to control some global properties of the flow like heat transfer or aerodynamic forces (Lin (2002); Duriez *et al.* (2008)).

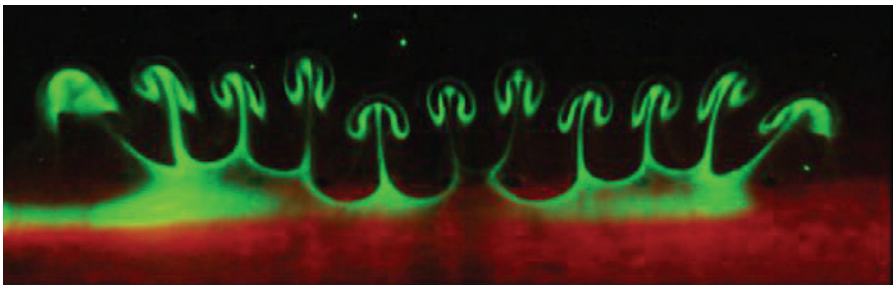


Fig. 1. Visualization of a row of counter-rotating streamwise vortices induced by a row of jet vortex generators.

One of the main difficulty in using VG is the large number of parameters the experimentalist has to choose: the type of VG (mechanical or fluidic, stationary or time-dependant), the dimensions, the spacing, the location relative to the flow to be controlled. In this paper we propose a short review describing the structures of the flows produced by two different mechanical VG (trapezoidal blades and cylinders) and continuous jets in a flat-plate boundary layer. The drawback and advantages of each of them will be underlined. The way

the longitudinal structures interact with a flat plate boundary layer will also be discussed. In the case of small cylinders it will be shown that one can define new physical properties that can be helpful to choose the proper parameters in the perspective of control of flow separation.

In a first step, we illustrate with both Particle Image Velocimetry (PIV) and visualizations the mechanisms of generation of streamwise vorticity in various examples. After recalling the classic mechanisms of vortex generation with winglets, we will show how "Bluff Body Vortex Generators" (BBVG) can be used to generate pairs of streamwise counter-rotating vortices. A comparison will also be made with Jet Vortex Generators (JVG) which allows an easier control of the perturbation through the jet velocity. In all cases, visualizations in a cross-section downstream the vortex generators exhibits the typical mushroom-like structures, characteristic of counter-rotating streamwise vortices, as shown on Fig. 1 in the case of JVGs.

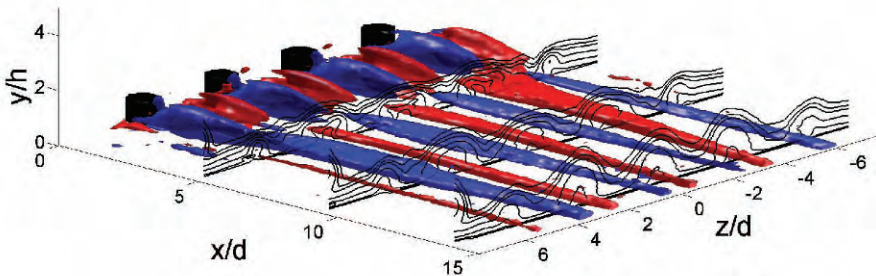


Fig. 2. Iso-surface of transversal velocity downstream a row of small cylinders. One can see the creation of pairs of counter-rotating vortices through alternate red (positive) and blue (negative) iso-surfaces. Isolines of longitudinal velocity show how the longitudinal velocity field is modulated by the longitudinal vortices.

In a second step, we focus on the downstream evolution of the perturbations induced by the Cylindrical VGs (CVG) in the boundary layer. A detailed study is carried out for different spacings between the CVGs and different Reynolds numbers. From 3D reconstruction of two-components horizontal PIV field (Fig. 2), we could extract meaningful informations quantifying the spatial transient growth of the perturbations. One example is illustrated on Fig. 3 where one can see the streamwise evolution of the amplitude of the harmonic mode of the longitudinal and spanwise perturbations induced by the VGs in the boundary layer.

From the difference between the base flow and the mean 3D longitudinal velocity field of the perturbed flow, one can also quantify the modification of the base flow through zero mode u_0^* :

$$u_0^*(x, y) = \langle U(x, y, z) - U_{base}(x, y, z) \rangle_z, \quad (1)$$

The global modification of the base flow is more easily quantified through the integral I_0 over the vertical direction of the $u_0^*(x, y)$ profiles :

$$I_0(x) = \int_0^\infty u_0^*(x, y) dy \quad (2)$$

Thanks to acquisition of the 3D mean longitudinal velocity field, one can compute $I_0(x)$ which is a measure of the global acceleration ($I_0 > 0$) or deceleration ($I_0 < 0$) of the 3D boundary layer. One can see on Fig. 4 that it is now possible to define precisely the exact longitudinal position ($x = L_{inv}$) where the CVG will accelerate the boundary layer and thus delay the separation. If the CVGs are placed at a longitudinal position $x < L_{inv}$ from the natural separation line, then they could trigger the separation instead of delaying it.

Finally we will show an example illustrating the application of the previously defined quantities to the control of boundary layer separation over a smoothly contoured ramp with the VGs.

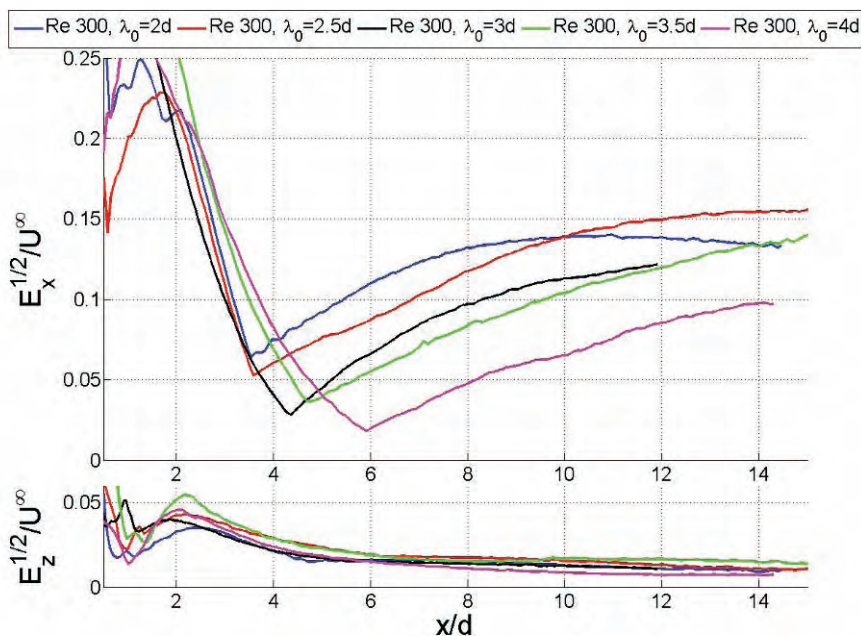


Fig. 3. Longitudinal evolution of the amplitude of the harmonic mode of the spatial perturbations induced by the VGs in a flat plate boundary layer for a Reynolds number based on the height of the VG $Re_h = 300$. One can see that the longitudinal evolution depends strongly on the spacing between the VG for both the longitudinal component (upper figure) and the spanwise component (lower figure).

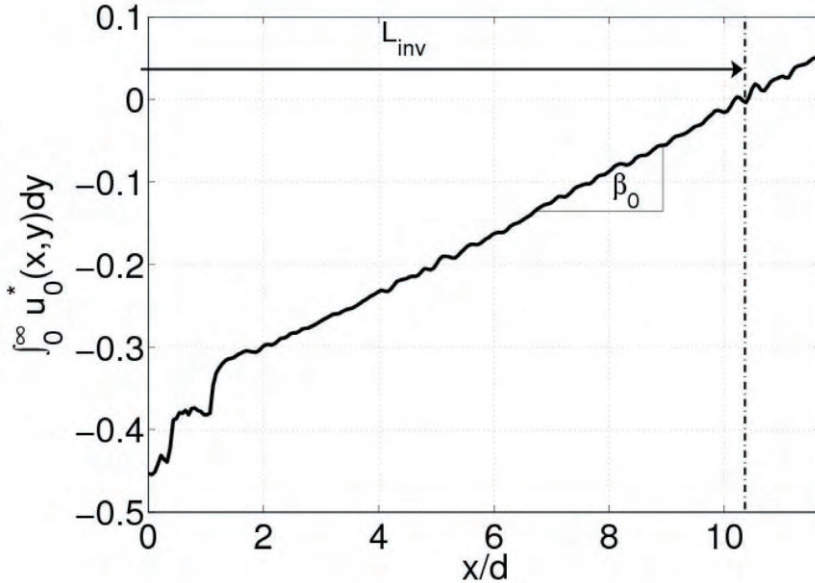


Fig. 4. Longitudinal evolution of the integral $I_0(x)$. It is possible to define a characteristic length L_{inv} where the boundary layer changes from globally decelerated to globally accelerated. Downstream this position, the separation of the boundary layer will be delayed.

References

- BETTERTON, J. G., HACKETT, H. C., ASHILL, P. R., WILSON, M. J., WOODCOCK, I. J., TILMAN, C. P. & LANGAN, K. J. 2000 Laser Doppler Anemometry investigation on sub boundary layer vortex generators for flow control. In *Proc. of the 10th Symposium on Application of Laser Techniques to Fluid Mechanics*. Lisbon, Portugal.
- DURIEZ, T., AIDER, J.-L. & WESFREID, J. E. 2008 Linear modulation of a boundary layer induced by vortex generators. In *4th Flow Control Conference, AIAA technical paper AIAA-2008-4076*. Seattle, USA.
- GODARD, G. & STANISLAS, M. 2006 Control of a decelerating boundary layer. part 1: Optimization of passive vortex generators. *Aerospace Science and Technology* **10**, 181–191.
- LIN, J. 2002 Review of research on low-profile vortex generators to control boundary-layer separation. *Prog. Aerospace Sci.* **38**, 389–420.

Modulated global mode of a controlled wake

V. Parezanović and O. Cadot

Unité de Mécanique - ENSTA, 91761 Palaiseau, France
vladimir.parezanovic at ensta.fr

1 Introduction

The 3D properties of the Bénard von Kármán global mode of the wake behind a 2D bluff body are investigated in an experimental study when a smaller, circular control cylinder is placed in the wake. Previous investigations [1, 2, 3], have shown the influence of a small control cylinder on the global frequency of the wake. The main effect is related to the interaction of vorticity produced by the control cylinder with the vorticity created by the bluff body. However, for certain positions of control, the envelope of the local velocity signal shows a modulation of amplitude. The search in the span-wise direction has shown the effects of the control cylinder's presence on existence and location of the modulation.

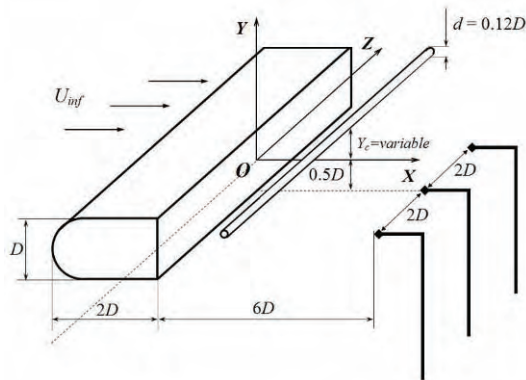


Fig. 1. The experimental setup.

2 Experiment

The schematic representation of the experimental setup is shown in Fig. 1. The bluff body is a "D" shape cylinder with $D = 25\text{mm}$, and a span of $L = 400\text{mm}$. It is situated in an Eiffel type wind tunnel, with the open side test section of $400\text{mm} \times 400\text{mm}$. The free stream velocity here is $U = 8\text{m/s}$, and the Reynolds number of the flow is $Re = \frac{UD}{\nu} \approx 12000$, based on the diameter of the primary cylinder. The secondary (control) cylinder has a circular cross section of diameter $d = 3\text{mm}$, and for the purpose of this investigation, it is displaced along lines parallel to Oy axis, at constant $x = 0.4D$ and $x = 1.8D$. Displacement is performed in 110 steps of 0.5mm . At each position of the control cylinder, three DANTEC hot-wire probes measure velocity, over 30 seconds, at a distance of $x_{p1,2,3} = 6D$ downstream from the trailing edge of the bluff body. As can be seen in Fig. 1., the three probes are all level with the lower edge of the bluff body ($y_{p1,2,3} = -0.5D$), with one of the probes at the span-wise center ($z_{p1} = 0$) and the other two at a distance of $2D$ on each side of the first probe ($z_{p2,3} = \pm 2D$). The probes are of a single wire type, oriented so as to be sensitive to velocity modulus in the xOy plane.

3 Results and discussion

The velocity spectra are displayed for each position of the control cylinder along the vertical lines $x_c = 1.8D$ in Fig. 2.(a,b,c) and $x_c = 0.4D$ in Fig. 2.(d,e,f). In the case of Fig. 2.(a,b,c), the frequency is a constant close to the natural frequency of the uncontrolled wake through all of the vertical positions. This is because the control cylinder is too far downstream of the recirculation zone to produce significant effects. The spectral properties are rather similar for the three span-wise locations in the wake. The width of the peaks is related to 3D effects in the wake such as dislocations [4]. When the control cylinder crosses vertically the recirculation zone at $x_c = 0.4D$, we can observe changes in the global mode frequency. At the extremes ($y_c = \pm D$) of the vertical path of the control cylinder, the frequency of the wake is not well defined (just as for the natural case) and is around the value of the natural frequency. As the control cylinder travels closer to the outer edge of the recirculation zone the frequency is reduced due to vorticity cancelation. At the inner edge the frequency is greatly increased, due to vorticity addition. Moving the control further into the bubble, the frequency is reduced to the natural value, and finally, it increases once more, as the control cylinder is at the center line $y_c = 0$. This increase is believed to be the result of the feedback effect of vorticity produced on the control cylinder, on the vorticity in the primary shear layers. If we analyze the structure of the spectrum peaks, we can observe in Fig. 2.(d,e,f) a drastic change compared to the natural wake. When the frequency is at its maximum the peak is better defined (the width is reduced) and this state is observable along the entire span. When the

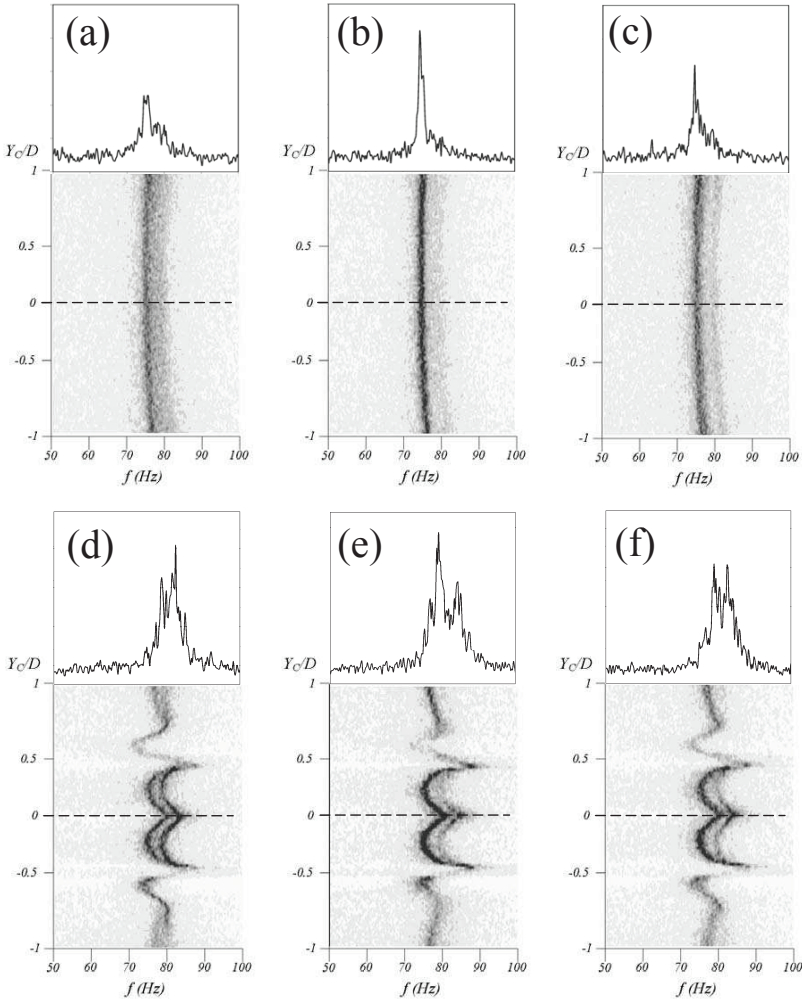


Fig. 2. Spectra of the wake for all the positions of the control cylinder when it is displaced along the Oy axis at a constant x , at three measurement points span-wise. For $x_c = 1.8D$, spectra are shown at $z_{p2} = 2D$ (a), $z_{p1} = 0$ (b) and $z_{p3} = -2D$ (c). For the downstream position of the control cylinder $x_c = 0.4D$, the corresponding measurements are shown in $z_{p2} = 2D$ (d), $z_{p1} = 0$ (e) and $z_{p3} = -2D$ (f). In each case the vertical axis shows the position of the control cylinder along Oy , the horizontal axis marks the frequency of the wake, while the graph intensity is the amplitude of the spectrum. Displayed above each graph is the spectrum of the middle position of the control cylinder ($y_c = 0$), marked by a dashed line in the corresponding picture below.

control cylinder is inside the bubble, we observe the presence of two distinct, well defined peaks, indicating a modulated wake. This modulation is not simultaneously recorded by the three probes, except for the control cylinder's position in the middle at $y_c = 0$.

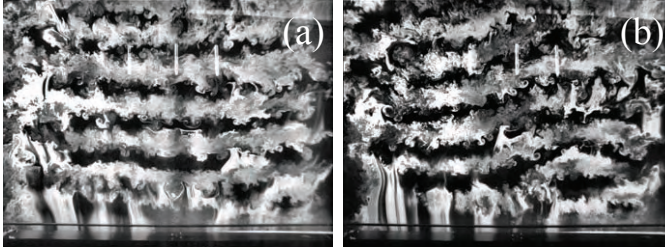


Fig. 3. Flow visualization for the position of the control cylinder at $x_c = 0.4D$, $y_c = 0$. (a) Parallel vortex shedding. (b) One-side vortex tube dislocation

We performed flow visualization of this configuration in the xOz plane. Fig. 3. shows the examples of parallel vortex shedding and the appearance of a dislocation. The dislocation originates from the presence of two global modes, each dominant on one side of the primary cylinder. The modulation takes place in the overlap region of the two global modes. When the control cylinder is at the middle position, the overlap region envelops the three probes.

4 Conclusion

In conclusion, the control cylinder in a turbulent wake can create a modulated state with two selected frequencies, or suppress it to a single frequency peak. Modulation is related to periodic appearance of dislocations in the wake, which are sensitive to the presence of a 2D stationary perturbation.

5 Acknowledgements

This work was supported by the ANR project no.06-BLAN-0363-01 "High-speed PIV".

References

1. P.J. Strykowski, K.R. Sreenivasan, *J. Fluid Mech.* **218**, 71-107, 1990.
2. H. Sakamoto, H. Haniu, *J. Fluids Eng.* **116**, 221-227, 1994.
3. B. Thiria, O. Cadot, J. F. Beaudoin, *J. Fluids Struct.* **25**(2), 2008.
4. C.H.K. Williamson, *J. Fluid Mech.* **243**, 393-441, 1992.

Swirl effects in turbulent pipe flow

F. Nygård and H.I. Andersson

Fluids Engineering Division, Department of Energy and Process Engineering,
NTNU, Trondheim, Norway

frode.nygard@ntnu.no

1 Introduction

DNSs of pipe flow with two different swirl strengths (S_1 and S_2) are carried out. The flow is driven by an axial pressure gradient sufficient to keep a constant bulk Reynolds number $Re_b = U_b D / \nu = 4900$. $U_p = 2U_b$ is the centerline velocity of the corresponding laminar flow. A body force in tangential direction is setting up a swirl in the near-wall region. The resulting mean tangential velocity profiles are shown in Fig. 1 a).

Swirling flow due to pipe rotation has been reported several times in the past, e.g. by DNS in [1, 2]. Their rotation number $N = 2V_{wall}/U_p$ defined the swirl strength and they considered $N = 0.5, 1,$ and 2 . In the present approach, the wall velocity is zero and the swirl is defined as $S = 2V_{max}/U_p$. By reading the maxima from Fig. 1 a) it can be found that $S_1 \approx 0.45$ and $S_2 \approx 0.85$. However, while S_1 increases the drag considerably, S_2 provides a slight drag reduction, as can be seen from the shear stress profiles in Fig. 1 b). In order to investigate the physics behind the differences in S_1 and S_2 , profiles of fluctuating vorticity and helicity, pdf-plots of helicity density, and visualizations of fluctuating velocities will be provided.

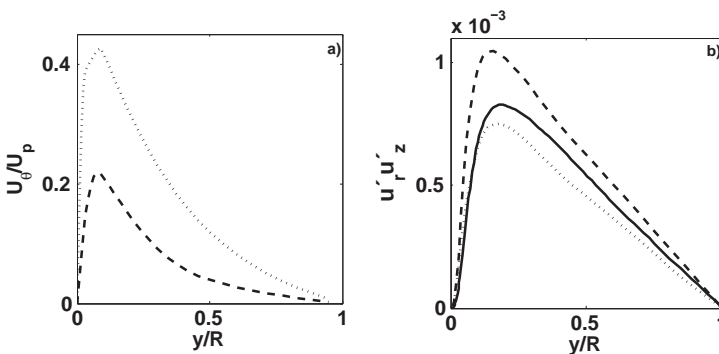


Fig. 1. a) Mean tangential velocity. b) Reynolds shear stress, $u'_r u'_z = \langle u'_r u'_z \rangle / U_p^2$. —, No swirl; ---, S_1 ; ···, S_2

2 Results

Figures 2 a) - c) show root-mean-square (rms) values of the vorticity fluctuations

$$\omega'_\theta = \frac{\partial u'_r}{\partial z} - \frac{\partial u'_z}{\partial r}, \quad \omega'_r = \frac{1}{r} \frac{\partial u'_z}{\partial \theta} - \frac{\partial u'_\theta}{\partial z}, \quad \omega'_z = \frac{1}{r} \frac{\partial r u'_\theta}{\partial r} - \frac{1}{r} \frac{\partial u'_r}{\partial \theta}, \quad (1)$$

for two swirling cases and the case without swirl for $y/R < 0.2$. A reduction of the tangential fluctuating vorticity in the near-wall region, as seen for S_2 , indicates a lower rate of cross-sectional mixing. The fluctuating radial vorticity is correlated to high- and low-speed streaks through $\partial u'_z/\partial \theta$ and Fig. 2 b) indicates therefore a reduction of streaks for S_2 compared to S_1 . The induced swirl increases the axial vorticity fluctuations in the near-wall region, as seen in Fig. 2 c). The swirl breaks up the even distribution of velocity-vorticity correlations and creates non-zero helicity. The tangential helicity component is mainly influenced by the induced u'_θ and $\partial u'_z/\partial r$. The region from the wall to the peak of the mean tangential velocity profiles (approximately $y/R < 0.1$, Fig. 1 a)) will experience inflow of axial high-speed fluid that also carries a high tangential velocity. Accordingly, this will result in a stronger radial gradient of u'_z which leads to a larger ω'_θ . The opposite effect will be experienced for excursions away from the wall. Consequently, $u'_\theta \omega'_\theta$ will be positive for both sweeps and ejections. In comparison to S_1 , the tangential velocity and vorticity fluctuations have become less correlated for S_2 as seen in Fig. 2 d). The radial fluctuating helicity component in Fig. 2 e) is about an order of magnitude smaller than the tangential and axial components as it is only indirectly influenced by the induced swirl. The axial helicity component is shown in Fig. 2 f). For $y/R < 0.1$ a sweep will represent a positive u'_z and an increase of the wall-normal gradient of u'_θ which results in a positive ω'_z . Correspondingly, an ejection results in negative u'_z and ω'_z . As seen in Fig. 2 f) the region dominated by sweeps and ejections is moved further away from the wall and has decreased for S_2 compared to S_1 .

The pdf of the helicity density fluctuations, $P(h')$, visualizes the alignment ϕ between the fluctuating vorticity and the fluctuating velocity vectors. Figures 3 a) - d) show that without swirl, ϕ tend to be $\approx \pi/2$ for $y/R \leq 0.2$ as u'_z and ω'_θ dominate the near-wall region. The swirls reduce the axial velocity fluctuations (not shown) together with the fluctuating azimuthal vorticity for $y/R \leq 0.2$. Consequently, a reduction of the misalignment between the fluctuating velocity and fluctuating vorticity vectors is observed for the swirling cases. For $y/R = 0.01$, orthogonality is still the most probable orientation with swirl, but the likelihood has almost halved. Only small deviations can be observed between the two swirl strengths. Moreover, for $y/R = 0.06$ seen in Fig. 3 b), it has become most likely to have either aligned or counter-aligned vectors. However, $P(h')$ is not far from being evenly distributed for S_2 due to roughly equal axial and azimuthal helicity of opposite sign at this position (see Fig. 2 d) and f)). For S_1 , the axial and tangential helicity show similar

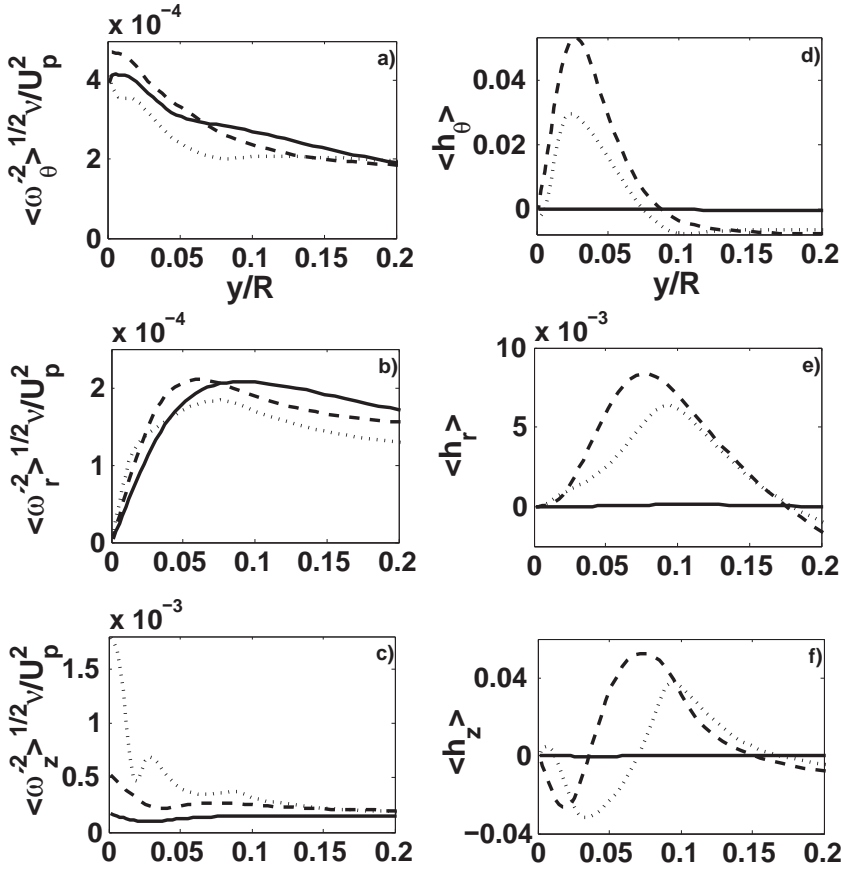


Fig. 2. a)-c) Mean fluctuating vorticity profiles. d)-f) Mean fluctuating helicity profiles, $\langle h_i \rangle = \langle u'_i \omega'_i \rangle / \nu U_p^3$. —, No swirl; --, S_1 ; ···, S_2

positive values at $y/R = 0.06$ and consequently the highest probability becomes alignment between the two vectors. At $y/R = 0.10$ the axial helicity is dominating (see Fig. 2 d) - f)) and implies alignment of the vectors in Fig. 3 c). At $y/R = 0.18$ the axial and azimuthal helicity fluctuations are negative and roughly equal. Therefore, the fluctuating velocity and the fluctuating vorticity vector tend to be counteraligned in Fig. 3 d). The differences in helicity and helicity probability between the friction-increasing S_1 and the drag-reducing S_2 are most noticeable around $y/R = 0.06$. At this point fluctuating helicity shows a more isotropic behaviour for S_2 than for S_1 and this might be one of the clues as to why only S_2 reduces the drag. Contour plots of the instantaneous u'_z at $y/R = 0.06$ are presented in Fig. 4 a)-c). The most striking difference between the case without swirl and the swirling cases is tilting of the structures. A closer look suggests that the S_2 -case exhibits reduced streak-lengths compared to the S_1 -case.

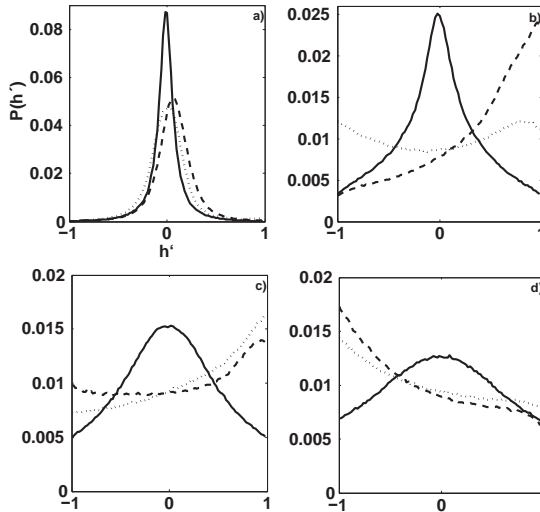


Fig. 3. Probability density function of the helicity density fluctuation, $P(h')$. $h' = (\mathbf{u}'\omega')/(\sqrt{|\mathbf{u}'|^2}|\omega|^2) = \cos\phi$. —, No swirl; --, S_1 ; \cdots , S_2 . a) $y/R = 0.01$, b) $y/R = 0.06$, c) $y/R = 0.10$, d) $y/R = 0.18$

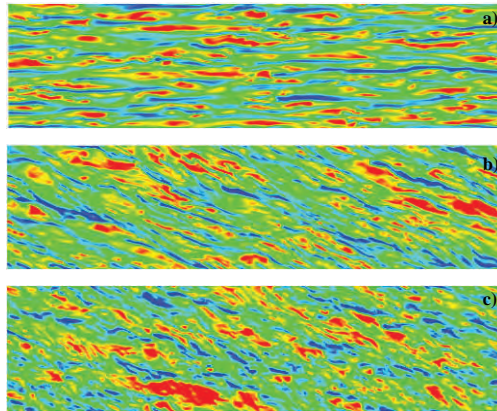


Fig. 4. Visualisation of u'_z/U_p at $y/R = 0.06$. Red and blue colours visualize positive and negative fluctuations (both shown as dark structures in the black and white version). a) No swirl b) S_1 ; c) S_2

To conclude, it seems that S_2 interferes more favourably with the sustainable turbulence cycle (i.e. reduces sweeps, ejections and streaks) than S_1 and therefore results in reduction of drag.

References

1. P. Orlandi, Phys. Fluids, **9**, 2045 (1997).
2. P. Orlandi and M. Fatica, J. Fluid Mech., **343**, 43 (1997).

Control of an axisymmetric turbulent wake by a pulsed jet

J.F. Morrison and A. Qubain

Department of Aeronautics, Imperial College, London SW7 2AZ
j.morrison@imperial.ac.uk

1 Introduction

It has been shown [1] that the axisymmetric wake is dominated by three types of instability mechanism: an axisymmetric “pumping” of the recirculation bubble at very low frequencies, antisymmetric fluctuations induced by a helical vortex structure that forms just downstream of the rear stagnation point and several higher-frequency, axisymmetric instability modes of the separated shear layer. The environmental requirement for drag reduction has placed a greater emphasis on base-pressure recovery of bluff bodies. The active control of separating flow around bluff bodies has tended to focus on 2D bodies [2, 3] demonstrating that large drag reductions are possible, usually by controlled blowing, at frequencies close to the von Kármán shedding frequency. However, in terms of control, 3D bluff bodies have received considerably less attention even though this configuration appears in many practical problems. Even then, active control has tended to focus on the delay of separation [4]. In the present work, we show that the base pressure of a blunt trailing edge may be increased by a high-frequency jet from a zero-net-mass-flux (ZNMF) device.

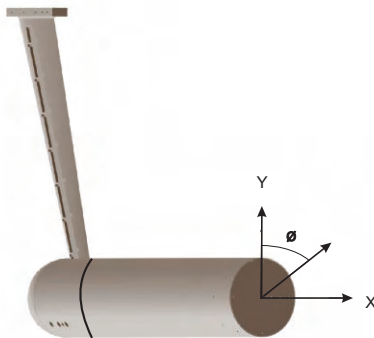


Fig. 1. Orthographic projection of model with sting. Freestream in x -direction.

2 Experimental Setup

In the present experiment, figure 1, the near wake of an axisymmetric cylinder with its axis aligned in the streamwise direction and a blunt trailing edge is subject to periodic forcing. The boundary layer is tripped just downstream of the sting. A high-fidelity speaker located inside the cylinder is used to generate an axisymmetric, pulsed jet of variable frequency and amplitude from a small circumferential gap located on the underside of the separating boundary layer. The ZNMF device is driven sinusoidally and does not operate at resonance. A detailed investigation of the response of the mixing layer, and in particular, the growth of the disturbances is performed using hot wires, PIV and base-pressure transducers. Further details are provided in [5].

3 Results

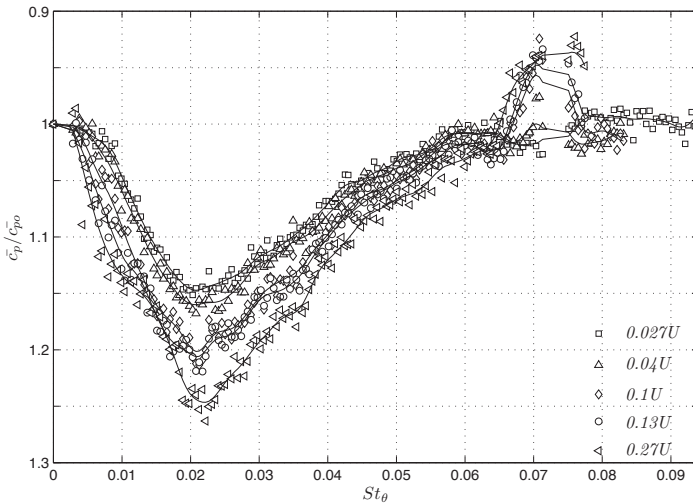


Fig. 2. Change in base pressure coefficient with forcing frequency, St_θ , for several different forcing amplitudes, v_f .

Figure 2 shows the base-pressure coefficient (averaged in time and over the radius of the base) for the forced case as a ratio of that for the unforced case, C_{p0} , where

$$\bar{C}_p = \frac{p - p_\infty}{\frac{1}{2}\rho U_\infty^2}, \quad (1)$$

and plotted against dimensionless forcing frequency, $St_\theta = f\theta/U_\infty$, where θ is the boundary-layer momentum thickness at separation. \bar{C}_p/\bar{C}_{p0} is shown for jet velocity amplitudes in the range $0.027 \leq v_f/U_\infty \leq 0.27$.

Figure 2 shows that the wake exhibits a specific response at three distinct forcing frequencies: at each one, contours of the phase-averaged vorticity in the (x, y) -plane are shown, figures 3 – 5, for $v_f/U_\infty = 0.27$. The averaging is performed at that part of the cycle where the jet switches from blowing to suction, that is at a phase angle $\phi = \pi$. Key features are as follows.

1. At very low frequencies ($St_\theta \approx 0.003$, or $St_D \approx 0.32$), there is a weak effect on the pumping mode, $St_D \approx 0.18$ via a “beat-coupling” effect in which the forcing frequency is at the boundaries to the lock-in region, even though it is closer to the frequency of the helical mode at $St_D \approx 0.255$. This is possible because the helical structures do not form until downstream of the rear stagnation point and is confirmed by the symmetrical response of the velocity field, figure 3. A phase-sequence through the blowing and suction phases of the forcing shows that the shear layer flaps in a varicose or “pumping” mode.
2. At $St_\theta \approx 0.024$, base pressure decreases as the amplitude of the forcing increases. The maximum amplification occurs at a frequency close to that predicted by a linear stability analysis for an initially laminar, plane mixing layer, $St_\theta = 0.016$ [6], and is even closer to that for a turbulent mixing layer, $St_\theta = 0.022$ [7]. The wavelength of the structures as deduced from PIV data (figure 4) and two-point hot-wire correlations shows that their convection velocity is $0.5U_\infty$ until they begin to merge for $x/D > 0.5$, approximately. Structures are formed as the jet switches from blowing to suction, that is, $\phi = \pi$.
3. At $St_\theta \approx 0.07$, there is a rise in base pressure over a restricted range of frequencies. The effect does not become apparent except for $v_f > 0.1U_\infty$ and saturates for $v_f > 0.2U_\infty$. Figure 5 apparently shows no structure: obviously in this case, the effects of short-wavelength forcing lead to more-or-less immediate merging. Velocity spectra indicate that there is a reduction of energy in the large scales but an enhancement of energy in the small scales and therefore of dissipation also. This effect does not appear to have been reported previously.

4 Discussion

A further experiment was conducted in which the jet was made three-dimensional by blocking the jet orifice with a uniform pitch to produce eight distinct jets, each with a width of $0.063D$. In this case, the rise in base pressure at $St_\theta \approx 0.07$ was not reproduced, presumably owing to the generation of streamwise vorticity. Further experiments indicate that forcing at one of the frequencies identified above can leave other modes unaffected. Forcing at $St_\theta \approx 0.024$ modified the bubble-pumping mode slightly, by increasing the energy and shifting it to a slightly higher frequency. This forcing frequency also modified the helical mode slightly. On the other hand, forcing at high frequencies, $St_\theta \approx 0.07$, leaves the helical mode unaffected, but does increase the energy associated with the bubble-pumping mode. These effects are discussed fully in [5].

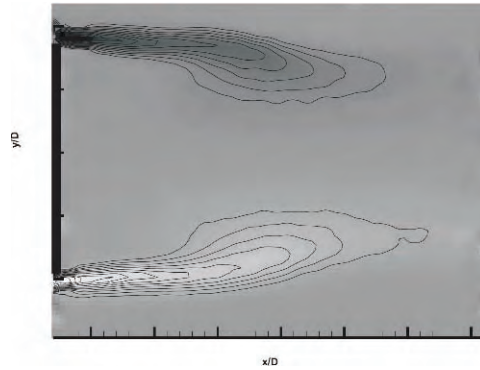


Fig. 3. Phase-averaged (x, y) -plane vorticity contours, $St_\theta = 0.003, v_f/U_\infty = 0.27$.

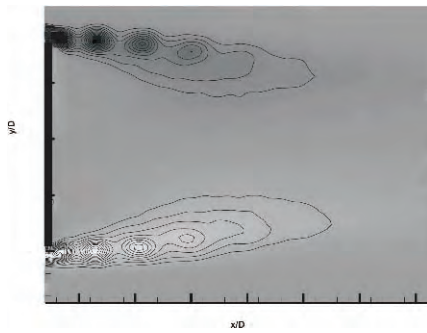


Fig. 4. Phase-averaged (x, y) -plane vorticity contours, $St_\theta = 0.024, v_f/U_\infty = 0.27$.

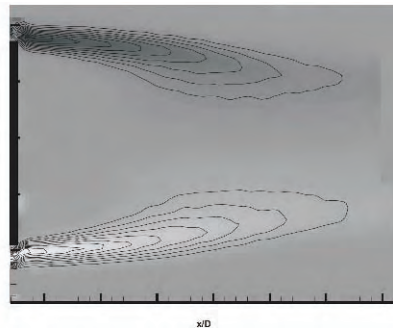


Fig. 5. Phase-averaged (x, y) -plane vorticity contours, $St_\theta = 0.07, v_f/U_\infty = 0.27$.

Acknowledgments

We are indebted to Ferrari S.p.A. for financial support.

References

1. E. Berger, D. Scholz and M. Schumm, *J. Fluids & Struct.* **4**, 231 (1990).
2. M. Pastoor, L. Henning, B. R. Noack, R. King & G. Tadmor, *J. Fluid Mech.*, **608**, 161 (2008).
3. H. Choi, W.-P. Jeon & J. Kim, *Ann. Rev. Fluid Mech.*, **40**, 113 (2008).
4. S. Jeon, J. Choi, W.-P. Jeon, H. Choi & J. Park., *J. Fluid Mech.*, **517**, 113 (2004).
5. A. Qubain & J. F. Morrison, In preparation (2009).
6. C.-M. Ho & P. Huerre, *Ann. Rev. Fluid Mech.*, **16**, 365 (1984).
7. S. C. Morris & J. F. Foss, *J. Fluid Mech.*, **494**, 187 (2003).

Direct Numerical Simulations of turbulent mixed convection in enclosures with heated obstacles

Olga Shishkina and Claus Wagner

Department Fluid Systems, Institute for Aerodynamics and Flow Technology,
German Aerospace Center (DLR), Göttingen, Germany
Olga.Shishkina@dlr.de and Claus.Wagner@dlr.de

1 Introduction

Investigation of turbulent mixed convection flows past heated obstacles has physical as well as engineering objectives, since such problems as climate control in buildings, cars or aircrafts, where the temperature must be regulated to maintain comfortable and healthy conditions, can be formulated as mixed convection problems. In this type of convection the flows are determined both by the buoyancy force like in natural convection and by inertia forces like in forced convection, while neither of these forces dominates.

Mixed convection is characterised by Archimedes number

$$Ar = Gr/\mathcal{R}e^2$$

of order 1, where

$$Gr = \alpha g \hat{D}^3 \Delta \hat{T} / \nu^2$$

denotes Grashof number and

$$\mathcal{R}e = \hat{D} \hat{u}_{inlet} / \nu$$

Reynolds number, α is the thermal expansion coefficient, ν the kinematic viscosity, g the gravitational acceleration, $\Delta \hat{T}$ the difference of the temperatures at the heated obstacles and in cold inlet flows, \hat{D} the width of the container and \hat{u}_{inlet} is the mean velocity of the inlet flow.

The objective of our study is to investigate by means of Direct Numerical Simulations (DNS) the instantaneous and statistical characteristics of turbulent mixed convection flows past heated obstacles, for different Gr and Ar .

2 Governing equations and numerical method

The considered computational domain is a box with 4 parallelepiped ducts connected to it (Fig. 1). The length, height and width (without ducts) of the

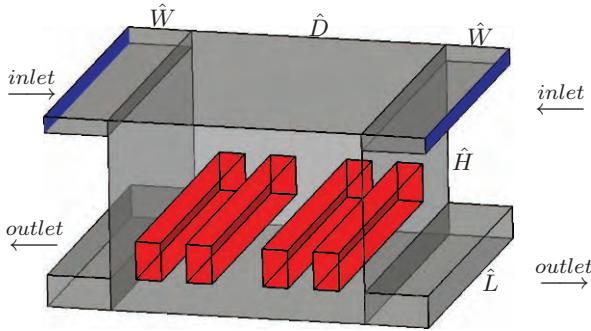


Fig. 1. Sketch of the computational domain and the boundary conditions. Warm obstacles and cold inlet flows are shown in red and blue, respectively.

domain are \hat{L} , \hat{H} and \hat{D} , respectively. Through 2 thin ducts, located close to the top, cold inlet flows come inside the box. The length, height and width of the ducts for the inlet flows are \hat{L} , $\hat{H}/150$ and \hat{W} , respectively. 2 ducts with the sizes $\hat{L} \times \hat{H}/20 \times \hat{W}$ for outlet flows are situated close to the bottom. There are 4 heated parallelepiped obstacles inside the box, which are raised at the distance $\hat{H}/20$ from the bottom.

The temperatures of the cold inlet flows and heated obstacles are fixed. At the outlets and outer rigid adiabatic walls $\partial\hat{T}/\partial\mathbf{n} = 0$, where \mathbf{n} is the normal vector. The velocities at the inlets are fixed, while at the outlets $\partial\hat{\mathbf{u}}/\partial\mathbf{n} = 0$ and at all solid walls $\hat{\mathbf{u}} = 0$. The working fluid is air, and all material properties are taken at 25°C.

To dimensionalize the governing equations we use the following reference constants: $\hat{x}_{ref} = \hat{D}$ for distance, $\hat{T}_{ref} = \Delta\hat{T}$ for temperature, where $\Delta\hat{T}$ is the temperature difference between the obstacles and the inlet flows, $\hat{u}_{ref} = (\alpha g \hat{D} \Delta\hat{T})^{1/2}$ for velocity, $\hat{t}_{ref} = \hat{x}_{ref}/\hat{u}_{ref}$ for time, $\hat{p}_{ref} = \hat{u}_{ref}^2 \rho$ for pressure.

Thus we get the following system of the governing dimensionless equations in Boussinesq approximation

$$\begin{aligned} \mathbf{u}_t + \mathbf{u} \cdot \nabla \mathbf{u} + \nabla p &= \mathcal{G}r^{-1/2} \Delta \mathbf{u} + T \mathbf{e}_x, \\ \nabla \cdot \mathbf{u} &= 0, \\ T_t + \mathbf{u} \cdot \nabla T &= \mathcal{G}r^{-1/2} \mathcal{P}r^{-1} \Delta T. \end{aligned}$$

Here \mathbf{u} is the velocity vector-function, T the temperature, \mathbf{u}_t and T_t their time derivatives, p the pressure, $\mathcal{P}r = \nu/\kappa$ Prandtl number, κ the thermal diffusivity, \mathbf{e}_x the unit vertical vector. All boundary conditions are taken in accordance with the above discussed. T equals 0.5 at the obstacles and -0.5 at the inlets.

To simulate turbulent mixed convection, we use fourth-order finite-volume discretization schemes in space and the explicit Euler-leapfrog discretization scheme in time within the Chorin ansatz [1], which is similar to that used in our DNS of turbulent Rayleigh–Bénard convection [3, 4, 5]. The Poisson solver, which is needed to compute the pressure, uses the capacitance matrix technique together with the separation of variables method [2]. The developed numerical method generally allows to conduct DNS of turbulent thermal convection using computational meshes, which are non-equidistant in all 3 directions and are irregular in any 2 directions.

3 Results

We investigate mixed convection in air in the above discussed domain by means of DNS, while varying the control parameters $10^8 \leq \mathcal{G}r \leq 10^{10}$, $1 \leq \mathcal{A}r \leq \infty$, the length of the computational domain $0.2 \leq \hat{L}/\hat{D} \leq 1.25$ and the width of the ducts $0 \leq \hat{W}/\hat{D} \leq 0.025$.

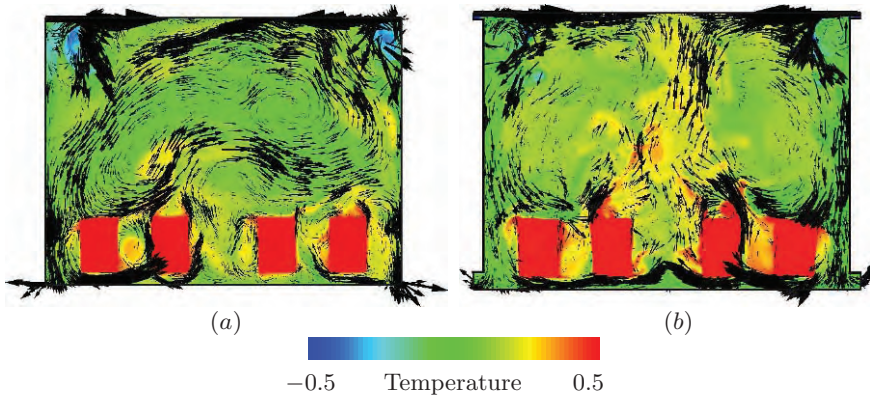


Fig. 2. Instantaneous temperature distribution with superimposed velocity vectors in a central vertical cross-section for $\mathcal{G}r = 10^9$, $\mathcal{A}r = 1$, $\hat{L}/\hat{D} = 0.2$, $\hat{W}/\hat{D} = 0.025$ as obtained in (a) two-dimensional and (b) three-dimensional direct numerical simulations.

It was shown that two-dimensional and three-dimensional direct numerical simulations produce principally different global flow structures (see Fig. 2 (a) and (b)). Indeed, in three-dimensional simulations 2 large rolls are observed in mixed convection for the case $\mathcal{A}r = 1$ and $\mathcal{R}a = 10^9$, while two-dimensional simulations for the same $\mathcal{A}r$ and $\mathcal{R}a$ produce a single large roll. Thus, the investigated mixed convection flows in enclosures with heated obstacles are shown to be turbulent and strongly three-dimensional even for relatively “thin” domains with $\hat{L}/\hat{D} = 0.2$.

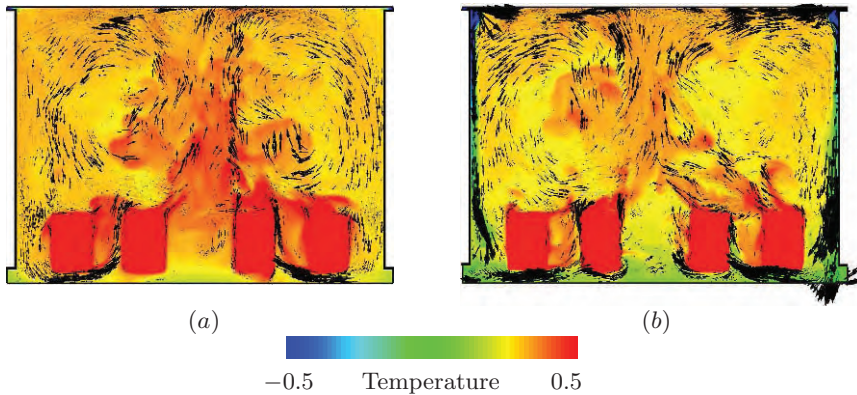


Fig. 3. Instantaneous temperature distribution with superimposed velocity vectors in a central vertical cross-section for $Gr = 10^9$, $\hat{L}/\hat{D} = 0.2$, $\hat{W}/\hat{D} = 0.025$ and (a) $Ar = \infty$, (b) $Ar = 4$ as obtained in three-dimensional direct numerical simulations.

Further, it is shown that the mean temperatures and velocities in mixed convection depend strongly on Ar . Thus, the mean temperature decreases with decreasing Archimedes number, while the mean absolute velocity increases with decreasing Ar (compare Fig. 2 (b) with Fig. 3 (a) and (b)).

At the conference further obtained instantaneous and mean mixed convection flows for different values of the control parameters will be discussed and compared to the corresponding natural convection flows ($Ar = \infty$).

4 Acknowledgements

The authors are grateful to the Deutsche Forschungsgemeinschaft (DFG) and Leibniz Supercomputing Centre (LRZ) for supporting this work.

References

1. A. J. Chorin & J. E. Marsden, *A Mathematical Introduction to Fluid Mechanics*, Springer-Verlag, 3rd ed., 1993.
2. O. Shishkina, A. Shishkin, C. Wagner, *J. Comput. Appl. Maths* **226**, 336 (2009).
3. O. Shishkina and C. Wagner, *J. Fluid Mech.* **599**, 383 (2008).
4. O. Shishkina and C. Wagner, *Phys. Fluids* **19**, 085107 (2007).
5. O. Shishkina and C. Wagner, *J. Fluid Mech.* **546**, 51 (2006).

On Drag Reduction in Turbulent Channel Flow over Superhydrophobic Surfaces

C. Peguero, and K. Breuer

Brown University, Providence, RI, USA
charles_peguero at brown.edu

1 Introduction

Recent simulations and experiments suggest that flow over superhydrophobic surfaces may exhibit significantly reduced drag in both laminar [8, 9] and turbulent [7, 10] regimes due to the existence of a thin layer of gas on the surface which allows a slip velocity. The current paper explores this using estimates of drag based on high-resolution PIV in a low-Reynolds number turbulent channel flow.

2 Superhydrophobic surfaces

Three superhydrophobic surfaces were tested, all of which exhibited static contact angles approaching 180° . The first surface examined was a textured surface manufactured in-house by laser etching $20 \times 20 \mu\text{m}$ (width \times depth) streamwise-oriented grooves into an aluminum test plate and subsequently coating the surface with a hydrophobic silane (Gelest, Inc.). The second surface was a sand-blasted aluminum plate (RMS roughness $\sim 15 \mu\text{m}$), SB, coated with a spray lacquer (G. J. Nikolas & Co., Inc) and dusted with a hydrophobic powder (Evonik). The final surface was “Nanograss” [6], consisting of arrays of posts ($350 \text{ nm } \emptyset$, $7 \mu\text{m}$ high, $1.25 \mu\text{m}$ spacing) etched in silicon and coated with a hydrophobic CF_x film.

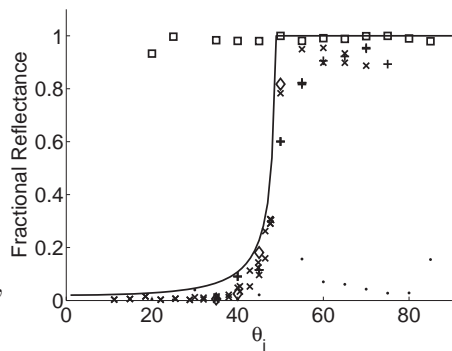


Fig. 1. Fractional reflection of incident light on a submerged surface. \times Grooves, \diamond SB, $+$ Nanograss, \square Mirror, \cdot Un-coated aluminum plate, $-$ Fresnel equation curve.

The presence of an air layer on the submerged superhydrophobic surfaces under turbulent flow conditions was confirmed by focusing a laser spot on the superhydrophobic surface and measuring the intensity of the reflected light as a function of the incident angle. The results from the superhydrophobic surfaces follow the theoretical curve (Fig. 1), according to Fresnel's equations, confirming the existence of an air layer under these conditions.

3 Experimental methods and determination of u^*

A 19 by 43 cm test surface was mounted on the lower wall of a turbulent channel flow facility [3]. PIV measurements, with wall-normal resolution (y) of 0.05 mm, were taken in the $x - y$ plane at the downstream end of baseline (hydrophilic) and superhydrophobic surfaces at $Re_b \cong 6000$; $Re^* \cong 200$ ($Re_b \equiv 2\delta U_{bulk}/\nu$; $Re^* \equiv \delta u^*/\nu$, where δ is the half-channel height). At these conditions, the characteristic turbulent scales are: $l^* \approx 100\mu\text{m}$ and $u^* \approx 10\text{mm/s}$. The typical PIV measurement uncertainty for the experimental data was 4 mm/s ($\approx 0.4u^*$), and valid experiment data was typically available starting from $y^+ \sim 2$.

Three methods were used to estimate the friction velocity from the velocity data. The methods were evaluated using DNS data [1, 2], perturbed using different levels of random noise. The first method used a cubic polynomial fit to the near-wall mean velocity profile [4], extended to allow for a non-zero slip velocity at the surface, U_s . This method is very sensitive to errors in the near-wall velocity, and the error in the estimate of u^* increased quickly, both with noise level and with the location of the first measured velocity point. A noise level of $0.4u^*$ resulted in a 24% error with the fit starting at $y^+ = 1$. As the starting point moved farther from the wall, the error increased to 83% at $y^+ = 5$. Note that the accuracy of this method is much higher if one enforces a no-slip condition at the wall [4].

The second method applied a linear fit to the total stress, $\tau = \mu dU/dy - \rho < u'v' >$, extrapolated to $y = 0$ to calculate u^* . This approach was less sensitive to error in the velocity data and was not dependent on availability of near-wall data. The error from the evaluation of this method was 2% at $0.4u^*$ noise. The final method relied on an integration the Reynolds stress to calculate u^* , based on Fukagata et al. [5], extended to allow for a non-zero wall velocity:

$$C_f = 2 \left(\frac{u^*}{U_b} \right)^2 = 12 \int_{y=-1}^{y=1} (y \cdot \overline{u'v'}) dy + \frac{12}{Re_b} (1 - \overline{U}_s). \quad (1)$$

This formula yields an average C_f for both channel walls (only one wall is superhydrophobic in our experiments). It is only weakly affected by uncertainty and availability of near-wall data. The effect of a slip velocity at the channel wall modified the laminar contribution to C_f . Any effect on the turbulent contribution was due to the Reynolds stress. The error when applied to the DNS data for $0.4u^*$ noise was 11%. The error for this method increased rapidly when data was unavailable for $y^+ \leq 5$ ($y^+ \leq 10$ for the no-slip case).

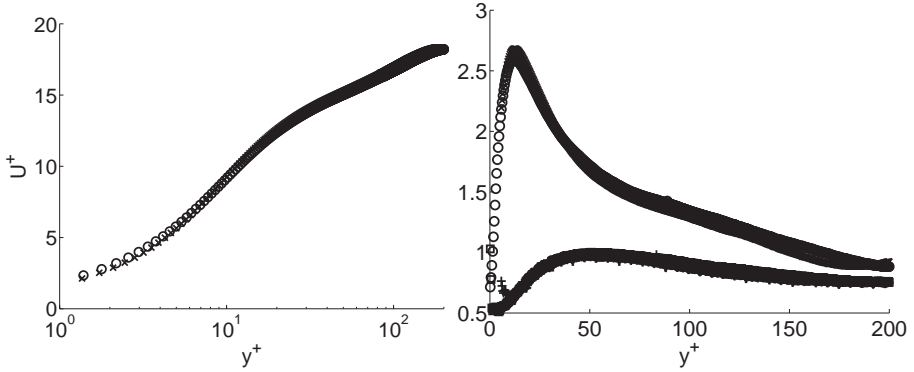


Fig. 2. PIV velocity and fluctuation profiles for both baseline (×) and Superhydrophobic (○) surfaces.

4 Results and Discussion

The methods described above were applied to data collected for each of the three superhydrophobic surfaces as well as the baseline flow (Figs. 2 and 3). Although there are differences between the tests, and some suggestions that drag reduction may be present, there is no definitive evidence, either from the mean and fluctuation profiles (e.g. Fig. 2) or the resultant values of C_f (Fig. 3), that drag reduction has been achieved using the superhydrophobic surface treatments.

The lack of drag reduction found here is in contrast to results from other groups [10], and may be due to several factors. Firstly, it is possible that the current experiments are in error. However, great care has been taken to reduce this possibility, and the experiments have been conducted multiple times over multiple surfaces. Secondly, it is possible that there is a moderate and subtle drag reduction that is not measurable using PIV-based techniques. This remains a possibility, given the scatter in the estimates for C_f found using the three different methods. Improving the PIV data (through larger samples and enhanced PIV processing), and continuing to improve the post-processing estimates for C_f are still areas where progress can be made to resolve these issues.

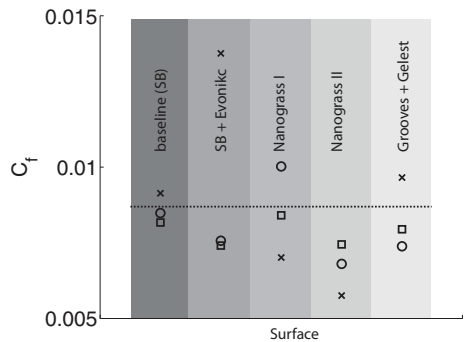


Fig. 3. C_f results from experimental PIV data using three methods: × Polynomial fit, ○ Total stress fit, □ Reynolds stress integration

However, the modifications to the mean velocity and fluctuation profiles due to superhydrophobicity that have been reported in previous work [7, 10] are quite dramatic and would clearly be visible in this data if they were present, leading us to believe that, even if there is some drag reduction, that the effect is subtle, and not comparable to other researchers' findings. Numerical DNS simulations [7] found drag reduction after the modification of the wall boundary condition to allow for a Navier slip velocity. However, in the real turbulent flow, an air layer also provides a wall-normal compliance which may obviate drag reduction [11]. Min and Kim [7] also showed that spanwise slip served to *increase* the drag, and it is possible that this is present in the current experiments (spanwise velocities were not measured). It is also possible that the current geometries tested are not optimal for drag reduction. The current grooves are somewhat large, and this may allow for the air layer to be compressed into the grooves, resulting in an effectively fully-wetted surface, although this still needs to be explored more fully.

References

1. J. C. del Alamo and J. Jimenez, Direct numerical simulation of the very large anisotropic scales in a turbulent channel. *Center for Turbulence Research Annual Research Briefs. Stanford University* 329-341 (2001).
2. J. C. del Alamo and J. Jimenez, Spectra of the very large anisotropic scales in turbulent channels. *Phys. Fluids* **15** 6 L41-L44 (2003).
3. K. S. Breuer, J. Park, and C. Henoeh, Actuation and control of a turbulent channel flow using Lorentz forces. *Phys. Fluids*, **16** 4 897-907 (2004).
4. F. Durst, H. Kikura, I. Lekakis, J. Jovanović and Q. Ye, Wall shear stress determination from near-wall mean velocity data in turbulent pipe and channel flows. *Experiments in Fluids*, **20** 417-428 (1996).
5. K. Fukagata, K. Iwamoto and N. Kasagi, Contribution of Reynolds stress distribution to the skin friction in wall-bounded flows. *Physics of Fluids*, **14** L73 (2002).
6. T. N. Krupenkin, J. A. Taylor, T. M. Schneider and S. Yang, From Rolling Ball to Complete Wetting: The Dynamic Tuning of Liquids on Nanostructured Surfaces. *Langmuir*, **20** 3824-3827 (2004).
7. T. Min and J. Kim, Effects of hydrophobic surface on skin-friction drag. *Physics of Fluids*, **16** L55 (2004).
8. J. Ou, B. Perot and J. P. Rothstein, Laminar drag reduction in microchannels using ultrahydrophobic surfaces. *Physics of Fluids*, **16** 4635 (2004).
9. J. Ou and J. P. Rothstein, Direct velocity measurements of the flow past drag-reducing ultrahydrophobic surfaces. *Physics of Fluids*, **17** 103606 (2005).
10. R. J. Daniello, N. E. Waterhouse and J. P. Rothstein, Turbulent drag reduction using superhydrophobic surfaces. *Physics of Fluids*, (2009). (in review).
11. S. Xu, D. Rempfer and J. Lumley, Turbulence over a compliant surface: numerical simulation and analysis. *J. Fluid Mech.*, **478** 11-34 (2003).

Response of Periodically Modulated Turbulence

H.E. Cekli and W. van de Water

Physics Department, Eindhoven University of Technology, 5600 MB Eindhoven, The Netherlands, h.e.cekli@tue.nl

Many turbulent flows are subject to periodic modulation, examples are the flow in an internal combustion engine, the pulsatile blood flow through arteries, and geophysical flows driven by periodic tides. When the modulation is slow, the turbulence will adjust adiabatically, but when the modulation period comes close to an internal time scale of the flow, the turbulence may resonate with the driving. Such a time scale may be the large-eddy turnover time. The possibility of resonance is intriguing as one may object that turbulence does not have a single time scale, but a continuum of strongly fluctuating times.

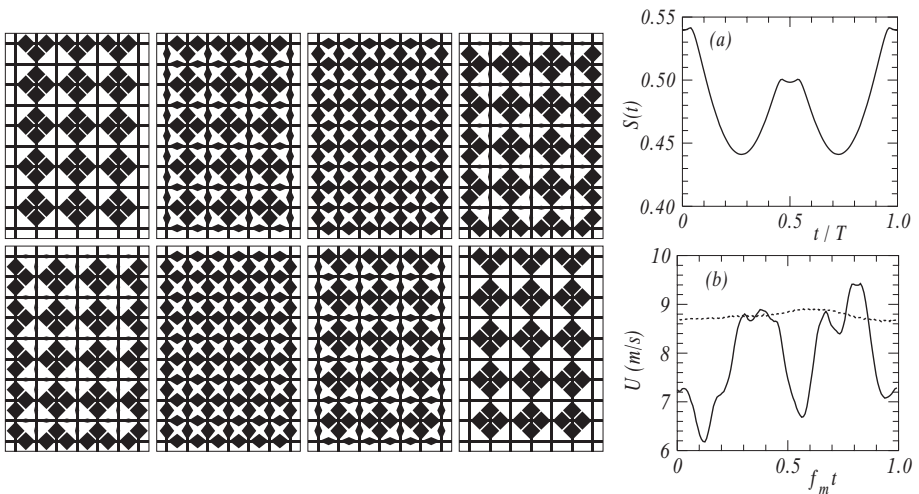


Fig. 1. Periodic pattern of active grid. (a) Its time-dependent transparency. (b) Full line: phase-averaged response at modulation frequency $f_m = 1\text{Hz}$, dashed line at 10 Hz.

We periodically modulate a strongly turbulent flow in a windtunnel using an active grid. Our active grid consists of a grid of rods with attached vanes that can be rotated by servo motors. We control the motion of the grid precisely by a computer which allows us to correlate the turbulent response with the instantaneous grid state.

Thus, the grid can be made to cycle periodically through a fixed series of patterns, or can be made to move completely randomly. The turbulent velocity field $u(y, t)$ is probed by an array of hot-wire anemometers, which gives access to the dissipation rate $\epsilon = 15\nu\langle\partial u/\partial x\rangle^2$. One of the ways to quantify the action of a grid is plotting its time-dependent transparency.

As figure 1 illustrates, the phase-averaged turbulent velocity adapts nearly adiabatically to the grid state at low driving frequencies f_m , while at large frequencies the turbulence is no longer able to follow the modulation.

Figure 2 shows a strong resonant response of the turbulence at a certain driving frequency. This frequency is close to the large-eddy turnover frequency. Thus, these experiments show that there are preferred frequencies with which to stir turbulence.

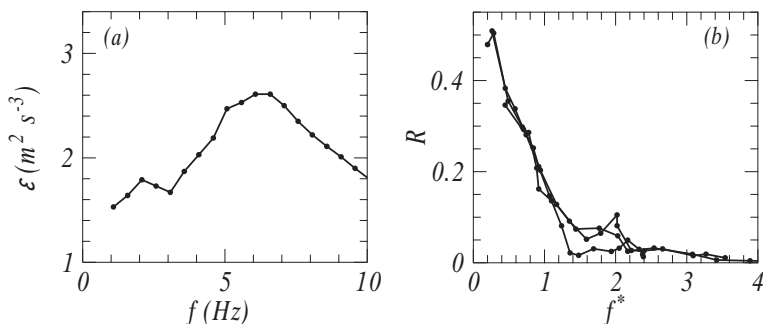


Fig. 2. (a) Large resonance effect in the averaged dissipation rate. (b) For several turbulence intensities the turbulence response R , defined as the fraction of the turbulent energy at the modulation frequency, show similar behavior as a function of the normalized driving frequency $f^* = f_m T$, with T the large-eddy turnover time.

There are several ways to realize the cyclic grid pattern of figure 1 and its associated transparency, for example by choosing different rotation senses of the axes. These details matter, however, defining the turbulence response in the same way as is done in numerical simulations [1, 2] results in similar behavior for all modes studied.

Periodic modulation of turbulence leaves its downwind trace as peaks in the spectrum at the modulation frequencies and its harmonics [3]. Also, periodic stirring may not be the optimal way to obtain large Reynolds numbers.

Random stirring has been explored by Mydlarski and Warhaft [3], with a simple protocol in which all axes rotate with the same frequency f , but with the direction of rotation changed randomly after a time T_r .

Although the turbulence spectrum is now no longer marred by sharp peaks, the correlation between the grid state and the turbulence remains strong. In our experiment, this correlation can be measured as we monitor the (random) grid state simultaneously with a measurement of the turbulence. The peak in the correlation function is shifted by x/U , where U is the mean velocity, signifying that the modulation is carried by the mean flow.

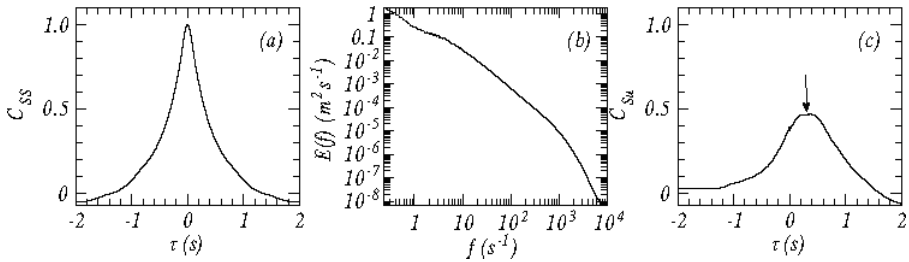


Fig. 3. Random modulation of turbulence using a protocol in which the direction of rotation of the grid axes is changed randomly. (a) Autocorrelation function of the grid transparency. (b) Turbulent spectrum at $x = 4.2\text{m}$ downstream of the grid. (c) Normalized cross correlation $C_{SU}(\tau)$ between the grid solidity and the turbulent velocity. The arrow indicates the time x/U .

The key question now is how to stir such that the correlation with the stirrer is weakest.

We will also present the relation of turbulence modulation to the fluctuation-dissipation theorem. A recent paper [4] showed that in order to test the physical relevance of the Fluctuation-Dissipation Relations response functions similar to the ones discussed here must be measured. The idea is that the size of turbulent fluctuations may be related to the response of the flow to small perturbations.

References

1. A. von der Heydt, S. Grossmann and D. Lohse, Phys. Rev. Lett., **68**, 066302-10 (2003)
2. A. K. Kuczaj, B.J. Geurts, D. Lohse and W. van de Water, Compt. Fluids, **37**, 816 (2008)
3. L. Mydlarski and Z. Warhaft, J. Fluid Mech. **320**, 331-368, (1996)
4. R. Monchaux, P.P. Cortet, P.H. Chavanis, A. Chiffaudel, F. Daviaud, P. Diribarne and B. Dubrulle, Phys. Rev. Lett., **101**, 174502, (2008)

Turbulent drag reduction by feedback: a Wiener-filtering approach

F. Martinelli¹, M. Quadrio¹, and P. Luchini²

¹Dipartimento di Ingegneria Aerospaziale, Politecnico di Milano, Milan, Italy
fulvio.martinelli@polimi.it

²Dipartimento di Meccanica, Università di Salerno, Fisciano (SA), Italy

In an attempt to devise control laws for reducing drag in turbulent wall flows, modern control theory has recently been employed for the design of linear controllers [1], state estimators [2], and compensators [3; 4]. These approaches led to encouraging results, revealing the potential of linear control in targeting significant dynamics in wall turbulence [5].

All the aforementioned works, however, rely on an approximate state-space representation of the system dynamics, obtained by linearization of the governing equations about a base flow profile. The state-space formulation reduces the compensator design problem to the solution of two matrix Riccati equations, a procedure that becomes computationally cumbersome for high-dimensional systems. Effects of nonlinearities and modeling errors are accounted for by introducing state and measurement noises with known (approximately modeled) statistics.

In contrast to previously proposed approaches, in this work we employ a linearized model of the wall-forced turbulent channel flow system in the form of an average impulse response function; such model is directly *measured* with DNS using the procedure proposed by Luchini et al. [6]. They introduced small velocity perturbations at the channel walls in the form of a space-time white noise, and computed runtime the cross-correlation between the flow state and the wall forcing. Leveraging a well known result in linear system theory, they used the computed correlation function to define a linear impulse response function, representing the average linear dynamics of a turbulent channel flow when impulsive wall forcing is applied.

A model given in the form of impulse response function would require first a state-space realization in order for standard Riccati-based control techniques to be applied. Instead of performing such realization – which would be impractical in the present very high-dimensional setting – we employ a frequency domain formulation of the optimal compensator design problem, that allows us to directly use the Fourier transform of the impulse response function (i.e. the frequency response function) in the compensator design pro-

cedure; this formulation has been first proposed by Luchini et al. [7; 8]. The block diagram of the feedback problem at hand is shown in fig. 1, where the feedback compensator having frequency response function $K(\omega)$ feeds the system, whose frequency response is $H(\omega)$, with a signal u determined on the basis of real-time measurement y , obtained with the sensor $C(\omega)$. Note that both the measurement and the state x are corrupted by disturbances d and noise n , respectively, that are supposed to be uncorrelated. The spectral density functions of the disturbances and noise will be denoted by $\phi_{dd}(\omega)$ and $\phi_{nn}(\omega)$, respectively, and may be functions of the frequency.

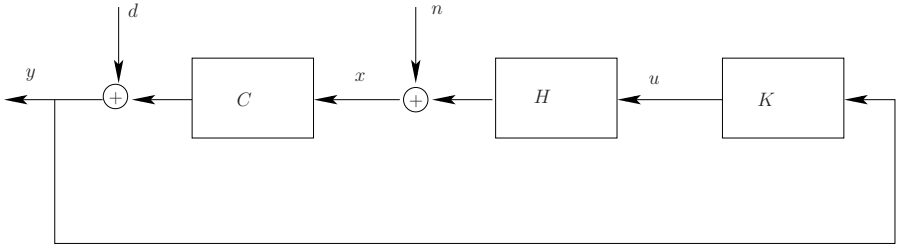


Fig. 1. Standard feedback control loop.

The goal is designing an optimal feedback compensator such that the usual LQG expectation functional

$$J = E\{x^H Q x + u^H R u\} \quad (1)$$

is minimized in the feedback controlled system; here, Q is a positive semidefinite hermitian matrix, and R is a positive definite weight of the control effort. Note that substitution of the closed loop relations in this functional leads to a form which is not quadratic in K . However, exploiting an Internal Model Control (IMC) approach, we can define a unique parametrization of all stabilizing compensators as

$$\bar{K} = (I - KCH)^{-1}K, \quad (2)$$

thus actually rewriting the feedback system in an equivalent open-loop form. This is a key step in the formulation, as the functional in (1) can now be written as a quadratic form of \bar{K} . Minimization of such functional with respect to \bar{K} then leads to a linear problem; causality of the compensator must be explicitly enforced so that the following Wiener-Hopf problem for \bar{K} is obtained:

$$(H^H Q H + R)\bar{K}_+ (C\phi_{nn}C^H + \phi_{dd}) + \Lambda_- = -H^H Q \phi_{nn}C^H. \quad (3)$$

In the above equation, plus and minus subscripts denote frequency response functions of causal and anticausal systems, respectively, and Λ is the Lagrange multiplier associated to the causality constraint for \bar{K} . It is noteworthy that

this procedure allows to design the optimal compensator in one single step, without the need to resort to the separation theorem. Note also that, in the single-input/single-output case, the coefficients of (3) are scalars, so that the optimal feedback compensator can be obtained from the solution of a scalar problem instead of two matrix Riccati equations, no matter how large is the number of states.

The spectral density functions of noise and disturbances appear in their functional form in the coefficients of (3); therefore, arbitrarily “colored” perturbations can be easily handled. We exploit this property by using, in the compensator design procedure, the true statistics of the flow as measured by DNS of an uncontrolled turbulent channel, thus accounting for the full spatio-temporal structure of the state noise; this is a fundamental difference with respect to previously proposed approaches, where approximate models for the noise statistics have been employed.

In the linearized setting, after Fourier transformation in streamwise and spanwise directions, the full control problem is reduced to a set of single-input/single-output control problems for each wavenumber pair (α, β) . Control laws are tested performing a DNS of turbulent channel flows, whose boundary condition on wall-normal velocity is computed runtime from the convolution integral

$$\hat{v}_{wall}(\alpha, \beta, t) = \int_0^t \hat{K}(\alpha, \beta, \tau) \hat{m}(\alpha, \beta, t - \tau) d\tau, \quad \forall \alpha, \beta;$$

here, hats denote Fourier coefficients, $\hat{K}(\alpha, \beta, t)$ is the impulse response function of the optimal compensator, and $\hat{m}(\alpha, \beta, t)$ denotes the history of the wall measurement. Upon inverse Fourier transformation to physical space, the spatial structure of the compensator can be recovered in the form of a convolution kernel; fig. 2 shows such kernel at zero time lag, i.e. the function $K(x, z, 0)$, for a kernel based on streamwise skin friction measurement.

We have designed and tested feedback compensators for turbulent channel flows at $Re_\tau = 100$ and $Re_\tau = 180$, using two state weighting matrices (namely, derived from the energy and dissipation norms), actuating with the wall-normal velocity at the walls, and measuring either one of the skin friction components or pressure fluctuations; this required about 300 DNS of controlled turbulent channel flows, that were performed on a computing system, located at the University of Salerno, dedicated to the simulation of wall turbulence.

A summary of the performance assessment is reported in Table 1. Results indicate that, employing any of the available measurements and for the two values of Re_τ considered, weighting matrix derived directly from the energy norm is ineffective in providing drag reducing compensators. This is consistent with previous findings by Lim [4], who succeeded in obtaining drag reduction only by employing weighting matrices derived from other relations, for instance from the output equation. On the other hand, our results demonstrate

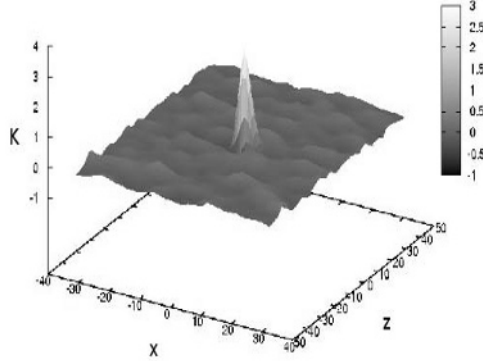


Fig. 2. Spatial representation of the impulse response function of the control kernel at zero time lag, $K(x, z, 0)$, when measurement of streamwise skin friction is employed.

	Dissipation			Energy		
Re_τ	τ_x	τ_z	p	τ_x	τ_z	p
100	2%	0%	0%	0%	0%	0%
180	8%	6%	0%	0%	0%	0%

Table 1. Best performance drag reduction results, as a function of Re , state weighting and measurement. Accuracy of the drag reduction is estimated to be $\approx \pm 1\%$. The values 0% indicate that no measurable difference in the average skin friction was obtained with respect to the uncontrolled case.

that state weighting matrix derived directly from the dissipation rate of turbulent kinetic energy leads to effective compensators. Among these, the best performing ones require the measurement of wall skin friction components, and the overall best performance result – obtained using streamwise skin friction measurement – yields a maximum drag reduction of $\approx 8\%$ at $Re_\tau = 180$. Since actuation with the wall-normal velocity component requires an energetic expenditure, it is interesting to quantify the net power saved when control is applied by the following ratio:

$$P.R. = 100 \frac{P_r - P_c}{P_r},$$

where P_r is the power required to drive the uncontrolled flow against viscous stresses, while P_c is that required to drive the controlled flow plus the control action, estimated as suggested in [9]. The power required for the control action was found to be $\approx 0.2\%$ of P_r , and the corresponding power reduction index is $P.R. \approx 7.7\%$.

It is interesting to note that compensators designed using the dissipation norm yield better performance at higher values of Re . This “inverse” Re -effect can be attributed to the fact that the ratio between the turbulent component (associated to turbulent fluctuations) and the mean component (associated to the mean flow) of the total dissipation rate increases with Re . As the present optimal compensators are designed to directly target turbulent fluctuations only (and, therefore, the turbulent component of the dissipation), their drag reducing capability increases with Re , probably up to a certain saturation limit to be determined in future work.

The present formulation allows the design of compensators accounting for the measured temporal and spatial structure of the noise statistics, as well as the measured average dynamics of wall-forced turbulent channel flow. As such, it actually represents an effective tool to devise the best possible linear time-invariant feedback control strategy for the problem at hand. In light of the results obtained in the present work, as well as of those reported in the recent literature, we emphasize the importance of selecting an appropriate objective function in the control design: it appears to be the most important degree of freedom for the present problem. Therefore, in future work we aim at exploiting the computational effectiveness of the present compensator design strategy to test a wide variety of objective functions, in order to quantitatively assess limiting performance of linear optimal compensators for drag reduction in wall turbulence.

References

- [1] M. Högberg, T.R. Bewley, and D.S. Henningson. Relaminarization of $Re_\tau = 100$ turbulence using gain scheduling and linear state-feedback control. *Phys. Fluids*, 15(11):3572–3575, 2003.
- [2] M. Chevalier, J. Höpfner, T.R. Bewley, and D.S. Henningson. State estimation in wall-bounded flow systems. Part 2. Turbulent flows. *J. Fluid Mech.*, 552:167–187, 2006.
- [3] K.H. Lee, L. Cortelezzi, J. Kim, and J. Speyer. Application of reduced-order controller to turbulent flows for drag reduction. *Phys. Fluids*, 13(5), 2001.
- [4] J. Lim. Control of wall-bounded turbulent shear flows using modern control theory Ph.D. Thesis, Univ. of California, Los Angeles, 2003
- [5] J. Kim and J. Lim. A linear process in wall-bounded turbulent flows. *Phys. Fluids*, 12(8):1885–1888, 2000.
- [6] P. Luchini, M. Quadrio, and S. Zuccher. Phase-locked linear response of a turbulent channel flow. *Phys. Fluids*, 18(121702):1–4, 2006.
- [7] P. Luchini, T.R. Bewley, M. Quadrio. An optimal feedback controller for the reduction of turbulent energy in 3D plane-duct flow. APS Meeting, Chicago, 2005

- [8] P. Luchini. Phase-locked linear response and the optimal feedback control of near-wall turbulence. *Mathematical Physics Models and Engineering Sciences*, Liguori Editore, Naples, 2008.
- [9] T.R. Bewley, P. Moin, R. Temam. DNS-based predictive control of turbulence: an optimal benchmark for feedback algorithms *J. Fluid Mech.*, 447:179–225, 2001.

**Part IV Vortex dynamics and structure
formation**

A driving mechanism of turbulent puff in pipe flow

M. Shimizu¹ and S. Kida²

Dep. Mech. Eng. Sci., Graduate School of Engineering, Kyoto Univ., Kyoto, Japan
¹shimizu@me.kyoto-u.ac.jp ²kida@mech.kyoto-u.ac.jp

Introduction Pipe flow is one of the most elemental and important problem in fluid mechanics. As noticed in Reynolds' experiments (1883), the flow can be partially turbulent at Reynolds number Re_m around 2000 – 3000, where $Re_m = 2a\bar{u}_z/\nu$ is based on the cross-sectional mean velocity \bar{u}_z , the pipe diameter $2a$ and the kinematic viscosity ν of fluid. Such localized turbulent regions are called "puffs". Wygnanski *et al.* (1975) investigated puffs in detail and observed an equilibrium puff at $Re_m = 2250$ which preserves its length indefinitely. Since then many works have been performed about an equilibrium puff as a fundamental object. The dynamical characteristics, in particular the driving mechanism of the puff, however, remain unsolved. Here we investigate numerically the spatio-temporal structure of an equilibrium puff. A driving mechanism of the puff is identified as the Kelvin-Helmholtz (KH) instability, and a self-sustenance mechanism is proposed.

DNS of Pipe Flow We consider the flow in a circular pipe of radius a driven by a constant body force. The Navier-Stokes equation for an incompressible viscous fluid of kinematic viscosity ν is described in the cylindrical coordinate (r, θ, z) and is solved numerically by the spectral method. The boundary

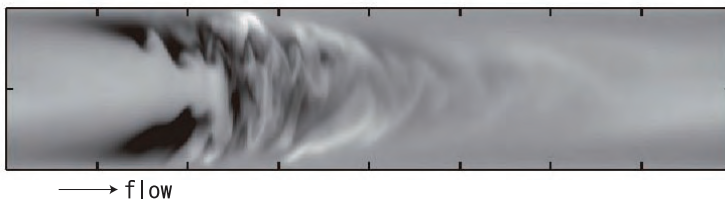


Fig. 1. Distribution of axial velocity $u_z - \langle u_z \rangle_{\theta, z}$ on a diametrical plane. Larger values in brighter regions. $t = 2000a/U$.

conditions are non-slip on the wall and periodic in the axial direction with period $L = 16\pi a (\simeq 50a)$. The Reynolds number is defined by $Re = Ua/\nu$ and set at 3000, the value around the laminar/turbulent transition Reynolds number. Here, U is the centerline velocity of the above HP flow. Using two scalar functions, ψ and ϕ , the velocity field is represented as $\mathbf{u} = \nabla \times (\hat{\mathbf{z}}\psi) + \nabla \times (\nabla \times (\hat{\mathbf{z}}\phi))$. These functions are expanded as

$$\begin{pmatrix} \psi \\ \phi \end{pmatrix} = \sum_{k=-K}^K \sum_{m=-M}^M \sum_{\substack{n=|m| \\ n+m=\text{even}}}^N \begin{pmatrix} \hat{\psi}_n^{mk} \\ \hat{\phi}_n^{mk} \end{pmatrix} \Phi_n^m(r) e^{i(m\theta + 2\pi kz/L)},$$

where Φ_n^m are the Zernike circular polynomials (Bhatia and Born (1954), Matsushima and Marcus (1995)). With the use of these polynomials, the analytic condition on the cylinder axis ($r = 0$) is guaranteed naturally and the CFL conditions there is not stiff. The evolution equations for $\hat{\psi}_n^{mk}$ and $\hat{\phi}_n^{mk}$ are solved numerically with the time step 0.005 and maximum mode number $(N, M, K) = (80, 31, 511)$ (see Shimizu and kida (2008) for details of the numerical method.) The initial condition is given by the Hagen-Poiseuille flow (corresponding to the body force) superposed by a disturbance of finite amplitude strong enough to cause turbulence.

Equilibrium puff After an initial transient period, $t < 200a/U$, a localized turbulent region of about $35a$ in length emerges. In Fig. 1 we show a snapshot of the distribution of axial velocity field on a diametrical plane over the whole computation box. A localized turbulent region is clearly observed. The upstream boundary of this region called the trailing edge is sharp, whereas that in the downstream called the leading edge is obscure. This turbulent region advects downstream nearly the mean flow velocity ($u_p \approx 0.96\bar{u}_z$). The axial length of this region varies between $30a$ and $40a$ throughout the computation time ($\leq 3000a/U$). Thus it may be regarded as an equilibrium puff.

As the usual wall-bounded turbulence, the streamwise vortices and the

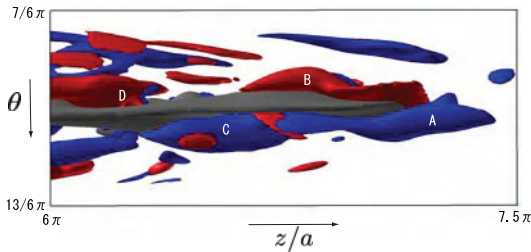


Fig. 2. A low-speed streak and accompanied streamwise vortices, viewed inward from the pipe wall.

associated low-speed streaks are repeatedly created and annihilated in the puff. In Fig. 2 are shown a low-speed streak and accompanied streamwise vortices. The regions of low axial velocity are plotted with light gray iso-

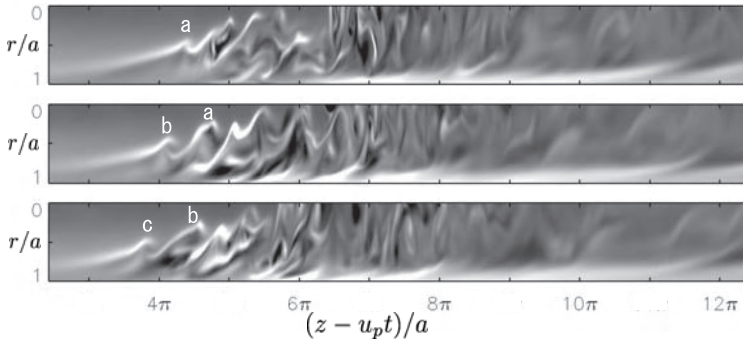


Fig. 3. Successive roll-ups of a vortex layer, viewed in the moving frame with the puff. $t = 2278, 2290$ and $2302a/U$ downward. Alphabets a, b and c identify the individual roll-ups.

surfaces, whereas streamwise vortices with iso-surfaces of positive (B and D) and of negative axial vorticity (A and C). Alphabets A, B, C and D identify the individual streamwise vortices. The flow is directed from left to right. Observe that the vortices A and C are inclined upward (to the negative azimuthal direction) toward downstream, whereas the B and D inclined downward. This is the characteristics commonly observed in wall turbulence.

Low-speed streaks and KH instability These low-speed streaks move upstream relative to the puff, across the trailing edge and create strong vortex layers together with the laminar flow coming from upstream. The vortex layers are unstable to roll up, through the KH instability, to induce velocity fluctuations which propagate downstream faster than the puff itself and enhance the

turbulent activity in it. In Fig. 3 are shown a series of roll-ups of a vortex layer above a low-speed streak. This is identified as the KH instability by comparing the wavelength with the linear stability theory (Betchov and Szewczyk 1963). Note that the width

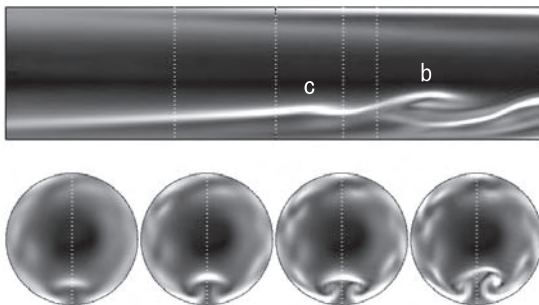


Fig. 4. A vortex layer above a low-speed streak (top) and its round cuts (bottom). $t = 2286a/U$.

(comparable to that of the low-speed streak underneath) is several times larger than the thickness as shown in Fig. 4. These roll-ups continuously produce disturbances at the trailing edge and sustain the puff.

Self-Sustenance Cycle The above observation suggests the following scenario of self-sustenance cycle of puffs.

- (i) The turbulence in the puff creates low-speed streaks (accompanied with streamwise vortices) along the pipe wall in the same way as many kinds of wall turbulence.
- (ii) These low-speed streaks move upstream relative to the puff and penetrate the trailing edge.
- (iii) Near-upstream of the puff strong shear layers are created between two counter flows, namely, the low-speed streaks and laminar flow coming down from far-upstream.
- (iv) These shear layers are rolled up through the KH instability to create new fluctuations.
- (v) The majority of these fluctuations propagate downstream faster than the puff, penetrate the trailing edge and enhance turbulent activity in the puff. Then the process goes back to (i).

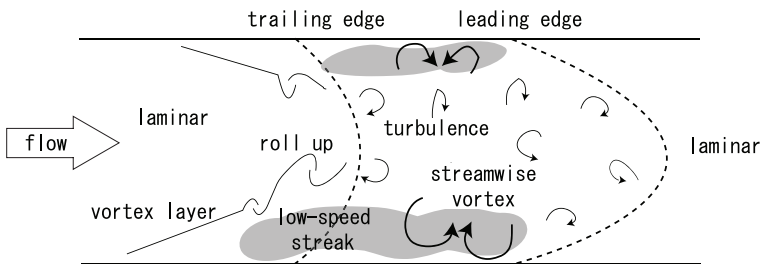


Fig. 5. Schematic of an equilibrium puff in pipe flow. The puff sandwiched by the leading edge and the trailing edge is advected with nearly the mean fluid velocity. The turbulent activity and the low-speed streaks in the puff as well as the vortex layer near-upstream of the trailing edge constitute a self-sustenance cycle together.

References

- Betchov, R. and Szewczyk, A., 1963. *Phys. Fluids*, **6**, 1391.
 Bhatia, A.B. and Born, M., 1954. *Proc. Cambridge Phil. Soc.*, **50**, 40.
 T. Matsushima, T. and Marcus, P.S. 1995. *J. Comp. Phys.* **120**, 365.
 Reynolds, O. 1883. *Phil. Trans. R. Soc. Lond.* **A 174**, 935.
 Shimizu, M. and Kida, S. 2008. *J. Phys. Soc. Jpn.* **77**, 114401.
 Wygnanski, I.J., Sokolov, M. and Friedman, D. 1975. *J. Fluid Mech.*, **69**, 283.

Wavelet tools to study vortex bursting and turbulence production

M. Farge¹, J. Ruppert-Felsot^{1,2}, and P. Petitjeans²

¹ LMD-IPSL-CNRS, Ecole Normale Supérieure, 24 rue Lhomond 75239 Paris Cedex 05, France, farge@lmd.ens.fr

² PMMH, ESPCI, 10 rue Vauquelin, 75231 Paris Cedex 05, France

Since there is not yet any agreement among specialists of turbulence about what coherent structures are and which method is the best to extract them, we propose an apophatic approach where, rather than stating what the coherent structures are, we make assumption about what they are not. We suppose that *coherent structures are different from noise*, and we thus define them as *what remains after denoising*. For the noise we use the mathematical definition of randomness, stating that a noise is homogeneously distributed in any functional basis.

To get started we choose the simplest hypothesis for the noise, namely that it is additive, Gaussian and white, *i.e.*, decorrelated. It has been demonstrated [2] that the optimal threshold (in a minmax sense) to remove an additive Gaussian white noise is $\epsilon = \sqrt{2\sigma^2 \log_e N}$, where σ^2 is the variance of the noise and N the resolution of the field to denoise. This value ensures a vanishing probability to the wavelet coefficients of the noise whose modulus is larger than the threshold. Since for turbulent flows the variance of the noise we want to remove is not known *a priori* and evolve in time, we have developed [1] a recursive algorithm to estimate it from the variance of the weakest wavelet coefficients to obtain the optimal threshold ϵ_{opt} . To extract coherent structures we have proposed [3] to split the vorticity field into two orthogonal components. One first computes the orthogonal wavelet transform of vorticity, then the wavelet coefficients whose modulus is larger than ϵ_{opt} are inverse wavelet transformed to reconstruct the coherent vorticity, which retains all coherent structures while the remaining incoherent component is structureless. This wavelet eduction method presents several advantages in comparison to previous ones [4]:

- it does not implicitly assume ensemble averaging and works for each flow realization independently of the others,
- it does not require to adjust any parameter, such as a threshold value, or a template,

- it is quite insensitive to the choice of the wavelet basis, since it is the multiresolution construction of the basis and not the wavelet shape which matters, *i.e.*, wavelets are not used as templates but as a way to organize the data in a scale-dependent fashion,
- it tracks coherent structures even when their shape and amplitude change due to, *e.g.*, pairing, stretching or tearing,
- it allows to process 'incomplete data', *i.e.*, when the dimensionality of the measured data is lower than the dimensionality of the flow itself,
- the computation is fast since it scales in $O(N)$ operations.

We apply the wavelet eduction method to analyze the bursting of a three-dimensional stretched vortex immersed in a steady laminar channel flow. The time evolution of a two-dimensional cut of the velocity field is measured by particle image velocimetry (PIV) during several successive bursts recorded at 15 double frame per second. At each instant we compute the vorticity component perpendicular to the observation plane and, using wavelet eduction, we split it into two orthogonal components: the coherent vorticity and the incoherent vorticity which are then analyzed independently. In Fig. 1 we show that the coherent vorticity evolution is very similar to the total vorticity evolution, both being highly non stationary and presenting the same coherent structures. In contrast, the incoherent vorticity remains stationary and homogeneous all along the bursting process. In Fig. 2 we observe that the spectral slope of enstrophy strongly varies in time, although the Kolmogorov scaling ($k^{+1/3}$ for enstrophy corresponding to $k^{-5/3}$ for energy) is recovered after averaging in time. We also find that before the vortex bursts the coherent component retains 98% of the total enstrophy Z . This proportion drops to about 60% Z when the vortex bursts, and later becomes negligible as the remnants of the vortex are swept out of the observation window. In contrast, the incoherent enstrophy remains negligible before vortex bursting and suddenly rises to 40% Z at the instant of bursting. We propose a new diagnostic, the coherency measure (CM), to estimate the instantaneous turbulence level and track the turbulence production when the vortex bursts. It is defined as the signal to noise ratio between the coherent enstrophy and the incoherent enstrophy [5]. In order to better understand the buildup of the turbulent cascade and to quantify the flow intermittency, we use the local intermittency measure (LIM) *i.e.*, the spatial variability of the enstrophy at each scale, or likewise the spatial deviation from the mean enstrophy spectrum. It allows us to find out when in time, where in space, and at which scale the nonlinear activity is dominant. We have thus found that the bursting process starts as an excitation of the small scales inside the vortex core, which then spreads in space and all over the inertial scales. This result is confirmed by visualizing the dye concentration recorded at 1000 frames per second using a fast camera.

Acknowledgements: JRF thanks the 'Agence Nationale pour la Recherche' (ANR) for financing his post-doctoral research and MF is grateful to the Association CEA-Euratom for supporting her research under contract n° V.3258.001.

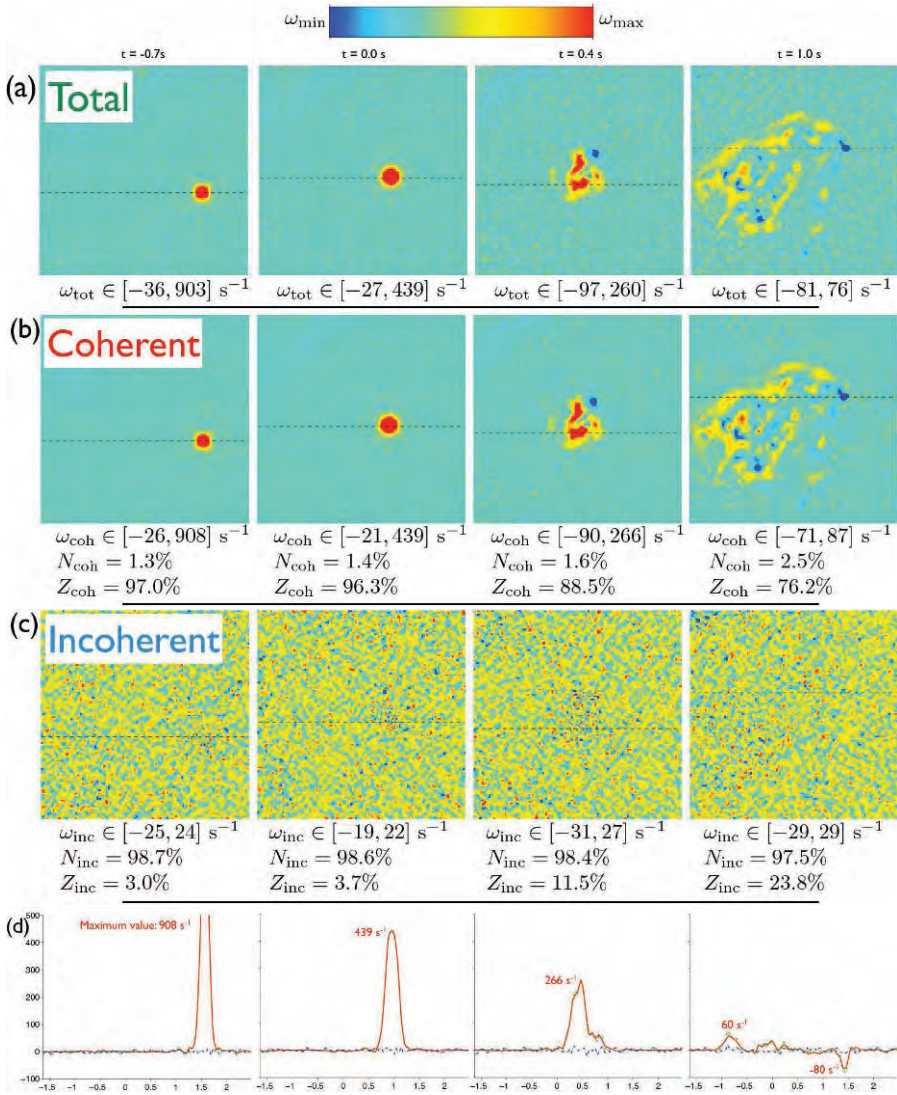


Fig. 1. Time evolution of the (a) total, (b) coherent and (c) incoherent vorticities at instants $t = \{-0.7, 0, 0.4, 1.0 \text{ s}\}$, with $t = 0$ the beginning of bursting. The number of coefficients and percentage of enstrophy retained in each component, and the extrema of vorticity are indicated below the snapshots. (d) 1D cuts along the vorticity at the location of the maxima. The dashed green, solid red, and dotted-dashed blue lines represent the total, coherent, and incoherent fields respectively.

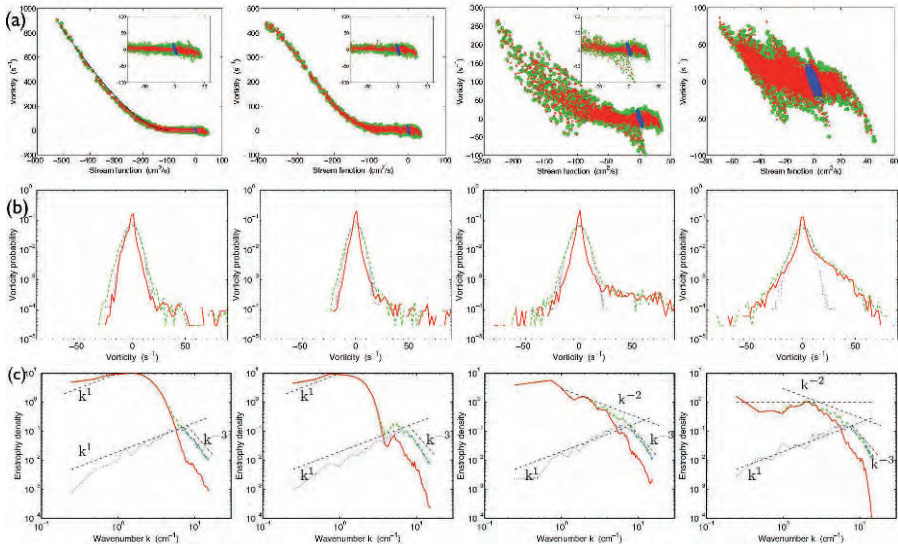


Fig. 2. Time evolution of the total (dashed green line), coherent (solid red line) and incoherent (dotted blue line) flows during one bursting event at instants $t = \{-0.7, 0, 0.4, 1.0 s\}$, with $t = 0$ the beginning of bursting. Top: **(a)** Scatter plot of the vorticity versus stream function characterizing the flow coherency. The total and coherent distributions are nearly indistinguishable and evolve in time, while the incoherent remains stationary and localized near the origin. Note that, since the flow is highly non-stationary, the scale on the plots changes in time. The insets show a zoom in a fixed region near the origin which corresponds to the limits on the last figure. Middle: **(b)** Probability distribution function (PDF) of vorticity. The total and coherent vorticities exhibit the same non-Gaussian PDF which evolves in time, while the incoherent vorticity remains Gaussian and stationary. Bottom: **(c)** Enstrophy spectrum. The total and coherent spectra have the same scaling at large scale which strongly varies in time, in contrast to the incoherent spectrum which remains stationary and close to the k^1 scaling of a Gaussian white noise.

References

1. A. Azzalini, M. Farge, and K. Schneider, *Appl. Comput. Harmonic Analysis*, **18**, 177–185 (2005).
2. D. Donoho and I. Johnstone, *Biometrika*, **81**, 425–455 (1994).
3. M. Farge, G. Pellegrino, and K. Schneider, *Phys. Rev. Lett.*, **87**(5), 054501 (2001).
4. A. K. M. F. Hussain, *J. Fluid Mech.*, **173**, 303–356 (1986).
5. J. Ruppert-Felsot, M. Farge, and P. Petitjeans, *J. Fluid Mech.*, revised (2009).

The minimum-entropy principle for decaying 2D turbulence in circular domains

G.H. Keetels, H.J.H. Clercx, and G.J.F. van Heijst

Physics Department, Eindhoven University of Technology, PO Box 513, 5600 MB Eindhoven, The Netherlands
h.j.h.clercx@tue.nl

Introduction

In several numerical and experimental studies [1, 2] on freely evolving or decaying two-dimensional (2D) turbulence on a square bounded domain it is observed that a flow, initially containing no net angular momentum (L), spontaneously acquires angular momentum by flow-wall interaction. From earlier work, by Li and Montgomery [3], it could be conjectured that on a circular domain with a no-slip boundary angular momentum production is absent. Decaying turbulence experiments in stratified fluids conducted a few years later by Maassen *et al.* [4] provided additional evidence supporting this conjecture. These observations have recently been confirmed by Schneider and Farge [5] for decaying 2D turbulence with substantially higher initial integral scale Reynolds numbers.

Set-up of the numerical simulations

We revisit this problem to analyse the late-time evolution in the framework of the minimum-entropy principle with emphasis on different decay scenarios. For this purpose the quasi-stationary final states of decaying 2D turbulence on a circular domain, with an initial flow field containing either no or a substantial amount of angular momentum, have been investigated numerically. Typical initial integral-scale Reynolds numbers, defined by the root-mean-square velocity of the flow and the radius of the container, is $Re \approx 5000$. This value is between those from the runs by Li and Montgomery [3] ($Re \approx 1000$) and by Schneider and Farge [5] ($Re \approx 5 \times 10^4$). This choice is a compromise as during the initial stage full 2D turbulence should be generated while still allowing long-time computations to access the full decay scenario. These simulations have been carried out with a 2D Fourier pseudospectral code. The no-slip boundary conditions are enforced by a volume-penalization method to mimick the solid geometry [6, 7]. The production of angular mo-



Fig. 1. Snapshots of the vorticity distribution of a $Re = 5000$ simulation initiated with $L = 0$. From left to right: early-time, intermediate and long-time flow evolution.

momentum is almost absent for these flows on a circular domain with a no-slip wall, see Fig. 1 for a few snapshots of the vorticity field during the flow evolution. In Fig. 2 we have shown the evolution of the (normalized) angular momentum (left) and the integral length scale of the flow for this particular run. It is clearly seen that the angular momentum remains approximately zero (dashed curve). Its presence or absence in the initial state essentially determines the character of the quasi-stationary final state.

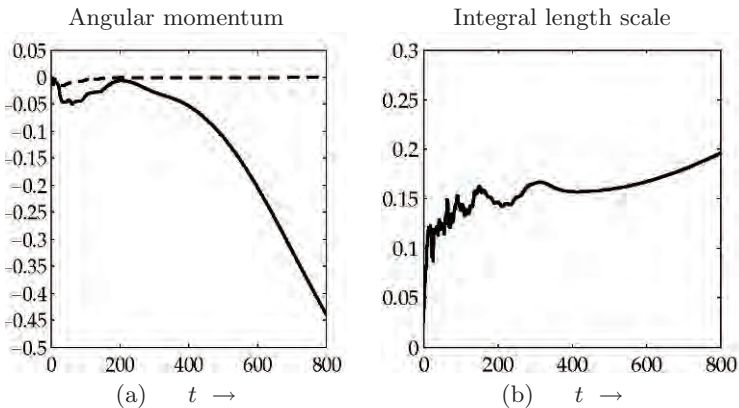


Fig. 2. (a) Angular momentum L normalized with $L_{sb}(t = 0)$ (dashed line) and $L_{sb}(t)$ (solid line) and (b) the integral length scale \mathcal{L} . Data correspond with the vorticity as shown in Fig. 1 with initial Reynolds number $Re = 5000$ and angular momentum $L = 0$.

Decaying 2D turbulence: late-time flow patterns

Based on a minimum-entropy principle a diagram can be constructed that provides insight in the development of the typical late-time flow patterns on a

circular domain with a no-slip wall. The quasi-stationary final states found in the present numerical study can be understood based on the predictions from the minimum-entropy principle. An example is provided in Fig. 3 where the quasi-stationary state observed in the simulations displayed in Fig. 1 can be understood in terms of a combination of two (local) minimum-entropy solutions.

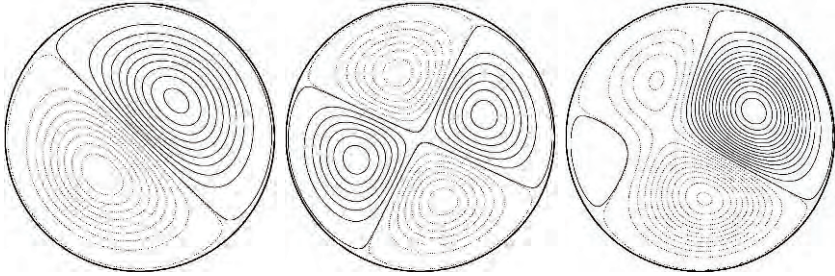


Fig. 3. Stream function distribution of two minimum-entropy solutions (with $L = 0$, left and middle panel) and a linear combination of the two (right panel).

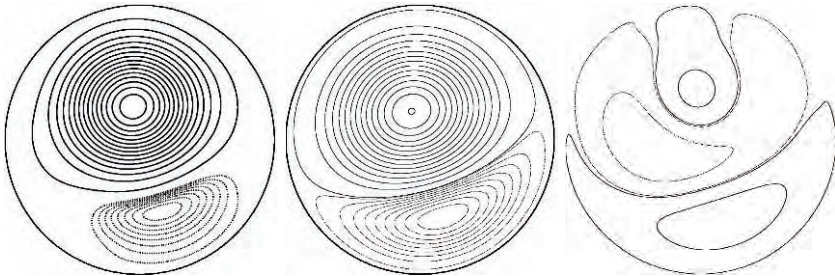


Fig. 4. a) Stream function for a decaying turbulence run with an initial field containing angular momentum (normalised angular momentum at $t = 0$: $L = 0.18$). Increments for negative (solid contours) and positive (dashed contours) values are different. b) Minimum entropy state based on the parameters of the snapshot shown in a). c) The stream function of the residual between minimum-entropy state and the stream function shown in a).

A further example concerns a decaying 2D turbulence run with an initial field containing angular momentum (normalised angular momentum at $t = 0$: $L = 0.18$). It can be shown that the flow relaxes directly towards the asymmetric dipole state [8]. There is no sign of dipole-quadrupole transitions like in the case without initial angular momentum, as shown in Fig. 1. In Fig. 4a we show the stream function for the quasi-stationary final state. To demonstrate the possibility to connect the data from the decaying turbulence simulations

with the minimum enstrophy states we use the data from this particular run. A comparison of these data with the minimum enstrophy state (for details, see Ref. [8]) reveals excellent agreement, see Figs. 4b and c. In Fig. 4b the minimum enstrophy state is shown based on the parameters of the snapshot shown in Fig. 4a. The right panel shows the stream function of the residual between minimum-enstrophy state and the stream function shown in Fig. 4a. The energy contained in the residual flow is less than 10% of the kinetic energy of the total flow.

Conclusions

Direct numerical simulations of decaying 2D turbulence on a circular domain with a no-slip boundary have been performed with a Fourier spectral approach with volume-penalization. The computations have been carried out at moderate Reynolds number (based on the initial rms velocity and the radius of the circle) and show similar behaviour as found in the numerical simulations of Li and Montgomery [3] and in the experiments conducted by Maassen *et al.* [4, 2] in density-stratified fluids. It was conjectured in these numerical and experimental studies that significant production of angular momentum is absent for flows on a circular domain with a no-slip wall. This conjecture is supported in the present numerical study (see also Ref. [5]). Therefore, the angular momentum of the initial condition has important consequences for the late-time evolution of the flow. Different flow initializations have been considered in the present study and its consequences for the quasi-stationary final states have been explored. Based on a minimum enstrophy principle a diagram is constructed that provides insight in the development of very typical flow patterns [8].

References

1. H.J.H. Clercx, S.R. Maassen and G.J.F. van Heijst, *Phys. Rev. Lett.*, **80**, 5129 (1998).
2. S.R. Maassen, H.J.H. Clercx and G.J.F. van Heijst, *Phys. Fluids*, **14**, 2150 (2002).
3. S. Li and D. Montgomery, *J. Plasma Phys.*, **56**, 615 (1996).
4. S.R. Maassen, H.J.H. Clercx and G.J.F. van Heijst, *Europhys. Lett.* **46**, 339 (1999).
5. K. Schneider and M. Farge, *Phys. Rev. Lett.* **95**, 244502 (2005).
6. E. Arquis and J.P. Caltagirone, *C. R. Acad. Sci. Paris*, **299** (1984).
7. Ph. Angot, C.-H. Bruneau and P. Fabrie, *Numer. Math.* **81**, 497 (1999).
8. G.H. Keetels, H.J.H. Clercx and G.J.F. van Heijst, *Physica D*, in press (2009).

Direct numerical simulation of a turbulent vortex ring

P.J. Archer, T.G. Thomas and G.N. Coleman

School of Engineering Sciences, University of Southampton, UK
pja@soton.ac.uk

1 Introduction

Engineers have been fascinated by vortex rings for over a hundred years, due to their numerous engineering and biological applications and their presence as a constituent of fully turbulent flow. Although the laminar ring has received much attention, the turbulent vortex ring is less well understood, due to the difficulty in its visualisation and measurement. Glezer and Coles [1] used ensemble averaging of experimental data to show that the radial expansion, circulation decay and slowing of the turbulent ring occur in a self-similar fashion. Circulation decreases in a staircase-like fashion [2] as the ring sheds hairpin vortices [3] into a wake. The radial growth of the ring is due to a slight excess in the amount of entrainment over detrainment [1]. The movement of dye within the ring suggests the existence of secondary vortices that wrap around the core, influencing the local entrainment, detrainment and production of turbulence [1]. In previous work [4], we investigated the laminar evolution of the ring and focused on the development of the Tsai-Widnall-Moore-Saffman (TWMS) instability [5, 6], and transition to turbulence. Here, we examine the temporal development of the turbulent vortex ring.

2 Numerical procedure

We perform a direct numerical simulation in which the incompressible Navier-Stokes equations are discretized on a staggered cartesian grid using second-order finite differences in space with Adams-Bashforth stepping in time; see Yao *et al.* [7] for further details. The method for prescribing the initial velocity field and the boundary conditions is reported in [4]. Of note, we employ a co-moving frame of reference and impose inflow and outflow boundary conditions in the direction of ring propagation, i.e. along the z -axis, rather than the periodic conditions used in the other directions. This prevents the ring from passing through its own wake and disturbing its dynamics. Furthermore, the

speed of the co-moving frame is adjusted to keep the ring in the centre of the computational box using a tracking system and controller.

The initial conditions are a laminar ring with a Gaussian distribution of vorticity. The ring is perturbed from being perfectly circular by addition to the local radius of a set of Fourier modes [1-32], which have random phase and an amplitude of $0.0002R_0$. The ring is susceptible to the TWMS instability, which displaces the core into a stationary wave around the circumferential axis of the ring and whose shedding marks the transition to turbulence [4]. Here, we present preliminary results for a ring of initial radius R_0 , circulation Γ_0 and slenderness ratio $\epsilon_0 = \delta_0/R_0 = 0.2$ (where δ_0 is the initial core radius), which propagates at Reynolds number $\text{Re} = \Gamma_0/\nu = 7500$. The cubic computational domain is of length $8R_0 \times 8R_0 \times 8R_0$ and uses 512^3 grid cells.

3 Results

The transition to turbulence is accompanied by the shedding of vorticity filaments into a wake [4], reducing the circulation of the ring. For the thin-core ring considered here, the rate of circulation loss is initially small (see figure 1(a), phase I) but then increases and is approximately linear (phase II) with a staircase-like behaviour, found in the experiments of Weigand and Gharib [2]. The initial period of lower circulation decay was not observed by Weigand

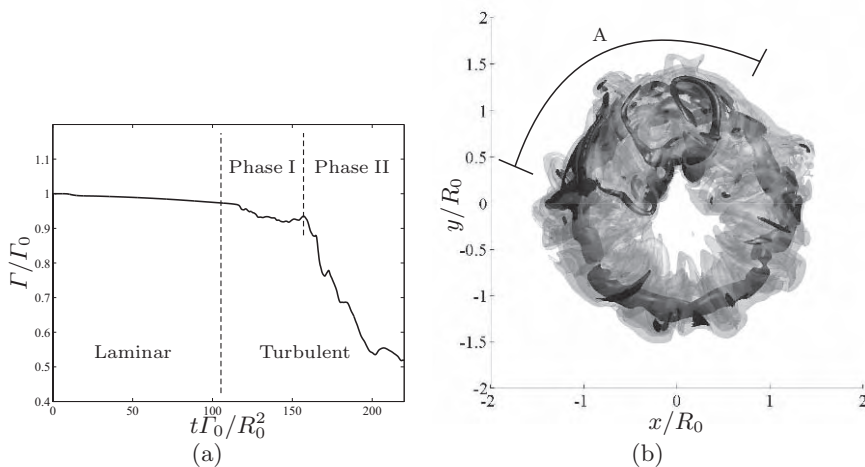


Fig. 1. (a) Decay of ring circulation against time (b) Vortical structure at time $t\Gamma_0/R_0^2 = 120.7$ visualised with isosurfaces of vorticity magnitude $|\omega|$, dark isosurface corresponds to high vorticity ($|\omega| R_0^2/\Gamma_0 > 10$), translucent light isosurface represents regions of low vorticity ($|\omega| R_0^2/\Gamma_0 > 1$). The region of more intense turbulence is marked with the letter ‘A’.

and Gharib [2]. This could be due to the more slender ring considered here. For our thin-core ring, the core initially breaks down to turbulence at the location of greatest wave growth of the TWMS instability. The onset of turbulence then ‘passes’ around the circumference of the ring and as a result is more intense in the region indicated in figure 1(b). By the end of phase I the ring is more equally turbulent around the entire circumference. This contrasts with our results for thicker-core rings (like those investigated by Weigand and Gharib), for which the TWMS instability develops more uniformly around the azimuth of the ring, leading to a more simultaneous onset of turbulence and an absence of the initially weak decay present in phase I.

In order to gain insight into the ring’s turbulent structure and statistics we interpolate the velocity field onto a cylindrical-polar grid with corresponding velocity components $\mathbf{u} = (u_r, u_\theta, u_z)$. A mean value (denoted with $\langle \rangle$) for each of the velocity components is defined by averaging around the circumference of the ring. The local fluctuations (denoted by a dash) from the mean velocity can then be obtained by

$$u'_r = u_r - \langle u_r \rangle, \quad u'_\theta = u_\theta - \langle u_\theta \rangle, \quad u'_z = u_z - \langle u_z \rangle. \quad (1)$$

The Reynolds stresses $\langle u'_i u'_j \rangle$ are defined similarly. The vertical normal stress $\langle u'_z u'_z \rangle$ is largest and concentrated mainly in the core region (figure 2(c)). The $\langle u'_r u'_r \rangle$ and $\langle u'_\theta u'_\theta \rangle$ stresses, on the other hand, are more intense near to the centreline of the ring, where vortex filaments trail into the wake and are stretched axially in the z -direction. The presence of the trailing vortical filaments is shown in contours of $\langle u_\theta \rangle$ (figure 2d).

Turbulence kinetic energy production P_r is defined in cylindrical coordinates as

$$\begin{aligned} P_r = & -\langle u'_r u'_r \rangle \frac{\partial \langle u_r \rangle}{\partial r} - \langle u'_\theta u'_\theta \rangle \left(\frac{1}{r} \frac{\partial \langle u_\theta \rangle}{\partial \theta} + \frac{\langle u_r \rangle}{r} \right) - \langle u'_z u'_z \rangle \frac{\partial \langle u_z \rangle}{\partial z} \\ & - \langle u'_r u'_\theta \rangle \left(\frac{\partial \langle u_\theta \rangle}{\partial r} + \frac{1}{r} \frac{\partial \langle u_r \rangle}{\partial \theta} - \frac{\langle u_\theta \rangle}{r} \right) - \langle u'_r u'_z \rangle \left(\frac{\partial \langle u_r \rangle}{\partial z} + \frac{\partial \langle u_z \rangle}{\partial r} \right) \\ & - \langle u'_\theta u'_z \rangle \left(\frac{\partial \langle u_\theta \rangle}{\partial z} + \frac{1}{r} \frac{\partial \langle u_z \rangle}{\partial \theta} \right). \end{aligned} \quad (2)$$

This quantity is mostly contained within the front half of the core (figure 2e), but there are also regions of negative production in the rear of the core. A weaker region also exists in the rear of the ring. The first three terms in (2) are of similar magnitude to Pr , with the others much smaller. Plots of the first and third terms (figures 2f & h) show good agreement with the experiments of Glezer and Coles [1]. The second term, is positive in the front and negative in the back half of the ring in agreement with Glezer and Coles’ prediction (figure 2g). We intend to refine the statistics through ensemble averaging of multiple simulations using different initial perturbations as part of ongoing work.

This research was supported by the UK Engineering and Physical Sciences Research Council (EPSRC) through a Platform grant on turbulence (Grant GR/582947/01). The work was done as part of the UK Turbulence Consortium, using the facilities of HPCx (Grant EP/D044073/1).

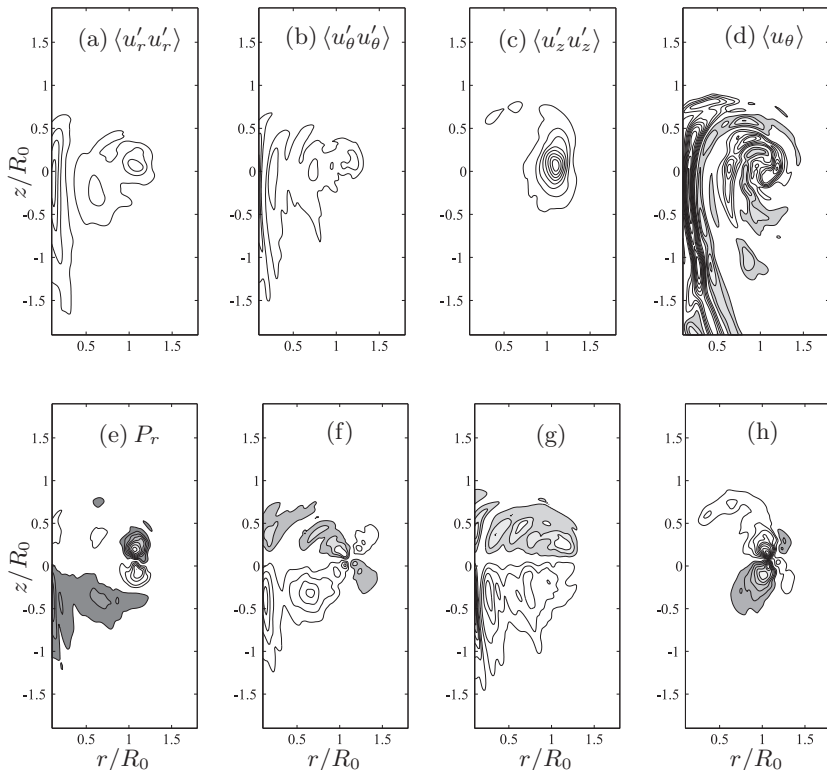


Fig. 2. Contour plots of various flow statistics for the turbulent ring at time $t\Gamma_0/R_0^2 = 128.3$. In plots with both positive and negative contours levels, the positive contours are filled. (a-c) Reynolds stresses $\langle u'_r u'_r \rangle$, $\langle u'_\theta u'_\theta \rangle$ and $\langle u'_z u'_z \rangle$ levels [min : increment : max] = $[-0.015 : 0.0015 : 0.015]$; (d) Mean azimuthal velocity $\langle u_\theta \rangle$ $[-0.03 : 0.003 : 0.03]$; (e) Turbulence Production P_r $[-0.004 : 0.0004 : 0.004]$; (f-h) Production terms $\langle u'_r u'_r \rangle dU_r/dr$ $[-0.002 : 0.0002 : 0.002]$, $\langle u'_\theta u'_\theta \rangle \left(\frac{1}{r} \frac{\partial \langle u_\theta \rangle}{\partial \theta} + \frac{\langle u_r \rangle}{r} \right)$ $[-0.001 : 0.0001 : 0.001]$, $\langle u'_z u'_z \rangle dU_z/dz$ $[-0.003 : 0.0003 : 0.003]$;

References

1. A. Glezer and D. Coles, *J. Fluid Mech*, **211**, 243 (1990)
2. A. Weigand and M. Gharib, *Phys. Fluids*, **38**, 3806 (1994).
3. M. Bergdorf, P. Koumoutsakos and A. Leonard *J. Fluid Mech*, **581**, 495 (2007)
4. P. J. Archer, T. G. Thomas, and G. N. Coleman, *J. Fluid Mech*, **598**, 201 (2008).
5. C-Y. Tsai and S. E. Widnall, *J. Fluid Mech*, **73**, 721 (1976).
6. D. W. Moore and P. G. Saffman, *Proc. R. Soc. London*, **346**, 415 (1975).
7. Y.F. Yao, T.G. Thomas, N.D. Sandham and J.J.R. Williams *Theoret. Comput. Fluid Dyn*, **14**, 337 (2001)

Reconnection of vortex bundles

Sultan Alamri, Anthony J. Youd, and Carlo F. Barenghi

School of Mathematics and Statistics, Newcastle University,
NE1 7RU Newcastle upon Tyne, United Kingdom
C.F.Barenghi@ncl.ac.uk

Recent experimental and theoretical studies have shown striking similarities between ordinary turbulence and quantum turbulence [1, 2]. Quantum turbulence is the turbulence of a superfluid, such as liquid helium (both ^4He and ^3He) and atomic Bose–Einstein condensates. Particularly interesting is the case in which the superfluid’s temperature is small enough that thermal excitations can be neglected. In this case, the superfluid almost becomes the physical realization of the textbooks’ concept of perfect (inviscid) Euler fluid, from which it differs in only two respects: firstly, superfluid vorticity is concentrated to thin filaments of fixed circulation κ and fixed core size ξ ; secondly, these vortex filaments can reconnect [4] even if the viscosity is zero. In superfluid ^4He we have $\kappa \approx 10^{-3} \text{ cm}^3/\text{s}$ and $\xi \approx 10^{-8} \text{ cm}$.

Vortex reconnections play an important role in the dynamics of both ordinary and quantum turbulence. In this work [5] we study numerically the reconnection of vortex bundles. We use two models: the nonlinear Schrödinger equation (NLSE) and the vortex filament model. The NLSE (also called the Gross–Pitaevskii equation) is

$$i\hbar \frac{\partial \psi}{\partial t} = -\frac{\hbar^2}{2m} \nabla^2 \psi + V|\psi|^2 \psi - E\psi, \quad (1)$$

where $\psi = Ae^{iS}$ is a complex order parameter of amplitude A and phase S , m is the mass of one boson (e.g. one helium atom), V is the potential of interaction between bosons and E is the chemical potential. A vortex filament solution of the NLSE is such that $A = 0$ on the vortex axis and S changes from 0 to 2π going around the axis. Approaching the vortex axis, the amplitude A drops from its bulk value to zero over the characteristic distance $\xi = \hbar/\sqrt{2mE}$ (coherence length). We make the equation dimensionless using ξ as the unit of length, \hbar/E as the unit of time and $\sqrt{E/V}$ as the unit of ψ ; the resulting dimensionless NLSE is

$$2i \frac{\partial \psi}{\partial t} = -\nabla^2 \psi + |\psi|^2 \psi - \psi, \quad (2)$$

By introducing the density $\rho = A^2$ and the velocity $\mathbf{v} = \nabla S$, it can be shown [3] that the NLSE can be transformed into a classical continuity equation and an Euler equation; the latter contains an extra term (called quantum stress) which is negligible away from vortices but, when vortices become close to each other, is responsible for vortex reconnections. The NLSE therefore models a reconnecting Euler fluid.

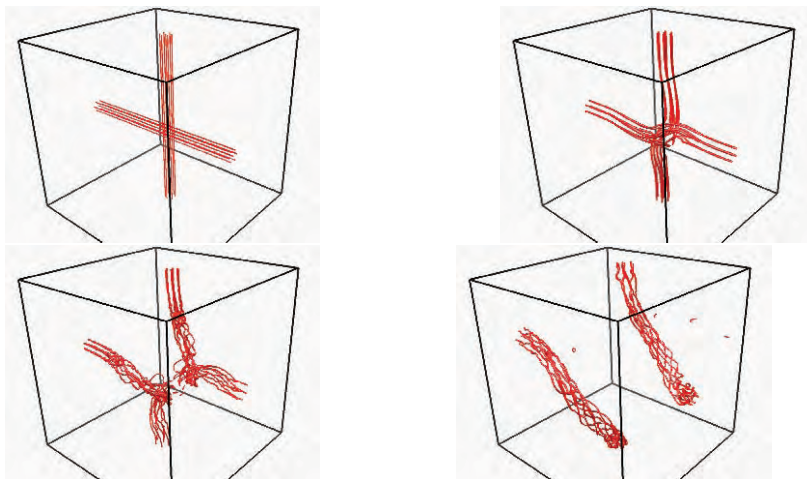


Fig. 1. Reconnection of vortex bundles of seven vortex lines each computed using Eq. (2). Top left and right: $t = 0$ and $t = 110$; Bottom left and right: $t = 320$ and $t = 800$.

The calculation is performed in the box $-128 \leq x, y, z \leq 128$. The typical reconnection scenario is shown in Fig. (1), which shows isosurfaces of ρ at the level 0.25 of the unit bulk density. Two rotating vortex bundles (of seven parallel vortex strands each) are initially ($t = 0$) set perpendicular to each other. The bundles interact, and individual vortices of the first bundle reconnect (one at the time) with individual vortices of the second bundle [4]. During the process, small vortex rings may be generated. The last stage of the reconnection often involves the formation of a "bridge" between the two bundles, similar to what observed in ordinary viscous vortex reconnections [7]; after the bridge breaks up, the bundles become completely free and move away from each other. The structural stability of the vortex bundles is remarkable.

We obtain the same scenario if instead of the NLSE we use the vortex filament model [6]. In this model a vortex filament is represented as a three-dimensional space curve $\mathbf{x} = \mathbf{x}(t, \xi)$ (where ξ is the arclength) which evolves in time according to the Biot–Savart law:

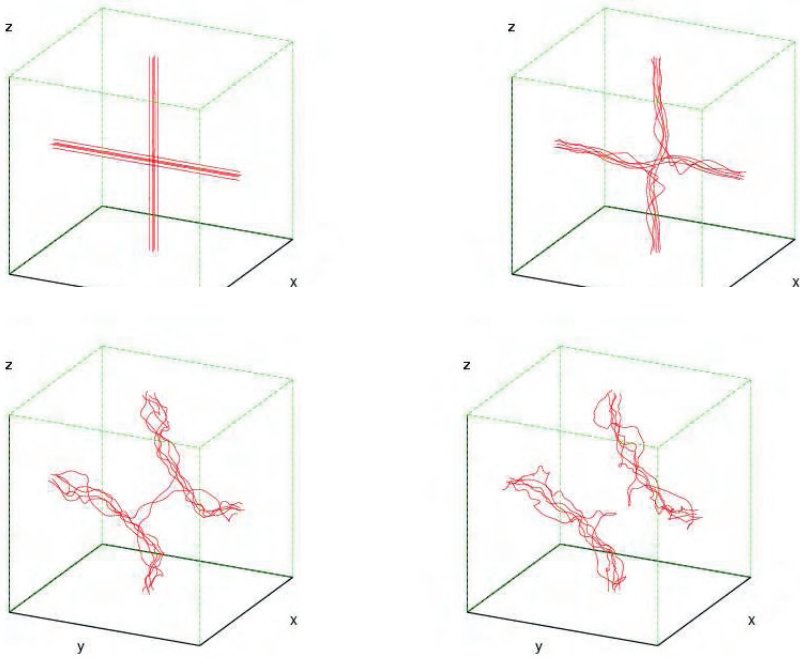


Fig. 2. Reconnection of two vortex bundles of five vortex lines each computed using Eq. (3). Top left and right: $t = 0$ s and $t = 32.5$ s; Bottom left and right: $t = 86.9$ s and $t = 112.1$ s.

$$\frac{d\mathbf{x}}{dt} = -\frac{\kappa}{4\pi} \oint \frac{(\mathbf{x} - \mathbf{z})}{|\mathbf{x} - \mathbf{z}|^3} \times d\mathbf{z}, \tag{3}$$

where the line integral extends over the entire vortex configuration. The techniques to de-singularise the Biot–Savart integral and to algorithmically perform a vortex reconnection when two vortex filaments come sufficiently close to each other are known in the literature [6]. Fig. (2) shows the reconnection of two vortex bundles which consist of five vortex strands each, computed using Eq. (3). The calculation is performed in the box $-1 \text{ cm} \leq x, y, z \leq 1 \text{ cm}$.

Fig. (3) illustrates two features of the process of vortex bundle reconnection. The first feature, shown at the left of the figure, is that the total length of the vortex filaments increases. The second feature is the generation of Kelvin waves (helical displacements of individual vortex lines), which are also visible in Fig. (1) and (2). The right hand side of Fig. (3) shows the time evolution of the PDF of $1/R$, where R is the local radius of curvature sampled along the filaments. Initially, when the vortex filaments are straight, $1/R = 0$; as the vortex bundles interact and reconnect, Kelvin waves are created of shorter and shorter wavelength, hence the PDF of $1/R$ moves to the right of the figure.

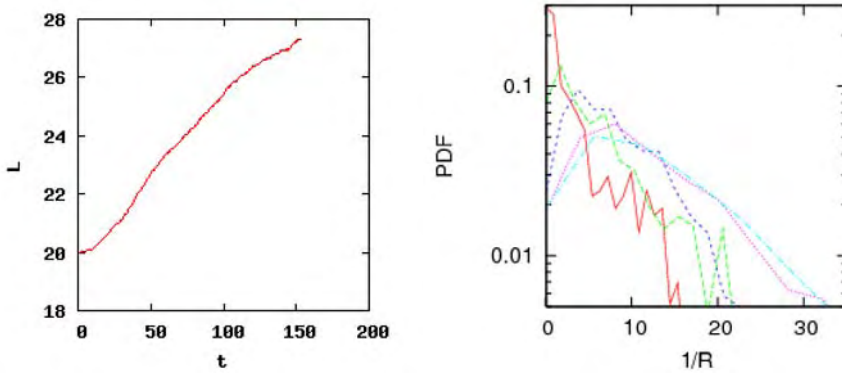


Fig. 3. Left: vortex length L (cm) vs time t (s). Right: PDF of $1/R$ at increasing time (moving from left to right): $t = 19.3$ s, $t = 32.5$ s, $t = 45.6$ s, $t = 86.9$ s and $t = 112.1$ s. The data refer to the reconnection shown in Fig. (2).

This process, which is important in the context of quantum turbulence [8], is called the Kelvin wave cascade, because, in analogy with the Kolmogorov energy cascade, shifts energy to smaller scales. Both cascade are thought to be present in quantum turbulence, the Kolmogorov cascade at scales larger than the typical intervortex separation, and the Kelvin cascade at smaller scales.

The large amount of coiling of vortex filaments which we observe during the reconnection process, represented by these Kelvin waves, confirms results of Kerr [9] and Holm & Kerr [10] about the generation of helicity in nearly singular vortex interactions of the classical Euler equation.

References

1. C.F. Barenghi, R.J. Donnelly and W.F. Vinen (eds.) *Quantized vortex dynamics and superfluid turbulence*, Springer (2001).
2. W.F. Vinen and J.J. Niemela, *J. Low Temp. Physics* **128**, 167 (2002).
3. C.F. Barenghi, *Physica D*, **237** 2195 (2008).
4. J. Koplik and H. Levine, *Phys. Rev. Lett.* **71** 1375 (1993).
5. S.Z. Alamri, A.J. Youd, and C.F. Barenghi, *Phys. Rev. Lett.* **101**, 215302 (2008).
6. K.W. Schwarz, *Phys. Rev.* **38**, 2398 (1988).
7. S. Kida and M. Takaoka, *Ann. Rev. Fluid Mech.* **26**, 169 (1994).
8. D. Kivotides, J.C. Vassilicos, D.C. Samuels and C.F. Barenghi, *Phys. Rev. Lett.* **86**, 3080 (2001); W.F. Vinen, M. Tsubota and A. Mitani, *Phys. Rev. Lett.* **91**, 135301 (2003); E. Kozik and B. Svistunov, *Phys. Rev. Lett.* **92**, 035301 (2004); V.S. L'vov, S. Nazarenko and O. Rudenko, *Phys. Rev. B* **76**, 024520 (2007).
9. R.M. Kerr, *Nonlinearity* **9**, 271 (1996);
10. D.D. Holm and R. Kerr *Phys. Rev. Lett.* **88**, 244501 (2002);

Turbulent energy cascade caused by vortex stretching

Susumu Goto

Department of Mechanical Engineering and Science, Kyoto University,
Yoshida-Honmachi, Sakyo, Kyoto 606-8501, Japan
goto@mech.kyoto-u.ac.jp

One of the most important characteristics of high-Reynolds-number turbulence is the small-scale universality: i.e. statistics at small scales are independent of larger-scale structures which depend on the boundary conditions and/or external forcing. It is the energy cascade that is the basis of this small-scale universality. More precisely, the energy supplied to turbulence at a large scale (the integral length L) transfers, scale by scale, to smaller scales until it is dissipated by the molecular viscosity at the smallest scale (the Kolmogorov length η). Then, the information of the large scales may well be forgotten through this cascade process, and therefore the small-scale universality is established. Although the Fourier analysis (see Ref. [1], e.g.) of turbulence has been shown to support this energy cascade picture, its physical mechanism is unknown.

Since the energy cascade is quite important in this research field, many attempts have been made to understand its physical mechanism. One pos-

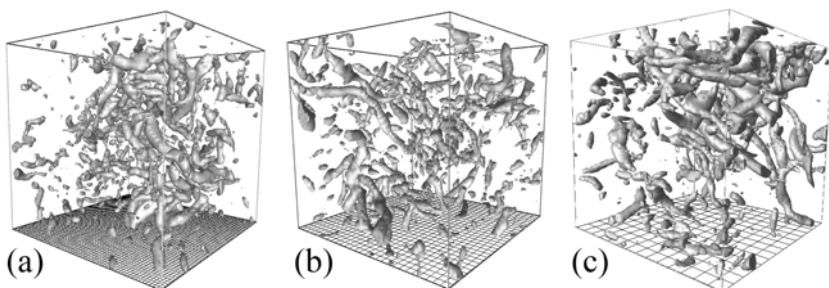


Fig. 1. Multi-scale coherent vortices in homogeneous isotropic turbulence (Taylor-length based Reynolds number R_λ is about 190). Iso-surfaces of enstrophy in coarse-grained fields are plotted for three different coarse-graining scales: (a) 74η , (b) 36η and (c) 18η . The bottom grid width is common (20η), whereas the size of the cubes is different. Coherent structures look statistically self-similar and have tubular shapes at these scales in the inertial subrange.

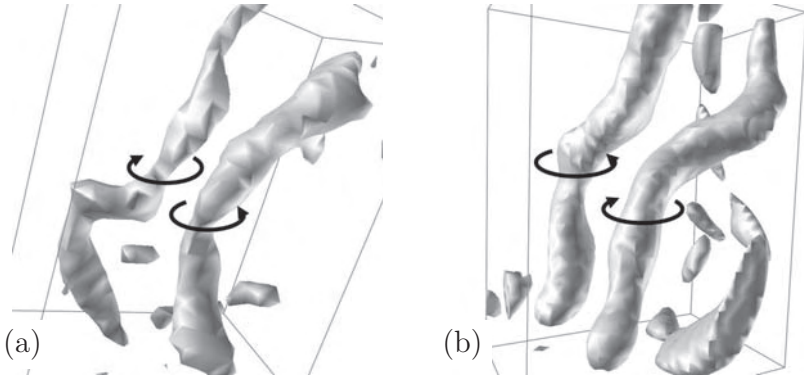


Fig. 2. Examples of an anti-parallel pair of vortex tubes at length scales much larger than the Kolmogorov length, η , (a) 170η and (b) 340η . The size of the shown boxes are (a) $1100\eta \times 870\eta \times 500\eta$ and (b) $1800\eta \times 1300\eta \times 900\eta$. $R_\lambda = 380$.

sibility was proposed by the author [2] recently based on the following two observations of numerically simulated turbulence: (i) Developed turbulence consists of the multi-scale vortex tubes (Fig. 1), and energy at each scale is predominantly confined within these coherent structures. (ii) Anti-parallel pairs of such vortex tubes (Fig. 2) are frequently observed in the turbulent field. The proposed scenario of the energy cascade is as follows.

1. Energy supplied to the large scale, i.e. the integral length L , is possessed by vortex tubes with large radii of $O(L)$.
2. When a pair (especially, an anti-parallel pair) of these vortex tubes encounter, a strong straining region is created around the pair. In this straining region, smaller-scale (i.e. thinner) vortices are stretched and created. In other words, the energy possessed by the fatter, $O(L)$, vortex tubes transfers to thinner scales (L' , say) by the process of the vortex stretching.
3. Thus created vortex tubes with radii of the intermediate length scale, L' , confine the energy inside them; and when a pair of them encounter, a strong straining region at the scale, L' , is created around the pair, and further smaller-scale (i.e. further thinner, L'') vortex tubes are stretched and created. Thus energy transfers from L' to L'' .
4. Such processes continue until Kolmogorov-scale vortex tubes are created, and the energy is finally dissipated by the molecular viscosity in strong straining regions around those smallest-scale vortices.

Examples supporting the above scenario are easily found (see an example in Fig. 3) in the numerically simulated homogeneous isotropic turbulence. That is, it is ubiquitous that anti-parallel pairs of fatter (i.e. larger-scale) vortex tubes stretch and create thinner (i.e. smaller-scale) vortex tubes, and

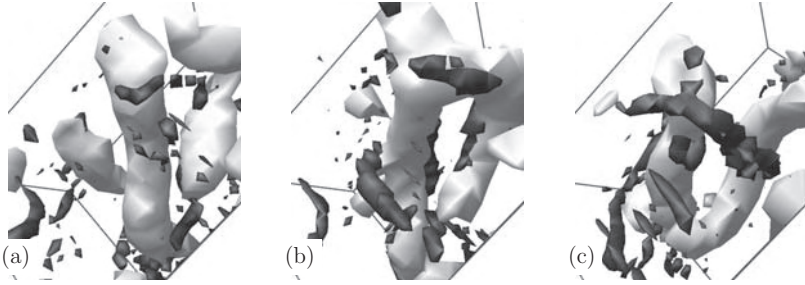


Fig. 3. An example of the creation of smaller-scale (18η) vortex tubes (black objects) by the stretching around an anti-parallel pair of larger-scale (74η) vortex tubes (white objects). $R_\lambda = 190$. Time elapsed from (a) to (c). Movies of this and similar events are available in the online version of Ref. [2].

that the energy transfers from larger to smaller scales. However, quantitative arguments are lacking, and it is open how important the vortex stretching by anti-parallel vortex pairs is in the cascade process.

In order to investigate the role of anti-parallel pairs of vortex tubes quantitatively, we employ a vortex identification method [3] to define the direction of each vortex tube at an arbitrary length scale, and to quantify their alignments. The vortex identification is based on the feature that the pressure on the centreline of vortex tube tends to be lower than around it because the swirling motion (which requires a centripetal force) of fluid particles inside a vortex tube must be due to the pressure gradient if the viscous force is negligible. Therefore, the centreline of each vortex tube may be defined by the connected points where the pressure becomes a local minimum on the plane defined by the two eigenvectors of the pressure Hessian at the centreline. We extend this method to identify vortex tubes at length scales in the inertial subrange, where the pressure field is obtained by solving the Poisson equation with the source term calculated from the coarse-grained velocity field.

Thus, we can define the distance r and angle θ between segments of two vortex tubes, unambiguously. Figure 4 shows the probability density function (PDF) of $\cos \theta$ for vortex tubes at the length scale 74η . The PDF is conditioned by the distance r as $80\eta < r < 160\eta$. Note that the PDF of $\cos \theta$ becomes constant if the distribution of the angle θ is isotropic. It is clearly observed in Fig. 4 that vortex tubes at this large scale (74η), indeed, tend to align in an anti-parallel manner in this range of distance. This result is consistent with the qualitative observations (Fig. 2), and supports the scenario of the energy cascade in terms of the vortex stretching in the straining fields created by anti-parallel pairs of the multi-scale vortex tubes, although further quantitative arguments (which should be shown in the conference) are needed.

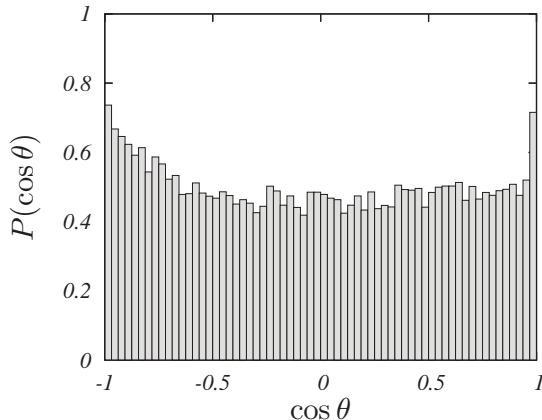


Fig. 4. PDF of the cosine of the angle θ between vortex pairs at the scale 74η . Conditioned by the distance r between the pairs as $80\eta < r < 160\eta$. Averaged over snapshots of turbulence ($R_\lambda = 190$).

Before closing this article, it may be worth mentioning the mechanism of the anti-parallel alignment of vortex tubes. A possible mechanism is the one which makes vortex filaments align in an anti-parallel manner [4]: i.e. when a part of an anti-parallel pair of vortex filaments approaches to each other, the mutual-induction bends them, and then self-induction (like a vortex ring) makes them further approach. However, it is still open whether this mechanism leads the anti-parallel pairing of vortex tubes such as observed in Fig. 2.

The direct numerical simulations were carried out on NEC SX-7/160M5 and Hitachi SR16000 with the support of the NIFS Collaborative Program.

References

1. J. A. Domaradzki & R. S. Rogallo, Local energy transfer and nonlocal interactions in homogeneous, isotropic turbulence. *Phys. Fluids A*, **2**, 413 (1990).
2. S. Goto, A physical mechanism of the energy cascade in homogeneous isotropic turbulence, *J. Fluid Mech.*, **605**, 355 (2008).
3. H. Miura & S. Kida, Identification of tubular vortices in turbulence, *J. Phys. Soc. Jpn.*, **66**, 1331 (1997).
4. E. D. Siggia, Collapse and amplification of a vortex filament, *Phys. Fluids*, **28**, 794 (1985).

Instabilities and transient growth of trailing vortices in stratified fluid

Claire Donnadieu¹, Jean-Marc Chomaz¹ and Sabine Ortiz^{1,2}

¹ *LadHyX, CNRS–Ecole Polytechnique F-91128 Palaiseau Cedex, France*

² *UME/DFA, ENSTA, chemin de la Hunière, 91761 Palaiseau Cedex, France*

ortiz at ladhyx.polytechnique.fr

1 Introduction

The wake, which forms behind an aircraft due to its lift, is a pair of horizontal counter-rotating vortices propagating downwards. Depending on the atmospheric conditions, such dipole can persist over a long time or be rapidly destroyed. This vortex pair, in homogeneous fluids, is unstable with respect to three-dimensional perturbations. Crow [1] has discovered a long-wavelength instability, symmetric with respect to the plane separating the two vortices. The existence of a short-wavelength elliptic instability has been revealed by Tsai & Widnall [2], Moore & Saffman [3] and numerous articles ever since for both symmetric and antisymmetric modes. Recently Donnadieu *et al.* [4] observed a novel oscillatory instability, less unstable than Crow and elliptic modes, for large Reynolds numbers. However, in many atmospheric situations, as such dipoles propagate downwards, they evolve under the influence of the stable stratification of the atmosphere. The three-dimensional dynamics of this vortex pair in stratified flow, has received much less attention: still Robins & Delisi [5] and Garten *et al.* [6] have discussed persistence of the Crow instability and Nomura *et al.* [7] of the short-wavelength instability.

2 2-D Evolution of the base flow in a stratified fluid

The base flow is obtained by integration of the non-linear two-dimensional Navier-Stokes equations with a pseudo-spectral method in Cartesian coordinates (x, z) and periodic boundary conditions (Delbende *et al.* [8]). The initial state is the superposition of two circular Lamb-Oseen vortices of initial circulation Γ_0 , initial radius a_0 and initial separation distance b_0 with $a_0/b_0 = 0.2$. The flow evolves in a stable linear vertically stratified flow characterized by the Brunt-Väisälä frequency N . The Reynolds number based on the initial circulation of the vortices is $Re_{\Gamma_0} = 2400$, and the Froude number $Fr = \frac{W_0}{Nb_0}$,

the ratio of the characteristic timescale of the stratification $1/N$ to the characteristic timescale of the flow (W_0 is the initial advection velocity of the dipole), is varied. As the counter-rotating vortices propagate downwards, they evolve under the influence of the stratification. Fig. 1 represents the axial vorticity of the vortex pair at two times rescaled by the Brunt-Väisälä frequency $Nt^* = 1$ and $Nt^* = 2$ (with $t^* = tW_0/b_0$) and for $Fr = 5$ and $Fr = 1$. The opposite-

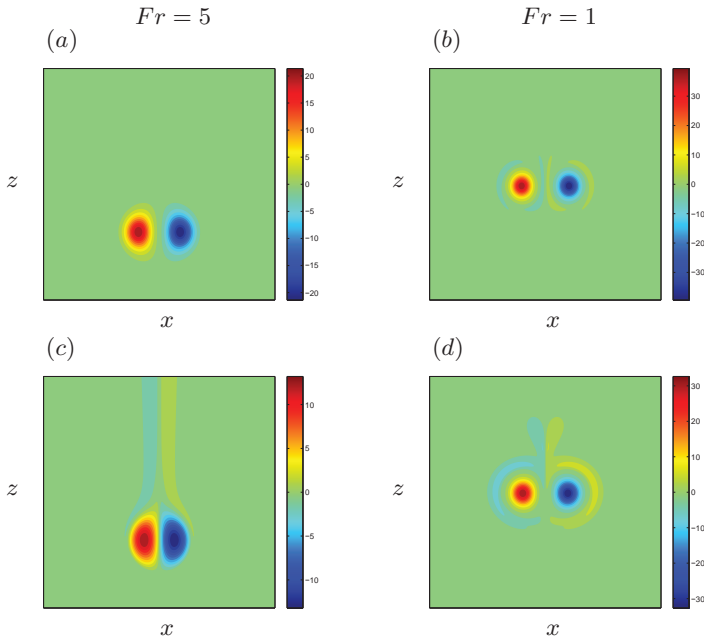


Fig. 1. Isovalues of the axial vorticity of the vortex pair in the (x, z) plane at (a)-(b) $Nt^* = 1$ and (c)-(d) $Nt^* = 2$ for (a)-(c) $Fr = 5$, (b)-(d) $Fr = 1$.

sign vorticity which appears around and behind the primary vortices on Fig. 1 is generated by the baroclinic torque and tends to push the vortices towards one another, hence to reduce the separation distance b between the vortices over time.

3 Quasy-steady approximation for the stability of the flow.

In the case of weak stratification (large Froude numbers Fr), as stratification acts on a long timescale $1/N$ compared to the advection time $\Gamma/2\pi b^2$ of the dipole, the base state can be considered as quasi-stationary and the

linear stability analysis of instantaneous base flow fields describes the leading order dynamics of the perturbation. Instantaneous growth rate of 3D perturbations are then computed solving the linearized Navier-Stokes equations with a pseudo-spectral code similar to the one used for the base flow coupled with a Krylov Arnoldi solver. Due to the symmetry of the base state, three dimensional perturbations are decomposed into symmetric and antisymmetric eigenmodes, calculated separately. Different bands of instabilities are

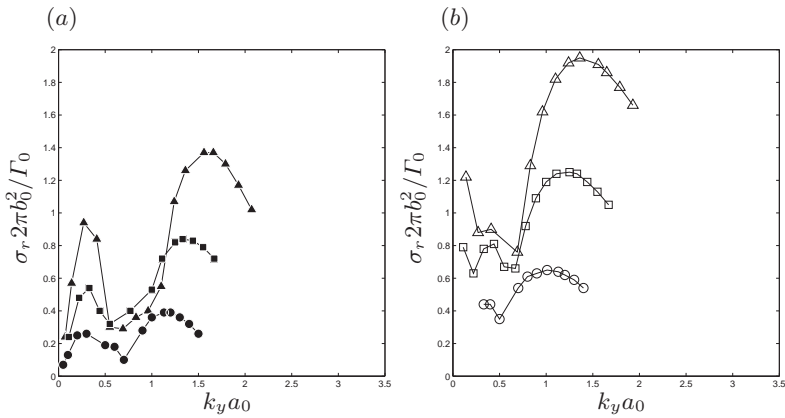


Fig. 2. Growthrates σ_r of symmetric (a) and antisymmetric modes as function of the axial wavenumber k_y scaled by the initial values of the radius a_0 , the separation distance b_0 and the circulation Γ_0 of the vortices for $Nt^* = 2$ for $Re_{\Gamma_0} = 2400$ and three Froude numbers $Fr = 10$ (\circ, \bullet), $Fr = 5$ (\square, \blacksquare) and $Fr = 2$ ($\triangle, \blacktriangle$).

observed. Long-wave symmetric instability on Fig. 2(a), corresponds both for the wavelength selection and the mode shape, to the Crow instability found in homogeneous case. Oscillatory instability (Fig. 2(b)), is found for the antisymmetric mode between $k_y a_0 = 0.2$ and $k_y a_0 = 0.5$ and is similar to the homogeneous case [4]. Short-wave instability leads dynamics for both symmetries, and corresponds in scale selection and perturbation form to elliptic instability adapted to the actual core size. Antisymmetric is the most amplified. These results agree with the direct numerical simulations of Nomura *et al.* [7] who have proposed, based on scale selection, that the short-wavelength instability mechanism is due to the elliptic instability for weak and moderate stratifications and that the growthrates nondimensionalized by the initial value of the strain, increase with the intensity of the stratification (Fig. 2).

4 Optimal perturbations

For strong stratification, $Fr = 1$, the unsteadiness of the flow makes instantaneous stability theory not legitimate, whereas optimal perturbation theory,

which computes the initial perturbation that experiences the largest energy growth at time τ , is still well posed and accessible via direct-adjoint technique [9] taking into account the evolution of the base flow. This analysis confirms that the dynamics is mainly inertial and due to the elliptic instability at intermediate times. Indeed the effect of the buoyancy force is to reduce the separation distance between the vortices of the base state. The optimal initial

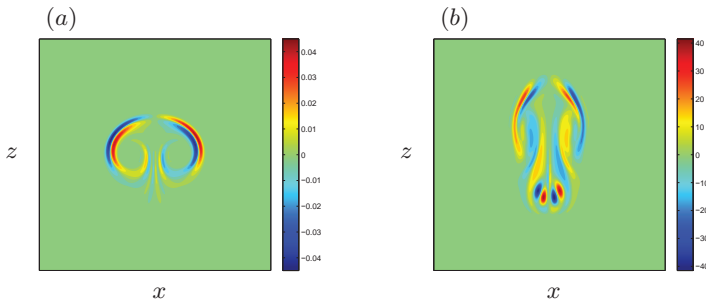


Fig. 3. Isovalues of the axial symmetric vorticity of the optimal initial perturbation (a) and optimal response (b) at $t^* = 4$ and $k_y a = 1.6$ and $Fr = 1$.

perturbation in the symmetric case, Fig. 3(a) is concentrated on the contracting manifold of the upper stagnation point. The optimal response Fig. 3(b) is mainly located in the core of the vortices where its shape is characteristic of the elliptic mode, the wake passively driven. At larger times of optimisation and for stronger stratifications (data not shown) the dynamics is driven by density effects and optimal response is concentrated in the wake of the dipole and not in the vortex cores.

References

1. S.C. Crow, *AIAA J.* **8** (12), 2172 (1970)
2. C.-Y. Tsai and S.E. Widnall, *J. Fluid Mech.* **73**, 721 (1976)
3. D.W. Moore and P. G. Saffman, *Proc. R. Soc. Lond. A.* **346**, 413 (1975)
4. C. Donnadieu, S. Ortiz, J.M. Chomaz and P. Billant, in revision for *Phys. Fluids* (2009)
5. R.E. Robins and D.P. Delisi, *AIAA J.* **36**, 981 (1998)
6. J. F. Garten, J. Werne, D.C. Fritts and S. Arendt, *J. Fluid Mech.* **426**, 1 (2001)
7. K.K. Nomura, H. Tsutsui, D. Mahoney and J.W. Rottman, *J. Fluid Mech.* **553**, 283 (2006)
8. I. Delbende, J.-M. Chomaz and P. Huerre 1998. *J. Fluid Mech.* **355**, 229-254.
9. P. Corbett and A. Bottaro, *Phys. Fluids* **12**, 120 (2000).

Implementation of Vortex Stretching into the Two-Dimensional Navier-Stokes Equations via Arbitrary External Straining

F. Sabetghadam, S. A. Ghaffari, and M. Dadashi

Mechanical and Aerospace Eng. Dept., Science and Research Branch, Islamic Azad University (IAU), Tehran, Iran.

fsabet@srbiau.ac.ir

1 Abstract

A modified vorticity-velocity formulation for the two-dimensional Navier-Stokes equations is proposed with the goal of imposing an arbitrary unsteady vortex stretching into the two-dimensional fluid flows. To this end, the velocity field is (Helmholtz) decomposed, allowing for presence of an arbitrary dilatation, which results in some modifications in both the continuity equation, and the vorticity transport equation. To show the applicability of the method, two entirely different classes of turbulent flows are analyzed; that is, the isotropic turbulence (solved via pseudospectral method), and the near-wall turbulent flow (simulated via the finite difference method). The results show ability of the method in mimicking some essential features of three-dimensional flows.

2 Introduction and mathematical formulation

Analysis of vortical flows in the presence of external straining has a long history from Burgers (in his studies on the Burgers vortex), to Bazant and Moffatt [1], which used sources and sinks to find a general class of similar and non-similar steady vortical structures. In the present work, a general vorticity-velocity formulation for the two-dimensional incompressible Navier-Stokes equations is proposed with the aim of including arbitrary unsteady vortex stretching.

According to Fig. 1, consider a two-dimensional velocity vector $\mathbf{u} = (u_1, u_2)$, defined on an arbitrary closed domain $\bar{\Omega} = (\Omega \cup \partial\Omega) \in \wp$, where \wp is a two-dimensional flat Euclidean plane ($\wp \in \mathbb{E}^2$), embedded in \mathbb{R}^3 . It is assumed that the two-dimensional flow (on $\bar{\Omega}$) is affected by external straining, which is modelled by appropriate injection or ejection of mass from the third direction (that is $\hat{\mathbf{e}}_3$), to the plane \wp . Then, capturing of dynamics of the resulting flow

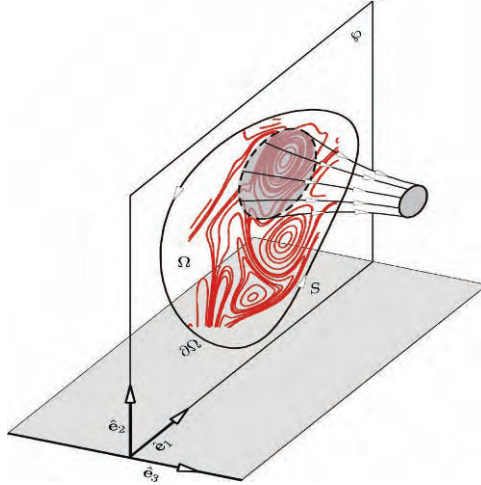


Fig. 1. Mass injection/ejection to the plane φ is modelled by appropriate dilatation.

field is aimed. For the sake of brevity, the ‘injection’ word will be used for both injection and ejection.

Using the Helmholtz–Leray decomposition for the velocity field $\mathbf{u} = \mathbf{u}^{\text{sol}} + \mathbf{u}^{\text{irr}}$, where \mathbf{u}^{sol} and \mathbf{u}^{irr} are divergence-free and curl-free parts respectively; one can find two Poisson’s equations for the flow kinematics

$$\nabla \cdot \mathbf{u}^{\text{irr}} = \nabla^2 \phi = \sigma, \quad (1)$$

$$\nabla^2 \mathbf{u}^{\text{sol}} = \hat{\mathbf{e}}_3 \times \omega, \quad (2)$$

where σ is dilatation due to mass injection, while $(u_1, u_2)^{\text{sol}} = (\partial_2 \psi, -\partial_1 \psi)$, and $\omega \hat{\mathbf{e}}_3 = \nabla \times \mathbf{u}^{\text{sol}}$.

Because \mathbf{u}^{sol} is divergence-free (and therefore, streamfunctions can be defined for it), appropriate boundary conditions for the Eq. (2) can be found directly, from the considered \mathbf{u}^{sol} at the boundaries. On the other hand, for the additional equation (1), the dilatation σ is just needed to be defined on Ω , and knowing the $\mathbf{u}(\mathbf{S})$, the boundary values of the \mathbf{u}^{irr} can be found from

$$\mathbf{u}^{\text{irr}}(\mathbf{S}) = \mathbf{u}(\mathbf{S}) - \mathbf{u}^{\text{sol}}(\mathbf{S}), \quad (3)$$

and then, the appropriate boundary conditions are appeared to be the Neumann ones

$$\nabla \phi \cdot \hat{\mathbf{n}} = \mathbf{u}^{\text{irr}}(\mathbf{S}) \cdot \hat{\mathbf{n}}, \quad (4)$$

where $\hat{\mathbf{n}}$ is the unit normal vector to \mathbf{S} .

On the other hand, beginning from conservative form of the vorticity transport equation, its modified form which governs time evolution (dynamics) of the

two-dimensional fluid flow, allowing for the mass injection, can be obtained as

$$\partial_t \omega = \nu \nabla^2 \omega - (\mathbf{u} \cdot \nabla) \omega - \sigma \omega. \tag{5}$$

Therefore, given the vorticity field ω and the dilatation distribution σ , dynamics of the flow field can be tracked from the Eqns. (1), (2) and (5), in conjunction with the above boundary conditions.

3 Applications

The method, unexpectedly, has shown a wide range of applicabilities, from the immersed solid-boundary implementation, to modification of the energy spectrum of the two-dimensional turbulent flows. As some primary examples, two entirely different classes of turbulent flows are analyzed in the present work; that is, the isotropic turbulence and the near-wall turbulence.

3.1 Isotropic decaying turbulence

There are appreciable differences between the two- and three-dimensional turbulence, mainly because of absence of the vortex stretching mechanism in the two-dimensional flows. As our first numerical example, an appropriate random dilatation σ is imposed in the isotropic decaying turbulence, in order to modelling of the vortex stretching. Distribution of σ is determined (at each timestep) from solution of a stochastic equation, which is solved (in

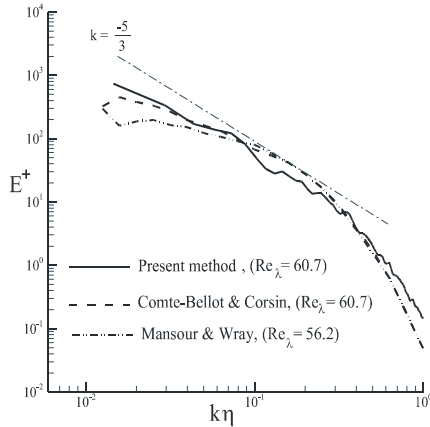


Fig. 2. A $k^{-5/3}$ decaying is appeared instead of the usual k^3 and k^{-3} (for the two-dimensional turbulence), which can be supposed as an evidence for establishment of a (direct) energy cascade and inertial subrange.

conjunction with the modified vorticity equations (1), (2) and (5)), using the Fourier pseudospectral method. It should be noted that because of non-periodicity of the dilatation term, a kind of windowing, more or less similar to [2], is needed when using the pseudospectral method. The results have shown direct energy cascade (in contrast to the two-dimensional turbulence); and a fairly close to $-\frac{5}{3}$ slope in the energy spectrum, which can be supposed as an evidence for establishing an inertial subrange (see Fig. 2).

3.2 Near-wall flow

In addition to the dissipation rate, the turbulence production is in the influence of vortex stretching as well. Formation and evolution of the hairpin vortices are chosen as an appropriate framework for analysis of the effects of vortex stretching. The results are shown that formation and dynamics of the three-dimensional hairpin vortices (at least in a statistical sense), can be simulated by appropriate definition of the dilatation in a two-dimensional flow behind an obstacle.

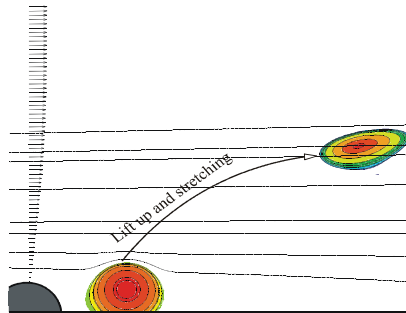


Fig. 3. A two-dimensional version for near-wall flow of [3] is generated by a semi-circle, mounted in a Blasius boundary layer.

References

1. M. Z. Bazant and H. K. Moffatt, *J. Fluid Mech.* (2005), vol. 541, pp. 55-64.
2. F. Sabetghadam, S. Sharafatmandjoor and F. Norouzi, *J. Comput. Phys.*, 228 (2009) 55-74.
3. H. M. Tufo, P. F. Fischer, M. E. Papka, M. Szymanski, Proceedings of SC99, 1999.

Turbulent cascade of a quantum fluid at finite temperature

E. Lévêque¹, C. F. Barenghi², P. Diribarne³ and P.-E. Roche⁴

(1) Laboratoire de Physique, ENS Lyon, CNRS / Université de Lyon, F-69364 Lyon, France

(2) School of Mathematics and Statistics, Newcastle University, Newcastle upon Tyne NE1 7RU, UK

(3) SBT, INAC CEA/ UJF, 38054 Grenoble cedex 9, France

(4) Institut Néel, CNRS / UJF, BP 166, F-38042 Grenoble cedex 9, France
philippe.roche at grenoble.cnrs.fr

1 Introduction : Motivation and Model

Quantum fluids (liquid ³He and ⁴He, atomic Bose-Einstein condensates) consist of two co-penetrating fluids: the superfluid, associated to the quantum ground state, and the normal fluid, associated to thermal excitations. In this work the turbulent inertial cascade undergone by a quantum fluid at small but finite temperature above absolute zero is simulated by DNS of two coupled Navier-Stokes equations[1]. Following the two-fluid model of Landau and Tisza, one equation accounts for the viscous normal fluid, while the other equation models superfluid dynamics on scales larger than the inter-vortex spacing.

The originality of our approach consists in introducing an artificial superfluid viscosity - as a turbulence closure - to model non-viscous processes taking place on scales smaller than the inter-vortex spacing, such as phonon emission. For simplicity, the fluids' coupling -often called "mutual friction"- is a simplified version of the coupling of the HVBK model[1]. With obvious notation, the governing equations of the two fluids are :

$$\frac{D\mathbf{v}_s}{Dt} = -\frac{1}{\rho_s} \nabla p_s + \nu_s \nabla^2 \mathbf{v}_s - \frac{\rho_n}{\rho} \frac{B}{2} |\boldsymbol{\omega}_s| (\mathbf{v}_n - \mathbf{v}_s)$$

$$\frac{D\mathbf{v}_n}{Dt} = -\frac{1}{\rho_n} \nabla p_n + \nu_n \nabla^2 \mathbf{v}_n + \frac{\rho_s}{\rho} \frac{B}{2} |\boldsymbol{\omega}_s| (\mathbf{v}_n - \mathbf{v}_s)$$

where the subscripts "n" and "s" stand for "normal fluid" and "superfluid", $\boldsymbol{\omega}_s$ is the superfluid vorticity, $B = 2$ and the velocity fields are solenoidal. This model allows us to take advantage of optimized parallelized codes in exploring the interaction between the two fluids. This paper is more focused on numerical aspects, the physical interpretation will be discussed elsewhere.

2 Numerical aspects

Numerical simulations refer to the integration of the previous dynamical equations in a cubic domain with periodic boundary conditions in the three directions. The simulations rely on a parallel (distributed-memory) pseudo-spectral solver[2]. Three grid sizes are considered, 128^3 , 256^3 and 512^3 respectively. The velocity Fourier modes are advanced in time by a second-order Adams-Bashforth scheme.

The ratio between the density of the normal fluid and the density of the superfluid is $\rho_n/\rho_s = 0.1, 1$ or 10 respectively for “low”, “intermediate” and “high” temperatures. The ratio between the kinematic viscosities is fixed at $\nu_n/\nu_s = 4$, which is a compromise chosen to separate the dissipative cut-off wavenumbers of the two fluids and maximize the extension of the inertial range of the superfluid.

In order to ensure (statistical) stationarity, a constant-energy flux is supplied to the Fourier modes in the shell of wave-vectors $1.5 < |\mathbf{k}| < 2.5$. This external energy flux applies to the normal fluid in the high-temperature and intermediate-temperature cases, and to the superfluid in the low-temperature case. This forcing scheme permits a rapid relaxation to a steady state, which is attained when the total dissipation fluctuates around the imposed energy input flux.

The transient from the initial state is monitored by the space-averaged enstrophies $\langle \omega_n^2 \rangle$, $\langle \omega_s^2 \rangle$ and $\langle (\omega_s - \omega_n)^2 \rangle$. The first three subplots of Fig. 1 show this transient.

3 Results

The fourth subplot of Fig. 1 shows that correlation between ω_s^2 and ω_n^2 is larger than 97% in steady state, indicating a strong locking of the two fluids. Fig. 2 illustrates this locking in physical space : the vorticity structures - slightly more intense in the superfluid - are indeed overlapping. A similar conclusion was reached recently in a numerical simulation performed at high temperature without coupling from the superfluid to the normal fluid [3].

Fig. 3 shows velocity power density spectra under various conditions; for both fluids there is clear evidence of an inertial range compatible with a $-5/3$ Kolmogorov-like scaling. This figure also shows the power spectra of the slip velocity $\mathbf{v}_s - \mathbf{v}_n$. We find that this quantity peaks at small scales, where ν_n efficiently damps the kinematic energy of the normal fluid. The spectra in the inset are obtained at different temperatures but with fixed ν_s , ν_n and total injected energy. They show that the extend of the inertial range varies with temperature, showing that the Reynolds number - defined using the separation of large and small scales - is a temperature dependent parameter in our two-fluid system.

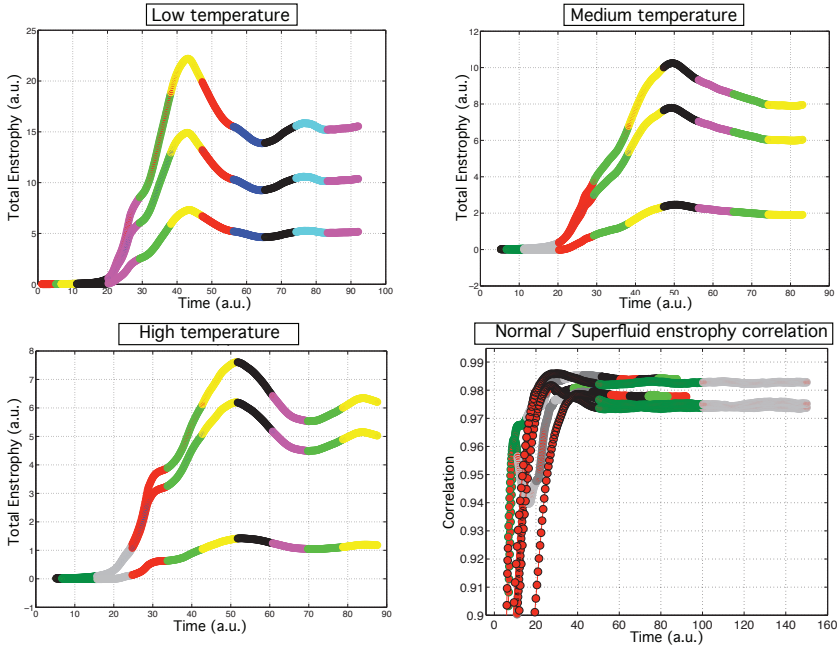


Fig. 1. Subplots 1,2 and 3 illustrate for different temperature the convergence to the steady state by monitoring the total entrophy of the superfluid $\langle \omega_s^2 \rangle$ (top curve), normal fluid $\langle \omega_n^2 \rangle$ (intermediate curve) and the slip entrophy $\langle (\omega_s - \omega_n)^2 \rangle$ (lower curve). These simulations were performed with grid resolution 512^3 . Subplot 4 shows the correlation between the superfluid and normal fluid entrophy fields during the transient to the steady state. These simulations were performed with grid resolution 256^3 and 512^3 .

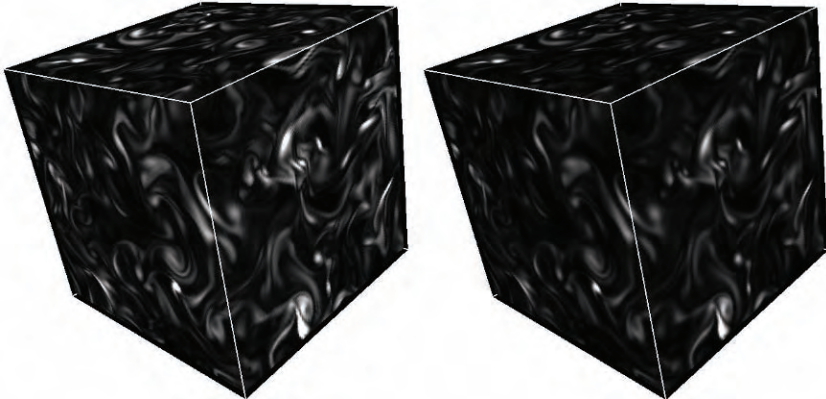


Fig. 2. Local entrophy of the superfluid (left) and normal fluid (right) at high temperature ($\rho_n/\rho_s = 10$). Grid resolution is 256^3 . This visualisation is generated with “Vapor” freeware. (www.vapor.ucar.edu)

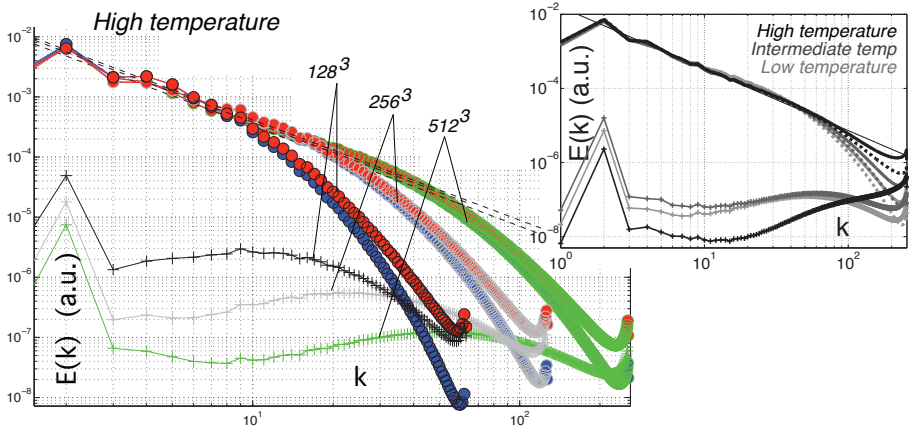


Fig. 3. Velocity spectra at high temperature for resolutions 128^3 , 256^3 and 512^3 . For each resolution, and from top to bottom : superfluid, normal fluid and slip velocities \mathbf{v}_n , \mathbf{v}_s and $\mathbf{v}_s - \mathbf{v}_n$. Dashed line : $-5/3$ scaling. Inset : Velocity spectra for fixed kinematic viscosities and total energy injection, at high (black), intermediate (black) and low (gray) temperatures. Continuous line : $-5/3$ scaling.

4 Conclusion

The locking between the superfluid and the normal fluid which we observe, as well as the Kolmogorov scaling, are consistent with the present theoretical understanding of quantum turbulence[4]. This work extends the numerical evidence over a wide temperature range, using a self-consistent coupling model between the two fluids. Two new features which we observe are the peaking of the slip velocity at small scales, and the temperature dependence of the Reynolds numbers for fixed energy injection and kinematic viscosities.

Acknowledgements : We thank L. Chevillard and J. Salort for useful discussions and support. CPU resources were provided by local computing facilities (PSMN at Ens-Lyon) and french supercomputing centers (CINES and CCRT-CEA). Supports from EPSRC (EP/D040892) and ANR TSF are acknowledged.

References

1. Quantized vortices in Helium II. Donnelly, R.J., Cambridge University Press(1991)
2. Leveque E. and Koudella C., Phys. Rev. Lett. **86**, 4033 (2001)
3. Morris, K., Koplik, J., and Rouson, D.W.I. Phys. Rev. Lett. **101**, 015301 (2008)
4. Vinen W. F., and Niemela J. J. J. Low Temp. Phys. **128** , 167 (2002)

Visualization of quantum turbulence in $^3\text{He-B}$ by thermal excitations

Y.A. Sergeev¹, C.F. Barenghi¹, and N. Suramlishvili²

¹Newcastle University, Newcastle upon Tyne NE1 7RU, United Kingdom

²Andronikashvili Institute of Physics, Tbilisi, 0177, Georgia

yuri.sergeev@ncl.ac.uk

Experiments at very low temperatures, in both ^3He and ^4He , have produced intriguing results which raise challenging questions to fluid mechanicians. The context of this work is quantum turbulence in superfluid $^3\text{He-B}$ at very low temperatures such that the viscous normal fluid component can be neglected, and quantum turbulence takes its purest form: a tangle of quantized vortex filaments (see Fig. 1) which move in a fluid without viscosity.

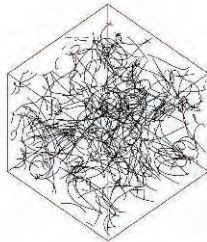


Fig. 1. Snapshot of a tangle of quantized vortices.

In the case of homogeneous quantum turbulence, the turbulence's intensity is characterized by the vortex line density L (vortex length per unit volume) inferring the typical distance between vortices, $\ell \sim 1/\sqrt{L}$. The current understanding [1] of quantum turbulence at very low temperatures is that, at length scales much larger than ℓ , the nonlinear interaction between vortex filaments results in partial alignment and polarization, such that, for $k \ll 1/\ell$, the superfluid supports an energy cascade from large to small scales, which manifests itself in the classical Kolmogorov energy spectrum, $E_k \sim k^{-5/3}$. This implies the existence of an energy sink, which is thought to be acoustic: energy decreases due to the emission of phonons by Kelvin waves (helical displacements of vortex filaments). The details of this scenario still need to be properly understood (in particular, recent experiments [2] suggest the existence of a new

form of turbulence – a less structured “ultraquantum” turbulence state). This and other problems require further theoretical and experimental study.

The experimental study of quantum turbulence would be greatly facilitated if better visualization techniques were available. A drawback of most of the existing techniques is that they only measure quantities averaged over a large region, while it is important to have local information about fluctuations. This problem has been recognized: in ^4He , at $T > 1\text{ K}$, a major breakthrough has been the implementation of the PIV technique. In the more difficult regime of very low temperature $^3\text{He-B}$, the Andreev reflection technique [3] has been a major advance in providing a tool for studying turbulence. The technique is based on the fact that the dispersion curve of quasiparticles (thermal excitations) is tied to the reference frame of the superfluid, so that one side of a vortex line presents a potential barrier to oncoming quasiparticles, which can be reflected back almost exactly becoming quasiholes (thermal excitations whose energy is below the Fermi level); the other side of the vortex lets the quasiparticles to go through. Quasiholes are reflected or transmitted in the opposite way. The vortex thus casts a symmetric shadow for quasiparticles at one side and quasiholes at the other thus enabling the experimentalist to detect vortices and infer the vortex line density.

In the presence of the flow field, $\mathbf{v}_s(\mathbf{r}, t)$, the energy of the thermal excitation is

$$E = \sqrt{\epsilon_p^2 + \Delta_0^2} + \mathbf{p} \cdot \mathbf{v}_s(\mathbf{r}, t), \quad (1)$$

where $\epsilon_p = p^2/(2m^*) - \epsilon_F$ is the kinetic energy of a quasiparticle ($\epsilon_p > 0$) or a quasihole ($\epsilon_p < 0$) of momentum \mathbf{p} measured with respect to the Fermi energy, $\epsilon_F = p_F^2/(2m^*) \approx 2.27 \times 10^{-16}$ erg, $m^* = 3.01m$ with m being a mass of ^3He atom, $\Delta_0 \approx 2.43 \times 10^{-19}$ erg is the superfluid energy gap. On a spatial scale larger than the coherence length, $\xi_0 \approx 0.85 \times 10^{-5}$ cm a thermal excitation can be regarded as a compact object, and Eq. (1) as an effective Hamiltonian yielding the equations of motion of a quasiparticle (quasihole) in the form

$$\frac{d\mathbf{r}}{dt} = \frac{\partial E}{\partial \mathbf{p}} = \frac{\epsilon_p}{\sqrt{\epsilon_p^2 + \Delta_0^2}} \frac{\mathbf{p}}{m^*} + \mathbf{v}_s, \quad \frac{d\mathbf{p}}{dt} = -\frac{\partial E}{\partial \mathbf{r}} = -\frac{\partial}{\partial \mathbf{r}}(\mathbf{p} \cdot \mathbf{v}_s). \quad (2)$$

We consider the two-dimensional model in which the quantized vortices become vortex points. Each vortex generates the velocity field $\mathbf{v}_s = \kappa(2\pi r)^{-1} \hat{\mathbf{e}}_\phi$, where $\kappa = \pi\hbar/m \approx 0.662 \times 10^{-3}$ cm²/s is the quantum of circulation in $^3\text{He-B}$, and $\hat{\mathbf{e}}_\phi$ is the azimuthal unit vector. In the vortex structure (e.g. vortex bundle) modeled by the system of N vortex points the fluid velocity at any point \mathbf{r} can be found as a superposition of velocity fields generated by all vortices, and each vortex moves as a fluid point in the flow field of all other vortex points.

In the case of one, stationary vortex Eqs. (2) possess the integrals of motion $E = \text{constant}$ and $J = p_\phi \rho_0 = \text{constant}$, the latter introducing the impact parameter, ρ_0 whose meaning is clear from the illustration of Andreev

reflection in Fig. 2. An approximate analytical solution of the equations of

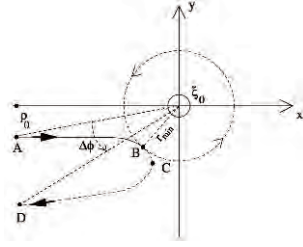


Fig. 2. Schematic trajectory of the quasiparticle Andreev reflected at position B.

motion was found [4] using the fact that $\epsilon_p/\Delta_0 \ll 1$. This solution enabled us to investigate ballistic trajectories of quasiparticles, find the locus of Andreev reflection, and calculate the Andreev reflection angle, $\Delta\phi$ (see Fig. 2) which, in agreement with previous studies, is very small so that the quasiparticle, having been Andreev reflected, practically retraces its trajectory as a quasi-hole. Calculated from our theory, the Andreev shadow of an isolated vortex is $S_0 = 3\pi\xi_0(\Delta_0/\epsilon_p)^2$.

When extrapolated to a disordered tangle, such that vortices are well separated (i.e. $\xi_0 \ll \ell$), the obtained solution enables us to calculate the fraction of heat, f_{tr} transmitted by quasiparticles through the vortex tangle. Provided f_{tr} is measured experimentally, the vortex line density can be inferred,

$$\ell = \left\{ -\frac{\Delta_0}{k_B T} \frac{3\pi\xi_0\mathcal{L}}{2 \ln f_{tr}} \right\}^{1/2}, \quad (3)$$

where \mathcal{L} is the size of the vortex system, in a good agreement with existing experimental estimates [3].

The situation becomes more complicated in the case where vortex rings and coherent vortex structures (e.g. bundles) are present. In this case \mathbf{v}_s becomes time dependent so that $E \neq \text{constant}$, and the equations of motion (2) have to be solved numerically [5]. The general result of such a solution is that in a structure consisting of N vortices the partial screening takes place so that the total Andreev shadow is not necessarily the sum of shadows of individual, isolated vortices, i.e. $S = S_1 + S_2 + \dots + S_N \neq NS_0$.

In all illustrations below the initial momentum of quasiparticles is $p_0 = 1.0001p_F$ in the x -direction; for this momentum the shadow of an isolated vortex is $S_0 \approx 269\xi_0$. We found that the total shadows of vortex-vortex and vortex-antivortex pairs (the latter being a 2D model of a vortex ring) depend on the distance, D between vortices and the angle θ between the line connecting the vortices and the direction of incident flux of quasiparticles. For $\theta = 90^\circ$, the dependence of the total shadow of the vortex-antivortex pair on D is shown in Fig. 3 (left) illustrating the partial screening and, hence,

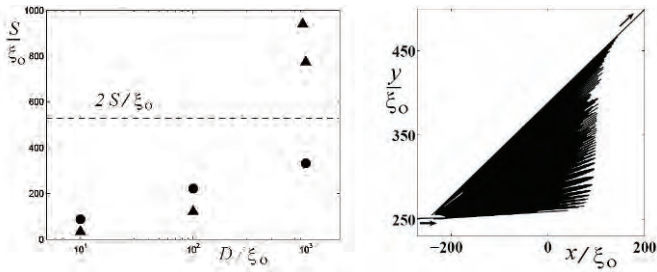


Fig. 3. Left: total Andreev shadow vs distance between vortices in a vortex-antivortex pair at $\theta = 90^\circ$; the pair moves: triangles – in the direction of the quasiparticles’ flux, circles – opposite to it. Right: multiple Andreev reflection in a system of 10 vortices. The quasiparticle turns into a quasihole many times before escaping as a quasiparticle.

substantial reduction in the total shadow. Even more dramatic reduction was found for larger clusters of vortex points. Thus, for some configurations of 5 vortex points the total shadow is smaller than $600\xi_0$ which is less than a half of $5S_0 = 1345\xi_0$, and for clusters of 10 vortices the total shadow can be an order of magnitude smaller than $10S_0$. This does not mean that the interpretation given to recent experiments is incorrect: it is possible that, for a large, random vortex system, the screening effects which we have found average out. If this is the case, screening effects can be taken into account by introducing a prefactor, hence for the vortex line density can be inferred.

Furthermore, we discovered that, interacting with vortex structures, the quasiparticle may experience multiple Andreev reflections, illustrated in Fig. 3 (right), resulting in the reflection angle which is no longer small. It should yet to be understood whether this is a typical situation, in which case an interpretation of experimental results might be seriously affected, or just a rare event which can be ignored.

References

1. W. F. Vinen and J. J. Niemela, *J. Low Temp. Phys.*, **128**, 167 (2002).
2. P. M. Walmsley, A. I. Golov, H. E. Hall, A. A. Levchenko and W. F. Vinen, *Phys. Rev. Lett.*, **99**, 265302 (2007).
3. S. N. Fisher, in *Vortices and Turbulence at Very Low Temperatures*, C. F. Barenghi and Y. A. Sergeev (eds.), CISM Courses and Lectures, Vol. 501, Springer, Wien New York, 2008, pp. 177-257.
4. C. F. Barenghi, Y. A. Sergeev and N. Suramlshvili, *Phys. Rev. B*, **77**, 104512 (2008).
5. C. F. Barenghi, Y. A. Sergeev, N. Suramlshvili and P. J. Van Dijk, *Phys. Rev. B*, **79**, 024508 (2008).

The 3D structure of a dipole in a shallow two-layer fluid

R.A.D. Akkermans, L.P.J. Kamp, H.J.H. Clercx and G.J.F. van Heijst

J.M. Burgerscentre for Fluid Dynamics & Dept. of Applied Physics, Eindhoven University of Technology, P.O. Box 513, 5600 MB Eindhoven, Netherlands.
r.a.d.akkermans@tue.nl

Introduction

The canonical laboratory setup to study two-dimensional (2D) turbulence is the electromagnetically driven shallow fluid layer. The argument used here is that whenever the vertical length scale is much smaller than the horizontal length scale the flow is presumed to behave in a 2D fashion. However, this assumption disregards the presence of a strong non-uniform magnetic field used to electromagnetically force the flow, a vertical component of the Lorentz force, and, most importantly, it oversimplifies the structure of 3D recirculating flows [1, 2]. The limitations of the single fluid layer setup have been recognized and now the two-layer fluid is commonly used for experimental 2D turbulence research.

In this contribution we will study experimentally and numerically the 3D motion inside a two-layer fluid. We will discuss the behaviour of the flow when decreasing the upper fluid layer thickness in steps down from 9 mm to 3.5 mm, the latter being the commonly used upper fluid layer thickness for 2D turbulence experiments. Surprisingly, the flow structures and evolution seen in the two-layer flow are qualitatively the same as in the single-layer flow.

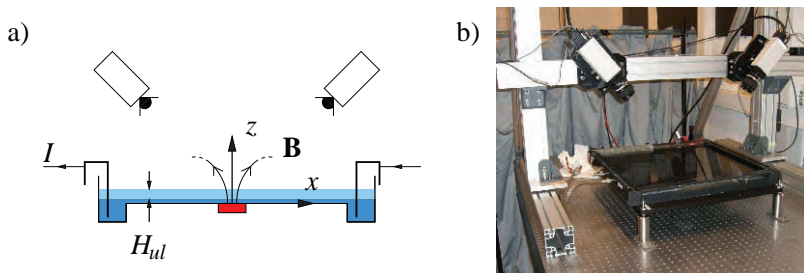


Fig. 1. Schematic cross-section (a) and photograph (b) of the experimental setup.

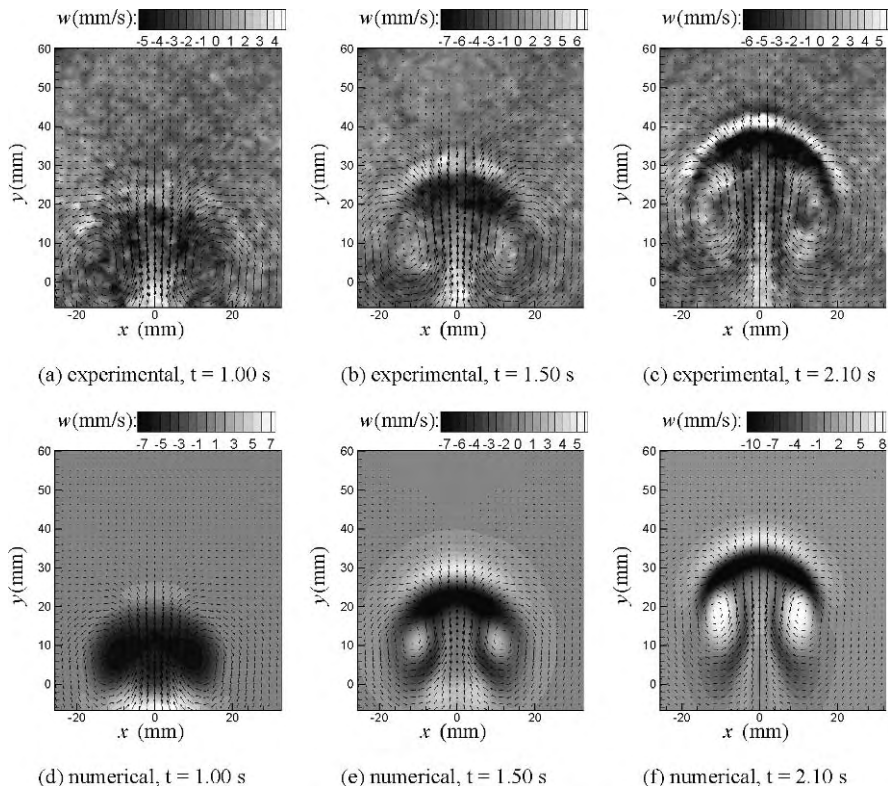


Fig. 2. Instantaneous velocity fields of a dipolar vortex in a horizontal plane at mid-depth of the top fluid layer ($H_{ul} = 7.0$ mm). Vectors represent horizontal velocity components and gray levels indicate the magnitude of the vertical velocity. Experimental results obtained with SPIV at (a) $t = 1.00$ s, (b) $t = 1.50$ s, and (c) $t = 2.10$ s. Numerical results obtained with a rigid internal interface at (d) $t = 1.00$ s, (e) $t = 1.50$ s, and (f) $t = 2.10$ s.

Experimental and numerical results

We present results from Stereoscopic-PIV measurements and full 3D numerical simulations of a dipolar vortex in a two-layer fluid, one of the most elementary coherent structures found in 2D turbulence. The experimental setup consists of a 52×52 cm² square tank with a magnet below the bottom and two electrodes on opposite sides of the tank (see Fig. 1). A salt solution (specific gravity = 1.0) of thickness H_{ul} serves as the conducting fluid enabling electromagnetic forcing, which lies on top of a 3 mm nonconducting heavier layer (specific gravity = 1.5). The forcing protocol constitutes of a 1 s pulse of constant current. The settings of the numerical simulations are identical to the experimental ones, except the internal interface is taken non-deformable in the simulations.

In Fig. 2 (upper row) experimentally obtained snapshots are displayed for the dipole at mid-depth of the top fluid layer ($H_{ul} = 7$ mm) at several time instances. In these figures we can identify several vertical structures. For example, in Fig. 2(b) upward vertical motion is present inside the two individual vortex cores surrounded by downward motion, strong upward motion in the tail, and band-like structures in front of the dipole. At an even later stage in the evolution [see Fig. 2(c)] an oscillatory motion is seen of the vertical velocity inside the two vortex cores. In the experimental result, the so-called “frontal circulation” [1–4] is seen at late stages of the evolution, i.e. a roll-like structure with upward motion and in front of that a downward motion. Note that these structures and their evolution show a great resemblance with the flow structures appearing in the dipolar vortex flow in a single fluid layer [1, 2].

Comparison of the numerical simulation results shown in Fig. 2 (lower row) with the corresponding experimental ones [Fig. 2 (upper row)] reveal a striking resemblance with respect to the structures and their evolution. However, the frontal circulation is not observed in the numerical simulation. This absence is illustrated in more detail in the vertical slice presented in Fig. 3. The frontal circulation, associated with negative ω_x , is not present in the upper fluid layer as it does not penetrate through the internal interface (the dashed white line in Fig. 3). In the numerical simulation the interface is taken flat, whereas in

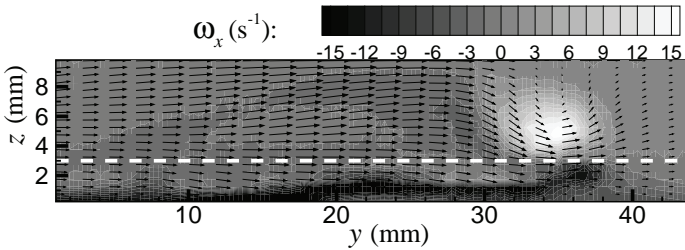


Fig. 3. Vertical slice through the symmetry plane of the dipole ($x = 0$) at time $t = 2.60$ s showing the ω_x distribution (gray levels), with vectors representing the flow in the yz -plane. The white dashed line indicates the internal interface between the fluid layers.

the experiment the interface will most likely deform as the density difference between the two fluids is rather low. This interface deformation is considered to be responsible for the development of the frontal circulation in the upper layer of the experiments. Furthermore, the magnitude of the vorticity component ω_x in the vertical slice of Fig. 3 turns out to evolve to significantly larger values than that of the “primary” vorticity component ω_z .

In Fig. 4(a) a snapshot for the case of a upper fluid depth $H_{ul} = 9.00$ mm is presented, so larger than the value 7.0 mm discussed above. Also, in Fig. 4(b-c) snapshots are displayed for smaller upper fluid depths $H_{ul} = 5.0$ mm and

3.5 mm, respectively. For all cases one observes a clear resemblance in the

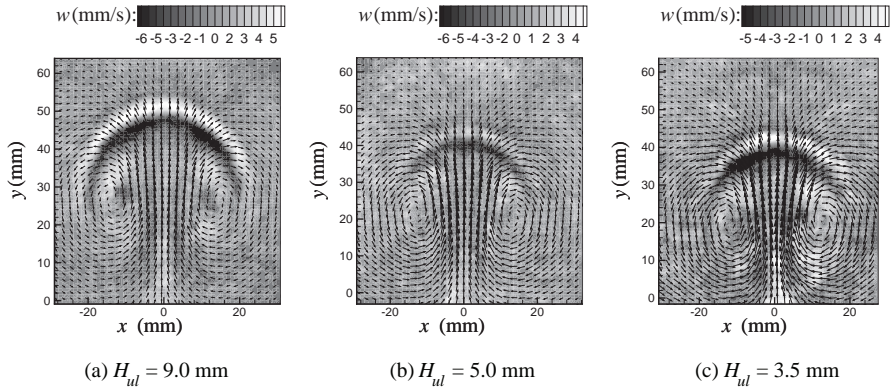


Fig. 4. Experimentally obtained velocity fields of a dipolar vortex in a horizontal plane at mid-depth of the top fluid layer having a thickness of (a) $H_{ul} = 9.0$ mm at $t = 2.6$ s, (b) $H_{ul} = 5.0$ mm at $t = 1.8$ s, and (c) $H_{ul} = 3.50$ mm at $t = 1.5$ s. Meaning of vectors and gray levels: see caption Fig. 2.

vertical motions. Clearly, the observed 3D structures in the $H_{ul} = 7.0$ mm case are representative of the other upper fluid depths. The same applies for the temporal evolution of the flow.

Conclusions

The experimental observations and numerical simulations show the presence of significant 3D motions in the two-layer configuration similar to those found in experiments on a single shallow fluid layer. As the dipole is one of the most elementary vortex structures in 2D turbulence, it is to be expected that decaying turbulence in shallow two-layer fluids will show similar 3D features.

Acknowledgments

This work is part of the research programme no. 36 “Two-Dimensional Turbulence” of the “Stichting voor Fundamenteel Onderzoek der Materie (FOM)”.

References

1. R.A.D. Akkermans, L.P.J. Kamp, H.J.H. Clercx, and G.J.F. van Heijst, *Europhys. Lett.*, **83**, 24001 (2008).
2. R.A.D. Akkermans, A.R. Cieslik, L.P.J. Kamp, R.R. Triefling, H.J.H. Clercx, and G.J.F. van Heijst, *Phys. Fluids*, **20**, 116601 (2008).
3. L.C. Lin, M. Ozgoren, and D. Rockwell, *J. Fluid Mech.*, **485**, 33 (2003).
4. D. Sous, N. Bonneton, and J. Sommeria, *Phys. Fluids*, **16**, 2886 (2004).

The 3D character of decaying turbulence in a shallow fluid layer

A.R. Cieslik, L.P.J. Kamp, H.J.H. Clercx, and G.J.F. van Heijst

Department of Applied Physics & J.M. Burgers Centre, Eindhoven University of Technology, 5600 MB Eindhoven, The Netherlands

L.P.J.Kamp@tue.nl

1 Introduction

A canonical laboratory setup to study two-dimensional (2D) turbulence is the electromagnetically driven shallow fluid layer. The argument used here is that whenever the vertical length scale is much smaller than the horizontal length scale the flow is presumed to behave in a 2D fashion with a Poiseuille-like structure in the vertical direction. However, this assumption disregards the presence of a strong non-uniform magnetic field used to electromagnetically force the flow, a vertical component of the Lorentz force, and, most importantly, it oversimplifies the structure of three-dimensional (3D) recirculating flows [1].

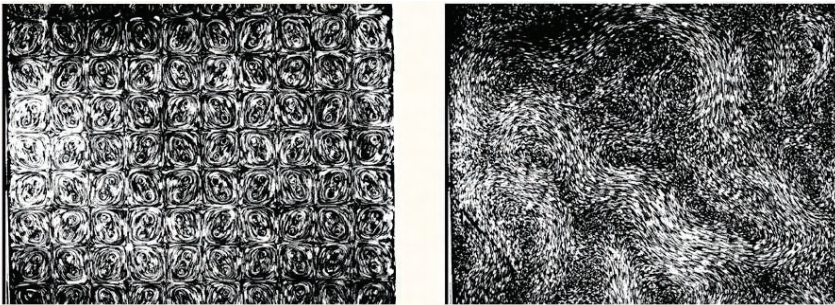


Fig. 1. Streak visualization of the flow at the end of the forcing stage ($t = 0$, left panel) and later in the evolution ($t = 30$ s, right panel).

2 Laboratory experiments

The experimental set-up consists of a shallow layer of electrolyte, in which the motion is created by electromagnetic forcing. Experiments were carried out with an array of 10×10 magnets with alternating polarity, yielding an initial flow field consisting of 10×10 flow cells, see Fig. 1 (left panel). The

fluid motion is visualized by adding small tracer particles to the fluid, their motion being recorded from above. Flow measurements were carried out at the free surface and at some horizontal cross sections of the fluid layer. In the latter experiments, the fluid was seeded with neutrally buoyant particles which were illuminated by a horizontal laser sheet. In both cases, quantitative information about the flow was obtained by (stereo-)PIV measurements.

After the forcing is switched off ($t = 0$ s), the flow shows a rather complex evolution, at some stage revealing the emergence of meandering flow patterns, extending over larger length scales, see Fig. 1 (right panel). This behaviour is in remarkable contrast with evolution of purely 2D flows, in which the inverse energy cascade is observed in the formation of larger coherent vortex structures. Figure 2 (upper row) shows the evolution of the vertical vorticity ω_z as

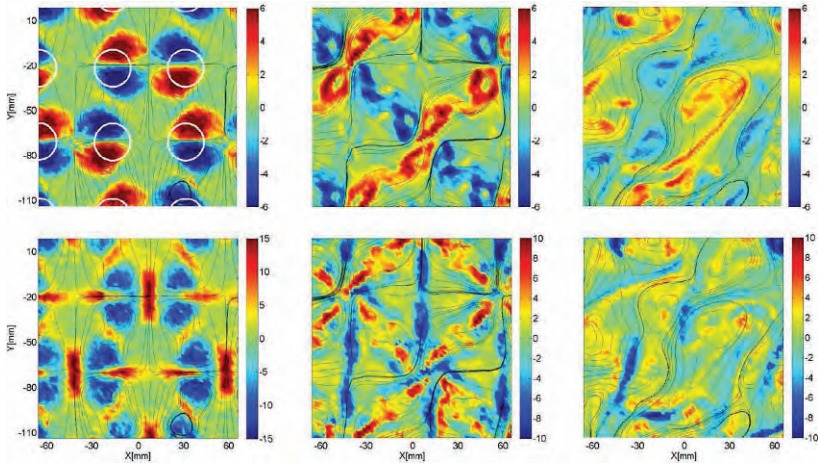


Fig. 2. Snapshots of the vertical vorticity ω_z (upper row; colours/shades indicate magnitude in 1/s) and the vertical velocity w (lower row; colours/shades indicate magnitude in mm/s) for $t = 0$ s (left), $t = 2$ s (middle) and $t = 5$ s (right).

well as the instantaneous streamline pattern of the horizontal flow component measured in a plane at $h = 5$ mm above the bottom obtained by SPIV measurements. The plots only cover a limited part of the domain. At the end of the forcing stage (upper row; left panel) one clearly observes a number of dipolar vortex structures. Owing to their self-propulsion these dipoles translate, which quickly leads to a sequence of head-on collisions between neighbouring dipoles all over the domain. During this process the initial symmetry of the flow is progressively broken and eventually the streamline pattern reveals meandering current structures extending over the whole measurement domain, while the vorticity is observed to become organized in elongated filaments rather than vortices (see Fig. 2 (upper row, middle and right panel)). Moreover, these vorticity filaments tend to be aligned with the streamlines.

A set of corresponding plots of the vertical velocity w measured at the same level $h = 5$ mm is also displayed in Fig. 2 (lower row). Throughout the evolution significant vertical motion is observed. Regions of pronounced upward flow are present at the front of each dipole, as well as at its rear; regions of downward motion are seen in the dipole cores (see Fig. 2 (left panels)). This is in agreement with the vertical flow structures found in single dipole vortices in a shallow fluid layer [1, 2]. The maximum value of the vertical velocities between two approaching dipoles is typically 20 mm/s, while the root-mean-square value of the horizontal flow components is 28 mm/s, indicating that locally the flow is fully three-dimensional. Regions of upward and downward flow remain visible in the next stages and the flow has taken the appearance of larger meandering structures (Fig. 2 (right panels)). The regions of downward motion tend to be correlated with the meandering flow structures, while the weaker upward motion is mainly observed inside vortical structures [3].

3 Numerical comparison between 3D and 2D flows

Full 3D numerical simulations based on the Navier-Stokes equation including a realistic representation of the electromagnetic forcing and corresponding 2D numerical simulations show considerable differences in the evolution of the vorticity (see Fig. 3 (upper row)). The 3D numerical simulations show meandering current structures at the surface and also at lower levels in the fluid layer. Fig. 3(b) illustrates the numerically calculated ω_z distribution in a horizontal cross-sectional plane at $h = 5$ mm above the tank bottom for $t = 21$ s. For comparison, Fig. 3(a) shows the ω_z distributions in a corresponding 2D simulation. Immediately after the forcing the flow patterns in the 3D and 2D simulations are still quite similar. In both cases one observes the emergence of elongated vorticity structures. However, as the flow evolves the vorticity distributions in the 3D and 2D simulations show considerable differences: while the flow in the 2D simulations is dominated by large-scale coherent structures (Fig. 3(a)), in the 3D simulations the horizontal flow is characterized by elongated patches of vorticity, indicating the presence of large-scale meandering currents (Fig. 3(b)).

Another feature studied numerically is the dispersion of passive tracer particles released at the free surface of the fluid layer, see Fig. 3 (lower row). For this purpose, a large number particles were initially distributed along a regular grid covering the full flow domain. In 2D simulations, they were advected without showing any clear concentration regions (see Fig. 3(c)). In the fully 3D simulations, however, they showed a very clear tendency to collect in elongated patches, coinciding with areas of negative horizontal divergence, i.e. where the vertical velocity $w < 0$ below the surface, see Fig. 3(d). For a more elaborate discussion we refer to Ref. [3].

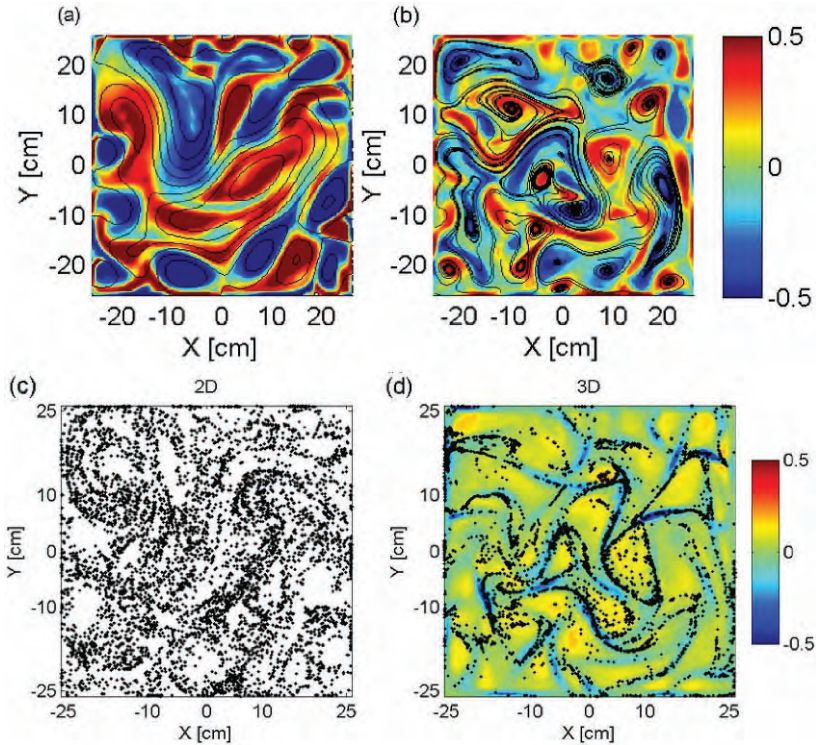


Fig. 3. Snapshots of the vertical vorticity ω_z (upper row; colours/shades indicate magnitude in 1/s) obtained from 2D (a) and 3D (b) numerical simulations at $t = 21$ s. The lower row shows the distribution of tracer particles for $t = 40$ s from the 2D simulation (c) and the 3D simulation (d), where colours/shades indicate the magnitude of the vertical velocity.

4 Conclusion

The laboratory experiments and the numerical simulations clearly demonstrated that these electro-magnetically forced shallow-layer flows are not 2D, not even quasi-2D: vertical velocities and vertical shear are substantial, and destroy the intuitive 2D picture that one originally might have had.

References

1. R.A.D. Akkermans, A.R. Cieslik, L.P.J. Kamp, R.R. Trieling, H.J.H. Clercx, and G.J.F. van Heijst, *Phys. Fluids*, **20**, 116601 (2008).
2. D. Sous, N. Bonneton, and J. Sommeria, *Phys. Fluids*, **16**, 2886 (2004).
3. A.R. Cieslik, L.P.J. Kamp, H.J.H. Clercx, and G.J.F. van Heijst, *Europhys. Lett.*, **85**, 54001 (2009).

Vortex dynamics in a Karman street behind a heated cylinder: defects and potentialities of acoustic diagnostics

V.V. Chernov⁽¹⁾, P.L. Soustov⁽¹⁾, P.R. Gromov⁽¹⁾, A.B. Ezersky^(1,2), and P. Paranthoen⁽³⁾

(1) Institute of Applied Physics, Russian Academy of Sciences 46 Ul'janov Street 603950 N. Novgorod, Russia

(2) CNRS 6143 M2C Universit de Caen 2-4 rue des Tilleuls, 14000 Caen, France
Alexander.Ezersky@unicaen.fr

(3) CNRS 6614 CORIA Site Universitaire du Madrillet BP12 Avenue de l'Universit 76801 Saint Etienne du Rouvray, France

In his paper reports results of experimental study of defects arising in a Karman vortex street in a wake behind a heated cylinder by means of remote acoustic diagnostics. This technique proved to be efficient for finding defects in a periodic structure by asymmetric shape of spectral picks of scattered sound.

A vortex street behind a heated cylinder is a classical object for investigation of heat transfer in flows. Until recently, investigations of a flow around a heated cylinder and of heated bodies in general were focused on the dependence of averaged characteristics of heat transfer (e.g., Nusselt number) on Reynolds number and on other flow parameters: degree of turbulence, roughness, and cylinder elongation. Nowadays the Karman street attracts the attention of researchers involved in fluid mechanics as a sample flow for testing new ideas in mixing of impurity, chaotic dynamics and so on. Detailed information about spatio-temporal dynamics of velocity and temperature fields is needed for these purpose. In this paper we show that heating of a streamlined cylinder can substantially change the regime in a wake and evoke the transition from a laminar state to spatio-temporal chaos of defects.

Under defects in a temperature-homogeneous von Karman vortex street one understands regions of the street where different modes determining the transition from a laminar to a turbulent regime are excited against the background of regular vortices. Such modes arise at $160 < Re < 230$ ($Re = U/d\nu$, where U is incident flow velocity, ν is kinematic viscosity, and d is diameter of the cylinder). If the cylinder is heated, then as was shown in [1], the amplitude and phase modulation increasing downstream occurs in the street at much smaller Reynolds numbers $60 < Re < 110$. This leads to formation of

regions with disturbed order, i.e., with defects. When such defects arise in the street, its spatial period depends on coordinate along the axis of the streamlined cylinder. If there is only one defect, then one of the half-planes contains one spatial period more than the other. Defects are localized in regions with the growing number of spatial periods. Characteristics of such defects were studied by records of time series at separate points, while no information about the spatial structure of the flow was obtained. Formore detailed investigation of defects arising in a von Karman vortex street behind a heated cylinder we staged experiments on visualization and remote acoustic diagnostics of the flow. Experiments were carried out in an air flow of IAP RAS low-turbulence (the level of turbulent velocity pulsations in an incident flow was less than 0.4%) wind tunnel with the size of the operating part 30 x 30 x 120 cm, velocity $U=2.7\text{m/s}$, and $Re=109$. The scheme of the experiment was analogous to that described in [2, 3, 4]. We studied ultrasound scattering with frequency $f_0=121.1\text{ kHz}$ (at the wavelength $\lambda_0 = 2.7\text{ mm}$) in a vortex behind a vertical cylinder with diameter $d=0.6\text{ mm}$ placed in the operating part of the wind tunnel. The temperature of the cylinder was calculated by the known empirical formula relating the Nusselt (dimensionless heat flux) and the Reynolds numbers. Structures were visualized by means of a thin wire $d_{sm} = 0.2\text{ mm}$ (smoke wire) that was stretched parallel to the base cylinder at distance $\approx 9d$ downstream. The wire was coated by oil, then direct current was passed through it giving rise to smoke in which structures could be visualized. The pictures were taken by a high-resolution digital camera. It was found that, in the absence of heating, vortex shedding occurred with a tilt. Spatio-temporal characteristics of vortex street depend on density of electric power P . For $P=80\text{ J/m}$, defects are observed in the wake. A typical picture of a vortex street with defects is presented in fig. 1.

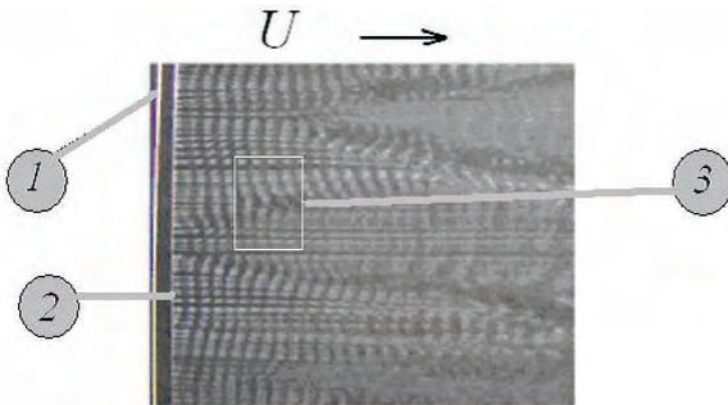


Fig. 1. Visualization of a wake in the regime with defects: 1 - streamlined cylinder, 2 - smoke wire, 3 - defect, the arrow points the direction of the flow U .

Such structures are observed up to $P \approx 200 J/m$. With a further increase of heating, the wake becomes regular and stable parallel vortex shedding occurs, but now with a larger spatial period. In order to obtain qualitative characteristics of a vortex street with defects we carried out experiments on ultrasound scattering. Parameters of ultrasound were measured by the high-frequency 4135 B&K microphone. The sound scattered at the vortex street had a narrow spectrum, hence the signal from the microphone was multiplied with the harmonic heterodyne signal $\cos(2\pi f_g)$ and the resulting signal was analysed in the 0-20 kHz range. The sound scattered at an infinite von Karman vortex street is known to be a set of harmonics propagating symmetrically to the direction of incident sound [2, 3, 4]. The propagation angle of each harmonic, ϕ_m , is found from the condition

$$\frac{2\pi f_0}{c} \sin(\psi) = \frac{2\pi f_0}{c} \sin(\phi_m) + \frac{2\pi m}{l} \tag{1}$$

where f_0 is the frequency of incident sound wave, c is sound velocity, ψ is the angle of acoustic wave incidence on the street, m stands for the number of the harmonic, and l is the spatial period of the street. The amplitude of each harmonic is determined by vortex circulation in the street, Γ , and by the quantity of heat, Q , transported by the vortices. The frequency of each harmonic is shifted relative to the incident sound frequency:

$$f_m = f_0 + m f_{Sh} \tag{2}$$

multiple to the vortex shedding frequency (Strouhal frequency f_{Sh}). If the medium is temperature homogeneous, then each vortex scatters the sound, primarily forward, and only the $+1$ -th and -1 -th harmonics are usually observed in experiment [2, 3]. In the case of the wake behind a heated cylinder, the temperature field makes a contribution mainly to even harmonics, and the velocity field to odd harmonics [4]. The scattered sound spectra and dispersion indexes of the fundamental harmonic $m=1$ were measured in experiment for different temperatures of cylinder heating. Examples of scattered sound spectra at angles corresponding to maximal amplitude of the fundamental harmonic are given in fig. 2.

It is clear from the spectra in fig. 2 that the vortex shedding frequency drops down with increasing cylinder temperature. This regularity was observed in many works (see, e.g., [1,5] and can be explained by temperature dependence of kinematic viscosity . Heating of a streamlined cylinder may be considered using the effective Reynolds number [1,5] The scattered sound spectra are symmetric for high and low heating temperatures (spectra 1 and 4 in fig. 2) and nonsymmetric for temperatures at which defects appeared in the Karman street (spectra 2 and 4, in fig. 2). Such a spectral pattern can be explained as follows: The arising defects lead to a decrease of vortex shedding frequency in definite regions of the street which make a contribution to the spectral components with frequencies less than . Analogous spectra of temperature pulsations were found in the work [1] in measurements by means of hot

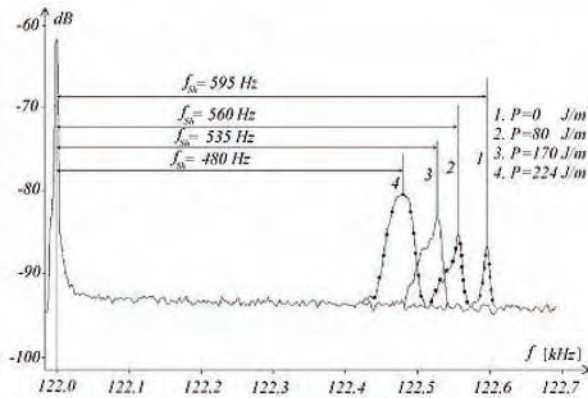


Fig. 2. Spectra of scattered sound at $Re=109$ for different power of cylinder heating P . Peak at $f=122.0$ Hz corresponds to the incident sound wave.

and cold wire anemometers in the wake behind a heated cylinder, where it was noted that the pulsation spectrum asymmetry is due to excitation of defects in the street. Measurement of scattering angles allowed us to determine the dependence of spatial period on cylinder heating. As heating was increased, the spatial period of the street increased too. This result is in good agreement with an increase of the spatial period of Karman street as the Reynolds number is decreased. Thus, by characteristics of scattered sound one can determine the action of heating on vortex wake parameters and arising in the Karman street of complex regimes with defects. In contrast to measurements at individual points, acoustic diagnostics enables one to determine characteristics of a vortex wake average over space. Our experiments demonstrated that temperature pulsation spectra determined by characteristics of scattered sound and measured at individual points are similar for different regimes of streamlining. This result is important for analysis of spatio-temporal disorder in wakes behind poorly streamlined bodies.

The research was done under financial support of the RFBR, grant No. 07-02-92175-CNRS-a and PICS CNRS grant No.3903

References

1. A.B.Ezersky, P.Paranthoen. Int. J. Transport Phenomena, **7**, 45 (2005).
2. P.R.Gromov, A.B.Ezersky, A.L.Fabrikant. Acoust. Phys., **28**, 763 (1982).
3. A.B.Ezersky, P.R.Gromov, P.L.Soustov, V.V.Chernov. Acoust. Phys., **51**, 212 (2005).
4. A.B.Ezersky, A.B.Zobnin, P.L. Soustov. Izv. VUZov, **38**, 832, (1995).
5. An-bang Wang, Z.Trvncek, K.-Ch. Chia. Physics of Fluids, **12**, 1401 (2006).

Asymmetric vortex shedding in the turbulent wake of a flat plate in a rotating fluid

Hatef A. Khaledi, Mustafa Barri, Helge I. Andersson

Department of Energy and Process Engineering NTNU, 7491 Trondheim, Norway
hatef.khaledi@ntnu.no

Summary. A numerical experiment of the turbulent flow behind a parallel-sided plate subjected to solid body rotation along the spanwise direction is performed. The Reynolds number $Re = U_\infty d/\nu$ based on inflow velocity and width of the plate equals 750, while the global Rossby number $Ro_g = U_\infty/2\Omega d$ varies from 1 to 0.16. The work provides an insight into several salient features of the spanwise rotating wake flow and revealed fascinating effects exerted by the Coriolis force on the wake flow turbulence.

1 Introduction

Due to their numerous important applications in geophysics and engineering such as turbo-machinery, turbulent and transitional shear flows in a rotating frame of reference with the rotating vector oriented along the span have been studied extensively. In these flows the local Rossby number, a characteristic number which measures the relative importance of inertial and Coriolis forces, can vary significantly. In tornadoes the Rossby number is on the order of 10^3 , in low pressure areas such as tropical storms, extratropical and sub-polar cyclones are on the order of 0.1-1 and around 2-3 in the wake of a large island. Several engineering applications motivated the scientists to conduct their very early experiments on rotating bounded flows and free shear flows such as the boundary layer over a flat plate as well as flow over bluff bodies subjected to solid body rotation. In the shear flow cases the effect of solid body rotation on the flow field depending on the cyclonic or anti-cyclonic sense of rotation can vary. Several experiments and numerical surveys have been devoted to study the influence of the Coriolis force on flow structure and turbulence. The Karman-type vortex shedding behind an obstacle can be suppressed for high rotation rates corresponding to a Rossby number below 0.1. If vortex shedding occurs, however, satellite photos of atmospheric vortex streets and laboratory experiments show that the vortex street exhibits an asymmetry with stronger cyclonic eddies and weaker anti-cyclonic eddies (e.g. [1]). The wake analysis

of a cylinder in a rotating frame of reference parallel to the spanwise direction was firstly studied by Witt and Joubert [2]. The asymmetry in the wake and turbulence quantities was the main feature of this flow. Boyer and Davis [3] went through and extensive experimental measurements for flow past a circular cylinder in a rotating water channel. Flow patterns were obtained over a range of several independent parameters such as Rossby number and Ekman number. In this paper preliminary results of direct numerical simulation of the flow over the flat plate subjected to solid body rotation will be presented. The paper is organized as follow. Following the introduction part the numerical simulation technique and flow field will be elaborated in section 2. In section 3 discussions will be presented. However due to space limitation, only a part of the extracted results is depicted here. Finally, concluding remarks will end this short article.

2 Computational approach and flow characteristics

The flow past a parallel-sided plate at a moderately high Reynolds number has been considered while the whole system was rotated about y axis. x , y and z are respectively the streamwise, spanwise and cross-streamwise directions. The size of computational domain for each coordinate direction is $Lx = 20$, $Ly = 6$ and $Lz = 16$. All spatial dimensions are normalized by the width of the plate and velocities are non-dimensionalized by the uniform inflow velocity U_∞ . The thickness of the plate is very small and equals to $0.02d$. The Reynolds number, based on the uniform inflow velocity U_∞ and width of the plate d is 750 which is sufficiently high to make even the near-wake turbulent. The rotation vector is oriented anti-parallel to the span direction i.e. $\Omega = (0, -\Omega, 0)$. In order to study the effect of rotation on the structure of the wake, four different global Rossby numbers, $Ro_g = 1$ and 0.16 were chosen. The Rossby number is based on the uniform inflow velocity, rotational rate of the frame of reference and width of the plate and is defined as $Ro_g = U_\infty / 2\Omega d$. The subscript g denotes the characteristic Rossby number based on inflow velocity. The simulation has been carried out with the well-documented finite-volume solver MGLET [4]. The three-dimensional Navier-Stokes equations for an incompressible fluid are approximated on a staggered Cartesian grid system. A 3^{rd} -order explicit Runge-Kutta scheme in time and a 2^{nd} -order accurate central-differencing scheme in combination with an iterative SIP (Strongly Implicit Procedure) for solving the Poisson equation are employed. A uniform velocity profile $U_\infty = 1$ was prescribed at the inlet without any free-stream perturbation and a Neumann boundary condition was used for the pressure. A free-slip boundary condition was applied on the top and bottom walls of the domain whereas foreseen homogeneity in spanwise direction enabled us to use periodic boundary conditions on the side walls.

3 Results and discussion

We first examine the three dimensional flow structures at two different Rossby numbers. In an attempt to better understand the evolution of the vortex structures in the complex wake of a flat plate subject to solid body rotation, it is important to determine and identify the relation between various vortical structures. In Figure 1 the instantaneous vorticity magnitude ($|\omega| = \frac{1}{2}(\omega_x^2 + \omega_y^2 + \omega_z^2)$) at $Ro_g = 1$ and $Ro_g = 0.16$ is shown. As it can be seen in the figure at $Ro_g = 1$, the turbulence within the cyclonic eddies which are rotating parallel to solid body rotation vector has been suppressed whereas the anti-cyclonic eddies are vigorously turbulent. The feature can clearly be observed also in Figure 2(a) where the 3D instantaneous iso-surface of spanwise vorticity ω_y has been depicted. On the cyclonic side of the wake the tendency of the flow structures to form Karman rollers is quite clear. The formation of Karman rollers on the cyclonic side of the wake is a manifestation of the two-dimensionalization. On the other side of the wake, i.e. at the anti-cyclonic regime, the streamwise longitudinal rib-like vortices seem to be reduced in magnitude downstream of the plate. The rib vortices are still apparent between the consecutive rollers in the very near wake of the flow on the anti-cyclonic side. A nearly complete relaminarisation of the wake is observed in Figures 1(b) and 2(b), obviously because $Ro_g = 0.16$ is beyond that of maximum destabilization of the anti-cyclonic eddies. These observations are broadly consistent with the stability analysis and LES of organized eddies in rotating turbulence by Cambon et al. [5].

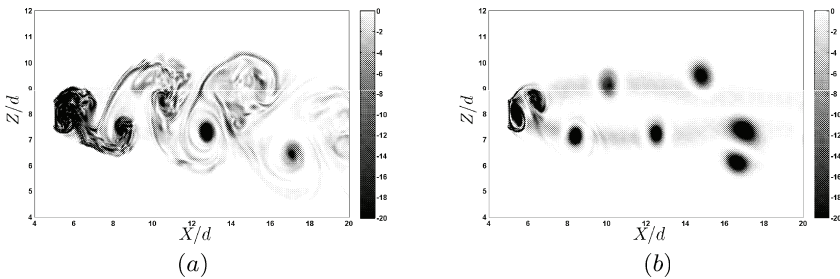


Fig. 1. Contour plot of instantaneous vorticity magnitude. (a) $Ro_g = 1$, (b) $Ro_g = 0.16$

4 Conclusions

Direct numerical simulations of the flow over a flat plate subjected to solid body rotation have been performed. The present numerical results have served



Fig. 2. Iso-surface plot of spanwise vorticity. (a) $Ro_g = 1$, (b) $Ro_g = 0.16$

to illustrate the strong and moderate effects of the Coriolis force on the 3-D structure of the shear in the near-wake flow after the plate. A distinguishing feature of the Coriolis force was to make the vortex Karman street asymmetric. Moreover, by increasing the rate of the rotation the two-dimensionalization of the vortex structures specifically on the cyclonic side of the wake was quite apparent.

References

- [1] D. ETLING Mesoscale vortex shedding from large islands: a comparison with laboratory experiments of rotating stratified flows. *Meteorol.Atoms.Phys.* **43**:145-151 (1990).
- [2] H.T. WITT, P.N. JOUBERT Effect of rotation on a turbulent wake. *Proc. 5th Symposium on Turbulent Shear Flows, Ithaca*: 21.25-21.30 (1985)
- [3] D.L. BOYER, P.A. DAVIES Flow past a circular cylinder on a β -plane. *Phil.Trans.R.Soc.Lond.A* **306**: 533-556 (1982)
- [4] M. MANHART A zonal grid algorithm for DNS of turbulent boundary layers. *Comput.Fluids* **33** : 435-461(2004)
- [5] C. CAMBON, J.P. BENOIT, L.SHAO, L.JACQUIN Stability analysis and large-eddy simulation of rotating turbulence with organized eddies, *J.Fluid Mech.* **278** : 175-200(1994).

Stability of steady vortices and new equilibrium flows from “Imperfect-Velocity-Impulse” diagrams

P. Luzzatto-Fegiz and C. H. K. Williamson

Sibley School of Mechanical and Aerospace Engineering, Cornell University
Ithaca, NY 14853-7501, USA
pl247 at cornell.edu

In 1875, Lord Kelvin proposed an energy-based argument for determining the stability of steady inviscid flows [1]. While the key underpinnings of the method are well established, its practical use has been the subject of extensive debate. In this work, we draw on ideas from dynamical systems and imperfection theory to construct a methodology that represents a rigorous implementation of Kelvin’s argument. Besides yielding stability properties, which are found to be in precise agreement with the results of linear analysis, our approach also implicitly yields new bifurcated solutions branches, as we shall describe below.

Kelvin’s original argument states that steady inviscid flows are associated with stationary points of the kinetic energy, for a given linear or angular impulse [1]. It appears that Kelvin found this statement to be self-evident, as he provided no proof for it; the first mathematical derivation was published more than a hundred years later by Benjamin [2] in 1976. Benjamin’s proof implies that, for example, for a two-dimensional vortical flow with excess kinetic energy E and angular impulse J , one can construct a functional H :

$$H = E - \Omega J, \tag{1}$$

such that the first variation δH with respect to vorticity-preserving perturbations vanishes if, and only if, the flow is in equilibrium when observed in a frame rotating with angular velocity Ω [3]. One may then proceed to establish stability of the solution as follows. Since E and J are both conserved in an inviscid flow, H is also a conserved quantity. If the stationary point is a maximum or a minimum in the solution space (implying that the second variation $\delta^2 H$ is positive or negative definite), then a displacement away from the solution would lead to a change in H , which is impossible; hence the solution must be stable to isovortical perturbations, thus yielding a sufficient condition for stability. Similarly, a necessary condition for instability to occur is that the stationary point is a saddle [1].

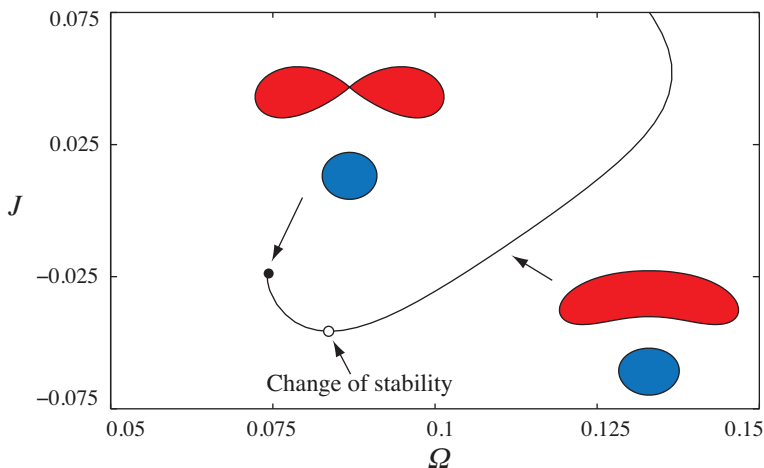


Fig. 1: “Velocity-Impulse” diagram for the opposite-signed pair with $A_1/A_2 = 0.3$. Our approach immediately points to a change of stability at a minimum in J (empty circle), after which the family ends with a limiting vortex shape (filled circle).

Stability can therefore be established by directly evaluating the second variation of H ; this approach carries over to all conservative systems for which a similar functional can be defined (see e.g. [4, 5]). However, implementing this methodology is not usually feasible, especially since steady solutions of practical interest are typically known only numerically. It is therefore common to resort to computing eigenvalues through a linear stability analysis, which is usually a process far more laborious than computing the steady solutions.

Saffman & Szeto [6], having numerically found steady solutions for two co-rotating vortices, proposed an approach to circumvent this difficulty as follows. Equation (1) can be interpreted as establishing extrema of E under the constraint that $J = \text{const.}$, with Ω taking the role of a Lagrange multiplier. A plot of E versus J then shows that, for a given J , there exist two E branches, joined at a fold point. The top branch was interpreted as a maximum (and hence stable), while the lower branch as a saddle (possibly unstable). This prediction was subsequently found to match the results of the linear stability analyses of Kamm [7] and Dritschel [8].

A fundamental objection to such an implementation of Kelvin’s argument was however posed by Dritschel [9], who pointed out that there seems to be no necessary link between the shape of a plot of E versus J and the curvature of the H surface. That is, one cannot determine whether the “highest” solution branch in a two-dimensional plot does actually correspond to a maximum in the solution space. Furthermore, Dritschel [9] pointed out that even if such correspondence could be established, additional changes of stability could also occur away from extrema in E and J by means of bifurcations to new families of solutions. This would render the method unreliable.

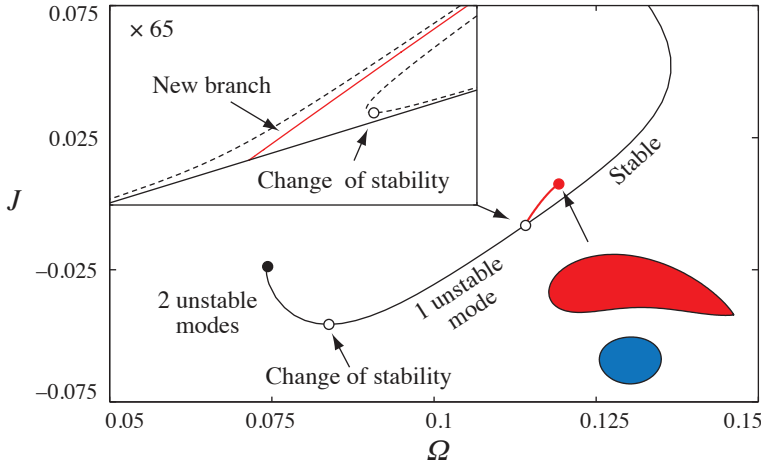


Fig. 2: “Imperfect-Velocity-Impulse” diagram for the opposite-signed pair with $A_1/A_2 = 0.3$. Re-computing the solutions with an imperfection (dashed lines in the inset) reveals an additional change of stability at a bifurcation associated with a new family of vortices, which display lesser symmetry (red line).

In a later work, Dritschel [8] provided an example for which the method fails to correctly predict the onset of instability. He considered the family consisting of two uniform vortices with equal vorticity magnitude, opposite sign, and unequal area, and inspected different area ratios A_1/A_2 , for which he computed both equilibrium states and linear stability properties. For families with A_1/A_2 fixed between 1 and 0.9, the extremum in E gave an accurate prediction for the onset of instability. However, below $A_1/A_2 \simeq 0.9$ the change of stability occurred before the location predicted by a plot of E versus J . This provided definitive proof that such an implementation of Kelvin’s argument does not always work.

In the light of such a rich history of developments, we have been stimulated to employ tools from dynamical systems theory to devise a new approach, which provides a rigorous link between extrema in a particular bifurcation diagram and changes in the second variation of a functional such as H . We show that the relevant plot is not one of impulse and energy, but of velocity and impulse, and establish a rigorous link between extrema in J and changes in stability properties.

Nevertheless, the second objection posed by Dritschel [9] would still stand, since, while an extremum in J is always associated with a change in the curvature of the H surface, changes in stability that occur through bifurcations would be undetected (without performing a linear stability analysis). We resolve this issue by employing the fact that joins in solution branches are not structurally stable (see e.g. [10]). Hence, by introducing a small imperfection and re-computing the equilibria, we obtain a new family of steady solutions

for which the solution branches will be distinct; thus any bifurcations are uncovered, and all changes of stability are apparent in an “Imperfect-Velocity-Impulse” (IVI) diagram.

Eager to verify whether this novel approach would work, we employed the “IVI diagram” methodology to re-examine the opposite-signed family studied by Dritschel [8]. Figure 1 shows the velocity-impulse diagram J versus Ω for $A_1/A_2 = 0.3$. Introducing a small imperfection and re-computing the equilibria breaks the family of solutions into distinct branches (dashed lines in the inset of Fig. 2), hinting at the presence of a bifurcation. Our method then reveals another extremum in J , which is associated with an additional change of stability. It turns out that the location of this change of stability, found using our approach based on IVI diagrams, agrees precisely with previous results from linear analysis. Finally, by bringing the imperfection to zero, our approach enables us to determine a new bifurcated branch (red line in Fig. 2), revealing a new family of solutions of lesser symmetry, whose vortex shapes are exhibited in Fig. 2.

In further work, we have applied the same approach to a wide range of classical solutions of the Euler equations, including for example the Kirchhoff elliptical vortices, the co-rotating vortex pair and its continuation into a singly connected shape [11], the finite-area Kármán vortex street [12], Stuart vortices [13], and other equilibrium flows. For all cases considered, we find precise correspondence with classical results from linear analysis, while additionally discovering new families of steady solutions. This work is to be found in Luzzatto-Fegiz & Williamson [14].

Partial support from ONR and from NSF is gratefully acknowledged (ONR Contract N00014-07-1-0303, NSF Grant CBET-0813835). We would like to thank Prof. S. Leibovich and Prof. P.H. Steen for several useful discussions.

References

1. W. Thomson, *Vortex statics*. Collected works **IV**, 115, (1875).
2. T.B. Benjamin, in: *Applications of Methods of Functional Analysis to Problems in Mechanics*. Springer, 1976.
3. P.G. Saffman, *Vortex dynamics*, Cambridge University Press, 1992.
4. D.D. Holm, J.E. Marsden, T. Ratiu & A. Weinstein, *Phys. Rep.* **123**, 1 (1985).
5. V.A. Vladimirov, H.K. Moffatt & K.I. Ilin, *J. Fluid Mech.* **390**, 127 (1999).
6. P.G. Saffman and R. Szeto, *Phys. Fluids* **23**, 2239 (1980).
7. J.R. Kamm, PhD thesis, California Institute of Technology, Pasadena (1987).
8. D.G. Dritschel, *J. Fluid Mech.* **293**, 269 (1995).
9. D.G. Dritschel, *J. Fluid Mech.* **157**, 95 (1985).
10. T. Poston and I. Stewart, *Catastrophe theory*, Dover, 1978.
11. C. Cerretelli & C.H.K. Williamson, *J. Fluid Mech.* **493**, 219 (2003).
12. P.G. Saffman & J.C. Schatzman, *J. Fluid Mech.* **117**, 171 (1982).
13. R.T. Pierrehumbert & S.E. Widnall, *J. Fluid Mech.* **114**, 59 (1982).
14. P. Luzzatto-Fegiz & C.H.K. Williamson, Submitted to *J. Fluid Mech.*

The Effect of Freestream Turbulence on Far Axisymmetric Wakes

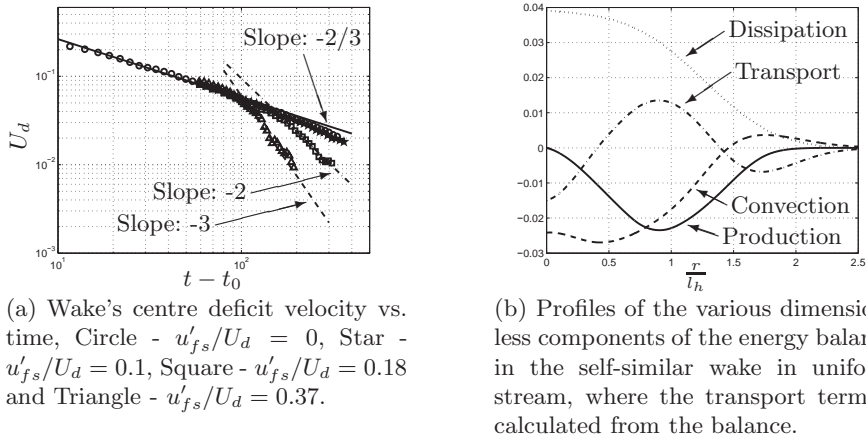
E. Rind and I.P. Castro

AFM Research Group, School of Engineering Sciences, University of Southampton,
Southampton SO17 1BJ, UK
elad.rind@soton.ac.uk and i.castro@soton.ac.uk

While far axisymmetric wakes in uniform streams have been studied thoroughly for many years (e.g. [3]), the effect of free-stream turbulence on them has come under much less scrutiny. Moreover, since the wake of any three-dimensional object becomes axisymmetric far enough downstream and is often enclosed in turbulent surroundings, we believe that our fundamental research is necessary to understand better many general problems.

Based on the extensive reported data on the effects of free-stream turbulence on the development of boundary layers, it may be anticipated that the major parameters affecting the wake's development would include u'_{fs}/U_d and L_x/l_h , where u'_{fs} and U_d are the rms velocity in the background turbulence ($\sqrt{\overline{u^2}}$) and the wake's centre-line deficit velocity, respectively, and L_x and l_h are the integral scale in the background turbulence and the r-location of the wake's half width (where the velocity deficit is one half of its maximum value) respectively.

We are undertaking numerical and wind tunnel experiments which include studies of axisymmetric far wakes in uniform and several turbulent surroundings and a comparison between them. The numerical experiments involve Direct Numerical Simulation (DNS) of a far axisymmetric wake developing in time, using a similar approach to that reported in [2]. The computational domain's dimensions are $4\pi \times 16\pi \times 4\pi$ and the number of Fourier modes is $512 \times 2048 \times 512$, using 512 processors on the UK's HPCx supercomputer. First, the self-similar time-developing wake was initiated using the experimental data reported by [1], with the turbulent statistics added to the mean velocity using a modified three-dimensional version of the digital filter of [7]. After a so-called correction stage, see [2], the wake was fully developed and reached its self-similar state, as can be seen for $u'_{fs}/U_d = 0$ in Figure 1(a), for $(t - t_0) \geq 20$, where t is the dimensionless time and t_0 is wake's virtual origin. By examining its development and statistical properties the wake was found to be qualitatively comparable with previously reported and current experimental data, e.g. [1, 3, 6], giving confidence in the chosen approach. The



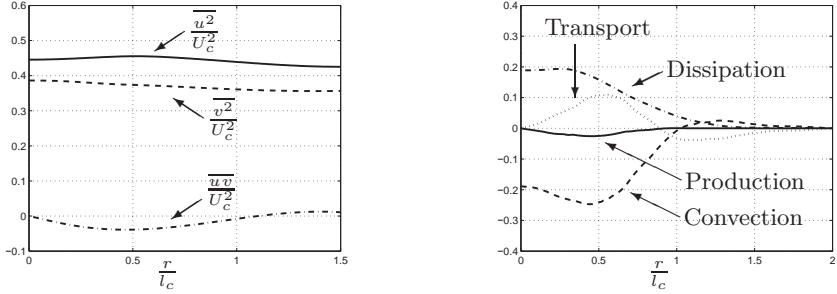
(a) Wake's centre deficit velocity vs. time, Circle - $u'_{fs}/U_d = 0$, Star - $u'_{fs}/U_d = 0.1$, Square - $u'_{fs}/U_d = 0.18$ and Triangle - $u'_{fs}/U_d = 0.37$.

(b) Profiles of the various dimensionless components of the energy balance in the self-similar wake in uniform stream, where the transport term is calculated from the balance.

Fig. 1. DNS Results of the wake in the uniform and turbulent surroundings

wake's turbulent energy balance for the same case ($u'_{fs}/U_d = 0$) is presented in Figure 1(b). Later, several isotropic turbulent fields were generated each having different initial ratios of turbulent intensity to wake deficit velocity ($u'_{fs}/U_d = 0.1, 0.18$ and 0.37). Finally, the self-similar wake and the turbulent background were combined with two constraints: the background turbulence was inserted at all locations outside the mean wake (defined by the region in which the velocity was below 1% of the centre-line value) and to all places inside the mean wake where the turbulence kinetic energy (TKE) was smaller than 5% of the maximum TKE.

Laboratory experiments are being undertaken in the University of Southampton's 3x2 wind tunnel on the far axisymmetric wake behind a disk in uniform and turbulent streams, with a disk Reynolds number based on its diameter, D , of about $Re_D = 15000$. The wind tunnel's test section dimensions are $0.6\text{m} \times 0.9\text{m} \times 4.5\text{m}$ and it is equipped with a speed control system, a two-dimensional automated traverse system and standard constant temperature hot wire anemometry systems. All those devices are controlled simultaneously by a single computer using the EnFlo software (from the University of Surrey) in order to reduce measurement errors – repeatability error in our flow measurements is less than 0.2%. The wind tunnel's free-stream intensity is below about 0.2%. Higher turbulence levels are generated using two aluminium bi-planar grids with the same solidity $d/M \cong 0.27$, where d is the square bar's diameter (12.7 mm) and M is the mesh spacing. A 90° conical disk with base diameter of $D = 10$ mm is mounted in the centre of the test section using a set of Berkley Whiplash Braid Moss Green fishing lines with cross-section diameter of 0.06 mm (the wire's Reynolds number is about 166 times smaller than the disk's) and with its base facing upstream and perpendicular to the flow. Measurements behind the disk in the uniform stream were found to be compa-



(a) Normalised Reynolds stresses profiles of the wake in turbulent background at the location $x/d = 85$, with $U_c = U_0 d^{2/3} (x - x_0)^{-2/3}$, $l_c = d^{2/3} (x - x_0)^{1/3}$ where U_0 is the free-stream velocity and x_0 was determined by extrapolating a linear fit to the data plotted as $(u'_{cl})^{-3/2}$ vs. x

(b) Profiles of the various dimensionless components of the energy balance in the self-similar wake in uniform stream, where the dissipation term is multiplied by 1.17 and the transport term is calculated from the balance.

Fig. 2. Experimental results of the wake in uniform and turbulent surroundings

able to previously reported data, e.g. [1, 3, 6], both in the wake’s decay rate and the TKE balance. For the latter, the dissipation rate was extracted from the energy spectra using its universal form in the inertial subrange, Equation 1, and then factored to ensure that the balancing transport term integrated to zero across the wake. The resulting TKE balance is presented in Figure 2(b) and the dissipation factor required was some 17%.

$$E_{11} = \frac{27}{55} \epsilon^{2/3} \kappa^{-5/3}, \tag{1}$$

where, E_{11} is the one-dimensional spectra in the axial direction of the wake, ϵ is the local dissipation rate and κ is wave number.

Not surprisingly, it was found from both the DNS and the experiments that the wake decays quicker with the presence of the free-stream turbulence. Moreover, our DNS results, presented in Figure 1(a), also show that the wakes decay increasingly quickly as the free-stream turbulence levels increase. We anticipate that our next set of experiments will confirm that result.

The DNS data also show that the effects of the turbulent free-stream do not occur instantaneously but over a period whose duration is a function of the ratio u'_{fs}/U_d , as can also be deduced from Figure 1(a) – the more intense is the free-stream turbulence, the shorter is this ‘penetration’ process. This feature will perhaps be less clear in the experiments, since in that case the free-stream turbulence is present right from the start of the disk’s wake and will effect the initial conditions of what would be, in the absence of free-stream turbulence, the self-similar far-wake region. Nevertheless, we do not anticipate

that this will prevent the general effect of increasingly rapid wake decay with increasing free-stream turbulence.

It was also noticed that after long times in the DNS or long distances in the experiments the rms velocities inside the wake are eventually determined by their values in the free stream; an example from the laboratory experiments is given in Figure 2(a). Since in the DNS the free-stream turbulence was isotropic one might think that with time the turbulence inside the wake would become isotropic also. Careful examination of the turbulent shear stress profiles reveals that that is not the case. The turbulent shear stress does not decay to zero, although the rms velocity profiles do tend to become uniform and equal to the external values. A similar trend was noticed in our experimental results, e.g. Figure 2(a), where (as usual with grid turbulence) the free-stream was not exactly isotropic but certainly had zero shear stress. It must thus remain true that the normal stress contributions to the momentum budget are small, so that the shear stress roughly follows the mean velocity gradient as usual ([5]) but with, no doubt, a continuously enhanced eddy viscosity.

In conclusion, our study has shown that the presence of free-stream turbulence strongly effects the wake's decay rate and effectively destroys its self-similar character. It is also clear that, as expected from the strongly enhanced decay rates, the turbulence in the free-stream eventually dominates turbulence inside the wake, although shear stress remains strongly linked to mean flow gradients.

We would like to acknowledge the School of Engineering Sciences at the University of Southampton for funding E.R. *via* a research scholarship. We also thank the UK's Turbulence Consortium, UKTC, for providing computer time on the UK EPSRC HPCx IBM supercomputer under EPSRC grant number EP/D044073/1. The experiments could not have been undertaken without the dedicated efforts of the School's technician staff, for whose help we are very grateful.

References

1. R. Chevray, *J. of Basic Engineering*, 275-284 (June 1968).
2. M. J. Gourlay, S. C. Arendt, D. C. Fritts and J. Werne, *Physics of Fluids*, **13**, 3783-3802 (2001).
3. S. B. Pope, *Turbulent Flows*, Cambridge University Press, Cambridge 2000.
4. J. A. Redford and G. N. Coleman, 5th international Symposium on Turbulence and Shear Flow Phenomena (TSFP-5 Conference), 561-566 (August 2008).
5. H. Tennekes and J. L. Lumley, *A First Course in Turbulence*, The MIT Press (1972).
6. M. S. Uberoi and P. Freymuth, *Physics of Fluids*, **13**(9), 2205-2210 (1970).
7. Z.-T. Xie and I. P. Castro, *Flow, Turbulence & Combustion*, **81**, 449-470 (2008).

Application of the deterministic turbulence method to study of LEBU-device mechanism

V.I. Borodulin, Y.S. Kachanov, and A.P. Roschektayev

Khristianovich Institute of Theoretical and Applied Mechanics, Siberian Branch of Russian Academy of Sciences, 630090 Novosibirsk, Russia
kachanov@itam.nsc.ru

Introduction. The deterministic turbulence method was developed in experiments [1] along with substantiation of the idea of existence of the deterministic wall turbulence. The present paper demonstrate how efficiently this approach can be used for investigations of various localized impacts on the turbulent boundary layers by the example of well-known Large Eddy Break-Up (LEBU) devices, the comprehensive explanation of functioning of which remained unclear. The present study clarifies the physics of this mechanism.

Definitions. The idea of the deterministic wall turbulence was advanced recently in [1] and [2] based on experimental data and on the idea on universality of turbulence production mechanisms in transitional and turbulent wall shear flows [3]. This idea consists in the following. By the *stochastic turbulence*, we mean the turbulence, which microscopic structure (the instantaneous spatial velocity field of fluid particles) can not be reproduced repeatedly (although the average structure - can be reproduced). By the *deterministic (causal) turbulence*, we mean the flow, which microscopic structure can be reproduced repeatedly from one realization to another at reproduction of the same initial conditions for perturbations incoming into the boundary layer.

Assumptions. There are some boundary layers in which *laws of flow evolution are deterministic*, while the *stochastic properties* result entirely from *external perturbations* amplified by various *instabilities*. We also assume that if all instabilities in these boundary layers *are convective* then weak stochastic external perturbations may not have enough time to be amplified. Under these assumptions the flow may *remain deterministic* even if it is *turbulent*.

Deterministic Turbulence. It was shown in [1] and [2] that the *deterministic (reproducible) turbulence actually exists* in nature and can be generated experimentally in some boundary-layer flows. Besides important *philosophical meaning*, this result provides investigators with a very *powerful tool* of subsequent turbulence research. An example of one of possible efficient application of this tool is presented below.

Present Approach. Similar to [1] and [2] the present experiment was performed in a self-similar boundary layer with Hartree parameter $\beta_H = -0.115$. The setup was also similar to that described in [1]. A special disturbance generator, called VS-II (see e.g. [4]) excited in a laminar boundary layer some weak initial 3D instability waves, which induced the laminar-turbulent transition. The excited disturbances had a pseudo-random component, which was periodic at very large time scales, which exceeded significantly all characteristic time-scales of the stream. Starting from certain streamwise coordinate the resulting flow was fully turbulent from the generally accepted viewpoint. This conclusion is supported by: (i) comparison of mean-velocity profiles with turbulent one measured in classical experiments [5] (Fig. 1, *left*), (ii) disturbance spectra with typical power laws: $-3/2$ one in Kolmogorov's range of inertial scales and -7 one in Heisenberg's small-scale range (Fig. 1, *right*), and (iii) wall-normal disturbance intensity profiles of very typical shape and amplitude near the wall (Fig. 2, *left*). However, simultaneously, this turbulent flow is deterministic, i.e. periodically reproducible (see fields of coherence coefficients $C = u/u_d$ in Fig. 3, *left*; here u is total fluctuation intensity, while u_d is its deterministic, ensemble averaged part. This flow was studied in detail by a hot-wire in absence and in presence of LEBU-devices. As the result, we have obtained several four-dimensional (x, y, z, t) data arrays used for subsequent analysis. Each of them represented a 'snapshot' of one (among infinite number) of possible realizations of the turbulent flow.

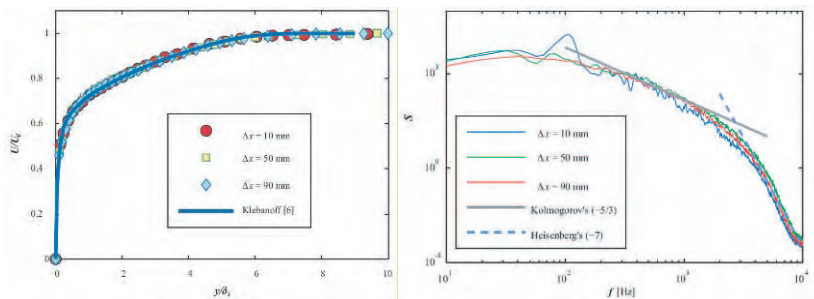


Fig. 1. Mean velocity profiles and spectra in post transitional boundary layer in absence of LEBU in comparison with [5] and power laws. Δx is distance from LEBU.

LEBU-Devices. LEBU-devices represented thin plates with chord lengths of 4 and 8 mm (LEBU #1 and #2) installed (one by one) at a distance of 4.2 mm from the wall (δ was about 8 mm) at streamwise coordinate $x=500$ mm from the leading edge. These devices were shown to produce 5 and 10% viscose drag reduction, respectively (see Fig. 2, *right*). The underlying physical mechanisms have been clarified based on analysis of the *instantaneous flow fields*, which were almost exactly the same upstream the LEBU location in all three studied cases (no LEBU, LEBU #1, and LEBU #2).

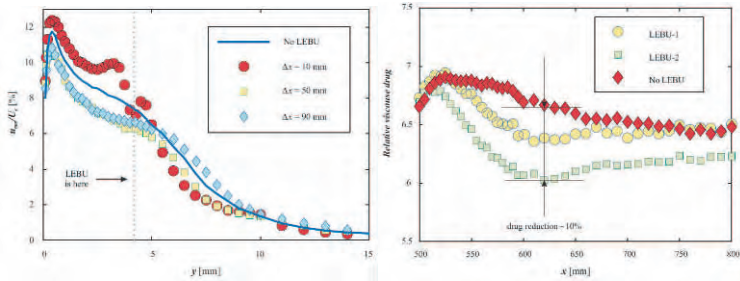


Fig. 2. Wall-normal disturbance profiles (left) and relative drag reduction (right).

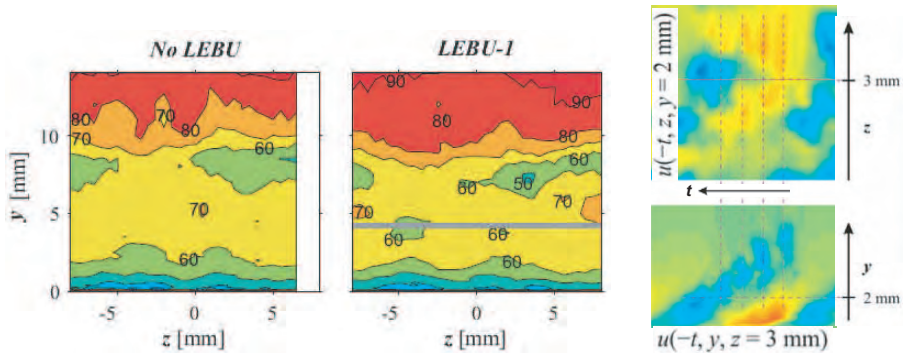


Fig. 3. Coherence field without and with LEBU (left) and positive spikes induced by ring-like vortices in wall region (right).

LEBU Mechanism. Shown in Fig. 4 are cross-sections by the (t, y) -plane of instantaneous fields of the streamwise velocity disturbance obtained in absence (a) and in presence (b) of LEBU #2 device. It is seen that far downstream LEBU suppresses near-wall structures. However, it is found that closer to the streamwise LEBU location the initial distortions are observed only at wall-normal distance of the LEBU-device position (not shown). As was found in previous experiments (see e.g. [3]), ring-like vortices generated continuously by Λ - (horseshoe-) vortices and propagated near the boundary-layer edge, induce in the near-wall region some strong disturbances ('positive spikes') (Figs. 3 *right* and 5), which enhance instantaneous and average friction and play a role of priming disturbances in launching new coherent vortical structures. Due to weakening of ring-like vortices by LEBU-devices (Figs. 5a, b) the wall domain becomes less perturbed (Figs. 5c, d) and the formation of new wall structures is partly blocked. These factors lead to a significant reduction of fluctuation intensities and skin friction (Fig. 2).

This work is supported by the Russian Foundation for Basic Research (grant N 08-01-91951).

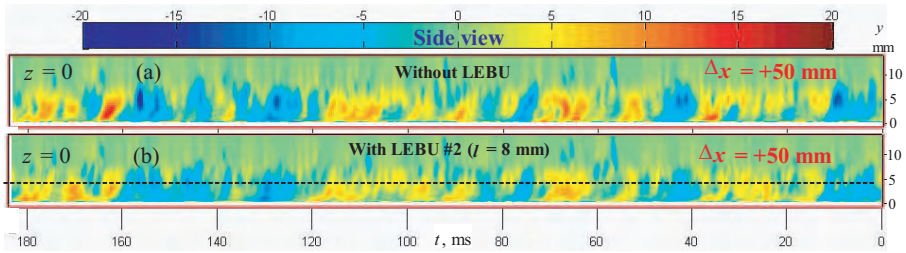


Fig. 4. Suppression of instantaneous vortical structures by LEBU (side view).

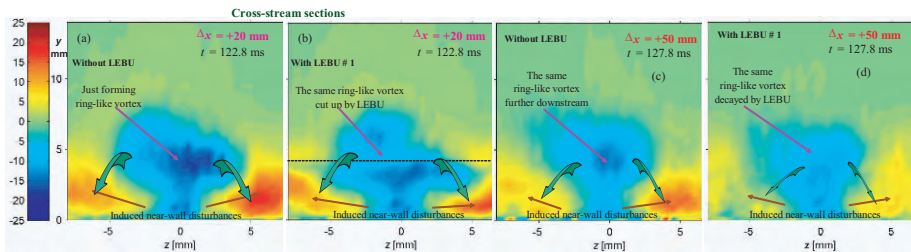


Fig. 5. Distortion of ring-like vortices by LEBU (*a, b*) resulting in reduction of them and near-wall 'positive spikes' observed downstream (*c, d*) (end view).

References

1. V.I. Borodulin, Y.S. Kachanov and A.P. Roschekhtayev, XIII International Conference on Methods of Aerophysical Research. Proceedings. Part I. - Novosibirsk: Inst. Publ. House "Parallel", pp. 46-52 (2007).
2. V.I. Borodulin, Y.S. Kachanov and A.P. Roschekhtayev, Advances in Turbulence XI. Proc. 11th EUROMECH European Turbulence Conference, June 25-28, 2007, Porto, Portugal / J.M.L.M. Palma and A. Silva Lopes, eds. - Heidelberg: Springer, pp. 176-178 (2007).
3. V.I. Borodulin, V.R. Gaponenko, Y.S. Kachanov, D.G.W. Meyer, U.Rist, Q.X. Lian and C.B. Lee, Theoret. Comput. Fluid Dynamics **15**, 317-337 (2002).
4. V.I. Borodulin, Y.S. Kachanov, D.B. Koptsev, Journal of Turbulence **3**, N 62, 1-38 (2002).
5. P.S. Klebanoff, Z.W. Diehl, NACA Report 1110 (1952).

The role of the intense vorticity structures in the turbulent structure of the jet edge

Ricardo J.N. Reis, Carlos B. da Silva and José C.F. Pereira

LASEF, Instituto Superior Técnico, Universidade Técnica de Lisboa, ät Av.
Rovisco Pais, 1049 Lisboa, Portugal
ricardo.reis at ist.utl.pt

1 Introduction

In free shear flows (jets, mixing layers and wakes) there is an highly contorted interface dividing the turbulent from the non-turbulent flow: the turbulent/non-turbulent (T/NT) interface. Across this interface important exchanges of mass, momentum and heat take place, in a process known as turbulent entrainment. Recently, the classical idea of the turbulent entrainment caused by engulfing [1] have been questioned, and it has been shown that the entrainment is mainly caused by small scale eddy motions (nibbling) [2, 3]). However, it is still argued that the entrainment rate is still largely governed by the large scale motions induced by the intense vorticity structures (IVS). The goal of the present work is to assess characterize the geometry and analyze the influence of these large scales structures in shaping the turbulent/nonturbulent interface.

2 Direct numerical simulation of a turbulent plane jet

The present work uses a direct numerical simulation (DNS) of a turbulent plane jet in temporal development at $Re_\lambda \approx 120$ [4]. The simulation uses a classical finite difference Navier-Stokes solver using pseudo-spectral schemes for spatial discretization and a 3rd order Runge-Kutta time stepping scheme for temporal advancement [4].

A well known result which can be easily observed in the DNS data bank (Fig. 1) is that the shape of the convolutions of the T/NT interface is of the order of the length scale of the large scale vortices.

3 Results and discussion

The intense vorticity structures (IVS) were detected and their axis was isolated using the procedure described in [5]. The statistics of the IVS were

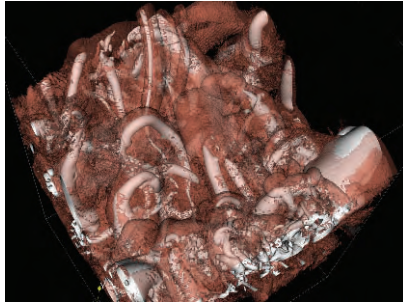


Fig. 1. Turbulent/non-turbulent interface with underlying large scale vortices identified through pressure contours.

computed in the whole turbulent region and then compared with results obtained in isotropic turbulence. Fig. 2 shows that the radius of the vortices near the edge of the plane jet tend to be bigger than in isotropic turbulence. Moreover, they tend to display stronger levels of vorticity and length. Moreover, in the jet these vortices tend to align with the tangent to the T/NT interface, particularly closest to the interface.

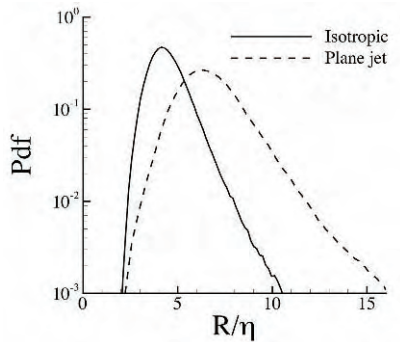


Fig. 2. Probability density functions (pdfs) of the vortex radius in kolmogorov units. In the plane jet case the higher values of the radius are due to the contribution of the vortices near the edge of the jet.

An interesting issue found in reference [4] concerns the existence of strong regions of intense, (almost) "irrotational" viscous dissipation near the T/NT interface. Some of these regions are displayed in red in Fig.(3). Either these regions are caused by small scale nibbling motions or by pure shear induced by the IVS. By decomposing the viscous dissipation field into local (caused by the near field vortices) and nonlocal (caused by background turbulence) as suggested by [6], we show that the irrotational dissipation regions are indeed caused by the presence of strong nearby IVS. This result has important

consequences in issues such as scalar dissipation in the edge of a jet diffusion flame, with impacts in mixing and combustion.

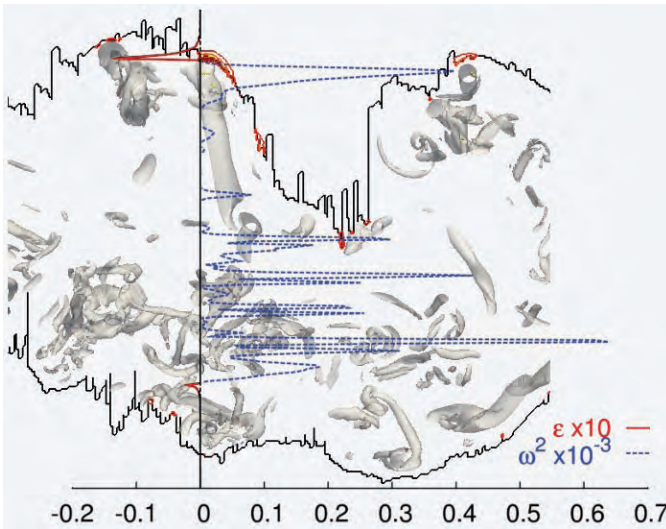


Fig. 3. Cut from the turbulent plane jet DNS. The figure shows the intense vorticity structures (grey) and the jet edge (T/NT- dark). An instantaneous profile of enstrophy (blue) and viscous dissipation (red) are also shown (the viscous dissipation is only shown outside the turbulent region).

References

1. A. A. Townsend. *The Structure of Turbulent Shear Flow*, Cambridge, 1976.
2. S. Corrsin & A. L. Kistler. Free-stream boundaries of turbulent flows. Technical Report TN-1244, NACA, 1955.
3. J. Westerweel, C. Fukushima, J.M. Pedersen & J.C.R. Hunt. Mechanics of the turbulent/non-turbulent interface of a jet. *Phys. Review Lett.*, 95:174501, 2005.
4. C. B. da Silva & J. C. F. Pereira. Invariants of the velocity-gradient, rate-of-strain and rate-of rotation tensors across the Turbulent/non-turbulent interface in jets. *Phys. Fluids*, 20:055101, 2008.
5. J. Jiménez, A. Wray, P. Saffman, & R. Rogallo, *J. Fluid Mechanics*, **225**, 65, 1993
6. Peter E. Hamlington, Jörg Schumacher, & Werner J. A. Dahm, *Physics of Fluids*, 111703 (2008)

Large Scale Dynamics of a Jet in a Counter Flow

C. Duwig*, and J. Revstedt

Fluid Mechanics/Energy Sciences, LTH, Lund University, P.O. Box 118, SE-22100, Lund, Sweden

`johan.revstedt@energy.lth.se`

Numerous studies of turbulent jets have contributed to a better understanding of the flow physics with applications in vehicle engineering, power generation or chemical industry. Different configurations (e.g. single jet in quiescent environment, jet in cross-flow) have received much attention whereas only few studies focused on the case of a jet issuing into a uniform counter-flow (JiCF). Among important studies, Bernero and Fiedler [1] evidenced some large scale flapping like motion but restricted their analysis to plane data. Tsunoda and Saruta [2] highlighted the bimodal shape of the scalar pdf as a consequence of the large scale fluctuation. The purpose of the present work is to further increase the understanding of the JiCF with the focus on identifying the large scale coherent structures using 3D LES data. In the LES framework, we consider the filtered incompressible continuity and momentum equations [3]. The subgrid scale (SGS) term is modeled using a classical eddy viscosity type model based on the Filtered Structure Function Model by Ducros et al. [4]. To solve the filtered governing equations on Cartesian grids a high-order finite difference code is used.

The spatial discretization is done using a fourth order centered scheme. However, for the convective terms a small portion of hyper-viscosity is added to the fourth order scheme, for stability reasons. A second order implicit finite difference scheme is used for time discretization. Multi-grid iterations are used to solve the implicit parts of the system. These advantages make the present approach suitable for LES of turbulent flows, in particular jets, e.g. Maciel et al. [5].

A commonly followed post-processing procedure consists of computing mean and RMS fields of the velocity variables. However, information related to large scale coherent motions is lost. We seek to supplement the mean and RMS fields by employing Proper Orthogonal Decomposition (POD) and we focus on the most energetic eddies/modes. Consequently, one seeks to project the turbulent flow field on a vector base that maximizes the turbulent kinetic

* also at Haldor Topsoe A/S, DK-2800 Lyngby

energy content for any subset of the base. It allows an accurate description of the turbulent data using only few modes [6]. The method results in solving a large eigenvalue problem, which we do using Sirovich's method of snap-shots (e.g Smith et al. [7]) to reduce the computational cost.

We consider a set-up similar to the experiments conducted by Bernero and Fiedler [1]. The numerical setup models a jet of diameter D issuing into a counter-flow area of $10D \times 10D$. The velocity ratio (jet bulk velocity / coflow bulk velocity) is set to 2.2 while the Reynolds number based on the jet bulk velocity (U_0) and the nozzle diameter is 2860. The computational grid consists of about $2 \cdot 10^6$ cells with 30 cells across the diameter D . The time step is set so that the Courant number is at most 0.3. The averages and POD modes are computed using around 1500 snapshots collected over $400T$, where $T = D/U_0$. Since the incoming fluctuation intensity is barely detectable in the experiments of Bernero and Fiedler [1] we model the jet inflow by a laminar top-hat profile for the streamwise component of the velocity vector. The counter flow is laminar and uniform. At the outlet, the flow is assumed to have a mass conservative zero gradient.

Figure 1 shows an instantaneous iso-surface of $0.5U_0$ (green) and a visualisation of the vortex cores using the λ_2 technique [8] (gray). One may notice that contrary to a jet issued into a quiescent surrounding or a co-flow, the jet in counter-flow exhibits a fast transition. The jet core is in this case only two nozzle diameters long and although the counter-flow is laminar and the flow issued from the nozzle has a fairly low Reynolds number the fluctuations become very high. This can be attributed to the continuous feed back upstream in the shear layer.

In order to focus on the large fluctuation dynamics, we decompose the flow in orthogonal proper modes. Figure 2 shows the first four POD modes in the centre plane of the jet. Mode 0 is the mean flow showing a short jet core and clean axi-symmetry. Mode 2 can be interpreted as an axial pulsation (azimuthal Fourier wave number $m=0$) which is strong about $4D$ downstream of the nozzle (at the end of the jet penetration). Unlike free jet, it barely affects the jet shearlayers and has its maximum at the centerline. The mode pair mode 1 and 3 can from this view be considered as a flapping motion, which is in fact how they were interpreted by Bernero and Fiedler [1]. However, considering the modes in the plane perpendicular to the main flow direction one can clearly see that this is a rotation of the jet core. This is visible in Figure 3 showing the first four modes at $6D$ down stream of the nozzle.

To find the frequencies of the modes one may Fourier transform the coefficients $a_i(t)$. In doing so we find that modes 1 and 3 are associated with Strouhal number $StfD/U_0 = 0.01$ describing a slow rotation around the axis. Mode 2 corresponds to $St = 0.013$, again the axisymmetric pulsation is slow compare to a typical shearlayer instability.

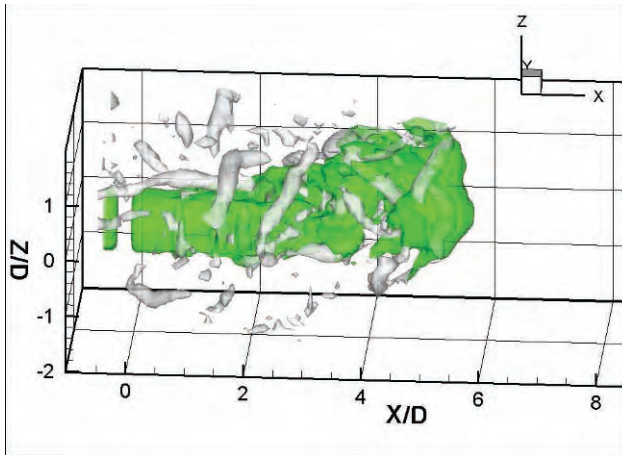


Fig. 1. A snapshot of the streamwise velocity in the plane $Y/D=0$

References

1. S. Bernero and H.E. Fielder, *Exp. Fluids*, **29**, 274, (2000)
2. H. Tsunoda and M.Saruta, *J. Turb.* **4**, 1, (2003)
3. P. Sagaut, *Large Eddy Simulation for Incompressible Flows*, Springer Verlag, Berlin 2001.
4. F. Ducros, P. Comte and M. Lesieur, *J. Fluid Mech.*, **326**, 1, (1996)
5. Y. Maciel, L. Facciolo, C. Duwig, L.Fuchs and H. Alfredsson, *Int.l J. Heat Fluid Flow*, **29**, 675, (2008)
6. G. Berkooz, P. Holmes and J.L. Lumley, *Ann. Rev. Fluid Mech.*, **25**, 539, (1993)
7. T. Smith, J. Moehlis and P. Holmes, *Nonlinear Dyn.*, **41**, 275, (2005)
8. J. Jeong and F. Hussain, *J. Fluid Mech.*, **285**,(1995)

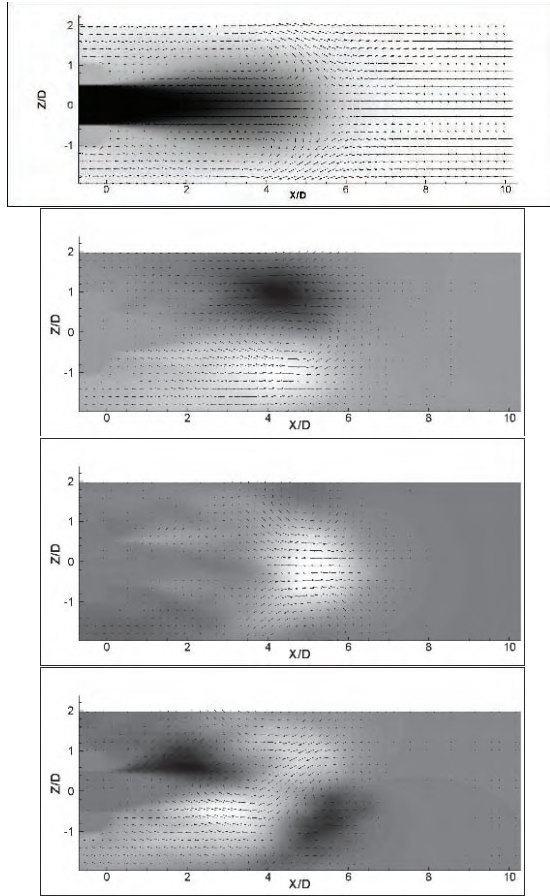


Fig. 2. The first four modes from POD in the centre plane of the jet.

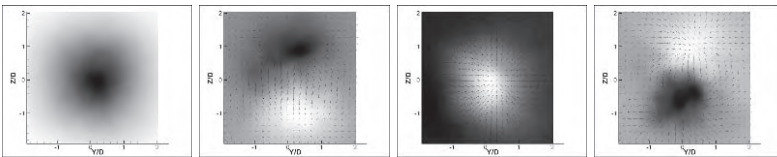


Fig. 3. The first four modes from POD at $Z/D=6$.

Dynamics of vortex filaments in turbulent flows and their impact on particle dispersion

A. Scagliarini¹, L. Biferale¹ and F. Toschi²

¹Department of Physics and INFN, University of Rome “Tor Vergata”, Rome, Italy

²Department of Applied Physics and Department of Mathematics and Computer Science, University of Technology of Eindhoven, Eindhoven, The Netherlands
`andrea.scagliarini at roma2.infn.it`

We study, by means of DNS up to 512^3 resolution (corresponding to $Re_\lambda \simeq 180$), the dynamics of pointwise particles passively advected by a turbulent fluid. To describe the particle dynamics we integrated numerically the Maxey-Riley equations for the so called “point-particle” model:

$$\frac{d\mathbf{v}}{dt} = \beta \frac{D\mathbf{u}}{Dt} + \frac{1}{\tau_S}(\mathbf{u} - \mathbf{v}). \quad (1)$$

Here \mathbf{v} is the particle velocity, while \mathbf{u} is the fluid velocity at the particle position, which is evolved by the (incompressible) Navier–Stokes equation

$$\frac{D\mathbf{u}}{Dt} \equiv \partial_t \mathbf{u} + (\mathbf{u} \cdot \nabla) \mathbf{u} = -\nabla P + \nu \Delta \mathbf{u} + \mathbf{f} \quad (2)$$

where P is the pressure and \mathbf{f} an external force injecting energy inside the system. The two parameters characterizing the type of particle are the density ratio $\beta = 3\rho_f/(\rho_f + 2\rho_p)$ (ρ_f and ρ_p being respectively the fluid and particle densities), and the Stokes time τ_S (or equivalently the Stokes number $St = \tau_S/\tau_\eta$, that is the ratio of the Stokes time over the Kolmogorov time). We focus on the connection between preferential concentration of particles with the underlying topological Eulerian structures in general and with vortex filaments in particular. We characterize the latter by tracking particles lighter than the fluid, which tend to accumulate around vortex filaments [1, 2], actually falling into them and remaining trapped [3, 4], and looking at the temporal evolution of the *momentum of inertia* of bunches of particles, $M(t)$ defined as

$$M(t) \stackrel{\text{def}}{=} \frac{1}{N} \sum_{i=1}^N [\mathbf{r}^{(i)}(t) - \mathbf{r}_{CM}(t)]^2 \quad (3)$$

where $\mathbf{r}_{CM}(t)$

$$\mathbf{r}_{CM}(t) = \frac{1}{N} \sum_{i=1}^N \mathbf{r}^{(i)}(t)$$

describes the barycentric motion of the bunch. For some bunch of light particles, the momentum of inertia may remain very small for long times, indicating a strong tendency toward preferential concentration inside vortex filaments [5]. The preferential concentration of heavy/light particles inside/outside vortex filaments can be also quantified by looking at the fluctuating autocorrelation time ($\tau_{1/2}$) of the instantaneous vorticity magnitude, $\omega(t) = \|\boldsymbol{\omega}(t)\|$, along particle trajectories:

$$\tau_{1/2} \stackrel{\text{def}}{=} \min \left\{ \tau \left| \frac{\omega(t+\tau)}{\omega(t)} = 1 \pm \frac{1}{2} \right. \right\} \quad (4)$$

In figure (1) the probability density functions of such autocorrelation times are plotted for different values of the density ratio $\beta \in [0; 3]$ at comparable values of the Stokes number. From their analysis we found a larger persistency of vorticity fluctuations along light particle paths than for heavy particles, supporting the idea that vortex filaments are somehow quasi-coherent objects moving randomly in the flow. The intense clustering of light particles, due

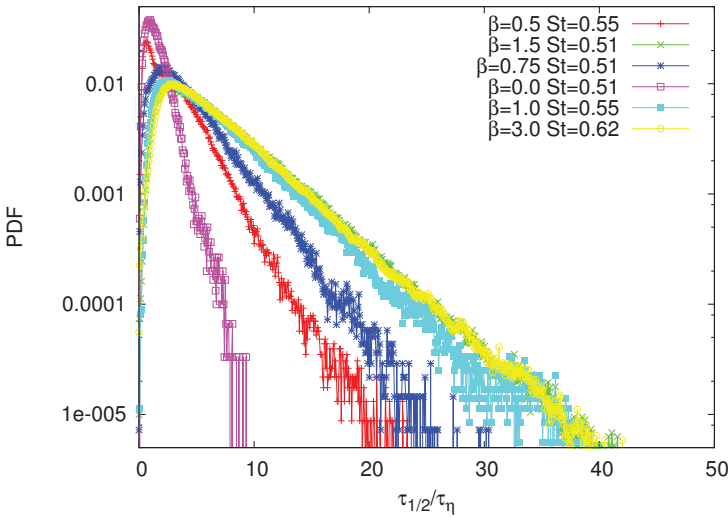


Fig. 1. Log–lin plot of the PDFs of “decoherence” times $\tau_{1/2}$ defined as the least instant of time at which $\omega(t + \tau_{1/2})/\omega(t) = 1 \pm 1/2$, $\omega(t)$ being the magnitude of the vorticity along the Lagrangian trajectory. It is to be noticed that for different particles, with approximately the same Stokes number (that is same degree of *inertia*), increasing β , hence going from heavy to light particles, one observes much larger tails, until values of around $\tau_{1/2} = 40\tau_\eta$.

to such trapping phenomena inside vortex filaments, has a dramatic impact on their long term pair dispersion. To show that, we study the statistics of relative distances among particles. In figure (2) we plot the probability density

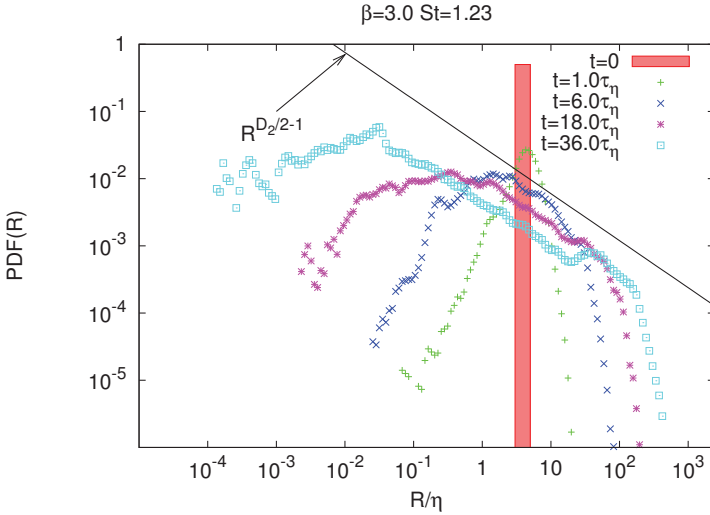


Fig. 2. Evolution of the PDF of light particles separations. Starting from a homogeneous initial condition (all particles displaced within relative distances $R \in [4\eta; 6\eta]$), light particles fill, as time goes on, the small-scale elliptic Eulerian topological structure and correspondingly the PDF develops a large tail at very low R values. Such tail shows a power law behaviour, which is consistent with the prediction $R^{\frac{D_2}{2}-1}$, as depicted by the solid straight line.

functions (PDF), at various instants of time, of distances of pairs of light particles ($\beta = 3.0$, $St = 1.23$) with a given initial separation (in particular we had $R \in [4\eta; 6\eta]$ at t_0 , with R and η being respectively the pair distance and the Kolmogorov length). The most interesting feature, signature of the clustering inside very small-scale vortex filaments, is the development of a fat tail at extremely low R values, which persists until times of the order of the integral time-scale. This is another example of small-scale focusing by turbulent flows. As it is also highlighted in the figure, such tail goes as a power law of R . From the exponent we can extract the value of the correlation dimension D_2 of the fractal set on which particles accumulate [6]. We find a value $D_2 \approx 0.6$, indicating that for those particles the small-scale attractor is less than one dimensional. At changing β and St one finds different D_2 dimensions [6]; as an example, in figure (3) we show the analogous of figure (2), that is the time evolution of the pair distances PDF, for a different kind of particles ($\beta = 2.0$, $St = 0.3$). In this latter case our estimate for the correlation dimension is $D_2 \approx 2.0$, thus confirming that the clustering becomes less intense when the density ratio β is lowered.

The strong clusterization of light particles inside very singular attractors is certainly one of the major problems for many applied modelisations of particle dispersion in turbulent flows.

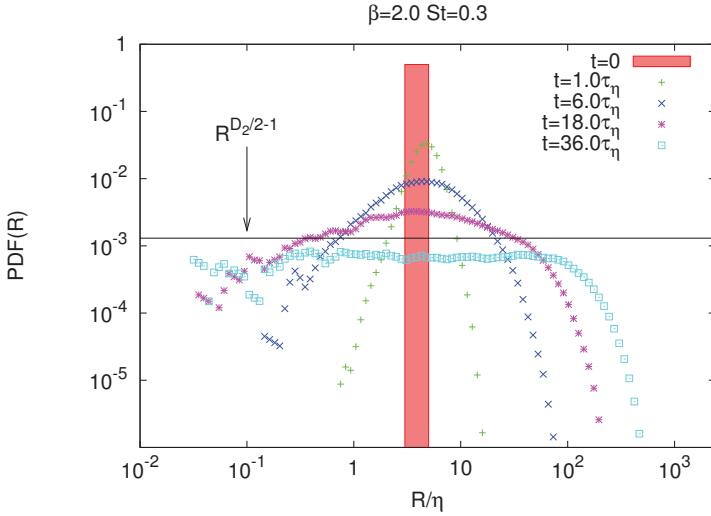


Fig. 3. PDFs of particle separations plotted according to the same criteria of figure (2) but for a case with lesser degree of clusterization ($\beta = 2.0$, $St = 0.3$). Again the self-similar power law filling of small scales is in agreement with the theoretical results [6] and from the stationary distribution we determine in this case $D_2 \approx 2.0$.

References

1. A. Vincent and M. Meneguzzi, “The spatial structure and statistical properties of homogeneous turbulence”, *J. Fluid Mech.* **225**, 1–25 (1991).
2. M. E. Brachet, D. I. Meiron, S. A. Orszag, B. G. Nickel, R. H. Morf and U. Frisch, “Small-scale structure of the Taylor–Green vortex”, *J. Fluid Mech.* **130**, 411–452 (1983).
3. S. Sundaram and L. R. Collins, “A numerical study of the modulation of isotropic turbulence by suspended particles”, *J. Fluid Mech.* **379**, 105 (1999).
4. S. Douady, Y. Couder and M. E. Brachet, “Direct observation of the intermittency of intense vorticity filaments in turbulence”, *Phys. Rev. Lett.* **67**, 983–986 (1991).
5. L. Biferale, A. Scagliarini and F. Toschi, “Focusing of light particles by turbulent flows”, in preparation.
6. J. Bec, L. Biferale, A.S. Lanotte, A. Scagliarini and F. Toschi, “Turbulent diffusion of inertial particles”, submitted to *J. Fluid Mech.* (2009).

The effect of coherent structures on the secondary flow in a square duct

A. Sekimoto¹, A. Pinelli², M. Uhlmann³ and G. Kawahara¹

¹Department of Mechanical Science, Osaka University, 560-8531 Osaka, Japan

²Modeling and Numerical Simulation Unit, CIEMAT, 28040 Madrid, Spain

³Institute for Hydromechanics, University of Karlsruhe, Germany

sekimoto@me.es.osaka-u.ac.jp

1 Introduction

The appearance of secondary flow of Prandtl's second kind is a well-known phenomenon in fully developed turbulent rectangular duct flow. The intensity of the secondary flow is two orders of magnitude smaller than that of the mean streamwise velocity; however, it plays an important role in the cross-streamwise momentum, heat and mass transfer. Our recent study [1] revealed that the mean secondary flow is a statistical footprint of the turbulent flow structures, i.e. streamwise vortices and streaks which are observed in the near-wall region, whose cross-sectional positions are constrained by the presence of the side walls at marginal Reynolds number (approximately 1100, based on the bulk velocity and the duct half width, corresponding to a friction Reynolds number of about 80). In this marginal case, one low-speed streak associated with a pair of counter-rotating streamwise vortices can exist over each wall and they are self-sustained [2]. When considering the higher Reynolds numbers, the increment of duct width in wall unit allows the simultaneous presence of multiple low velocity streaks and pairs of streamwise vortices upon the wall.

Direct numerical simulations of fully developed turbulent flow in a straight square duct were performed at moderate values of Reynolds numbers. The main motivation of our study is to unravel the relationship between coherent buffer layer structures and the mean secondary motion at Reynolds numbers larger than the marginal value.

2 Numerical methods

We consider an incompressible viscous fluid flowing through an infinite straight square duct. The Navier-Stokes equations are solved by means of a pressure correction method. We use an implicit scheme for the viscous terms, and a three-step Runge-Kutta method for the non-linear terms [3].

For the spatial discretization, Fourier expansion is employed in the streamwise (x) direction, while Chebyshev-polynomial expansions are used in the cross-streamwise (y, z) directions. The nonlinear terms are evaluated pseudo-spectrally with full dealiasing in the streamwise direction. The Helmholtz and Poisson problems for each Fourier coefficient are solved by the fast diagonalisation technique [4]. In the following we present results from simulations performed at several Reynolds numbers, $Re_b \equiv u_b h / \nu \leq 3500$ where u_b is the bulk mean velocity, h is half the duct width, and ν is the kinematic viscosity of the fluid. In our simulations a constant mass flow rate is imposed. Furthermore, for each case the number of Fourier modes was chosen such that the streamwise grid spacing was below 15 wall units, and the number of Chebyshev polynomials was adjusted such that the maximum cross streamwise grid spacing was less than 6 wall units.

3 Results

Figure 1 shows the mean streamwise vorticity and cross-streamwise velocity in the cross-section. At a bulk Reynolds number of $Re_b = 1500$ (corresponding to a skin friction Reynolds number of 100), the cross-streamwise length scale of streamwise vortices, is comparable with that of the mean secondary flow, implying that the mean secondary motion is a statistical footprint of the coherent structures whose cross-sectional positions are constrained by the presence of the side walls [1]. At higher Reynolds numbers, the smallest coherent structures which are still constrained by the side walls in the corner regions affect the mean streamwise vorticity near the corner, but the mean secondary flow seems to scale with the geometrical size of the duct possibly because of the presence of large scale motions. Figure 2 shows the time evolution of spanwise position of low speed wall streaks computed by extracting the local minimum points of wall shear profile from streamwise averaged instantaneous velocity fields. The number of low speed streaks, which are associated with counter-rotating quasi-streamwise vortices pairs constrained by the presence of the side walls, increases in an almost discrete fashion in the considered range of Reynolds numbers. It can be seen that at the lowest Reynolds number a single low speed streak meanders around the center of the duct edge in Fig.2 (a). When increasing the Reynolds number more than one simultaneous streak is detected. At the highest value of Re_b , the probability of finding a low speed streak becomes uniform along the edge (like in a plane channel flow) except for the corner regions. This behaviour is consistent with the observed fluttering of the local mean wall shear stress and the preferential location of low speed streaks in the corner region also contributes the local minimum in Figure 3 ($Re_b = 2200, 3500$). Therefore, a clear dependence of the mean flow upon the Reynolds number stems from the preferential number and positioning of buffer layer structures along the edge.

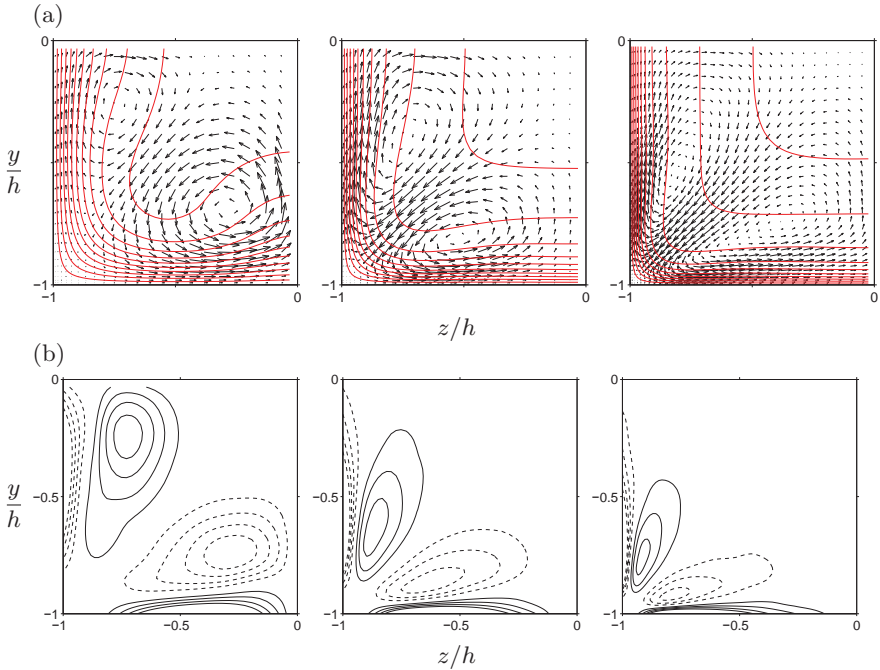


Fig. 1. (a) Secondary mean flow averaged over all quadrants represented by vectors. (left), $Re_b = 1500$; (center), $Re_b = 2200$; (right) $Re_b = 3500$. The cross-streamwise component is shown by vectors and the streamwise component is represented by iso-contours. (b) streamwise vorticity field: —, iso-contours of positive vorticity; ----, negative vorticity.

In summary, coherent buffer layer structures play a crucial role in the formation of the mean secondary motion and the characteristic profile of wall shear stress even when increasing the Reynolds number. However, in the present study the scale of coherent structures are not sufficiently separated from the largest duct-width scale. The more investigations at higher Reynolds numbers are needed to reveal other possible dependence upon the Reynolds number of the mean flow which is related with the largest allowed coherent motions.

References

1. M. Uhlmann, A. Pinelli, G. Kawahara and A. Sekimoto, *J. Fluid Mech.* **588**(2007), 153-162.
2. J. M. Hamilton, J. Kim, and F. Waleffe, *J. Fluid Mech.* **287**(1995), 317-348.
3. R. Verzicco and P. Orlandi, *J. Comput. Phys.* **123**(1996), 402-414.
4. P. Haldenwang, G. Labrosse, S. Abboudi, and M. Deville. *J. Comput. Phys.* **55**(1984), 115-128.

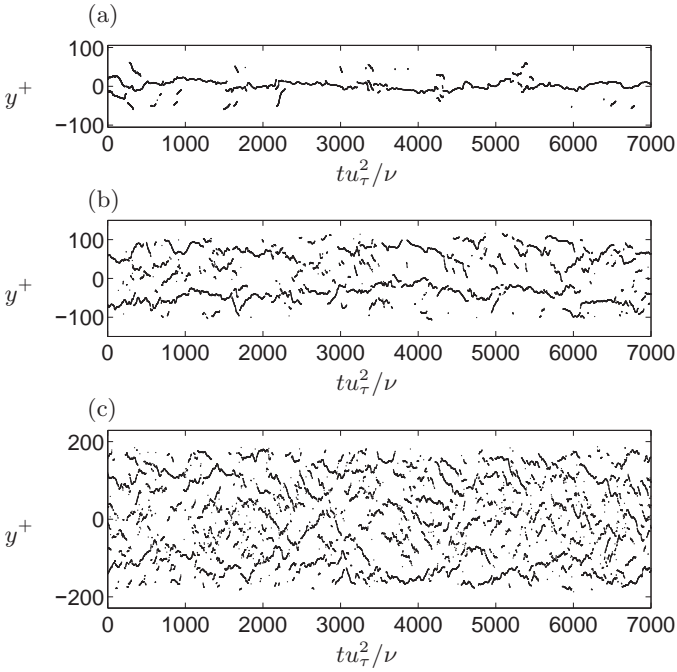


Fig. 2. Time evolution of local minimum point of the streamwise averaged wall shear stress on a wall. (a) $Re_b = 1500$; (b) $Re_b = 2200$; (c) $Re_b = 3500$.

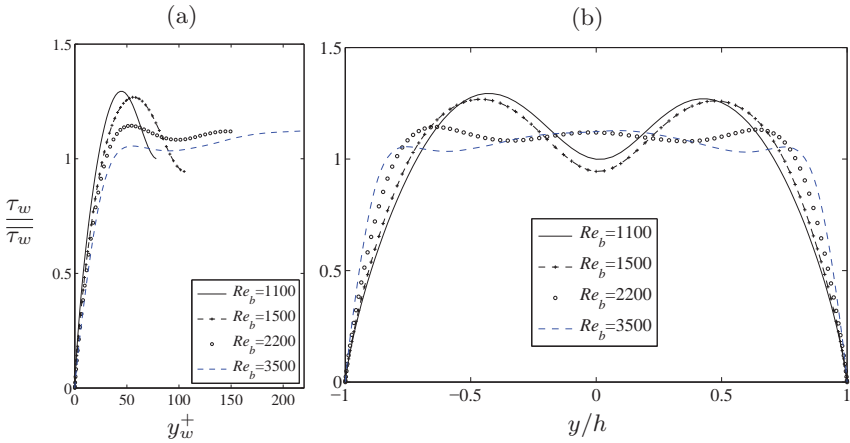


Fig. 3. Mean local wall shear stress normalized by the average over the whole walls, as a function of the distance (a) from the corner, y_w^+ in wall units, (b) from the wall bisector, y/h in outer unit.

Part V Multiphase and non-Newtonian flows

How to Discriminate Between Light and Heavy Particles in Turbulence

H.I. Andersson¹, P.H. Mortensen¹, J.J.J. Gillissen²
L.H. Zhao¹ & B.J. Boersma²

¹Dept. Energy & Process Engineering, NTNU, Norway

²Lab. Aero & Hydrodynamics, TU Delft, The Netherlands
`helge.i.andersson at ntnu.no`

Light and heavy particles behave completely different in a turbulent flow field. In the present communication we discuss how one can discriminate between light and heavy particle behavior and how the important class of intermediate particles is identified. This latter class of particles exhibit challenging dynamics since they are affected both by inertia and Stokes drag, i.e. $d\mathbf{v}/dt = St^{-1}(\mathbf{u} - \mathbf{v})$, where \mathbf{u} and \mathbf{v} are the Eulerian fluid and Lagrangian particle velocities. This Lagrangian equation is expressed in non-dimensional form where t and St denote time and particle relaxation time $\tau = 2/9(\rho_p/\rho_f)a^2/\nu_f$ normalized by an *arbitrarily* chosen time scale. This expression for τ is applicable for spherical particles with radius a smaller than the smallest length scales of the flow and provided that the particle Reynolds number is below unity. However, for the dimensionless particle relaxation time St , i.e. the so-called Stokes number, to play a distinguishing role in the particle dynamics, the choice of time scale becomes essential. With a properly selected time scale, the particle motion is dominated by Stokes drag if $St \ll 1$ and by inertia if $St > 1$.

The prevailing choice of time scale for particulate channel and pipe flow is the viscous time scale ν/u_*^2 (e.g. [1, 2]). This choice is convenient since u_* is readily available in LES and DNS studies. The viscous time scale is, however, consistently smaller than the Kolmogorov time scale $t_k = (\nu/\epsilon)^{1/2}$ in turbulent channel flows. The DNS data in Fig. 1 shows that the Kolmogorov time scale increases monotonically from about $2\nu/u_*^2$ at the wall to more than $10\nu/u_*^2$ beyond $z^+ = 100$ for some different Reynolds numbers. Here, Re is based on the friction velocity and the wall separation $2h$.

The role of the Stokes number on the particle dynamics is illustrated in Fig. 2 and 3, which show results from a DNS of particulate channel flow at Reynolds number $Re = 360$. Some results from these simulations focusing on the parti-

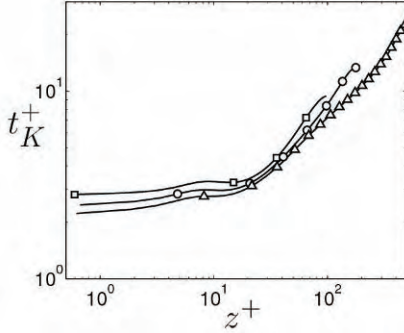


Fig. 1. Ratio between Kolmogorov time scale and viscous time scale. $Re=200$ (Squares), $Re=360$ (Circles), $Re=1000$ (Triangles)

cle spin have been presented by Mortensen et al.[2]. The streamwise particle-velocity correlation exceeds the fluid-velocity intensity even for the lightest particles ($St = 0.075$) but almost collapses with the conditionally-averaged fluid-velocities in the particle positions. It is well-known that particles tend to accumulate in regions of locally low streamwise fluid velocity near the wall. Such so-called preferential concentration has been addressed by Eaton and Fessler [3] and Marchioli and Soldati [4]. It is evident that the present light particles preferentially concentrate in low-speed regions and that inertia has no direct effect. The particle-velocity correlations of the heavier particles ($St = 2.24$) are substantially different from the fluid-velocity correlations due to the influence of Stokes drag.

The present results imply that the light and heavy particles behave fundamentally different, i.e. inertial effects are negligible for the lightest particles ($St = 0.075 < 1$) but not for the heavier ones ($St = 2.24$). Here, the Stokes number is based on the Kolmogorov time scale. If we instead followed the prevailing practice and scaled with the viscous time scale, the Stokes numbers for the light and heavy particles become 1 and 30, respectively. The latter choice of time scale does not suggest that the light particles are in the drag-dominated regime.

If the covariance $\langle u_i(x_p)v_i(x_p) \rangle^{1/2} \approx \langle v_i(x_p)v_i(x_p) \rangle^{1/2}$, it might be tempting to assume that $\langle u_i(x_p)u_i(x_p) \rangle^{1/2} \approx \langle v_i(x_p)v_i(x_p) \rangle^{1/2}$, as was incorrectly done by Vance et al. [5]. The covariance between the fluid and particle velocities has, however, to obey the Cauchy-Schwartz inequality:

$$\langle u_i(x_p)v_i(x_p) \rangle^2 \leq \langle u_i(x_p)u_i(x_p) \rangle \langle v_i(x_p)v_i(x_p) \rangle \quad (1)$$

If the covariance $\langle u_i(x_p)v_i(x_p) \rangle^{1/2} \approx \langle v_i(x_p)v_i(x_p) \rangle^{1/2}$, as for relatively light particles, it can be only be inferred that

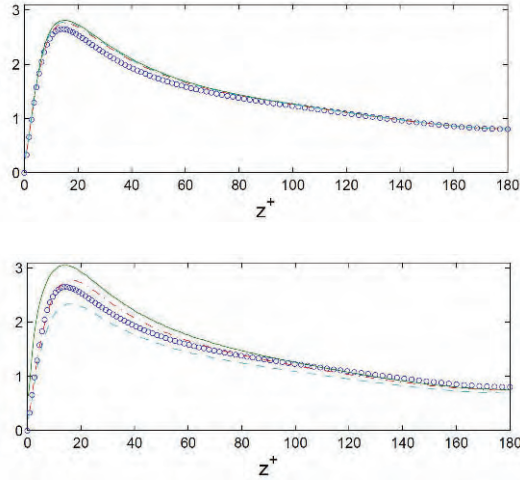


Fig. 2. Correlations between streamwise velocity fluctuations u_x and v_x for $Re = 360$. Stokes number based on the Kolmogorov time scale. $St=0.075$ (upper), $St=2.24$ (lower).

(ooo $u_{x,rms}$; -.- $\langle u_x(x_p)u_x(x_p) \rangle$; — $\langle v_x(x_p)v_x(x_p) \rangle$; - - - $\langle u_x(x_p)v_x(x_p) \rangle$)

$$\langle u_i(x_p)v_i(x_p) \rangle^{1/2} \leq \langle u_i(x_p)u_i(x_p) \rangle^{1/2} \tag{2}$$

It can therefore not be concluded that the particles passively follow the fluid and inertia does not play any role.

Particle concentrations $C(z^+)$ are shown in Fig. 4 and 5 for two different Reynolds numbers and four different Stokes numbers. At both Re , the particle concentration at the wall increases with particle response time and reaches a maximum when $St=3.0$ (i.e. of order unity). At both Reynolds numbers, the largest tendency of the particles to concentrate preferentially in the near-wall layer is found at $St=3.0$, while the concentration is lower both for lighter and heavier particles. The particle concentrations for $St=3.0$ seem to be independent of the Reynolds number, whereas the concentration increases with Re for the lighter particles. Picciotto et al.[6] found the maximum concentration at $St \approx 25$ for $Re=300$. They based their Stokes number on the viscous time scale which is an order of magnitude smaller than the Kolmogorov time scale.

In conclusion, the prevailing use of the viscous time scale is unsuitable to distinguish between light and heavy particles suspended in a turbulent wall-flow.

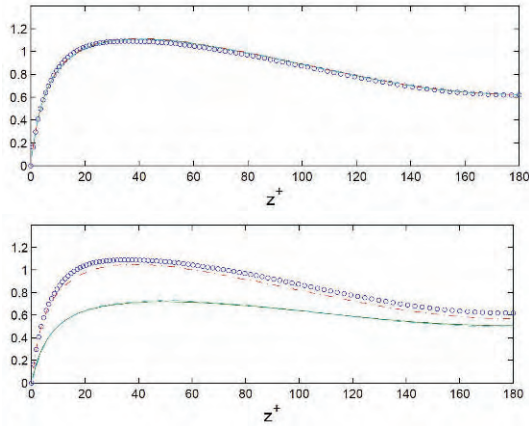


Fig. 3. Correlations between spanwise velocity fluctuations u_y and v_y for $Re = 360$. Stokes number based on the Kolmogorov time scale. $St=0.075$ (upper), $St=2.24$ (lower).

(ooo $u_{y,rms}$; - - - $\langle u_y(x_p)u_y(x_p) \rangle$; — $\langle v_y(x_p)v_y(x_p) \rangle$; - - - $\langle u_y(x_p)v_y(x_p) \rangle$)

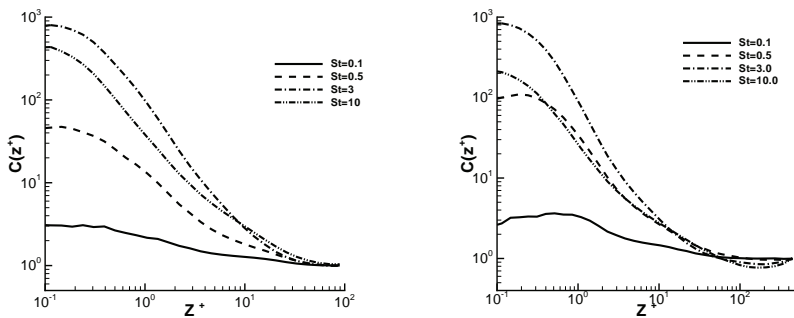


Fig. 4. Particle concentrations ($Re=200$) **Fig. 5.** Particle concentrations($Re=1000$)

References

1. C. Marchioli, A. Soldati, J.G.M. Kuerten, B. Arcen, A. Taniere, G. Goldensohn, K.D. Squires, M.F. Cargnelutti and L.M. Portela, *Int. J. Multiphase Flow*, **34**, 879 (2008).
2. P.H. Mortensen, H.I. Andersson, J.J.J. Gillissen and B.J. Boersma, *Phys. Fluids*, **19**, 078109 (2007).
3. J.K. Eaton and J.R. Fessler, *Int. J. Multiphase Flow*, **20**, 169 (1994).
4. C. Marchioli and A. Soldati, *J. Fluid Mech.*, **468**, 283 (2002)
5. M.W. Vance, K.D. Squires and O. Simonin, *Phys. Fluids*, **18**, 063302 (2006)
6. M. Picciotto, C. Marchioli and A. Soldati, *Phys. Fluids*, **17**, 098101 (2005).

Anisotropic clustering and particles velocity statistics in shear turbulence

P. Gualtieri, F. Picano, G. Sardina and C.M. Casciola

Dipartimento di Meccanica e Aeronautica, “Sapienza” Università di Roma , 00184 Rome, Italy

paolo.gualtieri@uniroma1.it

Dynamics of inertial particles is addressed in a homogeneous shear flow as the prototype of statistically steady anisotropic flows. In this simple flow, velocity fluctuations are strongly anisotropic at the largest scales where production of turbulent kinetic energy is active i.e. at scale separation $r > L_S$ ($L_S = \sqrt{\epsilon/S^3}$ denote the shear scale) while re-isotropization is expected for smaller separations $r < L_S$ [6]. Since anisotropy is strongly depleted through the inertial range, the advecting field anisotropy may be expected in-influential for the small scale features of particle dynamics. We find instead that the small scales of the particle distribution and particles velocity fluctuations are strongly affected by the geometry of turbulent fluctuations at large scales even in the range of scales where isotropization of velocity statistics occurs.

Inertial particles differ from perfectly Lagrangian tracers due to inertia which prevents them from following the flow trajectories. The main effect consists of “preferential accumulation” that leads to small-scale clustering for locally homogeneous and isotropic flows [1] and to turbophoresis in wall-bounded flows i.e. preferential spatial segregation at the boundary [3]. The statistically steady homogeneous shear flow retains most of the anisotropic dynamics of wall bounded flows still preserving, spatial homogeneity. This flow shares with the wall-layer streamwise vortices and turbulent kinetic energy production mechanisms. Velocity fluctuations are strongly anisotropic at the large scales driven by production while, for smaller separations, the classical energy transfer mechanisms become effective in inducing re-isotropization.

The main contribution of the present paper is the quantitative evidence that particles do not necessarily reduce their anisotropy at small scales both in terms of clusters geometry and velocity statistics. Rather it may even grow below the Kolmogorov length where the velocity field, is smooth and almost isotropic.

A visual impression of the instantaneous spatial distribution of particles is provided in figure 1, where slices of the domain in selected coordinate planes are displayed for $St_\eta = 1$. Clustering is apparent and the distribution exhibits

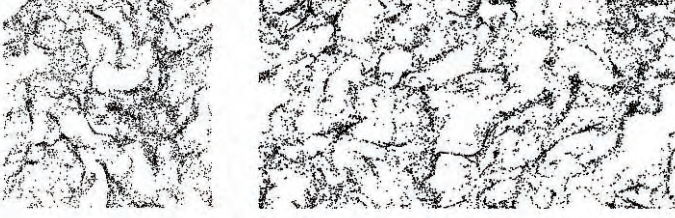


Fig. 1. Snapshots of particle positions for Stokes number based on Kolmogorov timescale $St_\eta = 1$. Left column thin slice in the $y-z$ plane; right column slice in the $x-y$ plane. The slice thickness is of the order of a few Kolmogorov scales. The mean flow is in the x direction $U = Sy$ with S the mean shear. DNS data with a resolution of $384 \times 384 \times 192$ collocation points in a $4\pi \times 2\pi \times 2\pi$ periodic box. The Kolmogorov scale is $\eta = 0.02$ corresponding to $K_{max}\eta = 3.1$. $L_s/\eta \simeq 35$ where $L_s = \sqrt{\epsilon/S^3}$ is the shear scale being ϵ the mean energy dissipation rate. Taylor-Reynolds number $Re_\lambda = \sqrt{5/(\nu\epsilon)}\langle u_\alpha u_\alpha \rangle \simeq 100$ and shear strength $S^* = S\langle u_\alpha u_\alpha \rangle/\epsilon = (L_0/L_s)^{2/3} \simeq 7$ where L_0 is the integral scale. Five populations of $N_p = 3 \cdot 10^5$ particles each are evolved with $St_\eta = 0.1, 0.5, 1.0, 5.0, 10.0$, see [4].

voids, correlated with enstrophy regions and intertwined thin “stretched” regions at the border of the voids where a large particle concentration is achieved. Recently particle clustering have been described in terms of other mechanisms such as the sweep-stick mechanism described in [7] which takes into account more complex topological information of the fluid acceleration field. The homogeneous shear flow manifest specific features associated with the large scale anisotropy. The shear-induced orientation is apparent from the bottom-left/top-right alignment of the sheet-like arrangement of particles in the shear plane $x-y$, see the right panels of figure 1.

The main statistical tool is the radial distribution function (RDF) of particle pairs $g(r)$ which is a function of radial distance r , see e.g. [2] for isotropic flows. The concept is extended to anisotropic cases by considering the number of pairs $d\mu_r = \nu_r(r, \hat{\mathbf{r}})d\Omega$ contained in a spherical cone of radius r , with axis along the direction $\hat{\mathbf{r}}$ and solid angle $d\Omega$. By this definition the number of pairs in the ball \mathcal{B}_r is $N_r = \int_\Omega \nu_r d\Omega$, hence $dN_r/dr = \int_\Omega d\nu_r/dr d\Omega$. We define the Angular Distribution Function (ADF) as

$$g(r, \hat{\mathbf{r}}) = \frac{1}{r^2} \frac{d\nu_r}{dr} \frac{1}{n_0}, \quad (1)$$

which retains information on the angular dependence of the distribution [4].

The RDF is the spherical average of the ADF $g(r) = 1/(4\pi) \int_\Omega g(r, \hat{\mathbf{r}})d\Omega$ and is shown in figure 2, where a scaling behavior is apparent in the range $r/\eta \in [.1 : 1]$. From the figure, particles with $St_\eta \sim 1$ exhibit maximum accumulation, i.e. the RDF diverges at a faster rate as r is decreased.

The strong anisotropy apparent in figure 1 however, needs a description in terms of the more complete ADF which allows for a systematic evaluation of

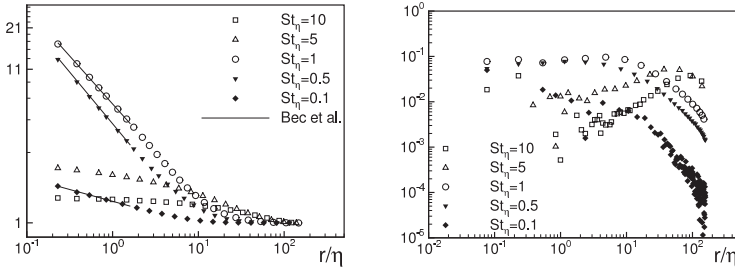


Fig. 2. *Left: radial distribution function vs separation, for different Stokes number $St_\eta = 10, 5, 1, 0.5, 0.1$ Right: ratio between the most energetic anisotropic sector (2, -2) normalized by isotropic sector as a function of separation for different Stokes number.*

anisotropy. For given separation r , its angular dependence can be resolved in terms of spherical harmonics, $g(r, \hat{\mathbf{r}}) = \sum_{j=0}^{\infty} \sum_{m=-j}^j g_{jm}(r) Y_{jm}(\hat{\mathbf{r}})$. In this notation, the classical RDF $g(r)$ is the projection of the ADF on the isotropic sector $j = 0$, namely $g_{00}(r) \equiv g(r) = \int_{\Omega} g(r, \hat{\mathbf{r}}) Y_{00}(\hat{\mathbf{r}}) d\Omega$. The ADF provides a quantitative account of the anisotropy induced by the fluid velocity field on the disperse phase and can be effectively used to parameterize the level of anisotropy through the scales in terms of the Stokes number.

The plot of figure 2 gives the normalized amplitude of the most energetic anisotropic mode in absolute value $|g_{2,-2}|/g_{0,0}$ for our set of Stokes numbers ranging from heavy to light particles. Focusing on the heaviest particles, $St_\eta = 10, 5$, the relative amplitude of the strongest anisotropic mode first increases towards the small scales to reach a maximum at $r \sim \ell_c$. Below this scale the anisotropy level decreases, until the very small scales become essentially isotropic.

Particles with smaller Stokes numbers behave in a different way. The anisotropy substantially increases to reach a saturation at small scales as Kolmogorov scale is approached. It keeps an almost constant value below η . In other words, the clustering process maintains its anisotropic features even below the dissipative scale for sufficiently small Stokes number particles. The saturation observed on the ratio $g_{2,-2}/g_{0,0}$ implies that the dominating anisotropic contribution inherits the same behavior of $g_{00} \propto r^{-\alpha}$. Looking at the data for our lightest population, we cannot exclude that the singularity exponent of the most significant anisotropic sector may even be larger than those inferred from the RDF. Conversely, heavy particles appear to preferentially concentrate on finite size patches, where they are more or less evenly and isotropically distributed.

The behavior of light inertial particles is completely different from that of velocity fluctuations which manifest two distinct isotropy recovery rates, a smaller one observed in the production range above the shear scale and a larger rate in the inertial transfer below, [6]. As a matter of fact, isotropy is always recovered at dissipative scales, provided the scale separation L_s/η is large

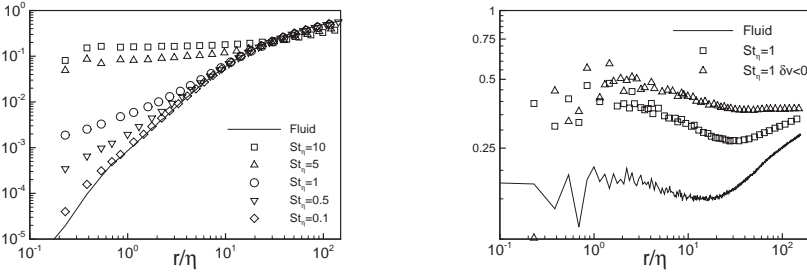


Fig. 3. *Left: isotropic projection of $\langle \delta v^2 \rangle$ vs separation for particles at different Stokes numbers (symbols) compared against corresponding projection of fluid velocity increments $\langle \delta u^2 \rangle$ (line) evaluated at the particle positions. Right: comparison of the anisotropy indicator $\langle \delta v^2 \rangle_{(2-2)} / \langle \delta v^2 \rangle_{(00)}$ for particle velocity increments (symbols) and fluid increments (solid line) at $St_\eta = 1$.*

enough, i.e. at sufficiently large Reynolds number. In this scenario we consider particles velocity statistics. In fact, at small scales, clustering is essentially anisotropic while the carrier phase is in the isotropy recovery range. In fact, we find that particles velocity statistics measured in terms of the disperse phase velocity increments $\langle \delta v^n(|\mathbf{r}|, \hat{\mathbf{r}}) \rangle$ differ considerably from those of the carrier fluid, see figure 3 where the isotropic projection of $\langle \delta v^2 \rangle$ is compared with $\langle \delta u^2 \rangle$ which denotes the carrier fluid velocity increments evaluated at the particle positions. A clear departure of the two statistics is observed at a length-scale which can be estimated dimensionally as $l_p = \sqrt{\epsilon \tau_p^3}$. Isotropy recovery of particle velocity fluctuations is addresses by considering the anisotropy indicator $\langle \delta v^2 \rangle_{(2-2)} / \langle \delta v^2 \rangle_{(00)}$ i.e. the most energetic anisotropic projection normalized with the isotropic sector, see figure 3. As the scale separation approaches the smallest scales where clusters are formed, particles velocity statistics are characterized by and enhancement of anisotropy in contrast to those of the carrier fluid which in the range from L_s to η and below shows instead a substantial decrease of directionality. Note the substantial increase of anisotropy in the particles statistics when only colliding pairs are considered ($\delta v < 0$) by comparing triangles and squares in figure 3. This might have a substantial impact for modeling particles collision kernels in anisotropic flows.

References

1. J. Bec et al., Phys. Rev. Lett. **98**, (2007)
2. S. Sundaram, L. R. Collins, J. Fluid. Mech. **335**, (1997)
3. D.W.I. Rouson, J.K. Eaton, J. Fluid. Mech. **428**, (2001)
4. P. Gualtieri, F. Picano, C.M. Casciola, in press J. Fluid. Mech. (2009)
5. B. Shotorban, S. Balachandar, Phys. Fluids **18**, (2006)
6. C. M. Casciola, P. Gualtieri, B. Jacob, R. Piva, Phys. Fluids **19**, (2007)
7. S. Goto, J.C. Vassilicos, Phys. Rev. Lett. **100**, (2008)

Direct Numerical Simulation of inertial particle accelerations in near-wall turbulence: effect of gravity

V. Lavezzo^a, S. Gerashchenko^b, Z. Warhaft^c, L. Collins^c and A. Soldati^a

^a Centro Interdipartimentale di Fluidodinamica e Idraulica and Dipartimento di Energetica e Macchine, University of Udine, 33100 Udine, Italy

^b California Institute of Technology, CA, USA

^c Sibley school of Mechanical and Aerospace Engineering, Cornell University, Ithaca, NY, USA

valentina.lavezzo@uniud.it, soldati@uniud.it

Introduction Particle acceleration in turbulent flows can be considered a key issue for many environmental and industrial applications e.g. cloud formation, atmospheric transport, combustion systems etc. It is thus, important to understand the nature of the acceleration since it affects the collision rate, the dispersion of droplets or particles in the carrier fluid.

Many experimental and numerical studies on particle acceleration can be found in literature, but most of them deal with homogeneous and isotropic turbulence rather than wall-bounded flows which represent the objective of the present work. Previous studies focus mainly on the effect of inertia on particle acceleration, the relationship between acceleration and fluid coherent structures and the coupling between sampling and filtering mechanisms exerted by the particles on the fluid.

Recent experiments in a turbulent boundary layer (Gerashchenko et al. 2008) revealed surprising trends for inertial particle accelerations in the near-wall region. In particular, acceleration variance was seen to increase with increasing inertia, contrary to what is found in isotropic turbulence (see Ayyalasomayajula et al. 2008, Bec et al. 2006 among others).

To gain further insight into these findings we perform Direct Numerical Simulations (DNS) of a horizontal channel flow with suspended inertial particles tracked in the Lagrangian frame of reference. The DNS parameters have been chosen to match those of the experiment, based on boundary layer scaling. Three swarms of particles with different Stokes numbers (0.8, 1.6 and 10.7) have been simulated. Results for the mean and rms profiles of particle acceleration are in good agreement with the experimental findings. A coupling between shear and gravity is considered the cause of high variance for high

Stokes number particles in proximity of the wall, as it will be discussed in the following paragraphs.

Numerical Methodology A pseudo-spectral Direct Numerical Simulation code has been used to compute the turbulent flow of air (incompressible and Newtonian) in a horizontal channel. The reference geometry consists of two infinite flat parallel walls with periodic boundary conditions in the streamwise (x) and spanwise (y) directions and no-slip conditions at the walls. Dimensions of the computational domain are $4\pi h \times 2\pi h \times 2h$ with $h = 0.04$ m or 300 wall units, discretized with $256 \times 256 \times 257$ grid nodes in x , y and z , respectively. For a better comparison with the experimental work by Gerashchenko et al. (2008), we chose the parameters for the simulation accordingly. The shear velocity has been chosen equal to $u_\tau = 0.112$ m/s, thus the shear Reynolds number becomes $Re_\tau = u_\tau h / \nu = 300$.

Three sets of 320,000 particles characterized by different diameter have been tracked in a Lagrangian frame of reference, into the air flow. As for the fluid we matched particle parameters with those employed by Gerashchenko and co-authors. The Stokes number, calculated as the ratio of the particle response time $\tau_p = D_p^2 \rho_p / 18\nu$ to the flow characteristic timescale $\tau_f = \nu / u_\tau a u^2$ has been set equal to $St = \tau_p / \tau_f = 0.80, 1.60$ and 10.7 . Since the particle density ρ_p is much higher than the one of the fluid, the equation for particle motion reduces to a balance of the Stokes drag and gravity. Initially, particle number concentration is uniform in the computational domain and particle position is randomly chosen. The assumptions for particle modeling are: (i) particles are point-wise (ii) nondeformable, (iii) rigid and spherical. The effect of particles on the fluid is neglected so one-way coupling is assumed between the dispersed and the carrier fluid.

Results and Discussion In this section results of the comparison between the experimental work of Gerashchenko et al. (2008) and the present simulation are presented. Before going into detail on particle acceleration it is useful, for the following discussion, to compare the two flows in which particles have been dispersed. In Figure 1 the mean fluid velocity profile in the two cases is plotted. Good agreement is found close to the wall, whereas a slight deviation is present at the center of the channel. This was expected, since the flow in the simulation is bounded by an upper wall while a free stream boundary can be considered in the experiments. Since the two flows compare well to each other in terms of velocity we can consider half of a channel a good approximation of a turbulent boundary layer and expect a good agreement also on particle behavior.

In Figure 2-(a) the mean acceleration profiles for three Stokes number particles are shown. In the streamwise direction, good agreement between the DNS results and the experiments is observed. Slight discrepancies for $Z^+ < 10$ can be the result of either difficulties in the measurements close to the wall or the presence of boundaries on which the particles are bouncing in the

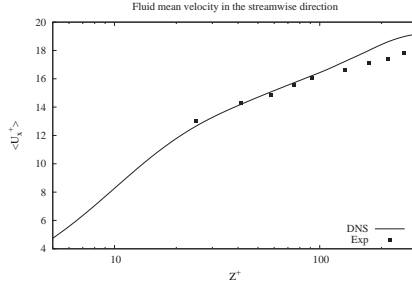


Fig. 1. Mean fluid velocity: streamwise component. Lines represent the simulations values at $Re_\tau = 300$, symbols the experimental ones at $Re_\tau = 470$.

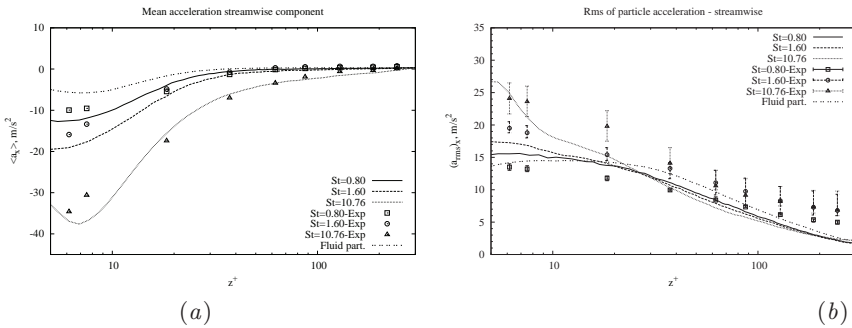


Fig. 2. Streamwise component of the mean particle acceleration (a) and of particle acceleration rms (b) varying with Z^+ . Lines represent the simulations values, symbols the experimental ones.

simulation. Comparing high order statistics it is possible to observe that experimental and simulation values compare well from a qualitative view point while quantitatively slight differences are present. This can be associated to the different fluid velocity faced by the particles in the two flows, as previously described. DNS results, indeed show lower values in correspondence to the channel core, as visible in Figure 2-(b), where the streamwise component of the rms of particle acceleration is plotted against the wall-normal direction. Furthermore we can notice that in correspondence to the wall, the variance is increasing with increasing Stokes number as described by Gerashchenko and co-authors. This result confirms the difference of a wall shear flow from homogeneous and isotropic turbulence where a decrease in acceleration variance is observed with increasing Stokes number as described in Bec et al.(2006).

In absence of gravity, particles are behaving as tracers, being their mean acceleration in the streamwise direction equal to fluid particles, as visible in Figure 3-(a). The slight deceleration close to the wall is found to be the result of shear stresses in this region. A deviation from fluid particles has

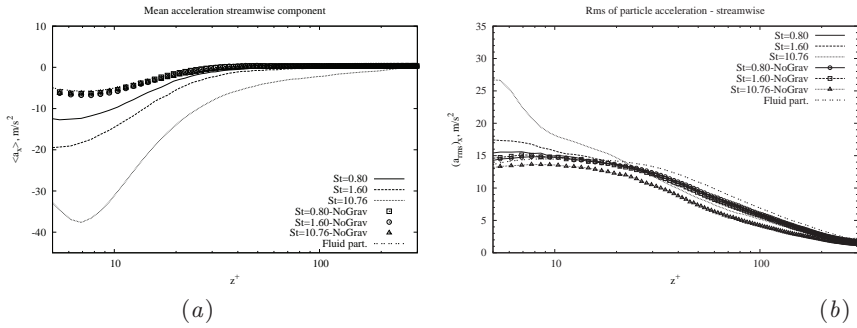


Fig. 3. Streamwise component of the mean particle acceleration (a) and of particle acceleration rms (b) varying with Z^+ in absence of gravity. Lines represent the simulations values, symbols the experimental ones.

been observed in the acceleration variance for $St = 10.7$ particles, as visible in Figure 3. Inertia plays an important role in decoupling particle velocity from fluid velocity. Inertial particles filter high-frequency small vortices, giving rise to a smaller acceleration variance close to the wall. Further analysis on the effect of gravity and inertia is currently under investigation and will be presented at the conference.

Conclusions Direct Numerical Simulation and Lagrangian particle tracking techniques have been used to study particle acceleration in a turbulent horizontal channel air flow. Results have been compared with the experimental work of (Gerashchenko et al. 2008) to have a better insight on their surprising trends for inertial particle accelerations in the near-wall region. Three sets of particles have been released in the turbulent flow to evaluate the effect of inertia on particle acceleration. Three main conclusions can be drawn: (i) we confirm the results of Gerashchenko and co-authors on an acceleration variance increasing close to the wall with increasing Stokes number, (ii) a coupling mechanism between shear and gravity forces is seen to be the main responsible for this increase and (iii) in absence of gravity particles are behaving as fluid tracers, but inertia effects are visible for larger particles.

1. S. Ayyalasomayajula, Z. Warhaft and L. R. Collins, “Modeling inertial particle acceleration statistics in isotropic turbulence”, *Phys. Fluids*, 2008, 20 –095104
2. S. Gerashchenko, N. Sharp, S. Neuscamman and Z. Warhaft, “Lagrangian measurements of inertial particle accelerations in a turbulent boundary layer”, *J. Fluid Mech.*, 2008, 617, 255–281
3. J. Bec, L. Biferale, G. Boffetta, A. Celani, M. Cencini, A. Lanotte, S. Musacchio and F. Toschi, “Acceleration statistics of heavy particles in turbulence”, *J. Fluid Mech.*, (2006), 550, 349–358

Simulating Fibre Suspensions: Lagrangian versus Statistical Approach

L.H. Zhao¹, H.I. Andersson¹, J.J.J. Gillissen² & B.J. Boersma²

¹Dept. Energy & Process Engineering, NTNU, Norway

²Lab. Aero & Hydrodynamics, TU Delft, The Netherlands

lihao.zhao at ntnu.no

INTRODUCTION

Fibre suspensions exhibit complex dynamical flow phenomena and are at the same time of immense practical importance, notably in the pulp and paper industries. NTNU and TU Delft have in a collaborative research project adopted two alternative strategies in the simulation of dilute fibre suspensions, namely a statistical approach [2] and a Lagrangian particle treatment [4]. The two approaches have their own advantages and disadvantages. In this paper we aim for the first time to compare the performance of the two.

In the statistical approach followed by Gillissen et al. [2],[3] the turbulent flow is handled from first principles, i.e. the turbulent field is obtained in a direct numerical simulation. The fibres are modeled as cylindrical rods, whose position and orientation are governed by a distribution function. This PDE is integrated along with the integration of the Navier-Stokes equations for the fluid motion by two-way coupling.

In the Lagrangian approach adopted by Mortensen et al. [4], [5] equations of translational and rotational motion are solved for each and every particle whereas the fluid motion is again obtained from a DNS. Forces and torques from the surrounding fluid act on the particles and without consideration of influence on the fluid, which is called one-way coupling. The fibres are modeled as prolate ellipsoids and analytical expressions for the force and torque are found in the literature[6]. Additional equations for the four Euler parameters are integrated in time to determine the particle orientation. The particle mass and shape are the essential parameters in this approach.

While the Lagrangian approach is limited to a finite number of particles, say 10^5 , the statistical approach assumes an infinite number of particles. On the other hand, the statistical model assumes massless particles whereas the

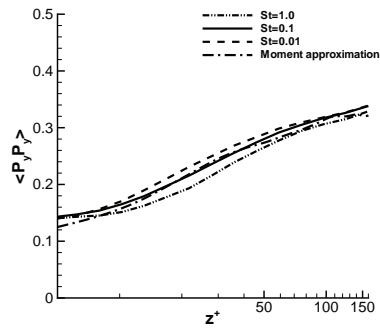
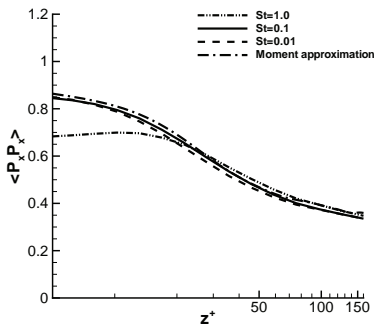


Fig. 1. Comparison of fibre orientation **Fig. 2.** Comparison of fibre orientation

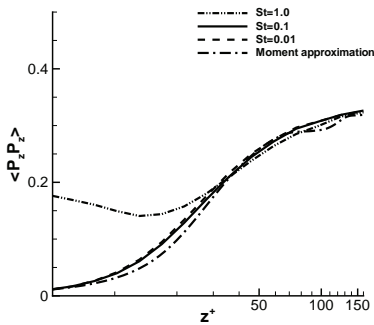


Fig. 3. Comparison of fibre orientation

Lagrangian model accounts for the particle mass through the particle response time. However, it should be possible to compare the two distinctly different approaches near the limit of zero mass, namely for small response times.

RESULTS

For this purpose we have used the Lagrangian approach and simulated ellipsoidal particles with aspect ratio 100 and with three rather different Stokes numbers, where the Stokes number is the ratio between the particle relaxation time and the Kolmogorov time scale. For comparison with the statistical approach, the moment approximation proposed by Gillissen et al. [3] is chosen. The fibre suspension is driven by a fixed pressure gradient through a plane channel. In the computation domain, x-axis, y-axis and z-axis are in the stream-wise, span-wise and wall-normal directions, respectively. The friction Reynolds number is 360 based on the wall distance.

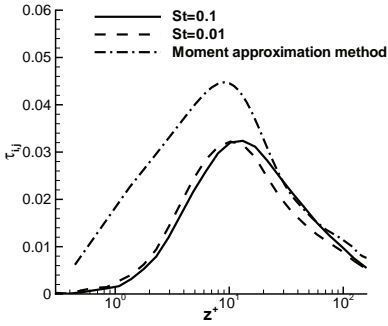


Fig. 4. Comparison of fibre stress $\bar{\tau}_{xx}$.

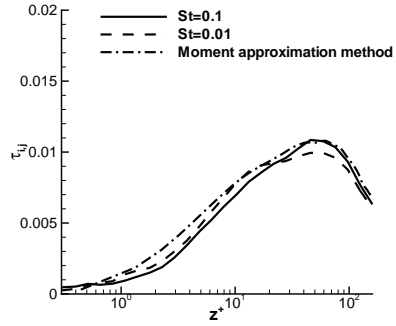


Fig. 5. Comparison of fibre stress $\bar{\tau}_{yy}$.

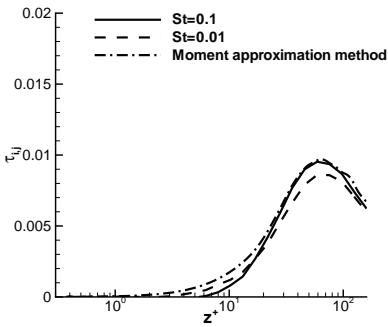


Fig. 6. Comparison of fibre stress $\bar{\tau}_{zz}$.

It is readily seen from Fig. 1, Fig. 2, Fig. 3 that the fibre orientations obtained with the two different approaches nearly collapse for Stokes numbers $St = 0.01$ and 0.1 , i.e. for very light particles. For $St = 1.0$, on the other hand, the heavier particles orient themselves rather differently from the massless particles in the near-wall region. However, all of the results show similar tendencies around the central region which means that particle orientations are almost identical in the middle of channel independently of the response time or Stokes numbers.

Further results of comparison of fibre mean stress are conducted. Results of fibre stress τ by the moment approximation method [2] are compared with the current Lagrangian approach with $St=0.01$ and $St=0.1$. Both results of mean fibre stress are computed based on the equation given by Doi and Edwards [1]:

$$\tau = 2\alpha \mathbf{S} : \langle \mathbf{p}\mathbf{p}\mathbf{p}\mathbf{p} \rangle \tag{1}$$

Here α is the fibre concentration parameter which is set to 1.0 in the current calculation; \mathbf{S} is the rate of strain tensor of fluid; $\langle \mathbf{pppp} \rangle$ is the fourth-order moment.

Results are shown in Fig. 4, Fig. 5, Fig. 6. Both cases of $St=0.1$ and $St=0.01$ gave reasonable agreement with the statistical approach. However, the case of $St=0.1$ gave better agreement than $St=0.01$ compared with results of the moment approximation method around the central region in the channel. This might be caused by the accumulation of numerical inaccuracies due to smaller particle time stepping needed for the very light particle as $St = 0.01$, i.e. the stiffness of the Lagrangian equation of motion.

Generally, in current work, the fibre orientations and the mean fibre stresses are studied by means of the Lagrangian approach and compared with results by statistical method of Gillissen et al.[2]. Three different cases of Stokes numbers are tested and results with small Stokes number are in reasonably agreement with results obtained with moment approximation method. Further results which tend to justify the linkage between the two rather different simulation approaches will also be presented.

References

1. Doi, M. and Edwards, S.F., 1986, *The Theory of Polymer Dynamics*, Clarendon, Oxford
2. J.J.J. Gillissen, B.J. Boersma, P.H. Mortensen and H.I. Andersson, *Phys. Fluids*, **19**, 115107 (2007).
3. J.J.J. Gillissen, B.J. Boersma, P.H. Mortensen and H.I. Andersson, *Phys. Fluids*, **19**, 035102 (2007).
4. P.H. Mortensen, H.I. Andersson, J.J.J. Gillissen and B.J. Boersma, *Phys. Fluids*, **20**, 093302 (2008).
5. P.H. Mortensen, H.I. Andersson, J.J.J. Gillissen and B.J. Boersma, *Int. J. Multiphase Flow*, **34**, 678 (2008).
6. H. Zhang, G. Ahmadi, F. G. Fan, and J. B. McLaughlin, *Int. J. Multiphase Flow*, **27**, 971 (2001).

Inertial particles in a turbulent pipe flow: spatial evolution

F. Picano, G. Sardina and C. M. Casciola

Dipartimento di Meccanica e Aeronautica, Sapienza Università di Roma, Via
Eudossiana 18, 00184 Roma, Italy
francesco.picano@uniroma1.it

Summary. Dynamics of small inertial particles transported by a turbulent flow is crucial in many engineering applications. For instance internal combustion engines or rockets involve the interaction between small droplets, chemical kinetics and turbulence. Small, diluted particles, much heavier than the carrier fluid, are essentially forced only by the viscous drag i.e. the Stokes drag. The difference between particle velocity V and fluid U produces various anomalous phenomena such as small-scale clustering or preferential accumulation at the wall even for incompressible flows. To stress the interaction between wall bounded flows and particle dynamics we have performed a direct numerical simulation of a fully-developed particle-laden pipe flow. Seven different populations of particles are injected at a fixed location on the axis of the pipe and their evolution is analyzed for a streamwise extension of $200R$ (with R the pipe radius) to assess the onset of turbophoresis.

1 Results & discussion

The friction Reynolds number of the simulation is about 200, the numerical code was tested in turbulent jets see [1] for details on the numerics. The whole domain is shown in the top panel of figure 1. Particles injected at the axis are dispersed by turbulent motions until they reach the wall where they accumulate due to turbophoretic effects. The injection rate is fixed at 900 particles per $\Delta t = R/U$, no gravity force is present in the simulation and no interaction between particles and back-reaction on the fluid are considered (one-way coupling). Note the trend towards a homogeneous distribution at large distance from the injection point.

The bottom panel represents the particles not too far from the injection point, the colours show the “smoke lines” traced by the heavy particles with different response time $\tau_p = 18d_p^2\rho_p/(\rho_f\nu)$ (d_p , ρ_p are the particle diameter and density respectively; ρ_f and ν are the fluid density and viscosity). Lines are corrugated by the fluid velocity fluctuations resulting in a different particle dispersion. This effect is due to the value of the Stokes number St^+ that is the ratio between τ_p and the characteristic time of the near wall region ν/U^{*2} . More generally it is possible to distinguish a developing region and a far field. In figure 2 two cross-flow slices in these two different zones are plotted. In the near region ($25R$, left panel) rod-

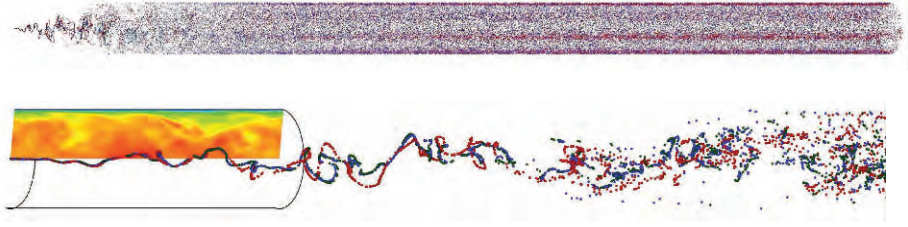


Fig. 1. Snapshots of particle positions ($St^+ = 0.1, 10, 100$ green, blue, and red spheres). Top panel, view of the whole computational domain plotted in arbitrary aspect ratio; bottom panel, enlargement of the near field region with colour encoded instantaneous axial fluid velocity isocontours.

like structures and void regions are present. All particles (except the lightest ones) show a preferential accumulation near the wall. In particular the heaviest ($St^+ = 100$) are distributed around the wall more intermittently compared to the blue ones ($St^+ = 10$). On the contrary, in the developed region particles fill the whole domain, although preferential accumulation is present near the wall especially for the heavier particles $St^+ = 10 \div 100$. Turbophoretic effects are negligible for lighter particles.

The mechanisms of particle dispersion and accumulation depends on the Stokes number, see figure 3 displaying the mean concentration for two Stokes numbers $St^+ = 0.1, 10$ as a function of the axial distance at four characteristic wall normal intervals i.e. viscous, buffer, log layer and bulk region. In the left panel ($St^+ = 0.1$) a uniform distribution for the whole section is reached at $z/R \cong 50$, below this value, the transient state can be observed with the gradual replenishment of all zones from the axis to wall. A different behavior characterizes particles with $St^+ = 10$ (middle panel) which present the maximum wall accumulation. In this case, at $z/R \cong 15$ the concentration in the buffer layer assumes the minimum value in the cross-section. Here particles tend to be expelled away from this region originating wall accumulation. In order to characterize with a single global index the particle dispersion along the developing region and the preferential accumulation in the far field, we make use of the Shannon's entropy associated to the mean particle concentration, as defined by:

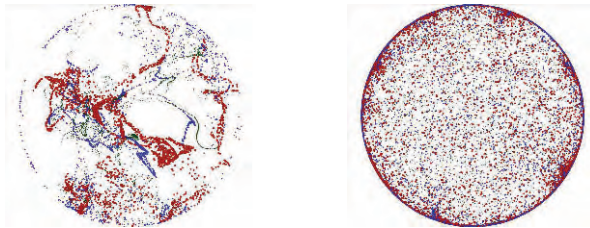


Fig. 2. Instantaneous particle positions in a thin cross flow slice of thickness $\sim R/10$ (same color coding as in fig. 1, symbol size increasing with St^+). Left, near field snapshot (distance from the releasing station $25R$); right, far field (at $200R$).

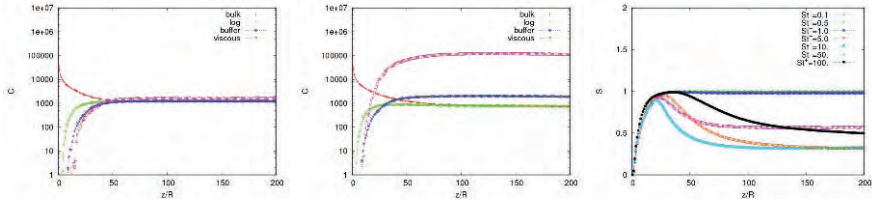


Fig. 3. Left ($St^+ = 0.1$) and middle ($St^+ = 10$) plots: mean particle concentration vs axial distance z/R in the four regions of the wall. Right plot: entropy of the mean particle concentration vs z/R for each particle population.

$$S(z) = - \sum_i \frac{N_i(z)}{N(z)} \ln \frac{N_i(z)}{N(z)}, \tag{1}$$

where N_i is the mean particle number in a shell with volume $\Delta z \pi (r_{out}^2 - r_{inn}^2)_i$, and i denotes the cell centered at r_i . All the shells share the same volume. N indicates the total number of particles in a given axial slice. In the right panel of figure 3 the entropy, normalized by the corresponding value of the uniform distribution, is reported as a function of the axial distance. Where the entropy is maximum particles tend to assume an even distribution in the section. In the far field values of entropy can give an indication of the preferential accumulation. From the right panel of figure 3, all the particles start from the null entropy since they are injected in a very small region on the axis. Downstream lightest particles ($St^+ \leq 1$) reach a uniform and homogeneous spatial distribution at $z \simeq 50R$. Intermediate particles ($St^+ = 5, St^+ = 10$) achieve a maximum of entropy with value smaller than one corresponding to a less homogeneous distribution. This behavior denotes that this kind of particles begins to accumulate at the wall before a complete dispersion takes place. Downstream, for $z/R \geq 110/120$, the entropy decreases corresponding to a strongly non-uniform particle concentration across the section. As far as the heaviest particles ($St^+ = 50$ and $St^+ = 100$) are concerned, the peak is almost one as for the lightest particles. Actually heaviest particles tend to distribute uniformly among the cross section before turbophoresis becomes relevant. Downstream the entropy decreases although more slowly compared to the medium size particles.

These results highlight that particles with different St^+ can achieve similar level of preferential accumulation, although at different distances from the injection point.

To investigate the origins of turbophoresis it is convenient to look at the average radial particle velocity conditioned to the velocity of the fluid (buffer layer), figure 4. The left panel refers to the developing region, while the right one concerns the fully developed state. Since lighter particles ($St^+ \leq 1$) exhibit conditional average velocities which almost exactly match the fluid velocity, their statistics are not reported here. Conditional average velocities are presented for particles which are most affected by turbophoresis, $St^+ \geq 5$. The immediate impression is that the difference between developing and far field does not emerge in the conditional statistics denoting a universal behavior of this observable. Very heavy particles, ($St^+ \geq 50$, circles and diamonds) present an almost vanishing mean conditional velocity, suggesting that their motion in the near wall region shows a weak dependence on the local fluid velocity also for very slow fluid motions. The most interesting results concern the intermediate range of Stokes numbers, $5 \leq St^+ \leq 10$. In this case the different

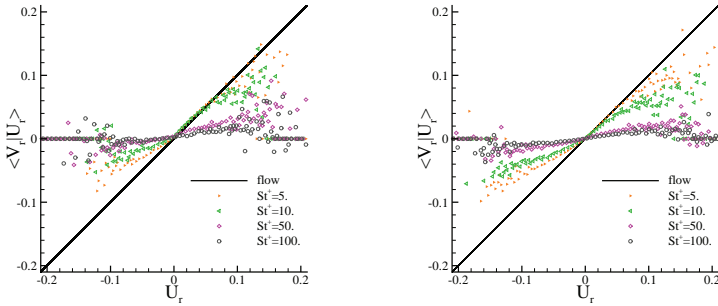


Fig. 4. Conditional particle radial velocity $\langle V_r | U_r \rangle$ vs fluid velocity for heavier particles: $St^+ = 5, 10, 50, 100$. Left panel refers to developing region ($z/R = 25$); right panel to far field ($z/R = 200$). The solid line gives the fluid velocity.

behaviors respectively associated with positive and negative fluid velocity are apparent. Specifically, weak and moderate intensity positive fluid velocity events are followed quite accurately by the particles in the range $0 \leq U_r \leq 0.04$. Stronger positive events see the particles trailing the fluid with a smaller velocity. On the contrary, particle inertia considerably filters the fluid excitation away from the wall, almost independently from the intensity, as apparent in the discontinuity in the slope of the plot at $U_r = 0$. This asymmetry between positive and negative conditional velocity distribution is the key to explain the fast accumulation rate of this kind of particles at the wall.

References

1. Picano F. & Casciola C.M.: Small scale isotropy and universality of axisymmetric jets, *Physics of Fluids* **19**, 118106. (2007)
2. Portela L.M., Cota P., Oliemans R.V.A.: Numerical study of the near-wall behaviour of particles in turbulent pipe flow. *Powder Tech.*, **125**, 149–157 (2002)
3. Marchioli C., Giusti A., Salvetti M.V., Soldati A.: Direct numerical simulation of particle wall transfer and deposition in upward turbulent pipe flow. *Journal of Multiphase Flow*, **129**, 1017–1038. (2003)
4. Rousson, D.W.I., Eaton, J.K.: On the preferential concentration of solid particles in turbulent channel flow. *Journal of Fluid Mechanics*, **428**, 149–169. (2001)

Heat transfer mechanisms in bubbly Rayleigh-Bénard convection

Paolo Oresta¹, Roberto Verzicco², Detlef Lohse¹, and Andrea Prosperetti¹

¹ Physics of Fluids group, Department of Applied Physics, J. M. Burgers Centre for Fluid Dynamics, and Impact-, MESA-, and BMTI-Institutes, University of Twente, P. O. Box 217, 7500 AE Enschede, The Netherlands,

² Department of Mechanical Engineering, University of Rome “Tor Vergata”, Via del Politecnico 1, 00133 Rome, Italy,

`d.lohse at utwente.nl`

This Proceeding contribution summarizes our results to be published in ref. [1]:

The effectiveness of boiling as a heat transfer mechanism has been known for centuries and the process has formed the object of a very large number of studies [2]. The emerging vapor bubbles introduce a new parameter to the classical Rayleigh-Bénard convection [3], namely the Jacob number

$$Ja = \frac{\rho c_p (T_h - T_{sat})}{\rho_V L} \quad (1)$$

in which L is the latent heat, ρ_V and ρ the vapor and liquid density, respectively, c_p the liquid specific heat and T_{sat} the saturation temperature of the liquid. Physically, Ja represents the ratio of the sensible heat to the latent heat. A very small Jacob number may be thought of as a very large value of the latent heat, which will tend to limit the volume change of the bubbles due to evaporation or condensation. For $Ja = 0$ the latent heat is effectively infinite and bubbles cannot grow or shrink.

Here we analyze the heat transfer mechanism in a liquid with a mean temperature close to its boiling point through numerical simulations with point-like [4, 5] vapor bubbles, which are allowed to grow or shrink through evaporation and condensation and which act back on the flow both thermally and mechanically. It is shown that the effect of the bubbles is strongly dependent on the Jacob number Ja . For very small Ja the bubbles stabilize the flow by absorbing heat in the warmer regions and releasing it in the colder regions. With an increase in Ja , the added buoyancy due to the bubble growth destabilizes the flow with respect to single-phase convection and considerably increases the Nusselt number, see figure 1, left.

Without bubbles, the cylinder is occupied by a single convective roll which rises along one side and descends along the opposite side. A picture of the flow

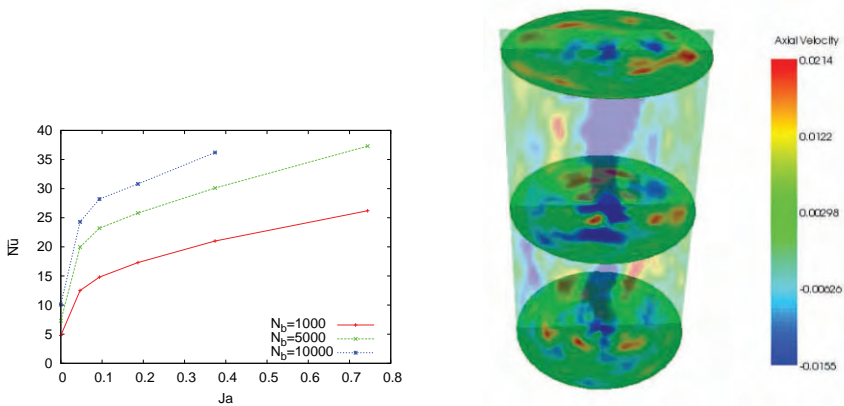


Fig. 1. Left: Nusselt number \bar{Nu} vs Jakob number for three different numbers of bubbles. Right: Vertical and horizontal cross sections (taken at $0.05H$, $0.5H$, and $0.95H$, respectively) of the vertical liquid velocity distribution in the cylinder for $Ja = 0$ and 5,000 bubbles. The blue structure near the axis is the descending region of the toroidal vortex which prevails for small Jakob numbers.

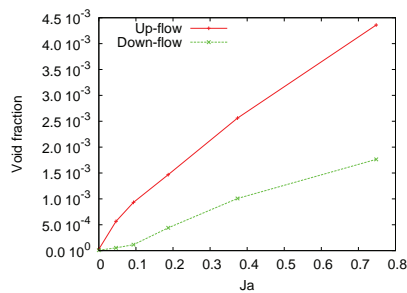


Fig. 2. Average void fraction in the up-flow and in the down-flow regions for $N_b = 5000$ bubbles.

for the 5,000 bubbles, $Ja = 0$ case is shown in Fig. 1, right, where one vertical and three horizontal cross sections color-coded with the vertical velocity field are displayed. The blue structure in the proximity of the cylinder axis is the descending region of a toroidal vortex, while the remaining green areas are those where the liquid rises, mostly with a smaller velocity, except for a few faster zones (yellow and red). It can be seen here that the volume occupied by the rising liquid is much greater than that occupied by the descending liquid, and this circumstance offers a likely explanation of the much smaller fraction of bubbles in the latter. If the Jakob number is increased, the toroidal circulation is reinforced with a marked increase in the maximum rising and descending velocities.

By calculating the volume of bubbles located in regions of positive and negative vertical liquid velocities we can look in detail at the effect of the increased buoyancy. Figure 2 shows the time- and volume-averaged vapor volume fractions for 5,000 bubbles as a function of the Jacob number. The results for the other cases are similar, with smaller void fractions for 1,000 bubbles (for $Ja = 0.35$, approximately 0.02% and 0.08%), and larger ones for 10,000 bubbles (for $Ja = 0.35$, approximately 0.16% and 0.36%). It is seen that the void fraction in the upflow regions is consistently much larger than in the downflow regions, thus providing strong evidence for the expected destabilizing effect of the buoyancy provided by the bubbles.

A comparison with the recent experiments of ref. [6] will be difficult as the bubble nucleation process is only very approximately modeled in this present work.

References

1. P. Oresta, R. Verzicco, D. Lohse, and A. Prosperetti, *Phys. Rev. E* **80**, to be published (2009).
2. V. Dhir, *Ann. Rev. Fluid Mech.* **30**, 365 (1998).
3. G. Ahlers, S. Grossmann, and D. Lohse, *Rev. Mod. Phys.* **81**, (2009).
4. J. Magnaudet and I. Eames, *Annu. Rev. Fluid Mech.* **32**, 659 (2000).
5. I. Mazzitelli, D. Lohse, and F. Toschi, *J. Fluid Mech.* **488**, 283 (2003).
6. J.-Q. Zhong, D. Funfschilling, and G. Ahlers, *Phys. Rev. Lett.* **102**, 124501 (2009).

Scaling of polymer drag reduction with polymer and flow parameters in turbulent channel flow

D. H. Lee and R. Akhavan†

University of Michigan, Department of Mechanical Engineering,
Ann Arbor, MI 48109-2125, USA

†corresponding author, e-mail: raa@umich.edu

Summary. The scaling of polymer drag reduction with polymer and flow parameters has been investigated using results from direct numerical simulations (DNS) of dilute, homogeneous polymer solutions in turbulent channel flow. Simulations were performed using a mixed Eulerian-Lagrangian scheme with a FENE-P dumbbell model of the polymer. The full range of drag reduction from onset to maximum drag reduction (MDR) is reproduced in DNS with realistic polymer parameters, giving results in good agreement with available experimental data. Onset of drag reduction is found to be a function of both the polymer concentration and the Weissenberg number, in agreement with the predictions of de Gennes[1]. The magnitude of drag reduction increases monotonically with decreasing viscosity ratio, β , for $1.0 > \beta > 0.98$, saturates to a plateau for $0.98 > \beta > 0.9$, and slowly decays for $0.9 > \beta$ when the solution ceases to be dilute. The magnitude of drag reduction at saturation is a strong function of the Weissenberg number. A $We_\tau \sim O(Re_\tau/3)$ is needed to achieve MDR. The presence of the polymer results in attenuation of the small scales along with enhancement of the large scales in the spectra of the streamwise turbulent velocity fluctuations, and attenuation of all scales in the spectra of cross-stream turbulent velocity fluctuations. The degree of attenuation and the range of affected scales increase with the Weissenberg number and with the polymer concentration up to the saturation concentration. At saturation concentration, the cross-stream size of the largest attenuated eddies in the streamwise spectra conform to the predictions of Lumley's theory[2, 3], while at concentrations below the saturation, they conform to a modified version of de Gennes's theory[1]. The net effect of the polymer can be represented by an effective viscosity with a peak magnitude of $\nu_{eff} \sim O(0.1\lambda u_\tau^2)$ at saturation, in agreement with the predictions of Lumley's theory[2, 3].

1 Introduction

While the phenomenon of drag reduction by dilute polymer solutions has been known for nearly sixty years, the scaling of polymer drag reduction with

polymer and flow parameters remains poorly understood. The two principal theories of polymer drag reduction suggested by de Gennes[1] and Lumley[2, 3] make vastly different predictions for the criteria for onset of drag reduction, saturation of drag reduction, Maximum Drag Reduction (MDR), and the range of turbulent scales attenuated by the polymer. In Lumley's theory, onset of drag reduction is assumed to be independent of the polymer concentration and to occur at $We_\tau|_{onset} \sim O(1)$, where $We_\tau \equiv \lambda u_\tau^2/\nu$ is the Weissenberg number, λ is the polymer relaxation time, u_τ is the wall-shear velocity, and ν is the kinematic viscosity of the solution. Saturation of drag reduction is assumed to occur when the effective viscosity introduced by the polymer reaches a magnitude of $\nu_{eff}|_{sat} \sim O(\lambda u_\tau^2)$, while MDR is assumed to occur when the viscous sublayer defined based on the saturation value of the effective viscosity extends all the way to the outer edge of the boundary layer or when $\delta \sim O(\lambda u_\tau)$ or $We_\tau|_{MDR} \sim O(Re_\tau)$. The largest turbulent scales damped by the polymer, r^* , are assumed to be those having a time-scale equal to λ . In de Gennes's theory, onset of drag reduction is assumed to be a function of both the polymer concentration and the Weissenberg number. In wall-bounded flows, it can be shown[4] that his onset criterion is equivalent to $(n_p k_B T)/(\rho u_\tau^2)|_{onset} \sim We_\tau^{-\frac{15n}{4}}$, where n_p is the polymer number density, k_B the Boltzmann constant, T the absolute temperature, ρ the density, and $0 < n \leq 2$ denotes the dimensionality of the polymer stretching. Saturation is assumed to occur when the unstretched polymer coils begin to overlap, or when $(n_p R_G^3) \sim 1$, where R_G denotes the radius of gyration of the polymer in the coiled state. In wall-bounded flows, this translates to[4] a saturation criterion of $(n_p k_B T)/(\rho u_\tau^2)|_{sat} \approx \beta We_\tau^{-1}$, where β denotes the ratio of the solvent viscosity to the zero shear viscosity of the polymer solution. MDR is assumed to occur when the largest scales affected by the polymer become comparable to the boundary layer thickness or when $r^* \sim \delta$. For wall-bounded flows, this reduces to $We_\tau|_{MDR} \sim O(Re_\tau)$, in agreement with the predictions of Lumley's theory. The largest turbulent scales damped by the polymer are assumed to have a scale $r^{**} < r^*$ such that the turbulence kinetic energy per unit volume at scale r^{**} is comparable to the elastic energy per unit volume stored in the polymer molecules. In wall-bounded flows, it can be shown[4] that $\frac{r^{**}}{r^*} = \left(\frac{1}{A} \frac{n_p k_B T}{\rho u_\tau^2} \frac{z^+}{We_\tau} \right)^{\frac{1}{2/3+\delta n/2}}$, where z^+ denotes the wall-normal coordinate in wall units, and A is a constant originally set to $A = 1$ by deGennes[1, 4]. In this study, we aim to evaluate these predictions using results from DNS.

2 Results and Discussion

The DNS studies were performed using a FENE-P dumbbell model of the polymer and a mixed Eulerian/Lagrangian numerical scheme, employing standard pseudo-spectral methods for the hydrodynamics and a backward-tracking Lagrangian particle method[5] for the polymer dynamics. Computations were

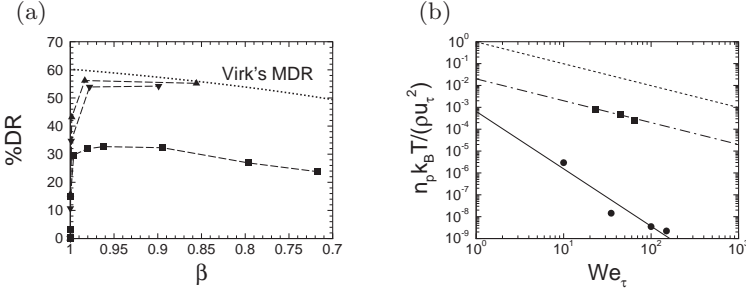


Fig. 1. (a) Dependence of drag reduction on We_{τ_b} and β observed in DNS, (b) Onset and saturation of drag reduction observed in DNS compared to theoretical predictions of deGennes. (a) \square , DNS results at $We_{\tau_b} \approx 35$; \blacktriangledown , DNS results at $We_{\tau_b} \approx 100$; \blacktriangle , DNS results at $We_{\tau_b} \approx 150$; \cdots , Virk's MDR asymptote; (b) \bullet , onset data from DNS; \blacksquare , saturation data from DNS; $—$, $\frac{n_p k_B T}{\rho u_\tau^2} = A We_\tau^{-15n/4} (z^+)^{(-1/2+15n/8)}$ with $A = 1 \times 10^{-4}$, $n = 0.7$, and $z^+ = 10$; $- \cdot -$, $\frac{n_p k_B T}{\rho u_\tau^2} = (1 - \beta) We_\tau^{-1}$ with $\beta = 0.98$; $---$, $\frac{n_p k_B T}{\rho u_\tau^2} = \beta We_\tau^{-1}$ with $\beta = 0.98$.

performed at a base Reynolds number of $Re_{\tau_b} = u_{\tau_b} h / \nu_b \approx 230$ in turbulent channel flows of size $40h \times 10h \times 2h$ or $10h \times 5h \times 2h$ with resolutions of $512 \times 256 \times 129$ and $128 \times 128 \times 129$, respectively. Simulations were performed for the range of $10 \leq We_{\tau_b} \equiv \lambda u_{\tau_b}^2 / \nu_b \leq 150$, polymer number densities $1.12 \times 10^{-10} \lesssim n_p k_B T / (\rho u_{\tau_b}^2) \lesssim 1.12 \times 10^{-2}$ (corresponding to $0.7 \leq \beta \leq 1.0$), and a polymer extensibility parameter of $b = 45,000$.

Fig. 1(a) shows the variation of drag reduction with We_{τ_b} and β . At all Weissenberg numbers, drag reduction sharply rises for $1 > \beta > 0.98$, saturates to a plateau for $0.98 > \beta > 0.9$, and slowly decays for $0.9 > \beta$. The magnitude of drag reduction at saturation is a strong function of the Weissenberg number. At $We_{\tau_b} \approx 35$, only $\sim 32\%$ DR is observed at saturation, while at $We_{\tau_b} \approx 100$ and $We_{\tau_b} \approx 150$, drag reductions of $\sim 54\%$ and $\sim 56\%$ are obtained, respectively. The magnitude of drag reduction observed at saturation at $We_{\tau_b} \approx 150$ is comparable to the range $57 - 60\%$ DR predicted by Virk's MDR asymptote. Fig. 1(b) shows the onset and saturation of drag reduction observed in DNS compared to the theory of de Gennes. Using the relation $\frac{1}{\beta} - 1 = \frac{n_p k_B T}{\mu_s} \lambda \frac{b}{b+3}$ [6] and for $b \gg 1$, the saturation condition $\beta \approx 0.98$ observed in DNS can be expressed as $(n_p k_B T) / (\rho u_\tau^2)|_{sat} \approx (1 - \beta) We_\tau^{-1}$. This criterion has the same scaling as $n_p k_B T / (\rho u_\tau^2)|_{sat} \approx \beta We_\tau^{-1}$ suggested by de Gennes[1] but is lower in magnitude by a factor of $(1 - \beta) / \beta$. Onset of drag reduction shows good agreement with de Gennes's theory with $n \approx 0.7$, which is comparable to $n = 2/3$ previously suggested based on analysis of experimental data[4]. Examination of the effective viscosity at saturation (not displayed) shows that the peak magnitude of ν_{eff} at saturation varies from $\nu_{eff} \sim 0.1(\lambda u_\tau^2)$ at $We_{\tau_b} \approx 10$ to $\nu_{eff} \sim 0.04(\lambda u_\tau^2)$ at $We_{\tau_b} \approx 150$, consistent with the predictions of Lumley's theory.

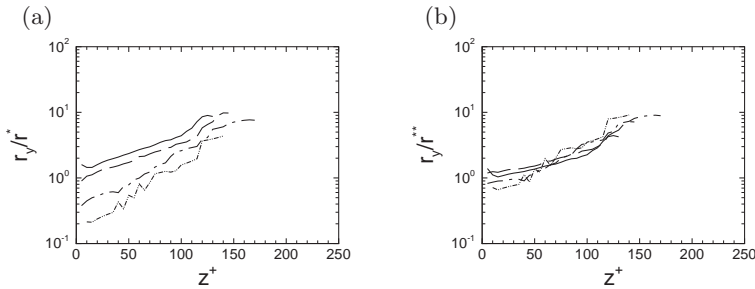


Fig. 2. The size of largest cross-stream scales, r_y , damped by the polymer at $We_{\tau_b} \approx 150$ compared to (a) r^* , and (b) r^{**} with $n = 2$ and $A = 1 \times 10^{-4}$. \cdots , $\beta \approx 0.9998$; $-\cdot-$, $\beta \approx 0.998$; $—$, $\beta \approx 0.98$; $- - -$, $\beta \approx 0.86$.

Fig. 2 shows the size of the largest cross-stream scales damped by the polymer at $We_{\tau_b} \approx 150$ for $1 > \beta > 0.86$ compared to r^* of Lumley's theory and r^{**} of de Gennes's theory, where $r_y = 2\pi/k_{y,c}$ and $k_{y,c}$ denotes the wavenumber of the largest damped scale in the spectra of $E_{uu}(k_y)$. It is observed that r_y/r^{**} with $n = 2$ provides a good collapse the data to $O(1)$ values, while r_y/r^* does not collapse the data and approaches $O(1)$ only at saturation. Overall, these results indicate that within the limitations of their underlying assumptions, the theories of Lumley[2, 3] and de Gennes[1] are both successful in describing the dynamics of turbulence in the presence of polymers. Lumley's theory does not attempt to account for the effect of polymer concentration, but correctly accounts for the effect of Weissenberg number at saturation concentrations. The theory of de Gennes is more complete and accounts for the effect of both the Weissenberg number and polymer concentration.

Further analysis of the data shown in Fig. 2 (not displayed) shows that at MDR, $r_y \sim O(3\lambda u_\tau)$ and $r_y \sim h$. Combining these two criteria gives the condition that to reach MDR a $We_\tau \sim O(Re_\tau/3)$ is required. This result is consistent with the predictions of both Lumley and de Gennes, who both predict a $We_\tau \sim O(Re_\tau)$ is needed to reach MDR.

References

1. P. G. de Gennes, *Physica*, **140A**, 9–25 (1986).
2. J. L. Lumley, *Annu. Rev. Fluid Mech.*, **1**, 367–384 (1969).
3. J. L. Lumley, *J. Polymer Sci.*, **7**, 263–290 (1973).
4. K. R. Sreenivasan and C. White, *J. Fluid Mech.*, **409**, 149–164 (2000).
5. P. Wapperom, R. Keunings and V. Legat, *J. Non-Newtonian Fluid Mech.*, **91**, 273–295 (2000).
6. R. B. Bird, P. J. Dotson and N. L. Johnson, *J. Non-Newtonian Fluid Mech.*, **7**, 213–235 (1980).

DNS study on “diameter effect” of drag reduction in viscoelastic-fluid flow

T. Ishigami, T. Tsukahara and Y. Kawaguchi

Department of Mechanical Engineering, Tokyo University of Science,
Yamazaki 2641, Noda-shi, Chiba 278-8510, Japan
tsuka@rs.noda.tus.ac.jp

1 Introduction

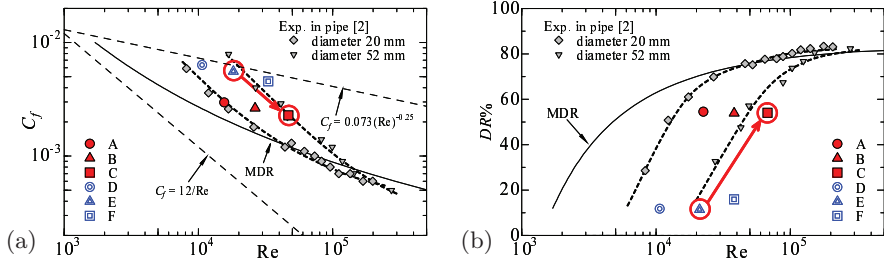
It is well known that the small amount of polymers or surfactant additives to flowing liquid give rise to drag reduction (DR) in turbulent flow [1]. However this mechanism has not been satisfactorily clarified. One of many interesting aspects is the so-called ‘diameter effect’, which has been observed experimentally [2, 3]. For instance, the discrepancy between results obtained by different pipe diameters represents the diameter effect (see Fig. 1): this effect is seen as additional dependence of the skin friction coefficient, C_f , on the pipe diameter (or channel width) as well as Reynolds number, Re . Although several experimental studies were published about the diameter effect, the relationship between the DR rate and rheological parameters (such as Weissenberg number, We) is still not clear. Therefore we have performed a series of direct numerical simulations (DNS) on a viscoelastic-fluid flow in a channel and discussed the diameter effect with focusing on effects of Re and We on the DR induced by polymers or surfactant additives.

2 Numerical conditions

In this study, the shear-thinning behaviour is considered to be negligible, and the elongational viscoelastic effect is attempted using the Giesekus model for a constitutive equation. We employed the code based on our previous studies, which have shown that obtained DNS data agree qualitatively well with experimental data (see [4, 5] for detail). The present Reynolds number ranges from $Re_\tau (= \rho u_\tau \delta / \eta_0) = 150$ to 395, where ρ is the density, $u_\tau (= \sqrt{\tau_w / \rho})$: τ_w is wall shear stress) the friction velocity, δ the channel half-width and η_0 the solution viscosity at zero shear rate. As for rheological properties, $We_\tau (= \rho u_\tau^2 \lambda / \eta_0)$ based on the relaxation time, λ , is set to be either 30 or 11. The solvent viscosity is assumed to be half of η_0 . The number of grid points

Table 1. Computational parameters and achieved drag-reduction rate.

Fluid	A	B	C	D	E	F
Re_τ	150	240	395	150	240	395
We_τ	30	30	30	11	11	11
η_0/η_{eff}	1.45	1.44	1.45	1.15	1.16	1.15
$DR\%$	54.6%	53.9%	54.0%	11.8%	11.4%	16.0%

**Fig. 1.** Variation of drag and its reduction rate with Reynolds number based on bulk velocity, 2δ and solvent kinematic viscosity. An arrow from E to C corresponds to Case- u —increasing in u_τ with constant fluid properties and δ .

is 128^3 for $Re_\tau = 150$ and 240, but 256^3 for $Re_\tau = 395$. The domain size is $12.8\delta \times 2\delta \times 6.4\delta$ in streamwise, wall-normal, and spanwise directions.

3 Results and discussion

The rate of DR, $DR\% = (C_f^D - C_f)/C_f^D$, obtained in the present study is given in Table 1. Here, C_f^D is the value estimated by the Dean's empirical correlation [6] for the Newtonian turbulent flow at the same bulk Reynolds number based on solvent viscosity. The actual C_f for each relevant non-Newtonian fluid is shown in Fig. 1(a) with comparing to the experimental data [2] and Virk's maximum-DR (MDR) asymptote [7]. Significant $DR\%$ of about 54% is accomplished in all of the present cases at $We_\tau = 30$, while the other cases exhibit a poor DR. It is obviously seen that high We_τ is responsible for the effective DR. In such case, the reduction of the effective viscosity at the wall [8], η_{eff} , is also remarkable (see Table 1). Moreover, the obtained values of $DR\%$ for each We_τ are almost constant regardless of Re_τ . This implies that when u_τ , η_0 and λ are constant (i.e., same fluid), the increasing of Re_τ is interpreted in two ways: firstly as an enlargement of channel width, and secondly as an increase in driving force, namely u_τ . These two protocols are hereafter referred to as 'Case- δ ' and 'Case- u ', respectively. In Case- δ , no noteworthy variation in $DR\%$ was recognized. For instance, the increase of Re_τ from 240 to 395, by increasing of δ with fixed u_τ and constant fluid properties, it is equivalent to changing fluid B \rightarrow C or fluid E \rightarrow F. In Case- u , on the other hand, the $DR\%$ significantly increases with increasing Re_τ due to additional change of We_τ ,

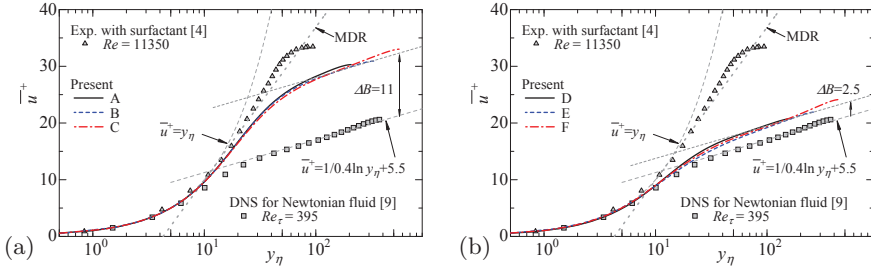


Fig. 2. Mean velocity profile in wall units: (a) $We_\tau = 30$, (b) $We_\tau = 11$.

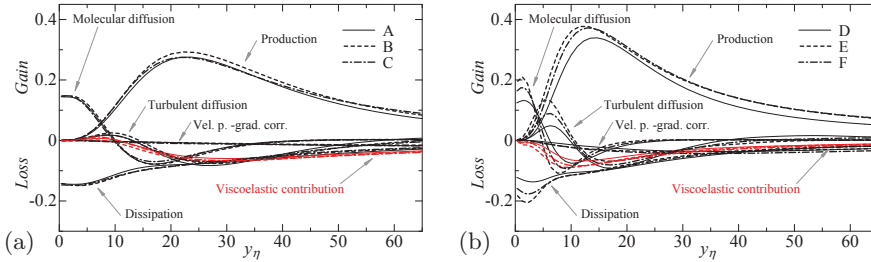


Fig. 3. Budget of streamwise normal stress, $\overline{u'u'}$, in wall units: (a) $We_\tau = 30$, (b) $We_\tau = 11$. All terms are normalized by $\eta_{\text{eff}}/\rho u_\tau^4$.

can be seen in Fig. 1(b). The shift from fluid E to C is an example of Case- u_τ . More specifically, whereas the increasing rate in Re_τ from 240 (fluid E) to 395 (fluid C) is about 1.65, that of We_τ equals to $1.65^2 \approx 30/11$. Hence, this causes inadequate scaling by Re to the prediction of DR in the case of rheologically identical fluids. The present DNS is in good agreement with the experimental observations [3]. In addition, it is important to note that the diameter effect can be demonstrated by simulations.

Figure 2 shows the mean velocity distributions plotted in \overline{u}^+ vs $\log y_\eta$. Here, $y_\eta = \rho u_\tau y / \eta_{\text{eff}}$. There exists a considerable difference in the profile between the high-DR flows (fluids A–C in Fig. 2(a)) and the low DR ones (fluids D–F in Fig. 2(b)). For the Newtonian fluid [9], the data closely follow the typical log law for $y_\eta > 30$. On the other hand, clear log-law regions with displacement are observed for the present non-Newtonian cases. In addition, the profiles for each We_τ are scaled well with wall units. For $We_\tau = 11$ there is an upshift $\Delta B \approx 2.5$ of logarithmic velocity profile of Newtonian fluid due to the presence of the additives, corresponding to the modest DR. In the case of high-DR ($We_\tau = 30$), the data follow Virk’s ultimate profile, $\overline{u}^+ = 11.7 \ln y_\eta - 17$, up to $y_\eta \approx 20$. These results suggest that We_τ is the most dominant parameter for ΔB and $DR\%$.

Figure 3 presents the budget terms of the transport equation for the Reynolds normal stress $\overline{u'u'}$, namely the production, the dissipation, the velocity pressure-gradient correlation (VPG), the turbulent and molecular diffusions, and the viscoelastic contribution terms. The last term does not appear

in the case of Newtonian fluid. At $We_\tau = 30$, the viscoelastic contribution is comparable in magnitude with the diffusion terms.

As is to be expected from the discussion on the $\overline{u^+}$ -profile, the budget of $\overline{u'u'}$ reveals to be less dependent on the Reynolds number, especially for the high-DR case as given in Fig. 3(a). The near-wall dissipation surprisingly does not depend on the Reynolds number. With increasing We_τ , the peak of production term drops and shift away from the wall, and other terms also apparently decreases in the vicinity of the wall. It is worth noting that the VPG term in Fig. 3(a) is negligible everywhere. (It is well-known that the pressure strain term contained in the VPG term plays a dominant role on the energy redistribution to other directional components.) In this case, the flow becomes anisotropic turbulence due to less redistribution, resulting high DR. On the other hand, the results obtained for three different Re_τ at each We_τ do not differ much from each other; at least to the extents of the present parameter ranges. However, when Re_τ (or u_τ) is varied with same fluid and channel (i.e., Case- u), a significant difference appears in the energy budget due to dependence of We_τ on u_τ .

4 Conclusion

The viscoelastic fluid in turbulent channel flow has been analyzed using DNS in the range of Re_τ from 150 to 395 for $We_\tau = 11$ and 30. We obtained two different results from the increasing Re_τ for rheologically identical fluids (with a fixed relaxation time). An increase of δ with a constant u_τ do not much affect $DR\%$, but that of u_τ with a constant δ gives rise to an effective DR. Moreover, $DR\%$ and flow properties, such as the log-law displacement in the mean velocity profile and the budget terms of $\overline{u'u'}$, are depend on We_τ but not on Re_τ . These results imply that We_τ is the most important parameter for prediction of $DR\%$ in increasing Re_τ .

Acknowledgements: This work was conducted in the Research Center for the Holistic Computational Science (HOLCS). The computations were performed with supercomputing resources at Cyberscience Center, Tohoku University.

References

1. B. A. Toms, *Proc. First Int. Cong. on Rheology*, 135 (1948).
2. K. Gasljevic and E. F. Matthys, *Proc. IMECE95* (1995).
3. K. Gasljevic, G. Aguilar and E. F. Matthys, *J. Non-Newtonian Fluid Mech.*, **84**, 131 (1999).
4. B. Yu, F. Li and Y. Kawaguchi, *Int. J. Heat & Fluid Flow*, **25**, 961 (2004).
5. B. Yu and Y. Kawaguchi, *J. Non-Newtonian Fluid Mech.*, **116**, 431 (2004).
6. R. D. Dean, *Trans. ASME I: J. Fluids Eng.*, **100**, 215 (1978).
7. P. S. Virk, *J. Fluid Mech.*, **45**, 225 (1971).
8. R. Sureshkumar, A. N. Beris and R. A. Handler, *Phys. Fluids*, **9**, 743 (1997).
9. H. Abe, H. Kawamura and Y. Matsuo, *Int. J. Heat & Fluid Flow*, **25**, 404 (2004).

Modifications of the turbulent structure in a bubbly boundary layer

B. Jacob, M. Miozzi, A. Olivieri, E. F. Campana and R. Piva*

INSEAN, via di Vallerano 139, Rome, Italy

* DMA, Sapienza Università di Roma, via Eudossiana 18, Rome, Italy.

b.jacob@insean.it

In recent years, evidence is accumulating on the fact that dispersing modest quantities of particles or bubbles in turbulent environments may lead to substantial modifications of the large scales of the flow, as well as of its global parameters. Interaction with the large-scale structures occurs even when the characteristic dimension of the dispersed phase lies below the smallest turbulent wavelength, and may be understood in terms of the significant inhomogeneities of the instantaneous concentration field associated to the preferential accumulation in the cores of vortical structures (for the case of bubbles). In turn, such large fluctuations in the bubble concentration dramatically modify the bulk properties of the underlying flow.

Here we report on a particular manifestation of this phenomenon, as observed in the context of a zero pressure gradient turbulent boundary layer laden with microbubbles (diameters of the order of the Kolmogorov length-scale $\eta \sim 100 \mu m$) at very low void fractions ($C_v \sim 10^{-3}$). The ultimate effect is a substantial reduction of the frictional drag, a phenomenon already observed in several wall-bounded configurations (see e.g. [1, 2] and references therein) but nonetheless still poorly understood. The experimental setup, depicted in Fig. 1 consists schematically of a 3.5 m long flat plate, horizontally positioned in a water channel run at a speed of 0.75 m s^{-1} . Roughly monodis-

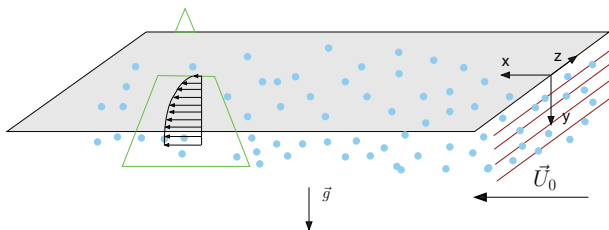


Fig. 1. The experimental setup: plate "on top", bubble-generating device and laser sheet arrangement for concentration and velocity measurements.

persed microbubbles are generated near the leading edge on the lower side of the plate, with gravity tending to push them towards the wall. Owing to their very small Weber number, bubbles retain their spherical shape and behaves like rigid spheres. The complex interplay of the different forces acting on the microbubbles (in particular lift, buoyancy and pressure-gradient forces) results in a strongly inhomogeneous distribution of the dispersed phase at the measurement station ($x = 2.5$ m, $Re_\theta = 3700$, $u_{\tau,0} = 0.029$ m/s) with a sharp peak in the buffer region of the base turbulent boundary layer, i.e. at $y^+ \approx 30$, see Fig. 2. Remarkably, no bubbles are found at the wall, suggesting that some statistical balance between vertical forces occurs in this region.

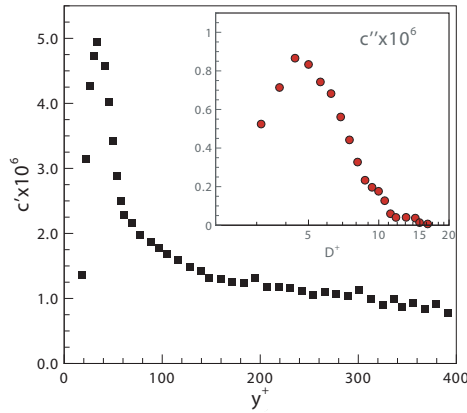


Fig. 2. Main panel: averaged bubble concentration, $10^6 \times c'$, against dimensionless wall-normal distance $y^+ = y/l_0$ and dimensionless bubble diameter $D^+ = D/l_0$, where $l_0 = \nu_0/u_{\tau,0}$ is the viscous length of the Newtonian boundary layer. The overall mean void fraction is $C_v = \int_0^\infty c'(D^+)dD^+ \approx 10^{-3}$. Inset: the histogram of bubble diameters, as measured at $y^+ = 25$, displaying an approximately log-normal behavior.

Velocity measurements of the liquid phase are obtained in the streamwise-wall normal plane by means of Feature Tracking techniques [3], which resolve only the displacements of neutrally buoyant tracers in the light plane generated by two Nd-Yag laser pulses. At the low concentrations typical of our measurements, scattering from the bubbles is limited, so that the quality of the data is preserved.

As mentioned before, the most noticeable effect of the presence of microbubbles is to be found in the values of the mean streamwise velocity and in the Reynolds stress profile near the wall. The reduction of the skin-friction coefficient derives from a substantial decrease of the mean velocity in the inner region, as shown in Fig. 3. As in most drag-reducing flows, this effect is

accompanied by a parallel depletion of the vertical flux of streamwise momentum, i.e. the Reynolds shear stress. Only marginal effects are seen instead on the velocity fluctuations profiles, a slight increase for both the streamwise and the wall-normal turbulent intensities being observed for the bubbly case.

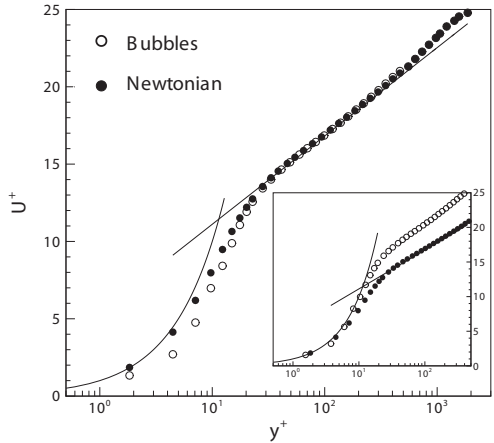


Fig. 3. The dimensionless streamwise mean velocity plotted against dimensionless wall-normal distance for both the Newtonian and the bubble-laden cases (filled and open symbols respectively). Inner scales relative to the Newtonian case are used for non-dimensionalizing the quantities. Inset: streamwise velocity profiles for the Newtonian and the bubbly flows, non-dimensionalized with the proper inner scales.

As a key to gaining an understanding of the underlying mechanism, the modification of the turbulent structure is analyzed in terms of the familiar two-point correlation tensor:

$$R_{ij}(y_0, r_x, y) = \langle u_i(x, y_0)u_j(x + r_x, y) \rangle / (u_{i,rms}(y_0)u_{j,rms}(y)) \quad (1)$$

from which all classical statistical observables, e.g., one-dimensional correlations or structure functions are straightforwardly derived. Additionally, this quantity directly conveys a complete qualitative picture of the spatial arrangement of the dominant turbulent structures. A comparison between the Newtonian and the bubbly behaviors, pertaining to a reference location in the base buffer region ($y_0^+ \approx 25$) where the peak of the void fraction occurs, is shown in Fig. 4 for two different components, R_{vu} and R_{uu} respectively. While the latter quantity, which reflects the well-known organization of near-wall structures into vortex packets, appears to be only little affected by the presence of the bubbles, marked differences are found instead for R_{vu} . In particular, consistently with the associated Reynolds stress, the intensity of the correlation peak at the origin is strongly reduced, indicating a marked decorrelation of the turbulent fluctuations. The most noteworthy feature is represented by

the characteristic scales of the energy production being strongly weakened, as indicated by the much shorter correlation length. A similar behavior is also observed for the vertical correlation component R_{vv} , which is usually assumed to be representative of some characteristic eddy dimension at the reference wall-normal distance y_0 .

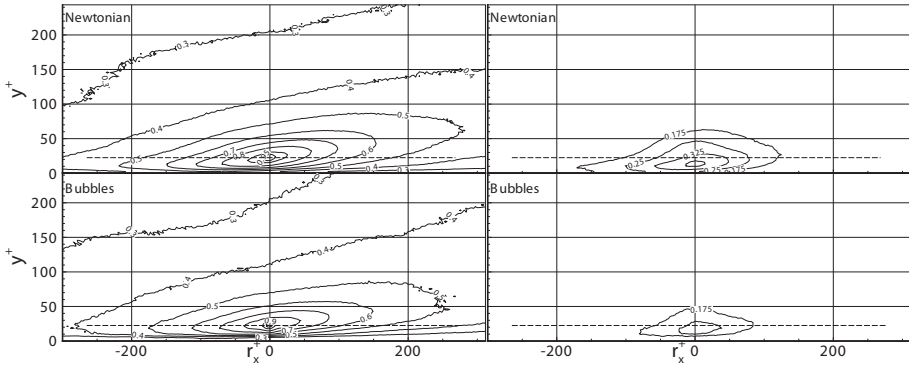


Fig. 4. Comparison between correlation maps estimated at $y_0^+ = 25$ in Newtonian (upper panels) and bubbly flows (lower panels). Left column: $R_{uu}(y_0, r_x, y)$, right column: $-R_{vu}(y_0, r_x, y)$. The dotted lines represent the wall-normal distance y_0 of the reference point. Distances are non-dimensionalised with the inner length scale l_0 .

Taken together, the above observations suggest that the mechanism responsible for the drag-reduction due to small bubbles at low void fractions can be identified with a fragmentation process of the near-wall vortical structures, arguably induced by the large instantaneous bubble concentrations that are observed in the buffer region of the base flow.

References

1. A. Ferrante and S. Elghobashi, *On the physical mechanisms of drag reduction in a spatially developing turbulent boundary layer laden with microbubbles*, JFM **506** (2004)
2. T. van den Berg, D. van Gils, D. Lathrop and D. Lohse, *Drag reduction in bubbly Taylor-Couette turbulence*, PRL **98**, 084501 (2007)
3. M. Miozzi, B. Jacob, A. Olivieri, *Performances of feature tracking in turbulent boundary layer investigation* Exp. Fluids **45**:765-780 (2008)

Budgets of polymer free energy in homogeneous turbulence

E. De Angelis, C.M. Casciola, and R. Piva

DIEM, Università di Bologna, 47100 Forlì, Italy
Dipartimento di Meccanica e Aeronautica, Università di Roma La Sapienza, 00184
Roma, Italy
e.deangelis@unibo.it

Turbulence in dilute polymer solutions has gained more and more interest over the last decades. Original studies were mainly oriented to drag reduction observed in wall bounded flows, however, recently studies have moved from applied problems to a more fundamental approach. In details a renewed interest has been devoted to problems different from bounded flows such as jets or basically homogeneous flows. On the other hand from a theoretical viewpoint some relevant development have appeared. In this contribution the analysis of spectral budgets of homogeneous and isotropic turbulence based on the set of equations derived in [1] is proposed. The study is performed on low-Reynolds number numerical results obtained for a dilute polymer solution in the mild stretch regime.

1 Mathematical formulation and results

Under mild stretching, the dynamics of the ensemble of polymers is described by the linear and homogeneous equation for the conformation tensor, \mathbf{R} , [1]

$$\frac{\partial \mathbf{R}}{\partial t} + \mathbf{u} \cdot \nabla \mathbf{R} = \mathbf{K} \mathbf{R} + \mathbf{R} \mathbf{K}^\dagger - \frac{2}{\tau} \mathbf{R}, \quad (1)$$

accounting for advection, stretching, re-orientation and linear elastic restoring force. As follows from its physical meaning, the conformation tensor must be a symmetric positive definite second order tensor. It can be factorized in terms of \mathbf{X} , the matrix of the right-eigenvectors, and $\mathbf{\Lambda}$, the diagonal matrix of the eigenvalues, as $\mathbf{R} = \mathbf{X} \mathbf{\Lambda} \mathbf{X}^\dagger$. As such, its square root, i.e. the tensor \mathbf{Q} such that $\mathbf{R} = \mathbf{Q} \mathbf{Q}^\dagger$ with $\mathbf{Q} = \mathbf{X} \sqrt{\mathbf{\Lambda}}$ exists and obeys the evolution equation

$$\frac{\partial \mathbf{Q}}{\partial t} + \mathbf{u} \cdot \nabla \mathbf{Q} = \mathbf{K} \mathbf{Q} - \frac{1}{\tau} \mathbf{Q}. \quad (2)$$

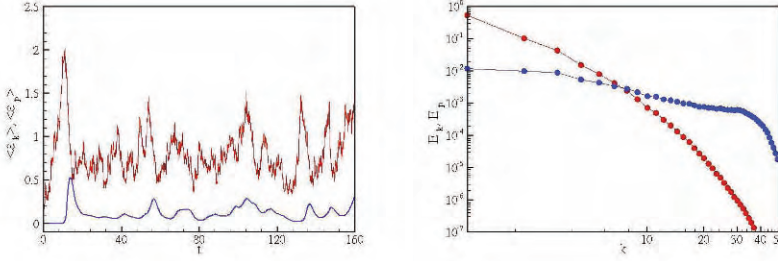


Fig. 1. Left: History of the two components of the energy, due to the solvent (red line) and to the microstructure (blue) respectively. Right: Spectra of the kinetic energy (red) and of the polymer free energy (blue).

It is straightforward to show that $\nabla \cdot \mathbf{Q}^\dagger$ (in Cartesian components $\partial Q_{ji}/\partial x_j$) tends exponentially to zero with a time constant given by τ . On the contrary, $\nabla \cdot \mathbf{Q}$ (in Cartesian components $\partial Q_{ij}/\partial x_j$) is not zero and is not conserved by the evolution implied by equation (2). In this framework, the elastic energy can be expressed as a quadratic form in terms of \mathbf{Q} , $\mathcal{E}_p(\mathbf{x}, t) := \nu_p/\tau \text{tr} [\mathbf{Q}(\mathbf{x}, t)\mathbf{Q}^\dagger(\mathbf{x}, t)]$ while the production term can be written as $\Pi_p(\mathbf{x}, t) = 2\nu_p/\tau \text{tr} [\mathbf{K}(\mathbf{x}, t)\mathbf{Q}(\mathbf{x}, t)\mathbf{Q}^\dagger(\mathbf{x}, t)]$. In other words the adoption of \mathbf{Q} as descriptor for the polymers allows the physical energy to be expressed as the natural L^2 -norm of the relevant field hence under the assumption of homogeneity, the averaged energy equation for the polymers takes the form

$$\frac{d\langle \mathcal{E}_p \rangle(t)}{dt} = \langle \Pi_p \rangle(t) - \frac{2}{\tau} \langle \mathcal{E}_p \rangle(t). \quad (3)$$

For the velocity, the average kinetic energy density, $\langle \mathcal{E}_k \rangle(t) = 1/2 \langle \mathbf{u} \cdot \mathbf{u} \rangle(t)$, follows a balance equation which for homogeneous fields reduces to

$$\frac{d\langle \mathcal{E}_k \rangle(t)}{dt} = \langle W \rangle(t) - \langle \epsilon_N \rangle(t) - \langle \Pi_N \rangle(t). \quad (4)$$

Homogeneous and isotropic turbulence has been simulated via a spectral code on 96^3 grid points for the dealiasing procedure and the time history of the two energy components is shown in the left panel of figure 1. The corresponding Newtonian simulation, i.e. with equivalent viscosity and energy input, was characterised by a $Re_\lambda = 80$ and the Deborah number based on the Newtonian Kolmogorov time scale is equal to 5.

The L^2 formulation previously discussed entails the spectral decomposition of the elastic energy. Actually, for a homogeneous field, the three-dimensional spectrum of elastic energy may be defined from the correlation tensor of the field \mathbf{Q} , $\mathbf{C}_p(\mathbf{r}, t) := \langle \mathbf{Q}(\mathbf{x}, t)\mathbf{Q}^\dagger(\mathbf{x} + \mathbf{r}, t) \rangle$, as

$$E_p^{(3D)}(\mathbf{k}, t) = \frac{1}{(2\pi)^3} \frac{\nu_p}{\tau} \int_{\mathbf{R}^3} \text{tr} [\mathbf{C}_p(\mathbf{r}, t)] e^{j\mathbf{k} \cdot \mathbf{r}} d^3 \mathbf{r} \quad (5)$$

where \mathbf{k} denotes the wave-vector which implies the related spectral decomposition of the elastic energy

$$\langle \mathcal{E}_p(t) \rangle = \int_{\mathbb{R}^3} E_p^{(3D)}(\mathbf{k}, t) d^3\mathbf{k} = \int_0^\infty E_p(k, t) dk . \quad (6)$$

where the spectrum of elastic energy is defined, as usual, as an integral on the solid angle Ω of $E^{(3D)}$. The corresponding evolution equation is obtained by the product of the Fourier transform of equation (2) with the conjugate transpose of the Fourier transform of \mathbf{Q} and reads

$$\frac{d}{dt} E_p(k, t) = H_{c_p}(k, t) + H_{s_p}(k, t) - \frac{2}{\tau} E_p(k, t) , \quad (7)$$

where H_{c_p} and H_{s_p} come from the convective term, $\mathbf{u} \cdot \nabla \mathbf{Q}$, and the stretching term, $\mathbf{K} \mathbf{Q}$, in equation (2), respectively. Equation (7) determines the elastic energy at wavenumber k as the result of the balance of feeding from the stretching term, redistribution due to convection and viscoelastic dissipation.

Regarding equation (7), the contribution, H_{c_p} , whose integral over k vanishes, has the meaning of a redistribution of spectral energy among different spectral bands with no net increase or decrease in the overall energy content. On the contrary, the stretching term H_{s_p} represents a net injection of energy into the polymeric sub-structure. For a statistically steady state (7) yields the equation

$$\int_0^\infty H_{s_p}(k) dk = \frac{2}{\tau} \int_0^\infty E_p(k) dk \geq 0 . \quad (8)$$

For the macroscopic field the evolution equation for the spectrum

$$\frac{d}{dt} E_k(k, t) = H_{c_k}(k, t) + H_{s_k}(k, t) - 2\nu k^2 E_k(k, t) + F(k, t) , \quad (9)$$

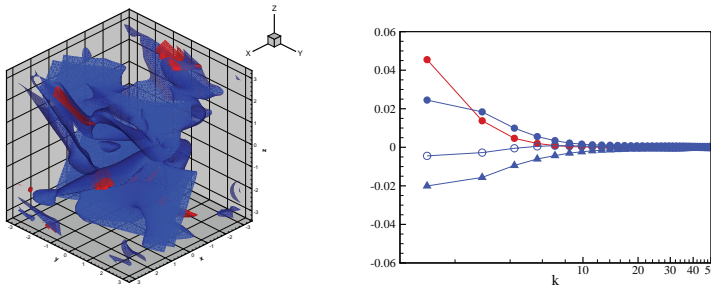


Fig. 2. Left: Three-dimensional plot of the two components of the dissipation, due to the solvent (red line) and to the microstructure (blue) respectively. Right: Spectral balance of the polymer free energy (blue curves), filled circles represent the stretching term H_{s_p} , the empty circles the convective term H_{c_p} and the triangles the dissipation. Superimposed is the stretching term K_{s_k} of the kinetic energy (red).

where F is the energy input from the external forcing \mathbf{f} . As in standard Newtonian turbulence, the net contribution over the entire spectrum of the convective term vanishes, leading to the following balance for the steady state

$$-\int_0^\infty H_{\text{sk}}(k) dk + 2\nu \int_0^\infty k^2 E_k(k, t) dk = \int_0^\infty F(k) dk \geq 0. \quad (10)$$

The definitions of the two spectra allow for a comparison of the energy content of the macro and microstructure at the different wavenumbers, see right panel of figure 2 a crossover identifies the wavenumbers where most of the energy is in the polymers. According to a standard argument, [4], the range of scales where the polymers can be stretched by the turbulence, hence where most of the energy should be, is confined below the scale $r_L = \sqrt{\langle \epsilon_T \rangle \tau^3}$. In the present simulation $r_L = 0.41$ and this value is consistent with the range of scales by the comparison of the spectra. In conditions such that $k_F \ll k_L \ll k_\eta$, one should expect a classical inertial range, with no polymer effect in the range $k_F \ll k \ll k_L$ where the energy flux is constant and given by the input power $\langle W \rangle = \langle \epsilon_T \rangle$. Below, one should observe a mixed inertial-elastic range, where the total energy flux is progressively reduced by the local dissipation of the polymers, see left panel of figure 2 for a three-dimensional plot. Equations (8) and (10) coincide with equations (3) and (4), respectively, consistently with the fact that

$$-\int_0^\infty H_{\text{sk}}(k) dk = \int_0^\infty H_{\text{sp}}(k) dk. \quad (11)$$

It should be stressed that, for each k , $-H_{\text{sk}}(k) \neq H_{\text{sp}}(k)$, as shown by the left panel of figure 2, even if for a steady state, the energy removed from the kinetic field by the polymers is positive and exactly the same amount of energy feeds the micro-structure, as shown by equation (11). However, this process is *not* occurring scale-by-scale, as already argued in [1].

More sophisticated analysis are hindered by the limited Reynolds number of the present data. Though further simulations are certainly needed in order to better exploit the capability of the proposed L^2 decomposition, we are confident that the present results corroborates the idea that the present scale by scale analysis provides an fundamental tool to study the energy transfer in dilute polymer solutions.

References

1. C.M. Casciola, E. De Angelis, Journal of Fluid Mechanics, **581**, 419 (2007).
2. E. De Angelis, C.M. Casciola, R. Benzi, R. Piva, Journal of Fluid Mechanics, **531**, 1 (2005).
3. R. Piva, C.M. Casciola, E. De Angelis, Proceedings of the XI European Turbulence Conference, Porto (2007).
4. J.L. Lumley, Annual Review of Fluid Mechanics, **1**, (1969).

Shear-induced self-diffusion in a Couette flow of a dilute suspension

E. S. Asmolov

Aero-Hydrodynamic Institute, Zhukovsky, Moscow region, 140180, Russia
aes@an.aerocentr.msk.su

Non-Brownian particles migrate randomly across the streamlines of a carrier flow in sheared suspensions at small Reynolds numbers. A random motion is very similar to that in turbulent flows but result not from a flow instability but from the hydrodynamic interactions of particles. It is characterized by the coefficient of particle self-diffusion D_s . Several mechanisms of diffusivity in dilute suspensions based on the interactions of two isolated particles were considered [1],[2]. The model of interactions of rough spheres [1] gives correct linear dependence of D_s on particle volume fraction ϕ . However, the experimental value of the diffusivity [3] is an order of magnitude greater than the theoretical predictions. Another mechanism of the diffusivity was proposed [2] for a wall-bounded shear flow. Two particles do not pass each other in such a configuration but exchange their positions in the normal direction. Swapping trajectories result in a particle cross-stream migration.

A new mechanism of the self-diffusion due to far-field collective hydrodynamic interactions in a wall-bounded shear flow has been studied very recently [4]. The motion of identical particles in a 3D rectangular Couette cell is simulated. The particle radius, $a = 0.025W$, where W is the separation between the walls, corresponds to the experimental value [3]. Large-scale particle density fluctuations induce fluid velocity disturbances with the lengthscale compared to W . Flow disturbances are due to particles freely rotating in a shear flow which are approximated at large distances by symmetric force dipoles. A point-particle approach neglecting short-range interactions appears suitable for large dilute systems. The boundary conditions are the no-slip conditions on the cell walls, and the periodic boundary conditions in the directions of the undisturbed velocity x and vorticity z . The solution of the Stokes equations for the disturbance flow in a confined geometry is obtained in terms of Fourier series. The particle velocities in a dilute suspension are the sum of the undisturbed velocity $y\mathbf{e}_x$ and the large-scale disturbances.

Both passing and swapping trajectories are obtained within the dipole approach depending on the initial cross-stream separation of the pair. Figure 1 shows the swapping trajectories of an isolated pair (dashed lines) relative to a

midpoint in the (x, y) – plane. The cell sizes are $L_x = L_z = 2W$. The particles start at points A and B , approach each other initially, then move across the streamlines, reverse their directions and separate without passing each other. The particle separation and distances to the walls remain always large compared to a , so the effect is due to large-scale velocity disturbances. In the periodic simulation cell, the swapping trajectories are close. Positions of the pair exchange back again because of interaction with periodically replicated opposite particles.

In dilute suspensions even close pairs experience effect of other particles. We seed randomly all particles except A and B over the cell at $t = 0$ with $\phi = 0.01$. Figure 1 illustrates the effect of other particles on the trajectories of A and B (solid lines). The dimensionless time required for the isolated pair to interact and move across the streamlines on the swapping trajectory is long, $t_{\text{swap}} = O(100\gamma^{-1})$, where γ is the shear rate, while the correlation time for large-scale concentration and velocity fluctuations is much shorter, $t_{\text{corr}} = O(\gamma^{-1})$. Multiple particle interactions lead to a loss in memory of a relative pair position during t_{corr} . Thus the cross-stream random migrations are due to large-scale fluctuations rather than to swapping trajectories.

The same conclusion follows from the behavior of the mean-square displacement curves for a homogeneous initial particle distribution. The curve is quadratic in time initially and shows the linear behavior corresponding to the diffusive regime after t_{corr} . The self-diffusivity is evaluated as the time rate of change of half the mean-square displacements,

$$D_s = \frac{1}{2} \frac{d}{dt} \langle \Delta y \Delta y \rangle. \quad (1)$$

The simulation time is usually $t_{\text{run}} = 400\gamma^{-1}$. The self-diffusivity is evaluated from (1) using the linear best-fits of the displacement curves. The diffusivity is evaluated as a function of initial particle positions y_{p0} by collecting statistics over particles in the slices $y_0 - h < y_{p0} < y_0 + h$, $h = 0.05W$, and by averaging over 30 runs. Figure 2 shows $D_s(y_0)$ for homogeneous suspension (solid lines). The diffusivity is maximum at the distances $0.3W$ from the walls. It is small for particles close to the walls because of the no-slip conditions for fluid velocity disturbances. In the middle part, $0.4W < y_0 < 0.6W$, it is less and close to the experimental one [3].

The diffusivity is linear in the shear rate γ . It is evaluated for different particle volume fraction ϕ . Figure 3 shows the calculated values (symbols) and the linear best fit (line). Thus D_s is linear in ϕ , in agreement with the experimental data [3]. The linear dependence can be explained within the fluctuation mechanism of the diffusivity following to the speculations for a sedimenting suspension [5]. The number fluctuations Δn for particles distributed randomly are $O(N^{1/2})$. As a result one has $D_s \propto \langle u^2 \rangle \propto \langle \Delta n^2 \rangle \propto N \propto \phi$.

Large-scale concentration inhomogeneities can be enlarged artificially. 5% of the total particle number is seeded randomly into the middle part, $W/3 < y_{p0} < 2W/3$, and the remaining particles uniformly over the whole cell. The

diffusivity (dashed lines in Fig. 2) increases significantly near the walls, i.e., far from the density inhomogeneity. These results also support the conclusion that the diffusivity in dilute suspensions is due to large-scale fluctuations rather than swapping-trajectories mechanism.

The research was supported by Russian Foundation for Basic Research (Grant No. 09-01-00335).

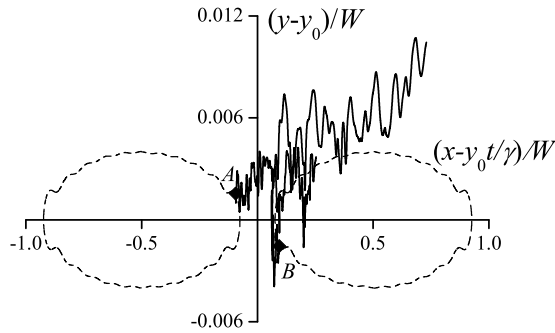


Fig. 1. Effect of other particles on reversing pair trajectories.

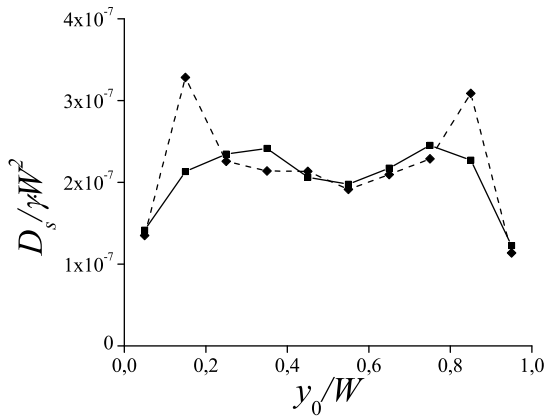


Fig. 2. Particle diffusivity across the cell width.

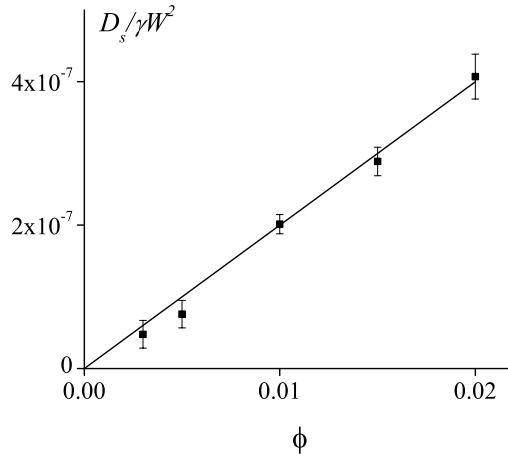


Fig. 3. Self-diffusivity as a function of particle volume fraction

References

1. F. R. Da Cunha and E. J. Hinch, *J. Fluid Mech.*, **309** 211, (1996).
2. M. Zurita-Gotor, J. Blawdziewicz, and E. Wajnryb, *J. Fluid Mech.*, **592** 447, (2007).
3. I. E. Zarraga and D. T. Leighton, *Phys. Fluids*, **14** 2194, (2002).
4. E. S. Asmolov, *Phys. Rev. E*, **77** 66312, (2008).
5. R. E. Caflisch and J. H. C. Luke, *Phys. Fluids*, **28** 759, (1985).

Part VI Atmospheric turbulence

Turbulent flow over rough walls

Ian P. Castro

School of Engineering Sciences, University of Southampton, Highfield,
Southampton SO17 1BJ

`i.castro@soton.ac.uk`

Summary. The nature of turbulent boundary layer flow over rough walls is discussed, with emphasis on the issues of zero-plane displacement, turbulence characteristics and how the latter may depend on roughness height and morphology.

1 Introduction

Despite the substantial literature on rough-wall boundary layers there remain many questions concerning their character, even in situations of zero pressure gradient. The classical assumption (usually attributed to Townsend [14]) is that sufficiently small roughness merely changes the surface stress, without altering the dynamics of the turbulence in either the inertial (log-law) region or the outer layer. Small roughness here means small h/δ – the ratio of mean roughness height to boundary layer depth. There is plenty of evidence that this is a reasonable assumption. For example, in reviewing a large body of data Jiménez [8] concluded that sufficiently small roughness means $h/\delta < \approx 3\%$. However, this view is not held universally and there is evidence that for certain types of roughness, even for those satisfying this height criterion, the measurable effects of the roughness on the turbulence structure extend into the outer flow (e.g. [10]). Of course, once h/δ becomes sufficiently large, the Townsend assumption must inevitably fail. But what is ‘sufficiently large’? And does universality fail first in the turbulence structure and only later in the mean flow behaviour? And when it does, how does the turbulence structure throughout the flow differ from smooth-wall behaviour and are the differences dependent on the precise morphology of the roughness?

Anticipating an earlier departure from universality in the turbulence than in the mean flow is at least plausible and we have already shown that, in fact, mean flow universality is surprisingly robust to increasing h/δ , certainly to beyond the point where there are structural changes in the turbulence ([1]). In that work, it was shown that mean flow correlations calculated on the basis of the usual two-parameter family (log-law plus law-of-the-wake) appear to be adequate for any type of fully three-dimensional roughness all the way up to

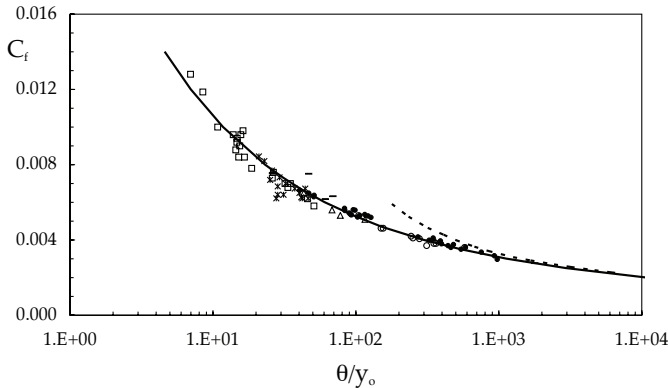


Fig. 1. Skin friction as a function of momentum thickness for fully rough, zero pressure gradient boundary layers. The heavy solid line is from classical two-parameter family analysis. Symbols refer to numerous different types of surface; dashed line is the classical smooth wall relation and the solid line is the rough wall equivalent (see text). From [1].

$h/\theta = 0.5$ (equivalently, $h/\delta < 0.2$), where θ is the usual momentum thickness. As an example, figure 1 shows the skin friction coefficient as a function of θ/y_0 which for fully aerodynamically rough surfaces replaces Re_θ as the controlling parameter. Data from a very wide range of three-dimensional roughness types are shown, compared with the implicit relation $\theta/y_0 = [(s - I)/s^2]e^{\kappa(s-K)}$, where $s = \sqrt{C_f/2}$ and $I = 7.03$, $K = -0.0542$. These numerical values follow from taking $\kappa = 0.41$ and a wake strength $\Pi = 0.7$ and the relation itself follows from the classical analysis (but in terms of θ/y_0 rather than Re_θ) and a quartic polynomial wake profile. There is no doubt that at the low end of the θ/y_0 range the turbulence structure is significantly different from that in a smooth-wall boundary layer – see §3. In this paper, the issues raised earlier, concerning how roughness affects turbulence structure, are discussed, by way of a brief consideration of some recent data from both laboratory and numerical (DNS) experiments.

First, however, we address a crucial fundamental issue that arises in analysing rough-wall data, obtained either from laboratory (or field) experiments or from numerical simulations.

2 Zero plane displacement and von Kármán's constant

With y measured upwards from zero at the (flat) surface on which the roughness elements sit, it is not obvious what value of y should be used as the ‘virtual origin’ of the flow. Expressing the usual log-law relation for a fully rough surface as $U/u_\tau = \frac{1}{\kappa} \ln \frac{y-d}{y_0}$, the zero-plane displacement, d , clearly cannot in general be zero. It has been almost universal practice to assume a classical

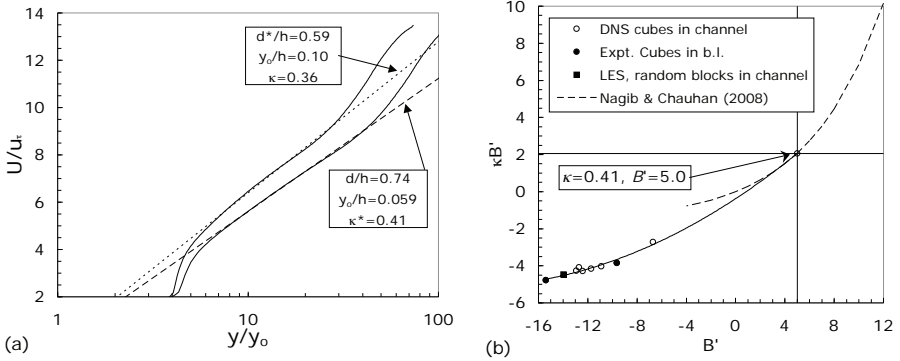


Fig. 2. (a), Velocity profile in rough-wall channel, DNS of [5]. Starred parameters in the boxes are fixed prior to fitting, which yields the other two parameters. (b), $\kappa B'$ vs. B' , the log law additive constant ($B' = B + \Delta U^+$, where Δ^+ is the usual roughness function).

value of κ (0.41, say) and deduce d by obtaining best fits to mean velocity data, ideally using an independently obtained friction velocity, u_τ , for otherwise there are too many unknowns to make the fitting process robust. This was the approach used for all the data in fig.1 and it always leads to a value of d a little below the height of the roughness, which is certainly reasonable physically. Provided the velocity at each height is a spatially averaged value, it is known that the log-law extends downwards into the roughness sublayer (where the flow is spatially inhomogeneous).

However, Jackson [7] showed that the usual derivations of the log-law imply that d is the height at which the total wall stress acts. His arguments assume that the inertial sub-layer does not depend on the detailed morphology of the surface except insofar as this determines the line of action of the drag force. As far as the author is aware, this is the only physically-based definition of d which has ever been proposed and, because it *is* physically based and is implicit in the log-law derivation, it is an appealing definition. It is only possible to determine this height unambiguously by measuring (or computing) the distribution of pressure forces acting on the roughness elements and the frictional forces acting on all surfaces. In cases of aerodynamically fully rough surfaces, where the latter are necessarily very small compared with the former (so that viscosity is not important), there have been a few attempts to measure (or compute) the pressure drag and thus deduce τ_w and d directly. These always lead to a value of d rather smaller than obtained by assuming $\kappa = 0.41$ and using a profile fitting process (e.g. [2, 9]). Consequently, mean velocity data can only be well-fitted to the log-law by choosing a lower value of κ .

We illustrate this in figure 2, which shows a spatially-averaged mean velocity profile obtained from well-resolved direct numerical simulations of a rough-wall channel flow. The rough surface comprised a staggered array of

cubes, height $h = H/16$ where H is the channel depth, and the mesh had grid lengths of $h/100$ over the cube height and over 35 million nodes in all. Reynolds numbers based on the roughness height and the bulk velocity or the friction velocity were about 7000 and 600, respectively. Full details are described in [11]. Two profile fits are shown in fig.2a, obtained either by fixing $\kappa = 0.41$ and choosing d to give the correct slope or by fixing d (obtained using the computed pressure and frictional forces) and choosing κ to give the best fit to a line of the correct slope. Note that in this channel flow case, u_τ is known independently because the total wall stress must balance the applied axial pressure gradient. There is little to choose between the two alternatives in terms of the adequacy of the profile fit. Figure 2b follows Nagib & Chauhan [12], who plotted the two log law coefficients (κ and the additive constant, B appropriate for the smooth log law) in a form which would yield a straight line if κ were a unique value. They used smooth-wall data from a wide variety of high Reynolds number flows including boundary layers with favourable or adverse pressure gradients. (Recall that the log law derivation requires sufficiently high Re.) Data from [11], LES and wind tunnel experiments for similar (rectangular block) surfaces are all seen to follow a reasonable extension of the Nagib & Chauhan fit, at least for the data which do not extend too far into the adverse pressure gradient region (for which $B' < \approx 0$).

One must conclude that either the appealing, physically based definition of zero-plane displacement is incorrect (for the rough-wall cases), or the Reynolds numbers for all these data are too low, or κ is not universal across different flow types and wall conditions. Spalart [13] has argued that to claim the latter amounts to ‘a frontal attack on the log law, not simply a refinement of it’; one therefore hesitates to accept it. Nagib & Chauhan, on the other hand, do not believe that a unique value of κ can be found for high-Re wall-bounded turbulent flows. As illustrated here, rough-wall data seem to be consistent with that statement, unless one forces a classical κ and allows d to ‘float’ appropriately. It is worth noting that the value of κ generally accepted by the meteorological community (atmospheric boundary layers are almost always fully rough) is significantly lower than 0.41 and there is evidence that for large roughness, where d certainly matters (e.g. urban situations), κ might even be as low as 0.35 [6]. No conclusion is offered here, except to say that, for significantly rough surfaces, if one rejects the notion that d is the effective height at which the surface drag acts, one would like an alternative physically sound definition; otherwise there is no hope of ever determining κ from either experiments or computations. Of course, another interpretation for d is certainly needed if the details of the flow in the inertial sublayer *do* depend on the surface morphology (contrary to Townsend’s and Jackson’s assumptions).

3 The near-wall turbulence

In the case of large enough h/δ , but not so large that the inertial sublayer ceases to exist, it seems intuitively likely, or at least possible, that features

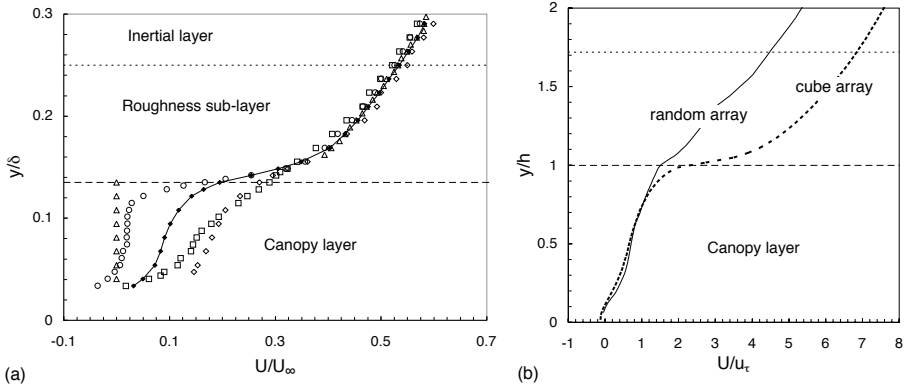


Fig. 3. (a) Velocity profiles in the wall region of a boundary layer over a staggered array of cubes, with $h/\delta \approx 0.07$; the solid line is the spatial average, other symbols are specific locations within the array and the dashed and dotted lines mark the upper boundary of the canopy and roughness sub-layers, respectively. From [2]. (b) Velocity profiles from DNS for a cube array in a channel (solid line) and LES for a random height array of blocks in a channel (dashed line), from [15]. Ratio of average roughness height h to channel half-height is 0.125 (cubes) and 0.1 (random blocks); the dotted line marks the height of the tallest element in the random array case. Note the different normalisations in the two figures.

of the flow in the sublayer and perhaps too the inertial layer *will* depend on the particular details of the roughness. There have been numerous studies of turbulence over plant canopies and, more recently, urban-like canopies. It has become evident that the qualitative features of these flows are much like those in the near-wall region of smooth-wall boundary layers. The flow is characterised by the presence of longitudinally-elongated low-speed streaks and corresponding shorter streamwise vortices, developing as ‘packet’ structures (e.g. [16] in the context of smooth walls, and [9] and [3] for flows over cube arrays). Flows over closely-packed plant canopies tend to be a little different, showing ‘large roller and rib’ structures similar to those typical of mixing layers. Finnigan [5] has argued that this is because, like classical mixing layers, the mean velocity profile has a strong inflection point around the top of the canopy, creating a rather different instability mechanism than would otherwise occur. But other types of surface (like arrays of sharp-edged rectangular blocks) also have a spatially averaged mean velocity profile which contains an inflection point, as illustrated in Figure 3. Similar results have been obtained from DNS and LES experiments on flows over both cube arrays and arrays of random height blocks ([3, 15]), although it is very noticeable that the strong velocity gradient evident over uniform arrays is very much weaker over the random-height roughness, as is clear from fig.3b.

Despite the qualitative structural similarities with the smooth wall case, at least for some kinds of rough surface, it is clear that there are quantitative

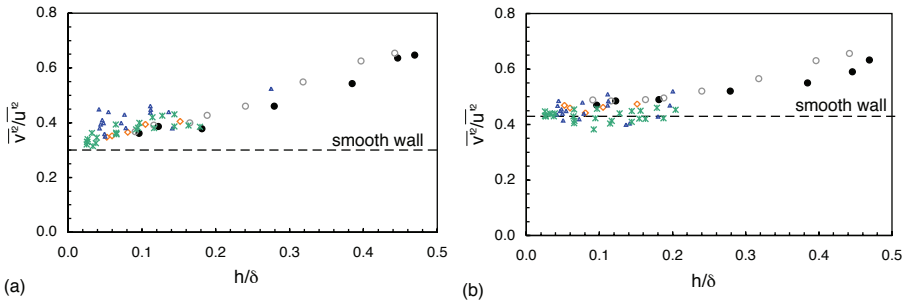


Fig. 4. Ratio of normal to axial Reynolds stress at $y/\Delta = 0.04$ (a) and 0.15 (b). Different symbols refer to different types of three-dimensional roughness, from expanded mesh to arrays of cubes and arrays of random height elements; $600 < Re_\theta < 10,000$.

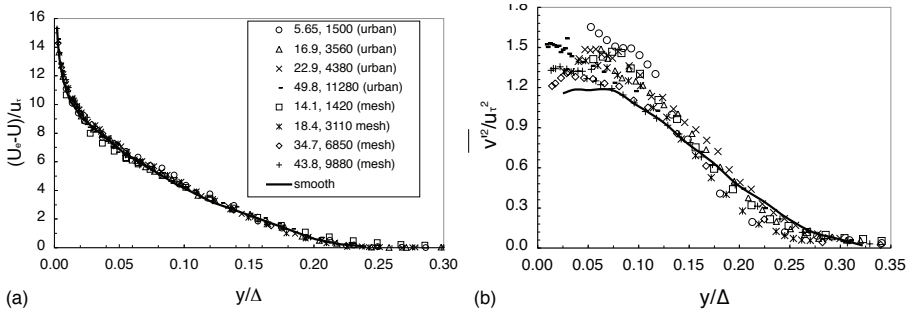


Fig. 5. (a) Velocity deficit profiles for mesh and random roughness, $0.025 < h/\delta < 0.3$; (b) corresponding normal Reynolds stress profiles. Solid line in both figures is smooth wall data [4]. Legend figures refer to values of δ/h and Re_θ .

differences in Reynolds stresses and, indeed, some of the averaged structural parameters. And these differences can extend to the outer flow even for relatively small h/δ . Figure 4 shows the ratio of wall-normal to axial Reynolds stresses, v^2/u^2 . Data from numerous different experiments, over various kinds of (three-dimensional) roughness are shown. Note that in this and subsequent figures, y and δ have been reduced by d in all cases. The results are plotted *vs.* h/δ for two different locations in the boundary layer, denoted by $y/\Delta = 0.04$ (fig.4a) and 0.15 (fig.4b), where Δ is the usual Clauser thickness. At both locations there is a noticeable rise in v^2/u^2 with increasing roughness height relative to boundary layer depth. At the near-wall location (fig.4a) this rise appears to begin even for very small roughness, whereas in the outer flow it is not really noticeable above the experimental scatter until h/δ exceeds about 0.15 . The implication is that turbulence structural changes occur first (not surprisingly) near the surface, but extend gradually into the outer flow as relative roughness height increases. For h/δ below a few percent, any changes in v^2/u^2 in the outer flow are only marginal.

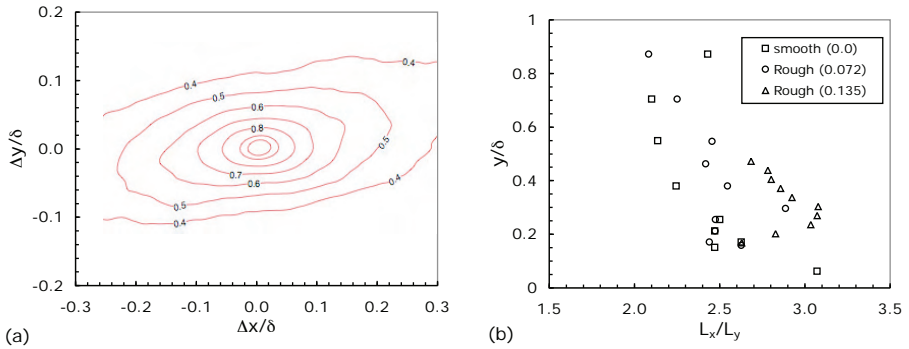


Fig. 6. (a) Contours of constant $R_{uu}(\Delta x, \Delta y)$ for $y/\delta = 0.17$, from PIV measurements; (b) Ratio of length scales defined by the separation distances $(\Delta x, \Delta y)$ from the reference point to the $R_{uu} = 0.5$ contour; legend shows values of h/δ .

However, Figure 5 suggests that even for $h/\delta = 0.025$, the wall-normal stress is still significantly higher than typical smooth-wall values for $y/\delta < 0.25$. The figure shows deficit mean velocity profiles (fig.5a) and profiles of $\overline{v'^2}/u_\tau^2$ (fig.5b) for two kinds of surface – a hexagonal wire mesh and an array of blocks of square plan section but random heights (and 25% plan area density). In all cases, even for $h/\delta = 0.3$, there is good universality in the mean flow but clear differences in the stress profiles. Note that the mesh roughness with $h/\delta = 1/43.8 = 0.023$ and the urban roughness with $h/\delta = 1/49.8 = 0.02$ both show elevated values of wall-normal stress over almost the entire lower quarter of the boundary layer ($y/\Delta < 0.07$), and even more in the urban case.

It would seem very unlikely that stress ratios could be affected by wall roughness without at least some changes to the quantitative details of the turbulence structure. Figure 6 shows that differences do indeed exist. PIV data have been obtained in a smooth-wall boundary layer ($Re_\theta \approx 5,500$) and two rough wall flows with different h/δ (0.072 and 0.135). A typical spatial correlation map of the axial velocity component, with the reference ‘probe’ at $y/\delta = 0.17$, is shown in Fig.6a (for the smooth wall case). Similar data were obtained for a set of y/δ heights in all three flows and a resulting measure of the average eddy shape is shown in fig.6b. L_x/L_y (defined in the caption) is close to the ratio of the major and minor axes of the roughly elliptical (and inclined) $R_{uu} = 0.5$ contour. As h/δ increases it is clear that the average eddy becomes more elongated and that this difference extends throughout at least half of the flow.

4 Conclusions

Whilst universality of mean velocity profiles in rough wall boundary layers appears to be maintained up to surprisingly large roughness to boundary layer height ratios (h/δ), evidence is accumulating that the turbulence character-

istics can be noticeably affected by roughness throughout the entire depth of the flow at much smaller h/δ . There is some evidence that for a specific h/δ the extent of the roughness influence is dependent on roughness morphology. A physically plausible definition of zero-plane displacement for very rough surfaces suggests, like recent high- Re_θ smooth-wall flow data, that von Kármán's coefficient varies with flow type. More work is needed to clarify the precise nature of the roughness influences. In particular, the dynamics of the near wall structures would be a fruitful area of study.

This work would not have been possible without significant input from a number of the author's colleagues at Southampton and elsewhere, not least Drs. Amir, Cheng, Reynolds and Leonardi, all of whom are gratefully acknowledged.

References

1. I.P. Castro, Rough-wall boundary layers: mean flow universality, *J. Fluid Mech.*, **585**, 469–485, 2007.
2. H. Cheng & I.P. Castro, Near-wall flow over urban-like obstacles, *Bound. Layer Meteorol.*, **104**, 229–259, 2002
3. O. Coceal, A. Dobre, T.G. Thomas, & S.E. Belcher, Structure of turbulent flow over regular arrays of cubical roughness, *J. Fluid Mech.*, **589**, 375–409, 2007.
4. H.H. Fernholz & P.J. Finley, The incompressible zero-pressure-gradient turbulent boundary layer: an assessment of the data, *Prog. Aero. Sci.*, **32**, 245–311, 1996.
5. J. Finnigan, Turbulence in plant canopies, *Ann. Rev. Fluid Mech.*, **32**, 519–571.
6. P. Frenzel & C.A. Vogel, On the magnitude of the apparent range of variation of the von Kármán constant in the atmospheric surface layer, *Bound. Layer Meteorol.*, **72**, 371–395, 1995.
7. P.S. Jackson, On the displacement height in the logarithmic profile, *J. Fluid Mec.*, **111**, 15–25, 1981.
8. J. Jiménez, Turbulent flow over rough walls, *Ann. Rev. Fluid Mech.*, **36**, 173–196, 2004
9. M. Kanda, R. Moriwaki & F. Kasamatsu, Large-eddy simulation of turbulent organised structures within and above explicitly resolved cube arrays, *Bound. Layer Meteorol.* **112**, 343–368, 2004.
10. P.-A. Krogstad and R.A. Antonia, Comparison between Rough- and Smooth-wall Turbulent Boundary Layers, *J. Fluid Mech*, **245**, 2008.
11. S. Leonardi & I.P. Castro, Turbulent flow over urban canopies, AIAA Paper, June 2008.
12. H.M. Nagib & K.A. Chauhan, Variations of von Kármán coefficient in canonical flows, *Phys. Fluids*, **20**, 101518, 2008.
13. P. Spalart, private communication, 2009.
14. A.A. Townsend, *The Structure of Turbulent Shear Flow*, Cambridge University Press, Cambridge 1976.
15. Z.-T. Xie, O. Coceal & I.P. Castro, Large-eddy simulation of flows over random urban-like obstacles, *Bound. Layer Meteorol.*, **129**, 1–23, 2008.
16. J. Zhou, R.J. Adrian, S. Balachandra & T. Kendall, Mechanisms for generating coherent packets of hairpin vortices in channel flow, *J. Fluid Mech.*, **387**, 353–396, 2004.

Top-down and bottom-up eddy motion in wall bounded turbulence

P. Carlotti¹, F. Laadhari²

(1) Université Paris est, Centre Scientifique et Technique du Bâtiment, Champs sur Marne, France

(2) Université Claude Bernard, Lyon, France

Pierre.Carlotti@cstb.fr

Many people argue that turbulence structure in a turbulent boundary layer is dominated by motion created by viscous instabilities in the near-wall region (see [4] and references quoted there). This analysis is based on observations made for a smooth wall up to height of order $50 y^+$, and generalised to rough walls. This is what is called the bottom-up theory of turbulent boundary layers.

On the other hand, other people think that the turbulence characteristics in the boundary layer are dominated by the way eddies coming from a higher layer are distorted when impinging onto the ground, in a top-down manner. It is mainly supported by people coming from the meteorological community and practitioners, who are influenced by the way wind patterns evolves on the sea surface or on agricultural fields (so called "cat-paws"), see [5], and by work on very high Reynolds number rough boundary layers, with typical viscous height $\nu/u_* \approx 10^{-4}$ m, roughness height from 0.1 to 10 m, and measurement height from 10 to 100 m.

It should be stressed that Taylor's frozen eddy hypothesis (see [7], and also [1]) relies on the assumption that turbulent eddies, being carried by the mean flow, are neither top-down nor bottom up.

The target of this work is to discuss some measurable data supporting the bottom-up or the top-down theory for very high Reynolds number turbulence.

The present work compares atmospheric rough-wall boundary layers and smooth-wall boundary layers. It is therefore useful to use notations compatible with both flows. In the following, x is the streamwise direction and y the vertical direction, and y_* is defined by $y_* = \nu/u_*$ where ν is the kinematic viscosity and u_* the friction velocity.

For a smooth wall boundary layer, the velocity profile in the log layer is $U = \frac{u_*}{\kappa} \ln E y^+$ where $y^+ = y/y_*$ and $E = 8$ to 10 . For a rough wall, it is $U = \frac{u_*}{\kappa} \ln y/y_0$ where y_0 is the roughness height. Thus, the corresponding heights are y_*/E and y_0 . The following notation is therefore used in the present paper for rough wall boundary layers:

$$y^+ = \frac{y}{Ez_0}$$

As an order of magnitude, common atmospheric boundary layers correspond to $z_0 = 4$ to 10 cm, the log layer height is of order 200 m and the boundary layer height is of order 1000 m. Thus, $y^+ = 100$ corresponds to a height $y \approx 40$ to 100m.

1 Use of sweeps and ejections

Here, $(U, 0, 0)$ is the mean velocity field and (u, v, w) is the fluctuating velocity field. It is said that there is an *ejection* at (x, y, z) and at time t if $u(x, y, z, t) < 0$ and $v(x, y, z, t) > 0$. It is said that there is a *sweep* at (x, y, z) and at time t if $u(x, y, z, t) > 0$ and $v(x, y, z, t) < 0$.

Sweep and ejection always dominate the other events when velocity increases with height, $U(y) = S(y - y_1) + U(y_1)$ at least locally for $y \approx y_1$ a given height. Consider a ball of air at height y_1 at time t_0 . The velocity of this fluid element is $(U(y_1) + u, v, w)$. The fluctuations are of zero mean. At time $t + dt$, the fluid element is advected to the height $y_1 + vdt$. When dt is very small, forces did not have time to modify the velocity of the fluid element, which is still the same, while the mean velocity of fluid at the new height is now $U(y_1) + Svdt$. Therefore the new value of the fluctuation is now $(u - Sv dt, v, w)$. Therefore, if $v > 0$, the probability for a negative horizontal velocity fluctuation increased, and similarly, if $v < 0$, the probability for a positive horizontal velocity fluctuation increased. As a consequence, the probability for a sweep or an ejection to occur is larger than the probability of complementary events.

The balance of sweep and ejections was investigated by many groups. In [2], figure 10 shows that in a rough atmospheric surface layer, for $y^+ = 22, 70$ and 120, sweeps dominate ejections, thus supporting the top-down picture of boundary layer turbulence. In their figure 12, it is shown that sweeps dominate when counted as number of events, but that the contribution of ejections dominates the momentum flux.

However, the domination of sweep and/or ejection may not mean that the eddy motion is top-down or bottom-up, as the following very simplified toy-model will show. For a two-dimensionnal vortex pair impinging onto a wall, an exact solution of Euler equation can be computed with the method of images. Whatever the direction (top-down or bottom-up) of the vortex pair, the velocity field is symmetrical, and sweeps balance exactly ejections. *Therefore it is not possible to use the balance between sweeps and ejections to conclude on the top-down or bottem-up nature of the motion!* The toy-model shows that the preferential direction of movement can be seen through the identification of the double vortex, a pattern that may be qualified as 'eddy'.

2 Eddy identification with a vorticity threshold

In the turbulent general case, because of incompressibility and homogeneity on horizontal planes, the vertical volume flux is zero, i.e. $\langle w \rangle = 0$. Therefore, top-down (as the bottom-up) conceptual model cannot simply be a preferential direction of the flow. It relies on the belief that some part of the flow are more important than other, and defining this part as 'eddies'.

One option is to define 'eddies' as intense events. A good way of quantifying this is to compute $\langle w^3 \rangle$. However, in the above toy-model, $\langle w^3 \rangle = 0$ because of the symmetry of the flow, showing that this approach is not able to discriminate between top-down and bottom-up motion in this simple case.

Eddies are now defined as zones of intense vorticity $\omega = \text{curl } \underline{u}$ (note that ω is the vorticity of the velocity fluctuation field only). Define the local enstrophy $\Omega = |\underline{\omega}|^2$. The characteristic scale for vorticity is the local mean shear $S = \frac{\partial U}{\partial y}$. We shall say that vorticity is intense if the ratio of the square root of local enstrophy to local mean shear is above a threshold α , and we define a sampling conditionnal to this threshold. This allows to separate the vertical velocity field into 3 components, which can be averaged as follows:

$$0 = \langle w \rangle = \left\langle w \left| (\sqrt{\Omega} < \alpha |S|) \right. \right\rangle + \left\langle w \left| (\sqrt{\Omega} \geq \alpha |S| \text{ and } w \leq 0) \right. \right\rangle + \left\langle w \left| (\sqrt{\Omega} \geq \alpha |S| \text{ and } w > 0) \right. \right\rangle$$

For a given α , area plot are defined as follows (see figure 1):

- green colour if $\sqrt{\Omega} \leq \alpha |S|$,
- blue colour if $\sqrt{\Omega} > \alpha |S|$ and $w \leq 0$,
- red colour if $\sqrt{\Omega} > \alpha |S|$ and $w > 0$.

This shows that for heights between 20 and 100 in wall units, most of the zones of intense vorticity have a positive vertical velocity, thus not supporting the top down picture of boundary layers in terms of eddy motion. On the other hand the plot of $\langle w | (\sqrt{\Omega} \geq \alpha |S| \text{ and } w \leq 0) \rangle + \langle w | (\sqrt{\Omega} \geq \alpha |S| \text{ and } w < 0) \rangle$ as function of height which shows negative values for relevant values of α , showing that zones of high enstrophy and negative w are smaller than zones of high enstrophy and positive w , but more intense.

The present data are based on direct numerical simulations performed with a pseudo-spectral code using the Chebychev- τ formulation in the wall-normal direction y , and Fourier expansion in the streamwise x , and spanwise z , directions where periodic boundary conditions are applied. A detailed description of the numerical method is given in [3]. The simulation was carried out at a Reynolds number R_c , based on the centerline velocity and the channel half-width h , of 12580 and a friction Reynolds number $hu_*/\nu = 590$ (see [6]).

Further investigation is still necessary to close completely the issue. A lagrangian tracking of high enstrophy blobs would be necessary as a next step.

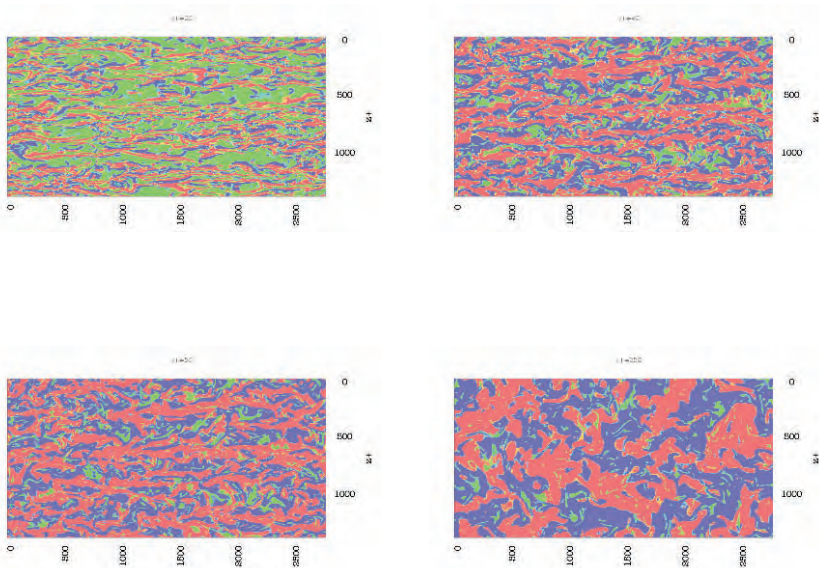


Fig. 1. For $\alpha = 1$, area plots are defined as follows defined in the text, with: top left: $y^+ = 20$; top right: $y^+ = 40$; bottom left: $y^+ = 50$; bottom right: $y^+ = 250$.

References

1. D.J.C. Dennis and T.B. Nickels On the limitations of Taylor's hypothesis in constructing long structures in a turbulent boundary layer, *Journal of Fluid Mechanics*, 614:197-206, 2008
2. Ph. Drobninski, P. Carlotti, J-L. Redelsperger, R.M. Banta, and R.K. Newson, Numerical and experimental investigation of the neutral atmospheric surface layer, *Journal of Atmospheric Sciences*, 64:137-156, 2007
3. F. S. Godeferd and L. Lollini, Direct numerical simulations of turbulence with confinement and rotation, *Journal of Fluid Mechanics*, 393, 257308 (1999).
4. P. Holmes, J.L. Lumley and G. Berkooz, *Turbulence, coherent structures, dynamical systems and symmetry*, Cambridge University Press, Cambridge 1996.
5. J.C.R. Hunt and J.M. Morrison Eddy structure in turbulent boundary layers, *Eur. J. Mech. B - Fluids*, 19, 673694, 2000
6. F. Laadhari, Reynolds number effect on the dissipation function in wall-bounded flows, *Phys. Flu.*, 19, 2007
7. A.A Townsend, *The structure of turbulent shear flow*, Cambridge University Press, Cambridge 1976

A study of turbulent Poiseuille-Ekman flow at different rotation rates using DNS

A.Mehdizadeh, and M. Oberlack

Department of Mechanical Engineering, Technische Universität Darmstadt, 64289 Darmstadt, Germany

1 Abstract

Turbulent Poiseuille-Ekman flow at different rotation rates has been investigated. A series of direct numerical simulations has been conducted at various rotation rates for Reynolds number 180 based on the friction velocity in the non-rotating case. In this paper the results of both statistical and instantaneous eddy structures are presented and discussed briefly.

2 Introduction

Rotating flows are of great importance in many engineering applications. In these flows the structure of turbulence and the mechanism of momentum transport are highly affected by additional body forces namely centrifugal and coriolis forces. The simplest wall dominated flow mode in this category is a pressure driven turbulent channel flow, with a arbitrary rotating vector, which can be decomposed into componential rotation vectors in the streamwise, the spanwise and the wall-normal directions. Among them, the spanwise and the streamwise rotating channel flows have been investigated by many authors [2], [3] and [4] to name only a few. However turbulent channel flow with wall-normal rotation has been rarely studied. Because of the important role played by Ekman type boundary layer in this flow, we shall refer to it as Poiseuille-Ekman flow. Since there is no possible experimental approach to investigation of these flows, direct numerical simulation (DNS) is the only available method to examine them. A series of DNS of various rotation numbers is carried out to establish the effects of the rotation on the flow. In the Figure.1 the flow geometry is sketched. No slip boundary condition at both walls and periodic boundary conditions are employed in the streamwise and the spanwise direction. Note that all variables are non-dimensionalized by the friction velocity in the non-rotating case (U_{τ_0}) and the channel half height (h). For the entire analysis of the flow, only rotation rate, i.e. Ω_2 or alternatively

$Ro = \frac{2\Omega_2 h}{U_{\tau_0}}$, is to be varied. The Reynolds number, $Re_{\tau_0} = \frac{U_{\tau_0} h}{\nu}$ based on the friction velocity in non rotating case is kept constant.

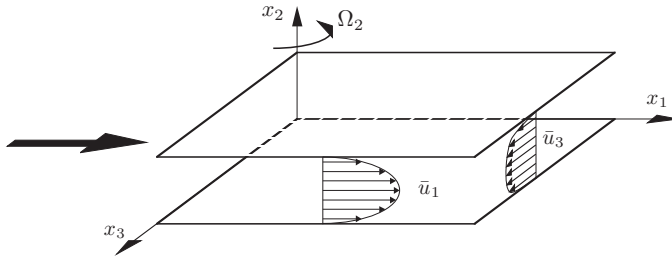


Fig. 1. Sketch of the geometry of Poiseuille-Ekman flow

3 DNS of turbulent Poiseuille-Ekman flow

The numerical technique presently employed is a standard spectral method with Fourier decomposition in the streamwise and the spanwise directions and Chebyshev decomposition in the wall-normal direction. The numerical code for channel flow was developed at KTH/Stockholm [7]. Additional features such as wall-normal rotation have been added during the project. Seven simulations have been conducted to show the effects of the rotation on the flow. The numerical results indicate that the flow is very sensitive to the rotation. Even a very small rotation number can induce a strong secondary motion in the spanwise direction and at the same time reduce the streamwise mean velocity substantially. Due to a further increase in the rotation rate, the streamwise mean velocity monotonically decreases. In contrast the spanwise mean velocity first increases, reaches a maximum at around $Ro = 0.054$ and then monotonically decreases by further increase in the rotation rate, (Figure.2). Further increase of the rotation rate causes that the turbulent intensity to be damped and as a result, the flow reaches a quasi laminar state. The Reynolds number of this state is lower than the critical Reynolds number obtained by Hoffmann and Busse [5], using stability analysis of the flow. In this parameter region the flow exhibits different behavior in the spanwise and the streamwise directions compared to fully turbulent region. In the streamwise direction, the velocity profile reaches its maximum close to the wall and its minimum in the middle of the channel. In the spanwise direction the velocity profile develops a nearly constant region in the core of the flow. Also an inflection point in the mean velocity profiles in both directions is visible, which can be clearly observed in the streamwise velocity profiles. However the inflection points in

the spanwise velocity profiles are not as clear as the ones in the streamwise direction, (Figure.3). apart from the statistical quantities in this parameter region very elongated structures (roll vortices) are observed, which are general features of Ekman type boundary layers. Their existence based upon the theory proposed by Faller [6], and Brown [1], is due to the inflection point in the velocity profile. These structures can be seen in Figure.4. By further increasing the rotation rate ($Ro > 0.273$), turbulence disappears and the flow reaches a fully laminar state. These three state against the rotation rate have been indicated in Figure.5.

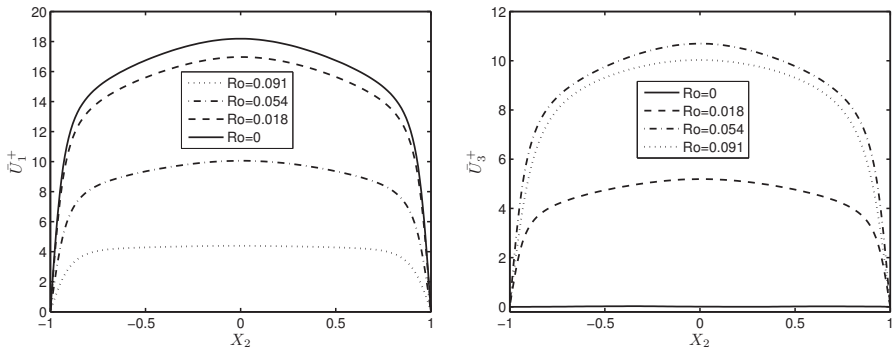


Fig. 2. Mean velocity in the streamwise (left) and in the spanwise (right) directions for different rotation numbers in the fully turbulent region.

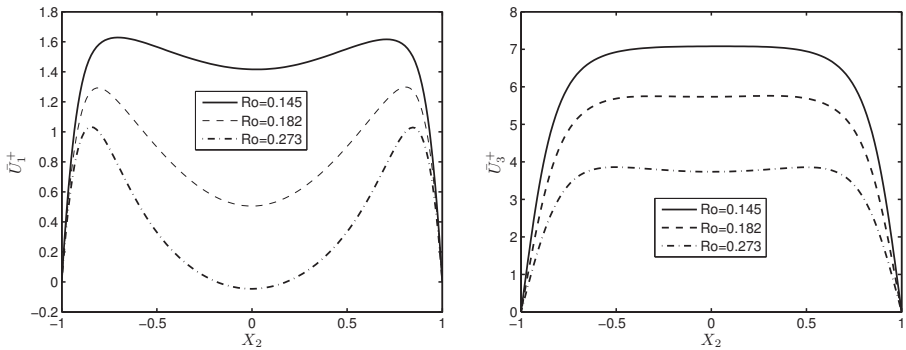


Fig. 3. Mean velocity in the streamwise (left) and in the spanwise (right) directions for different rotation numbers in the quasi laminar region.

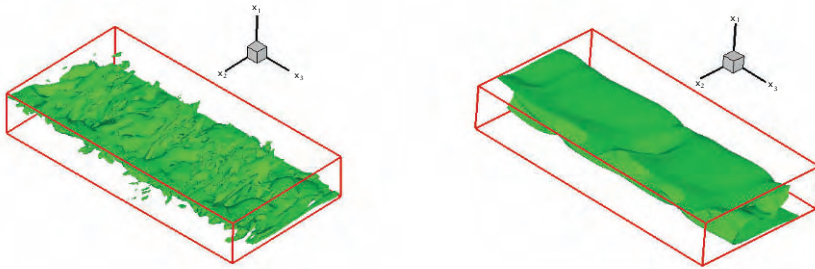


Fig. 4. Elongated coherent structures in the quasi laminar region for $Ro = 0.145$ (left) and $Ro = 0.273$ (right).

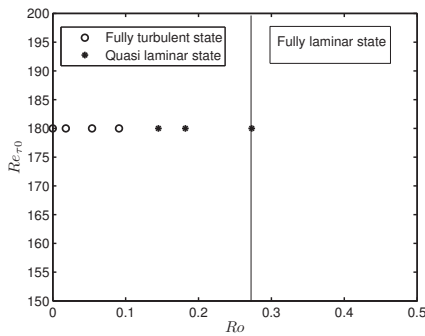


Fig. 5. Fully turbulent, quasi-laminar and fully turbulent state against the rotation number for $Re_{\tau=0} = 180$

References

1. R.A. Brown, Analytical methods in planetary boundary-layer modeling Wiley and Sons, 1974.
2. J.P. Johanson, R.M. Halleen and D. K. Lezius, J. Fluid Mech., **56**, 533 (1972).
3. O. Grundestam , S. Wallin Halleen and V. Johanson. A, J. Fluid Mech., **598**, 177 (2008).
4. M. Oberlack, W. Cabot, B.A Pettersson Reif and T. Weller., J. Fluid Mech., **562**, 383 (2006).
5. N.P. Hoffmann and F.H. Busse, Phys. Fluids ., **13**, 2735 (2001).
6. A.J. Faller , J. Atmos Sci., **22**, 176 (1965).
7. Lundbladh, A. Henningson, D. and Johanson, A, Aeronautical Research Institute of Sweden, Bromma., **FFA-TN 1992-28**, (1992).

Experimental study of forced stratified turbulence

P. Augier, P. Billant, E. Negretti and J.-M. Chomaz

LadHyX, Ecole polytechnique, 91128 Palaiseau, France
pierre.augier@ladhyx.polytechnique.fr

Recent results have shown that strongly stratified turbulence has a three dimensional dynamic instead of a quasi-two dimensional dynamic conjectured previously. The structures are strongly anisotropic with an aspect ratio scaling like the Froude number $l_v/l_h \sim F_h$ [1]. A direct cascade of energy from large scales to small scales associated with a $k_h^{-5/3}$ horizontal kinetic energy spectrum has been predicted and observed in DNS of forced stratified turbulence when the buoyancy Reynolds number \mathcal{R}^t is sufficiently large [2]. In contrast, for small \mathcal{R}^t , the flow is dominated by vertical viscous effects even if the Reynolds number is large [3, 4].

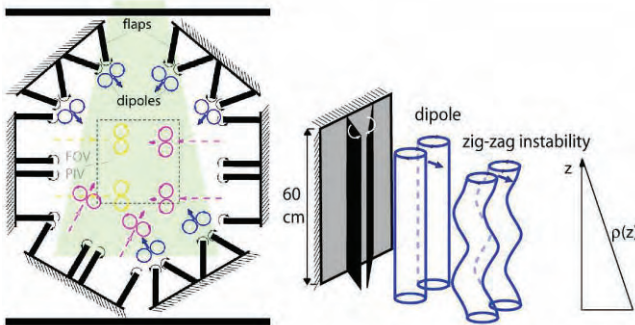


Fig. 1. Sketch of the experimental apparatus.

In order to investigate the turbulent regime experimentally with a sufficiently high buoyancy Reynolds number, we have set-up a new experiment where the flow is generated by 12 vortex generators (flaps) placed on the side of a large stratified tank (Fig. 1). Each generator produces periodically and independently a counter-rotating vertical columnar vortex pair which propagates toward the central part of the tank. The interactions between all the

randomly produced vortex pairs give rise to a forced turbulent flow with a low Froude number F_h and a large Reynolds number Re . The buoyancy Reynolds number based on the characteristics of the vortices generated by the flaps is $\mathcal{R}^s \equiv ReF_h^2 \sim 100$ while the buoyancy Reynolds number based on the injection rate of energy ϵ : $\mathcal{R}^t \equiv \epsilon/(\nu N^2)$, is order unity. As seen on figure 2, the mean kinetic energy of the flow is statistically stationary but with high fluctuations typical of turbulent flows.

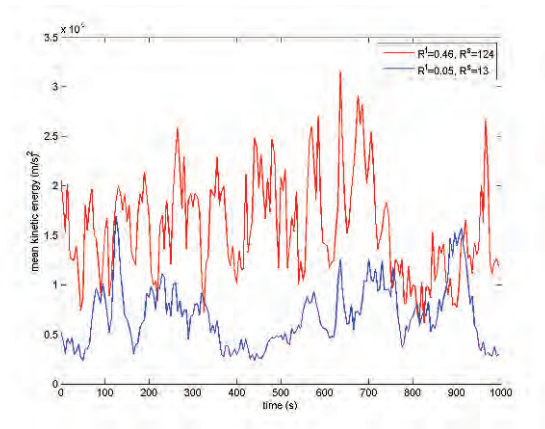


Fig. 2. Mean kinetic energy as a function of time.

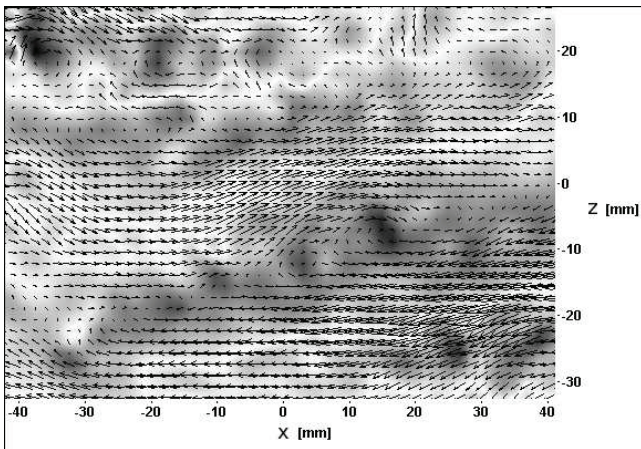


Fig. 3. Vertical cross-section of the velocity field. The background color represents the horizontal vorticity $|\omega_y|$ perpendicular to the cross-section. In heavy shaded regions, $|\omega_y| \sim N$.

PIV measurements in vertical cross-sections show that the flow is organised into horizontal layers (Fig. 3). This layering arises spontaneously via the zigzag instability of individual vortex pairs [5]. When the buoyancy Reynolds number is increased, shear instabilities and intermittent overturning become more and more visible between layers in agreement with [3, 6].

Horizontal velocity spectra exhibit a narrow $k_h^{-5/3}$ inertial domain at intermediate scales ($0.2 \text{ rad/mm} \lesssim k_h \lesssim 0.7 \text{ rad/mm}$) even for the lowest \mathcal{R}^t investigated (Fig. 4). This inertial range becomes more and more flat as \mathcal{R}^t increases as observed in DNS of forced stratified turbulence [3].

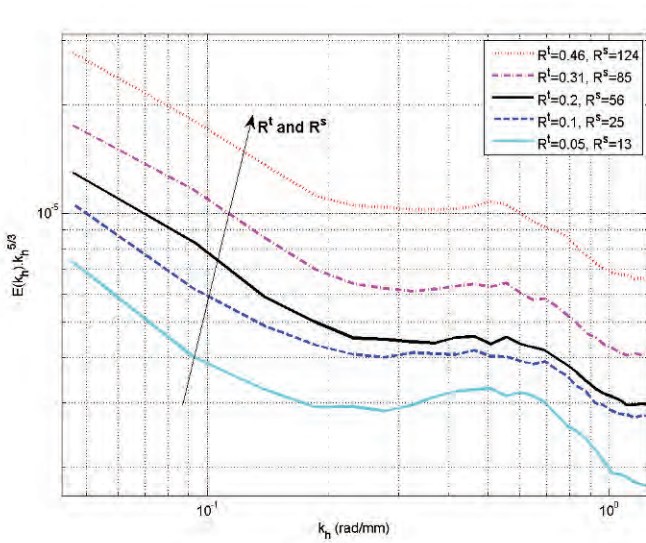


Fig. 4. Compensated 1D kinetic energy spectrum : $E(k_h)k_h^{5/3}$ as function of the horizontal wave number k_h for different buoyancy Reynolds numbers.

As shown in figure 5, the rotational and divergent parts of the horizontal velocity are of the same order at all scales even if the forcing is purely vortical. This is consistent with the scaling law $l_v/l_h \sim F_h$ for which the dynamic of waves and vortices can not be separated [1, 3]

We have set-up a novel experiment on forced strongly stratified turbulence with buoyancy Reynolds number of order one. For the first time, a $k_h^{-5/3}$ inertial range has been observed experimentally in agreement with theoretical predictions, DNS and atmospheric measurements.

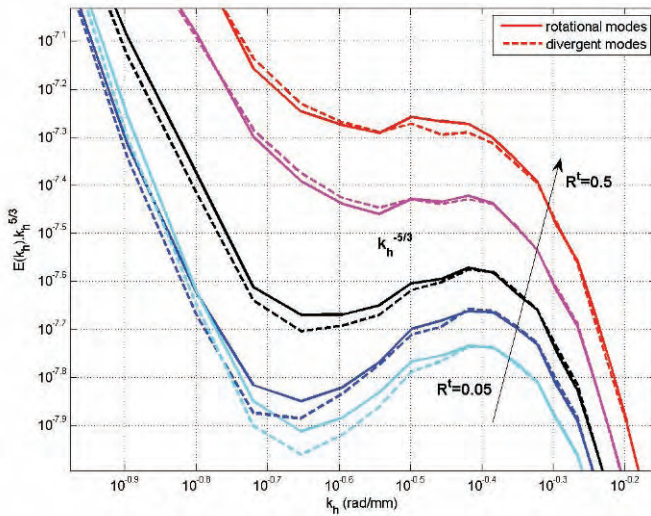


Fig. 5. Compensated 2D kinetic spectrum of the vortical and divergent parts of the horizontal velocity.

References

1. P. Billant and J.-M. Chomaz, Self-similarity of strongly stratified inviscid flows, *Phys. Fluids*, 13 (2001)
2. E. Lindborg. The energy cascade in a strongly stratified fluid, *J. Fluid Mech.*, 550 (2006)
3. G. Brethouwer, and P. Billant, and E. Lindborg, and J.-M. Chomaz. Scaling analysis and simulation of strongly stratified turbulent flows, *J. Fluid Mech.*, 585 (2007)
4. O. Praud and A.M. Fincham and J. Sommeria, Decaying grid turbulence in a strongly stratified fluid, *J. Fluid Mech.*, 522 (2005)
5. P. Billant and J.-M. Chomaz. Experimental evidence for a new instability of a vertical columnar vortex pair in a strongly stratified fluid, *J. Fluid Mech.*, 418 (2000)
6. A. Deloncle, P. Billant and J.-M. Chomaz. Nonlinear evolution of the zigzag instability in stratified fluids : a shortcut on the route to dissipation, *J. Fluid Mech.*, 599 (2008)

DNS of the turbulent cloud-top mixing layer

J. P. Mellado^a, H. Schmidt^b, B. Stevens^c, N. Peters^a

^a Institut für Technische Verbrennung, RWTH Aachen University, 52056 Aachen, Germany

^b Zuse Institute, FU Berlin

^c Max Planck Institute for Meteorology, Hamburg

`jpmellado at itv.rwth-aachen.de`

The turbulent cloud-top mixing layer is studied using direct numerical simulation (DNS). This configuration models the top of stratocumulus clouds and is employed to investigate the role of latent heat effects. A partial description of the turbulent flow that develops when the cloud and the cloud-free air mix under buoyancy reversal conditions is presented in this paper.

1 Introduction

Cloud effects remain one of the largest sources of uncertainty in model-based estimates of climate sensitivity. In particular entrainment rates in stratocumulus-topped boundary layers need better models [3] in order to improve predictions obtained with large-eddy simulations and Reynolds average Navier-Stokes equations.

This work continues previous studies (see [2] and references therein) of small-domain systems specifically designed to investigate the effects of the latent heat of water, to gain understanding of the local dynamics at the top of the cloud deck over length-scales below 5 m, which is the typical grid step used in recent large-eddy simulations of the boundary layer [5]. The cloud-top mixing layer is an idealized configuration formed by an unbounded horizontal two-layer system, the upper layer warm and subsaturated and the lower cool and saturated, the gravity force acting downwards. When they mix, buoyancy reversal due to evaporative cooling may occur under certain thermodynamic conditions, creating mixtures heavier than the environment. The physical model, as used in the past, is based on a mixture fraction variable χ , a conserved scalar that represents the amount of mass in a fluid particle that originates from the upper layer. It only retains the effects of water phase transition, and no further detail of the micro-physics of the cloud is represented.

The problem is reduced to the Boussinesq approximation with the buoyancy term in the vertical momentum equation related to the mixture fraction

by a nonlinear function $b^e(\chi)$, the so-called buoyancy mixing function. The typical shape of this function is shown in Fig. 1 (left), non-dimensionalized with the inversion value b_1 formed by the density difference between the two layers. The mapping $b^e(\chi)$ is characterized by the saturation value χ_s that indicates the mixture with the minimum buoyancy $b_s = -Db_1$; D is the buoyancy reversal parameter. The interval of mixtures between $\chi = 0$ and the cross-over value $\chi_c = (\chi_s + D)/(1 + D)$ with negative buoyancy represents the buoyancy reversal.

The two-layer system in terms of the conserved variables leads to a three-layer system in terms of the density, with the middle layer heavier than the cloud below if buoyancy reversal occurs. This structure is unstable and the associated instability is the buoyancy reversal instability [1]. This instability leads to a turbulent state of the lower cloudy layer, even for the low values $D < 0.1$ characteristic of real stratocumulus.

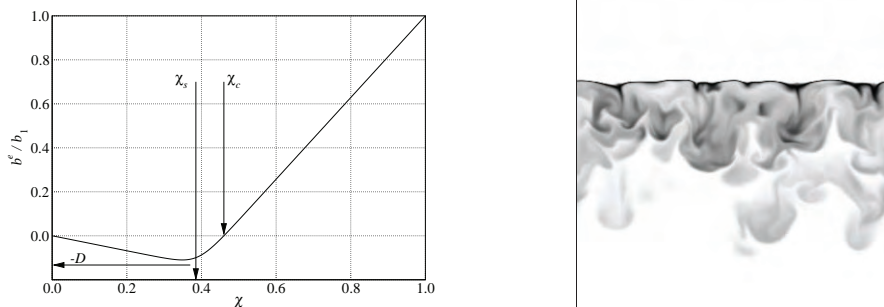


Fig. 1. Nondimensional buoyancy mixing function (left). Negative buoyancy field (right) at the final time of the simulation $\tau_3 = 5.40$.

2 Results

A DNS of the reference case $D = 0.031$ and $\chi_s = 0.09$ taken from field measurements in nocturnal marine stratocumulus in the DYCOMS-II study [4] has been performed on a cubic domain L_0^3 using a uniform grid of size 1024^3 . The Prandtl number is $Pr = 1$ and the Grashof number $Gr = L_0^3 b_1 / \nu^2 = 6.4 \times 10^9$, which corresponds to a domain size $L_0 \simeq 2$ m when atmospheric values for the viscosity ν and the inversion buoyancy b_1 are used. The flow is temporally evolving and the horizontal planes are statistically homogeneous, so that statistics depend on the vertical distance z/L_0 and on a nondimensional time $\tau = t \sqrt{|b_s|}/L_0$.

Figure 1 (right) depicts qualitatively the state of the turbulent flow by means of the negative buoyancy field at the final time, using a gray scale

ranging from zero buoyancy (white) to b_s (black). The forcing is to be found in the vertical downdrafts of cool fluid that develop between the domes observed at the inversion, which suffer then shear instabilities and transfer turbulent energy to the horizontal motion. The inversion remains relatively thin and its mean position is not significantly displaced in the vertical direction.

Quantitatively, the evolution of the mixture fraction is presented in Fig. 2. The mean profile $\langle \chi \rangle$ shows the penetration of the mixing region into the neutrally-stable lower layer. The mean values of mixture fraction inside the mixing region are small compared to the inversion value, even smaller than the cross-over value $\chi_c = 0.12$, and the evolution is only clearly observed in the inset of Fig. 2 (left). On the other hand, the inversion remains located at about the initial position $z = 0$, with a small thickening towards the upper layer consistent with the conservation property of the mixture fraction, and seemingly dominated by diffusion processes.

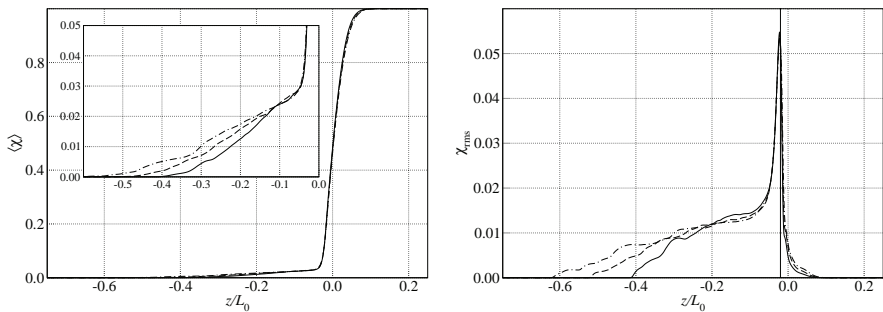


Fig. 2. Mean (left) and r.m.s. (right) profiles of mixture fraction at different times: $\tau_1 = 4.03$, solid; $\tau_2 = 4.70$, dashed; $\tau_3 = 5.40$, dot-dashed. The cross-over mixture fraction separating negatively from positively buoyant mixtures is $\chi_c = 0.12$ and the vertical line indicates the corresponding position of that reference inversion plane.

The fluctuation of the mixture fraction is illustrated by Fig. 2 (right), where the profile of the root-mean-square (r.m.s.) is plotted. First, there is a broad zone below $z/L_0 \simeq -0.1$, corresponding to the turbulent region, with fluctuation values about 1%; compared with χ_c , the value that seems to cap the turbulent motion at the inversion, that turbulence intensity is of the order of 10%. Second, there is a strong peak of χ_{rms} at about $z/L_0 \simeq -0.02$, which does not vary strongly in time and that approximately corresponds to the point of maximum mean gradient observed in Fig. 2 (left). The location of this maximum gradient is not at $z = 0$ because the problem is asymmetric, and it is more related to the position of the reference inversion plane based on the initial background profile and the cross-over value χ_c . That strong maximum in χ_{rms} represents the oscillation of the stable inversion.

In terms of the velocity, the mean is zero due to the statistical homogeneity along the horizontal planes and the solenoidal character of the velocity field.

The velocity turbulence intensity $\sqrt{2k}$, k being the turbulent kinetic energy per unit mass, is plotted in Fig. 3 (left). The turbulent kinetic energy continuously increases due to the positive turbulent buoyancy flux, Fig. 3 (right), generated by the downdrafts, and this growth is in magnitude as well as in broadening towards the lower layer. The Taylor-scale Reynolds number is $Re_\lambda = w' \lambda_z / \nu \simeq 65$, where w' is the vertical velocity r.m.s. and the Taylor microscale is $\lambda_z = w' / \sqrt{\langle (\partial w' / \partial z)^2 \rangle}$. The turbulent Richardson number is large, $Ri_t = b_1 k^{1/2} / \epsilon \simeq 300$, with ϵ the average turbulent dissipation rate, which explains why the turbulent zone is constrained by the inversion on top, as observed again in Fig. 3, without intense engulfment of the upper laminar layer into the mixing region.

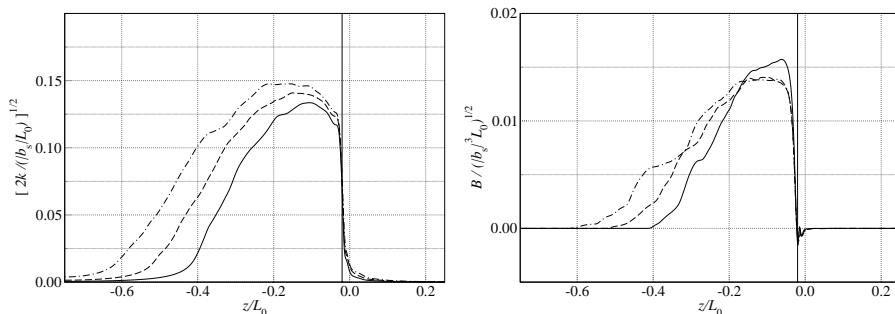


Fig. 3. Turbulent kinetic energy (left) and turbulent buoyancy flux (right) at different times. Same legend as in Fig. 2.

Partial financial support for this work was provided by the Deutsche Forschungsgemeinschaft within the SPP 1276 Metström program.

References

1. J. P. Mellado, B. Stevens, H. Schmidt, and N. Peters. Buoyancy reversal in cloud-top mixing layers. *Q. J. Roy. Meteorol. Soc.*, 2009.
2. S. T. Siems and C. S. Bretherton. A numerical investigation of cloud-top entrainment instability and related experiments. *Q. J. Roy. Meteorol. Soc.*, 118:787–818, 1992.
3. B. Stevens. Entrainment in Stratocumulus-topped mixed layers. *Q. J. Roy. Meteorol. Soc.*, 128:2663–2690, 2002.
4. B. Stevens, D-H-Lenschow, I. Faloona, C. H. Moeng, D. K. Lilly, B. Blomquist, G. Vali, A. Bandy, T. Campos, H. Gerber, S. Haimov, B. Morley, and C. Thornton. On entrainment rates in nocturnal marine Stratocumulus. *Q. J. Roy. Meteorol. Soc.*, 129(595):3469–3493, 2003.
5. T. Yamaguchi and D. A. Randall. Large-eddy simulation of evaporatively driven entrainment in cloud-topped mixed layers. *J. Atmos. Sci.*, 65:1481–1504, 2008.

Modeling and Simulation of Momentum and Heat Transfer in the Atmospheric Boundary Layer over Rough Surface: Study with Improved Turbulence Model *

A.F. Kurbatskiy^{1,2} and L.I. Kurbatskaya³

¹ Khristianovich Institute of Theoretical and Applied Mechanics of Russian Academy of Sciences, Siberian Branch kurbat@nsu.ru

² Novosibirsk State University kurbat@nsu.ru

³ Institute of Computational Mathematics and Mathematical Geophysics RAS, Siberin Branch L.Kurbatskaya@ommgp.sccc.ru

1 Introduction

In the present study we are focused on the mesoscale simulation of turbulent momentum and heat transfer in the stably stratified boundary layer over a flat urbanized surface by using the improved three-parameter turbulence model in which buoyancy effects are accurately taken into account [1]. A horizontal inhomogeneity of a mechanical nature is accompanied by a thermal inhomogeneity. In some field studies, urbanized surfaces were observed to be generally warmer than the adjacent vicinities. This situation is referred to as an urban heat island [2]. Aerodynamic roughness and the urban heat island produce significant disturbances in the wind and temperature fields due to an intense upward flow of warm unstable air. This flow is induced by the horizontal temperature gradient between the more strongly heated air over the urbanized surface and the less heated air over its environs [1]. In this case, vertical turbulent heat transfer has a nonlocal (countergradient) character [3].

2 Anisotropic three-parameter turbulence model

Below we will present completely explicit anisotropic expressions for the turbulent momentum and heat fluxes in which the effects of buoyancy on turbulent transfer are taken into account physically correctly. The details and

* Authors acknowledge support of the Russian Foundation for Basic Research (grant No. 09-05-00004a, 07-05-00673)

approximations of their derivation can be found in [1]. The expressions for the momentum and heat fluxes may be written as

$$\langle\langle uw \rangle\rangle, \langle\langle vw \rangle\rangle = -K_M \left(\frac{\partial U}{\partial z}, \frac{\partial V}{\partial z} \right), \quad (1)$$

$$\langle w\theta \rangle = -K_H \frac{\partial \Theta}{\partial z} + \gamma_c, \quad (2)$$

$$K_M = E\tau S_M, \quad K_H = E\tau S_H, \quad (3)$$

$$S_M = \frac{1}{D} \left\{ s_0 [1 + s_1 G_H (s_2 - s_3 G_H)] + s_4 s_5 (1 + s_6 G_H) (\tau \beta g)^2 \frac{\langle \theta^2 \rangle}{E} \right\}, \quad (4)$$

$$S_H = \frac{1}{D} \left\{ \frac{2}{3} \frac{1}{\tilde{c}_{1\theta}} (1 + s_6 G_H) \right\}, \quad (5)$$

$$\gamma_c = \frac{1}{D} \left\{ 1 + \frac{2}{3} \alpha_2^2 G_M + s_6 G_H \right\} \alpha_5 (\tau \beta g) \langle \theta^2 \rangle, \quad (6)$$

where γ_c is the countergradient term, which is absent in the 2.5-order closure models [4-7].

$$G_H \equiv (\tau N)^2, \quad G_M \equiv (\tau \Sigma)^2,$$

$$N^2 = \beta g \frac{\partial \Theta}{\partial z}, \quad \Sigma^2 \equiv \left(\frac{\partial U}{\partial z} \right)^2 + \left(\frac{\partial V}{\partial z} \right)^2, \quad \tau = E/\varepsilon, \quad E = 1/2 \langle u_i u_i \rangle.$$

The coefficients in the equations (4-6) are given as

$$D = 1 + d_1 G_M + d_2 G_H + d_3 G_M G_H + d_4 G_H^2 + [d_5 G_H^2 - d_6 G_m G_h] G_H$$

$$d_1 = \frac{2}{3} \alpha_2^2, \quad d_2 = \frac{10}{3} \frac{\alpha_3}{\tilde{c}_{1\theta}}, \quad d_3 = \frac{2}{3} \alpha_2 \frac{\alpha_3}{\tilde{c}_{1\theta}} (\alpha_2 - \alpha_5)$$

$$d_4 = \frac{11}{3} \left(\frac{\alpha_3}{\tilde{c}_{1\theta}} \right)^2, \quad d_5 = \frac{4}{3} \left(\frac{\alpha_3}{\tilde{c}_{1\theta}} \right)^3, \quad d_6 = \frac{2}{3} \alpha_2 \alpha_5 \left(\frac{\alpha_3}{\tilde{c}_{1\theta}} \right)^2$$

$$s_0 = \frac{2}{3} \alpha_2, \quad s_1 = \frac{1}{\alpha_3} \frac{\alpha_3}{\tilde{c}_{1\theta}}, \quad s_2 = \alpha_2 - \alpha_5, \quad s_3 = \alpha_5 \left(\frac{\alpha_3}{\tilde{c}_{1\theta}} \right)$$

$$s_4 = \alpha_3 \alpha_5, \quad s_5 = \alpha_5 + \frac{4}{3} \alpha_2, \quad s_6 = \frac{\alpha_3}{\tilde{c}_{1\theta}}$$

$$\alpha_1 = \frac{4}{3} \frac{1 - c_2}{c_1}, \quad \alpha_2 = \frac{1 - c_2}{c_1}, \quad \alpha_3 = \frac{1 - c_3}{c_1}, \quad \alpha_4 = (1 - c_{2\theta}), \quad \alpha_5 = \frac{1 - c_{2\theta}}{\tilde{c}_{1\theta}} \quad (7)$$

Numerical values of the constants in expressions of (7) for turbulent momentum and heat fluxes (1) and (2) are $c_1 = 2$, $c_2 = 0.54$, $c_3 = 0.8$, $c_{1\theta} = 3.28$, $c_{2\theta} = 0.5$. The kinetic energy E , its spectral consumption ε and variance $\langle \theta^2 \rangle$ are obtained from the solution of transport equations (see in [1]). The slow terms of the pressure-temperature correlation have been modeled as follows:

$$\Pi_i^{\theta(1)} \equiv \langle p \frac{\partial \theta}{\partial x_i} \rangle \approx -\frac{c_{1\theta}}{\tau_{p\theta}} \langle u_i \theta \rangle,$$

where $\langle u_i \theta \rangle$ is the heat flux. In the many second-order closure models further assume that $\tau_{p\theta} \sim \tau = E/\varepsilon$. However, this assumption may not necessarily apply to the stratified flows. Indeed, in the original work of Weinstock [8] it is shown, that the return-to-isotropy time scale $\tau_{p\theta}$ in the presence of stable stratification assumed to be equal

$$\tau_{p\theta} = \frac{\tau}{1 + a\tau^2 N^2}, \tag{8}$$

where $a = 0.04$ if $N^2 > 0$, and $a = 0$ if $N^2 \leq 0$. Here N is the *Brunt – Väisälä* frequency . The physical reason behind (8) is that in stably stratified flows eddies lose kinetic energy for work against a gravity and this energy will be converted to potential energy. Taking into consideration of (8), it is easy to write the modified expression of coefficient $c_{1\theta}$ so as to exhibit its dependence on :

$$\tilde{c}_{1\theta} = c_{1\theta}(1 + a\tau^2 N^2). \tag{9}$$

3 Turbulent Prandtl number in a Stably Stratified Boundary Layer over Rough Surface

Figure 1 shows the dependence of the inverse turbulent Prandtl number $Pr_t^{-1} = K_h/K_m$ as a function of the gradient Richardson number (defined as $Ri = N^2/S^2$, and S is the vertical shear of the horizontal velocity), calculated at the numerical simulation of the stably stratified boundary layer with use an anisotropic algebraic model for turbulent momentum and heat fluxes and the RANS three-parametric turbulence model [1]. The general trend of the inverse Prandtl number compares with the laboratory measurements and the atmospheric data [9, 10]. Our simulation result is obtained by the physically correct damping of turbulent vortices by the stable stratification according to modifications of (8, 9). Indeed, the dash-dot line on Figure 1 correspond to the calculation with help the 'standard' approximation: $\tau_{p\theta} = \tau$, but this dependence does not answer experimentally observed to decrease of inverse Prandtl number with growth of thermal stability of a boundary layer (increasing the gradient Richardson's number). The result $Pr_t^{-1} < 1$ is usually associated with the presence of the internal gravity waves in the SBL. They are presumed to enhance the momentum transfer through pressure terms in the Navier-Stokes equations, whereas gravity waves do not affect the heat flux (e.g. [11]). At the same time it is necessary to note, the result $Pr_t^{-1} > 1$ was obtained in recent large-eddy simulation (LES) studies of the SBL (e. g. [12]). Also in [13] reported $Pr_t^{-1} > 1$ from their LES simulations. In particular, is noted [13], that in a boundary layer (up to 150 m), (almost) all results of simulations give value $Ri/Ri_f \sim 0.7$ (Ri_f is the flux Richardson number). Nevertheless, 'mainstream' the given measurements and observations, apparently, specifies in a diminishing trend of inverse Prandtl number with increasing of thermal stability (increasing of the gradient Richardson's number) of the SBL.

References

1. A. F. Kurbatskiy, L. I. Kurbatskaya, *Meteorology and Atmospheric Physics*,4, DOI: 10. 1007/s0703-009-0017-8 (2009).
2. T. R. Oke, *Boundary Layer Climates*, London, Methuen and CO LTD 1978.
3. A.F. Kurbatskiy, *Izv. Atmos. Ocean. Phys*, 44, 160 (2008).
4. G. L. Mellor, T. Yamada, *Journal of Atmospheric Sciences*, 31, 1791 (1974).
5. G. L. Mellor, T. Yamada, *Reviews of Geophysics and Space Physics*, 20, 851 (1982).
6. Y. Cheng, V. M. Canuto, A. M. Howard, *Journal of Atmospheric Sciences*, 59, 1550 (2002).
7. V. M. Canuto, A. Howard, Y. Cheng, I. H. Esau, *Journal of Atmospheric Sciences*, 65, 2437 (2008).
8. J. Weinstock, *Journal of Fluid Mechanics*, 202, 319(1989).
9. E. J. Strang, H. J. S. Fernando, *J. Phys. Oceanography*, 31, 2006 (2001).
10. P. Monti, H. J. S. Fernando, M. Princevac, W. C. Chan, T. A. Kowalewski, E. R. Paradyjak, *Journal of Atmospheric Sciences*, 59, 2513 (2002).
11. A. Monin, A.Yaglom, *Statistical Fluid Mechanics: Mechanics of Turbulence. Vol. 1.* The MIT Press, Cambridge, Massachusetts 1975.
12. R. J. Beare, and Coauthors, *Boundary-Layer Meteorology*, DOI: 10. 1007/s10546-004-2820-6.
13. S. Basu and F. Porte-Agel, *Journal of Atmospheric Sciences*, 63, 2074 (2006).

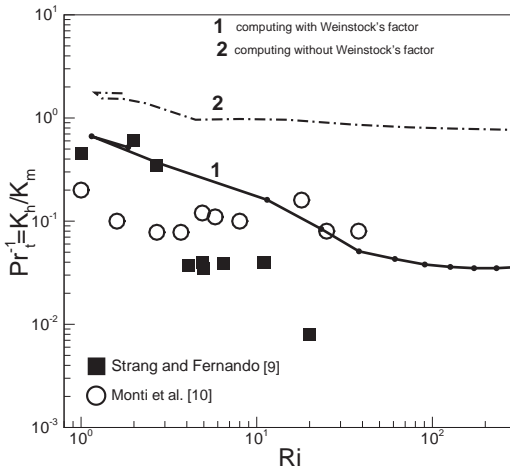


Fig. 1. Inverse Prandtl number, $Pr_t^{-1} = K_h/K_m$, as a function of Ri . Solid line 1 shows prediction by the improved turbulence model [1] with the correction of (8), and dash dot line 2 shows prediction without correction (8). Black square symbols show data by Strang and Fernando [9] and open circle are data by Monti et al. [10]

Wind Direction Effects on Urban Like Roughness: an LES Study

J.M. Claus, I.P. Castro and Z.-T. Xie

AFM, SES, University of Southampton, Southampton SO17 1BJ, U.K.
jean.claus@soton.ac.uk

1 Introduction

In research on flow characteristics above and within urban areas, recent studies have used uniform cube arrays as simple models of an urban canopy [1, 2, 3, 4]. In most of these studies the flow direction was normal to the faces of the cubes. So as to bridge the gap between this simple model and real urban environments it is now required to investigate the effects of more parameters, such as variations in surface morphology or, as in the present paper, the wind direction.

2 Numerical Approach

A flow was numerically simulated above and within a staggered array of uniform cubes of height h as shown in fig. 1. Two domain sizes were used; the first, $4h \times 4h \times 4h$, comprised 4 cubes and the second, $8h \times 8h \times 4h$, 16 cubes. The domains were discretised on regular grids of hexahedral cells. The dimensions of the cells were $(\frac{h}{16})^3$ for the coarse grid and $(\frac{h}{25})^3$ for the fine grid (only used

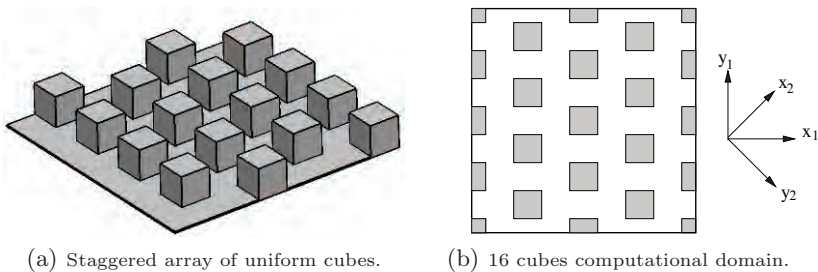


Fig. 1. Surface studied.

on the 4-cubes domain). The vertical boundaries were set as periodic and the top of the domain was a slip boundary.

The flow was forced by a pressure gradient in the x_2 -direction – see coordinate system on fig. 1(b). Global and roughness Reynolds numbers are: $Re = U_{ref}h/\nu \approx 4000$, $Re_\tau = u_\tau h/\nu = 434$, respectively, with U_{ref} the velocity at the top of the domain and u_τ the friction velocity. Both the spatial and time discretisation scheme were second order accurate. The flow was simulated using LES with Smagorinsky subgrid scale (SGS) model and a Lilly damping function.

3 Results

3.1 Mean Flow

The velocity components were time averaged and spatially averaged in horizontal layers. Mean velocity profiles from the three simulations are compared in fig. 2(a). The angle between the resulting mean flow and the direction of the pressure gradient is represented in fig. 2(b). The results show that the flow is highly skewed, especially within the canopy where the flow is deviated by more than 40 degrees below $z = 0.5 h$. It is also interesting to notice that even at the top of the domain the flow is not aligned with the direction of the forcing which could indicate that the domain is not high enough. This issue will be investigated in future simulations.

Within the canopy, the spatial rms of the velocity components, presented in fig. 3(a) and 3(b), are however of the same order as the velocity components themselves so that the direction of the mean flow has more statistical than physical sense. The spatial rms also indicate that the top of the roughness sublayer is around $z = 1.7 h$.

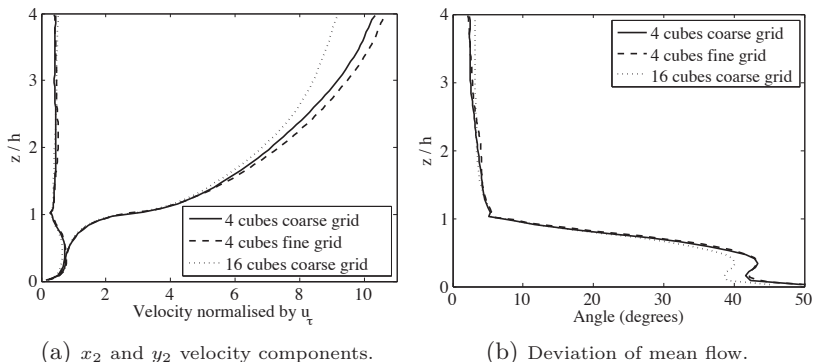


Fig. 2. Velocity and mean flow deviation from the direction of the forcing (x_2).

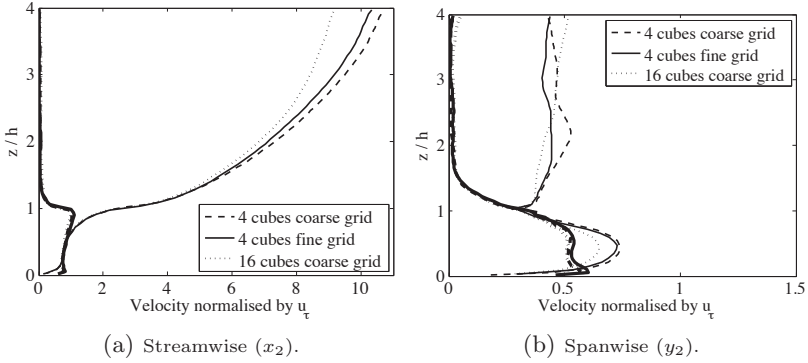


Fig. 3. Horizontally averaged mean flow (faint) and spatial rms (bold).

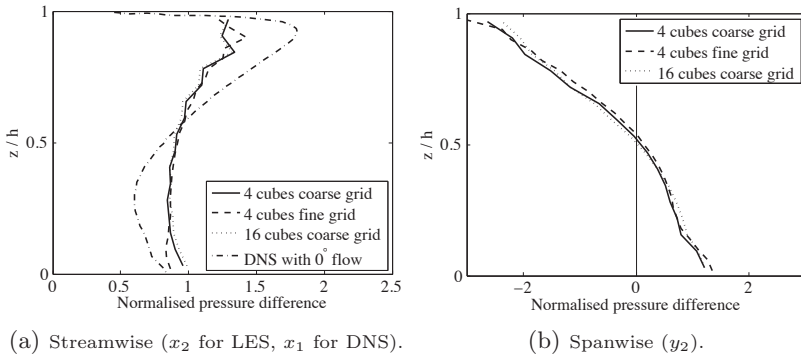


Fig. 4. Horizontally averaged pressure difference on cubes.

3.2 Drag and lift forces

The pressure on the faces of the cubes has been averaged from the 4 or 16 cubes, depending on the domain, and then averaged horizontally. The vertical distributions of pressure difference in the streamwise and spanwise directions, normalised by the integral of their absolute value, are represented in fig. 4(a) and 4(b). The streamwise pressure difference is compared to DNS results from Coceal *et al* [2] obtained for a flow at 0 degree – in the x_1 -direction.

For the 0-degree case, the top third of the building contributes to half the pressure drag and the peak is situated around $z = 0.9 h$. In a study with random-height obstacles, Xie *et al* [4] showed that the tallest buildings presented similar vertical distribution which resulted in their contribution to the total drag being much higher than their contribution to the total frontal area (by a factor of about two). For the 45-degree case, however, the vertical distribution of the drag proves to be much more uniform. It would thus be interesting to study whether or not the tallest buildings remain predominantly responsible for the drag of the random array with a 45-degree flow.

For the 0-degree case, the form drag represented more than 90% of the total drag and LES results collapsed well with DNS and wind tunnel data, because the influence of the (probably inadequately captured) viscous forces was quite small. For the 45-degree case, however, the pressure drag is only of the order of 80% of the total drag, the 20% remaining being thus the viscous drag. Given that the downfall of LES is often the poor representation of the viscous forces, and in the absence, to our knowledge, of DNS or experimental data for this configuration, this issue will have to be carefully investigated.

4(b) shows that the spanwise pressure difference is positive in the lower half of the canopy and negative in the top half, which implies that a moment is exerted on the cubes. Furthermore, by vertical integration of the spanwise pressure difference we obtain a non-zero pressure ‘lift’ exerted on the cubes. The ratio of the pressure lift to the pressure drag is of the order of 3%. The global forces on the whole domain shows that this lift can only be balanced by an opposing viscous force in the spanwise direction. The pressure force – hence the viscous force – in the spanwise direction is directly related to the deviation of the mean flow so that, once more, how well the viscous forces are represented could reflect on the quality of the flow simulation.

4 Conclusions

The 45-degree simulations have shown new features in the flow above cube arrays. Given the very good LES results for the 0-degree flow we can be confident about the qualitative features of the 45-degree flow: highly skewed mean flow, greater uniformity in the vertical distribution of drag, exertion of a pressure lift on the cubes. However, the seemingly increased importance of the viscous forces (at least in the main flow direction) and their possibly poor representation by LES perhaps raises questions about the quantitative accuracy of the results. The forthcoming wind tunnel experiments, whose results will be presented at the conference, are intended to shed some light on this issue.

References

1. Cheng H. and Castro I. P. (2002) Near wall flow over urban-like roughness. *Bound. Layer Meteorol.*, 104:229–259.
2. Coceal O., Thomas T. G., Castro, I. P. and Belcher, S. E. (2006) Mean flow and turbulence statistics over groups of urban-like obstacles. *Bound. Layer Meteorol.*, 121:491–519.
3. Xie Z-T. and Castro I. P. (2006) LES and RANS for turbulent flow over arrays of wall-mounted obstacles. *Flow Turbulent Combustion*, 76:291–312.
4. Xie Z-T., Coceal O. and Castro I. P. (2008) Large-eddy simulation of flows over random urban-like obstacles. *Bound. Layer Meteorol.*, 129:1–23.

**Part VII Geophysical and astrophysical
turbulence**

Anisotropy in turbulent rotating convection

R.P.J. Kunnen^{1,*}, H.J.H. Clercx^{1,2}, and B.J. Geurts^{2,1}

¹ Fluid Dynamics Laboratory, Dept. of Physics, Eindhoven University of Technology, P.O. Box 513, 5600 MB Eindhoven, The Netherlands

² Department of Applied Mathematics, University of Twente, P.O. Box 217, 7500 AE Enschede, The Netherlands

* Current address: Institute of Aerodynamics, RWTH Aachen University, Wüllnerstrasse 5a, 52062 Aachen, Germany

h.j.h.clercx@tue.nl

Introduction

A simple model for many geophysical and astrophysical flows, such as oceanic deep convection and the convective outer layer of the Sun, is found in rotating Rayleigh–Bénard convection: a horizontal fluid layer heated from below and cooled from above is rotated about a vertical axis. Three dimensionless parameters characterise this flow: the Rayleigh number Ra describes the strength of the destabilising temperature gradient, the Prandtl number σ relates the diffusion coefficients for heat and momentum of the fluid, and the Rossby number Ro is the ratio of buoyancy and Coriolis forces ($Ro = \infty$ when rotation is absent and $Ro \ll 1$ for rotation-dominated flow). We investigate the effect of rotation on the flow anisotropy in turbulent convection in an upright cylinder of equal height and diameter, with experiments and numerical simulations.

Anisotropy quantified

A method to visualise and quantify flow anisotropy has been introduced by Lumley [2]. It is based on the Reynolds stress tensor $R_{ij} \equiv \overline{u_i u_j}$, with u_i the i th velocity component ($i = 1, 2, 3$) and the overbar indicating spatial averaging. Define the Reynolds stress anisotropy tensor

$$b_{ij} \equiv \frac{R_{ij}}{R_{kk}} - \frac{1}{3}\delta_{ij}, \quad (1)$$

where δ_{ij} is the second-order Kronecker tensor, and summation is implied over repeated indices. b_{ij} is a symmetric tensor with zero trace. The second and third tensor invariants of b_{ij} , denoted with II and III , respectively, are

$$II \equiv -b_{ij}b_{ji}/2, \quad III \equiv \det(b_{ij}). \quad (2)$$

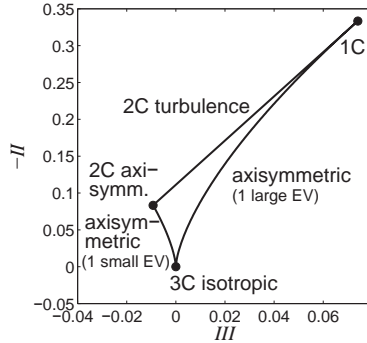


Fig. 1. The Lumley triangle [2] is the map of allowed turbulence states in terms of the anisotropy tensor invariants II and III .

The so-called Lumley triangle allows for a graphical evaluation of the anisotropy based on the invariants II and III , see Fig. 1. All possible turbulence states are found within this triangle. Isotropic three-component (3C) turbulence is found in the origin. The limiting case of two-component (2C) turbulence with axial symmetry is the leftmost point, while the rightmost point represents turbulence with only one nonzero velocity component (1C). On the left-hand side, the bounding curve represents the situation where one eigenvalue (EV) of b_{ij} is smaller than the other two (which are equal in magnitude), representing so-called ‘pancake-shaped’ or ‘disk-like’ turbulence [2]. Conversely, on the right-hand side one EV of b_{ij} is larger than the other two, and ‘cigar-shaped’ or ‘rod-like’ turbulence is found [2].

Experimental and numerical methods

The full 3C velocity vector must be known to apply the aforementioned procedure. In the experiments velocity measurements are carried out in the convection cell using stereoscopic particle image velocimetry (SPIV). This measurement resolves the three components of velocity simultaneously on many positions in a planar cross-section of the flow domain. The seeded fluid is illuminated with a laser light sheet that crosses the cylinder horizontally. Two different heights are considered, viz. $z = 0.5H$ and $0.8H$ (H is the cylinder height). Two cameras are placed above the cell at different viewing angles. With this stereoscopic view vertical displacements of the seeding particles in the light sheet can be detected in addition to in-plane displacements.

In the simulations the equations of motion (the Navier–Stokes and heat equations in Boussinesq form with incompressibility) are written in cylindrical coordinates and discretised using second-order accurate finite-difference formulations. The procedure is described in detail elsewhere [3].

The experiments and simulations are performed at a constant Rayleigh number $Ra = 10^9$ and the convection fluid is water ($\sigma = 6.4$). The rotation

rate is varied between runs. The Rossby number Ro takes values between $Ro = 0.045$ and 11.52 in the simulations; in the experiments $0.09 \leq Ro \leq \infty$.

Results

Some typical results of the anisotropy evaluation from the simulations are shown in Fig. 2. The invariants describe a certain trajectory in time inside the Lumley triangle. When rotation is negligibly small (a, b), the invariants take values covering most of the triangle. Under strong rotation (c, d) different trends are observed. At mid-height (c) the trajectory is pressed against the lower right-hand side boundary, indicating a turbulent state where velocity fluctuations in one direction (the vertical direction) dominate over the other two directions. Closer to the top plate (d) the trajectory is confined to a small region near the isotropic limit, indicating nearly isotropic turbulence.

An overview of these effects as a function of Ro is obtained by plotting the time-averaged values of the invariants in the Lumley triangle at the various Ro values. These averages are drawn in Fig. 3 for both experiment (a) and simulation (b). Both methods show the same trends: at $z = 0.5H$ rotation increases the anisotropy toward ‘cigar-shaped turbulence,’ while at $z = 0.8H$ a near-isotropic state is approached. Thus a strong vertical inhomogeneity is found.

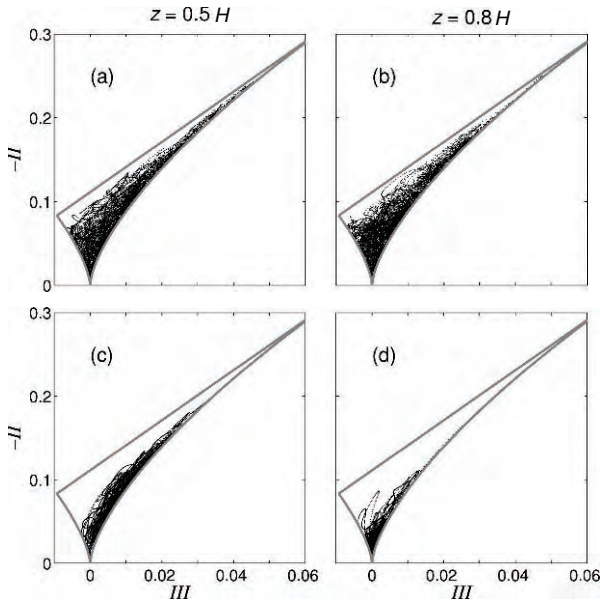


Fig. 2. Time series plots of the invariants in the Lumley triangle from simulations at (a, b) $Ro = 11.52$ (negligible rotation) and (c, d) $Ro = 0.045$ (strong rotation). Figures (a, c) are for $z = 0.5H$, while (b, d) are for $z = 0.8H$.

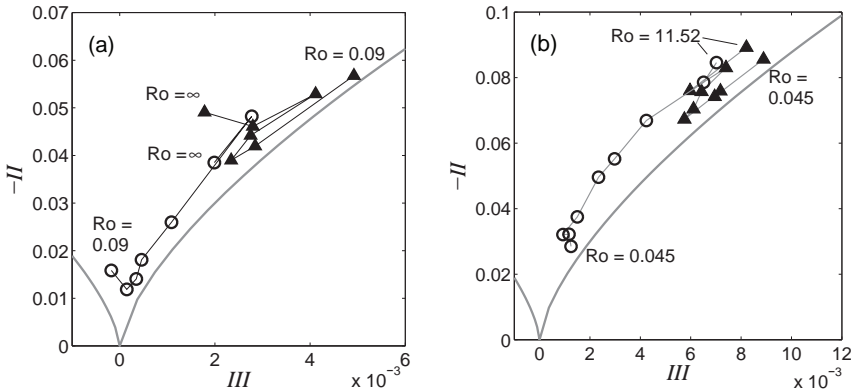


Fig. 3. Averaged trajectories in the Lumley map as a function of Ro , taken at $z = 0.5H$ (circles) and at $z = 0.8H$ (triangles). (a) Experiment; Ro increases with factors 2 from 0.09 to 2.88; $Ro = \infty$ is also included. (b) Simulation. Ro increases with factors 2 from 0.045 to 2.88; $Ro = 11.52$ is also included.

Discussion and conclusion

Rotation has profound effects on the turbulence anisotropy in convection. In the central region there is a tendency toward ‘cigar-shaped’ turbulence with one preferential direction. This is remarkably different from non-convective rotating turbulence [4], where the opposite limit of two-component ‘pancake-shaped’ turbulence is approached. The current ‘cigar-shaped’ turbulence anisotropy agrees with the vertical convective forcing and the formation of narrow vortical tube-like plumes that account for the vertical transport of heat and fluid [5]. When approaching the vertical walls it is found that rotation actually promotes isotropy. The vertical inhomogeneity is unexpected from the Taylor–Proudman theorem, which predicts a flow field without vertical gradients. It is thus important to take into account the vertical dependence when modelling rotating convection.

References

1. R.P.J. Kunnen, H.J.H. Clercx and B.J. Geurts, *Phys. Rev. Lett.*, **101**, 174501 (2008).
2. J.L. Lumley, *Adv. Appl. Mech.*, **18**, 123 (1978); K.-S. Choi and J.L. Lumley, *J. Fluid Mech.*, **436**, 59 (2001); A.J. Simonsen and P.-Å. Krogstad, *Phys. Fluids*, **17**, 088103 (2005).
3. R. Verzicco and P. Orlandi, *J. Comput. Phys.*, **123**, 402 (1996); R. Verzicco and R. Camussi, *J. Fluid Mech.*, **477**, 19 (2003).
4. L.J.A. van Bokhoven, PhD thesis, Eindhoven University of Technology (2007).
5. K. Julien et al., *J. Fluid Mech.*, **322**, 243 (1996); S. Sakai, *J. Fluid Mech.*, **333**, 85 (1997); P. Vorobieff and R.E. Ecke, *J. Fluid Mech.*, **458**, 191 (2002).

Nonlocal interactions and condensation in forced rotating turbulence

L. Bourouiba¹ and D. Straub²

¹Department of Mathematics and Statistics, York University, Canada

²Department of Atmospheric and Oceanic Sciences, McGill University, Canada
lydia.bourouiba@mail.mcgill.ca

1 Introduction

The Rossby number, $Ro = U/L2\Omega$, is the non-dimensional number characterizing rotating flows. Here U is the characteristic velocity, L the characteristic length scale, and 2Ω is the Coriolis parameter. When $Ro \rightarrow 0$ the nonlinearity of the equations of motion becomes weak, and the theories of weak wave interactions apply. The normal modes of the flow can be decomposed into zero-frequency 2D large scale structures and inertial waves (3D).

Rotating turbulent flow experiments and simulations are known to generate large-scale two-dimensional (2D) columnar structures from initially isotropic turbulence. Decaying turbulence simulations show this generation to be dependent on Rossby number, with three distinct regimes appearing [1]. These are the *weakly* rotating Ro regime, for which the turbulent flow is essentially unaffected by rotation, the *intermediate* Ro range, characterized by a strong transfer of energy from the wave to the 2D modes (with a peak at around Ro 0.2), and the *small* Ro range for which the 2D modes receive less and less energy from the wave modes as $Ro \rightarrow 0$.

The nonlinear processes involved in the generation of the intermediate Ro regime include the contribution of resonant and near-resonant inertial waves. The role of near-resonant was highlighted in forced turbulence at a moderately small Ro [2]. Discreteness effects on such interactions were quantified and a range of Ro over which both resonant and near-resonant interactions play important roles in finite domains was found [3]. These results allow us to undertake a robust numerical study of regime separation in forced rotating turbulence.

In this paper, we discuss the study of forced rotating homogeneous turbulence comparing various forcing schemes and numerical domains. We summarize our findings and turn our attention to the nature of the dominant interactions (found to be nonlocal) and to the generation of a condensate in the long-time limit.

2 Method and results

We used direct numerical simulations of homogeneous rotating turbulent flows in triply periodic domains. The resolutions and forcing schemes were selected according to the results obtained in [3] in order to ensure that all key interactions are captured by the simulations in finite domains. Forcings in both small and large scales and at various resolutions (e.g. 128^3 and 200^3) were compared. The range of rotation rates spanned Rossby numbers from approximately 10^{-2} to 2.

We found a robust regime separation in forced rotating turbulent flows. The three regimes found in decaying flows have their analogue in forced flows and are robust to the variation of resolutions and forcing configurations. The rate of energy transfer from the 3D to the 2D modes peaks for Ro around 0.2, independently of the chosen horizontal forcing scale.

Figure 1 shows 2D and 3D horizontal spectra for a flow forced at small 3D scales ($39 \leq k_h \leq 42$) with a 200^3 resolution. We recover a 2D horizontal energy spectrum of $\approx k_h^{-3.7}$ for $5 \leq k_h \leq 20$ with a less steep slope of $\approx k_h^{-2}$ for $20 \leq k_h \leq 50$. Note that similar spectral slopes were obtained when changing the resolution, while applying an analogous small scale 3D forcing. The steep slope is characteristic of the intermediate Ro regime and is consistent with previous forced simulations of rotating turbulence despite the use of different forcing schemes [4]. This shows the robustness of this steep slope, but does not explain its origin. Scaling theories are difficult to formulate for

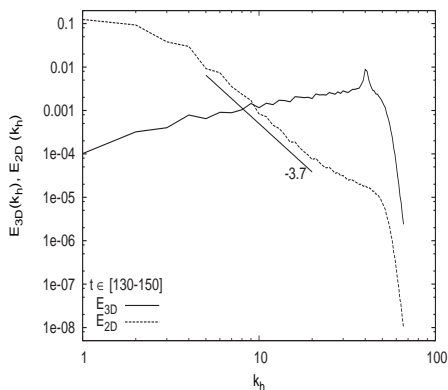


Fig. 1. Time-averaged horizontal 2D and 3D energy spectra for a simulation forced at small 3D horizontal scales.

rotating turbulence due to the lack of understanding of the elementary processes contributing to the energy transfers, particularly between the 3D and 2D modes. In order to clarify this discussion for the intermediate Ro regime,

we investigate the nonlocal or local nature of the dominant interactions, with a particular focus on the interactions between the triads with two 3D modes and one 2D mode, denoted $33 \rightarrow 2$.

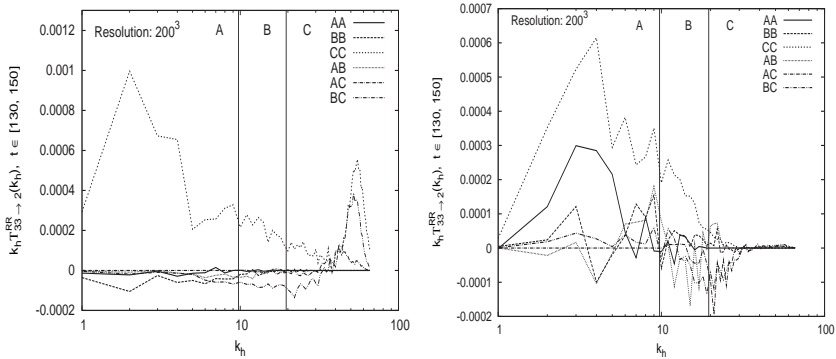


Fig. 2. Time-averaged horizontal energy transfer spectra for simulations forced in (left) small and (right) large 3D horizontal scales. Both simulations were performed at 200^3 resolution and the transfers were averaged over time $t \in [130, 150]$.

Figure 2 shows the energy transfers due to $33 \rightarrow 2$ interactions, where we filtered the contribution of 3D modes of different horizontal scales. This filtering allows us to identify the scales involved in the dominant 3D-2D triads of the intermediate Ro regime. We split the spectral scales into three regions (for example in Fig. 2 *A*, *B* and *C*, correspond to $k_h < 9.75$, $9.75 \leq k_h < 19.5$ and $k_h \geq 19.5$, respectively). Both forcings at small (region *C*) and large scales (region *A*) lead to dominant nonlocal transfers of energy. The dominant triads involve two small scale 3D modes directly injecting energy into a large horizontal 2D mode. This non-locality of the interactions was found to be robust to the change of forcing schemes and resolutions.

The nonlocal direct injection of energy into relatively large horizontal 2D scales shows that the steep ≈ -3 slope observed in the present and previous forced rotating turbulence flow simulations is not due to an inverse energy cascade range as would be expected when assuming a local interaction with such a small scale 3D forcing. In fact, a direct calculation of the 2D energy and enstrophy transfers showed that the energy injected in 2D modes in region *A* is transferred upscale, while the steep slope of the 2D spectrum corresponds to a spectral region of downscale enstrophy transfer to the dissipation scales (not shown).

Finally, using long-time simulations and various forcings, we find that the 2D dynamics of the forced intermediate Ro range reach a condensate state similar to that observed in classical two-dimensional turbulence and in MHD turbulence, in which energy accumulates in the largest scales of the finite

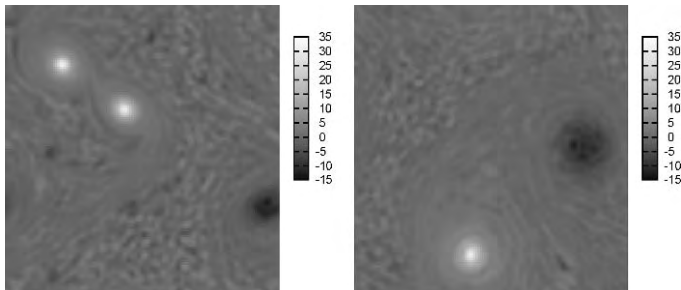


Fig. 3. Snapshots of a horizontal slice of the 2D vorticity ω_{2D} of a flow forced at (3D) wave scales of $26 \leq k_h \leq 28$, $k_z \neq 0$. They are shown at times (left) $t_1 = 167.4$ and (right) $t_2 = 317.4$ (condensate state), where turbulence is dominated by nonlocal interactions between small-scale 3D and large-scale 2D modes.

domain. A small 3D scale forcing was applied to a rotating flow during a long simulation run up to 14700 rotation timescales $(2\Omega)^{-1}$. Fig. 3 shows the snapshots of 2D vorticity fields, corresponding to 3800 and 7000 rotation periods. The 2D energy spectra associated with these snapshots are steeper than -3.25 with a clear accumulation of energy in the larger scales of the domain. The condensate formation explains the steep spectral slope observed.

3 Conclusion

Forced numerical simulations of rotating homogeneous turbulence have shown a robust regime separation analogous to that found in decaying turbulence in Ref. [1]. The intermediate Rossby regime in forced turbulence is characterized by a steep 2D energy spectrum, dominated by nonlocal interactions between wave and zero-frequency modes. These interactions transfer energy directly from the small wave scales to the large 2D scales. Forced simulations of rotating flows eventually lead to the formation of a condensate where the energy is concentrated in two dominant (2D) vortices of opposite sign. The steep 2D spectral slope of the forced intermediate Ro regime is not associated with an inverse energy cascade. This is true regardless of the scale of the 3D forcing.

References

1. L. Bourouiba and P. Bartello, *J. Fluid Mech.* **587**, 139 (2007).
2. L. Smith and Y. Lee, *J. Fluid Mech.* **535**, 111 (2005)
3. L. Bourouiba, *Phys. Rev. E* **78** 056309 (2008).
4. L. Bourouiba, Numerical and Theoretical Study of Homogeneous Rotating Turbulence, PhD dissertation, McGill University, (2008).

Structural Features of Rotating Sheared Turbulence

F.G. Jacobitz¹, W.J.T. Bos², K. Schneider³, and M. Farge⁴

¹Mechanical Engineering Program, University of San Diego, San Diego, CA 92110, USA, [jacobitz at sandiego.edu](mailto:jacobitz@sandiego.edu)

²LMFA-CNRS, Ecole Centrale de Lyon, Université de Lyon, 69134 Ecully, France

³M2P2-CNRS, Université de Provence, 13453 Marseille Cedex 13, France

⁴LMD-IPSL-CNRS, Ecole Normale Supérieure, 75231 Paris Cedex 5, France

Rotation and shear are important features of many geophysical flows and engineering applications (see for example Miesch [6]). Direct numerical simulations with constant vertical shear $S = \partial U_1 / \partial x_2$ and system rotation with constant Coriolis parameter $f = 2\Omega$ are considered in this study. The rotation axis is perpendicular to the plane of shear and points in the spanwise direction x_3 . It is therefore parallel or anti-parallel to the mean flow vorticity. The Cartesian coordinates x_1 , x_2 , and x_3 refer to the streamwise, vertical, and spanwise directions, respectively.

In previous studies by Bradshaw [2] and Tritton [10] the effect of rotation was found to be destabilizing in the anti-parallel configuration with $0 < f/S < 1$ and stabilizing otherwise. A comprehensive investigation of this flow was performed by Salhi and Cambon [8], Brethouwer [3], as well as Jacobitz, Liechtenstein, Schneider, and Farge [5].

The direct numerical simulations performed here are based on the continuity equation for an incompressible fluid and the unsteady three-dimensional Navier-Stokes equation. In the direct numerical approach, all dynamically important scales of the velocity field are resolved. The equations are solved in a frame of reference moving with the mean flow (Rogallo [7]) and periodic boundary conditions for the fluctuating components of the velocity field are applied. A spectral collocation method is used for the spatial discretization and the solution is advanced in time with a fourth-order Runge-Kutta scheme. The simulations are performed on a parallel computer using a grid with 256^3 points.

The results presented here are based on nine simulations of rotating sheared turbulence. The rotation ratio f/S was varied from -10 to 10 . Negative values of f/S correspond to a parallel orientation of system rotation and mean flow vorticity axes. Positive values of f/S correspond to an anti-parallel orientation. All simulations are initialized with isotropic turbulence fields. The initial Taylor microscale Reynolds number $Re_\lambda = 45$ and the ini-

tial shear number $SK/\epsilon = 2$ are matched in all cases. The Reynolds number reaches values as high as $Re_\lambda = 120$ and the shear number assumes a value of about $SK/\epsilon = 6$ in the simulations. The simulations analyzed in this study are identical to the ones reported in Jacobitz *et al.* [5].

Figure 1a shows the evolution of the turbulent kinetic energy K for the series of simulations in which the rotation ratio f/S is varied. Due to the isotropic initial conditions, the turbulent kinetic energy first decays. The non-rotating case with $f/S = 0$ shows eventual exponential growth of K . For moderate rotation ratios, the anti-parallel case with $f/S = +0.5$ leads to strong growth of the turbulent kinetic energy, while the parallel case with $f/S = -0.5$ results in decay of K . For strong rotation ratios, however, both the anti-parallel case with $f/S = +10$ and the parallel case with $f/S = -10$ lead to strong decay of K due to the importance of linear effects. These observations agree with previous results by Bradshaw [2], Tritton [10], and Brethouwer [3].

Figure 1b shows the dependence of the components of the Reynolds shear stress anisotropy tensor $b_{ij} = \overline{u_i u_j} / \overline{u_k u_k} - \delta_{ij}/3$ on the rotation ratio f/S at non-dimensional time $St = 5$. The diagonal components of b_{ij} correspond to the distribution of energy on the velocity components. For most rotation ratios, an ordering $b_{11} > b_{33} > b_{22}$, or streamwise $>$ spanwise $>$ vertical, is observed. Only in the anti-parallel cases with $0 < f/S < 1$ this ordering is changed to $b_{22} > b_{33} > b_{11}$, or vertical $>$ spanwise $>$ streamwise. The magnitude of the off-diagonal component b_{12} is largest for $f/S = +0.5$, corresponding to the strongest growth of the turbulent kinetic energy K . Note that the normalized turbulence production rate $P/(SK) = -2b_{12}$ is directly related to the anisotropy features of the flow.

Figure 2 shows the directional energy of the flow for two cases with (a) $f/S = +0.5$ and (b) $f/S = +5$ at non-dimensional time $St = 5$. Orthogonal wavelets allow to give an alternative description with additional information of the anisotropy of the flow [1]. Wavelets, similar to structure functions, are sensitive to velocity differences in the different directions. This allows to characterize longitudinal and transversal anisotropy. Furthermore, orthogonal wavelets have the advantage that the energy contained in the different direction sums up to the total energy, unlike structure functions or one-dimensional Fourier spectra. For the strongly growing case with $f/S = +0.5$ the spanwise differences of vertical velocity contain most of the energy, followed by the spanwise differences of downstream velocity. For the strongly decaying case with $f/S = +5$, however, the vertical differences of spanwise and downstream velocities contain most of the energy, while vertical velocity is reduced.

In order to investigate the effect of shear and rotation on the turbulence structure volume visualizations of the magnitude of fluctuating vorticity are considered [4]. Figure 3 shows vortical structures for two cases with (a) $f/S = +0.5$ and (b) $f/S = +5$ at non-dimensional time $St = 5$. The vortical structures are inclined in the vertical direction to the downstream direction by an angle α . This angle is larger for the strongly growing case with $f/S = +0.5$

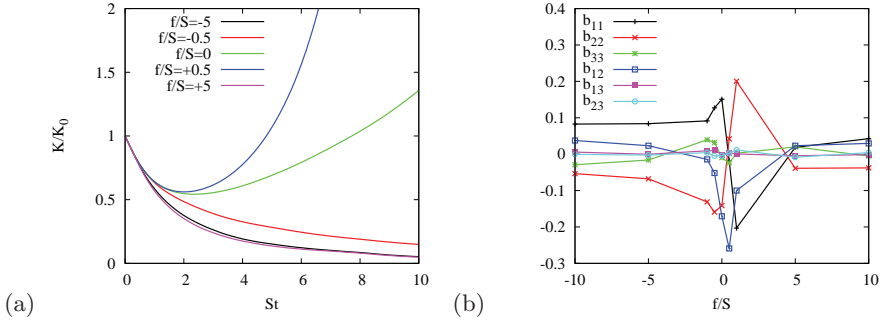


Fig. 1. (a) Evolution of the turbulent kinetic energy k in non-dimensional time St . (b) Dependence of the components of the Reynolds stress anisotropy tensor b_{ij} on the rotation ratio f/S at non-dimensional time $St = 5$.

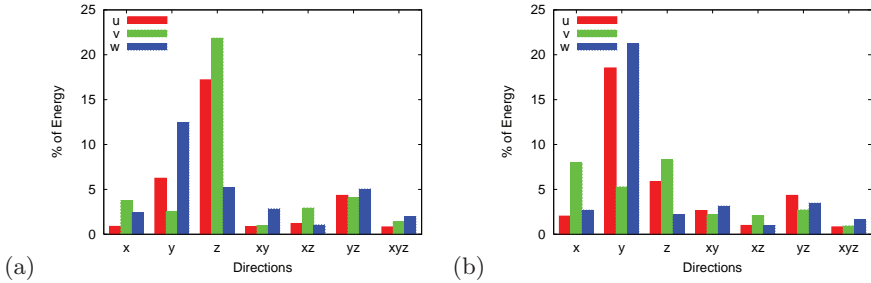


Fig. 2. Wavelet-based directional energy for cases with (a) $f/S = +0.5$ and (b) $f/S = +5$ at non-dimensional time $St = 5$.

compared to the decaying case with $f/S = +5$. The inclination angle α of vortical structures directly influences the strength or turbulence growth or decay. In the decaying case with $f/S = +5$, the vortical structures are patchy and somewhat resemble structures found in stratified flows. Salhi [9] pointed out similarities between rotation and stratification effects in homogeneous shear flow using rapid distortion theory.

Additional geometrical information about the flow can be obtained from the relative helicity of velocity h_u and relative helicity of vorticity h_ω :

$$h_u = \frac{\mathbf{u} \cdot (\nabla \times \mathbf{u})}{\|\mathbf{u}\| \|\nabla \times \mathbf{u}\|} \quad h_\omega = \frac{\omega \cdot (\nabla \times \omega)}{\|\omega\| \|\nabla \times \omega\|}$$

The relative helicity measures the cosine of the angle between the two vector quantities. Figure 4 shows the PDFs of relative helicity of (a) velocity and (b) vorticity. The relative helicity of velocity h_u allows to distinguish between helical structures (swirling motion) for which h has values of ± 1 , which correspond to alignment or anti-alignment of vorticity and velocity, respectively. Two-dimensionalization of the flow, i.e., vorticity is perpendicular to velocity,

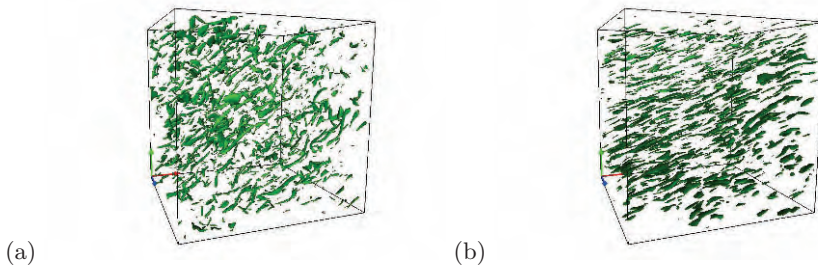


Fig. 3. Volume visualization of vortical structures for cases with (a) $f/S = +0.5$ and (b) $f/S = +5$ at non-dimensional time $St = 5$.

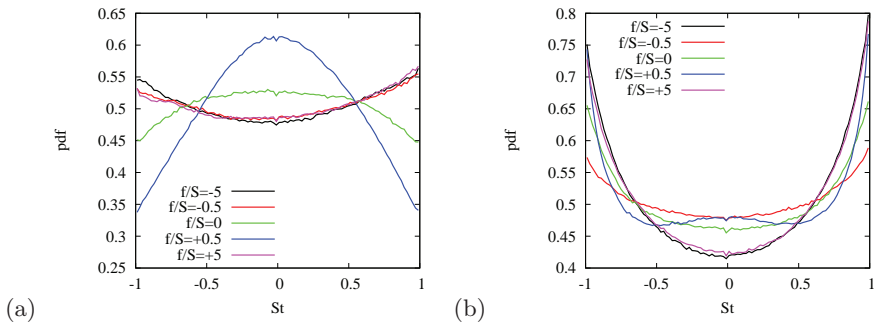


Fig. 4. Helicity distribution of (a) velocity H_u and (b) vorticity H_ω at non-dimensional time $St = 5$.

results in $h = 0$. The PDFs of h_u show a maximum for $h_u = 0$ for growing cases and a maximum for $h_u \pm 1$ for decaying cases. The PDFs of h_ω show a maximum for $h_\omega \pm 1$ for all cases.

We thank B. Kadoch for the preparation of the volume visualizations.

References

1. W.J.T. Bos, L. Liechtenstein, K. Schneider, Phys. Rev. E, **76**, 046310 (2007).
2. P. Bradshaw, J. Fluid Mech., **36**, 177 (1969).
3. G. Brethouwer, J. Fluid Mech., **542**, 305 (2005).
4. J. Clyne, P. Mininni, A. Norton, M. Rast, New J. Phys., **9**, 301 (2007).
5. F.G. Jacobitz, L. Liechtenstein, K. Schneider, M. Farge, Phys. Fluids, **20**, (2008).
6. M.S. Miesch, Living Rev. Solar Phys., **2**, 1 (2005).
7. R.S. Rogallo, Technical Report TM 81315, NASA, Moffett Field, CA, (1981).
8. A. Salhi and C. Cambon, J. Fluid Mech., **347**, 171 (1997).
9. A. Salhi, Theoret. Comp. Fluid Dyn., **15**, 339 (2002).
10. D.J. Tritton, J. Fluid Mech., **241**, 503 (1992).

Structure functions and energy transfers in a decaying rotating turbulence experiment

F. Moisy, L. Agostini, and G. Tan

Université Paris-Sud; Université Pierre et Marie Curie; CNRS. Laboratoire FAST (Fluides, Automatique et Systèmes Thermiques), Bâtiment 502, 91405 Orsay, France

moisy at fast.u-psud.fr

A key feature of rotating turbulence is the anisotropic transfer of energy towards horizontal modes, normal to the rotation axis $\mathbf{\Omega} = \Omega\hat{\mathbf{z}}$, eventually driving turbulence to a quasi-two-dimensional state [1, 2, 3]. While nonrotating homogeneous and isotropic turbulence shows direct energy cascade towards small scales, the energy may be transferred in homogeneous rotating turbulence both in scale and direction.

In isotropic turbulence, the energy transfers are classically described in the physical space using the 3rd order structure function, $S_3(r) = \langle \delta_r u^3 \rangle$, where $\delta_r u = [\mathbf{u}(\mathbf{x} + \mathbf{r}) - \mathbf{u}(\mathbf{x})] \cdot \mathbf{r}/r$ is the longitudinal velocity increment. Exact results for this quantity are $S_3 = -\frac{4}{5}\epsilon r$ in 3D turbulence, and $S_3 = +\frac{3}{2}\epsilon r$ in 2D turbulence, with ϵ the rate of energy injected in the system. The sign of $S_3(r)$ is indeed related to the direction of the energy flux: positive (resp. negative) for transfers towards larger (resp. smaller) scales. To date, no exact anisotropic extension of the 4/5th law has been derived for homogeneous rotating turbulence. A recent attempt to derive a quasi-isotropic form of the 4/5 law under weak rotation has been carried out by Chakraborty and Bhattacharjee (2007) [4].

Recently, several experiments have reported the possibility of a change of sign of the 3rd order structure function for separations in the plane normal to $\mathbf{\Omega}$ [5, 6, 7]. In the experiment of Baroud et al. [6], where turbulence is forced by radial jets originating from a circular array of source holes in a rotating annulus, a change of sign is observed on S_3 . A change of sign of $S_3(r)$ has also been reported in our experiment of decaying grid-generating turbulence in a rotating tank [7]. This change of sign is found to occur at a scale r_0 which is decreasing during the decay, although this trend was not characterized in details in this work.

We present here experimental results of decaying turbulence in a rotating frame [7, 8, 9], aiming to further investigate the influence of the background rotation on the 3rd order structure function. The experiment consists in a water filled tank of square section, of side 35 cm and height 44 cm, rotating

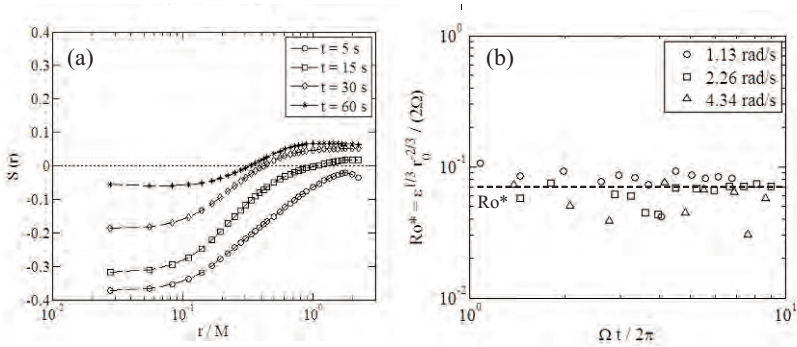


Fig. 1.1. (a) Skewness of the longitudinal velocity increments, $S(r) = S_3(r)/S_2(r)^{3/2}$, measured in the plane normal to the rotation axis, at four times during the decay. The scale r_0 where S_3 changes sign is a decreasing function of time. (b) The local Rossby number (1.1) computed at the scale r_0 , for different rotation rates.

at constant angular velocity. Turbulence is generated by towing a co-rotating square grid from the bottom to the top of the tank. Structure functions are computed from the horizontal components of the velocity in a horizontal plane at mid height of the tank, using a corotating Particle Image Velocimetry system.

Figure 1.1(a) shows that the skewness of the velocity increments, $S(r) = S_3(r)/S_2(r)^{3/2}$, measured in a plane normal to Ω , crosses zero at a scale r_0 , with r_0 being a decreasing function of time. This change of sign suggests that scales $r \ll r_0$ transfer energy towards small scales, whereas larger scales, $r \gg r_0$, show a behavior consistent with transfers towards larger scales. Although a positive S_3 can be clearly associated to an inverse energy cascade for forced turbulence [6], its physical signification is unclear in the case of decaying turbulence, since no energy is supplied at scale r_0 .

This scale r_0 can be tentatively interpreted as the crossover scale separating 3D turbulence at small scales with no influence of the rotation (large Rossby number), and a flow at larger scales dominated by the rotation (low Rossby number), in analogy with the Ozmidov scale of stratified turbulence [10, 11]. This interpretation can be indeed tested by computing a local Rossby number, defined as

$$Ro(r) = S_2(r)^{1/2} / (2\Omega r) \quad (1.1)$$

where $S_2(r) = \langle \delta_r u^2 \rangle$ is the 2nd order structure function. Accordingly, $Ro(r)$ should take a constant value of order unity at scale $r = r_0$, which we denote $Ro(r_0) = Ro^*$. Assuming that the 2/3 law remains verified for $r = r_0$, i.e. $S_2(r) \simeq (\epsilon r)^{2/3}$, one has $Ro^* = \epsilon^{1/3} r_0^{-2/3} / (2\Omega)$. This quantity, plotted in Fig. 1(b) as a function of time for various rotation rates, is indeed approximately constant, $Ro^* \simeq 0.07 \pm 0.03$, confirming this simple picture.

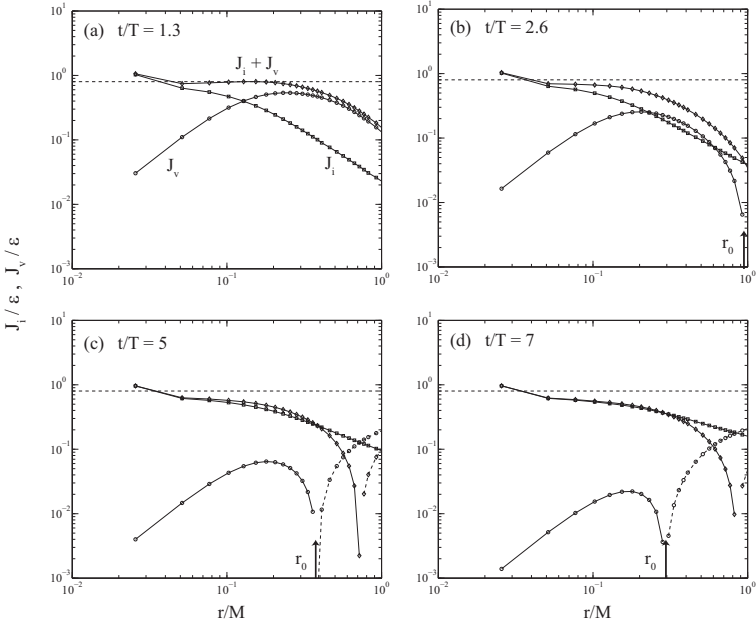


Fig. 1.2. The 2 contributions of the von Kármán-Howarth equation (1.2), $J_i = -S_3/r$ and $J_v = 6\nu\partial S_2/\partial r$, and their sum $J_i + J_v$, non-dimensionalized by the instantaneous dissipation rate ϵ , at 4 different times during a decay experiment with $\Omega = 1.13 \text{ rad s}^{-1}$. The horizontal dashed line shows the value $4/5$ expected for isotropic turbulence.

Since no accumulation of energy at large scale is observed in decaying turbulence (in particular, $S_2(r)$ is found to decrease in time for all r), the interpretation of a positive $S_3(r)$ for $r > r_0$ in terms of an inverse cascade is questionable. In particular, the relationship between the sign of S_3 and the direction of the energy transfers holds only in the isotropic case. For anisotropic turbulence, there is the possibility that the horizontal velocity actually cascades towards large scales, while the vertical velocity, behaving as a passive scalar advected by the horizontal motion, cascades towards small scales. Since $S_3(r)$ is related only to the horizontal velocity here, it may be indeed related to the direction of the energy cascade for the horizontal mode.

Another possibility is that the viscous effects may start to play a role in the energy decay at large times, for $r \simeq r_0$. In order to test the effect of the viscosity in the energy decay, we can measure the different contributions of the von Kármán-Howarth equation,

$$-\frac{S_3}{r} + \frac{6\nu}{r} \frac{\partial S_2}{\partial r} = \frac{4}{5}\epsilon, \quad (1.2)$$

which reduces to the $4/5$ th law in the inertial range in the limit of large Reynolds numbers. Although this equation is not valid for anisotropic turbu-

lence, we aim to check to what extent it remains verified at small times in decaying rotating turbulence, for measurements restricted to the horizontal plane.

The two terms of the left-hand side of Eq. (1.2), noted J_i (inertial) and J_v (viscous), are plotted in figure 1.2 at 4 times. At small time, the sum of the two terms remains close to the value expected for isotropic turbulence, $J_i + J_v = \frac{4}{5}\epsilon$, for all r . As time proceeds, when the inertial contribution J_i crosses zero at $r = r_0$, the viscous contribution J_v becomes gradually dominant, so that the sum $J_i + J_v$ remains positive at $r = r_0$. This would suggest that, although the nonlinear terms shows a trend towards inverse energy transfer, this effect is actually hidden by the viscous effects, resulting in an overall decay at all scales. A zero crossing of the sum $J_i + J_v$ may possibly be present at even larger scales, but this effect can not be checked by the presently available data.

More insight into the behavior of the 3rd order structure function in rotating turbulence could be gained from an isotropic generalization of the von Kármán-Howarth relation, for separations r normal and perpendicular to the rotation axis. In particular, it would be of first interest to check whether the zero crossing of $S_3(r)$, observed both in forced [5, 6] and decaying [7] turbulence, is an artifact of the restriction to horizontal velocity measurements, or a true effect that could be related to an inverse energy cascade of the 2D mode.

This work was supported by the ANR project no. 06-BLAN-0363-01 “HiSpeedPIV”.

References

1. F. Waleffe, *Phys. Fluids A* **5** (3), 677 (1993).
2. C. Cambon, N. N. Mansour, and F. S. Godeferd, *J. Fluid Mech.* **337**, 303 (1997).
3. S. Galtier, *Phys. Rev. E* **68**, 015301R (2003).
4. S. Chakraborty, J.K. Bhattacharjee, *Phys. Rev. E* **76**, 036304 (2007).
5. C. Simand, F. Chillà, and J.-F. Pinton, *Europhys. Lett.* **49** (3), 336 (2000); **49** (6), 821 (2000).
6. C. N. Baroud, B. B. Plapp, Z.-S. She, and H. L. Swinney, *Phys. Rev. Lett.* **88**, 114501 (2002).
7. C. Morize, F. Moisy and M. Rabaud, *Phys. Fluids* **17**, 095105 (2005).
8. C. Morize, and F. Moisy, *Phys. Fluids* **18**, 065107 (2006).
9. J. Seiwert, C. Morize and F. Moisy, *Phys. Fluids* **20**, 071702 (2008).
10. O. Zeman, *Phys. Fluids* **6**, 3221 (1994).
11. Y. Zhou, *Phys. Fluids* **7**, 2092 (1995).

Table-top rotating turbulence: an experimental insight through particle tracking

L. Del Castello¹, H.J.H. Clercx¹, R.R. Trieling¹, and A. Tsinober²

1. JM Burgerscentrum and Fluid Dynamics Laboratory, Dept. of Applied Physics, Eindhoven University of Technology, The Netherlands
2. Inst. Math. Sciences and Dept. of Aeronautics, Imperial College London, United Kingdom
l.delcastello at tue.nl

Introduction

Background rotation may seriously affect the dynamics of fluid flows when the relative importance of the nonlinear acceleration over the Coriolis force becomes small enough. It has a relevant effect on turbulent dispersion and mixing in geophysical and engineering flows, and acts with different mecha-

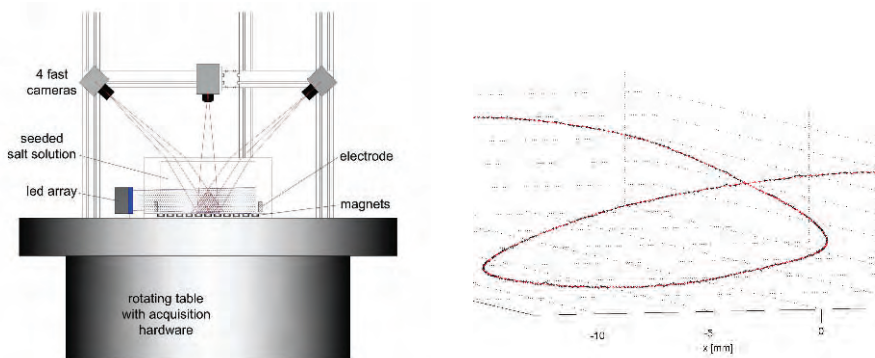


Fig. 1. Left panel: sketch of the setup on the rotating table. Right panel: a typical trajectory as recovered through PTV.

nisms: the Coriolis force makes the flow strongly anisotropic and reduces the energy dissipation [1, 2]. The background rotation reduces the overall dispersion and particularly in the direction parallel to the rotation axis. At the same time, it leads to the formation of Ekman layers close to the horizontal no-slip boundaries, responsible for an enhancement of the vertical mixing by pumping effects.

The Lagrangian viewpoint in turbulent diffusion is not only natural, but also practical. Yeung [3] points to a major lack of experimental data in the Lagrangian setting. However, in the last few years the development of tracking techniques allowed to access multi-particle statistics directly in the Lagrangian frame, e.g. Ref. [4, 5].

Exploratory experiments in rotating turbulence

The aim of this work is to feed the fundamental investigation of turbulence with experimental data, giving further insight into the anisotropic effects of rotation. Experiments of electromagnetically forced turbulence are performed in a confined tank put on a rotating table (see Fig. 1): the forcing acts in the bottom region, inducing a turbulent flow ($Re_\lambda \sim 150$) which decays along the upward vertical direction. The Rossby number $Ro = \frac{U^2/L}{2U\Omega}$ (with the typical length scale L chosen as the magnet spacing, U the rms velocity, and Ω the rotation rate) is varied between ∞ and 0.013. A 3D-PTV technique, based on the code developed at ETH (Zurich) [6], is used to extract trajectories in a volume comparable with the integral scale.

A first set of experiments allowed us to fully characterise the flow in the Eulerian frame, and also to define the appropriate set of parameters for additional experiments suitable for computing long-time velocity correlations, and single-particle and particle-pairs dispersion. The Eulerian analysis showed

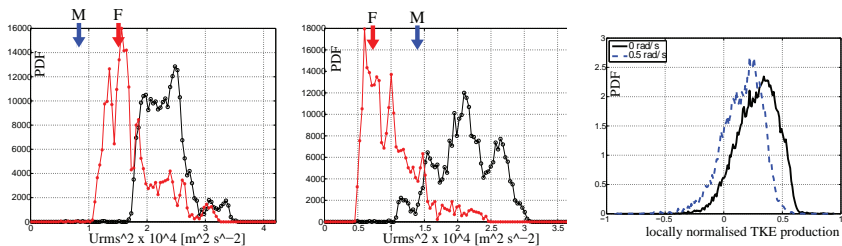


Fig. 2. Left and central panels: PDFs of kinetic energy, from the reference non-rotating experiment and a 0.5 rad/s run, respectively. The PDFs correspond to the total flow (black) and the fluctuating part (red/grey), and the arrows indicate the average energy value of the mean flow (M) and the fluctuating one (F). Right panel: PDF of locally normalised TKE production $\frac{-\langle u_i u_j \rangle S_{ij}}{\sqrt{\langle u_i u_j \rangle \langle S_{ij} S_{ij} \rangle}}$ for the same two experiments.

that a considerable part of the kinetic energy is transferred from the fluctuating field to the time-averaged flow when increasing the rotation rate, as illustrated in the left and central panels of Fig. 2: the mean flow overcomes the fluctuating flow in terms of energy content, this being a clear indication of the regularisation effect of the background rotation. The overall energy

dissipation is reduced, and the Kolmogorov scales increased. Moreover the distribution of the turbulent kinetic energy production shows a reduction of its positive skewness with increasing rotation rate; when this quantity is made non-dimensional using the local magnitude of the mean flow strain rate tensor and the one of the Reynolds stress tensor (as done in [7]), its probability density function still shows a reduction of its positive skewness with increasing rotation rate (see Fig. 2, right panel). This indicates that the TKE production is diminished also due to the reduced correlation of the two tensors. Both these features characterise all rotating runs, clearly distinguishable with a mild rotation of 0.5 rad/s already, and even more pronounced for faster rotation rates.

The analysis of particle-pairs dispersion out of the first set of experiments

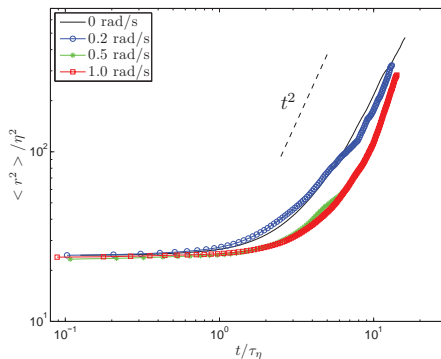


Fig. 3. Normalised mean-squared separation of particle-pairs, showing the t^2 -slope typical of the initial ballistic regime.

shows well-known features at short times: as shown in Fig. 3, the ensemble average curves reach the t^2 -slope characteristic of the initial ballistic regime for all rotating runs. For longer times, data do not permit robust statistics, nevertheless it is clear that the effect of rotation is anisotropic: the damping of the slope of the curves is greater for the vertical component (parallel to the rotation axis) than for the horizontal ones, at all rotation rates.

Ongoing experiments

In order to proceed with the analysis, a new set of experiments is performed: the measurement volume is increased of a 20% in size along each of the three directions (now 100^3 mm^3); the number of tracked particles is roughly doubled (up to 2500 tracked particles on average between time-steps); the recording time is extended to 30 eddy turn-over times. The new data (sample velocity and vorticity fields are shown in Fig. 4) show the same features in the Eulerian frame as described above, and it will allow us to quantify in a wider range

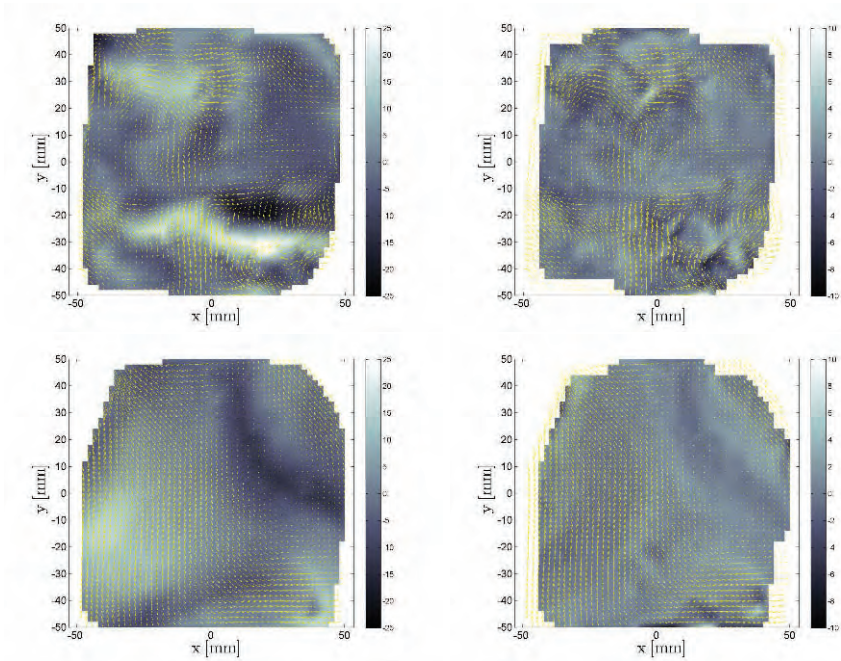


Fig. 4. Mid-height horizontal slices of instantaneous velocity fields from the latest experiments, interpolated on regular grid. Left column: vector map of horizontal velocity components and grey scale map of vertical velocity component (mm/s); right column: vector map of horizontal velocity components and grey scale map of vertical vorticity (mm/s and mm/s², respectively). First row: reference non-rotating experiment; second row: fast rotating (5 rad/s) experiment.

of the turbulence spectrum the dispersion of single particles and of particle-pairs, together with Eulerian and Lagrangian time-correlations of velocity. The description of the effects of rotation will also include the distribution and the auto-correlation of particle accelerations.

References

1. L. Jacquin, O. Leuchter, C. Cambon, J. Mathieu: *J. Fluid Mech.* **220**, 1 (1990)
2. P. Orlandi: *Phys. Fluids* **9**, 1 (1997)
3. P.K. Yeung: *Annu. Rev. Fluid Mech.* **34**, 115 (2002)
4. S. Ott, J. Mann: *J. Fluid Mech.* **422**, 207 (2000)
5. B. Lüthi, S. Ott, J. Berg, J. Mann: *J. Turbulence* **8**, 45 (2007)
6. H.G. Maas, A. Gruen, D. Papantoniou: *Exp. Fluids* **15**, 133 (1993)
7. A. Liberzon, M. Guala, W. Kinzelbach, A. Tsinober: *Phys. Fluids* **18**, 125101 (2006)

On the structure of rapidly-rotating, decaying turbulence

P.A. Davidson and P.J. Staplehurst

Department of Engineering, Cambridge University, Cambridge, UK, CB2 1PZ
pad3@eng.cam.ac.uk

Laboratory experiments of rotating turbulence at a Rossby number of order unity show three robust phenomena: (i) the rapid formation of columnar eddies aligned with the rotation axis; (ii) a dominance of cyclonic eddies over anti-cyclones; and (iii) a reduction in the rate of energy decay [1], [2]. We review recent experimental results which confirm that the observed columnar eddies are simply transient Taylor columns formed by linear inertial wave propagation [2], a phenomenon which was predicted earlier on the basis of angular momentum conservation [1]. We also offer an explanation for the dominance of cyclones. Finally, we provide evidence that the kinetic energy decays as $u^2 \sim (\Omega t)^{-1}$, a result which can be explained in terms of the conservation of a Loitsyansky-like integral.

Introduction

We consider rotating turbulence in which the velocity in the rotating frame, \mathbf{u} , is smaller than, or of the order of, $|\boldsymbol{\Omega}|\ell$, where $\boldsymbol{\Omega} = \Omega\hat{e}_z$ is the rotation vector and ℓ an integral scale. It is well known that such turbulence is characterised by the presence of large columnar eddies aligned with the rotation axis [1], [2], [3], and there has been much discussion as to the mechanism by which these columnar structures form. The various theories differ in detail but all agree that inertial waves play an important rôle. Nearly all theories focus on the case of small Rossby number, $Ro = u/\Omega\ell \ll 1$, and suggest that anisotropy results from a weak non-linear coupling of the waves; so-called resonant triads [4]. However, a quite different, and simpler, explanation for the growth of the columnar eddies was put forward in [1]. It too is posed in the context of $Ro \ll 1$, but does not require non-linearity. Rather, it relies on the idea that the large energy-containing eddies in the turbulence will elongate along the rotation axis by radiating energy in the form of linear inertial waves. This leads to the prediction that the large eddies, and hence the integral scale parallel to $\boldsymbol{\Omega}$, will elongate at a rate set by the group velocity of inertial waves.

How columnar eddies form

We start by summarizing the linear theory of [1], which offers a simple explanation for the growth of columnar structures at low Ro . Consider the initial value problem of a localised blob of vorticity sitting in an otherwise quiescent, rapidly-rotating fluid. Let the characteristic scale of the blob be δ and a typical velocity be u . If $Ro \ll 1$, then the subsequent motion consists of a spectrum of linear inertial waves whose group velocity is dictated by the initial distribution of wavenumbers, \mathbf{k} , in accordance with $\mathbf{c}_g = \pm 2\mathbf{k} \times (\boldsymbol{\Omega} \times \mathbf{k})/k^3$. Thus the energy will disperse in all directions with a typical speed $c_g \sim \Omega\delta$. However, this radiation of energy is subject to a powerful constraint, which systematically favours dispersion of energy along the rotation axis. Let V_R be a cylindrical volume of infinite length that circumscribes the vortex blob at $t = 0$. Then it is shown in [1] that the axial component of angular momentum held within V_R is conserved for all time. In short, angular momentum can disperse along the rotation axis only.

This constraint systematically biases the dispersion of energy. For example, as the energy radiates to fill a volume whose size grows as $(\delta\Omega t)^3$, conservation of energy requires that the velocity outside V_R falls as $u \sim u_0(\Omega t)^{-3/2}$. However, inside V_R the angular momentum is confined to a cylindrical region of size $\Omega t\delta^3$, and so a typical velocity inside V_R falls more slowly, as $u \sim u_0(\Omega t)^{-1}$. (These predictions can be confirmed by direct calculation using stationary phase.) Thus the energy density inside V_R is always greater than that outside, and so the dominant effect of inertial wave radiation is to spread the energy of the vortex along the rotation axis. In short, the eddy splits to form pairs of Taylor columns whose length grows as $\ell_z \sim \delta\Omega t$, as shown in Fig. 1(a).

Now consider an initial condition consisting of many such vortex blobs randomly, but uniformly distributed in space. Each vortex will behave as above, spontaneously forming columnar eddies, and it is readily confirmed that, for $\Omega t \gg 1$, the two-point velocity correlations are self-similar when r_z is scaled by $\Omega\delta t$ [2]. This admits the simple physical interpretation that all of the eddies grow in the axial direction at the rate $\ell_z \sim \delta\Omega t$, which is the hallmark of energy dispersion by linear inertial waves. Crucially, this prediction provides a simple test to distinguish between columnar vortex formation via linear and non-linear mechanisms.

The experimental evidence at $Ro \sim 1$

We now turn to the experiments [2]. Here Ro drifts down towards unity as the energy of the flow decays. Four robust phenomena were observed: (i) when Ro reaches a value close to unity, columnar eddies start to form and these eventually dominate the large, energy-containing scales; (ii) during the formation of these columnar eddies, the integral scale parallel to the rotation axis grows linearly in time, $\ell_z \sim \ell_0\Omega t$; (iii) more cyclones than anticyclones are observed; (iv) the energy decay rate is reduced by rotation.

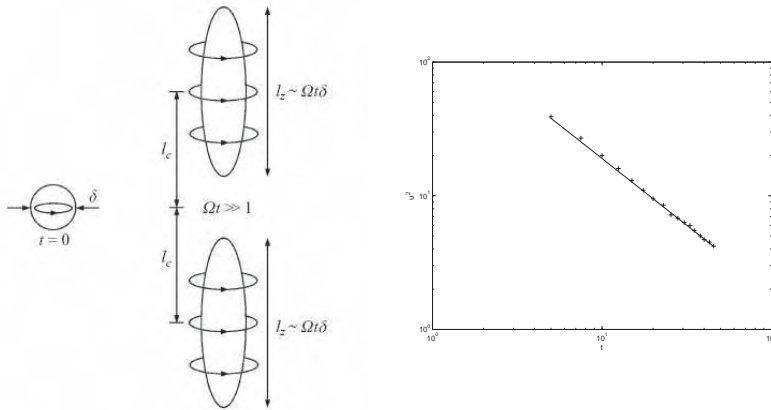


Fig. 1. (a) An initial blob of vorticity converts itself into a pair of columnar eddies (Taylor columns) via linear inertial wave propagation, $Ro \ll 1$. (b) Plot of energy against time from the experiments of [2]. The solid line is $u^2 \sim t^{-1}$.

The fact that the integral scale grows as $l_z \sim \ell_0 \Omega t$ is highly suggestive that the columnar eddies form by linear wave propagation, and not by resonant triad interactions. This is perhaps surprising, since $Ro \sim 1$. In order to check this hypothesis, two-point velocity correlations were measured as a function of r_z and t . This was done for four different experiments which had varying values of Ω and ℓ_0 , but were otherwise similar. According to linear theory, the velocity correlations from all four experiments and at all times in each experiment should collapse onto a single universal curve, provided r_z is normalised by $\Omega \ell_0 t$. This is exactly what was found, so there is no doubt that the columnar vortices seen in [2] were formed by linear wave propagation, despite the fact that $Ro \sim 1$.

Why linear behaviour at $Ro \sim 1$?

Let us now consider the curious observation that linear wave propagation can persist up to a Rossby number of $Ro \sim 1$. Numerical simulations were undertaken in [5] to investigate this very point, in which a single eddy (blob of vorticity) was allowed to evolve in the presence of background rotation. A range of initial values of Ro was considered, from 0.1 to 4.0, and both cyclones and anticyclones were computed. For small Ro the eddies evolved into columnar structures as shown in fig. 1 (a), and of course there is no difference between the behaviour of cyclones and anticyclones in the linear regime. At high Ro , on the other hand, the vortices behave very differently, bursting radially outward under the influence of the centrifugal force. Perhaps the most surprising aspect of the computations, though, is that the transition

from linear to fully non-linear behaviour is abrupt. In the case of cyclones the transition occurs in the narrow range $1.4 < Ro < 3.0$, with columnar vortex formation below $Ro = 1.4$ and centrifugal bursting for $Ro > 3.0$. The equivalent range for anticyclones is also surprisingly narrow, $0.4 < Ro < 1.6$. These findings illustrate how quasi-linear inertial wave propagation can persist up to Rossby numbers of $Ro \sim 1$, which is consistent with the experiments of [2].

The results of [5] are also interesting from the point of view of the observed dominance of cyclones over anticyclones. Notice that the transition range of Ro is different for cyclones and anticyclones, with the anticyclones requiring a lower value of Ro to form columnar structures. Now in the experiments of [2] we start with a high value of Ro , but as Ro drifts down towards $Ro \sim 1$, columnar eddies start to appear. From the asymmetry described above, we might expect the first columnar structures to be cyclones, with significantly lower values of Ro needed to generate anti-cyclonic columns.

The Decay of Energy

We conclude by discussing the energy decay rate, which is known to be suppressed by rotation. It is shown in [6] that, subject to certain caveats, homogeneous turbulent flows which are statistically axisymmetric possess a Loitsyansky-like invariant. This includes MHD, stratified and rotating turbulence. If the large scales in such a flow are self-similar, this then requires $u_{\perp}^2 \ell_{\perp}^4 \ell_z = \text{constant}$. Moreover, we have already seen that, once the Rossby number falls below unity, ℓ_z grows as $\ell_z \sim \ell_0 \Omega t$. It follows that, in freely-decaying, rapidly-rotating turbulence, $u_{\perp}^2 \ell_{\perp}^4 \ell_0 \sim (\Omega t)^{-1}$. This is interesting because $\ell_{\perp} \sim \text{constant}$ during the linear growth of ℓ_z and the decay data of [2], which is shown in fig.1(b), seems to follow the power law $u_{\perp}^2 \sim (\Omega t)^{-1}$, consistent with $u_{\perp}^2 \ell_{\perp}^4 \ell_0 \sim (\Omega t)^{-1}$.

References

1. P.A. Davidson, P.J. Staplehurst, S.B. Dalziel, *J. Fluid Mech.* **557** (2006).
2. P.J. Staplehurst, P.A. Davidson, S.B. Dalziel, *J. Fluid Mech.* **598** (2008).
3. C. Morize, F. Moisy, M. Rabaud. *Phys. Fluids* **17** (2007).
4. L.M. Smith, F.J. Waleffe, *Fluid Mech.* **451** (2002)
5. B. Sreenivasan, P.A. Davidson, *Phys. Fluids* **20** 2008.
6. P.A. Davidson, *Turbulence*, Oxford University Press (2004).

Large-eddy simulations of gravity current flows past submerged cylinders

E. Gonzalez-Juez ¹, E. Meiburg ¹, G. Constantinescu ², and T. Tokyay ²

¹ Department of Mechanical Engineering, University of California at Santa Barbara

² Department of Civil and Environmental Engineering, University of Iowa
meiburg@engineering.ucsb.edu

As the offshore oil and gas industry moves towards deeper ocean environments, submarine structures such as oil and gas pipelines become increasingly exposed to less understood hazards, among them gravity and turbidity currents. Our incomplete understanding of the interaction between gravity currents and submarine structures has motivated several recent experimental [1, 2] and numerical [3, 4, 5, 6, 7] investigations. Whereas previous studies focus on the force exerted on submerged cylinders and on the two-dimensional dynamics of the interaction, the current investigation places emphasis on the magnitude of the wall shear stresses near the cylinder calculated from three-dimensional simulations. This shear stress is related to the process of scour near submarine structures [8].

We use the flow configuration shown in figure 1, and solve numerically the Navier-Stokes equations in the Boussinesq approximation with the large-eddy-simulation method developed by Pierce [9]. The simulation code has been validated for the simulation of gravity currents [10] and gravity current flows past submerged cylinders [4]. As governing dimensionless parameters we identify the Reynolds and Schmidt numbers, respectively, $Re = \sqrt{g'h}h/\nu$ and $Sc = \nu/\kappa$, where g' is the reduced gravity, h the lock height, ν represents the kinematic viscosity, and κ the molecular diffusivity. In addition, there are various geometrical parameters, cf. figure 1, the most important ones being H/h , D/h , and G/h . The gravity current front speed is denoted with V . In the following, we discuss results from a representative three-dimensional simulation with the following parameters: $Re = 45,000$, $Sc = 1$, $H/h = 2.5$, $D/h = 0.1$, and $G/h = 0.03$.

As the current approaches the cylinder, cf. Figs. 2a and 3a, the wall shear stress right below the cylinder increases, and reaches a maximum value when the current impacts the cylinder, cf. Fig. 3b. Notice in Fig. 2a the lobe and cleft structure at the current front [11], as well as the Kelvin-Helmholtz billows further upstream. Also notice in Figs. 3a and 3b the effect of the lobe and cleft structure on the wall shear stress. The larger wall shear stress near the

lobes may trigger localized scour. After impact, the head of the current plunges downstream of the cylinder, producing a high level of wall shear stresses there, cf. Fig. 3c. Later on, the flow around the cylinder reaches a quasisteady stage, and the gravity current reestablishes itself downstream of the cylinder, cf. Fig. 2b. For sufficiently large gaps, the wall shear stress downstream of the cylinder fluctuates due to vortex shedding, cf. Fig. 3d. Hence lee wake erosion may occur [8]. The magnitude of the wall shear stress at impact is observed to be 2.6 times higher than that during the quasisteady stage, for a wide range of parameters [7]. Therefore, aggressive tunneling erosion can occur at impact, which represents a key difference between the scour dynamics of gravity current and constant density flows.

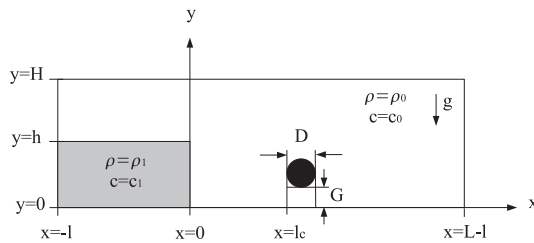


Fig. 1. Sketch of the flow configuration. A channel of length L and height H is filled with ambient fluid of density ρ_0 . Submerged in it is a lock of length l and height h , which contains the denser fluid of density ρ_1 . The difference in density between the fluids is assumed to be produced by different concentrations of a solute. When the vertical gate at $x = 0$ is opened, a current of the denser fluid forms and propagates towards the right along the floor of the channel. After traveling a distance l_c , it encounters a circular cylinder of diameter D , placed a distance G above the non-erodible bottom wall.

The above comments are based on wall shear stress data obtained from simulations for non-erodible beds. Clearly, future research should extend the scope of the simulations to erodible boundaries, and it should involve comparisons with corresponding laboratory experiments.

References

1. E. V. Ermanyuk and N. V. Gavrilov, *J. Appl. Mech. Tech. Phys.* **46**, 216-223 (2005).
2. E. V. Ermanyuk and N. V. Gavrilov, *J. Appl. Mech. Tech. Phys.* **46**, 489-495 (2005).

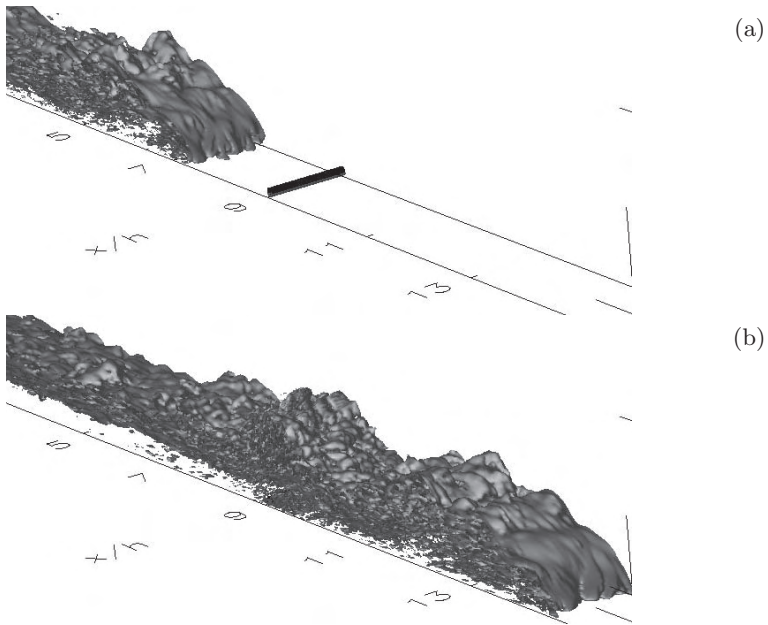


Fig. 2. Spanwise vorticity isosurfaces ($\omega_z/(V/h) = 1$) at $t/(h/V) = 7.3$ (a) and 14.6 (c). These isosurfaces highlight the interface between the fluids. The gravity current moves from left to right in the x -direction. The cylinder is at $x/h = 9 - 9.1$.

3. E. Gonzalez-Juez, G. Constantinescu, and E. Meiburg, Proceedings of the 26th International Conference on Offshore Mechanics and Arctic Engineering.
4. E. Gonzalez-Juez, E. Meiburg, and G. Constantinescu, Accepted for publication in *J. Fluid Mech.* (2009).
5. E. Gonzalez-Juez, E. Meiburg, and G. Constantinescu, Accepted for publication in *J. Fluid Struct.* (2009).
6. E. Gonzalez-Juez and E. Meiburg, Submitted to *J. Fluid Mech.* (2009).
7. E. Gonzalez-Juez, E. Meiburg, T. Tokyay, and G. Constantinescu, Submitted to *J. Fluid Mech.* (2009).
8. B. Sumer and J. Fredsøe, *The Mechanics of Scour in the Marine Environment*, World Scientific, 2002.
9. C. D. Pierce, Ph. D. Thesis, Stanford University, 2001.
10. S. Ooi, G. Constantinescu, and L. Weber, *J. Hyd. Eng.* **133**, 1037-1047 (2007).
11. J. Simpson, *Gravity Currents in the Environment and the Laboratory*, Cambridge University Press, 2007.

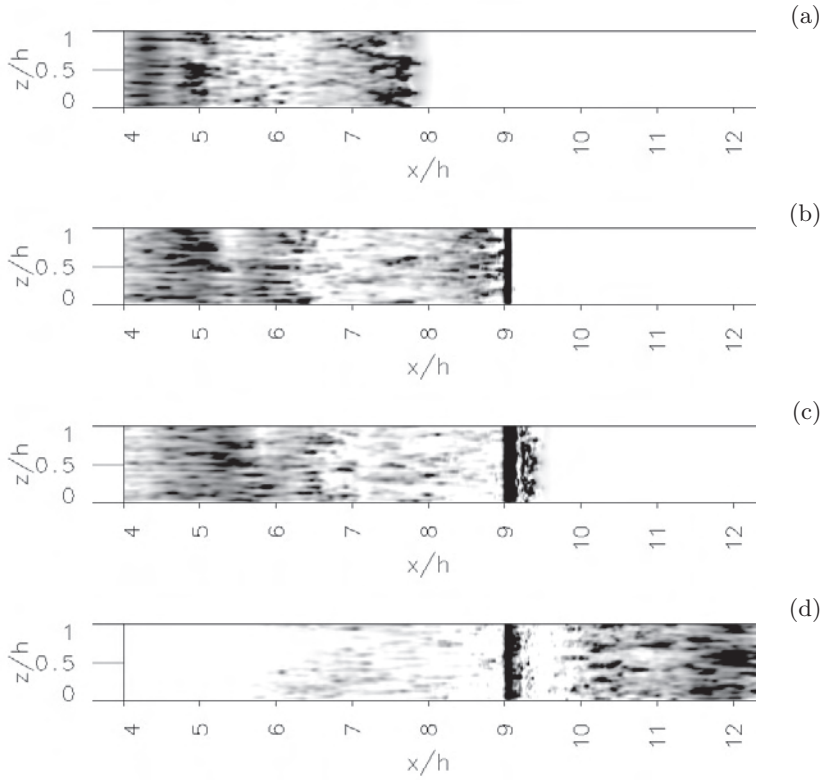


Fig. 3. Wall shear stress magnitude contours ($|\tau_w|/\rho_0 V^2$) at different times: $t/(h/V) = 7.7$ (a), 8.9 (b), 9.4 (c), and 16.7 (d). The cylinder is at $x/h = 9 - 9.1$. Darker shades indicate a higher wall shear stress. The front of the gravity current is approximately at $x_f/h \approx 7.9$ (a), 9 (b), 9.3 (c), or $x_f/h > 12$ (d).

Large scale quasi-2D structures and the problem of nonlinear bottom friction

*A.A. Khapaev*¹, *S.V. Kostrykin*^{1,2**} and *I.G. Yakushkin*^{1*}

1) A.M.Obukhov Institute of Atmospheric Physics, Russian Academy of Sciences, Moscow, Russia

2) Institute of Numerical Mathematics, Russian Academy of Sciences, Moscow, Russia

*iyakushkin@yandex.ru, **kostr@inm.ras.ru

In recent years much attention has been focused on the study of large scale structures in ideal and viscous fluids. Such nonlinear effect as cyclonic-anticyclonic asymmetry is observed in geophysical flows and in laboratory or numerical experiments [1, 2]. In the case of quasi-2D structures smaller than Rossby-Oboukhov scale the main role belongs to the nonlinear friction at the underlying surface. In this study an approximate theory is constructed to describe quasi-two-dimensional flows of rotating viscous incompressible fluid. The two-dimensional description of large scale vortical flows, which is based on the concept of linear or weak nonlinear bottom friction, is valid only for moderate Reynolds or for small Rossby numbers [3, 4]. This study takes into account a circulation in the vertical plane and related two-dimensional divergence of the vortex flow [5]. The role of nonlinear terms that are due to the interaction between the vortical and potential components of two-dimensional velocity or between vortices with vertical and horizontal axes is analyzed. This interaction leads to nonlinear Ekman pumping of fluid and forms the boundary (Ekman) layer with effective height. For rotating flows the different height of Ekman layer determines the different behavior of cyclonic and anti-cyclonic vortices. For non-rotating flows with strong vorticity the boundary layer similar to Ekman layer is also formed. The results of the proposed theory are compared with experimental data, which were obtained from laboratory study of a spatially periodic flow.

Let us consider a flow in a thin layer of a viscous homogeneous incompressible fluid rotating in the gravity field. We assume that the flow is created by vertically homogeneous vortical force. In the quasi-static approximation the equation for horizontal velocity is written as

$$\frac{d\mathbf{U}}{dt} + [f\mathbf{e}_z \times \mathbf{U}] - \nu \frac{\partial^2 \mathbf{U}}{\partial z^2} = F_0[\mathbf{e}_z \times \nabla G(\frac{x}{l}, \frac{y}{l})] - g\nabla\eta(x, y)$$

where $z = h + \eta(x, y)$ is the equation of the free surface, f - Coriolis parameter, ν - kinematic viscosity, $h \ll l, \nu \ll Ul$.

The boundary conditions for horizontal and vertical velocity components are

$$\mathbf{U} = 0(z = 0), \frac{\partial \mathbf{U}}{\partial z} = 0(z = h), w = 0(z = 0, z = h)$$

It is convenient to use Helmholtz decomposition of vector field

$$\mathbf{U} = [\mathbf{e}_z \times \nabla \Psi] + \nabla \Phi, \nabla = \mathbf{e}_x \frac{\partial}{\partial x} + \mathbf{e}_y \frac{\partial}{\partial y}$$

and describe the fluid motion in terms of vertical component of vorticity $\omega = \Delta \Psi$ and divergence of horizontal velocity $\delta = \Delta \Phi$. The divergent term is connected with circulation in the vertical plane. Let us assume that

$$\Psi = \Psi_0(x, y) + \Psi_1(x, y, \frac{z}{\sigma_0}),$$

$$\Phi = \Phi_0(x, y) + \Phi_1(x, y, \frac{z}{\sigma_0}),$$

where Ψ_1, Φ_1 are non-vanishing only in the boundary layer $\sigma_0 \ll h, h\Phi_0(x, y) = - \int \Phi_1(x, y, \frac{z}{\sigma_0}) dz$

The following scaling relations for flow are derived from the basic equations

$$\begin{aligned} \Psi_0 &= \omega_0 \psi_0(x, y, \frac{f}{\omega_0}), \\ \Phi_0 &= \omega_0 \frac{\sigma_0}{h} \phi_0(x, y, \frac{f}{\omega_0}), \\ \Psi_1 &= \omega_0 \psi_1(x, y, \frac{f}{\omega_0}, \frac{z}{\sigma_0}), \\ \Phi_1 &= \omega_0 \phi_1(x, y, \frac{f}{\omega_0}, \frac{z}{\sigma_0}), \\ \sigma_0 &= (2 \frac{\nu}{\omega_0})^{\frac{1}{2}} \sigma(\frac{f}{\omega_0}). \end{aligned}$$

Under the balance condition between forcing and dissipation we get

$$\omega_0 = (\frac{F_0^2 h^2}{2\nu})^{\frac{1}{3}}.$$

We assume that without rotation and at small Rossby numbers the symmetric distribution of cyclonic and anticyclonic vorticity is generated. For moderate Rossby numbers the antisymmetric component is also important. The approximate solution of boundary layer equations allows us to determine the relationship between two flow components and to derive the approximate closed equation for surface flow. This equation takes into account nonlinear bottom friction and it is valid for flows with strong vorticity at arbitrary

Rossby numbers. As a solution of this equation we obtain the vorticity distribution at the fluid surface.

The experimental flow was realized in a rectangular tank filled with conducting fluid. The tank was placed on the rotating platform. On the sides of the tank was mounted electrodes with help of which an electric current was passed through the fluid. The vortex flow in the thin fluid layer was created by means of the system of permanent magnets. We have received a number of cyclonic and anticyclonic vortices. The velocity field of this flow was measured on the surface. Second and third moments of vorticity were calculated.

The experimental data obtained at different values of current strength $I \sim F_0$ and rotation period - T are in a good agreement with results of approximated theory. These results correspond to the scaling relations $\tilde{\omega} = q\omega, \tilde{T} = q^{-1}T, q = (I_0/I)^{2/3}$, as it is shown on the Fig.1 and 2. The value of third moment of vorticity shows an asymmetry between anticyclones and cyclones that is maximal at Rossby number equal to unit. Our investigation demonstrate that intense quasi-2D vortices generate circulation in the vertical plane due to friction at the underlying layer and form effective Ekman layer. Obtained results allow us to interpret the amplification of anticyclonic eddies and weakening cyclonic eddies observed in the experiment.

The work is supported by RFBR (projects 08-05-00764,07-05-00112).

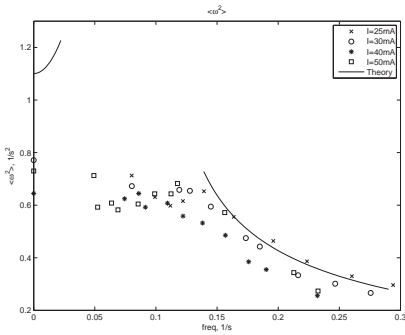


Fig. 1. Dependencies of the second moment of vorticity from the rotation frequency for different values of forcing with account of the scaling parameter $q = (I_0/I)^{2/3}$. Experiment: crosses - $I = 25$ mA, circles - $I = 30$ mA, stars - $I = 40$ mA, squares - $I = I_0 = 50$ mA. The solid curve - theoretical results.

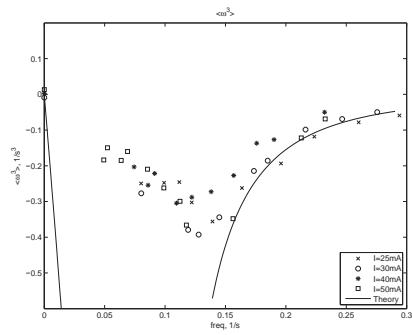


Fig. 2. Dependencies of the third moment of vorticity from the rotation frequency for different values of forcing with account of the scaling parameter $q = (I_0/I)^{2/3}$. Experiment: crosses - $I = 25$ mA, circles - $I = 30$ mA, stars - $I = 40$ mA, squares - $I = I_0 = 50$ mA. The solid curve - theoretical results.

References

1. L.P.Graves, J.C.McWilliams and M.T. Montgomery, *Sov. Geophys. and Astrophys. Fluid Dyn.* **100**, 151 (2006)
2. G. Pere, A.Stenger, *Phys. of Fluids*, **18**, 1 (2006)
3. F.V.Dolzhanskii, V.A.Krymov, D.Yu.Manin, *Sov.Phys.Uspekhi*, **33**(7), 495, (1990).
4. L.Zavala Sansón and G.J.F.Van Heijst, *J.Fluid Mech.*, **412**, 75 (2000).
5. V.M. Ponomarev, A.A. Khapaev and I.G.Yakushkin, *Izv. of Atm. and Ocean. Phys.* **44**, 45 (2008)

Double-period oscillation of passive scalar flux in stratified turbulence

H. Hanazaki, T. Miyao and T. Okamura

Department of Mechanical Engineering and Science, Kyoto University,
Yoshida-Honmachi, Sakyo-ku, Kyoto 606-8501, Japan
hanazaki@mech.kyoto-u.ac.jp

Scalar fluxes in decaying stratified turbulence are investigated when vertical mean gradients of density and passive scalar coexist. While there have been many studies on stratified turbulence, behavior of passive scalars in that system has rarely been studied. In this study, we have compared the DNS results with RDT (rapid distortion theory) [1], particularly for the time development of turbulent diffusion coefficients of density ($K_\rho = -\overline{\rho w}/N^2$, w : vertical velocity, N : Brunt-Väisälä frequency) and passive scalar ($K_c = \overline{c w}/(\overline{dc}/dz)$, $\overline{c}(z)$: mean passive scalar distribution), and investigated the effects of molecular diffusions and initial conditions which might lead to differential diffusions of density (active scalar) and passive scalar [2], while $K_\rho = K_c$ has been assumed in many applications. Results of DNS show temporal oscillations of a passive scalar flux (Fig. 1b) at double-period of the density flux (Fig. 1a), in agreement with RDT (Fig. 2). The results also show that, at low Froude numbers ($Fr = 0.1 \ll 1$), RDT gives quantitatively good prediction even at moderate Reynolds numbers ($Re = 100$). The period doubling depends on the molecular diffusion of the scalars, in agreement with RDT. For a passive scalar with high Schmidt number ($Sc > 2Pr/(1 + Pr)$, Pr : Prandtl number of density, Sc : Schmidt number of passive scalar), the slowly oscillating mode becomes dominant at large times ($Nt/2\pi > 1$), and K_c decays slowly (Fig. 3a). On the other hand, at low Schmidt numbers ($Sc < 2Pr/(1 + Pr)$), the slowly oscillating mode suffers strong initial decay, so that fastly oscillating components becomes dominant at large times (Fig. 3b). These results illustrate the importance of molecular diffusivity, initial conditions and unsteadiness in strongly stratified turbulence, along with the possibility of differential diffusion of scalars.

References

1. H. Hanazaki, *Phys. Fluids* **20**, 055106 (2008).
2. Z. Warhaft, *Q. J. R. Meteorol. Soc.* **102**, 703 (1976).

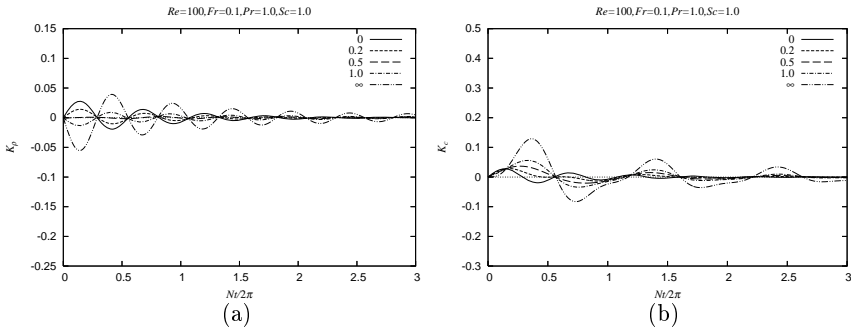


Fig. 1. DNS results (256^3) for the turbulent diffusion coefficient of (a) density K_ρ and (b) passive scalar K_c at $Re = 100$, $Fr = 0.1$ and $Pr = Sc = 1$. Five lines in each figure correspond to different initial potential energy ratio to the kinetic energy (PE_0/KE_0). Initial fluctuations are assumed to be isotropic.

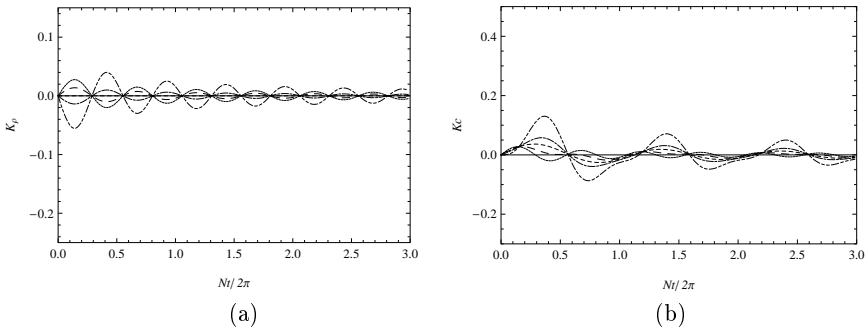


Fig. 2. RDT results corresponding to Fig. 1 at the same conditions.

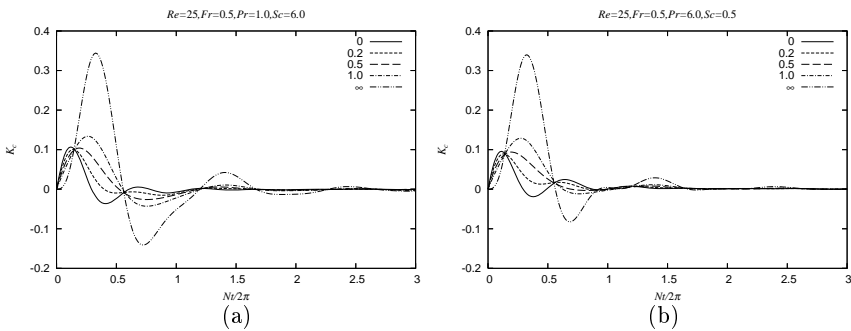


Fig. 3. DNS results for K_c at different Pr and Sc . (a) $Pr = 1$, $Sc = 6$ ($Sc > 2Pr/(1 + Pr)$); (b) $Pr = 6$, $Sc = 0.5$ ($Sc < 2Pr/(1 + Pr)$).

Energy spectra of stably stratified turbulence

Y. Kimura¹ and J. R. Herring²

¹Graduate School of Mathematics, Nagoya University,
Furo-cho, Chikusa-ku, Nagoya 464-8602 JAPAN

² National Center for Atmospheric Research, P.O. Box 3000,
Boulder, Colorado, 80307-3000, U.S.A.
kimura at math.nagoya-u.ac.jp

In this paper, the energy spectra of forced stably stratified turbulence are investigated numerically using the Direct Numerical Simulations (DNS) with 1024^3 grid points ($R_\lambda \sim 300$). The simulation is done by solving the 3D momentum equation under the Boussinesq approximation pseudo-spectrally with stochastic forcing applied to the large horizontal velocity scales. Similar types of numerical simulations have discussed the features of the energy spectrum for stratified turbulence¹⁻⁶. In this paper we will present more detailed analysis on the anisotropy of the spectrum⁷.

One of the most striking features of stratified turbulence is dynamical and statistical anisotropy that develops in flows, and because of this anisotropy, stratified turbulence exhibits various different aspects from homogeneous isotropic turbulence. To investigate such anisotropy, it is crucial to employ proper methods, and as a useful tool for this purpose, the Craya-Herring decomposition which has a close relation with the toroidal-poloidal decomposition, is widely known.

For the Craya-Herring decomposition, the following orthonormal coordinates are introduced,

$$\mathbf{e}_1(\mathbf{k}) = \frac{\mathbf{k} \times \hat{\mathbf{z}}}{\|\mathbf{k} \times \hat{\mathbf{z}}\|} = \frac{1}{\sqrt{k_x^2 + k_y^2}} \begin{pmatrix} k_y \\ -k_x \\ 0 \end{pmatrix}, \quad (1)$$

$$\mathbf{e}_2(\mathbf{k}) = \frac{\mathbf{k} \times \mathbf{k} \times \hat{\mathbf{z}}}{\|\mathbf{k} \times \mathbf{k} \times \hat{\mathbf{z}}\|} = \frac{1}{\sqrt{k_x^2 + k_y^2 + k_z^2} \sqrt{k_x^2 + k_y^2}} \begin{pmatrix} k_z k_x \\ k_z k_y \\ -(k_x^2 + k_y^2) \end{pmatrix}, \quad (2)$$

$$\mathbf{e}_3(\mathbf{k}) = \frac{\mathbf{k}}{\|\mathbf{k}\|} = \frac{1}{\sqrt{k_x^2 + k_y^2 + k_z^2}} \begin{pmatrix} k_x \\ k_y \\ k_z \end{pmatrix}, \quad (3)$$

where $\hat{\mathbf{z}} = (0, 0, 1)^t$ is the unit vector in the z -direction. By projecting the fourier component of an incompressible velocity vector in 3D, $\tilde{\mathbf{u}}(\mathbf{k})$, onto the

above coordinates, we obtain the following decomposition

$$\mathbf{u}(\mathbf{k}) = \phi_1 \mathbf{e}_1(\mathbf{k}) + \phi_2 \mathbf{e}_2(\mathbf{k}) . \tag{4}$$

where the coefficients ϕ_1, ϕ_2 in terms of the cartesian coordinates of $\tilde{\mathbf{u}}(\mathbf{k}) = (\tilde{u}, \tilde{v}, \tilde{w})^t$, are given as

$$\phi_1 = \frac{1}{\sqrt{k_x^2 + k_y^2}} (k_y \tilde{u} - k_x \tilde{v}) = \frac{i}{\sqrt{k_x^2 + k_y^2}} \tilde{\omega}_z , \tag{5}$$

$$\phi_2 = -\frac{\sqrt{k_x^2 + k_y^2 + k_z^2}}{\sqrt{k_x^2 + k_y^2}} \tilde{w} . \tag{6}$$

In the above expression, $\tilde{\omega}$ is the fourier transform of the z-component of vorticity.

Using the Craya-Herring decomposition, the velocity field is divided into the vortex mode (ϕ_1) and the wave mode (ϕ_2). With the initial kinetic energy being zero, the ϕ_1 spectra as a function of horizontal wave numbers, $k_\perp = \sqrt{k_x^2 + k_y^2}$, first develops a k_\perp^{-3} spectra for the whole k_\perp range, and then $k_\perp^{-5/3}$ part appears at large k_\perp with rather a sharp transition wave number. **Fig. 1** shows ϕ_1 spectra for $N^2 = 1, 10, 50, 100$ (from the top to the bottom) where N is the Brunt-Väisälä frequency. We can observe that the small k_\perp parts collapse to a single spectrum of $\sim k_\perp^{-3}$, while the large k_\perp parts have the same slope of $k_\perp^{-5/3}$ but with different coefficients depending on N .

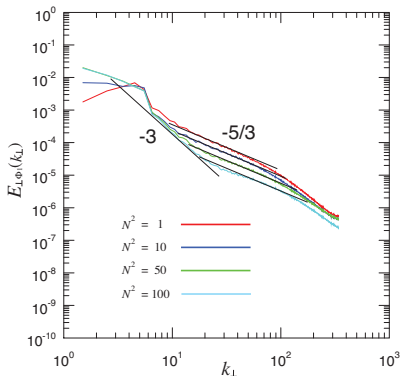


Fig. 1. ϕ_1 spectra as a function of k_\perp for $N^2 = 1, 10, 50, 100$

For scaling these spectra, we use the following two points as criterions; (1) the large scales do not depend on N , (2) we expect that the Kolmogorov constant is universal for the isotropic subset of anisotropic data, and we propose the functional form as;

$$E_{\perp\phi_1}(k_\perp) = \begin{cases} \alpha \eta_{\perp\phi_1}^{2/3} k_\perp^{-3} & (k_\perp < k_c) \\ C_K \varepsilon_{\perp\phi_1}^{2/3} k_\perp^{-5/3} & (k_\perp > k_c) \end{cases} , \tag{7}$$

where

$$\varepsilon_{\perp\phi_i} = 2\nu \int_0^\infty k_\perp^2 E_{\perp\phi_i}(k_\perp) dk_\perp \quad (i = 1, 2), \tag{8}$$

$$\eta_{\perp\phi_i} = 2\nu \int_0^\infty k_\perp^4 E_{\perp\phi_i}(k_\perp) dk_\perp \quad (i = 1, 2). \tag{9}$$

By the dimensional analysis, the coefficient of k_{\perp}^{-3} should have the unit of $[T]^{-2}$ where T represents the time scale. Often the buoyancy spectrum assumes N^2 for this coefficient, but we excluded this possibility from the criterion. We tested various quantities and concluded that the above $\eta_{\perp\Phi_1}$, the 2D enstrophy dissipation rate, provides reasonable agreement for the large scale part.

Meanwhile the Kolmogorov type spectrum fits for the small scale part. However, instead of the 3D energy dissipation rate, ε , the above 2D horizontal energy dissipation rate, $\varepsilon_{\perp\Phi_1}$ provides closer value to the widely accepted value for the 3D Kolmogorov constant of ~ 1.5 .

The transition wave number k_c can be calculated by equating the two terms in (1) as

$$\alpha\eta_{\perp\Phi_1}^{2/3}k_c^{-3} = C_K\varepsilon_{\perp\Phi_1}^{2/3}k_c^{-5/3} \rightarrow k_c = \left(\frac{\alpha}{C_K}\right)^{3/4} \sqrt{\frac{\eta_{\perp\Phi_1}}{\varepsilon_{\perp\Phi_1}}}. \quad (10)$$

From the compensated spectra with respect to (1), we can estimate the coefficient α as 0.02 for all N^2 examined. By using the numerical values of $\varepsilon_{\perp\Phi_1}$ and $\eta_{\perp\Phi_1}$ and $C_k \sim 1.5$, the transition wavenumbers for $N^2 = 1, 10, 50, 100$ are calculated as 7.557, 8.536, 10.662 and 11.888, respectively.

Figure 2 shows $E_{\perp\Phi_2}(k_{\perp})$ for $N^2 = 1, 10, 50, 100$. There are significant differences from the Φ_1 spectra. First, little effect of forcing is observed in the large scale. Second, for most cases of stratification, $-5/3$ spectra are observed, but for $N^2 = 100$, $\sim k_{\perp}^{-2}$ spectrum is obtained with a transition to $-5/3$. For these spectra, we propose the following functional forms;

$$E_{\perp\Phi_2}(k_{\perp}) = \begin{cases} \beta\sqrt{N\varepsilon_{\perp\Phi_2}}k_{\perp}^{-2} & (k_{\perp} < k_c) \\ C_K\varepsilon_{\perp\Phi_2}^{2/3}k_{\perp}^{-5/3} & (k_{\perp} > k_c) \end{cases}, \quad (11)$$

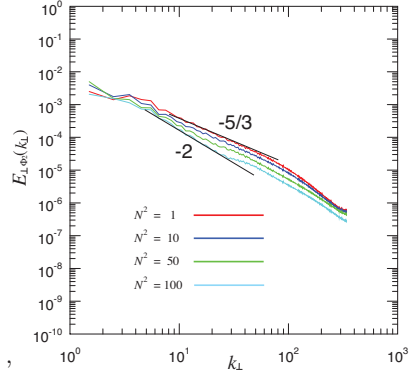


Fig. 2. ϕ_1 spectra as a function of k_{\perp} for $N^2 = 1, 10, 50, 100$

With the same procedure, the transition wave number k_c for the above spectra can be calculated by equating the two terms in the right hand side as

$$\beta\sqrt{N\varepsilon_{\perp\Phi_2}}k_c^{-2} = C_K\varepsilon_{\perp\Phi_2}^{2/3}k_c^{-5/3} \rightarrow k_c = \left(\frac{\beta}{C_K}\right)^3 \sqrt{\frac{N^3}{\varepsilon_{\perp\Phi_2}}} \quad (12)$$

Using the estimated values of C_K and β , the transition k_{\perp} s, for $N^2 = 1, 10, 50, 100$ are calculated as 3.31×10^{-2} , 0.350, 2.634 and 6.021, respectively. The estimated transition wave number is smaller than 1 for $N^2 = 1$ and 10, and it is consistent with the fact that the transition points are not

seen on the spectra in Figure 2. The square-root part of the right hand side of (12) has the form of the Ozmidov scale being different from the original one by the fact that the dissipation rate is horizontal for the Φ_2 energy.

References

1. Riley, J. J. & DeBruyn Kops, S. M. 2003 Dynamics of turbulence strongly influenced by buoyancy *Phys. Fluids* **15**, 2047–2059.
2. Waite, M. L. & Bartello, P. 2004 Stratified turbulence dominated by vortical motion *J. Fluid Mech.* **517**, 281–308.
3. Waite, M. L. & Bartello, P. 2006 Stratified turbulence generated by internal gravity waves *J. Fluid Mech.* **546**, 313–339.
4. Lindborg, E. 2006 The energy cascade in a strongly stratified fluid *J. Fluid Mech.* **550**, 207–242.
5. Riley, J. J. & Lindborg, E. 2008 Stratified Turbulence: A Possible Interpretation of Some Geophysical Turbulence Measurements *J. Atmos. Sci.* **65**, 2416–2424.
6. Kurien, S., Wingate, B. & Taylor, M. A. 2008 Anisotropic constraints on energy distribution in rotating and stratified turbulence. *Europhy. Lett.* **84**, 24003.
7. Y. Kimura and J. R. Herring, Energy spectra of stably stratified turbulence, in preparation.

The wind-driven turbulent oscillating channel flow subjected to a stable stratification

W. Kramer^{1,2}, V. Armenio³, and H. J. H. Clercx^{1,2,4}

¹ Fluid Dynamics Laboratory, Department of Applied Physics, Eindhoven University of Technology, P.O. Box 513, 5600 MB Eindhoven, The Netherlands
w.kramer@tue.nl

² J.M. Burgers Centre, Research School for Fluid Dynamics, The Netherlands

³ Dipartimento di Ingegneria Civile é Ambientale, Università di Trieste, Italy

⁴ Department of Applied Mathematics, University of Twente, The Netherlands

Introduction

The tide in estuaries drives a turbulent slowly-oscillating flow. To investigate the effects of wind and density stratification on such flows, we have performed Large Eddy Simulations in a cubic fluid column of depth h . The velocity field \mathbf{u} is obtained from the Navier-Stokes equation under the Boussinesq approximation,

$$\frac{D\mathbf{u}}{Dt} = -\nabla p + \frac{1}{\text{Re}}\nabla^2\mathbf{u} - \text{Ri}\rho'e_z + \mathbf{f}_p. \quad (1)$$

Here, p is the kinematic pressure and ρ' the fluctuating part of the density with respect to a reference density ρ_0 . The mimic a tidal flow an oscillating pressure gradient, $\mathbf{f}_p \sim \cos \omega t$, with frequency ω is applied. At the free surface a wind stress τ_{wind} is present, which can be oriented at arbitrary angles. The dimensionless Reynolds and Richardson numbers are, $\text{Re} = \frac{Uh}{\nu}$ and $\text{Ri} = \frac{g}{\rho_0} \left| \frac{\partial \rho}{\partial z} \right| \frac{h^2}{U^2}$, respectively, with ν the kinematic viscosity and g the gravitational acceleration. Here, the (constant) density gradient $\frac{\partial \rho}{\partial z}$ at the free surface is used. For the typical velocity scale U we take the friction velocity at the free surface, $u_\tau = \sqrt{\tau_{\text{wind}}/\rho_0}$.

Turbulent oscillating channel flow

When the wind stress is aligned with the pressure gradient a pulsating mean flow is observed in the same direction. Turbulence is created in the wall shear layer, but subsequently fills the entire fluid column [1]. Additionally, turbulence is also produced in a thin layer beneath the free surface due to the

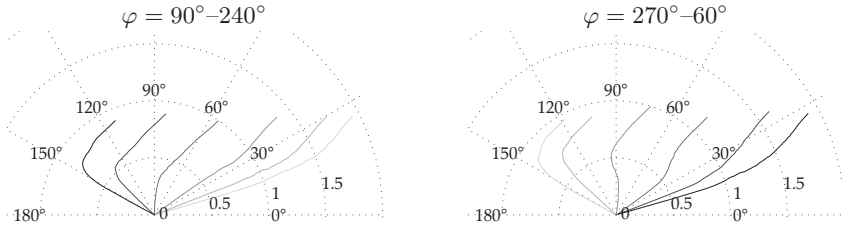


Fig. 1. Hodograph of the mean velocity with the darker-colored lines representing later phases in the tidal cycle for $Re = 800$ and $Ri = 0$. Each point on the line gives the direction and amplitude of the velocity vector for a certain height.

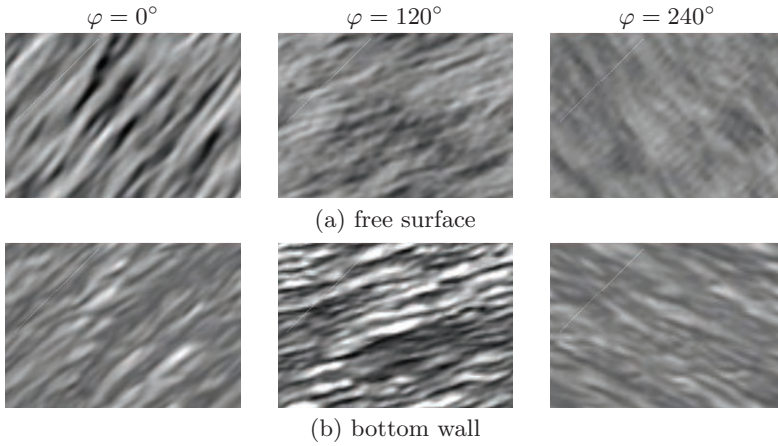


Fig. 2. Greyscale plot of the streamwise velocity fluctuations revealing turbulent streaks in (a) the free surface layer and (b) the bottom wall layer at three different phases in the tidal cycle. For the present simulations: $Re=800$ and $Ri=0$.

wind stress [2]. Now, consider a wind stress at a 45° angle to the tidal flow component. The orientation of the mean velocity will then change over depth (Fig. 1). At the bottom in the viscous sublayer shear and velocity are aligned. The shear leads to the strong turbulent streaks in this layer, which are aligned with the mean velocity (Fig. 2). Going upwards from the logarithmic boundary layer towards the free surface the mean velocity changes orientation. In the free-surface layer shear and mean velocity are not aligned. Streaks are present at the free surface, but the pattern is more irregular than in the bottom boundary layer. Streaks are still aligned with the mean velocity, but they are disturbed by a pattern oriented parallel to the imposed wind stress. When shear and mean velocity are almost aligned at $\varphi = 0^\circ$ a clear pattern of streaks is observed. The turbulence is then essentially dominated by one component. The streamwise fluctuations are stronger than the spanwise and vertical fluctuations. For the wind stress at a certain angle with the tidal

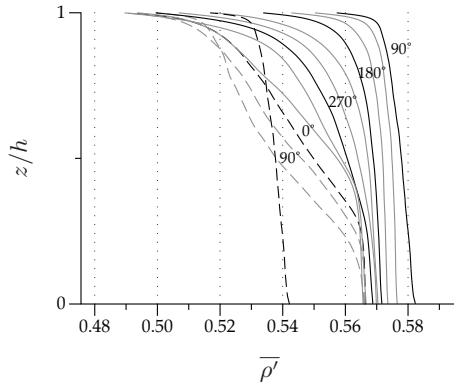


Fig. 3. The density $\bar{\rho}'$, averaged over the horizontal plane for $Re = 400$ and $Ri = 1000$. The black lines are given for $\varphi = 90^\circ, 180^\circ, 270^\circ$ (drawn) and for $\varphi = 0^\circ, 90^\circ$ in the next period (dashed). The gray lines are the density profiles for intermediate phases.

flow two-component turbulent fluctuations are observed, with the horizontal fluctuations being about equal but dominating over the vertical fluctuations. Two-component turbulence originates from the free-surface layer but can disperse into a larger part of the fluid column.

Stably stratified turbulent oscillating channel flow

Now consider the case where the sun is heating the free surface at a constant rate and assume an adiabatic estuary bottom. The constant heat flux at the free surface results in a linear warming of the fluid column. However, there is a temperature difference, and hence a density stratification of the fluid, with the top layer being warmer and lighter than the bottom layer (Fig. 3). For simplicity, the wind stress is now kept aligned with the driving pressure gradient. Turbulence is most intense in the deceleration phase of the first half cycle (90° – 180°), when wind and tide are in the same direction (Fig. 4). During this phase the density is well mixed in the complete fluid column except for a thin layer at the free-surface. In the second half cycle (180° – 360°) intensity of the turbulence decreases due to a lower wall stress. The density stratification then extends to deeper fluid layers, until only the bottom layer remains well mixed in the accelerating phase of the first half cycle (0° – 90°). When the decelerating phase is then reached again, mixing increases abruptly in the entire domain, leading to an abrupt change of the density profile.

Turbulent fluctuations are suppressed by a stable density stratification and, hence, the mean velocity is altered. Deviations from the unstratified case firstly appear in the upper layers of the flow. The mean velocity is here

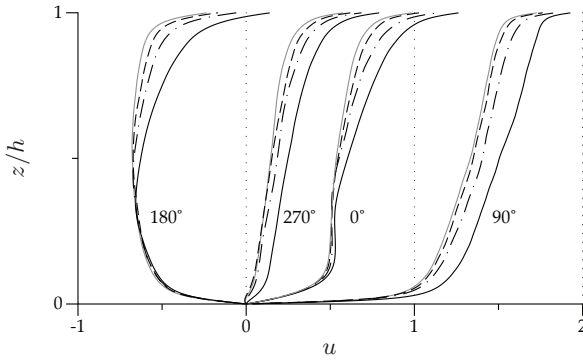


Fig. 4. The oscillating pressure gradient and the wind stress in the same direction results in a pulsating mean flow. The mean streamwise velocity profiles are given for four different phases of the driving pressure gradient. Richardson numbers are $Ri = 0$ (gray), 200 (dashed), 500 (dash-dot) and 1000 (drawn).

stronger affected by the wind stress, as the vertical velocity fluctuations are less intense. When the stratification increases deviations appear in deeper layers. In the case the density is well mixed ($\varphi = 90^\circ$) the velocity differs over nearly the complete fluid column. The viscous sublayer at the no-slip bottom, however, remains unaffected.

Conclusion

Overall, the case of turbulent oscillating channel flow subjected to a wind stress and/or a surface heating results in a flow with a strong change of the turbulent dynamics and the stratification over one period. Turbulent streaks reorientate with the changing mean flow direction. In the free-surface layer the pattern of the turbulent fluctuations is also affected by the wind stress. During a cycle the density stratification can penetrate deeper into the fluid column, while for other phases the density is well mixed in the major part of the fluid column. Future research is necessary, as large effects can be expected for the dispersion of particles in these kind of flows, which is relevant to sedimentation and the plankton ecosystem.

References

1. S. Salon, V. Armenio and A. Crise J. Fluid Mech., **570**, 253 (2007)
2. W. Kramer, H. J. H. Clercx and V. Armenio, Phys. Fluids (submitted for publication).
3. J. R. Taylor, S. Sarkar and V. Armenio, Phys. Fluids. **17**, 116602 (2005).

Numerical studies of turbulence in breaking internal waves

S.N. Yakovenko^{1,2}, T.G. Thomas¹ and I.P. Castro¹

¹ University of Southampton, Highfield, Southampton SO17 1BJ, UK
yakovenk@soton.ac.uk, tgt@soton.ac.uk, i.castro@soton.ac.uk

² Novosibirsk State University, ITAM SB RAS, Novosibirsk 630090, Russia
yakovenk@itam.nsc.ru

To explore the steady internal wave breaking observed in stably stratified flows past obstacles [1], we use well-resolved DNS/LES methods [2]. Internal waves are generated by an obstacle inserted in the flow with a linear upstream density variation and constant inflow velocity U [3]. A sponge-layer procedure with forcing terms in governing equations has been incorporated to prevent reflection from inflow/outflow boundaries. Initially, the domain was extended from $x/h = 0$ to 200 with the obstacle located in the middle. The sponge layers allowed us to reduce the domain by a factor of two (over the range $x/h = 50$ to 150) and use run times up to $tU/h = 250$ without significant differences with corresponding long-domain computations. The finest applied grid ($5120 \times 512 \times 512$) had a resolution of $\Delta x = \Delta y = \Delta z = h/51.2$. The wave breaking is captured at low values of the Froude number F_h (based on the obstacle height h), with turbulence generation at $Re = Uh/\nu > 2000$ as in experiments [1]. Following the preliminary results [3] at $Sc = 700$, we present DNS data for the 2D case at $Re = 4000$, $F_h = 0.6$, $Sc = 1$.

The recirculation zone arising from wave overturning and breaking generates turbulence activity, which in turn destroys the recirculation structure, but maintains a quasi-steady fully mixed zone (Fig. 1,2). The transition mechanism includes Rayleigh-Taylor instability (RTI) of mushroom type (Fig. 3), generating the small toroidal vortices seen from vorticity invariant contours and noted also in [4]. Exponential growth of RTI at $tU/h \sim 25$ leads to turbulence ‘explosion’ in the breaking region, and the vortex structure scale is increased later up to $\lambda \sim 2.5h$. This is also seen from the y -spectra (Fig. 4) having the corresponding peak at $tU/h > 22.5$ and the higher-frequency peak $\lambda \sim 0.5h$ at $22.5 \leq tU/h < 27.5$ related to RTI. To break the 2D flow symmetry, small ‘white-noise seeding’ (with an amplitude of 2% from the inflow density change over the obstacle height) was applied to the scalar field at $tU/h = 7.5$. The initial perturbation gradually decays, the flow remains laminar until $tU/h \sim 20$, then extracts from the white noise and amplifies unsteadiness of above-mentioned wavelengths and its harmonics. The spectra

and statistical moments (Fig. 5) show quasi-steady behavior of the wave-breaking turbulence at $tU/h \geq 35$. Both time and spatial spectra produced in some points of the mixed zone contain clear parts of the ‘ $-5/3$ ’ inertial range and high-frequency dissipative range (Fig. 4,6). (Note that the wavenumber $n = L_y/\lambda$ [4] is the number of periods over the domain width $L_y = 10h$.) The velocity spectra shows no unrealistic features (such as peaks at the inertial-range end which would suggest the need for a subgrid-scale model). Thus, at least at $Sc \sim 1$ and the moderate Reynolds number $Re = 4000$, the use of the DNS approach is reasonable and sufficient. For the case of $Sc \sim 700$, the subgrid-scale model may be needed to remove the ‘pile-up’ effects of the density spectra at $fh/U \geq 0.5$.

Careful scrutiny of second-moment and t.k.e. balance dynamics (Fig. 5,7) provides the following mechanism of turbulence generation/maintenance. At $tU/h \sim 22.5$ (Fig. 1), with a significant unstable density gradient over the small vertical distance between $z/h = 1.65$ and 2.35 , the large vertical turbulent scalar flux $\langle w'f' \rangle$ is generated which in turn enhances vertical velocity fluctuations and t.k.e via the buoyancy production G_k . The initial Reynolds-stress anisotropy is strong ($\langle w'w' \rangle \gg \langle u'u' \rangle \gg \langle v'v' \rangle$), and lateral velocity fluctuations are smaller due to delaying effect of 2D symmetry. The G_k term becomes small again at $tU/h > 30$ because of the suppressing effect of the buoyancy source in the $\langle w'f' \rangle$ equation, and this initial cycle of G_k variation generates weak unsteadiness in the second moments and t.k.e. balance terms with the period $TU/h \sim 8$ (which gradually decay later). The viscous dissipation D_k appears last to compensate the production terms when they become large, whereas the advection terms A_k provide a significant additional sink. Turbulent and pressure diffusion terms D_t , D_p are of lower order, and viscous diffusion is negligibly small. The residual term $k_t = \partial k / \partial t$ correlates well with the G_k variations and time history of velocity fluctuations.

In the breaking zone, over the quasi-steady period, roughly $35 \leq tU/h \leq 55$, Figure 5 shows that the global balance (averaged over y , and within the breaking region) is largely between mean-shear production, dissipation and advection, and turbulence is almost isotropic with slight preference of $\langle w'w' \rangle$. Locally, however things are quite different. Figure 7 shows that the axial and spanwise stresses, integrated over the span, have noticeable peaks at the edges of the breaking region, buoyant production is certainly not negligible but has antisymmetric peaks almost as strong as those of the (symmetric) shear production, and dissipation is greatest around the middle of the turbulent patch. Further analysis of these data is in hand.

References

1. I. P. Castro, W. H. Snyder, *J. Fluid Mech.*, **255**, 195 (1993).
2. T. G. Thomas, J. J. R. Williams, *J. Wind Eng. Ind. Aero.*, **67&68**, 155 (1997).
3. S. N. Yakovenko, T. G. Thomas and I. P. Castro, *Proceedings of DLES7*, Springer, Berlin 2009, 6 p. (in press)
4. F. Gheusi, J. Stein and O. F. Eiff, *J. Fluid Mech.*, **410**, 67 (2000).

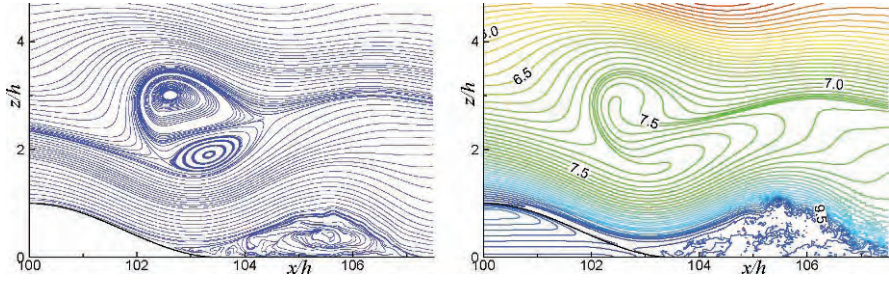


Fig. 1. Fluid particle pathlines (left), density contours (right), $y = 5h$, $t = 22.5h/U$.

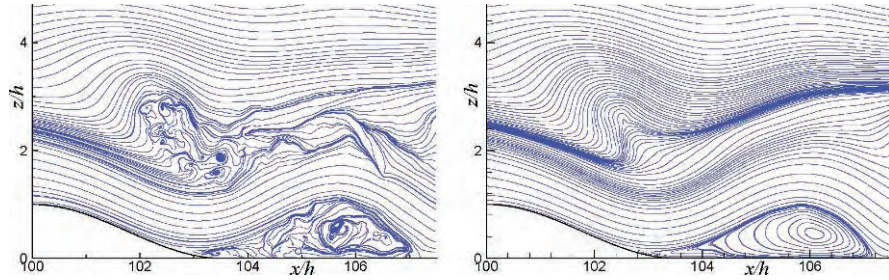


Fig. 2. Fluid particle pathlines, $y = 5h$ (left), averaged along y (right), $t = 40h/U$.

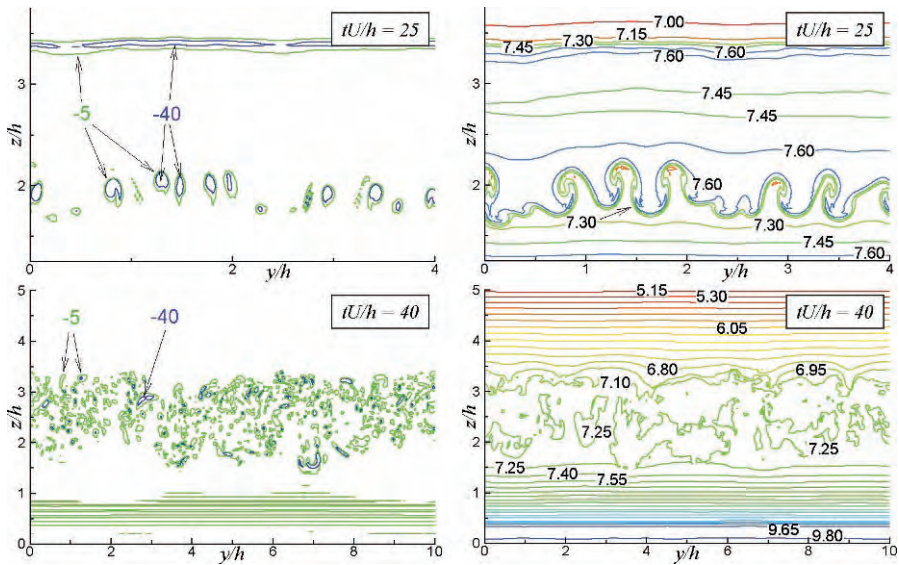


Fig. 3. Second invariant of vorticity (left), density contours (right) at $x/h = 102.5$.

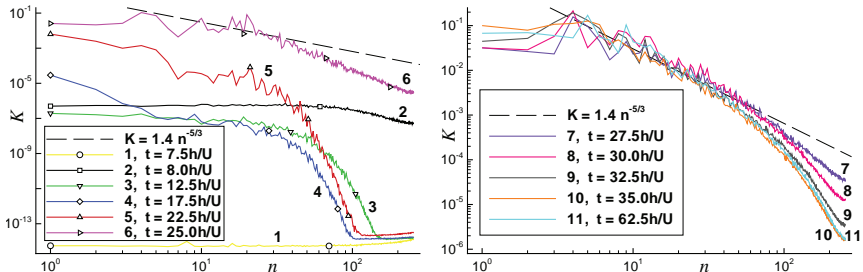


Fig. 4. Spatial t.k.e. spectra in y -direction averaged at $101.8 < x/h < 102.3$, $2.4 < z/h < 2.9$: transition (left); turbulence (right).

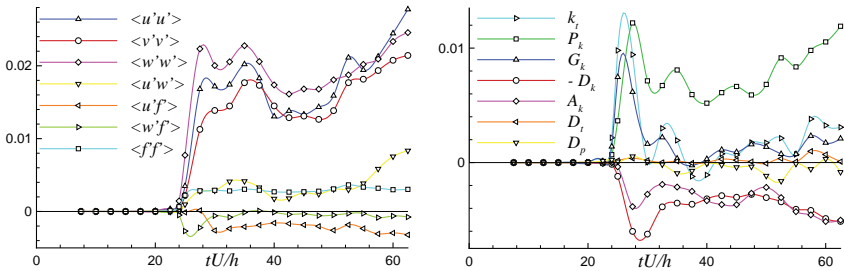


Fig. 5. Global values of second moments and t.k.e. balance terms (normalized using U and h) averaged along y and at $101.25 < x/h < 105.00$, $1.25 < z/h < 3.75$.

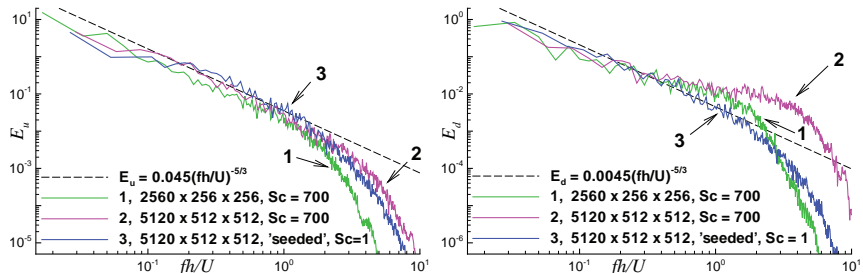


Fig. 6. Temporal horizontal velocity (left) and density (right) spectra at $x/h = 102.5$, $z/h = 2.5$ averaged over 64 points along y .

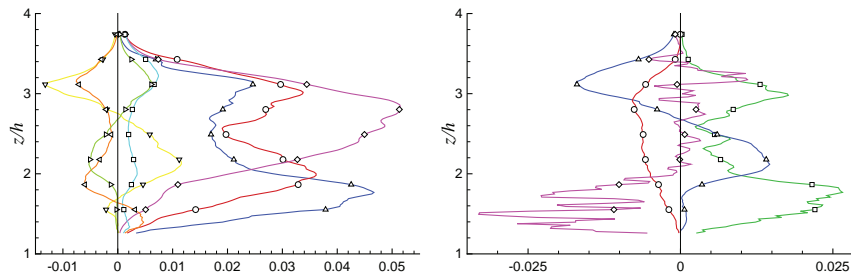


Fig. 7. Second moments (left) and t.k.e. balance terms (right), averaged along y (at $x/h = 102.5$), and from $tU/h = 35$ to 55. Legends are as for Fig. 5.

Vortex self-similarity and the evolution of unforced inviscid two-dimensional turbulence

D.G. Dritschel, R.K. Scott, C. Macaskill, G.A. Gottwald, and C.V. Tran

School of Mathematics and Statistics, University of St Andrews, St Andrews KY16
9SS, UK `dgd` at `mcs.st-and.ac.uk`

It has been recognized for some time that the k^{-3} decay of the energy spectrum in two-dimensional, freely-decaying turbulence, found independently by Batchelor (1969) and Kraichnan (1967), is not sufficient to explain the frequently observed steeper spectra (see for example McWilliams, 1984). The theories on which the k^{-3} spectrum are based are local in wavenumber space and do not take into account the nonlocal effect of vortices in transporting energy and enstrophy. Since then, several scaling theories have been proposed stressing the importance of vortices for the energy transport in spectral space. Benzi *et al.* (1988,1992) linked the statistics of vortex populations to the energy spectrum. They numerically fitted an algebraically decaying vortex population with number density $n(A, t) \sim A^{-\xi}$ (where $n(A, t)dA$ gives the average number of vortices with areas between A and $A + dA$ over a sample area A_s in the plane) to deduce that the energy spectrum associated with the vortices decays more steeply than predicted by the Batchelor scaling.

The temporal scaling of the vortex number density was addressed in Carnevale (1991) and Weiss & McWilliams (1993), who assumed that, in addition to energy, the maximal vorticity during vortex interactions is conserved. Dimensional arguments lead to an algebraic decay in time of the vortex number density $n(A, t)$. Their analysis however assumes vortices of one particular size, and does not predict the value of the scaling exponent. In Dritschel *et al.* (2008, hereafter D08) we unified the spatial and temporal scaling theories by postulating the emergence of a unique, self-similar vortex population in two-dimensional turbulence. This population is characterised by a vortex number density $n(A, t) \propto t^{-2/3} A^{-1}$. This corresponds to an energy spectrum $\mathcal{E}(k, t) \propto t^{-2/3} k^{-5}$ over the range of scales containing the vortex population. Moreover, this implies that the enstrophy in the vortex population decays like $t^{-1/3}$ through partially destructive interactions, which produce incoherent filamentary debris carrying nearly all of the enstrophy to small scales at late times. Meanwhile, and for consistency, the mean radius of the largest vortices slowly grows like $t^{1/6}$, sending energy to progressively larger scales at a diminishing rate proportional to $t^{-5/6}$. The predictions are consistent with

previous numerical simulations (Benzi *et al.* 1992; Bracco *et al.* 2000; Weiss & McWilliams, 1993); in D08, an ensemble of ultra-high resolution numerical simulations verified the predicted scaling laws, in particular showing a $t^{-1/3}$ enstrophy decay holding for 90% of the simulation duration (Fig. 5 therein).

To this vortex self-similarity we now add a description of the evolution at scales larger than any vortex. Again, we use an infinite domain to examine the limit $t \rightarrow \infty$ without the effects of domain boundaries or periodicity. As the flow evolution slows down at late times, the large-scale evolution approaches equipartition (Kraichnan, 1967; Fox & Orszag 1973), with energy becoming equally distributed among Fourier modes over an increasing range of scales. This tendency has been verified using a novel point-vortex experiment starting from small-scale initial conditions that produces a large-scale k^1 energy spectrum over a range of almost three decades (Dritschel *et al.* 2009).

We combine the vortex self-similarity of D08 and large-scale equipartition in a simple model of the long-time turbulent decay incorporating three basic elements:

- (1) large-scale equipartition over a range $k \lesssim m(t)$,
- (2) a self-similar vortex population over a range $m(t) \lesssim k \lesssim f(t)$, and
- (3) a filamentary cascade over a range $f(t) \lesssim k \lesssim d(t)$.

A simple spectral form with these properties is

$$\mathcal{E}(k, t) = \frac{ck(1 + k^2/f^2)}{(k^2 + m^2)^3}. \quad (1)$$

This spectrum is not a mathematical model like the equipartition spectrum proposed by Fox & Orszag (1973), but rather is chosen simply to deduce the spectral transition wavenumbers m and f . Here $m(t)$ is the wavenumber associated with the maximum vortex size. The wavenumber $f(t)$ marks the transition scale from vortices to filaments, and $d(t)$ is the leading edge of the ‘enstrophy front’, assumed to be increasing exponentially. The final coefficient $c(t)$ is proportional to the vortex density (D08).

At sufficiently late times, vortex self-similarity predicts $c(t) \sim t^{-2/3}$ and $m(t) \sim t^{-1/6}$ (D08), but does not predict the ‘filament transition’ wavenumber $f(t)$. Here we determine $f(t)$ from conservation of energy E and enstrophy Q , together with the assumption that the smallest scales stretch exponentially fast (at a constant rate). The model then predicts that the steep k^{-5} energy spectrum associated with the vortex population slowly spreads over the range $m(t) \lesssim k \lesssim f(t)$, with $f(t) \sim t^{1/6}$ and $m(t) \sim t^{-1/6}$. Meanwhile, the shallower k^{-3} energy spectrum associated with filamentary debris retreats to ever higher wavenumbers, $k \gtrsim f(t) \sim t^{1/6}$.

This model is supported by a large ensemble of high resolution numerical simulations. The vorticity field at two times in one simulation is shown in Figure 1 to illustrate prevalence of filamentary structures at early times and

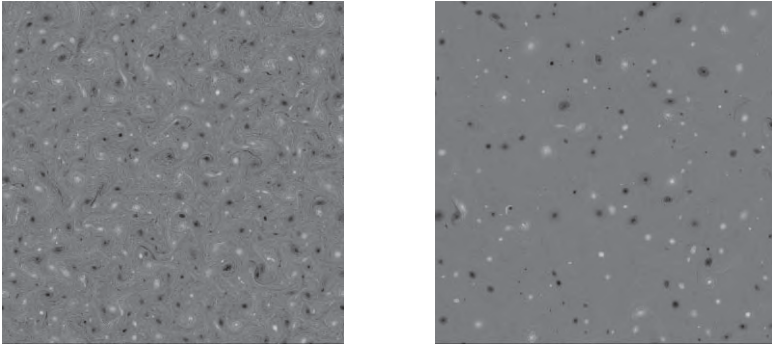


Fig. 1. Vorticity at $t = 6$ (left) and $t = 24$ (right) in one representative simulation. A linear greyscale is used from the minimum (black) to maximum (white) values.

the emergence of vortices at later times. In fact the flow is dominated by vortices at all but the earliest times.

Figure 2 (left) shows the enstrophy spectrum at early, intermediate and late times. Each spectrum is multiplied by $t^{2/3}$ so that, in theory, the intermediate ‘vortex wavenumber range’ remains steady. At low wavenumbers, we observe a k^3 spectrum (which eventually saturates when energy reaches the domain scale), while at small scales we see a slowly retreating k^{-1} range. A comparison of the numerical and ideal model enstrophy spectra at an intermediate time of $t = 40$ is shown (right). The ideal spectrum is more peaked but captures the spectral transitions around $k = m$ and $k = f$, and closely matches the k^{-1} tail. Importantly, the spectral parameters are *not* sensitive to the form of the ideal spectrum we have chosen.

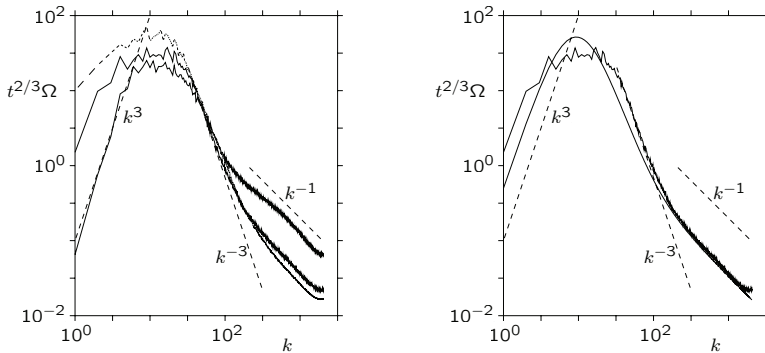


Fig. 2. Left: Ensemble-averaged scaled enstrophy spectra $t^{2/3}\Omega(k, t)$ at $t = 10$ (bold solid line), 40 (thin solid line) and 160 (dashed line). Right: $t^{2/3}\Omega(k, t)$ at $t = 40$ (bold solid line) compared with the ideal scaled spectrum using (1). The temporal scaling is intended to collapse the spectra over the range of scales occupied by vortices, $m \lesssim k \lesssim f$. Various slopes are indicated.

In conclusion, we have developed a new model for the late-time evolution of inviscid, unforced two-dimensional turbulence, whose predictions are well-supported by high resolution numerical experiments. The model builds upon vortex self-similarity over a slowly-expanding intermediate range of scales (D08). Here, we propose that the scales larger than any vortex approach a state of equipartition, with energy spread uniformly among Fourier modes (except at ultra-large scales, where the spectrum is bounded by a constant times $t^2 k^3$, see Tran & Dritschel, 2006a). Whereas ideal equipartition is a statistically-steady state, in our model the energy spectrum at large scales slowly grows like $\mathcal{E}(k, t) \propto t^{1/3} k^1$, and slowly cascades to ever larger scales, $k \lesssim m(t) \propto t^{-1/6}$. At small scales, Batchelor's k^{-3} spectrum is gradually replaced at its upper end around $k = f(t) \propto t^{1/6}$ by the steeper spectrum $\mathcal{E}(k, t) \propto t^{-2/3} k^{-5}$ associated with a self-similar population of vortices (D08). The k^{-3} spectrum, we argue, spreads to high k exponentially fast, implying that the spectrum decays like t^{-1} there.

References

1. BATCHELOR, G. K. 1969 Computation of the energy spectrum in homogeneous two-dimensional turbulence. *Phys. Fluids* **12**, 233–239.
2. BENZI, R., PATARNELLO, S. & SANTANGELO, P., 1988 Self-similar coherent structures in two-dimensional decaying turbulence. *J. Phys. A* **21**, 1221–1237.
3. BENZI, R., COLELLA, M., BRISCOLINI, M. & SANTANGELO, P., 1992 A simple point vortex model for two-dimensional decaying turbulence. *Phys. Fluids* **4**, 1036.
4. BRACCO, A., MCWILLIAMS, J. C., MURANTE, G., PROVENZALE, A. & WEISS, J. B. 2000 Revisiting freely decaying two-dimensional turbulence at millennial resolution. *Phys. Fluids* **12**, 2931–2941.
5. CARNEVALE, G. F, MCWILLIAMS, J. C., POMEAU, Y., WEISS, J. B. & YOUNG, W. R., 1991 Evolution of vortex statistics in two-dimensional turbulence. *Phys. Rev. Lett.* **66**, 2735–2737.
6. DRITSCHEL, D. G., SCOTT, R. K., MACASKILL, C., GOTTWALD, G. A. & TRAN, C. V. 2008 Unifying scaling theory for vortex dynamics in two-dimensional turbulence. *Phys. Rev. Lett.* **101**, 094501.
7. DRITSCHEL, D. G., SCOTT, R. K., MACASKILL, C., GOTTWALD, G. A. & TRAN, C. V. 2009 Late time evolution of unforced inviscid two-dimensional turbulence. *J. Fluid Mech.* submitted.
8. FOX, D. G. & ORSZAG, S. A. 1973 Inviscid dynamics of two-dimensional turbulence. *Phys. Fluids* **16(2)**, 169–171.
9. KRAICHNAN, R. H. 1967 Inertial ranges in two-dimensional turbulence. *Phys. Fluids* **10**, 1417–1423.
10. MCWILLIAMS, J. C, 1984 The emergence of isolated coherent vortices in turbulent flow. *J. Fluid Mech.* **146**, 21–43.
11. WEISS, J. B. & MCWILLIAMS, J. C. 1993 Temporal scaling behavior of decaying two-dimensional turbulence. *Phys. Fluids* **5**, 608–621.

Large Eddy Simulation of compressible magnetohydrodynamic turbulence in the local interstellar medium

A.A. Chernyshov, K.V. Karelsky, and A.S. Petrosyan

Theoretical section, Space Research Institute of the Russian Academy of Sciences,
Profsoyuznaya 84/32, 117997, Moscow, Russia
apetrosy@iki.rssi.ru

There is growing interest in observations and explanation of the spectrum of the density fluctuations in the interstellar medium. These fluctuations are responsible for radio wave scattering in the interstellar medium and cause interstellar scintillation fluctuations in the amplitude and phase of radio waves. Kolmogorov-like $k^{-5/3}$ spectrum of density fluctuations have been observed in wide range of scales in the local interstellar medium (from an outer scale of a few parsecs to scales of about 200 km. Motivated by these observations Zank, Matthaeus et al. [1] developed "nearly incompressible" theory describing compressive effects in hydrodynamical and magnetic fluids. This singular asymptotic theory coupled convective fluid motions with high-frequency acoustic fluctuations in which leading order fluctuations are incompressible modes. According to this theory, Dastgeer and Zank [2] investigated inertial range turbulence properties using two-dimensional neutral fluid simulations and found that density fluctuations behave as passive scalar, reproduce incompressible Kolmogorov spectra and obey anisotropic properties. An origin of the density fluctuations spectrum observed in the local interstellar medium was explained by direct numerical simulations (DNS) of the three-dimensional time dependent compressible magnetohydrodynamic (MHD) fluid and nearly incompressible model is used to interpret results.

For study of three-dimensional compressible MHD turbulence in interstellar medium we use potentials of large eddy simulation (LES) method [3, 4, 5]. We use Smagorinsky model for compressible MHD case for subgrid-scale (SGS) parametrization that showed accurate results under various range of similarity numbers [3].

The initial isotropic turbulent spectrum was chosen for kinetic and magnetic energies in Fourier space to be close to k^{-2} with random amplitudes and phases in all three directions. The choice of such spectrum as initial conditions is due to velocity perturbations with an initial power spectrum in Fourier space similar to that of developed turbulence. This is some way equivalent to

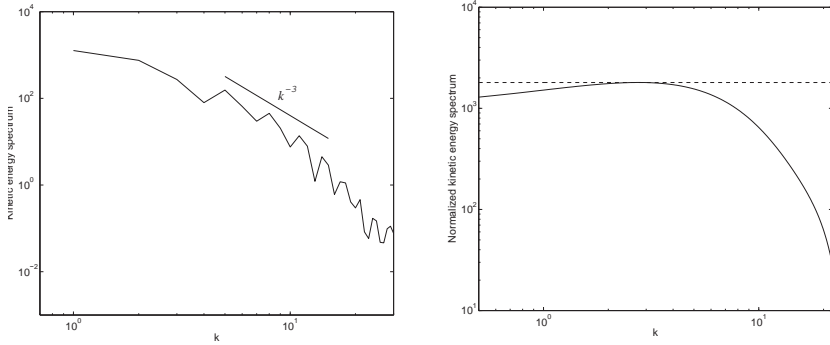


Fig. 1. The kinetic energy spectrum (left). Normalized and smoothed spectrum of kinetic energy, multiplied by $k^{5/3}$ (right). Notice that the spectrum is close to $\sim k^{-3}$ in a forward cascade regime of decaying turbulence. However, there is well-defined inertial Kolmogorov-like range of $k^{-5/3}$.

start with developed turbulence. In addition, the choice of such spectrum is physically motivated by its rapid convergence as the inertial range spectrum of the energy yields a k^{-3} spectrum through a forward cascade mechanism. Moreover, any single discontinuous shock waves also have such a power spectrum as that for simple the Fourier transform of a step function. Taking the Fourier transform of many shocks do not change this power law. Nevertheless, most distributions with k^{-2} spectra do not contain shocks. Initial conditions

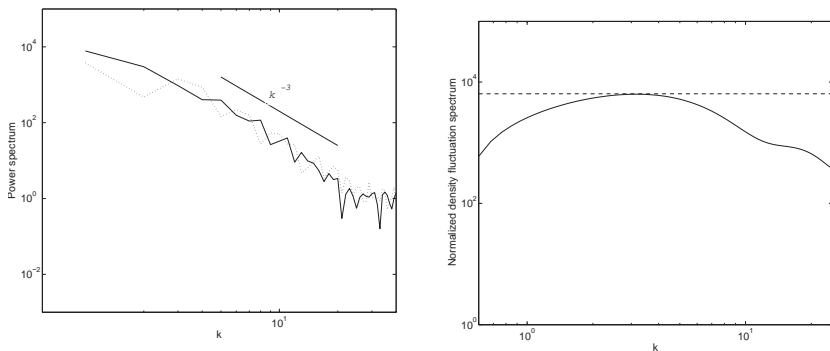


Fig. 2. The density spectrum is the solid line and the density fluctuations spectrum is the dot line (left). Normalized and smoothed spectrum of density fluctuations, multiplied by $k^{5/3}$ (right). Both graphs (in the left figure) have spectral index close to $\sim k^{-3}$. Moreover, there is well-defined inertial Kolmogorov-like range of $k^{-5/3}$ that confirms observation data.

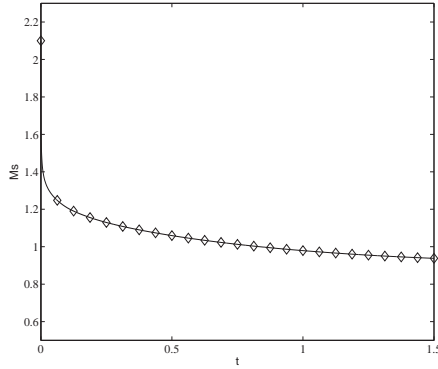


Fig. 3. Decay of turbulent small-scale Mach number \check{M}_s with time. A transition from a supersonic $\check{M}_s > 1$ to a subsonic $\check{M}_s < 1$ can be observed.

for the velocity and the magnetic field have been obtained in physical space using inverse Fourier transform.

In this work compressible MHD turbulence in local interstellar medium is studied using LES method for turbulence modeling and subsequent numerical solution of system of resolved magnetohydrodynamic equations. Notwithstanding the fact that supersonic flows with high value of large-scale Mach numbers are characterized in interstellar medium, nevertheless, there are subsonic fluctuations of weakly compressible components of interstellar medium. These weakly compressible subsonic fluctuations are responsible for emergence of a Kolmogorov-type spectrum in interstellar turbulence which is observed from experimental data. In this work, it is shown that density fluctuations are a passive scalar in a velocity field in weakly compressible magnetohydrodynamic turbulence and demonstrate Kolmogorov-like spectrum in a dissipative range of the energy cascade (Fig. 1 and Fig. 2). The spectral indexes of density fluctuations and kinetic energy are almost coincident and close to k^{-3} spectrum. It is represented that the range with Kolmogorov-like spectrum of density fluctuations exists the same as kinetic energy spectrum, with the same wave numbers. The decrease of energy-containing large eddies and inertial range with time, and the increase of dissipative scale are also represented. It is shown in Fig. 3, that the turbulent sonic Mach number decreases significantly from a supersonic turbulent regime ($\check{M}_s > 1$), where the medium is strongly compressible, to a subsonic value of Mach number ($\check{M}_s < 1$), describing weakly compressible flow. This conclusion about reduction of a role of compressibility in turbulent fluctuations confirms by time evolution of velocity divergence which decreases and tends zero (but not zero). In interstellar medium, the transition of MHD turbulent flow from a strongly compressible to a weakly compressible state not only transforms the characteristic supersonic motion into subsonic motion, but also attenuates plasma magnetization,

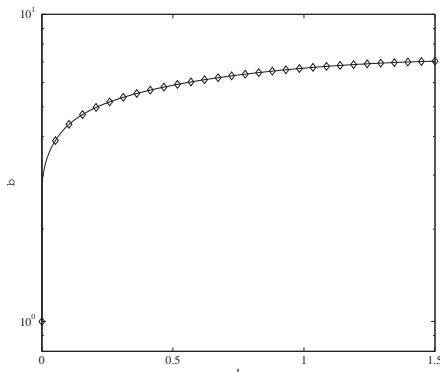


Fig. 4. Time evolution of the turbulent plasma beta $\check{\beta}$ in compressible MHD turbulence. The MHD plasma is strongly magnetized initially and then, as the turbulence evolves, the plasma becomes less magnetized.

which is shown in Fig. 4 because plasma beta $\check{\beta}$ increases with time, thus, role of magnetic energy decreases in comparison with plasma pressure. Besides, the anisotropy of turbulent flow is considered and it is demonstrated that large-scale flow shows anisotropic properties while small-scale structures are isotropic. We quantitatively distinguish local spectral transfer of the velocity field in Fourier space by decomposing the spectrum into its x -, y - and z -components of velocity. Numerical simulation shows various behaviour of the velocity components in spectral cascade at the lower wave number and almost lack of distinctions for large Fourier modes. This indicates that larger scales show a greater anisotropization. In order to estimate the isotropy and the symmetry we use the Shebalin angles (it is also called the anisotropy angles). After short initial time interval, anisotropy of velocity and magnetic field does not change almost and achieves a saturation level.

LES method is shown to be effective in solving interstellar turbulent problem.

References

1. G. P. Zank & W. H. Matthaeus. *Phys. Fluids A*, 5, 257 (1993)
2. S. Dastgeer & G. P. Zank. *Nonlin. Processes Geophys.*, 12, 139 (2005)
3. A. A. Chernyshov, K. V. Karelsky, & A. S. Petrosyan. *Physics of Fluids*, 19, 055106 (2007)
4. A. A. Chernyshov, K. V. Karelsky, & A. S. Petrosyan. *Phys. Plasmas*, 13, 032304 (2006)
5. A. A. Chernyshov, K. V. Karelsky, & A. S. Petrosyan. *Physics of Fluids*, 20, 085106 (2008)

Part VIII Transport and mixing

Experimental Studies of Turbulent Rayleigh-Bénard Convection

Ke-Qing Xia

Department of Physics, The Chinese University of Hong Kong, Hong Kong, China
kxia@phy.cuhk.edu.hk

Rayleigh-Bénard (RB) convection has become a paradigm for the study of convective thermal turbulence. Understanding convective thermal turbulence is important for several reasons. First, as an important class of turbulent flows, convective thermal turbulence differs from other types of turbulence in many ways. Studying convective turbulence would therefore provide new insight and perspectives on the general turbulence problem itself. Secondly, it is a phenomenon occurring widely in geophysical and astrophysical systems, such as atmospheric and ocean circulations; convection in the Earth mantle and its outer core; stellar convection like that in the Sun. Thirdly, heat transfer and mixing are important engineering problems. The state of motion in a thermally driven convecting fluid is governed by the Boussinesq equations, plus the incompressibility condition:

$$\frac{\partial \mathbf{v}}{\partial t} + \mathbf{v} \cdot \nabla \mathbf{v} = -\frac{1}{\rho} \nabla p + \nu \nabla^2 \mathbf{v} + g\alpha \delta T \hat{z} \quad (1)$$

$$\frac{\partial T}{\partial t} + \mathbf{v} \cdot \nabla T = \kappa \nabla^2 T \quad (2)$$

$$\nabla \cdot \mathbf{v} = 0 \quad (3)$$

When the above are recast into dimensionless form, two parameters appear in the equations of motion for the temperature and velocity fields; these are the Rayleigh number $Ra = \alpha g \Delta T H^3 / (\nu \kappa)$ and the Prandtl number $Pr = \nu / \kappa$, where ΔT is the applied temperature difference, H is the height of the cell, g is the acceleration due to gravity, and α , ν , and κ are, respectively, the volume expansion coefficient, kinematic viscosity, and thermal diffusivity of the fluid. In any laboratory convection experiment a lateral sidewall is inevitably present, so the aspect ratio ($\Gamma = \text{diameter}/\text{height}$; therefore, $\Gamma = D/H$ for a cylinder of height H and diameter D) enters this problem as another control parameter. A measure of the heat transfer enhancement by convective flow is the Nusselt number $Nu = J / (\chi \Delta T / H)$, which is the ratio between the actual

convective heat transfer and the heat that would be transferred if there exists only conduction, here χ is the thermal conductivity of the working fluid in quiescent state. Another response parameter is the well-known Reynolds number Re . Therefore, the system has three control parameters: Ra , Pr and Γ , and two response parameters: Nu and Re . Figure 1 shows an illustration of the Rayleigh-Bénard convection cell with all the important structures or “components” of the flow, i.e. the thermal plumes (both sheetlike and mushroom-like), the large-scale circulation, and the boundary layers (an aspect ratio one cylinder, the most popular configuration, is used here).

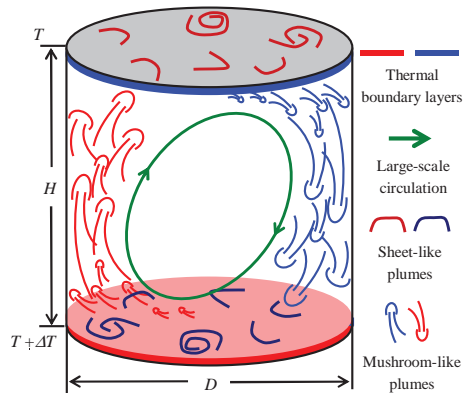


Fig. 1. Sketch of the Rayleigh-Bénard convection system showing all the important structures: thermal plumes, large-sale circulation (the wind), and the boundary layers.

Traditionally, there are five major issues or areas in the studies of convective thermal turbulence: 1. Turbulent Heat Transfer; 2 Boundary Layer Dynamics; 3. Dynamics of the Large-scale Flow; 4. Small-scale Turbulence; and 5. Thermal Plumes. The state of the affair and the progresses made in the past decade in the first three areas, i.e. heat transfer, boundary layers, and coherent structures have been discussed in great detail in the recent review article by Ahlers, Grossmann and Lohse [1] and those in the fourth area, i.e. small-scale properties of the velocity and the temperature fields, have been reviewed recently by Lohse and Xia [2]. Here I will provide only a brief summary on the status of the major issues and then present and discuss some experimental results from my own laboratory.

Turbulent Heat Transfer — A central issue in convective turbulence is to understand how heat is transported by highly turbulent flows. Specifically, we ask how the Nusselt number Nu depends on the three control parameters of the system at very high levels of turbulence, i.e. $Nu(Ra, Pr, \Gamma) = ?$ For moderately large Ra and over a wide range of Pr , the behavior of Nu can be adequately

described by a theoretical model proposed by Grossmann and Lohse (GL) [3], which decomposes the kinetic energy and thermal dissipation rates into boundary layer (BL) and bulk contributions. For very large Ra and small to moderate Pr , an earlier model proposed by Kraichnan [4], and also the GL model itself, predicts that Nu should scale with Ra with an exponent of $1/2$. The current status of this so-called ultimate (or Kraichnan) regime of thermal convection is that no convincing experimental evidence exists that supports its existence and the recent experimental [5] and numerical [6] measurements that have reached the values of Ra for which the Kraichnan scaling is supposed to rule have all found a scaling exponent of $1/3$. A conclusive confirmation or negation of this regime remains a central challenge in the study of turbulent thermal convection. Instead of focusing on the Nu itself, a fruitful way to tackle this problem would be to look for transitions in the boundary layers, as the Kraichnan regime requires the boundary layer becoming turbulent. Figure 2 shows a photo of a large convection facility, the Hong Kong Giant Cell, for which investigations along this line of research have been planned.

Boundary Layer Dynamics — The existence of strong temperature fluctuations near the horizontal plates makes the measurement of viscous boundary layer a challenge. Nevertheless, it is necessary to make direct measurements of the viscous boundary layer in order to critically differentiate various models. This is because different models have very different assumptions about the boundary layer, but all have similar predictions for the scaling between Nu and Ra . For example, the GL theory assumes a laminar Prandtl-Blasius boundary layer, which is a key ingredient in that theory. Recently, Sun *et al.* have made high-resolution measurements of the properties of the velocity boundary layer and found that, despite the intermittent emission of plumes, the Blasius-type laminar boundary condition is indeed a good approximation, in time-averaged sense, both in terms of its scaling and its various dynamic properties [7]. As already mentioned, future research should focus on any departures from the laminar boundary layer behavior (at highest Ra achievable), not just in connection to the search for the ultimate regime, but also to see how the eruption of thermal plumes (or temperature as an active scalar) changes the dynamics of the boundary layer and its time-averaged properties.

Large-scale Flow Dynamics — A fascinating feature of turbulent RB convection is the emergence of a well-defined and nearly coherent circulating roll spanning the height of the convection cell (for $\Gamma \simeq 1$) in defiance of the turbulent background. This large-scale circulation (LSC), also known as the wind of turbulent convection, has many intriguing dynamic features, such as azimuthal rotations and occasional cessations (momentary vanishing of its circulation speed) and reversals (of its circulation directions). Most strikingly is its coherent three-dimensional bulk oscillation. Energetically, the LSC is driven by the plumes as shown in both thermal and flow visualizations and quantitative measurements [8, 9]. Recently, however, it has been shown [10]

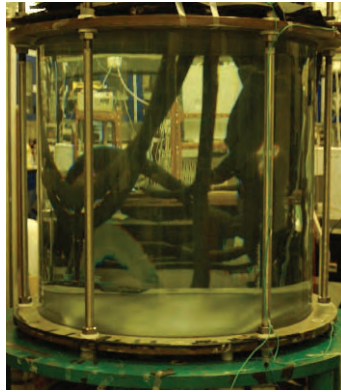


Fig. 2. The Hong Kong Giant Cell of 1-meter diameter and height varying from 1 to 4 meters (1 meter high is shown). Water is the working fluid. Both heat transport and boundary layer measurements have been planned for this large convection facility.

that the intricate three-dimensional flow dynamics, manifested by the torsional [11] and sloshing modes [13] of the LSC, are not dictated by thermal plume emissions or boundary layer dynamics, rather the plumes behave passively as far as oscillatory dynamics is concerned.

Small-scale Turbulence — What is the physical mechanism that drives the cascades of the velocity and temperature fields in buoyancy-driven turbulence, such as turbulent thermal convection, has been a long-debated issue. Specifically, does the classical Bolgiano-Obukhov scaling (BO59) exist above the so-called Bolgiano scale ℓ_B ? To answer this question, one needs to make direct measurements of the spatial velocity and temperature structure functions instead of inferring them from time-domain data. Such attempts have been made recently by Sun *et al.* [12] who made high-resolution multipoint measurements of both the velocity and the temperature fields. Using particle image velocimetry (PIV) and the multi-thermistor-probe technique, they measured respectively the two-dimensional velocity field and the temperature difference along the vertical direction, from which the real-space structure functions of both velocity and temperature were obtained. Basically, Sun *et al.* found that in the central region both velocity and temperature exhibit the same scaling behavior that one would find for the velocity and for a passive scalar in homogeneous and isotropic Navier-Stokes turbulence. However, as discussed by Lohse and Xia [2], due to the opposite behavior of the global ($\langle \ell_B \rangle$) and local ($\ell_B(\mathbf{x})$) Bolgiano scale with respect to Ra , and the lack of wide separation of scales between η (the Kolmogorov dissipation scale), ℓ_B and L (the integral scale), as well as theoretical inconsistencies of the Bolgiano argument itself, the existence of the Bolgiano scale (i.e. BO59-type of scaling above ℓ_B and K41-type scaling below ℓ_B) remains unsettled.

Thermal Plumes — The thermal plumes, both as thermal and geometrical objects, play an important role in heat transport, and there are a number of studies devoted to this subject. Recognizing that thermal plumes produce cliff and ramp structures in the measured local temperature time series and using the criterion $T_{\tau_\eta} > T_{RMS}$ (where T_{τ_η} is the temperature increment $T_\tau = T(t + \tau) - T(t)$ over the dissipative timescale τ_η and T_{RMS} is the RMS value of the temperature T), Zhou and Xia [14] were able to effectively extract plume signals from the measured temperature time series. Examples of hot and cold plumes extracted using this method are shown in Fig. 3 and it is seen that these structures are large temperature excursions from the mean which can reach close to $10T_{RMS}$. In contrast to “ramp-cliff” structures for passive scalars, these extracted plume signals clearly exhibit “cliff-ramp” structures (corresponding to the cap of plumes) that exhibit log-normal distribution. In a recent study of morphological transformation from mushroom-like to sheet-like plumes using liquid crystal imaging of the temperature field, Zhou *et al.* [16] found that several other properties of plumes, such as the area, circumference and heat content (of sheetlike plumes, see Fig. 3(c)), also exhibit log-normal distributions, suggesting that long-normality may be a generic feature of plume-related quantities. In addition, plumes in the bulk (see Fig. 3(b)) are found to be always associated with strong vertical vorticity [16], implying that mushroomlike plumes are essentially vortical structures. When simultaneous velocity and temperature data are available, more sophisticated schemes can be used to extract plume properties. In a numerical study of RB convection, Jullien *et al.* [17] identified plumes using several criteria that are combinations of temperature, vertical velocity and vertical vorticity satisfying certain thresholds. Ching *et al.* [18] obtained plume velocity by calculating the conditional average of velocity on temperature that were measured simultaneously in a RB experiment in water [19] and decomposed the velocity signal into a sum of plume velocity $\mathbf{v}_p(t) \equiv \langle \mathbf{v} | T(t) \rangle$ and a background one that is uncorrelated with the temperature. With this method, they were able to separate the measured local heat flux into those carried by the plumes and those by the background velocity. While in [16] individual sheetlike plumes were extracted manually, Shishkina and Wagner [20] identified them using the properties of temperature, thermal dissipation rate and vorticity in a DNS study of RB convection.

In addition to the kinetic, or viscous, boundary layer that has been discussed above, the thermal boundary layer plays a crucial role in the determination of the heat transport. Several length scales can be associated with the thermal boundary layer. Here we use λ_{th} to denote the thermal boundary layer thickness which is based on the mean temperature profile $T(z)$ (where z is the distance from one of the horizontal plates of the cell, see Fig. 4) and is defined through the slope of $T(z)$ near the plate, i.e. λ_{th} is located at the intersection between the extrapolation of the linear slope of $T(z)$ and the horizontal line equaling T_c the mean temperature at cell center. This definition is the most widely used. Another length scale is based on the profile $T_{RMS}(z)$

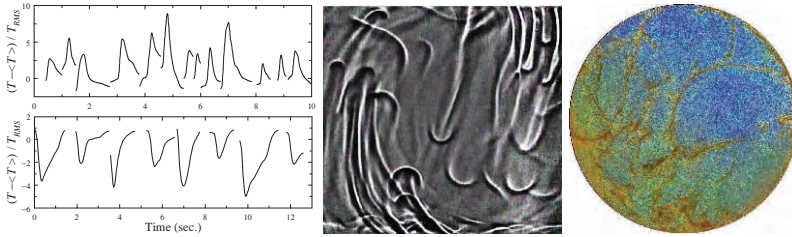


Fig. 3. Left panel: Examples of plume signals extracted from temperature time series measured in water: hot plumes (upper panel; $Ra=1.8 \cdot 10^{10}$) and cold plumes (lower panel; $Ra=5.4 \cdot 10^9$); the cliff-ramp structures (such as fast ‘rise’ and slow ‘decay’, in either direction from the mean) are apparent here. Time origins for the plumes are arbitrary. It is clear from the figures that the ‘front’ or ‘cap’ of plumes become sharper as Ra increases. Adapted from [15]. Middle panel: Shadowgraph image (side view) of mushroom-like plumes obtained ($Ra = 6.8 \cdot 10^8$ and $Pr = 596$). Adapted from [9]. Right panel: Liquid crystal image (top view) of the temperature field taken at 2 mm from the top plate showing sheetlike plumes ($Ra = 2.0 \cdot 10^9$ and $Pr = 5.4$). Adapted from [16].

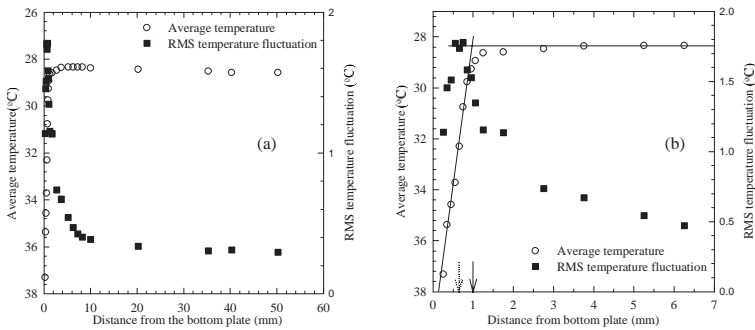


Fig. 4. (a) Profiles of the mean $T(z)$ and RMS $T_{RMS}(z)$ temperatures as a function of the distance z measured from the lower plate of a cylindrical convection cell ($Ra= 7.0 \times 10^9$). (b) Enlarged portions of profiles in (a) near the plate; also shown are the definitions of the two length scales λ_{th} and δ_{RMS} . Adapted from [22].

of the RMS value of the temperature. We denote this length scale as δ_{RMS} and it is defined as the position of the maximum of $T_{RMS}(z)$. Definitions of the two length scales are illustrated in Fig. 4(b). In many cases, these two values are very close to each other and so it has been suggested that these two can be used interchangeably [21]. Here we show that this is in general not the case. In Fig. 5(a) we show the Ra -dependence of both λ_{th} and δ_{RMS} measured in an aspect ratio $\Gamma = 1$ cylindrical cell using water as the working fluid. Figures 5(b) and (c) show the same quantities but measured in cells with $\Gamma = 0.5$ and 4.4. These figures show clearly that the length scale δ_{RMS} has a strong aspect-ratio dependence. This is summarized in Fig. 5(d) and

can also be quantified by the power-law fittings (the solid lines in the figures, $\Gamma = 2$ results not shown):

$$\text{For } \Gamma = 0.5, \quad \begin{cases} \lambda_{th}/H = (2.48 \pm 0.04)Ra^{-(0.287 \pm 0.003)} \\ \delta_{RMS}/H = (0.29 \pm 0.05)Ra^{-(0.21 \pm 0.01)} \end{cases} \quad (4)$$

$$\text{For } \Gamma = 1.0, \quad \begin{cases} \lambda_{th}/H = (2.22 \pm 0.04)Ra^{-(0.284 \pm 0.005)} \\ \delta_{RMS}/H = (0.32 \pm 0.05)Ra^{-(0.20 \pm 0.01)} \end{cases} \quad (5)$$

$$\text{For } \Gamma = 2.0, \quad \begin{cases} \lambda_{th}/H = (2.54 \pm 0.08)Ra^{-(0.285 \pm 0.003)} \\ \delta_{RMS}/H = (0.34 \pm 0.05)Ra^{-(0.22 \pm 0.01)} \end{cases} \quad (6)$$

$$\text{For } \Gamma = 4.4, \quad \begin{cases} \lambda_{th}/H = (3.9 \pm 0.1)Ra^{-(0.309 \pm 0.004)} \\ \delta_{RMS}/H = (7.0 \pm 0.9)Ra^{-(0.34 \pm 0.01)} \end{cases} \quad (7)$$

From the above it is obvious that λ_{th} and δ_{RMS} are in general *two different quantities* in terms of both their Ra-scaling exponents and their magnitudes. We can also see that the power-law exponent for λ_{th} varies somewhat among different aspect ratios, which may be understood as a result of crossing different regimes due to the change of Ra over five decades. Whereas the exponent for δ_{RMS} clearly changes more drastically as aspect ratio is changed. Bear in mind that δ_{RMS} is the position of maximum temperature fluctuations and that the large-scale flow pattern depends on the aspect ratio. Therefore, the results here suggest that the position of maximum temperature fluctuations depends more sensitively on the flow patterns than the thickness of thermal boundary layer which is intrinsically related to heat transport.

Acknowledgement: The author wishes to thank Quan Zhou for his help in preparing many of the figures and S.-Q. Zhou and S.-L. Lui for making their, respectively, plume signal and thermal boundary layer data available to him. He also acknowledges support from the Hong Kong Research Grants Council (Grant Nos. 403806, 403807).

References

1. G. Ahlers, S. Grossmann and D. Lohse, Rev. Mod. Phys., **81**, April-June (2009).
2. D. Lohse and K.-Q. Xia, Ann. Rev. Fluid. Mech., (2010).
3. S. Grossmann and D. Lohse, J. Fluid Mech., **407**, 27 (2000); Phys. Rev. Lett., **86**, 3316 (2001); Phys. Rev. E, **66**, 016305 (2002); Phys. Fluids, **16**, 4462 (2004).
4. R. H. Kraichnan, Phys. Fluids, **5**, 1374 (1962).
5. J. J. Niemela and K. R. Sreenivasan, J. Fluid Mech., **557**, 307 (2006); A. Nikolaenko, E. Brown, D. Funfschilling and G. Ahlers, J. Fluid Mech., **523**, 251 (2005).
6. G. Amati, *et al.*, Phys. Fluids, **17**, 121701 2005.
7. C. Sun, Y.-H. Cheung and K.-Q. Xia, J. Fluid Mech., **605**, 79 (2008).

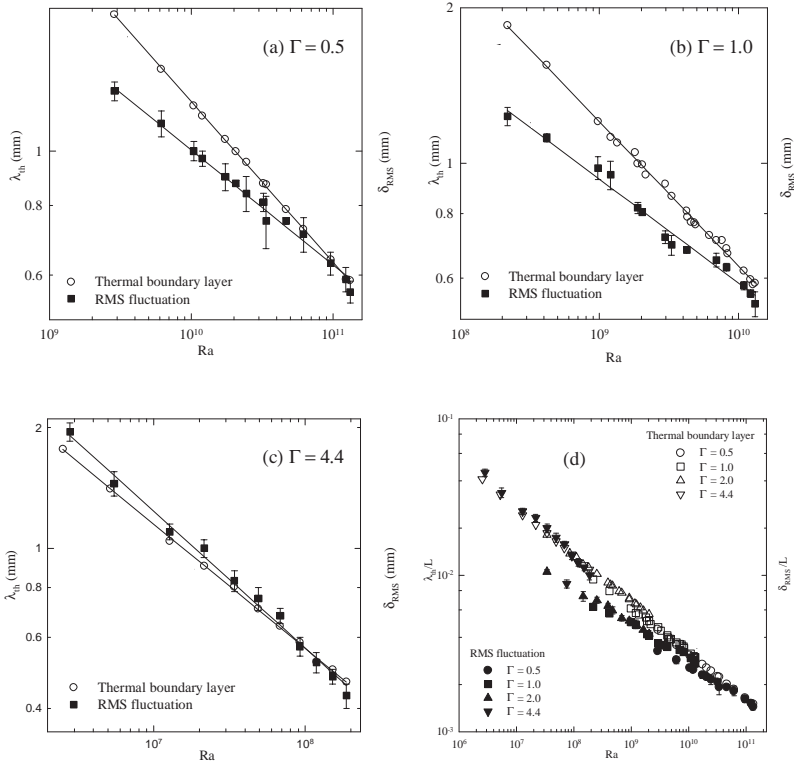


Fig. 5. Ra-dependence of the two length scales λ_{th} and δ_{RMS} measured in cylindrical cells with aspect ratio (a) $\Gamma = 0.5$; (b) $\Gamma = 1.0$; (c) $\Gamma = 4.4$; and (d) All four aspect ratios: 0.5, 1.0, 2.0, and 4.4. Adapted from [22].

8. K.-Q. Xia, C. Sun and S.-Q. Zhou, *Phys. Rev. E*, **68**, 066303 (2003).
9. H.-D. Xi, S. Lam and K.-Q. Xia, *J. Fluid Mech.*, **503**, 47 (2004).
10. H.-D. Xi, *et al.*, *Phys. Rev. Lett.*, **102**, 044503 (2009).
11. D. Funfschilling and G. Ahlers, *Phys. Rev. Lett.*, **92**, 194502 (2004).
12. C. Sun, Q. Zhou and K.-Q. Zhou, *Phys. Rev. Lett.*, **97**, 144504 (2006).
13. Q. Zhou, H.-D. Xi, S.-Q. Zhou, C. Sun and K.-Q. Xia, *J. Fluid Mech.*, in press.
14. S.-Q. Zhou and K.-Q. Xia, *Phys. Rev. Lett.*, **89**, 184502 (2002).
15. S.-Q. Zhou, PhD Thesis, The Chinese University of Hong Kong (2002).
16. Q. Zhou, C. Sun and K.-Q. Xia, *Phys. Rev. Lett.*, **98**, 074501 (2007).
17. K. Jullien, *et al.*, *J. Fluid Mech.*, **391**, 151 (1999).
18. E. S. C. Ching, *et al.*, *Phys. Rev. Lett.*, **93**, 124501 (2004).
19. X.-D. Shang, *et al.*, *Phys. Rev. Lett.*, **90**, 074501 (2003).
20. O. Shishkina and C. Wagner, *J. Fluid Mech.*, **599**, 383 (2008).
21. A. Tilgner, A. Belmonte and A. Libchaber, *Phys. Rev. E*, **47**, R2253 (1993).
22. S.-L. Lui, MPhil Thesis, The Chinese University of Hong Kong (1997).

Various flow amplitudes in 2D non-Oberbeck-Boussinesq Rayleigh-Bénard convection in water

Enrico Calzavarini¹, Siegfried Grossmann^{2*}, Detlef Lohse¹, and Kazuyasu Sugiyama¹

¹ Physics of Fluids group, Department of Applied Physics, J. M. Burgers Centre for Fluid Dynamics, and Impact-, MESA-, and BMTI-Institutes, University of Twente, P. O. Box 217, 7500 AE Enschede, The Netherlands,

² Fachbereich Physik, Philipps-Universität Marburg, 35032 Marburg, Germany,

*grossmann at physik.uni-marburg.de

The flow organization in Rayleigh-Bénard turbulence including Non-Oberbeck-Boussinesq (NOB) effects is numerically analyzed. The working fluid is water, the aspect ratio is $\Gamma = 1$, and we restrict ourselves to two-dimensional flow. We focus here on a summary of the structure of the velocity field. A more detailed analysis of the flow structure as well as on the temperature profiles, the center temperature and the Nusselt number is given in [1].

The thermal flow develops several large scale coherent structures and thus has to be described by several velocity amplitudes (or Reynolds numbers). These include the volume and time averaged energy based velocity amplitude

$$Re^E = \left\langle \frac{1}{2} \mathbf{u}^2 \right\rangle_{V,\tau}^{1/2} \cdot L/\nu, \quad (1)$$

and local wind amplitudes $Re(x_j) = \left\langle \frac{1}{2} \mathbf{u}^2(x_j) \right\rangle_{\tau}^{1/2} \cdot L/\nu$ for certain characteristic positions x_j , e.g. in the cell center, at the profiles' maxima, in the corner rolls etc. Correspondingly, one also has to introduce and study several velocity profiles, area averaged or local ones. These together describe the various features of the rather complex flow organization.

Our results for the center temperature T_c are presented both as functions of the Rayleigh number Ra (with Ra up to 10^8) for fixed temperature difference Δ between top and bottom plates and as functions of Δ (which measures the “non-Oberbeck-Boussinesqness”) for fixed Ra with Δ up to 60K (see Figure 1). All results are consistent with the available experimental NOB data for the center temperature T_c and the Nusselt number ratio Nu_{NOB}/Nu_{OB} . Here, the labels OB and NOB mean that the Oberbeck-Boussinesq conditions are either valid or are not guaranteed any more, respectively, i.e., $Nu_{NOB} \equiv Nu$ is the actually measured Nusselt number.

For the temperature profiles we find – due to plume emission from the boundary layers – increasing deviations from the extended Prandtl-Blasius boundary layer theory presented in [2] with increasing Ra , while the center temperature itself is surprisingly well predicted by that theory.

For given non-Oberbeck-Boussinesqness Δ both the center temperature T_c and the Nusselt number ratio Nu_{NOB}/Nu_{OB} only weakly depend on Ra .

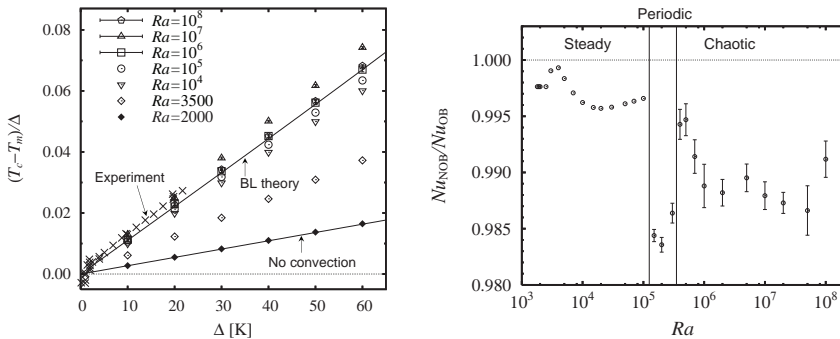


Fig. 1. Left: Relative deviation $(T_c - T_m)/\Delta$ of the horizontally area (and time) averaged center temperature T_c from the arithmetic mean temperature T_m in terms of Δ versus the temperature difference Δ for water at fixed $T_m = 40^\circ\text{C}$ for various values of Ra . Right: Nusselt number ratio Nu_{NOB}/Nu_{OB} vs. Rayleigh number Ra for water at fixed values for $T_m = 40^\circ\text{C}$ and $\Delta = 40\text{K}$. It is also indicated where the state is steady, periodic, or chaotic. Apparently there is a tiny reduction of the heat flux Nu due to deviations from Oberbeck-Boussinesq conditions, about 1% or so.

Concerning the flow structure we find that beyond $Ra \approx 10^6$ the flow consists of a large diagonal center convection roll and two smaller rolls in the upper and lower corners, respectively (“corner flows”), see Figure 2. In the NOB case the center convection roll is still characterized by only one velocity scale. In contrast, the top and bottom corner flows are then of different strengths, the velocity amplitude of the bottom corner roll being a factor 1.3 larger (for $\Delta = 40\text{K}$) than the top one. We attribute this to the lower viscosity in the hotter bottom boundary layer.

Under OB-conditions we find a scaling of the volume averaged energy based velocity amplitude as $Re_{OB}^E \propto Ra^\gamma$ with an exponent $\gamma = 0.62$. As the NOBness increases, the enhanced lower corner flow as well as the enhanced center roll lead to an enhancement of the energy based Reynolds number Re^E of about 4% to 5% for $\Delta = 60\text{K}$. Trying to understand this we consider the free fall velocity of fluid elements in thermal convection $v \propto \sqrt{\beta g L \Delta}$, leading to $Re_{NOB}^E/Re_{OB}^E \propto (\beta(T_c)/\beta(T_m))^{0.5}$. Here $\beta(T)$ is the thermal expansion coefficient, taken either at the center T_c or the arithmetic mean temperature T_m between top and bottom plate temperatures. The β -ratio as a function of

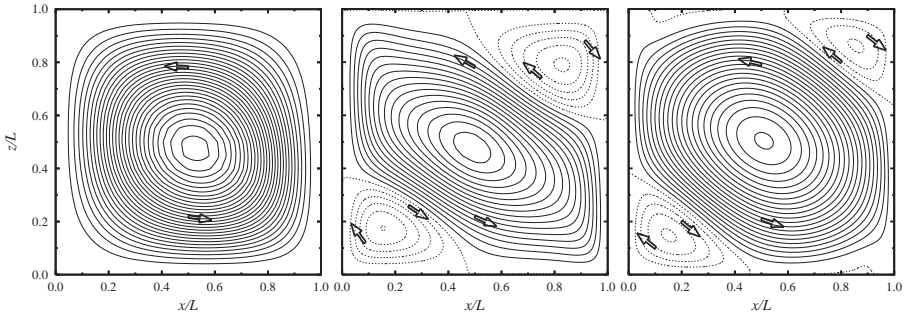


Fig. 2. Lines of constant values for the conditionally time averaged velocity field $\bar{\mathbf{u}}(x, z)$ at different Rayleigh numbers $Ra = 10^4, 10^6, 10^8$ in Rayleigh-Bénard convection. (Conditional time averaging takes the time dependent rotational direction of the wind into account.) Counterclockwise velocity direction (as indicated by arrows) is drawn with solid lines, while the clockwise ones are indicated by dotted lines. The OB flow structure, which already develops secondary (counter) rolls enjoys top-bottom symmetry, which is broken for the shown NOB case. There are major secondary rolls only in those corners, where the downcoming or the upgoing wind is directed towards the bottom or top plates, respectively.

the NOBness is included in Figure 3 a. It seems to be consistent with the numerical Reynolds number data, also in their dependence on Ra . - To support this, we artificially switched off the temperature dependence of β in the numerics. Then the NOB modifications of Re^E is less than 1% even at $\Delta = 60K$, revealing the temperature dependence of the thermal expansion coefficient as the main origin of the NOB effects on the global Reynolds number in water.

The found ratio-relation might suggest that the NOB Reynolds number can be related to the OB one by simply allowing for the temperature variation of $\beta(T)$ due to the NOB-shift $T_m \rightarrow T_c$ in the Rayleigh number, keeping the other material parameters at their fixed values ν_m, κ_m . One then has $\tilde{Re}_{NOB}^E \propto (\beta(T_c)gL^3\Delta/\nu_m\kappa_m)^{0.62} = (\beta(T_c)/\beta(T_m))^{0.62} \cdot Ra_m^{0.62} \propto (\beta(T_c)/\beta(T_m))^{0.62} \cdot Re_{OB}$. This leads to an analogous Re^E and β ratio relation as before, but with the numerical exponent 0.62 (Figure 3 (b)). For larger Ra the ratio $(\beta(T_c)/\beta(T_m))^{0.62}$ is even closer to the numerical Re_{NOB}^E/Re_{OB}^E data. - But note that $\beta(T)gL^3\Delta/\nu_m\kappa_m$ no longer is the physical control parameter!

Of interest are also the various flow profiles, e.g. the area averaged velocity amplitudes $U_x(z)$ as a function of height $0 \leq z/L \leq 1$ as well as the side wall wind $U_z(x)$ as a function of the wall distance $0 \leq x/L \leq 1$. These amplitudes are defined as $U_x(z) = \langle \overline{u_x} \rangle_{x(z)}(z)$ and $U_z(x) = \langle \overline{u_z} \rangle_{z(x)}(x)$, where the overline denotes the time average and $\langle \dots \rangle$ indicates averaging along the x -direction for fixed z etc. In Figure 4 we summarize one of our profile results.

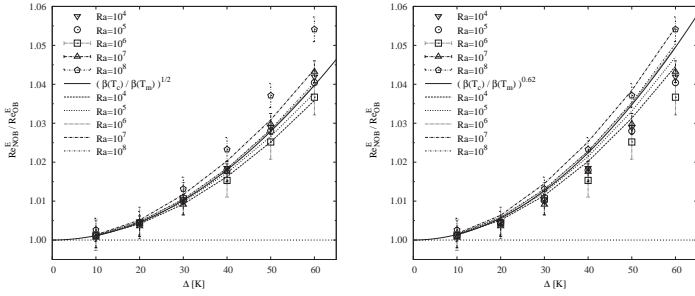


Fig. 3. NOB effect on the Reynolds number ratio Re_{NOB}^E/Re_{OB}^E as function of the NOBness Δ , compared with $(\beta_c/\beta_m)^\gamma$. Left: $\gamma = 1/2$, according to free fall velocity; right: $\gamma = 0.62$. Apparently, it is the NOB deviation of $T_m \rightarrow T_c$ in the expansion coefficient which is the main NOB effect on the wind amplitude.

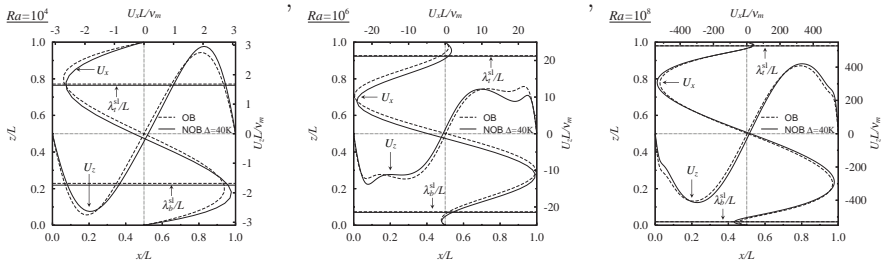


Fig. 4. The vertical and horizontal velocity profiles $U_x(z)$ and $U_z(x)$ as derived from the conditionally time averaged velocity components $\overline{u_x}$ and $\overline{u_z}$ at three different Ra numbers $10^4, 10^6, 10^8$. The abscissa and ordinate scales are the dimensionless width and height. The upper scales show the horizontal velocity profiles nondimensionalized with ν_m/L , i.e., $Re_x(z)$; the right scales show the vertical velocity's $U_z(x)$ profiles, also nondimensionalized by ν_m/L . Dashed lines indicate the OB case, full lines NOB case. In both cases $\Delta = 40K$. Also indicated are the corresponding thermal slope BL widths $\lambda_{b,t}^{sl}$, which strongly decrease with increasing Ra .

References

1. Kazuyasu Sugiyama, Enrico Calzavarini, Siegfried Grossmann, and Detlef Lohse, *Flow organization in non-Oberbeck-Boussinesq Rayleigh-Bénard convection in water*, accepted in JFM, 2009.
2. Guenter Ahlers, Eric Brown, Francisco Fontenele Araujo, Denis Funfschilling, Siegfried Grossmann, and Detlef Lohse, *J. Fluid Mech.* 569, 409 - 445 (2006).

A comparison of turbulent thermal convection between conditions of constant temperature and constant heat flux boundaries

Hans Johnston¹ and Charles R. Doering²

¹Department of Mathematics & Statistics, University of Massachusetts, Amherst, MA 01003-9305 USA

²Departments of Mathematics & Physics, and Center for the Study of Complex Systems, University of Michigan, Ann Arbor, MI 48109-1043 USA

High resolution direct numerical simulations of two-dimensional Rayleigh-Bénard convection are used to study the influence of temperature boundary conditions on turbulent heat transport. The extreme cases of fixed heat flux and fixed temperature both display power law scaling $Nu \approx 0.138 \times Ra^{.285}$ with a scaling exponent indistinguishable from $2/7 = .2857\dots$ above $Ra = 10^7$ up to the highest Rayleigh number measured, $Ra = 10^{10}$. This work [1] was supported in part by NSF Awards PHY-0555324 and SCREMS-0619492.

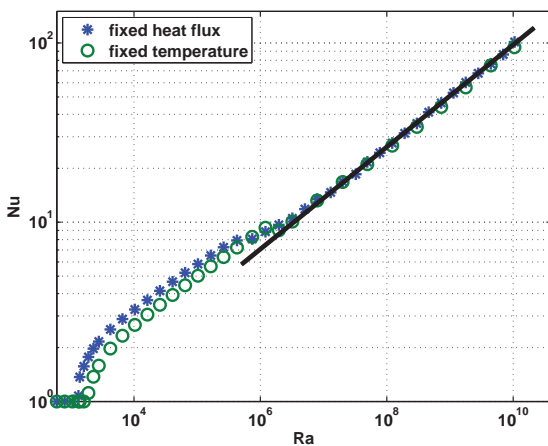


Fig. 1. Comparison of heat transport data for fixed-flux and fixed-temperature simulations in a cell of aspect ratio 2. The solid line is $Nu = 0.138 \times Ra^{.285}$

[1] H. Johnston and C. R. Doering, Phys. Rev. Lett. **102**, 064501 (2009).

Diffusion of heavy particles in turbulent flows

A.S. Lanotte¹, J. Bec², L. Biferale³, M. Cencini⁴, A. Scagliarini³, F. Toschi⁵

¹CNR ISAC, Rome and INFN Sezione di Lecce, Italy a.lanotte@isac.cnr.it

² CNRS UMR6202, OCA, Nice, France

³ University of Tor Vergata, Rome, Italy

⁴INFN-CNR, SMC University La Sapienza, Rome, Italy

⁵ CNR IAC & University of Eindhoven, Eindhoven, The Netherlands

Relative dispersion of tracers - i.e. very small, neutrally buoyant particles-, is particularly efficient in incompressible turbulent flows. Due to the non smooth behaviour of velocity differences in the inertial range, the separation distance between two trajectories, $\mathbf{R}(t) = \mathbf{X}_1(t) - \mathbf{X}_2(t)$, grows as a power of time superdiffusively, $\langle R^2(t) \rangle \propto t^3$, as first observed by L.F. Richardson [1]. This now well established result has no counterpart in the theory of heavy particle suspensions, namely finite-size particles with a mass density much larger than that of the carrier fluid. The complete knowledge of particle properties of mixing in turbulent flows -yet an open problem-, is of great importance in cloud physics, or in estimating pollutant dispersion for hazardous safety purposes.

Here we present results of three-dimensional direct numerical simulations of heavy particles transported by an incompressible, homogeneous and isotropic turbulent fluid flow at Taylor-microscale Reynolds number $Re_\lambda \sim 400$. Details can be found in [2]. We consider particles much heavier than the fluid and much smaller than the Kolmogorov scale η of the flow. Moreover, they are passively advected by the fluid, and do not interact among themselves. Within these assumptions, particles feel the flow through a viscous drag only, so that the trajectory $\mathbf{X}(t)$ of any such particle obeys the Newton equation $\ddot{\mathbf{X}} = (1/\tau_s)(\mathbf{u}(\mathbf{X}, t) - \dot{\mathbf{X}})$. Particle response time τ_s is non-dimensionalized by the Kolmogorov time scale τ_η , to define the Stokes number $St = \tau_s/\tau_\eta$ that measures inertia. A complete description in the position-velocity phase space (X, V) characterizing particle dynamics is performed. After relaxation of transients, pairs of initially close particles are identified and recorded along their Lagrangian motion.

Turbulent pair dispersion for tracers is classically based on the application of similarity theory for Eulerian velocity statistics: depending on the value of space and time scales, velocity increment statistics of the underlying flow differently affect the way tracers separate. This results in different regimes for relative dispersion. In the case of inertial particles, a similar reasoning holds, so that to analyze the way inertial pairs separate in time, the stationary statis-

tics of particles velocity differences has to be investigated first. It is well known that inertia is responsible of the formation of *caustics*: at increasing inertia, heavy particles velocity differences at a given scale do not smoothly go to zero as the scale decreases to zero. In the limit of very large inertia, two particles at a very small distance tend to have uncorraleted motion, with a relative velocity difference that can be very large.

We analyze the stationary distribution of heavy particles velocity increments, by measuring the velocity difference among two particles located at distance R , without any conditioning on their initial separation. It is clear that inertia

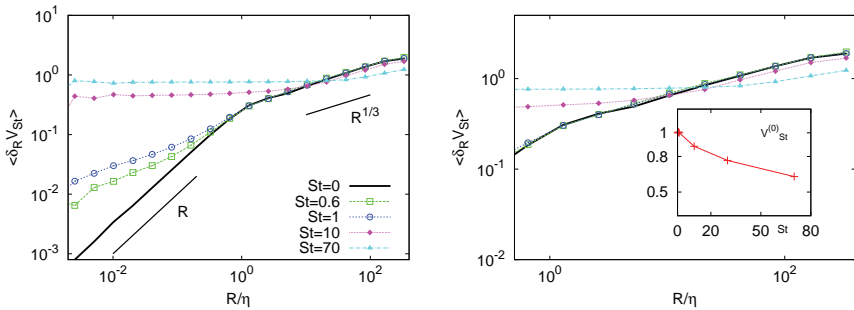


Fig. 1. Right figure: log-log plot of average particle velocity increment $\langle \Delta_R V_{St} \rangle$ versus the scale R/η , for various Stokes numbers. The statistics for fluid tracers ($St = 0$) correspond to the solid line. The differentiable scaling behaviour $\propto R$ in the dissipative range, and the Kolmogorov K41 behaviour $\propto R^{1/3}$ in the inertial range of scales are also shown. Left figure: zoom-in of the inertial range, same symbols as right. Inset: behaviour of the amplitude prefactor, V_{St}^0 as a function of the Stokes number St .

affects the heavy particles stationary velocity statistics, with two main consequences.

The first concerns the small-scale behaviour of the particle velocity statistics. At small scales $R \ll \eta$ and for Stokes numbers large enough, caustics make the particle velocity increments not differentiable. At changing the inertia of the particles, the statistical weight of caustics might monotonically vary as follows: at small St , inertial particles should behave as tracers and their stationary velocity distribution should approach the differentiable Eulerian statistics of tracers; at large values $St \rightarrow \infty$, on the contrary particles that do not feel underlying fluid fluctuations at all and their velocity difference statistics should approach the discontinuous rough limit $\Delta_R V_{St} \sim R^0$.

The second effect of inertia concerns the particle velocity statistics at larger scales, still in the inertial range. For any fixed Stokes number and for a Reynolds number large enough, there will be a scale at which inertia ceases to be dominant in particle dynamics. If we define the scale dependent Stokes number as $St(R) \sim St [\eta/R]^2/3$, such scale corresponds to having $St(R^*) \simeq 1$. We expect that inertia becomes weaker and weaker, by going to larger and

larger scales $R \gg R^*(St)$. In such case, particle velocity increments are expected to approach the underlying fluid velocity increments scaling behaviour. The mark of inertia is only visible in the damped large-scale amplitude of the velocity increment, which approaches the value U^0/V_{St}^0 , where U^0 is the large scale amplitude for tracers velocity and V_{St}^0 is an adimensional constant varying between 1 and 0, for very small and very large Stokes numbers respectively. This is shown in the inset of the right panel in Fig. 1.

How do the stationary velocity statistics affect relative dispersion?

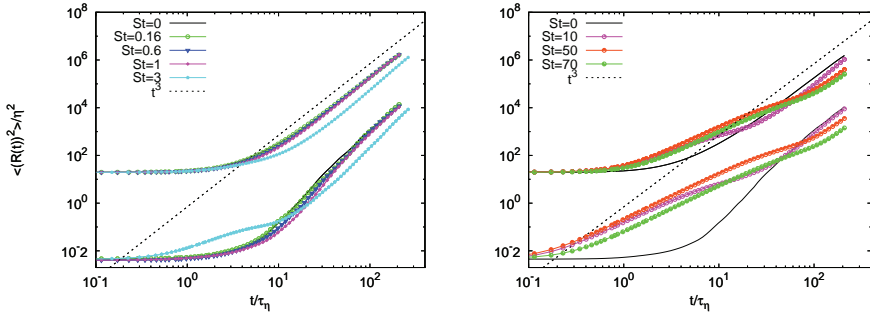


Fig. 2. Log-log plot of the time evolution of mean squared separation for pairs of heavy particles, with initial separations $R_0 \in [0 - 1]\eta$ (shifted below for the plotting purposes) and with $R_0 \in [4 - 6]\eta$, for different values of the Stokes number. The dashed line gives the Richardson scaling $\langle R^2(t) \rangle \sim t^3$. Notice the strong dependency on the values of R_0 and of St .

We expect that depending on the value of the Stokes number St and on that of their initial distance R_0 , particles will start separating with an initial velocity differences that can be much larger than that of tracers at the same R_0 . Later on, when their velocities have eventually relax onto their tracer counterpart, heavy particles will separate recovering the standard Richardson regime for sufficiently large separations in the inertial range of scales.

In Fig. 2, it is plotted the squared separation vector $\mathbf{R}(t)$ among two initially close particles of equal inertia, for various values of the Stokes number. The large times behaviour *à la* Richardson is recovered by pairs of any Stokes numbers considered. However, at intermediate times, when the dependence on the initial state- i.e. initial separation and initial velocity difference-, has not been yet forgotten, clear deviations from the tracers behaviour take place. These are due to pairs that have much larger separations compared the tracers case, which is the statistical signature of the presence of caustics in the initial relative velocity distribution. In a zero order approximation, such pairs initially separate almost ballistically, until their initially large velocity difference have relaxed onto the the underlying fluid velocity fluctuations. This regime lasts for a time scale of the order of the particle response time τ_s .

The above analysis made in terms of the stationary velocity statistics of par-

ticles is very informative, since it explains how it takes place the cross-over among the initial separation regime dominated by inertia at small separations, and the Richardson regime, appearing at large scales. It is also interesting to look at particle relative velocity statistics during the separation process, that is with a conditioning on the value of the initial separation. For this, we fix a number of thresholds scales: at the moment, these thresholds are reached for the first time by the particles pair, we measure their velocity difference at that scale. This is a sort of *exit time* statistics, originally proposed in [3], which turns out to be useful to disentangle different scale dependent behaviours. Notice, in Fig. 3, that the smallest Stokes numbers already at the first thresh-

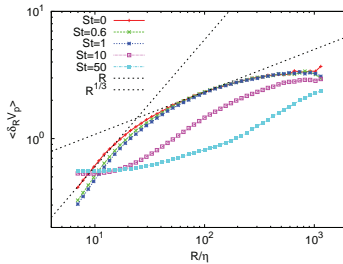


Fig. 3. Log-log plot of average particle velocity increment $\langle \delta_R V_{St} \rangle$ versus the scale R/η , measured along the separating trajectories with $R_0 \in [4 - 6]\eta$. The statistics for fluid tracers ($St = 0$) correspond to the solid line. The differentiable scaling $\propto R$, and the Kolmogorov K41 scaling $\propto R^{1/3}$ are also shown with dashed lines.

olds have a velocity difference which is smaller than that of tracers, and reach tracers velocity difference only at large scale. Pairs with very large Stokes numbers start with a finite and large velocity difference, and then approach tracers velocity differences only at the largest separation, never recovering the scaling behaviour $R^{1/3}$ in the inertial range.

Relative dispersion of heavy inertial pairs exhibit substantial differences with respect to the tracers case: inertia plays different roles at different separations. To understand these results, a mean field argument can be proposed, based on the role of inertia at the different scales of the flow [2].

References

1. L. F. Richardson, Proc. R. Soc. Lond. A **110**, 709 (1926).
2. J. Bec, L. Biferale, A.S. Lanotte, A. Scagliarini, and F. Toschi, "Turbulent pair dispersion of inertial particles" in preparation (2009).
3. V. Artale, G. Boffetta, A. Celani, M. Cencini, and A. Vulpiani, Phys. Fluids A **9** 3162 (1997).

Quantification of heavy particle segregation in turbulent flows: a Lagrangian approach

E. Meneguz (1), M.W. Reeks (1) and A. Soldati (2)

(1) School of Mechanical and Systems Engineering, University of Newcastle Upon Tyne, Stephenson Building, Claremont Road, NE1 7RU Newcastle Upon Tyne U.K.

(2) Dipartimento di Energetica e Macchine, Universita' degli Studi di Udine, via delle Scienze 208, 33100 Udine Italy

`e.lena.meneguz at ncl.ac.uk`

The way particles suspended in a turbulent flow are transported and segregated by turbulent structures is crucial in many atmospheric and industrial applications such as powder production and formation and growth of PM10 particulate. In recent years, this phenomenon has been studied from different viewpoints; lately, Osipov [1] proposed an alternative approach to quantify particle segregation, later followed by [2] and [3]. This method, referred to as 'Full Lagrangian approach (FLA)', evaluates the size of an infinitesimally small volume of particles and its changes in the course of time along each particle trajectory. The rate of deformation of this volume is related to the compressibility of the particle velocity field (e.g. [4]) which is an indicator of particle concentration. This method presents high computational efficiency in comparison with traditional Eulerian methods such as 'box-counting', for which a large number of particles is required to obtain accurate statistics. We decided to exploit FLA in a simple two-dimension synthetic turbulent flow field Direct Numerical Simulations of homogeneous isotropic turbulence, and to compare it with the MEPPV, a method proposed by [5] et al. essentially based on box counting. Preliminary results of the spatially averaged statistics of the rate of deformation are also presented, showing that the presence of singularities increases for large St numbers. In this work, we study the dispersion of identical, rigid and spherical particles in a carrier flow of mass density ρ and kinematic viscosity ν . Particles are assumed to be heavy (i.e. $\rho_p/\rho \gg 1$ where ρ_p is the particle density) with radii a_p much smaller than the smallest length scale of the flow. Upon neglecting gravity and Brownian effects, the equations of motion are [6]:

$$\frac{d\mathbf{x}_p}{dt} = \mathbf{v}, \quad \frac{d\mathbf{v}}{dt} = \frac{1}{St}(\mathbf{u} - \mathbf{v}), \quad (1)$$

where \mathbf{x}_p and \mathbf{v} are the position and velocity of the particle respectively, and $\mathbf{u} = \mathbf{u}(\mathbf{x}_p, t)$ denotes the velocity of the carrier flow at the position of the particle. All variables have been made dimensionless by a typical time scale \mathcal{T} and a typical velocity scale \mathcal{U} . The parameter $St = 2\rho_p a_p^2 / (9\rho\nu\mathcal{T})$ is the Stokes number, which represents the ratio between the inertia driving the particle and the viscous damping action of the fluid.

For the continuity equation, along the trajectory of a particle which moves with velocity $\bar{\mathbf{v}}$, we have [7]:

$$\frac{dn}{dt} = -n(\nabla \cdot \bar{\mathbf{v}}). \tag{2}$$

where $\nabla \cdot \bar{\mathbf{v}}$ denotes the *compressibility* of the particle velocity field. For sufficiently small Stokes numbers, $\bar{\mathbf{v}} = \mathbf{u} - St\mathbf{u} \cdot \nabla\mathbf{u} + \mathcal{O}(St^2)$ [7], and consequently in an incompressible flow:

$$\nabla \cdot \bar{\mathbf{v}} \simeq -St\nabla \cdot (\mathbf{u} \cdot \nabla\mathbf{u}) = -StQ, \tag{3}$$

To implement the FLA, we consider the fractional volume of particles surrounding the particle and follow its evolution as the particle moves through the turbulent carrier flow. Upon defining a unit deformation tensor as $J_{ij} \equiv \partial x_{p,i}(\mathbf{x}_0, t) / \partial x_{0,j}$, we can differentiate Eq. 1 with respect to \mathbf{x}_0 in order to obtain [1, 2, 3]:

$$\frac{dJ_{ij}}{dt} = \dot{J}_{ij}, \quad \frac{d}{dt} \dot{J}_{ij} = \frac{1}{St} \left(J_{kj} \frac{\partial u_i}{\partial x_k} - \dot{J}_{ij} \right). \tag{4}$$

Along a particle trajectory $|J| \equiv |\det(J_{ij})| = n^{-1}$, so that using Eq. 2 and averaging over all particle trajectories gives a relation between J and $\nabla \cdot \bar{\mathbf{v}}$ [4]:

$$\frac{d}{dt} \langle \ln |J| \rangle = \langle \nabla \cdot \bar{\mathbf{v}} \rangle. \tag{5}$$

Février et al.[5] have proven that the velocity of particles dispersed in turbulent flows can be seen as the sum of two contributions: a continuous turbulent velocity field shared by all particles called the Mesoscopic Eulerian Particle Velocity Field (MEPVF) and denoted by $\bar{\mathbf{v}}$, and a random velocity component we refer to as Random Uncorrelated Motion (RUM) [2]. The latter component is dominant in the case of large inertia, thus leading to a ballistic particle motion, and negligible in the case of infinitesimally small particles. The MEF approach provides a way to calculate $\nabla \cdot \bar{\mathbf{v}}$ [5, 8], based upon a division of the calculation domain into grid cells. Averaging the velocities of all the particles inside a cell gives $\bar{\mathbf{v}}$, defined in the center of a cell. By taking the spatial derivatives using a finite difference method, one can obtain $\nabla \cdot \bar{\mathbf{v}}$ at each cell center.

We note that Eq. 4 may result in J becoming equal to zero, which is equivalent to a singularity in the particle velocity field ($\nabla \cdot \bar{\mathbf{v}} = -\infty$). Therefore the

FLM is expected to be able to detect singularities in the spatial distribution of particles, in contrast to the MEF which is ultimately based on a difference equation.

We compare the FLM and the MEF in a simple two-dimensional synthetic flow field. Particles are injected at random positions $\mathbf{x}_0 = \mathbf{x}_p(0)$ inside the periodic domain $[0, 2\pi] \times [0, 2\pi]$ with the same velocity as the fluid at the corresponding position, $\mathbf{v}(0) = \mathbf{u}(\mathbf{x}_0, 0)$. Using Eq. 1, we trace 10^6 particles to determine the value of $\langle \nabla \cdot \bar{\mathbf{v}} \rangle$ with the MEF with 60 grid cells in each direction. Alternatively we follow 10^4 particles using Eqs. 1 and 4, and determine $\langle \nabla \cdot \bar{\mathbf{v}} \rangle$ from Eq. 5. We present the results from both methods in Fig. , together with the estimate for small St, Eq. 3. For a small Stokes number such as $St = 0.05$ (Fig. a), the three lines collapse. This is expected, since Eq. 3 is exact in the limit of infinitely small St. If we increase the St number, as shown in Fig. 1b for $St = 2$, the graph contains sharp negative peaks in the value of $\langle \nabla \cdot \bar{\mathbf{v}} \rangle$. These intermittent events correspond to a sudden collapse of the volume occupied by the particles so that $J \sim 0$ and $\langle \nabla \cdot \bar{\mathbf{v}} \rangle \rightarrow -\infty$. This phenomenon is due to RUM, i.e. singularities in the flow field where particle trajectories cross and J vanishes. The agreement between the MEF and the FLM is nonetheless very good, although the peaks tend to be a bit steeper in the Lagrangian method.

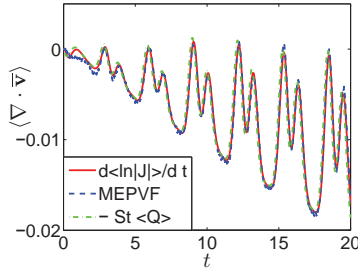


Fig.2 displays the particle-averaged value of the compressibility, as a function of time, evaluated with the FLA and with the MEF, in a Direct Numerical Simulation of homogeneous isotropic turbulence. The main simulation parameters are the turbulent Reynolds number and the Stokes number (namely the particle relaxation time normalized by the Kolmogorov time scale). Except for an initial transient, the correspondence between the two methods is very good. The small difference is probably due to the influence of random uncorrelated motion whose effects are included in the quantification of J but not in the MEF. In other words, in agreement with theory and previous simulations, the Lagrangian method used accurately predicts the compressibility of the particle velocity field even when the latter is characterized by singularities, which take place when the instantaneous particle concentration becomes infinite.

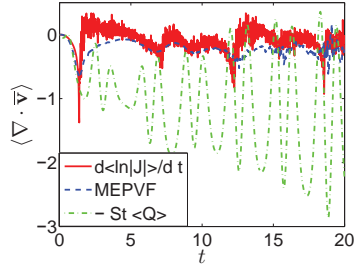


Fig. 1. (Color online) Compressibility of the particle velocity field in the synthetic flow ($A = \pi$, $\omega = 1$) as a function of time, measured by the FLM ($d\langle \ln |J| \rangle / dt$; red solid line), and by the MEF (MEPVF; blue dashed line). Maxey's estimate, Eq. 3, is plotted as well (green dash-dotted line). a) $St = 0.05$, b) $St = 2$.

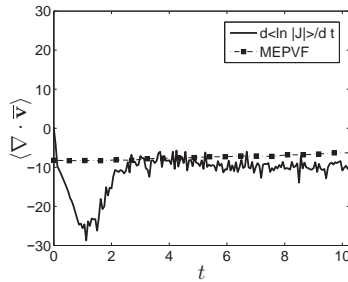


Fig. 2. Compressibility of the particle velocity field versus time in a DNS of turbulence, $St = 1$. The solid line denotes the compressibility measured by the Lagrangian method ($d \ln |J| / dt$), whereas the dotted line represents the Eulerian method using the MEPVF.

References

1. A. N. Osipov, *Astrophysics and Space Science*, **274**, 377-386 (2000).
2. M. W. Reeks, In *Proc. of IUTAM Symposium on Computational Modelling of Dispersed Multiphase Flow*, (ed. S. Balachandar and A. Prosperetti), 21-30 (2004).
3. D. P. Healy and J. B. Young, *Proc. R. Soc. London A*, **461(2059)**, 2197-2225 (2005).
4. R. Aris, *Vectors, tensors and the basic equation of fluid mechanics*, Dover Press, Dover 1989.
5. P. Février, O. Simonin and K. D. Squires, *J. Fluid Mech.*, **553**, 1 (2005).
6. M. R. Maxey and J. J. Riley, *Phys. Fluids* **26(4)**, 883 (1983).
7. E. Balkovsky, G. Falkovich, and A. Fouxon, *Phys. Rev. Lett* **86**, 2790 (2001).
8. O. Simonin, L. I. Zaichik, V. M. Alipchenkov and P. Février, *Phys. Fluids*, **18**, 125107 (2006).

The dispersion of lines written in a turbulent jet flow

M. Mirzaei¹, N.J. Dam^{1,2}, J.J. ter Meulen¹ and W. van de Water^{1,2}

¹Institute of Molecules and Materials, Radboud University, 6525 AJ Nijmegen, The Netherlands, and ²Physics Department, Eindhoven University of Technology, 5600 MB Eindhoven, the Netherlands

m.mirzaei@science.ru.nl

We write patterns, such as dots, lines and crosses, in a strongly turbulent air flow by fusing N_2 and O_2 molecules to NO, which is then used as a tracer. This photosynthesis is done in the focus of a strong UV laser (ArF excimer Λ Physik, LPX 150). A while (tens of μs) later, the written patterns are made visible through inducing fluorescence with a second (UV) laser. The deformed and dispersed pattern of NO molecules is photographed in the UV using a fast intensified camera [1]. This technique allows us to create tracer patterns at will, and with sizes comparable to the smallest length scale in turbulence. This would have been very hard using seeded particles, such as in particle tracking velocimetry.

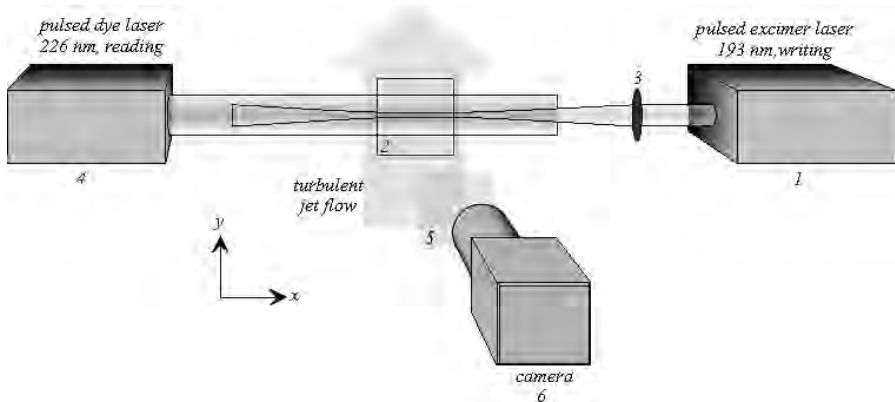


Fig. 1. Experimental Setup. The pulsed ArF excimer laser (1) creates a line of NO particles and the flow displaces and wrinkles the lines. The pulsed dye laser (4) visualizes the NO particles fluorescence, while the ICCD camera (6) collects fluorescence signals within the readout area (2).

The initial width of our tracer pattern, a line, is $\sigma_0 = 50 \mu\text{m}$. We trace the backbone $y_0(s)$ of deformed lines in images by fitting Gaussians $I \sim \exp(-(y - y_0(s))^2/\sigma^2(s))$, to their cross sections and thus find the line width $\sigma(s)$, with s the coordinate along the line (see figure 2).

The turbulent flow emanates from a jet, and the turbulent velocity u is varied by varying its plenum pressure. In this manner the Kolmogorov scale η is varied from $\eta = 50 \mu\text{m}$ at the smallest turbulent velocity to $\eta = 17 \mu\text{m}$ at the largest u . Thus, at the smallest u , our lines embrace one small eddy, and a few Kolmogorov lengths at the largest u .

Our written patterns wrinkle and blur due to molecular diffusion and turbulent dispersion. The key question is about their combined effect: will molecular diffusion enhance or diminish the effect of turbulent dispersion [2].

From collected statistics on 4×10^3 images at each time delay t we measure how the average line width σ increases with the delay time t between writing and reading. We express this dispersion by the effective diffusion coefficient $D = (\sigma^2(t) - \sigma_0^2)/4t$.

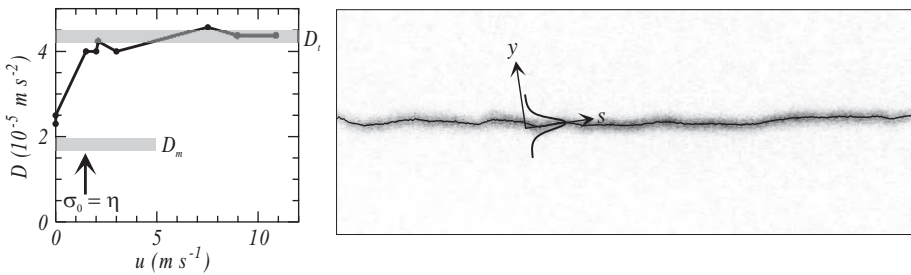


Fig. 2. The width of a dispersed line (length 6.4 mm) is measured by fitting Gaussians to its cross section. Our surprising finding is that the effective dispersion jumps from its molecular value D_m to the turbulent D_t , which appears to be independent on the turbulence level. At $u = 1.5 \text{ ms}^{-1}$, $\sigma_0 \approx \eta$.

Figure 2 shows that at small turbulence levels the spreading rate relaxes to a value slightly larger than the molecular diffusion coefficient, $D_m = 1.8 \times 10^{-5} \text{ ms}^{-2}$, and increases quickly to its turbulent value once the Kolmogorov scale η drops below the initial line width.

A point of concern is the intrusiveness of our method: the creation of tracer molecules is a nonlinear optical process which during a brief time interval raises the temperature and decreases the density of the air. Consequently, the rate of spreading of our molecular clouds in still air is faster than the diffusion coefficient of NO molecules D_m . This was verified in a model for the enhanced convection of molecules out of the focus of the writing laser. As figure 3 shows, a temperature rise $\Delta T \approx 100 \text{ K}$ explains the enhanced diffusion.

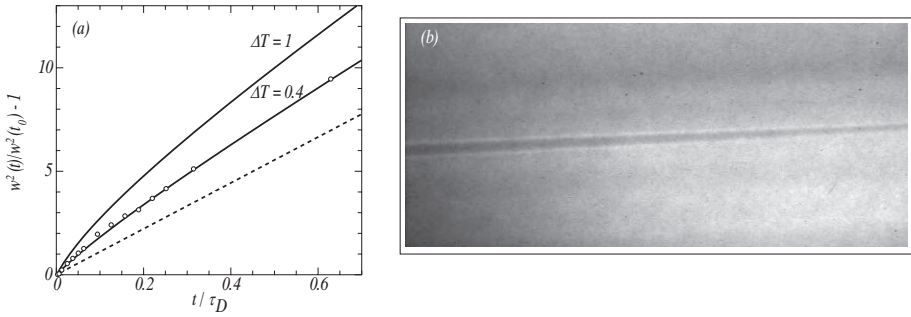


Fig. 3. Writing in air comes with a temperature rise at the instant of writing. This results in a slightly anomalous diffusion. (a) Open circles: measured linewidths $\sigma^2(t)$ in still air after a time t normalized by the diffusion time $t_D = \sigma_0^2/D_m$. Full lines result of a model calculation with the initial temperature rise $\Delta T/T_a$ as a parameter, $T_a = 293\text{K}$. Dashed line: ordinary diffusion ($\Delta T = 0$). The excellent fit of the model to the experiment suggests that the initial temperature increase in the experiment is $\approx 100\text{K}$. (b) Density profile of the air at $t = 3 \mu\text{s}$ after writing.

Figure 3(b) shows that the brief rise in temperature results in a local dilution of the ambient air, which can be visualized using Raleigh scattering at wavelengths away from those causing fluorescence of NO.

Molecular diffusion, which blurs written patterns, sets the precision with which they can be followed in order to do velocimetry. Naively one may say that tracing its molecules is the best way to perform velocimetry of a gas. However, because mass diffuses at approximately the same rate as momentum in a gas, and because the size of the smallest scales in turbulence is set by the diffusion of momentum, the smallest scales in turbulence will remain fundamentally unresolved in molecular velocimetry. In current experiments we are therefore employing heavy molecules which can be made visible using phosphorescence.

References

1. J. Bominaar, M. Pashtropanska, T. Elenbaas, N. Dam, J.J. ter Meulen and W. van de Water, *Phys. Rev. E* **77**, 046312 (2008).
2. P. G. Saffman, *J. Fluid Mech.* **8**, 273 (1960).

PDF modeling of vapour micromixing in turbulent evaporating sprays

Gaurav Anand and Patrick Jenny

Institute of Fluid Dynamics, ETH Zurich, CH 8092 Zürich, Switzerland
anand at ifd.mavt.ethz.ch

Spray combustion is a complex phenomena finding its application in many combustion devices like gas turbines, diesel engines, liquid-fueled rocket engines etc. This phenomena is characterised by the break up of the liquid fuel sheet, followed by atomisation, droplet dispersion and its evaporation, mixing of the fuel vapour with the oxidiser and eventually its combustion. However, the present study is focused on the turbulence modification of the carrier phase (i.e. gas) and the fuel vapour mixing. Flows seeded with droplet volume fraction less than 10^{-3} are considered so that the inter-droplet collision effects are negligible.

Molecular mixing specially in or near the flame fronts plays an important role in turbulent combustion. Although, micromixing of gaseous fuel and oxidiser has been an active area of study, but the micromixing of vapour with the air lacks proper attention. Pera et al [1] proposed a subgrid scale model for the mixture fraction variance in large eddy simulation (LES) of evaporating sprays. In the present study, a probability density functions (PDF) model for the micromixing of the fuel vapour with the oxidiser is proposed. Such PDF methods have certain advantages over closure methods. The turbulence reaction interactions and all convective terms (including scalar dissipation) in the PDF transport equation appear in closed form and for molecular mixing the joint velocity-composition PDF, which can be quite arbitrary, can be considered. In comparison to DNS and LES, PDF methods are computationally inexpensive.

For this purpose, an Eulerian-Lagrangian-Lagrangian approach as presented in [2] is employed. For the gas phase, a joint velocity-composition PDF method [3] is used. For the droplet phase, the mass density function (MDF, density-weighted PDF) of droplet velocity, droplet diameter, droplet temperature, droplet composition (if the fuel is multicomponent), “seen” gas temperature, “seen” gas velocity and “seen” gas composition is calculated. This provides a unified formulation to consistently address the various modeling issues associated with such two-phase systems. Because of the high dimensionality, particle methods are employed to solve the PDF transport equations.

Micromixing of the fuel vapour depends highly on the turbulence of both the gas and the droplet phases. Thus its highly important to correctly predict the gas and the droplet phases turbulence. One way coupling, i.e. the influence of the gas turbulence on the droplet turbulence, might not be sufficient to predict the flow behaviour accurately in some applications. For instance in reacting flows, modification of the gas turbulence structure due to droplet turbulence will influence the gas motion and thereby its composition, which is required for the prediction of the heat release rate. A new stochastic model based on individual particle separation and a decorrelation length scales is proposed to capture the influence of turbulence modulation of the gas due to the droplet presence. The model has been validated with the experiments of Poelma et al [4] as shown in figure 1. Next, computation experiments were performed in order to study the influence of gravity and the model on the decay of carrier phase turbulence. Figure 2 shows the comparison of the results obtained from various computational experiments.

To model the micromixing of fuel vapour with the oxidiser, a new model based on droplet decorrelation frequency (which is a function of droplet turbulence length scale) has been proposed. Depending on the individual separation between the droplet and the surrounding gas particles, the probability of the vapour (formed due to evaporation) mixing with the surrounding gas is evaluated. For gas phase molecular mixing, interaction by exchange with mean (IEM) model [5, 6] has been employed.

The proposed model is compared with the LES results of Pera et al [1] for the micromixing of vapour formed in an evaporating spray evolving in spatially decaying homogenous turbulence. Meyer and Jenny [7] proposed parameterised scalar profiles (PSP) mixing model based on constructing distributions of one-dimensional scalar profiles (e.g. temperature or vapour mass fraction) and showed significant improvements over IEM mixing model. Based on their study, it is expected that employment of PSP model might further help in improving the results.

References

1. C. Pera, J. Reveillon, L. Vervisch and P. Domingo, *Combustion and Flame*, **146**, 635 (2006).
2. G. Anand and P. Jenny, *Journal of Computational Physics*, **228**, 2063 (2009).
3. P. Jenny, S. B. Pope, M. Muradoglu and D. A. Caughey, *Journal of Computational Physics*, **166(2)**, 218 (2001).
4. C. Poelma, J. Westerweel, and G. Ooms, *Journal of Fluid Mechanics*, **589**, 315 (2007).
5. J. Villermaux and J. C. Devillon, *Second International Symposium on Chemical Reaction Engineering*, , 1 (1972).
6. C. Dopazo and E. E. O'Brien, *Acta Astronaut*, **1**, 1239 (1991).
7. D. W. Meyer and P. Jenny, *Physics of Fluids*, **18**, 035105 (2006).

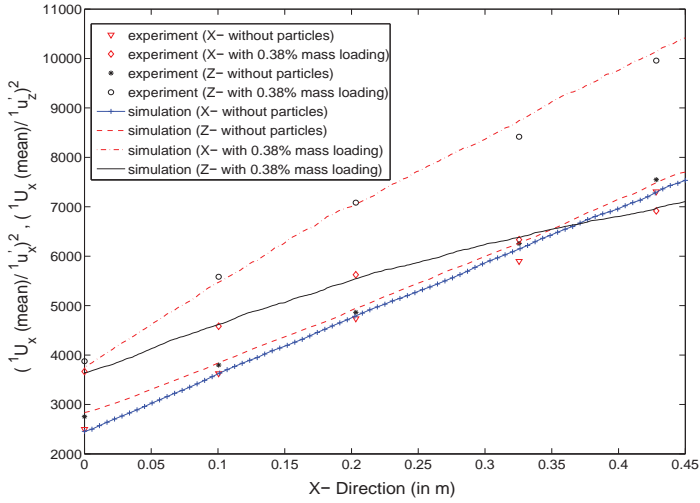


Fig. 1. Comparison of the decay of the normalized variance of the fluid velocity (“X-” represents variance of the longitudinal component; “Z-” represents variance of the transverse component) with and without ceramic particles. X- direction refers to downstream and Z- direction, transverse to the flow.

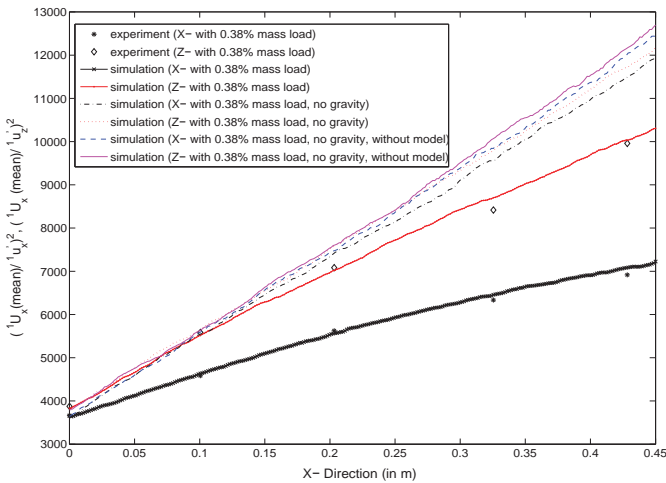


Fig. 2. Comparison of the decay of the normalized variance of the fluid velocity (“X-” represents variance of the longitudinal component; “Z-” represents variance of the transverse component). Water seeded with ceramic particles having 0.10% volume loading with and without gravity, and with and without models. X- direction refers to downstream and Z- direction, transverse to the flow.

Forces on light particles in stratified turbulence

M. van Aartrijk and H.J.H. Clercx

Fluid Dynamics Laboratory, Department of Physics, Eindhoven University of Technology, The Netherlands

h.j.h.clercx@tue.nl

Introduction

The dispersion of light particles, like plankton, algae and sand, plays an important role in geophysical environments such as estuaries. In these geophysical flows often a negative vertical density gradient is present, which suppresses to a certain extent vertical fluid motions. In this work we study the effect of different hydrodynamic forces on the behavior of light particles, which have a density ρ_p that is of the same order as that of the surrounding fluid (ρ_f), in stratified turbulence by means of direct numerical simulations (DNS). The code solves the flow field in a Eulerian manner, and particle trajectories are computed from the Lagrangian point of view [1, 2].

Forces on light inertial particles

Usually, the limit of heavy particles ($\rho_p \gg \rho_f$) is studied. For heavy-particle dispersion in stratified turbulence, see Ref. [3]. Contrary to these studies, for light particles the full Maxey-Riley equation needs to be resolved [4]. Particle trajectories are obtained from $\frac{d\mathbf{x}_p}{dt} = \mathbf{u}_p$, with \mathbf{x}_p the particle position and \mathbf{u}_p its velocity. The velocities of the inertial particles (light and heavy) are then obtained by solving:

$$\begin{aligned} m_p \frac{d\mathbf{u}_p}{dt} &= 6\pi a \nu \rho_f \left(\mathbf{u} - \mathbf{u}_p + \frac{1}{6} a^2 \nabla^2 \mathbf{u} \right) + m_f \frac{D\mathbf{u}}{Dt} \\ &+ (m_p - m_f) \mathbf{g} + \frac{1}{2} m_f \left(\frac{D\mathbf{u}}{Dt} - \frac{d\mathbf{u}_p}{dt} + \frac{1}{10} a^2 \frac{d}{dt} \nabla^2 \mathbf{u} \right) \\ &+ 6\pi a^2 \nu \rho_f \int_0^t d\tau \frac{d\mathbf{u}/d\tau - d\mathbf{u}_p/d\tau + \frac{1}{6} a^2 d\nabla^2 \mathbf{u}/d\tau}{[\pi \nu (t - \tau)]^{1/2}}. \end{aligned} \quad (1)$$

The particle mass is given by m_p , a is the radius of the particle and m_f is the mass of a fluid element with a volume equal to that of the particle. The

fluid velocity is denoted by \mathbf{u} , ν is the kinematic viscosity. The Maxey-Riley equation is derived for a small ($a \ll \eta$, with η the Kolmogorov length scale) isolated rigid sphere in a non-uniform velocity field, under the assumption of a low particle Reynolds number. A measure of the particle inertia is the particle response time, $\tau_p = 2a^2\rho_p/(9\rho_f\nu)$, which will be expressed in the following using the Stokes number $St = \tau_p/\tau_\kappa$ (τ_κ the Kolmogorov time). The forces on the right-hand side of this equation are viscous drag, a local pressure gradient in the undisturbed fluid, gravitational forces, added mass and the Basset history force, successively. Because the particles are small, the smallest scales of the flow are the most important for the strength of the forces that act on a particle. It is found that the history term has to be calculated over a time interval of at least one Kolmogorov time. For the runs presented here a history of about $2\tau_\kappa$ is chosen; increasing this time does not significantly change any of the forces acting on a particle. Since the density of the particles is close to that of the surrounding fluid, and a background density gradient is present in the flow, the density ratio ρ_p/ρ_f is changing continuously and care needs to be taken in calculating particle statistics. Luckily, these changes are small (about 1‰) and the initial positions of the particles are chosen such that they will not cross the top or bottom boundaries of the domain [2]. Particles are released when the stratified turbulent flow has reached a stationary state and velocity and position time series of 4000 particles are collected for about 10 eddy turnover times.

The strength of the different forces that are acting on the particles in stratified turbulence is shown in Fig. 1. For light particles, with $\rho_p/\rho_f = \mathcal{O}(1)$, almost all

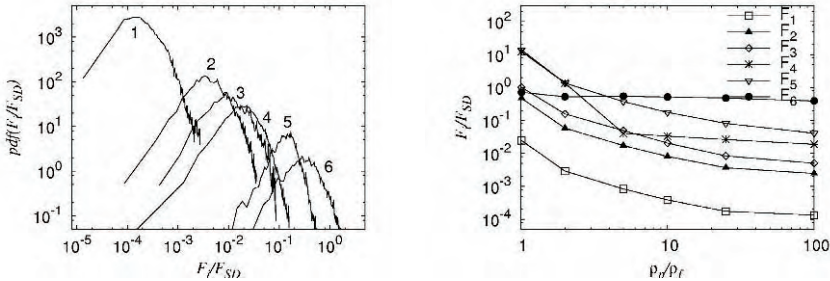


Fig. 1. Left: PDF of the forces F_i normalised by the Stokes drag F_{SD} ; F_1 : added mass Faxén correction, F_2 : Basset force Faxén correction, F_3 : Stokes drag Faxén correction, F_4 : added mass, F_5 : pressure gradient, F_6 : Basset force. Particle properties: $St=0.55$ and $\rho_p/\rho_f=10$. Right: Average value of the normalised force F_i as function of the density ratio. For both graphs the buoyancy frequency $N = 0.3 \text{ s}^{-1}$.

forces have magnitudes comparable to that of the Stokes drag (see Fig. 1b). With increasing density ratio the relative importance of the different forces decreases.

Particle dispersion: the role of the Basset force

The dispersion results of light particles in stratified turbulence are compared to those obtained for heavy particles. Both in the horizontal and in the vertical direction the mean-squared displacement of both types of particles show similar behavior when displayed as a function of the Stokes number. The results obtained for the vertical dispersion are shown in Fig. 2. For small Stokes

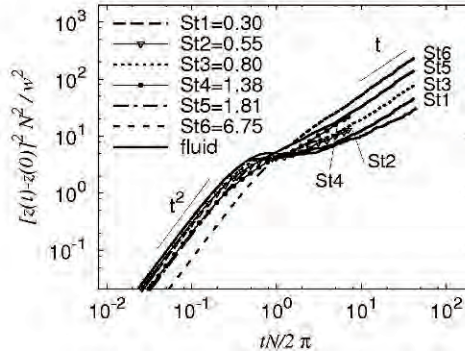


Fig. 2. Vertical single-particle dispersion for fluid particles, light particles (particles with $St2=0.55$ and $St4=1.38$) and heavy particles. Lowest curve (long-time limit) shows the fluid particle result, which is included for reference.

numbers the dispersion behavior is similar to that of fluid particles. Only the length of the plateau is shorter for the light particles which might be an indication that also at these small Stokes numbers the different forces affect light particle dispersion. This would be in contradiction with the assumption that is often used in the literature that the dispersion of inertial particles with $St \approx 1$ can be described using fluid particles. For Stokes numbers larger than about 0.5 a reduced dispersion can be seen for short times (reduced rms-velocity) and for longer times the plateau - typical for stratified turbulence [5] - becomes less pronounced and the dispersion increases with increasing St . The influence of the forces on the vertical dispersion statistics is shown in Fig. 3. These results are computed from trajectories of particles with a density ratio of 25.0, because their dispersion behavior shows deviations from that of fluid particles, but at the same time also other forces than the drag force are relevant. It can be seen that if the Basset force is switched off, the vertical dispersion increases by about 15 – 20%. For the horizontal dispersion the influence of any other force than the drag force can be neglected. The influence of the Basset history force on vertical dispersion of light inertial particles in stably stratified turbulence has two causes. The vertical motion of the particles in stratified turbulence occurs on much smaller scales (scales at which the forces act on the particles), and the oscillatory wave-like motion

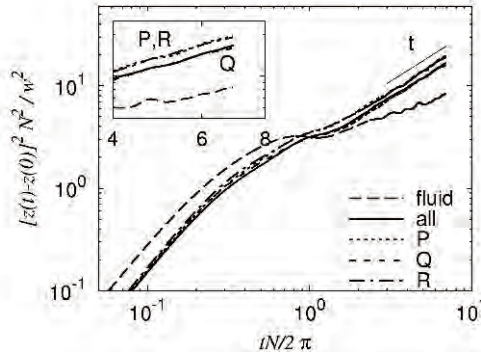


Fig. 3. Vertical mean-squared displacement of fluid particles and light particles for $N = 0.3 \text{ s}^{-1}$. For the particles denoted with “all” all the forces are incorporated except for gravity (particles denoted “St4=1.38” in Fig. 2). For particles P the Basset forces are switched off, for particles Q all Faxén correction terms are set equal to zero and for particles R only the Stokes drag, the pressure gradient and the added mass force are taken into account.

of the particles induces considerable accelerations and decelerations. Several other kernels are proposed in the literature for the history force, as adaptations of the original one derived by Basset [6, 7, 8]. It has been tested whether a kernel with a stronger decay at large times ($(t - \tau)^{-2}$) influences the results. The conclusion that the history force needs to be included when studying light particle dispersion in stratified turbulence is found to be independent of the choice of the history force kernel.

Conclusions

We conclude that the the Basset force cannot be neglected with regard to light particle dispersion in stratified turbulence. Moreover, light inertial particles with $St \approx 1$ cannot be described using fluid particles.

References

1. M. van Aartrijk, H.J.H. Clercx and K.B. Winters, *Phys. Fluids* **20**, 025104 (2008).
2. M. van Aartrijk, *Dispersion of inertial particles in stratified turbulence*, Eindhoven University of Technology 2008.
3. M. van Aartrijk and H.J.H. Clercx, *Phys. Fluids* **21**, 033304 (2009).
4. M.R. Maxey and J.J. Riley, *Phys. Fluids* **26**(4), 883(1983).
5. Y. Kimura and J.R. Herring, *J. Fluid Mech.* **328**, 253(1996).
6. J. Magnaudet and I. Eames, *Annu. Rev. Fluid Mech.* **32**, 659(2000).
7. R. Mei and R.J. Adrian, *J. Fluid Mech.* **237**, 323(1992).
8. P.M. Lovalenti and J.F. Brady, *J. Fluid Mech.* **256**, 607(1993).

Renormalized transport of inertial particles

M. Martins Afonso¹, A. Celani², A. Mazzino³, and P. Olla⁴

¹ Institut de Mécanique des Fluides de Toulouse, Groupe Ecoulements Et Combustion, Allée du Professeur Camille Soula, 31400 Toulouse, France
marcomar@fisica.unige.it

² CNRS, URA 2171, Institut Pasteur, 28 Rue du docteur Roux, 75015 Paris, France

³ Department of Physics - University of Genova,
and CNISM & INFN - Genova Section, via Dodecaneso 33, 16146 Genova, Italy

⁴ ISAC-CNR & INFN - Cagliari Section, 09042 Monserrato (CA), Italy

We investigate the long-time asymptotic properties of inertial particles in flowing fluids by means of analytical computations, and we show the comparison with results derived from simple numerical simulations.

Namely, we focus our attention on the terminal “renormalized” velocity, more precisely on its deviation from the corresponding “bare” value observed in still fluids. Specifically, we analyze two distinct cases, which allow us to perform: 1) either an ordinary perturbation expansion at small inertia, using the second-quantization formalism; 2) or a strong-sweep approach “à la Maxey” [1], in which the deviations from the original rectilinear trajectory due to the flow disturbances are small. We are thus able to investigate (both separately and as an interplay) the effects of several physical properties of the particles and of the flow: inertia, gravity, particle molecular diffusivity, turbulence intensity, space dimension, compressibility degree, density ratio and the flow spatio-temporal profile. We deduce that, depending on these parameters, and in particular on the presence of areas of oscillation or recirculation, both an increase and a reduction in settling/sweeping can occur.

In case 1) we focus on regular incompressible flows $\mathbf{u}(\mathbf{x}, t)$, steady or periodic in time and cellular or symmetric in space [2, 3]. Taking into account both gravity (\mathbf{g}) and diffusivity in the particle dynamical evolution equation [4], we can consider particles of any density (by introducing the covelocity variable and a simplified added-mass effect, in which the fluid acceleration is computed following the particle trajectory rather than along the fluid path), and we can also model the evolution of small micro-organisms with limited capacity of autonomous movement by means of Brownian motion. We analytically obtain a set of partial differential equations which provide the expansion at small Stokes number (St) of the particle probability density function, more

precisely of its projection from the phase space onto the physical space. This set is then solved by means of direct numerical simulations for a specific class of two-dimensional flows [5],

$$\begin{cases} u_1 = \sin(kx_1) \cos[x_2 + 2 \sin(\omega t)] \\ u_2 = -k \cos(kx_1) \sin[x_2 + 2 \sin(\omega t)] \end{cases}, \quad (1)$$

and the resulting vertical terminal velocity (Δw along $x_2 \parallel \mathbf{g}$) is compared with the outcome of our corresponding Lagrangian simulations performed directly on the original dynamical equation. This kind of flow (1) is physically relevant because it is universally used to mimic thermal rolls in Rayleigh–Bénard convection or Langmuir circulation, i.e. the wind-driven helical circulation on the sea surface. Moreover, it has also been employed for both numerical and analytical studies in several domains, ranging from front propagation to polymer transport, and from anomalous diffusion to chaotic maps. Our findings lead to the following conclusion of interest in the realm of applications: any attempt to model the effect of flows on particle sedimentation cannot avoid taking into account the full details of the flow field, e.g. its vertical-oscillation frequency ω or its cell aspect ratio k . Indeed, changing these two parameters, one can verify or even invert the usual picture about the dependence of Δw on St , which associates Stokes numbers smaller (larger) than a critical value with an increase (decrease) of the falling/ascending velocity — as shown in figure 1 for two different values of the Péclet number. Figure 2 proves the correctness of our aforementioned small- St expansion (quadratic, in this case), which enables us to find Δw by means of a rigorous field approach rather than via the so-called continuum approximation [6].

It also turns out that the expression of the renormalized velocity can be obtained by means of a standard multiple-scale expansion, whose following order gives rise to an eddy-diffusivity tensor [7], which in turn might be investigated using this same formalism. Our future plan is to study also the possibility of anomalous transport in the horizontal direction.

In case 2) we analyze random flows with a generic compressibility degree [8]. Our approach is thus applicable both to sedimentation and, more interestingly, to the study of floaters dragged by wind on the water surface. In particular, we concentrate ourselves on stochastic flows and we compute the leading-order correction to the bare drift for Gaussian velocity fields, which as a first approximation is maximum for perfectly compressible (potential) flows and occurs at higher orders for incompressible ones. We are able to identify an important dynamical feature of the carrying flow, i.e. the way through which it decorrelates in time. Our main result is that, in general, a small (large) degree of recirculation is associated with a decrease (increase) of streaming with respect to a quiescent fluid. The presence of this effect is also confirmed numerically, away from the perturbative limit. However, the previous picture can be reversed in the presence of incompressibility, even if it does not seem to depend on the space dimension. Moreover, we extend our approach to in-

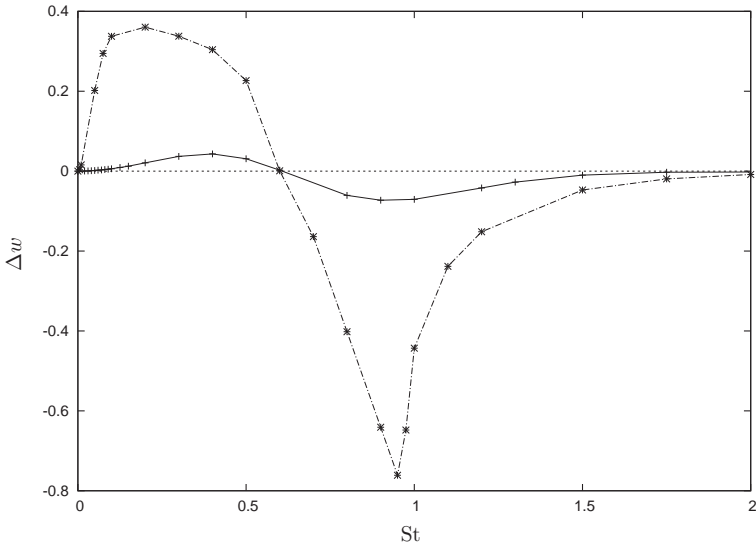


Fig. 1. Variation of the falling velocity, for very heavy particles, as a function of the Stokes number for the flow (1) at $\omega = 0$ and $k = 1$, from Lagrangian simulations of the original dynamical equations. The solid and dash-dotted lines refer to Péclet numbers of 5 and 1000, respectively.

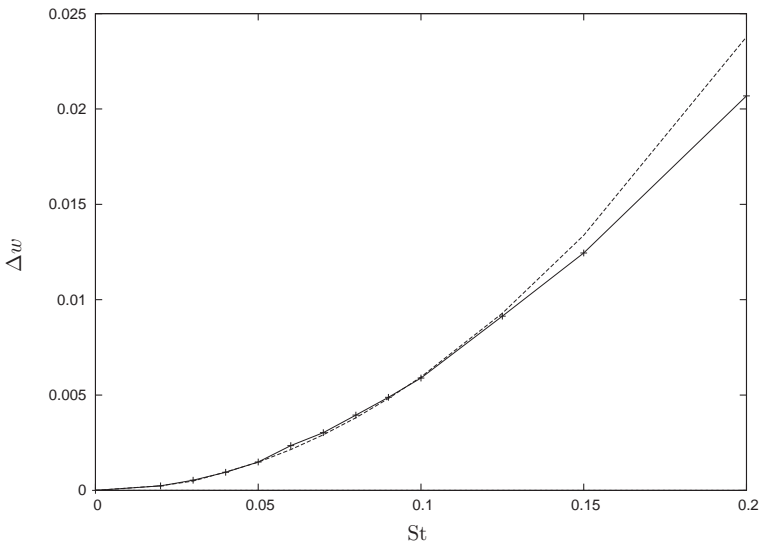


Fig. 2. Comparison between Lagrangian simulations (solid line) of the original dynamical equations — i.e. simply a zoom of the solid line in figure 1 near the origin — and the parabola (dashed line) resulting from direct numerical simulations of our set of partial differential equations for the particle probability density function.

investigate the particle effective diffusivity, and thus the relative efficiency of diffusive and ballistic transport. The crossover time, after which the latter becomes predominant over the former, can show a resonance peak. We find the important result that, for a specific class of flows, the compressibility degree has no influence on the total diffusivity, but only on its components parallel and orthogonal to the unperturbed straight trajectory; namely, if the recirculation degree is small or inertia is large, we show that parallel (orthogonal) diffusion dominates for incompressible (potential) flows.

References

1. M. R. Maxey, *J. Fluid Mech.*, **174**, 441 (1987).
2. A. Celani, M. Martins Afonso and A. Mazzino, *Advances in Turbulence XI: Proceedings of the 11th EUROMECH European Turbulence Conference*, Springer Proceedings in Physics, **117**, 61 (2007).
3. M. Martins Afonso, *J. Phys. A: Math. Theor.*, **41**, 385501 (2008).
4. M. R. Maxey and J. J. Riley, *Phys. Fluids*, **26**, 883 (1983).
5. T. H. Solomon and J. P. Gollub, *Phys. Rev. A*, **38**, 6280 (1988).
6. E. Balkovsky, G. Falkovich and A. Fouxon, *Phys. Rev. Lett.*, **86**, 2790 (2001).
7. G. A. Pavliotis and A. M. Stuart, *Physica D*, **204**, 161 (2005).
8. M. Martins Afonso, A. Mazzino and P. Olla, submitted to *J. Phys. A: Math. Theor.* (2009).

Turbulence modification in the vicinity of a solid particle

Aurore Naso¹ and Andrea Prosperetti²

¹Laboratoire de Physique, Ecole Normale Supérieure de Lyon and CNRS, 46, allée d'Italie, 69364 Lyon Cedex 07, France

²Johns Hopkins University, Department of Mechanical Engineering, Baltimore MD 21218, USA

`aurore.naso at ens-lyon.fr`

The turbulent transport of material particles is a very general phenomenon, occurring in many natural (dust storms, pollutants in the atmosphere, plankton in the ocean, ...) and industrial (fluidized beds, chemical reactors, ...) systems. The dynamics of particles suspended in a turbulent flow depends on their size and on their mass density. Very small neutrally buoyant particles behave as passive tracers, co-moving with the fluid, whereas inertial and finite-size effects are expected to occur for larger objects which are buoyant or denser than the fluid. The dynamics of very small heavy particles has been studied by modeling the hydrodynamic forces acting on them as the sum of a (possibly corrected) Stokes drag, added mass, and other forces; in this way it has been possible to simulate the dynamics of millions of particles (see e.g. [1]).

However, the dynamics of finite size (in practice, larger than the Kolmogorov scale) particles is not yet understood. Recent experiments have been carried out in order to characterize the influence of the particles' size on their acceleration statistics [1, 2, 3, 4]. However, in order to understand the underlying mechanisms one needs to investigate the flow around the objects. Such an information is not yet available in the experiments. Simulations based as much as possible on the first principles must therefore be carried out [5, 6, 7].

For this purpose, we use the Physalis algorithm, specifically designed to integrate the Navier-Stokes equation in the presence of solid spheres [8, 9, 10]. This method exploits the no-slip condition to linearize the flow around a solid-body rotation/translation in the vicinity of each particle. In this way, an analytical solution, valid very close to the surface of the object, can be calculated. In the particle rest frame, this problem is indeed reduced to the resolution of the Stokes equation with the condition of vanishing velocity on a sphere. The most general solution of this problem is expressed as a sum of spherical harmonics multiplied by coefficients depending on the external

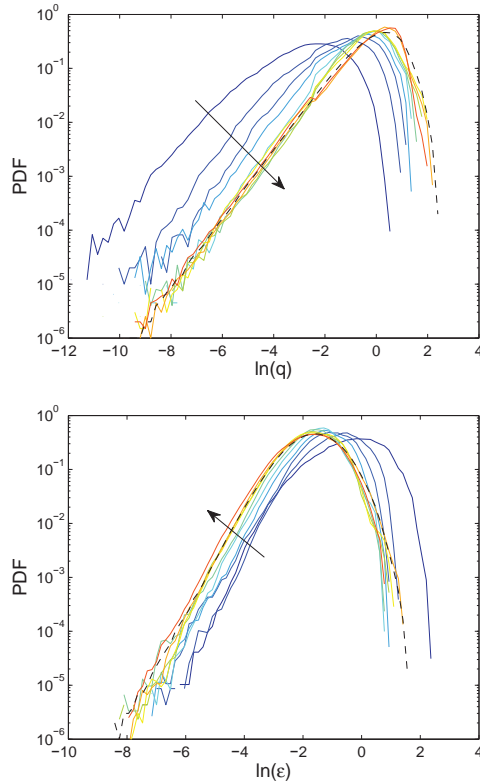


Fig. 1. Probability density functions of kinetic energy (top) and dissipation (bottom) around the particle, in thin spherical shells of radius $R(1+\alpha)$: $\alpha = 0.125, 0.25, 0.375, 0.5, 0.75, 1, 1.5, 2, 4, 6$ in the direction of the arrow. The dashed lines are the results of a simulation without particle.

boundary conditions, in our case the flow in the rest of the computational domain. This flow is calculated by a finite difference scheme, using a standard projection method. The existence of the analytical solution, valid in a very thin shell surrounding the particle, allows us to use a uniform mesh, irrespective of the presence of the objects, in the whole domain. We have at our disposal a dual representation of the flow (analytical/numerical), matching on a cage of nodes surrounding the object.

In this communication we limit ourselves to the case of a single particle kept fixed (neither translating nor rotating) in homogeneous turbulence, with a zero mean flow. The level of turbulence is kept stationary by using a linear forcing [11]: $\mathbf{F} = A\mathbf{u}$, where \mathbf{F} is a force per unit mass, \mathbf{u} is the fluid velocity and A is a parameter whose value is kept fixed during the simulation. Our choice for this forcing was motivated by two criteria: (i) it acts in the phys-

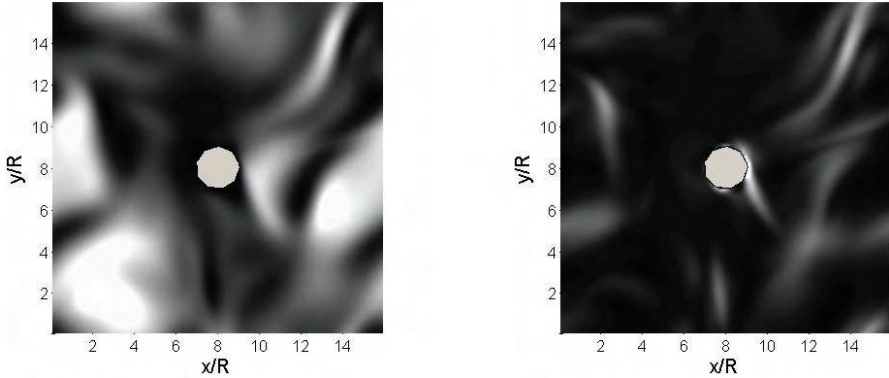


Fig. 2. Instantaneous kinetic energy (left) and dissipation (right) densities in a plane diametral to the sphere: $z/R = 8$. Increasing values from black to white. At the particle surface, the no-slip condition is satisfied (left), resulting in a local enhancement of the dissipation (right).

ical space; (ii) it tends towards zero as one approaches the particle surface. Details on the numerical procedure can be found in [10]. The computational domain is a cubic box of linear size equal to 16 times the particle radius, R . The grid resolution was 128^3 , which results in a number of nodes per radius equal to 8. The particle is located at the center of the computational domain, and periodic boundary conditions are imposed in each direction. The particle Reynolds number, $Re_p \equiv 2Ru_{rms}/\nu$, is close to 20, and the object diameter is close to $8\eta \sim L/2$, where η is the Kolmogorov scale and L the integral scale. The Courant number based on the instantaneous maximal velocity was always smaller than 0.5.

In order to investigate the local modification of the flow due to the presence of the object, we measured the statistics of kinetic energy, q , and of energy dissipation, ε , at different distances from its surface. The probability distribution functions of these quantities in spherical shells of different radii are plotted in Fig. 1. At the largest distances, the statistics measured in single-phase flow are recovered, showing that the computational domain is large enough to avoid any influence of the virtual neighbor particles implied by the use of periodic boundary conditions. As expected, the presence of the particle results in a dramatic damping of the kinetic energy close to its surface (no-slip and no-penetration condition) (Fig. 1, top). The dissipation rate is drastically enhanced in the vicinity of the object (Fig. 1, bottom), which can be explained by the fact that, because of the vanishing velocity condition on the object, the velocity derivatives normal to its surface are relatively large. Both effects are significant at distances r up to $3R$ from the particle surface, which can be shown more accurately by plotting the moments of both quantities as a function of r (not shown here). Thus, the volume of fluid affected

by the particle is more than one order of magnitude greater than the particle volume fraction. As a comparison, a rough estimate of the boundary layer thickness l gives: $l \sim R/\sqrt{Re_p} \approx 0.22R$.

To illustrate the enhancement of energy dissipation close to the particle surface, we have plotted in Fig. 2 the densities of kinetic energy and of dissipation in a plane passing through the center of the object. Interestingly, a region of high energy is approaching the particle surface (right-hand sides of the figures). Because of the vanishing velocity condition, the major part of this energy is clearly dissipated (Fig. 2, right).

This study will be completed by the investigation of other quantities, such as the velocity components and the pressure.

The calculations were performed at the Pôle Scientifique de Modélisation Numérique at the Ecole Normale Supérieure de Lyon.

References

1. R. Volk, E. Calzavarini, G. Verhille, D. Lohse, N. Mordant, J.-F. Pinton and F. Toschi, *Physica D*, **237**, 2084 (2008).
2. R. Volk, N. Mordant, G. Verhille and J.-F. Pinton, *Europhys. Lett.*, **81**, 34002 (2008).
3. N.M. Qureshi, M. Bourgoïn, C. Baudet, A. Cartellier and Y. Gagne, *Phys. Rev. Lett.*, **99**, 184502 (2007).
4. N.M. Qureshi, U. Arrieta, C. Baudet, A. Cartellier, Y. Gagne and M. Bourgoïn, *Eur. Phys. J. B*, **66**, 531 (2008).
5. P. Bagchi and S. Balachandar, *J. Fluid Mech.*, **581**, 95 (2004).
6. T.M. Burton and J.K. Eaton, *J. Fluid Mech.*, **545**, 67 (2005).
7. L.Y. Zeng, S. Balachandar, P. Fischer and F. Najjar, *J. Fluid Mech.*, **594**, 271 (2008).
8. Z. Zhang and A. Prosperetti, *J. Appl. Mech.*, **70**, 64 (2003).
9. Z. Zhang and A. Prosperetti, *J. Comput. Phys.*, **210**, 292 (2005).
10. A. Naso and A. Prosperetti, *Proceedings of the International Conference on Multiphase Flows*, Leipzig, Germany (2007).
11. C. Rosales and C. Meneveau, *Phys. Fluids*, **17**, 095106 (2005).

Particle Transport in Turbulent Wakes Behind Spherical Caps

N.G.W. Warncke, R. Delfos, and J. Westerweel

Laboratory for Aero- & Hydrodynamics, Delft University of Technology, 2628CA
Delft, The Netherlands
`n.g.w.warncke@tudelft.nl`

1 Introduction

Flows around spherical-cap objects have been studied for decades ([1], [2], [3]). The problem we consider here is how suspended particles in a flow interact with the wake behind rising spherical-cap bubbles. The fundamental question is whether — and if so, how — particles become trapped in the wake of a rising bubble [4]. An important industrial application of this mechanism is the cleaning of liquid steel from μm -sized inclusions (Flotation). We examine the wake trapping mechanism by analyzing the wake of a solid spherical-cap model in water.

2 Methods

A two-camera PIV-system was used to simultaneously measure the velocity fields of the fluid phase (EBM FLUOSTAR tracer) and the dispersed phase (hollow glass spheres, $\rho = 0.22\text{g/cm}^3$, $d=50 \dots 60\mu\text{m}$) in the wake of a brass 50° -spherical-cap model (Fig. 1) of diameter $d_{eff} = 11\text{mm}$. This obstacle is placed in a vertical tube and is approached with an upward turbulent flow. Turbulence is created by a grid placed upstream of the obstacle.

To discriminate between the two phases a beam splitter and optical filters mounted in front of the cameras were used. The alignment between the two camera images was realized by calculating a linear mapping function of reference images recorded without the filters in the optical path and subsequent averaging. The averaged mapping function was later used to correct the second cameras double frames prior to the PIV analysis. Our tests using this alignment method have shown remaining errors to be below 0.4 px.

For every node, mean and variance of the velocity were calculated from the acquired vector fields of both phases. The flux over a boundary was determined by integrating the bilinear interpolated normal velocity at that boundary. Measuring the particle concentration was done by analyzing the reflected light intensity of the dispersed phase by evaluating the raw PIV images directly.

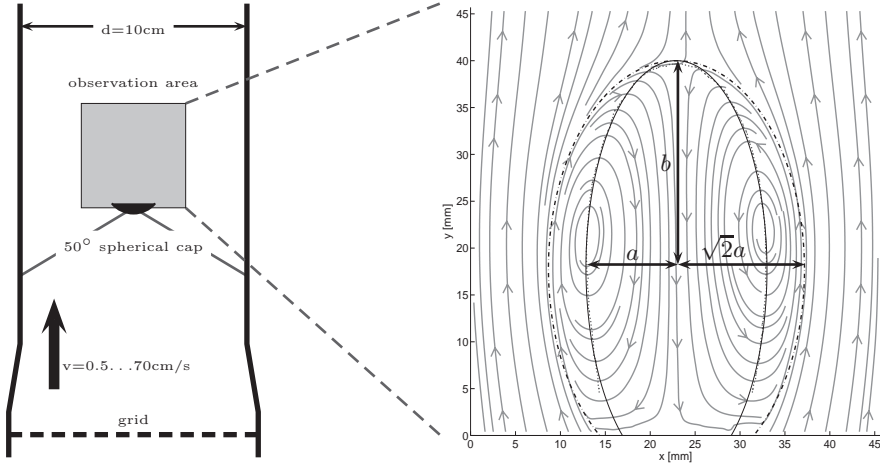


Fig. 1. Schematic view of the experimental setup (left), stream line plot (right) of the averaged velocity field, with ellipse fit (solid line) to the zero-crossings (dotted) of u_z , and scaled ellipse (dashed)

3 Results

A detailed description of wakes behind spherical-cap objects was given in [2] and [3]. To allow a comparison with Argon bubbles rising in molten steel, the parameters for the performed experiment were chosen to match these conditions ($Re = 500 \dots 10^4$). This resulted in Reynolds numbers far beyond the stable, laminar range. Though one can argue that the lowest used Reynolds number ($Re = 840$) is still transitional, the observed wakes were open and turbulent. Nevertheless the averaged velocity fields, in particular for the higher Re numbers, are in good congruence with a Hill vortex, only being elongated by about 50% in the direction of the mean flow.

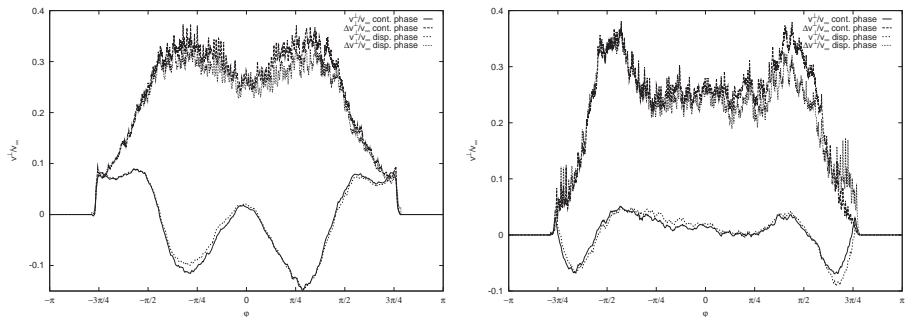


Fig. 2. Velocities normal to elliptic boundaries, fitted ellipse (left) and scaled ellipse (right), $Re = 2300$

	Re	\dot{V}	$\Delta\dot{V}$	$\dot{V}/\Delta\dot{V}$		Re	\dot{V}	$\Delta\dot{V}$	$\dot{V}/\Delta\dot{V}$
continuous	840	14.65	70.41	0.21	continuous	840	-179.9	44.13	-4.07
phase,	2300	-1.38	84.39	-0.016	phase,	2300	-10.95	68.70	-0.16
(a, b)	6600	-2.75	79.98	-0.034	$(\sqrt{2}a, b)$	6600	-21.82	58.79	-0.37
dispersed	840	25.01	65.01	0.38	dispersed	840	-157.8	42.89	-3.68
phase,	2300	-3.85	80.67	-0.048	phase,	2300	-8.74	64.91	-0.13
(a, b)	6600	-2.24	70.09	-0.032	$(\sqrt{2}a, b)$	6600	-2.49	54.62	-0.046

Table 1. Measured fluxes $\dot{V}/\Delta\dot{V}$ over the wake boundary for the continuous phase (top) and dispersed phase (bottom)

The concentration measurements were realized by averaging and low-pass filtering of the recorded PIV images. There was no indication for a higher average light intensity inside the wake area. Therefore the focus of the following analysis will be on the flow measurements.

To determine the particle transport from the outer flow to the wake, a smooth boundary was needed. An ellipse was fitted to the zero-crossings of the z-component of the continuous phase, making use of the similarity ([1]) between the averaged velocity field of a spherical-cap wake and a Hill vortex. From the Stokes stream function of a Hill vortex with radius R , the velocity can be derived as

$$\mathbf{v} = 1.5 \left((2\mathbf{x}^2 \mathbf{u}_\infty - (\mathbf{u}_\infty \cdot \mathbf{x})\mathbf{x}) / R^2 - \mathbf{u}_\infty \right) . \tag{1}$$

Requiring that the velocity component parallel to \mathbf{u}_∞ is zero gives $0 = \mathbf{u}_\infty \cdot \mathbf{v}$, and using the simplification $\mathbf{u}_\infty = (0, 0, u_\infty^z)$ in cylindrical coordinates gives

$$1 = \frac{r^2}{R^2/2} + \frac{z^2}{R^2} , \tag{2}$$

an equation for an ellipse with the half axes $a = R/\sqrt{2}$ perpendicular and $b = R$ parallel to \mathbf{u}_∞ . This ellipse together with one whose smaller half-axis was multiplied by $\sqrt{2}$ (the “fitted” and “scaled ellipse”, see Fig. 1) were used as boundaries to interpolate the normal velocities from the PIV vector field.

The volume flow is assumed to be axis-symmetric around the z-axis, giving

$$\dot{V} = 2\pi \int_{-\pi}^{\pi} v^\perp r(\phi) \sqrt{\left(\frac{dr}{d\phi}\right)^2 + \left(\frac{dz}{d\phi}\right)^2} d\phi \approx \sum_i v_i^\perp A_i/2 = 1/2 \mathbf{v}^\perp \cdot \mathbf{A} \tag{3}$$

for the volume flow over the boundary of a body of revolution. The sum on the right is the used approximation for this integral, with $A_i/2$ being the surface area of point i of the elliptic boundary, taking into account that only half of the ellipse must be rotated to get an ellipsoid. Similarly,

$$\Delta\dot{V} \approx 1/2 \sqrt{\mathbf{A}^T \text{COV}(\mathbf{v}^\perp) \mathbf{A}} \tag{4}$$

gives an estimate for the standard deviation of the measured volume flow according to the propagation of uncertainty, including turbulent fluctuations of the normal velocity as well as statistical measurement errors.

In table 1 the fluxes \dot{V} relative to the strength of the estimated fluctuations $\Delta\dot{V}$ for both phases and different Reynolds numbers are given. In general the averaged particle transport is about one order of magnitude smaller than the estimated fluctuations. Exceptions are the values for the scaled ellipse at $Re = 840$: at this low flow speed the averaged velocity field of the wake close to the obstacle was more strongly distorted compared to an elongated Hill vortex, resulting in an elliptical fit with a larger value for the smaller half-axis. In this case the boundary did not intersect with the spherical cap, neglecting the flow passing between the boundary and the obstacle. For the measurements done at the low flow speed and a transitional wake, the criterion used to determine the wake boundary was found to be less applicable.

Figure 2 displays polar plots of the mean normal velocity \mathbf{v}^\perp and its estimated fluctuations $\Delta\mathbf{v}^\perp = \text{diag}(\text{COV}(v^\perp))$. For the fitted-ellipse boundary the averaged normal velocity is positive (outflow) close to the obstacle, negative (inflow) further behind and zero directly at the boundary of the obstacle. For the scaled-ellipse boundary the normal velocities are smaller on average with a small outflow further behind and slightly higher values (inflow) directly behind the obstacle. In both cases there is marginal difference between the continuous and the dispersed phase. Additionally, the turbulent velocity fluctuations ($\Delta v^\perp/v_\infty$) of about 30% are much higher than the averaged normal velocities.

4 Discussion and Conclusion

The measurement results show that the velocity component normal to the elliptic boundaries is clearly dominated by the turbulent velocity fluctuations. Furthermore, the integrated volume flow over these boundaries is negligible compared to its estimated standard deviation for both the continuous and the dispersed phase. Considering that there was no indication of differences in concentration in the intensity data, it can be concluded that the dispersed phase does not underlie any effect of preferred concentration. In summary, the experimental results show no indication for an effect of wake trapping of the examined particles under the examined conditions.

Acknowledgments: This project was funded by STW and Corus RD&T. Special thanks to EBM for providing tracers, and to IMCD for the test particles.

References

1. P.P. Wegener, J-Y. Parlange: *Spherical-cup bubbles*. Annu.Rev.Fluid Mech. 1973.5:79-100
2. J.H.C. Coppus, K. Rietma, S.P.P. Ottengraf: *Wake Phenomena Behind Spherical-Cup Bubbles and Solid Spherical-Cap Bodies*. TRANS. INSTN CHEM, ENGRS, Vol 55, 1977
3. Ch. Brückner: *3-D Scanning-Particle-Image-Velocimetry: Technique and Application to a Spherical Cap Wake Flow*. Appl. Sci. Res, 1999
4. M. Schlüter, S. Scheid, S. John, N. Rübiger: *Fluidization of Fine Particles In Bubble Wakes Affects Hydrodynamics in Three-Phase Flows*. Journal of Chemical Engineering of Japan, Vol. 37(8), 947-954, 2004

Turbulent heat transfer and large-scale flow in convection cells with aspect ratio $\Gamma > 1$

Mohammad S. Emran, Jorge Bailon-Cuba, and Jörg Schumacher

Institut für Thermo-und Fluidodynamik, Technische Universität Ilmenau, D-98693 Ilmenau, Germany
mohammad.emran@tu-ilmenau.de

1 Introduction

One of the most comprehensively studied turbulent flow is the Rayleigh-Bénard convection, in which a complex three-dimension turbulent motion is initiated by heating the fluid from below and cooling from above. Detailed measurements of the turbulent heat transfer [1, 2], the statistics of the temperature fluctuations and its gradients [3, 4] and the analysis of coherent thermal plumes [5, 6] haven been conducted in the past. The variation of the global heat transfer with respect to two of the three dimensionless control parameters—the Rayleigh number Ra and the Prandtl number Pr – in thermal convection was the focus of most of the laboratory experiments and simulations [7]. The dependence of the third control parameter – the aspect ratio, $\Gamma = D/H$, with D the diameter and H the height of the cell – has been studied much less extensively. Only a few systematic analyses of high-Rayleigh number convection in flat cells with $\Gamma > 1$ have been conducted [7], although it is relevant in geophysics and astrophysics. Even more surprisingly, an explicit aspect ratio dependence of the heat transfer in turbulent convection is absent in the existing scaling theories. Within the framework of this study, we perform a systematic analysis of the aspect ratio dependence of convective turbulence in cylindrical cells by three-dimensional direct numerical simulation. Our parameter ranges are: $Ra = 10^7 - 10^9$, $\Gamma = 0.5 - 12$ for fixed $Pr = 0.7$. Our analysis is focused on the following questions: Does the turbulent heat transfer at fixed Ra depend on Γ ? Which changes in the the global flow structures are associated with an aspect ratio variation and which fraction of the total kinetic energy and heat transfer is contained in the large-scale circulation (LSC)? It is found that the global heat transfer, as measured by the Nusselt number Nu , varies up to 10% for aspect ratio variation. It is also observed that the primary mode of the LSC is responsible for carrying almost 50% of the turbulent kinetic energy for $\Gamma > 1$.

2 Dependence of heat transfer on aspect ratio

The global heat transfer in the convection cell as measured by the Nusselt number, Nu , is given by

$$Nu = \frac{1}{H} \int_0^H Nu(z) dz = 1 + \frac{H}{\kappa \Delta T} \langle u_z T \rangle_{V,t}, \quad (1)$$

with κ the thermal diffusivity, T the temperature, ΔT the temperature difference between the hot and cold plates and u_z the vertical velocity. The symbol $\langle \cdot \rangle_{V,t}$ denotes an average over the cell volume and an ensemble of statistically independent snapshots.

Figure 1 shows Nu as a function of Γ for three different Ra , namely $Ra = 10^7, 10^8$ and 10^9 . At $Ra = 10^7$ (Fig. 1(a)), Nu decreases with increasing Γ , attains a minimum value at $\Gamma = 2$, then increases up to a maximum value close to $\Gamma = 8$ and finally saturates. Similar trends are observed for higher Rayleigh numbers in the same figure. The variations in Nu , as defined by the difference between the maximum and minimum Nu , are 10.6%, 7.5% and 4.9% for $Ra = 10^7, 10^8$ and 10^9 respectively, within our parameter range. We have also fitted power law $Nu = A \times Ra^\beta$ at a fixed Ra by varying Γ . It turns out $(A, \beta) = (0.165, 0.287), (0.145, 0.294), (0.127, 0.300), (0.110, 0.309)$ for $\Gamma = 0.5, 1, 2, 3$ respectively, which reveals that the prefactors and exponents follow systematic trends.

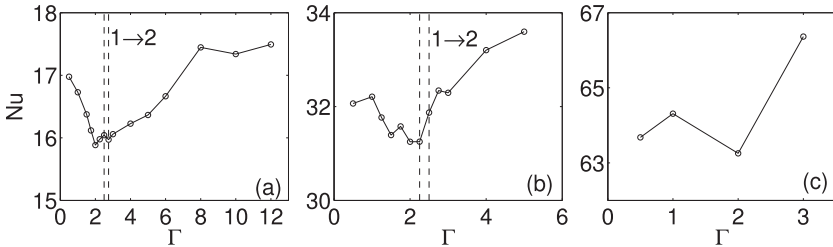


Fig. 1. Nusselt number Nu (as in Eq. (1)) as a function of the aspect ratio Γ with (a) $Ra = 10^7$, (b) $Ra = 10^8$, (c) $Ra = 10^9$. The crossover from one circulation roll to two rolls is indicated in (a) and (b) by two parallel dashed lines. The statistics is gathered over at least 109 statistically independent turbulent samples.

3 Large-scale circulation (LSC)

We investigate the behaviour of the LSC in the convection cell with the help of the time-averaged velocity field. This procedure removes not only all small-scale fluctuations of the velocity field, but also oscillations of the LSC. Figure 2

shows the LSC patterns for two aspect ratios, $\Gamma = 2.5$ and 6, at $Ra = 10^7$. Between $\Gamma = 2.5$ and 2.75, the system bifurcates from a one-roll to a two-roll pattern [8]. The LSC patterns are more complex at higher aspect ratio, e.g., $\Gamma = 6$, as the single roll break down in to smaller ones.

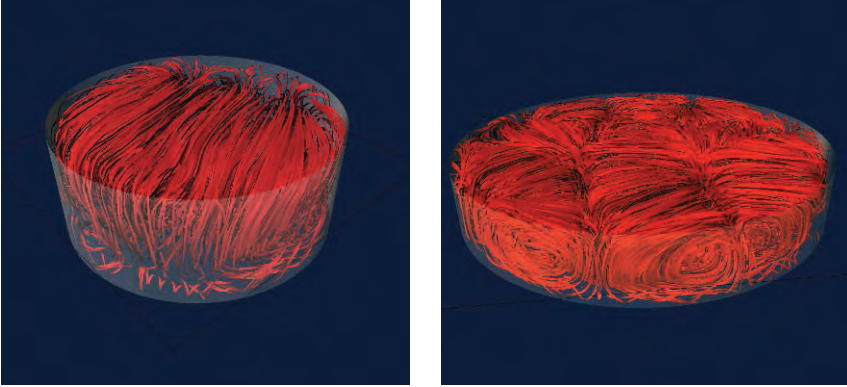


Fig. 2. Flow patterns at different aspect ratios. Streamlines of the time-averaged velocity field at $\Gamma = 2.5$ on the left and $\Gamma = 6$ on the right for $Ra = 10^7$. All data are obtained by time averaging of a sequence of 50 statistically independent snapshots.

3.1 Proper Orthogonal Decomposition (POD)

Turbulent heat transfer is the sum of contributions by the LSC and turbulent fluctuations. In order to disentangle both contributions, the so-called Karhunen-Loève or POD analysis [8, 9] is employed here. We decompose turbulent velocity field as $u_i(\mathbf{x}, t) = \sum_{m=1}^{N_T} a_i^{(m)}(t) \phi_i^{(m)}(\mathbf{x})$ and the temperature fluctuation as $\theta(\mathbf{x}, t) = \sum_{m=1}^{N_T} a_4^{(m)}(t) \phi_4^{(m)}(\mathbf{x})$, with $i = 1, 2, 3$, N_T the number of snapshots. The coefficients $a_i^{(m)}(t)$ correspond to the projection of flow field at time t to the POD-mode $\phi^{(m)}(\mathbf{x})$. The Nusselt number definition in Eq. (1) then translates to

$$Nu = 1 + \frac{H}{\kappa \Delta T} \sum_{m,n=1}^{N_T} \left\langle a_3^{(m)}(t) \phi_3^{(m)}(\mathbf{x}) a_4^{(n)}(t) \phi_4^{(n)}(\mathbf{x}) \right\rangle_{V,t} \quad (2)$$

In Figure 3, we plot the contribution of various POD modes to the global heat transfer as in Eq. (1). Since the analysis is conducted here with 80 snapshots, the values of Nu deviate slightly from Figure 1. The primary POD mode carries to up 31.8, 48.2, 47.6, 46.2 and 56.6% of Nu for aspect ratios $\Gamma = 0.5, 1, 2, 2.5$ and 3 respectively. For flow patterns with a single-roll circulation ($\Gamma = 1, 2$, and 2.5), the contribution to the heat transfer by the primary POD mode

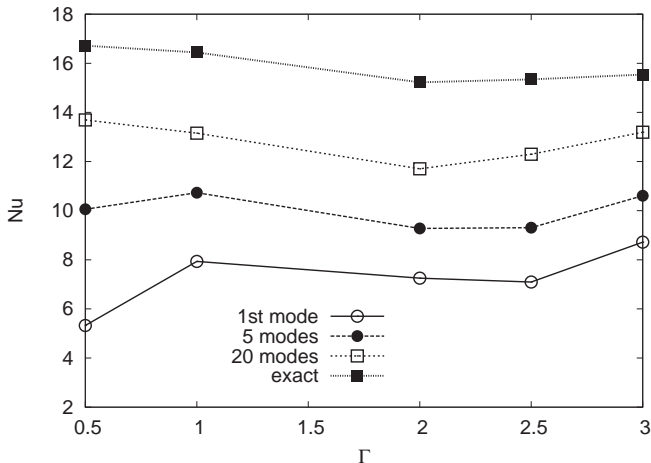


Fig. 3. Contributions of various POD modes (as indicated in the legend) to the global heat transfer Nu (exact in the legend). The analysis is conducted for 5 different aspect ratios at $Ra = 10^7$.

is roughly the same, which is about one-half of Nu . It increases by 10% due to the transition from a single-roll to a double-roll pattern (cross over from $\Gamma = 2.5$ to 3). The slender cell ($\Gamma = 0.5$) has a lower Nu fraction, which can be attributed to the complex flow configuration with different roll-orientation. The first POD mode reproduces the LSC pattern as depicted in Figure 2 [8].

This work is supported by the Deutsche Forschungsgemeinschaft under the grants SCHU 1410/2-1 and SCHU 1410/5-1. We also acknowledge the support by the Jülich Supercomputing Center (Germany) under the grant HMR09.

References

1. B. Castaing, G. Gunaratne, F. Heslot, L. Kadanoff, A. Libchaber, S. Thomae, X.-Z. Wu, S. Zaleski and G. Zanetti, *J. Fluid Mech.* **204**, 1 (1989).
2. K. Xia, S. Lam, and S. Zhou, *Phys. Rev. Letters* **88**, 064501 (2002).
3. M. S. Emran and J. Schumacher, *J. Fluid Mech.* **688**, 13 (2008).
4. X. He and P. Tong, *Phys. Rev. E* **79**, 026306 (2008).
5. Q. Zhou, C. Sun and K. Xia, *Phys. Rev. Letters* **98**, 074501 (2007).
6. O. Shishkina and C. Wagner, *J. Fluid Mech.* **599**, 383 (2008).
7. G. Ahlers, S. Grossmann, and D. Lohse, *Rev. Mod. Phys.* **81**, xx (2009).
8. J. Bailon-Cuba, M. S. Emran and J. Schumacher, *J. Fluid Mech.*, submitted (2009).
9. T. R. Smith, J. Moehlis and P. Holmes, *Nonlin. Dyn.* **41**, 275 (2005).

Shot noise of thermal plumes : Evidence of a boundary layer instability consistent with the onset of Kraichnan's Regime of convection

F. Gauthier, and P.-E. Roche

Institut Néel, CNRS / UJF, BP166, F38042 Grenoble cedex 9, France
philippe.roche at grenoble.cnrs.fr

1 Introduction and Motivation

In 1997, an enhancement of heat transfer has been reported [1] in Rayleigh Bénard convection for Rayleigh numbers $Ra \gtrsim 10^{12}$. This new regime -named "Ultimate Regime" in the original paper- was interpreted as the regime predicted by Kraichnan in 1962 [2] and which is characterized by the turbulence of the boundary layers of the convection cell. Although this interpretation has been indirectly supported by specific experimental tests, including the observation of the $Nu \sim Ra^{1/2}$ scaling predicted by Kraichnan for asymptotically high Ra [3], a direct evidence of fluctuations in the boundary layer was still missing. We report such an observation based on the measurement of the shot-noise induced by thermal plumes in the heating plate [4].

2 Experimental set-up

Probing fluctuations directly within the boundary layer itself raises instrumentation challenges due to its thinness, estimated as a tenth of a millimeter in cells such as the one used in [1]. To overcome this difficulty, we measured the low-frequency temperature fluctuations of the heating plate of the convection cell, which was Joule heated at a constant flux. As explained in [4], operation at cryogenic temperatures (around 6 K) makes this measurement possible thanks to the thermal characteristic times of the fluid (He) compared to those of the bottom plate material (OFHC annealed copper).

The cell (insert of Fig.1) is similar to the one used in [1]. The bottom plate temperature is monitored by 2 Ge thermistors (letter "T" on Fig.1), distant from each other by a plate's radius. At the frequency of interest (of order 10–100 mHz) they give consistent signal. The thermistors' time response was measured with the 3ω method. As displayed on Fig 1: their characteristic frequency response is significantly larger than the frequencies of interest.

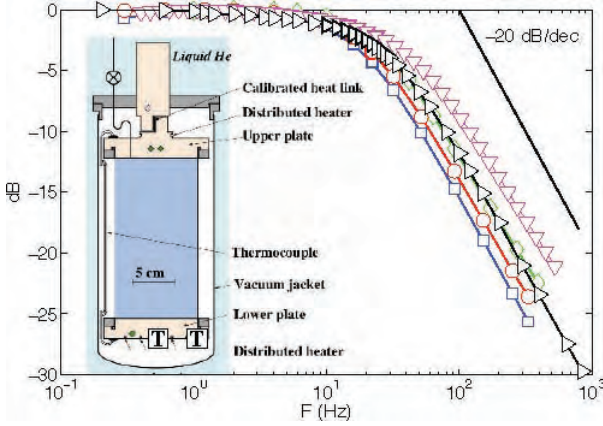


Fig. 1. Frequency response of the various thermistances of the set-up, measured in-situ by the 3ω technique. Insert : the cylindrical cryogenic convection cell. The letters “T” represents the thermometers used to measure temperature fluctuations.

3 Results : a new signatures of the transition to the Ultimate Regime

The insert of Fig.2 shows temperature spectra for $5 \times 10^{10} < Ra < 6 \times 10^{13}$ and for Prandtl numbers of order 1 ($1.0 \leq Pr \leq 2.8$). At low frequency, spectral density plateaus $E_{plateau}$ can be fitted on data. The main figure shows the spectra rescaled by $E_{plateau}$ and by arbitrary frequencies F_c .

The spectral densities $E_{plateau}$ can be made dimensionless with the temperature difference across the cell Δ , its height h and the kinematic viscosity of the fluid ν : $P^* = E_{plateau} \nu / (h \Delta)^2$. Fig.3 (black symbols on the main plot) shows that P^* roughly scales like $Ra^{-2/3}$ below $Ra \simeq 2 \times 10^{12}$ but increases faster with Ra above. This threshold Ra is the same as the one for which the heat transfer across the cell improves significantly, compared to the “hard turbulence” regime present at lower Ra . This is illustrated by the insert of Fig.3 showing the Nusselt number Nu (compensated by $Ra^{1/3}$) versus Ra .

As illustrated by the histograms and the skewness of the temperature fluctuations (see Fig.4), the plate’s fluctuations differ significantly from a gaussian distribution above $Ra = 2 \times 10^{12}$.

4 Interpretation and Conclusion : a boundary layer instability

Interestingly, for $Ra < 2 \times 10^{12}$, the low-frequency spectral density P^* of the plate temperature spectra coincides with the corresponding quantity in the bulk of the flow (measured previously in a similar experiment) but not above

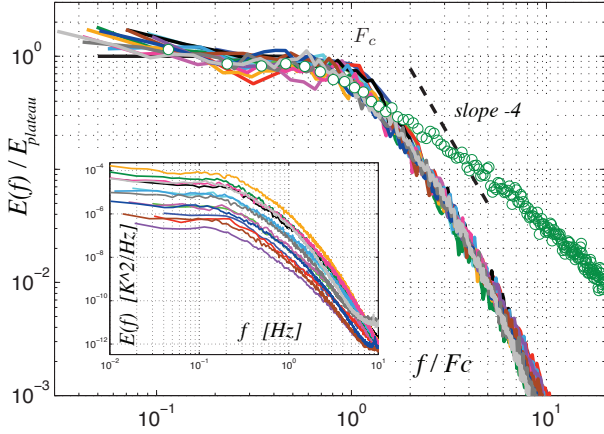


Fig. 2. Temperature power spectra of the bottom plate (continuous line) and of a local probe located in the core of the flow (circles) [1]. In the main plot, the spectra are rescaled by 2 ad-hoc parameters $E_{plateau}$ and F_c .

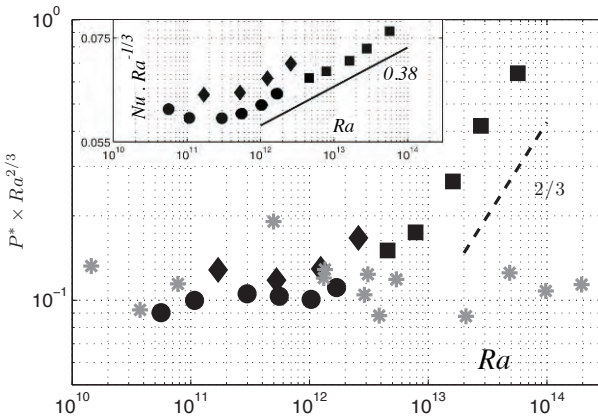


Fig. 3. Compensated spectral density of the low frequency temperature fluctuations of the bottom plate (\bullet : $Pr=1.0$, \blacklozenge : $Pr=1.3$, \blacksquare : $Pr=2.8$) and of the bulk of the flow (*). Insert : Nusselt number Nu , compensated by $Ra^{1/3}$, versus Ra showing departure from a typical $Ra^{1/3}$ scaling above $Ra \simeq 10^{12}$.

$Ra \sim 2 \times 10^{12}$ (see Fig.3). A straightforward interpretation, consistent with the time scales of the system [4], consists in assuming that the temperature of the plate follows the slow temperature fluctuations of the well-mixed core region of the flow, with an offset corresponding to the temperature drop across the thermal boundary layer. On average, this temperature drop is $\Delta/2$. The present results indicate that the boundary layer becomes significantly “noisy” -compared to the residual fluctuations in the core of the flow- above a threshold of order $Ra \sim 10^{12}$. This is consistent with the occurrence of an instability in

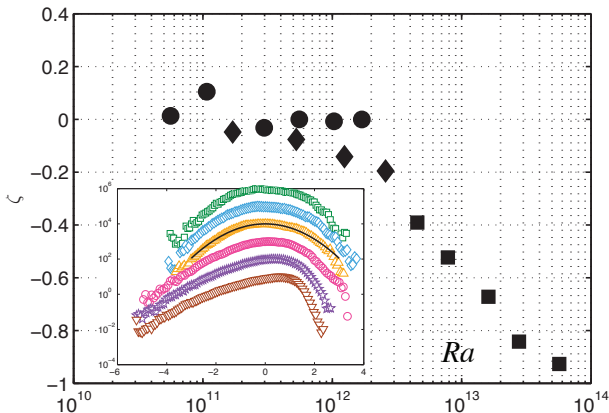


Fig. 4. Skewness of the temperature fluctuations of the plate versus Ra with same symbols as Fig.3. Insert : Histograms of the (centered) temperature fluctuations normalized by the standard deviation. Ra from top to bottom : 5.6×10^{10} , 5.5×10^{11} , 1.7×10^{12} , 4.5×10^{12} , 1.6×10^{13} and 5.7×10^{13} . The continuous line corresponds to a gaussian.

the thermal boundary layer, which would cause an increase of the fluctuations of the temperature drop across it.

In 1962, R. Kraichnan predicted that the thermal boundary layers in Rayleigh-Bénard convection should become unstable at high enough Rayleigh number, leading to an improved heat transfer. The increase in heat transfer $Nu(Ra)$ reported for $Ra \sim 10^{12} - 10^{13}$ in several experiments (since 1997) has been interpreted following Kraichnan’s prediction. The present result confirms the occurrence of a boundary layer instability and is consistent with this interpretation.

Acknowledgements : We thank F. Chilla, Y. Gagne and B. Castaing for stimulating discussions.

References

1. Observation of the ultimate regime in Rayleigh-Bénard convection. Chavanne, X. et al., Phys. Rev. Lett. **79**, 3648 (1997)
2. Turbulent thermal convection at arbitrary Prandtl numbers. Kraichnan, R., Phys. Fluids **5**,1374 (1962)
3. Observation of the 1/2 power law in Rayleigh-Bénard convection. Roche P.-E. et al., PRE, **63**,045303(R) (2001)
4. Evidence of a boundary layer instability at very high Rayleigh number. Gauthier F. and Roche P.-E, EPL **83**,24005 (2008)

Scalar mixing in turbulent confined flow

D. Kolomensky¹, B. Kadoch¹, W.J.T. Bos², K. Schneider¹ and P. Angot³

¹ M2P2–UMR 6181 CNRS CMI, Aix-Marseille Université, Marseille, France

² LMFA–UMR 5509 CNRS, Ecole Centrale de Lyon–Université Claude Bernard Lyon 1–INSA de Lyon, Ecully, France

³ LATP–UMR 6632 CNRS CMI, Aix-Marseille Université, Marseille, France
kadoch@L3m.univ-mrs.fr

Summary. We study the influence of solid boundaries on the scalar transport and mixing in two-dimensional decaying turbulence. It was shown previously that walls have a strong influence on Lagrangian statistics. Two distinct geometries are considered: a square with periodic boundary conditions and a circular domain with no-slip boundary conditions for velocity and no-flux for the scalar. Direct numerical simulations are performed with a pseudo-spectral code, where a penalization method is used to take into account the boundary conditions. Our study shows that the mixing is more pronounced in the confined case due to the stronger production of scalar gradients.

Key words: Mixing, passive scalar, turbulence

Transport and mixing in confined domains is an important issue for many applications, such as chemical reactors or ventilation systems. Numerous studies have been carried out in the context of homogeneous isotropic turbulence [3, 7]. Moreover, two-dimensional approximation can be used in many applications, *e.g.* atmospheric pollutant mixing. In our study we are interested in the influence of boundaries on the transport and mixing properties of two-dimensional decaying turbulence. The influence of no-slip boundary conditions on Lagrangian statistics was studied in [2] for a circular container. It was shown that the generation and separation of vortices near the walls has a strong influence on the statistics of the Lagrangian acceleration. The aim of the present contribution is to explore the effect of boundaries on passive scalar mixing. Numerical simulations are performed using a Fourier pseudo-spectral method. Different geometrical shapes and boundary conditions are modelled with a volume penalization technique [4].

In the following the physical model and the numerical method are explained and parameters and initial conditions are described. Then the results regarding the passive scalar mixing and the Lagrangian transport are shown. Finally, conclusions are drawn.

We consider two different cases: the first one is a square 2π -biperiodic domain; the second is a circular container of radius $R = 2.8$, which is immersed in a biperiodic domain. No-slip boundary conditions for the velocity and no-flux conditions for the passive scalar are imposed at the wall. We shall refer to these two configurations as

the ‘periodic case’ and the ‘circular case’, respectively. The fluid flow is governed by the incompressible Navier–Stokes equations, which we recast in the form of the non-dimensional penalized vorticity equation:

$$\frac{\partial \omega}{\partial t} + \mathbf{u} \cdot \nabla \omega - \nu \nabla^2 \omega = -\frac{1}{\eta_u} \nabla \times (\chi \cdot \mathbf{u}) \quad (1)$$

where the velocity $\mathbf{u} = (u_1, u_2)$ is divergent-free, $\nabla \cdot \mathbf{u} = 0$, its curl is the vorticity, $\omega = \nabla \times \mathbf{u}$, and ν is the kinematic viscosity. The right-hand side of (1) corresponds to the penalization term, which is used to impose the no-slip boundary condition, and which equals zero in the periodic case. The mask function χ equals 1 inside the solid and 0 inside the fluid, where the original (not penalized) vorticity equation is recovered. The permeability η_u is required to be sufficiently small for a given ν in order to minimize the modelling error, since the physical idea behind the volume penalization method is to consider solids as porous media with vanishing permeability, such that the velocity of the surrounding fluid vanishes at the interface.

To study mixing, we consider the advection–diffusion equation of a passive scalar:

$$\frac{\partial \theta}{\partial t} + ((1 - \chi)\mathbf{u}) \cdot \nabla \theta = \nabla \cdot ([\kappa(1 - \chi) + \eta_\theta \chi] \nabla \theta), \quad (2)$$

where θ is the passive scalar, which can represent the concentration or the temperature, κ is its diffusivity, and η_θ is the penalization parameter. The right-hand side of (2) corresponds to the penalized diffusion term, which incorporates the no-flux boundary condition at the wall [4]. Zero flux through the fluid–solid interface can be achieved by imposing vanishing diffusivity inside the solid domain. In the periodic case without boundaries this term simply equals $\kappa \nabla^2 \theta$.

We are using a classical pseudo-spectral discretization in space with the resolution $N = 512^2$ and semi-implicit time stepping scheme with $\Delta t = 10^{-4}$ [5]. The penalization parameters equal $\eta_u = 10^{-4}$ and $\eta_\theta = 10^{-7}$ in equations (1) and (2), respectively. The kinematic viscosity ν is 10^{-4} and the Schmidt number is $Sc = \nu/\kappa = 1$.

In both the periodic and the circular cases the initial condition for the vorticity is a random Gaussian noise with enstrophy $Z = 1/2 \langle \omega^2 \rangle = 55.8$, where $\langle \cdot \rangle$ denotes space averaging. The eddy turnover time is $T_e = 1/\sqrt{2Z} = 0.096$ and the Taylor microscale is $\lambda = \sqrt{E/Z} = 0.095$, where $E = 1/2 \langle u^2 \rangle$ is the initial kinetic energy. The Reynolds number $Re = S\sqrt{E}/\nu$ is about 45000 and 40000 for the periodic and the circular domains, respectively. S is the characteristic size of the fluid domain: $S = 2\pi$ in the periodic case and $S = 2R$ in the circular case. The initial condition for the passive scalar is a Gaussian blob placed in the center of the domain. Its characteristic size equals 1 in the periodic case, and in the circular case it is such that the mean concentrations are equal for both cases.

Fig. 1 shows a visualization of the passive scalar field θ at $t = 104 T_e$ for the circular geometry. The scalar is advected by coherent vortices which are present in the flow. Near the boundary of the circle it slips in the tangential direction, but far from the boundaries the dynamics are similar both in the circular and the periodic cases, the passive scalar is stretched, folded and diffuses. In Fig. 2 (left) the time evolution of the variance of the passive scalar field, $\sigma^2(t) = \langle (\theta(t) - \langle \theta(t) \rangle)^2 \rangle$, shows that the mixing is more pronounced in the circular case. Note that the variance is decaying faster starting from $t \sim 10 T_e$, when the blob approaches the wall. Fig. 2 (right) displays the time evolution of the scalar dissipation rate, defined as

$\Lambda(t) = \langle |\nabla\theta(t)|^2 \rangle$. In the beginning it is just slightly lower in the circular case, but after $t = 211 T_e$ the difference increases. Noteworthy, in the chaotic regime at smaller Reynolds numbers [1] the action of the boundaries is different, since they inhibit mixing in that case. This difference can be explained by the fact that in turbulent flows mixing is driven by the vorticity, and walls produce it.

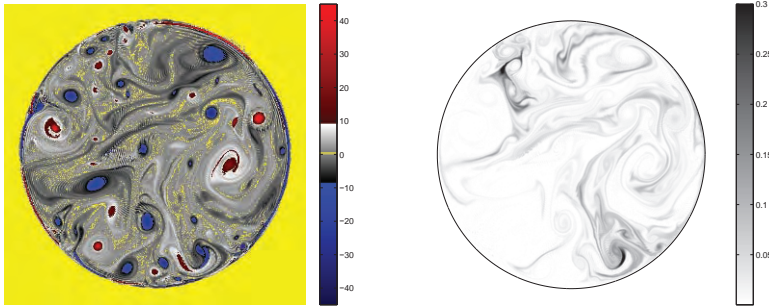


Fig. 1. Vorticity field (left) and scalar field (right) at $t = 104 T_e$. Solid line indicates the circular wall.

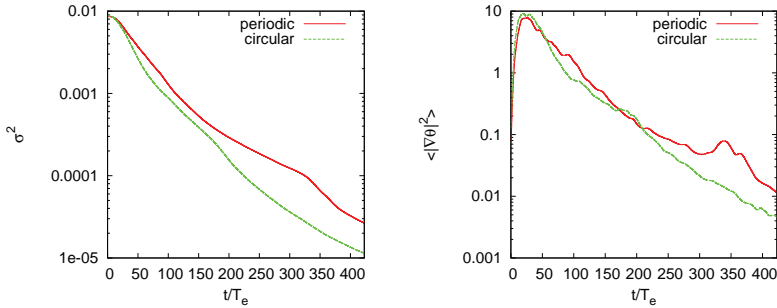


Fig. 2. Time evolution of the variance σ^2 (left) and the dissipation rate Λ (left) of the scalar in the periodic and the circular cases.

The Lagrangian viewpoint is helpful for understanding how the walls influence the scalar transport. We consider passive particles advected by the fluid, such that $\mathbf{u}_L(t) = d\mathbf{x}/dt = \mathbf{u}[\mathbf{x}(t), t]$. They do not diffuse, which corresponds to an infinite Schmidt number. The Lagrangian quantities are obtained by interpolation of the Eulerian data and integration in time using a second-order Runge-Kutta scheme. The Lagrangian acceleration is defined as a sum of the pressure gradient and the diffusive term. The Lagrangian statistics are obtained by averaging over 10000 particles, which are initially distributed uniformly over the surface of the blob. The statistics are made stationary by dividing the Lagrangian quantities $L(t)$ by their instantaneous standard deviation $\sigma(t)$ computed from all particles at each time [6]. Time averaging is then performed over the interval $[0, 190 T_e]$.

The PDFs of the Lagrangian velocity, Fig. 3 (left), have Gaussian-like profiles both in the periodic and the circular cases. A small peak in the circular case reflects the increased probability of zero velocity near the boundary. Fig. 3 (right) shows the PDFs of the Lagrangian acceleration. Its behaviour is similar to that first observed in [2]. Indeed, the circular case displays extreme events, which manifest in heavy ‘tails’ for large acceleration values. This actually corresponds to the transport of particles by vortices generated at the boundary.

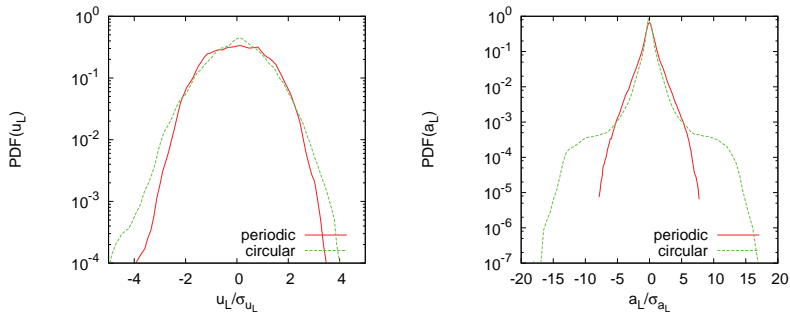


Fig. 3. Left: PDFs of the Lagrangian velocity u_L/σ_{u_L} . Right: PDFs of the Lagrangian acceleration a_L/σ_{a_L} .

To conclude, our study indicates a significant influence of boundaries on turbulent transport and mixing. This is most pronounced in the Lagrangian acceleration. Second-order statistics of the passive scalar are less sensible to the presence of the walls, but mixing is still more efficient in the circular container than in the biperiodic domain.

DK, KS acknowledge financial support from the French-German University Project S-GRK-ED-04-05.

References

1. E. Gouillard, N. Kuncio, O. Dauchot, B. Dubrulle, S. Roux, and J.-L. Thiffeault. *Phys. Rev. Lett.*, 99:114501, 2007.
2. B. Kadoch, W. J. T. Bos, and K. Schneider. *Phys. Rev. Lett.*, 100:184503, 2008.
3. J.M. Ottino. *The Kinematics of Mixing: Stretching, Chaos, and Transport*. Cambridge Univ. Press, Cambridge, 1989.
4. I. Ramière, P. Angot, and M. Belliard. *Comput. Methods Appl. Mech. Engrg.*, 196:766, 2007.
5. K. Schneider. *Comput. Fluids*, 34:1223, 2005.
6. P.K. Yeung and S.B. Pope. *J. Fluid Mech.*, 207:531, 1989.
7. P.K. Yeung, S. Xu, D.A. Donzis, and K.R. Sreenivasan. *Flow, Turb. & Combust.*, 72:333, 2004.

Prandtl-, Rayleigh-, and Rossby-number dependence of heat transport in turbulent rotating Rayleigh-Bénard convection

Richard J.A.M. Stevens¹, Jin-Qiang Zhong², Herman J.H. Clercx³,
Roberto Verzicco⁴, Detlef Lohse¹, Guenter Ahlers²

¹Dept. of Applied Physics, University of Twente, Enschede, The Netherlands

²Dept. of Physics and iQCD, University of California, Santa Barbara, USA

³Dept. of Physics, Eindhoven University; Dept. of Mathematics, Twente University

⁴Dept. of Mech. Eng., Università di Roma "Tor Vergata", Roma, Italy

r.j.a.m.stevens at tnw.utwente.nl

For given aspect ratio and given geometry, the nature of Rayleigh Benard convection (RBC) is determined by the Rayleigh number $Ra = \beta g \Delta L^3 / (\kappa \nu)$ and by the Prandtl number $Pr = \nu / \kappa$. Here, β is the thermal expansion coefficient, g the gravitational acceleration, $\Delta = T_b - T_t$ the difference between the imposed temperatures T_b and T_t at the bottom and the top of the sample, respectively, and ν and κ the kinematic viscosity and the thermal diffusivity, respectively. The rotation rate Ω (given in rad/s) is used in the form of the Rossby number $Ro = \sqrt{\beta g \Delta L} / (2\Omega)$.

We present both experimental measurements (fig. 1) and results from direct numerical simulation (DNS) (fig. 2). They cover different but overlapping parameter ranges and thus complement each other. The convection apparatus was used in the experiments is described in detail as the “medium sample” in Ref. [1]. All measurements were made at constant imposed Δ and Ω , and fluid properties were evaluated at $T_m = (T_t + T_b)/2$ [2].

In the DNS we solved the three-dimensional Navier-Stokes equations within the Boussinesq approximation in a three dimensional cylindrical domain [3, 4, 5]. The resolution is sufficient to represent the small scales both inside the bulk of turbulence and in the boundary layers (BLs) (where the grid-point density has been enhanced) for the parameters employed here. Nu is calculated as in ref. [6] and its statistical convergence has been controlled [2].

The heat-flux enhancement can be as large as 30% and depends strongly on Pr and Ra (fig. 1 and 2). The increased heat transfer is due to Ekman pumping; i.e. due to the rotation, rising or falling plumes of hot or cold fluid are stretched into vertical vortices that suck fluid out of the thermal BLs adjacent to the bottom and top plates (fig. 3). For $Pr = 6.4$ thermal structures

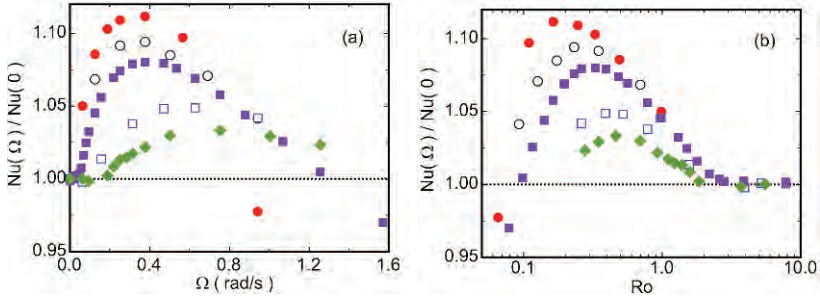


Fig. 1. The ratio of the Nusselt number $Nu(\Omega)$ in the presence of rotation to $Nu(\Omega = 0)$ for $Pr = 4.38$ ($T_m = 40.00^\circ\text{C}$). (a): Results as a function of the rotation rate in rad/sec. (b): The same results as a function of the Rossby number Ro on a logarithmic scale. Red solid circles: $Ra = 5.6 \times 10^8$ ($\Delta = 1.00$ K). Black open circles: $Ra = 1.2 \times 10^9$ ($\Delta = 2.00$ K). Purple solid squares: $Ra = 2.2 \times 10^9$ ($\Delta = 4.00$ K). Blue open squares: $Ra = 8.9 \times 10^9$ ($\Delta = 16.00$ K). Green solid diamonds: $Ra = 1.8 \times 10^{10}$ ($\Delta = 32.00$ K). Here and in fig. 2 experimental uncertainties are typically no larger than the size of the symbols [2].

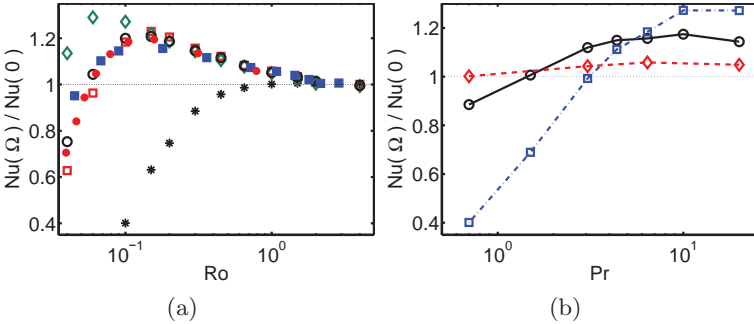


Fig. 2. (a): The ratio $Nu(\Omega)/Nu(\Omega = 0)$ as function of Ro on a logarithmic scale. Red solid circles: $Ra = 2.73 \times 10^8$ and $Pr = 6.26$ (experiment). Black open circles: $Ra = 2.73 \times 10^8$ and $Pr = 6.26$ (DNS). Blue solid squares: $Ra = 1 \times 10^9$ and $Pr = 6.4$ (DNS) [5]. Red open squares: $Ra = 1 \times 10^8$ and $Pr = 6.4$ (DNS). Green open diamonds: $Ra = 1 \times 10^8$ and $Pr = 20$ (DNS). Black stars: $Ra = 1 \times 10^8$ and $Pr = 0.7$ (DNS). (b): Numerical result for the ratio $Nu(\Omega)/Nu(0)$ as function of Pr for $Ra = 10^8$ and $Ro = 1.0$ (red open diamonds), $Ro = 0.3$ (black open circles), and $Ro = 0.1$ (blue open squares) [2].

are basically confined to these vortices, whereas for $Pr = 0.7$ they are much shorter and broadened, because the larger thermal diffusion which makes the Ekman pumping inefficient, which results in a decreasing heat transfer at lower Pr (fig. 3) [2].

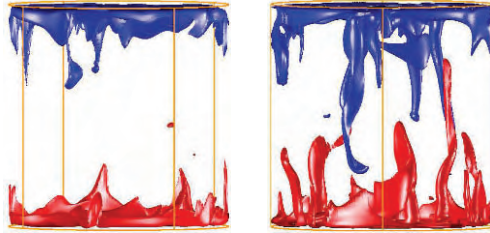


Fig. 3. 3D visualization of the temperature isosurfaces in the cylindrical sample of $\Gamma = 1$ at 0.65Δ (red) and 0.35Δ (blue), for $Pr = 6.4$, $Ra = 10^8$ and $Ro = \infty$ (left) $Ro = 0.30$ (right). The snapshots were taken in the respective statistically stationary regimes [2].

For the weakly rotating case a sharp transition from a turbulent state with nearly rotation-independent heat transport to another turbulent state with enhanced heat transfer is observed at a critical inverse Rossby number $1/Ro_c$ (fig. 4a). To characterize the flow field, we numerically calculated the rms velocities averaged over horizontal planes and over the entire volume, respectively. The maximum rms azimuthal and radial velocities near the top and bottom wall have been used to define the thickness of the kinetic BL, which is shown in the inset of Fig. 4a for $Ra = 2.73 \times 10^8$ and $Pr = 6.26$. The critical inverse Rossby number clearly distinguishes between two regimes: one with a constant BL thickness (in agreement with the presence of the LSC and the Prandtl-Blasius BL) and another one with decreasing BL thickness for $1/Ro \gtrsim 0.38$. The scaling with rotation rate is in agreement with Ekman BL theory $\lambda_u/L \sim Ro^{1/2}$. For $1/Ro > 1/Ro_c$ the normalized (by the value without rotation) volume-averaged vertical velocity fluctuations w_{rms} strongly decrease, indicating that the LSC becomes weaker, see Fig. 4b. The decrease in normalized *volume averaged* vertical velocity fluctuations coincides with a significant increase of the *horizontal average* at the edge of the thermal BLs indicating enhanced Ekman transport. These averages provide support for the mechanism of the sudden transition seen in Nu and indicate an abrupt change from a LSC-dominated flow structure for $1/Ro < 1/Ro_c$ to a regime where Ekman pumping plays a progressively important role as $1/Ro$ increases [7].

Our interpretation for the two regimes is as follows: Once the vertical vortices organize so that Ekman pumping sucks in the detaching plumes from the BLs, those plumes are no longer available to feed the LSC which consequently diminishes in intensity. A transition between the two regimes should occur once the buoyancy force, causing the LSC, and the Coriolis force, causing

Ekman pumping, balance. The ratio of the respective velocity scales is the Rossby number. For $Ro \gg 1$ the buoyancy-driven LSC is dominant, whereas for $Ro \ll 1$ the Coriolis force and thus Ekman pumping is stronger. The transition between the two regimes should occur at $Ro = \mathcal{O}(1)$, consistent with the observed $Ro_c \approx 2.6$ [7].

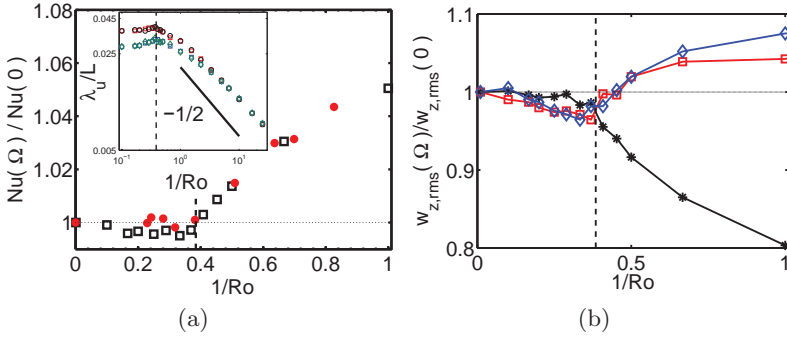


Fig. 4. a) $Nu(\Omega)/Nu(\Omega = 0)$ for $Ra = 2.73 \times 10^8$ and $Pr = 6.26$. Red solid circles: experimental data. Open black squares: numerical results. The experimental error coincides approximately with the symbol size and the numerical error is approximately 0.5%. Inset: Thickness of the kinetic BL. For dashed vertical lines and inset: The thickness of the kinematic top and bottom BLs based on the maximum rms azimuthal (upper symbols: black (red) for top (bottom) BL) and radial (lower symbols: green (blue) for top (bottom) BL) velocities. The vertical dashed lines in both graphs represent $1/Ro_c$ and indicates the transition in boundary-layer character from Prandtl-Blasius (left) to Ekman (right) behavior. b) The normalized averaged rms vertical velocities w_{rms} for $Ra = 4 \times 10^7$ (left) and $Ra = 2.73 \times 10^8$ (right) as function of $1/Ro$. The black line indicates the normalized *volume averaged* value of w_{rms} . The red and the blue line indicate the normalized *horizontally averaged* w_{rms} at the edge of the thermal BL based on the slope at respectively the lower and upper plate. The vertical dashed lines again indicate the position of $1/Ro_c$ [7].

References

1. E. Brown, D. Funfschilling, A. Nikolaenko, and G. Ahlers, *Phys. Fluids* **17**, 075108 (2005).
2. J.-Q. Zhong *et al.*, *Phys. Rev. Lett.* **102**, 044505 (2009).
3. R. Verzicco and P. Orlandi, *J. Comput. Phys.* **123**, 402 (1996).
4. P. Oresta, G. Stingano, and R. Verzicco, *Eur. J. Mech.* **26**, 1 (2007).
5. R. P. J. Kunnen *et al.*, *Europhys. Lett.* **84**, 24001 (2008).
6. R. J. A. M. Stevens, R. Verzicco, and D. Lohse, *Radial boundary layer structure and Nusselt number in Rayleigh-Bénard convection*, 2009.
7. R. J. A. M. Stevens *et al.*, (2009), submitted to *Phys. Rev. Lett.*

Oscillations of Large-Scale Structures in turbulent Mixed Convection in a rectangular enclosure

A. Westhoff, D. Schmeling, J. Bosbach and C. Wagner

German Aerospace Center (DLR) Göttingen - Institute of Aerodynamics and Flow Technology - Bunsenstr. 10, D-37073 Göttingen, Germany
andreas.westhoff@dlr.de

1 Introduction

The term mixed convection (MC) is used to describe the process of heat transfer in fluids where forced convection (FC) and thermal convection (TC) coexist. Mixed convection is an often occurring flow condition e.g. in the oceans, atmosphere, indoor climatisation or industrial processes and applications [1]. In many flow situations convection is the prevalent transport mechanism of heat whereas the heat transfer strongly depends on the dynamics of the large-scale structures. In this study we investigate the formation of large-scale circulation (LSC) in mixed convection and the influence of the dynamics of the LSC, also known as *mean wind*, on the heat transfer. Measurements of the heat transfer $\dot{Q}(t) \sim (T_{out}(t) - \bar{T}_{in}) / \Delta T$ (T_{in} : temperature of the flow at the inlet, T_{out} : temperature of the flow at the outlet) in mixed convection revealed very low frequency oscillations for \dot{Q} [5], which strongly depend on the magnitude of the Reynolds number Re and Rayleigh number Ra as well as on the Archimedes number Ar .

For the investigations presented here a simple rectangular container in which a fluid layer is confined between two isothermal horizontal plates heated from below, cooled from above and can be exposed to forced convection was chosen. The problem is defined by five dimensionless parameters, i.e. the Rayleigh number $Ra \equiv \Delta T \beta g H^3 / \kappa \nu$, the Reynolds number $Re \equiv UH/\nu$, the Prandtl number $Pr \equiv \nu/\kappa$ and the aspect ratios of the rectangular container $\Gamma_{xz} \equiv W/H$ and $\Gamma_{yz} \equiv L/H$. Here β denotes the isobaric thermal expansion coefficient, g the acceleration due to gravity, ΔT the applied temperature difference, κ the thermal diffusivity, ν the kinematic viscosity, U the characteristic velocity, W the width, L the length and H the height of the cell. An additional parameter used for mixed convection is the Archimedes number $Ar = Ra/(Re^2 \times Pr) = \Delta T \beta g H^3 / U^2$ which is the ratio of buoyancy

and inertia forces. For $Ar \ll 1$ the flow is primarily driven by inertia forces, whereas for $Ar \gg 1$ the flow is dominated by buoyancy forces.

2 Experimental set up

To cover a large parameter range of $600 < Re < 3 \times 10^6$ and $1 \times 10^5 < Ra < 1 \times 10^{11}$ two convection cells have been constructed using air as working fluid under different pressure conditions with an aspect ratio of $\Gamma_{xy} = 1$ and $\Gamma_{xz} = 5$. The cells are equipped with an air inlet at the top and an air outlet at the bottom. The in- and outlet channels are located at the same side of the cell, are rectangular and span the whole length of the cell. The inlet channel has a height of $H_{in} = \frac{1}{20} \times H$ and a length of $L_{in} = 30 \times H_{in}$ to assure a well defined fully developed channel flow at the cell inlet, while the outlet channel has a height of $H_{out} = \frac{3}{5} \times H_{in}$ and a length of $L_{out} = 30 \times H_{out}$. All side walls are thermally insulated by a layer system with an insulating sheath of air between two transparent windows. Hence we nearly realise adiabatic boundary conditions while maintaining the optical accessibility of the cell. The bottom is equipped with a heating plate and the top with a heat exchanger with cooling fins. One of the cells with the dimensions $W \times H \times L = 0.1 \text{ m} \times 0.1 \text{ m} \times 0.5 \text{ m}$ was designed to be operated under high pressure conditions of up to 100 bar. The second convection cell has been designed to work under ambient pressure conditions with the same aspect ratio, but its dimensions are scaled by a factor of 5.

In this article particle image velocimetry (PIV) results of the flow in the large cell under ambient pressure are presented, analysed and compared to results of temperature measurements conducted in the small cell at 10 bar. Two-dimensional two-component (2D2C) PIV has been carried out in different cross sections. Additionally two-dimensional three-component (2D3C) PIV has been performed in a longitudinal cross section. The 2D2C measurement planes are located at $0.5 \times L$, $0.375 \times L$, $0.25 \times L$ and $0.1 \times L$ while the 2D3C cross section is located at $0.5 \times W$. The instantaneous velocity fields have been acquired with a repetition rate of 2/3 Hz. For the forced convection case 800 and for the mixed convection case 4800 instantaneous velocity fields have been measured. Additionally results of a Proper Orthogonal Decomposition (POD) of the instantaneous velocity fields are presented, which have been calculated using the snapshots method by Sirovich [4].

3 Results

In the cell forced convection is induced by a pressure gradient between the in- and outlet. As a result a nearly two-dimensional vortex structure develops, with a core which is stationary (Fig. 1). The mean wind behaves in the core like a solid body rotation (Rankine vortex) and the angular frequency is found

to be $\omega_{FC} = 0.32 \text{ s}^{-1}$. The other mechanism that drives the heat transport in mixed convection is the buoyancy force. In the buoyancy driven case hot plumes are rising from the bottom thermal boundary layer and cold plumes are descending from the top. As a result of this plume-motion coherent flow structures develop and form a LSC [3]. In the here used enclosure the plume-motion induces four LSCs, which are arranged in longitudinal direction. One of these LSCs is presented in Fig. 1 in terms of the time averaged velocity fields. Additionally, the contours in Fig. 1 depict the out of plane velocity component w . At the top (coloured red) the air which enters the cell through the inlet and at the bottom (coloured blue) the flow in direction of the outlet dominate.

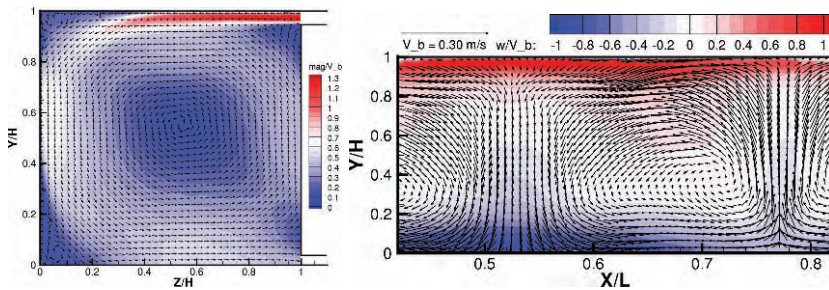


Fig. 1. Left: Time averaged velocity field of forced convection at $Ar = 0$ with $Re = 1.0 \times 10^4$ at $0.15 \times L$. Colour coded normalised velocity magnitude. Right: Time averaged velocity field of the 2D3C-PIV measurement for mixed convection at $Ar = 3.3$ with $Ra = 2.4 \times 10^8$, $Re = 1.0 \times 10^4$ at $0.5 \times W$. All velocities are normalised with the buoyancy velocity $V_b = \sqrt{\beta H^3 \Delta T g}$. Only every fifth velocity vector is plotted.

Analysing the measured temperature data spatial temperature variations over the length of the outlet depending on the orientation of the buoyancy induced LSCs have been found. In regions of rising plumes T_{out} is elevated and in regions where plumes are falling a lower T_{out} can be observed. For cases $Ar > 1$, the temperature signal locally fluctuates in time (subplot Fig. 2). The corresponding powerspectrum of the local temperature fluctuations at $0.5 \times L$ (Fig. 2) reveals two characteristic frequencies. One of these characteristic frequencies is $\omega = 0.32 \text{ s}^{-1}$, which equals the angular frequency $\omega_{FC} = 0.32 \text{ s}^{-1}$ of the role structure found in the PIV results of forced convection in the large cell. Although the temperature measurements were performed at 10 bar (small cell experiment), the same frequency appears and we assume this frequency to be associated with the dynamics of the role structure induced by forced convection. The second characteristic frequency $\omega_{low} = 0.008 \text{ s}^{-1}$ (Fig. 2) is much lower than ω_{FC} and the angular frequency associated with the thermal convection induced LSCs $\omega_{TC} \approx 0.5 \text{ s}^{-1}$.

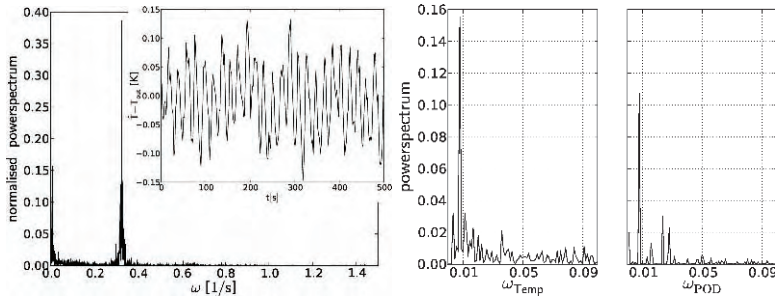


Fig. 2. Left: Powerspectrum of T_{out} at $0.5 \times L$ for $Ar = 3.3$, $Ra = 2.4 \times 10^8$ and $Re = 1 \times 10^4$ at 10 bar. The subplot shows the first 500 of 5000 s of the time series of the outlet temperature ($0.5 \times L$). Right: Powerspectrum of the low frequency oscillations of T_{out} and the powerspectrum of ζ_1^{MC} .

To investigate if the above frequencies are related to the dynamics of any characteristic flow structures a POD analysis of the 2D3C PIV data obtained for forced and mixed convection has been performed. For both, forced and mixed convection, eigenfunctions with eigenvalues $\lambda_1^{\text{MC}} = 73\%$ and $\lambda_1^{\text{FC}} = 90\%$ of the total energy were obtained. Additionally the coefficient of the eigenfunction ζ which corresponds to the highest eigenvalue has been analysed. The powerspectrum ζ_1 of the forced convection case reveals no characteristic frequency contrarily to the powerspectrum of the mixed convection case. The latter contains the same low characteristic frequency that has been found in the temperature measurements at 10 bar. Due to the concurrence of these frequencies it is concluded that this low frequency oscillation in the heat transfer is the result of the dynamics of the buoyancy induced LSCs. Even more, we assume that the oscillations are a result of torsional oscillations of the buoyancy induced LSCs in agreement with findings in Rayleigh-Bénard convection by Funfschilling et al. [2].

References

1. P. F. Linden, The fluid mechanics of natural ventilation, *Annu. Rev. Fluid Mech.*, **31**, 201, 1999.
2. D. Funfschilling, E. Brown and G. Ahlers, Torsional oscillations of the large-scale circulation in turbulent Rayleigh-Bénard convection, *J. Fluid Mech.*, **607**, 119, 2008.
3. X.-L. Qui and P. Tong, Large-scale velocity structures in turbulent thermal convection, *Phys. Rev. E*, **64**, 036304, 2001.
4. L. Sirovich. Turbulence and the dynamics of coherent structures part ii: Symmetries and transformation, *Quarterly of Applied Mathematics*, **45(3)**, 573, 1987.
5. A. Westhoff, J. Bosbach, and C. Wagner. Scaling of mixed convection in aircraft cabins. 26th International Congress of the Aeronautical Sciences, 2008.

Interaction between slope flows and an urban heat island

Marco Giorgilli, Monica Moroni, Paolo Monti and Antonio Cenedese

Department of Hydraulics, Transportations and Roads, Sapienza University of Rome at Rome, via Eudossiana 18, 00184, Italy

E-mail: marco.giorgilli@uniroma1.it

1 Introduction

The local atmospheric circulation due to a city located at the bottom of a valley is reproduced by laboratory experiments analyzing the interaction between an urban heat island (UHI) and anabatic or katabatic slope flows. Slope flows are generated by the horizontal temperature difference between air adjacent to a mountain slope and the ambient air at the same altitude over the neighboring plane (or over the valley center). The thermal disomogeneity is a consequence of the daily heating due to the solar radiation and to the nightly cooling related to the infrared radiation emitted by the ground. Assuming clear sky and weak synoptic wind conditions, the slope flow is upslope (anabatic) during the daytime and downslope (katabatic) during the nighttime. The cool air settles down in the valley, starting the cold pool formation, a still and steady stratified environment. The slope flows present counter current compensating flows of lower velocity and larger thickness. The circulation associated to slope flows was studied in the past via field observations (Manins and Sawford, 1979; Hunt et al., 2003), analytical (Prandtl, 1952; Horst and Doran, 1983), numerical (Tripoli and Cotton, 1989) and experimental investigations (Fernando et al., 2000; Cenedese and Monti, 2004). Buoyancy-driven UHI circulation has been investigated in experimental and analytical study by Lu et al. (1997). The experiments described here are performed in a temperature controlled water-tank, the same employed by Cenedese and Monti (2003) and (2004) to investigate urban heat islands and sea-breeze flows, respectively.

2 Experimental setup

Tests on a physical model that reproduces a symmetrical valley between two smooth and uniformly 20° tilted slopes, with a heat island in the middle are presented here (Figure 1). Both slopes are made of $14.5 \times 32 \text{ cm}^2$ sized aluminium plates with two series of six Peltier cells inside.

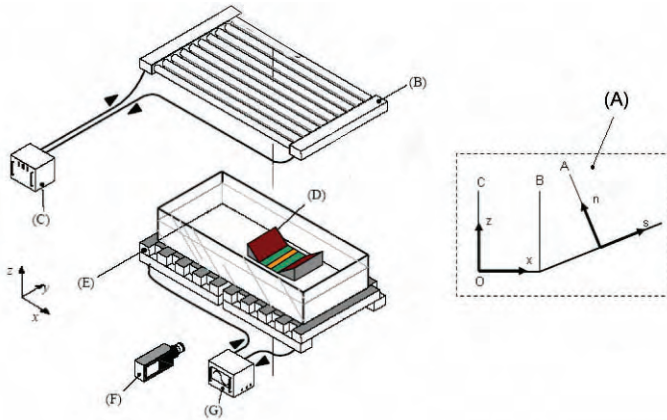


Fig. 1. Experimental apparatus: A) Reference systems and locations of temperature arrays, B) Free surface heat exchanger, C) Free surface thermostat, D) Valley model, E) Bottom surface heat exchanger, F) Camera, G) Bottom surface thermostat.

The Peltier cells allow heating the slopes by electrical continuous current (anabatic case), or their cooling by reversing the polarity (katabatic case). The UHI has been realized by a rectangular electrical resistance embedded in a $5 \times 15 \text{ cm}^2$ sized plastic tape pasted on the aluminium plate. The slope model is inserted in a test section filled with water till a height of 12 cm. The test section is $170 \times 60 \times 21 \text{ cm}^3$ sized and presents aluminium bottom and glass side walls. Two heat exchangers are placed below the bottom and on the free surface respectively. They are fed with water from two different thermostats and fix the bottom and free surface temperature in order to achieve a linear profiled stable stratification. One progressive scan CCD camera of 764×576 pixel and 25 Hz frequency allowed acquiring the images of well reflecting passive tracer particles. 26 thermocouples have been employed to detect the temperature profiles. Since the valley was designed symmetric, the resulting cross-valley circulation associated to the thermal anomalies is expected to be two-dimensional and symmetric with respect to the valley center. The velocity field was then detected by using the 2D Feature Tracking (FT) technique (Moroni and Cenedese, 2005).

3 Results

Here we present streamlines and velocity profiles for three cases (see Table below). Streamlines are reconstructed starting from velocity fields interpolated on a regular grid (25 rows and 76 columns) averaging data for 20 seconds. Figure 2a and 2b well describe the katabatic case features: the downslope flow close to the slope and the return current farther from the slope are correctly

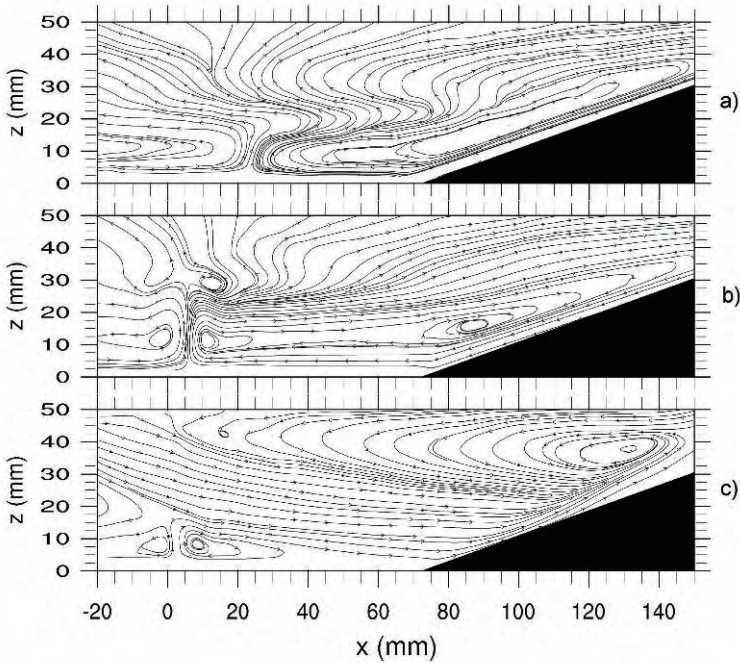


Fig. 2. Streamlines right-hand, time 480 s: a) Exp #1, b) Exp #2, c) Exp #3.

Experiment #	Description	Gradient stratification ($^{\circ}\text{C cm}^{-1}$)	Slope heat flux (kW m^{-2})	UHI heat flux (kW m^{-2})
1	Katabatic	0.7	1.0	
2	Katabatic + UHI	0.7	1.0	0.6
3	Anabatic + UHI	0.7	1.5	0.6

visualised. A close circulation characterizes each slope region. The presence of the heat island constraints the symmetrical shape of the circulations. This is not the case for Exp #1 due to a slight different heat flux provided to the two slopes. Figure 2c well describes the upslope flow associated to the anabatic case. A close circulation forms here as well but it interests a thicker fluid layer. A strong interaction between the UHI and anabatic-katabatic winds occurs and it determines a higher UHI plume in the katabatic case than in the anabatic one. Figure 3a compares the velocity component along the slope for profile A and for the three experiments. The reference system axis s is positive oriented upslope (Figure 1). The largest absolute velocity value is reached in Exp #3 (anabatic wind), because thermals triggered by the heat flux provided in this case break the stable stratification and increase the upslope motion.

The maximum absolute velocity is larger for Exp #2 than Exp #1 because the circulation driven by the urban heat island moves and warms the air in

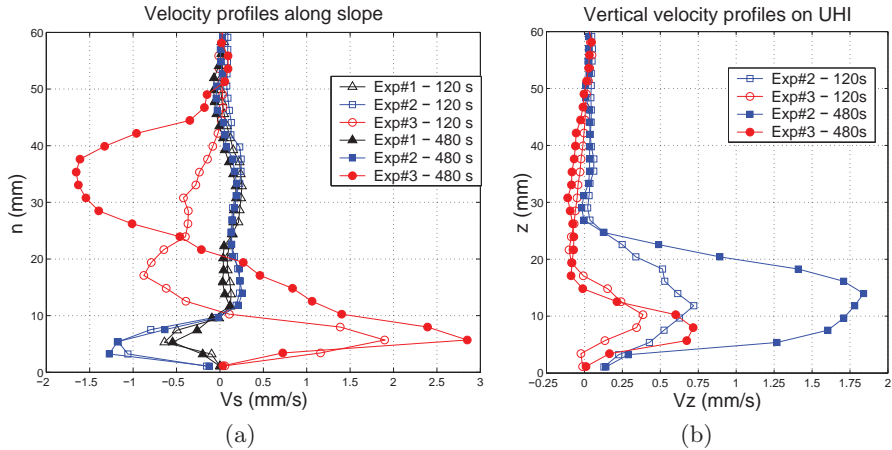


Fig. 3. a) velocity components along the slope for profile A; - b) vertical velocity component along profile C.

the valley inhibiting the stabilization of the nocturnal cold pool. Hence air will move toward the valley with a weaker resistance. The slope flow thickness is larger in Exp #3 than in other two cases, which are indeed very similar. The maximum velocity and plume height are larger for Exp #2 than Exp #3 (Figure 3b). This is due to the resistance opposed by the anabatic wind to the motion of air toward the city and to the UHI plume flattening induced by the compensating flow.

References

1. A. Cenedese, P. Monti, *J. Appl. Meteor.*, **42**, 1569 (2003).
2. A. Cenedese, P. Monti, *J. Fluid Mech.*, **510**, 1 (2004).
3. H.J.S. Fernando, M. Princevac, J.C.R. Hunt, E.R. Pardyjak, 5th International Symposium on Stratified Flows, 10-13 July, Canada, 2000.
4. T.W. Horst, J.C. Doran, *J. Atmos. Sci.*, **40**, 708 (1983).
5. J.C.R. Hunt, H.J.S. Fernando, M. Princevac, *J. Atmos. Sci.*, **60**, 2169 (2003).
6. J.S. Lu, P. Arya, W.H. Snyder, R.E. Lawson Jr., *J. Appl. Meteor.*, **36**, 1377 (1997).
7. P.C. Manins, B.L. Sawford, *J. Atmos. Sci.*, **36**, 619 (1979).
8. M. Moroni, A. Cenedese, *Meas. Sci. Tech.*, **16**, 2307 (2005).
9. L. Prandtl, *Essentials of fluid dynamics*, Hafner 1952.
10. G.J. Tripoli, W.R. Cotton, *Mon. Wea. Rev.* **117**, 273 (1989).

Origin of the small-scale anisotropy of the passive scalar fluctuations

J. Kalda and A. Morozenko

CENS, Institute of Cybernetics, Tallinn University of Technology, 12618 Tallinn, Estonia
kalda at ioc.ee

Mixing in fully developed incompressible turbulent flows is known to lead to highly intermittent scalar fields. The main feature of these fields is the presence of a cascade of fractal discontinuity fronts of the tracer density; while most of the fronts are characterized by relatively small values of the density drop, there are also some segments of the fronts (the so-called *mature fronts*), where the density drop is of the order of the amplitude of the global density variations [1]. One of the consequences of such a geometrical structure is the anomalous scaling of the structure function scaling exponents.

Another intriguing aspect of the intermittency of the tracer fields is the small-scale anisotropy of the passive scalar fluctuations [2]: the anisotropy of the large-scale forcing of the scalar field is reflected in the anisotropy of the fluctuations of the smallest (dissipation) scale. More specifically, if the fluid temperature plays the role of the tracer field, and there is a turbulent fluid motion between a cold wall, and a hot wall, then the temperature profile obtains a *ramp-cliff* structure: a slow growth of the temperature is followed by a rapid fall. A quantitative measure of this anisotropy is provided by the third order (sign-sensitive) structure function scaling exponent ζ_3 , which, according to the experimental data is close to unity.

It appears that several features of the intermittent tracer fields can be successfully analysed by using the method of linear eddy modelling [3, 4] In particular, by combining this model with additional approximations, we were able to derive an analytical expression for the structure function scaling exponent ζ_p , which is in a good agreement with the experimental and numerical data [5]. Here we extend our method to address the phenomenon of the small-scale anisotropy of the passive scalar fluctuations.

First, we provide a simple qualitative explanation for the ramp-cliff structure of the tracer density profile. To begin with, let us recall the basic idea of the linear eddy modelling. Instead of considering the full three-dimensional problem, described by convective diffusion equation

$$\partial_t \theta + \mathbf{v} \nabla \theta = \kappa \nabla^2 \theta + f(\mathbf{r}, t), \quad (1)$$

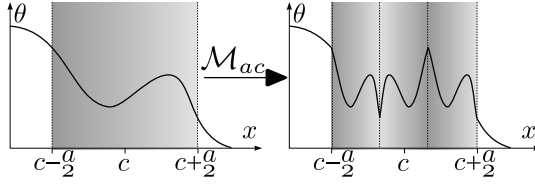


Fig. 1. Mapping $\mathcal{M}_{a,c}$ modelling the effect of a single vortex of size a on the tracer profile $\theta(x)$.

we study only the evolution of the scalar density $\theta(\mathbf{r}, t)$ along a one-dimensional cut, i.e. $\theta(x, t)$. Here, $\mathbf{v}(\mathbf{r}, t)$ is a turbulent velocity field, $f(\mathbf{r}, t)$ is a forcing, and the seed diffusivity $\kappa > 0$ is assumed to be very small. We assume that the velocity field is non-smooth, obeys Gaussian statistics, and can be characterised by the smoothness exponent ξ ($0 \leq \xi \leq 2$). Fully developed Kolmogorov turbulence corresponds to $\xi = 4/3$.

In order to understand the effect of the turbulent mixing, we focus first on the effect of a single eddy of certain size. It can be argued [5] that the integral effect of it on the evolution of the tracer profile $\theta(x, t)$ is essentially the same as applying the Kerstein’s triplet map [3, 4]:

$$\theta_{t+1}(x) = \mathcal{M}_{a_t, c_t}[\theta_t(x)], \tag{2}$$

where a_t is the centre of the vortex and c_t — its diameter, see Fig 1. Index t denotes the time and corresponds to the situation before the given vortex has produced a mixing effect; $t + 1$ corresponds to the later stage, when the mixing has been already taken place.

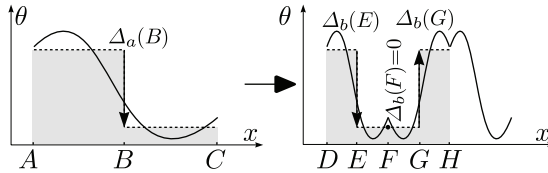


Fig. 2. As a result of the mapping $\mathcal{M}_{2a,B}$, the old value of the mean density difference $\Delta_a(B)$ defines the possible range of new values at trice smaller scale $b = a/3$, the smallest value is $\Delta_b(F) = 0$, and the largest one $\Delta_b(E) = \Delta_b(G) = \Delta_a(B)$.

In order to analyse this process analytically, we have introduced the probability density function (PDF) $f_a(\Delta_a)$, which characterizes the probability that the difference between the mean tracer densities between two neighbouring windows of width a is larger than Δ_a . Based on several approximations, we have shown that this PDF satisfies a self-convolution equality, connecting its values at different scales a : denoting $b = \frac{a}{3}$,

$$f_b(\Delta) = \int_{\Delta}^1 f_a(\Delta') \frac{d\Delta'}{\Delta'} \tag{3}$$

This equality assumes that the maximal value of Δ is 1, which is defined by amplitude of the forcing at the largest scale $a = 1$. The self-convolution reflects the fact that the triplet mapping transfers the density drop Δ_a at scale a to a density drop Δ_b with the range of possible values $\Delta_b \in [0, \Delta_a]$. Which value of Δ_b is realized from this range, depends on the mutual position of the averaging windows and the triplet map. see Fig. 2. Based on this self-convolution equality and assuming an approximately constant PDF at the input scale, $f_1(\Delta) \equiv 1$, one can derive, for instance, an expression for the p -th order structure function scaling exponent, $\zeta_p = (2 - \xi) \log_3(p + 1)$; this result is in a good agreement with a wide spectrum of experiments.

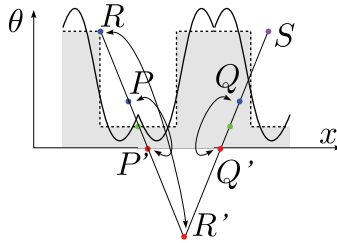


Fig. 3. For the triplet map, most of the points have a symmetric counterpart, which yields a mean density drop of equal amplitude and opposite sign (e.g. the point pairs P and P' ; Q and Q' ; R and R'). The only non-symmetric point S is characterized by the largest possible value of the density drop.

Now, let us suppose that there is an asymmetry at the input scale $a = 1$, and consider, how the asymmetry of the difference of the mean values of the tracer density between the neighbouring regions is transferred towards the smaller scales by the triplet map, see Fig. 3. Let us assume that at a larger scale a , there is a left-to-right asymmetry in the statistics of the mean density differences. Upon applying a triplet map, for almost all the positions of the point at which we study the density difference, there will be a symmetric position with a density drop of opposite sign. So, at point P , there is a small left-to-right drop $\Delta_b(P)$, and at point P' , there is a right-to-left drop of equal amplitude, $\Delta_b(P') = -\Delta_b(P)$. The same applies to the pair of points Q' and Q . However, there are only three positions R , R' , and S , which realize the largest density drop (equal to the largest drop at the initial scale a). Of those three, two are symmetric to each other: $\Delta_b(R) = -\Delta_b(R') = \Delta_a$. However, there is no symmetric counterpart for the third point S ; this is the only site at which the initial asymmetry survives.

To summarize, along one-dimensional cuts of the turbulent fluid, the vortices can be modelled as the triplet maps. The triplet maps produce almost always symmetric regions with left-to-right and right-to-left tracer density

drops — except for the sites, where the modulus of the density drop has the maximal possible value. Therefore, the asymmetry is transferred from the input scale, down to the dissipation scale, at the sites of highest density drop (by modulus). This corresponds precisely to the experimentally observed ramp-cliff structure [2]: the only asymmetric sites are the cliffs, where the density drops almost by the same amplitude as at the input scale, and the direction of the drop is dominantly in the same direction as in the case of the large-scale density differences at the input scale (due to asymmetric forcing).

These qualitative observations can be also formulated mathematically, similarly to the procedure of deriving the structure function scaling exponents [5]. Using certain approximations, it is possible to derive the exponent for the third order sign-sensitive structure function, $\tilde{\zeta}_3 = 1 + 2(2 - \xi)3^{-1/(2-\xi)}/(e \ln 3)$; for the Kolmogorov turbulence ($\xi = \frac{4}{3}$), this yields $\tilde{\zeta}_3 \approx 1.1$, which is in a reasonable agreement with the experimental data. This result is also supported by our numerical simulations, based on the linear eddy modelling.

References

1. Celani A, Matsumoto T, Mazzino A and Vergassola M 2002 *Phys. Rev. Lett.* **88** 054503
2. Warhaft Z 2000 *Annual Review of Fluid Mechanics* **32** 203–240
3. Kerstein A R 1991 *Journal of Fluid Mechanics* **231** 361–394
4. Kerstein A R 1999 *Journal of Fluid Mechanics* **392** 277–334
5. Kalda J and Morozenko A 2008 *New Journal of Physics* **10** 093003 (11pp)

Mixing asymmetry in variable density turbulence

D. Livescu and J. R. Ristorcelli

Los Alamos National Laboratory, Los Alamos, NM 87545, USA
livescu@lanl.gov

Molecular mixing as a consequence of stirring by turbulence is an important process in many practical applications. If the microscopic densities of the fluids participating in the mixing are very different, we refer to such flows as variable density (VD) flows in contrast to the Boussinesq approximation in which the densities are close. In such flows, due to the tight coupling between the density and velocity fields, in addition to the quadratic non-linearities of the incompressible Navier-Stokes equations, new cubic nonlinearities arise and the velocity field is no longer solenoidal. Many of these flows are driven by acceleration (e.g. gravity in geophysical and astrophysical flows) which, because the density is not uniform, leads to large differential fluid accelerations. If the acceleration is constant and the fluid configuration is unstable (i.e. density gradient points opposite to the body force), a fluid instability is generated in which small perturbations of the initial interface between the two fluids grow, interact nonlinearly, and lead to turbulence. This instability is known as the Rayleigh-Taylor (RT) instability.

The homogenization of a heterogeneous mixture of two pure fluids with different densities by molecular diffusion and stirring induced by buoyancy generated motions is studied using Direct Numerical Simulations in two configurations: a) classical Rayleigh-Taylor instability (RTI) using a 3072^3 data set [1, 2] and b) an idealized triply periodic Rayleigh-Taylor flow named hereafter homogeneous Rayleigh-Taylor (HRT), using up to 1024^3 meshes [3, 4]. The data-sets used represent the largest simulations to date for each configuration. The RTI simulation achieves bulk Reynolds number, $Re = 32,000$ at an Atwood number, $A \equiv \frac{\rho_2 - \rho_1}{\rho_2 + \rho_1} = 0.5$, where ρ_1, ρ_2 are the pure fluid densities, and a Schmidt number, $Sc = 1$. The HRT flow starts from rest, with the two fluids in a non-premixed state corresponding to a double-delta density PDF. Turbulence is generated as the two fluids move in opposite directions due to the body force and eventually dies as the fluids become molecularly mixed. The cases considered cover the range $A = 0.05 - 0.5$, in order to examine small departures from the Boussinesq approximation as well as large A effects.

The flows in both configurations are governed by the same set of equations, continuity and momentum transport, with the velocity divergence related to the density field. In non-dimensional form, with the usual notations, these are:

$$\rho_{,t} + (\rho u_j)_{,j} = 0 \tag{1}$$

$$(\rho u_i)_{,t} + (\rho u_i u_j)_{,j} = -p_{,i} + \tau_{ij,j} + \frac{1}{Fr^2} \rho g_i \tag{2}$$

$$u_{j,j} = -\frac{1}{Re_0 Sc} (\ln \rho)_{,jj} \tag{3}$$

with $\tau_{ij} = \frac{1}{Re_0} (u_{i,j} + u_{j,i} - \frac{2}{3} u_{k,k} \delta_{ij})$. Equations (1)-(3) have triply periodic boundary conditions in HRT, while in RT slip wall conditions are applied in the vertical direction.

In HRT, the the density PDF starts as a double delta, then evolves towards a quasi-Gaussian as the fluids become molecularly mixed. At low A (Boussinesq approximation) the PDF remains symmetrical at all times (figure 1). At higher A, the PDF becomes rapidly skewed and, only at long times and low density fluctuations it relaxes towards a Gaussian shape. At intermediate times, the two pure fluids mix differently, with the light pure fluid mixing faster than the heavy pure fluid.

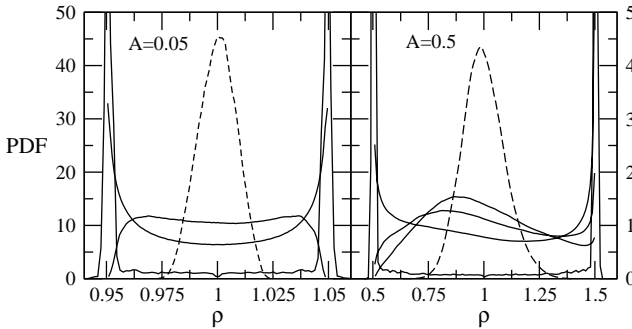


Fig. 1. Density PDF at different times in HRT for two Atwood numbers

The asymmetry of the density PDF in the VD case can be understood from the skewness, $S \equiv \langle \rho'^3 \rangle / (\langle \rho'^2 \rangle^{3/2})$, equation:

$$\frac{d}{dt} S = -\frac{S}{2Re_0 Sc} \frac{\langle \rho_{,j} \rho_{,j} \rangle}{\langle \rho'^2 \rangle} - \frac{3}{4} \frac{\langle \rho' (\rho_{,j} \rho_{,j}) \rangle}{\langle \rho_{,k} \rho_{,k} \rangle \langle \rho'^2 \rangle^{1/2}} \tag{4}$$

As the flow begins with $S = 0$, it is the second term, the production, that generates the skewness of the PDF. The quantity $\langle \rho' \rho_{,j} \rho_{,j} \rangle$ is weighted towards large squared density gradient events occurring in lower than average density regions so that $S > 0$ at early times. In other words, the light fluid blobs

become more fragmented at higher A . As the mixing proceeds, the production term approaches zero and one obtains a simple skewness decay.

The density PDF skewness generation mechanism, $\langle \rho' \rho_{,j} \rho_{,j} \rangle$, is determined, through changes in the magnitude of the density gradient, by the eigenvalues of the strain rate tensor and the relative alignment between $\nabla \rho$ and the eigenvectors of s_{ij} :

$$\frac{d}{dt} \langle \rho_{,j} \rho_{,j} \rangle = -2 \langle \rho_{,j} s_{ij} \rho_{,j} \rangle - \langle u_{i,i} (\rho_{,j} \rho_{,j} + 2\rho \rho_{,jj}) \rangle \tag{5}$$

where the second term, which depends on the velocity divergence, is small after the initial transients. Let χ_1, χ_2 , and χ_3 , be the angles between $\nabla \rho$ and the α -, β -, and γ -eigenvectors, which correspond to the eigenvalues labeled using the usual convention $\alpha > \beta > \gamma$. In isotropic turbulence, it is known that passive scalar gradients tend to align with the most compressive (γ) eigenvector of s_{ij} . Similar results are obtained in HRT, however there are important differences between the low and high A cases:

- **Low A :** The relative alignment and the magnitude of the eigenvectors are about the same in the light and heavy fluid regions.
- **High A :** Both the eigenvalues and the alignment of $\nabla \rho$ with the principal axes of s_{ij} are different in the light and heavy fluids (figure 2).

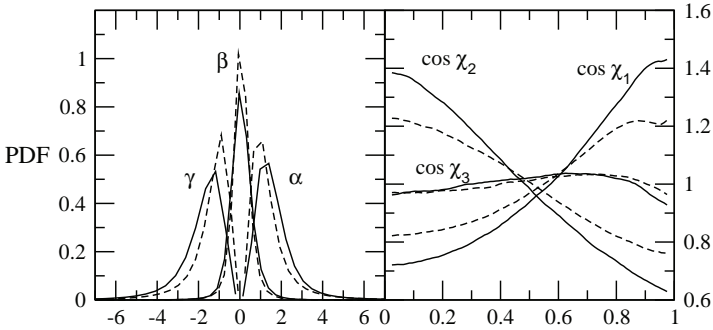


Fig. 2. PDFs of the a) eigenvalues of s_{ij} and b) cosines of the angles between $\nabla \rho$ and the eigenvectors of s_{ij} in the light fluid, $\rho < \bar{\rho}$ (continuous lines), and heavy fluid, $\rho > \bar{\rho}$ (dashed lines), at $A = 0.5$.

In the light fluid, the eigenvalues α and γ have larger magnitudes as the reduced inertia allows higher deformation rates of a fluid particle. Moreover, the alignment of $\nabla \rho$ with the γ -eigenvector weakens in the heavy fluid regions, as the inertia of the heavy fluid particles tends to make them less responsive to deformations due to the local strain. The net result is a decrease in the magnitude of $\langle \rho_{,j} s_{ij} \rho_{,j} \rangle$ (note that this quantity has negative sign) in the heavy fluid regions compared to the light fluid regions. Consequently, the inertia of the heavy fluid inhibits the growth of the density gradients and,

thus, reduces the rate at which heavy fluid regions are broken up by stirring, ultimately leading to reduced mixing.

The density PDF varies considerably across the RT mixing layer. At the top of the RT layer the PDF is spiked at the heavy fluid end and includes some mixed fluid. At the bottom of the layer the PDF is spiked at the light fluid end (figure 3). At large density differences, the HRT findings suggest that molecular mixing proceeds differently on the two sides of the RT layer. Experiments to date have not investigated this possibility. One consequence of the mixing asymmetry identified in HRT is that the penetration distance of the pure heavy fluid is larger than that of the pure light fluid. Thus, figure 3 shows that the density PDF is not symmetrical at the centerline: the peak is at $\rho < 2$ and the amount of pure heavy fluid is larger than the amount of pure light fluid. The mixing asymmetry is likely also the cause of the bubble-spike anomaly (higher growth rate on the spike side compared to the bubble side), which was observed experimentally [5].

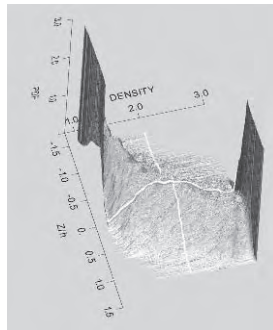


Fig. 3. Density PDF as a function of vertical position in RT

Los Alamos National Laboratory is operated by the Los Alamos National Security, LLC for the U.S. Department of Energy NNSA under contract no. DE-AC52-06NA25396. This publication and part of the research described herein were made possible by funding from the LDRD program at Los Alamos National Laboratory through project numbers 20090058DR and 20090195ER.

References

1. W. H. Cabot and A. W. Cook, *Nature Phys.* **2**, 562 (2006).
2. D. Livescu, J.R. Ristorcelli, R. A. Gore, S. H. Dean, W. H. Cabot and A. W. Cook, to appear *J. Turb.* (2009).
3. D. Livescu and J. R. Ristorcelli, *J. Fluid Mech.* **591**, 43 (2007).
4. D. Livescu and J. R. Ristorcelli, *J. Fluid Mech.* **605**, 145 (2008).
5. G. Dimonte and M. Schneider, *Phys. Fluids* **12**, 304 (2000).

Turbulent transport close to a wall

G. Boffetta¹, F. De Lillo¹, and A. Mazzino²

¹Dipartimento di Fisica Generale and INFN, Università di Torino, via P.Giuria 1, 10125 Torino (Italy)

²Dipartimento di Fisica, Università di Genova, INFN and CNISM, via Dodecaneso 22, 16146 Genova (Italy)
delillo@to.infn.it

Summary. We investigate the problem of tracer mixing in presence of boundaries by means of direct numerical simulation of a Couette flow at small Reynolds number and in kinematic simulations of a chaotic flow. Scalar profiles close to the boundary are computed. Their shape and time evolution are found to agree with published theoretical predictions.

A passive scalar θ advected by an incompressible velocity field \mathbf{u} obeys the equation

$$\frac{\partial \theta}{\partial t} + \mathbf{u} \cdot \nabla \theta = \kappa \nabla^2 \theta \quad (1)$$

where κ is the molecular diffusivity, and appropriate initial and boundary conditions are set for θ . In general \mathbf{u} is subject to its own set of equations, the typical case being Navier-Stokes equations, together with some external forcing. However some general predictions on the evolution of θ can be made, with few rather general assumptions. We follow the theoretical analysis in [2] To simplify the notation, but without loss of generality, we assume the flow to be two-dimensional, with (x, y) the coordinates parallel and normal to the wall ($y = 0$ corresponding to the wall) and (u, v) the associated velocity components.

As a consequence of no slip ($\mathbf{u}(x, y = 0) = 0$) and incompressibility ($\nabla \cdot \mathbf{u} = 0$) conditions, there is a region close to the wall, characterized by the scaling $\langle u^2(y) \rangle \sim y^2$ and $\langle v^2(y) \rangle \sim y^4$ (where by $\langle \cdot \rangle$ we indicate the double average with respect to the coordinates parallel to the wall and velocity realizations). The velocities in the bulk of the container or duct are therefore much more intense with respect to the ones in the layers close to the wall, and the passive scalar evolution becomes faster and faster as one moves away from the wall. Starting from these considerations, it is possible to describe the evolution of a passive tracer initially concentrated in a layer of thickness δ close to the wall in term of a turbulent diffusivity. Averaging (1), the equation for the y -evolution of the scalar profile is

$$\partial_t \langle \theta \rangle = \mu \partial_y [y^4 \partial_y \langle \theta \rangle] + \kappa \partial_y^2 \langle \theta \rangle. \tag{2}$$

The first term in the rhs of (2) describes the role of chaotic advection in terms of an eddy diffusivity, which close to the wall is defined by $D = \int_0^\infty \langle v(y, 0)v(y, t) \rangle dt = \mu y^4$. Dimensional analysis suggests that the evolution of the profile is dominated by advection as long as $\delta \gtrsim r_{bl} = (\kappa/\mu)^{1/4}$, the thickness of the diffusive boundary layer. Under this condition, the diffusive contribution can be neglected and (2) becomes

$$\partial_t \langle \theta \rangle = \mu \partial_y y^4 \partial_y \langle \theta \rangle \tag{3}$$

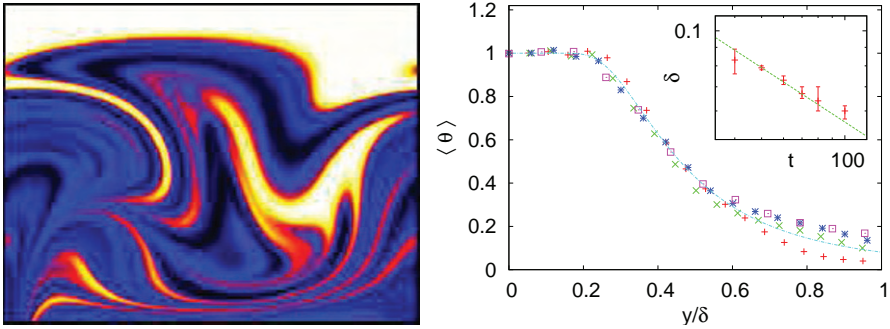


Fig. 1. *Left panel:* Snapshot of passive tracer concentration close to a wall placed on the top. White correspond to high concentration, black to low concentration. The initial condition is a step function in the vertical direction. Tracers is advected according to (1) with a two-dimensional synthetic velocity field. *Right panel:* Profile of the scalar density θ at different times in the Couette channel rescaled with respect to $\delta(t)$ and compared with the theoretical prediction (4) (continuous line). The inset shows the fitted values of δ at different times and the prediction $\delta \simeq t^{-1/2}$.

Taking as initial condition for the scalar a distribution concentrated at the wall with $\theta(x, 0; 0) = 1$ and $\lim_{y \rightarrow \infty} \theta(x, y; t) = 0$, the asymptotic solution of (3) for large times according to [2] is

$$\langle \theta(y, t) \rangle = \left[\operatorname{erf} \left(\frac{\delta}{2y} \right) - \frac{\delta}{\sqrt{\pi}y} \exp \left(-\frac{\delta^2}{4y^2} \right) \right] \tag{4}$$

i.e. the profile has a universal form, whose evolution in time is given by simple rescaling by the thickness $\delta = (\mu t)^{-1/2}$. The concentration (4) gives a practically constant concentration for $y \lesssim \delta/4$, making the boundary conditions for the scalar irrelevant in the advective stage. We remark that although (1) obviously conserves the average scalar $\langle \theta \rangle$, from (4) one has that $\int \langle \theta(y, t) \rangle dy = \delta(t)/\sqrt{\pi} \simeq t^{-1/2}$ is time dependent. The reason is that in deriving (4) the bulk is considered as an infinite reservoir for the scalar which has therefore zero average.

Neglecting diffusion, the advection equation (1) holds for any moment of scalar concentration $\langle \theta^n \rangle$, which will then obey the same law as (4) for all n . From this observation, we expect a strong intermittency in the evolution of the scalar field. Indeed the trace of such intermittency can be seen in the left panel of Figure 1 in which $\langle \theta^n \rangle$ is dominated by the white regions in which $\theta = 1$.

We simulated scalar transport close to a no-slip wall in plane Couette flow and in a synthetic chaotic flow [1]. Direct numerical simulations of a plane Couette flow are performed by means of a standard pseudo-spectral Fourier-Chebyshev code at resolution $128 \times 65 \times 128$ on a domain of size $L_x \times 2L_y \times L_z = 8 \times 2 \times 8$, at a Reynolds number $Re = U_0 L_y / \nu \simeq 600$ (with U_0 the velocity of each wall and ν the kinematic viscosity).

The trajectories of $N = 10^7$ particles, representing the concentration of tracer, are integrated according to the equation $\dot{\mathbf{x}}(t) = \mathbf{u}(\mathbf{x}, t)$. The initial condition for the particles is an uniform distribution in the x and z directions in a layer close to the wall $y \leq 0.04L_y$.

In the right panel of Fig. 1 we plot the mean profile $\langle \theta(y, t) \rangle$ at different times compared with the theoretical curve (4). The value of the thickness δ at different time is obtained from the fit of the profiles with (4) and its dependence on t is compatible with the prediction $\delta = (\mu t)^{-1/2}$.

Scalar profiles in the bulk deviate from the theoretical curve at large y , because of the limited extension of the viscous layer. In order to extend the range of scaling, we performed simulations of scalar transport in a kinematic velocity field. We define a two-dimensional velocity field in terms of a synthetic stream function $\Psi(x, y) = \Phi(x, y)G(y)$, where $\Phi = \sin(k_x x + \varphi_x(t)) \sin(k_y y + \varphi_y(t))$ represents a time-dependent cellular flow while $G(y)$ is tailored to reproduce the correct scaling at the wall. The phases of the cellular flow are given by a random process with a finite correlation time. The velocity field generated by Φ is placed on a grid of size $L_x = \pi$ and $2L_y = 4\pi$ at resolution 512×2048 where the evolution of (1) is integrated by means of a pseudo-spectral code, with periodic boundary conditions. Scaling regions extend approximatively to $L_s = 4$. The time unit is chosen so that the correlation time of the velocity field is $T = 1$. In these units we have $\mu \simeq 2.66$ and $\kappa = 3.42 \times 10^{-6}$ and therefore the width of the diffusive boundary layer is $r_{bl} \simeq 0.034L_y$. As initial condition we choose a distribution null in the bulk and concentrated at the walls in two smoothed-step functions of size $L_y/4$. The results are based on ensemble average over 100 realizations of the random noise driving the kinematic velocity field.

In the left panel of Fig. 2 the profile $\langle \theta(y, t) \rangle$ is compared, at different times, with the theoretical curve. In order to accurately resolve the region close to the wall, the extension of the domain in the bulk is not large enough for the approximation of an infinite bulk to be valid. Therefore, because of the conservation of $\langle \theta \rangle$, after a short transient a relevant amount of scalar accumulates in the central region of the domain, thus affecting the overall shape of the profile. In order to compare the numerical results with the the-

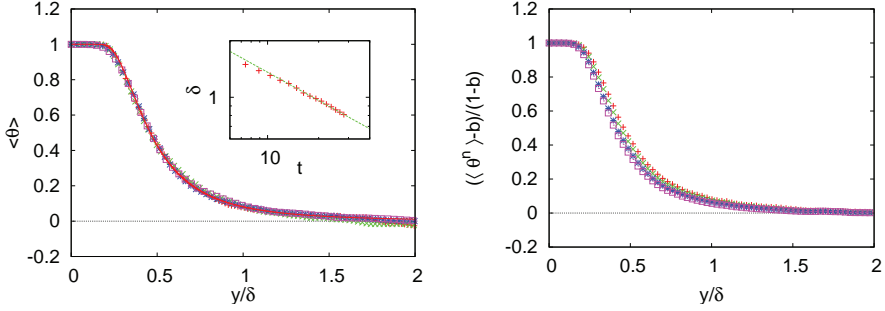


Fig. 2. *Left panel:* Average profile of the scalar density θ at different times rescaled with respect to δ and the bulk average b (see text) and compared with (4) (continuous line). In the inset, the thickness of the profile is shown together with the prediction $t^{-1/2}$ dependence. *Right panel:* Average profiles of moments of scalar density $\langle \theta^n \rangle$ for $n = 1$ (+), $n = 2$ (x), $n = 4$ (*) and $n = 6$ (□) at fixed time in the two-dimensional kinematic simulation.

oretical prediction based on an infinite basin, we computed the profile of the auxiliary field $\tilde{\theta} = (\theta - b)/(1 - b)$, where $b(t)$ is the time-dependent value of θ in the bulk (averaged over x). Figure 2 shows the remarkable agreement obtained between theory and numerics, indicating that the profile (4) can be easily extended to the general case of advection in a finite vessel. From the fitting procedure we get the values of the parameter δ , which is found to follow accurately the prediction $\delta(t) = (\mu t)^{-1/2}$ with $\mu \simeq 2.13$ (see inset of Fig. 2, left).

The right panel of Fig. 2 shows the profiles of different moments of scalar concentration $\langle \theta^n(y, t) \rangle$ computed at an intermediate time. All the moments collapse on the prediction (4), confirming the fact that in this stage diffusion is negligible and mixing of the scalar is dominated by eddy diffusivity according to (3).

This work was supported by Piedmont Industrial Research Grant INUMI-CRO.

References

1. G. Boffetta, F. De Lillo, A. Mazzino, *J. Fluid Mech.*, **624**, 151 (2009)
2. Lebedev, V. V. and Turitsyn, K. S., *Phys. Rev. E*, **69**, 036301 (2004)

Persistence of inhomogeneity of the turbulence generated by the static grid structures

Ö. Ertunc*, N. Özyılmaz**, H. Lienhart* and F. Durst***

* Lehrstuhl für Strömungsmechanik Erlangen, Friedrich-Alexander-Universität Erlangen-Nürnberg, D-91058, Germany

** Institut für Technische Mechanik, TU-Clausthal, D-38678 Clausthal-Zellerfeld, Germany

*** FMP Technology GmbH, D-91058 Erlangen, Germany
ertunc@lstm.uni-erlangen.de

Abstract

The homogeneity of turbulence, generated by static grid structures, was investigated in a complementary manner with the help of hot-wire measurements in a wind tunnel and direct numerical simulations based on the lattice Boltzmann method. The measurements were conducted downstream a grid having 64% porosity by varying the mesh Reynolds number in the range 4000-8000. The direct numerical simulations were performed at a constant mesh Reynolds number of 1400, varying the grid porosity from 53% to 82%. It is shown that the mean streamwise velocity becomes rapidly homogeneous, whereas the Reynolds stresses do not become homogeneous, at all, downstream of uniform grids. The reported investigations revealed no dependence of the inhomogeneity of Reynolds stresses on mesh Reynolds number and grid porosity. The analysis of the simulations showed that the early homogenization of the mean velocity field hinders the homogenization of the turbulence field.

1 Introduction

Owing to the translational invariance of homogeneous turbulence, decay processes in undistorted flows and the effects of mean velocity distortion on this kind of turbulent flows have constituted the framework of understanding and modeling of turbulent flow phenomena [1]. In experimental investigations, turbulence, which is homogeneous in planes perpendicular to the flow direction, has commonly been produced by static grid structures. After Corrsin [2], it became a rule of thumb to employ grids having porosities larger than 57%

in order to generate a turbulent flow field, which could be expected to be spatially homogeneous. However, there are only a few studies in the literature which directly investigated the homogeneity of the grid-generated turbulence. Although, in those studies [3, 4, 5], turbulent stresses were reported to be inhomogeneous even for grids having porosities higher than 57%, homogeneity of grid-generated turbulence remained as an ad hoc assumption for highly porous grids.

For some of the authors' investigations on homogeneous turbulence, it was essential to determine the extent of spatial homogeneity of grid-generated turbulence. For this purpose, detailed hot-wire measurements and direct numerical simulations (DNS) [6, 7] were conducted to yield information about the Reynolds stresses in the wake of static grid structures which had porosities ranging from 53% to 82%. The carried out investigations revealed inhomogeneous Reynolds stress fields far downstream of the grids ($x_1/M > 40$) over the whole porosity range. In this work, we summarize the results of our experimental and numerical investigations and provide explanation for the persistence of the inhomogeneity of Reynolds stresses far downstream of the grid with the help of DNS.

2 Results and Discussion

The velocity measurements were conducted in the wake of a grid having 64% porosity, which was installed in the test section of the wind tunnel of LSTM-Erlangen. The measurements were performed by using a hot-wire anemometer [6]. The measurements were conducted at different mesh Reynolds numbers ($Re_M = \bar{U}_1 M / \nu$) between 4000 and 8000, where M was the mesh size of the static grid. The hot-wire measurements in the wind tunnel comprised scans in planes, which were perpendicular to the grid, located at the center of the test section and extending 1060 mm in the streamwise direction and 50 mm in the transverse direction. The transverse and streamwise resolutions of the scan were 1 mm and 10 mm, respectively. For the DNS, a standard Lattice-Boltzmann BGK method (LBGK) was employed. The simulations were performed for static grids having porosities ranging between 53% and 82% at $Re_M = 1400$. There were $2400 \times 160 \times 160$ lattice points in the computational domain [7].

The scanned planes consist of N_{x_1} points in the flow direction and N_{x_2} points in the transverse direction, such that the spatial resolutions of the scan in both directions are Δx_1 and Δx_2 . In order to visualize the homogeneity of any one of the measured mean quantities, say \bar{H} , in the scanned plane, the inhomogeneity parameter $I_{\bar{H}}$ is defined as:

$$I_{\bar{H}}(x_1, x_2) = \frac{\bar{H}(i\Delta x_1, j\Delta x_2)}{\left| \frac{1}{N_{x_2}} \sum_{j=1}^{N_{x_2}} \bar{H}(i\Delta x_1, j\Delta x_2) \right|} 100, \quad (1)$$

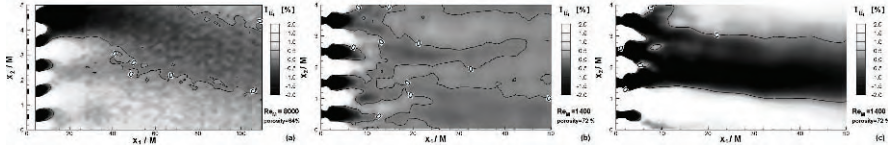


Fig. 1. Inhomogeneity of the mean velocity field (a) in experiments, in simulations (b) with uniform grid structure and (c) with non-uniform grid structure.

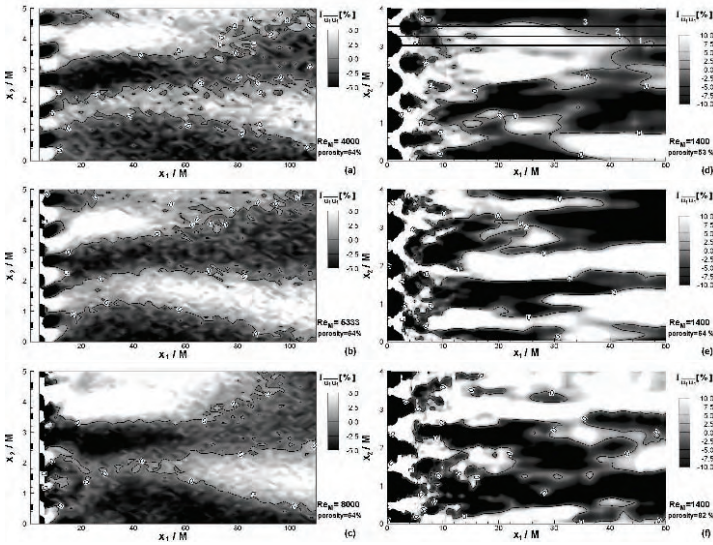


Fig. 2. $I_{\overline{u_1 u_1}}$ field in the wake of the grid (a-c) in the wind tunnel at different mesh Reynolds numbers and (d-f) in the simulations with different porosities.

which is the percentage deviation of the variable $\overline{H}(x_1, x_2)$ from the absolute value of its average value calculated along a line $x_1 = \text{constant}$.

In the experiments and simulations, the inhomogeneity of the mean streamwise velocity $I_{\overline{U_1}}$ decreased rapidly with increasing distance downstream of the grid structures (Fig. 1 a and b). Simulations performed with slightly non-uniform grid structure caused inhomogeneous mean velocity distributions (Fig.1 c). In contrast to the mean streamwise velocity behind uniform grid structures, the Reynolds stresses revealed regions having periodic deviations from the mean in the transverse direction. The inhomogeneous field consisting of elongated positive and negative stripes and coalescing with each other. As an example, the measured and simulated inhomogeneity fields of the streamwise normal Reynolds stress ($I_{\overline{u_1 u_1}}$) are shown in Fig. 2 (a)-(c) and (d)-(f), respectively. Measurements did not reveal any dependence of the inhomogeneity level on the grid Reynolds number and the simulations showed the inhomogeneity of Reynolds stresses over the whole investigated porosity range, however at higher levels. Moreover, the location of the inhomogeneity

stripes of Reynolds stresses remained almost at the same locations despite increased Re_M in the experiments. These findings on the inhomogeneity of grid-generated turbulence are in accordance with those of Grant & Nisbet [3] and show the dependency of measured mean quantities on the relative position of the measurement location with respect to the grid structure.

To understand the persistence of inhomogeneity of Reynolds stresses far downstream of the grid, the terms in the transport equation of the turbulence kinetic energy k were further analyzed for the 53% porosity grid case along the lines shown in Fig.2 (d). As a result of the rapidly decreasing mean velocity gradients (Fig. 3 a), the turbulence production becomes rapidly inactive (Fig. 3 b), so that the large scale mixing process stops and the remaining viscous diffusion term is insufficient to homogenize turbulence before it decays completely.

The presented results demonstrate that far downstream of the uniform static grid structures certain amount of inhomogeneity of Reynolds stresses persists regardless of the grid porosity. Any kind of study which does not take this fact into consideration can be misleading.

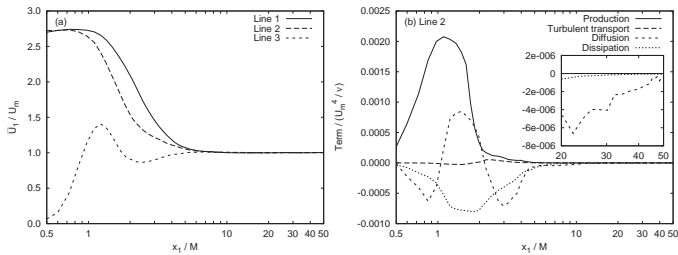


Fig. 3. (a) Development of the streamwise mean velocity along the three lines in Fig. 2 (d) and (b) the development of the terms in the transport equation of the turbulence kinetic energy k along line 2.

References

1. J. N. Gence, *Annu. Rev. Fluid Mech.*, **15** 201 (1983).
2. S. Corrsin, *Handbuch der Physik-Encyclopedia of Physics*, S. Flüge and C. Truesdell, Springer-Verlag,(1963).
3. H. L. Grant and I. C. T. Nisbet, *J. Fluid Mech.*, **2** 263 (1957).
4. R. I. Loehrke and H. Nagib, *AGARD Report*, **No. 598** (1972).
5. R. Liu, D. S. K. Ting and G. W. Rankin, *Experimental Thermal and Fluid Science*, **28** 307 (2004).
6. Ö. Ertunç, *Experimental and numerical investigations of axisymmetric turbulence*. PhD Thesis, Friedrich Alexander Universität Erlangen-Nürnberg, 2007.
7. Ö. Ertunç, N. Özyilmaz, H. Lienhart, F. Durst and K. Beronov, submitted to *J. Fluid Mech.*,(2008).

On the energy decay of grid generated turbulence

P.-Å. Krogstad¹ and P.A. Davidson²

Dept. Energy & Process Eng., NTNU, Trondheim, Norway

Dept. Engineering, University of Cambridge, Cambridge, U.K.

Introduction

There is a long tradition of studying the decay of turbulent energy generated by grids. The main reason for this is that it is probably the simplest turbulent flow that exists. Despite its simplicity there are many aspects of the flow that are still not fully understood. This is demonstrated e.g. by the fact that there is still considerable doubt as to how fast the energy decays. It is generally accepted that $(u/U_{mean})^2$ decays as $[(x-x_0)/M]^{-n}$, where u and U are the rms and mean components of the streamwise velocity, respectively, x is the streamwise distance and M is the size of the mesh. A number of theories exist that predict n to vary from 1 to 10/7 and the range of experimental values is even larger. In a recent study Kurian and Fransson[1] showed that n depends on the mesh Reynolds number and appears to decrease towards $n \approx 1.2$ at high Re. This agrees well with Krogstad and Davidson[2].

There are a number of reasons which may account for the large scatter in the experimental data in the literature. The main reason is probably that the wind tunnels where the flow has been studied have often been quite small. Therefore the setup has been a compromise between spatial resolution, the number of meshes needed to assure that the effects of the side walls are small and the possibility to map the flow to large values of x/M . This has often resulted in the streamwise distance being limited to less than $x/M = 100$. Ignoring the first 30 to 40 meshes where the flow may still be developing, this leaves a rather limited range to study the flow.

Experimental details

The present investigation was performed in a wind tunnel with a test section that is 11m long and with a cross section of 2.7 x 1.9m². We used a monoplane grid with a mesh size of 40 x 40mm². The mesh was made by punching 30 x 30mm² holes in 2mm thick plates, giving a solidity of $\sigma = 44\%$. It has been demonstrated in previous investigations (e.g. [3, 4]) that the flow isotropy is improved if a contraction is mounted downstream of the grid. In the

present case the grid was mounted near the exit of the contraction upstream of the test section, giving a contraction ratio of about 1.4 downstream of the grid before the flow entered the test section. This gave a grid of about 80 by 60 meshes and the flow could be mapped from $x/M \approx 30$ to 275.

The streamwise uniformity of the mean flow was investigated by a number of traverses along the test section. From $x/M \approx 45$ to 250, U was found to be constant within -0.6% and $+0.3\%$. Similarly the spanwise homogeneity of the flow was examined at a number of cross sections and was found to be within $\pm 0.3\%$ at all positions. Also the homogeneity of the higher order moments up to 4th order was mapped and the highest spanwise scatter was found in the flatness which was found to be constant within $\pm 0.8\%$ at all cross sections.

All three velocity components were measured using a combination of two component LDA, single and X-wire anemometry. The large scale isotropy was found to be good with $0.94 < \langle q^2 \rangle / 3 \langle u^2 \rangle = (\langle u^2 \rangle + \langle v^2 \rangle + \langle w^2 \rangle) / 3 \langle u^2 \rangle < 0.97$ throughout the measurement range.

Results

Fig. 1(a) shows the decay of $\langle u^2 \rangle / U_{mean}^2$ and $\langle q^2 \rangle / U_{mean}^2$. The decay exponents were obtained using three different strategies. The first method is based on the work by Mohamed and LaRue[5]. Since it is not known which part of the data that satisfies the decay equation

$$\frac{\langle u^2 \rangle}{U^2} = a \left(\frac{x}{M} - \frac{x_0}{M} \right)^{-n}, \tag{1}$$

it is essential to sort out the data that suffers from initial development and where the final decay or system noise starts to affect the data. Hence, the range is sought that gives the least squares fit to a limited range of the data. This was found to be for $45 < x/M < 200$. For $x/M < 45$ the flow was still affected by the velocity increase in the contraction and for $x/M > 200$ noise appeared to affect the fit.

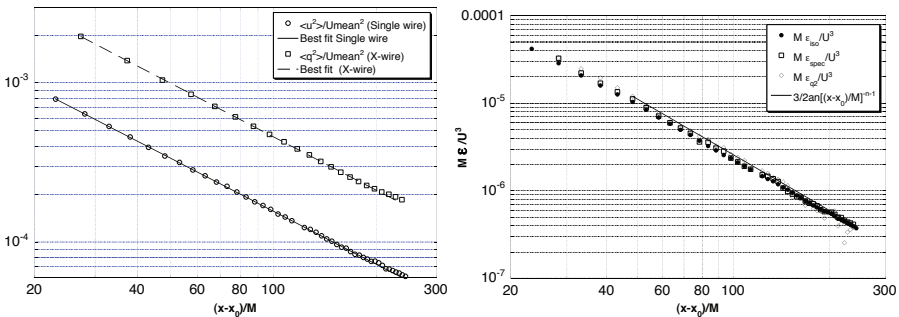


Fig. 1. Decay of streamwise normal stress (left) and 3 estimates of the dissipation rate (right).

Measurements were taken for every $\Delta x/M=2.5$. The high spatial resolution allows the local decay exponent to be determined directly from the data by differentiation (Fig. 2(a)). Finally we applied the method of Lavoie et al.[4]. The idea here is that instead of trying to find all three fit constants a , x_0 and n simultaneously, considerable improvement can be obtained in the accuracy if one constant is assumed to be known. By keeping x_0 constant the other constants were sought for various subsets of the data. The x_0 that gave the most extended range of constant n is assumed to produce the optimal fit of Eq. (1) to the data (Fig. 2(b)). In this way the decay exponent was found to be $n = 1.13$ with an uncertainty of ± 0.02 when applying the three methods to both the $\langle u^2 \rangle / U_{mean}^2$ and $\langle q^2 \rangle / U_{mean}^2$ data.

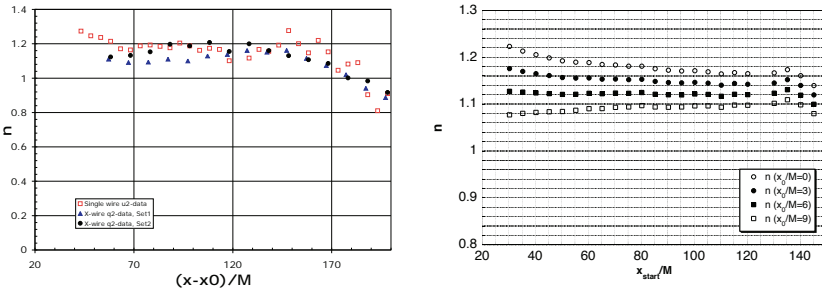


Fig. 2. Decay exponents from local gradients (left) and the method of Lavoie et al, 2007 (right).

The small streamwise distance between measurements also allowed local gradients of the kinetic energy to be estimated. Using the balance equation $\frac{1}{2}Udq^2/dx = -\epsilon_{q2}$ the dissipation was found and compared to estimates assuming isotropic turbulence ($\epsilon_{iso} = 15\nu < (\partial u/\partial x)^2 >$) and from the inertial subrange ($E_{uu}(k) = C\epsilon_{spec}^{2/3}k^{-5/3}$), see Fig. 1(b). As expected ϵ_{q2} has more scatter than the other two estimates for large x/M . This is because reliable estimates for the gradients of the energy distribution are increasingly more difficult to obtain as q^2 becomes small for large x . Finally we have included the dissipation rate that can be estimated from the fit of the decay equation, Eq. (1), to the $\langle u^2 \rangle / U_{mean}^2$ data, i.e.

$$\frac{M\epsilon}{U^3} = -\frac{3}{2} \frac{d(\langle u^2 \rangle / U^2)}{d(x/M)} = \frac{3}{2} na \left(\frac{x - x_0}{M} \right)^{-n-1}. \tag{2}$$

(The distribution obtained from the fit to $\langle q^2 \rangle / U_{mean}^2$ gave virtually identical results and has therefore not been included.) The agreement between the methods is seen to be good.

We also computed the integral length scale of u , i.e. $\ell_{uu} = \int_0^\infty \frac{\langle u(x)u(x+r) \rangle}{\langle u^2 \rangle} dr$ which is shown in Figure 3(a). This is frequently used in the empirical, but well established relationship

$$\frac{du^2}{dt} = -A \frac{u^3}{\ell}, \quad A = \text{constant} . \tag{3}$$

where A is of order 1. The assumption that A is a constant is fundamental to most decay laws in the literature. This leads e.g. to the Saffman decay exponent of $n = 6/5 = 1.2$. In Figure Figure 3(b) we show that the measurements indicate that A is not a constant, but decays steadily with x/M . Krogstad and Davidson[2] showed that this has serious consequences for the decay exponent in Eq. (1). If A depends on x as $A \sim x^{-p}$ then the decay exponent is modified to $n(1 - p)$. We have included a best fit to the data which suggests that A decays as $A \sim (x - x_0)^{-0.075}$. This implies a decay exponent of about $n = 1.11$ which is within the range of the present measurements.

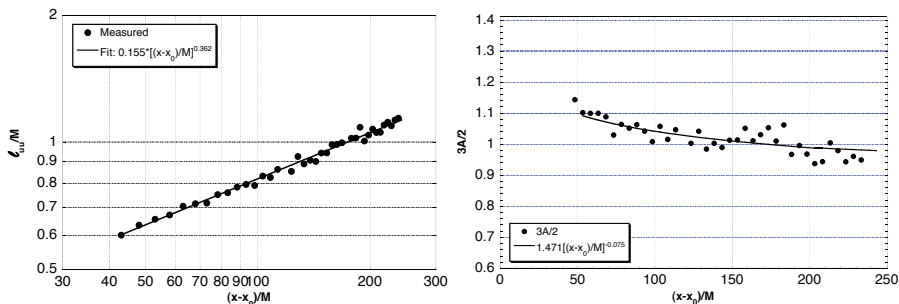


Fig. 3. Development of integral length (left) and dissipation coefficient (right).

Conclusions

This study of the flow downstream of a monoplane grid suggests that the assumption of a fixed constant of proportionality, A , in Eq. (1) may not in general be true. In the present experiment it was found that A decayed as $A \sim x^{-0.075}$. This has implications for the exponent in the expression for turbulent kinetic energy decay. The decay exponent of $n = 1.13$ observed in the experiment is consistent with the exponent predicted for Saffman turbulence ($n = 6/5$) if the reduction caused by the slow streamwise decay of A is accounted for.

References

1. T. Kurian and J.H.M. Fransson, /it Fluid Dyn. Res., **41**, (2009).
2. P.-Å. Krogstad and P.A. Davidson, Submitted /it J. Fluid Mech., (2009).
3. G. Comte-Bellot and S. Corrsin, /it J. Fluid Mech., **25**, (1966).
4. P. Lavoie, L. Djenedi and R.A. Antonia, /it J. Fluid Mech., **585**, (2007).
5. M.S. Mohamed and J.C. LaRue, /it J. Fluid Mech. **219**, (1990).

Turbulent Entrainment in Jets: The role of Kinetic Energy

Rodrigo M. R. Taveira, Carlos B. da Silva and J. C. F. Pereira

IDMEC/IST, Pav. Mecânica I/LASEF, Av. Rovisco Pais 1049-001 Lisboa,
Portugal
rodrigo.taveira@ist.utl.pt

1 Introduction

In free shear flows the flow field can be divided into two distinct regions that find themselves separated by a thin contorted front entitled turbulent/non-turbulent interface. In the outer region the flow is largely irrotational whereas in the inner region the flow is turbulent. *Turbulent entrainment* is the process through which fluid parcels from the outer region acquire vorticity, thus becoming turbulent. Recently, the classical assumption, where large scale “*engulfing*” motions are the main responsible for the jet growth [?], has been questioned *e.g.* Mathew & Basu [?] and Westerweel *et. al.* [?]. Instead, these works provided ample support to the original model of Corrsin & Kistler [?], where the entrainment is mainly governed by small scale eddy motions (“*nibbling*”).

2 DNS of a turbulent plane jet

The present work uses a direct numerical simulation (DNS) of a fully developed turbulent plane jet at $Re_\lambda \approx 120$ [?, ?] (Fig. ??) to analyze the dynamics of the kinetic energy and the role of the intense vorticity structures (IVS) (Fig. ??) in the turbulent entrainment mechanism, as well as the thickness of the interfacial layer, whose detection is determined by means of a vorticity norm threshold $|\vec{\Omega}| = 0.7 \frac{U_j}{H}$ (Fig. ??), as in Bisset *et. al.* [?]. Specifically, we employ conditional statistics from the distance to the turbulent/non-turbulent (T/NT) interface y_I , that separates the turbulent from the irrotational flow regions (Fig. ??).

3 Results and Discussion

The conditional vorticity components (Fig. ??) show the existence of a sharp jump at the interface with a width close to the Taylor micro-scale, in agree-

ment with Westerweel *et. al.* [?], but in contrast to Holzner *et. al.* [?]. Additionally, Fig. ?? demonstrates that, locally, the Taylor micro-scale is the characteristic scale for the vorticity scaling. Moreover, the conditional normal Reynolds stresses (Fig. ??) show the existence of significant values at the irrotational region, near the T/NT interface, also in agreement with reference [?]. Such values result from intense velocity fluctuations produced by a sharp pressure gradient near the interface. Figures ?? and ?? show conditional mean profiles of all the terms from the total and fluctuating (turbulent) kinetic energy transport equations. Notice that all major transport mechanisms are restricted to a confined region, in vicinity of the T/NT interface, in strong contrast with classical mean profiles for these terms. Moreover, the growth of irrotational kinetic energy is caused by an inviscid mechanism resulting from pressure/velocity interactions. Analysis of the instantaneous fields showed that the advection term is the dominant mechanism at the turbulent regions, transferring energy from the inner regions into the vicinity of the T/NT interface ($\frac{y_I}{\lambda} \lesssim 2$). An interesting result is the realization that the turbulent production term is important only very close to the T/NT interface $y_I/\lambda \lesssim 3$. Furthermore, turbulent diffusion drains energy from the regions of intense production and injects it at the interface $y_I/\lambda \lesssim 1$. The results indicate the mechanisms driving the growth of the kinetic energy during the turbulent entrainment process, and the small scales associated with these. From this it is possible to infer the resolution requirements that are necessary to correctly capture the vorticity, energy and scalars transfers across the T/NT interface, with huge impact in issues such as mixing and turbulent combustion.

References

1. A. A. Townsend. The Structure of Turbulent Shear Flow, Cambridge, 1976.
2. J. Westerweel, C. Fukushima, J.M. Pedersen and J.C.R. Hunt. Mechanics of the turbulent/non-turbulent interface of a jet. *Phys. Review Lett.*, 95:174501, 2005.
3. J. Mathew & A. Basu. Some characteristics of entrainment at a cylindrical turbulent boundary. *Phys. Fluids.*,14(7):2065-2072, 2002.
4. S. Corrsin & A. L. Kistler. Free-stream boundaries of turbulent flows. Technical Report TN-1244, NACA, 1955.
5. C. B. da Silva & J. C. F. Pereira. Invariants of the velocity-gradient, rate-of-strain and rate-of-rotation tensors across the turbulent/non-turbulent interface in jets. *Phys. Fluids*, 19:071702, 2007.
6. C. B. da Silva & J. C. F. Pereira. Erratum: "Invariants of the velocity-gradient, rate-of-strain and rate-of-rotation tensors across the turbulent/non-turbulent interface in jets". *Phys. Fluids* 21, 019902, 2009.
7. D. K. Bisset, J. C. R. Hunt and M. M. Rogers. The turbulent/non-turbulent interface bounding a far wake. *J. Fluid Mech.*, 451:383-410, 2002.
8. M. Holzner, A. Liberzon, N. Nikitin, W. Kinzelbach and A. Tsinober, Small-scale aspects of flows in proximity of the turbulent/nonturbulent interface, *Phys. Fluids* 19, 071702, 2007.

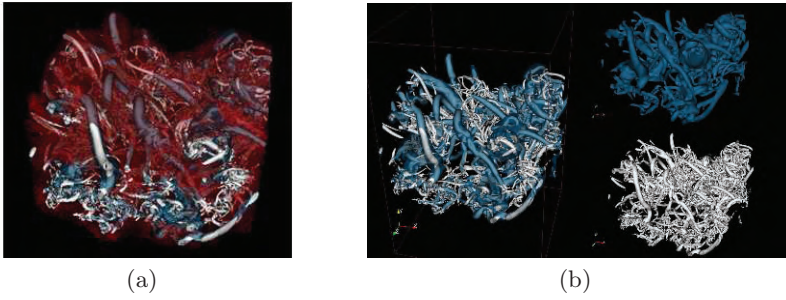


Fig. 1. (a) Plane Jet: T/NT interface (red) and intense vorticity structures. (b) Individualized visualization of large eddies (blue) and small vorticity structures (white).

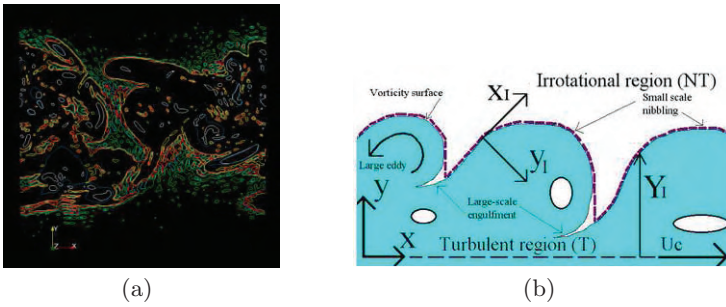


Fig. 2. (a) Vorticity norm threshold levels for interface detection. (b) Sketch of the T/NT interface, where a local frame is used to perform the conditional statistics.

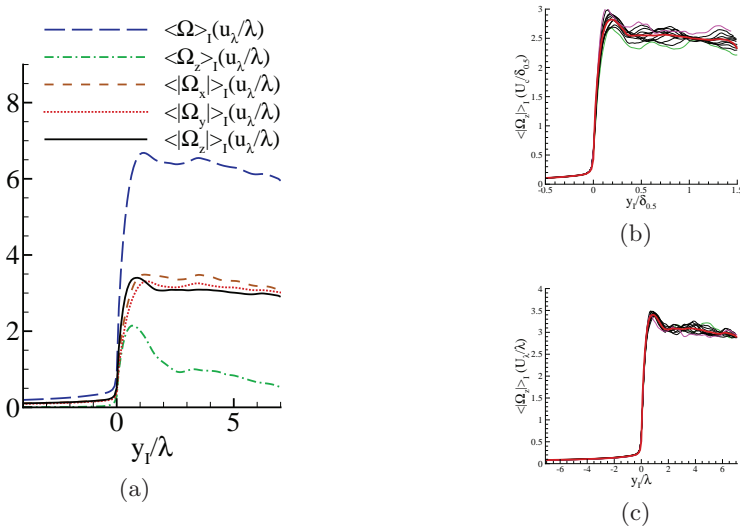


Fig. 3. (a) Conditional mean profiles of the vorticity norm and components, relative to the distance from the T/NT interface. Vorticity norm non-dimensionalized by: b) Centreline velocity (U_c) and jet half-width ($\delta_{0.5}$) and (c) Taylor micro-scale “velocity” (v) and length scale (λ).

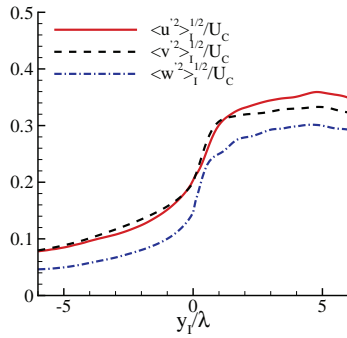


Fig. 4. Conditional mean profiles of the Reynolds stresses.

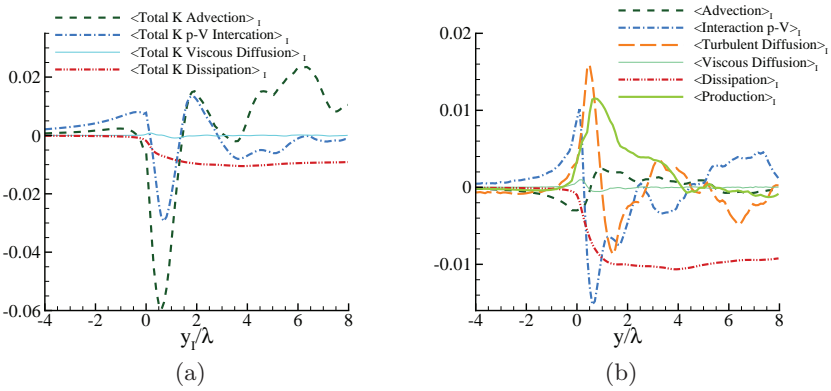


Fig. 5. (a) Total kinetic energy transport equation and, (b) turbulent kinetic energy transport equation. Advection (---); pressure-velocity interaction (- · -); viscous diffusion (—); viscous dissipation (- · · -); production (—); turbulent diffusion (—).

Fast and slow changes of the length of gradient trajectories in homogeneous shear turbulence

P. Schäfer, M. Gampert, L. Wang and N. Peters

Institut für Technische Mechanik, RWTH-Aachen, Templergraben 64, Aachen
n.peters@itv.rwth-aachen.de

Introduction

Gradient trajectories in scalar fields have recently received attention in the context of dissipation elements [1], [2] which in turn are of interest for the flamelet concept in nonpremixed combustion [3]. Dissipation elements are space filling regions in a scalar field defined such that gradient trajectories starting from any point within the element in ascending and descending directions reach the same minimum and maximum points. Gradient trajectories advance preferentially through regions of the scalar field that have been smoothed by the combined action of diffusion and extensive strain. Since the extensive strain in these regions is of the order of the inverse of the integral time scale τ , dimensional analysis predicts the mean length l_m of dissipation elements to be of the order of the Taylor length [4].

The space filling property of dissipation can be used to reconstruct statistical properties of the entire scalar field from mean values within the dissipation elements [2]. For this purpose the properties of the elements need to be parameterized. Since elements are elongated in one direction and thin in the other two directions, a suitable parameter to characterize them is the linear length of an element l which is the distance between its minimum and maximum point.

In [1], considering at first the random cutting and reconnection processes of elements arranged in one dimension, an equation describing the time evolution of the probability density of the distance between two Poisson points along a line has been derived from first principles. These are fast processes that result in integral terms in the equations, similar to the integral term resulting from molecular collision processes in the Boltzmann equation. In addition, the linear length of elements is changed by slow processes, namely diffusion of extremal points towards each other and straining by the flow field [2]. For elements arranged in one direction, and likewise for the length of gradient trajectories, the evolution equation takes the form

$$\begin{aligned} \frac{\partial P(l,t)}{\partial t} + \frac{\partial[v_D(l,t)P(l,t)]}{\partial l} + \frac{\partial[a(l,t)lP(l,t)]}{\partial l} &= 2\lambda \int_0^\infty P(l+z,t)dz \\ - lP(l,t) + 2\mu \int_0^l \frac{y}{l} P(l-y,t)P(y,t)dy - 2\mu P(l,t) - P(l,t)\bar{a}(l,t), \end{aligned} \quad (1)$$

where $P(l,t)$ is the probability density of the length, $v_D(l,t)$ is the diffusion drift velocity, $a(l,t)$ is the conditional mean strain rate of elements, λ is the cutting frequency per time and length and μ is the frequency of reconnection. The removal of elements by the last term containing the weighted mean strain rate $\bar{a}(l,t) = \int_0^\infty a(l,t)lP(l,t)dl$ is needed to obtain a stationary solution. Finally the drift velocity has been approximated by the following expressions [1] [2]

$$v_D = -\frac{4D}{l} \{1 - c[1 - \exp(-1.5l/l_m)]\}, \quad (2)$$

where l_m is the mean linear length and D is the viscosity.

A stochastic simulation of the cutting, reconnection and molecular diffusion process using the random superposition of Gaussian profiles satisfying the one-dimensional diffusion equation has confirmed the theory [4], but showed that the imposed frequency of addition these profiles becomes irrelevant for profiles having a width representing turbulent eddies. The cutting frequency is then of the order of the inverse of the integral scalar time, calculated from the scalar variance and scalar dissipation rate.

Once a model for the evolution equation is well established and validated by comparison with DNS data, unconditional mean properties can be calculated from conditional means from the elements. For instance, it has been shown in [2] that the mean viscous dissipation rate $\langle \varepsilon(t) \rangle$ can be reconstructed from the conditional mean $\langle \varepsilon/l \rangle$ when the distribution function $P(l,t)$ is known. Applying this to the evolution equation for $P(l,t)$ one then may derive an equation for $\langle \varepsilon(t) \rangle$ which, in the case of homogenous shear turbulence, agrees well with the modeling of the ε -equation in the widely used k - ε -model, except that the modeling constants turn out to be Reynolds number dependent.

Analysis

The purpose of the proposed paper is to determine the cutting and reconnection frequencies as well as the conditional mean strain rate in eq. (1) by sending Lagrangian particles through the scalar field and by analyzing the length of gradient trajectories that originate from the particles in ascending and descending directions as a function of time. These trajectories are expected to display the fast and slow processes to which elements are subjected. When a minimum or a maximum disappears due to molecular diffusion, or is created due to turbulent motions, trajectories will proceed to another extremal point and their lengths will change abruptly. On the other hand, strain and diffusion will continuously change the length of elements.

In practice, turbulent displacement fluctuations of a particle close to the in-

terface between dissipation elements may affect the lengths of gradient trajectories from Lagrangian particles as well, because the particle may enter into another dissipation element that has a different linear length. Trying to remove this effect, we have adopted a five points diagnosis arranged in a plane perpendicular to the direction of the local trajectory. The Lagrangian point in the center is surrounded by the other four auxiliary companions arranged in a square configuration. In 2D the method is illustrated in Fig. 1. Besides the Lagrangian point p , other two companions p_1 and p_2 are chosen at a fixed separation distance from p . The alignment of the three point is perpendicular to the local trajectory. If at time t the Lagrangian point p lies in the vicinity of the interface between two elements $DE1$ and $DE2$, then after a short time step Δt , if p moves from $DE2$ to $DE1$, the length of its trajectory will have a fast change, while the lengths of trajectories from p_1 and p_2 have only slow changes. If the length of the trajectory from p and either p_1 or p_2 or both change simultaneously rapidly, then the dissipation element in which p is located, has changed its length due to the disappearance or creation of an extremal point. In this way it is possible to exclude fast jumps due to turbulent displacement fluctuations or, likewise, surface motion fluctuation, from those by the abrupt changes of the length of dissipation elements. In the simulations to be presented below, this effect accounted for approximately 50% of the fast processes that were identified.

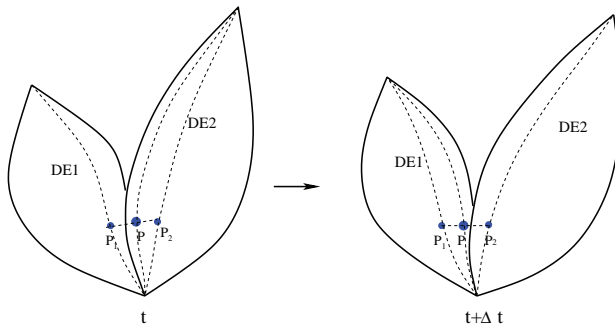


Fig. 1. Schematic structure of triple point array diagnosis to exclude the effect of Lagrangian particles crossing the interfaces of dissipation elements.

Results

A DNS using 512^3 grid points and a mean shear gradient $\partial\langle u_1 \rangle / \partial x_2 = 0.5$ with a diffusion coefficient $D = 0.003$ has been performed. The resolution Δx was 0.66 times the Kolmogorov scale $\eta = 0.0186$ and the Taylor Reynolds number was $Re_\lambda = 100.3$. An example of the fast and slow changes of the length of an element is shown in Fig. 2. One observes slow increases or decreases of the length over a larger time period and as well as abrupt changes.

The former are due to the straining or compression of elements while the latter correspond to cutting and reconnection. After an appropriate filtering and by analyzing over $4 \cdot 10^6$ trajectories one may obtain the conditional mean strain rate a , shown in Fig. 3.

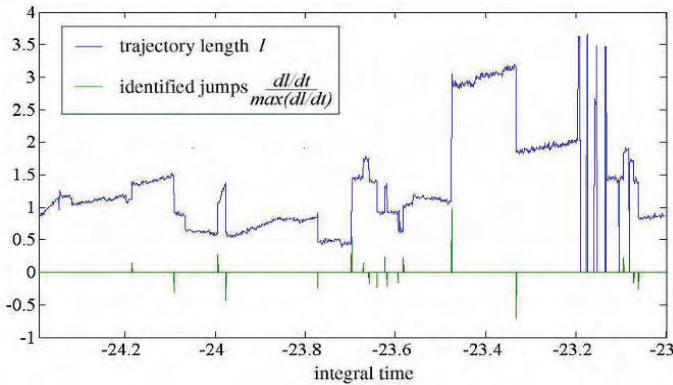


Fig. 2. Arclength of the gradient trajectory originating from a Lagrangian particle. The normalized time derivative is plotted only for those jump that have been identified as physically meaningful.

When the effect from crossing the interfaces has been removed, the frequencies of cutting and reconnection can be calculated as a function of the length. The results in Fig. 4 show an approximately linear dependence of λl on l , from which λ can be calculated by differentiation. The reconnection frequency μ varies between 0.75 and 0.25, approximately.

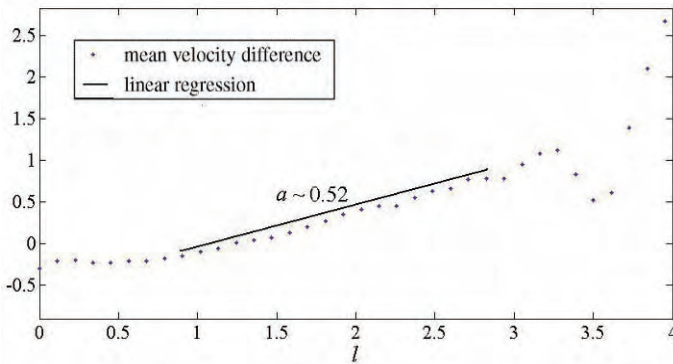


Fig. 3. Mean velocity difference at the ending points of the trajectory as a function of trajectory length. The mean strain rate a is determined from the slope.

Note that by taking the derivative with respect to the arclength of trajectories in Fig. 3 and 4 rather than with respect to the linear length of dissipation elements, one obtains a different strain rate a and a different cutting frequency λ than those in Eq. (1). Nevertheless, in order to compare the order of magnitude of these coefficient, Eq. (1) is solved numerically by the method outlined in [1]. Two eigenvalues can thereby be calculated. With the prescribed values of $D = 0.003$, $a = 0.52$ and $l_m = 1.185$ from the analysis of the DNS data, one obtains from these eigenvalues the coefficients $\lambda = 0.48$ and $\mu = 0.13$. The values of λ from the DNS and the solution of the evolution equation agree favorably while those for μ differ by more than a factor 2. Nevertheless, the method of gradient trajectories originating from Lagrangian particles seems to confirm the hypotheses about fast and slow changes of the linear length of dissipation elements.

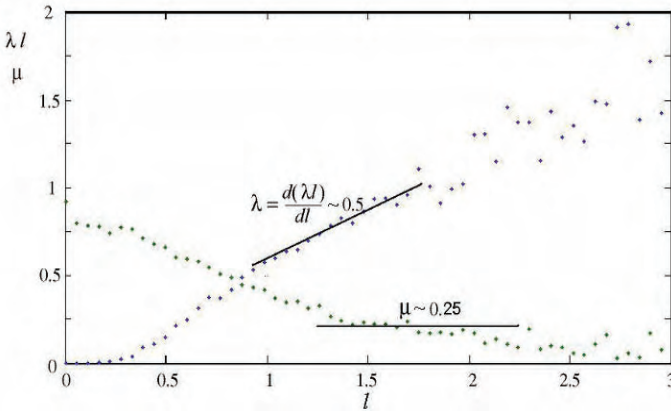


Fig. 4. Mean cutting frequency λ and mean reconnection frequency μ as a function of the length before the of the trajectories.

Acknowledgement The authors acknowledge the funding of this work by the Deutsche Forschungsgemeinschaft under Grant Pe 241/38-1.

References

1. L. Wang and N.Peters, *J.Fluid Mech.*, **554**, 457 (2006).
2. L. Wang and N.Peters, *J.Fluid Mech.*, **608**, 113 (2008).
3. N.Peters, 32nd Symposium on Combustion, Montreal, (2008)
4. N.Peters and L.Wang, *C.R.Mechanique*, **334**, 493 (2006).

Part IX Wall bounded flows

Coherent streaky structures and optimal perturbations of turbulent boundary layers

C. Cossu¹, G. Pujals^{1,2}, and S. Depardon²

¹LadHyX, CNRS-École Polytechnique, Palaiseau, France

²PSA Peugeot Citroën, Centre Technique de Velizy, France

carlo.cossu at ladhyx.polytechnique.fr

The presence of persistent streaky structures is a well established robust feature of turbulent shear flows. A large amount of research has been dedicated to the understanding of the mechanisms by which streaks are generated and of their relevance on the turbulent dynamics. In the near wall region of the boundary layer these streaks, with characteristic mean spacing of about one hundred wall units, are thought to play an essential role in a turbulent self sustained mechanism. The ‘lift-up’ effect by which low energy streamwise vortices can induce large energy streaks is an important process embedded in this self sustained mechanism. Recent studies have also demonstrated that the well controlled optimal transient growth of artificially forced streaks can be efficiently used to manipulate at leading order laminar shear flows. Such a paradigm has been successfully applied to stabilize Tollmien-Schlichting waves in a laminar boundary layer [1] and to effectively delay transition to turbulence [4]. In these investigations, roughness elements were used to create nearly optimal vortices in the upstream part of the boundary layer that induced well controlled streamwise streaks downstream. A still not addressed extension of such a kind of approach would consist in the manipulation of turbulent boundary layers with optimal or nearly optimal vortices and streaks, the first step in this direction being to compute the optimal perturbations of the turbulent boundary layer.

We compute the optimal energy growth sustained by a turbulent boundary layer without pressure gradients. The two-scales composite expression proposed by Monkewitz et al. [9] is assumed for the turbulent mean flow. Such an expansion has proven to be an excellent fit to experimental data at large Reynolds number. The motion of small coherent perturbations to the turbulent mean flow is modelled following the approach used by del Álamo & Jiménez [3] for the turbulent Poiseuille flow case: the mean flow equations are linearized near the turbulent mean flow and the effect of small scales is modelled with an effective viscosity in equilibrium with the turbulent mean flow. This results in a generalized Orr-Sommerfeld-Squire system including

the effect of the variable viscosity. Here we do not use the operators used in Ref.[3], but the ones detailed in Refs.[11, 2] that are consistent with previous investigations.

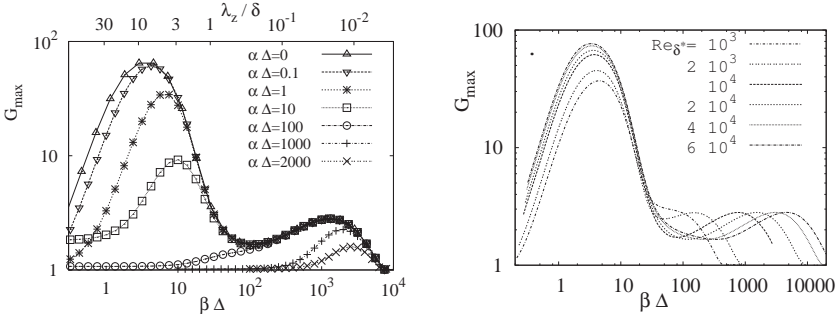


Fig. 1. Left: Dependence of the maximum growth G_{max} on the spanwise wavenumber $\beta\Delta$ obtained for selected streamwise wavenumbers ($\alpha\Delta = 0, 0.1, 1, \dots$) at $Re_{\delta_*} = 17300$. Right: Maximum growth G_{max} of streamwise uniform ($\alpha = 0$) perturbations versus the spanwise wavenumber $\beta\Delta$ for the selected Reynolds numbers Re_{δ_*} .

The considered turbulent mean profiles are found to be linearly stable at all Reynolds numbers, but they can support transient energy growths. Without loss of generality, the perturbations are assumed periodic in the spanwise and the streamwise directions with wavelengths respectively λ_z and λ_x (and wavenumbers β and α). The maximum energy growth G_{max} , defined as the maximum ratio of the kinetic energy contained in the perturbations to the kinetic energy of the initial condition, is then computed using standard methods. It is found that only disturbances with $\lambda_x > \lambda_z$ are noticeably transiently amplified (see Fig. 1). The most amplified perturbations are streamwise uniform ($\alpha = 0$) and correspond to streamwise streaks originated by streamwise vortices. We have computed the maximum transient growth of the (most amplified) streamwise uniform ($\alpha = 0$) perturbations for a set of Reynolds numbers Re_{δ_*} extending from 1000 to 60000 (where Re_{δ_*} is the Reynolds number based on the free-stream velocity U_e and the displacement thickness δ_*). The results are reported in Fig. 1. For sufficiently large Reynolds numbers (roughly $Re_{\delta_*} > 1500$) two distinct peaks of locally higher growth $G_{max}(\lambda_z, \lambda_x = \infty)$ exist. The growth corresponding to the primary peak increases with Re_{δ_*} . The corresponding optimal perturbations consist in very large scale structures with a spanwise wavelength of the order of 8δ , but perturbations with scales between ≈ 3 and $\approx 20\delta$ are also strongly amplified. The optimal vortices are centred near the edge of the boundary layer. The associated optimal streaks spread into the whole boundary layer (see Fig. 2(b)), scale in outer variables in the outer region and in wall units in the inner region of the boundary layer, there being proportional to the mean flow velocity. These outer streaks therefore protrude far into the near wall region, having still 50% of their maximum

amplitude at $y^+ = 20$. The moderate growth associated to the secondary peak is essentially independent of Re_{δ_*} and is shifted to larger β (smaller λ_z) when Re_{δ_*} is increased. The secondary peak exactly scales in inner units and that it is attained for $\lambda_z^+ \approx 100$ ($\lambda_z^+ = 81.6$ in this case) exactly like for the turbulent Poiseuille flow case [3, 11]. This inner peak is associated with optimal structures corresponding to the most probable streaks and vortices observed in the buffer layer (see Fig. 2(a)). The existence of two different peaks for the optimal growth with an outer-scaling peak whose amplitude increases with the Reynolds number and with the distance from the wall is furthermore compatible with the experimental results of [6] and [10] among others.

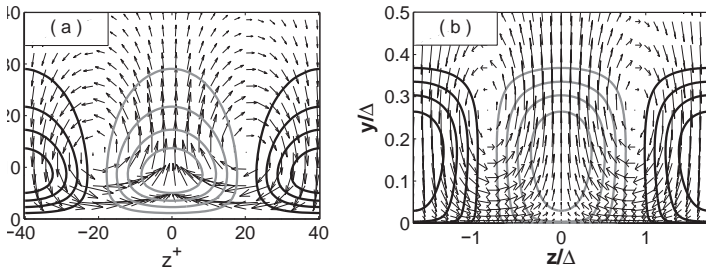


Fig. 2. Cross-stream view of the $v-w$ component of the optimal initial vortices (arrows) and of the u component of the corresponding maximally amplified streak (contour-lines) for $\alpha = 0$. (a) the secondary peak optimal is plotted in internal units while (b) the primary peak optimal is plotted in external units. Black contours represent positive u while grey contours represent negative u .

A still open question is the one of the relation existing between the optimally amplified streaks and the large-scale coherent streaks measured in experiments and in direct numerical simulations. The optimal perturbation approach provides a measure of the maximum amplification of streaks with given streamwise and spanwise scales but this amplification is only part of more complicated processes leading to the ‘refuelling’ of the vortices that induce the streaks. The secondary instability of the streaks is for instance primordial to generate streamwise non-uniform perturbations leading to the refuelling of the quasi-streamwise vortices in the models of self-sustained turbulent cycles [5, 12]. These additional processes select particular streamwise and spanwise scales in the flow. The self-sustained scales that are actually observed, are therefore selected by all the different mechanisms embedded in the self-sustained process. For the turbulent Poiseuille [3, 11] and Couette [7] the optimal spanwise wavelength corresponding to the primary peak correspond well to the sizes of the observed large scale coherent structures, but in the present turbulent boundary layer case the optimal scale ($\lambda_z \approx 8\delta$) is larger than the scale ($\lambda_z \approx \delta$) actually observed for the coherent large-scale streaks [8] denoting an important difference between these situations. Even

if the actual reason for this different behaviour is not actually clear, it could well be that in the turbulent Couette and Poiseuille flows, the scale selection of self-sustained large scale structures from the additional processes is weak and therefore the lift-up selection is the one dominating in the end, while this is not the case for the turbulent boundary layer. It could also be however that very large scale structures have simply not been measured with large enough acquisition windows in the turbulent boundary layer case. Extensive investigations are currently under way on all these issues.

Even if open questions remain about scale selection of ‘unforced’ large-scale streaks, the present results may have some relevance in applications where large-scale, streamwise uniform streaks would be artificially forced in the boundary layer. In that case, our results predict that streamwise uniform structures with spanwise wavelength ranging roughly from ≈ 3 to $\approx 30\delta$ would be the most amplified. The induced large scale streaks would then be felt in all the boundary layer.

References

1. C. Cossu and L. Brandt. Stabilization of Tollmien-Schlichting waves by finite amplitude optimal streaks in the Blasius boundary layer. *Phys. Fluids*, 14:L57–L60, 2002.
2. C. Cossu, G. Pujals, and S. Depardon. Optimal transient growth and very large scale structures in turbulent boundary layers. *J. Fluid Mech.*, 619:79–94, 2009.
3. J. C. del Álamo and J. Jiménez. Linear energy amplification in turbulent channels. *J. Fluid Mech.*, 559:205–213, 2006.
4. J. Fransson, A. Talamelli, L. Brandt, and C. Cossu. Delaying transition to turbulence by a passive mechanism. *Phys. Rev. Lett.*, 96:064501, 2006.
5. J.M. Hamilton, J. Kim, and F. Waleffe. Regeneration mechanisms of near-wall turbulence structures. *J. Fluid Mech.*, 287:317–348, 1995.
6. M. H. Hites. *Scaling of high-Reynolds number turbulent boundary layers in the National Diagnostic Facility*. Ph. D. Thesis, Illinois Inst. of Technology, 1997.
7. Y. Hwang and C. Cossu. Optimal amplification of large scale streaks in the turbulent couette flow. In *same proceedings*, 2009.
8. J. Jiménez. Recent developments on wall-bounded turbulence. *Rev. R. Acad. Cien. Serie A Mat.*, 101:187–203, 2007.
9. P. A. Monkewitz, K. A. Chauhan, and H. M. Nagib. Self-consistent high-reynolds-number asymptotics for zero-pressure-gradient turbulent boundary layers. *Phys. Fluids*, 19:115101, 2007.
10. J. M. Österlund, A. V. Johansson, H. M. Nagib, and M. H. Hites. Spectral characteristics of the overlap region in turbulent boundary layers. In *Extended abstract to Intl Congr. Theor. Appl. Math.*, Chicago, 2000.
11. G. Pujals, M. García-Villalba, C. Cossu, and S. Depardon. A note on optimal transient growth in turbulent channel flows. *Phys. Fluids*, 2009. In press.
12. F. Waleffe. Hydrodynamic stability and turbulence: Beyond transients to a self-sustaining process. *Stud. Appl. Math.*, 95:319–343, 1995.

Time-mean description of turbulent bluff-body separation in the high-Reynolds-number limit

B. Scheichl^{†*}, A. Kluwick[†], and F. T. Smith[‡]

[†]Institute of Fluid Mechanics and Heat Transfer, Vienna University of Technology, A-1040 Vienna, Austria,

^{*}Austrian Center of Competence for Tribology, A-2700 Wiener Neustadt, Austria,

[‡]Department of Mathematics, University College London, London WC1E 6BT, UK
bernhard.scheichl at tuwien.ac.at

1 Motivation

A most reliable prediction of the position of time-mean gross separation of incompressible turbulent boundary layer (BL) flow from the smooth impervious surface of a rigid and more-or-less blunt body not only still defies theoreticians but, needless to say, is also of great interest from an engineering point of view. The undeniable vital progress in computational techniques made in the recent past does not master this challenge presently in the form of sufficiently accurate solutions of the full (unsteady) Navier–Stokes equations. This is largely due to the fact that for practical applications, e.g. in aerodynamics, the relevant Reynolds numbers are still too high to be dealt with adequately.

It is desirable to gain a profound insight into two fundamental aspects, constituting the core problem: (i) the behaviour of the nominally two-dimensional and steady flow in the vicinity of separation, and (ii) how the local theory, describing (i), fits into the global picture of the flow past the obstacle under consideration. In the following, all flow quantities are non-dimensional, respectively, with the speed \tilde{U} of the unperturbed oncoming uniform flow, a typical body dimension \tilde{L} , the (constant) kinematic fluid viscosity $\tilde{\nu}$, and the (constant) fluid density. As the basic assumption, the globally formed Reynolds number $Re := \tilde{U}\tilde{L}/\tilde{\nu}$ takes on arbitrarily large values. In the first instance, analytical methods, such as matched asymptotic expansions, then provide the appropriate means of choice to establish a rational theory.

The asymptotic splitting of the initially attached turbulent BL in the limit $Re \rightarrow \infty$ that aims at a local description of the separation process has already been tackled by other researchers; for references and discussion of the, as we feel, apparent formal shortcomings of these approaches see [1, 2]. As demonstrated in [3, 4], a fully self-consistent flow structure that provides a match of the BL region with the (asymptotically small) region of pronounced laminar–turbulent transition near the leading edge of the obstacle essentially

agrees with the well-known picture of a two-tiered turbulent BL: it consists of a fully turbulent outer main region that exhibits a small defect of the streamwise velocity component u with respect to its value u_e imposed by the external potential flow and where the Reynolds shear stress dominates over its viscous counterparts, and the viscous wall layer, where both are of comparable magnitude. However, here that classical asymptotic structure is relaxed insofar as also to account for “underdeveloped” turbulence, i.e. for a BL having a level of turbulence intensity below that referring to fully developed turbulence.

The asymptotic concept which allows for describing this type of a “transitional” BL on the basis of the time- or Reynolds-averaged Navier–Stokes equations, i.e. the Reynolds equations, was originally proposed in [1]. In its form adopted here, two perturbation parameters are employed: a measure for the velocity defect, ϵ , and one, δ , for the BL thickness. By setting $\gamma := 1/\ln Re$, we deal with “underdeveloped” turbulent flow if $\delta \ll \gamma \ll \epsilon \ll 1$, which eventually assumes its fully developed form if both δ and ϵ are of $O(\gamma)$. However, as has been pointed out recently in [3, 4], the process of laminar–turbulent transition provides a source of hampering the BL from becoming a fully developed turbulent one. Self-consistency is confirmed by considering the local asymptotic splitting of the BL close to separation: a rigorous description of the locally strong viscous/inviscid interaction process requires the v. Kármán number δ^+ , namely, the ratio of the inner and the outer layer thicknesses, to vary merely algebraically with Re rather than exponentially, as in the limiting classical case. The detailed analysis in [4] of a turbulent BL evolving from the leading edge towards the location of separation indicates that the first situation applies by considering a specific distinguished double limit $\epsilon \rightarrow 0$, $\delta/\epsilon \rightarrow 0$ as $Re \rightarrow \infty$, determining the maximum turbulence intensity level possible.

To be more precise, turbulent separation is found to be associated with a quite complex interplay of an “outer” and an “inner” mechanism of local viscous/inviscid interaction. Below we present some recent results regarding the former mechanism, which is of paramount importance for the understanding of the drastic change of the flow in the wall layer as it undergoes separation, governed by the “inner” interaction. Here we only note that the latter gives rise to a novel internal triple-deck structure, detected at the base of the BL.

2 Asymptotic picture of the flow near separation

We analyse the flow in the vicinity of the point \mathcal{O} where in the inviscid limit $Re \rightarrow \infty$ the irrotational free-stream flow separates tangentially from the body surface, cf. Fig. 1 (a): here x , y , ψ , p denote natural coordinates along and perpendicular to the body surface, respectively, with origin in \mathcal{O} , the stream function, and the pressure. We write $[\psi, p] \sim [\psi_0, p_0](x, y) + O(\epsilon\delta)$, $Re \rightarrow \infty$, so that the subscript 0 indicates the inviscid-flow limit. It is characterised by the free streamline \mathcal{S} that separates the oncoming irrotational flow from a cavity or an inviscid backflow eddy in the slipstream of the body for $x > 0$.

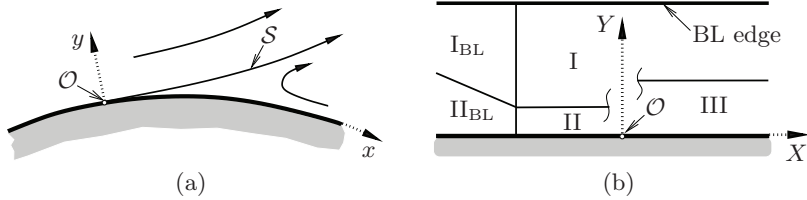


Fig. 1. (a) global situation: arrows on streamlines (*solid*) indicate flow direction, (b) local splitting of small-defect tier: regions I_{BL} , II_{BL} refer to incident BL flow.

Close to \mathcal{O} , the potential flow is conveniently described in terms of polar coordinates $r := (x^2 + y^2)^{1/2}$, $\theta := \arctan(y/x)$, $\pi \geq \theta > 0$, cf. [3, 4]:

$$\psi_0/u_{\mathcal{O}} \sim r \sin \theta + \hat{\psi}(r, \theta) + O(r^2), \quad \hat{\psi} := -(4k/3)r^{3/2} \cos(3\theta/2), \quad r \rightarrow 0. \quad (1)$$

Herein, $u_{\mathcal{O}}$ denotes the value of the surface speed $u_e = \partial_y \psi_0|_{y=0}$ at \mathcal{O} , and the value of the positive parameter k depends on the a priori unknown position of \mathcal{O} and measures the strength of the well-known Brillouin–Villat (BV) singularity there, expressed by (1). Accordingly, $u_e/u_{\mathcal{O}} \sim 1 + 2k(-x)^{1/2} + O(-x)$, $x \rightarrow 0_-$. For $x \rightarrow 0_+$, the expansion (1) breaks down passively for $y = O(y_S)$ such that $x, y_S \sim (4k/3)x^{3/2} + O(x^{5/2})$ gives the position of \mathcal{S} where $\psi_0 = 0$.

For the subsequent considerations we refer to Fig. 1 (b). The analysis carried out in [4] indicates that in the outer tier of the BL $\partial_y p_0$ and $\partial_x p_0$ become of the same order of magnitude when $x = O(\delta)$ and, consequently, the conventional BL approximation ceases to be valid. In addition, the BL thickness is found to remain of $O(\delta)$ there (region I). We introduce suitable local variables $[X, Y, \Psi] := [x, y, \psi/u_{\mathcal{O}}]/\delta$. Inspection of the Reynolds equations and matching the asymptotic representations of the velocity defect in the oncoming BL and in region I then shows that in the latter the expansion

$$\Psi \sim Y + \delta^{1/2} \Psi_{ir,1}(X, Y) + \epsilon \Psi_{BL}(Y) + \delta \Psi_{ir,2}(X, Y) + \epsilon \delta^{1/2} \Psi_{rot}(X, Y) + O(\epsilon \delta) \quad (2)$$

holds. It describes a predominantly inviscid flow: the Reynolds stresses are of $O(\epsilon \delta)$ and thus only affect terms of the same magnitude in (2). Furthermore, the subscripts “ir” and “rot” in expansion (2) refer to contributions that account for, respectively, the imposed irrotational flow and induced rotational flow: the latter results from the interaction of the external potential flow with the locally “frozen” velocity defect of the oncoming BL, captured by the term of $O(\epsilon)$ in (2). It comprises the celebrated logarithmic law of the wall,

$$\Psi_{BL} \sim \kappa^{-1} Y \ln Y + cY + O(Y^2 \ln Y), \quad Y \rightarrow 0, \quad (3)$$

where κ denotes the v. Kármán and c a further (flow-dependent) constant.

By substitution of (2) into the Reynolds equations and elimination of the pressure in standard manner one readily obtains $\Delta \Psi_{ir,1} = 0$, $\Delta := \partial_{XX} + \partial_{YY}$. Let $\Psi^*(X, Y) := \Psi_{ir,1} - \hat{\psi}(R, \theta)$, $R := (X^2 + Y^2)^{1/2}$, with $\theta = \arctan(Y/X)$ according to (1), such that $\Delta \Psi^* = 0$. Hence, matching with the attached

portion of the near-wall flow demands $\Psi^*(X, 0) = 0$ for $X \leq 0$. Moreover, $\Psi^* = o(R^{3/2})$ as $R \rightarrow 0$, since the BV singularity can only be avoided by taking into account viscous/inviscid interaction if the representation of the Euler flow near \mathcal{O} is not more singular than in the non-interactive case. Finally, we consider the irrotational velocity perturbations provoked in the ambient free-stream flow: consistency of their pressure feedback in the oncoming BL with the original small-defect structure of the latter requires $\delta^{3/2}\Psi^* = o(\delta^2)$ for $r = O(1)$, giving $\Psi^* = o(R^{-1/2})$ as $R \rightarrow \infty$. One then infers from the above properties of Ψ^* , by adopting methods of potential theory, that $\Psi^* \equiv 0$, i.e. $\Psi_{\text{ir},1} = \hat{\psi}(R, \theta)$. In turn, exploitation of the Reynolds equations and the conditions of matching with the oncoming flow yields the crucial result that the turbulence-induced inviscid vortex flow is governed by the Poisson equation

$$\Delta\Psi_{\text{rot}} = -\Psi_{\text{BL}}'''(Y)\hat{\psi}(R, \theta), \quad Y > 0. \quad (4)$$

The investigation of (4) reveals a contribution adding to the logarithmic portion of the velocity profile given by (3) upstream of separation, which is superseded by a stronger singular behaviour immediately downstream:

$$Y \rightarrow 0: \quad \Psi_{\text{rot}} \sim 2\kappa^{-1}k \begin{cases} [(-X)^{1/2}Y \ln Y] + O(Y), & X < 0, \\ X^{3/2} \ln Y + O(Y \ln Y), & X > 0. \end{cases} \quad (5)$$

For $X < 0$, in the wall layer u varies quite rapidly with u_e according to $u/u_e \sim \epsilon u^+(y^+) = O(1)$, $y^+ := Y/\delta^+$, with $u^+ \sim \kappa^{-1} \ln y^+ + O(1)$, $y^+ \rightarrow \infty$; see [4]. The apparent mismatch with region I requires the introduction of the sublayer II where $Y = O(\delta)$. On the other hand, for $X > 0$ the separated-flow region III where $Y = O(\delta^{3/2})$ has to be considered. Note that the asymptotic structure outlined so far closely resembles that of the turbulent BL flow past the trailing edge of an inclined flat plate in uniform stream, studied first in [5].

3 Current research and further outlook

The gradual transition between the two limiting forms given in (5) is analysed by considering the behaviour of Ψ_{rot} in the limit $R \rightarrow 0$, θ kept fixed. Once found, this determines the extent of a further region close to \mathcal{O} , which is of salient importance for the understanding of the conversion of region II into region III and accounts for the “inner” (nonlinear) interaction process. Most important, the latter is expected to fix the dependence of ϵ and δ on Re .

References

1. A. Neish and F. T. Smith, *J. Fluid Mech.*, **241**, 443 (1992).
2. B. Scheichl and A. Kluwick, *J. Fluids Struct.*, **24**(8), 1326 (2008).
3. B. Scheichl, A. Kluwick, and M. Alletto, *Acta Mech.*, **201**(1-4), 131 (2008).
4. B. Scheichl and A. Kluwick, AIAA paper 2008-4348 (2008).
5. R. E. Melnik and R. Chow, NASA Technical Report 1-12426 (1975).

Isotropic Free-stream Turbulence Promotes Anisotropy in a Turbulent Boundary Layer

S. Torres-Nieves¹, B. Brzek¹, J. Lebrón¹, R.B. Cal², H.S. Kang³, C. Meneveau³, and L. Castillo¹

¹ Rensselaer Polytechnic Institute, Troy, NY, 12180, USA torres@rpi.edu

² Portland State University, Portland, OR, 97207, USA

³ The Johns Hopkins University, Baltimore, MD, 21218, USA

The study of how external conditions affect turbulent boundary layers is important since such effects are often present in common engineering applications. Earlier investigations on surface roughness have shown its effect on the mean velocity and Reynolds stress profiles. Similarly, the effects of free-stream turbulence have been well documented [1, 2, 3]. However, the results available until now are limited to low Reynolds numbers. Hence, the aim of this investigation is to study the effects of high free-stream turbulence on rough surface turbulent boundary layers, at relatively high Reynolds numbers. This investigation focused on the penetration mechanisms of free-stream turbulence into the boundary layer, identifying the length scales that dominate these mechanisms and studying the effects on the resulting turbulence anisotropy [4]. These effects will also be studied in turbulent boundary layers subject to favorable pressure gradients.

A 2D turbulent boundary layer experiment was performed over a smooth and a rough surface. The boundary layer developed over a 6.7m long flat plate, and measurements were taken using Laser Doppler Anemometry at two locations downstream of the leading edge ($L_1 = 3.15\text{m}$ and $L_2 = 4.76\text{m}$). For the rough cases, the flat plate was covered with a 24-grit continuous abrasive sheet. The rough surface is characterized by a roughness parameter, $k^+ \approx 53$, and measurements are performed at Reynolds numbers of up to $Re_\theta \approx 11,300$. The upstream turbulence was generated with an active grid (AG), resulting in free-stream turbulence levels of up to 6.2% and ratio of free-stream integral length-scale to boundary layer thickness, $\frac{L_\infty}{\delta_{99}}$, of up to 0.97.

Results show that, although significant augmentation of the streamwise Reynolds stress profiles is observed throughout the entire boundary layer, the increase due to free-stream turbulence in the Reynolds wall-normal and shear stress profiles is only seen in the outer part of the boundary layer (fig. 1). However, unlike the streamwise component, the wall-normal Reynolds stress feels the presence of the wall through the pressure field. Hence, as a result

of the nearly isotropic turbulence in the free-stream, there is a portion of the boundary layer, from $y/\delta_{95} \approx 0.07$ to 0.7 , that shows an increase in anisotropy. In order to quantify which turbulence length-scales contribute mostly to this trend, second order structure functions for velocity components u and v are examined at various distances from the wall. Figure 2 shows that the anisotropy created by adding nearly isotropic turbulence in the free-stream resides strictly in the largest scales of the flow, in a range between $r/\delta_{95} = 3$ and 10 , where r is a spatial separation.

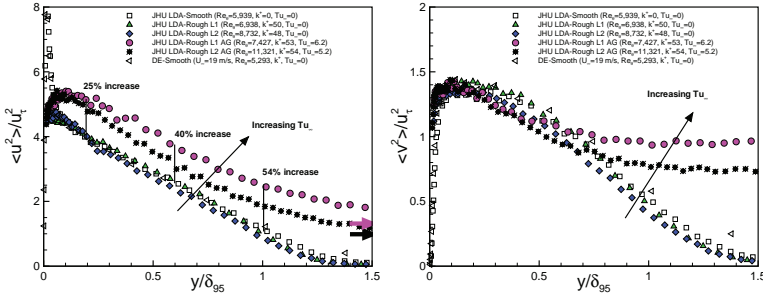


Fig. 1. Streamwise (left) and wall-normal (right) Reynolds stress profiles as function of y/δ_{95}

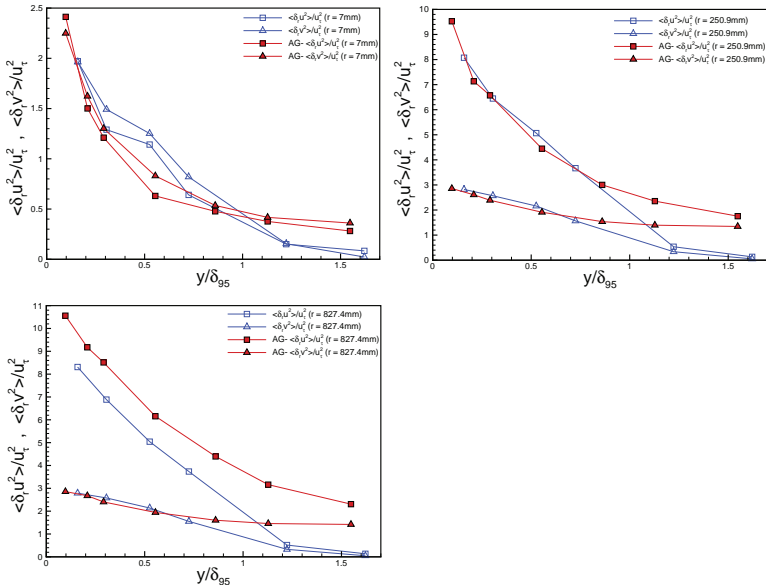


Fig. 2. Second order structure function versus y/δ_{95} , at fixed values of r (top left: $r/\delta_{95} \approx 0.07$; top right: $r/\delta_{95} \approx 3$; bottom: $r/\delta_{95} \approx 10$)

Moreover, LDA and, more recently, hotwire measurements were performed, under similar initial conditions, for a turbulent boundary layer subject to a favorable pressure gradient. The boundary layer developed over a 3.6m long, inclined plate, and measurements were taken using Laser Doppler Anemometry and hotwire anemometry, at two locations downstream of the leading edge ($L1= 1.7\text{m}$ and $L2= 2.7\text{m}$). For the rough cases, the plate was covered with the 24-grit continuous abrasive sheet and, with an upstream velocity of 10 m/s, the rough data is characterized by roughness parameters ($k^+ \approx 70$) in the transitionally rough regime. To generate the favorable pressure gradient, the plate was tilted at an angle $\alpha= 5^\circ$ with respect to the horizontal, resulting in an acceleration parameter, $K \approx 2 \times 10^{-7}$, that corresponds to a strong favorable pressure gradient. Measurements are carried out at $Re_\theta \leq 4,300$ and the active grid generated upstream turbulence results in FST levels of up to 7%.

Results for the favorable pressure gradient cases also show discrepancies between the behavior of the streamwise and wall-normal components of the Reynolds stresses when higher levels of free-stream turbulence are present. Streamwise Reynolds stress profiles show a significant augmentation due to free-stream turbulence, throughout the entire boundary layer. In the contrary, the increase in the Reynolds wall-normal and shear stress profiles is only seen in the outer part of the boundary layer (fig. 3). Future data analysis will examine second order structure functions for favorable pressure gradient turbulent boundary layers to understand the effect of adding nearly isotropic turbulence in the free-stream on the development of the boundary layer. Moreover, the energy spectrum, at various distances to the wall, will be analyzed to better explain the effects of surface roughness, pressure gradient and high levels of isotropic free-stream turbulence in the turbulent boundary layer.

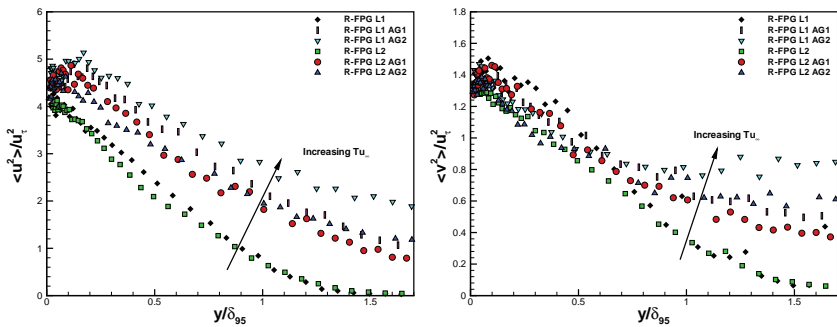


Fig. 3. Streamwise (left) and wall-normal (right) Reynolds stress profiles as function of y/δ_{95} for favorable pressure gradient, turbulent boundary layers

References

1. B. Stefes and H.H. Fernholz, Skin friction and turbulence measurements in a boundary layer with zero-pressure gradient under the influence of high intensity free-stream turbulence. *Euro. J. Mech. B/Fluids* **23**, 303318, 2005.
2. P.E. Hancock and P. Bradshaw, The effect of free-stream turbulence on turbulent boundary layers. *J. Fluids Eng.* **105**, 284289, 1983.
3. K.A. Thole and D.G. Bogard, High free-stream turbulence effects on turbulent boundary layers. *J. Fluids Eng.* **118**, 276844, 1996.
4. B. Brzek, S. Torres-Nieves, J. Lebrón, R.B. Cal, C. Meneveau, and L. Castillo, Effects of free-stream turbulence on rough surface turbulent boundary layers. *J. Fluid Mech.*, accepted on March 2009.

Travelling waves in a straight square duct

M. Uhlmann¹, G. Kawahara² and A. Pinelli³

¹Institut für Hydromechanik, Universität Karlsruhe, 76131 Karlsruhe, Germany

²Department of Mechanical Science, Osaka University, 560-8531 Osaka, Japan

³Modeling and Numerical Simulation Unit, CIEMAT, 28040 Madrid, Spain

markus.uhlmann@ifh.uka.de

1 Introduction

Isothermal, incompressible flow in a straight duct with square cross-section is known to be linearly stable [1]. Direct numerical simulation, on the other hand, has revealed that turbulence in this geometry is self-sustained above a Reynolds number value of approximately 1100, based on the bulk velocity and the duct half-width [2].

Numerous non-linear equilibrium solutions have already been identified in plane Couette, plane Poiseuille and pipe flows [3, 4, 5], and their role in the transition process as well as their relevance to the statistics of turbulent flow have been investigated [6, 7, 8]. No non-linear travelling-wave solutions for the flow through a square duct have been published to date.

In the specific case of square duct flow, it can be anticipated that travelling wave solutions will help to shed further light on the origin of mean secondary flow, whose appearance has been linked to the near-wall coherent structures [2]. Here we will present results obtained by applying an iterative solution strategy to the steady Navier-Stokes equations in a moving frame of reference. In the absence of a “natural” primary bifurcation point, we resort to the method proposed by Waleffe [9], where streamwise vortices are artificially added to the base flow and forced against viscous decay, leading to streaks, which are in turn linearly unstable, feeding back into the original vortices. The non-linear solution is then continued back to the original problem, i.e. the unforced flow.

2 Numerical method

Our method is an extension of the classical spectral approach often used e.g. in plane channel flow [4]. Here we employ a primitive variable formulation. The dependent variables $\varphi = \{u, v, w, p\}$ are expanded as follows:

$$\varphi(\mathbf{x}, t) = \sum_{n=-N_x}^{N_x} \sum_{m=0}^{N_y-k^{(\varphi)}} \sum_{l=0}^{N_z-k^{(\varphi)}} \varphi_{nml} \phi_m^{(\varphi)}(y) \phi_l^{(\varphi)}(z) \exp(in\alpha(x - ct)), \quad (1)$$

where α is the streamwise wavenumber and c the (real-valued) phase speed and $i = \sqrt{-1}$. The functions $\phi^{(\varphi)}$ are modified Chebyshev polynomials which incorporate odd/even parities and—in the case of φ being a velocity component—the wall boundary conditions. The pressure field has two polynomial degrees less than the velocity field, i.e. $k^{(p)} = 2$ and $k^{(u_i)} = 0$. A Galerkin method is employed in the streamwise (Fourier) direction, and the collocation method is applied in the cross-stream (Chebyshev) directions. In our case, the collocation points for pressure are chosen as the *Gauss* points, i.e. pressure is staggered w.r.t. the usual *Gauss-Lobatto* grid used for velocity, thereby avoiding spurious pressure modes. The solution of the resulting non-linear algebraic system is performed via Newton-Raphson iteration; continuation is implemented by means of a standard arc-length procedure. The methodology has been validated by comparison with available data for plane channel flow [4]; our code also reproduces the linear results of [10] perfectly.

3 Results

Similar to what has been proposed in [9, 11] we construct the initial conditions for our non-linear procedure as a superposition of various ingredients: (i) the laminar base flow, (ii) streamwise rolls (taken as one of the least decaying eigenmodes of the Stokes operator on the square), (iii) the streaks induced by the rolls, and (iv) neutrally stable linear perturbations (with specific parities I to IV, according to the nomenclature of [1]) of the roll/streak flow. Contrary to [12] we have focused upon initial conditions constructed from roll/streak-instabilities with type-II and type-III parities. After continuing various initial fields towards a state with zero forcing we have obtained different families of travelling waves. In the following we will present results corresponding to the fourth Stokes mode and roll/streak-instabilities of type-II.

Figure 1(a) shows the perturbation energy of this solution family at various values for the streamwise wavenumber α . Figure 1(b) shows that these three curves are cutting the solution region near the two extremes in α (1.58 and 0.6) and around the center (1.0), with the lower wavenumbers leading to considerably higher perturbation energies. The smallest Reynolds numbers, however, are obtained close to $\alpha = 1$, for which this family yields $Re_{b,min} \approx 600$. Concerning the wall friction, it can be seen from the graph in figure 1(c) that values around and above the extrapolation from the turbulent regime are obtained for the travelling-waves with smaller streamwise wavenumber, with the lower branch yielding a flow near the laminar limit; for large wavenumbers, both upper and lower solution branch are only little removed from the laminar friction value. Figure 1(d) shows the energy of the secondary motion induced

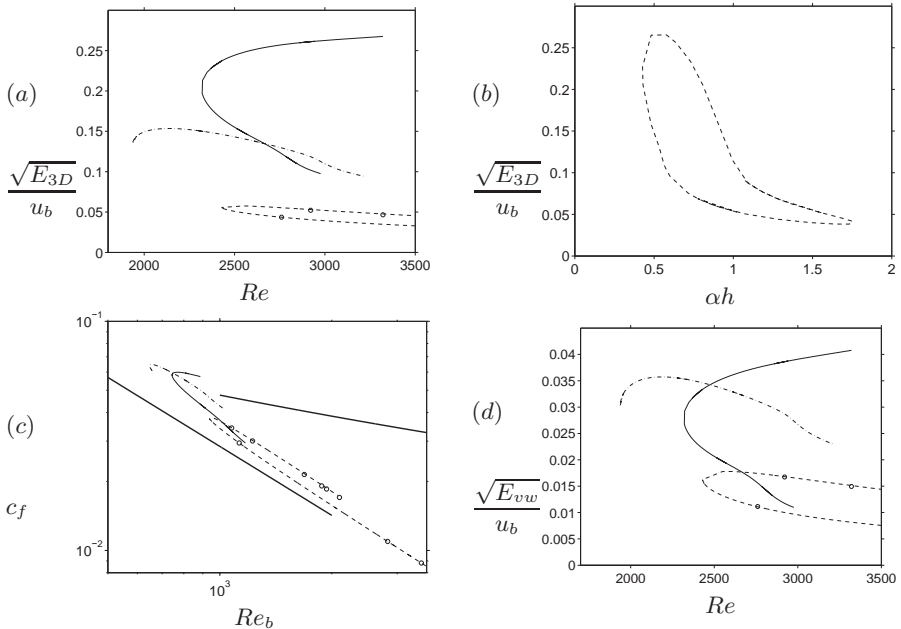


Fig. 1. Results for truncation levels $N_x = 2$, $N_y = N_z = 30$ (lines) and $N_x = 4$, $N_y = N_z = 32$ (symbols). In (a), (c), (d) the different lines correspond to wavenumber values: ----, $\alpha = 1.58$; - · -, $\alpha = 1.0$; —, $\alpha = 0.6$. E_{3D} is the total perturbation energy of the velocity field, excluding the streamwise constant mode; E_{vw} corresponds to the energy of the streamwise-averaged secondary flow. Whereas the other plots show continuation lines varying the value of the Reynolds number, the graph (b) shows a solution curve when varying α with fixed $Re = 3321$ (based on maximum base flow velocity). In (c) the thick straight lines indicate the friction factor for laminar and fully turbulent flow. Note that Re is the Reynolds number based upon the maximum laminar base flow velocity and duct half width.

by the travelling wave. As a comparison, in fully-turbulent flow at marginal Reynolds numbers ($Re_b \approx 1100$) we have measured an intensity of $\sqrt{E_{vw}}/u_b \approx 0.09$ [2], roughly twice as much as the largest value in figure 1(d). The shape of the streamwise averaged secondary flow is shown in figure 2(a), exhibiting eight streamwise vortices—similar to time-averaged turbulent flow. Figure 2(b) shows isosurfaces of the total streamwise velocity and of streamwise vorticity. The structure above an individual wall is very much alike the one obtained in a periodic cell of plane Poiseuille flow [9], with a single slightly undulating streak flanked by a pair of staggered streamwise vortices.

It can be concluded that the present family of travelling waves appears to be highly relevant to turbulent duct flow at low-Reynolds numbers. In fact, our solutions represent the first non-linear equilibrium state which exhibits eight-vortex secondary flow, and can therefore be expected to contribute to further

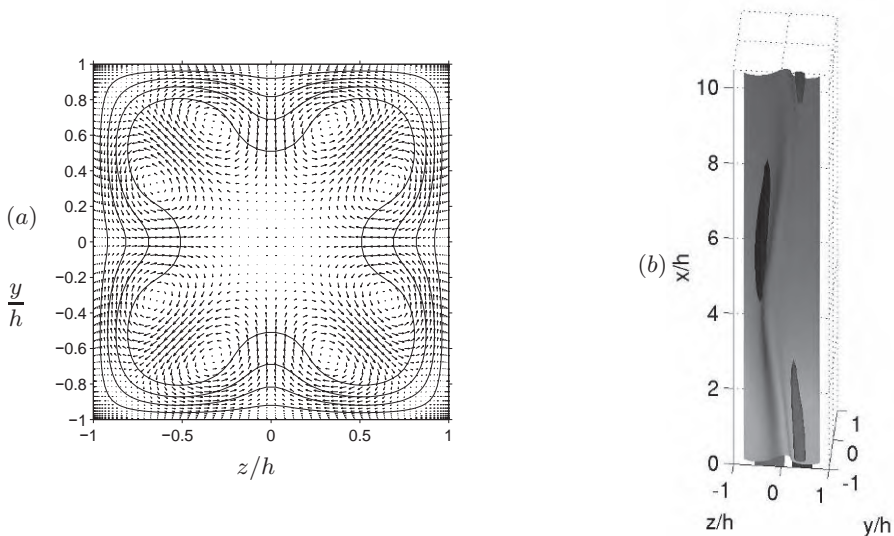


Fig. 2. Shape of a travelling wave on the upper branch at $Re_b = 760$ and $\alpha = 0.6$, having a phase speed of $c/u_b = 1.44$. (a) Streamwise averaged secondary flow vectors and primary flow contours; (b) isosurfaces of $u = 0.45 \max(u)$ (light grey sheet) and $\omega_x = \pm 0.3 \max(\omega_x)$ (dark grey tubes) shown above one wall, with the other three sectors (delimited by the cross-sectional diagonals) cut away for clarity.

the understanding of the generation mechanism of secondary flow. In order to establish a direct link with turbulence, however, an in-depth investigation of its dynamical properties needs to be carried out.

References

1. T. Tatsumi, T. Yoshimura: *J. Fluid Mech.* **212**, 437–449 (1990)
2. M. Uhlmann, A. Pinelli, G. Kawahara, A. Sekimoto: *J. Fluid Mech.* **588**, 153–162 (2007)
3. M. Nagata: *J. Fluid Mech.* **217**, 519–527 (1990)
4. U. Ehrenstein, W. Koch: *J. Fluid Mech.* **228**, 111–148 (1991)
5. H. Faisst, B. Eckhardt: *Phys. Rev. Lett.* **91**, (2003) art. 224502.
6. J. Jiménez, G. Kawahara, M. Siemens, M. Nagata, M. Shiba: *Phys. Fluids* **17**, 015105 (2005)
7. B. Eckhardt, T. Schneider, B. Hof, J. Westerweel: *Annu. Rev. Fluid Mech.* **39**, 447–468 (2007)
8. J. Gibson, J. Halcrow, P. Cvitanović: *J. Fluid Mech.* **611**, 107–130 (2008)
9. F. Waleffe: *Phys. Fluids* **15**, 1517–1534 (2003)
10. M. Uhlmann, M. Nagata: *J. Fluid Mech.* **551**, 387–404 (2006)
11. H. Wedin, R. Kerswell: *J. Fluid Mech.* **508**, 333–371 (2004)
12. H. Wedin, D. Biau, A. Bottaro, M. Nagata: *Phys. Fluids* **20**, 094105 (2008)

Thermal boundary layers in turbulent Rayleigh-Bénard convection

R. du Puits, C. Resagk, and A. Theiss

Institute of Thermodynamics and Fluid Mechanics,
Ilmenau University of Technology, Ehrenbergstrasse 29, 98693 Ilmenau, Germany.
ronald.dupuits@tu-ilmenau.de

Summary. We report high-resolution local temperature measurements in the upper and the lower boundary layer of turbulent Rayleigh-Bénard (RB) convection in air ($Pr = 0.71$) complemented by local heat flux measurements at the surface of both horizontal plates. Two series of measurements were undertaken - a first one with fixed aspect ratio $\Gamma = 1.13$ and variable Rayleigh number $5 \times 10^5 < Ra < 10^{12}$ and a second one in which we varied the aspect ratio and kept the Rayleigh number constant. The primary purpose of the work is to preserve a comprehensive data set of the temperature field against which various phenomenological theories and numerical simulations can be tested. In our talk we show the mean temperature profiles $\vartheta_h(z)$ at the heating and $\vartheta_c(z)$ at the cooling plate. We demonstrate, that the corresponding profiles do not collapse even at low Rayleigh numbers and that the measured bulk temperature ϑ_b strongly deviates from the mean between the heating and the cooling plate $\vartheta_{b,t}$.

1 Introduction

Thermal convection is an ubiquitous type of flows in nature. This class of highly turbulent flows is characterized by very strong velocity and temperature fluctuations compared with their mean. For a systematic study of these flows the Rayleigh-Bénard (RB) system – a closed box with a heated bottom plate and a cooled top plate as well as adiabatic sidewalls – represents a well-defined model, which has been investigated in great detail in the past (see eg. [1, 2]). For a long time this system was considered as a symmetric problem as long as the applied temperature difference between both horizontal plates is small enough to satisfy the Boussinesq approximation. However, recent experimental, numerical, and theoretical works (see e.g. [3, 4]) showed that this assumption is not invariably justified. The authors of those works found that the temperature measured in the bulk of the RB cell ϑ_b deviates from the predicted mean between the heating and the cooling plate $\vartheta_{b,t} = 1/2(\vartheta_{hp} + \vartheta_{cp})$. Insights into a potential asymmetry of the temperature field close to both horizontal boundaries are still missing but those differences might be crucial for the scaling of the global heat transport through the cell.

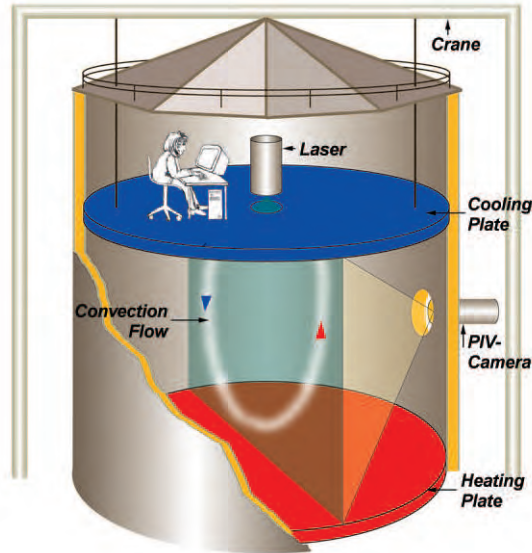


Fig. 1. Experimental facility: Sketch of the large scale RB facility ("Barrel of Ilmenau")

We present temperature measurements at a large-scale RB experiment simultaneously undertaken at the top and the bottom plate using ultra-small microthermistors with a size of $125 \mu\text{m}$. The convection apparatus - known as the "Barrel of Ilmenau" - is a cylindrical box with an inner diameter of $D = 7.15 \text{ m}$. It is filled with air ($Pr = 0.71$). An electrical heating plate at the bottom and a free hanging cooling plate at the top trigger the convective flow. Top and bottom plate are maintained at a very homogeneous temperature circulating water inside. The distance H between both plates can be adjusted between $0.05 \text{ m} < H < 6.30 \text{ m}$. In order to guarantee the adiabatic boundary condition at the sidewall the experiment is shielded with an electrical compensation heating system. In progress to our work in the past [5] the new measurements profit from several improvements of the experimental facility and the measurement technique:

- A new heating plate overlay has been installed in 2006 keeping the temperature deviations over its surface at less than $\pm 0.5 \text{ K}$ ($\pm 5 \text{ K}$ in the past). This is the same high quality of thermal boundary condition as the cooling plate already satisfied.
- Heating and cooling plate temperature were adjusted in a way that their mean has been kept constant at $T_b = 30^\circ\text{C}$ except for the highest Ra number of $Ra = 9.59 \times 10^{11}$.
- A new designed temperature sensor significantly improves the accuracy of the measurements particularly very close to the surface of the heating/ cooling plate.
- An independent heat flux sensor mounted at the surface of both plates near the temperature sensor simultaneously measures the local heat flux at the surface of the heating plate simultaneously to the temperature measurements.

This facility permits the investigation of highly turbulent RB convection in air in a parameter domain ranging from $Ra = 10^5$ ($\Gamma = D/H = 143$), $\Delta\vartheta = 4$ K to $Ra = 10^{12}$ ($\Gamma = 1.13$, $\Delta\vartheta = 60$ K). A sketch of the experimental facility is shown in figure 1. A more detailed description can be found in [5].

2 Experimental Results

In a first series of experiments we fixed the aspect ratio at the lowest possible value of $\Gamma = 1.13$ and we changed the Rayleigh number between $5 \times 10^5 < Ra < 10^{12}$ by the variation of the temperature difference applied to the heating and the cooling plate from $\Delta\vartheta = 2.4$ K to $\Delta\vartheta = 60$ K. We measured the profiles of the mean temperature $\bar{\vartheta}(z)$ simultaneously at both plates along the central axis of the convection cell. The measurements were undertaken using ultra-small microthermistors of a size of $s = 125 \mu\text{m}$. Each of them was mounted on a high precision positioning system and could be moved in steps of $\Delta z = 10 \mu\text{m}$. The measurements have been complemented by local heat flux measurements at the surface of both plates using commercial heat flux sensors of a size of 20 mm in diameter and about 1 mm in height. They were glued at the surface of both horizontal plates close to the temperature sensors. Applying Fourier’s law $q_d|_{z=0} = -\lambda(T)\partial T/\partial z$ they give an independent value of the local gradient of the mean temperature and permit to verify our temperature measurements particularly very close to the wall. A typical example of the obtained profiles of the normalized mean temperature $\Theta(z) = (\vartheta_{hp} - \vartheta(z))/(\vartheta_{hp} - \vartheta_{cp})$ at the smallest possible aspect ratio $\Gamma = 1.13$ and at a Rayleigh number of $Ra = 7.5 \times 10^{11}$ is plotted in figure 2.

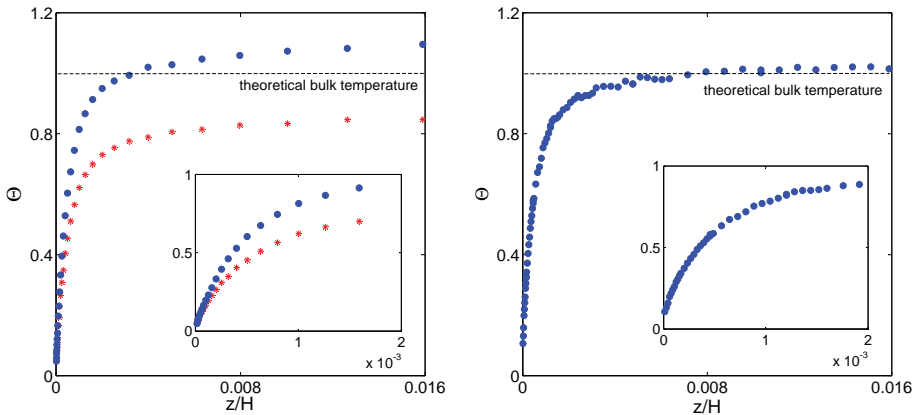


Fig. 2. Profiles of the normalized mean temperature $\Theta(z)$ near the heating (*) and the cooling (●) plate at $Ra = 7.5 \times 10^{11}$ and $\Gamma = 1.13$ on the left compared with our old measurements at the cooling plate on the right [5].

The graph clearly demonstrates the differences between the mean temperature profiles at the heating and the cooling plate and it also shows that the temperature

in the bulk deviates from the average between them. This observed asymmetry is in a good agreement with recently reported non-boussinesq effects found in RB convection in pressurized ethane [3]. While in that small-scale experiment only global quantities like Nusselt number or bulk temperature ϑ_b could be studied, we have also access to the local temperature field inside the boundary layers at both horizontal plates. In our talk we will discuss the typical shape of the mean temperature profiles, its fluctuations and its higher order moments. Furthermore we will analyze typical length scales and the relation between the global and the local heat transport and how this all depends on Rayleigh number and aspect ratio.

References

1. Castaing, B., Gunaratne, G., Heslot, F., Kadanoff, L., Libchaber, A., Thomae, S., Wu, X.-Z., Zaleski, S., Zanetti, G.: Scaling of hard thermal turbulence in Rayleigh-Bénard convection. *J. Fluid Mech.* **204**, 1-30 (1989).
2. Siggia, E. D.: High Rayleigh Number Convection. *Annu. Rev. Fluid Mech.* **26**, 137-168 (1994).
3. Ahlers, G. Araujo, F. F., Funfschilling, D., Grossmann, S.; Lohse, D.: Non-Oberbeck-Boussinesq Effects in Gaseous Rayleigh-Bnard Convection. *Phys. Rev. Lett.* **98**, 054501 (2007).
4. Sun, C., Cheung, Y.-H., Xia, K.-Q.: Experimental study of the viscous boundary layer properties in turbulent RB convection. *J. Fluid Mech.* **605**, 79-113 (2008).
5. R. du Puits, C. Resagk, A. Tilgner, F. H. Busse, A. Thess. Structure of thermal boundary layers in turbulent Rayleigh-Bénard convection. *J. Fluid Mech.* **572**, 231-254 (2007).

DNS of turbulent transport of scalar concentration in various thermally stratified boundary layers

H. Hattori, S. Yamazaki and Y. Nagano

Department of Mechanical Engineering, Nagoya Institute of Technology,
Gokiso-cho, Showa-ku, Nagoya 466-8555, Japan
hattori at heat.mech.nitech.ac.jp

This paper presents phenomena involving the turbulent transport of concentration of passive contaminants in various thermally-stratified boundary layers by means of direct numerical simulation (DNS), because it is essential to know such detailed phenomena in a spatially-developing and buoyancy-affected boundary layer. The various thermally-stratified boundary layers have been simulated by DNS [1, 2]. The DNS of thermally-stratified boundary layers shows intriguing results, in which the counter-gradient diffusion phenomena (CDP) in turbulent momentum and heat transfer are observed in the strongly-stratified stable boundary layer (SSBL), i.e., Reynolds shear stress and the wall-normal turbulent heat flux indicate a negative sign despite the positive gradients of mean velocity and temperature. It is well-known that CDP disturb the transport of turbulent quantities due to reductions of the effective diffusivities for momentum, heat and passive contaminants. On the other hand, the transport phenomena of the unstable boundary layer (UBL) is also revealed in the DNS, in which an enhancement of near-wall turbulence is obviously shown in the UBL. Meanwhile, passive contaminants such as suspended particulate matter (SPM) and smog which lead to environmental deterioration infrequently occur in the natural environment, or environmentally-safe passive contaminants are utilized for various purposes in industrial machinery. Thus, passive contaminants must be controlled in various situations, it is important to know that the concentration of passive contaminants is transported in the thermally-stratified boundary layer. Therefore, in the present study, the turbulent transport phenomena of concentrations of passive contaminants in various thermally-stratified boundary layers are investigated and explored using DNS. Two cases of discharge methods for passive contaminants are carried out in the DNS. In the first case, passive contaminants are provided from the wall in a short region. In the second case, the contaminants are supplied at the outer region of the turbulent boundary layer. Thus, the transport phenomena of concentration of passive contaminants affected by the thermally-stratified

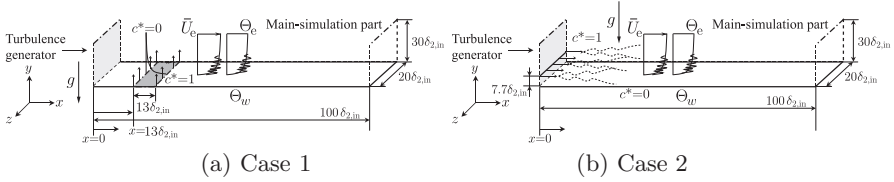


Fig. 1. Computational domain and coordinate system

turbulent boundary layer are investigated in detail. Also, the effects of Schmidt numbers are revealed in the present DNS.

In the present DNS, the transport equations for momentum, heat and passive contaminants as indicated below are solved using the high accuracy finite difference method [2], in which the Boussinesq approximation is approved for the Navier-Stokes equation. Thus, the thermal field affects the velocity field through the buoyant term, but the passive contaminants field does not influence the velocity field. The computational domain and coordinate system are shown in Fig. 1. The basic distributions of turbulent quantities in various thermally-stratified boundary layers are shown in Fig. 2, in which the characteristic distributions of turbulent quantities are revealed in detail. Thus, two cases of discharge methods are considered as follows: in the case 1, the near-wall turbulent transport phenomena of passive contaminants which are provided from the wall at the region between $x/\delta_{2,in} = 13$ and 26 are explored, where $\delta_{2,in}$ is the momentum thickness at the inlet of the driver part which generates turbulence of both the velocity and thermal fields. Since CDP occurs remarkably in the region in the case of SSBL, a passive contaminants is supplied from here so as to also investigate the effects of CDP for a concentration of passive contaminants. In the case 2, in order to investigate the transport phenomena of passive contaminants in the outer region of the turbulent boundary layer, the passive contaminants are discharged at $y/\delta_{2,in} = 7.7$ which is in the outer region of the turbulent boundary layer as indicated in

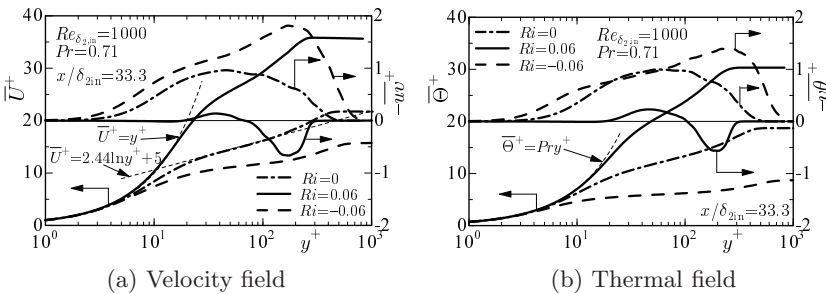


Fig. 2. Profiles of turbulent quantities in various thermally-stratified boundary layers

Fig. 1 (b). The basic parameters of the present DNS are: Reynolds number $Re_{\delta_2} = 1000$, Prandtl number $Pr = 0.71$ and Schmidt number $Sc = 1$. In order to reproduce a thermally-stratified boundary layer, bulk Richardson numbers, Ri_{δ_2} , are set at -0.06 for the unstable boundary layer (UBL), 0 for the neutral boundary layer (NBL), and 0.06 for the stable boundary layer (SBL). Also, in order to investigate the effect of the properties of passive contaminants, Schmidt numbers are changed for $Sc = 0.1$ and 2 . The boundary conditions of the concentration of passive contaminants are: $c^* = (C_e - c)/(C_e - C_r) = 1$ at the wall in case 1 and at the discharge point in case 2 and $c^* = 0$ at other points, where C_e is the concentration of the main stream, and C_r is the concentration of the reference point.

The results of the present DNS are shown in Figs. 4~6. Since passive contaminants are not provided from the wall in the downstream direction, the mean passive contaminants concentrations are observed to suddenly decrease in case 1. At $x/\delta_{2,\text{in}} = 33.3$, where the passive contaminants are not provided from the wall, a narrower region of turbulent flux of the concentration is observed in the SBL than in the region of NBL due to the appearance of CDP in the SBL. In the UBL of case 1, the concentration remarkably decreases in the downstream region, where the concentration almost vanishes, but the turbulent flux of the concentration remains in the boundary layer. In the case 2, a diffusing concentration is observed in the downstream region. In the NBL and SBL regions, the concentration distributes almost evenly to the outer and inner boundary layers. However, the disproportionate distribution of concentration is clearly observed in the UBL, because the wall-normal turbulent flux for concentration increases near the inner layer as indicated in Fig. 5(b). The effects of Schmidt numbers are also shown in Figs. 6(a) and (b). Obviously, in the case of a lower Schmidt number ($Sc = 0.1$), the concentration of passive contaminants distributes upward in the boundary layer.

As mentioned above, the phenomena involving in the turbulent transport of the concentration of passive contaminants in various thermally-stratified boundary layers are investigated in detail by means of DNS, in which different distributions of concentration are revealed by the various Richardson numbers of the flow fields and Schmidt numbers of the concentration field.

This study was partially supported by a Grant-in-Aid for Scientific Research (S), 17106003, from the Japan Society for the Promotion of Science (JSPS).

References

1. H. Hattori, M. Tagawa and Y. Nagano., Turbulent structures and modelling of specially developing thermally-stratified turbulent boundary layers, Proc. ETMM7, 175 (2008).
2. H. Hattori, T. Houra, and Y. Nagano, Direct numerical simulation of stable and unstable turbulent thermal boundary layers, Int. J. Heat and Fluid Flow, **28**, 1262 (2007).

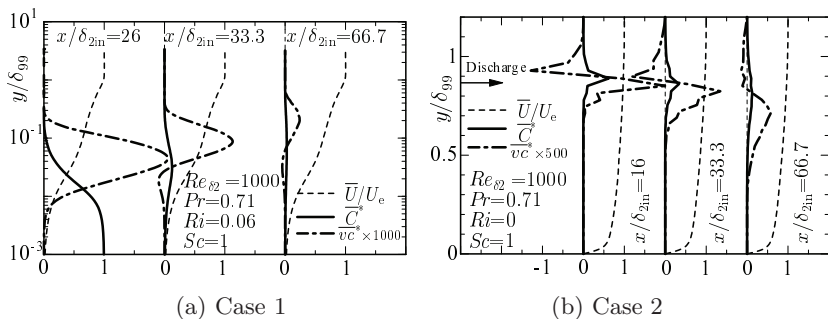


Fig. 3. Distributions of turbulent quantities of passive contaminants in neutral boundary layer ($Sc = 1, Ri = 0$)

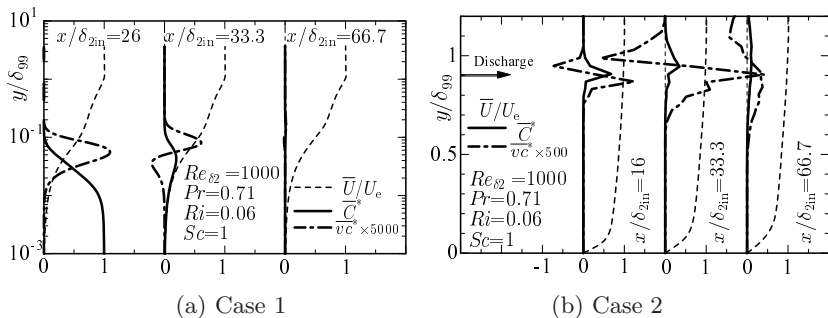


Fig. 4. Distributions of turbulent quantities of passive contaminants in stable boundary layer ($Sc = 1, Ri = 0.06$)

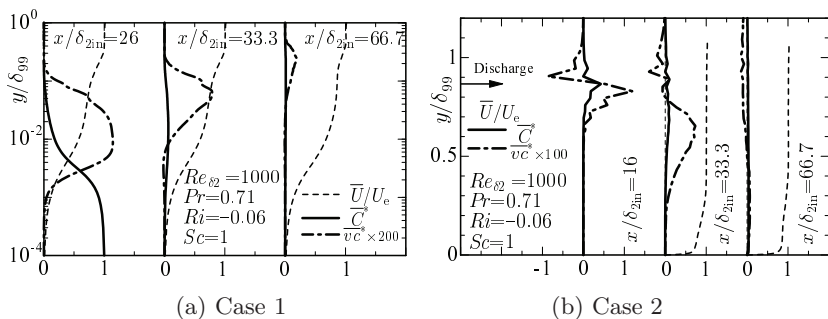


Fig. 5. Distributions of turbulent quantities of passive contaminants in unstable boundary layer ($Sc = 1, Ri = -0.06$)

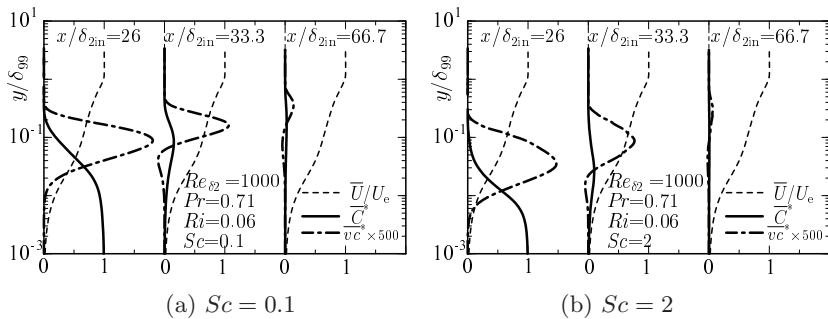


Fig. 6. Distributions of turbulent quantities of passive contaminants in various Schmidt numbers

Wall turbulence without walls

Yoshinori Mizuno¹ and Javier Jiménez^{1,2}

¹ School of Aeronautics, Universidad Politécnica de Madrid, 28040 Madrid, Spain

² Centre for Turbulence Research, Stanford University, CA 94305, USA

yoshi@torroja.dmt.upm.es, jimenez@torroja.dmt.upm.es

1 Introduction

The dynamics of the inner layer of wall turbulence are now fairly well understood[1]. The next target are the overlying outer layers, including the logarithmic layer. There is increasing evidence that those layers, which account for most of the flow thickness, are relatively independent of the near-wall region, mainly from rough- and active-wall experiments and simulations[2, 3], but it is unclear whether a physical wall is required for their canonical behaviour. On the other hand, this is an interesting physical question, and sets a baseline requirement for LES, because the buffer layer often has to be modelled differently from the rest of the flow.

Wall turbulence is a non-uniformly sheared flow characterised by length-scales that become larger away from the wall[4]. To test whether this is its fundamental feature, we present direct simulations (DNS) in which the wall at $y = 0$ is substituted by a boundary condition on a wall-parallel plane $y = y_b$. It mimics the scale gradient by rescaling and shifting the instantaneous velocity field of another interior ‘reference’ plane αy_b , where α is the rescaling factor. The rescaling implements the scale gradient of the real flow, and the shifting takes care of the different advection velocities of the reference and boundary planes. The procedure also conserves the appropriate Reynolds stress. In Fourier space,

$$u(k, \alpha y_b) \mapsto u(\alpha k, y_b) e^{i\alpha k \Delta X}, \quad (1)$$

where ΔX is a wall-parallel translation calculated by integrating in time the spatially-averaged velocity difference between the two planes, and k is the wavenumber. The layer $y < y_b$ is not simulated. Although written here in one dimension, (1) is applied to the two wall-parallel directions of every velocity component. The shifting transformation without rescaling had been previously used as a boundary condition for homogeneous shear[5].

2 Numerical experiment

We have simulated channel flows whose numerical box size is $L_x \times L_y \times L_z = 4\pi h \times 2h \times 2\pi h$, where the subscripts x and z stand for the streamwise and spanwise directions, by solving Navier-Stokes equation for the velocity (u, v, w) and pressure. Assuming homogeneity in x and z we enforce periodic boundary conditions in these directions, and employ the off-wall boundary technique mentioned above in $y \in (0.1h, 1.9h)$. Space discretisation is Fourier-spectral for x and z , and compact finite differences on a non-uniform grid for y . A third-order Runge-Kutta method is used for time marching. The number of the grid points is $N_x \times N_y \times N_z = 1536 \times 277 \times 1536$. The reference planes are placed at the positions separated by $0.1h$ from the boundaries, and the rescaling factor α is set to 2. The flows generated in this way reach statistical equilibrium. The friction velocity u_τ is estimated by extrapolating to $y = 0$ the value of the total shear stress. The friction Reynolds number is about 890, comparable to the DNS in [6] of a full channel flow at $Re_\tau = 934$. The grid spacings against the Kolmogorov length scale η in the resulting flow are $\eta < \Delta x (= 2\Delta z) < 3\eta$, and $1.1\eta < \Delta y < 1.5\eta$.

3 Results

To compare the statistics of the wall-less and full channels in a common frame, it is useful to shift the coordinate in y by an offset y_{off} , which is the origin of the logarithmic profile of the mean streamwise velocity U . It is obtained as the origin of a linear profile of $(dU/dy)^{-1}$ in the logarithmic layer. Though the channels with $Re_\tau \approx 900$ do not have logarithmic layers, their U exhibit a ‘logarithmic’ profile in the outer layers, and the offsets obtained from it are $y_{off} = 0.0266h$ and $-0.0596h$ for the wall-less and full channels. From numerical and experimental data [7, 8], the offset seems to scale in wall units in wall-bounded flows for high Reynolds numbers ($y_{off}^+ \approx -15$), while its Reynolds number dependence is still unclear in the wall-less channels. Using this offset, a new coordinate and scales are defined as,

$$y' = y - y_{off}, \quad u'_\tau = u_\tau(1 - y_{off}/h)^{1/2}, \quad h' = h(1 - y_{off}/h).$$

The resulting U in the two channels agree well, as shown in Fig.1(a). Under these coordinate and scales the fluctuation intensities are also in good agreement, apart from the region near the boundary, as shown in Fig.1(b).

Figure 2(a) shows the premultiplied one-dimensional spectrum of the wall-normal component v as a function of λ_z/h' and y'/h' , where λ_z is the wavelength in the spanwise direction. Around the reference plane, whose position is indicated by the dashed line, a linear dependence of the length-scale is realized. The spectrum above it agrees well with that in the full channel. The spectra for the other components are also in good agreement (not shown).

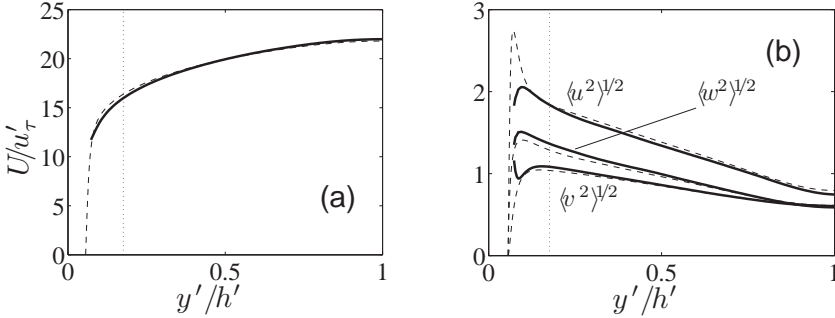


Fig. 1. (a) Mean streamwise velocity U normalized by u'_τ . Solid line, wall-less channel; dashed line, full (walled) channel. (b) Turbulent intensities normalized by u'_τ . Lines as in (a). Dotted lines indicate the position of the reference plane.

Below the reference plane, the spectra of the two channels disagree, because this range of the full channel is the buffer layer (in the shifted coordinate, the reference plane goes to $y^+ \approx 106$ in the full channel). One possible reason for the discrepancy in the statistics near the boundary is this mismatch of the length-scale gradient, as well as artifacts in the boundary condition. We are running a higher Reynolds number case to clarify this issue.

Inactive motions in the wall-parallel velocity components are a significant feature of wall turbulence[4]. Since they span the full flow width without changing their wall-parallel sizes, their spectra do not satisfy (1), and the rescaling destroys the inactive motions at the boundary. To which extent the inactive motions are modified by the rescaling can be observed in a spectrum of u integrated only over $4 < \lambda_x/h' < 7$ as representative of large-scale motions, which is shown in Fig.2(b). While large-scale modes extend to the buffer layer without changing their wall-parallel sizes in the full channel, they are blocked by the rescaling in the wall-less channel. However, this happens only below the reference plane, and the inactive motions survive above it. Therefore replicating the large-scale modes representing the inactive motions at the off-wall boundaries is not necessary for creating the outer layer.

The full channel has structures near the wall that are long in x and narrow in z . These modes are also observed in other channels, and found to be confined below $y^+ = 40$ [9]. These modes are absent in the wall-less channel, which does not include a buffer layer. They do not affect the outer layer, even though their length scale in x is comparable to the outer one.

4 Conclusions

We have performed DNS of turbulent channel flows without the near-wall region by using a new off-wall boundary technique. The new boundary condition mimics the inhomogeneity of the length-scale of the fluctuations in full

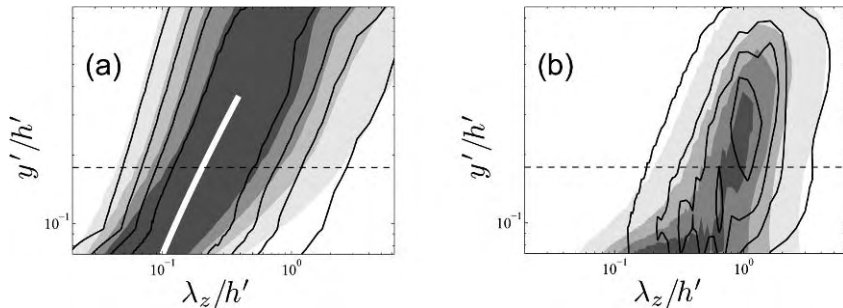


Fig. 2. (a) Premultiplied one-dimensional spectra of v as a function of λ_z/h' and y'/h' , normalized by the intensity at each height. Line contours, wall-less channel; Shaded contours, full channel. White line has the unit slope. (b) Premultiplied one-dimensional spectra of u as a function of λ_z/h' and y'/h' , integrated over the range of $4 < \lambda_x/h' < 7$, normalized by $u_\tau'^2$. Contours as in (a).

channel flows, and is able to maintain the sheared flow. The resulting statistics and spectra agree well with those in the outer layer of a full channel with comparable Reynolds number, using coordinates shifted and scales modified by an offset which is defined from the self-similar behaviour of the outer layers. In conclusion, the spatial length-scale gradient seems to be the essential ingredient that the outer layers of wall turbulence receive from the wall. Other contributions are smaller, in agreement with the weak dependence of the outer layer on the inner one, found in rough- and active-wall experiments and simulations.

This work is financially supported by the CICYT grant TRA2006-08226. YM is supported by the Spanish Ministry of Education and Science, under the Juan de la Cierva program.

References

1. J. Jiménez and R. D. Moser, *Phil. Trans. R Soc. London A*, **365**, 715 (2007).
2. J. Jiménez, *Ann. Rev. Fluid Mech.*, **36**, 173 (2004).
3. O. Flores and J. Jiménez, *J. Fluid Mech.*, **566**, 357 (2006).
4. A. Townsend, *The Structure of Turbulent Shear Flow*, 2nd ed. (Cambridge University Press, Cambridge 1976).
5. J. Jiménez, *CTR Ann. Res. Briefs*, Stanford, CA, 367 (2007).
6. J. C. del Álamo, J. Jiménez, P. Zandonade, and R. D. Moser, *J. Fluid Mech.* **500**, 135 (2004).
7. D. B. DeGraaff and J. K. Eaton, *J. Fluid Mech.* **422**, 319 (2000).
8. S. Hoyas and J. Jiménez, *Phys. Fluids*, **18**, 011702 (2006).
9. J. C. del Álamo and J. Jiménez, *Phys. Fluids* **15**, L41 (2003).

Turbulent flow and heat transfer in eccentric annulus

N.V. Nikitin¹, S.I. Chernyshenko² and H.L. Wang²

¹ Institute of Mechanics, Moscow State University, 1 Michurinsky prospect, 119899 Moscow, Russia

² Department of Aeronautics, Imperial College London, SW7 2AZ London, United Kingdom

hengliang.wang07@imperial.ac.uk

1 Introduction

An eccentric annular duct is a prototype element in a number of engineering applications. Numerous modeling and experimental efforts have been made to investigate the details of the flow field and heat transfer characteristics in such kind of ducts [1, 2, 3]. As for the turbulent flow in eccentric annular duct, it is interesting from a fundamental point of view since it presents an ideal model for investigating inhomogeneous turbulent flows, where the conditions of turbulence production vary significantly within the cross-section.

The present work aims to provide a DNS-based data of turbulent flow and heat transfer for the fully turbulent case, i.e. when the region of turbulent fluctuations occupies the entire duct's cross-section.

2 Research approach and methods

We consider non-isothermal flow of an incompressible viscous fluid through a straight duct which has an eccentric annular cross-section. The flow is governed by the Navier-Stokes and energy equations. The no-slip conditions and periodic boundary conditions are applied at the rigid duct's walls and in the streamwise z direction, respectively. The problem is solved using curvilinear bipolar coordinates (ξ, η) introduced in the cross-sectional plane of the duct. Direct Numerical Simulations (DNS) is the main investigation approach in this work. Numerical solution is obtained by using the method of Nikitin [4].

3 Results and discussions

The simulation was carried out at Reynolds number $Re = 8000$ for the duct with diameter ratio $r_1/r_2 = 0.5$ and eccentricity $e = 0.5$.

3.1 Law of the wall

The validity of the universal logarithmic mean-velocity distribution

$$U_z^+ = A \log d^+ + B \tag{1}$$

in eccentric annulus has been discussed in a number of investigations [3]. In our present simulation, the logarithmic distribution with constants $A = 2.65, B = 4.5$ is only visible in the wide gap for the outer profiles (Fig. 1). The logarithmic region in the inner profiles has a less steep slope. The corresponding constants are $A = 2.35, B = 5.5$. The set of nine normal-to-walls lines $\eta = \eta_j, j = 0, \dots, 8$ (η is the coordinate in the circumferential direction) chosen for the data presentation are equally spaced in the circumferential direction within the upper half of the cross-section.

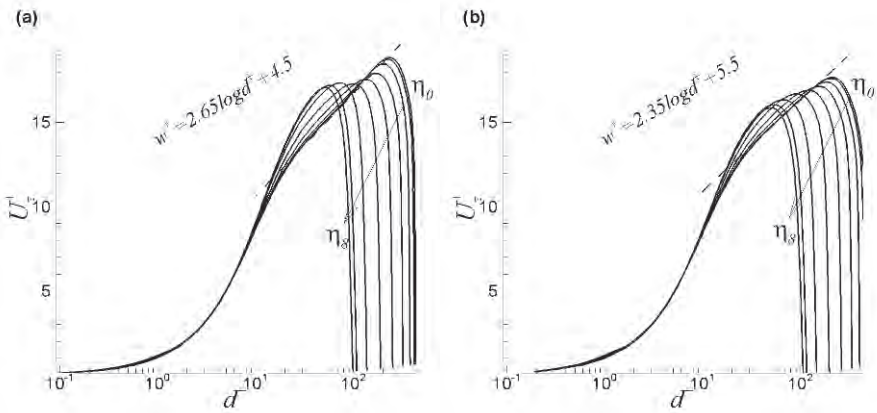


Fig. 1. Mean-velocity profiles. (a) outer profiles; (b) inner profiles.

3.2 Reynolds stress tensor

The components of the Reynolds stresses tensor are also investigated (Fig. 2). The shape of normal stress $\langle u'_z u'_z \rangle$ with maximum values in the near-wall region is fairly predictable in the most part of the duct cross-section. The shape of shear stress $\langle u'_\xi u'_z \rangle$ may be interpreted by considering wall-normal velocity fluctuations acting across the longitudinal mean-velocity gradient. Here, d is the distance measured along the line from the midpoint between the cylinder walls.

3.3 Secondary motion

Anisotropy of Reynolds stresses in the circumferential direction causes an appearance of a secondary motion in the cross-sectional plane of the duct. The

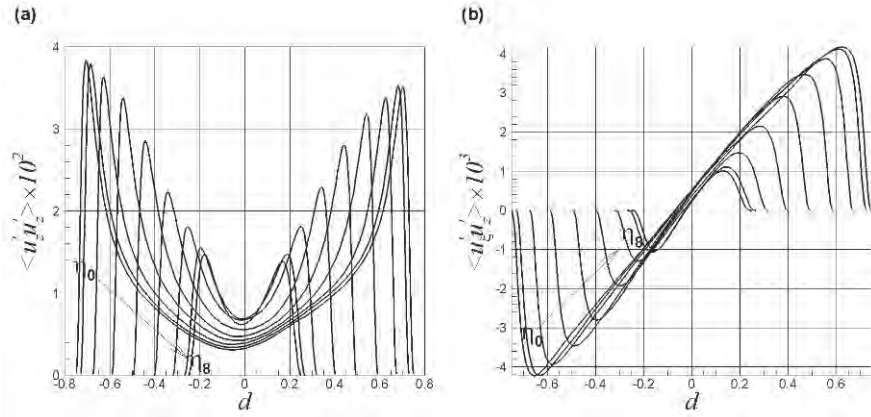


Fig. 2. Radial profiles of Reynolds stresses tensor components. (a) $\langle u'_z u'_z \rangle$; (b) $\langle u'_\xi u'_z \rangle$

streamlines of the secondary flows and its intensity are presented in Fig. 3. The maximum velocity in the secondary motion is about 1.5% of the bulk velocity in the flow and is attained in the vicinity of the inner wall. Here, the flow is statistically symmetric about the plane $y = 0$, therefore the lower-half distribution is not shown.

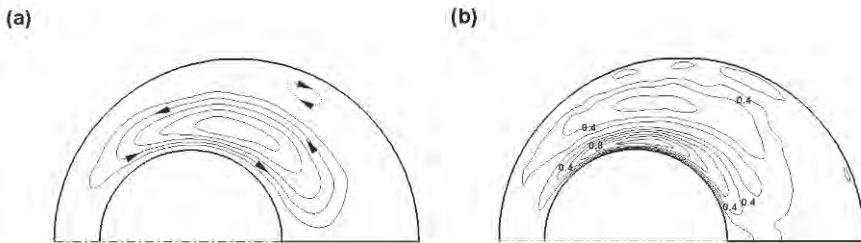


Fig. 3. Streamlines of secondary motion, (a), and its intensity $\sqrt{U_\xi^2 + U_\eta^2} \times 100$, (b). Solid and dashed streamlines correspond to a counterclockwise and a clockwise rotation, respectively

3.4 Intensity of the temperature fluctuations

As for each η_j , the temperature fluctuations (T_{rms} , which is $\langle T' T' \rangle^{\frac{1}{2}}$) in the wide-gap region are about two times larger near the inner wall than those near the outer wall (Fig. 4). This may suggest that the main mechanism of temperature fluctuations in the flow is the action of radial velocity fluctuations

across the mean temperature gradient which is twice more steep in the inner wall region than that in the outer wall one.

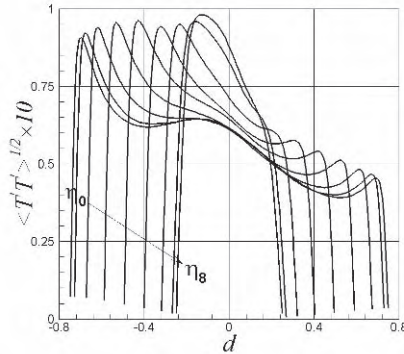


Fig. 4. Profiles of temperature fluctuations T_{rms} .

4 Conclusions and further Work

The present work has revealed some flow details which were not known from the experiment. A number of flow characteristics such as components of the Reynolds stress tensor, temperature-velocity correlation and some others were obtained for the first time for such kind of a flow. According to Nikitin [4], partly turbulent flow may exist in some geometrical configurations. In such kind of eccentric pipes, the region of a turbulent flow occupies the wide gap part and the region of a laminar flow occupies the narrow gap part. The analysis concerned with partly turbulent flow is going to be undertaken in future work.

References

1. DEISSLER, R.G. & TAYLOR, M.F., Analysis of fully developed turbulent heat transfer and flow in an annulus with various eccentricities. NACA TN, no. 3451 (1955).
2. DODGE, N.A., Friction losses in annular flow. The American Society of Mechanical Engineers, Paper no. 63-WA-11(1963).
3. JONSSON, V.K. & SPARROW, E.M., Experiments on turbulent-flow phenomena in eccentric annular ducts, J. Fluid Mech, **25**, 65-86 (1966).
4. NIKITIN, N., Direct simulation of turbulent flow in eccentric pipes, Comp. Maths Math. Phys, **46**, 489-504 (2006).

On imperfect hot-wire resolution issues and their effect on mean quantities

R. Örlü, J. H. M. Fransson and P. H. Alfredsson

Linné Flow Centre, KTH Mechanics, SE-100 44 Stockholm, Sweden
hal@mech.kth.se

1 Introduction

Spatial averaging when measuring small scale turbulence is a well known problem when using hot-wire anemometry. However the literature—despite a few well known and often cited studies—is rather inconclusive and incomplete, since spatial resolution effects can also be obscured by Reynolds number effects. As long as the sensing part of the hot-wire is sufficiently small and can respond to changes to the highest frequencies encountered in the flow, the measurements are believed to be free from spatial and temporal resolution issues.

Within the last decade there has been a renewed interest in high Reynolds number laboratory studies (see e.g. [1, 2]), due to the need to test asymptotic theories or scaling laws as well as to ensure that known phenomena at laboratory Reynolds numbers are representative for practical engineering situations. In order to make it possible to resolve the turbulent scales at high Reynolds numbers with the measurement techniques available today, large size facilities have to be set up (see discussion in Ref. [3]). The use of existing laboratory facilities to reach high Reynolds numbers by increasing the free stream velocity (U_∞) or the density (ρ) brings along a reduction of the viscous scale ($\ell_* = \mu/(\rho u_\tau)$, where μ and u_τ denote the dynamic viscosity and friction velocity, respectively). This increases the relative wire length when compared to the smallest scales. Since the sensing length can not be reduced *ad infinitum* in order to fulfil the requirements for well-resolved turbulence measurements [4], the effect of spatial resolution needs to be re-evaluated in the light of concurrent experiments in high Reynolds number wall-bounded flows.

Recently Hutchins *et al.* [5] studied the effect of spatial resolution on the streamwise turbulence intensity (u'^+) and spectral distribution in turbulent boundary layer flows and concluded that spatial attenuation is not—as usually assumed—restricted to the region adjacent to the near-wall peak in u'^+ , but rather a complex function of the inner-scaled wall distance (y^+) and hot-wire length (L^+), as well as the Reynolds number. An example of this is

the second peak in the u'^+ -distribution usually encountered in high Reynolds number wall-bounded flow experiments [1], which is unmasked as a symptom of spatial resolution rather than a new high Reynolds number phenomenon.

2 Motivation and Strategy

Reconciling, that a truncated skewed probability density distribution (pdf) alters the area under the pdf and recalling that the first moment, the mean, is nothing else than the centre of gravity of the described area, it can legitimately be questioned whether the mean remains unaffected under the influence of spatial averaging. The answer to this question is of considerable importance, especially in the light of the current debate regarding the proper scaling of the streamwise mean and rms velocity distribution in the overlap region.

In the following, newly performed zero-pressure gradient turbulent boundary layer experiments obtained in the MTL wind tunnel at KTH are analysed in the light of the above stated question. The set-up was similar, to the one used in [2], and comprised a 7 m long flat plate. The measurements were performed at downstream distances of 1.62 and 3.62 m from the leading edge by means of hot-wire anemometry and were supplemented by oil-film interferometry measurements in order to provide an independent measure of the skin friction.

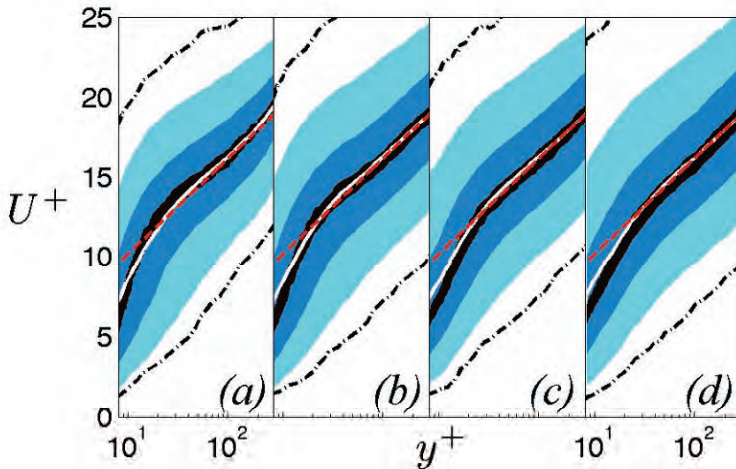


Fig. 1. Mean streamwise velocity in inner-scaled variables (white line) plotted on top of its pdf for (a) $L^+ = 15$ and $Re_\theta = 2532$, (b) $L^+ = 26$ and $Re_\theta = 8105$ (c) $L^+ = 46$ and $Re_\theta = 7561$, and (d) $L^+ = 61$ and $Re_\theta = 18661$. The three shaded areas indicate the confidence intervals for 3, 50 and 98.5 %, whereas the dash-dotted line gives the extreme values of the pdf. The log law with the von Kármán constant of 0.384 and an additive constant of 4.17 is shown through the dashed line.

3 Results and Discussion

As mentioned in the Introduction, Reynolds number and spatial resolution effects are interconnected whenever the Reynolds number is varied by means of U_∞ or ρ , since both change L^+ . It is usually assumed that the mean streamwise velocity is immune against spatial resolution effects and independent of the Reynolds number, as long as it is above a certain threshold value. Figure 1 displays, however, a different scenario. Here, U^+ vs. y^+ is shown above its pdf distribution within the inner region for varying Re_θ and L^+ values, where Re_θ is based on U_∞ and the momentum-loss thickness. While a clear deviation from a Gaussian pdf distribution is present in (a) below $y^+ = 100$, the deviation becomes smaller when successively decreasing the spatial resolution, i.e. for increasing L^+ and Re_θ in (b) to (d). While for (a) the mean velocity profile in the overlap region does not even extend to $y^+ = 300$, due to the low Reynolds number of $Re_\theta = 2532$, a successively longer part in inner-law scaling is covered for (b)–(d) and agrees nicely with the log law. The reason for the apparent differences can be sought within Reynolds number and/or spatial resolution effects. Note, that the subplots are sorted in order of increasing L^+ , and implicate therefore a dependence on spatial resolution effects. Particularly the plot in (b) is from a slightly higher Reynolds number than the one shown in (c), but was measured with a wire with a nearly half as large L^+ value. The comparison of these subplots therefore supports the view put forward by Johansson & Alfredsson [4], viz. that spatial resolution effects can overwhelm Reynolds number effects. Regardless of which of the two reasons

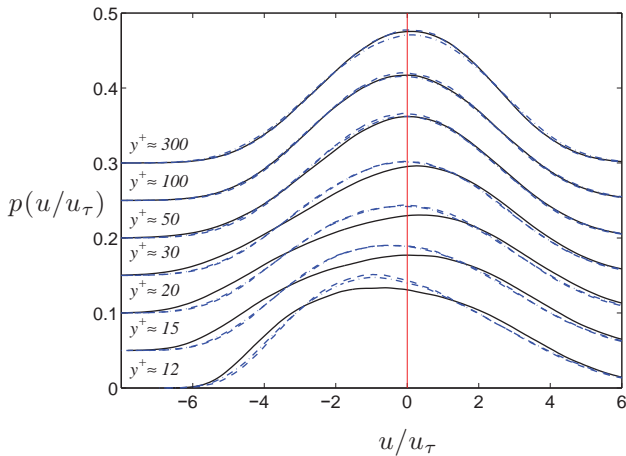


Fig. 2. Probability density distribution of the streamwise velocity fluctuations scaled by u_τ : solid ($L^+ = 26$, $Re_\theta = 8105$), dashed ($L^+ = 46$, $Re_\theta = 7561$), and dash-dotted ($L^+ = 46$, $Re_\theta = 8792$) line for different y^+ positions, each y^+ -position is shifted for visual aid by 0.05.

is the main cause, a subtle difference in the mean quantity compared to the log law is discernable.

A more quantitative assessment is given when comparing measurements with (fairly) matched Reynolds numbers, but differing L^+ , as shown in Fig. 2. Here the pdf is scaled by u_τ , rather than its rms value, since the latter is known to be reduced and would therefore mask spatial resolution effects. It is evident that the longer wires are especially insufficient when it comes to detect the low speed fluctuations and hence smooth out the highly non-Gaussian shape of the pdf within the buffer region. As apparent from the shift in the peak position of the pdf, the most effected region corresponds to the overshoot over the log law shown in Fig. 1.

4 Final Remarks

The present study found discernable differences within the pdf distribution of the streamwise velocity fluctuations when measured with $L^+ = 26$ and 46. These were in turn related to a weak reduction of U^+ within the buffer region. In this context it may also be of interest to ask the more philosophical question: since the mean value is in principle formed from the pdf of the fluctuating signal and if the fluctuating signal is not measured correctly, is it then possible to get the mean value correctly? The general answer to this question is *no*.

The present results show the importance of small L^+ and throw doubt on statements regarding the scaling of higher order moments or even the mean when based on hot-wire data with an order of magnitude longer wires than employed here (see e.g. [6]).

References

1. J. F. Morrison, B. McKeon, W. Jiang & A. J. Smits, Scaling of the streamwise velocity component in turbulent pipe flow. *J. Fluid Mech.* **508**, 99–131 (2004).
2. J. M. Osterlund, Experimental studies of zero pressure-gradient turbulent boundary layer flow. *Ph. D. thesis, KTH Mechanics, Stockholm, Sweden* (1999).
3. A. Talamelli, F. Persiani, J. H. M. Fransson, P. H. Alfredsson, A. V. Johansson, H. M. Nagib, J.-D. Rüedi, K. R. Sreenivasan, & P. A. Monkewitz, CICLoPE – a response to the need for high Reynolds number experiments. *Fluid Dyn. Res.* **41**, 021407 (2009).
4. A. V. Johansson & P. H. Alfredsson, Effects of imperfect spatial resolution on measurements of wall-bounded turbulent shear flows. *J. Fluid Mech.* **137**, 409–421 (1983).
5. N. Hutchins, T. B. Nickels, I. Marusic, & M. S. Chong, The influence of spatial resolution due to hot-wire sensors on measurements in wall-bounded turbulence. *16th Australasian Fluid Mechanics Conference, Gold Coast, Australia* (2007).
6. R. Zhao & A. J. Smits, Scaling of the wall-normal turbulence component in high-Reynolds-number pipe flow. *J. Fluid Mech.* **576**, 457–473 (2007).

The diagnostic plot - a new way to appraise turbulent boundary-layer data

P. H. Alfredsson¹, R. Örlü¹, T. Kurian¹, J. H. M. Fransson¹, A. Segalini²,
J.-D. Ruedi² and A. Talamelli^{1,2}

¹Linné Flow Centre, KTH Mechanics, S-10044 Stockholm, Sweden

²DIEM, Università di Bologna, 47100, Forlì, Italy

hal at mech.kth.se

1 Introduction

During the last decade there has been a renewed interest in how averaged quantities of the turbulent boundary layer vary in the direction normal to the wall, especially with regard to the mean and fluctuation velocity distributions (see e.g. [1, 2]). Comparing data from different facilities and/or different techniques are, however, often inconclusive since the inaccuracies of the measured quantities may be larger than the trends one wants to investigate.

For such studies most measurements of the streamwise mean (U) and fluctuating (u') velocity distributions are made with hot-wire anemometry using single wires. The resolution in the normal direction to the wall (y) is usually not a problem since wires with a diameter of $2.5\ \mu\text{m}$ or smaller are used routinely and the viscous length scale ($\ell_* = \nu/u_\tau$, where u_τ is the friction velocity) for typical studies is larger than $10\ \mu\text{m}$ ($\ell_* = 10\ \mu\text{m}$ corresponds to a free stream velocity, U_∞ , of about $40\ \text{m/s}$). The spatial resolution in the spanwise direction may however be an issue, since sensing elements with a spanwise length larger than about $20\ \ell_*$ will give an averaging of the signal that affects the fluctuation level, especially in the near wall region (see e.g. [3]). Another issue which becomes important close to the wall is heat conduction to the wall itself, which may be seen as an increase in the velocity and a decrease in the turbulence intensity. A further complication is that the hot-wire needs to be calibrated down to quite low velocities. Even in the buffer region at $y^+ = (y/\ell_*^+) = 15$ the lowest velocities encountered in the probability density function are approximately $2\ u_\tau$.

A quantity of major importance is the wall shear stress (τ) or rather the friction velocity (u_τ). Since u_τ scales the mean velocity and also determines ℓ_* , and thereby the coordinate y^+ , the accuracy with which different measurements can be compared is utterly dependent on the accuracy of u_τ itself. Also u' is usually scaled with u_τ although there is a slight Reynolds number

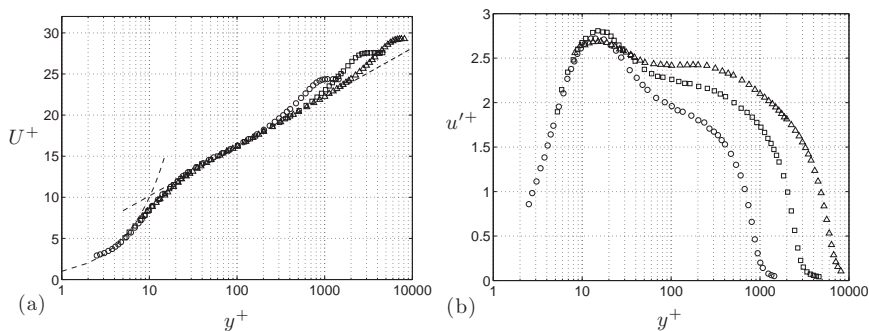


Fig. 1. Profiles of the (a) mean and (b) rms streamwise velocity in inner-law scaling. $U^+ = y^+$ and $U^+ = \kappa^{-1} \ln y^+ + B$, with $\kappa = 0.384$ and $B = 4.17$ are given as dashed lines. \circ : $Re_\theta = 2540$, \square : $Re_\theta = 8100$, \triangle : $Re_\theta = 18700$.

effect in the near-wall region [2]. For boundary layers, the oil-film technique can now be used to determine u_τ with an accuracy better than 1%, but is neither standard practice in most laboratories, nor simple enough to do in a short time for diagnostic purposes.

Finally the determination of the probe position relative to the wall is crucial. This may at first look like a trivial problem but to determine the position with an accuracy of better than one ℓ_* is not easy if it has to be done from outside the wind-tunnel test section. A possibility is to fit the mean velocity profile to some pre-described distribution for the near-wall behaviour. However in that case it is necessary that the measurements of the mean velocity are accurate in themselves.

In this short paper we introduce a new way to plot boundary layer data (in the following called *the diagnostic plot*) that can be used to check whether the velocity data measured close to the wall conform to expected physical characteristics or if they are affected by spatial averaging or other near wall effects. The diagnostic plot allows us to do this without having to determine either the position of the wall or the friction velocity. It also allows us to characterize the flow in the outer region.

2 The diagnostic plot

Most turbulent boundary-layer data are obtained with hot-wire anemometry which gives access both to the distributions of U and u' . Typical plots of U and u' are shown in Fig. 1, for three different Re_θ , viz. 2540, 8100 and 18700 measured in the MTL wind tunnel at KTH (Re_θ is the Reynolds number based on the momentum-loss thickness and free-stream velocity and the first is taken at $x = 1.62$ m and the two other at $x = 3.62$ m from the leading edge of the plate). Both U and u' are normalized with the friction velocity u_τ (based on oil-film interferometry) and plotted as a function of y^+ , i.e. the normal

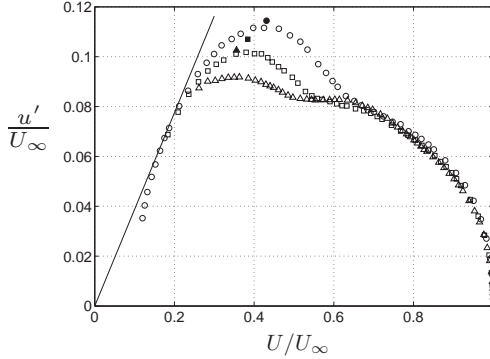


Fig. 2. The data from Fig. 1(a),(b) shown in the *diagnostic plot*. Filled symbols correspond to values for the maximum in u_{rms} obtained from the correlation in [2] and assuming that the maximum is located at $y^+ = 15$. Solid line indicates the tangent to the near-wall data and has a slope of 0.40. The measured points below this line for $U/U_\infty < 0.15$ are clearly affected by the wall.

coordinate y normalized with ℓ_* . The probe lengths for the three cases are, 15, 26 and 60 ℓ_* , respectively, which would give fairly good resolution for the two smallest Re_θ but rather large spatial averaging effects in the near-wall region for the highest Re_θ .

If instead u' is plotted as function of U , where both quantities are normalized by the free stream velocity (U_∞) (i.e. the *diagnostic plot*), any uncertainties in both the wall position and u_τ are avoided. For boundary layers in equilibrium that are plotted in this way, distributions of U and u' that are taken at the same Re , should fall on top of each other if accurately measured (or simulated).

Close to the wall ($y^+ < 10$) we would expect that the distribution should be nearly self similar and independent of Re . The relative level of the rms of the wall shear-stress fluctuations, τ'/τ is related to u' as

$$\frac{\tau'}{\tau} = \lim_{y \rightarrow 0} \frac{u'}{U} \tag{1}$$

The value of τ'/τ is around 0.40 for typical laboratory Reynolds numbers (see e.g. [4]) however it may increase slightly with Re [2]. Since U varies linearly with y near the wall Eq. 1 shows that u' also varies linearly with y with a constant slope (i.e. $u' = 0.40U$). Simulations and experiments show that this linear variation reaches up to, at least, $y^+ = 3$ (corresponding to $U/U_\infty \sim 0.1$ for typical laboratory experiments) and thereafter the slope decreases. As can be seen in Fig. 2 the points closest to the wall deviate below the straight line indicating that the measured u' values are too small and/or the U values are too high. Hence the diagnostic plot indicates at what position the measured values show a wall interference effect, which is not evident in Fig. 1.

Also in the outer region the distributions at different Reynolds numbers previously shown in Fig. 1 nicely overlap in the diagnostic plot. This indicates that in the outer region the u'/U_∞ versus U/U_∞ distribution is nearly self similar with only a weak Reynolds-number dependence.

The behaviour of the near-wall peak (located around $y^+ = 15$, corresponding to $U^+ \approx 11$) is also of interest. As can be seen in Fig. 2 the maximum value in this scaling decreases, although the large difference between the two highest Re is an effect mainly of the spatial averaging. Marusic & Kunkel [2] give an expression for how the maximum increases with Re_θ that can be used to find the variation of u'/U and is given by the solid symbols. As can be seen there is a good correspondence between the present experiments and their expression. Hence, the location in the diagnostic plot of the maximum in u_{rms} can be used as an indication on the accuracy of the measurements in the buffer region.

3 Final remarks

It has been shown that the diagnostic plot may distinguish between accurately measured data in the near-wall region and data which may suffer from various problems. The diagnostic plot also has the interesting property that both the inner ($y^+ < 10$) and outer regions can be made to collapse in the same plot. There is unfortunately not yet enough well-resolved data of u' for high Reynolds numbers to clarify how u' scales in the outer region although in Ref. [1] scaling with U_∞ gives the smallest scatter when plotted against the wall distance normalized with the boundary-layer thickness. When better data becomes available it will be interesting to see how the diagnostic plot varies with Re in the outer region. If the Reynolds number variation is small the diagnostic plot may be used to estimate the boundary-layer free-stream velocity from a few measurement points in the outer region of u' and U , which may be helpful when studying atmospheric boundary layers.

References

1. P. A. Monkewitz, K. A. Chauhan and H. M. Nagib, Self-consistent high-Reynolds-number asymptotics for zero-pressure-gradient turbulent boundary layers. *Phys. Fluids* **19**, 115101 (2007).
2. I. Marusic and G. J. Kunkel, Streamwise turbulence intensity formulation for flat-plate boundary layers. *Phys. Fluids* **15**, 2461–2464 (2003).
3. A. V. Johansson and P. H. Alfredsson, Effects of imperfect spatial resolution on measurements of wall bounded turbulent shear flows. *J. Fluid Mech.* **137**, 409–421 (1983).
4. P. H. Alfredsson, A. V. Johansson, J. H. Haritonidis and H. Eckelmann, On the fluctuating wall shear stress and velocity field in the viscous sublayer. *Phys. Fluids* **31**, 1026–1033 (1988).

DHMPIV and Tomo-PIV measurements of three-dimensional structures in a turbulent boundary layer

O. Amili, C. Atkinson, and J. Soria

Department of Mechanical and Aerospace Engineering, Monash University , VIC 3800, AUSTRALIA
omid.amili@eng.monash.edu.au

Summary. In turbulent boundary layers, a large portion of total turbulence production happens in the near wall region, $y/\delta < 0.2$. The aim of the present work is to measure three-dimensional velocity field in a turbulent boundary layer at a moderately high Reynolds number. Tomographic particle image velocitmetry (Tomo-PIV) was used to extract the 3C-3D velocity field using a rapid and less memory intensive reconstruction algorithm. It is based on a multiplicative line-of-sight (MLOS) estimation that determines possible particle locations in the volume, followed by simultaneous iterative correction. Application of MLOS-SART and MART to a turbulent boundary layer at $Re_\theta=2200$ using a 4 camera Tomo-PIV system with a volume of $1000 \times 1000 \times 160$ voxels is discussed. In addition, near wall velocity measurement attempt made by digital holographic microscopic particle image velocimetry (DHMPIV). The technique provides a solution to overcome the poor axial accuracy and the low spatial resolution which are common problems in digital holography [5]. By reducing the depth of focus by at least one order of magnitude as well as increasing the lateral spatial resolution, DHMPIV provides the opportunity to resolve the small-scale structures existing in near wall layers.

1 Experimental setup

A 4 camera Tomo-PIV system was set up in a 500×500 mm cross-section horizontal water tunnel at the Laboratory for Turbulence Research in Aerospace and Combustion (LTRAC) at Monash University, to provide measurements of a turbulent boundary layer at $Re_\theta = 2200$. A detailed characterization of this boundary layer can be found in [4]. The tunnel was set to a free-stream velocity of $U_\infty=0.422$ m/s with measurements performed 3.7 m downstream of a tripping device. Four PCO 4000 (4008×2672 pixel) CCD arrays were used in combination with 200 mm focal length lenses and arranged in the same plane at angles shown in Fig.1(a), in order to measure a wall-normal stream-wise region of the flow. Prisms were used to reduce the distortion created by the water-air interface and the Scheimpflug condition was set to maximize focus throughout the measurement volume. A 3 mm laser sheet was

generated by a two-cavity 200 mJ 532 nm Nd:YAG laser using a system of spherical and cylindrical lenses. The tunnel was seeded with 60 mm nylon spheres with a particle density of 1030 kg/m^3 . Calibration was performed using the Soloff method [6], with a calibration target aligned parallel to the light sheet then translated through the light sheet thickness, from $z = -2.5 \text{ mm}$ to $z = +2.5 \text{ mm}$ in steps of $500 \mu\text{m}$.

The schematic diagram of the experimental setup for digital holographic microscopic PIV is shown in Fig. 1(b). Appropriate spherical converging lenses were used to expand the laser beam generated by two Nd:YAG pulsed lasers (532 nm and 200 mJ per pulse) and suitable neutral density filters were implemented to reduce the laser energy. The collimated laser beam illuminates the object volume; diffracted light beams from the particles form the object waves while un-diffracted ones are the reference waves. A $10\times$ SemiApochromat microscope objective located in front the digital camera was used to magnify holograms. The microscope objective has the working distance of 21 mm, the numerical aperture of 0.25, and optical resolution of $1.298 \mu\text{m}$. A PCO Pixelfly camera with the CCD array of 1280×1024 pixels was used as the recording medium and flow was seeded by $11 \mu\text{m}$ Potters hallow spherical particles. More detailed information for hologram recording, numerical particle field reconstruction, and imaging resolution can be found in [1].

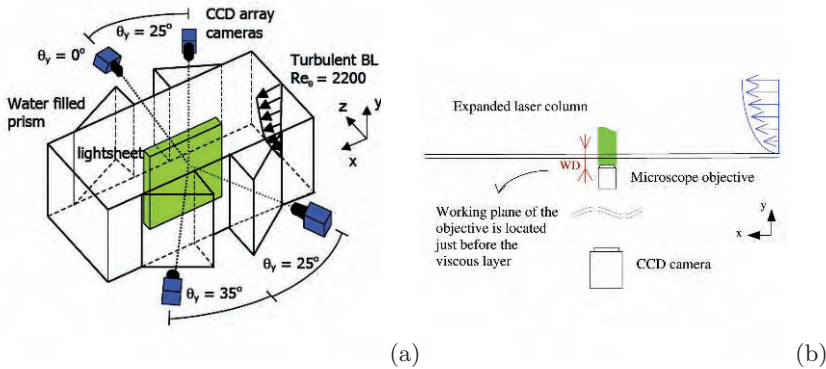


Fig. 1. a) Schematic of Tomo-PIV camera set up for wall-normal stream-wise turbulent boundary layer measurements, b) Front view of Digital holographic microscopic PIV setup for near wall velocity measurement.

2 Results

Tomographic reconstruction was performed using the standard 5 iterations of MART, a MLOS estimation and multiple MLOS-SMART iterations. A standard initial solution and relaxation parameter of unity was used for MART reconstruction, with relaxation parameter of both $\mu=1$ and $\mu=3$ applied to MLOS-SMART. All images were pre-processed to remove the background intensity as required by the MLOS-SMART algorithm and typically used in MART based Tomo-PIV [3]. This

involved an averaged background intensity subtraction, thresholding and Gaussian smoothing (3×3 pixels). To examine the velocity fields produced by these volumes cross-correlation was performed using an in-house multi-pass 3D PIV program. Interrogation regions of 643 voxels with 50% overlap were used, providing fields of $30 \times 30 \times 4$ vectors. Approximately 6% of vectors were rejected, mostly due to areas of low seeding density. This reconstructed particle field density prevented the use of smaller interrogation regions. The same pre-processed images and vector discretization was used for all cases. For more details reader is referred to [2]. Typical instantaneous velocity fields resulting from MART and MLOS-SMART reconstruction are shown in Fig. 2 with the convection velocity removed. The greatest deviation appears in the out-of-plane velocity w , exaggerated in this case by use of discrete iso-contours. A sample field produced by 10 MART iterations has been included for comparison. Using only the MLOS estimation a larger variation in w can be observed, with a much smaller difference between the velocity fields resulting from 40 MLOS-SMART iterations.

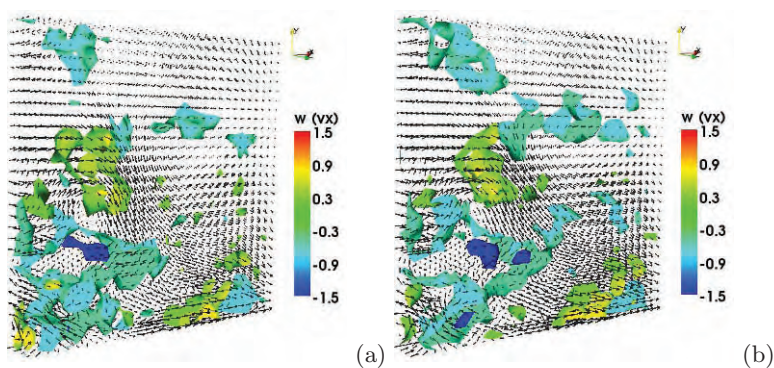


Fig. 2. Instantaneous velocity vectors and iso-contours of out-of-plane velocity for $0.31\delta \times 0.31\delta \times 0.05\delta$ region of a turbulent boundary layer with convection velocity removed. Iso-contours of $w = -1.5, -0.5, 0.25, 0.5$ pixels; a) MART 10 iterations, b) MLOS-SMART 40 iterations $\mu=1.0$.

In order to measure near wall velocity profile, microscopy was applied to digital in-line holography by recording magnified holograms. The elongated dimension of $11 \mu\text{m}$ particle in depth direction was calculated as 130 and $70 \mu\text{m}$ based on the 75% of the peak intensity with the imaging resolution of 1.16 and $0.508 \mu\text{m}/\text{px}$ respectively. Reconstruction of a 11 micron particle using digital holographic microscopy is shown in Fig. 3. More detailed information regarding measuring imaging resolution and particle detection can be found in the study by [1]. This shows the ability of DHM to improve the depth of focus problem where in a non-magnified reconstruction this elongated length is more than two orders of magnitude. As a result, the technique is applicable to measure near wall velocity profile over the turbulent boundary layer in the region of $y^+ < 5$ and consequently to measure wall shear stress. However, due to small number of particles in the vicinity of the wall, reconstruction of flow field is not possible with the current setup. Appropriate local condense seeding is needed to have reasonable number of particles for cross-correlation.

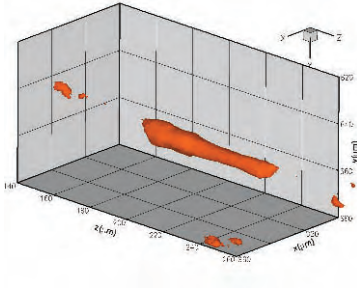


Fig. 3. Reconstruction of a 11 micron particle using digital holographic microscopy, imaging resolution= $0.508 \mu\text{m}$. The technique has the capability of reconstructing a particle field in a seeded flow with the concentration over 10,000 particles per mm^3 which is a very high dense cloud of particles in comparison with the order of 10 used in conventional digital in-line holographic PIV measurements.

3 Conclusion

Application of MART and MLOS-SMART to a turbulent boundary layer at $\text{Re}_\theta=2200$ using a 4 camera Tomo-PIV setup system with a volume of $1000 \times 1000 \times 160$ voxels and a seeding density of 0.01 ppp is presented. Results indicate that the vector difference between velocity fields resulting from 10 MLOS-SMART iterations and 5 MART iterations converge to within the sub-pixel experimental error of Tomo-PIV. In addition, digital in-line holographic microscopic PIV was used to examine the near wall velocity profile. However, due to small number of particles in the vicinity of the wall, reconstruction of flow field is not possible with current setup.

References

- [1] AMILI, O. & SORIA, J. 2008 Application of digital holographic microscopic piv to a water jet. *Proceedings of the 5th Australian Conference on Laser Diagnostics in Fluid Mechanics and Combustion* pp. 51–54.
- [2] ATKINSON, C. H., DILLON-GIBBONS, C. J. & SORIA, J. 2008 Efficient tomographic particle image velocimetry techniques for application to a turbulent boundary layer. *Proceedings of the 5th Australian Conference on Laser Diagnostics in Fluid Mechanics and Combustion* pp. 55–58.
- [3] ELSINGA, G. E., SCARANO, F., WIENEKE, B. & VAN OUDHEUSDEN, B. W. 2006 Tomographic particle image velocimetry. *Experiments in Fluids* **41** (6), 933–947.
- [4] HERPIN, S., WONG, C. Y., STANISLAS, M. & SORIA, J. 2008 Stereoscopic piv measurements of a turbulent boundary layer with a large spatial dynamic range. *Experiments in Fluids* **45** (4), 745–763.
- [5] SHENG, J., MALKIEL, E. & KATZ, J. 2006 Digital holographic microscope for measuring three-dimensional particle distributions and motions. *Applied Optics* **45** (16), 3893–3901.
- [6] SOLOFF, S. M., ADRIAN, R. J. & LIU, Z. . 1997 Distortion compensation for generalized stereoscopic particle image velocimetry. *Measurement Science and Technology* **8** (12), 1441–1454.

LDA measurements of Reynolds stresses in a swirling turbulent pipe flow

B. Z. Genç, Ö. Ertunç, J. Jovanović and A. Delgado

Lehrstuhl für Strömungsmechanik Erlangen, Friedrich-Alexander-Universität
Erlangen-Nürnberg, D-91058, Germany
bgenc@lstm.uni-erlangen.de

Abstract

This study concentrates on turbulent swirling flows, which are constrained in a stationary and straight circular pipe. Aim was to determine the sole effect of swirl component and its decay on a developing turbulent pipe flow. For this purpose, velocity statistics of a pipe flow with a Reynolds number of $Re_D = U_m D/\nu \cong 30,000$ were measured at several downstream positions up to $z/D = 17.3$. The strength of inlet swirl was adjusted to the desired swirl numbers of $N = 0.3$ (weak) and $N = 1.0$ (strong). Emphasis was put on generating a solid-body rotation type of swirl while maintaining axisymmetric inlet conditions. Consequently, the determined mean velocity and Reynolds stress profiles showed almost no deviation from axisymmetry. Furthermore, non-zero Reynolds shear stresses were determined. Both findings contradict some results in the literature. Subtle increase in the magnitude of Reynolds stresses was observed as the swirl component decayed partially.

1 Background

Swirling flows are an important class of flows not only due to their basic features, but also due to their technical relevance for engineering and abundance in nature. However, their challenging complexity poses serious problems in their modeling and understanding [1]. Due to this fact, swirling flows have been studied for a long time and an abundant number of publications can be found in the literature [2, 3, 4]. These studies reveal the fact that, depending on the boundary conditions, swirling flows can undergo totally different scenarios and flow field can exhibit different dynamical features: A great number of these studies concentrate on the effects of swirl, when the swirling flow is created and subjected to gradual-sudden expansion in pipes or injected as a free jet (unconstrained) [5, 6]. In these kind of flows, swirl component decays

rapidly due to the action of adverse pressure gradient and sometimes *vortex core breakdown* phenomenon occurs [5]. Other studies consider the case, when the swirl component was created by a rotating pipe, where swirl component was constantly imposed onto the axial flow [6, 7]. In such a flow, a parabolic tangential velocity profile develops and it does not decay along the axis of the pipe [6].

In contrast to these, present study concentrates on the relatively less studied case [2, 3, 4, 8, 9, 10] when the swirl is generated at the inlet of a straight circular pipe and constrained in it. In such a flow, the swirl component decays gradually due to the action of viscosity. Regarding to this kind flow, a number of different effects were reported; like stabilizing-destabilizing effect of swirl on turbulence [8], effect of swirl decay on breaking of axisymmetry [3], relaminarization of flow profile [7], annihilation of Reynolds shear stresses [4]. From the literature survey and our previous experiments [10], it can be concluded that axial velocity distribution and the generation of swirl at the inlet of the pipe determine the downstream distribution of mean and turbulent flow quantities to a great extent. Therefore, in this study, a solid body rotation type of swirling inlet condition was carefully created to maintain axisymmetry at the inlet of the pipe. Aim is to determine the sole effect of swirl and its decay on the statistics of flow quantities along the pipe. The obtained results are evaluated taking into account the above-mentioned effects reported in the literature.

2 Experimental Facility

In this study, the refractive-index-matched pipe flow facility of LSTM-Erlangen was used (Fig. 1). The working fluid in the pipe was diesel oil. A refractive-index-matched test section with a length of 1 m, filled with diesel oil, provided optical access for the simple 1-C laser Doppler anemometer (LDA) system, which was mounted on a traversing table [10, 3]. The swirl generator used in previous studies [10, 3] was reconstructed to obtain axisymmetric flow conditions at the inlet. A 300 mm long polycarbonate honeycomb insert was carefully machined into a cylindrical form to obtain an axisymmetric distribution of its cells. This insert was then tightly fitted into a piece of pipe out of steel, which could be rotated with an AC Motor and as such the strength of the inlet swirl could exactly be adjusted to the desired swirl numbers ($N = U_{\theta_{max}}/U_m$) up to ca. $N = 1.3$.

3 Results and Conclusions

All results were normalized with avg. axial velocity $U_m = 2.34 \text{ m/s}$. The mean velocities depict some typical effects of swirl, which were also observed in the literature, like rounding of the axial mean flow profiles for strong swirl

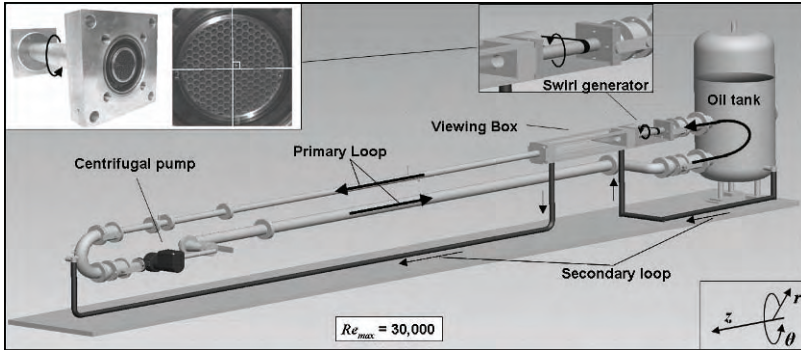


Fig. 1. The refractive-index-matched turbulent pipe flow facility of LSTM-Erlangen with a close up view of the swirl generator and its honeycomb insert. Cylindrical coordinates are used, where z denote the axial direction

(Fig. 2). Reynolds stresses substantially increase, especially when the strong swirl component decays along the pipe (Fig. 3 and 4). The observed increase of Reynolds stresses is most pronounced in the near-wall region and penetrates into the center of the pipe at downstream locations. Apart from $\overline{u_r u_z}$, magnitudes of Reynolds stresses increase with increasing swirl number owing to the increased shearing of flow in θ -direction.

Another important observation is that the measured profiles show almost no sign of deviation from axisymmetry, at least until the measured downstream position $z/D = 17$ (Fig. 2, 3, 4). This contradicts some results for similar cases in the literature, in which the swirl was held responsible for the appearance of asymmetries in the profiles of flow quantities [8, 3, 2]. It was therefore concluded that the inlet conditions should first carefully be checked for axisymmetry, before any claim can be made about the effect of swirl. Furthermore, contrary to another investigation [4], no annihilation of Reynolds shear stresses was observed and even the Reynolds stresses increased in magnitude (Fig. 4). No evidence of vortex core breakdown phenomenon could be observed (like tendency to flow reversal in the center) and properties did not change abruptly along the pipe [3]. The swirl component of flow decayed gradually along the pipe.

References

1. S. Jakirlić, K. Hanjalić, and C. Tropea, *AIAA Journal*, **40** 1984 (2002).
2. W. Steenbergen, *Turbulent pipe flow with swirl*. Ph.D. thesis, Eindhoven University of Technology, 1995.
3. M. Pashtrapanska, J. Jovanović, H. Lienhart and F. Durst, *Exp. Fluids*, **41** 813 (2006).
4. G. Rocklage-Marliani, M. Schmidts and V. I. V. Ram, *Flow Turbulence and Combustion*, **70** 43 (2003).
5. F. Novak and T. Sarpkaya, *AIAA Journal*, **38** 1671 (2000).

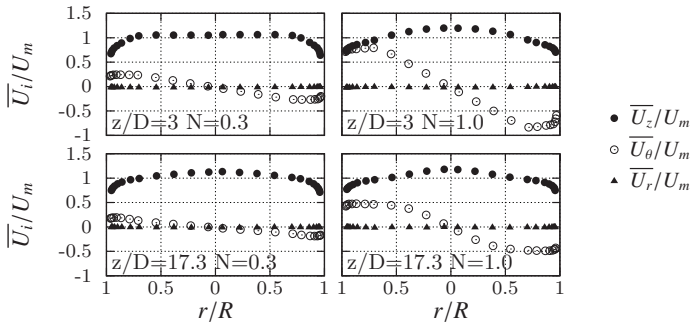


Fig. 2. Mean velocity profiles at $z/D = 3, 17.3$ for swirl numbers $N = 0.3, 1.0$.

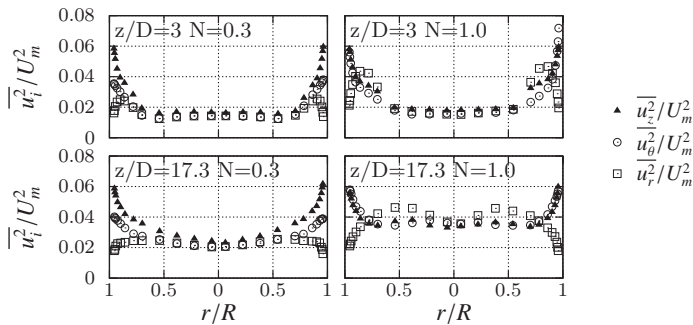


Fig. 3. Reyn. normal stress profiles at $z/D = 3, 17.3$ for swirl numbers $N = 0.3, 1.0$.

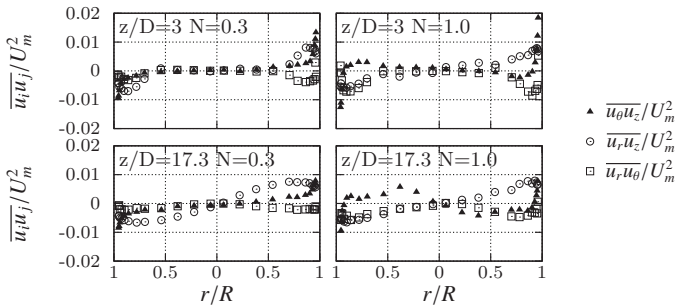


Fig. 4. Reyn. shear stress profiles at $z/D = 3, 17.3$ for swirl numbers $N = 0.3, 1.0$.

6. L. Facciolo, N. Tillmark, A. Talamelli and P. Henrik Alfredson, *Physics of Fluids*, **19** 035105 (2007).
7. K. Nishibory, K. Kikuyama and M. Murakami, *Bull. JSME*, **30** 255 (1987).
8. O. Kito, *Bull. JSME*, **27** 683 (1984).
9. O. Kitoh, *J. Fluid Mech.*, **225** 445 (1991).
10. B. Z. Genç, J. Jovanović and F. Durst, 13. GALA Fachtagung "Lasermethoden in der Strömungsmechanik", 2005.

Time-resolved stereoscopic PIV of the log-layer in fully developed turbulent pipe flow

S. Große, D.J. Kuik, and J.Westerweel

Laboratory of Aero and Hydrodynamics, TU Delft University, 2628 CA Delft, The Netherlands, s.grosse at aia.rwth-aachen.de

1 Introduction

Turbulent pipe flow is supposed to be confined by the flow geometry and the boundary layers evolving on ‘opposite’ sides of the center line are expected to interact with each other even at high Reynolds numbers. An obvious evidence of this interaction is the negative two-point correlation of streamwise fluctuations across the centerline $R_{u_z u_z}(r)$. It is, however, not clear how a possible interaction takes place and how far a ‘sloshing’, i.e., a meandering of the pipe flow core region, is related to the large-scale (LSM) and very large-scale motion (VLSM), which were found in the logarithmic and wake region [1, 2, 3, 4].

Therefore, measurements of fully developed turbulent pipe flow were performed using stereoscopic high-speed PIV at Reynolds numbers $Re_b = 10\,000 \div 44\,000$. The data allows to reconstruct all velocity components. Since only a single measurement plane is observed Taylor’s hypothesis is applied to reconstruct the streamwise extension of the flow field. The high recording frequency allows to ‘track’ the development of coherent motion from instantaneous velocity fields along the streamwise direction. Approximately 150 bulk scales are continuously recorded such that even the largest expected scales reaching up to $7 R$ [3] are captured. The flow field is resolved with approximately $8 \div 36 l^+$ at the Reynolds numbers in the experiments, respectively.

The simultaneous assessment of the entire flow field allows to gain valuable information on the growth of coherent motion. The azimuthal extent, to which large-scale low-momentum zones in the logarithmic region meander, can be investigated, which is an interesting point in the study of the interaction of ‘opposite’ boundary layers in pipe flow.

2 Experimental Setup

The measurements are performed in the flow facility of the Laboratory of Aero- and Hydrodynamics at TU Delft. The pipe possesses a diameter of

$D = 40 \text{ mm}$ and a total length of 28 m . The fluid is filtered tap water at $T = 20 \pm 0.1^\circ\text{C}$. The Reynolds number based on the bulk velocity $Re_b = U_b D / \nu$ can be determined to within 0.4% . The flow enters the pipe section through a settling chamber with a flow straightener of approximately 5 mm core size and several meshes. The contraction possesses a $5 : 1$ contraction ratio (based on the diameter). The entire pipe is thermally isolated. This design allows to keep the flow in the pipe laminar up to $Re_b = 30\,000$. Hence, it is necessary to trip the flow artificially downstream of the inlet. All measurements are carried out at about 25 m downstream of the tripping device, i.e., at $600 L_e / D$, to ensure fully developed flow conditions at the measurement section [5, 6]. A further description of the setup can be found in [7, 8]. Stereo high-speed PIV recordings at $500 \div 1\,000 \text{ Hz}$ and at Reynolds numbers of $Re_b = 10\,000 \div 44\,000$ have been performed. The recording time of single sequences corresponds to approximately 150 integral scales based on the bulk velocity U_b and the radius of the pipe R . In total, the low and high-speed data spans over 3 000 bulk scales such that the data can statistically be discussed.

3 Preliminary Discussion of Results

Two-point correlations of the streamwise fluctuations across the centerline $R_{u_z u_z}(r)$ calculated from the PIV recordings at $Re_b = 10\,000$ are shown in figure 1(a), evidencing the correlation function to reach negative values at distances from the centerline $r/R = 0.0 \div 0.5$ for distances of the reference point from the centerline being less than $-0.4 r/R$. At positions of the reference point closer to the wall the correlation across the centerline decays toward zero. Similar results have been found in square duct flow, where the correlation peaks negatively opposite of the centerline. Data of 2D-channel flow is not available yet such that it can not further be investigated how far the flow confinement has an influence on the interaction. Whether or not the negative trend of the two-point correlations across the centerline can also be observed in DNS data of turbulent pipe flow will need further investigation.

It is still under research how a possible interaction takes place and how far a ‘sloshing’, i.e., a meandering of the pipe flow core region might be related to or induced by the large-scale (LSM) and very large-scale motion (VLSM). There is evidence from instantaneous streamwise velocity fields in the cross-section indicating an extra-ordinary growth of near-wall coherent motion into the near-center wake region causing a strong influence on the entire flow field, but further investigation is necessary.

Similarly, in figure 1(b) the distribution of $R_{u_z u_z}(\Theta)$ indicates a negative correlation at $\Theta \approx \pi$ close to the centerline. Note, the graph can only be read along lines of constant radius/wall-distance. At larger r/R , lobe-like regions of negative correlation indicate the co-existence of low- and high-momentum zones in the azimuthal plane. The distance between the extrema decreases

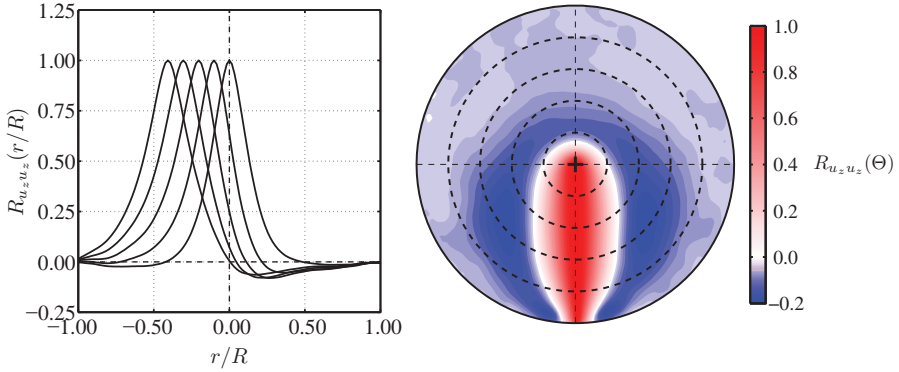


Fig. 1. (left) Spatial correlation of streamwise fluctuations as function of radius $R_{u_z u_z}(r/R)$ across the centerline at $Re_b = 10000$. (right) Distribution of the spatial correlation $R_{u_z u_z}(\Theta)$ at $Re_b = 10000$. Note, the graph can only be read along lines of constant radius.

with increasing r/R . Figure 1(b) further indicate two distinct lobes very close to the wall at $Re_b = 10000$. A region of less negative correlation values at approximately $r/R = 0.7 \div 0.9$ indicates a larger order of different scales present in the flow, whereas the strong negative correlation in the regions at $r/R \leq 0.7$ and $r/R \geq 0.9$ indicate a rather uniform scale of structures. The distance between the negative lobes in the vicinity of the wall reaches approximately $100 l^+$, i.e., 100 viscous scales, which is in good agreement with the spacing of the near-wall cycle reported in the literature (e.g. [9, 10, 11, 12]). At the highest Reynolds number this near-wall region can not sufficiently be resolved. To further assess the scaling, the azimuthal dimension of the correlation function has been estimated similarly to [1, 13, 4]. The distance from the reference point, at which the correlation value drops below a level of $R_{u_z u_z} \leq 0.05$, is defined by $l_z/2$. In figures 2(a) and 2(b) the azimuthal dimension l_z is given as a function of y/R and compared to values in the literature. The azimuthal dimension in these graphs is scaled with the local value of $2\pi r$ and R , respectively. The results at the highest Reynolds number show excellent agreement with the data of [1, 4]. At lower Reynolds number the curves indicate a decrease of the azimuthal scaling close to the wall and the distributions drop to values similar to those reported for turbulent boundary layer flow [13, 14]. This might indicate that the near-wall cycle in the vicinity of the wall is little influenced by the geometric confinement that the flow experiences at higher regions. It is, however, remarkable that the fields of streamwise velocity fluctuations indicate similar structures of meandering bands of low-momentum and high-momentum fluid almost throughout an region ranging from $0.05 \leq y/R \leq 0.50$, which would rather indicate a strong interaction of the flow field at different heights in the boundary layer.

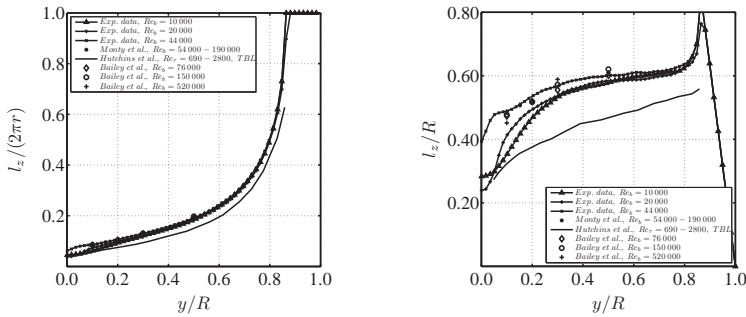


Fig. 2. Azimuthal length-scale l_z in different scalings. l_z is the azimuthal dimension of the two-sided correlation peak using a threshold of $R_{u_z u_z} \geq 0.05$.

4 Outlook

First results from the measurements evidence the high quality of the recorded PIV data. The long integral time span, over which individual sequences are recorded, the high recording frequency, the coverage of the entire azimuthal velocity plane, and the simultaneous assessment of all three velocity components will allow a valuable and in-depth investigation of further features of turbulent pipe flow including further characteristics of the recently found superstructures, an ‘inter-scale’ interaction and a possible meandering (‘sloshing’) of the core region. First full-field statistics of turbulent pipe flow presented in this work show very good agreement with data obtained by the hot-wire technique with arrays covering the azimuthal plane at constant radius.

References

1. S. C. C. Bailey et al., *Journal of Fluid Mechanics*, **366**, 121-138, 2008.
2. M. Guala et al., *Journal of Fluid Mechanics*, **554**, 521-542, 2006.
3. K. C. Kim and R. J. Adrian, *Physics of Fluids*, **11(2)**, 417-422, 1999.
4. J. P. Monty et al., *Journal of Fluid Mechanics*, **589**, 147-156, 2007.
5. F. Durst et al., *Journal of Fluids Engineering - Transactions of the ASME*, **120**, 496-503, 1998.
6. M. V. Zagarola and A. J. Smits, *Journal of Fluid Mechanics*, **373**, 33-79, 1998.
7. C. W. H. van Doorne, TU Delft University, 2004.
8. C. W. H. van Doorne and J. Westerweel, *Experiments in Fluids*, **42**, 259-279, 2007.
9. S. Große and W. Schröder, *AIAA Journal*, **47(2)**, 314-321, 2009.
10. H. P. Kreplin and H. Eckelmann, *Journal of Fluid Mechanics*, **95(2)**, 305-322, 1979.
11. M. K. Lee et al., *Journal of Fluid Mechanics*, **66(1)**, 17-33, 1974.
12. R. D. Moser et al., *Physics of Fluids*, **11**, 943-945, 1999.
13. N. Hutchins et al., *Journal of Fluid Mechanics*, **541**, 21-54, 2005.
14. N. Hutchins and I. Marusic, *Journal of Fluid Mechanics*, **579**, 1-28, 2007.

Massive separation in rotating turbulent flows

Mustafa Barri¹, George K. El Khoury², Helge I. Andersson¹ and Bjørnar Pettersen²

¹ Dept. of Energy and Process Engineering, Norwegian University of Science and Technology, NO-7491 Trondheim, Norway. mustafa.barri@ntnu.no

² Dept. of Marine Technology, NTNU, NO-7491 Trondheim, Norway

1 Motivation

Turbulent flow over a backward facing step can be of great assist to demonstrate the effect of system rotation on separating flows. Depending on the magnitude and orientation of the imposed background vorticity 2Ω relative to the mean flow vorticity ω in the rotating frame of reference, a variety of different flow phenomena may occur. Cyclonic (anti-cyclonic) rotation if mean vorticity vector is parallel (anti-parallel) to the system rotation vector. Cambon *et al.*[1] and Metais *et al.*[2] indicated the stabilization effect in the cyclonic rotation regimes in terms of reducing turbulence level and decreasing the momentum interchange (compared to the situation with no rotation). On the other hand, the destabilization effect associated with increase in momentum interchange dominates the moderate anti-cyclonic rotation regimes. Beyond a certain rotation rate the anti-cyclonic regimes begin to restabilize.

The aim of the present study is to explore separated turbulent flows in a rotating frame of reference. To this end we consider the turbulent flow over a backward facing step with a distance of $2h$ between the two walls. The step is mounted at the anti-cyclonic side of the channel with step height of $1h$. According to Barri *et al.*[3] the turbulent inflow boundary conditions are induced by velocity profiles taken from a precursor simulation of turbulent plane Poiseuille flow with periodic boundary conditions in streamwise and spanwise directions. The imposed system rotation vector is aligned in the positive spanwise direction and the stepped wall becomes the anti-cyclonic side. The Reynolds number is $Re \equiv U_{bulk}h/\nu = 5600$.

The relative importance of the imposed system rotation is given by the rotation number $Ro \equiv 2\Omega h/U_{bulk}$. Different rotation numbers have been considered (0.0, 0.1, 0.2 and 0.4). We therefore performed direct numerical simulations of turbulent BF-step with periodic boundary conditions in the spanwise direction and exit boundary conditions in the streamwise direction.

The stabilization, at the cyclonic region before the expansion, increases the possibility of the attached shear layer to separate under deceleration. In the

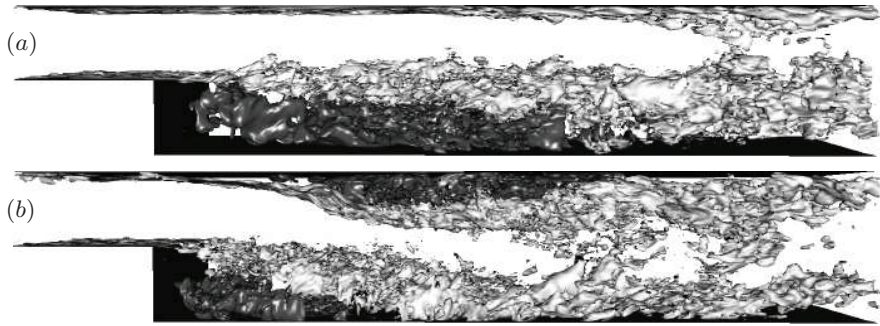


Fig. 1. u' iso-surfaces. Positive and negative contours are distinguished by light and dark shading, respectively. (a) $Ro = 0.0$, (b) $Ro = 0.4$.

mean time, the boundary layer at the anti-cyclonic flow region separates from the edge of the step, being shed downstream as an anti-cyclonic free shear layer (figure 1). The simulations show significant increase in the spreading rate of the mixing layer by increasing the system rotation rate due to destabilization effect (figure 2). According to this fact, the size of the anti-cyclonic recirculation region after the step reduces by increasing the system rotation. In an opposite manner, the cyclonic recirculation region increases in size by increasing the system rotation due to the decrease in turbulence level.

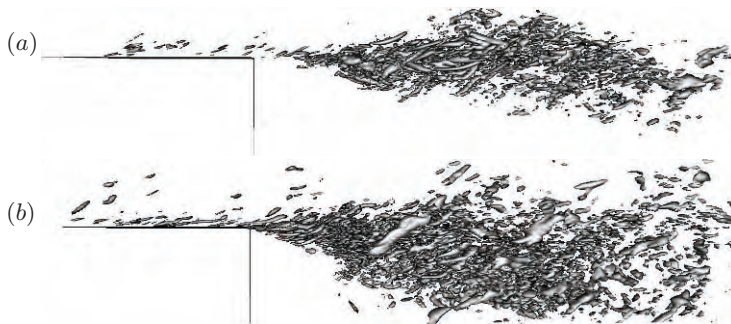


Fig. 2. $-\lambda_2' \omega_x'$ iso-surfaces (positive contour level). (a) $Ro = 0.0$, (b) $Ro = 0.4$.

2 Results

Results for the highest rotation number $Ro = 0.4$ compared with the non-rotating case $Ro = 0.0$ are shown in figures 3 & 4. To facilitate comparisons between the two different cases, the contour level increased by a factor of two in the rotating case compared with the contour levels used in the non-rotating.

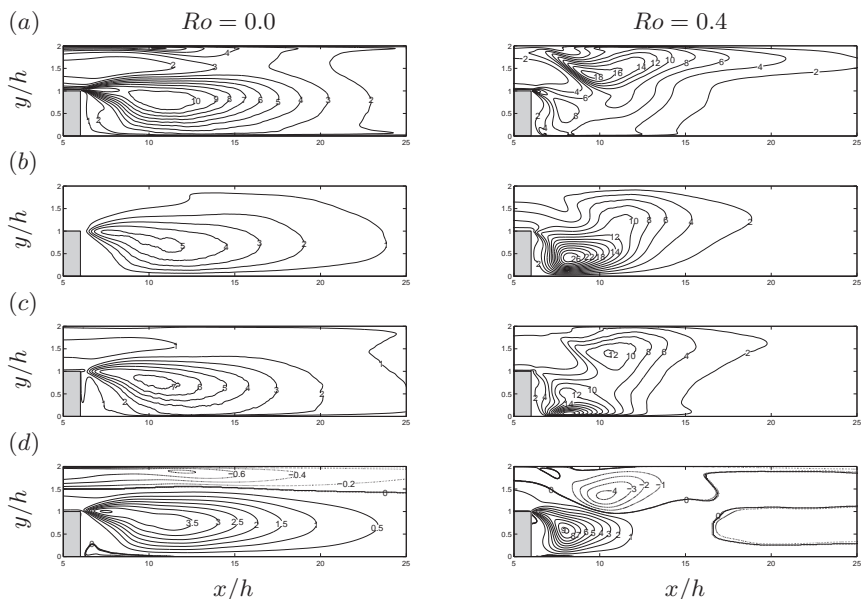


Fig. 3. Contour plots of Reynolds stresses. (a) $\overline{u'u'}$, (b) $\overline{v'v'}$, (c) $\overline{w'w'}$, (d) $-\overline{u'v'}$.

For the sake of clarity, the cross-stream length scale has been enlarged in figures 3 & 4.

The results in figure 3 show that the high levels of turbulent stresses occur in the mixing layer originating from the corner of the step. The anti-cyclonic regions downstream of the step (the mixing layer and the recirculation zone at the lower wall) express a reversal anisotropy $v'_{rms} > w'_{rms} > u'_{rms}$ at high rotation rates, whereas the cyclonic regions (the recirculation zone at the upper wall) conserve the conventional anisotropy behavior $u'_{rms} > w'_{rms} > v'_{rms}$. In counter-clockwise rotation ($Ro = 0.4$), the stepped wall becomes the pressure side of the channel, and the rotational production G_{22} in Table 1 becomes positive, thereby increasing $\overline{v'v'}$ in figure 3b in comparison with the non-rotating case.

	$i = 1, j = 1$	$i = 2, j = 2$	$i = 3, j = 3$	$i = 1, j = 2$
P_{ij}	$-2(\overline{u'u'} \frac{\partial U}{\partial x} + \overline{v'v'} \frac{\partial U}{\partial y})$	$-2(\overline{u'v'} \frac{\partial V}{\partial x} + \overline{v'v'} \frac{\partial V}{\partial y})$	0	$-(\overline{u'u'} \frac{\partial V}{\partial x} + \overline{v'v'} \frac{\partial U}{\partial y})$
G_{ij}	$4\Omega \overline{u'v'}$	$-4\Omega \overline{u'v'}$	0	$-2\Omega(\overline{u'u'} - \overline{v'v'})$

Table 1. Production terms in two dimensional mean flow.

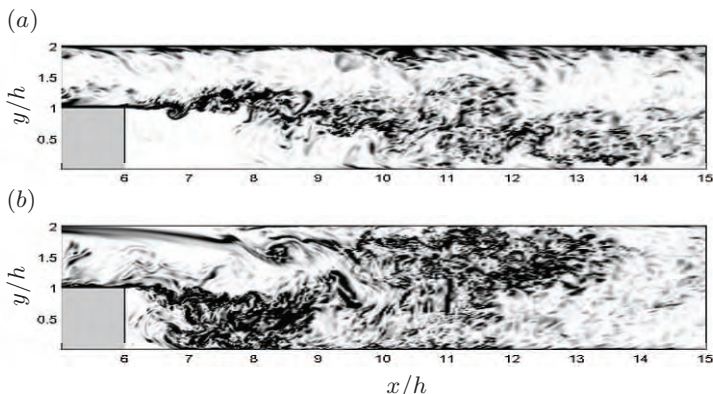


Fig. 4. Contour levels of the instantaneous enstrophy fluctuations $\omega'_i\omega'_i$. (a) $Ro = 0.0$, (b) $Ro = 0.4$.

By increasing $\overline{v'v'}$ the magnitude of the shear production term P_{12} is also increased and the shear stress level $-\overline{u'v'}$ is further increased. On the other hand, $G_{11} < 0$ tends to reduce the streamwise turbulent intensity in figure 3a. The overall effect of anti-cyclonic rotation is therefore to enhance the turbulence level downstream of the step edge. The increased mixing inevitably increases the spreading rate of the mixing layer, thereby reducing the anti-cyclonic recirculation region below the layer.

The vortical topology associated with high turbulent kinetic energy can be investigated using the enstrophy field shown in figure 4. The reattachment region in the non-rotating case is due to turbulent kinetic energy reduction in the mixing layer region farther downstream of the step. In contrast, the mixing layer is forced to reattach by the effect of system rotation and the vortex sheet has not been allowed to develop in space. Thereby not only the mixing layer region has higher turbulence level compared to the non-rotating case but even the reattachment region as can be seen from figure 4b.

The support for this work from the Research Council of Norway through a research grant (Contract no 171725/V30) and a grant of computing time (Programme for Supercomputing) is gratefully acknowledged.

References

1. C. Cambon, J. Benoit, L. Shao and L. Jacquin, *J. Fluid Mech.*, **278**, 175 (1994).
2. O. Metais, C. Flores, S. Yanase, J. Riley and M. Lesieur, *J. Fluid Mech.*, **293**, 47 (1995).
3. M. Barri, G.K. El Khoury, H.I. Andersson and B. Pettersen, *Int. J. Numer. Meth. Fluids*, **60**, 227 (2009).

Scaling of torque in turbulent Taylor-Couette flow with background rotation

R. Delfos¹, F. Ravelet^{1,2} and J. Westerweel¹

¹Laboratory for Aero and Hydrodynamics, Delft University of Technology, Leeghwaterstraat 21, 2628 CA Delft, the Netherlands

²LEMFI, ENSAM-ParisTech, 151 Bld de l'hôpital, 75013 Paris, France
`r.delfos at tudelft.nl`

We did an experimental study on Taylor-Couette flow in between two coaxial cylinders of length $L = 220$ mm and radii $r_i = 110$ and $r_o = 120$, respectively, the fluid-filled 'Taylor-Couette gap' or TC-gap being $h = 10$ mm, thus gap ratio $\eta = r_i/r_o = 0.917$, and gap aspect ratio $L/h = 22$). Both cylinders are rotating independently, with angular frequencies $\omega_{i,o}$. The torque T on the inner cylinder is measured through the axis driving the inner cylinder with a co-rotating torque meter.

The system is characterised with parameters as given by Dubrulle *et al.* [3]: a shear Reynolds number $Re_S = 2/(1 + \eta) |\eta Re_o - Re_i|$ and a Rotation number $Ro = (1 - \eta) (Re_i + Re_o)/(\eta Re_o - Re_i)$, where $Re_{i,o} = (r_{i,o}\omega_{i,o}h/\nu)$ are inner and outer Reynolds number. With this choice, Re_S is based on the laminar shear rate S ; $Re_S = h^2S/\nu$. The Rotation number Ro compares mean rotation to mean shear; its sign determines cyclonic ($Ro > 0$, stabilising) or anti-cyclonic ($Ro < 0$, destabilising) flow. Two other relevant values are $Ro_i = \eta - 1 \simeq -0.083$ and $Ro_o = (1 - \eta)/\eta \simeq 0.091$ for the inner and the outer cylinder rotating alone, respectively.

We have estimated the wall shear stress at the inner wall by $\tau_{W,i} = T/(2\pi r_i^2 L)$, and from this the friction factor c_F , i.e. non-dimensional wall shear stress, $c_F = \tau/\rho(Sh)^2$ is obtained. We have done this for a range of Re_S values far beyond those presented in Andereck's classical work [1]. Andereck investigated the occurrence of flow structures in laminar and low turbulent TC flows up to $Re_S = 4 \cdot 10^3$. Our results up to $Re_S = 5 \cdot 10^4$ are shown in Fig. 1. We observe that, for a given Ro , the friction factor c_F decreases monotonically with increasing Re_S . This torque-scaling is discussed in much detail in [4], with many references. In [6, 7], we summarise this briefly, and show that we retrieve in our system up to $Re_S = 2 \cdot 10^5$ very similar torque scaling exponents for $Ro = Ro_i$ as in [5].

We further observe that for a given constant Re_S the friction factor c_F strongly depends on Ro : Friction increases monotonically when Ro decreases especially at lower Reynolds numbers, which clearly shows the role of rotation

in the stability of the mean flow. For the highest Re_S , c_F however gets constant at some fairly small negative Rotation, ($Ro = Ro_{Plat}$) until roughly $Ro = \eta - 1$ (inner alone), from which the shear stress further increases.

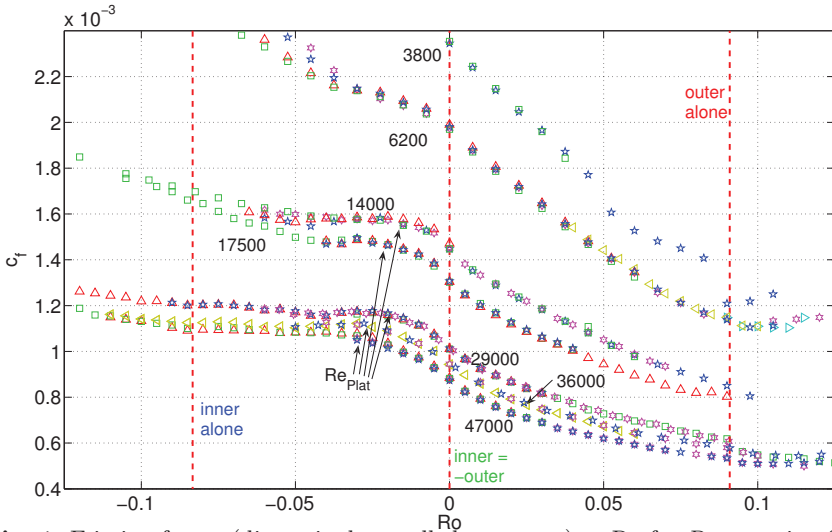


Fig. 1. Friction factor (dimensionless wall shear stress) vs Ro for Re_S ranging from 4.10^3 till 50.10^3 . Axes for 'inner alone', 'counter rotation' and 'outer alone' indicated.

Towards the other end of the curve, increasing Ro , torque gradually diminishes. A small step attributed to system friction (bearings) is visible at Ro_o , where the inner cylinder reverses its sense of rotation. Where flow visualisations with micro-fibers shows a gradual laminarisation of the flow around $Ro = Ro_o$, the torque does not drop accordingly. This is attributed to a non-idealness of our system: Besides torque produced in the 'Taylor-Couette gap', the system measures as well the torque as exerted on the upper and lower horizontal ends of the inner cylinder that forms at both ends a ± 2 mm high fluid-filled gap with equally flat ends of the outer cylinder. For laminar flow with a high-viscosity corn syrup, the deviation was found to be a constant, as much as some 40% larger than that of the analytical result for the outer wall alone, which we thus consider as 'end effects' as common in rheometric instruments. Under transitional and turbulent conditions, the dynamics of such torsional shear layers, or 'von Kármán' layers is complex and still under study, [2], with many references. Unfortunately, measuring with only the lower vK-gap filled or with a partially-filled TC-gap to estimate the torque by the vK-gap was not feasible under turbulent flow conditions because of the entrapment of air; the system can only be run entirely fluid filled. Therefore, establishing the contribution of the end effect was not reliable. But certainly at relaminarised flow in the TC-gap, the torque in the vK-gap will dominate; hence the magnitude of our measured torques is of limited value at high Ro .

Finally, exact counter rotation $Ro = 0$ appears to be an inflection point; though c_F and its change with Ro are continuous; the second derivative clearly changes sign for all Re_S investigated. In the following we will briefly discuss possible mechanisms behind the behaviour of the torque curve.

In [6, 7] we show Stereoscopic-PIV measurements in the radial-axial plane in the TC-gap. In these measurements, at an intermediate Re_S investigated here, i.e. $Re_S = 14.10^3$. Though the flow is turbulent, there is as well a pattern of large-scale azimuthal (Taylor-like) vortices or 'rolls' of alternating sense of rotation in the flow when time-averaging. At inner alone, i.e. at $Ro = Ro_i$ they contribute around the centre of the gap for at least 50% to the torque, the remainder of the transport still being by turbulent shear stress (correlated radial-azimuthal velocity fluctuations).

The magnitude of the rolls is measured by matching an idealised stream function Ψ_{Sec} to the 'secondary', i.e. radial-axial flow field: $\Psi_{Sec} = \sin[\pi(r - r_i)/h] \times (A_1 \sin[\pi(z - z_0)/\ell] + A_3 \sin[3\pi(z - z_0)/\ell])$, with A_1 , A_3 , z_0 , and ℓ as free fit parameters; ℓ and z_0 describing height and origin of a roll; A_1 and A_3 describing the fundamental mode and the first possible symmetric harmonic. The (radial) velocity amplitude is given as $u_{rad,Max} = |\partial\Psi_{Sec}/\partial z| = \pi(A_1/\ell + 3A_3/\ell)$.

We verified that the fit parameters are stationary; we also measured with both increasing and decreasing values for Ro such to check for a possible hysteresis. We plot in Fig. 2 the velocity amplitudes associated with the simple model (fundamental mode \diamond), and with the complete model (including the harmonic, \bullet).

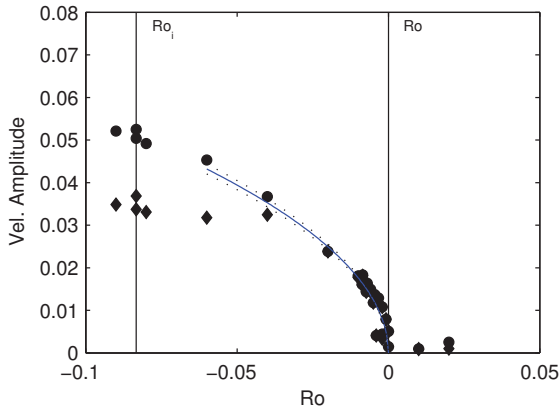


Fig. 2. velocity magnitude normalised by hS of fundamental mode (\diamond), and both modes (\bullet) vs. Ro at $Re_S = 1.4.10^4$, including a curve fit of form $A = a(-Ro)^{1/2}$

All data fall on a single curve; the changes being smooth and without hysteresis. For positive Ro , the fitted modes have negligible amplitudes, (there are no secondary flow structures visible in the time-average field [6]). As soon as

$Ro < 0$, *i.e.*, the inner cylinder rotates faster than the outer, secondary flow occurs, and the fundamental mode starts to grow in amplitude, with $A_3 \simeq 0$; the secondary mean flow thus being well described by pure sinusoidal structures. For $Ro \leq -0.04$, the vortices start to deform to a more elongated shape, with wider cores and more narrow regions of large radial velocities in between the adjacent vortices; the first harmonic is then necessary to adequately describe the secondary flow. The fundamental mode becomes saturated in its amplitude in this region of $Ro < Ro_{Sat}$. Finally, we give in Fig. 2 a curve fit to the measured velocity amplitudes of the form: $A = a(-Ro)^{1/2}$. The velocity magnitude of the secondary flow behaves like the square root of the distance to $Ro = 0$, a situation reminiscent to a classical supercritical bifurcation, with A as order parameter, and Ro as control parameter.

Now combining the results for flow patterns and torque, it is remarkable that the similarity is limited: Where Taylor vortices are expected to positively contribute to the torque, the emergence of the rolls at $Ro = 0$ rather seems to suppress the growth of c_F , as visible from the inflection point in the torque. Further, the resemblance of saturations in torque and secondary flow magnitude showed to be accidental: Torque saturation, at $Ro_{Plat} = -0.02$, is significantly separated from saturation of the fundamental mode at $Ro_{Sat} = -0.035$ for the same shear Reynolds number. We thus conclude that the two phenomenons of saturation are at least not as directly related as expected. A more detailed analysis of the velocity data including the turbulence statistics is required.

References

1. Andereck, C.D., Liu, S.S. and Swinney, H.L. Flow regimes in a circular Couette system with independently rotating cylinders. *J. Fluid Mech.* **164:155** (1986).
2. Ravelet, F., Chiffaudel, A., Daviaud, F. *et al.* Supercritical transition to turbulence in an inertially driven van Kármán closed flow. *J. Fluid Mech.* **601:339** (2008).
3. Dubrulle, B., Dauchot, O., Daviaud, F. *et al.* Stability and turbulent transport in Taylor-Couette flow from analysis of experimental data. *Phys. Fluids* **17-9**, 1-19 (2005).
4. Eckhardt, B., Grossman, S. and Lohse, D. Torque scaling in Taylor-Couette flow between independently rotating cylinders. *J. Fluid Mech.* **581:221** (2007).
5. Lewis, G.S. and Swinney, H.L. Velocity structure functions, scaling, and transition in high-Reynolds number Couette-Taylor flow. *Phys. Review E.* **59**, 5457-67 (1999).
6. Ravelet, F., Delfos, R. and Westerweel, J. Experimental studies of turbulent Taylor-Couette flow. *Proc. 5th Int. Symp. on Turb. Shear Flow Phen.* p.1211, Munich, Germany (2007).
7. Ravelet, F., Delfos, R. and Westerweel, J. Influence of global rotation and Reynolds number on the large-scale features of a turbulent Taylor-Couette flow. submitted to *Phys. Fluids.* (2009).

Velocity gradient statistics in a turbulent channel flow

Dmitry Krasnov, Thomas Boeck and Jörg Schumacher

Institut für Thermo- und Fluidodynamik, Technische Universität Ilmenau, 98693
Ilmenau, Germany
`dmitry.krasnov@tu-ilmenau.de`

Turbulence is associated with large fluctuations of velocity gradients which appear preferentially at the smallest scales of the flow. The amplitudes of the fluctuations exceed the mean values by orders of magnitude when the Reynolds number of the flow is sufficiently large. This behaviour is known as small-scale intermittency. The small-scale structure and statistics of turbulence has been mostly studied for the case of homogeneous, isotropic and statistically stationary turbulence. Much less work on the subject is reported for wall-bounded shear flows. Several reasons for this circumstance can be given. First, it is more challenging to measure all nine derivatives of the velocity gradient tensor with a sufficient resolution in an open shear-flow-setup (see e.g. [1] for a review). Secondly, a wall-bounded shear flow consists of a boundary layer which is dominated by coherent streamwise structures and a central bulk region in which they are basically absent. The statistics in the wall-normal direction is inhomogeneous and requires a height-dependent analysis. Finally, it is frequently believed that shear flow turbulence is in a state of local isotropy at the small-scale end for larger Reynolds numbers. Recent experimental and numerical studies demonstrated however that significant deviations persist, in particular when higher-order moments are discussed [2]. All this suggests to our view a systematic study of the height-dependence of the statistics of the velocity gradient fields in turbulent shear flows.

Here, we want to make a first step in this direction and conduct an analysis of the small-scale statistics of the velocity gradient in a wall-bounded shear flow. The analysis is based on three-dimensional direct numerical simulations of a turbulent channel flow at $Re_\tau = 180$ defined as

$$Re_\tau = \frac{u_\tau L}{\nu}. \quad (1)$$

Here u_τ is the wall friction velocity whereas L and ν stand, correspondingly, for the half-channel height and the kinematic viscosity. Figure 1 illustrates the geometry. The applied pseudospectral method is based on Fourier series in the horizontal directions x and y and a Chebyshev polynomial expansion

in the vertical z -direction [3, 4]. Our study is focused on two fields, the local enstrophy field and the energy dissipation rate field.

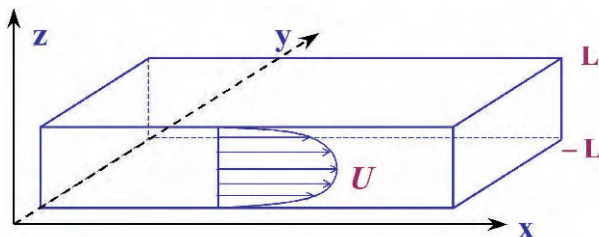


Fig. 1. Sketch of the channel flow geometry and the coordinates. The simulation domain is $L_x \times L_y \times L_z = 4\pi \times 2\pi \times 2$ in units of the half-width L .

The gradient tensor m_{ij} of the velocity fluctuations \mathbf{v}' can be decomposed into a symmetric and an antisymmetric part as

$$m_{ij} = \frac{\partial v'_i}{\partial x_j} = a_{ij} + s_{ij}. \quad (2)$$

The local enstrophy field, $\omega^2 = (\nabla \times \mathbf{v}')^2$ (see Fig. 2), probes the magnitude of the antisymmetric part $a_{ij} = -\epsilon_{ijk}\omega_k/2$ of the velocity fluctuation gradient tensor. Here ϵ_{ijk} is the fully antisymmetric Levi-Civita tensor. The energy dissipation rate field, $\epsilon = 2\nu s_{ij}s_{ji}$ (also shown in Fig. 2), measures the magnitude of the symmetric part s_{ij} of m_{ij} . The ensemble average of both fields are connected by $\langle \epsilon \rangle = \nu \langle \omega^2 \rangle$ for homogeneous isotropic turbulence. This does however not imply that the local statistical fluctuations are synchronized. In addition to homogeneous isotropic turbulence, we have to conduct the statistical analysis for both fields as a function of distance from the wall and to separate the turbulent fluctuations from the mean flow.

The accurate statistical analysis of velocity gradients requires considerably better spectral resolution than it is commonly used when only low-order moments are considered. Our channel simulation at the resolution of 512^3 collocation points shows considerable differences for the probability distribution functions (PDF) of the enstrophy and energy dissipation when compared with PDFs from a coarser simulation with 128^3 collocation points. For this lower resolution, which is adequate for second-order moments such as the Reynolds stresses [3], the far tails of the PDFs are considerably shorter.

The effect of the wall distance is examined at four locations, namely in the viscous buffer layer ($z^+ = 10$), at the beginning of the logarithmic layer where the Reynolds shear stress has its maximum ($z^+ = 30$), in the logarithmic region ($z^+ = 72$), and in the midplane of the channel ($z^+ = 180$). We find that the variations of both fields about their mean values are strongest in the

logarithmic layer which can be interpreted as a result of the recently observed hairpin vortex packet formation [1]. The fluctuations decrease slightly towards the channel centre and significantly towards the wall.

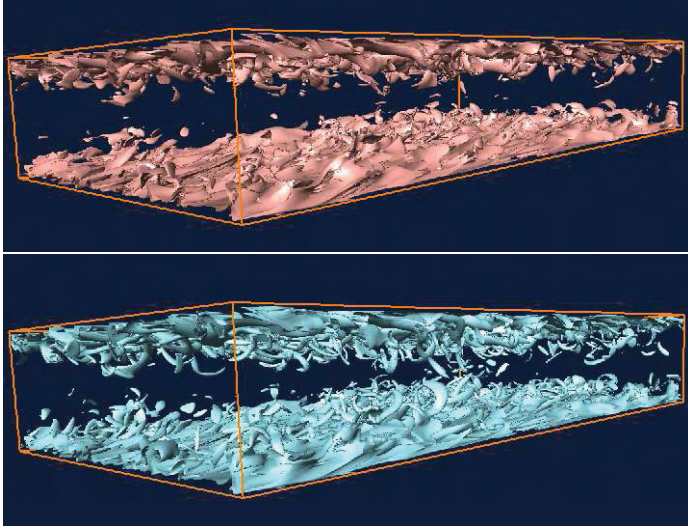


Fig. 2. Isosurfaces of the energy dissipation rate (upper figure) and the local enstrophy (lower figure). The isolevels are taken at $1.4\langle\epsilon\rangle$ and $1.4\langle\omega^2\rangle$, respectively.

The strong height-dependence is also manifest in the joint statistics of both fields [5]. Fig. 3 shows the joint PDF of ϵ and ω^2 normalized by both single quantity PDFs, i.e.

$$\Pi(\epsilon, \omega^2) = \frac{p(\epsilon, \omega^2)}{p(\epsilon)p(\omega^2)}. \tag{3}$$

High amplitudes of Π indicate a strong statistical correlation between both fields. The PDF of the data in the midplane has the broadest support. Very high-amplitude events of dissipation and vorticity are strongly correlated as indicated by the local maximum which is stretched out into the upper right corner of the plane. This maximum is even more pronounced in the logarithmic layer as can be seen in the upper right panel of Fig. 3. The local maximum of Π in the outer right corner becomes narrower with decreasing distance from the wall. It is in line with an overall decrease of the support for highly correlated events. The observed trend is consistent with our observations for the single quantity statistics. If we plot the line $\epsilon = \nu\omega^2$ (in white), it can be seen that the broad range of amplitudes of both fields is basically concentrated around this line.

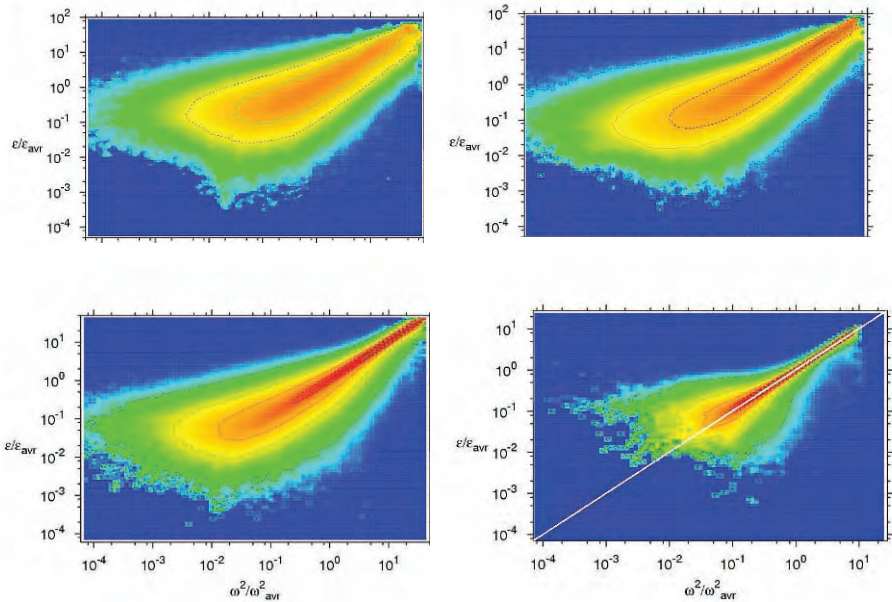


Fig. 3. Joint and normalized PDFs given by Eq. (3). Upper left: $z^+ = 180$. Upper right: $z^+ = 72$. Lower left: $z^+ = 30$. Lower right: $z^+ = 10$. Results of DNS with 512^3 grid points are shown, the joint PDF fields are normalized by the product of separate PDFs for ϵ/ϵ_{avr} and ω^2/ω_{avr}^2 . The white diagonal line in the lower right figure corresponds with $\epsilon = \nu\omega^2$. The colour coding is the same in all four figures and given in units of decadic logarithm. It varies from 10^0 (red) to 10^{-4} (blue).

To conclude, at all distances from the wall there is a strong statistical correlation between the local enstrophy and the dissipation. Close to the wall high-amplitude events of both fields seem to become synchronized. The support of the statistically correlated events varies significantly across the channel.

This work is supported by the Deutsche Forschungsgemeinschaft under grants BO 1668/2-3 (Emmy Noether Program) and SCHU 1410/4-1 (Heisenberg Program) and by the Jülich Supercomputing Centre (Germany) under grants HIL01.

References

1. R. J. Adrian, *Phys. Fluids* **19**, 041301 (2007).
2. L. Biferale and I. Procaccia, *Phys. Rep.* **414**, 43 (2005).
3. J. Kim, P. Moin and R. Moser, *J. Fluid Mech.* **177**, 133 (1987).
4. D. Krasnov, M. Rossi, O. Zikanov and T. Boeck, *J. Fluid Mech.* **596**, 73 (2008)
5. T. Boeck, D. Krasnov and J. Schumacher, *Physica D*, submitted (2008).

Channel flow LES with stochastic modeling of the sub-grid acceleration

R. Zamansky, I. Vinkovic and M. Gorokhovski

LMFA UMR 5509 CNRS Ecole Centrale de Lyon Université Claude Bernard
Lyon 1, 36 avenue Guy de Collongue, 69134 Ecully Cedex, France
remi.zamansky@ec-lyon.fr, ivana.vinkovic@ec-lyon.fr,
mikhael.gorokhovski@ec-lyon.fr

In [1] the large eddy simulation with stochastic modeling of the sub-grid acceleration (LES-SSAM) for homogeneous turbulence was proposed. The main motivation of this approach is to account for intermittency of the flow at sub-grid scales, by emphasizing the role of sub-grid acceleration. In this paper, we develop further this approach in order to simulate a high Reynolds number channel flow. We proposed a new sub-grid acceleration model and compared it with DNS and standard LES.

In LES-SSAM approach of [1], the total acceleration is decomposed on filtered (resolved) and unresolved part, in a way that the instantaneous model velocity field \hat{u}_i is resolved by:

$$\hat{a}_i = \frac{\partial \hat{u}_i}{\partial t} + \hat{u}_k \frac{\partial \hat{u}_i}{\partial x_k} = -\frac{1}{\rho} \frac{\partial \hat{p}}{\partial x_i} + \frac{\partial}{\partial x_k} (\nu + \nu_t) \left(\frac{\partial \hat{u}_i}{\partial x_k} + \frac{\partial \hat{u}_k}{\partial x_i} \right) + \hat{a}'_i; \quad \frac{\partial \hat{u}_k}{\partial x_k} = 0 \quad (1)$$

where ν is the viscosity, and ν_{turb} is given by the Smagorinsky model.

In the modeling of the non-resolved acceleration \hat{a}'_i for turbulent channel flow, our assumption is to emulate its modulus, $|\hat{a}'_i|$, by the product of the typical velocity increment, $u_*^2/\nu\Delta$ (u_* is the friction velocity and Δ is the characteristic cell size) and the frequency, f , considered as stochastic variable:

$$\hat{a}'_i = |a|(t)e_i(t) = fu_*^2/\nu\Delta e_i \quad (2)$$

Here e_i is a random unit vector of orientation, also simulated in this paper. The frequency f is supposed to be evolved with non-dimensional parameter $\tau = -\ln\left(\frac{h-y}{h}\right)$, where h represents the channel half-width, and y is the distance from the wall. The stochastic equation is derived here in the framework of scaling symmetry [2], and has the following form:

$$df = [\langle \ln\alpha \rangle + \langle \ln^2\alpha \rangle/2]fd\tau + \sqrt{\langle \ln^2\alpha \rangle/2}fdW(\tau) \quad (3)$$

$dW(\tau)$ is a Wiener process. The parameters of eq. 3 are $-\langle \ln \alpha \rangle = \langle \ln^2 \alpha \rangle = Re_+^{1/3}$, where $Re_+ = u_* h / \nu$. For the starting condition, $\tau = 0$, in this stochastic process, we introduce the characteristic value of frequency prescribed on the wall $f_+ = \lambda / u_*$, where λ is determined, as Taylor scale, but in the framework of definitions of wall parameters. This is done as follows: the Reynolds number, based on friction velocity, is $Re_+ = u_* h / \nu = h / y_0 \approx Re_h^{3/4}$ where y_0 is the thickness of the viscous layer, and Re_h is the Reynolds number based on the center-line velocity. One then yields: $\lambda \approx h Re_h^{-1/2} \approx h Re_+^{-2/3}$. Similar to Kolmogorov-Oboukhov 62, the starting condition for the random path, given by eq. 3, is sampled from the stationary log-normal distribution of f/f_+ with parameters $\sigma^2 = \ln 2$ and $\mu = -\frac{1}{2}\sigma^2$, such that $\langle f \rangle = (\langle f^2 \rangle - \langle f \rangle^2)^{1/2} = f_+$. Hence this stochastic process for frequency will relax f from a log-normal distribution on the wall ($\tau = 0$) to the power distribution with increasing the distance to the wall ($\tau \rightarrow \infty$). The distributions of the frequency predicted by this stochastic process, on different wall-normal distances, are compared in fig. 1a with the evolution of the frequency computed from DNS, via eq. 2. It is seen that the model of frequency allows to predict the DNS relatively well.

In addition to the stochastic simulation of the unresolved modulus of acceleration, we simulate also the orientation vector e_i . This is done by a random walk evolving on the surface of a sphere of unity radius. First the computation of e_i from DNS was performed. The result are shown in fig. 1b. It is seen that e_i relaxes toward isotropy with increasing distance from the wall. In order to represent this tendency toward isotropy, we implement the Kubo oscillator with a real coefficient α for the random motion on the sphere. Each position increment of the random walk is given by $\zeta = \alpha dW(\tau) = \sqrt{\frac{\ln Re_+}{2}} W(\tau)$, and the direction β , at each time step, is chosen randomly from the uniform distribution. As τ increases, the random walk covers all the surface of the sphere. In fig. 1b the simulated distribution of $\theta = \sin^{-1}(e_y)$ (e_y is the normal to the wall direction) is compared with unresolved acceleration from DNS. The last one was computed as difference between actual acceleration, given by DNS and its filtered value on the scale Δ .

The *a posteriori* tests of this model is performed by comparing the LES-SSAM with standard LES and DNS, for three Reynolds numbers, $Re_+ = 590$, $Re_+ = 1000$ and $Re_+ = 2000$. We used our own DNS data, as well as the DNS data from [3] and [4]. For LES and LES-SSAM simulations the classical Smagorinsky model with a wall damping function for the turbulent viscosity has been applied. The grid size is $64 \times 64 \times 64$, and its resolution is: $\Delta x^+ \times (\Delta y_{min}^+ \sim \Delta y_{max}^+) \times \Delta z^+ = 87 \times (0.71 \sim 29) \times 29$, $147 \times (1.2 \sim 49) \times 49$ and $295 \times (2.4 \sim 98) \times 98$ for $Re_+ = 590$, 1000 and 2000 respectively. As shown on fig. 2, the profiles of mean velocity and of standard deviation of the velocity fluctuations, predicted by LES-SSAM approach, are improved notably. Fig. 3a illustrates the computation of turbulent and viscous stresses. It is seen that computation of momentum fluxes in the wall-normal direction, is

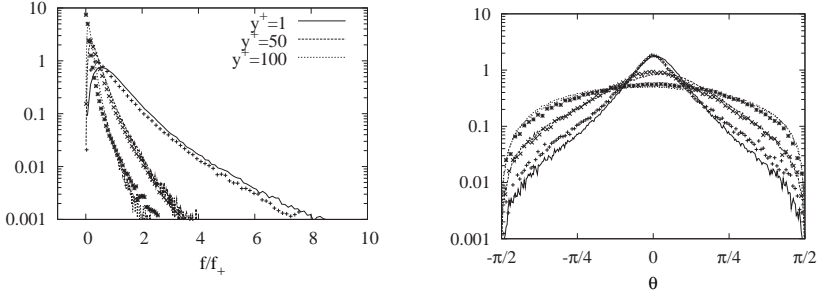


Fig. 1. (a): Distribution of f/f_+ from SSAM (cross) and comparison with DNS (line) at $Re_+ = 590$, for several distances from the wall. (b): Distribution of $\theta = \sin^{-1}(e_y)$ for unresolved acceleration from DNS (line) and from SSAM (cross), for $Re_+ = 590$, and for several distances from the wall ($y^+ = 3, y^+ = 10$ and $y^+ = 30$).

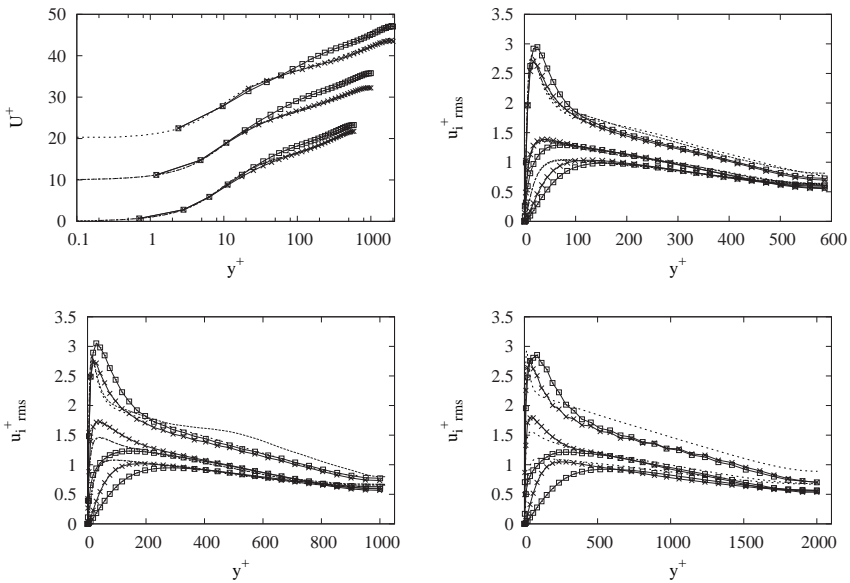


Fig. 2. (a): Streamwise mean velocity, for $Re_+ = 590, Re_+ = 1000$ and $Re_+ = 2000$ from bottom to top, respectively, shifted by 10 wall units upward. Standard deviation of streamwise (u), spanwise (w) and normal (v) velocity (in wall unites), for (b): $Re_+ = 590$, (c): $Re_+ = 1000$ and (d): $Re_+ = 2000$. Square: LES; cross: LES-SSAM; dash: DNS (only for $Re_+ = 590$ and $Re_+ = 1000$); dots: DNS from [3] for $Re_+ = 590$ and from [4] for $Re_+ = 1000$ and $Re_+ = 2000$.

improved in comparison with LES. Velocity spectra are shown in fig. 3b. The excessive damping of energy on small scales, which is inherent to LES, is reduced by LES-SSAM. Fig. 3c represents the evolution of the longitudinal autocorrelation coefficient for the streamwise velocity component along the channel. Improvement of the decorrelation length can be seen as well, when LES-SSAM is used. Fig. 3d displays distribution of acceleration component in the spanwise direction. In agreement with the DNS, the LES-SSAM distribution exposes stretched tails, as a manifestation of the close to the wall intermittency, which is not the case by using LES.

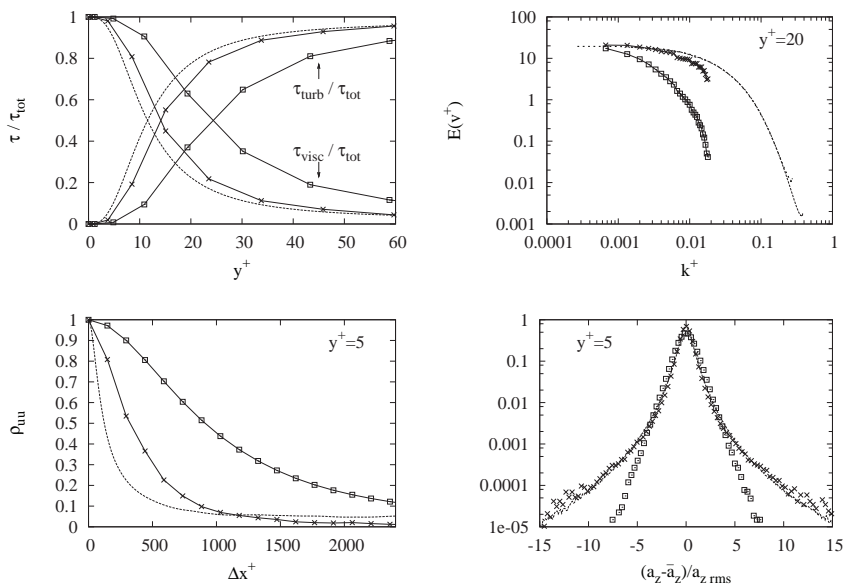


Fig. 3. Reynolds number of $Re_+ = 1000$. (a): Fractions of turbulent $\tau_{turb} = -\rho\langle u'v' \rangle$ and viscous $\tau_{visc} = -\rho\nu\langle \frac{\partial u}{\partial y} \rangle$ stresses compared to the total one $\tau_{tot} = \tau_{visc} + \tau_{turb}$. (b): Normalized longitudinal 1-D spectra of streamwise velocity for $y^+ = 20$. (c): Longitudinal autocorrelation of streamwise velocity at $y^+ = 5$. (d): Distribution of spanwise component of acceleration for $y^+ = 5$. Square: LES; cross: LES-SSAM; dash: DNS; dots: DNS from [4] (uniquely for (b)).

References

1. V. Sabelnikov, A. Chtab & M. Gorokhovski, Advances in Turbulence XI, 11th EUROMECH European Turbulence Conference, **117** 209-211 (2007).
2. M. Gorokhovski & V. L. Saveliev, J. Phys. D: Appl. Phys. **41**, 085405 (2008).
3. R. D. Moser, J. Kim & N. M. Mansour, Phys. Fluids **11**, 943-945 (1999).
4. S. Hoyas & J. Jiménez, Phys. Fluids **20**, 101511 (2008).

DNS of three-dimensional separation in turbulent diffuser flows

Johan Ohlsson¹, Philipp Schlatter¹, Paul F. Fischer² & Dan S. Henningson¹

¹ Linné Flow Centre, KTH Mechanics, Stockholm, Sweden

johan@mech.kth.se

² MCS, Argonne National Laboratory, Argonne, USA

The spectral-element method (SEM), is a high-order numerical method with the ability to accurately simulate fluid flows in complex geometries. SEM has opened the possibility to study – in great detail – fluid phenomena known to be very sensitive to discretization errors, e.g. flows undergoing pressure-induced separation [4]. Recently, Cherry *et al.* [1] performed experiments using Magnetic Resonance Velocimetry (MRV) of turbulent diffuser flow exhibiting unsteady three-dimensional separation at $Re = 10\,000$ based on bulk velocity and height of the inflow duct. Two geometries with different opening angles were investigated and it was found that the flow was extremely sensitive to slight changes in the geometrical setup. To understand this sensitivity and to analyze its causes, we present a direct numerical simulation (DNS) of one of these cases (denoted by “Diffuser 1” in [1]) by means of the SEM. Here, we focus on careful analysis of mean flow results in order to assess the quality of the simulation data. The incompressible Navier-Stokes equations are

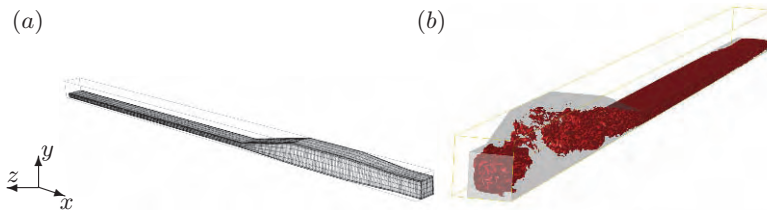


Fig. 1. (a) Grid of one of the diffuser geometries (“Diffuser 1”) showing the development region, diffuser expansion, converging section and outlet. (b) Snapshot showing isocontours of $0.4 \cdot u_b$.

solved using the Legendre polynomial based SEM code `nek5000`, developed by Fischer *et al.* [2]. The computational domain shown in Fig. 1a, is set up in close agreement to the diffuser geometry in the experiment. It consists of the inflow development duct, the diffuser expansion and the converging section. The resolution of approximately 172 million grid points is obtained by a total of 127 750 local tensor product domains (elements) with a polynomial order of 11 respectively. The simulation was performed on 32 768 cores on the

Blue Gene/P at Argonne National Laboratory and turbulent statistics over ~ 100 convective time units were collected. A snapshot clearly highlighting the complex unsteady features of the flow is given in Fig. 1*b*. In the inflow duct, turbulence is triggered by means of an unsteady trip forcing, which eliminates artificial temporal frequencies which may arise from inflow recycling methods. The outflow condition specifies zero pressure at the outflow plane, which mimics the real experiment. In addition, a sponge region is added at the end of the contraction in order to smoothly damp out turbulent fluctuations, thereby eliminating spurious pressure waves to arise when energetic turbulent structures hit the outflow boundary, as well as ensure the stability of the computation by preventing these structures from recirculating back into the domain. The turbulent inflow duct was studied in detail to ensure that a fully developed turbulent flow is reached at the end of the development section. Mean velocity profiles as a function of y^+ and z^+ respectively taken from a middle plane a short distance upstream of the diffuser opening are shown in Fig. 2*a*. Good agreement with turbulent channel flow simulation at $Re_\tau =$

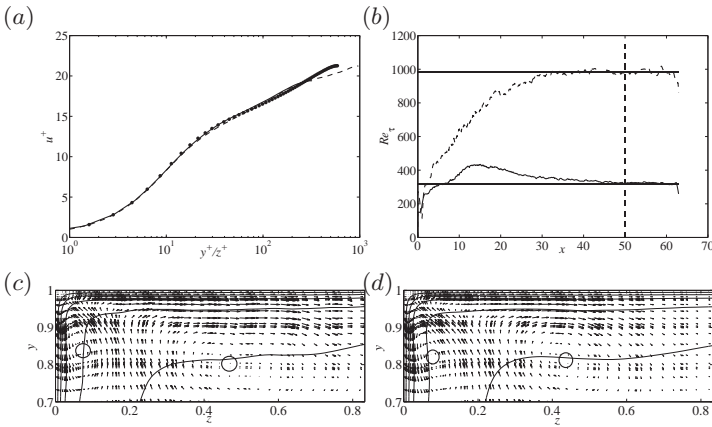


Fig. 2. (a) Mean centerplane velocity profile 13 units upstream of the diffuser throat, (b) evolution of Re_τ in a middle plane of the inflow section, solid horizontal lines showing Re_τ for a periodic duct and vertical dashed line location of the selected velocity profile in (a). — $u^+(y^+)$, - - - $u^+(z^+)$, ····· turbulent channel flow simulation at $Re_\tau = 590$ [3] (c) Time-averaged flow field in one of the corners showing the secondary flow compared to (d) periodic duct simulation. Circles show approximate location of vortex centers.

590 [3] can be inferred. In particular, the linear profile in the viscous sublayer and the *log law* is captured with good accuracy. Monitoring the streamwise development of the friction Reynolds number, Re_τ , see Fig. 2*b*, helps to detect where a fully turbulent flow is reached. The secondary flow in the corners of the duct also give a good indication on the development of the flow and are known to be important for the correct separation behavior [1]. As can be seen in Fig. 2*c* the corner vortices are captured well, compared to results from a periodic duct simulation in Fig. 2*d*. From the measures listed above,

we conclude that the flow has converged to a statistically stationary state well upstream of the diffuser throat.

Turning to the actual diffuser, a qualitative analysis focusing on identifying the size and location of the separated region is made by selecting crossflow planes in Fig. 3. It can be clearly seen that our simulation captures the mean

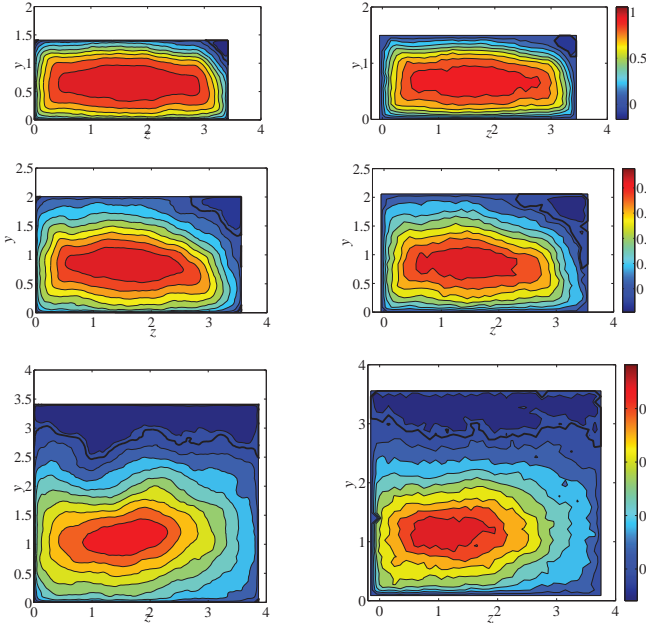


Fig. 3. Crossflow planes of streamwise velocity 2, 5 and 12 units downstream of the diffuser throat. *Left column:* Computation by nek5000. *Right column:* Experiment by Cherry *et al.* [1] Each streamwise position has its own colorbar on the right. Thick black line corresponds to the zero velocity contour.

separation, which starts in the uppermost right corner and gradually spreads to the top expanding wall. It should be pointed out that the separated region experiences a highly unsteady behavior and structures with time scales on the order of one flow through time were detected in the time history of the data. Considering this, it is remarkable that the simulation data experiences less fluctuations (i.e. indicating a more averaged state) than the experimental data. A more quantitative comparison is made in Fig. 4, where mean velocity profiles are selected in a spanwise midplane. Generally, excellent agreement is observed. In particular, the upward movement of the velocity peak is well captured. The presence of the large separated region on the upper inclined wall forces the flow upwards, however only slightly, due to the originally high momentum content in the flow. A movement of the peak is also present in the spanwise direction, which can be seen in Fig. 3 in both data sets. Interestingly, here, the motion is reversed, i.e., the peak moves away from the side expanding wall. The reason for this is the boundary layer thickening created as the side wall expands. The shear layer on top of this boundary layer acts as a barrier

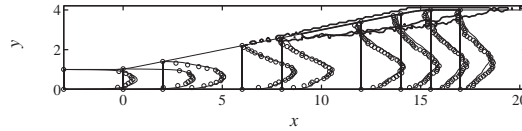


Fig. 4. Mean centerplane velocity $3 \cdot \langle u \rangle + x$ in the diffuser. *Velocity data:* — nek5000, \circ experiment by Cherry *et al.* *Separated region:* — nek5000, ---- experiment by Cherry *et al.*

for the flow, which then has to turn slightly to the left. If, however, the angle for the side wall would have been larger with a resulting separation, the flow would instead be forced to the right due to the lower pressure in this area, as is the case on the top expanding wall. This suggests that as soon as separation appears in the flow, the motion will change completely (e.g. change mean flow direction as seen here) and will be dictated by the location of the separated flow region. Moreover, the size and location of the separated region (here defined as a region with negative velocity) in a spanwise midplane, seen in Fig. 4, is in good agreement with the experimental data.

Diffuser flows are numerically hard to treat in general, not only due to their sensitivity to discretization errors, but also — as a cause of the slow, separated flow — the need for long (and expensive) time integration to obtain converged turbulent statistics. Three-dimensional diffusers, in particular, are even more challenging due to the lack of statistically homogeneous directions, and hence the possibility to average over these. Taking into account these difficulties and the fact that a Reynolds number of 10 000 can be considered fairly high in the context of DNS, the mean flow results presented here show excellent agreement with experimental studies. As the quality of the data is now assessed, the complex flow physics in the three-dimensional separation can be investigated. In particular, turbulent statistics not accessible from the experimental data, i.e. Reynolds stress budgets including e.g. the entire pressure field, will be investigated to get a more detailed picture of the flow. In addition, as turbulence modeling in separated flows continues to be large area of research, this data can serve as a reference database, where particular interest might be the transport of turbulent kinetic energy and dissipation subject to three-dimensional separation.

References

1. E. M. Cherry, C. J. Elkins, and J. K. Eaton. Geometric sensitivity of three-dimensional separated flows. *Int. J. Heat Fluid Flow*, 29, 2008.
2. P. Fischer, J. Kruse, J. Mullen, H. Tufo, J. Lottes, and S. Kerke-meier. NEK5000 - Open Source Spectral Element CFD solver. <https://nek5000.mcs.anl.gov/index.php/MainPage>.
3. R. D. Moser, J. Kim, and N. Mansour. Direct numerical simulation of turbulent channel flow up to $Re_\tau = 590$. *Phys. Fluids*, 11(4), 1999.
4. J. Ohlsson, P. Schlatter, P.F. Fischer, and D.S. Henningson. Direct and large-eddy simulation of turbulent flow in a plane asymmetric diffuser by the spectral-element method. In *DLES7. ERCOFTAC WORKSHOP Direct and Large-Eddy Simulations 7* University of Trieste, Italy, September 8-10, 2008.

Optimal amplification of large scale streaks in the turbulent Couette flow

Y. Hwang and C. Cossu

LadHyX, CNRS-École Polytechnique, F-91128 Palaiseau, France
carlo.cossu at ladhyx.polytechnique.fr

Abstract:

The optimal response of the turbulent Couette mean flow to initial conditions, harmonic and stochastic forcing is computed at $Re = 750$. The equations for the coherent perturbations are linearised near the turbulent mean flow and the effect of small scales is modelled with the standard eddy viscosity. The mean flow is linearly stable but it is shown to amplify coherent streamwise streaks from streamwise vortices. The largest amplifications are realized by streamwise uniform structures associated to spanwise wavelengths of $4.3h$ for largest amplifications of the energy of initial conditions, $5.1h$ for the maximum amplification of the variance of stochastic forcing. These spanwise scales compare well with the ones of the coherent large-scale streaks observed in experimental realisations and direct numerical simulations of the turbulent Couette flow. The optimal response to the harmonic forcing can be very large and is obtained with steady forcing of structures with larger spanwise wavelength ($7.4h$).

1. Introduction

The fully developed turbulent plane Couette flow is one of the canonical cases in which very large coherent and persistent streaky structures have been observed. Lee & Kim (1991) observed structures elongated in the streamwise direction with a roughly circular cross-section in their direct numerical simulation of the fully developed turbulent Couette flow. In order to understand if the spanwise size of these large scale structures was the largest possible, Komminaho *et al.* (1996) repeated the simulations at $Re_h = 750$ using a huge computational box ($L_x \times L_y \times L_z = 28\pi \times 2 \times 8\pi$). They found that the most probable spanwise spacing of these vortical structures is about $4h$ where h is the half height of channel and that these structures can be suppressed by rotation around the spanwise axis. Very recently, Kitoh *et al.* (2005) and Kitoh & Umeki (2008) experimentally studied these structures at $Re_h = 3750$ and found typical spanwise wavelengths of the order of $4 \sim 5h$.

At the same time similar large scale structures were found in direct numerical simulations and experiments in the plane pressure driven channel flow and in the turbulent boundary layer. Recent investigations (del Álamo & Jiménez 2006; Cossu *et al.* 2008; Pujals *et al.* 2008) have revealed a possible connection between the observed large scale structures and the optimal perturbations of the turbulent mean flows. In all these studies, analytical expressions that matched the mean velocity profiles and the turbulent eddy viscosity, were used to compute the optimal perturbations leading to the maximum transient growth. In the turbulent Poiseuille flow case it was found that the maximum transient growth was realized by streamwise uniform structures with a spanwise wavelength proportional to the outer scale h and in good agreement with that of dominant streaky structures in the outer layer. No results are, to our knowledge, currently available for the optimal transient growth sustained by the turbulent Couette flow nor for the optimal response of turbulent mean flows to harmonic and stochastic forcing. The scope of this investigation is to fill these gaps.

2. Results and discussion

Unlike previous investigation of the turbulent Poiseuille and boundary layer flows, no analytical model is currently available to model the Couette turbulent mean flow and the associated eddy viscosity. We therefore use direct numerical simulations to obtain the turbulent mean flow at $Re_h \equiv Uh/\nu = 750$. We `channelflow` code (Gibson *et al.* 2008; which is based on a spectral method with Fourier-Galerkin representation in the streamwise (x) and spanwise (z) directions, and Chebyshev-tau representation in the transverse direction (y). For time-integration, semi-implicit method with a third-order Runge-Kutta scheme for nonlinear term and a second-order Crank-Nicolson scheme for the diffusion term is used. We follow Komminaho *et al.* (1996) in the choice of the large computational box ($L_x \times L_y \times L_z = 28\pi \times 2 \times 8\pi$) and grid point ($N_x \times N_y \times N_z = 340 \times 55 \times 170$) to obtain well converged solutions. Turbulent statistics are obtained with averaging time interval $T_{average} = 1000$ ($T \in [500, 1500]$). Fig. 1 shows the mean velocity profile obtained by the present DNS, which shows good agreement with DNS results by Komminaho *et al.* (1996) and Tsukahara *et al.* (2006). Using this mean flow, eddy viscosity is also obtained to use for computing optimal perturbations: i.e. $\nu_T = dU/dy^{-1}(u_\tau^2 - \nu dU/dy)$ where ν_T and U are eddy viscosity and turbulent mean flow, respectively.

The three canonical types of optimal perturbations have been computed: the temporal energy growth, the response to harmonic excitations and the variance to white-noise stochastic forcing. The corresponding optimal amplification curves are reported in Fig. 2. In all the cases the maximum growth is obtained for streamwise uniform disturbances ($\alpha h = 0$), and their spanwise spacings are $\lambda_z = 4.3h$ for the temporal growth, $\lambda_z = 7.4h$ for the harmonic response and $\lambda_z = 5.1h$ for the stochastic forcing. These values are in very good agreement with the spanwise spacing of the large-scale streaks

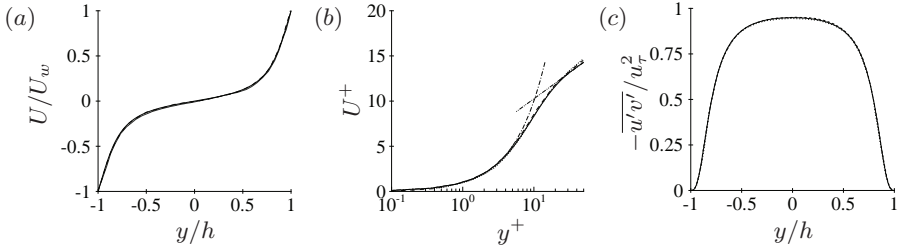


Fig. 1. Turbulent mean velocity profile and shear stress from direct numerical simulations. (a) Mean velocity profile expressed in outer units, (b) Same profile expressed in inner units $U^+ \equiv (U + U_w)/u_\tau$ and $y^+ = (y + h)u_\tau/\nu$ and compared to the curves $U^+ = y^+$ (---) and $U^+ = (1/0.4) \log y^+ + 4.5$ (-----), (c) Turbulent mean shear stress $-\overline{u'v'}/u_\tau^2$. Here, the present DNS (—), Komminaho *et al.* (1996) (---) and Tsukahara *et al.* (2006) (·····); the curves are almost undistinguishable.

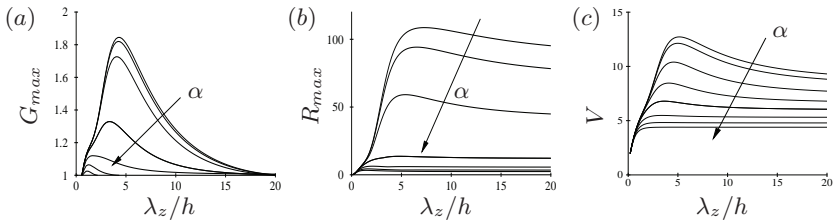


Fig. 2. Responses to optimal perturbations with λ_z/h for $\alpha h = 0.0, 0.1, 0.25, 0.5, 1.0, 2.0, 3.0, 4.0$: (a) optimal transient growth, G_{max} ; (b) optimal harmonic response, R_{max} ; (c) variance excited by stochastic forcing, V .

reported in previous studies (Komminaho *et al.* 1996; Kitoh *et al.* 2005; Kitoh & Umeki 2008) except for the response to harmonic forcing, that is probably more related to the sensitivity to deterministic forcing induced e.g. by boundary conditions or control devices. The velocity field of the optimal initial perturbation maximizing the transient energy growth in time, and the corresponding optimal response, reported in Fig. 3, consist of streamwise vortices and streamwise streaks respectively. Also the structure of the optimal streaks is strikingly similar to the one obtained by DNS (Komminaho *et al.* 1996; Tsukahara *et al.* 2006). These results are further confirmations of the strong relations that seem to exist between large-scale streaky structures and the optimal coherent perturbations of the turbulent mean flow.

References

1. LEE, M. J. & KIM, J. 1991 The structure of turbulence in a simulated plane Couette flow. *Eighth Symp. on Turbulent Shear Flow Tech. University of Munich, Sept. 9-11*, 5.3.1-5.3.6.

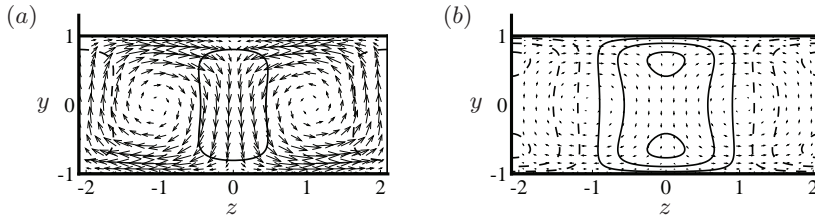


Fig. 3. Cross-stream view of the optimal perturbation velocity fields for the initial value problem obtained for $\lambda_{z_{max}}/h$ ($\simeq 4.2$) and $\alpha_{max}h$ ($= 0$): (a) initial disturbance, (b) optimal response at t_{max} . Here, the solid and dashed contours denote $u \geq 0$ and $u < 0$, respectively, with increment 0.3. The v and w are superimposed as vectors.

2. KOMMINAHO, J., LUNDBLADH, A., & JOHANSSON, A. V. 1996 Very large structures in plane turbulent Couette flow. *J. Fluid Mech.* **320**, 259.
3. KITO, O., NAKABAYASHI, K., & NISHIMURA, F. 2005 Experimental study on mean velocity and turbulence characteristics of plane Couette flow, low Reynolds number effects and longitudinal vortical structure. *J. Fluid Mech.* **539**, 199.
4. KITO, O., & UMEKI, M. 2008 Experimental study on large-scale streak structure in the core region of turbulent plane Couette flow. *Phys. Fluids* **20**, 025107.
5. DEL ÁLAMO, J. C., & JIMÉNEZ, J. 2006 Linear energy amplification in turbulent channels. *J. Fluid Mech.* **559**, 205.
6. COSSU, C., PUJALS, G. & DEPARDON, S. 2009 Optimal transient growth and very large scale structures in turbulent boundary layers. *J. Fluid Mech.* **619**, 79–94.
7. PUJALS, G., GARCÍA-VILLALVA, M., COSSU, C., & DEPARDON, S. 2009 A note on optimal transient growth in turbulent channel flow. A note on optimal transient growth in turbulent channel flows. *Phys. Fluids* **21**, 015109.
8. GIBSON, J. F., HALCROW, J., & CVITANOVIĆ, P. 2008 Visualizing the geometry of state space in plane Couette flow. *J. Fluid Mech.* **611**, 107., see also <http://www.channelflow.org/>.
9. TSUKAHARA, T., KAWAMURA, H. & SHINGAI, K. 2006 Dns of turbulent Couette flow with emphasis on the large-scale structure in the core region. *J. Turbulence*. **42**.
10. TSUKAHARA, T., IWAMOTO, K. & KAWAMURA, H. 2007 POD analysis of large-scale structures through DNS of turbulence Couette flow. In *Advances in Turbulence XI*, pp. 245–247. Porto, Portugal, June 25–28.

Symmetry of Coherent Vortices in Plane Couette Flow

T. Itano¹, S.C. Generalis², S. Toh³ and J.P. Fletcher²

¹Faculty of Engineering Science, Kansai University, 564-8680 Osaka, Japan
itano at kansai-u.ac.jp

²School of Engineering & Applied Sciences, Aston University, B4 7ET
Birmingham, UK.

³Department of Physics and Astronomy, Graduate School of Science, Kyoto
University, Kyoto 606-8502, Japan

A numerical continuation method is carried out in a homotopy space connecting two different flows, the Plane Couette Flow (PCF) and the Laterally Heated Flow in a vertical slot (LHF). This numerical continuation method enables us to obtain an exact steady solution in PCF[6]. The *new solution* has the shape of hairpin vortices (HVS: hairpin vortex solution, see Fig.1), which is observed ubiquitously in turbulent shear flows.

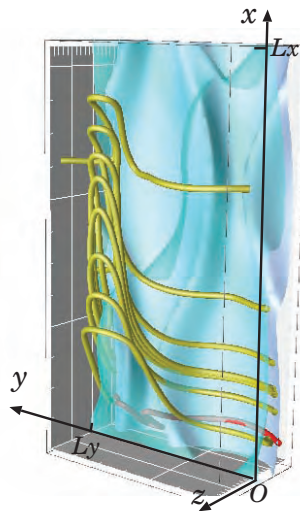


Fig. 1. The *hairpin vortex solution* (HVS) in plane Couette flow (PCF) at $Re = 200$. (Yellow) curves are vortex lines across the channel mid-plane, underneath which there are low-speed structures visualised as (cyan) isosurfaces. Here x, y, z denote the stream-, span-wise and wall coordinates.

The HVS satisfies three distinct symmetries, which lead to the apparent spanwise reflection symmetry across a plane ($y = L_y/4$ or $3L_y/4$) as seen in Fig.1. By contrast, only two of the three symmetries are satisfied by the streamwise vortex solution (SVS), which was previously obtained as a coherent structure typical of wall turbulence in Refs.[1, 2, 3, 4]. Thus, the SVS is expected to bifurcate from the HVS via breaking of the spanwise reflection symmetry depicted in Fig.1. In the present study, we show evidence that the SVS bifurcates from the HVS in the homotopy space between the PCF and the LHF.

We first consider an incompressible Boussinesq fluid with $Pr = 0$ filling a vertical slot of thickness $2\tilde{h}$. The boundaries of the gap are two rigid parallel planes of infinite extent heated laterally with temperatures $\tilde{T}_0 \pm \Delta\tilde{T}$, and which move relative to each other with speed $2\Delta\tilde{U}$ in the x-direction of the Cartesian coordinate system. In terms of the two non-dimensional parameters, $Re = (\tilde{A} + \Delta\tilde{U})\tilde{h}/\tilde{\nu}$ and $\epsilon = \tilde{A}/(\tilde{A} + \Delta\tilde{U})$, where $\tilde{A} = \tilde{\gamma}\tilde{g}\Delta\tilde{T}\tilde{h}^2/6\tilde{\nu}$, the perturbation from the static state of our system is governed by the incompressibility and momentum equations respectively:

$$\nabla \cdot \mathbf{u} = 0 \quad , \quad \mathbf{u} \cdot \nabla \mathbf{u} = -\nabla p + \frac{6\epsilon}{Re} z \mathbf{e}_x + \frac{1}{Re} \nabla^2 \mathbf{u} .$$

Here, the parameter ϵ plays an important role in our analysis; solutions obtained with $\epsilon = 0$ are exact states of PCF, while those with $\epsilon = 1$ are exact solutions of LHF.

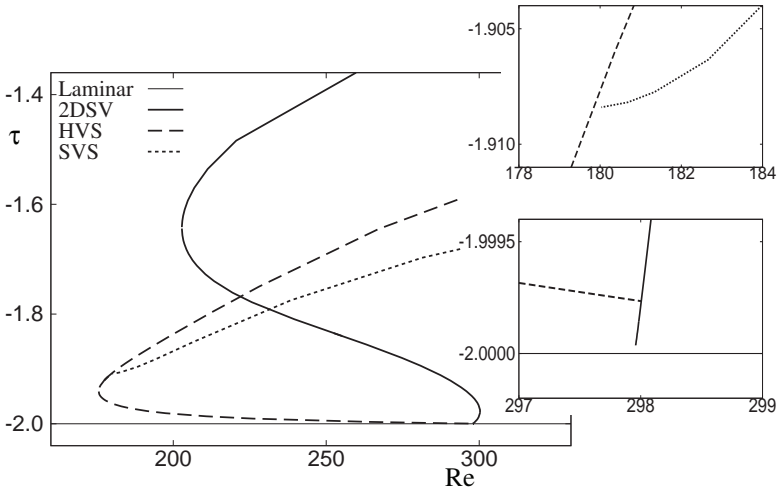


Fig. 2. Transition in LHF($\epsilon = 1$): $(\alpha, \beta) = (2.0, 0)$ for the 2DSV (2D spanwise vortex), $(\alpha, \beta) = (1.0, 2.0)$ for the tertiary state (abbreviated as “HVS”) and the SVS.

Fig.2 shows the bifurcation diagram obtained in LHF ($\epsilon = 1$), where the mean shear rate at the boundary, τ , is adopted as an order parameter to characterise solutions. The secondary branch in LHF ($\epsilon = 1$) that bifurcates from the laminar state in LHF (see the right-bottom inset of Fig.2) consists of the two-dimensional spanwise vortical (2DSV) structures, which exhibit cat’s-eye roll patterns occupying the whole channel width (cf. Ref.[5]). The branch satisfies the following symmetries: “Spanwise translational symmetry” $\mathbf{u}(x, y, z) = \mathbf{u}(x, y + \Delta y, z)$, and “Rotational symmetry with respect to the y axis” $[u_x, u_z]^T(x, y, z) = [-u_x, -u_z]^T(-x, y, -z)$.

The tertiary branch that bifurcates from 2DSV, termed as “HVS” in the diagram, is the new hairpin vortex solution reported recently in [6]. The branch satisfies the following three independent symmetries:

- \mathcal{A} “Streamwise translational and spanwise reflectional symmetry”,
 $[u_x, u_y, u_z]^T(x, y, z) = [u_x, -u_y, u_z]^T(x + L_x/2, -y, z)$,
- \mathcal{B} “Parity symmetry with respect to $(x, y, z) = (L_x/4, L_y/4, 0)$ ”,
 $[u_x, u_y, u_z]^T(\frac{L_x}{4} + x, \frac{L_y}{4} + y, z) = [-u_x, -u_y, -u_z]^T(\frac{L_x}{4} - x, \frac{L_y}{4} - y, -z)$,
- \mathcal{C} “Parity symmetry with respect to the origin”,
 $[u_x, u_y, u_z]^T(x, y, z) = [-u_x, -u_y, -u_z]^T(-x, -y, -z)$,

where L_x and L_y are the streamwise and spanwise wave-lengths of the HVS. The spanwise reflection symmetry of HVS, $[u_x, u_y, u_z]^T(x, L_y/4 + y, z) = [u_x, u_y, u_z]^T(x, L_y/4 - y, z)$, can be deduced by the symmetries \mathcal{A} , \mathcal{B} and \mathcal{C} . By employing the numerical continuation method, this branch connects to a solution at the PCF limit ($\epsilon = 0$), which contains a hairpin-shaped bundle of vortex lines depicted in Fig.1.

Furthermore, a branch (termed as “SVS” in the diagram) bifurcates from HVS at $Re = 180$ (see also the right-top inset of Fig.2). This bifurcation takes place via breaking of the symmetry \mathcal{C} of HVS (details of this bifurcation will be given elsewhere [7]). The continuation method guarantees that this branch also connects to a solution at PCF limit ($\epsilon = 0$), which corresponds to the streamwise vortex solution (SVS) previously obtained. In the homotopy parameter space spanned by ϵ and Re , the SVS is the quaternary (or higher) solution branch, while HVS is the tertiary branch in the bifurcation sequence for the laminar state. This discovery would provide us with an understanding of the vortex nature in shear flows, that would reconcile the historical controversy with respect to the distinction between the streamwise (SVS) and hairpin vortices (HVS) in turbulent shear flows.

Acknowledgement

Both of us would like to dedicate the result to our families, whose continued support enabled us to research in the field of canonical shear flows. In particular we are grateful to our fathers who over the years installed on us the enthusiasm to pursue vigorously the unknown in order to establish the truth. T.I. is grateful for the financial support received from Aston University under

the Visiting Scholars Fund Scheme and EPSRC (GR/S70593/01). S.C.G. is grateful to a Research Invitation from the Kansai University. This work has been also supported in part by KAKENHI (19760123).

References

1. M.Nagata, J. Fluids Mech., **217**, 519 (1989).
2. R. Clever and F.Busse, J. Fluids Mech., **344**, 137 (1997).
3. F.Waleffe, Phys. Rev. Lett., **81**, 4140 (1998).
4. F.Waleffe, Phys. Fluids, **15**, 1517 (2003).
5. M.Nagata and F.Busse, J. Fluids Mech., **135**, 1 (1983).
6. T. Itano and S.C. Generalis, Phys. Rev. Lett., **102**, 114501 (2009).
7. T. Itano and S.C. Generalis, *in preparation*, (2009).

Universal character of perturbation growth in near-wall turbulence

N. Nikitin

Institute of Mechanics, Moscow State University
Michurinsky prospect 1, 117192 Moscow, Russia. nvnikitin@mail.ru

1 Introduction

Instability and unpredictability may be considered as essential parts of the definition of turbulence. The difference between the instantaneous velocity fields of two turbulent flows will grow no matter how small it might be initially. Considerable theoretical and experimental effort has been devoted to tackling the problem of turbulence predictability (see for references [1]). However, there were no quantitative results up to now except in the paper [2]. In that work, the Lyapunov spectra corresponding to turbulent channel flow at very low Reynolds number was calculated.

In present work, spatial growth of small perturbations introduced into an inlet cross-section of turbulent pipe flow is investigated via DNS. Turbulent inflow field is extracted from auxiliary streamwise-periodic simulation running in parallel with the main spatial simulation. Downstream evolution of perturbations is analyzed by comparing two flows, with and without perturbations.

2 Formulation and numerical method

We consider a flow of viscous incompressible fluid through a long circular pipe driven by a given unsteady inflow velocity. The flow is governed by the Navier–Stokes and continuity equations with a no-slip boundary condition on the rigid wall. Initial $\mathbf{u}|_{t=0}$ and inflow $\mathbf{u}|_{x=0}$ velocity fields are extracted from an auxiliary turbulent flow simulation with streamwise-periodic conditions. The procedure of generating the streamwise-periodic solution $\mathbf{u}_t(\mathbf{x}, t)$ is standard for DNS of turbulent pipe flow.

At first, the auxiliary simulation is run alone until a statistically steady state is achieved. The instantaneous velocity field at this time, which is referred to as $t = 0$, is taken as the initial condition for the main simulation. After that, the auxiliary simulation is run in parallel with the main simulation. At each time instant $t > 0$, the velocity distribution in the cross-sectional plane

$x = 0$ of the auxiliary simulation is transferred into the inlet cross-section of the main simulation. In addition, a certain small-amplitude artificial perturbation is introduced into the inlet.

In the present paper, we are focused on the spatio-temporal evolution of the perturbation field, which is defined as the difference between the actual $\mathbf{u}(\mathbf{x}, t)$ and unperturbed velocity fields, the latter being presented by the streamwise-periodic solution $\mathbf{u}_t(\mathbf{x}, t)$ of the auxiliary simulation [3].

The intensity of perturbation is characterized by a mean-square amplitude $\varepsilon(x, t)$, defined as a cross-sectional average

$$\varepsilon^2(x, t) = \frac{1}{|S|} \int \int |\mathbf{u}(x, y, z, t) - \mathbf{u}_t(x, y, z, t)|^2 dS. \quad (1)$$

Here, S is the cross-sectional area.

The Navier-Stokes equations in a cylindrical coordinate system (x, r, θ) are solved using a second-order finite-difference discretization scheme in space and a third-order semi-implicit Runge-Kutta method in time. A detailed description of the numerical method is given in [4].

3 Results

Spatially evolving turbulent flow in a circular pipe at Reynolds number $Re = 5300$ was investigated in [3]. It was shown that after a certain transitional stage the flow does not depend on the initial condition. It takes the form of a streamwise-periodic flow of the auxiliary simulation with superimposed spatially growing perturbation. The mean perturbation amplitude

$$\bar{\varepsilon}(x) = \left[\frac{1}{T} \int_{t_0}^{t_0+T} \varepsilon^2(x, t) dt \right]^{1/2}, \quad (2)$$

behaves exponentially, $\bar{\varepsilon}(x) \sim \exp(\sigma x)$. The growth rate was estimated as $\sigma \approx 0.36$ ¹. More careful examination of the [3] data reveals that a better approximation for the growth rate is $\sigma = 0.38$.

Some additional simulations at $Re = 5300$ were performed in present work. It was shown that the growth rates of small perturbations does not depend from the origin and the character of the flow perturbation. It is insensitive to variations of the grid resolution, length of the computational domain and size of the streamwise period of the auxiliary simulation.

The growth of perturbations means that the actual flow departs from the oncoming streamwise-periodic flow of the auxiliary simulation in terms of instantaneous velocity fields. It is important, however, that the two flows remain basically the same turbulent flow in terms of mean quantities.

¹ Here and in what follows the pipe radius R is taken as the length scale.

Similar simulations were conducted at two other Reynolds numbers, $Re = 4000$ and $Re = 10000$. In all cases, the mesh spacing was adequate for accurate representation of the main statistical characteristics.

It was expected that the rate of perturbation growth would be an increasing function of Reynolds number. The results of the simulations support this supposition. The resulting graphs $\bar{\varepsilon}(x)$ for different Reynolds numbers are presented in figure 1(a). In all cases, there is a distinct region of exponential growth in $\bar{\varepsilon}(x)$ with the growth rate increasing from $\sigma \approx 0.29$ at $Re = 4000$ to $\sigma \approx 0.71$ at $Re = 10000$.

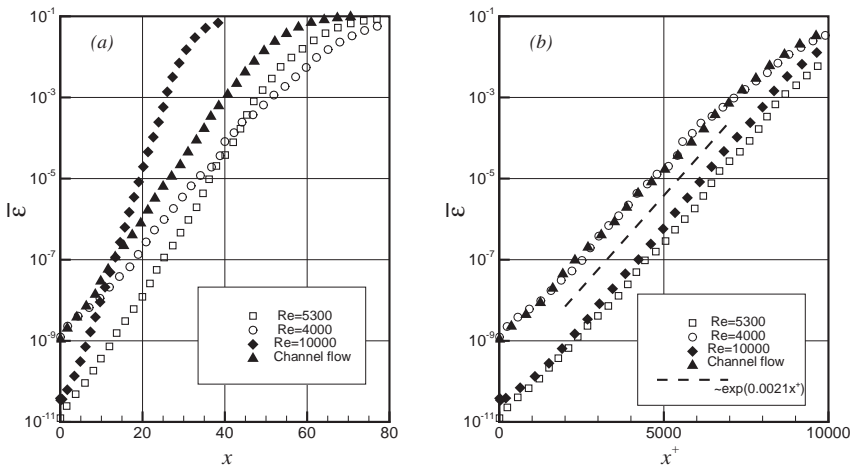


Fig. 1. Growth of mean perturbation amplitude as function of (a), x and (b), x^+ .

In figure 1(b), the variation of $\bar{\varepsilon}$ with distance from the inlet is shown as a function of $x^+ \equiv xRe_\tau$, where $Re_\tau = u_\tau R/\nu$. In this representation, the graphs $\bar{\varepsilon}(x^+)$, remarkably, have the same growth rate $\sigma^+ = \sigma/Re_\tau$ in the range $0.0021 - 0.0022$ in all cases. The observation that the growth rate of small perturbations is constant when normalized by a friction length, suggests that instability of turbulent flow is a purely near-wall phenomenon with low dependence on the outer flow.

The near-wall character of instability in turbulent pipe flow suggests that instability with similar properties may be observed in other near-wall flows. To check the validity of this hypothesis, evolution of perturbations in plane channel flow was investigated following the procedure described in the previous sections for pipe flow. Simulation was performed at Reynolds number $2hU_b/\nu = 5600$. Spatial evolution of the mean perturbation amplitude is shown in figure 1. Perturbation growth rate $\sigma^+ \approx 0.002$ was obtained in chan-

nel flow. This is in reasonable agreement with the values $\sigma^+ \approx 0.0021 - 0.0022$ observed in pipe flow.

3.1 Temporal evolution of perturbations

Spatial growth of perturbations can be interpreted as temporal growth in a moving frame of reference translating downstream with the propagation velocity C_f . The propagation velocity can be estimated by monitoring the position x_f of the front edge of the exponential part in the $\varepsilon(x, t)$ distribution at the initial stage of flow evolution. Although the front edge can be defined only within a certain tolerance, the graph $x_f^+(t^+)$ demonstrates a constant propagation velocity $C_f^+ = dx_f^+/dt^+ \approx 10$.

Another way to estimate propagation velocity follows from the supposition that the maximum amplification of perturbation takes place in a critical layer, where propagation velocity coincides with the velocity of a base flow. Since the maximum perturbation amplitude is at distance $d^+ \approx 13$ from the wall where the mean velocity U^+ in the base turbulent flow is equal to 10, it is reasonable to expect that the propagation velocity of the most growing perturbation is also close to $C_f^+ = 10$.

Given the rate of spatial growth σ and the velocity of spatial propagation C_f , the rate of temporal growth λ can be found as $\lambda = C_f\sigma$. Thus, for the values obtained in the present work, we can estimate $\lambda^+ \approx 0.021$.

The obtained rate of temporal growth agrees well with the results of Keefe, Moin & Kim [2]. They estimated dimension of the turbulent attractor underlying plane channel flow at very low Reynolds number $Re_\tau = 80$ and calculated Lyapunov spectra. Lyapunov exponents were calculated using two time steps $\Delta tu_\tau/h = 0.003$ and $\Delta tu_\tau/h = 0.0015$. The highest Lyapunov exponent, which characterizes the growth rate of the most growing small perturbation, was estimated as $\lambda_1 h/u_\tau \approx 1.4$ for the larger time step and $\lambda_1 h/u_\tau \approx 1.6$ for the smaller one. When normalized by viscous scales, these values give $\lambda_1^+ \approx 0.0175$ and $\lambda_1^+ \approx 0.02$, respectively.

Acknowledgments

The research was started during the author's visit to the School of Engineering Sciences, University of Southampton, UK, which was supported by EPSRC under grant EP/D050871/1. The work was supported also by the Russian Foundation for Basic Research under grant 08-01-00489-a.

References

1. N. Nikitin, *J. Fluid Mech.*, **614**, 495 (2008).
2. L. Keefe, P. Moin and J. Kim, *J. Fluid Mech.*, **242**, 1 (1992).
3. N. Nikitin, *Phys. Fluids*, **19**, 091703 (2007).
4. N. Nikitin, *J. Comput. Phys.*, **217**, 759 (2006).

Experimental assessment of turbulent drag reduction by wall traveling waves

M. Quadrio, F. Auteri, A. Baron, M. Belan and A. Bertolucci

Dipartimento di Ingegneria Aerospaziale, Politecnico di Milano, 20156 Milano, Italy

maurizio.quadrio at polimi.it

Waves of spanwise velocity applied at the wall of a turbulent channel flow and traveling in the streamwise direction have been recently discovered in a numerical study by Quadrio *et al.* [1] to alter the natural turbulent friction significantly. In particular, depending on the parameters that define the waves, drag can be either increased or decreased, and at low Re full relaminarization has been achieved. Large drag reductions are obtained at the expense of very limited expenditure in energy, thus resulting in a largely positive overall energy budget. This paper presents the first experimental assessment of the performance of the streamwise-traveling waves in a turbulent pipe flow.

The waves considered in [1] are described by:

$$w_w(x, t) = A \sin(\kappa_x x - \omega t), \quad (1)$$

where w_w is the spanwise (z) component of the velocity vector at the wall, x is the streamwise coordinate and t is time, A is the oscillation amplitude, κ_x is the wave number in the streamwise direction and $\omega = 2\pi/T$ is the oscillation frequency. One important parameter of the waves is their phase speed $c = \omega/\kappa_x$. Such waves include and generalize the particular cases of the oscillating wall [2] and the stationary transverse waves described at the last ETC conference [4].

The effects exerted by the wall traveling waves on the turbulent plane channel flow are summarized in figure 1, adapted from [1]. The flow has a Reynolds number of $Re = 3170$ based on the bulk velocity U_b and the channel half-width h . The amplitude A of the waves is kept fixed at $A = 0.75U_b$. The effect of waves on the drag varies widely depending on their spatial and temporal frequency. The largest drag reduction (about 45% for this value of A) is observed for slowly forward-traveling waves over a wide range of not-too-large wavelenghts. The maximum drag reduction pertains to backward-traveling waves when the wavelength $\lambda = 2\pi/\kappa_x$ of the waves exceeds $\lambda \approx 6h$. At a relatively well-defined phase speed c (indicated in this plot by straight lines passing through the origin), the effect of the waves abruptly becomes

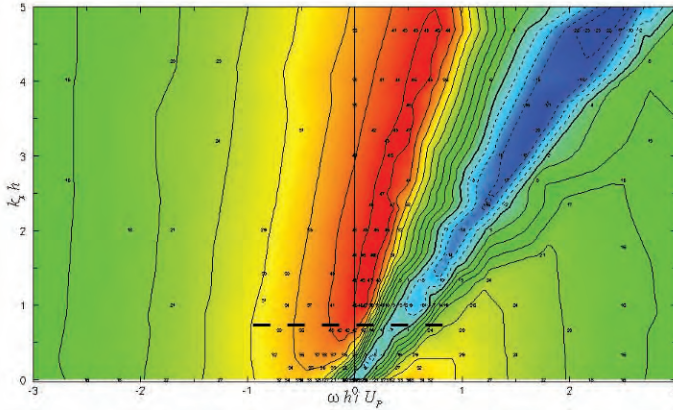


Fig. 1. Map of friction drag reduction (percentage) in the $\omega - \kappa_x$ plane for $A = 0.75U_b$ and $Re = 3170$. Contours are spaced by 5% intervals, loci of zero DR are indicated by thick lines and negative values are represented by dashed lines. The numbers indicate percentage drag reduction at measured points. On the horizontal axis, $U_p = 3/2U_b$. The thick dashed line indicates the range explored in the present experiment, see later fig. 3.

that of drag increase. The straight line with $c = 0.7U_b$ identifies the locus of maximum drag increase.

Aim of the present work is to give the results contained in [1] an experimental confirmation. The cylindrical geometry lends itself to an easier implementation of the traveling waves, owing to the natural periodic spanwise (azimuthal) direction offered by a cylindrical pipe. The wall motion implied by Eq. (1) in the cartesian geometry is implemented by imposing different rotation rates to different longitudinal sections of the pipe, so realizing a discretization of the sinusoidal space variation. In addition to the traveling waves, the setup can be used to obtain both purely temporal (when all the pipe sections have an in-phase alternating motion) and purely spatial (when all the pipe sections steadily rotate at different speed) oscillations.

Water is chosen as the working fluid. The bulk velocity of the flow is $U_b = 0.11$ m/s and the value of the Reynolds number equals $Re = 2450$ (based on pipe inner radius R of 25 mm and U_b), i.e. somewhat lower than the one employed in the DNS for the planar case. The oscillating frequencies of interest are of the order of 1 Hertz; the pressure drop across the moving section is small but still measurable. Most of the difficulties encountered during the present work are related to the need of measuring very small pressure differences.

The longitudinal sinusoidal variation of the transversal velocity required by (1) is discretized through up to 6 independent pipe segments for each wavelength. Each segment has an axial length of 36.55 mm. The total length of the pipe section with rotating segments is about 2.2 m, that amounts to no less than 10 wavelengths. The lineup of the different segments is achieved

by mounting each segment with two rolling-contact bearings co-axial to the pipe and aligned to a steel rail. The need for controlling the frequency of the sinusoidal variation of the angular speed, and in particular for implementing a constant-speed motion, poses a number of constraints on the transmission system, that is based on timing belts moved by 6 independent D.C. motors, each driven by a purposely designed closed-loop controller. The pipe section with rotating segments is part of a large closed-circuit pipe. The whole apparatus is approximately 250 diameters long, thus ensuring a fully developed turbulent flow. Fig.2 illustrates the experimental setup.

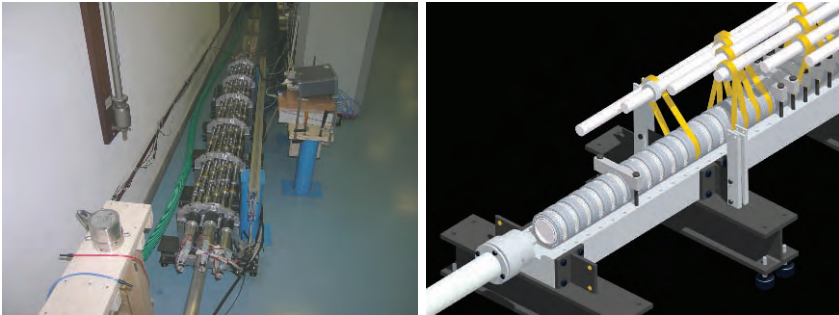


Fig. 2. Left: picture of the experimental setup. The return pipe can be seen on the far left, the moving segments are on the center, hidden by the transmission shafts and 3 D.C. motors. Right: close-up of a schematic of the trasmission system: shafts, belts and segments.

A preliminary set of results is shown in figure 3. Percentage changes in friction drag are plotted against the oscillation frequency; the oscillation amplitude is kept fixed at $A = 0.73U_b$. Each sinusoid in space is discretized with 6 segments, thus yielding a wavelength of $\lambda = 8.78R$. The frequency of the wave is varied, thus observing how the turbulent friction changes along the points indicated by the dashed line in fig.1. Drag is evaluated by measuring the pressure drop between two points located immediately upstream the first rotating segment and immediately downstream the last one.

The results strongly resemble the data available for the cartesian geometry. Friction drag is reduced over a wide range of frequencies, except for a small range where drag increases. The maximum of drag is attained for the wave with phase speed of $c = 0.57U_b$, whereas the drag minimum takes place for slowly backward-traveling wave, with $c = -0.05U_b$. The actual amount of maximum drag reduction, however, turns out to be underestimated by approximately 50%. More than one reason can explain this discrepancy. First of all, the main mechanism suggested [3] to drive the modification of turbulent friction drag in plane channel flow is quantitatively different from what happens in the cylindrical geometry. Moreover, our experimental setup differs in some respects from the idealized setting of a DNS. Most important is the presence

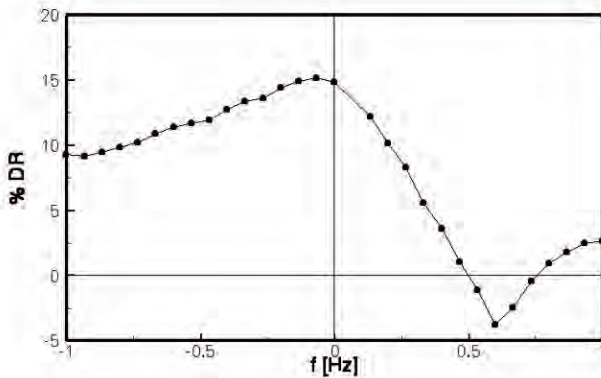


Fig. 3. Friction drag reduction (in percentage of the reference friction) due to waves with $\lambda = 8.78R$ and $A = 0.73U_b$, as a function of the oscillation frequency.

of a spatial transient, where the turbulent friction gradually decreases from the unperturbed level. Our estimate, based on the DNS in cartesian geometry, is that this transient region extends over thousands of wall units. However, the measured pressure drop is an integral measure over the entire length of the active pipe, and as such it yields an underestimated drag reduction. Moreover, the friction factor for the pipe with fixed segments is higher than expected. This may be due to localized roughness effects, either due to the design of the pipe segments, or – most probably – due to debris that accumulates in the measuring section. We are still working to sort out this issue.

In conclusion, the experiment described here has successfully demonstrated the capability of the wall traveling waves to yield large reductions of drag in the laboratory. We are still working towards a better quantitative characterization of their performance. An accompanying effort is that of understanding the traveling wave working mechanism in the cylindrical geometry.

References

1. Quadrio, M., Ricco, P., Viotti, C. Streamwise oscillation of spanwise velocity at the wall of a channel for turbulent drag reduction. *J. Fluid Mech.* In press, 2009.
2. Karniadakis, G.E., Choi, K.-S. Mechanisms on Transverse Motions in Turbulent Wall Flows. *Ann. Rev. Fluid Mech.*, **35**, 45–62, 2003
3. Quadrio, M. Streamwise-traveling waves of spanwise velocity at the wall of a turbulent channel flow. iTi Conference on Turbulence, Bertinoro (I), Oct. 2008.
4. Viotti, C., Quadrio, M., Luchini, P. Skin-friction drag reduction via steady streamwise oscillations of spanwise velocity. *Advances in Turbulence XI*, Palma and Silva Lopez eds., p.659–661, 2007.

Effects of very-large roughness in turbulent channel flow

D.M. Birch* and J.F. Morrison

Department of Aeronautics, Imperial College, London SW7 2AZ
d.birch@surrey.ac.uk

Summary. The streamwise velocity statistics in fully-developed rough-wall channel flow have been investigated over grit- and mesh-type surface topologies. The flow was demonstrated to be fully-developed and two-dimensional up to the fourth moment of velocity. Though the flow over both surface types appear to exhibit a limited logarithmic region, the regions of inner and outer scaling over the mesh surface fail to overlap. The influence of the spanwise periodicity of the mesh upon the outer scaling is discussed.

1 Introduction

The scaling of flows over rough walls has been of considerable recent interest. The model originally proposed by (7; 3; 9; 10; 11) suggests that the near-wall inhomogeneities in the flow arising from the local effect of the individual roughness elements are limited to a thin ‘roughness sublayer’, analogous to the viscous sublayer in smooth-wall flows. Any influence of the specific roughness topology upon the flow is therefore assumed to be contained within this layer, so any influence of the roughness upon the flow outside of this layer relative to the smooth-wall case must be attributable to the global increase in the wall friction velocity u_τ alone. For roughness which is large relative to the viscous length scale ν/u_τ (but still small relative to the integral length scale δ), the roughness size replaces viscosity in the near-wall scaling while sufficient scale separation remains that an overlap region may exist. Then, the usual log-law may be expressed in the form

$$\frac{u}{u_\tau} = \frac{1}{\kappa} \ln\left(\frac{y-d}{y_0}\right) \quad (1)$$

where y_0 is a geometry-dependent roughness length, and d is a zero-plane displacement.

Despite its comparative simplicity, considerable support exists for this model. After a review of available literature, Jimenez (8) proposed the condition $k/\delta \lesssim 2.5\%$ (where k is the roughness height) for these scaling conditions to be met. Flack *et al.* (6) demonstrated collapse of the outer-scaled velocity moments up to the third order for $k/\delta < 2.2\%$, while appropriately-scaled mean velocities have been shown to scale well for values of k/δ as high

*Faculty of Engineering and Physical Sciences, University of Surrey, Guildford, GU2 7XH, UK

as 20 % in rough-wall boundary layers (4; 5; 2). Internal flows, on the other hand, are constrained by the additional boundary condition and are therefore more likely to exhibit evidence of inner-outer interaction for larger values of k/δ . In the present study, the streamwise velocity statistics in very rough-wall channel flow (with k/h ranging up to $\sim 8\%$, where h is the channel half-height) have been studied in order to investigate the extent of the similarity. Special attention is given to the higher-order velocity moments, as these quantities are more sensitive to any changes in the flow structure.

2 Experimental details

Hot-wire scans of the streamwise velocity component were carried out in a rectangular channel with half-height $h = 50.8$ mm, width $W = 15h$ and total streamwise fetch $L = 134h$. The critical parameters of the two roughness surfaces tested are included in Table 1. The estimated error bounds on the experimental results are as follows: u_τ , 6%; mean velocities, 0.5%; second-order moments, 1.5%; velocity skewness and kurtosis, 6% and 10%, respectively.

Surface	k_{max} (mm)	\bar{k} (mm)	k_{rms} (mm)	\bar{k}/h (%)	k_{max}/h (%)
Grit	2.0	0.74	0.41	1.46	3.94
Mesh	4.0	1.27	1.31	2.50	7.87

Table 1. Key roughness parameters

3 Results and discussion

In the present study, the values of the roughness length y_0 and zero-plane offset d were determined by fitting the time-mean velocity profiles to Equation (1), assuming that $\kappa = 0.41$ and requiring that the logarithmic region began at the wall-normal distance where the flow became spanwise homogeneous. The critical flow parameters for the various cases tested are included in Table 2.

Line	Case	U_{cl} (m s ⁻¹)	\bar{U} (m s ⁻¹)	Re_τ	$Re_h \times 10^{-4}$	d mm	y_0 mm	k^+	k_s^+
— · — · — ·	Grit (G1)	24.5	21.0	4780	7.27	1.35	0.13	186	359
————	Grit (G2)	26.6	22.8	5190	7.87	1.30	0.13	200	389
— · — · — ·	Grit (G3)	28.5	24.4	5530	8.43	1.45	0.13	216	415
— · — · — · — ·	Mesh (M1)	21.0	17.3	5290	6.23	1.90	0.43	410	1402
— — —	Mesh (M2)	23.1	18.8	5890	6.84	2.60	0.43	458	1561
— —	Mesh (M3)	25.0	20.5	6280	7.38	2.00	0.43	493	1664

Table 2. Experimental parameters for grit and mesh roughness. k^+ based on k_{max}

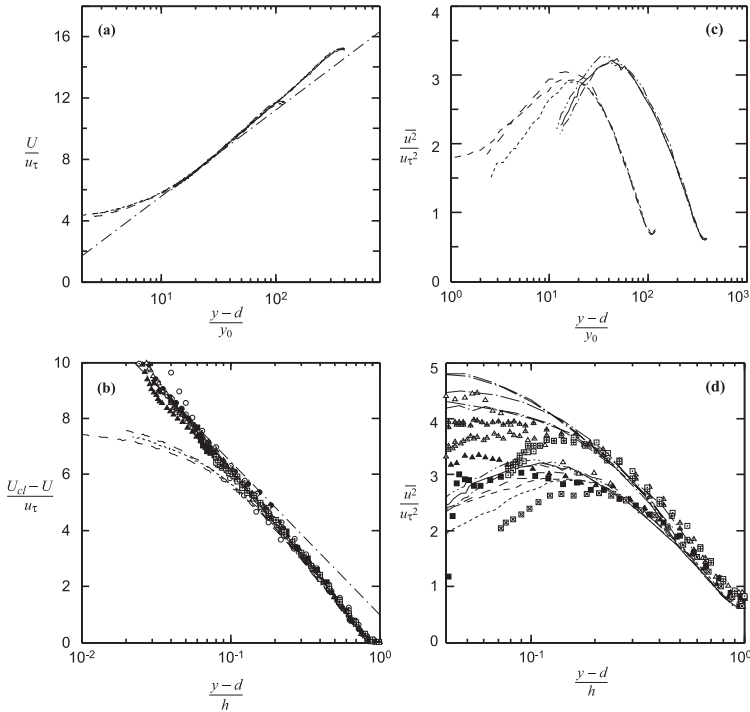


Fig. 1. Mean velocity profiles in (a) inner scaling and (b) outer scaling, and standard deviation in (c) inner scaling and (d) outer scaling.

Figure 1(a) shows the inner-scaled mean velocity profiles for all cases tested. The excellent collapse observed was, to some extent, artificially imposed in obtaining y_0 and d by fitting the data to Equation 1. A limited logarithmic region appears over both the grit-type and mesh-type roughness for $15 \lesssim (y-d)/y_0 \lesssim 30$. Figure 1(b) shows the outer-scaled velocity deficit profiles, together with selected rough-wall channel results from Bakken *et al.* (1), at similar Re_τ . The profiles over the grit surface collapse with those of Bakken *et al.*. The profiles over the mesh-type surface do not collapse below $(y-d)/h \sim 0.30$, corresponding to $(y-d)/y_0 \sim 35$. This result indicates that the regions of inner- and outer-scaling over the mesh-type surface did not overlap, and consequently a logarithmic region could not have existed. The apparent agreement of the data with Equation 1 observed in Figure 1(a) may therefore have been spurious and artificially imposed. In addition, velocity statistics were affected by the spanwise variation of the mesh, since results were obtained at a single spanwise location only, at the centre of the depression.

Figure 1(c) shows the inner-scaled second velocity moment $\overline{u'^2}$ profiles over the grit and mesh surfaces. The profiles collapse remarkably well, and are indistinguishable above $(y-d)/y_0 \gtrsim 50$ and 30 , respectively. The outer-scaled profiles are included in Figure 1(d), together with selected results from Bakken *et al.* The present data collapse together regardless

of surface type for $(y-d)/h \gtrsim 0.2$, though Re_τ -independent collapse with the data of Bakken *et al.* is only observed for $(y-d)/h \gtrsim 0.4$.

4 Conclusions

Experimental measurements of the streamwise velocity statistics in very-rough-wall channel flow over mesh- and a grit-like roughness surfaces have been carried out. The inner-scaled mean velocity near the wall demonstrated good agreement with previous studies, and the flow over both the mesh and the grit surfaces appeared to exhibit a limited logarithmic region; however, the lack of simultaneous overlap of the regions of inner and outer scaling over the mesh indicated that a logarithmic region could not exist. The lack of an overlap region may have been the result of the spanwise variation in the flow over the mesh, and the scaling of spanwise spatial averages of the time-mean velocity profiles is presently being examined.

References

- [1] Bakken, O.M., Krogstad, P.A., Ashrafian, A., Andersson, H.I.: Reynolds number effects in the outer layer of the turbulent flow in a channel with rough walls. *Phys. Fluids* **17**, 065,101 (2005)
- [2] Castro, I.P.: Rough-wall boundary layers: mean flow universality. *J. Fluid Mech* **585**, 469–485 (2007)
- [3] Clauser, F.H.: The turbulent boundary layer. *Adv. Appl. Mech.* **4**, 1–51 (1956)
- [4] Connelly, J.S., Schultz, M.P., Flack, K.A.: Velocity defect scaling for turbulent boundary layers with a range of relative roughness. *Exp. Fluids* **40**, 188–195 (2006)
- [5] Flack, K.A., Schultz, M.P., Connelly, J.S.: Examination of a critical roughness height for outer layer similarity. *Phys. Fluids* **19**, 095,104 (2007)
- [6] Flack, K.A., Schultz, M.P., Shapiro, T.A.: Experimental support for townsend's reynolds number similarity hypothesis on rough walls. *Phys. Fluids* **17**, 035,102 (2005)
- [7] Hama, F.: Boundary-layer characteristics for smooth and rough surfaces. *Trans. Soc. Naval Arch. and Marine Eng.* **62**, 333–358 (1954)
- [8] Jiménez, J.: Turbulent flows over rough walls. *Annu. Rev. Fluid Mech.* **36**, 173–196 (2004)
- [9] Rotta, J.C.: Turbulent boundary layers in incompressible flow. *Prog. Aero. Sci.* **2**, 1–219 (1962)
- [10] Townsend, A.A.: *The Structure of Turbulent Shear Flow*, 1st Ed. Cambridge University Press (1956)
- [11] Townsend, A.A.: *The Structure of Turbulent Shear Flow*, 2nd Ed. Cambridge University Press (1976)

Roughness effects in a rotating turbulent channel

Vagesh D. Narasimhamurthy and Helge I. Andersson

Fluids Engineering Division, Department of Energy and Process Engineering,
Norwegian University of Science and Technology, Trondheim, 7491, Norway
vagesh@ntnu.no

The distinction between d -type and k -type roughness on wall turbulence is well established [1] and related to the pitch-to-height ratio λ/k , where λ is the separation between roughness elements of height k . The results of the present study show that a k -type roughness with $\lambda/k = 8$ is turned into d -type roughness by the action of the Coriolis force due to imposed system rotation.

We considered a rod-roughened plane channel flow where both walls were roughened by square rods with height $k = 0.1h$ (h being the channel half-width) and $\lambda/k = 8$. The rods were positioned in a non-staggered arrangement, as depicted in figure 1(a). The mean flow and turbulence statistics will therefore exhibit a symmetry about the midplane in the absence of rotation [2], [3]. In order to explore the effect of system rotation direct numerical simulations (DNS) of pressure-driven flow in the rod-roughened channel have been performed. The driving pressure-gradient $-dP/dx$ was prescribed such that the Reynolds number based on the channel half-width h and the wall-friction velocity $u_\tau = (-\rho^{-1}hdP/dx)^{1/2}$ was equal to 400. This is essentially the same Reynolds number as the medium Re case reported by Moser et al. [4] for smooth channel flows and by Ashrafian et al. [3] for a rod-roughened channel flow. The computational domain was $8\lambda (= 6.4h)$ long and $4\lambda (= 3.2h)$ wide and thus comprised eight rods on each wall. Cyclic (i.e. periodic) boundary conditions were imposed in the streamwise and spanwise directions. A Coriolis force term was implemented in the Navier-Stokes solver to account for system rotation. The mean velocity field and the turbulence statistics have been deduced by first averaging in time and in the homogeneous spanwise direction. Advantage was then taken of the streamwise periodicity over the pitch length λ to further improve the quality of the sampling. In this paper we report results of a marginally resolved DNS using $256 \times 128 \times 128$ grid points. A fully resolved simulation is underway. The rotation number $Ro = 2\Omega h/u_\tau$ was set to 6.3 and data for a non-rotating case are included for comparative purposes.

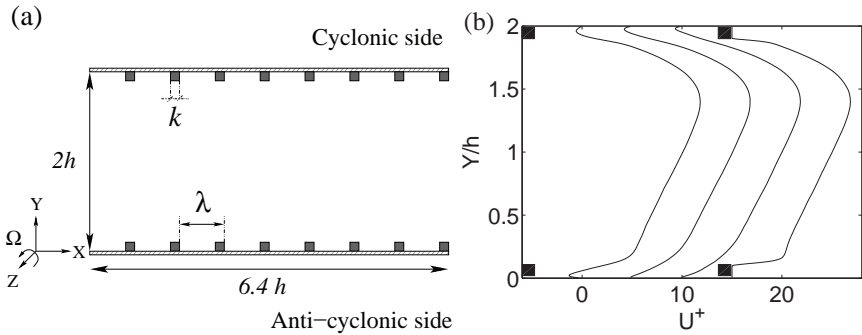


Fig. 1. (a) flow configuration; (b) streamwise mean velocity profiles in anti-clockwise rotation (note that for clarity profiles have been shifted to the right by 5).

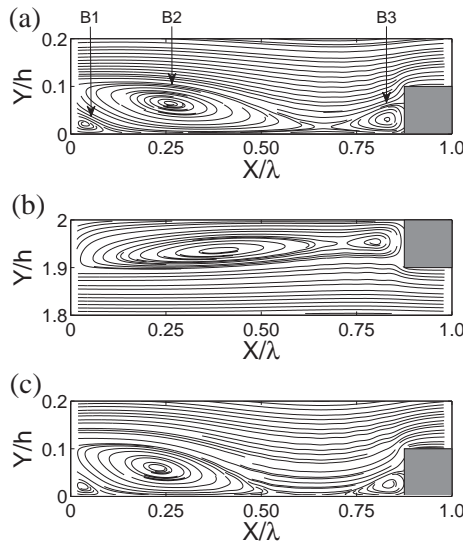


Fig. 2. Streamlines illustrating the separated flow regions in the vicinity of the roughness elements. (a) non-rotating channel; (b) rotating channel: cyclonic side; (c) rotating channel: anti-cyclonic side.

When the channel is rotated with a constant angular velocity Ω about a spanwise axis, cyclonic and anti-cyclonic behaviours are observed along the two channel walls, similarly as in the rotating smooth-walled channel studied by Kristoffersen & Andersson [5]. The mean velocity profiles in figure 1(b) show that $U(Y)$ exhibits a substantial region with a linearly increasing velocity. The slope is close to 2Ω , which implies that the absolute mean vorticity is driven to zero, just as in the smooth-walled case [5]. The peak of U^+ is shifted towards the cyclonic side of the channel due to the rotation.

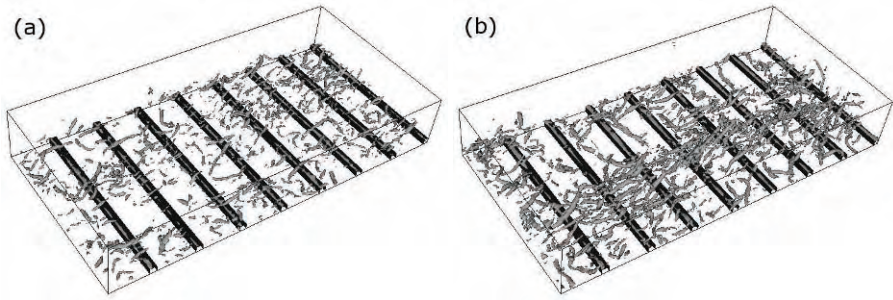


Fig. 3. Instantaneous vortical structures near the lower wall: (a) non-rotating channel; (b) rotating channel. The flow direction is from left to right.

The mean velocity profiles also show that the near-wall behaviour is rather different on the two sides. At the lower wall where the flow is anti-cyclonic, the reverse flow within the cavity between two subsequent rods is modest, whereas the reverse flow extends over the entire cavity near the top wall where the flow is cyclonic. This rotational-induced asymmetry is even more distinctly seen from the streamlines depicted in figure 2. This flow configuration corresponds to k -type roughness in the absence of rotation since the flow separated from one rod re-attaches at the bottom of the downstream cavity, as can be seen in figure 2(a). The streamlines at the cyclonic side in figure 2(b), however, show that the rotation has turned it into d -type roughness where the recirculating flow fills the entire cavity and shelters the outer flow from the wall.

The explanation of this remarkable phenomenon may either be that cyclonic vortices are more stable than anti-cyclonic vortices, as convincingly argued by Cambon et al. [6], or that the turbulent fluctuations are enhanced near the anti-cyclonic side and dampened near the cyclonic side [5] and thus promotes or reduces the spreading of the mixing-layer emanating from the downstream corner of a rod.

The perspective views of the instantaneous vorticity field in figure 3 suggest that the turbulent vorticity has been enhanced along the anti-cyclonic side as compared to the non-rotating case. The Reynolds shear stress $\langle uv \rangle$ and the mean turbulent kinetic energy k are shown in figure 4(a),4(b) and figure 4(c),4(d), respectively at some representative streamwise locations. The imposed system rotation has broken the conventional anti-symmetric variation of the turbulent shear stress since $\langle uv \rangle$ is enhanced near the anti-cyclonic side and reduced near the cyclonic side. The turbulence level, i.e. turbulent kinetic energy, is similarly damped along the cyclonic wall as a result of the interactions between the instantaneous Coriolis force and the instantaneous velocity vector which nearly suppress the wall-normal velocity fluctuations.

The complex non-linear influences of the system rotation will be further exploited by means of data from the refined simulation.

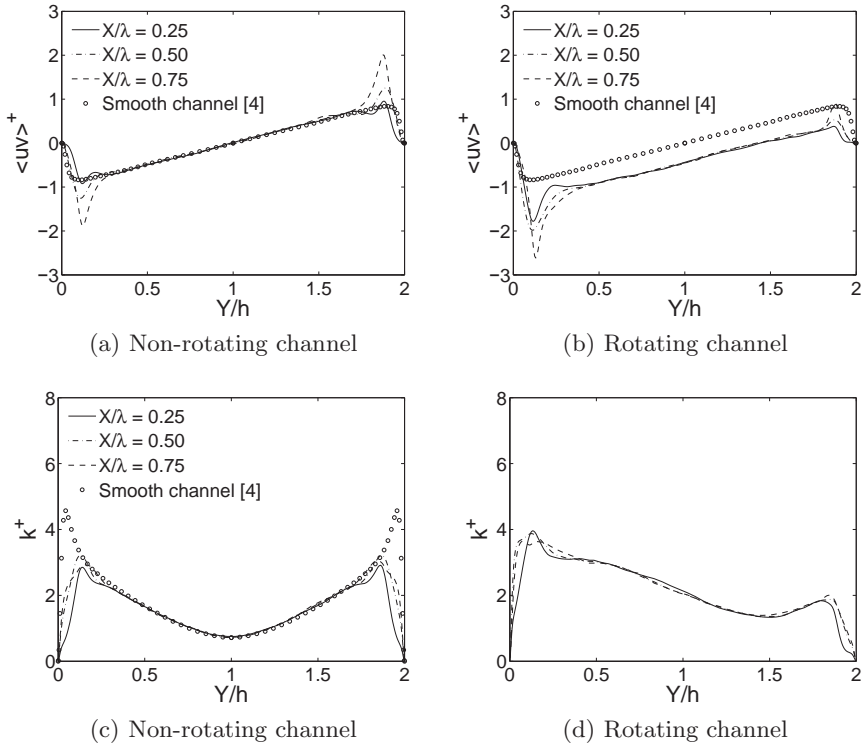


Fig. 4. Reynolds shear stress $\langle uv \rangle^+$ and mean turbulent kinetic energy k^+ profiles normalized by u_τ^2 at different X/λ positions.

This work has received support from The Research Council of Norway (Programme for Supercomputing) through a grant of computing time and a research fellowship for VDN.

References

1. J. Jiménez, *Annu. Rev. Fluid Mech.*, **36**, 173 (2004).
2. P.-Å. Krogstad, H. I. Andersson, O. M. Bakken and A. Ashrafian, *J. Fluid Mech.*, **530**, 327 (2005).
3. A. Ashrafian, H.I. Andersson and M. Manhart, *Int. J. Heat Fluid Flow*, **25**, 337 (2004).
4. R.D. Moser, J. Kim and N.N. Mansour, *Phys. Fluids*, **11**, 943 (1999).
5. R. Kristoffersen and H. I. Andersson, *J. Fluid Mech.*, **256**, 163 (1993).
6. C. Cambon, J.-P. Benoit, L. Shao and L. Jacquin, *J. Fluid Mech.*, **278**, 175 (1994).

Mean Flow and Turbulence over Rough Surfaces

M. Amir and I.P. Castro

School of Engineering Sciences, University of Southampton, Highfield,
Southampton SO17 1BJ
m.amir@soton.ac.uk, i.castro@soton.ac.uk

In real engineering applications involving wall-bounded boundary layer flow, the roughness of the wall surface is an important design parameter because it influences characteristics such as the transport of heat, mass and momentum. Previous experimental studies on the effects of surface roughness have been well reviewed by a number of researchers, for example, Jiménez [1]. Such reviews support the wall similarity hypothesis of Townsend [2] which states that the turbulent flow in the region outside the roughness sublayer is independent of surface roughness at sufficiently large Reynolds numbers. There is evidence that this is not always true (e.g. [3]) and, clearly, for sufficiently large surface protuberances it must fail. Quite apart from the various geometrical parameters defining the particular topology of the roughness, h/δ must have a role in controlling the extent of the roughness influence. The issue of just how large h/δ must be for the whole flow to be affected, $(h/\delta)_c$ say, has not yet been explicitly addressed but $(h/\delta)_c$ may well depend on the roughness topology. If Townsend's [2] hypothesis is valid for small h/δ , then how large must h/δ become before it becomes untenable and does the critical value of h/δ depend on the geometrical characteristics of the roughness? The work presented here is part of an ongoing effort to answer such questions.

Experiments were conducted in a wind tunnel and the surfaces consisted of i) a regular diamond-patterned wire mesh with a total mesh height of about 3 mm and ii) an urban-type rough surface with 5 mm square elements of random heights (mean and maximum heights of 5 and 8.6 mm, respectively) arranged in a staggered pattern (Fig.1). Measurements of both mean velocity and turbulence stresses were obtained using a two-component LDA system.

Fig. 2a shows the mean velocity profiles for both the surfaces plotted in inner variables. The solid line is the smooth wall data from [4]. Both rough surfaces display the usual linear log region shifted by ΔU^+ below the smooth profile. It is of note that at higher values of h/δ the roughness function is higher for the urban-type surface at nominally the same unit Reynolds number since the mean height is about 1.7 times that of the mesh surface. The urban

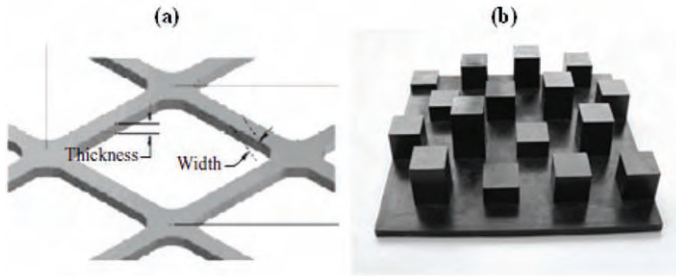


Fig. 1. Rough surfaces used. (a) Mesh roughness. (b) Urban-type 5 mm cubes of random height

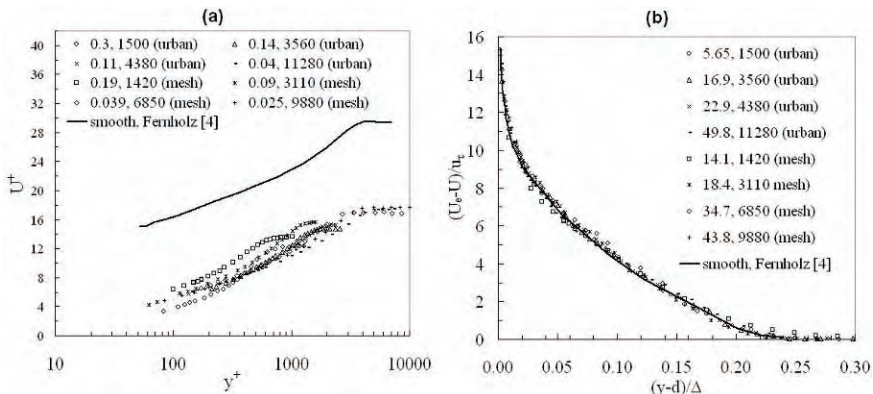


Fig. 2. (a) Mean velocity profiles in wall coordinates, with the legend giving values of (first) h/δ and Re_θ . (b) Deficit velocity profiles, with the legend giving values of θ/y_o and Re_θ . Solid lines are smooth-wall data from Fernholz [4].

and mesh surface produced roughness functions of $\Delta U^+ = 11.8$ and 9.84 at higher values of h/δ , whereas far downstream where h/δ is quite small both the surfaces have about the same roughness function. The mean velocity profiles in defect form for both surfaces are presented in Fig. 2b. These are plotted using standard Rotta [5] scaling (i.e. normalising $(y - d)$ by Δ , the Clauser thickness). The zero plane displacement d has been subtracted from the wall normal distance. The velocity defect profiles exhibit good collapse in the overlap and outer regions of the boundary layer. Fig.2b supports a universal velocity defect profile for rough and smooth walls and also lends support to the boundary layer similarity hypothesis of Townsend [3]. It is important to note that only at small fetches, corresponding to relatively large values of h/δ , are there perhaps noticeable deviations. Castro [6] found that the classical universality ideas adequately describe the mean flow profile of fully-rough boundary layers independently of the nature of the roughness up to surprisingly large h/δ . This conclusion was based on values of $h/\delta < 0.2$, but Fig. 2b shows that even at $h/\delta = 0.3$ for the urban-type roughness case

the universality of the velocity profile is still evident, giving further evidence for the robustness of mean flow profiles to roughness type or size.

The normalised streamwise, $\overline{u'^2}/u_\tau^2$, and wall-normal, $\overline{v'^2}/u_\tau^2$, Reynolds stress profiles for both roughness types are presented in Fig. 3. The differences in the stresses from smooth-wall values are seen both near the surface and into the outer region of the boundary layer. Reasonably good collapse of $\overline{u'^2}/u_\tau^2$ profiles are seen in the outer regions of the boundary layer at lower values of h/δ . For both surfaces at the lowest fetches (where values of h/δ are the largest) the changes in both $\overline{u'^2}/u_\tau^2$ and $\overline{v'^2}/u_\tau^2$ are the largest. Even though a significant increase in $\overline{u'^2}/u_\tau^2$ is evident at the lowest fetches, Fig. 3a does not exhibit an obvious trend, whereas Fig. 3b clearly shows that $\overline{v'^2}/u_\tau^2$ increases with decreasing fetch, at least in the inner region. In the outer region, however, noticeable differences from the smooth wall are still evident at higher values of h/δ , with stresses here falling somewhat below smooth-wall values. Fig. 3b also shows that at the highest values of h/δ for each roughness type, i.e. 0.30 for urban and 0.19 for mesh, the effects on $\overline{v'^2}/u_\tau^2$ extend up to nearly the same distance suggesting that $(h/\delta)_c$ must be higher for the urban roughness. The exact values of $(h/\delta)_c$ are not possible to determine from these results; further measurements are required at even larger values of h/δ . Note that for the mesh surface with $h/\delta = 0.025$ the augmentation in $\overline{v'^2}/u_\tau^2$ is observed up to a distance of $(y-d)/\Delta = 0.075$ which is equivalent to about $12h$. Above this distance, the wall normal stress profile collapses fairly well on to the smooth wall. Krogstad *et al.* [3] also noted a large increase in $\overline{v'^2}/u_\tau^2$ well into the outer region of the boundary layer. They attributed this to an increase in the inclination angle of the large-scale structures, which tended to make turbulence in the outer region more isotropic. They observed differences up to $y/\delta = 0.7$ for the mesh surface, whereas in our case the differences are seen up to $y/\delta = 0.27$ only.

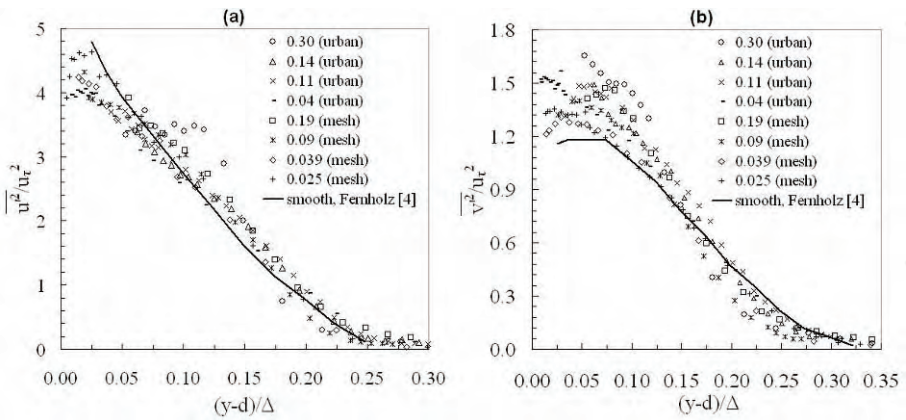


Fig. 3. Streamwise (a) and wall normal (b) Reynolds stresses, with the legend giving values of h/δ . Solid lines are smooth-wall data from Fernholz [4].

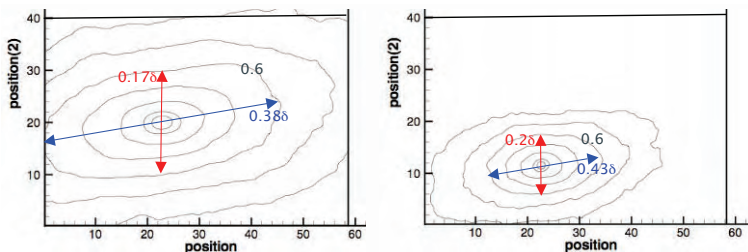


Fig. 4. Contours of time-averaged spatial correlation, R_{uu} , of the axial velocity fluctuations. (a) urban-type roughness, $\delta = 120\text{mm}$; (b) smooth wall, $\delta = 80\text{mm}$. Axis scales are in mm, origins are arbitrary, but the reference location – i.e. the centre of the ‘average’ structure – is $y = 0.7\delta$ in both cases. The height and extent of the structure, as determined from the $R_{uu} = 0.6$ contour, are shown as fractions of δ .

Figure 4 shows some structural information for a smooth wall and the urban surface ($h/\delta = 0.04$), obtained using PIV techniques, in the outer region of the flow. Apart from the overall scale, which is larger over the rough surface because of the larger δ , the time-averaged structure looks similar in the two cases. We are currently assessing the extent to which structure inclinations depend on scale, but it is clear that at least for this ‘overall-averaged’ structure there is little significant difference between the two cases, despite the differences in normal stresses.

We conclude that the velocity defect profiles are independent of roughness type and collapse fairly satisfactorily up to surprisingly large values of h/δ . Turbulence data, however, provide evidence that the roughness effects are not just confined to the near-wall region but the outer region is also affected, increasingly so as h/δ increases. At the lowest measured values of h/δ , the differences in wall normal Reynolds stresses extend well outside the roughness sub-layer, but in the outer regions of the boundary layer the stress profiles for the smooth and rough surfaces collapse and at least some features of the eddy structures are very similar.

References

1. J. Jimènez, Turbulent Flows over Rough Walls, *J. Fluid Mech.* 530, 327-352, 2004.
2. A.A. Townsend, *The Structure of Turbulent Shear Flow*, CUP, 1976.
3. P-A. Krogstad, R.A. Antonia & L. Browne, Comparison between rough and smooth wall turbulent boundary layers, *J Fluid Mech.* 245, 599-617, 1992.
4. H.H. Fernholz and P.J. Finley, *The Incompressible Zero-Pressure Gradient Turbulent Boundary Layer: An Assessment of the Data*, *Prog. Aerospace Sci.*, 32, pp. 245-311, 1996.
5. J.C. Rotta, *The Calculation of the Turbulent Boundary Layer*, *Prog. Aeronaut. Sci.* 2, 1-219, 1962.
6. I.P. Castro, Rough-wall boundary layers: mean flow universality, *J. Fluid Mech.*, 585, 469-485, 2007.

Part X Intermittency and scaling

DNS of vibrating grid turbulence

G. Khujadze and M. Oberlack

Chair of Fluid Dynamics, Technische Universität Darmstadt, Germany
khujadze@fdy.tu-darmstadt.de

Direct numerical simulation of the turbulence generated at a grid vibrating normally to itself using spectral code [1] is presented. Due to zero mean shear there is no production of turbulence apart from the grid. Action of the grid is mimiced by the function implemented in the middle of the simulation box:

$$f_i(x_1, x_2) = \frac{n^2 S}{2} \left\{ \left| \frac{\delta_{i3}}{4} \cos\left(\frac{2\pi}{M}x_1\right) \cos\left(\frac{2\pi}{M}x_2\right) \right| \sin(nt) + \frac{\beta_i}{4} \right\},$$

where M is the mesh size, $S/2$ – amplitude or stroke of the grid, n – frequency. β_i are random numbers with uniform distribution. The simulations were performed for the following parameters: $x_1, x_2 \in [-\pi; \pi]$, $x_3 \in [-2\pi; 2\pi]$; $Re = nS^2/\nu = 1000$; $S/M = 2$; Numerical grid: $128 \times 128 \times 256$. The time evolution of the mean depth of a turbulent/non-turbulent interface was obtained in the paper [2]: $H(t) = A(t - t_0)^m + B$, where A, m, B are constants. One of the aims of the presented DNS was to validate this law and find the values of the constants. Fig. 1 shows $H(t)$ in the logarithmic scaling with constants: $A = 1.7 \cdot 10^{-3}$; $B = 0.5 \cdot 10^{-2}$; $t_0 = 0$; $m = 0.4$. Numerics shows good agreement with the theoretical [2] and experimental [3] results.

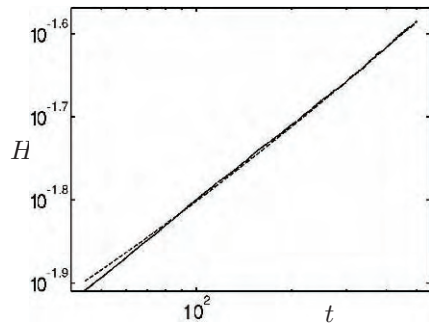


Fig. 1 $H(t)$: — theory; --- DNS.

References

1. M. Iovieno, C. Cavazzoni, D. Tordella, *Comp Phys Comm*, **141**, 365 (2006).
2. M. Oberlack, S. Guenther, *Fluid Dynamics Research*, **33**, 453 (2003).
3. M. Kinzel, M. Holzner, B. Lüthi, C. Tropea, W. Kinzelbach and M. Oberlack, 14th Int Symp on Appl of Laser Techn to Fluid Mech, Lisbon, Portugal (2008).

Step onset from an initial uniform distribution of turbulent kinetic energy.

D. Tordella and M. Iovieno

Diasp, Politecnico di Torino, 10129 Torino, Italy. michele.iovieno@polito.it

1 Introduction

We consider the time decay of a field with an initially uniform turbulent energy distribution where the macroscale has been slightly varied in two adiacent regions. The flow is studied by means of Direct Numeical Simulation carried out in a parallepiped, see fig. 1 b. The interesting observation is that the time evolution of the field shows the onset of a step of turbulent energy. It is sufficient to introduce a slight dishomogeneity associated to the integral scale that the nonlinear interaction is able to induce a dishomogeneity also in the kinetic energy. We present here a set of results from experiments where we actually follow the temporal decay of two isotropic turbulences (of initial equal turbulent kinetic energy, but of different integral scales) that machth over a thin region $\Delta(t)$. The two isotropic regions are characterized by a different shape of the spectrum in the low wavenumber range, as shown in figure 1, see , a thing which was obtained by means of a high-pass filter (see [5]).

2 Results and discussion

The present simulations are performed on a parallelepiped domain with periodic boundary conditions in all directions, see the scheme in figure 1. The Navier-Stokes equations are solved by means of a fully dealiased Fourier-Galerkin pseudospectral method with explicit fourth order time integration [7]. The initial conditions are obtained by matching two fields, coming from simulations of homogeneous and isotropic turbulence, over a thin region by means of a smoothing function [5]. The two fields are characterized by a different shape of the spectrum in the low wavenumber range, as shown in figure 1. The fields with a steeper spectrum in the low wave number range, and thus a smaller integral scale, have been obtained by the application of a high-pass filter to a same reference field, which produces a k^α slope with α between 2 and 4. As a conseuence, the integral scales of the two interacting

isotropic turbulences are different and a scale gradient is present across the initial matching layer. The Taylor microscale Reynolds number Re_λ is 150. The simulations show that the flows with a smaller integral scale decay faster and have higher decay exponents, that range from 1.1 up to 1.65. The smaller the macroscale, the higher is the exponent value. These different decay rates are in agreement with previous literature [1, 2, 3, 4] which suggests that the shape of the spectrum at low wavenumbers determines the decay rate at least for low to moderate Reynolds numbers.

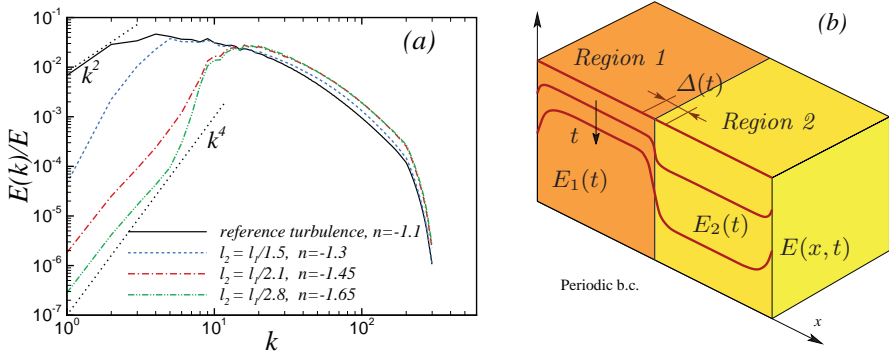


Fig. 1. (a) Initial three-dimensional spectra $E(k)$ normalized with the initial energy E . Continuous line: homogeneous region ($Re_\lambda = 150$) with the larger scale ℓ_1 ; other lines: spectra of the other fields to be mixed, with integral scale $\ell_2 < \ell_1$; n is the decay exponent found in the simulation. Reference k^2 and k^4 slopes are also shown. (b) Scheme of the flow and of the kinetic energy distribution during the decay.

Another interesting point is that, due to the different decay, an energy gradient, always concurrent to the integral scale gradient, soon emerges during the decay. It is maximum after about one eddy-turnover time $\ell/E^{1/2}$, then it is gradually reduced while the ratio of kinetic energy between the two regions still increases, see fig. 2 (a, c). The thickness of the induced kinetic energy layer increases while the two flow interact, see fig. 2 (b). The scale and energy mixing layer becomes immediately intermittent and the intermittency level is close to the that found in the shearless mixings with imposed gradients discussed in ref. [5, 6]. The instantaneous level of velocity skewness and kurtosis is comparable with the one which can be seen in the shearless mixings with higher energy ratios but uniform scale, see fig. 3 (a). The departure from the almost gaussian initial conditions always follows the same path, see figure 3(b), which is shared not only by the present mixings but also by the mixings with an imposed energy gradient. Another common aspect is the anisotropy of the velocity moments in the mixing layer: for the second order moments deviations of about a 10% of the isotropic value of $1/3$ are visible, while for the third order moments about half of the total kinetic energy flow was contributed by the velocity fluctuations in the direction of the mixing. This

property seems related to the behaviour of the pressure-velocity correlations in absence of shear [6].

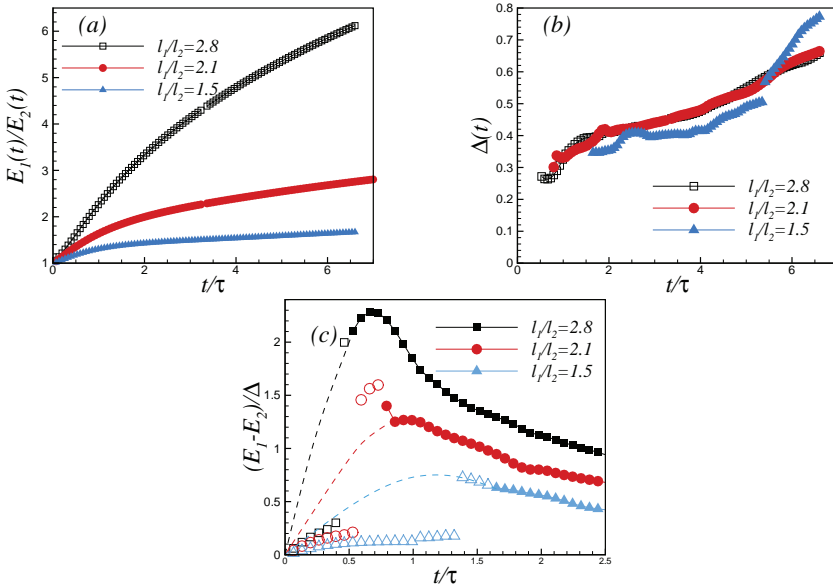


Fig. 2. (a) Time evolution of energy ratio E_1/E_2 , where E_1 and E_2 are the energy of the homogeneous regions with the largest and smallest macroscale; τ is the initial eddy turnover time. (b) Mixing layer thickness, conventionally defined as the distance between the points with normalized energy $(E(x, t) - E_2(t))/(E_1(t) - E_2(t))$ equal to 0.75 and 0.25 [5, 6]. (c) Time evolution of the energy gradient.

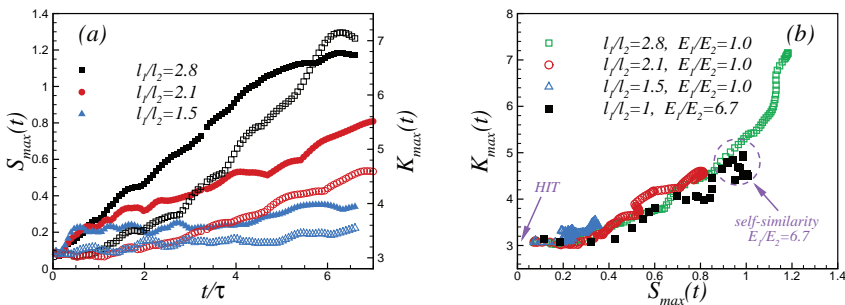


Fig. 3. (a) Maximum of the velocity skewness (filled symbols) and kurtosis (empty symbols) in the mixing layer. (b) Comparison of the intermittency level with a mixing with an initially uniform integral scale, each point corresponds to one time instant.

References

1. G.K. Batchelor, Q. Appl. Maths **6**, 97-116 (1948).

2. W.K. George, *Phys. Fluids* **4**, 1492-1509 (1992).
3. W.K. George, L. Davidson, *AIAA J.* **42**, 438-446 (2004).
4. P. Lavoie, L. Djenidi, R.A. Antonia, *J.Fluid Mech.* **585**, 395-420 (2007).
5. D. Tordella, M. Iovieno, *J. Fluid Mech.* **549**, 441-454, (2006).
6. D. Tordella, M. Iovieno, P.R. Bailey, *Phys. Rev. E* **77**, 016309 (2008).
7. M. Iovieno, C. Cavazzoni, D. Tordella, *Comp. Phys. Comm.* **141**, 365-374 (2001).

Fractal-generated turbulent scaling laws from a new scaling group of the multi-point correlation equation

M. Oberlack and G. Khujadze

Chair of Fluid Dynamics, Technische Universität Darmstadt, 64289 Darmstadt, Germany
 oberlack@fdy.tu-darmstadt.de, khujadze@fdy.tu-darmstadt.de

Investigating the multi-point correlation (MPC) equations for the velocity and pressure fluctuations in the limit of homogeneous turbulence a new scaling symmetry has been discovered. Interesting enough this property is not shared with the Euler or Navier-Stokes equations from which the MPC equations have originally emerged. This was first observed for parallel wall-bounded shear flows in [1]. Presently using this extended set of symmetry groups a much wider class of invariant solutions or turbulent scaling laws is derived for the decay of homogeneous-isotropic turbulence which is in stark contrast to the classical power law decay. In particular, we show that the experimentally observed specific scaling properties of fractal-generated turbulence i.e. a constant integral and Taylor length scale and the exponential decay of the turbulent kinetic energy (see [2, 3]) fall into this new class of solutions. The latter new scaling law may have been the first clear indication towards the existence of the extended statistical scaling group.

1 Multi-point equation of homogeneous turbulence

We investigate the symmetry structure of the infinite set of multi-point correlation (MPC) equations [4] for the velocity and pressure fluctuations $\mathbf{u}(\mathbf{x}, t)$ and $p(\mathbf{x}, t)$ respectively in the limit of homogeneous turbulence

$$\begin{aligned}
 & \frac{\partial R_{i_{\{n+1\}}}}{\partial t} + \sum_{l=1}^n \left(-\frac{\partial P_{i_{\{n\}}[0]}}{\partial r_{m_{(l)}}} \Big|_{[m_{(l)} \mapsto i]} + \frac{\partial P_{i_{\{n\}}[l]}}{\partial r_{i_{(l)}}} \right) - \nu \sum_{l=1}^n \sum_{m=1}^n \left(\frac{\partial^2 R_{i_{\{n+1\}}}}{\partial r_{k_{(m)}} \partial r_{k_{(l)}}} \right. \\
 & + \left. \frac{\partial^2 R_{i_{\{n+1\}}}}{\partial r_{k_{(l)}} \partial r_{k_{(l)}}} \right) + \sum_{l=1}^n \left(-\frac{\partial R_{i_{\{n+2\}}[i_{(n+1)} \mapsto k_{(l)}]}[\mathbf{x}_{(n+1)} \mapsto \mathbf{x}]}{\partial r_{k_{(l)}}} \right. \\
 & \left. + \frac{\partial R_{i_{\{n+2\}}[i_{(n+1)} \mapsto k_{(l)}]}[\mathbf{x}_{(n+1)} \mapsto \mathbf{r}_{(l)}]}{\partial r_{k_{(l)}}} \right) = 0, \quad \text{for } n = 1 \dots \infty . \quad (1)
 \end{aligned}$$

The system (1) is extended by its corresponding continuity equations (see [4]). In the latter equations the MPC tensor is defined as

$$R_{i_{\{n+1\}}} = R_{i_{(0)i_{(1)}\dots i_{(n)}} = \overline{u_{i_{(0)}}(\mathbf{x}_{(0)}) \cdot \dots \cdot u_{i_{(n)}}(\mathbf{x}_{(n)})}, \quad (2)$$

and the four variations of it appearing in (1) are defined accordingly [4].

2 Invariant solutions and turbulent decay scaling laws

In the limit of $|\mathbf{r}| \gg \eta_K$, i.e. for length scales beyond the viscosity dominated Kolmogorov scale [4], we find a new scaling symmetry \mathbf{G}_{s3} of the system (1). The system also admits the classical scaling groups \mathbf{G}_{s1} and \mathbf{G}_{s2} representing the independent scaling of space and time

$$\mathbf{G}_{s1} : \tilde{t} = t, \tilde{r}_{i_{(l)}} = r_{i_{(l)}}e^{a_1}, \tilde{R}_{ij} = R_{ij}e^{2a_1}, \tilde{R}_{ijk} = R_{ijk}e^{3a_1}, \dots, \quad (3)$$

$$\mathbf{G}_{s2} : \tilde{t} = e^{a_2}t, \tilde{r}_{i_{(l)}} = r_{i_{(l)}}, \tilde{R}_{ij} = R_{ij}e^{-2a_2}, \tilde{R}_{ijk} = R_{ijk}e^{-3a_2}, \dots, \quad (4)$$

$$\mathbf{G}_{s3} : \tilde{t} = t, \tilde{r}_{i_{(l)}} = r_{i_{(l)}}, \tilde{R}_{ij} = R_{ij}e^{a_3}, \tilde{R}_{ijk} = R_{ijk}e^{a_3}, \dots. \quad (5)$$

It is important to note that \mathbf{G}_{s3} is clearly distinct from the classical scaling groups in fluid mechanics. This property is not shared with the Euler or Navier-Stokes equations from which the MPC equations have originally emerged. Hence it is a purely statistical property of the equations (1).

Beside the above symmetries the system (1) admits the classical symmetry translation in time

$$\mathbf{G}_t : \tilde{t} = t + a_4, \tilde{r}_{i_{(l)}} = r_{i_{(l)}}, \tilde{R}_{ij} = R_{ij}, \tilde{R}_{ijk} = R_{ijk}, \dots. \quad (6)$$

Classical theories on decaying turbulence such as Birkhoff's and Loitsyansky's integrals entirely rely on the groups \mathbf{G}_{s1} and \mathbf{G}_{s2} . There these two groups give rise to a one-parameter family of similarity solutions with power law behavior.

Presently using the above extended set of symmetry groups (3)-(6) a much wider class of invariant solutions or turbulent scaling laws is derived. For this we need to employ the concept of invariant solutions, usually called similarity solution. This includes the three ideas of (i) infinitesimal transformations, (ii) condition of invariance of a differential equation and (iii) the invariant solution (for details see i.e. [5] or [4]).

For the present case the infinite set of equations (1) leads to the invariant surface condition

$$\frac{dt}{a_2t + a_4} = \frac{dr_{(i)}}{a_1r_{(i)}} = \frac{dR_{(ij)}}{[2(a_1 - a_2) + a_3]R_{(ij)}} = \dots \quad (7)$$

with the group parameters a_1 - a_4 descending from the groups (3)-(6).

It is important to note that any solution for an arbitrary set of group parameters of the latter system allows for an invariant solution of (1).

Firstly we consider the case without (5) i.e. $a_3 = 0$. Further assuming $a_1 \neq a_2$ and $a_4 \neq 0$ we find the following invariants of the system (7)

$$\hat{\mathbf{r}}_{(1)} = \frac{\mathbf{r}_{(1)}}{(t + t_0)^n} , \quad R_{ij}(\mathbf{r}_{(1)}, t) = (t + t_0)^{-m} \hat{\mathcal{R}}_{ij}(\hat{\mathbf{r}}_{(1)}) , \quad \dots \quad (8)$$

with $n = a_1/a_2$, $t_0 = a_4/a_2$ and $m = 2(1 - a_1/a_2)$. The variables $\hat{\mathbf{r}}_{(1)}$ and $\hat{\mathcal{R}}_{ij}$ are the constants of integration of (7) and are to be taken as new independent and dependent variables of the system (1) leading to a similarity reduction. Therein $m = 6/5, n = 2/5$ and $m = 10/7, n = 2/7$ respectively correspond to Birkhoff’s and Loitsiansky’s integrals.

For the present purpose of primarily understanding the scaling behaviour of fractal generated turbulence we need to consider both the breaking of the two classical scaling groups due to external symmetry breaking quantities. Hence, we set $a_1 = a_2 = 0$. Further, for the present case a non-zero a_3 related to the new scaling group is needed in order to allow for the construction of an invariant solution at all. Hence, employing the latter into (7) we observe two important conclusions.

Following the methodology above this leads to a similarity solution for the infinite set of MPC tensors (1) where the first term in the row, i.e. the two-point tensor, has the following form

$$\hat{\mathbf{r}}_{(1)} = \mathbf{r}_{(1)} , \quad R_{ij}(\mathbf{r}_{(1)}, t) = e^{-t/t_0} \mathcal{R}_{ij}(\hat{\mathbf{r}}_{(1)}) , \quad \dots \quad (9)$$

where \mathcal{R}_{ij} is the similarity variable of the reduced set of MPC equations independent of time and $t_0 = -a_4/a_3$.

We introduce the Reynolds stress tensor $\overline{u_i u_j}$ and the integral length scale L_i as functionals of R_{ij}

$$\overline{u_i u_j} = R_{ij}(\mathbf{r} = 0, t) \quad \text{and} \quad L_i = \frac{1}{2K} \int R_{kk}(\mathbf{r}) dr_i . \quad (10)$$

Employing these definitions and implementing (8) and (9) into the latter we respectively obtain the rather different turbulent scaling laws

$$\overline{u_i u_j} \sim (t + t_0)^{-m} , \quad L_i \sim (t + t_0)^n \quad (11)$$

and

$$\overline{u_i u_j} \sim e^{-t/t_0} , \quad L_i \sim const. \quad (12)$$

where the first one is the classical algebraic decay law while the second one corresponds to a new exponential decay law.

In [2] it was first reported that fractal-generated turbulence in a wind tunnel experiment may lead to an exponential decay law for the turbulent kinetic energy and a constant integral length scale according to (12) and it was more fully consolidated in [3]. A variety of different fractal grids were employed for the experiment. The key parameter therein is t_r the thickness ratio defined

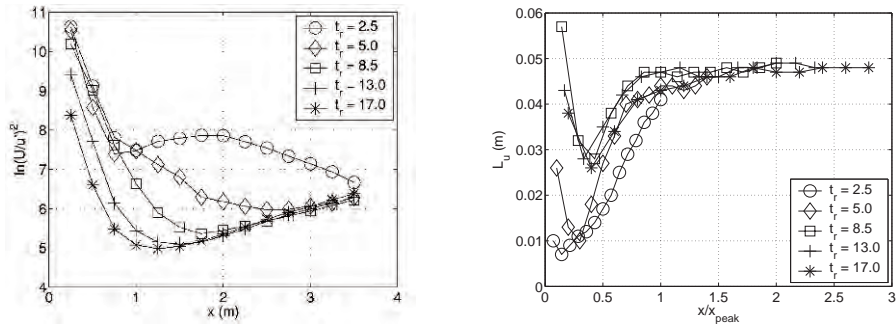


Fig. 1. $\ln[(U/u)^2]$ and L_u as functions of x (and x/x_{peak}) for all five space-filling fractal square grids. In particular for large t_r the turbulence decay curves asymptote to an exponential in agreement with equation (12). Accordingly the integral scales approach a constant downstream of the grid. t_r defines the scaling factor between the largest to smallest bar thicknesses. All results are taken from [2].

as the scaling factor between the largest to smallest bar thicknesses. The data for the turbulent kinetic energy and the integral length scale showing both the behaviour according to (12) are given in figure 1.

We observe that only the higher thickness ratios allow for the establishment of an exponential decay law i.e. beginning with $t_r = 8.5$ and higher. Second, the development of the exponential decay downstream of the grid becomes faster for increasing thickness ratios and is the largest for $t_r = 17$.

The physical interpretation of the latter results and in particular the fact that for large t_r the new scaling laws are established faster are due to the fact that a broad bandwidth of external scales have been imposed on the flow. As a result we observe a symmetry breaking of a_1 and a_2 i.e. $a_1 = a_2 = 0$ which directly leads to the given multi-point scaling law (9) or the related one-point scaling law (12).

References

1. Khujadze, G., and Oberlack, M., “DNS and scaling laws from new symmetry groups of ZPG turbulent boundary layer flow”, TCFD, **18**, pp. 391-411, (2004).
2. Hurst, D., and Vassilicos, J.C., “Scalings and decay of fractal-generated turbulence”, *Phys. Fluids*, **19**, pp. 035103, (2007).
3. Seoud, R.E., and Vassilicos, J.C., “Dissipation and decay of fractal-generated turbulence”, *Phys. Fluids*, **19**, pp. 105108, (2007).
4. Oberlack, M., 2000, *Symmetry, Invariance and Selfsimilarity in Turbulence*, Habilitation Thesis, RWTH Aachen.
5. Bluman, G.W., and Kumei, S., *Symmetries and Differential Equations*. In: Applied Mathematical Sciences, Vol. 81, Springer, Berlin, (1989).

Casimir Cascades in Two-Dimensional Turbulence

John C. Bowman

Department of Mathematical and Statistical Sciences, University of Alberta,
Edmonton, Alberta T6G 2G1 Canada `bowman at math.ualberta.ca`

Summary. The Kraichnan–Leith–Batchelor theory of two-dimensional turbulence is based on the fact that the nonlinear terms of the two-dimensional Navier–Stokes equation conserve both energy and enstrophy. In an infinite domain and in the limit of infinite Reynolds number, the net energy and enstrophy transfers out of a low-wavenumber forcing region must consequently be independent of wavenumber. The resulting dual cascade of energy to larger scales and enstrophy to smaller scales is readily observed in numerical simulations of two-dimensional turbulence in a finite domain.

While it is well known that the nonlinearity also conserves the global integral of any arbitrary C^1 function of the scalar vorticity field, the direction of transfer of these quantities in wavenumber space remains unclear. Numerical investigations of this problem are hampered by the fact that pseudospectral simulations, which necessarily truncate the wavenumber domain, do not conserve these higher-order Casimir invariants.

A fundamental question is whether these invariants also play an underlying role in the turbulent cascade, in addition to the *rugged* quadratic (energy and enstrophy) invariants, which do survive spectral truncation. Polyakov’s minimal conformal field theory model [1] has suggested that the higher-order Casimir invariants cascade to large scales, while Eyink [2] suggests that they might instead cascade to small scales.

In this work we develop estimates for the degree of nonconservation of the Casimir invariants and demonstrate, using sufficiently well-resolved simulations, that the fourth power of the vorticity cascades to small scales.

1 Two-Dimensional Turbulence

We begin with the 2D incompressible Navier–Stokes equation for the *vorticity* $\omega \doteq \hat{\mathbf{z}} \cdot \nabla \times \mathbf{u}$:

$$\frac{\partial \omega}{\partial t} + \mathbf{u} \cdot \nabla \omega = -\nu \nabla^2 \omega + f, \quad (1)$$

where the constant ν is the kinematic viscosity and f is an external stirring force. In the inviscid unforced limit $\nu = f = 0$, both the *energy* $E \doteq \frac{1}{2} \int u^2 \, d\mathbf{x}$ and *enstrophy* $Z \doteq \frac{1}{2} \int \omega^2 \, d\mathbf{x}$ are conserved.

However, as is well known, inviscid unforced 2D turbulence has uncountably many other *Casimir* invariants: any continuously differentiable function g of the (scalar) vorticity is conserved by the nonlinearity:

$$\begin{aligned} \frac{d}{dt} \int g(\omega) d\mathbf{x} &= \int g'(\omega) \frac{\partial \omega}{\partial t} d\mathbf{x} = - \int g'(\omega) \mathbf{u} \cdot \nabla \omega d\mathbf{x} \\ &= - \int \mathbf{u} \cdot \nabla g(\omega) d\mathbf{x} = \int g(\omega) \nabla \cdot \mathbf{u} d\mathbf{x} = 0. \end{aligned}$$

Do these invariants also play a fundamental role in the turbulent dynamics, in addition to the quadratic (energy and enstrophy) invariants? In particular, do they exhibit *cascades*? In the theoretical literature, this remains an open question: Polyakov [1] has predicted that the higher-order Casimir invariants cascade to large scales, while Eyink [2] suggests that they might cascade to small scales. What is certain is that only the quadratic invariants are *rugged*, meaning that their conservation, being a consequence of detailed triadic balance, survives high-wavenumber truncation. To see this, let us express (1) in Fourier space:

$$\frac{\partial \omega_{\mathbf{k}}}{\partial t} + \nu k^2 \omega_{\mathbf{k}} = \sum_{\mathbf{p}, \mathbf{q}} \frac{\epsilon_{\mathbf{k}\mathbf{p}\mathbf{q}}}{q^2} \omega_{\mathbf{p}}^* \omega_{\mathbf{q}}^* + f_{\mathbf{k}}, \quad (2)$$

where $\epsilon_{\mathbf{k}\mathbf{p}\mathbf{q}} \doteq (\hat{\mathbf{z}} \cdot \mathbf{p} \times \mathbf{q}) \delta(\mathbf{k} + \mathbf{p} + \mathbf{q})$ is antisymmetric under interchange of any two indices. When $\nu = f_{\mathbf{k}} = 0$, the enstrophy is readily seen to be conserved:

$$\frac{d}{dt} \sum_{\mathbf{k}} |\omega_{\mathbf{k}}|^2 = \sum_{\mathbf{k}, \mathbf{p}, \mathbf{q}} \frac{\epsilon_{\mathbf{k}\mathbf{p}\mathbf{q}}}{q^2} \omega_{\mathbf{k}}^* \omega_{\mathbf{p}}^* \omega_{\mathbf{q}}^* = 0.$$

In the absence of high-wavenumber truncation, the invariance of $Z_3 \doteq \int \omega^3 d\mathbf{x}$ also arises from a product of antisymmetric and symmetric tensors:

$$0 = \sum_{\mathbf{k}, \mathbf{r}, \mathbf{s}} \left[\sum_{\mathbf{p}, \mathbf{q}} \frac{\epsilon_{\mathbf{k}\mathbf{p}\mathbf{q}}}{q^2} \omega_{\mathbf{p}}^* \omega_{\mathbf{q}}^* \omega_{\mathbf{r}}^* \omega_{\mathbf{s}}^* + 2 \text{ other similar terms} \right].$$

However, the absence of an explicit $\omega_{\mathbf{k}}$ in the first term means that setting $\omega_{\ell} = 0$ for $\ell > K$ breaks the symmetry in the summations. Nevertheless, since the missing terms involve $\omega_{\mathbf{p}}$ and $\omega_{\mathbf{q}}$ for p and q higher than the truncation wavenumber K , one might expect that a very well-resolved simulation would lead to almost exact invariance of Z_3 . Indeed, we will see that this is the case.

In terms of the nonlinearity $S_{\mathbf{k}} \doteq \sum_{\mathbf{p}, \mathbf{q}} \frac{\epsilon_{\mathbf{k}\mathbf{p}\mathbf{q}}}{q^2} \omega_{\mathbf{p}}^* \omega_{\mathbf{q}}^*$, the enstrophy spectrum $Z(k)$ is seen to satisfy a balance equation of the form

$$\frac{\partial}{\partial t} Z(k) + 2\nu k^2 Z(k) = 2T(k) + G(k),$$

where $T(k)$ and $G(k)$ are the angular averages of $\text{Re} \langle S_{\mathbf{k}} \omega_{\mathbf{k}}^* \rangle$ and $\text{Re} \langle f_{\mathbf{k}} \omega_{\mathbf{k}}^* \rangle$, respectively. It is convenient to define the *nonlinear enstrophy transfer function* $\Pi(k)$, which measures the cumulative nonlinear transfer of enstrophy into $[k, \infty)$:

$$\Pi(k) = 2 \int_k^\infty T(p) dp.$$

On integrating from k to ∞ , we find

$$\frac{d}{dt} \int_k^\infty Z(p) dp = \Pi(k) - \epsilon(k),$$

where $\epsilon(k) \doteq 2\nu \int_k^\infty p^2 Z(p) dp - \int_k^\infty G(p) dp$ is the total enstrophy transfer, *via* dissipation and forcing, *out* of wavenumbers higher than k . A positive (negative) value for $\Pi(k)$ represents a flow of enstrophy to wavenumbers higher (lower) than k . When $\nu = f_{\mathbf{k}} = 0$ enstrophy conservation implies that

$$0 = \frac{d}{dt} \int_0^\infty Z(p) dp = 2 \int_0^\infty T(p) dp,$$

so that

$$\Pi(k) = 2 \int_k^\infty T(p) dp = -2 \int_0^k T(p) dp. \tag{3}$$

We note that $\Pi(0) = \Pi(\infty) = 0$. Moreover, in a steady state, $\Pi(k) = \epsilon(k)$; this provides an excellent numerical diagnostic for validating a steady state.

The cumulative nonlinear enstrophy transfer Π_3 for the globally integrated invariant $Z_3 = \int \omega^3 d\mathbf{x}$ can be defined similarly and measured numerically. However, we found no systematic cascade: Z_3 appears to slosh back and forth between the large and small scales. In hindsight, this should be expected since ω^3 is not a sign-definite quantity.

Of much more interest is the determination from a pseudospectral code of the cascade direction of a sign-definite quantity like the fourth-order Casimir invariant $Z_4 \doteq \int \omega^4 d\mathbf{x}$. If we Fourier decompose $Z_4 = N^3 \sum_j \omega^4(x_j)$ in terms of N spatial collocation points x_j , we find

$$Z_4 = \sum_{\mathbf{k}, \mathbf{p}} \omega_{\mathbf{k}} \omega_{\mathbf{p}} \omega_{\mathbf{q}} \omega_{-\mathbf{k}-\mathbf{p}-\mathbf{q}}.$$

In terms of the nonlinear source term $S_{\mathbf{k}}$, the evolution of Z_4 follows

$$\begin{aligned} \frac{d}{dt} Z_4 &= \sum_{\mathbf{k}} \left[S_{\mathbf{k}} \sum_{\mathbf{p}} \omega_{\mathbf{p}} \omega_{\mathbf{q}} \omega_{-\mathbf{k}-\mathbf{p}-\mathbf{q}} + 3\omega_{\mathbf{k}} \sum_{\mathbf{p}} S_{\mathbf{p}} \omega_{\mathbf{q}} \omega_{-\mathbf{k}-\mathbf{p}-\mathbf{q}} \right] \\ &= N^2 \sum_{\mathbf{k}} \left[S_{\mathbf{k}} \sum_j \omega^3(x_j) e^{2\pi i \mathbf{j} \cdot \mathbf{k} / N} + 3\omega_{\mathbf{k}} \sum_j S(x_j) \omega^2(x_j) e^{2\pi i \mathbf{j} \cdot \mathbf{k} / N} \right] \\ &\doteq \sum_k T_4(k). \end{aligned} \tag{4}$$

To determine the cascade direction of Z_4 , we considered a double-periodic pseudospectral simulation forced at wavenumber 2, with the dissipation

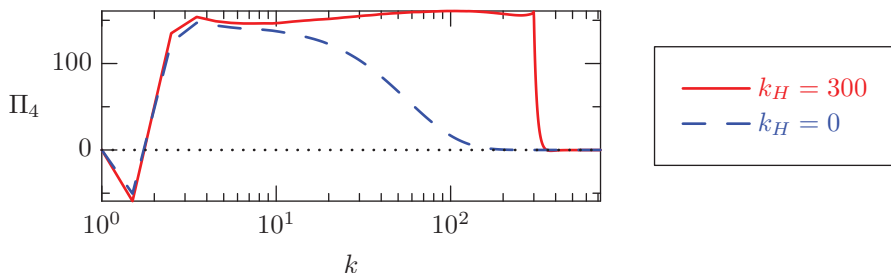


Fig. 1. Downscale nonlinear transfer Π_4 of Z_4 averaged over $t \in [200, 450]$.

term νk^2 replaced by $\nu k^2 H(k - k_H)$, where H is the Heaviside step function. A positive cutoff k_H mimics a pristine inertial range, à la Kolmogorov. In Fig. 1, we see that the time-averaged nonlinear transfer Π_4 of Z_4 exhibits the clear signature of a downward cascade (positive Π_4 in the enstrophy inertial range) at small scales. As a check that sufficient numerical resolution has been used to resolve the contribution of the nonlinear terms to the evolution of Z_4 , we note that $\Pi(0) = \Pi(\infty) = 0$, as desired. An important point to emphasize in computing Z_4 is that (4) requires the computation of a double convolution, in terms of the Fourier transform of the cubic quantity ω^3 . Correctly dealiasing therefore requires a 2/4 zero padding rule (instead of the usual 2/3 rule for a quadratic convolution). This means that even though a 2048×2048 pseudospectral simulation was used, the maximum physical wavenumber retained in each direction was 512.

We also point out an important distinction between nonlinear enstrophy *transfer* and *flux*. The mean rate of enstrophy transfer to $[k, \infty)$ is given by (3). In a steady state, $\Pi(k)$ will thus trivially be constant throughout an inertial range. In contrast, the enstrophy flux through a wavenumber k , as considered by Kolmogorov, is the amount of enstrophy transferred to small scales *via* triad interactions involving mode k . Independence of the flux on k is highly nontrivial, based on the conjectured self-similarity of the inertial range.

Even though higher-order Casimir invariants do not survive wavenumber truncation, it appears possible, with sufficiently well-resolved simulations, to check whether they cascade to large or small scales. In this work, we computed the transfer function of the globally integrated ω^4 inviscid invariant and provided strong numerical evidence supporting Eyink's conjecture that in the enstrophy inertial range there is a direct cascade of (positive-definite) high-order invariants to small scales.

References

1. A.M. Polyakov, PUPT-1369 (1992).
2. Gregory L. Eyink, Physica D 91 (1996) 97-142.

The development of truncated inviscid turbulence and the FPU-problem

G. Ooms, and B.J. Boersma

J.M. Burgerscentrum, Delft University of Technology, Faculty of Mechanical Engineering, Laboratory for Aero - & Hydrodynamics, Mekelweg 2, 2628 CD Delft, The Netherlands

Gijs Ooms at g.ooms@tudelft.nl

As is well known Fermi, Pasta and Ulam [1] studied the energy redistribution between the linear modes of a one-dimensional chain of particles connected via weakly nonlinear springs. To their surprise no apparent tendency to equipartition of energy was observed in their numerical experiments. Much more knowledge is now available about this problem (see, for instance, the recent book by Gallavotti [2] or the review by Cambell et al. [3] in the focus issue on the FPU-problem in the journal *Chaos*). According to more recent studies an exponential localization of the energy distribution in normal mode space is observed on a very short time scale τ_1 . It possesses a core with a few modes that are strongly excited, and a tail of exponentially weakly excited modes. Below an energy threshold there is a slow pumping of energy from the core of the distribution into its tail. This process ultimately brings the system to equipartition, but on a much larger time scale τ_2 ($\tau_2 \gg \tau_1$).

In this paper we present the results of an investigation of another system of non-linearly coupled normal modes to find out whether results similar to the FPU-results are found. This system is truncated, inviscid turbulence. To that purpose we carried out direct numerical simulations of the turbulent flow of an inviscid fluid inside a 3-D box. Only a limited number of modes was taken into account. The purpose of our calculations was to start with energy in one normal mode and then study the development of the energy spectrum as function of time with special interest for the influence of the amount of initial energy on the development, to see whether results were found similar to the FPU-problem. The equation of motion describing the flow inside the box is given by

$$\frac{\partial \mathbf{v}}{\partial t} + (\mathbf{v} \cdot \nabla) \mathbf{v} = -\frac{1}{\rho_f} \nabla p, \quad (1)$$

in which \mathbf{v} is the fluid velocity, p the pressure, ρ_f the fluid density and t the time. We assumed periodic boundary conditions at the walls of the box. Equation (1) was solved by means of direct numerical simulation (DNS). The

velocity and pressure field is represented as a truncated Fourier series. Spatial derivatives were calculated in Fourier space. The non-linear term has been evaluated in physical space. The time integration was performed with a standard second-order Adams-Basforth method.

We present now the results for the influence of decreasing energy E_0 of the initial mode on the spectrum development while keeping the time scale T_0 for this mode constant. As velocity scale of the initial mode is chosen $V_0 = E_0^{1/2}$. So the length scale for the mode is given by $L_0 = V_0 T_0 = E_0^{1/2} T_0$, which means that this length scale decreases with decreasing energy of the initial mode. We keep the length scale of the total system constant. This was also the case for the FPU-problem, i.e. the distance between the two walls remained the same when the amplitude of the excitation was changed. The aim of our study is to simulate as much as possible for truncated inviscid turbulence the conditions for the FPU problem and then investigate the possible similarities.

We present in Fig. 1 the spectral development for an initial spectrum with one (arbitrarily chosen) excited mode. Then we decrease the initial energy E_0 by a factor of 4, while decreasing the length scale L_0 of the initial mode by a factor of 2 and calculate again the spectral development. We repeat such calculation, but this time by decreasing the initial energy by a factor of 25 and the length scale of the initial mode by a factor of 5. The results are respectively given in Fig. 2 and Fig. 3, in which τ_Λ is the integral time scale (chosen equal to T_0). It can be seen from the figures, that with decreasing

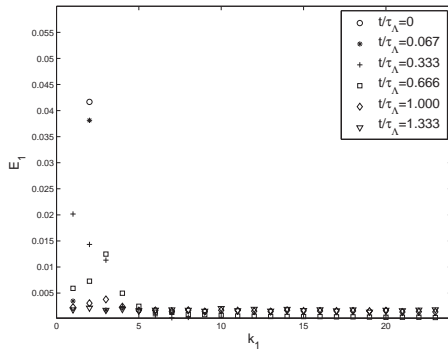


Fig. 1. Spectrum E_1 as a function of wave number k_1 at six values of t/τ_Λ for the case of one excited initial mode. k_1 is the component of the wave vector in the x_1 -direction. $E_1(k_1, t) = \frac{1}{2} v_1(k_1, t)^2$ in which $v_1(k_1, t)$ is the velocity component in the x_1 -direction.

energy the equipartition of energy is increasingly delayed. For a decrease in energy of a factor 4 the equipartition takes about a factor 3 more time than for the base case shown in Fig. 1 and for a decrease in energy of a factor of 25 equipartition is already delayed by a factor of 10. At first a few modes are

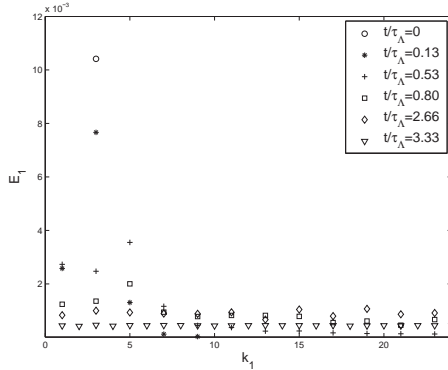


Fig. 2. Spectrum E_1 as a function of wave number k_1 at six values of t/τ_A for the case of one excited initial mode. The initial energy is a factor 4 smaller than for the case shown in Fig. 1 and the length scale of the initial mode is a factor of 2 smaller.

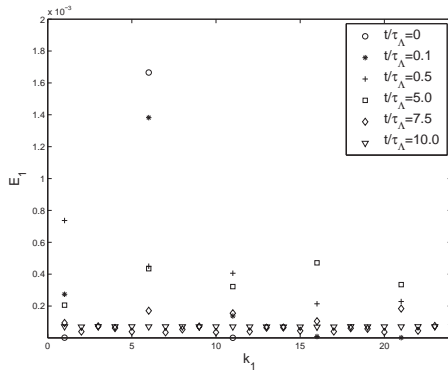


Fig. 3. Spectrum E_1 as a function of wave number k_1 at six values of t/τ_A for the case of one excited initial mode. The initial energy is a factor 25 smaller than for the case shown in Fig. 1 and the length scale of the initial mode is a factor of 5 smaller.

generated and the change in energy of these modes continues for a relatively long time. Then the remaining modes suddenly appear and equipartition of energy is rather quickly established. This can even better be seen in Fig. 4, in which the results of Fig. 3 are plotted with a log scale for the energy axis. For the results shown in Fig. 2 and Fig. 3 we have made an estimate of the time scale τ_1 for the initial localization of the energy distribution with a few excited modes in normal mode space and for the time scale τ_2 for reaching equipartition. For Fig. 2 the ratio τ_2/τ_1 is approximately equal to 15, whereas for Fig. 3 the ratio τ_2/τ_1 is approximately 50. As the time scale τ_1 is nearly the same for the two cases, this means that the time scale τ_2 for reaching equipartition is strongly increasing with decreasing initial energy. This is in qualitative accordance with the results for the FPU problem. FPU

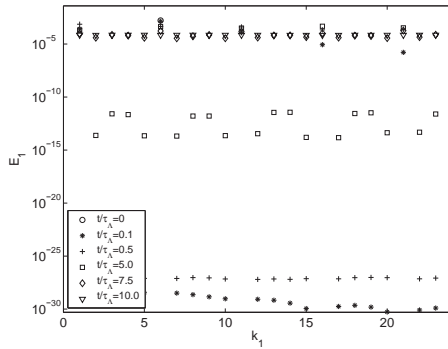


Fig. 4. Spectrum E_1 as a function of wave number k_1 as shown in Fig. 3, but now with a log scale for the energy axis. As can be seen the spectrum possesses a few modes that are strongly excited and there is a rather flat spectrum of weakly excited modes. Only rather late in the spectral development they increase in strength and equipartition is established.

observed recurrences during the development of the spectrum of almost all the energy into the initially excited mode. Such surprising recurrences were not observed by us for the turbulence problem. However, recurrence is not a universal feature of the FPU problem. If the energy in the FPU chain is reduced beyond the values originally used by FPU, recurrence will become partial, with less and less energy flowing back and forth.

The conclusion is that although the FPU-problem deals with a different physical problem (dynamics of a 1-D chain of particles connected via springs) than our problem (dynamics of an inviscid fluid flow inside a 3-D box), the influence of a decrease in the energy of the system on the delay in the development of the energy spectrum is rather similar for both problems. Details are given by Ooms and Boersma [4]

References

1. E. Fermi, J. Pasta and S. Ulam, Los Alamos Report LA-1940, (1955), Also published in *Collected Papers of Enrico Fermi*, edited by E. Segre, University of Chicago Press, Chicago, 1965.
2. G. Gallavotti, Lecture notes in physics, " No. 728: The Fermi-Pasta-Ulam problem: A status report", Springer, 2007.
3. D.K. Campbell, P. Rosenau and G.M. Zaslavsky, *Chaos*, **15**, 015101 2005.
4. G. Ooms and B.J. Boersma, *Chaos*, **18**, 043124 2008.

The renormalized eddy-fragmentation equation and its exact solutions

V. L. Saveliev and M. Gorokhovski

¹ Institut of Ionosphere, Academy of Science, Kamenskoe Plato, 050020 Almaty, Kazakhstan

² LMFA, CNRS Ecole Centrale de Lyon INSA Lyon Université Claude Bernard Lyon 1, 36 avenue Guy de Collongue, 69134 Ecully Cedex, France
saveliev@topmail.kz ; mikhael.gorokhovski@ec-lyon.fr

The fragmentation equation describes the evolution in time of particles system, when particles break up. The turbulent eddy decay is an example of such fragmentation. A collection of tangled trajectories of fluid particle, associated with a turbulent concentrated structure, resembles a “wool ball” of a typical scale r . Once a fluid particle is subjected to an intense acceleration, a new “wool ball” is formed, containing a part of total energy of flow. The population of newly appeared “wool balls” is assumed to be governed by the fragmentation equation, requiring conservation of the total kinetic energy injected on large scales. The question raised is how this energy is distributed in statistical ensemble of such “wool balls”. In this paper, the renormalized form of the fragmentation equation is obtained for arbitrary functions for the spectrum and for frequency of fragmentation. If the frequency of fragmentation is a power function of size, a simple exact solution to this equation is obtained, providing for stationary flux of energy, from large scales towards zero scales. A simple stochastic generation of random field with presumed fractal properties is illustrated. Also, presuming the spectrum of breakup and its frequency in the form of power functions, the exact self-similar solution is obtained on the basis of specifically introduced scaling transformations. Here the specific case is considered, when the breakup frequency is decreasing with decreasing of r . This work contributes to the group-theoretical description of statistically homogeneous turbulence, developed recently by authors in [1, 2, 3].

1. *The fragmentation equation* has the following form:

$$\frac{\partial F(r)}{\partial t} = (q_0 \widehat{I}_+^p - 1) \nu(r) F(r); \widehat{I}_+^p F = \int_0^1 \frac{d\alpha}{\alpha} Q(\alpha) F\left(\frac{r}{\alpha}\right); \int_0^1 Q(\alpha) d\alpha = 1 \quad (1)$$

where $F(r)$ is the number distribution function; $Q(\alpha)$ is the probability density function of breakup (spectrum of fragmentation), $\nu(r)$ is the breakup

frequency, q_0 is the mean number of new statistical particles produced by one breakup.

2. *The energy distribution function.* With evolution in time, the total energy is conserved and not the total number of statistical particles. This motivates to introduce the energy distribution function $f(r)$, instead of using the number distribution function $F(r)$; the norm of the former one will not change. The relation between both functions, $f(r) = r^\beta F(r)$, leads to the following expression: $q_0 = \frac{1}{\langle \alpha^\beta \rangle_Q}$, and then to the following fragmentation equation:

$$\frac{\partial f(r)}{\partial t} = (\hat{I}_+ - 1) \nu(r) f(r); \quad \hat{I}_+ f = \int_0^1 \frac{d\alpha}{\alpha} q(\alpha) f\left(\frac{r}{\alpha}\right) \tag{2}$$

$$q(\alpha) = \frac{\alpha^\beta Q(\alpha)}{\langle \alpha^\beta \rangle_Q}; \quad \int_0^1 q(\alpha) d\alpha = 1 \tag{3}$$

Note that in the case of the constant breakup frequency, the invariance of (2) to the Kolmogorovs scaling transformation ($r \rightarrow \gamma^{3/2}r$; $t \rightarrow \gamma t$) requires $\beta = -2/3$.

3. *Renormalized form of the fragmentation equation and its exact solution for an arbitrary fragmentation spectrum $q(\alpha)$.* The fragmentation term in (2) represents the difference between two terms; each of them can be very large, and even infinite (if to give up the normalization requirement of spectrum $q(\alpha)$). In order to overcome this problem, the renormalization of (2) can be obtained, describing evolution of an infinite system of particles in the form of continuity equation:

$$\frac{\partial f(r)}{\partial t} = \frac{\partial}{\partial r} J \tag{4}$$

where energy flux in the r -space is given by the following expression:

$$J = r \left[\langle -\ln \alpha \rangle + \frac{\langle (-\ln \alpha)^2 \rangle}{2!} \hat{\sigma} + \dots + \frac{\langle (-\ln \alpha)^{n-1} \rangle}{(n-1)!} \hat{\sigma}^{n-2} + \frac{\langle (-\ln \alpha)^n \rangle}{n!} \hat{\sigma}^{n-1} \hat{I}_+^{(n)} \right] \nu(r) f(r) \tag{5}$$

Here

$$\hat{\sigma} = \frac{\partial}{\partial r} r; \quad \langle (-\ln \alpha)^n \rangle = \int_0^1 (\ln \alpha)^n dq(\alpha) d\alpha; \quad \hat{I}_+^{(n)} = \int_0^1 d\alpha q_n(\alpha) e^{-\ln \alpha \hat{\sigma}} \tag{6}$$

$$q_n(\alpha) = \frac{n}{\langle (-\ln \alpha)^n \rangle} \int_0^1 q(\alpha\beta) (-\ln \beta)^{n-1} d\beta; \quad \int_0^1 q_n(\alpha) d\alpha = 1 \tag{7}$$

The number of terms in (5) can be chosen arbitrary ($n = 1, 2, 3, \dots$). If $n = 1$, the renormalized fragmentation equation has the following form:

$$\frac{\partial f}{\partial t} = \frac{\partial}{\partial r} r \langle -\ln \alpha \rangle \hat{I}_+^{(1)} \nu f; \quad q_1(\alpha) = \frac{1}{\langle -\ln \alpha \rangle} \int_0^1 q(\alpha\beta) d\beta \tag{8}$$

In the case when $\nu(r) = cr^\mu$, a simple solution to this equation, verifies to be a power (scaling symmetry) distribution:

$$f(r, t) = \frac{j_0}{\langle -\ln \alpha \rangle} r^{-(\mu+1)} + t j_0 \delta(r); \quad 0 \leq r < \infty \tag{9}$$

The principal point here is that with accumulation of statistical particles of zero size (zero energy), this solution provides for stationary energy flux j_0 (sec^{-1}), from infinity towards zero size.

4. *Stochastic simulation of random field with presumed fractal properties.* We sample an ensemble of stochastic particles from a power function $r^{-(\mu+1)}$; their sum represents the total energy. Additionally to the scaling symmetry, we impose the translational symmetry on the random position of each particle (thereby conserving the total energy): once a sampled particle walks out from the box of presumed size L ($|r| > L$), it is reset to the box in the position with its period L . In fig. 1, an example of results of such a simulation is given for four identical sampling procedure but with four different values of power $\mu = 0., 0.5, 1.5, 2.5$. A strong clustering of particles in the phase space is seen with increasing power μ .

4. *Self-similar solutions.* It is also possible to construct the exact self-similar solution to eq. (8). To this end, we define the scaling transformation with parameter η :

$$\phi(r, t) = \frac{1}{|\eta|^{1/\mu}} f\left(\frac{r}{|\eta|^{1/\mu}}, t\right) = e^{-\frac{1}{\mu} \ln |\eta| \hat{\sigma}} f(r, t) \tag{10}$$

and, respectively, its inverse transformation:

$$f(r, t) = |\eta|^{1/\mu} \phi\left(|\eta|^{1/\mu}, t\right) = e^{\frac{1}{\mu} \ln |\eta| \hat{\sigma}} \phi(r, t) \tag{11}$$

where η is chosen to be linear function of time, $\eta(t) = 1 + \tau^{-1}t$, τ is some positive or negative constant. When $\mu > 0$, the duration of relaxation process is infinite, and only positive value of parameter τ is considered. Then $\eta(t)$ is positive, and $\frac{|\eta|}{\eta} = 1$. In this case, using (10)-(11) for transformation of (8), the stationary solution $\phi(r)$, is governed by the following equation:

$$\frac{\partial}{\partial r} r \left[-\frac{1}{\mu\tau} + \langle -\ln \alpha \rangle \widehat{I}_+^{(1)} \nu \right] \phi(r) = 0 \tag{12}$$

When the spectrum of breakup $q(\alpha)$ is a power function, $q(\alpha) = (\gamma+1)\alpha^\gamma$, one gets: $\widehat{I}_+^{(1)} = \widehat{I}_+$, $\langle -\ln \alpha \rangle = (\gamma+1)^{-1}$, and, consequently, the exact solution (12) can be found. This solution verifies to be as follows:

$$\phi(r) = \text{const } r^\gamma e^{-\gamma cr^\mu} \tag{13}$$

To this solution, according to (11), corresponds the self-similar solution to starting equations, equivalently, (2) or (8):

$$f(r, t) = \text{const } (1 + \tau^{-1}t)^{\frac{\gamma+1}{\mu}} r^\gamma e^{-\gamma c(1+\tau^{-1}t)r^\mu} \tag{14}$$

References

1. V. L. Saveliev and M. Gorokhovski, Group-theoretical model of developed turbulence and renormalization of Navier-Stokes equations. *Phys.l Rev. E* **72**, 016302 (2005).
2. V. L. Saveliev and M. Gorokhovski, Description of group-theoretical model of developed turbulence. *Phys. Scr.* **T132**, 014005 (2008).
3. M. A. Gorokhovski and V. L. Saveliev, Statistical universalities in fragmentation under scaling symmetry with a constant frequency of fragmentation. *J.Phys.D: Appl. Phys.* **41**, 085405 (2008).

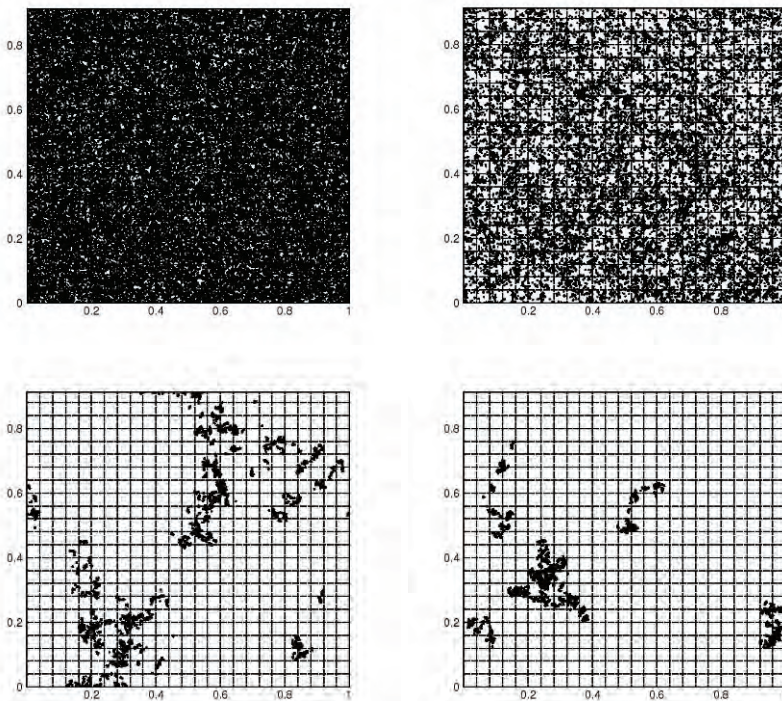


Fig. 1. Sampling from $r^{-(\mu+1)}$ along with periodic conditions; combination of scaling and translation symmetries; $\mu = 0., 0.5, 1.5, 2.5$; the total number of sampled particles is the same. A strong clustering of particles in the phase space is seen with increasing power μ .

Determination of the statistics of the velocity gradient tensor as a function of scale : solution of the tetrad model

A. Naso and A. Pumir

Laboratoire de Physique, Ecole Normale Supérieure de Lyon, 46, Allée d'Italie,
F-69007, Lyon, France
alain.pumir at ens-lyon.fr

The transfer of energy from large to small scales in turbulent flows rests on the properties of the velocity gradient tensor. Understanding the properties of the velocity gradient tensor, $m_{ab} = \partial_a u_b$, as well as the dependence on scale of m coarse-grained over a scale r : $M_{ab} = (1/V) \int_V m_{ab} d^3x$, is one of the most important modelling issues in turbulence, in particular in the context of LES.

The lagrangian approach provides a natural way to address the problem of evolution of the (coarse-grained) velocity gradient tensor. To describe the evolution of M , it is necessary to also follow the evolution of the volume (parameterized by a tetrad of lagrangian particles) over which m is coarse-grained. The model, introduced in [1] thus involves, besides the matrix M , a set of vectors $\rho_{i,a}$ describing the geometry of the tetrad, and obeying, provided the scale r is in the inertial range of scales :

$$\frac{d}{dt} \rho_{i,a} = \rho_{i,b} M_{ba} + u_{i,a} \quad (1)$$

$$\frac{d}{dt} M = -(1 - \alpha) (M^2 - \Pi \text{tr}(M^2)) + \eta \quad (2)$$

The tensor Π is defined by $\Pi \equiv \frac{g^{-1}}{\text{tr}(g^{-1})}$, where g is the moment of inertia tensor, defined by $g_{ab} = \sum_i \rho_{i,a} \rho_{i,b}$. The terms u (resp. η), on the right-hand side of Eq. 1 (resp. 2), are postulated to be gaussian, white in time, and with the following correlation : $\langle u_{i,a}(0) u_{j,b}(t) \rangle = C_u \rho^2 \sqrt{\text{tr}(MM^T)} \delta_{ab} \delta_{ij} \delta(t)$ and $\langle \eta_{ab}(0) \eta_{cd}(t) \rangle = \frac{C_\eta \epsilon}{\rho^2} \left[\delta_{ac} \delta_{bd} - \frac{1}{3} \delta_{ab} \delta_{cd} \right] \delta(t)$. The properties of the velocity gradient tensor at a scale r in the inertial range can be inferred by integrating the system of equations 1, 2 and by using the fact that the velocity gradient tensor is (essentially) gaussian at the integral scale. The determination of the velocity gradient tensor at scale r can be formulated as a stochastic problem,

amenable in principle to a numerical solution by using Monte Carlo methods [2].

One of the most significant difficulties in solving such problems comes from the fact that a straightforward sampling of the possible configurations leads to contributions that vary over many orders of magnitude, thus leading to vastly inefficient algorithms. One way to address the problem is to look for the configuration that contributes most to the probability, the so-called semi-classical method [3]. The approach followed here is rather to use the importance sampling strategy [4], that consists in sampling preferentially configurations that contribute most to the weight. Various strategies have been developed in order to keep track only of the trajectories in phase space that contribute most to the statistical weight. Details of the scheme actually implemented here will be provided elsewhere [5]. Implementing such methods has allowed us to compute the evolution of the pdf of the velocity gradient tensor down to scales of $r = L/16$. Fig. 1 shows the probability distribution function (PDF) in the plan of the invariants $R = -\frac{1}{3}\text{tr}(M^3)$ and $Q = -\frac{1}{2}\text{tr}(M^2)$. The numerical solution is in qualitatively very good agreement with the known DNS [3] and experimental [6] results.

The scaling of the second moments, such as the strain $\langle S^2 \rangle$ ($S = (M + M^T)/2$) and the vorticity $\langle \Omega^2 \rangle$ ($\Omega_a = \epsilon_{abc}M_{bc}$), and for the third order invariants of M , the vortex stretching $\langle \Omega \cdot S \cdot \Omega \rangle$ and the quantity $\langle \text{tr}(M^2 M^T) \rangle$, related to the energy transfer [1]. Fig.2 shows a close agreement with the standard Kolmogorov scalings : $M \propto r^{-2/3}$, so the second moments go as $r^{-4/3}$ and the third moments go as r^{-2} . In addition, the signs of $\langle \Omega \cdot S \cdot \Omega \rangle$ is positive, thus revealing the presence of vorticity production, and $\langle \text{tr}(M^2 M^T) \rangle$ is negative, consistent with an energy flux towards small scales.

Last, the model correctly reproduces the main features of the density of vorticity, strain, vortex stretching and $\text{tr}(M^2 M^T)$, Fig.3.

Further improvement of the algorithm should allow us to determine the solution at much smaller scale. The hope is that it will permit us to address several important questions regarding the physics of turbulence. The aim of studying the evolution of the PDF in the (R, Q) plane as a function of r is to provide a qualitative understanding of the structures occurring in turbulent flows, as a function of scales. Higher moments of the correlation function can be readily determined from this work. It will be interesting to investigate systematically the intrinsic invariants of the velocity gradient tensor [7] with our method. One obvious generalisation of this work consists in incorporating a large scale gradient, such as a shear [8] or other mean gradients [9]. The possibility to measure directly these quantities in an experiment offers fascinating perspectives for this work. In particular, our hope is that it will not only allow us to find optimal parameters for the model, but more importantly, to test precisely the limitations of the model itself, and suggest improvements.

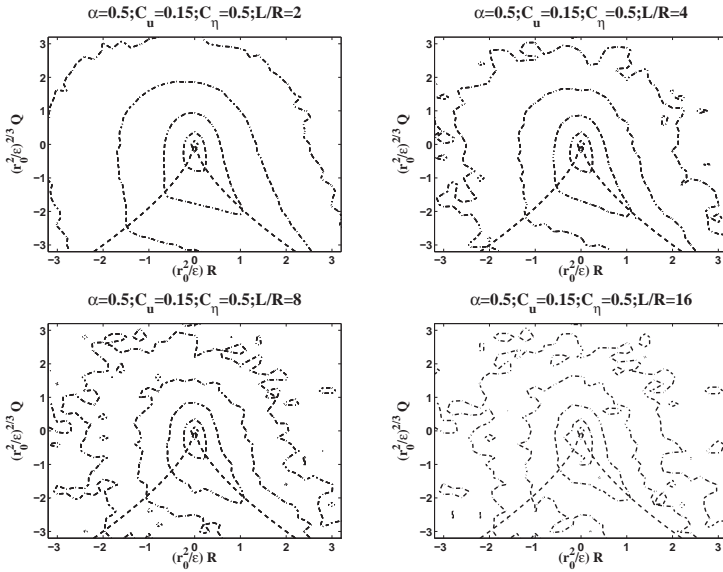


Fig. 1. Joint pdf of the invariants (R, Q) , scaled by the variance of the rate of strain tensor, at $r/L = 0.5$ (top left), $r/L = 0.25$ (top right), $r/L = 0.125$ (bottom left) and $r/L = 0.0625$ (bottom right). The dashed lines are isoprobability lines, logarithmically spaced, and separated by a factor 10. The values of the parameters are $\alpha = 0.5$. $C_u = 0.15$ and $C_\eta = 0.5$. The increased amount of noise is a consequence of the difficulty in adequately sampling the phase space as the ratio r/L decreases.

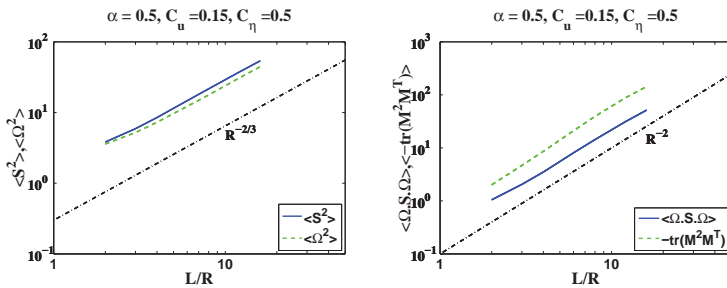


Fig. 2. The scaling behavior of the second moments (strain and vorticity variance, left) as a function of scale, and of the third moments (stretching and $\langle \text{tr}(M^2 M^T) \rangle$), right). These moments follow the standard Kolmogorov prediction, as indicated by the dash-dotted lines.

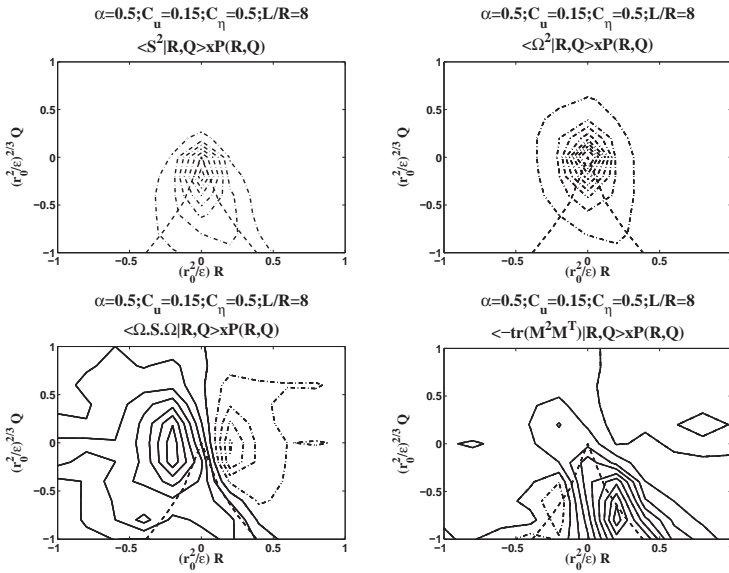


Fig. 3. The density of strain (top left), vorticity (top right), vorticity stretching (bottom left) and $\text{tr}(M^2 M^T)$ in the (R, Q) plane. The patterns are generally comparable to what has been obtained in other numerical studies [1] or in experiments [6].

References

1. M. Chertkov, A. Pumir and B. Shraiman, *Phys. Fluids* **11**, 2394 (1999).
2. A. Naso, A. Pumir and M. Chertkov, *J. Turbulence* **8**, N39 (2007).
3. A. Naso and A. Pumir, *Phys. Rev.* **E72**, 056318 (2005).
4. M. Denny, *Eur. J. Phys.* **22**, 403 (2001).
5. A. Naso, A. Pumir and B. Shraiman, in preparation (2009).
6. H. Xu et al., in preparation (2008).
7. E. D. Siggia, *Phys. Fluids* **24**, 1934 (1981).
8. A. Naso, M. Chertkov and A. Pumir, *J. of Turb.* **7**, N41 (2006).
9. S. Ayyakasonmayajula and Z. Warhaft, *J. Fluid Mech.* **566**, 273 (2006).

TSF Experiment for comparison of high Reynold's number turbulence in He I and He II : first results.

P. Diribarne^{1,6}, J. Salort², C. Baudet^{5,6}, B. Belier⁸, B. Castaing³, L. Chevillard³, F. Daviaud⁴, S. David⁸, B. Dubrulle⁴, Y. Gagne^{5,6}, A. Girard¹, B. Rousset¹, P. Tabeling⁷, P. Thibault¹, H. Willaime⁷ and P.-E. Roche²

¹ Service des Basses Températures/CEA/INAC, Grenoble, France

² Institut Neel/CNRS Grenoble, France

³ Laboratoire des Écoulements Géophysiques et Industriels/CNRS, Grenoble, France

⁴ École Normale Supérieure de Lyon/CNRS, Lyon, France

⁵ Service de Physique de l'État Condensé/DSM/CEA Saclay, CNRS, Gif-sur-Yvette, France

⁶ Université Joseph Fourier, Grenoble, France

⁷ LMMN, ESPCI / CNRS, Paris, France

⁸ IEF, Université d'Orsay / CNRS, Orsay, France
`pantxo.diribarne@cea.fr`

Summary. Superfluid turbulence (TSF) project uses liquid helium for the fundamental study of turbulent phenomena behind a passive grid and is able to work both in HeI and in HeII. Local and semi-local instrumentation was developed specifically for the purpose of this experiment (e.g. sub-micrometer anemometer, total head pressure tube and second sound tweezer). The difficulties encountered with this local and fragile instrumentation are discussed. Global characterization of the flow is presented including velocity, pressure, temperature stability and turbulence intensity. Finally, first results obtained with semi local measurements (total head pressure tube and second sound tweezer) both in the two phases of helium are presented.

1 Experimental facility and sensors

The experiment is a closed loop, containing three main sections : a pump, a heat exchanger and the experimental section. The helium flow is generated by the cryogenic pump. The temperature is controled by means of the heat exchanger immersed in a liquid Helium saturated bath. This experiment takes profit of the CEA Grenoble refrigerator (nominal capacity of 400 Watt at 1.8 K) to remove the heat due to the energy dissipated in this high Reynolds num-

ber experiment. Thermodynamical characteristics of the flow are summarized in table b of fig.1.

The experimental section (see fig. 1) is made of a 27.2 mm inside diameter tube fitted with specifically designed sensor inserts. Much care was taken to avoid wall discontinuities due to the presence of the sensor mountings. The grid mesh size is $M = 3.9$ mm with 3.1mm square holes with 0.8 mm wide boundaries.

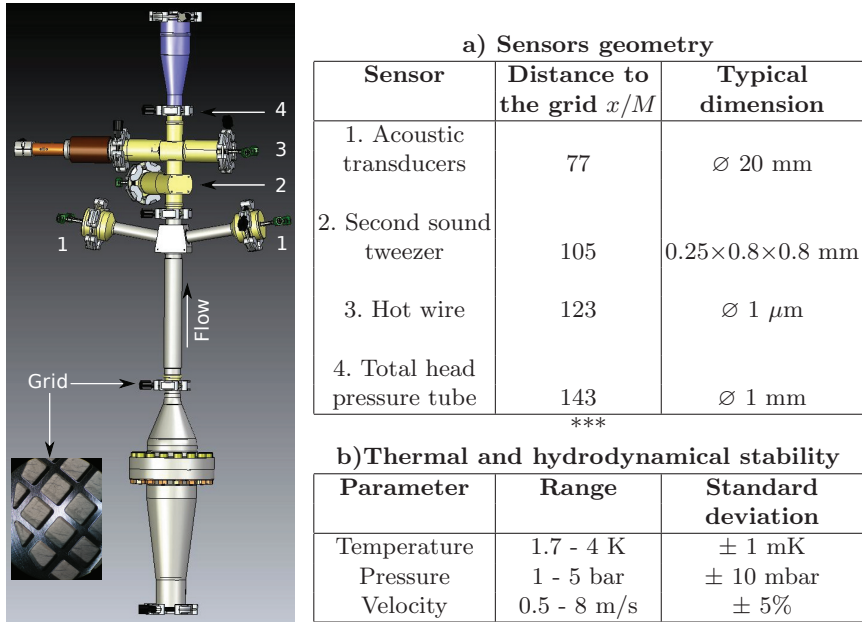


Fig. 1. Left : a sketch of the experimental section of TSF. Right : table **a** summarize position and spatial resolution of the probes, table **b** shows the thermodynamical parameters range and stability.

Four types of probes are available on TSF facility. Their location and typical spatial resolution are summarized in table b of fig. 1.

Ultrasonic vorticity probe is based on scattering of ultrasonic waves by the flow vorticity at a chosen wave vector [3, 1]. In order to insure the non-invasiveness of the probe, it was necessary to add a thin wall between the transducers (transmitter and receiver) and the flow. Unfortunately, in those conditions, the resulting signal could not be properly interpreted.

Second sound tweezer was used to measure the quantized vortex density L_0 . It is based on the attenuation of a second standing wave between an emitter (heating surface) and a very sensitive superconducting temperature probe [5].

Superconducting hot wire is designed following the principle of Cas-taing [2]. A bulk NbTi wire is used instead of a coated glass fiber in order to improve the spatial resolution and the sensitivity of the probe. The active part of the wire is obtained by locally reducing its cross section. This leads to a very fragile probe and few data could be acquired. Those measurements are not discussed in the present paper.

Total head pressure tube is inserted at the end of the experimental section. As in the experiment of Maurer and Tabeling [4], the pressure fluctuations at the stagnation point are assumed to be proportionnal to velocity fluctuations. This probes is thus used as an anemometer working both in He I and He II.

2 First results

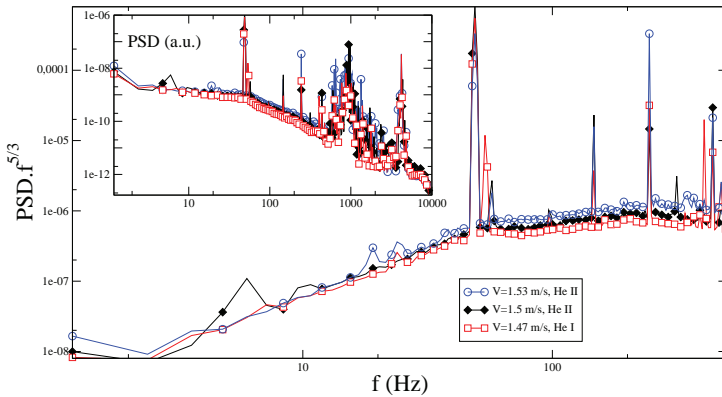


Fig. 2. Main graph : power spectral density (PSD) of the velocity compensated with $f^{-5/3}$. Inset : rough PSD in arbitrary units. Above 500 Hz the signal is strongly altered by a Helmholtz resonance in the pressure tube

In this section we show two preliminary results obtained with the total head pressure tube and the second sound tweezer.

In fig. 2 we have plotted the Power Spectral Density of the velocity. We see from the compensated spectrum that the PSD is compatible with a $f^{-5/3}$ power law, both in He I and He II. The similarity between the upper inertial range in He I and II has already been reported by Maurer and Tabeling [4] in von Kármán flow with a higher turbulence intensity. Here, computed turbulence intensity is about 2%, consistent with expected values in such configurations, and does not depend on the helium phase. The geometry of the probe will now be improved to reach higher spatial and temporal resolution.

Preliminary results of the second sound tweezer are shown in fig. 3. We see that the amplitude of the temperature wave decreases with velocity. This is

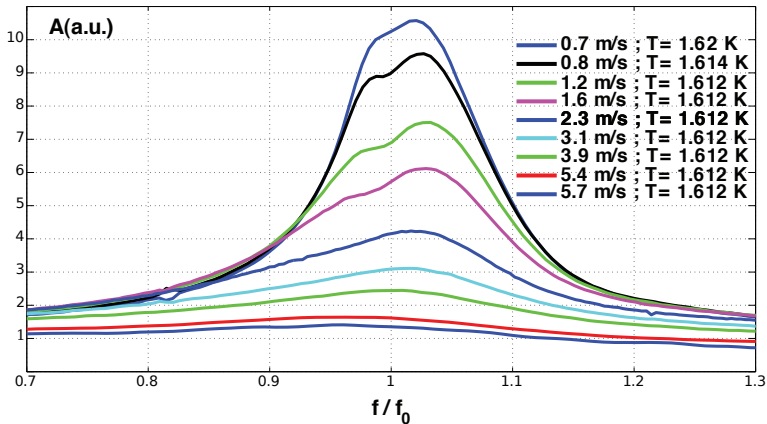


Fig. 3. Amplitude \mathbf{A} of the measured temperature standing wave as a function of the driving frequency normalized with the expected resonance frequency f_0 . From top to bottom the curves correspond to increasing velocities.

due to increasing vortex lines density L_0 in the flow. Since L_0 can be viewed as the superfluid enstrophy, it provides a direct integral information about the smallest scales of the superfluid flow. Thus, the increase of L_0 versus the flow Reynolds number reflects the increase of the depth of the superfluid cascade.

3 Conclusion

We have succeeded in stabilizing a high Reynolds steady superfluid flow. First results of TSF experiment tend to confirm the present understanding of superfluid turbulence and particularly the similarity with classical turbulence at large scale in a grid experiment. On-going work include quantitative analysis of the Reynolds number dependence of the superfluid cascade depth and velocity fluctuation measurements with improved space and time resolution.

References

1. C. Baudet, S. Ciliberto, and J. F. Pinton. Spectral analysis of the von kármán flow using ultrasound scattering. *Phys. Rev. Lett.*, 67(2):193–195, Jul 1991.
2. B. Castaing, B. Chabaud, and B. Hébral. Hot wire anemometer operating at cryogenic temperatures. *Rev. of Sci. Inst.*, 63(9):4167–4173, 1992.
3. F. Lund and C. Rojas. Ultrasound as a probe of turbulence. *Physica D*, 37:508–514, 1989.
4. J. Maurer and P. Tabeling. Local investigation of superfluid turbulence. *Europhys. Lett.*, 43 (1):29, 1998.
5. P.-E. Roche, P. Diribarne, T. Didelot, O. Français, L. Rousseau, and H. Willaime. Vortex density spectrum of quantum turbulence. *EPL*, 77:66002, 2007.

Extraction of the non-equilibrium energy spectrum in high Reynolds number turbulence

K. Horiuti¹⁾, Y. Tsuji²⁾ and K. Saitou¹⁾

1) Dept. Mechano-Aerospace Eng., Tokyo Institute of Technology, Tokyo, Japan

2) Dept. Energy Engineering and Science, Nagoya University, Nagoya, Japan
khorciuti at mes.titech.ac.jp

The structure of the energy spectrum in the inertial subrange is studied using the DNS data for turbulence in a periodic box at high Reynolds numbers. The Kolmogorov spectrum, $E_0(k) = C_K \langle \bar{\varepsilon}^{2/3} \rangle k^{-5/3}$, can be regarded as an accurate description of turbulent motion, and forms a base state for the energy spectrum in the inertial subrange, where k is the wavenumber and ε is the dissipation rate of turbulent energy. (Because ε is strongly intermittent, ε is averaged in the whole computational domain and denoted as $\bar{\varepsilon}$.) However, the spectrum which exhibits a scaling different from the $-5/3$ power is often depicted in turbulent flows, e.g., [1, 2]. In fact, perturbation expansion about the Kolmogorov spectrum yields a correction with the $-7/3$ power [3, 4]. $\langle \bar{\varepsilon} \rangle$ denotes the long-term average of $\bar{\varepsilon}$. When the expansion is extended to higher orders, we obtain the formula as

$$E(k) = E_0(k) + C_1 \dot{\bar{\varepsilon}} \bar{\varepsilon}^{-2/3} k^{-7/3} + C_2 (\ddot{\bar{\varepsilon}} \bar{\varepsilon}^{-1} - 2\dot{\bar{\varepsilon}}^2 \bar{\varepsilon}^{-2}) k^{-9/3} + \dots \quad (1)$$

in which the non-equilibrium spectrum is induced by the fluctuation of the dissipation rate. The factors in the $-7/3$ and $-9/3$ power components are induced by the derivative of the preceding $-5/3$ and $-7/3$ spectra with respect to time, respectively, thus this expansion possesses a hierarchical structure. The long term temporal average removes the $-7/3$ component. When a conditional sampling on the sign of $\dot{\bar{\varepsilon}}$ is applied, $-7/3$ component can be extracted. In the period in which $\dot{\bar{\varepsilon}} \geq 0$ (Phase 1), we get $E^+(k) = E_0(k) + E_1^+(k)$, and in the period in which $\dot{\bar{\varepsilon}} < 0$ (Phase 2), $E^-(k) = E_0(k) + E_1^-(k) = E_0(k) - E_1^+(k)$.

Figure 1 (a) shows the spectra, $E_0(k)$ and $E_1^+(k)$, obtained using the DNS data for homogeneous isotropic turbulence at $R_\lambda \approx 240$ in which the forcing with constant amplitude and random phase is applied in the wavenumber range $1 \leq k \leq 2.5$. It is seen that $E_0(k)$ fits $-5/3$ power ($C_K \approx 1.60$) and $E_1^+(k)$ fits $-7/3$ power over one decade in the inertial subrange ($0.01 \lesssim k\eta \lesssim 0.1$). We note that as R_λ is increased, the extent of wavenumber range in which $E_1^+(k)$ fits $-7/3$ power increases. In figure 1 (a), absolute value of $E_1^+(k)$ is shown. In the actual value of $E_1^+(k)$, the switchover of the sign in $E_1^+(k)$ occurs

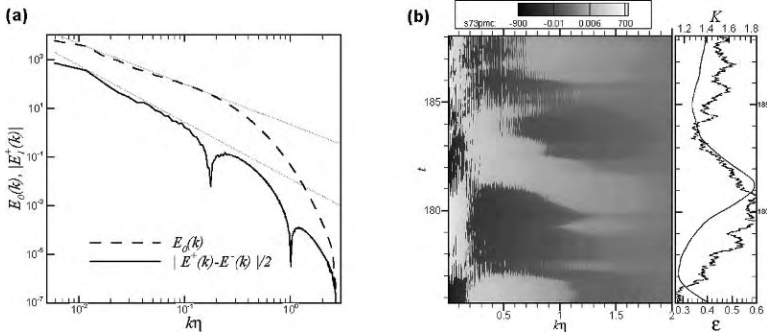


Fig. 1. Energy spectra normalised by $(\langle \bar{\varepsilon} \rangle \nu^5)^{1/4}$ obtained using DNS data at $Re_\lambda \approx 240$ are plotted versus $k\bar{\eta}$. (a) The distribution of $E_0(k)$ is plotted using dashed line, $|E_1^+(k)|$ using solid line. The dotted lines indicate scaling with $k^{-5/3}$ and $k^{-7/3}$. (b) Isocontours of $E_1^+(k)$ and $E_1^-(k)$ normalised by $(\bar{\varepsilon}\nu^5)^{1/4}$ as functions of the wavelength $k\bar{\eta}$ and t . The small frame shows the temporal variations of K and $\bar{\varepsilon}$.

at $k\bar{\eta} \approx 0.17$, at which a bump is discernible in $E_0(k)$. Figure 1 (b) shows the temporal variations of the energy spectra. The contours of the deviation of the spectra from $E_0(k)$ are shown, i.e., $E_1^+(k)$ in Phase 1 and $E_1^-(k)$ in Phase 2 as functions of the wavenumber $k\bar{\eta}$ and t . The period of the oscillations in K and $\bar{\varepsilon}$ is comparable to the eddy turnover time due to forcing, but the variation of $\bar{\varepsilon}$ lags in phase against that of K . In Phase 1, the deviation is positive in the low-wave number range, $0.01 \lesssim k\bar{\eta} \lesssim 0.2$, and negative in the high-wave number range during the time period $177.0 \lesssim t \lesssim 181.0$. In other periods, e.g., $181.0 \lesssim t \lesssim 184.0$ (Phase 2), the sign is reversed and becomes negative and positive in the low- and high-wave number ranges, respectively. As a result, the turbulent energy is maximal in Phase 1 because the large-scale eddy carries the large energy. The energy cascades to the higher-wavenumber range in Phase 2, and the energy becomes minimal in Phase 2.

As is indicated in Eq. (1), the magnitude of the $-7/3$ component becomes small in the period in which $\bar{\varepsilon}$ is minimal or maximal ($\dot{\bar{\varepsilon}} \approx 0$). In this period, the contribution of the $-9/3$ component becomes large because $\ddot{\bar{\varepsilon}}$ is large. Figure 2 (a) shows the energy spectrum averaged in the time interval $t_{\text{minimal}} \leq t \leq t_{\text{minimal}} + 10\tau_K$, where t_{minimal} is the time when $\bar{\varepsilon}$ is minimal and τ_K is Kolmogorov time scale ($= (\nu/\langle \bar{\varepsilon} \rangle)^{1/2}$). The solid line shows the average spectrum $E_0(k)$, and the deviation of the spectra from $E_0(k)$, $E_1(k)$, is plotted using the symbols. The small circles show the absolute values of $E_1(k)$ and large circles show only positive values of $E_1(k)$. It can be seen that $E_1(k)$ is mostly positive and fits the $-9/3$ power in the inertial subrange. Similar results are obtained in the period around the time when $\bar{\varepsilon}$ is maximal. In these time intervals, the contribution of the $-7/3$ component becomes small and the $-9/3$ component predominates.

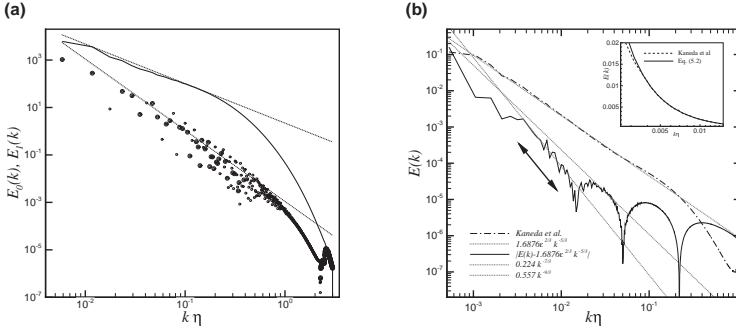


Fig. 2. Energy spectra normalised by $(\langle \bar{\varepsilon} \rangle \nu^5)^{1/4}$ are plotted versus $k\bar{\eta}$. (a) DNS data at $R_\lambda \approx 240$. $E_0(k)$ is plotted using solid line, $|E_1(k)|$ using solid line. The dotted lines indicate scaling with $k^{-5/3}$ and $k^{-9/3}$. (b) DNS data at $R_\lambda \approx 1200$. $E(k)$ using dashed-dotted line, $|E(k) - E_0(k)|$ using solid line. The dotted lines indicate scalings with $k^{-7/3}$ and $k^{-9/3}$. The inset shows a log-linear plot of $E(k)$ versus $k\bar{\eta}$.

The dissipation terms according to the $-7/3$ and $-9/3$ components are given respectively as

$$\nu \int_{k_L}^{k_d} k^2 \dot{\bar{\varepsilon}} \bar{\varepsilon}^{-2/3} k^{-7/3} dk \approx \frac{3}{2} \nu^{1/2} \dot{\bar{\varepsilon}}, \tag{2}$$

$$\nu \int_{k_L}^{k_d} k^2 (\ddot{\bar{\varepsilon}} \bar{\varepsilon}^{-1} - 2\dot{\bar{\varepsilon}}^2 \bar{\varepsilon}^{-2}) k^{-9/3} dk \approx (\ddot{\bar{\varepsilon}} \bar{\varepsilon}^{-1} - 2\dot{\bar{\varepsilon}}^2 \bar{\varepsilon}^{-2}) \left(-\frac{3}{4} \nu \log \nu + \frac{1}{4} \nu \log \bar{\varepsilon} \right), \tag{3}$$

where k_L and k_d denote the wavenumbers corresponding to the integral scale and the Kolmogorov dissipation scale, respectively. In the limit of $\nu \rightarrow 0$, the corrections to the dissipation in both (2) and (3) vanish. Both $-7/3$ and $-9/3$ components provide no contribution to the dissipation. However, it was shown in [5] and [6] that the borderline steepness capable of sustaining an energy cascade in the inertial subrange (if it exists) is $k^{-8/3}$ in the limit of $\nu \rightarrow 0$.

We analyse the energy cascade using the transfer function $T(k)$ as

$$T(k) = \frac{1}{2} \text{Im} \left[\sum_{k-1/2 \leq |\mathbf{k}'| \leq k+1/2} \tilde{u}_i^*(\mathbf{k}') P_{ijk}(\mathbf{k}') \sum_p \tilde{u}_j(\mathbf{p}) \tilde{u}_k(\mathbf{k}' - \mathbf{p}) \right], \tag{4}$$

where $\tilde{u}_i(\mathbf{k})$ is the Fourier transform of the velocity $u_i(\mathbf{x})$, $\tilde{u}_i^*(\mathbf{k})$ is the complex conjugate of $\tilde{u}_i(\mathbf{k})$, $P_{ijk}(\mathbf{k})$ is the orthogonalising operator, \mathbf{k} is the wavenumber vector [7]. The temporal development of the deviatric part of $T(k)$ is similar to that shown in the contours of the energy spectrum in figure 1 (b) except that the switchover of the sign occurs at $k\bar{\eta} \approx 0.5$ (figure not shown). Gain in the low-wavenumber range ($k\bar{\eta} \lesssim 0.5$) is larger than the long-term average in Phase 1, while gain in the high-wavenumber range ($k\bar{\eta} \gtrsim 0.5$) is

larger in Phase 2, i.e., the energy contained in the large scales in Phase 1 is transferred to the small scales in Phase 2. In these time intervals, the $-7/3$ power component predominates. In the transition period between Phase 1 and Phase 2 when the $-9/3$ component prevails, the magnitude of the deviatric part of $T(k)$ becomes very small (figure not shown) and the energy cascade ceases on average. These results are consistent with those obtained in [5, 6].

In [1], it was shown that the slope in the inertial subrange is steeper than $-5/3$ by $\mu \approx 0.1$ at $R_\lambda \approx 1200$. Similar result was obtained in [2]. We investigate on this deviation using the data from Run 4096-1 ($R_\lambda \approx 1200$) in [1]. The long-term ensemble average of (1) yields

$$E(k) = C_K \langle \bar{\varepsilon}^{2/3} \rangle k^{-5/3} + C_2 \langle \bar{\varepsilon}^2 \bar{\varepsilon}^{-2} \rangle k^{-9/3}. \quad (5)$$

When the spectrum is fitted using the function $E(k) = C_K \bar{\varepsilon}^{2/3} k^{-(5/3+\mu)}$ by the least square method, $\mu \approx 0.083$ and $C_K \approx 2.24$. The fitting is done using the data in the range $0.00369 \leq k\bar{\eta} \leq 0.0132$. μ is close to that in Kaneda *et al.* (2003), whereas C_K is larger than the generally accepted values ($C_K = 1.6 - 1.7$). When the spectrum is fitted using the function $E(k) = C_K \bar{\varepsilon}^{2/3} k^{-5/3} + C_3 k^{-9/3}$, $C_K \approx 1.688$ and $C_3 \approx 0.557$. (Because the value of $\langle \bar{\varepsilon}^2 \bar{\varepsilon}^{-2} \rangle$ was not available, the coefficient of $k^{-9/3}$ term, C_3 , is optimised as a whole.) We note that when the exponent of the second term is determined using the function $E(k) = C_K \bar{\varepsilon}^{2/3} k^{-5/3} + C_3 k^{-\alpha}$, $\alpha \approx 2.92$ ($C_K \approx 1.675$, $C_3 \approx 0.5045$). α is indeed close to 3. Figure 2 (b) shows the energy spectra, $E(k) = C_K \bar{\varepsilon}^{2/3} k^{-5/3} + C_3 k^{-9/3}$, $E(k) = C_1 k^{-7/3}$, $E(k) = C_3 k^{-9/3}$, where $C_K = 1.688$, $C_1 = 0.224$ and $C_3 = 0.557$. It is seen that the deviation of the spectrum from $E_0(k)$ approximately fits the function $C_3 k^{-9/3}$ in the region $0.00369 \lesssim k\bar{\eta} \lesssim 0.0132$ (indicated by the bald solid line and the arrows). It is shown that the deviation from $-5/3$ power can be approximated using the $-9/3$ term. These results indicate that the $-9/3$ component plays important roles as well as the $-7/3$ component at high R_λ .

References

1. Y. Kaneda *et al.*, Phys. Fluids, **15**, L21 (2003).
2. Y. Tsuji, Phys. Fluids, **16**, L43 (2004).
3. A. Yoshizawa, Phys. Rev. E, **49**, 4065 (1994).
4. S. L. Woodruff and R. Rubinstein, J. Fluid Mech., **565**, 95 (2006).
5. P.-L. Sulem and U. Frisch, J. Fluid Mech., **72**, 417 (1975).
6. C. R. Doering and J.D. Gibbon, Physica D, **165**, 163 (2002).
7. J. A. Domaradzki and R. S. Rogallo, Phys. Fluids A, **2**, 413 (1990).

Universality of Kolmogorov law in spectrally condensed turbulence in thin layers

H. Xia, M.G. Shats, and H. Punzmann

Research School of Physics & Engineering, The Australian National University,
Canberra, ACT 0200, Australia
hua.xia@anu.edu.au

The four-fifth Kolmogorov law relates the third-order structure function and the energy dissipation rate ϵ in three-dimensional turbulence (see, e.g. [1]. This law for 2D turbulence reads: $S_{L3} = (3/2)\epsilon r$, where $S_{L3} = \langle \delta v_L^3 \rangle$ is the third moment of the longitudinal velocity increments at the scale r . Angular brackets denote averaging over the box size and time. This relationship allows the energy dissipation rate, or the energy flux within the inertial range to be determined by analyzing the third-order velocity moments in laboratory experiments or in observational data. The Kolmogorov law has been confirmed in direct numerical simulations of 2D turbulence [2], however previous experimental attempts to derive ϵ from the third-order longitudinal structure functions were not successful [3], probably due the insufficient statistics in the calculations of $\langle \delta v_L^3 \rangle$. In this paper we present the results of the $S_3(r)$ measurements in quasi-2D turbulence in laboratory experiments. We are particularly interested in estimating the energy flux in the energy inertial interval and in comparison of its value with independently obtained energy dissipation rate.

Another practically interesting question is how the presence of the self-generated coherent flows in 2D turbulence affects the Kolmogorov law in the regime of spectral condensation. We investigate this in the thin stratified layers of fluid where turbulence is driven electromagnetically as described in [4, 5]. When the flow is bounded the inverse energy cascade leads to the accumulation of the spectral energy at the scale close to the boundary size and generation of mean flow. By controlling the bottom dissipation rate (via the thickness of the fluid layers) and the size of the boundary, large vortices of different strengths, or condensates, can be obtained as discussed in [5].

Figure 1 shows time-averaged (over about 100s) velocity fields measured with the boundary size of $L=0.11$ m for 3 different damping rates. The large-scale vortex becomes more symmetric as its turnover time becomes shorter and approaches the inverse damping rate $1/\alpha$.

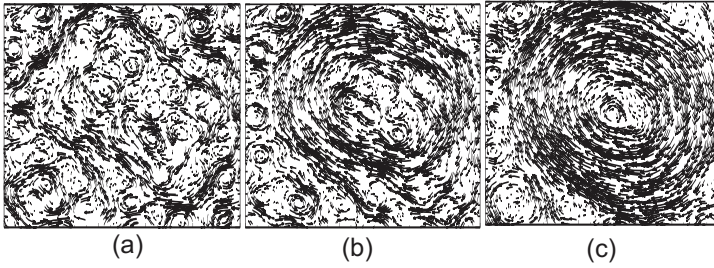


Fig. 1. Time-averaged velocity field of the condensate at $L \approx 0.10$ m with different linear damping rate: (a) $\alpha = 0.25$ s $^{-1}$, (b) $\alpha = 0.15$ s $^{-1}$ and (c) $\alpha = 0.05$ s $^{-1}$.

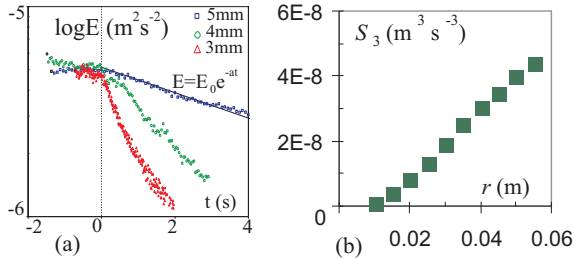


Fig. 2. (a) Time evolution of the kinetic energy during turbulence decay for the 3 cases of Fig. 1. (b) 3rd-order structure function computed for the case of Fig. 1(c) by subtracting mean flow velocity.

The presence of the mean flow greatly affects the velocity moments, as discussed in [5]. However by subtracting mean (time-averaged) velocity field from instantaneous fields before computing the 3rd-order structure function $S_3 = (S_{3L} + S_{3T})/2$ one recovers physically meaningful values of $\epsilon = S_3/r$. This is verified by comparing ϵ with the energy dissipation rate derived from the time evolution of the turbulence energy in the initial stage and during the decay: $dE/dt - \alpha E = \epsilon$. During the decay $\epsilon \approx \alpha E$, while at the early stage of the turbulence development $dE/dt \approx \epsilon$. This result has been confirmed at different strengths of the condensate flow, even in the regimes when the presence of the condensate leads to the onset of non-Gaussian statistics in condensed turbulence (larger flatness).

References

1. U.Frisch, *Turbulence: The Legacy of A.N. Kolmogorov* (Cambridge, 1995).
2. G. Boffetta, A. Celani and M. Vergassola, *Phys. Rev. E* **61**, R29, (2000).
3. J. Paret and P. Tabeling, *Phys. Fluids* **10**, 3126, (1998).
4. M.G. Shats et al., *Phys. Rev. Lett.* **99**, 164502, (2007).
5. H. Xia et al., *Phys. Rev. Lett.* **101**, 194504, (2008).

Multi-scale correlations in regular and fractal-generated turbulence

R. Stresing¹, J. Peinke¹, R. E. Seoud², and J. C. Vassilicos^{2,3}

¹ Institute of Physics, Carl-von-Ossietzky University of Oldenburg, Germany

² Department of Aeronautics, Imperial College, London, UK

³ Institute for Mathematical Sciences, Imperial College, London, UK

Summary. We present a stochastic analysis of turbulence data, which provides access to the joint probability of finding velocity increments at several scales. The underlying stochastic process in form of a Fokker-Planck equation can be reconstructed from given data, including intermittency effects. We analyze turbulence generated by a space-filling fractal square grid and find that in contrast to other types of turbulence, like free-jet turbulence, the n -scale statistics of the velocity increments and the coefficients of the Fokker-Planck equation are independent of the Reynolds number over the entire range of Re_λ from 150 to 740.

Introduction

Standard statistical analysis of small-scale turbulence is based on two-point correlations and their dependence on the scale r . A central quantity is the (longitudinal) velocity increment $u(r)$,

$$u(r) = v(x + r, t) - v(x, t), \quad (1)$$

where v denotes the velocity component in the direction of r . A characterization of the scale-dependent disorder of turbulence by means of one-scale (= two-point) statistics like structure functions can be extended to multi-scale statistics. It has been shown for several different turbulent flows that these multi-scale statistics can be treated within the framework of Markov processes, and that the corresponding stochastic differential equation is the Fokker-Planck equation [1, 2, 3].

If the stochastic process for the evolution of the velocity increments from scale to scale has Markov properties, i.e. if

$$p(u_1, r_1 | u_2, r_2; \dots; u_n, r_n) = p(u_1, r_1 | u_2, r_2) \quad (2)$$

(where we assume $r_1 < r_2 < \dots < r_n$), the n -scale joint probability density function (pdf) of the velocity increments can be expressed by a product of conditional pdfs:

$$p(u_1, r_1; u_2, r_2; \dots; u_n, r_n) = p(u_1, r_1 | u_2, r_2) \dots p(u_{n-1}, r_{n-1} | u_n, r_n) p(u_n, r_n). \quad (3)$$

The stochastic process for the conditional pdfs can be described by a Kramers-Moyal expansion. If the fourth-order Kramers-Moyal coefficient $D^{(4)}$ is zero, the expansion truncates after the second term and becomes a Fokker-Planck equation, also called Kolmogorov equation:

$$-\frac{\partial}{\partial r} p(u, r | u_0, r_0) = -\frac{\partial}{\partial u} \left[D^{(1)}(u, r) p(u, r | u_0, r_0) \right] + \frac{\partial^2}{\partial u^2} \left[D^{(2)}(u, r) p(u, r | u_0, r_0) \right], \quad (4)$$

where drift and diffusion functions $D^{(1)}$ and $D^{(2)}$ can be estimated as Kramers-Moyal coefficients pointwise by:

$$D^{(k)}(u, r) = \lim_{\Delta r \rightarrow 0} \frac{r}{k! \Delta r} \int_{-\infty}^{+\infty} (\tilde{u} - u)^k p(\tilde{u}, r - \Delta r | u, r) d\tilde{u}. \quad (5)$$

The experimental pdfs and conditional pdfs of the velocity increments can be reproduced by integration of the Fokker-Planck equation, including intermittency effects.

Results for fractal-generated turbulence

We analyze hot wire measurement data from turbulence generated by a fractal square grid¹, measured for two different flow velocities at five different down-stream positions in the decay region, where the turbulence is small-scale homogeneous and isotropic [5, 6]. We confirm the result of [6], that the Taylor microscale λ is almost independent of the flow velocity and the down-stream position, so that we obtain an unusually wide range of Taylor-based Reynolds numbers Re_λ from 153 to 740.

We find that the stochastic process for the velocity increments has Markov properties for scale separations Δr greater than the *Einstein-Markov coherence length* l_{EM} , which is defined as the smallest distance $\Delta r = r_i - r_{i-1}$, for which eq. (2) still holds. We estimate l_{EM} with the (Mann-Whitney-)Wilcoxon test, which is a parameter-free statistical test to decide whether two samples, in this case, the left and right hand side of eq. (2) for $n = 3$, have the same distribution [2]. We find a constant ratio of $l_{EM}/\lambda = 0.73 \pm 0.09$, which is comparable to results for other turbulent flows, where $l_{EM}/\lambda \approx 0.8$ [4].

We determine the Kramers-Moyal coefficients with two different methods. The first, “classical” method directly uses definition (5), determining the limit

¹ The grid has a thickness ratio $t_r = 17$, that is, the thickest bars are 17 times thicker than the thinnest bars of the grid. It is space-filling in the sense that it has the maximal possible fractal dimension, $D_f = 2$. For more details see [5, 6].

of $\Delta r \rightarrow 0$ with a linear fit to the conditional moments on the right hand side of eq. (5) in the range $l_{EM} \leq \Delta r \leq 2l_{EM}$, following [2, 3]. The drift and diffusion functions at each scale r can then be approximated by linear and second-order functions in u , respectively:

$$D^{(1)}(u, r) = -d_{11}(r) u \tag{6}$$

$$D^{(2)}(u, r) = d_{20}(r) - d_{21}(r) u + d_{22}(r) u^2 \tag{7}$$

The second method uses numerical optimization to find the coefficients $d_{ij}(r)$ of eq. (6) and (7), which minimize the (Kullback-Leibler) distance between the empirical conditional pdf $p(u_{i-1}, r_{i-1} | u_i, r_i)$, and the conditional pdf obtained by numerical integration over the Fokker-Planck equation (4) [7].

By convention, the velocity increments $u(r)$ are given in dimensionless units of their standard deviation in the limit $r \rightarrow \infty$, σ_∞ [2]. This normalization allows us to compare the Kramers-Moyal coefficients of different flows.

Renner et al. [2, 3] showed for free-jet turbulence and for Reynolds numbers up to $Re_\lambda \approx 1200$, that the coefficients d_{20} , d_{21} , and d_{22} strongly depend on the Reynolds number. In contrast to this result, we do not find any significant dependence of d_{20} on Re_λ for fractal-generated turbulence. For d_{21} and d_{22} , we do find a dependence on the Reynolds number for the “classical” estimates, but no such dependence for the estimates obtained by numerical optimization, which are the ones that reproduce the empirical conditional pdfs best. In Fig. 1, we look at d_{20} , which is linear in r and thus can be approximated by:

$$d_{20}(r) = d_{20}^* \frac{r}{\lambda}. \tag{8}$$

The slope d_{20}^* follows a power law in Re for the free jet, $d_{20}^* \propto Re^{-3/8}$ [3], but is approximately constant for the fractal grid turbulence.

As a final verification of the indicated findings of the Reynolds number independence of the statistical properties we investigate the conditional pdfs $p(u, r | u_0, r_0)$. Note that these are the fundamental quantities which contain the information of the stochastic process integrated over a range of scales. Most important the conditional pdfs do not contain the errors and uncertainties which arise in estimating the Kramers-Moyal coefficients. Fig. 2 shows the conditional pdfs $p(u, r | u_0, r_0)$ and pdfs $p(u, r)$ for two different Reynolds numbers for the free jet (a), and fractal grid (b), for large scale separations $r_0 - r$. For the fractal grid, these (conditional) pdfs are practically identical, indicating that the stochastic process is indeed independent of the Reynolds number.

We conclude that the n-scale statistics of fractal generated turbulence can be described by a Markov process governed by a Fokker-Planck equation, with an Einstein-Markov coherence length l_{EM} in the order of magnitude of the Taylor microscale λ . The coefficients of the stochastic process equations and the conditional pdfs $p(u, r | u_0, r_0)$ for fractal-generated turbulence do not depend significantly on the Reynolds number, which differs substantially from the findings for free-jet turbulence in [2, 3].

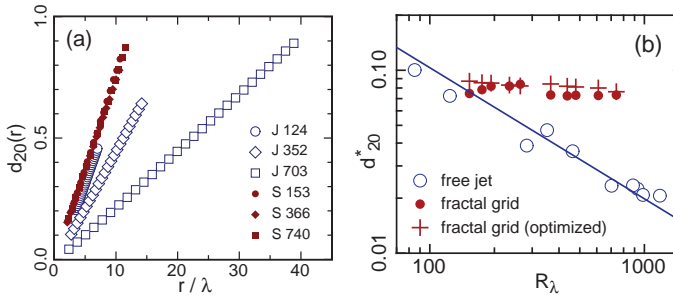


Fig. 1. (a) $d_{20}(r)$ for the free jet (J) and fractal square grid (S), estimated by the “classical” method. Reynolds numbers Re_λ are given in the legend. (b) slopes d_{20}^* from eq. (8) as functions of Re_λ for the free jet (o) and fractal grid (●), estimated with the “classical” method, and for the fractal grid after numerical optimization (+). The free-jet data are taken from [3]. The straight line represents a power law $d_{20}^* = 2.8 Re^{3/8}$ from [3], where we use $Re_\lambda = Re^{0.5233}$.

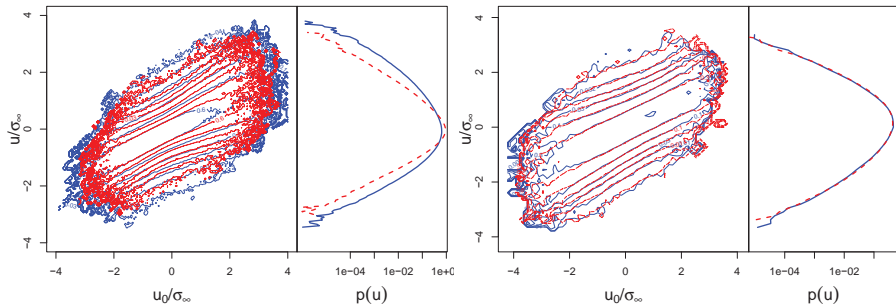


Fig. 2. Contour plots of $p(u, r|u_0, r_0)$, and plots of $p(u, r)$, rotated by 90° . Left: free jet at $Re_\lambda = 124$ (solid) and $Re_\lambda = 352$ (dashed) for $r = 4l_{EM}$ and $r_0 = 8l_{EM}$. Right: fractal square grid at $Re_\lambda = 154$ (solid) and $Re_\lambda = 740$ (dashed) for $r = 6l_{EM}$ and $r_0 = 12l_{EM} \approx L$.

References

1. R. Friedrich, J. Peinke, Phys. Rev. Lett. **78** 863 (1997)
2. C. Renner, J. Peinke, R. Friedrich, J. Fluid Mech. **433** 383 (2001)
3. C. Renner, J. Peinke, R. Friedrich, O. Chanal, B. Chabaud, Phys. Rev. Lett. **89** 124502 (2002)
4. S. Lück, C. Renner, J. Peinke, R. Friedrich, Phys. Lett. A **359** 335 (2006)
5. D. Hurst, J.C. Vassilicos, Phys. Fluids, **19** 035103 (2007)
6. R.E. Seoud, J.C. Vassilicos, Phys. Fluids, **19** 105108 (2007)
7. A.P. Nawroth, J. Peinke, D. Kleinhans, R. Friedrich, Phys. Rev. E **76** 056102 (2007)

On an alternative explanation of anomalous scaling and how inertial is the inertial range

M. Kholmyansky^a, and A. Tsinober^{a,b}

^aDepartment of Fluid Mechanics and Heat Transfer, Faculty of Engineering, Tel-Aviv University, Tel-Aviv 69978, Israel

^bInstitute for Mathematical Sciences and Department of Aeronautics, Imperial College, SW7 2PG London, United Kingdom
tsinober@eng.tau.ac.il

*There are a variety of models of higher statistics that have meager or nonexistent deductive support from the Navier–Stokes equations but can be made to give good fits to experimental measurements [1]. These include ‘explanations’ of what is called anomalous scaling, observed experimentally for higher-order structure functions of velocity and temperature increments, such that their scaling exponents, $\zeta_p = p/3 - \mu_p < p/3$, are nonlinear concave functions of the order p . Starting with refined similarity hypotheses by Kolmogorov and Oboukhov, numerous phenomenological models have been proposed to describe these deviations. The dominant of these models has been the multifractal formalism, others claimed the Reynolds number dependence as responsible. The common in all these approaches is the basic, widely accepted premise that *in the inertial range, the viscosity plays in principle no role* [2] so that *nonlinear dependence of the algebraic scaling exponents ζ_p on the moment order p is a manifestation of the inertial-range intermittency* [3] with the *inertial range* defined as $\eta \ll r \ll L$ (with η being the Kolmogorov and L — some integral scale). Thus the issue is directly related to what is called inertial (sub)range and how inertial it is.*

The main point of this communication is that there is a considerable number of very strong events contributing significantly to the PDF of $\Delta u_i(r)$ in the nominally-defined inertial range, for which viscosity/dissipation is of utmost importance at high Reynolds number. This contribution is largest to the tails of the PDF of $\Delta u_i(r)$. In other words, the inertial range is ill-defined in the sense that not all, but almost all statistics of $\Delta u_i(r)$ is independent of viscosity. As long as one deals with low-order statistics of $\Delta u_i(r)$ (as Kolmogorov did) this is of little (but still not negligible, see below) importance. However, it appears that these events contribute significantly to the higher-order structure functions and thereby a non-negligible contribution to their values is dominated by viscosity. In other words, the ‘anomalous scaling’ as exhibited by the behavior of higher-order structure functions is to a large

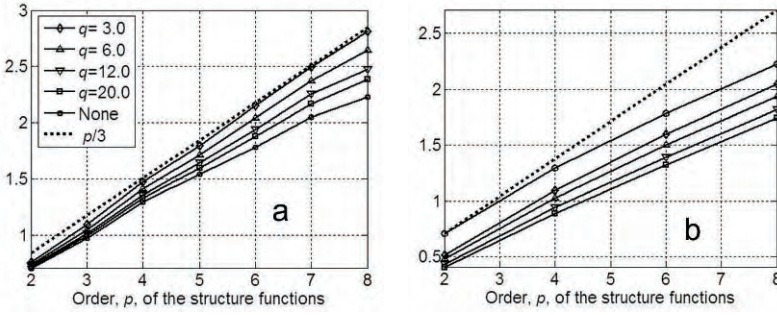


Fig. 1. (a) Scaling exponents of structure functions at $Re_\lambda \sim 10^4$ for the longitudinal velocity component corresponding to the full data and the same data in which the strong dissipative events (when at least at one point x or $x+r$ the instantaneous dissipation $\epsilon > q\langle\epsilon\rangle$) with various thresholds q were removed. (b) Scaling exponents for the strong events themselves.

extent due to significant contribution of viscosity/dissipation in the *inertial range* as commonly defined. The higher the order of the structure function, the stronger is the contribution due to viscosity (i.e., mainly from the tails of the PDFs of $\Delta u_i(r)$) and the weaker is the ‘inertial’ contribution (i.e., from the core of those PDFs) to the structure function. Thus it seems problematic to speak about inertial-range behavior of higher-order structure functions.

The support for the above view comes from a recent analysis of high-Reynolds-number data in field experiments [4, 5]. The experimental facilities and related matters are described in these papers and references therein. A selection of results is shown in Fig. 1 — Fig. 4.

Fig. 1 (a) shows the scaling exponents of longitudinal structure functions $S_p(r) = \langle (\Delta u_1)^p \rangle$ up to order 8, corresponding to the full data, and the same data in which the strong dissipative events with various thresholds were removed. By an event we mean here a velocity increment, $\Delta u_1 \equiv u_1(x+r) - u_1(x)$. It is qualified as a strong dissipative event if at least at one of its ends ($x, x+r$) the instantaneous dissipation $\epsilon > q\langle\epsilon\rangle$ for $q > 1$. We have chosen $q = 3, 6, 12$ and 20 . This corresponds to the instantaneous Kolmogorov-like scales $0.76, 0.64, 0.54$ and 0.47 of the conventional Kolmogorov scale η based on the mean dissipation $\langle\epsilon\rangle$. It is seen that the removal of the strong dissipative events results in an increase of the exponents ζ_p . For example, with the removal of the dissipative events between the threshold $3\langle\epsilon\rangle$ (0.76η) and $6\langle\epsilon\rangle$ (0.64η) the dependence of ζ_p on p becomes pretty close to the Kolmogorov $p/3$. The strong events themselves have different scaling properties, Fig. 1 (b).

The next example in Fig. 2 shows that the removal of the strong dissipative events results not only in narrowing of the tails, but also makes a non-negligible contribution in the core of the $\Delta u_1(r)$ distribution.

The effect of the removal of the strong dissipative events is much stronger for higher-order structure functions. For example, there are only 5% of dissipative events (Fig. 3 (a)) for $q = 6$ sitting mostly at tails of the PDF of $\Delta u_i(r)$ for $r/\eta = 400$ (i.e. deep in the ‘inertial’ range), which contribute about 36% to

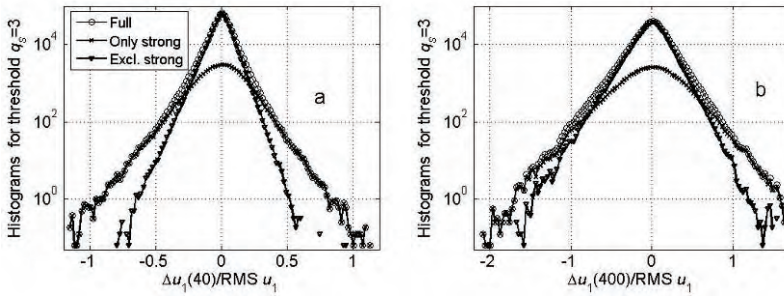


Fig. 2. Histograms of the increments of the longitudinal velocity component for the same data as in Fig. 1 for the threshold $q = 3$. $r/\eta = 40$ (a). $r/\eta = 400$ (b).

the total dissipation (Fig. 3 (b)). They contribute nearly 60% to the value of $S_8^u(r)$ at $Re_\lambda \sim 10^4$ (Fig. 4 (a)). The same events change the $S_2^u(r)$ by about 11.5% (Fig. 4 (b)), but contribute about 9% to $S_3^u(r)$ (see Fig. 4 (c)).

It is noteworthy that the data used here ([4, 5]) was somewhat spatially underresolved, $1 \div 3\eta$. This means that the conclusions are to some extent qualitative. However, with properly resolved data the strong dissipative events, lost in the underresolved ones, would enhance the tendencies just described above. This is in agreement with the fact that essentially the same results are obtained using the same data smoothed over up to eight sequential samples. Additional support comes from reference [3], indicating that the underresolved data reproduce faithfully the flow at scales about two times smaller than those resolved ($\sim 0.6\eta$) at least as concerns the instantaneous dissipation rate. Finally, using enstrophy ω^2 and/or the surrogate $(\partial u_1/\partial x_1)^2$ as a criterion for the threshold instead of the true dissipation ϵ gives the same qualitative (but not quantitative) results.

Along with the fact that velocity increments (let alone structure functions and their scaling if such exists) are not the only objects of interest and *do not constitute a representation basis for a flow* [1], they are not a good object to define a perfect inertial range. Such a definition seems to be not possible in principle due to a variety of nonlocal effects [6, 7].

A special remark is about the contribution of the dissipative events as defined/described above to the low order statistics and in particular to the 4/5 law. These events *do* contribute to the 4/5 law, and removing them leads to an increase of the scaling exponent above unity, see Fig. 1 (a) and Fig. 4 (c). An important point here is that the neglected viscous term in the Karman–Howarth equation does not contain all the viscous contributions. Those which are present in the structure function S_3 itself remain and keep the 4/5 law precise. In this sense the 4/5 law is not a pure inertial law. In fact, the contribution of the strongly-dissipative events is non-negligible also in the core of the PDFs of Δu_1 (but not dominating as in their tails) as seen from Fig. 2.

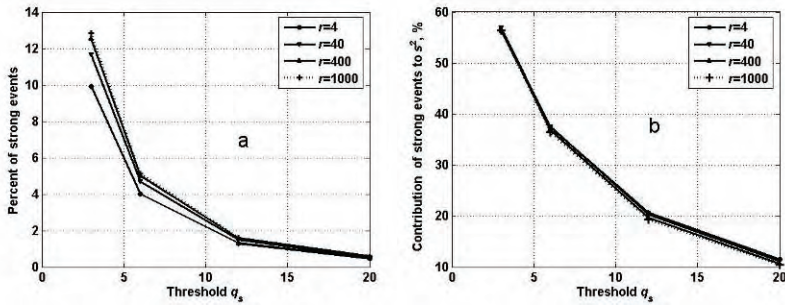


Fig. 3. Percent of the strong dissipative events as defined in the text (a) and their contribution to the total dissipation (b) as a function of the threshold q for various separations r .

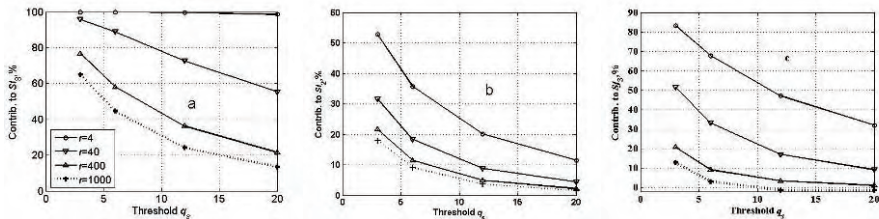


Fig. 4. Contributions of the strong dissipative events, as defined in the text, to the eighth-order structure function (a), the second-order structure function (b) and the third-order structure function (c) as a function of the threshold q for various separations r .

Among the main challenges for future work is an experiment similar to that described in references [4, 5] but with sub-Kolmogorov resolution. This includes also the issue of passive scalar. So far, we have pretty crude qualitative results (due to poor resolution and quality of the data) concerning the passive scalar [8], which show the same trends as described above and which raise similar questions concerning the anomalous scaling of passive scalars.

References

1. T. Goto and R.H. Kraichnan, *Physica*, **D 193**, 231–244 (2004).
2. D. Ruelle, *Physics Reports*, **103**, 81–85 (1984).
3. J. Schumacher, K.R. Sreenivasan and V. Yakhot, *New J. Physics*, **9**, 89 (1–19) (2007).
4. M. Kholmyansky, A. Tsinober and S. Yorish, *Phys. Fluids*, **13**, 311–314 (2001).
5. G. Gulitski, M. Kholmyansky, W. Kinzelbach, B. Lüthi, A. Tsinober and S. Yorish, *J. Fluid Mech.*, **589**, 57–81 (2007).
6. A. Tsinober, *An informal conceptual introduction to turbulence*, Springer, 2009, in press.
7. M. Kholmyansky, and A. Tsinober, *Phys.Fluids*, **20**, 041704/1–4 (2008).
8. G. Gulitski, M. Kholmyansky, W. Kinzelbach, B. Lüthi, A. Tsinober, and S. Yorish, *J. Fluid Mech.* **589**, 103–123 (2007a).

Phenomenological relation between the Kolmogorov constant and the skewness in turbulence

L. Chevillard, B. Castaing, E. Lévêque and A. Arneodo

Laboratoire de Physique de l'Ecole Normale Supérieure de Lyon, CNRS, Université de Lyon, 46 allée d'Italie, F69007 Lyon, France
laurent.chevillard@ens-lyon.fr

The phenomenology of velocity statistics in turbulent flows, up to now, relates to different models dealing with either signed or unsigned longitudinal velocity increments, with either inertial or dissipative fluctuations. Based on experimental longitudinal velocity profiles, we show that velocity statistics can be completely understood phenomenologically with the help of two sets of parameters, a parameter function $\mathcal{D}(h)$, well known in the multifractal formalism as the singularity spectrum (in the inviscid limit) and an additional universal constant \mathcal{R}^* (i.e. independent on the Reynolds number and the geometry of the flow). The measurable parameter function $\mathcal{D}(h)$ is well known in the turbulence literature [1]. It encodes several crucial inertial range informations [1] such as K41 predictions (namely, the ‘-5/3’ law of the power spectrum) and intermittent corrections. Furthermore, it allows a quantitative prediction of the behavior of the even order structure functions in the intermediate and far-dissipative ranges (see for instance [2]).

However, an additional universal constant has to be given in order to reproduce known facts of turbulence, namely the Kolmogorov constant c_K and the skewness (or signed third order structure function) of velocity increments. This is the purpose of the present contribution [4, 5]. This constant has been claimed for a long time to have a universal value, namely $\mathcal{R}^* \approx 52$ (see [3] and references therein). It is fully defined through the fluctuating nature of the dissipative scale, i.e. $\eta(h)/L = (\mathcal{R}_e/\mathcal{R}^*)^{-1/(h+1)}$, where L is the integral scale, \mathcal{R}_e the Reynolds number and h the local Hölder exponent [2]. Including the constant \mathcal{R}^* in this definition of $\eta(h)$ has strong implications on averaged measurable quantities such as the mean dissipation: $\langle \epsilon \rangle = \frac{15}{\mathcal{R}^*} \frac{\sigma^3}{L}$, where σ^2 is the variance of the large scale velocity increment $\delta_L u$. Then, neglecting intermittent corrections, it can be shown that the Kolmogorov constant is linked to \mathcal{R}^* in the following way: $c_K = (\mathcal{R}^*/15)^{2/3} \approx 2.3$ [4], in relative good agreement with experimental findings [1].

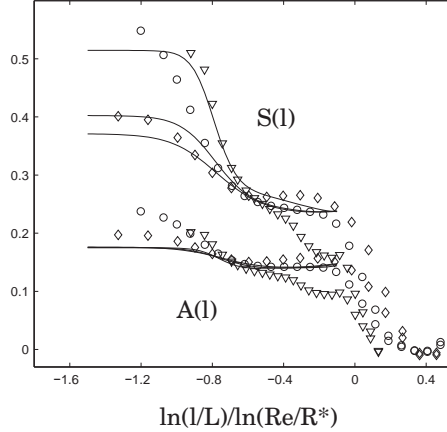


Fig. 1. Asymmetry factor $\mathcal{A}(\ell) = -\langle(\delta_\ell u)^3\rangle/\langle|\delta_\ell u|^3\rangle$ and Skewness $\mathcal{S}(\ell)$ estimated from various experimental velocity profiles: (\diamond) Turbulent low temperature gaseous helium jet for $\mathcal{R}_\lambda = 208$; (\circ) Air Jet for $\mathcal{R}_\lambda = 380$; (∇) Wind tunnel for $\mathcal{R}_\lambda = 2500$ [5]. The solid curves correspond to our theoretical predictions using the multifractal formalism (see [5])

Using the Karman-Howarth relation (in the inertial range), i.e. $\langle(\delta_\ell u)^3\rangle \approx -\frac{4}{5}\langle\epsilon\rangle\ell$, it can be easily shown that neglecting intermittency corrections, the Skewness of velocity increments $\mathcal{S}(\ell) = -\langle(\delta_\ell u)^3\rangle/\langle(\delta_\ell u)^2\rangle^{3/2}$ should display a universal plateau (independent on both scales and Reynolds numbers) $\mathcal{S}(\ell) = 12/\mathcal{R}^*$. Thus the constant \mathcal{R}^* explains both the value of c_K and the Skewness of velocity increments in the inertial range: this is our proposed phenomenological relation between c_K and the skewness [5].

More precise predictions can be obtained using the multifractal formalism, including intermittent corrections and dissipative corrections to the Karman-Howarth equation. This theoretical predictions were shown to compare quite well with experimental data as shown in Fig. 1 ([5]). Note that no vertical shifts were used in this figure.

References

1. U. Frisch, *Turbulence* (Cambridge University Press, Cambridge, 1995).
2. G. Paladin and A. Vulpiani, Phys. Rev. A **35**, 1971 (1987). M. Nelkin, Phys. Rev. A **42**, 7226 (1990). U. Frisch and M. Vergassola, Europhys. Lett. **14**, 439 (1991). C. Meneveau, Phys. Rev. E **54**, 3657 (1996).
3. Y. Gagne et al., Phys. Fluids **16**, 482 (2004).
4. L. Chevillard, B. Castaing, E. Lévêque, Eur. Phys. J. B **45**, 561567 (2005).
5. L. Chevillard, B. Castaing, E. Lévêque, A. Arneodo, Physica D, **218**, 77 (2006).

Kolmogorov scaling and intermittency in Rayleigh-Taylor turbulence

G. Boffetta⁽¹⁾, S. Musacchio⁽¹⁾, A. Mazzino⁽²⁾, and L. Vozella⁽²⁾

⁽¹⁾Dipartimento di Fisica Generale and INFN, Università di Torino, via P.Giuria 1, 10125 Torino (Italy)

⁽²⁾Dipartimento di Fisica, Università di Genova, INFN and CNISM, via Dodecaneso 33, 16146 Genova (Italy)

Summary. Three-dimensional Rayleigh-Taylor turbulence is studied by means of high resolution Direct Numerical Simulations of Boussinesq equations. The spatio-temporal predictions of a recently proposed phenomenological theory are confirmed and Kolmogorov-Obukhov scaling is observed.

We investigate the breakdown of the dimensional theory at small scale due to intermittency effects. Acceleration probability density functions and statistics of kinetic energy dissipation are found to be very close to the same quantities measured in homogeneous, isotropic turbulence.

At the level of global quantities, we show that the time-dependent Nusselt and Reynolds numbers scale with Rayleigh number according to the Kraichnan ultimate state of thermal convection.

We consider the 3D, incompressible ($\nabla \cdot \mathbf{v} = 0$), miscible Rayleigh-Taylor flow in the Boussinesq approximation

$$\partial_t \mathbf{v} + \mathbf{v} \cdot \nabla \mathbf{v} = -\nabla p + \nu \Delta \mathbf{v} + \beta \mathbf{g} T \quad (1)$$

$$\partial_t T + \mathbf{v} \cdot \nabla T = \kappa \Delta T \quad (2)$$

where T is the temperature field, proportional to density via the thermal expansion coefficient β , ν the kinematic viscosity, κ the molecular diffusivity and $\mathbf{g} = (0, 0, g)$ is the gravitational acceleration.

At time $t = 0$ the system is at rest with cooler (heavier) fluid placed above the hotter (lighter) one. This corresponds to $\mathbf{v}(\mathbf{x}, 0) = 0$ and to a step function for the initial temperature profile: $T(\mathbf{x}, 0) = -(\theta_0/2)\text{sgn}(z)$ where θ_0 is the initial temperature jump which fixes the Atwood number $A = (1/2)\beta\theta_0$. The development of the instability leads to a mixing zone of width h which starts from the plane $z = 0$ and is dimensionally expected to grow in time according to $h(t) = \alpha A g t^2$ [1]. Inside this mixing zone, turbulence develops in space and time. The phenomenological theory [2] predicts for velocity and temperature fluctuations the scaling laws

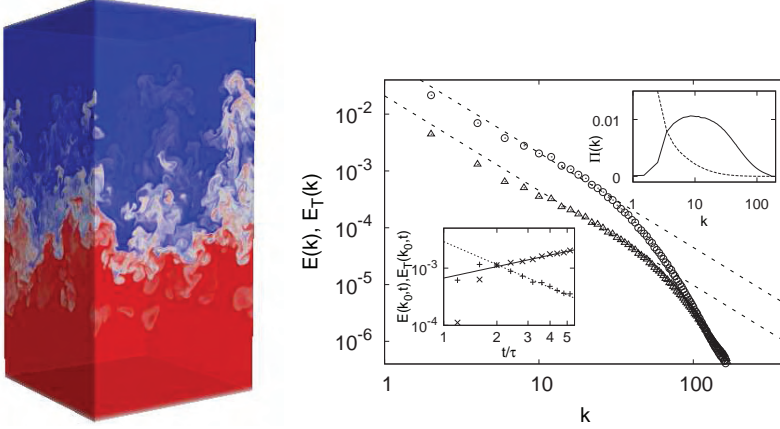


Fig. 1. (a) Snapshot of the temperature field for a simulation of Rayleigh-Taylor turbulence. Red (blue) corresponds to light (heavy) fluid turbulent pipe flow showing a transient. (b) Two-dimensional kinetic energy spectrum (\circ) and temperature spectrum (\triangle) at $R_\lambda = 245$. Dashed lines represent Kolmogorov scaling $k^{-5/3}$. Lower inset: evolution in time of the amplitude of kinetic energy (\times) and temperature ($+$) spectra at fixed wavenumber $k_0 = 12$. Lines represent the dimensional predictions $t^{2/3}$ (continuous) and $t^{-4/3}$ (dashed) given by (3) and (4). Upper inset: inertial (continuous) and buoyancy (dashed) contributions to kinetic energy flux $\Pi(k)$ in Fourier space.

$$\delta_r v(t) \simeq (Ag)^{2/3} t^{1/3} r^{1/3} \quad (3)$$

$$\delta_r T(t) \simeq \theta_0 (Ag)^{-1/3} t^{-2/3} r^{1/3} \quad (4)$$

The first relation represents Kolmogorov scaling with a time dependent energy flux $\epsilon \simeq (Ag)^2 t$. From the above scaling laws one obtains that the buoyancy term $\beta g T$ becomes subleading at small scales in (1), consistently with the assumption of passive transport of temperature fluctuations.

We integrate equations (1-2) by a standard 2/3-dealiased pseudospectral method on a periodic domain with uniform grid spacing, square basis $L_x = L_y$ and aspect ratio $L_x/L_z = r$ with a resolution up to $512 \times 512 \times 2048$ ($r = 1/4$). Time evolution is obtained by a second-order Runge-Kutta scheme with explicit linear part. In all runs, $Ag = 0.25$, $Pr = \nu/\kappa = 1$, $\theta_0 = 1$. Viscosity is sufficiently large to resolve small scales ($k_{max}\eta \simeq 1.2$ at final time). In the results, scales and times are made dimensionless with the box scale L_z and the characteristic time $\tau = (L_z/Ag)^{1/2}$.

Figure 1a shows a snapshot of the temperature field for a simulation with $r = 1/2$ at advanced time. Large scale structures (plumes) identify the direction of gravity and break the isotropy. Nonetheless, we find that at small scales isotropy is almost completely recovered: the ratio of vertical to horizontal rms velocity is $v_z/v_x \simeq 1.8$ while for the gradients we have $\partial_z v_z/\partial_x v_x \simeq 1.0$. The

horizontally averaged temperature $\langle T(z) \rangle$ follows closely a linear profile within the mixing layer where, therefore, the system recovers statistical homogeneity.

Figure 1b shows the kinetic energy $E(k)$ and temperature $E_T(k)$ spectra within the similarity regime. From (3) and (4), we expect the following spatial-temporal scaling of spectra: $E(k, t) \sim t^{2/3}k^{-5/3}$ and $E_T(k, t) \sim t^{-4/3}k^{-5/3}$. Kolmogorov scaling $k^{-5/3}$ is evident for both velocity and temperature fluctuations. Moreover, self-similar temporal evolution of spectra is well reproduced, as shown in the lower inset. Also in Fig. 1b the two contributions to kinetic energy flux in spectral space are shown. Buoyancy contribution, dominant at large scale, becomes subleading at smaller scales. The above results, together with previous simulations [1, 3] and theoretical arguments [2], give a coherent picture of RT turbulence as a Kolmogorov cascade of kinetic energy forced by large scale temperature instability.

In this contribution we push this analogy one step ahead by showing that small scale fluctuations in RT turbulence display intermittency corrections typical of usual Navier–Stokes (NS) turbulence. Intermittency in turbulence is a consequence of non-uniform transfer of energy in the cascade which breaks down scale invariance. As a consequence, scaling exponents deviates from mean field theory and cannot be determined by dimensional arguments [4]. Several studies have been devoted to the intermittent statistics in NS turbulence, where the main issue concerns the possible universality of anomalous scaling exponent with respect to the forcing mechanisms and the large scale geometry of the flow. While universality has been demonstrated for the simpler problem of passive scalar transport, it is still an open issue for nonlinear NS turbulence.

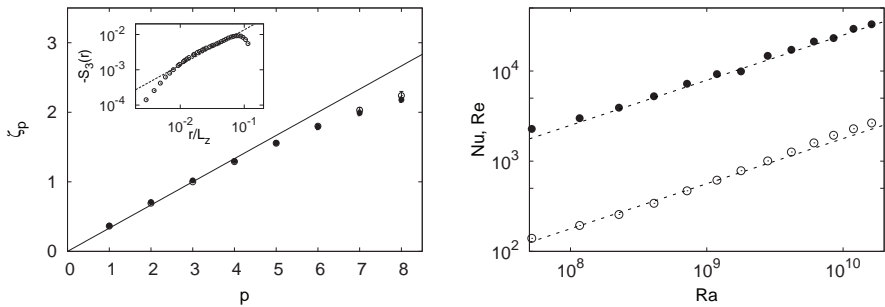


Fig. 2. (a) Scaling exponents of isotropic longitudinal velocity structure functions for the late stage of RT turbulence (open circle). Filled circles: scaling exponents from simulations of homogeneous, isotropic turbulence at $R_\lambda = 381$ [5]. Line represents dimensional prediction $\zeta_p = p/3$. Inset: third-order isotropic longitudinal structure function $S_3(r)$. The line represents Kolmogorov’s four-fifth law $S_3(r) = -4/5\epsilon r$. (b) The scaling of Nusselt number (open circles) and Reynolds number (solid circles) as functions of Rayleigh number. Lines represent the ultimate state predictions.

Figure 2a shows the first longitudinal scaling exponents computed from our simulations exploiting the extended self-similarity procedure which allows for a precise determination of the exponents at moderate Reynolds numbers. A deviation from dimensional prediction $\zeta_p = p/3$ is clearly observable for higher moments. Fig. 2a also shows the scaling exponents obtained from a homogeneous, isotropic simulation of NS equations at a comparable R_λ [5]. The two sets agree within the error bars, this gives further quantitative evidence in favor of the equivalence between RT turbulence and NS turbulence in three dimensions.

We end by discussing the behavior of turbulent heat flux and rms velocity fluctuations as a function of the mean temperature gradient. In terms of dimensionless variables, these quantities are represented respectively by the Nusselt number $Nu = 1 + \langle v_z T \rangle L / (\kappa \theta_0)$, the Reynolds numbers $Re = v_{rms} L / \nu$ and Rayleigh number $Ra = AgL^3 / (\nu \kappa)$. Experiments have reported both simple scaling laws $Nu \sim Ra^\beta$ with exponent β scattered around $\beta = 0.3$ [6, 7] and, more complicated behavior [8, 9] partially in agreement with a phenomenological theory [10]. However, in the limit of very large Ra , Kraichnan [11] predicted an asymptotic scaling $Nu \sim Re \sim Ra^{1/2}$ now called the ultimate state of thermal convection. This regime is expected to hold when thermal and kinetic boundary layers become irrelevant, and it is therefore natural to expect that the ultimate state scaling arises in RT convection where boundaries are absent. Fig. 2b shows that the ultimate state scaling is indeed observed in our simulations of RT convection.

References

1. W.H. Cabot and A.W. Cook, *Nature Phys.* **2**, 562 (2006).
2. M. Chertkov, *Phys. Rev. Lett.* **91**, 115001 (2003).
3. N. Vladimirova and M. Chertkov, *Phys. Fluids* **21**, 015102 (2009).
4. U. Frisch “Turbulence: The Legacy of AN Kolmogorov”, Cambridge University Press (1995).
5. T. Gotoh and D. Fukayama and T. Nakano, *Phys. Fluids* **14**, 1065 (2002).
6. J.A. Glazier and T. Segawa and A. Naert and M. Sano, *Nature* **398**, 307 (1999).
7. J.J. Niemela and L. Skrbek and K.R. Sreenivasan and R.J. Donnelly, *Nature* **404**, 837 (2000).
8. X. Xu and K.M.S. Bajaj and G. Ahlers, *Phys. Rev. Lett.* **84**, 4357 (2000).
9. A. Nikolaenko and G. Ahlers, *Phys. Rev. Lett.* **91**, 084501 (2003).
10. S. Grossmann and D. Lohse, *J. Fluid Mech.* **407**, 27 (2000).
11. R.H. Kraichnan, *Phys. Fluids* **5**, 1374 (1962).

Observation of weak turbulence spectra of capillary waves

H. Punzmann, M.G. Shats, H. Xia

Research School of Physics and Engineering, The Australian National University, Canberra ACT 0200, Australia

Turbulence of capillary waves is often studied in laboratory experiments by parametrically exciting waves in vertically shaken containers (Faraday waves). Above the threshold of parametric instability the waves become nonlinear and generate multiple harmonics which form complex chaotic wave fields which resemble turbulence. Such states are characterized by discrete frequency spectra (e.g. [1, 2]), which are often compared with the predictions from weak turbulence theory (WTT) of capillary waves [3, 4]. It should be noted that WTT assumes that interacting waves are weakly nonlinear and that their phases are almost random. The latter assumption has never been tested in experiments.

In this paper we present experimental studies of capillary waves which show that two distinctly different regimes can be achieved in a system of parametrically excited waves: a discrete spectrum of capillary waves dominated by the coherent-phase interactions and a continuous spectrum in which the spectral transfer occurs due to random-phase three-wave interactions.

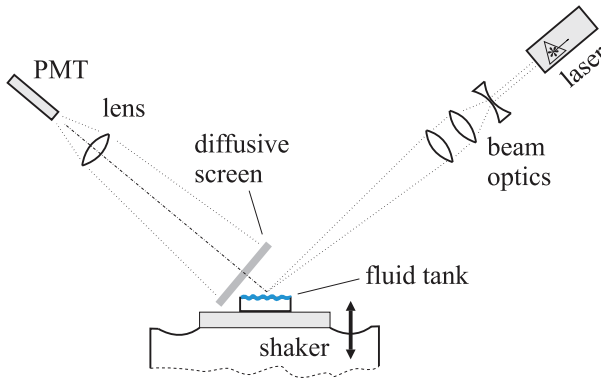


Fig. 1. Experimental setup.

The experiments are performed in a vertically shaken cylindrical container (100 mm in diameter, 30 mm deep). The surface perturbations by capillary

waves are detected using the reflection of the laser beam off the water surface, similarly to the method described in [1]. A laser beam is reflected by the water surface onto a diffusive screen which is imaged into a photo-multiplier tube. The reflected light intensity is proportional to the tilt angle $\nabla\eta$, or the gradient of the surface elevation $\eta(r, t)$. A schematic of the experimental setup is shown in Figure 1.

In the reported experiments a monochromatic excitation is used. A parametrically driven $f_0/2$ subharmonic wave is excited above a certain acceleration threshold and generates a large number of harmonics $f_n = n f_0/2$. An example of the discrete spectrum is given in Figure 2(a) for which $f_0 = 40$ Hz and $f_1 = 20$ Hz. More than $n = 50$ harmonics are observed. The increase in the drive (vertical acceleration) leads first to a substantial broadening of the harmonics and eventually to the generation of a continuous broadband spectrum, Fig. 2(b). This spectrum has a power law fit $S(f) \propto f^{-m}$, where $m \approx 3$.

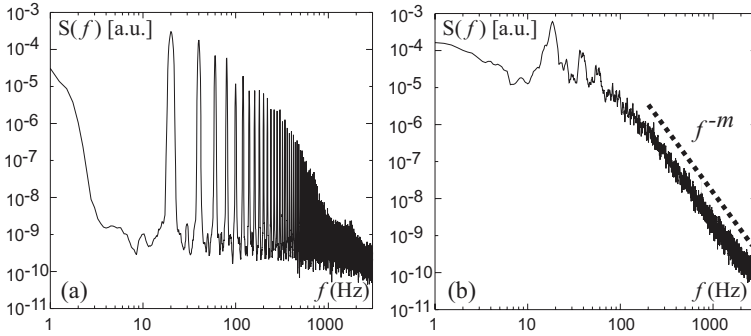


Fig. 2. (a) Discrete and (b) continuous spectra of capillary waves driven by the parametrically excited wave at $f_1 = f_0/2 = 20$ Hz. The r.m.s. acceleration is (a) $A = 2.5g$ and (b) $A = 15g$. Dotted line corresponds to a power-law fit of f^{-3} .

Capillary waves can interact via a three-wave interaction process which is possible due to the decay-type dispersion relation, $\omega_k = (\sigma/\rho)^{1/2} k^{3/2}$, where σ is the surface tension coefficient and ρ is the fluid density. Such a dispersion allows three-wave resonant conditions for the frequencies and for the wave numbers to be satisfied simultaneously: $\omega = \omega_1 + \omega_2$ and $k = k_1 + k_2$. The phase coupling in the spectra is characterized by the normalized bispectrum [5], or the *auto-bicoherence*. The auto-bispectrum of the reflected laser power $P(t)$ is defined as

$$B(f_1, f_2) = \langle F_f F_{f_1}^* F_{f_2}^* \rangle = \langle A_{f_1} A_{f_2} A_f e^{\phi_f - \phi_{f_1} - \phi_{f_2}} \rangle, \quad (1)$$

where $f = f_1 + f_2$, $F(f) = A_f e^{\phi_f}$ is the Fourier transform of $P(t)$, and $*$ denotes a complex conjugate. If phases of waves at f_1, f_2 and f are statistically random, the average value of the bispectrum is zero. The auto-bicoherence is the squared auto-bispectrum normalized by the auto power spectra of the

interacting waves:

$$b_f^2(f_1, f_2) = \frac{\left| \langle F_f F_{f_1}^* F_{f_2}^* \rangle \right|^2}{\langle F_f F_f^* \rangle \langle F_{f_1} F_{f_1}^* \rangle \langle F_{f_2} F_{f_2}^* \rangle}. \quad (2)$$

It changes between 0 (no phase coupling) and 1 (coherent waves) and reflects the strength of the three-wave interactions. We also compute the summed bicoherence, $SB(f) = \sum_{f=f_1+f_2} b_f^2(f_1, f_2)$. This quantity gives a measure of the total phase coupling to the frequency f from all frequencies f_1 and f_2 in the spectrum satisfying $f = f_1 + f_2$.

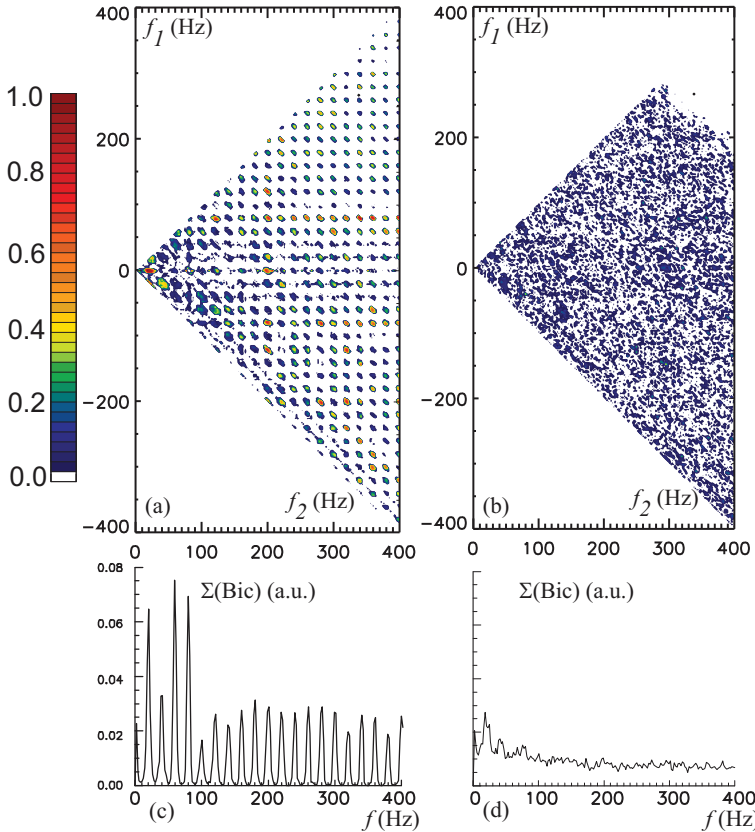


Fig. 3. (a,b) The auto-bicoherence of the reflected light intensity and (c,d) the summed bicoherence computed for the conditions of (a,c) discrete spectrum of Fig. 2(a), and (b,d) continuous spectrum of Fig. 2(b).

Fig. 3 shows the auto-bicoherence corresponding to the spectra of Fig. 2. The degree of the phase coupling between all discrete harmonics is very high,

$b_f^2 = (0.5 - 0.9)$, Fig. 3(a,c), which is indicative of highly coherent phase interaction. In the broadband turbulence, Fig. 3(b,d), the level of the bicoherence drops below 0.2 at all frequencies, even at the strongest harmonics of the pumping wave. This suggests that the waves participating in the three-wave interactions have almost random phases. In our experiments a gradual increase in the bandwidths of the interacting waves leads to a gradual overlapping of the adjacent harmonics and eventually leads to the sharp breakdown in the coherence and to the transition to the random-phase three wave interactions. The level of the summed bicoherence in the continuum increases, while it drops in the wave harmonics, as seen in Fig. 3(c,d). Further increase in the pumping leads to the increase in the level of the spectral continuum until the spectrum develops a power law of $S(f) \propto f^{-m}$. This spectrum gradually steepens with the increase in the acceleration until reaching its limit of about $m = 3$, as in Fig. 2(b).

Summarizing, we observe that transitions from discrete to continuous spectra of parametrically generated capillary waves occur via a sudden change in the degree of the phase coupling in the three-wave interactions. The coherent phase interaction is replaced by the interactions of a much larger number of modes having nearly random phases. Such a transition changes the nature of the energy transfer between interacting modes from continuous reversible transfer between coherent harmonics to asymmetric and irreversible transfer between the random-phase waves [6]. The regime relevant to the weak turbulence theory is realized in the latter case.

References

1. M. Yu. Brazhnikov *et al.* *Europhys. Lett.*, **58**, 510 (2002).
2. D. Snouck, M.-T. Westra, W. van de Water, *Phys. Fluids*, **21**, 025102 (2009).
3. V.E. Zakharov and N.N. Filonenko, *J. Appl. Mech. Tech. Phys.* **8**, 62 (1967).
4. A.N. Pushkarev and V.E. Zakharov, *Physica D* **135**, 98 (2000).
5. Y. C. Kim, E.J. Powers, *IEEE Trans. Plasma Sci.* **PS-7**, 120 (1979).
6. V.N. Tsytovich. *Nonlinear Effects in Plasma*, Plenum, New York (1970).

A new numerical methodology to follow the time-decay of turbulence

G. Sardina, P. Gualtieri, and C.M. Casciola

Dipartimento di meccanica e aeronautica, "Sapienza" Università di Roma , 00184 Rome, Italy

`gaetano.sardina at uniroma1.it`

Homogeneous isotropic turbulence in time decay has longly been a paradigm in turbulence. Since the very first investigations it clearly appeared that certain scaling laws characterize the time decay, i.e. the turbulent kinetic energy decreases in time as a power law with exponent n ($k = A_k(t - t_0)^{-n}$). From experiments [2] it immediately appeared that the values of n are strongly sensitive to the specific forcing and to the geometry of the apparatus. Ever since, there are been a number of attempts to understand this dispersion of data, under the assumption that the value of n should be universal. The theory described in [1] states that the decay exponent n is strongly affected by initial conditions and for large Reynolds number it assumes the value $n = 1$. Under this respect DNS simulations in triperiodic box ([5],[6]), are highly influenced by initial conditions i.e. by the spectrum of the velocity field. In particular it is strongly affected by the behavior of the spectrum near $k = 0$. Recent experiments [3] with space-filling square fractal grids show that the generated turbulence is characterized by the property that the Taylor scale remains constant during the decay. George [4] theoretically derived under the assumption of a constant characteristic scale that the turbulence described in [3] decays with an exponential law instead of the classical power law decay. He also states that this exponential solution is not restricted to low Reynolds number but its valid also for finite Reynolds number.

A basic property of self-similar decay is that the squared Taylor scale $\lambda^2 = 10\nu k/\epsilon = (10\nu/n)(t-t_v)$ increases linearly in time independently of the scaling exponent n , while the proportionality constant is n -dependent. It follows that the decaying exponent n can be estimated from the local slope $d\lambda^2/dt$. This procedure is exploited for the data presented in Fig. 1, concerning a simulation with an initial spectrum peaked at $k = 10$. In the first stages, consistently with previous predictions, we find that a scaling exponent emerges, $n = 1$, resulting in a constant Taylor-Reynolds number Re_λ . The process of turbulence decay essentially amounts to an unbound increase of the spatial scale according to $\ell = \ell_0 t^{1/2}$. However for longer times the scaling properties change since the

turbulent scales become comparable with the box size and can not increase further. In these conditions the value of the decay exponent begins to increase and might assume unphysical values greater than 2.5 that are not allowed by theoretical considerations.

In this paper we introduce a new numerical methodology to follow the time decay of homogeneous isotropic turbulence which is free from confinement effects. The idea behind the new technique we present here is to map the Navier-Stokes equations in a fixed domain in computational space corresponding to an expanding box in physical space. To map our equations in computational space we introduce suitable time-dependent velocity and length scales $U(t)/u_0 = (t/t_0)^{-\alpha/2}$, $L(t)/\ell_0 = (t/t_0)^{1/2}$ where α is up to now an unspecified real parameter.

The equations in the transformed space, $\mathbf{u}^* = \mathbf{u}/U(t)$, $\mathbf{x}^* = \mathbf{x}/L(t)$, read

$$\nabla_* \cdot \mathbf{u}_* = 0$$

$$\frac{\partial \mathbf{u}_*}{\partial \tau_*} + e^{\frac{1-\alpha}{2}\tau_*} \mathbf{u}_* \cdot \nabla_* \mathbf{u}_* = -\nabla_* p_* + \frac{1}{Re} \nabla_*^2 \mathbf{u}_* + \frac{\alpha}{2} \mathbf{u}_* + \frac{1}{2} \mathbf{x}_* \cdot \nabla_* \mathbf{u}_* \tag{1}$$

where $\tau_* = \ln(t/t_0)$ and $Re = u_0 \ell_0 / \nu$ is the nominal Reynolds number.

The solution $\mathbf{u}(\mathbf{x}, t)$ is α -independent and this invariance is preserved by any reasonably accurate numerics.

The equations in the Fourier space are the following:

$$j\mathbf{k}_* \cdot \widehat{\mathbf{u}}_* = 0$$

$$\frac{\partial \widehat{\mathbf{u}}_*}{\partial \tau_*} + e^{\frac{1-\alpha}{2}\tau_*} \mathbf{u}_* \cdot \widehat{\nabla}_* \mathbf{u}_* = -j\mathbf{k}_* \widehat{p}_* - \frac{1}{Re} k_*^2 \widehat{\mathbf{u}}_* + \frac{\alpha - 3}{2} \widehat{\mathbf{u}}_* - \frac{1}{2} \mathbf{k}_* \cdot \frac{\partial \widehat{\mathbf{u}}_*}{\partial \mathbf{k}_*} \tag{2}$$

As a matter of fact a computational box of fixed edges $\Lambda_i^0 = 2\pi$ $i = 1, 2, 3$ corresponds to an expanding box in physical space of edges $\Lambda_i(t) = \Lambda_i^0 (t/t_0)^{1/2}$. During decay, the physical box is continuously adjusted thus providing room for the enlarging energy containing modes. Since Kolmogorov and integral scale grow in time as $\eta = (\nu^3/\epsilon)^{1/4} \propto t^{(n+1)/4}$ and $L_0 = k^{3/2}/\epsilon \propto t^{(1-n/2)}$, respectively, for $n > 1$ the dissipative scales grow quicker than the box size, while the integral scale grows slower. At $n = 1$ all scales increase at the same rate. As a consequence, if the system is properly resolved at $t = 0$ and as far as $n \geq 1$ (the only cases of relevance here), at any $t > 0$ we have $L_0(t) < \Lambda_i(t)$ and $\eta(t) > \Lambda_i(t)/N_i$, with $\Lambda_i(t)/N_i$ the grid spacing and N_i the number of grid points in direction i . Concerning the algorithm, we use a standard pseudo-spectral method with the so-called three-halves dealiasing rule for the non-linear terms, coupled with a low storage, four stages, third order Runge-Kutta scheme for time advancement.

We performed a simulation in the expanding box from the same initial condition. The initial dimensions of the box are $2\pi \times 2\pi \times 2\pi$ and the resolution

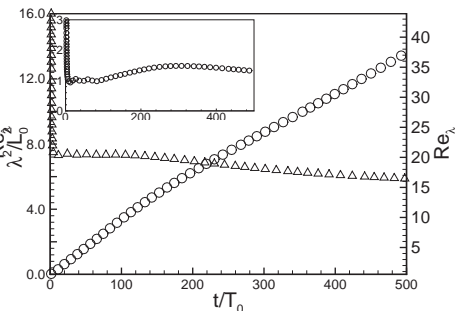
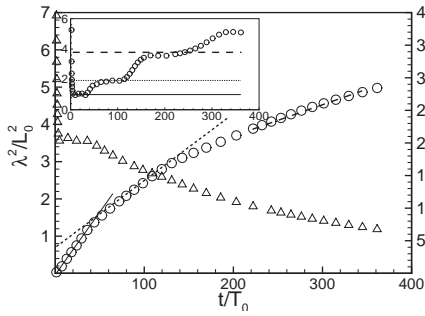


Fig. 1. Fixed box simulation. Left axis: squared Taylor’s scale (circles) and its fit (solid line) normalized by the integral scale at $t = 0$, L_0 . Right axis: Taylor-Reynolds number (triangles). Time on abscissa is made dimensionless with the eddy turn over time at $t = 0$. In the inset the local scaling exponent $n = 10\nu/d\lambda^2/dt$. The horizontal line is the fit in the range [2 : 18], $n = 2.3$.

Fig. 2. Expanding box simulation. Left axis: squared Taylor’s scale (circles) and its fit (solid line) normalized by the integral scale at $t = 0$, L_0 . Right axis: Taylor-Reynolds number (triangles). Time on abscissa is made dimensionless with the eddy turn over time at $t = 0$. In the inset the local scaling exponent $n = 10\nu/d\lambda^2/dt$.

is $384 \times 384 \times 384$. Looking at Fig. 2 it can be observed that, in this case, a constant Taylor Reynolds number is preserved for time intervals larger than those of the fixed box simulation—six times larger—where the value of the exponent n is one. The departure from $n = 1$ seen at larger times in fig 2 is presumably due to numerical accuracy issues since the very small values of the turbulent kinetic energy in computational space.

Fig. 3 summarizes the previous data to highlight the different behavior for the fixed and expanding simulations respectively.

The integral scale versus time is shown in fig. 4. In the unconfined simulation this variable increases with time while in the confined case it reaches a limit comparable with the box length. In the expanding box run, the integral length scales with the same power law of the Taylor scale and also of the Kolmogorov scale such that the ratios between the different turbulent characteristic scales tend to remain constant in time also when the turbulent intensity decays.

It is intriguing that at very late simulation time the exponent n reaches the value of 2.5 as predicted theoretically in the final period of decay.

In conclusion, by using the expanding box procedure it is possible to remove confinement effects that are the main causes of the different decay exponent n measured both in experiments and numerical simulations.

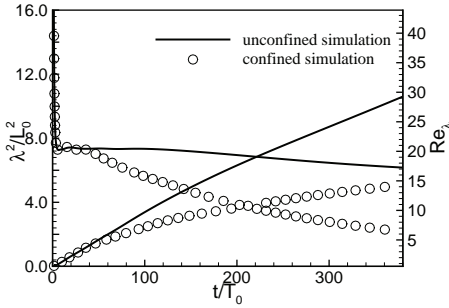


Fig. 3. Comparison between confined (circles) and unconfined (straight line) simulations in terms of Squared Taylor scale and Taylor Reynolds number.

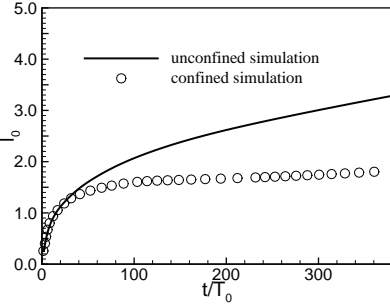


Fig. 4. Comparison between confined (circles) and unconfined (straight line) simulations in terms of integral scale.

References

1. W.K. George, Phys. Fluids, **A(4)**, 1492 (1992).
2. G. Comte-Bellot and S. Corrsin, J. Fluid Mech., **25**, 657 (1966).
3. D. Hurst and J. C. Vassilicos, Phys. Fluids, **19**, 035103 (2007).
4. W.K. George, Phys. Fluids, **21**, 025108 (2009).
5. N. N. Mansour and A. A. Wray, Phys. Fluids, **6**, 808 (1994).
6. Ishida, T., Davidson, P.A. and Kaneda, Y., J. Fluid Mech., **564**, 455 (2006).

Velocity kinematic relations in decaying turbulent flow past a grid

R. Gurka¹, G. Kopp², A. Liberzon^{3*}, P. Sarathi², and A. Tsinober³

¹Department of Chemical Engineering, Ben Gurion University,

²Boundary Layer Wind Tunnel Laboratory, University of Western Ontario,

³School of Mechanical Engineering, Tel Aviv University

*alexlib@eng.tau.ac.il

Introduction. Three recent publications^{1–3} stressed out that some kinematic relations of velocity increments $\Delta u_i = u_i(x+r) - u_i(x)$ comprise a manifestation of nonlocal effects, e.g. large and small scale quantities are correlated. This feature invalidates the so-called random sweeping hypothesis that large and small scales are statistically independent. It is noteworthy that, pure kinematic relations that emphasize the non-local effects thereby become dynamically significant. Some kinematic relations could be used for the validation of experimental results.

Authors of Ref. [2,3] presented a number of experimental results obtained using a multi-hot-wire probe in high Reynolds number flows estimated through the time series in a single point. The main objective of this contribution is to examine whether similar kinematic relations exist in lower range of Reynolds numbers, in a homogeneous decaying grid turbulence. Moreover, it is of our interest to test whether particle image velocimetry (PIV) (an experimental method that spatially resolves the flow fields but suffers from spatial low-pass filtering effects), is capable of capturing such kinematic relations. For this purpose, we measured the decaying turbulent flow past a grid in a water channel at the initial Reynolds number of 5000 (based on mean velocity and grid mesh size).

Experimental setup and methods of analysis. Figure 1 shows an overview of the water tunnel consists of an inlet reservoir, where water are introduced into the tunnel, followed by a settling chamber consisting of a honeycomb and screens, an 8:1 contraction, the test section, and a 90 degree turn to return the water to the sump through a control valve. The present set-up allows a maximum flow rate of 0.036 m³/s, corresponding to a maximum average of uniform mean velocity profile within 1% and turbulence intensity of less than 1% in the test section. The length of the test section was chosen to be 10 times the height of the test section. The width, W , and height, H , of the test section are 600 mm and 300 mm, respectively.

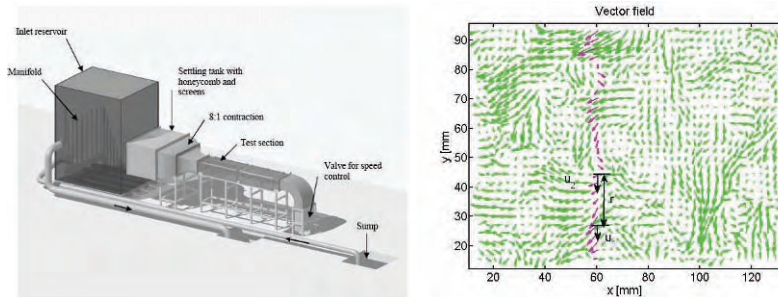


Fig. 1. Left: experimental setup of the wind tunnel. Right: Schematic description of the analysis: velocity field measured using PIV and an example of the single column of vectors marked. Only the vertical component is used, $u_1(x) = v(y)$ and $u_2(x+r) = v(y+\Delta y)$, $r = \Delta y$.

Measurements were carried out in the grid turbulence generated by a square mesh grid interwoven of stainless steel rods of 6.35 mm diameter and a spacing of $M = 25.4$ mm, placed perpendicular to the flow at the beginning of the test section. Measurements were made at five locations downstream past the grid ($x = 100, 500, 600, 800$ and 900 mm).

The flow was seeded using Silicon Carbide particles with an average diameter of $2 \mu\text{m}$ and a density of 3200 kg/m^3 . The PIV system makes use of a double pulse Nd:YAG laser operating at 15 Hz with an energy of 120 mJ/pulse that produces a light sheet at a wavelength of 532 nm illuminating the seeded flow field. The scattered light from the particles is collected into a CCD camera located 90 degrees to the light sheet. The CCD has an array of 1024×1024 pixels with an 8 bit dynamic range operating in double exposure mode. The images are then subsequently transferred to a computer for the completion of a two frame cross-correlation analysis. The time interval between two sequential images was set to be 2.5 msec corresponding to a mean velocity of 0.20 m/sec. The interrogation area was set to 64×64 pixels with 50% overlap resulting in 2048 velocity vectors per instantaneous map. A total of 2000 velocity maps were acquired per each experiment.

The kinematic relations are derived directly from the measured data. For every velocity field, the vertical velocity component v (along the homogeneous direction) is utilized to calculate the u_+ and the u_- along the vertical coordinate (Fig. 1 right). Homogeneity enables to average all the increments at a given distance r (limited to half-height of the observation field). The time steadiness of the decaying turbulence behind a grid enables the ensemble average at a given streamwise coordinate x .

Results. Two distinct types of the kinematic relations are presented: I) two-point relations such as Hosokawa's $\langle u_-^3 \rangle = -3\langle u_+^2 u_- \rangle$, II) mixed-type relations that mix the single- and two-point quantities such as $\langle (\Delta u)^2 \rangle = -2\langle u_1 \Delta u \rangle = 2\langle u_2 \Delta u \rangle$, which can appear as symmetric or asymmetric. In addition, a dis-

tion is made between the kinematic relations and dynamical relations, such as the Hosokawa's $\langle u_+^2 u_- \rangle = \langle \epsilon \rangle r / 30$, associated with the 4/5 law.

Kinematic relations. Two relations are presented in Fig. 2: two-point kinematic relation $\langle u_-^3 \rangle / \langle u_+^2 u_- \rangle$ and an analogous asymmetric relation $\langle (\Delta u)^3 \rangle / -2 \langle u_1 (\Delta u)^2 \rangle$.

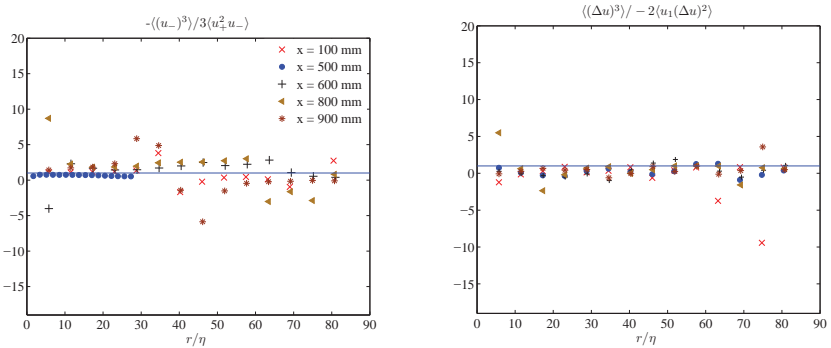


Fig. 2. (Left) Two-point kinematic relation $\langle u_-^3 \rangle / \langle u_+^2 u_- \rangle$ at different distances from the grid, $x = 100, 500, 600, 800$ and 900 [mm]. (Right) An asymmetric relation $\langle (\Delta u)^3 \rangle / -2 \langle u_1 (\Delta u)^2 \rangle$ analogous to the Hosokawa's relation on the left.

Dynamical relations associated with the 4/5 law. Hosokawa's relation $\langle u_+^2 u_- \rangle = \langle \epsilon \rangle r / 30$ and the direct 4/5 law are shown in the following Figure 3.

We would like to emphasize that for relatively low Reynolds numbers, it would be of interest to compare the dynamical relations without neglecting the viscous term in the 4/5 law. Namely, $\langle (\Delta u)^3 \rangle / [-(4/5) \langle \epsilon \rangle r + 6\nu d\{\langle (\Delta u)^2 \rangle / dr\}]$ and $\langle u_+^2 u_- \rangle / [\langle \epsilon \rangle r / 30 - \nu d\{\langle (u_-)^2 \rangle / dr\}]$, as well as considering the variation along the streamwise coordinate x . This will be a part of our future publication.

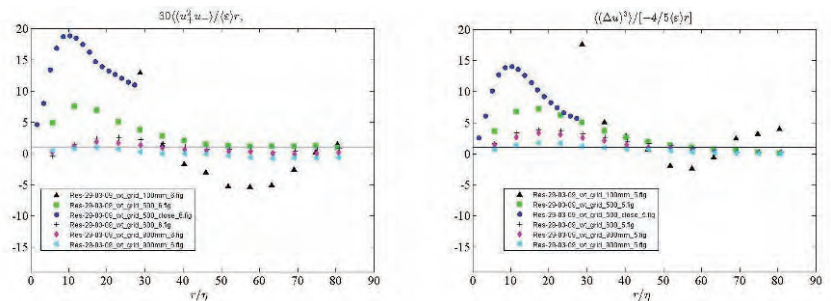


Fig. 3. (Left) Hosokawa's relation $\langle u_+^2 u_- \rangle = 30\epsilon / r$. (Right) Kolmogorov's 4/5 law in the form: $\langle (\Delta u)^3 \rangle = -4/5 \langle \epsilon \rangle r$

Summary and discussion. We demonstrate that the kinematic relations similar to those introduced by Hosokawa¹⁻³ can be obtained in a moderate Reynolds number flow of decaying turbulence past a mesh grid. The relations are shown to be sensitive to the homogeneity of the flow, as it appears in the results from the non-homogeneous region of the flow ($x = 100$ mm). Therefore, the kinematic relations are qualitatively different from the widely used single point statistics, that exhibit cut-offs at high wavenumbers due to the intrinsic low-pass filtering effect of the PIV experimental method. The dynamic relations presented by Hosokawa, $\langle u_+^2 u_- \rangle = \langle \epsilon \rangle r / 30$ and the 4/5 law hold for data obtained using PIV in grid turbulence despite the relatively low Reynolds number. The tests based on the kinematic and the dynamic relations can be recommended as a procedure to examine the homogeneity of turbulent flows under investigation.

References

1. Hosokawa, I. "A Paradox concerning the refined similarity hypothesis of Kolmogorov for isotropic turbulence," *Prog. Theor. Phys.* **118**, 169 (2007).
2. Kholmyansky, M. and Tsinober, A. "Kolmogorov 4/5 law, nonlocality, and sweeping decorrelation hypothesis", *Phys. Fluids* **20**, 041704 (2008).
3. Kholmyansky, M., Sabelnikov, V. and Tsinober, A., "New developments in field experiments in ASL: Kolmogorov 4/5 law and non-locality", 18th Symposium on Boundary Layers and Turbulence, American Meteorological Society, Stockholm, 2008.
4. Praskovsky, A., Gledzer, E.B., Karyakin, M. Yu. and Zhou, Y. "The sweeping decorrelation hypothesis and energy-inertial scale interaction in high Reynolds number flows", *J. Fluid Mech.*, **248**, 493511 (1993)
5. Sarathi, P., Kopp, G.A., Martinuzzi, R.J., Sullivan, P.J. and Gurka, R., "Design and performance of an open-return water tunnel", sub judice in *Journal of Wind Engineering and Industrial Aerodynamics* (2009)

Lagrangian intermittency and time-correlations in two-dimensional turbulence

K. Schneider¹, S. Neffaa¹, B. Kadoch¹ and W.J.T. Bos²

¹M2P2-CNRS & CMI, Université de Provence, Marseille, France

²LMFA-CNRS Ecole Centrale de Lyon, Université de Lyon, Ecully, France

The intermittent nature of turbulent flows constitutes a major challenge to modellers. Whereas the statistics of the complex dynamics of scale-invariant Lagrangian dynamics could be modelled by a Gaussian process, intermittency impedes this. Large fluctuations in the velocity increments and fluid particle accelerations would be largely underestimated by such an approach. Advances in numerical and experimental methods have recently boosted the research on and understanding of the intermittent nature of turbulent flows, in particular from the Lagrangian viewpoint [1]. For example, in two dimensions, it was recently shown that Lagrangian intermittency can exist even if it is completely absent in the Eulerian reference frame [2]. Moreover, it was hypothesized that Lagrangian long-time correlations might be a key to the understanding of intermittency [3].

In the present work we will investigate the validity of this hypothesis. We start with a model for two-dimensional turbulence, well known in the magnetically confined fusion community. This model, due to Hasegawa and Wakatani [4], bares resemblances with both 2D Navier-Stokes turbulence and 2D geostrophic turbulence. One parameter, the adiabaticity c , allows to vary continuously from one limit to the other. This model reads

$$\frac{\partial \omega}{\partial t} + (\mathbf{u} \cdot \nabla) \omega = \nu \nabla^2 \omega + c(\psi - n), \quad (1)$$

$$\frac{\partial n}{\partial t} + (\mathbf{u} \cdot \nabla) n = D \nabla^2 n - u \frac{\partial \bar{n}}{\partial x} + c(\psi - n). \quad (2)$$

with ω the vorticity, n an advected scalar, ψ the stream-function, ν and D viscosity and diffusivity, respectively, and $\partial \bar{n} / \partial x$ an imposed mean scalar gradient. For $c \rightarrow 0$ one approaches the 2D Navier-Stokes limit, whereas for $c \rightarrow \infty$ the geostrophic Charney model is obtained. The coupling term $c(\psi - n)$ allows the system to access to a saturated turbulent state even in the absence of external forcing.

Equations (1,2) were solved using a fully dealiased pseudo-spectral method at a resolution of 1024^2 gridpoints. 10^4 particles were injected, equally spaced,

in the statistically stationary regime, and their velocity and acceleration were monitored during several large-scale turn-over times. Details on the simulations of equations (1,2) can be found in [5] and on the Lagrangian part of the study in [6] in which a similar investigation was performed for Navier-Stokes turbulence. The adiabaticity is varied between $c = 0.01$ and $c = 2$, to obtain different flow regimes. Visualizations of the vorticity-field for two flow regimes are shown in Figure 1.

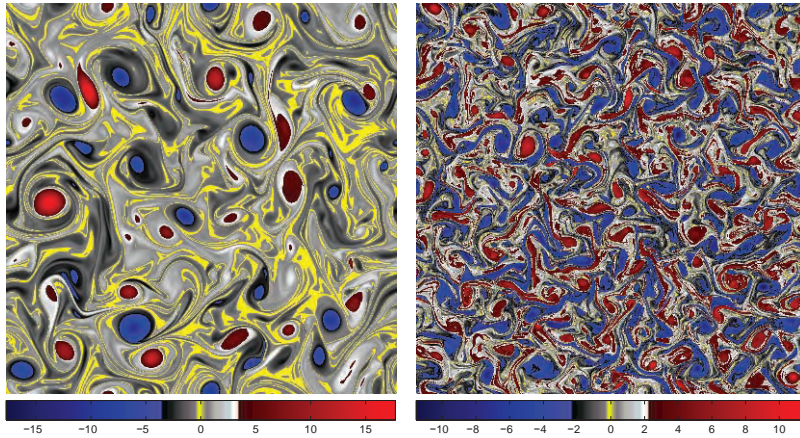


Fig. 1. Visualisations of the vorticity field for two different values of the adiabaticity. Left: $c = 0.01$, right: $c = 2$.

In Figure 2 (left), the PDFs (probability density functions) of the Lagrangian acceleration are shown for different values of c . It is observed that the PDF evolves from a close to exponential form for large c to a stretched exponential for $c = 0.01$. It was argued by Holzer and Siggia [7] that an exponential distribution for the pressure gradient PDF (which is supposed to resemble the Lagrangian acceleration for large Reynolds number), can be obtained from Gaussian (non-intermittent) velocity fields. More puzzling are the stretched exponentials, found for small c , similar to the stretched exponentials observed in Navier-Stokes turbulence. To quantify the stretching of the PDFs, we plot in Figure 2 (right) the flatness of the velocity increment PDFs as a function of the timelag τ . For small τ this quantity yields the flatness of the acceleration PDFs. This flatness is seen to vary between approximately 8 and 60. Note that for a perfect exponential distribution the flatness is equal to 6. The flatness of the velocity PDFs can be obtained by evaluating the value for large τ . Except for $c = 0.01$, all cases yield a flatness close to three, which is the Gaussian value. For the case $c = 0.01$, the value of the flatness at large τ is approximately 5.5. For timelags $0.5 < \tau < 5$, the flatness can be fitted with a power-law.

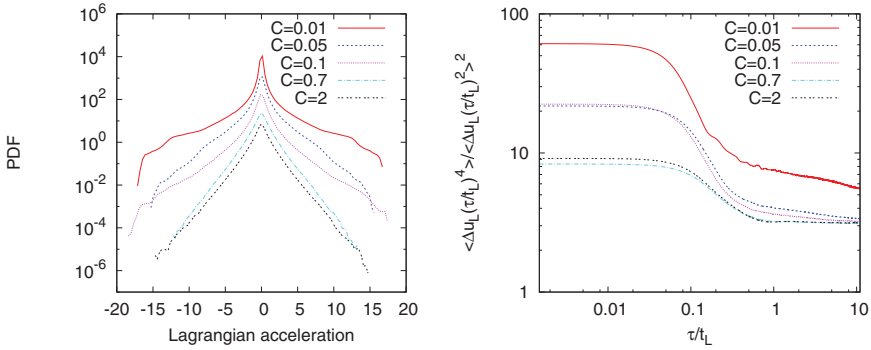


Fig. 2. Left: PDFs of Lagrangian acceleration for different values of c . Right: flatness of the velocity increments as a function of τ .

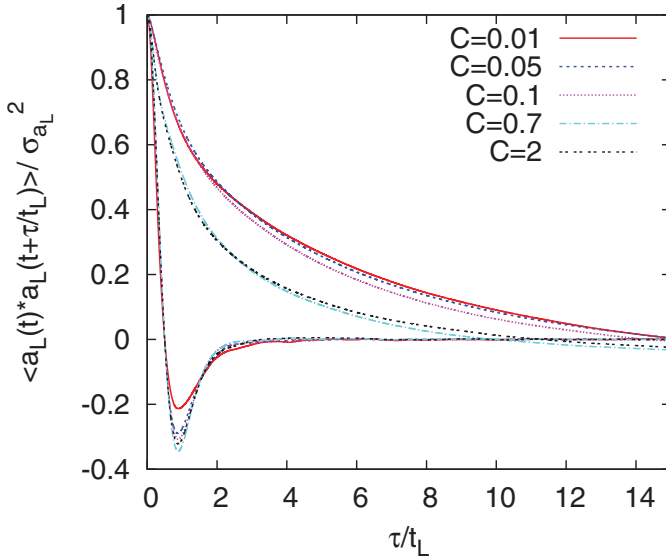


Fig. 3. Autocorrelations of the acceleration and of its norm for the five cases.

Mordant *et al.* [3] proposed that the origin of the intermittent behavior of the Lagrangian acceleration might be related to the long time-correlation of the norm of the acceleration. To test this assumption, we show in Figure 3 the time-correlations of the components of the acceleration and of their norm. Note that at large times the correlation of the norm takes small negative values. This is, as explained in Yeung and Pope [8], due to a slow convergence of the statistics at long time intervals. This can be reduced by preprocessing the data, which is not attempted in the present work. The timelag is normalized by the first zero-crossing of the time-correlation of the components of the ac-

celeration. These correlations thereby almost collapse. The time-correlation of the norm of the acceleration varies slightly. The cases $c = 0.7$ and $c = 2$ show shorter time correlations than the other cases ($c = 0.01$; 0.05 ; 0.1). However, in between these last three cases no significant difference is observed, whereas the flatness of the PDF of the acceleration varies between 20 and 60. We can therefore not conclude, for the moment, whether or not long time-correlations are the key to intermittency.

References

1. F. Toschi and E. Bodenschatz. Lagrangian properties of particles in turbulence. *Annu. Rev. Fluid Mech.*, 41:375, 2009.
2. O. Kamps and R. Friedrich. Lagrangian statistics in forced two-dimensional turbulence. *Phys. Rev. E*, 78:036321, 2008.
3. N. Mordant, J. Delour, E. Leveque, A. Arneodo, and J.-F. Pinton. Long time correlations in Lagrangian dynamics: a key to intermittency in turbulence. *Phys. Rev. Lett.*, 89:254502, 2002.
4. A. Hasegawa and M. Wakatani. Plasma edge turbulence. *Phys. Rev. Lett.*, 50:682, 1983.
5. W.J.T. Bos, S. Futatani, S. Benkadda, M. Farge, and K. Schneider. Role of coherent vorticity in turbulent transport in resistive drift-wave turbulence. *Phys. Plasmas*, 15:072305, 2008.
6. B. Kadoch, W.J.T. Bos, and K. Schneider. Extreme lagrangian acceleration in confined turbulent flow. *Phys. Rev. Lett.*, 100:184503, 2008.
7. M. Holzer and E. Siggia. Skewed, exponential pressure distributions from Gaussian velocities. *Phys. Fluids A*, 5:2525, 1993.
8. P.K. Yeung and S.B. Pope. Lagrangian statistics from direct numerical simulations of isotropic turbulence. *J. Fluid Mech.*, 207:531, 1989.

Part XI Large eddy simulation

Implicit Large-Eddy Simulation: Theory and Application

N. A. Adams and S. Hickel

Institute of Aerodynamics, Technische Universität München
Nikolaus adams at tum.de

Large-Eddy Simulation has been recognized as one of the major tools for the numerical simulation of complex turbulent flows, in events when more accessible alternative approaches, such as statistically averaged Navier-Stokes equations (Reynolds-averaged Navier-Stokes equations - RANS), fail. This is in particular the case, when complex flow phenomena (reaction, fluid-structure interaction, interfaces, shocks) introduce additional non-turbulent temporal or spatial scales. It is known since quite some time that the nonlinear truncation error of some classes of discretization schemes for the Navier-Stokes equations not only interferes with explicitly added subgrid-scale (SGS) models but also can provide some SGS closure when no model is added at all. More recent analyses of such schemes have outlined the way to a more systematic procedure for such no-model approaches, leading to what is called now implicit LES (ILES). With ILES no subgrid-scale model is added to the discretized Navier-Stokes equations, and SGS modeling is left solely to the numerical truncation error. In this contribution we will outline a theory of ILES which allows for physically motivated modeling of the nonlinear truncation error, called adaptive local deconvolution method (ALDM), and demonstrate its feasibility for reliable LES of a wide range of turbulent flow configurations.

1 General Concept of ILES

For simplicity we consider the initial-value problem for a generic scalar nonlinear transport equation for the variable v

$$\frac{\partial v}{\partial t} + \frac{\partial F(v)}{\partial x} = 0 . \quad (1)$$

On a mesh with equidistant spacing h the grid function v_N represents a discrete approximation of $v(x)$ by $v_j \doteq v(x_j)$. For finite h the representation of the continuous solution $v(x)$ by the grid function v_N results in a subgrid-scale error or residual

$$\mathcal{G}_{SGS} = \frac{\partial F_N(v_N)}{\partial x} - \frac{\partial F_N(v)}{\partial x} \quad (2)$$

which arises from the nonlinearity of $F(v)$. The modified differential equation (MDE) for v_N is

$$\frac{\partial v_N}{\partial t} + \frac{\partial F_N(v_N)}{\partial x} = \mathcal{G}_{SGS} . \quad (3)$$

Since for LES the ratio between characteristic flow scale and grid size h never can be considered as asymptotically small \mathcal{G}_{SGS} cannot be neglected for proper evolution of v_N but requires approximation by modeling closures.

A similar MDE is obtained from a finite-volume discretization of eq. (1) which corresponds to a convolution with the top-hat filter. The resulting finite-volume approximation of eq. (1) is given by

$$\frac{\partial \bar{u}_N}{\partial t} + G * \frac{\partial \tilde{F}_N(u_N^*)}{\partial x} = 0 , \quad (4)$$

where $u_N^* \doteq u_N$ results from an approximate inversion $u_N^* = Q * \bar{u}_N$ of the filtering $\bar{u}_N = G * u$. This equation approximates the exact filtered equation

$$\frac{\partial \bar{v}}{\partial t} + G * \frac{\partial F(v)}{\partial x} = 0 , \quad (5)$$

Similar considerations hold for filter kernels other than the top-hat filter. We recall that although the inverse-filtering operation is ill-posed, an approximation u_N^* of u on the grid x_N can be obtained by regularized deconvolution.

Once deconvolution operation and numerical flux function are determined, the modified-differential-equation analysis of eq. (4) leads to an evolution equation of \bar{u}_N in the form of

$$\frac{\partial \bar{u}_N}{\partial t} + G * \frac{\partial F_N(u_N)}{\partial x} = \mathcal{G}_N , \quad (6)$$

where

$$\mathcal{G}_N = G * \frac{\partial F_N(u_N)}{\partial x} - G * \frac{\partial \tilde{F}_N(u_N^*)}{\partial x} \quad (7)$$

is the truncation error of the discretization scheme. If \mathcal{G}_N approximates $\bar{\mathcal{G}}_{SGS}$ in some sense for finite h we obtain an implicit subgrid-scale model implied by the discretization scheme. Note that this requirement is similar to that for \mathcal{G}_{SGS} and different from classical asymptotic truncation-error analysis, where \mathcal{G}_N approximates $\bar{\mathcal{G}}_{SGS}$ for $h \rightarrow 0$.

2 The Modified Differential Equation

Central element of implicit LES modeling is the modified differential equation analysis (MDEA). Considering the initial-value problem of the generic one

dimensional conservation law of eq. (1) with the generic semi-discretization eq. (4) we obtain as solution a grid function $u_N = \{u_j\}$. Assuming that this grid function decays sufficiently fast with $x \rightarrow \pm\infty$ it possesses a discrete Fourier transform. As explained by Vichnevetsky and Bowles [21] the same Fourier transform applies to the continuous function $u(x)$ which is the continuous interpolation of the grid function u_N by virtue of the Whittaker cardinal function. The interpolated function is smooth $u(x) \in C^\infty$ and can be expanded as a Taylor series at each x_j . Note that $u(x)$ represents jumps in u_N , which are approximations of discontinuities in terms of the grid function, by a smooth approximation. Also, any filtering applied to u_N can be formally inverted by application of the inverse filter kernel to \hat{u}_N since as a grid function u_N has compact support in Fourier space, and accordingly does $u(x)$.

Given $u(x)$ as continuous interpolation of u_N , and given that this function is sufficiently smooth, the question is what differential equation is solved exactly by $u(x)$. Since $\bar{u}(x_j) = \bar{u}_j$, and $\bar{u}_j \doteq \bar{v}(x_j)$ is only an approximation of the solution of eq. (5) certainly $\bar{v}(x)$ and $\bar{u}(x)$ differ in general. Therefore, also the differential equation whose exact solution is $\bar{v}(x)$ differs from eq. (5). Given that \bar{u}_N is the the solution of eq. (4) obtained by a consistent discretization, the differential equation for $\bar{u}(x)$ should differ from eq. (5) for $\bar{v}(x)$ by the truncation error, which for consistent schemes should become small with small grid- and time-step sizes. As we consider here only spatial semi-discretizations it is the spatial truncation error, which is relevant. Now it is clear that eq. (6) can be rewritten in terms of $u(x, t)$ as

$$\frac{\partial \bar{u}}{\partial t} + G * \frac{\partial F(u)}{\partial x} = \mathcal{G}, \tag{8}$$

where the continuous spatial truncation error \mathcal{G} can be obtained by inserting the Taylor expansion of $u(x)$, after $u(x)$ has been reconstructed from $\bar{u}(x)$ by inverse filtering or deconvolution.

For more general transport equations and more complex, e.g. nonlinear, discretization schemes the derivation of the modified differential equation becomes very complex. Also, when incompressible flows are considered, the spatial truncation error involves contributions of the divergence constraint. If zero divergence is satisfied by projection these analytical contributions require the solution of a Poisson equation by suitable Green functions. Overall, the real space modified-differential-equation analysis is hardly tractable for more complex discretizations and more general transport equations. One of the essential requirements for a SGS model is that for isotropic turbulence it has to recover the proper energy transfer between represented and non-represented scales. Only then one can expect that the kinetic-energy spectrum develops a Kolmogorov inertial range. Most suitable for such analyses is a representation of the truncation error in spectral space, leading to the MDEA in spectral space [7].

3 Review of ILES approaches

3.1 The Volume Balance Procedure of Schumamm

With the Volume-Balance Procedure [16] the incompressible Navier-Stokes equations are averaged over finite volumes using a staggered arrangement of the grid for the different components of the momentum equation. The main focus is posed on physically motivated modeling of the SGS stresses. For this purpose isotropic and inhomogeneous contributions are considered separately. A particular truncation-error term arising from the discretization, or volume-averaging, respectively, is modeled, whereas not the full truncation error is considered. In this respect the volume-balance procedure rather can be considered as explicit LES model, but the notion that the discrete equations should be the starting point of modeling is shared with implicit LES modeling.

3.2 The Kawamura-Kuwahara scheme

A linear implicit LES method has been proposed by Kawamura and Kuwahara [13] for incompressible flow. The method is based on a standard pressure-correction scheme with non-staggered arrangement of grid points for the discretization of momentum and pressure-Poisson equations. While for the discrete derivative operators in the Poisson equation and in the friction term of the momentum equations second-order central differences are used, the essence of this simple implicit model is in the discretization of the convective terms in the momentum equations by a particular combination of directional upwind schemes.

3.3 The Piecewise-Parabolic Method

The Piecewise-Parabolic Method (PPM) was proposed by Woodward and Colella [22] for the numerical solution of gas-dynamics problems, see also Ref. [5, chapter 4b], and applied to turbulence flows by Porter *et al.* [15]. Basis of PPM is a MUSCL (Monotone UPstream-centered Scheme for Conservation Laws) [14] reconstruction of the unfiltered solution by quadratic local approximation polynomials. From these differences a so-called fractional error can be computed which serves as a measure of the local smoothness of the solution. Based on this reconstruction procedure and the accompanying smoothness measure a MUSCL-type, formally third-order accurate spatial discretization can be constructed, where the interpolation procedure for compressible flow problems is commonly applied to the Riemann variables (i.e. to a local characteristic projection of the transport equations). To maintain nonlinear stability a slope limiting is introduced. For contact discontinuities a steepening operation is constructed. With this framework PPM introduces a method for the reconstruction of subgrid information which is motivated by its function as approximate Riemann solver for gas dynamics.

3.4 The Flux-Corrected-Transport Method

For implicit SGS modeling the discretization scheme has to be specifically designed so that the truncation error has physical significance. In a numerical analysis [3] several approaches to implicit LES are investigated and difficulties in satisfying this requirement are demonstrated. It was found that artificial dissipation introduced by common nonlinearly-stable discretizations indeed stabilizes under-resolved turbulence simulations. For the investigated schemes, however, small scales suffer from excessive numerical damping such that the probability-density functions of velocity increments and pressure exhibit the typical behavior of low Reynolds-number flows rather than that of high Reynolds-number turbulence. Thus it appears that for these schemes the prediction accuracy of subgrid effects is poor, although some general trends were reproduced. With a certain Flux-Corrected Transport Method (FCT), however, good results for a wide range of complex flows have been reported [4].

3.5 The MPDATA Method

The Multidimensional Positive Definite Advection Transport Algorithm (MPDATA) has been introduced by Smolarkiewicz [17, 18] for meteorological applications. Reviews of MPDATA can be found in Refs. [20, 19]. Essential to MPDATA is upwinding of the numerical error, which is achieved in a two-step scheme, where a spatially first-order upwind step is followed by an anti-diffusive step, involving upwinding of the truncation error. Overall second-order in space is achieved. Applied to incompressible Navier-Stokes turbulence the MPDATA method was analyzed by Domaradzki *et al.* [2]. Simulations for isotropic incompressible turbulence at formally infinite Reynolds number for fixed numerical parameters (resolution and time-step size). It was found that the compensated inertial-range spectra approximate the value for the Kolmogorov constant in a quality comparable to classical explicit LES models. A spectral-space MDEA reveals that the spectral numerical viscosity is in the range of the theoretically predicted spectral eddy viscosity, does not, however return the plateau values and does not reproduce the cusp near the cut-off wavenumber.

3.6 The Optimum Finite-Volume Scheme

Starting point of the Optimum Finite-Volume Scheme of Zandonade *et al.* [23] is the finite-volume discretization of the incompressible Navier-Stokes equations. As with the Volume-Balance Method the problem of modeling the cell-face fluxes is considered directly which is then subjected to stochastic estimation. In effect, the above ansatz leaves all finite-volume stencil weights free for optimization. Numerical requirements, such as consistency or stability, are not enforced by constraining the optimization and have to be recovered by

the estimation procedure. Also, as the ansatz is linear, it cannot be expected that the resulting model can adapt locally to the flow character, whether turbulent or laminar. An optimum parameter set was identified for isotropic turbulence.

3.7 Implicit LES by Adaptive Local Deconvolution

The Adaptive Local Deconvolution Method (ALDM) constitutes a general framework for ILES which is inherently solution adaptive and involves only few discretization parameters which can be identified by incorporating theoretical knowledge about turbulence physics. For any discretization parameters ALDM results in a consistent spatial discretization scheme which is at least second-order accurate. A one-dimensional development of ALDM for the Burgers equation has been given by Ref. [1]. This fundamental concept of ALDM has been extended to the incompressible [7] and the compressible Navier-Stokes equations [12]. ALDM also has been formulated for scalar transport [9].

The generic discretized conservation law eq. (6) is considered subjected to a real-space top-hat filter. For the filtered flux term an approximation of the unfiltered solution at the left and right faces of each cell is required. The top-hat filtering being equivalent to a finite-volume discretization allows for a primitive-function reconstruction of $u(x)$ from \bar{u}_N as proposed by Harten *et al.* [6]. For this purpose a set of local interpolation polynomials is introduced, operating on admissible interpolation stencils. Whereas for ENO or weighted-ENO (WENO) approaches a single interpolation-polynomial order is chosen, here a quasi-linear combination of all possible interpolation polynomials up to a certain order is constructed. Finally, an appropriate numerical flux function \tilde{F}_N needs to be devised which approximates the physical flux F . Details are given in Ref. [1, 7]

ALDM for the incompressible Navier-Stokes equations has been applied to a wide range of flows. A representative result for homogeneous turbulence is the transition of the three-dimensional Taylor-Green vortex, whose dissipation evolution is very well captured by ALDM, see fig. 1. Inhomogeneous turbulent flows also are well reproduced by ALDM, this holds e.g. for turbulent channel flow [8], see fig. 2, and for massively separated boundary layer flows [10, 11].

References

1. N. A. Adams, S. Hickel, S. Franz, Implicit subgrid-scale modeling by adaptive deconvolution, *J. Comput. Phys.* 200:412-431, 2004
2. J. A. Domaradzki, Z. Xiao, P. K. Smolarkiewicz, Effective eddy viscosities in implicit large eddy simulations of turbulent flows, *Phys. Fluids* 15:3890-3893, 2003
3. E. Garnier, M. Mossi, P. Sagaut, P. Comte, M. Deville, On the use of shock-capturing schemes for large-eddy simulation, *J. Comput. Phys.* 153:273-311, 1999
4. F. F. Grinstein, C. Fureby, From canonical to complex flows: recent progress on monotonically integrated LES, *Comp. Sci. Eng.* 6:36-49, 2004

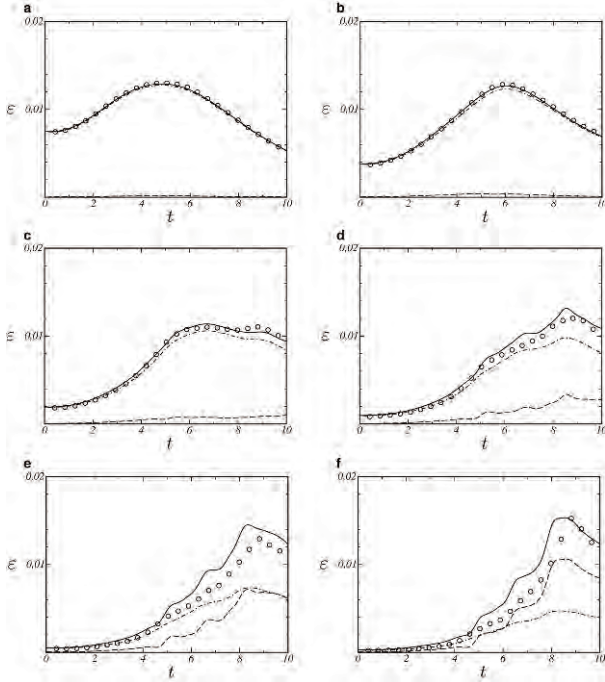


Fig. 1. Contributions to energy dissipation in ALDM for LES of the TaylorGreen vortex at $Re =$ (a) 100, (b) 200, (c) 400, (d) 800, (e) 1600, (f) 3000; — — — molecular dissipation, - - - - implicit SGS dissipation, ——— total dissipation, symbols DNS data. For details see [7].

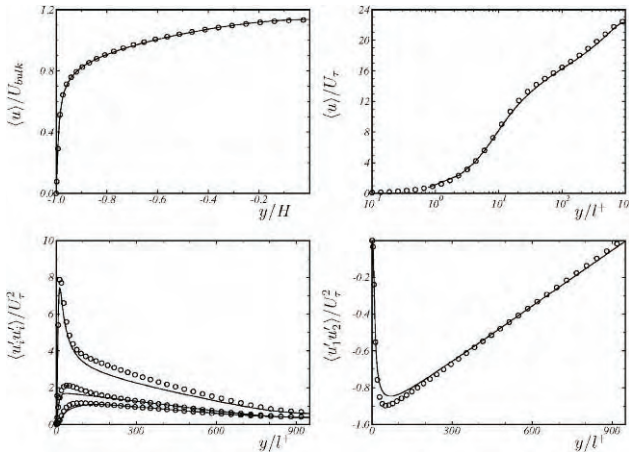


Fig. 2. Mean velocity profile and resolved Reynolds stresses for LES of turbulent channel flow at $Re_\tau = 950$. Lines: ALDM, symbols: DNS, For details see Ref. [8].

5. F. F. Grinstein, L. G. Margolin, W. J. Rider, *Implicit Large Eddy Simulation - Computing Turbulent Fluid Dynamics* Cambridge University Press, 2007.
6. A. Harten, B. Engquist, S. Osher, S. R. Chakravarty, Uniformly high order accurate essentially non-oscillatory schemes, III, *J. Comput. Phys.* 71:231-303, 1987
7. S. Hickel, N. A. Adams, J. A. Domaradzki, An adaptive local deconvolution method for implicit LES, *J. Comput. Phys.* 213:413-436, 2006
8. S. Hickel, N. A. Adams, On implicit subgrid-scale modeling in wall-bounded flows, *Phys. Fluids* 19:105106, 2007
9. S. Hickel, N. A. Adams, N. N. Mansour, Implicit subgrid-scale modeling for large-eddy simulation of passive-scalar mixing, *Phys. Fluids* 19:095102, 2007
10. S. Hickel, N. A. Adams, Implicit LES applied to zero-pressure-gradient and adverse-pressure-gradient boundary-layer turbulence, *Int. J. Heat Fluid Flow* 29:626-639, 2008
11. S. Hickel, N. A. Adams, Implicit large-eddy simulation applied to turbulent channel flow with periodic constrictions, *Theor. Comput. Fluid Dyn.* 22:227-242, 2008
12. S. Hickel, J. Larsson, An adaptive local deconvolution model for compressible turbulence, *Proceedings of the CTR Summer Program 2008*, Center for Turbulence Research, Stanford University, 2008
13. T. Kawamura, K. Kuwahara, Computation of high Reynolds number flow around a circular cylinder with surface roughness, *AIAA-paper* 84-0340, 1984
14. B. van Leer, Towards the Ultimate Conservative Difference Scheme, V. A Second Order Sequel to Godunov's Method, *J. Comput. Phys.* 32:101-136, 1979
15. D. H. Porter, P. R. Woodward, A. Pouquet, Inertial range structures in decaying compressible turbulent flows *Phys. Fluids* 10 :237-245, 1998
16. U. Schumann, Subgrid scale model for finite difference simulations of turbulent flows in plane channels and annuli, *J. Comput. Phys.* 18:376-404, 1975
17. P. K. Smolarkiewicz, A simple positive definite advection scheme with small implicit diffusion, *Mon. Weather Rev.* 111:479-486, 1983
18. P. K. Smolarkiewicz, A fully multidimensional positive definite advection transport algorithm with small implicit diffusion, *J. Comput. Phys.* 54:325-362, 1984
19. P. K. Smolarkiewicz, Multidimensional positive definite advection transport algorithm: an overview, *Int. J. Num. Meth. Fluids* 50:1123-1144, 2006.
20. P. K. Smolarkiewicz, L. G. Margolin, MPDATA: A finite-difference solver for geophysical flows, *J. Comput. Phys.* 140:459-480, 1998
21. Fourier analysis of numerical approximations of hyperbolic equations. *SIAM Studies in Applied mathematics*, SIAM Philadelphia, 1982.
22. P. R. Woodward, P. Colella, The numerical solution of two-dimensional fluid flow with strong shocks, *J. Comput. Phys.* 54:115-173, 1984
23. P. S. Zandonade, J. A. Langford, R. D. Moser, Finite-volume optimal large-eddy simulation of isotropic turbulence, *Phys. Fluids* 16:2255-2271, 2004

A challenging new problem for LES: the flow near the turbulent/nonturbulent interface

Carlos B. da Silva

IDMEC/IST, Pav. Mec. I/LASEF,
Av. Rovisco Pais 1049-001 Lisboa,
Portugal
`Carlos.Silva@ist.utl.pt`

1 Introduction

This work addresses a challenging and new problem for large-eddy simulations (LES) that exists in free shear flows. These flows can be divided into two regions: in the outer region the flow is largely irrotational whereas in the inner region the flow is turbulent. These two regions are separated by a sharp interface - the turbulent/nonturbulent (T/NT) interface - where the turbulent entrainment, by which a given fluid element from the irrotational flows region becomes turbulent, takes place. It was assumed in the past that the turbulent entrainment was mainly caused by large-scale engulfing motions [1], but recent experimental and numerical works [2, 3] give support to the original idea from [4] where the entrainment is caused by small scale eddy-motions (nibbling).

Moreover, it has been show that important Reynolds stresses exist in the irrotational flow region near the T/NT interface [5]. Since the Reynolds stresses affect the small scale mixing near the T/NT interface it is important to study the influence of several subgrid-scale models in this new and challenging context, since a deficient prediction of these stresses near the T/NT interface will affect important issues such as mixing and combustion, which take place at that location.

2 Direct numerical Simulation of turbulent plane jets

Direct and large-eddy simulations (DNS/LES) were used. The reference DNS is from a developed turbulent plane jet at $Re_\lambda \approx 120$ [6] (Fig. 1(a)). Specifically, we do *a-priori* and *a-posteriori* tests based on this data bank, using conditional statistics *i.e.* statistics in relation to the distance from the turbulent/non-turbulent (T/NT) interface y_I , that separates the turbulent from the irrotational flow regions (Fig. 1(b)).

To show the interest of these statistics, the conditional vorticity components are shown in Fig. 2(a), displaying the existence of a sharp jump at the T/NT interface with a width close to the Taylor micro-scale, in agreement with Westerweel *et al.* [2]. Moreover, the conditional normal Reynolds stresses near the T/NT interface (Fig. 2(b)) show the existence of significant values at the irrotational region.

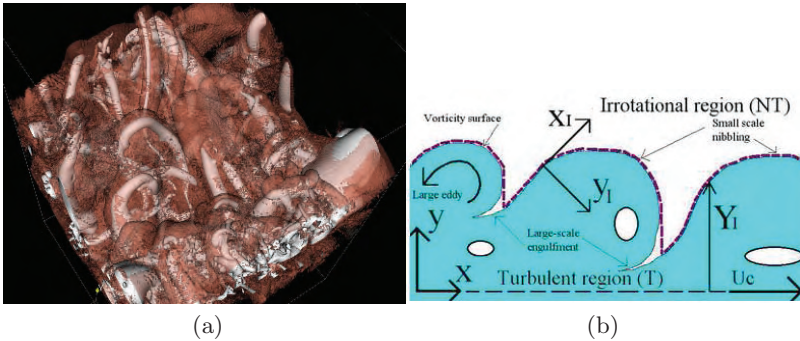


Fig. 1. (a) Intense vorticity structures (white) and the T/NT interface (red); (b) Sketch of the T/NT interface, where a local reference frame is used to perform the conditional statistics.

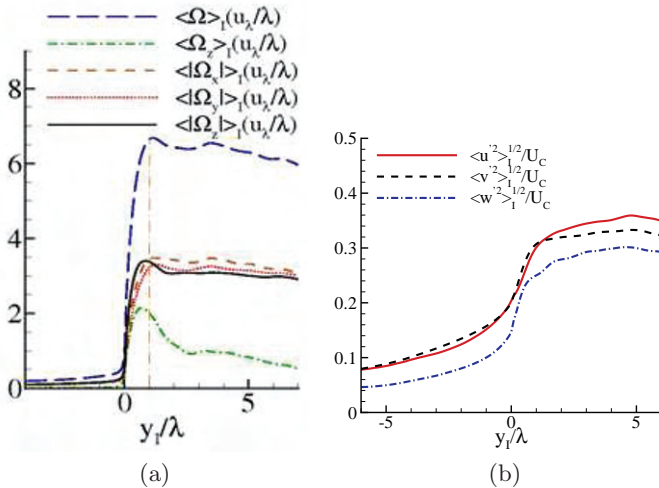


Fig. 2. (a) Conditional mean profiles of the vorticity components; (b) Conditional mean profiles of Reynolds stresses (DNS).

3 Results and discussion

Figure 3(a) illustrates the challenge faced by LES in this context. The figure displays conditional profiles of twice the total kinetic energy $u_i u_i$, SGS kinetic energy τ_{ii} , and the ratio between these quantities. Deep inside the turbulent region $y_I/\lambda \approx 4$ only a small fraction of the energy (10-15%) is at the subgrid-scales, however, the value increases near the T/NT interface, where near 80% of the energy is at the unresolved scales due to the small level of total energy there.

The model constants from current subgrid-scale models near the T/NT interface can be determined in *a-priori* tests using the equilibrium assumption between production $\Pi = -\tau_{ij} \overline{S_{ij}}$ and dissipation of subgrid-scale kinetic energy $\varepsilon^\Delta = \nu \left[\frac{\partial \overline{u_i}}{\partial x_j} \frac{\partial \overline{u_i}}{\partial x_j} - \frac{\partial \overline{u_i}}{\partial x_j} \frac{\partial \overline{u_i}}{\partial x_j} \right]$. Figure 3(b) shows the Smagorinsky model constant C_S . As can be seen the model constant C_S is much too high near the irrotational region and should be corrected to avoid excessive dissipation of the Reynolds stresses at that location. A similar trend is observed for other classical subgrid-models such as the Structure Function or the Gradient models.

A-priori and *a-posteriori* tests showed that the dynamic procedure, although improving the results, does not solve the problem. This is due to the classical plane averaging procedure of the dynamics constant C_D that does not separate between turbulent and irrotational regions.

Several correcting measures to the SGS models are proposed that can improve the results for the Reynolds stresses near the T/NT interface, with consequences for mixing and combustion at the edge of a jet or a mixing layer.

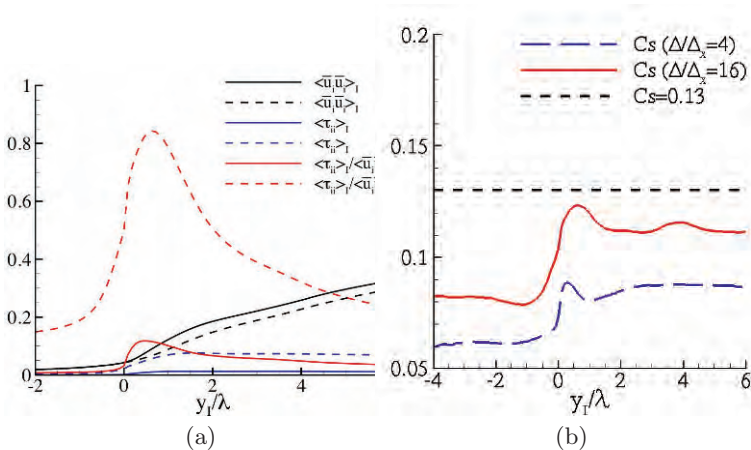


Fig. 3. Conditional mean profiles of: (a) Fraction of SGS energy at the SGS scales; (b) Smagorinsky model constant.

References

1. A. A. Townsend. *The Structure of Turbulent Shear Flow*, Cambridge, 1976.
2. J. Westerweel, C. Fukushima, J.M. Pedersen and J.C.R. Hunt. Mechanics of the turbulent/non-turbulent interface of a jet. *Phys. Review Lett.*, 95:174501, 2005.
3. J. Mathew and A. Basu. Some characteristics of entrainment at a cylindrical turbulent boundary. *Phys. Fluids*, 14(7):2065–2072, 2002.
4. S. Corrsin & A. L. Kistler. Free-stream boundaries of turbulent flows. Technical Report TN-1244, NACA, 1955.
5. D. K. Bisset, J. C. R. Hunt, and M. M. Rogers. The turbulent/non-turbulent interface bounding a far wake. *J. Fluid Mech.*, 451:383–410, 2002.
6. C. B. da Silva & J. C. F. Pereira. Invariants of the velocity-gradient, rate-of-strain and rate-of rotation tensors across the Turbulent/non-turbulent interface in jets. *Phys. Fluids*, 19:071702, 2007.

Towards practical large-eddy simulations of complex turbulent flows

J. Boudet^(a), A. Cahuzac^{(a),(b)}, P. Borgnat^(b), E. Lévêque^(b), F. Toschi^(c)

(a) Laboratoire de Mécanique des Fluides et d'Acoustique, Ecole Centrale de Lyon, Université de Lyon, CNRS, France

(b) Laboratoire de Physique, École normale supérieure de Lyon, Université de Lyon, CNRS, France

(c) Technische Universiteit Eindhoven, The Netherlands

`emmanuel.leveque at ens-lyon.fr`

Turbulence that occurs in nature, or in engineering flows, is usually not, even approximatively, homogeneous. There are frequent variations of the mean velocity with position. By explicating the scale-by-scale energy budget of non-homogeneous turbulence, it has been argued that the subgrid-scale (SGS) stress tensor should encompass two types of interactions [1, 2]: (i) between the mean velocity and the resolved fluctuating velocities (the rapid part of the SGS stress) and (ii) among the resolved fluctuating velocities themselves (the slow part of the SGS stress). The rapid part is related to the large-scale distortion, while the slow part is associated with the Kolmogorov's energy cascade [3]. Interestingly, these developments end up with a *shear-improved Smagorinsky model* (SISM) [1], for which the SGS viscosity writes

$$\nu_{\text{sgs}} = (C_s \Delta)^2 (|\bar{\mathcal{S}}| - \mathcal{S}). \quad (1)$$

$C_s \simeq 0.2$ is the Smagorinsky constant, Δ is the grid size and $|\bar{\mathcal{S}}| \equiv (2\bar{S}_{ij}\bar{S}_{ij})^{1/2}$ is the norm of the resolved rate-of-strain. Finally, $\mathcal{S} \equiv |\langle \mathcal{S} \rangle|$ is the *characteristic shear* associated with the mean flow. In practical simulations, $\mathcal{S} \simeq |\langle \bar{\mathcal{S}} \rangle|$.

Interestingly, the SISM does not call for any adjustable parameter nor ad-hoc damping function. It does not use any kind of dynamic adjustment either. However, a special care must be taken in estimating the ensemble-averaged rate-of-strain, $\langle \bar{\mathcal{S}} \rangle$. Ensemble average may be replaced by space average over homogeneous directions (whenever it is possible) or time average. This is adapted to simple-geometry flows or (statistically) stationary turbulent flows. This was the case of our first tests (which focused on SGS modeling errors) concerning a bi-periodic plane-channel flow [1] and a backward-facing step flow [4]. These results are promising as they indicate that the SISM possesses a predictive capacity essentially equivalent to the dynamic Smagorinsky model [5] but with a computational cost and a manageability comparable to the Smagorinsky model [6].

It is now our motivation to examine how the SISIM behaves in CFD solvers, which usually rely on a coarser grid and a lower-order discretization scheme, and apply to complex-geometry unsteady flows [8]. A procedure is introduced to evaluate the mean flow from the running velocity field. Our proposal is based on temporal smoothing that highlights longer-term trends or cycles but erases short-term fluctuations. Our physical assumption is that the mean velocity is given by the “low-frequency component” of the velocity, and that the turbulent part of the velocity adds itself to this “unsteady mean”. An exponentially-weighted moving average (or exponential smoothing) is considered.

At a given grid-point, the idea behind exponential smoothing is to update (at each time step) the previous estimate of the mean by taking into account the new instantaneous value. Let $u^{(n)}$ stand for a component of velocity and $[u]^{(n)}$ the estimated mean, at time n . The update writes

$$[u]^{(n+1)} = (1 - c_{exp.})[u]^{(n)} + c_{exp.}u^{(n+1)}, \quad (2)$$

where $[u]^{(0)} = u^{(0)}$ and $0 < c_{exp.} < 1$ is the smoothing factor. This algorithm acts as a low-pass filter with cut-off frequency f_c (at which the amplitude is reduced by half) approximated by $c_{exp.} \simeq 2\pi f_c \Delta t / \sqrt{3}$ (first-order filter), where Δt is the simulation time-step. In our fluid mechanical context, f_c should be identified with a “characteristic frequency of the flow”. The main advantage of this algorithm is its simplicity, both conceptually and in its implementation.

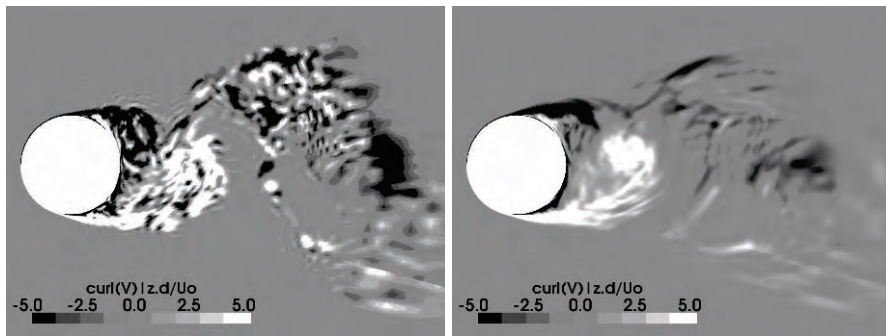


Fig. 1. Cylinder, $Re_D = 47000$. *Left:* instantaneous vorticity (non-dimensionnal). *Right:* vorticity of the exponentially-smoothed flow (non-dimensionnal).

The flow past a circular cylinder at $Re_D = 47000$ based on diameter D has been examined to test our modeling. In this regime, the flow develops laminar boundary-layers, moving separations, shear-layer transitions and vortex shedding. It is therefore a challenging test-case [7]. The LES was performed by using the *Turb'Flow* solver [8]. The numerical grid extends over $10D$ in the radial direction and $3D$ in the spanwise direction (with a periodic boundary condition). This grid encompasses 3×10^6 mesh-points with a resolution

$\Delta r^+ \lesssim 1$, $(D/2)\Delta\theta^+ \lesssim 20$ and $\Delta z^+ \lesssim 25$ (in wall units) in the turbulent separated region, following standard recommendations for LES [9]. In the smoothing algorithm, f_c is fixed at twice the value of the expected vortex-shedding frequency. This prescription *a priori* ensures that large eddies that detach from the cylinder are captured in the mean-flow reconstruction. Indeed, as shown in Fig.1, while the instantaneous flow presents numerous turbulent scales, the smoothed flow mostly captures the vortex shedding.

	simulation	data in literature
St : Strouhal number of the vortex shedding	0.19	[0.18, 0.20] ($Re_D = 4.8 \cdot 10^4$) [10] [0.185, 0.195] ($10^4 \leq Re_D \leq 10^5$) [11]
θ_s : mean separation angle	88°	$\simeq 83^\circ$ ($4.0 \cdot 10^4 \leq Re_D \leq 4.5 \cdot 10^4$) [11]
C_D : mean drag coefficient	1.34	[1.0, 1.35] ($Re_D = 4.8 \cdot 10^4$) [10] 1.35 ($Re_D = 4.3 \cdot 10^4$) [12] [1.0, 1.3] ($Re_D = 4.8 \cdot 10^4$) [13] [1.1, 1.3] ($10^4 \leq Re_D \leq 10^5$) [11]
C'_D : rms drag coefficient	0.09	[0.08, 0.1] ($Re_D = 4.8 \cdot 10^4$) [14] 0.16 ($Re_D = 4.3 \cdot 10^4$) [12] [0.05, 0.1] ($10^4 \leq Re_D \leq 10^5$) [11]
C'_L : rms lift coefficient	0.77	[0.4, 0.8] ($Re_D = 4.8 \cdot 10^4$) [14] [0.45, 0.55] ($Re_D = 4.3 \cdot 10^4$) [12] [0.6, 0.82] ($10^4 \leq Re_D \leq 10^5$) [11]

Table 1. Comparison of flow characteristics with experimental data.

The key flow characteristics are summarized in Table 1. The agreement is good with experimental data, concerning the vortex-shedding frequency and the mean or fluctuating forces. The mean separation angle appears over-estimated, but the numerical resolution in the region of the boundary-layer separation is about 2° ; the discrepancy is thus only two grid-points. In Fig.2, the angular profile of the mean-pressure coefficient is consistent with experimental data. The angular profile of the root-mean-squared fluctuations of the pressure coefficient is displayed in Fig.3. The overall behavior is well captured, with a maximum around the mean separation angle, but over-estimated. However, the data reported in the figure indicate a dependence on the Reynolds number which may explain, to some degree, the observed discrepancy.

In conclusion, our numerical results demonstrate the good predictive capacity of the method. From a computational viewpoint, this method deserves interests since it is “low-cost” and entirely local in space. It is therefore well adapted for parallelization. A refinement of the smoothing algorithm, in terms of a Kalman filter that adapts its smoothing frequency to the recent history of the signal, is currently investigated.

Acknowledgements: the simulation has been performed by using the local computing facilities, PSMN at ENS-Lyon.

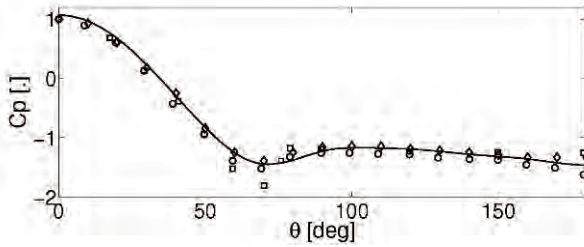


Fig. 2. Mean pressure coefficient around the cylinder. —: simulation at $Re_D = 4.7 \cdot 10^4$; \circ : exp. data at $Re = 4.0 \cdot 10^4$ [12]; \diamond : exp. data at $Re = 4.6 \cdot 10^4$ [15]; \square : exp. data at $Re = 10^5$ [13].

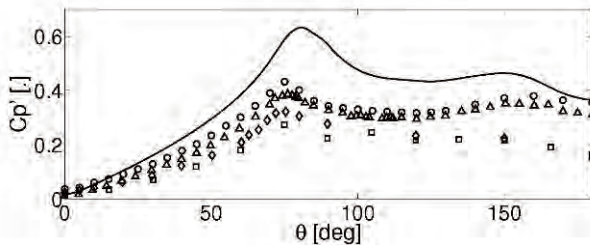


Fig. 3. RMS fluctuations of the pressure coefficient around the cylinder. —: simulation at $Re_D = 4.7 \cdot 10^4$; \circ : exp. data at $Re = 6.1 \cdot 10^4$ [17]; \triangle : exp. data at $Re = 6.1 \cdot 10^4$ [19]; \square : exp. data at $Re = 10^5$ [18]; \diamond : exp. data at $Re = 10^5$ [16].

References

1. E. L ev eque, F. Toschi, L. Shao & J.-P. Bertoglio, *J.Fluid Mech.* **570**, 491 (2007).
2. L. Shao, S. Sarkar & C. Pantano, *Phys. Fluids* **11**(5), 1229–1248 (1999).
3. S. Pope, *Turbulent Flows*, Cambridge University Press, Cambridge, UK (2000).
4. F. Toschi, H. Kobayashi, U. Piomelli & G. Iaccarino, *Proceedings of the Summer Program 2006*, Center for Turbulent Research, Stanford, USA (2006).
5. M. Germano *et al.*, *Phys. Fluids A*, **3**, 1760 (1991).
6. J. Smagorinsky, *Mon. Weather Rev.* **91**, 99 (1967).
7. M. Breuer, *Heat and Fluid Flow* **21**, 648 (2000).
8. J. Boudet *et al.*, *Journal of Thermal Science*, **16**(4), 328–336 (2007).
9. P. Sagaut, *Large Eddy Simulation for Incompressible Flows*, Springer (2001).
10. B. Cantwell and D. Coles. *J.Fluid Mech.* **136**, 321–374 (1983).
11. M. M. Zdravkovich, *Oxford University Press* (2002).
12. S. Szepessy and P. W. Bearman. *J.Fluid Mech.* **234**, 191–217 (1992).
13. E. Achenbach. *J. Fluid Mech.* **34**, 625–639 (1968).
14. J. H. Gerrard. *J.Fluid Mech.* **11**, 244–256 (1961).
15. E. A. Anderson and A. A. Szewczyk. *Exp. in Fluids* **23**, 161-174 (1997).
16. S. Yokuda and B. R. Ramaprian. *Phys. Fluids A* **2** (5), 784–791 (1990).
17. H. Nishimura and Y. Taniike. *J. Wind Eng. Ind. Aerodyn.* **89**, 713-723 (2001).
18. J. P. Batham. *J. Fluid Mech.* **57**, 209 (1973).
19. C. Norberg. *J. Fluids Struct.* **17**, 57-96 (2003).

Coherent Vortex Simulation: application to 3D homogeneous isotropic turbulence

N. Okamoto¹, K. Yoshimatsu², K. Schneider³, M. Farge⁴ and Y. Kaneda²

¹ Center for Computational Science, Graduate School of Engineering, Nagoya University, Nagoya, 464-8603, Japan okamoto@ccs.engg.nagoya-u.ac.jp

² Department of Computational Science and Engineering, Nagoya University, Nagoya, 464-8603, Japan

³ M2P2–CNRS & CMI, Université de Provence, 39 rue Frédéric Joliot-Curie, 13453 Marseille Cedex 13, France

⁴ LMD–IPSL–CNRS, Ecole Normale Supérieure, 24 rue Lhomond, 75231 Paris Cedex 05, France

1 Introduction

Self-organization and formation of active regions in fully developed turbulent flow are observed in many physical quantities, such as vorticity or energy dissipation. The regions are not distributed homogeneously and exhibit spatial intermittency. Wavelet analysis is a prominent tool to allow a sparse representation of intermittent fields [1]. Wavelets, well-localized functions both in physical and spectral space, decompose a given flow field into scale-space contributions.

The Coherent Vortex Extraction (CVE) method, a wavelet nonlinear filtering method based on orthogonal wavelet, has been introduced in [2]. The coherent vorticity ω_c is reconstructed from few wavelet coefficients of ω , whose modulus is larger than a given threshold motivated by denoising theory [3]. The coherent vortices are thus retained, together with most of the energy and the statistics are similar to the one of the total vorticity. The incoherent vorticity field ω_i reconstructed from the remaining wavelet coefficients is structureless and contains no vortex tubes.

A turbulence model based on CVE, called coherent vortex simulation (CVS), has been proposed in [2, 4]. The CVS method is a technique for computing and modeling turbulent flows. It is based on the deterministic computation of the evolution of coherent flow in an adaptive wavelet basis, while neglecting the influence of the remaining incoherent background flow to model turbulent dissipation. The wavelet filter dynamically adapts to the flow evolution and thus changes with time. A safety zone is hence required to predict the translation of coherent vortices and the generation of smaller scales due to their nonlinear interaction [5]. The efficiency of CVS is directly

related to flow intermittency and thus increases with the Reynolds number as suggested in [6].

In this paper, we examine the potential of CVS for three-dimensional decaying homogeneous isotropic turbulence at the initial Taylor-microscale Reynolds number $R_\lambda = 167$ [7]. This canonical flow allows to assess the performance of CVS in the fully developed turbulent regime. Due to its statistical homogeneity, this turbulent flow is the most challenging flow to test the validity and performance of CVS.

2 Methodology

The CVE method decomposes $\boldsymbol{\omega}$ into $\boldsymbol{\omega}_c$ and $\boldsymbol{\omega}_i$, satisfying $\boldsymbol{\omega} = \boldsymbol{\omega}_c + \boldsymbol{\omega}_i$. Applying the Biot-Savart operator $-\nabla^{-2}\nabla\times$ to $\boldsymbol{\omega}$, $\boldsymbol{\omega}_c$ and $\boldsymbol{\omega}_i$, we obtain the total \mathbf{u} , coherent \mathbf{u}_c and incoherent \mathbf{u}_i velocity fields, respectively. Each velocity field satisfies the divergence free condition. The wavelet filtered Navier-Stokes equations, written in vorticity-velocity formulation, are obtained by substituting the coherent-incoherent decompositions of the total vorticity and velocity into the equation. Neglecting the influence of $\boldsymbol{\omega}_i$ and \mathbf{u}_i , we get the evolution equation for $\boldsymbol{\omega}_c$,

$$\partial_t\boldsymbol{\omega}_c + \mathbf{u}_c \cdot \nabla\boldsymbol{\omega}_c - \boldsymbol{\omega}_c \cdot \nabla\mathbf{u}_c - \nu\nabla^2\boldsymbol{\omega}_c = \mathbf{0}, \quad (1)$$

where ν denotes the kinematic viscosity.

Retaining the coherent wavelet coefficients only is not sufficient to catch the flow evolution and adding a safety zone in the vicinity of the retained wavelet coefficients is of primordial importance, as shown in [8]. Here, we set a safety zone in space, direction and scale in the wavelet space by the same way as that used in [5].

3 Numerical Results

We performed two numerical simulations of freely-decaying homogeneous isotropic turbulence, one DNS reference computation and one CVS computation with the safety zone. For the numerical solutions of equation (1) we use a classical Fourier pseudo-spectral code based on the velocity-pressure formulation and a fourth-order Runge-Kutta method for time marching. The resolution is $N^3 = 256^3$, the kinematic viscosity $\nu = 7.0 \times 10^{-4}$ and the time increment $\Delta t = 1.0 \times 10^{-3}$. An initial velocity field for each simulation is a statistically stationary flow of isotropic turbulence at $R_\lambda = 167$ obtained by DNS [9]. These simulations are carried out up to $3T_0$. Here, T_0 is one large eddy turn over time defined by L/u' . The symbol L is the integral length scale defined by $L = \pi/(2u'^2) \int_0^\infty k^{-1}E(k)dk$, $E(k)$ is the energy spectrum and $u'^2 = \langle \mathbf{u}^2 \rangle / 3$.

Figure 1 shows time evolutions of the kinetic energy for DNS and CVS. The two curves almost superimpose. The ratio of the number of degrees of freedom including the safety zone in CVS to that of DNS is about 30% and almost independent of time. Energy spectra $E(k)$ for DNS and CVS at $t = T_0$ are plotted in Fig. 2. The spectrum of CVS is in good agreement with that of DNS all along the inertial range. In the dissipative range, i.e. for $k\eta \gtrsim 0.3$, the spectrum of CVS differs from that of DNS, although CVS preserves a significant contribution in the dissipative range.

4 Conclusions and Discussions

We have performed CVS with a safety zone and DNS of three-dimensional decaying homogeneous isotropic turbulence at the initial Taylor microscale Reynolds number $R_\lambda = 167$ and resolution $N^3 = 256^3$. CVS retains only 30% of the wavelet coefficients compared to that of DNS, while CVS preserves low-order statistics of the flow.

In large eddy simulation, large scales in the inertial range are resolved and the effect of the discarded subgrid scales onto grid scales must be modeled by the retained grid scales with the aid of statistical theory of turbulence. In contrast, in CVS, the flow evolution can be computed without taking into account the effect of the discarded incoherent modes on the resolved coherent modes.

Fully adaptive CVS computations of three-dimensional turbulent flows can reduce both the memory requirements and the CPU time of the computations. The first example for three-dimensional weakly compressible mixing layers using an adaptive multiresolution method is shown in Ref. [10].

We will discuss high order statistics and different choices of the safety zone in [7], which shows that its appropriate choice reduces the degrees of freedom of CVS by a factor of six with respect to DNS, and that CVS preserves high-order statistics of turbulence as well as the above low order statistics.

Acknowledgement. The authors express their thanks to T. Ishihara for providing us with the DNS data at $R_\lambda = 167$.

References

1. M. Farge, *Annu. Rev. Fluid Mech.*, **24** 395, (1992)
2. M. Farge, K. Schneider and N. Kevlahan, *Phys. Fluids*, **11**, 2187, (1999).
3. D. Donoho, *IEEE Transaction on Information Theory* **41**, 613, (1995)
4. M. Farge and K. Schneider, *Flow. Turbul. Combust.*, **66**, 393, (2001).
5. K. Schneider, M. Farge, G. Pellegrino and M. Rogers, *J. Fluid Mech.*, **534**, 39, (2005).
6. N. Okamoto, K. Yoshimatsu, K. Schneider, M. Farge and Y. Kaneda. *Phys. Fluids*, **19**, 115109, (2007).

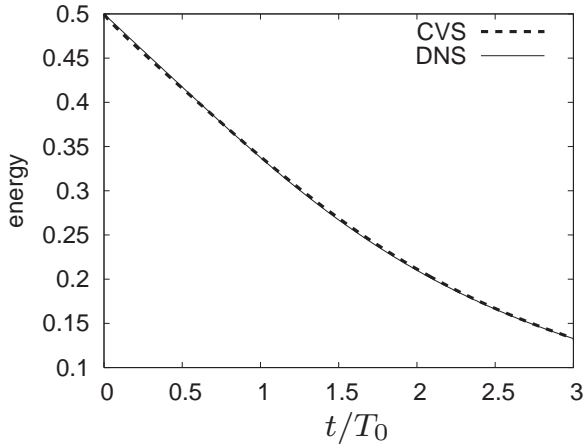


Fig. 1. Time evolution of kinetic energy for DNS and CVS.

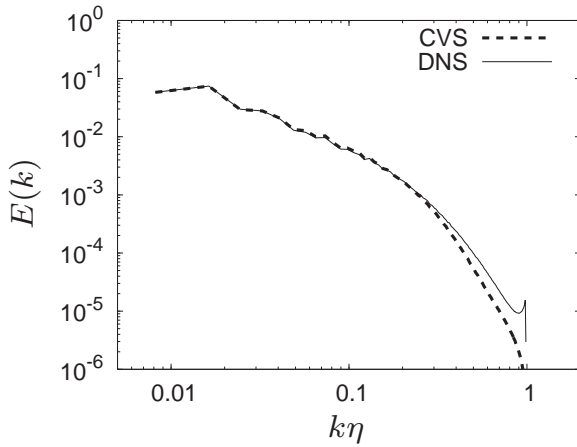


Fig. 2. Energy spectra for DNS and CVS at $t = T_0$. The wavenumber is normalized by the Kolmogorov length scale η of DNS at $t = T_0$.

7. N. Okamoto, K. Yoshimatsu, K. Schneider, M. Farge and Y. Kaneda (submitted)
8. K. Schneider, M. Farge, A. Azzalini and J. Zuber, *J. Turbul.*, **7** No. 44, 1, (2006).
9. Y. Kaneda, T. Ishihara, M. Yokokawa, K. Itakura, and A. Uno, *Phys. Fluids*, **15**, L21-L24, (2003).
10. O. Roussel and K. Schneider, under revision.

LES of a Non-Premixed Flame with an Assumed Tophat FDF

A.M. Kempf* and A. Kronenburg⁺

* Department of Mechanical Engineering, Imperial College London, UK

⁺ Institut für Technische Verbrennung, Universität Stuttgart, Germany

a.kempf@imperial.ac.uk, kronenburg@itv.uni-stuttgart.de

For Large-Eddy Simulation (LES) of combustion, the subgrid distribution of the reacting scalars must be known to calculate the thermochemical state and the reaction progress. In non-premixed combustion, the scalar concentrations can often be derived from a single 'passive' scalar, the mixture fraction f , of which the subgrid distribution or filtered density function (FDF) is often described by an assumed function. This assumed FDF is normally parameterised with the mixture fraction and its variance. The type of function can vary, but in the context of Reynolds Averaged Navier Stokes (RANS) simulations, where the equivalent probability density function (PDF) must be described, the β -function has proven to be a relatively simple and accurate description. Based on its success in RANS, the β -function has also been applied to LES.

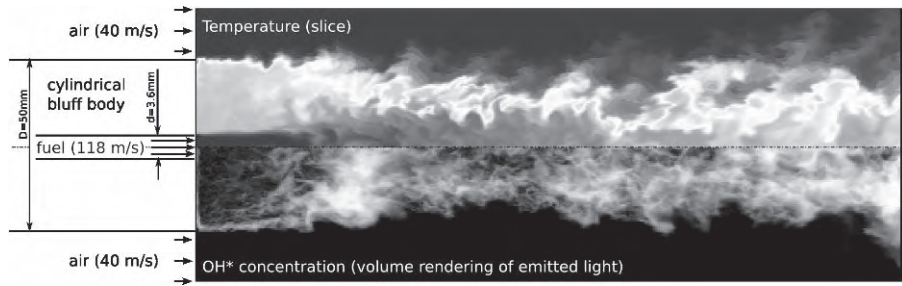


Fig. 1. Setup and instantaneous snapshots of the temperature field (top) and a view of the flame. The image-resolution corresponds to the grid-resolution.

However, Floyd et al. [1] have shown that while the β -function is well justified in RANS, the tophat function may be a more consistent FDF for LES than the β -function. The tophat-FDF shows the correct convergence behaviour for f''^2 approaching 0, whereas the β -function implies infinite scalar gradients in physical space. The tophat-FDF is also more consistent with the

typical LES-variance models and works well for multi-stream mixing. Interestingly, the inconsistencies of a β -FDF remain largely hidden when applied to an LES, as the type of the assumed FDF function becomes less important for small variances [8]. A very significant advantage of the tophat function is the improved computational efficiency and simplicity of the description. Where the β -integration requires non-trivial special treatments for variances approaching the maximum value or zero, the tophat-integration only requires a special treatment for the limit of zero. Most numerical implementations using assumed FDFs or PDFs rely on pre-integrated tables, which are two-dimensional when using β -FDFs, whereas the one-dimensional anti-derivative of the original table is sufficient with a tophat function – leading to reduced complexity, lower memory consumption, and faster table access-time.

The suitability of the tophat FDF is illustrated for the LES of the Sydney Bluff-Body burner [2], a much investigated non-premixed bluff-body stabilised methane-hydrogen flame, that has long been a target flame of the workshop on turbulent non-premixed flames (TNF) [3]. Aside from various RANS simulations of the flames, Large-Eddy Simulations have been presented by Raman and Pitsch [4], Navarro-Martinez and Kronenburg [5], and Kempf et al. [6], using grid-resolutions of typically one to three million cells. The flame as shown in Fig. 1 is stabilised on a cylindrical bluff-body located in a co-axial stream of air ($u_{air} = 40\text{m/s}$) that acts as oxidiser. The methane/hydrogen fuel (50/50 vol.) is injected into the recirculation zone downstream of the bluff-body, ejected from a central nozzle at $U_{jet} = 118\text{m/s}$. The air-flow and the jet-flow create two toroidal vortices downstream of the bluff-body with a recirculation zone inbetween, which provides hot combustion products to the unburnt fuel and air mixture, stabilising the flame.

The flow was simulated using the incompressible combustion LES code ‘ $\Psi\Phi$ ’ (PsiPhi) for general transported fields Φ and derived fields Ψ , which is based on structured, equidistant grids with collocated cells. It uses a third-order Runge-Kutta scheme and second-order central discretisation of all but the convective scalar fluxes: convection of the mixture fraction quantity $\tilde{\rho}\tilde{f}$ is discretised through a CHARM-TVD scheme, as numerical oscillations cannot be afforded due to the strong functional dependence of the density on mixture fraction ($|\partial\rho/\partial f|$ exceeds values of 20kg/m^3). Consistency of the density from transport and the combustion model was ensured using a projection method. The unresolved turbulent stresses are modelled with the classical Smagorinsky model providing a turbulent viscosity ν_t , that is also used to calculate the scalar subgrid fluxes from an eddy diffusivity model with the diffusion coefficient $D_t = \nu_t/\sigma_t$ involving the turbulent Schmidt number $\sigma_t = 0.7 \approx \sigma_{laminar}$. Pseudo turbulent inflow conditions satisfying both the Reynolds stress tensor and a realistic length-scale were created using an extended version [9] of Klein’s inflow-data generator. The chemical state is computed from a steady flamelet model for a single strain rate $a = 100/s$, calculated from a chemical mechanism by Lindstedt et al. [6]. The computational domain ($150^2 \times 200\text{mm}^3$) was discretised by approximately 40 million

cubic cells of 0.5^3 mm^3 . The simulations were run on 12 processor cores for 40 million nodes until a real time of 0.1s was reached after two times ten days.

The inflow conditions were taken from extrapolating the available experimental data upstream to ensure a good prediction of the flow-field, in a similar way as in previous simulations [4, 6]. Interestingly, previous simulations have shown that the total flame-length is largely determined by the width of the boundary layer on the outside of the bluff-body. Setting this boundary layer too thick will lead to a long recirculation zone, setting it thin will keep the recirculation zone short. However, if the flow-field is predicted properly, the scalar field can be compared to the experiments.

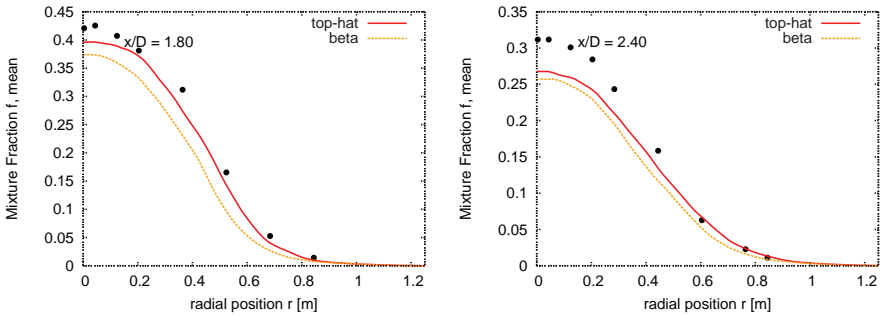


Fig. 2. Mean mixture fraction at axial distances of 1.8 and 2.4 nozzle diameters downstream of the exit plane.

Figure 2 shows the mixture fraction profiles at 1.8 and 2.4 burner diameters downstream of the bluff-body, illustrating that the flow and mixing fields do not change significantly when the β FDF is replaced with the top-hat function.

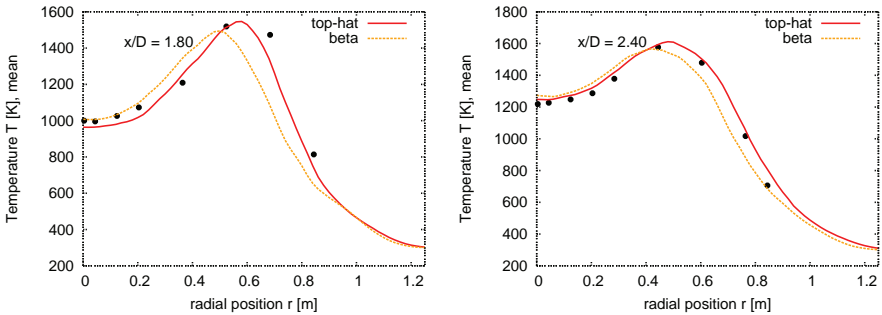


Fig. 3. Mean temperatures at axial distances of 1.8 and 2.4 nozzle diameters downstream of the exit plane.

Figure 3 shows radial profiles of the mean temperature at two different axial locations for two simulations using a top-hat FDF and a beta FDF respectively. Overall, the results agree well with the measurements, and on this fine grid, the move to the simpler, more consistent top-hat FDF does alter the results significantly. The results agree well with the experiment, however, the experimental data for the inflow-boundary condition is not sufficient to ensure a reproducible simulation.

The difference between simulations using the β -function and the tophat function are generally small due to the small subgrid variance in the scalar field. Implementing a tophat FDF is simple and less prone to error than implementing a β -function, as it avoids the special treatments required for variances approaching the maximum value. The tophat FDF also saves at least two orders of magnitude in storage space, as the dimensionality of the chemistry table is reduced by one. For this reason, the tophat FDF appears to be a natural choice for more sophisticated chemistry models, which require significant amounts of memory to store the chemical state as a function of many parameters.

The authors would like to acknowledge the support from EPSRC through COCCFEA (Consortium on Computational Combustion for Engineering Applications).

References

1. Floyd, J., Kempf, A., Kronenburg, A., Ram, R.H., A Simple Model for the Filtered Density Function for Passive Scalar Combustion LES, accepted (11/2008) for publication in Combustion Theory and Modelling.
2. Dally, B., Masri, A., Barlow, R., et al., Instantaneous Mean Compositional Structure of Bluff-Body Stabilized Non-Premixed Flames, Combust. Flame 114 (1998) 119-148.
3. Barlow, R., Proceedings of the International Workshop on Turbulent Non-premixed Flames, <http://www.ca.sandia.gov/TNF/>
4. Raman, V., Pitsch, H., Large-eddy simulation of a bluff-body-stabilized non-premixed flame using a recursive filter-refinement procedure, Combust. Flame 142 (2005) 329-347.
5. Navarro-Martinez, S., Kronenburg, A., LES-CMC simulations of a turbulent bluff-body flame, Proc. Combust. Inst. (2007) 1721-1728
6. Kempf, A., Lindstedt, R., Janicka, J., Large-eddy simulation of a bluff-body stabilized nonpremixed flame, Combust. Flame 144 (1-2) (2006) 170-189.
7. J. Smagorinsky, General circulation experiments with the primitive equations., Mon. Weather Rev. 91 (3) (1963) 99-164.
8. Jimenez, J., Linan, A., Rogers, M., Higuera, F., A priori testing of subgrid models for chemically reacting non-premixed turbulent shear flows, J. Fluid Mech. 349 (1997) 149-171.
9. Kempf, A., Klein, M., Janicka, J., Efficient generation of initial- and inflow-conditions for transient turbulent flows in arbitrary geometries, Flow, Turb. Combust. 74 (2005) 670-84.

Closure models for inhomogeneous turbulence

R. Rubinstein¹, W.J.T. Bos², D. Livescu³, and S.L. Woodruff⁴

¹Newport News, Virginia, USA

²LMFA-CNRS Ecole Centrale de Lyon, Université de Lyon, Ecully, France

³CCS Los Alamos National Laboratory, Los Alamos NM USA

⁴Florida State University, Tallahassee FL USA

arubin@hra.org

If ‘ideal’ turbulence is in a homogeneous, isotropic Kolmogorov steady state, then ‘non-ideal’ turbulence can occur due to time-dependence, anisotropy, or inhomogeneity. Whereas in kinetic theory, significant departure from a weakly perturbed local Maxwellian is exceptional, the analogous state of non-ideal turbulence is what is typical; although it would be inaccurate to state that homogeneous isotropic turbulence is more common in theory than in practice, the absence of a usable and defensible theory of inhomogeneous turbulence should not be ignored.

Although Kraichnan formulated the direct interaction approximation for inhomogeneous anisotropic turbulence [1] as early as 1964, such two-point closure theories have never been applied because of their apparent computational intractability. But the difficulties are also conceptual: whereas triad interactions provide a simple key to the physical meaning of closure in the homogeneous case, nothing comparable appears to exist for inhomogeneity. This study hopes to suggest ways to extract information from these seemingly unusable theories by restricting attention to problems in which the flow region exhibits enough symmetry to allow useful kinematic simplifications.

First consider inhomogeneous turbulence in free space, so that the flow domain admits arbitrary spatial translations. Given the two-point correlation $U(\mathbf{x}, \mathbf{x}')$, define $U(\mathbf{x}, \mathbf{x}'; \mathbf{K}) = \int d\mathbf{y} U(\mathbf{x} + \mathbf{y}, \mathbf{x}' + \mathbf{y}) \exp(i\mathbf{y} \cdot \mathbf{K})$. Then

$U(\mathbf{x}, \mathbf{x}') = \int d\mathbf{K} U(\mathbf{x}, \mathbf{x}'; \mathbf{K})$, and the ‘representation’ property [2]

$U(\mathbf{x} + \mathbf{a}, \mathbf{x}' + \mathbf{a}; \mathbf{K}) = U(\mathbf{x}, \mathbf{x}'; \mathbf{K}) \exp(-i\mathbf{K} \cdot \mathbf{a})$ imply a decomposition of the correlation function into components $U(\mathbf{x} - \mathbf{x}'; \mathbf{K}) \equiv U(\mathbf{x} - \mathbf{x}', \mathbf{0}; \mathbf{K})$. For a homogeneous flow field, $\mathbf{K} = 0$. Fourier transformation in the difference variable leads to the inhomogeneous field descriptors $U(\mathbf{k}; \mathbf{K})$, in terms of which two-time closure [1] has the form

$$\begin{aligned} \dot{U}(\mathbf{k}; \mathbf{K}) = & -2P(\mathbf{k} + \mathbf{K})G(\mathbf{p}; \mathbf{P})P(\mathbf{p} + \mathbf{P})U(\mathbf{q}; \mathbf{Q})U(\mathbf{k} + \mathbf{K}; \mathbf{K}) \\ & + P(\mathbf{k} + \mathbf{K})P(\mathbf{k} + \mathbf{K})U(\mathbf{p}; \mathbf{P})U(\mathbf{q}; \mathbf{Q})G(\mathbf{k} + \mathbf{K}; \mathbf{K}) \end{aligned} \quad (1)$$

where \mathbf{P} is the nonlinear coupling with the pressure eliminated and \mathbf{G} is the response tensor [1]. Tensor indices, time arguments and time integrations have been suppressed. Integration over \mathbf{p} and \mathbf{P} is understood, with the conditions $\mathbf{K} = \mathbf{P} + \mathbf{Q}$ and $\mathbf{k} + \mathbf{K} = \mathbf{p} + \mathbf{q}$. Finally, we note that in a Markovianized theory [3], a tensor, but assume for simplicity, a scalar relaxation time $\Theta(\mathbf{k}, \mathbf{p}, \mathbf{q}; \mathbf{K}, \mathbf{P}, \mathbf{Q})$ enters in order to replace two-time quantities by single-time counterparts. Eq. (1) is found by transforming integrals in [1] $a(\mathbf{x}, \mathbf{x}') = \int d\mathbf{y} b(\mathbf{x}, \mathbf{y})c(\mathbf{y}, \mathbf{x}')$ into $a(\mathbf{k}; \mathbf{K}) = \int d\mathbf{P} b(\mathbf{k}; \mathbf{P})c(\mathbf{k} + \mathbf{P}; \mathbf{Q})$ where $\mathbf{K} = \mathbf{P} + \mathbf{Q}$. Eq. (1) exhibits inhomogeneous turbulence as the nonlinear interaction of the quasi-homogeneous quantities $\mathbf{U}(\mathbf{k}; \mathbf{K})$.

The reduction to closure for homogeneous turbulence when $\mathbf{K} = \mathbf{P} = \mathbf{Q} = 0$ is immediate, and homogeneous turbulence trivially satisfies the general inhomogeneous closure equation. Despite the striking resemblance to the homogeneous equations, there is a crucial modification of the nonlinear coupling by the translation of the wavevector arguments of \mathbf{P} and the appearance of the modified triad condition $\mathbf{k} + \mathbf{K} = \mathbf{p} + \mathbf{q}$. In homogeneous turbulence, the properties of $\mathbf{P}(\mathbf{k})$ are crucial to Kraichnan's detailed conservation property for wavevector triads $S(k|p, q) + S(p|q, k) + S(q|k, p) = 0$. The absence of any analogous general relation for the quantities $S(\mathbf{k}, \mathbf{p}, \mathbf{q}; \mathbf{K}, \mathbf{P}, \mathbf{Q})$ defined by the right side of Eq. (1) is the most important effect of inhomogeneity, which couples transfer with respect to both \mathbf{k} and \mathbf{K} .

Some basic properties of inhomogeneous turbulence can be formulated and analyzed in these terms.

1. *inviscid truncated system*: The tendency of the truncated Euler system to inviscid equipartition implies both the development of small scale excitation and the suppression of inhomogeneity. The first trend suggests the transfer of energy to modes with large k , whereas the second indicates the opposite tendency to transfer energy to nearly homogeneous modes with $K \approx 0$. Equivalently, turbulence is expected to become fine-grained and at the same time to spread out, not contract. These trends should be consistent with Eq. (1).
2. *recovery of homogeneity at small scales*: Although the scale of inhomogeneity described by \mathbf{K} is not restricted, it is natural to consider the turbulence scales that are smaller than the scales of the inhomogeneity, so that $k \ll K$. Then it is evident that since K/k becomes smaller as $k \rightarrow \infty$, small scales are 'more homogeneous' than large scales.
3. *return to homogeneity*: We expect that during free relaxation of initially inhomogeneous turbulence with $\mathbf{K} \neq 0$, $U(\mathbf{k}, \mathbf{K})/U(\mathbf{k}, \mathbf{0}) \rightarrow 0$ ($U = \text{tr}U$) with increasing time. This property should be a consequence of properties 1 and 2.
4. *Nonlinear coupling between inhomogeneity and anisotropy* is a consequence of Eq. (1) because the wavevector arguments $\mathbf{k} + \mathbf{K}$ make the distribution of energy in \mathbf{k} anisotropic as soon as $\mathbf{K} \neq 0$. It should be noted that

this coupling does not occur in simpler spherically averaged models of inhomogeneous turbulence like that of [4], where anisotropy can only be generated by linear mechanisms or assumed as an initial condition.

A systematic theory of *perturbation about homogeneous, isotropic turbulence* generalizing the analysis of time dependence alone in [5] can be developed that makes contact with Yoshizawa’s two-scale direct interaction approximation [6]. For this, begin with a spatially homogeneous solution $U(\mathbf{k}) = U(k; \varepsilon, \mathcal{E})P_{ij}(\mathbf{k})$, where ε and \mathcal{E} are the dissipation rate and turbulent kinetic energy. Next consider the inhomogeneous ‘normal solution’ $U^0(\mathbf{k}; \mathbf{K}) = U^0(k; \varepsilon(\mathbf{K}), \mathcal{E}(\mathbf{K}))P_{ij}(\mathbf{k})$ which is inhomogeneous only through $\varepsilon(\mathbf{K})$ and $\mathcal{E}(\mathbf{K})$. Substitution in Eq. (1) generates error terms due to inhomogeneity; following [5], adding a locally isotropic correction U_i^1 to the correlation generates an inhomogeneous integral equation for U_i^1 . The compatibility conditions to solve it yield closed equations for $\varepsilon(\mathbf{K})$ and $\mathcal{E}(\mathbf{K})$. The adjoint solutions needed to form the compatibility conditions are exactly the same as those for perturbations that are homogeneous and isotropic, but time-dependent.

As stated in property 4 above, substitution of U^0 in Eq. (1) will also generate anisotropic terms which cannot be balanced by U_i^1 . This issue requires the representation theory of the rotation group [7]. In terms of this theory, lowest order anisotropy is described by two second rank trace-free tensors H^e and H^z by [8]

$$\begin{aligned}
 U_a^1(\mathbf{k}; \mathbf{K}) = & -15\Pi(\mathbf{k})H^e(k; \mathbf{K}) : \mathbf{k}\mathbf{k} + 5[\Pi(\mathbf{k})H^z(k; \mathbf{K})\Pi(\mathbf{k}) \\
 & + \Pi(\mathbf{k})H^z(k; \mathbf{K}) : \mathbf{k}\mathbf{k}]
 \end{aligned}
 \tag{2}$$

Here, Π is the transverse projection operator; for unambiguous index notation, refer to [8]. Adding the correction U_a^1 to the perturbation expansion, and separating the error terms generated by inhomogeneity into irreducible components under the rotation group, the compatibility conditions to cancel these errors will provide relations for integrals over the k arguments of H^e and H^z . These averages will be connected to the *structure tensors* of Kassinos and Reynolds [9]. We stress that the result in this case will be ‘algebraic’ models that express the relevant averages of H^e and H^z (including the Reynolds stresses: compare [8]) as explicit functionals of $\varepsilon(\mathbf{K})$ and $\mathcal{E}(\mathbf{K})$. A different formalism is required to obtain a stress transport model; this question will be addressed briefly below.

The usual introduction of sum and difference variables [4, 10] states exactly the same geometric ideas, but representation theory has an advantage if we consider the less elementary problem of turbulence in the half-space $z \geq 0$; this problem illustrates the treatment of boundaries, which has not been possible in previous inhomogeneous theories without severe truncation of the dynamics [10]. The flow domain admits arbitrary translations in the $\mathbf{x} = (x, y)$ plane, but translations in z are replaced by scaling transformations $z \rightarrow \lambda z$ with $\lambda > 0$. The invariant fields have the self-similar struc-

ture $U(\mathbf{x}, \mathbf{x}'; z, z') = U\left(\frac{\mathbf{x} - \mathbf{x}'}{z'}; \frac{z}{z'}\right)$ used in Lumley's analysis [11] of energy transfer in wall-bounded flows; compare also the self-similar properties of the problem analyzed by Oberlack and Günther [12]. Define

$$U(\mathbf{x}, \mathbf{x}'; z, z' : \mathbf{K}; \lambda) = \int d\mathbf{y} \int \frac{d\alpha}{\alpha} U(\mathbf{x} + \mathbf{y}, \mathbf{x}' + \mathbf{y}; \alpha z, \alpha z') \exp i(\mathbf{y} \cdot \mathbf{K}) \alpha^{i\lambda} \quad (3)$$

so that the invariant fields have $\mathbf{K} = 0$ and $\lambda = 1$. Note that $d\alpha/\alpha$ is the invariant measure on the scaling group: the construction (3) using invariant integration and multiplication by group characters is a standard formulation in group representation theory [2]. We repeat that this is not a decomposition into 'modes,' but into quantities with distinct transformation properties under the symmetry operations admitted by the flow domain.

We omit the straightforward expression of the closure equations in these variables that is analogous to Eq. (1). We assume that the self-similar state $\mathbf{K} = 0$, $\lambda = 1$ is known completely, and we ask how it behaves under perturbations that break the scaling invariances responsible for self-similarity [12]. Properties analogous to those of turbulence in free space can be formulated, including the recovery of self-similarity at small scales and a return to self-similarity in time under removal of symmetry-breaking perturbations.

The deductive theory of perturbations about a self-similar state has one important new feature, namely that the reference state must be anisotropic. In this case, the anisotropic descriptors of Eq. (2) appear in the lowest order solution. Departure from self-similarity will generate error terms depending on gradients of H^e and H^z ; the compatibility conditions to cancel these error terms will be transport equations for suitable moments of H^e and H^z .

References

1. R. H. Kraichnan, *Phys. Fluids*, **7**, 1049 (1964).
2. N. Y. Vilenkin, *Special functions and the theory of group representations*, American Mathematical Society 1968.
3. R. H. Kraichnan, *J. Fluid Mech.* **56**, 287 (1972).
4. D. Besnard, F. H. Harlow, R. M. Rauenzahn, and C. Zemach, *Theor. Comput. Fluid Mech.*, **8**, 1 (1996).
5. S. L. Woodruff and R. Rubinstein, *J. Fluid Mech.*, **565**, 95 (2006).
6. A. Yoshizawa, *Phys. Fluids* **27**, 1377 (1984).
7. I. Arad, V.S. L'vov, and I. Procaccia, *Phys. Rev. E*, **59**, 6753 (1999).
8. C. Cambon and R. Rubinstein, *Phys. Fluids* **18**, 085106 (2006).
9. S. Kassinos, W. C. Reynolds and M. Rogers, *J. Fluid Mech.* **428**, 213 (2000).
10. H. Touil, *Dissertation*, Lyon I (2002).
11. J. L. Lumley, *Phys. Fluids*, **7**, 190 (1964).
12. M. Oberlack and S. Guenther, *Fluid Dyn. Res.*, **33**, 453 (2003).

Statistical Mechanics of Fluid Turbulence based on the Cross-Independence Closure Hypothesis

Tomomasa Tatsumi

Kyoto University (Professor Emeritus)

1.1 Introduction

Statistical theory of turbulence based on the *cross-independence closure hypothesis* has been constructed successfully for *homogeneous isotropic turbulence* by Tatsumi & Yoshimura (2004, 2007). Now it is extended to *inhomogeneous turbulence*. The basic equations for the one-point velocity distribution and the velocity-sum and velocity-difference distributions are obtained. As the first step to inhomogeneous turbulence, *turbulent wakes* behind a spherical or cylindrical body are obtained by the superposition of an one-point binormal velocity distribution and a uniform flow.

1.2 Cross-independence Closure Hypothesis

Complete statistical description of turbulence is given by an infinite set of the Lundgren-Monin equations (1967) for the multi-point velocity distributions $f^{(n)}(\mathbf{v}_1, \dots, \mathbf{v}_n; \mathbf{x}_1, \dots, \mathbf{x}_n; t)$, where \mathbf{v}_m ($m = 1, \dots, n$) denote the probability variables corresponding to the turbulent velocities $\mathbf{u}_m = \mathbf{u}(\mathbf{x}_m, t)$. In practice, we have to deal with its finite subset and then encounter the difficulty of *unclosedness* since the equation for the distribution $f^{(n)}$ always includes a distribution $f^{(n+1)}$ as new unknown. In order to overcome this difficulty, a *closure hypothesis* is introduced. The simplest hypothesis is the "quasi-normal approximation" relating the one- and two-point velocity distributions as

$$f^{(2)}(\mathbf{v}_1, \mathbf{v}_2; \mathbf{x}_1, \mathbf{x}_2; t) = f(\mathbf{v}_1, \mathbf{x}_1, t) f(\mathbf{v}_2, \mathbf{x}_2, t). \quad (1.1)$$

This relation is valid for large distance $r = |\mathbf{r}| = |\mathbf{x}_2 - \mathbf{x}_1|$ but definitely not for small r , and actually the latter defect is the common weakness of the theories based on this sort of approximation.

On the other hand, if we consider the *sum* $\mathbf{u}_+ = (\mathbf{u}_1 + \mathbf{u}_2)/2$ and the *difference* $\mathbf{u}_- = (\mathbf{u}_2 - \mathbf{u}_1)/2$ of the velocities \mathbf{u}_1 and \mathbf{u}_2 , and assume the similar relation as (1.1) for the one and two-body distributions,

$$g^{(2)}(\mathbf{v}_+, \mathbf{v}_-; \mathbf{x}_1, \mathbf{x}_2; t) = g_+(\mathbf{v}_+; \mathbf{x}_1, \mathbf{x}_2; t) g_-(\mathbf{v}_-; \mathbf{x}_1, \mathbf{x}_2; t), \quad (1.2)$$

this relation gives a new hypothesis which may be called the *cross-independence closure hypothesis* (Tatsumi (2001)). Unlike the former hypothesis, this hypothesis is shown to be valid for both large and small values of r , and the latter validity, which has been proved experimentally by Sreenivasan et al.(1998), is crucial for the present case since the equation for the distribution $f^{(n)}$ includes the higher distributions $f^{(n+1)}$ only in their degenerate forms of vanishing distances $|\mathbf{x}_{n+1} - \mathbf{x}_m| \rightarrow 0$ ($m = 1, \dots, n$).

It may be noted that this hypothesis is similar to Kolmogorov’s (1941) hypothesis which assumes the independence of small eddies represented by the velocity-difference $\Delta \mathbf{u} = 2\mathbf{u}_-$ from large eddies represented by the velocities \mathbf{u}_1 and \mathbf{u}_2 . This is true, but it should be noted that his theory assumes *steady* turbulence while the present theory is concerned with *decaying* homogeneous turbulence.

1.3 Inhomogeneous Turbulence

First, the turbulent velocity $\mathbf{u}(\mathbf{x}, t)$ is decomposed into its probability mean $\bar{\mathbf{u}}(\mathbf{x}, t) = \langle \mathbf{u}(\mathbf{x}, t) \rangle$ and the fluctuation around the mean $\hat{\mathbf{u}}(\mathbf{x}, t) = \mathbf{u}(\mathbf{x}, t) - \bar{\mathbf{u}}(\mathbf{x}, t)$. If we take the fluctuation velocities at two points $\hat{\mathbf{u}}_i(t) = \hat{\mathbf{u}}(\mathbf{x}_i, t)$ ($i = 1, 2$), the joint probability distributions of these velocities are defined as $f(\mathbf{v}_1, \mathbf{x}_1, t)$ and $f^{(2)}(\mathbf{v}_1, \mathbf{v}_2; \mathbf{x}_1, \mathbf{x}_2; t)$ which is written according to Eq.(1.2) as

$$f^{(2)}(\mathbf{v}_1, \mathbf{v}_2; \mathbf{x}_1, \mathbf{x}_2; t) = 2^{-3} g^{(2)}(\mathbf{v}_+, \mathbf{v}_-; \mathbf{x}_1, \mathbf{x}_2; t) = 2^{-3} g_+(\mathbf{v}_+; \mathbf{x}_1, \mathbf{x}_2; t) g_-(\mathbf{v}_-; \mathbf{x}_1, \mathbf{x}_2; t). \quad (1.3)$$

Thus, the equations for the one-point velocity distribution f , the velocity-sum distribution g_+ and the velocity-difference distribution g_- are obtained in a closed form using the Lundgren-Monin equations for the distributions f and $f^{(2)}$ and the *cross-independence closure hypothesis*. Here, only the equation for the distribution f is cited as follows:

$$\left[\frac{\partial}{\partial t} + (\bar{\mathbf{u}} + \mathbf{v}) \cdot \frac{\partial}{\partial \mathbf{x}} - \left(\frac{\partial}{\partial \mathbf{x}} \cdot \mathbf{v} \right) \bar{\mathbf{u}} \cdot \frac{\partial}{\partial \mathbf{v}} - \nu \left| \frac{\partial}{\partial \mathbf{x}} \right|^2 + \alpha(\mathbf{x}, t) \left| \frac{\partial}{\partial \mathbf{v}} \right|^2 - \frac{\partial}{\partial \mathbf{v}} \cdot \frac{\partial}{\partial \mathbf{x}} \beta(\mathbf{v}, \mathbf{x}, t) \right] f(\mathbf{v}, \mathbf{x}, t) = 0, \quad (1.4)$$

$$\alpha(\mathbf{x}, t) = \varepsilon(\mathbf{x}, t) / 3 = \frac{2}{3} \lim_{\mathbf{r} \rightarrow 0} \left| \frac{\partial}{\partial \mathbf{r}} \right|^2 \int |\mathbf{v}_-|^2 g_-(\mathbf{v}_-; \mathbf{x}, \mathbf{r}; t) d\mathbf{v}_-, \quad (1.5)$$

$$\beta(\mathbf{v}, \mathbf{x}, t) = \frac{1}{4\pi} \int \int \frac{1}{|\mathbf{r}|} \left((\mathbf{v} + 2\mathbf{v}_-) \cdot \frac{\partial}{\partial \mathbf{r}} \right)^2 \left(1 + \mathbf{v}_- \cdot \frac{\partial}{\partial \mathbf{v}} \right) g(\mathbf{v}_-; \mathbf{x}, \mathbf{r}; t) \, d\mathbf{r} d\mathbf{v}_-, \tag{1.6}$$

where the suffixes are omitted and $\varepsilon(\mathbf{x}, t) = \nu \sum_{i,j=1}^3 \langle (\partial \hat{u}_i(\mathbf{x}, t) / \partial x_j)^2 \rangle$ denotes the *energy-dissipation rate* as a function of \mathbf{x} and t .

The set of equations for the distributions f , g_+ and g_- together with that for the mean velocity $\bar{\mathbf{u}}$ constitute the closed set of dynamic equations for *inhomogeneous turbulence* in general. In principle, all kinds of inhomogeneous turbulence can be dealt with by means of this set of equations under appropriate initial and boundary conditions. As a simple example, *turbulent wakes* are dealt with below.

1.4 Turbulent Wakes

An *elementary velocity distribution* in inhomogeneous turbulence is expressed by the inertial binormal distribution centered at a point \mathbf{x} ,

$$f(\mathbf{v}, \mathbf{x}, t) = f_0(\mathbf{v}, \mathbf{x}, t) = \left(\frac{t}{4\pi\alpha_0(\mathbf{x}, t)} \right)^{3/2} \exp \left[-\frac{|\mathbf{v}|^2 t}{4\alpha_0(\mathbf{x}, t)} \right]$$

$$\alpha_0(\mathbf{x}, t) = \frac{\alpha_{00}}{(4\pi\nu t)^{3/2}} \exp \left[-\frac{|\mathbf{x}|^2}{4\nu t} \right], \tag{1.7}$$

with the kinetic energy distribution $E(\mathbf{x}, t)$ and the total energy $E(t)$,

$$E(\mathbf{x}, t) = \frac{1}{2} \langle |\mathbf{u}(\mathbf{x}, t)|^2 \rangle = 3\alpha_0(\mathbf{x}, t) / t = \frac{3\alpha_{00}t^{-1}}{(4\pi\nu t)^{3/2}} \exp \left[-\frac{|\mathbf{x}|^2}{4\nu t} \right]$$

$$E(t) = \int E(\mathbf{x}, t) \, d\mathbf{x} = 3\alpha_{00}t^{-1}. \tag{1.8}$$

Taking the linear combination of this type of elementary distributions we can construct various types of free turbulence, including the *turbulent wakes* of axisymmetric type $E(\mathbf{x})$ and two-dimensional type $E(x, y)$ with $\mathbf{x} = (x, y, z)$, the uniform flow $\mathbf{U} = (U, 0, 0)$ and the drag of the solid body D ,

$$E(\mathbf{x}) = \frac{D}{4\pi\nu x/U} \exp \left[-\frac{y^2 + z^2}{4\nu x/U} \right]$$

$$E(x, y) = \frac{DU}{(4\pi\nu x/U)^{1/2}} \exp \left[-\frac{y^2}{4\nu x/U} \right]. \tag{1.9}$$

The energy distributions represented by Eq.(1.9) are in general agreement with experimental results.

1.5 References

- A.N. Kolmogorov, Dokl. Akad. Nauk SSSR, **30**, 301-305 (1941).
T.S. Lundgren, Phys. Fluids, **10**, 969-975 (1967).
A.S. Monin, PMM J. Appl. Math. Mech. **31**, 1057-1068 (1967).
K.R. Sreenivasan & B. Dhruva, Prog. Theo. Phys. (Suppl.) **130**, 103-120 (1998).
T. Tatsumi, In T. Kambe ed. *Geometry and Statistics of Turbulence*. Kluwer, pp.3-12 (2001).
T. Tatsumi & T. Yoshimura, Fluid Dyn. Res. **35**, 123-158 (2004).
T. Tatsumi & T. Yoshimura, Fluid Dyn. Res. **39**, 226-266 (2007).

Large-Eddy Simulation of a Two-Phase Plane Mixing-Layer

M. Dianat, Z. Yang and J. J. McGuirk

Department of Aeronautical and Automotive Engineering
Loughborough University, UK
m.dianat@lboro.ac.uk

1 Introduction

This paper describes the Large-Eddy Simulation (LES) of a droplet laden mixing layer. The method uses an Eulerian description of the carrier flow with a Lagrangian formulation for the dispersed phase. Special treatment of inlet conditions for both phases is critical. Sub-grid scale dispersion effects are investigated, predictions of Sauter Mean Diameter and concentration agree closely with experimental data. The performance of a hybrid droplet/parcel approach for improved efficiency has also been investigated.

2 Flow and Boundary Conditions

The experiment reported in [3], has been used previously [2] as a test case for droplet models. This test case comprises a 2D high Re turbulent plane mixing layer created when an air stream containing water droplets discharges into stagnant air. As in all LES predictions, unsteady correlated inlet conditions must be specified. For the gas phase, the re-scaling approach of [4], has been extended to specify all three components of mean and fluctuating velocity. Within specially created inlet blocks in the multi-block mesh, the velocities are re-scaled at every time step using measured and spatially averaged computed mean and rms velocities. For the droplets, the inlet profile is divided into segments and pdfs of droplet size/number are constructed for each segment to match measured SMD levels and pdfs. The volume-size distribution is approximated using square-root normal distribution adjusted to yield measured data. The number-size distribution is derived and a Cumulative Distribution Function is obtained via integration. This CDF is finally used to determine inlet droplet conditions using random sampling.

3 Results and Discussion

3.1 Gas-phase

A typical normal to wall direction spatial correlation of the axial velocity in the inlet boundary layer is shown in Fig. 1. The correct shape of this confirms the velocity fluctuations are spatially well correlated. The deduced integral length scale (Fig. 1), suggests the scale lies between 2 and 3mm. With an alternative, more complex digital filter approach for inlet conditions, a length scale of 2.5mm was found necessary for correct mixing layer spreading [2]. The current re-scaling methodology generates its own length scales consistent with [2]. Fig. 2 shows that the predicted mean and rms profiles of axial velocity in the mixing layer are in excellent agreement with the experiments.

3.2 Liquid-phase

Fig. 3 shows the effects of SGS dispersion [5] on the predictions of SMD and droplet concentration. SGS dispersion effects seem to improve concentration profiles slightly but lead to higher SMD near the outer edge. Experiments confirm the presence of an outer higher SMD level [3] as correctly predicted at $x=25.4\text{cm}$. The spreading of the mixing layer for both phases is shown in Fig. 4. The agreement with experiments is very good and an improvement on [2]. Note the model successfully predicts the initial non-linear, and subsequent linear, spreading of concentration. Fig. 5 shows SMD and concentration profiles using an all droplets tracked and a hybrid droplet/parcel approach [1]. For the former 10.5M droplets are tracked, with a computational overhead of $\sim 680\%$ with reference to the gas-phase only LES time. For the hybrid approach, the number of droplets for parcel creation was 20 and the number of parcel bins 5. With these parameters, the total number of droplets/parcels tracked reduces to 1.7M/1.9M. This leads to a computational overhead of $\sim 180\%$, a significant reduction without compromising accuracy.

4 Conclusions

The results presented show that the current method for generating gas and liquid-phase inlet conditions is simple and efficient, leading to accurate predictions of flow statistics in close agreement with experiments. The method relies only on parameters that are likely to be available from experiments. Incorporation of an SGS dispersion model tends to improve the predictions of concentration slightly. The results show that a hybrid droplet/parcel approach offers an effective means of reducing computational overhead without compromising accuracy.

5 Acknowledgement

This work received funding from the EU project TIMECOP-AE (AST5-CT-2006-030828). It reflects only the author's views and the Community is not liable for any use that may be made of the information contained therein.

References

1. S. V. Apte, M. Gorokhovski, P. Moin, *Int. J. Mult. Flow*, **29**, 1503 (2003).
2. M. Bini and W. P. Jones, *J. Fluid Mech.*, **614**, 207 (2008).
3. B. J. Lazaro and J. C. Lasheras, *J Fluid Mech*, **235**, 143 (1992).
4. C. D. Pierce, PhD Thesis, Stanford University (2001).
5. C. Wang, Z. Yang, J. J. McGuirk, 2nd Int. Conf. on Turb. and Interact. (2009).

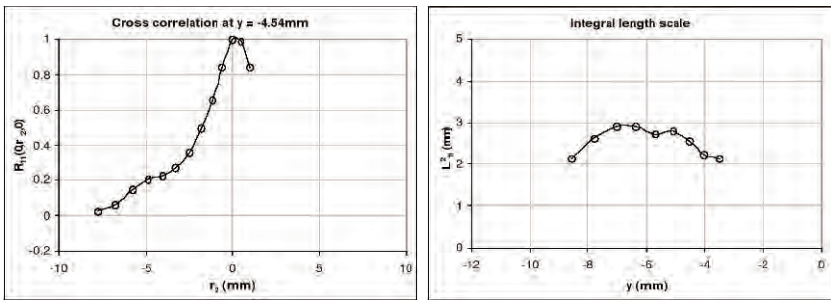


Fig. 1. Typical predicted normal to wall cross-correlation profile of axial velocity (left) and integral length scale of turbulence (right) in the inlet boundary layer.

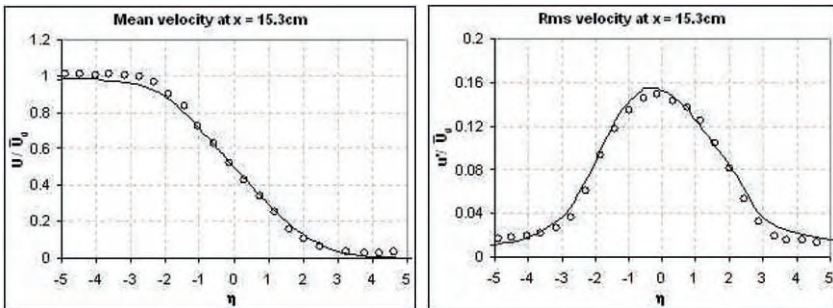


Fig. 2. Profiles of mean (left) and rms (right) axial velocities in the mixing layer. Symbols: data, solid-line: predictions.

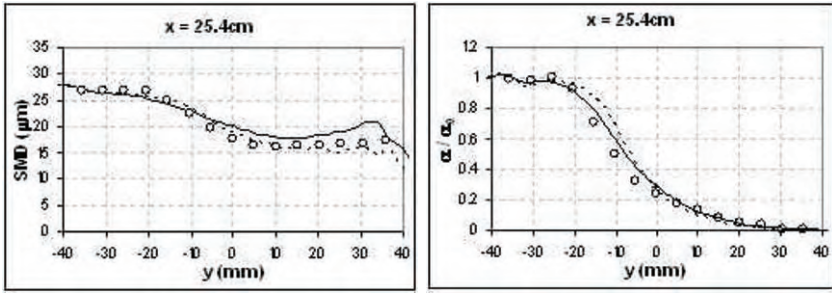


Fig. 3. Dispersion effects on the predicted SMD (left) and concentration (right). Symbols: data, solid-line: with SGS dispersion, dashed-line: no dispersion.

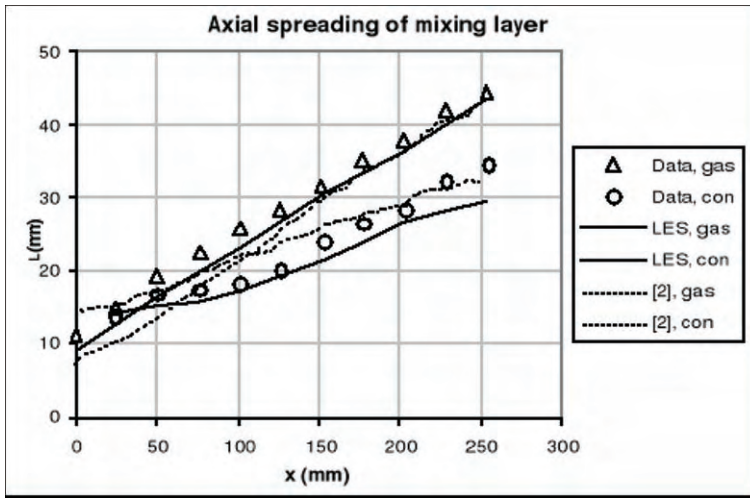


Fig. 4. Axial spreading of the mixing layer for gas and liquid phases using 0.1-0.9 level thickness.

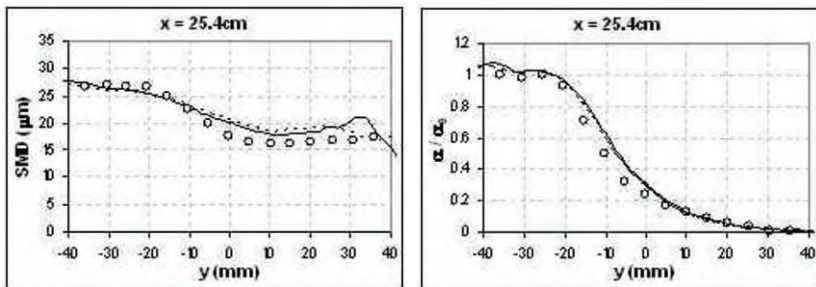


Fig. 5. Predicted SMD (left) and concentration (right) using all droplets and hybrid models. Symbols: data, solid-line: all droplets, dashed-line: hybrid.

Subgrid particle resolution for the turbulent transport of a passive scalar

G.-H. Cottet, G. Balarac and M. Coquerelle

CNRS and Université de Grenoble, 38041 Grenoble Cedex 9, France
Georges-Henri.Cottet@imag.fr

1 Introduction

The transport of passive scalar in turbulent flows remains a challenging and important problem for several reasons. First, the passive scalar spectra exhibit various behaviors depending on the molecular Schmidt number value (see [3]). The passive scalar spectrum with a high Schmidt number exhibits thus a k^{-1} scaling between the Kolmogorov scale and the Batchelor scale [1]. This suggests that it is more demanding in terms of spatial resolution than the momentum. Moreover, capturing accurately advected scalar quantities is of crucial importance in reacting flows, as concentrations control reaction rates [5]. In Large Eddy Simulations, classical subgrid-scale models, which only focus on dissipation related to the transfer of energy to small scales, are not sufficient to predict adequately the effect of non-resolved small scales of the advected concentrations on the large scales involved in the reactions. Another field where passive scalar requires special care is the case of free surface multiphase flows when interfaces and surface tensions are captured by a level set method. The idea of using a different resolution for the scalar and the momentum is therefore natural. This paper investigates the use of a subgrid particle method to predict accurately small scales while keeping the computational cost at a reasonable level.

2 The numerical method

We consider the incompressible Navier-Stokes equation, written in the vorticity formulation, coupled with an advection equation for a passive scalar:

$$\omega_t + (\mathbf{u} \cdot \nabla)\omega - (\omega \cdot \nabla)\mathbf{u} - Re^{-1}\Delta\omega = 0 \quad (1)$$

$$\phi_t + (\mathbf{u} \cdot \nabla)\phi = 0. \quad (2)$$

This system is solved by a remeshed particle method [2]. This method can be summarized as follows: particles are initialized in the support of the initial

vorticity and scalar fields. At each time-step they are advected by the local velocity field then remeshed on a regular fixed using high order interpolation formulas. On that grid a classical diffusion finite-difference formula is used to update vorticity values and velocity is deduced by FFT-based fast solvers. To advect particles in the next step, velocity values are interpolated on particle locations using the same formula as in the remeshing step. A validation of the method against spectral method in DNS of homogeneous isotropic turbulence can be found in [2]. The method exhibits two features which are particularly important in the context of the advection of passive scalar. Particles remain in the support of the advected quantities and the method is not constrained to usual CFL stability conditions. This means that if particles are used at a higher resolution for the simulation of the scalar than for the vorticity, it is not necessary to use smaller time-steps to update the scalar field. If in addition the scalar is concentrated on small parts of the computational domain, subgrid particle resolution can be used at a marginal additional cost.

3 Results

We first consider a jet at a low Reynolds number carrying a passive scalar. The Schmidt number is taken infinite. We compare two experiments. In the first one, both vorticity and scalar are under-resolved. In the second one, the vorticity is under-resolved but the scalar use a three times finer resolution. Figure 1 is a volume rendering visualization of the density for both cases. Although the second experiment takes only 20% more CPU time than the first one - due to the spatial localization of the scalar - there is a clear gain, at least from a qualitative point of view, in the visualization of the intermediate scales.



Fig. 1. Left pictures: volume rendering comparison of a low (left pictures) and high (right pictures) resolution of scalar in an under-resolved jet. The right pictures are a close-up view of the top part of the jet.

We next give more quantitative illustrations on a classical turbulence experiment. The flow and scalar are initialized by turbulent fields in a periodic

box, with a spectral peak at a low wave number. The initial Reynolds number based on the Taylor micro-scale is 48.4 corresponding to a viscosity $\nu = 0.01$. The Schmidt number is chosen equal to 10. We compare the results obtained on the one hand by a full DNS using $N = 128$ grid points in each direction for both the flow and the scalar, to the results given on the other hand by a simulation combining a LES of the flow with $N = 32$ with a DNS of the scalar using $N = 128$ points (we will refer to this later simulation as an *hybrid LES-DNS*). In order to be able to compare side by side scalar visualizations, we have used in the second case the velocity field obtained by filtering the full DNS field, with a top-hat filter in the Fourier space. We show in figure 2 the spectra for the scalar at two given times ($t = 0.6$ and $t = 1.4$). One may observe on the spectra that the hybrid LES-DNS gives a satisfactory scalar spectrum all the way to the smallest scale. It can be noticed that the spectrum shows a plateau that extends a k^{-1} scaling further than in the full DNS. This k^{-1} scaling is not the Batchelors scaling but this spectral behavior has already been found by Lesieur and Rogallo [4]. They explain this spectral behavior as a result of the shearing by large-scale velocity gradients. Whether in the present case this is a desirable behavior will be seen by comparing these spectra with DNS using $N = 256$ grid points for the scalar.

Figure 3 gives a visualization of the surfaces for the same scalar value 0.9 together with the contours of the scalar in a plane through the middle of the computational box. This comparison shows that the hybrid LES-DNS captures

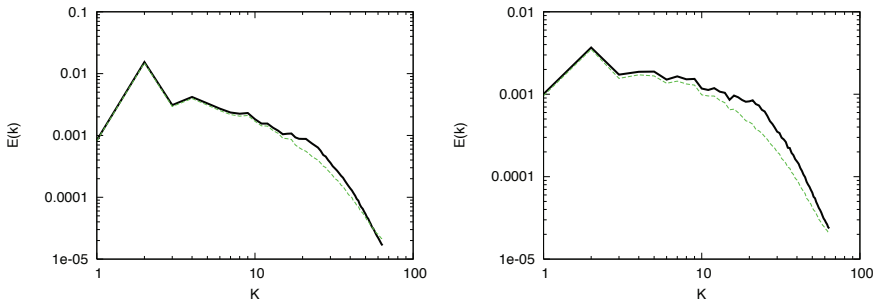


Fig. 2. Scalar spectra in a homogeneous turbulence experiment by a full 128^3 DNS (green dotted line), and a 128^3 scalar DNS in a filtered flow with $N = 32$ (solid black line) at times $t = 0.6$ (left picture) and $t = 1.4$ (right picture).

all the visible scales obtained in the full DNS. Some additional small scale details are also obtained in parts of the flow. This observation is confirmed by looking at the filtered scalar fields corresponding to these two simulations (bottom pictures of Figure 3). Whether these additional features are desirable or numerical artifact is the subject of ongoing higher resolution simulations.

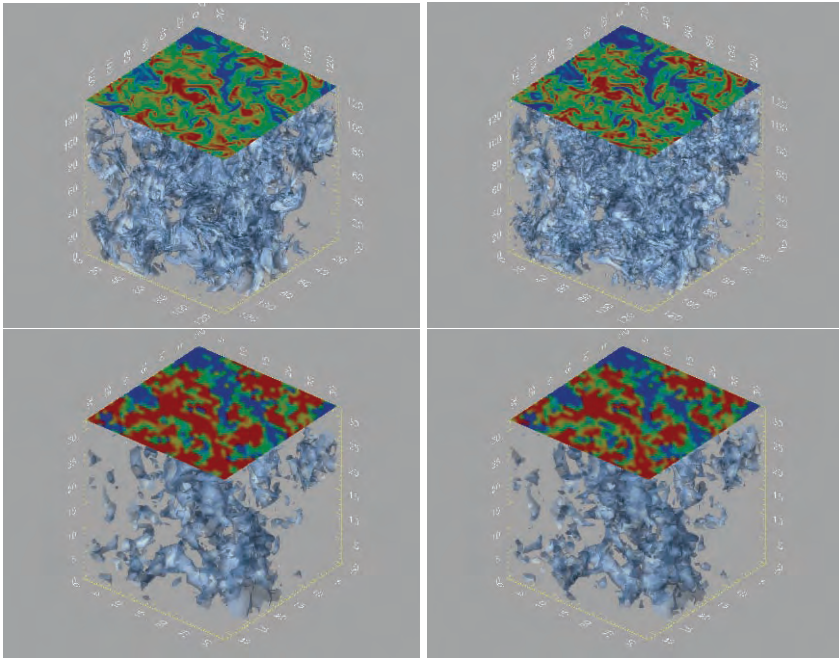


Fig. 3. Isosurface corresponding to $\phi = 0.9$ and contours through the middle of the computational box for the scalar in a full DNS (top-left picture) and in an hybrid LES-DNS (top-right picture). Bottom pictures: scalar fields filtered at $k = 1/32$.

4 Conclusion

We have described a numerical technique based on particle methods for the turbulent transport of scalar combining LES models for the momentum and DNS for the scalar. Numerical validations on homogeneous turbulent flows indicate that this method has the ability to reproduce fine scales for the scalar with a minimal computational effort and can thus be viewed as an LES tool for the scalar transport. Ongoing works concern a systematic use of this approach to explore spectrum decay as a function of the Schmidt number and its application to interface capturing in multiphase flows.

References

1. G.K. Batchelor. *J. Fluid Mech.*, **5**, 1959.
2. G.-H. Cottet, B. Michaux, S.Ossia and G. Vanderlinden, *J. Comp. Phys*, **175**, 2002.
3. M. Lesieur, *Turbulence in Fluids* 4th Edition, Springer, 2008.
4. M. Lesieur and R. Rogallo, *Phys. Fluids A* **1**, 718, 1989.
5. H. Pitsch, *Annu. Rev. Fluid Mech.* **38**, 453, 2006.

An adaptive local deconvolution method for general curvilinear coordinate systems

Stefan Hickel,¹ Dominic von Terzi² and Jochen Fröhlich³

¹ Lehrstuhl für Aerodynamik, Technische Universität München

² Institut für Thermische Strömungsmaschinen, Universität Karlsruhe

³ Institut für Strömungsmechanik, Technische Universität Dresden

Turbulence modeling and the numerical discretization of the Navier–Stokes equations are strongly coupled in large-eddy simulations (LES). The truncation error of common approximations for the convective terms can outweigh the effect of a physically sound subgrid-scale (SGS) model, which generally operates on a range of scales that is marginally resolved by any discretization scheme. This mutual interference can have large and generally unpredictable effects on the accuracy of the solution. On the other hand, one can exploit this link by developing discretization methods from subgrid-scale models, or vice versa. Approaches where the SGS model and the numerical discretization scheme are fully merged are called implicit LES (ILES) methods.

A suitable environment for the design of discretizations with implicit SGS model is provided by Schumann’s concept of a finite–volume method [1]. The numerical truncation error of finite–volume methods readily appears as a divergence of a tensor which is advantageous with respect to physically motivated implicit modeling. Finite–volume discretizations involve averaging and reconstruction steps that are related to filtering and deconvolution well known in explicit SGS modeling. Explicit deconvolution-type SGS models have so far been limited to linear deconvolution. By employing methods that are well established for essentially non-oscillatory finite–volume discretizations, the concept of approximate deconvolution was extended to the solution-adaptive nonlinear case. The resulting adaptive local deconvolution method (ALDM) for implicit LES is based on a nonlinear deconvolution operator and a numerical flux function [2, 4]. Free parameters inherent to the discretization allow to control the truncation error. They are calibrated in such a way that the truncation error acts as a physically motivated SGS model, which combines an implicit tensor–dissipation regularization with a generalized scale–similarity approach. The method is established for LES of turbulent flows governed by the incompressible Navier–Stokes equations and for passive-scalar mixing [6, 7]. The subject of this paper is the extension of ALDM to incompressible turbulent flows with irregular boundaries and non-Cartesian grid topologies.

The work presented here is motivated by the desire to perform LES for complex flows. Such flows are frequently connected to complex geometries that, in the framework of a finite-volume method, can be addressed by three distinct approaches:

(1) The method may be based on discretizations for general volume elements as partitioning of the computational domain. These unstructured meshes are, in general, poorly suited for wall-bounded shear layers. In particular, the performance of SGS models can degrade due to strongly inhomogeneous filter widths making the method ill-suited for ALDM-based ILES.

(2) Cartesian-grid methods with zonal embedding are considerably more appropriate for implicit LES, since local refinement can be easily accounted for. The disadvantage is that computational domain boundaries may not coincide with geometric boundaries of the considered configuration so that boundary conditions have to be applied at the subcell level.

(3) The approach pursued here is based on boundary-fitted block-structured meshes, which offer considerable computational advantages for predicting wall-bounded turbulence. The implementation is based on the flow solver LESOCC2 [8]. It employs non-orthogonal curvilinear grids, a cell centered variable arrangement, and Cartesian velocity components. The convective fluxes are discretized by the simplified adaptive local deconvolution (SALD) method [5]. SALD preserves the good performance of ALDM while computational costs are reduced significantly. Another advantage of SALD is that it allows for a straight-forward application to curved grids: the reconstruction of the unfiltered solution at cell faces by Harten-type deconvolution polynomials can be set up along curved grid lines. Viscous fluxes are based on centered differences. The pressure-velocity coupling is maintained by employing a momentum-interpolation technique.

Simulations of the incompressible turbulent flow in a channel with a periodic arrangement of smoothly curved hills are performed for validation. This complex flow, which exhibits anisotropic, inhomogeneous turbulence statistics, is a standard test case for numerical methods and has been investigated extensively in the recent past. A strong streamwise adverse pressure gradient causes highly unsteady flow separation shortly after the crest of the hill. The flow reattaches at the channel bottom roughly in the middle between two hills. For the present study, the Reynolds number based on the hill height H and the bulk velocity above the crest of the hill is $Re = 10595$. Reference data are provided by experimental results of Rapp [9] and by a well resolved LES of Breuer [3]. The computational domain has the extents $9H \times 4.5H \times 3.03H$ and is discretized by $80 \times 100 \times 30$ cells in the present work. This grid with about 240 thousand cells is rather coarse compared to Breuer's LES, which uses about 13 million cells. Aside of comparing implicit LES results with the reference data we also performed an explicit LES with a central discretization and the well established dynamic Smagorinsky model using the same computational grid. Figures 1 and 2 show mean velocity profiles and Reynolds stresses for the separated flow at $x/H = 2$ and for the reattached flow at $x/H = 6$,

respectively. The predictions of both LES are in good agreement with experimental data and the well-resolved simulation. Discrepancies observed for $\langle u'u' \rangle$ at the bottom wall can be attributed to the coarse grid resolution and vanish on refined grids. The implicit model performs at least as well as the dynamic Smagorinsky model.

In the presentation, we will discuss in detail the theoretical and numerical background of the new method. Computational results will be shown for turbulent flow in a channel, over a circular cylinder, and over periodic hills.

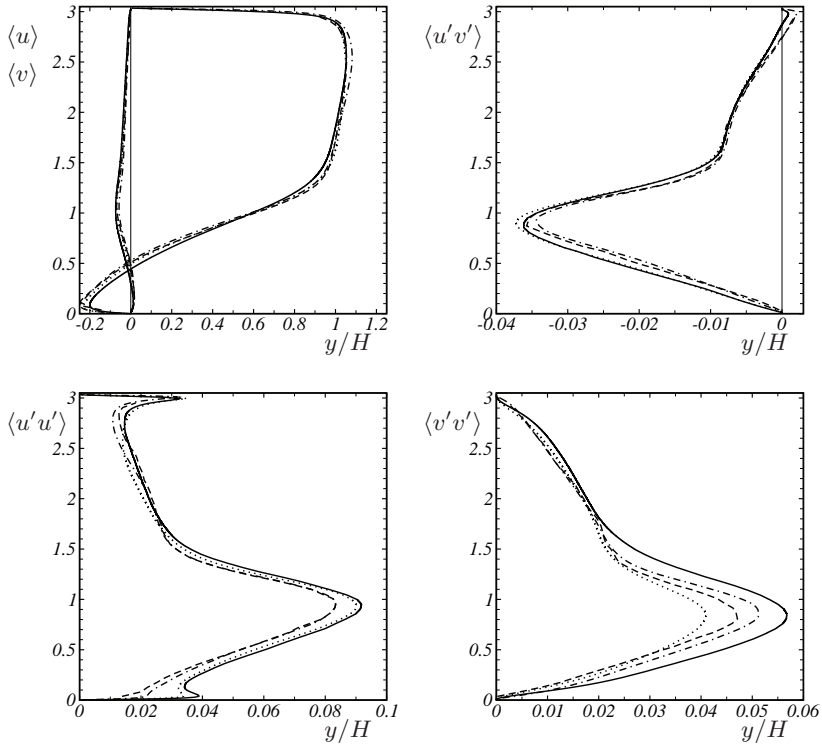


Fig. 1. LES of the flow over periodic hills using a grid with 2.4×10^5 hexahedral cells. Mean velocity profiles and Reynolds stresses at $x/H = 2$ for ——— implicit LES with ALDM, explicit LES with dynamic Smagorinsky SGS model, - - - - Experiment [9], ·-·-·- well-resolved LES on a grid with 13×10^6 cells [3].

References

1. U. Schumann. Subgrid scale model for finite-difference simulations of turbulence in plane channels and annuli. *J. Comp. Phys.*, 18:376–404, 1975.
2. N. A. Adams, S. Hickel, and S. Franz. Implicit subgrid-scale modeling by adaptive deconvolution. *J. Comp. Phys.*, 200:412–431, 2004.

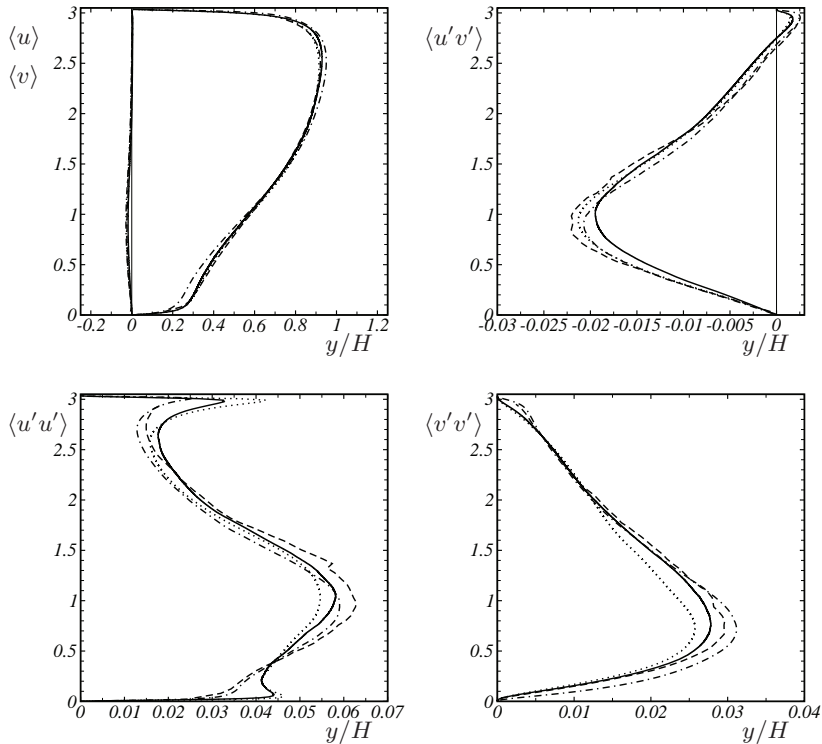


Fig. 2. LES of the flow over periodic hills using a grid with 2.4×10^5 hexahedral cells. Mean velocity profiles and Reynolds stresses at $x/H = 6$ for ——— implicit LES with ALDM, explicit LES with dynamic Smagorinsky SGS model, - - - - Experiment [9], - · - · - well-resolved LES on a grid with 13×10^6 cells [3].

3. M. Breuer. New reference data for the hill flow test case, 2005. <http://www.hy.bv.tum.de/DFG-CNRS/>
4. S. Hickel, N. A. Adams, and J. A. Domaradzki. An adaptive local deconvolution method for implicit LES. *J. Comp. Phys.*, 213:413–436, 2006.
5. S. Hickel and N. A. Adams. Efficient implementation of nonlinear deconvolution methods for implicit large-eddy simulation. In *High Performance Computing in Science and Engineering*, 293–306. Springer, 2006.
6. S. Hickel and N. A. Adams. On implicit subgrid-scale modeling in wall-bounded flows. *Phys. Fluids*, 19:105106, 2007.
7. S. Hickel, N. A. Adams, and N. N. Mansour. Implicit subgrid-scale modeling for large-eddy simulation of passive-scalar mixing. *Phys. Fluids*, 19:095102, 2007.
8. C. Hinterberger. Dreidimensionale und tiefengemittelte Large-Eddy-Simulation von Flachwasserströmungen. PhD thesis, University of Karlsruhe, 2004.
9. C. Rapp. Experimentelle Studie der turbulenten Strömung ueber periodische Huegel PhD thesis, Technische Universität München, 2008.

On under-resolved simulation of atmospheric convection

Z.P. Piotrowski^{1,3}, P. K. Smolarkiewicz², S. P. Malinowski¹, and A. A. Wyszogrodzki²

¹ Institute of Geophysics, University of Warsaw, Warsaw, Poland

² National Center for Atmospheric Research, Boulder, CO, USA

³ Institute of Meteorology and Water Management, Warsaw, Poland
zbych@igf.fuw.edu.pl

Intrigued by the regularity of convective structures observed in simulations of mesoscale flow past realistic topography, we take a deeper look into computational aspects of a classical problem of the flow over a heated plane. We find that the numerical solutions are sensitive to viscosity, either incorporated a priori or effectively realized in computational models. In particular, anisotropic viscosity can lead to regular convective structures that mimic naturally realizable Rayleigh-Bénard (RB) cells but are unphysical for the problem at hand. This is becoming important since the advent of “cloud resolving” numerical weather prediction (NWP) [1, 2] and a rapid progress towards the petascale computing. Even with a relatively fine (for NWP) horizontal resolution $\delta x \sim \mathcal{O}(10^3)$ m numerical filtering is practically unavoidable [2], hence the simulated convection remains grossly under-resolved. The linear theory [3, 4] shows that anisotropic viscosity (characteristic of under-resolved NWP) modifies the range of unstable classical RB modes [5]. In particular, for an effective viscosity much larger in the horizontal than in the vertical unphysically broad RB cells may be observed.

A large series of simulations of thermal convection, with various degrees of idealization, were conducted using the computational model EULAG [6]. Figure 1 shows the structure of idealized RB convection over heated plane; the resolution, surface thermal forcing and timing of the results are representative of mesoscale weather simulations. The left panel shows the solution with small constant viscosity, whereas the right panel shows the result with the same small viscosity in the vertical but with a much larger value in the horizontal.

To better understand the impact of an effective model viscosity on the structure of convective fields, we performed an extensive convergence study and documented differences between the well resolved (viz. realistic) cellular convection and spurious structures. Comparing various means of enhancing the effective viscosity in the horizontal — while keeping the anisotropy ratio $r = \nu_h/\nu_v$ constant — we showed that details of filtering are inessential. The

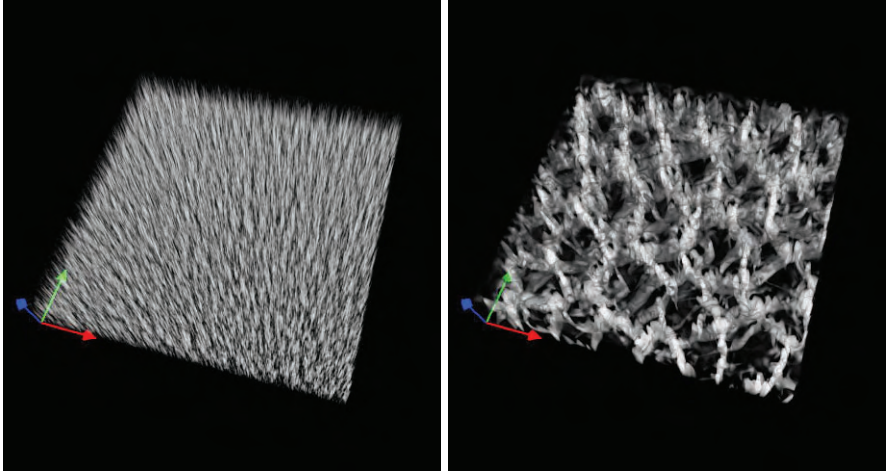


Fig. 1. Convective cells over heated plane, vertical velocity field (bright volumes depict updrafts). The only difference between the two solutions is the value of viscosity in the horizontal entries of the stress tensor $\nu_h = 2.5$ and $70 \text{ m}^2\text{s}^{-1}$ in the left and right panel, respectively; the vertical entry $\nu_v = 2.5 \text{ m}^2\text{s}^{-1}$ in both cases.

common denominator of the scale selection is consistent with the classical linear theory, extended to small anisotropy ratios at moderately supercritical Rayleigh numbers realized (effectively) in under-resolved convection simulations. In particular, there is an approximate inverse proportionality of the band of unstable modes' wavelengths λ to \sqrt{r} , as shown in Figure 2.

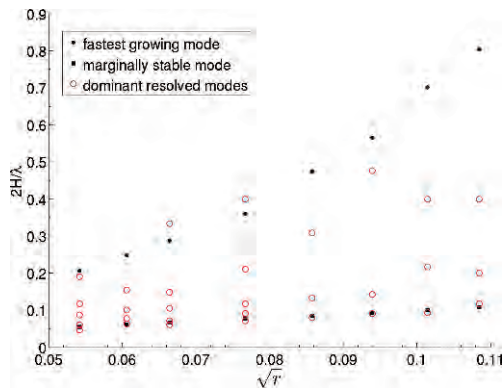


Fig. 2. The dependence of dominant modes' wavelength on square root of the viscosity anisotropy ratio, where H denotes boundary layer height. The lines marked with full circles and squares are, respectively, the linear theory estimates of the fastest growing modes and the marginally stable modes.

On the practical side, our study shows that some numerical approaches may be preferable when the resolution is inadequate to capture the realism of convective fields. While control of effective viscosity is certainly the key to the quality results, resorting to non-dissipative numerics is not a cure. We found that implicit large-eddy simulation (ILES) approach [6] based on non-oscillatory forward-in-time MPDATA advection [7] minimizes numerical viscosity and its anisotropy, and produces results superior compared to more standard LES models.

References

1. M. Satoh & coauthors, *J. Comput. Phys.*, **227**, 3486 (2008).
2. W.C. Skamarock, B. Klemp, *J. Comput. Phys.*, **227**, 3465 (2008).
3. P. Sheu, E. Agee, J. Tribbia, *J. Meteor. Soc. Japan*, **58**, 489 (1980).
4. Z.P. Piotrowski & coauthors, *J. Comput. Phys.*, submitted.
5. A.V. Getling, *Rayleigh-Benard Convection Structures and Dynamics*, World Scientific, 1998
6. J.M. Prusa, P.K. Smolarkiewicz, A.A. Wyszogrodzki, *Computers & Fluids*, **37**, 1193 (2008).
7. P.K. Smolarkiewicz, *Int. J. Num. Meth. Fluids*, **50**, 1123 (2006).

The Multispectral Method: Progress and Prospects

Malcolm Roberts¹, John C. Bowman¹, and Bruno Eckhardt²

¹Dept. of Mathematics, University of Alberta, Edmonton, AB, T6G 2G1, Canada

²Fachbereich Physik, Philipps-Universität Marburg, 35032 Marburg, Germany
mroberts at math.ualberta.ca

1 Introduction

Simulations of high Reynolds-number turbulence require a large number of Fourier modes, with no natural scale separation of which we might take advantage. The underlying hyperbolic system of equations is too large to be simulated on any available computer system.

The technique of *spectral reduction* [1] is a decimation scheme that allows one to simulate large systems on uniformly-coarsened spectral grids. The *multispectral method* uses a hierarchy of differently-coarsened grids in Fourier space, retaining all large-scale modes while approximating the smaller scales.

2 The models in question

Since high-Reynolds number simulations of the Navier–Stokes equations are not currently tenable, we introduce two shell models of turbulence, the DN [3] model,

$$\frac{du_n}{dt} = ik_n (au_{n-1}^2 - \lambda au_n u_{n+1} + bu_{n-1} u_n - \lambda bu_{n+1}^2)^* - \nu k_n^2 u_n, \quad (1)$$

and the GOY [4, 5] model,

$$\frac{du_n}{dt} = ik_n \left(\alpha u_{n+1} u_{n+2} + \frac{\beta}{\lambda} u_{n-1} u_{n+1} + \frac{\gamma}{\lambda^2} u_{n-1} u_{n-2} \right)^* - \nu k_n^2 u_n, \quad (2)$$

where $*$ denotes complex conjugation. These are heuristic models that mimic the form and many statistical properties of the spectral Navier–Stokes equations. Because of these features, they are excellent test beds for theories about turbulence.

The modal amplitude u_n associated with the geometrically spaced wavenumber $k_n = k_0 \lambda^n$ represents a characteristic complex amplitude of the modes

$\mathbf{u}(\mathbf{k})$ for $|\mathbf{k}| \in [k_n, k_{n+1}]$. That is, u_n represents a typical velocity for a three-dimensional shell with inner radius k_n and outer radius k_{n+1} , as shown in Fig. 1. The combination of averaging and geometric spacing allows one to reach high wavenumbers, and hence very high Reynolds numbers, with a small number of modes, as shown in Fig. 2.

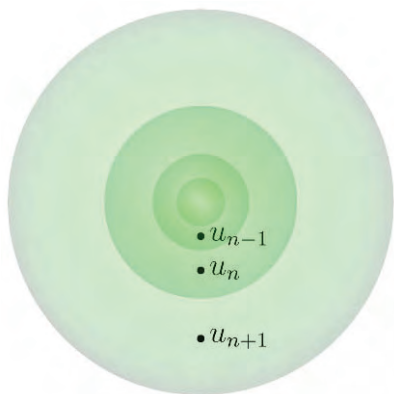


Fig. 1. Spectral domain for mode u_n .

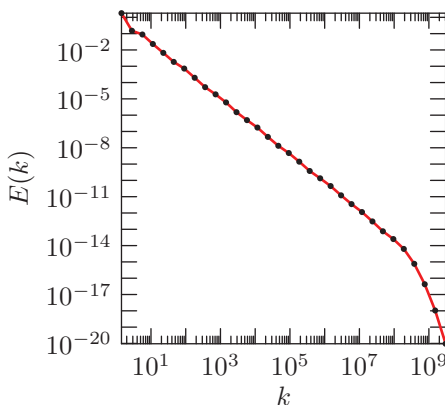


Fig. 2. Energy spectrum of shell-model turbulence.

3 Spectral Reduction

Spectral reduction allows one to take two modes, say u_{2n} and u_{2n+1} , and replace them with an average of the two full-resolution modes u_{2n} and u_{2n+1} :

$$u_{n,1} = \frac{u_{2n} + u_{2n+1}}{2}. \tag{3}$$

This uniform coarsening allows one to simulate a binned energy spectrum using half as many modes. Spectral reduction can be applied iteratively to the system until there are too few remaining independent modes to capture the energy injection, inertial-range transfer, and dissipation.

An equation for $\frac{d}{dt}u_{n,1}$ follows on taking the derivative of equation (3) and substituting either equation (1) or (2), depending on whether one is simulating the DN or GOY models, respectively. The resulting system will conserve the binned energy $E_1 = \frac{1}{2} \sum 2|u_{n,1}|^2$. An easy calculation shows that spectral reduction reduces the GOY model to the DN model, which is then a fixed point of the map, with each reduction modifying the parameters a , b and ν as per equation (4):

$$a \rightarrow \frac{a}{2}, \quad b \rightarrow \frac{b}{2} \quad \nu \rightarrow \nu \frac{1 + \lambda^2}{2} \tag{4}$$

The energy spectrum of a singly decimated system is shown in Fig. 3.

4 Interpolation

The binned mode $u_{n,1}$ represents two quantities. We can recapture some of this structure by replacing equation (3) with

$$u_{n,1} = \frac{u_{2n} + \sigma_n^* u_{2n+1}}{1 + |\sigma_n|^2}, \quad \sigma_n = \frac{u_{2n+1}}{u_{2n}}. \tag{5}$$

The complex quantity σ_n accounts for the slope of the amplitude across a bin. If σ_n is constant with respect to time, then the energy $E_1 = \frac{1}{2} \sum_n (1 + |\sigma_n|^2) |u_{n,1}|^2$ is conserved. This interpolated spectral reduction can also be applied iteratively, with the caveat that energy is conserved only when σ is constant during a time step and over each coarse bin. In order to close the system, we let

$$\sigma_n = \sqrt[4]{\frac{\langle |u_{n,1}|^2 \rangle}{\langle |u_{n+1,1}|^2 \rangle}} \tag{6}$$

where $\langle \dots \rangle$ is a windowed time average. The energy spectrum of an interpolated singly decimated system is shown in Fig. 3.

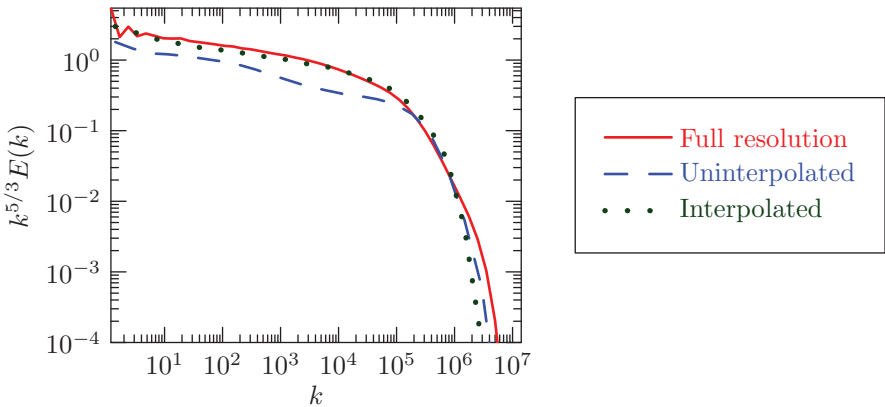


Fig. 3. Rescaled energy spectrum of spectrally reduced shell-model turbulence.

5 The Multispectral Method

The method of spectral reduction allows one to represent a large system on a uniformly coarsened spectral grid. However, the low-wavenumber modes are typically of greater physical importance: one would like to coarsen just the high-wavenumber, small-scale modes in favour of keeping all of the low-wavenumber, large-scale modes. Unfortunately, this modifies the system's Liouville theorem, and the inviscid, unforced energy spectrum is not correctly reproduced.

The *multispectral method* was designed to alleviate this problem. Since we are unable to decimate a single grid non-uniformly, we must use two grids which have been decimated to different degrees, as shown in Fig. 4.

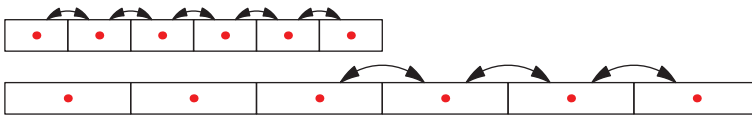


Fig. 4. Schematic diagram for the DN model with the multispectral method showing nonlinear interactions.

To evolve this system forward in time, redundant interactions are first removed. One then evolves the fine grid from time t to $t + dt$ using an explicit integrator. The result of this integration is projected onto the coarse grid, which is then also evolved from from time t to $t + dt$ using a (possibly different) explicit integrator. Finally, the two grids are synchronised by prolonging from the coarse grid to the fine grid.

The resulting system reproduces the essential behaviour of the full-resolution system, keeps all the large-scale modes, but is much less costly to simulate.

References

1. Bowman, Shadwick, and Morrison, *Phys. Rev. Lett.* **83**, 5491 (1999).
2. J. C. Bowman, C. R. Doering, B. Eckhardt, J. Davoudi, M. Roberts, and Jörg Schumacher, *Physica D* **218**, 1-10 (2006).
3. V. N. Desnyansky and E. A. Novikov, *Prikl. Mat. Mekh.* **38**, 507 (1974)
4. E. B. Gledzer, System of hydrodynamic type admitting two quadratic integrals of motion, *Sov. Phys. Dokl.*, **18**, 216-217, (1973)
5. Yamada, Michio and Ohkitani, Koji, Asymptotic formulas for the Lyapunov spectrum of fully developed shell model turbulence, *Phys. Rev. E* **57**, 6257-6260 (1998)

Discretization errors and subgrid scale implementations in Large Eddy Simulations

A. Viré and B. Knaepen

Physique Statistique et des Plasmas, Faculté des Sciences, Université Libre de Bruxelles, Belgium

avire at ulb.ac.be

The aim of large eddy simulations (LES) is to reproduce with accuracy the large scale properties of a turbulent flow at a much lower computational cost than required by direct numerical simulations (DNS). The main challenge of LES is thus to appropriately model the influence of the subgrid scales on the resolved scales. Here, the attention is restricted to finite volume methods, without explicit filtering. In this framework, the subgrid scale modeling is related to the volume averaging on the coarse mesh and is responsible for the destruction of small scale information. Because the mesh is coarse, the discrete operators needed for differentiations and interpolations introduce further errors that might be significant. For differentiation operators, the severity of this problem increases with the order of the derivative taken, so that the physical relevance of the numerical results becomes questionable.

The present study analyzes the impact of discretization errors on the performance of the Smagorinsky model. To avoid difficulties related to solid boundaries, we focus on decaying homogeneous turbulence. The computations are performed using the CDP code developed at the Center For Turbulence Research (Stanford / NASA-Ames) [1, 2, 3]. This code uses a collocated discretization of the incompressible Navier–Stokes equations in a node-based formulation. The spectral results of [4] are used as the benchmark case. Two implementations of the Smagorinsky model are compared. The first implementation of the turbulent viscosity, referred to as SM1, is

$$(\nu_{e,1})_P = -2C\overline{\Delta}^2 \sqrt{2(\overline{S}_{ij})_P(\overline{S}_{ij})_P}, \quad (1)$$

where $\overline{S}_{ij} = (\partial_i \overline{u}_j + \partial_j \overline{u}_i)/2$. The focus here being on isotropic turbulence, we choose $C = 0.0225$ [5] and $\overline{\Delta} = L_{box}/N_x$, with L_{box} and N_x respectively the computational box size and the number of cells in one direction. Moreover, the strain is computed explicitly at the control volume's center P using a central difference scheme. To introduce the second implementation of the turbulent viscosity, we make use of the identity:

$$\overline{S}_{ij}\overline{S}_{ij} = -\overline{u}_i\partial_j\overline{S}_{ij} + \partial_j(\overline{u}_i\overline{S}_{ij}). \quad (2)$$

Based on this identity, we define an alternative subgrid scale viscosity, referred to as SM2,

$$(\nu_{e,2})_P = -2C\bar{\Delta}^2 \sqrt{2\mathcal{D}[\overline{\mathcal{S}}_{ij}\overline{\mathcal{S}}_{ij}]_P}, \tag{3}$$

where $\mathcal{D}[\overline{\mathcal{S}}_{ij}\overline{\mathcal{S}}_{ij}]_P$ represents the discretization of the right-hand-side of Eq. (2).

The discretization error is evaluated *a priori* by comparing the average strain rate computed through the spectral code to $\mathcal{S}^{(a)} = \langle (\overline{\mathcal{S}}_{ij})_P (\overline{\mathcal{S}}_{ij})_P \rangle$ and $\mathcal{S}^{(b)} = \langle \mathcal{D}[\overline{\mathcal{S}}_{ij}\overline{\mathcal{S}}_{ij}]_P \rangle$. The initial spectral DNS field at the resolution $N = N_x \times N_y \times N_z = 512^3$ is filtered down to different resolutions ($32^3, 64^3, 128^3, 256^3$). The corresponding average strain rate is denoted \mathcal{S}^{DNS_f} and we define $\delta_{\mathcal{S}^*} = \mathcal{S}^* / \mathcal{S}^{DNS_f}$. The asterisk stands for the superscript (a) or (b). The corresponding $\delta_{\mathcal{S}^*}$ are plotted in figure 1 (left) as a function of the truncation level $K = (N/N_{DNS})^{1/3}$ (defined as the ratio of the filtered resolution to the initial DNS resolution). We observe an increase of $\delta_{\mathcal{S}^*}$ as K increases for both $\mathcal{S}^{(a)}$ and $\mathcal{S}^{(b)}$. This is of course expected, since discretization errors should decrease when the grid is refined. At $N = 256^3$, which is the finest resolution considered here, $\delta_{\mathcal{S}^*}$ reaches 94% for $\mathcal{S}^{(b)}$ and 74% for $\mathcal{S}^{(a)}$. We also analyze the convergence of $(\overline{\mathcal{S}}_{ij})_P (\overline{\mathcal{S}}_{ij})_P$ and $\mathcal{D}[\overline{\mathcal{S}}_{ij}\overline{\mathcal{S}}_{ij}]_P$ with respect to the resolution by smoothing the velocity field. To that end, we apply a spectral cutoff filter to our initial 32^3 instantaneous velocity field. This procedure has the advantage of being less demanding in terms of computational resources than a mesh refinement. Figure 1 (right) shows $\delta_{\mathcal{S}^*}$ as a function of the cutoff length Δ_c (the lowest value of Δ_c corresponds to a cutoff wave-number of $k_c = 15$ and the highest value to $k_c = 1$). It is again clear that $\mathcal{S}^{(b)}$ predicts significantly better the average strain rate. Furthermore, all the strain rates ($\mathcal{S}^{(a)}$, $\mathcal{S}^{(b)}$ and spectral), converge to the same value as the velocity field is filtered and smoothed.

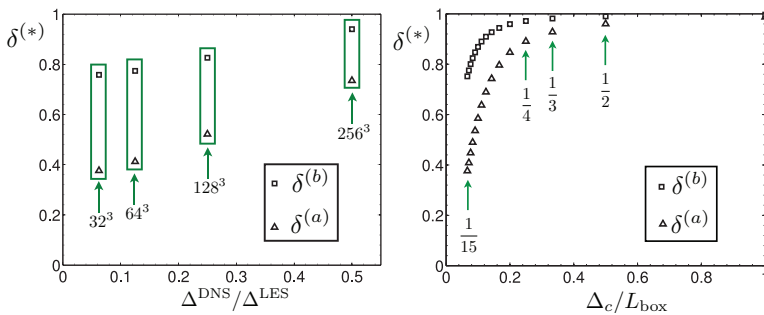


Fig. 1. Left: fraction $\delta_{\mathcal{S}^*}$ of the strain rate captured initially for different mesh refinements. Right: fraction $\delta_{\mathcal{S}^*}$ for different cutoff lengths at $N = 32^3$.

The two models are finally compared, *a posteriori*, at the resolution $N = 32^3$. The measured microscale Reynolds number for the initial field is $Re_\lambda =$

84.1, the Reynolds number based on the integral length-scale is $Re = 380$ and the viscosity is set to $\nu = 0.006$. In the figures, time is normalized by the initial eddy-turnover time $\tau_{tu} = 0.238s$, and is denoted t^* . Figure 2 (left) shows the time evolution of the resolved kinetic energy, defined by

$$E_R = \frac{1}{V_{tot}} \int_V \frac{\bar{u}_i \bar{u}_i}{2} dV \approx \frac{1}{2V_{tot}} \sum_P \bar{u}_{i,P} \bar{u}_{i,P} V_P, \quad (4)$$

with $V_{tot} = \sum_P V_P$ and V_P is the volume of the control volume centered on point P . Aside from the LES runs, the unresolved simulation performed without model (UDNS) is also presented to emphasize the role of the LES modeling. As is obvious from the figure, UDNS severely underestimates the decay rate of energy. In addition, the decay obtained with SM1 is better than that obtained using SM2 since it is closer to the spectral prediction. The time evolution of the subgrid dissipation rate, computed as $\epsilon_{sgs} = 2\nu_e \sum_P V_P \mathcal{D}[\bar{S}_{ij} \bar{S}_{ij}]_P$ (ν_e being the eddy-viscosity), is illustrated in figure 2 (right). The most important fact is that the subgrid scale dissipation generated by the SM1 model is much too low. Although the SM2 model also underestimates the dissipation at the very beginning of the simulation, its behavior is however significantly closer to the spectral result. The improvements provided by SM2 are also observed for the viscous dissipation and kinetic energy spectra (not shown here).

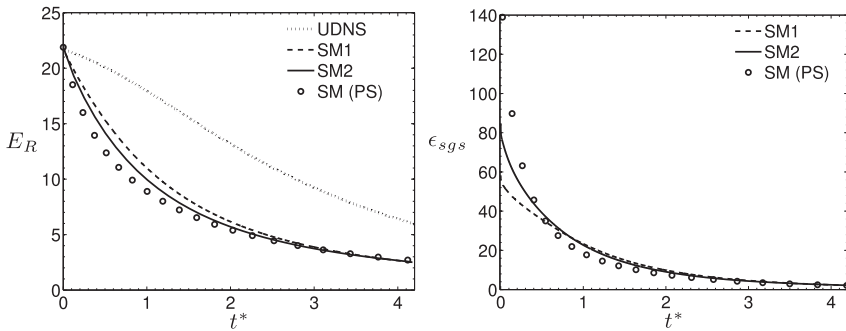


Fig. 2. Left: time evolution of the resolved kinetic energy. Right: time evolution of the subgrid dissipation rate computed from the right-hand-side of Eq. (2).

A question that arises is the possibility that the large differences observed in the computation of $\bar{S}_{ij} \bar{S}_{ij}$ through $\mathcal{S}^{(a)}$ or $\mathcal{S}^{(b)}$ might be related to the present manner of initializing the simulations. Indeed, our initial condition is obtained by truncating a 512^3 spectral DNS field to a 32^3 resolution. This produces, on the real space grid, a signal that has sharp gradients and for which it is expected that second-order derivatives cannot be fairly computed. Over time, one could speculate that the numerical solution might evolve towards

a state more easily captured by the finite volume discretization and that the ratio $R = \mathcal{S}^{(b)}/\mathcal{S}^{(a)}$ would converge to unity. Figure 3 shows that this is not the case, as R even increases for the LES runs with the SM1 model. The difference between $\mathcal{S}^{(a)}$ and $\mathcal{S}^{(b)}$ is not fortuitous. The uncertainty is due to the fact that a LES signal has a significant content at scales close to the grid size and that discrete operators cannot resolve those scales without ambiguity [6].

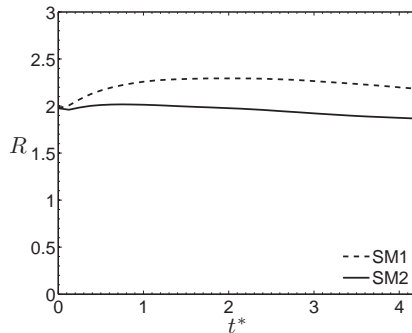


Fig. 3. Time evolution of the ratio $R = \frac{\mathcal{S}^{(b)}}{\mathcal{S}^{(a)}}$.

References

1. K. Mahesh, G. Constantinescu, S. Apte, G. Iaccarino, F. Ham and P. Moin, Annual Research Briefs, Center for Turbulence Research, NASA Ames/Stanford University, 115 (2002).
2. F. Ham and G. Iaccarino, Annual Research Briefs, Center for Turbulence Research, NASA Ames/Stanford University, 3 (2004).
3. F. Ham, K. Mattsson and G. Iaccarino, Annual Research Briefs, Center for Turbulence Research, NASA Ames/Stanford University, 243 (2006).
4. B. Knaepen and P. Moin, Phys. Fluids, **16**, 1255 (2004).
5. S. B. Pope, Turbulent flow, Cambridge University Press, Cambridge 2000.
6. A. Viré and B. Knaepen, J. Comput. Phys., in press (2009), doi: 10.1016/j.jcp.2008.12.024.

Part XII Magnetohydrodynamical turbulence

Reversals of the magnetic field generated by a turbulent flow

S. Fauve, E. Dormy, C. Gissinger and F. P  tr  lis

Ecole Normale Sup  rieure, LPS - CNRS, 24 Rue Lhomond, 75005 Paris, France.
fauve@lps.ens.fr

When averaged on a few thousands years, the Earth's magnetic field can be roughly described as the one of an axial dipole. As shown by paleomagnetic records, it has frequently reversed its polarity on geological time scales. Field reversals have also been reported in several numerical simulations of the geodynamo and more recently, in a laboratory experiment involving a von Karman swirling flow of liquid sodium (VKS). We first recall some of the main experimental results and understand them using phenomenological models and numerical simulations. In particular, we show that all the regimes of the magnetic field observed in the experiments reported so far, can be understood in the framework of low dimensional dynamical system theory: two modes of the magnetic field, with dipolar (respectively quadrupolar) symmetry, can be generated by the turbulent flow of liquid sodium, and their interaction can lead to the observed dynamics (oscillations, random reversals, symmetric or asymmetric bursts). Turbulent fluctuations alone do not drive these dynamical regimes that only occur when a symmetry of the flow is broken. Although the flow in the Earth's core strongly differs from the one of the VKS experiment, a similar model but based on a different broken symmetry, can be used. It explains several features observed in paleomagnetic recordings of the Earth's magnetic field reversals.

1 A dynamo generated by a von Karman swirling flow

The generation of magnetic field by the flow of an electrically conducting fluid, i.e., the dynamo effect, is an instability that has been mostly studied to understand the magnetic fields of planets and stars [1]. Flows in the interiors of planets or stars have huge kinetic Reynolds numbers, $Re = VL/\nu$, where V is the typical velocity, L is its integral length scale and ν is the kinematic viscosity. For instance, $Re \sim 10^9$ in the Earth's liquid core or $Re \sim 10^{15}$ in the convective zone of the Sun. The main control parameter for dynamo action is the magnetic Reynolds number, $R_m = \mu_0\sigma VL$. It relates transport

and stretching of the magnetic field by the flow to Ohmic diffusion (σ is the electrical conductivity and μ_0 is the magnetic permeability of vacuum). $P_m = R_m/Re = \mu_0\sigma\nu$ is the magnetic Prandtl number of the fluid. For planetary or stellar interiors, $P_m < 10^{-6}$. For liquid metals used in laboratory experiments, its maximum value is obtained with liquid sodium $P_m \sim 10^{-5}$. A necessary condition for dynamo action being R_m large enough in order to overcome Ohmic dissipation (in the range 10 – 100 for many dynamos), the dynamo threshold can be reached only when the flow is strongly turbulent (Re of order 10^6 or larger). This provides both the difficulty and the interest of the problem. An instability that develops on a fully turbulent flow involves several open questions: Do turbulent fluctuations inhibit or enhance the growth rate of the magnetic field? What is the magnetic energy density that can be generated by a turbulent flow [2]? At which spatial scales is it maximum [3]? The first successful experiments on fluid dynamos involved flows with a geometrical confinement to aim at the suppression of large scale turbulence [4]. In contrast, the motivation for the von Karman geometry was to study the generation of a magnetic field by a strongly turbulent flow. The flow of liquid sodium is driven in a cylinder by two counter-rotating disks fitted with eight blades (see figure 1a). $Re \sim 5 \cdot 10^6$, thus $R_m \sim 50$ can be reached, and turbulent fluctuations are comparable to the mean flow (time averaged). The motivation for choosing this flow resulted from its strong differential rotation and the absence of mirror symmetry (in the counter-rotating case). In addition, this flow was known to generate tornado-like vorticity filaments [5] involving large velocity increments as displayed by pressure measurements [6]. All these features were known to favor dynamo action [7]. The generation of magnetic field by the VKS flow has been widely reported [8, 9, 10, 11] and we refer to these publications for a description of the experimental results. Our purpose here is to present various models and numerical simulations that provide an explanation for several experimental observations.

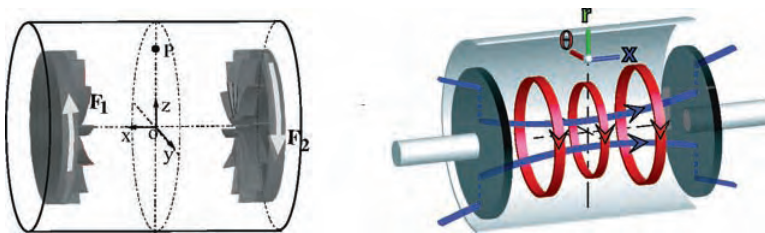


Fig. 1. a) Sketch of the von Karman swirling flow geometry. b) Sketch of the mean magnetic field generated for exact counter-rotation of the propellers, $F_1 = F_2$.

2 Geometry of the mean magnetic field: equatorial versus axial dipoles

Several early attempts to predict the magnetic field generated by the VKS flow and to understand the underlying mechanisms were presented in [12]. An equatorial dipole was found (as the one displayed in figure 2 (left)) whereas the magnetic field observed in the experiment involved a strong axial dipolar component (see figure 1, right). These calculations were based on the mean flow of the VKS experiment. This one being axisymmetric, the generated magnetic field should break axisymmetry according to Cowling theorem [7] and this is achieved by an equatorial dipole. The experimental observation of an axial dipole thus shows that non axisymmetric velocity fluctuations play an important role in the VKS dynamo that is not generated by the mean flow alone. It has been proposed that the vortical flow radially ejected by the blades of the rotating impellers generate an axial mean field from an $\alpha-\omega$ mechanism [13]. This mechanism has been qualitatively illustrated using the mean field induction equation [14]. It has been checked using the direct numerical simulation displayed in figure 2 (right) [15]. It has been also shown by direct simulations of a flow generated by two propellers in a spherical domain, that an axial dipole is generated as soon as turbulent fluctuations are large enough [16].



Fig. 2. Numerical simulations of the magnetic field at dynamo threshold: left: an equatorial dipole is obtained when only the mean flow is taken into account. Right: an axial dipole is generated when non axisymmetric components in the form of vortices generated by the blades are included in the velocity field.

Thus, the VKS dynamo is not generated by the mean flow alone in contrast to Karlsruhe and Riga experiments, and non-axisymmetric fluctuations play an essential role in the dynamo process. Note also that it has been observed so far only when impellers made of soft iron have been used. It has been shown

that magnetic boundary conditions corresponding to the high permeability limit significantly decrease the dynamo threshold [17]. However, other mechanisms due to the iron disks can be also put forward (see for instance [13]).

3 Broken symmetries and dynamics of the large scale magnetic field

The most striking feature of the VKS experiment is that time dependent magnetic fields are generated only when the impellers rotate at different frequencies [9]. We will show that this can be related to the additional invariance under \mathcal{R}_π when $F_1 = F_2$ (rotation of an angle π along any axis in the mid-plane). We indeed expect that in that case, the modes involved in the dynamics are either symmetric or antisymmetric. Such modes are displayed in figure 3. A dipole is changed to its opposite by \mathcal{R}_π , whereas a quadrupole is unchanged. More generally, we name “dipole” (respectively “quadrupole”), modes with dipolar (respectively quadrupolar) symmetry even though they might involve a more complex spatial structure.

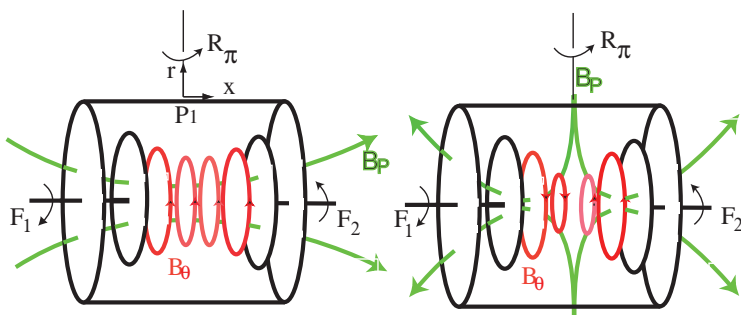


Fig. 3. Possible eigenmodes of the VKS experiment. The two disks counter-rotate with frequency F_1 and F_2 . Left: magnetic dipolar mode. Right: magnetic quadrupolar mode. Poloidal, B_P , and toroidal, B_θ , components are sketched.

We assume that the magnetic field is the sum of a dipolar component with an amplitude D and a quadrupolar one, Q . We define $A = D + iQ$ and we assume that an expansion in power of A and its complex conjugate \bar{A} is pertinent close to threshold in order to obtain an evolution equation for both modes. Taking into account the invariance $\mathbf{B} \rightarrow -\mathbf{B}$, *i.e.* $A \rightarrow -A$, we obtain

$$\dot{A} = \mu A + \nu \bar{A} + \beta_1 A^3 + \beta_2 A^2 \bar{A} + \beta_3 A \bar{A}^2 + \beta_4 \bar{A}^3, \quad (1)$$

where we limit the expansion to the lowest order nonlinearities. In the general case, the coefficients are complex and depend on the experimental parameters.

Symmetry of the experiment with respect to \mathcal{R}_π when the disks exactly counter-rotate, amounts to constraints on the coefficients. Applying this transformation to the magnetic modes, changes D into $-D$ and Q into Q , thus $A \rightarrow -\bar{A}$. We conclude that, in the case of exact counter-rotation, all the coefficients are real. When the frequency difference $f = F_1 - F_2$ is increased from zero, we obtain that the real parts of the coefficients are even and the imaginary parts are odd functions of f . When the coefficients are real, the growth rate of the dipolar component is $\mu_r + \nu_r$ and that of the quadrupolar component is $\mu_r - \nu_r$. The dipole being observed for exact counter-rotation implies that $\nu_r > 0$ for $f = 0$. By increasing f , we expect that ν_r changes sign and favors the quadrupolar mode according to the experimental results (see figure 3 in [10]). We will explain in the next section how modifying the parameters of (1) leads to bifurcation to time dependent solutions.

4 A mechanism for oscillations and reversals

As shown in [18], the planar system (1) explains the dynamical regimes observed so far in the VKS experiment [10]. It is invariant under the transformation $\mathbf{B} \rightarrow -\mathbf{B}$. Thus, in the case of counter-rotating impellers, $F_1 = F_2$, it has two stable dipolar solutions $\pm D$ and two unstable quadrupolar solutions $\pm Q$. When the frequency difference f is increased, these solutions become more and more mixed due to the increase of the strength of the coupling terms between dipolar and quadrupolar modes. Dipolar (respectively quadrupolar) solutions get a quadrupolar (respectively dipolar) component and give rise to the stable solutions $\pm B_s$ (respectively unstable solutions $\pm B_u$) displayed in figure 4. When f is increased further, a saddle-node bifurcation occurs, i.e. the stable and unstable solutions collide by pairs and disappear. This generates a limit cycle that connects the collision point with its opposite. This result can be understood as follows: the solution $B = 0$ is unstable with respect to the two different fixed points, and their opposite. It is an unstable point, whereas one of the two bifurcating solutions is a stable point, a node, and the other is a saddle. If the saddle and the node collide, say at B_c , what happens to initial conditions located close to these points? They cannot be attracted by $B = 0$ which is unstable and they cannot reach other fixed points since they just disappeared. Therefore the trajectories describe a cycle. The associated orbit contains $B = 0$ since, for a planar problem, in any orbit, there is a fixed point. Suppose that the orbit created from B_c is different from the one created by $-B_c$. These orbits being images by the transformation $\mathbf{B} \rightarrow -\mathbf{B}$, they must intersect at some point. Of course, this is not possible for a planar system because it would violate the uniqueness of the solutions. Therefore, there is only one cycle that connects points close to B_c and $-B_c$.

This provides an elementary mechanism for field reversals in the vicinity of a saddle-node bifurcation. First, in the absence of fluctuations, the limit cycle generated at the saddle-node bifurcation connects $\pm B_c$. This corresponds to

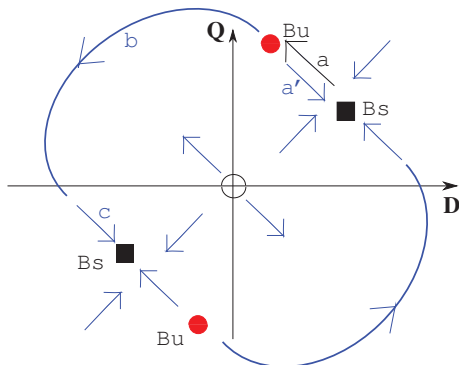


Fig. 4. A generic saddle-node bifurcation in a system with the $\mathbf{B} \rightarrow -\mathbf{B}$ invariance: below threshold, fluctuations can drive the system against its deterministic dynamics (phase a). If the effect of fluctuations is large enough, this generates a reversal (phases b and c). Otherwise, an excursion occurs (phase a').

periodic reversals. Slightly above the bifurcation threshold, the system spends most of the time close to the two states of opposite polarity $\pm B_c$. Second, in the presence of fluctuations, random reversals can be obtained slightly below the saddle-node bifurcation. B_u being very close to B_s , even a fluctuation of small intensity can drive the system to B_u from which it can be attracted by $-B_s$, thus generating a reversal.

The effect of turbulent fluctuations on the dynamics of the two magnetic modes governed by (1) can be easily modeled by adding some noisy component to the coefficients [18]. Random reversals are displayed in figure 5 (left). The system spends most of the time close to the stable fixed points $\pm B_s$. We observe in figure 5 (right) that a reversal consists of two phases. In the first phase, the system evolves from the stable point B_s to the unstable point B_u (in the phase space sketched in figure 4). The deterministic part of the dynamics acts against this evolution and the fluctuations are the motor of the dynamics. That phase is thus slow. In the second phase, the system evolves from B_u to $-B_s$, the deterministic part of the dynamics drives the system and this phase is faster.

The behaviour of the system close to B_s depends on the local flow. Close to the saddle-node bifurcation, the position of B_s and B_u defines the slow direction of the dynamics. If a component of B_u is smaller than the corresponding one of B_s , that component displays an overshoot at the end of a reversal. In the opposite case, that component will increase at the beginning of a reversal. For instance, in the phase space sketched in figure 4, the component D decreases at the end of a reversal and the signal displays an overshoot. The component Q increases just before a reversal.

For some fluctuations, the second phase does not connect B_u to $-B_s$ but to B_s . It is an aborted reversal or an excursion in the context of the Earth

dynamo. Note that during the initial phase, a reversal and an excursion are identical. In the second phase, the approaches to the stationary phase differ because the trajectory that links B_u and B_s is different from the trajectory that links B_u and $-B_s$. In particular, if the reversals display an overshoot this will not be the case of the excursion (see figure 5 (right) and the sketch of the cycle in figure 4).

Other regimes observed in the VKS experiment such as symmetric or asymmetric bursts [10] have been also described in the vicinity of more complex bifurcations of equation (1) [18].

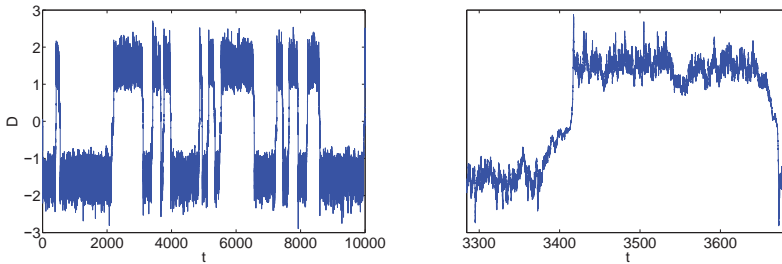


Fig. 5. Reversals of the magnetic field modeled by (1).

5 A simple model for Earth's magnetic field reversals

The above model of reversals of magnetic field in the vicinity of a saddle-node bifurcation in a system with the invariance $\mathbf{B} \rightarrow -\mathbf{B}$ explains many intriguing features of the reversals of Earth magnetic field [19]. The most significant output is that the mechanism predicts specific characteristics of the field obtained from paleomagnetic records [20], in particular their asymmetry: the Earth's dipole decays on a slower time scale than it recovers after a reversal. In addition, it displays an overshoot that immediately follows the reversals. Other characteristic features such as excursions as well as the existence of superchrons are understood in the same framework.

Although the symmetries of the flow in the Earth's core strongly differ from the ones of the VKS experiment, dipolar and quadrupolar modes can be defined with respect to equatorial symmetry such that model (1) can be transposed for Earth's magnetic field. From an analysis of paleomagnetic data, it has been proposed that reversals involve an interaction between dipolar and quadrupolar modes [21]. We thus obtain an interesting prediction about the liquid core in that case: if reversals involve a coupling of the Earth's dipole with a quadrupolar mode, then this requires that the flow in the core has broken mirror symmetry. In contrast, another scenario has been proposed in

which the Earth's dipole is coupled to an octupole, i.e., another mode with a dipolar symmetry. This does not require additional constraint on the flow in the core in the framework of our model. In any case, the existence of two coupled modes allows the system to evolve along a path that avoids $\mathbf{B} = \mathbf{0}$. In physical space, this means that the total magnetic field does not vanish during a reversal but that its spatial structure changes.

Finally, we note that reversals are also observed in purely hydrodynamic systems, in which a large scale flow driven by a turbulent background in thermal convection or in periodically driven flows, randomly reverses its direction [22]. A similar type of models can be used to understand the large scale dynamics that result from these bifurcations from turbulent flows.

References

1. Ya. B. Zeldovich, A. A. Ruzmaikin and D. D. Sokoloff, *Magnetic fields in astrophysics*, Gordon and Breach, New York 1983.
2. F. Pétrélis and S. Fauve, *Eur. Phys. J. B* **22**, 273-276 (2001).
3. S. Fauve and F. Pétrélis, *C. R. Physique* **8**, 87-92 (2007).
4. R. Stieglitz and U. Müller *Phys. Fluids*, **13**, 561 (2001); A. Gailitis et al., *Phys. Rev. Lett.* **86**, 3024 (2001).
5. S. Douady, Y. Couder and M. E. Brachet, *Phys. Rev. Lett.* **67**, 983-986 (1991)
6. S. Fauve, C. Laroche and B. Castaing, *J. Physique II* **3**, 271-278 (1993).
7. H. K. Moffatt, *Magnetic field generation in electrically conducting fluids*, Cambridge University Press, Cambridge 1978.
8. R. Monchaux et al., *Phys. Rev. Lett.* **98**, 044502 (2007).
9. M. Berhanu et al., *Europhys. Lett.* **77**, 59001 (2007).
10. F. Ravelet et al., *Phys. Rev. Lett.* **101**, 074502 (2008).
11. R. Monchaux et al., *Phys. Fluids* **21**, 035108 (2009).
12. L. Marié et al., *Eur. Phys. J. B* **33**, 469-485 (2003); M. Bourgoïn et al., *Phys. Fluids* **16**, 2529-2547 (2004); F. Ravelet et al., *Phys. Fluids* **17**, 117104 (2005); F. Stefani et al., *Eur. J. Mech. B* **25** 894 (2006).
13. F. Pétrélis, N. Mordant and S. Fauve, *G. A. F. D.*, **101**, 289-323 (2007).
14. R. Laguerre et al., *Phys. Rev. Lett.* **101**, 104501 (2008); **101**, 219902 (2008).
15. C. Gissinger, in preparation (2009).
16. C. Gissinger, E. Dormy and S. Fauve, *Phys. Rev. Lett.* **101**, 144502 (2008).
17. C. Gissinger et al., *Europhys. Lett.* **82**, 29001 (2008).
18. F. Pétrélis and S. Fauve, *J. Phys.: Condens. Matter* **20**, 494203 (2008).
19. F. Pétrélis et al., *Phys. Rev. Lett.* **102**, 144503 (2009).
20. J.-P. Valet, L. Meynadier and Y. Guyodo, *Nature* **435**, 802 (2005).
21. P. L. McFadden et al., *J. Geophys. Research* **96**, 3923 (1991).
22. R. Krishnamurti and L. N. Howard, *Proc. Natl. Acad. Sci.* **78**, 1981 (1981); J. Sommeria, *J. Fluid Mech.* **170**, 139 (1986); B. Liu and J. Zhang, *Phys. Rev. Letters*, **100**, 244501 (2008) and references therein.

Direct measurement of turbulent magnetic diffusivity in liquid metal flow

P. Frick, S. Denisov, V. Noskov, and R. Stepanov

Institute of Continuous Media Mechanics, Perm, Russia

frick@icmm.ru

In the mean field MHD-theory, an increase in the effective magnetic diffusivity (decrease of electric conductivity) of the developed turbulent flow of conducting fluid is commonly referred to as the β -effect. In spite of the fact that the effect seems to be quite obvious (in comparison with a far more sophisticated α -effect), up to now there have been no reliable direct measurements of effective electric conductivity in turbulent flows. We present the results of experiments, which intend to isolate the contribution of turbulence to the magnetic diffusivity.

The experimental set up is a rigid frame, which is used as a support for a rotating circular toroidal channel with dielectric walls (structural fabric-base laminate) [1]. The torus radius is $R = 0.0875$ m, the radius of the channel cross-section is $r_1 = 0.0225$ m. The channel is filled with a low-temperature gallium alloy (Ga-87.5%, Sn-10.5%, Zn-2%; melting point 19°C). It is fasten on the horizontal axis, which is also used for mounting a driving pulley, a system of sliding contacts and a disk braking system. The channel rotates with a frequency up to 55 r.p.s. and the flow in the channel is generated by abrupt braking - the braking time is no more than 0.1 sec. The maximal section-averaged velocity of the flow relative to the channel walls reaches at the full stop of the channel about 70 % of the linear velocity of the channel axis before braking. This means that the Reynolds number $Re = Ur_1/\nu$ (ν is the kinematic viscosity of the alloy) reaches at a maximum the value $Re \approx 10^6$, which corresponds to the magnetic Reynolds number $Rm \approx 1$.

The idea of the experiment consists in measuring the inductance of the toroidal coil embracing the channel, which depends on the electrical conductivity of the metal in the channel. The coil is a part of successively connected RLC-circuit (Fig. 1), and the measurements are made in the vicinity of the resonance because conductivity variations are small (of order of a percent). The variable to be determined is the difference in phase between sinusoidal voltage and current in the circuit. The measurements were made at two frequencies: 166.12 Hz and 963.90 Hz, at which the thickness of the skin layer is correspondingly about 8 and 20 mm.

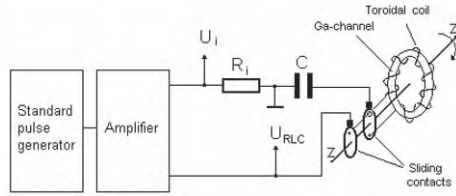


Fig. 1. Scheme of the experimental set up.

To calibrate the measurement system we performed a test thermal experiment on the channel at rest: the phase shift $\delta\Theta(T)$ dependence was determined at the stationary inductive heating of the channel. The aim of the test is to determine the temperature coefficient of the alloy resistivity, using this dependence and known thermal expansion coefficient of the alloy, materials of the channel wall, and coil wire. The measurements were performed at both resonant frequencies. Fig. 2 shows the measurement results. According to these results, the resistivity temperature coefficients are $(1.02 \pm 0.05) 10^{-3} \text{ K}^{-1}$ and $(0.98 \pm 0.07) 10^{-3} \text{ K}^{-1}$, which are close to the reference value of $(1.04 \pm 0.05) 10^{-3} \text{ K}^{-1}$.

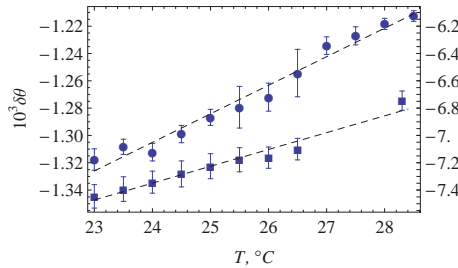


Fig. 2. Phase shift versus gallium temperature in the channel: $\omega = 166 \text{ Hz}$ (squares), $\omega = 964 \text{ Hz}$ (circles).

Fig. 3 shows the time dependence of the phase shift for various initial rotation frequencies. Each line is a result of averaging over 20 measurements. It is seen that the turbulent flow is developed in the channel with the beginning of braking; the intensity of this flow is maximal at the time of the complete stop of the channel. At this time, the phase shift is also maximal. Turbulence after the channel stop degenerates along with the mean flow and the phase shift decreases to the noise level.

Lack of velocity measurements and the nonstationarity prevent direct definition of the Reynolds number. However, the studies of similar water flows showed that in considered regimes the maximum of the Reynolds number, achieved in the nonstationary flow, at the same braking moment is proportional to the channel rotation speed before braking. In Fig. 4 the maximal

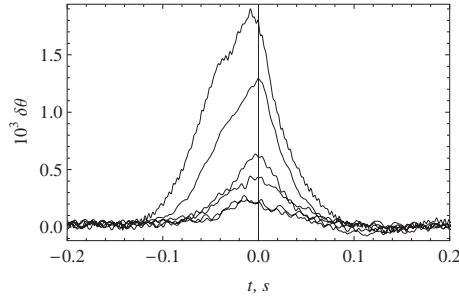


Fig. 3. Time dependence of the phase shift for the initial torus rotation frequencies (from top to bottom) 55, 50, 45, 40, and 35 s⁻¹. The resonant frequency is 964 Hz.

deviation of electrical conductivity measured at two frequencies ω for different rotation speeds are shown. For the maximal rotation speed $\Omega = 55$ r.p.s., which corresponds to $Rm \approx 1$, this deviation reaches about 1%.

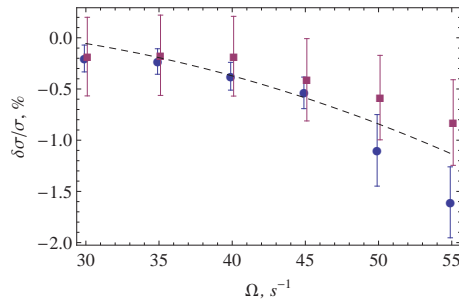


Fig. 4. Maximal relative variation of conductivity as a function of channel rotation speed: $\omega = 166$ Hz (squares), $\omega = 964$ Hz (circles).

So, the measurement of electric conductivity in the nonstationary fully developed turbulent ($Re \sim 10^6$) flow of gallium alloy in a closed channel shows that the effective conductivity decrease with the Reynolds number. In the range of the magnetic Reynolds number, available in the gallium experiment described above (see also [2]), the dependence looks like a quadratic $\beta \sim (Rm)^2$, which corresponds to general conceptions of the beta-effect. Apparently, the quadratic law will not hold at $Rm \rightarrow Re \gg 1$ because the turbulent viscosity in pipe flows at high Re increases as $\nu_t \sim Re^{1/2}$ and we have no reason to suppose that both turbulent transport coefficients develop in quite different ways. We have also no reasons to extend the obtained dependence to the case of homogeneous turbulence. However, in view of the fact that the problem of measuring the examined characteristic in the real flows is very complicated and the experimental data are completely absent, measurements of the effective electric conductivity in the turbulent medium even

in one particular case is an important step to experimental substantiation of general MHD-dynamo conceptions.



Fig. 5. Torus 2 (titanium).

Of special interest is the extension of the range of magnetic Reynolds number, available for measurement of effective conductivity in the turbulent flow. To achieve this goal we modify the experimental set up. The new set up includes a titanium channel (Fig. 5) - the torus radius is $R = 0.180$ m, the radius of the channel cross-section is $r_1 = 0.080$ m, which is filled with liquid sodium. High electro conductivity and low viscosity of liquid sodium allow us to achieve magnetic Reynolds number $Rm \approx 20$ (for channel rotation speed 40 r.p.s.). The essential growth of energy which must be dissipated during the braking requires modernization of the braking system and the transition to sodium requires a thermally-stabilized box around the channel. The set up modernization is in progress. We expect to made the first measurements in the summer and present the results in our talk.

The financial support from ISTC under project #3726 is kindly acknowledged.

References

1. R. Stepanov, R. Volk, V. Noskov, S. Denisov, P. Frick, and J.-F. Pinton, Phys. Rev. E, **73**, 046310 (2006).
2. S. Denisov, V. Noskov, R. Stepanov, and P. Frick, JETP Letters, **88**, 167 (2008).

Shell models of MHD turbulence

T. Lessinnes[†], D. Carati[†], M.K. Verma[‡] and F. Plunian[★]

[†] Service de Physique Statistique et des Plasmas,
Faculty of Sciences, Université Libre de Bruxelles B-1000 Bruxelles, BELGIUM

[‡] Department of Physics,
Indian Institute of Technology Kanpur, 208016 Kanpur, INDIA

[★]Laboratoire de Géophysique Interne et Tectonophysique,
Université Joseph Fourier, B.P. 53, 38041 Grenoble Cedex 9, FRANCE

Corresponding author: `Thomas.Lessinnes@ulb.ac.be`

Understanding the existence and the dynamics of the magnetic field of the Earth, of the Sun and, in general, of other celestial bodies (dynamo effect) remains one of the most challenging problems of classical physics. Analytical approaches of this problem are extremely complicated while numerical efforts are limited to a range of parameter space that is often quite distant from the realistic systems. For instance, in certain astrophysical bodies as well as in laboratory experiments, the kinematic viscosity ν of the fluid is six orders of magnitude smaller than its resistivity η . The two dissipation processes therefore take place at very different time scales. This property makes direct numerical simulations of dynamo intractable. Due to these reasons, we resort to simplified models.

Shell models specifically belong to this class of simplified approaches [1]. They have been constructed to describe interactions among various scales without any reference to the geometric structure of the problem. They were first introduced for fluid turbulence with the quite successful GOY shell model [2, 3] and have been extended to MHD turbulence [4, 5, 6, 7].

In shell models, a drastically reduced number of degrees of freedom (usually only one complex number) is used to describe the entire information provided by a shell of Fourier modes in wavevector space. A typical model considers N shells which are separated by a set of spheres concentric at the origin of the Fourier space. Their radii form a geometric progression of ratio $\lambda > 1$. Each shell s_i is associated to a typical wave number $k_i = k_0 \lambda^i$. Any observable quantity that was represented by its Fourier modes $\mathbf{x}_{\mathbf{k}}$ in MHD will be described in the model by N complex components $x_{i \in \{1, \dots, N\}}$, each of which representing the state of the Fourier modes $\mathbf{x}_{\mathbf{k}}$ lying in the i -th shell. These N components are gathered in a state vector \mathbf{X} . The scalar product of two fields (useful to define energies and helicities) is defined in the model by analogy with Parseval's identity: $\langle \mathbf{X} | \mathbf{Y} \rangle = \frac{1}{2} \sum_{i=1}^N (x_i y_i^* + y_i x_i^*)$.

The state of the system is contained in the two N-dimensional vectors \mathbf{U} (velocity field) and \mathbf{B} (magnetic field). The original MHD partial differential equations are simplified in this approach to a reduced set of ordinary differential equations. It provides a simplified tool for studying the energy and helicity exchanges between different scales at a significantly reduced numerical cost.

Emphasising on the antisymmetry of the non linear terms under $\mathbf{u} \leftrightarrow \mathbf{b}$ exchange, the incompressible MHD equations are in Fourier space

$$\frac{d\mathbf{u}_k}{dt} = \mathbf{n}_k(\mathbf{u}, \mathbf{u}) - \mathbf{n}_k(\mathbf{b}, \mathbf{b}) - \nu k^2 \mathbf{u}_k + \mathbf{f}_k, \tag{1}$$

$$\frac{d\mathbf{b}_k}{dt} = \mathbf{n}_k(\mathbf{u}, \mathbf{b}) - \mathbf{n}_k(\mathbf{b}, \mathbf{u}) - \eta k^2 \mathbf{b}_k, \tag{2}$$

with $\mathbf{n}_k(\mathbf{x}, \mathbf{y}) = i \mathbf{P}(\mathbf{k}) \cdot \sum_{\mathbf{p}+\mathbf{q}=-\mathbf{k}} (\mathbf{k} \cdot \mathbf{x}_q^*) \mathbf{y}_p^*$ and $P_{ij}(\mathbf{k}) = \frac{k^2 \delta_{ij} - k_i k_j}{k^2}$. It is remarkable that the first non linear term in the equation of evolution of \mathbf{b} , corresponding to the advection of the magnetic field by the velocity field, is not modifying the overall energy in the magnetic field: $\sum_{\mathbf{k}} \mathbf{n}_k(\mathbf{u}, \mathbf{b}) \cdot \mathbf{b}_k^* = 0$.

A shell model is therefore asked to be of the form [8]:

$$d_t \mathbf{U} = \mathbf{Q}(\mathbf{U}, \mathbf{U}) - \mathbf{Q}(\mathbf{B}, \mathbf{B}) - \nu \mathbf{D}(\mathbf{U}) + \mathbf{F}, \tag{3}$$

$$d_t \mathbf{B} = \mathbf{Q}(\mathbf{U}, \mathbf{B}) - \mathbf{Q}(\mathbf{B}, \mathbf{U}) - \eta \mathbf{D}(\mathbf{B}), \tag{4}$$

where the terms proportional to ν and η account for the viscous and Joule dissipations. The linear operator \mathbf{D} is defined by $\mathbf{D}(\mathbf{X}) = (k_1^2 x_1, k_2^2 x_2, \dots, k_N^2 x_N)$. The \mathbf{F} term describes the forcing. The operator \mathbf{Q} , often asked to be quadratic, models the operator \mathbf{n}_k .

In previous works [7], the non linear parts of these equations were asked to conserve a number of quadratic invariants. Letting \mathbf{W} and \mathbf{A} be respectively the vorticity and the potential vector¹, the conserved quantities are the total energy $\mathcal{E} = \frac{1}{2} (\langle \mathbf{U} | \mathbf{U} \rangle + \langle \mathbf{B} | \mathbf{B} \rangle)$, the cross helicity $\mathcal{H}^c = \langle \mathbf{U} | \mathbf{B} \rangle$ and the magnetic helicity $\mathcal{H}^m = \langle \mathbf{A} | \mathbf{B} \rangle$ as well as, in case of vanishing magnetic field ($\mathbf{B} = 0$), the kinetic energy $\mathcal{E}^k = \frac{1}{2} \langle \mathbf{U} | \mathbf{U} \rangle$ and helicity $\mathcal{H}^k = \langle \mathbf{U} | \mathbf{W} \rangle$.

However, the conservation of the magnetic energy by the advection term in the induction equation (2) has not been exploited so far. In a recently submitted article [8], we proposed to take this conservation into account thereby imposing that $\langle \mathbf{Q}(\mathbf{U}, \mathbf{B}) | \mathbf{B} \rangle = 0 \forall \mathbf{U}, \mathbf{B}$. This allows to recognise the first term in (4) as responsible for an energy exchange between magnetic variables only (letting the overall magnetic energy unchanged). The second non linear terms in (3,4) are then responsible for energy exchanges between the two fields.

The dynamo process involves growth of magnetic energy that is supplied from the kinetic energy via the non-linear interactions. A clear and unambiguous identification of the various energy fluxes and energy exchanges between the velocity and the magnetic fields is very important in the study of dynamo

¹ These quantities must be defined in function of \mathbf{U} and \mathbf{B} in the model (see [7] and [9] for two viable choices)

effects. This is one of the main motivations for the development of the present approach.

Introducing the notation $\mathbf{X}_i = (0, \dots, 0, x_i, 0, \dots, 0)$ for the projection of the vector \mathbf{X} on its i -th component, the energy e_i^x in the i -th shell of the \mathbf{X} field is defined by $e_i^x = \frac{1}{2} \langle \mathbf{X}_i | \mathbf{X}_i \rangle$. These quantities evolve as

$$d_t e_i^u = T(\mathbf{U} \rightarrow u_i) + T(\mathbf{B} \rightarrow u_i) - 2 \nu k_i^2 e_i^u + \langle \mathbf{F} | \mathbf{U}_i \rangle, \quad (5)$$

$$d_t e_i^b = T(\mathbf{B} \rightarrow b_i) + T(\mathbf{U} \rightarrow b_i) - 2 \eta k_i^2 e_i^b, \quad (6)$$

where $T(\mathbf{X} \rightarrow y_i)$ is the rate of energy transfer from the field \mathbf{X} to the i -th component of the \mathbf{Y} field. These transfers are defined in [8] as $T(\mathbf{U} \rightarrow u_i) = \langle \mathbf{Q}(\mathbf{U}, \mathbf{U}) | \mathbf{U}_i \rangle$, $T(\mathbf{B} \rightarrow u_i) = \langle \mathbf{Q}(\mathbf{B}, \mathbf{B}) | \mathbf{U}_i \rangle$, $T(\mathbf{B} \rightarrow b_i) = \langle \mathbf{Q}(\mathbf{U}, \mathbf{B}) | \mathbf{B}_i \rangle$ and $T(\mathbf{U} \rightarrow b_i) = \langle \mathbf{Q}(\mathbf{B}, \mathbf{U}) | \mathbf{B}_i \rangle$. The flux of magnetic energy $\Pi_B(n)$ from the big scale $k \leq k_{\text{sphere}}$ of \mathbf{B} to the small scales $k > k_{\text{sphere}}$ of \mathbf{B} through a sphere of radius $k_{\text{sphere}} = k_0 \lambda^n$ can be estimated [8] by

$$\Pi_B(n) = \sum_{j=n+1}^N T(\mathbf{B} \rightarrow b_j) = \sum_{j=n+1}^N \langle \mathbf{Q}(\mathbf{U}, \mathbf{B}) | \mathbf{B}_j \rangle, \quad (7)$$

One of the main advantages of the present formalism is that this flux is independent of the unknown circulating transfer appearing in the related past work by Dar et al. [10, 11].

This procedure has been applied in [8] to a specific class of shell models based on first neighbour couplings, known as the GOY model. It has been shown that the general constraints naturally lead to the already derived GOY-MHD shell model [7]. However, the interpretation of the energy fluxes appears to be simpler in the present formalism.

This model, together with our fluxes definitions, point out a magnetic-to-magnetic inverse cascade of energy at high magnetic Reynolds number. The flux Π_B is shown here in function of the delimiting sphere's radius k_{sphere} . For the low magnetic Reynolds number $R_m \propto \eta^{-1}$ (dotted curves) which are in reach of DNS [12, 13], the flux is positive and energy flows from the big scales to the small ones (direct energy cascade). However as R_m gets larger, there is a growing region of k_{sphere} for which the flux is negative indicating a reverse cascade of magnetic energy (i.e. from the small scales to the large ones). The value of k_{sphere} for which the flux changes sign seems to correspond to the typical Joule dissipation wave number k_η . This indicates that this reverse cascade is piloted by R_m and the scale of the magnetic dissipative structures rather than by the Prandtl number $P_m = \nu/\eta$. Moreover, if the model is correct, in actually developed MHD turbulence of $P_m < 1$, at scales within the kinetic and magnetic inertial ranges, the magnetic energy undergoes a *reversed* energy cascade.

We are currently studying this intriguing aspect with helical [9] and non-local [14] shell models.

This work has been supported by the contract of association EURATOM - Belgian state. The content of the publication is the sole responsibility of the

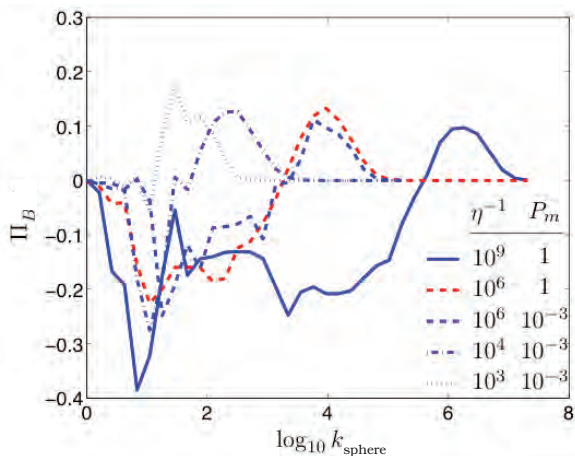


Fig. 1. Magnetic-to-magnetic energy fluxes for various values of η and of the Prandtl number $P_m = \nu/\eta$ in function of the logarithm of k_n . The forcing is applied in the region $10^{0.63} < k < 10^{1.25}$; $\lambda = (1 + \sqrt{5})/2$.

authors and it does not necessarily represent the views of the Commission or its services. D.C. and T.L. are supported by the Fonds de la Recherche Scientifique (Belgium). MKV thanks the Physique Statistique et Plasmas group at the University Libre de Bruxelles for the kind hospitality and financial support during his long leave when this work was undertaken.

References

1. L. Biferale. *Ann. Rev. Fluid Mech.*, 35:441–468, 2003.
2. E.B. Gletzer. *Soviet Phys., Doklady*, 18(216), 1973.
3. M. Yamada and K. Ohkitani. *Journal of the Physical Society of Japan*, 56, 1987.
4. C. Gloaguen, J. Léorat, A. Pouquet, and R. Grappin. *Physica D*, 17:154–182, 1985.
5. P. Frick and S. Sokoloff. *Phys. Rev. E*, 57(4), 1998.
6. T. Gilbert and D. Mitra. *Phys. Rev. E*, 69(5, Part 2), MAY 2004.
7. R. Stepanov and F. Plunian. *Journal of Turbulence*, 7(39), 2006.
8. T. Lessinnes, D. Carati and M. Verma. *Energy transfers in shell models for MHD turbulence*, submitted to *Phys. Rev. E*, 2009.
9. T. Lessinnes, D. Carati and F. Plunian. *Helical shell models for MHD*, submitted to *Theoretical and Computational Fluid Dynamics*, 2009.
10. G. Dar, M.K. Verma and V. Eswaran. *Physica D*, 3:207–225, 2001.
11. M. K. Verma. *Phys. Report*, 401: 229–380, 2004.
12. D. Carati, O. Debligny, B. Knaepen, B. Teaca and M. Verma. *Journal of Turbulence*, 51(7), 2006.
13. A. Alexakis, P.D. Mininni, and A. Pouquet. *Phys. Rev. E*, 72:046301, 2005.
14. F. Plunian and R. Stepanov. *New Journal of Physics* **9**, 294 (2007).

Turbulence induced by magnetic fields

K. Bajer, and K.A. Mizerski

¹ Institute of Geophysics, University of Warsaw, Poland
kbajer@fuw.edu.pl

² Department of Applied Mathematics, University of Leeds, UK
krzysztof.mizerski@gmail.com

Externally imposed magnetic field is usually a factor that stabilises flows of electrically conducting fluids. One long-known example, among many, is the archetypal Taylor-Couette flow between solid cylinders

A surprising counterexample is the magnetorotational instability (MRI) discovered by Chandrasekhar [6] and elucidated by Balbus and Hawley [3]. Ever since it attracts great interest as a possible mechanism of enhancing turbulence in accretion disks and may thus be responsible for the efficient transport of angular momentum inferred from observations [12].

In the weak-field limit the onset and the growth rate of the MRI is independent of the field strength, so even a seed field is a trigger of the powerful exchange-type *flow instability*. In this paper we describe the destabilising ef-

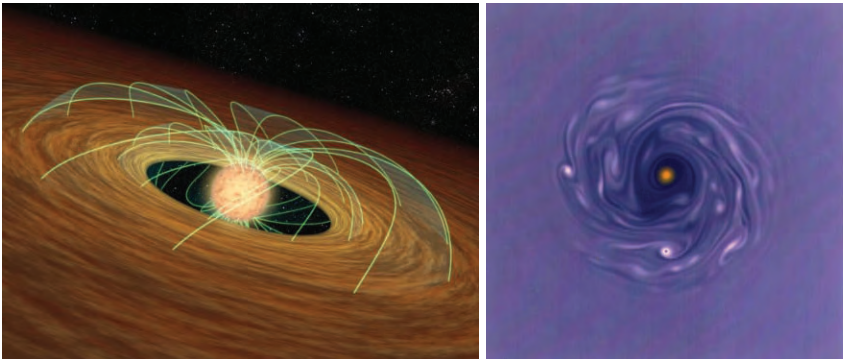


Fig. 1. Left: The artist's concept shows a dusty planet-forming disk in orbit around a whirling young star. The green colour marks the magnetic field lines dragged by the disk rotating more slowly than the star. NASA's Spitzer Space Telescope found evidence that disks like this one can slow stars down [1]; Right: Vorticity field in a Keplerian disk. Persistent anti-cyclonic vortices that emerge from an initially turbulent, freely decaying perturbation and survive for a long time [5].

fect of the magnetic field on recirculating flows with *elliptical* rather than circular streamlines [10, 2]. Such non-axisymmetric vortical flows are subject to the well-known elliptical instability (EI) [11, 4]. The EI is suppressed by cyclonic as well as by strong anticyclonic background rotation. We show that in anticyclonic vortices they may be triggered by a seed magnetic field just like the exchange instability (MRI) is triggered in otherwise stable axisymmetric flows.

Disruptions of the zonal flow in an accretion disc are likely to produce non-axisymmetric vortical structures just like ‘cat’s eyes’ appearing in a perturbed two-dimensional shear flow (fig. 1). When the zonal flow has outward-decreasing angular velocity, the emerging vortices will be anticyclonic. The

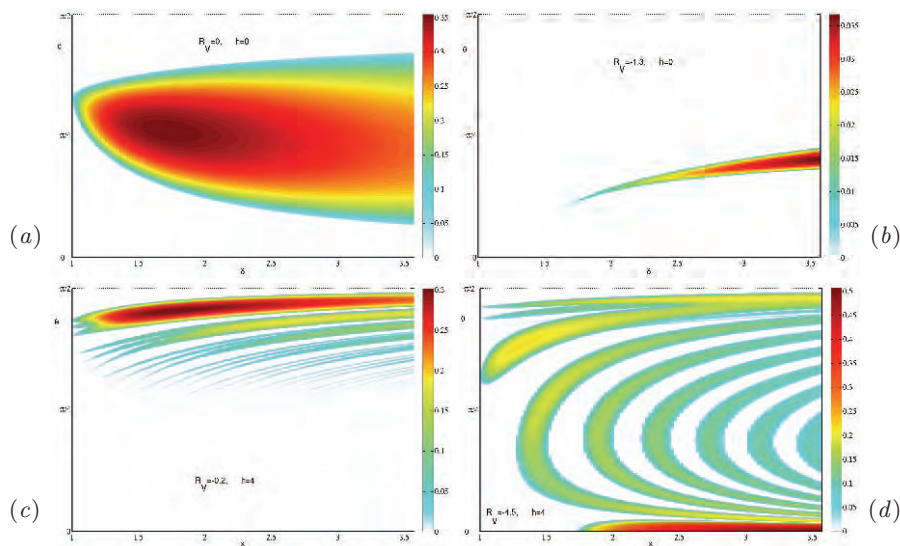


Fig. 2. Grey-scale plots of the growth rates of elliptical instability as functions of eccentricity parameter δ (horizontal axis) and inclination of the wave vector θ (vertical axis): (a) Neither background rotation nor magnetic field is present ($R_{\sigma}^{-1} = h = 0$). This case was analysed by Bayly [4]; (b) Background rotation is present but there is no magnetic field ($R_{\sigma}^{-1} = -1.3$, $h = 0$). This case was considered by Miyazaki and Fukumoto [8, 9]; (c) Weak background rotation and magnetic field are present ($R_{\sigma}^{-1} = -0.2$, $h = 4$). The tips ($\delta \rightarrow 0$) of the ‘tongues’ of instability (location and shape) agree with the asymptotic calculations (field present, no background rotation) of Lebovitz and Zweibel [7] (cf. [10]); (d) Strong background rotation and magnetic field are present ($R_{\sigma}^{-1} = -4.5$, $h = 4$). Although either factor in isolation is stabilising, the combination triggers the so-called ‘horizontal instability’ (elongated dark region near the horizontal axis) which is more powerful than any other unstable mode. Its domination over other modes increases with the rate of background rotation.

linear stability of an MHD flow of an ideal fluid is considered. The frame of reference is rotating with constant angular velocity $\boldsymbol{\Omega}$. The basic flow is two-dimensional, $\mathbf{U}_0 \perp \boldsymbol{\Omega}$, linear in Cartesian coordinates, has elliptical streamlines and is penetrated by the uniform magnetic field perpendicular to the plane of the flow, $\mathbf{B}_0 \parallel \boldsymbol{\Omega}$.

We find that for an anticyclonic basic flow the presence of magnetic field, however weak, may trigger a fast and powerful instability. The magnetic field may thus enable elliptical instability of anticyclonic vortices and therefore may ‘catalyse’, rather than suppress turbulence. Besides the well-known magnetorotational instability this may be an important mechanism of generating turbulence in accretion disks and tidally forced planetary cores.

Analysis

Let us consider the dynamics of a steady flow $\mathbf{u}(\mathbf{x}, t)$ of an ideal fluid penetrated by a magnetic field $\mathbf{B}(\mathbf{x}, t)$ and conducting electric current $\mathbf{j}(\mathbf{x}, t)$ with negligible resistivity. We write the equations of ideal MHD with respect to a frame of reference steadily rotating with angular velocity $\boldsymbol{\Omega} = \Omega \hat{\mathbf{e}}_z$,

$$\frac{\partial \mathbf{u}}{\partial t} + (\mathbf{u} \cdot \nabla) \mathbf{u} = -\rho^{-1} \nabla P - 2\boldsymbol{\Omega} \times \mathbf{u} + \rho^{-1} \mathbf{j} \times \mathbf{B}, \quad (1a)$$

$$\frac{\partial \mathbf{B}}{\partial t} + (\mathbf{u} \cdot \nabla) \mathbf{B} = (\mathbf{B} \cdot \nabla) \mathbf{u}, \quad (1b)$$

$$\nabla \cdot \mathbf{u} = 0, \quad \nabla \cdot \mathbf{B} = 0, \quad \mathbf{j} = \mu^{-1} \nabla \times \mathbf{B}, \quad (1c)$$

where ρ is fluid density, μ its permeability and $P(\mathbf{x}, t)$ is the pressure field including the potential of the centrifugal force.

We consider linear stability of a vortical flow with elliptical streamlines [4] and with uniform magnetic field aligned with the axis of rotation,

$$\mathbf{U}_0 = \gamma [-(1+\epsilon)y, (1-\epsilon)x, 0], \quad \mathbf{B}_0 = B_0 \hat{\mathbf{e}}_z, \quad (2)$$

where $-1 < \epsilon < 1$ is a measure of eccentricity.

The characteristic scales of time, velocity and length in this basic flow are given by γ^{-1} , $u_A = B_0(\rho\mu)^{-1/2}$, $u_A\gamma^{-1}$, where 2γ is the (uniform) relative vorticity and u_A is the Alfvén speed. We denote the (non-dimensional) inverse of the angular frequency of the vortex $\delta = \omega^{-1} = (1 - \epsilon^2)^{-1/2}$. The magnitude of the background rotation is characterised by the Rossby number, $R_o = \gamma/\Omega$, or its inverse, $R_v = R_o^{-1} = \Omega/\gamma$. When R_o and R_v are positive (negative) the vortex is called cyclonic (anticyclonic).

When we linearise (1) around the basic state (2) we find that they admit solutions in the form of Kelvin modes,

$$[\mathbf{u}', \mathbf{B}', P'] = [\mathbf{v}(t), \mathbf{b}(t), p(t)] \times e^{i\mathbf{k}(t) \cdot \mathbf{x}}, \quad (3)$$

where $\mathbf{k} = k_0 (\sin \vartheta \cos [\omega (t - t_0)], E \sin \vartheta \sin [\omega (t - t_0)], \cos \vartheta)$ with k_0 and ϑ arbitrary constants and $E = (1 + \epsilon)^{1/2} (1 - \epsilon)^{-1/2}$ yet another measure of eccentricity. Pressure can be eliminated by projection and (1c) are two conditions on \mathbf{u} and \mathbf{b} , so there remain altogether only four independent components of the Kelvin mode amplitudes jointly denoted as $\mathbf{s} = (v_x, v_y, b_x, b_y)$.

This vector satisfies a set of linear ODEs, $\dot{\mathbf{s}} = \widehat{\mathcal{S}}(t) \mathbf{s}$, where $\widehat{\mathcal{S}}(t)$ is a *periodic* 4×4 matrix [10]. The solutions are combinations of Floquet modes of the form $\mathbf{s}(t) = e^{\sigma t} \mathbf{f}(t)$ (see, e.g., lecture notes by Gerald Teschl [13]).

We have computed the Floquet exponents σ in a large region of the space of parameters $(\delta, \vartheta, R\bar{\sigma}^{-1}, k_0)$. The results are summarised in fig. 2. When the field is present the parameter h used in fig. 2 is the same as k_0 . Without the field the problem has no length scale, so σ does not depend on k_0 (all modes have the same growth rate). The main conclusion transpires that when background rotation (or R_v) has large negative value, the otherwise stable situation is violently destabilised even by weak magnetic field.

References

1. http://gallery.spitzer.caltech.edu/Imagegallery/image.php?image_name=ssc2006-15a
<http://www.jpl.nasa.gov/news/news.cfm?release=2006-094>.
2. K. Bajer and K. A. Mizerski. Elliptical flow instability triggered by a magnetic field. *Phys. Rev. Lett.*, 2009. (submitted).
3. S. A. Balbus and J. F. Hawley. A powerful local shear instability in weakly magnetized disks. I. Linear analysis. *Astrophys. J.*, 376(1):214–222, 1991.
4. B. J. Bayly. Three-dimensional instability of elliptical flow. *Phys. Rev. Lett.*, 57:2160–2163, 1986.
5. A. Bracco, P. H. Chavanis, A. Provenzale, and E. A. Spiegel. Particle aggregation in a turbulent keplerian flow. *Phys. Fluids*, 11(8):2280–2287, Aug. 1999.
6. S. Chandrasekhar. The stability of non-dissipative couette flow in hydromagnetics. *Proc. Nat. Acad. Sci.*, 46(2):253–257, Feb. 1960.
7. N. R. Lebovitz and E. Zweibel. Magnetoelliptic instabilities. *Ap. J.*, 609(1):301–312, 2004.
8. T. Miyazaki. Elliptical instability in a stably stratified rotating fluid. *Phys. Fluids A*, 5:2702–2709, 1993.
9. T. Miyazaki and Y. Fukumoto. Three-dimensional instability of strained vortices in a stably stratified fluid. *Phys. Fluids A*, 4(11):2515–2522, Nov. 1992.
10. K. A. Mizerski and K. Bajer. The magnetoelliptic instability of rotating systems. *J. Fluid Mech.*, 2009. In print.
11. R. T. Pierrehumbert. Universal short-wave instability of two-dimensional eddies in an inviscid fluid. *Phys. Rev. Lett.*, 57(17):2157–, Oct. 1986.
12. G. Rüdiger and R. Hollerbach. *The Magnetic Universe: Geophysical and Astrophysical Dynamo Theory*. Wiley, 1 edition, 2004.
13. G. Teschl. Ordinary differential equations and dynamical systems. <http://www.mat.univie.ac.at/~gerald/>, 2009.

Spin-up in MHD turbulence

S. Neffaa¹, W.J.T. Bos² and K. Schneider¹

¹M2P2-CNRS CMI, Université de Provence, Marseille, France

²LMFA-CNRS Ecole Centrale de Lyon, Université de Lyon, Ecully, France

In fusion plasmas, spontaneous large-scale poloidal rotation is beneficial for the confinement as it suppresses turbulence and radially extended structures, which are largely responsible for anomalous transport [1, 2]. This reduction of turbulent activity plays a key role in the transition to an improved confinement state (L-H transition) [3]. The absence of this transition would jeopardize the success of the ITER project. The understanding of large scale poloidal rotation is therefore primordial. It is generally admitted that the poloidal rotation of tokamaks is due to the asymmetry of the charge distribution. However, in recent work [4] the link was made between the L-H transition and the inverse cascade of two-dimensional turbulence. A neutral fluid can therefore also give rise to poloidal large-scale rotation.

The phenomenon of spontaneous generation of large-scale rotation-cells in two-dimensional fluid turbulence was discovered by Clercx *et al.* [5]. The importance of the non-axisymmetry of the geometry was recently demonstrated by Keetels *et al.* [6], and an interpretation in terms of statistical mechanics was obtained by Taylor *et al.* [7]. All these studies were performed for non-conducting fluids, using either the Navier–Stokes, or Euler equations. In MHD turbulence the question was investigated for the first time only very recently [8], where it was shown that spin-up in MHD turbulence is also present and that it can be enhanced by increasing the magnetic fluctuations. These observations were however done at low Reynolds numbers in square and circular geometries. In the present work we will confirm these results at higher Reynolds numbers in three different geometries, a square, a circle and an ellipse. It is shown that the tendency to generate angular momentum is stronger at higher Reynolds number. The tendency to generate angular fields is still present at these Reynolds numbers.

We present results of pseudo-spectral simulations of two-dimensional MHD turbulence in bounded domains. An efficient method to compute these flows is the penalization method, which was applied for the first time to MHD turbulence in [9].

The initial conditions consist of correlated noise, with a prescribed energy spectrum, peaked at the low wavenumbers. The initial fields contain zero or little angular momentum and angular field, defined respectively as

$$L_u = \int_{\Omega} \mathbf{e}_z \cdot (\mathbf{r} \times \mathbf{u}) dA, \quad L_B = \int_{\Omega} \mathbf{e}_z \cdot (\mathbf{r} \times \mathbf{B}) dA. \quad (1)$$

in which Ω is the flow domain and r is the position vector with respect to the center of the domain. Simulations are performed at a resolution of 512^2 grid-points. The magnetic Prandtl number is unity and the initial Reynolds number, based on the root mean square velocity, and domain-size is of the order of 10^4 . Ten simulations were carried out in each geometry and we present the results of the simulations in which the generation of angular momentum is maximal. The time is normalized by $D/\sqrt{2E_u(t=0)}$, D being the typical lengthscale of the fluid domain.

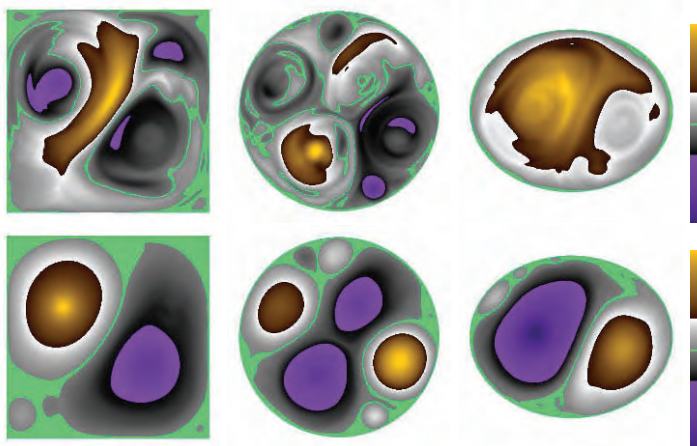


Fig. 1. The stream-function ψ (top), and the vector potential a (bottom) for the square, circular and elliptic geometries. The three columns correspond (from left to right) to the time instants $t^* = 3, 2, 2.7$ for which L_u (Fig. 2) is maximal. The time is normalized by the initial turn-over time.

Visualizations of the stream-function and the vector-potential are displayed in Figure 1. It is observed that both the velocity-field and the magnetic field exhibit a tendency to generate large-scale structures. To quantify the extent to which a large-scale swirling structure dominates the flow, we plot in Figure 2 the angular momentum in the three geometries. It is observed that strong spin-up takes place in the square and in the ellipse. The generation of the angular momentum is spontaneous, after a short time interval $t \approx 3$ and one observes that the amplitude is close to 0.4 in the square and 0.3 in the ellipse. This implies that, in the square container, the fluid reaches an

angular momentum which corresponds to approximately 40% of the angular momentum which would possess a fluid in solid-body rotation containing the same energy at $t = 0$. There is practically no spin-up in the circular container.

In Figure 2, bottom, the magnetic angular momentum is evaluated in all geometries. Surprisingly, in the square in which the generation of kinetic angular momentum was the strongest, L_B remains close to zero. However, in other simulations a small amount of L_B was generated in the square geometry. In the other two geometries, Figure 2 shows that an amount of L_B is created, however, this magnetic spin-up takes place on a time-scale which is larger than for its kinetic counterpart. Furthermore it can be observed that once L_B is created it remains almost constant over time.

In [8] we derived the equation for L_u in the case of MHD turbulence. It reads

$$\frac{dL_u}{dt} = \nu \oint_{\partial\Omega} \omega(\mathbf{r} \cdot \mathbf{n}) ds + \oint_{\partial\Omega} p^* \mathbf{r} \cdot d\mathbf{s} \quad (2)$$

with ν the kinematic viscosity, ω the vorticity, \mathbf{n} the unit-vector perpendicular to the wall, $p^* = p + B^2/2$ is the sum of the hydrodynamic and magnetic pressure. It was discovered by Clercx et al. [5] that spontaneous generation of angular momentum in hydrodynamic turbulence is observed in square domains, whereas it is absent in a circular domain. Subsequently, it was explained to be an effect due to the pressure [6], the last term in equation (2). Indeed, this term vanishes in a circular domain. In MHD, the presence of the magnetic pressure allows to vary the importance of the pressure term, while keeping the other parameters constant, by changing the value of the magnetic fluctuations. This is illustrated in Figure 2, right. The ratio E_B/E_u is varied, with E_B the mean-square of the magnetic fluctuations and E_u the mean-square of the velocity fluctuations. It is observed that the tendency to spin-up is significantly increased in the square geometry. It is thus shown that both geometry and magnetic pressure can play a role in the generation of zonal flows.

In [8], the tendency to generate angular fields was also investigated by computing the value of L_B . It was observed that angular fields were observed, even in the circular geometry. In Figure 2 bottom, we show that at higher Reynolds numbers the generation of this 'magnetic angular momentum' is weak but persistent. In the square geometry it is absent. Writing the equation for L_B , we find

$$\frac{dL_B}{dt} = \eta \oint_{\partial\Omega} j(\mathbf{r} \cdot \mathbf{n}) ds - 2\eta I. \quad (3)$$

where I denotes the net current through the domain, defined by $I = \int_{\Omega} j dA$. The pressure plays thus no direct role and only the net current or resistive magnetic stress can generate angular fields. We suspect that the observed spin-up of the magnetic field is related to the presence of a mean current through the circular domain. However, for the moment the reason is not understood and thus requires further investigation.

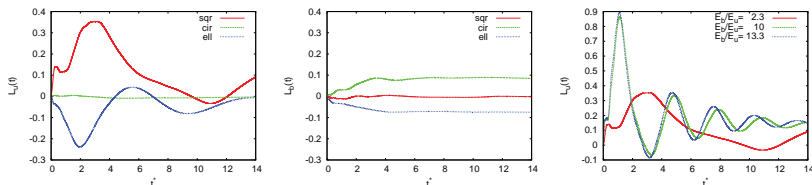


Fig. 2. Time-dependence of the angular momentum L_u (left) and angular field L_B (center) in the square, circular and elliptic geometry, normalized by $\mathcal{L}_u(0)$ and $\mathcal{L}_B(0)$, respectively. Right: The influence of the magnetic pressure on the spin-up in the square container is illustrated by changing the ratio E_B/E_u , while keeping E_u fixed.

Acknowledgments

We thankfully acknowledge financial support from the ANR, project M2TFP.

References

1. H. Biglari, P.H. Diamond, and P.W. Terry. Influence of sheared poloidal rotation on edge turbulence. *Phys. Fluids B*, 2:1, 1990.
2. X. Shan and D.C. Montgomery. Magnetohydrodynamic stabilization through rotation. *Phys. Rev. Lett.*, 73:1624, 1994.
3. F. Wagner *et al.* Regime of improved confinement and high beta in neutral-beam-heated divertor discharges of the ASDEX tokamak. *Phys. Rev. Lett.*, 49:1408, 1982.
4. M. G. Shats, H. Xia, and H. Punzmann. Spectral condensation of turbulence in plasmas and fluids and its role in low-to-high phase transitions in toroidal plasma. *Phys. Rev. E*, 71:046409, 2005.
5. H. J. H. Clercx, S.R. Maassen, and G.J.F. van Heijst. Spontaneous spin-up during the decay of 2d turbulence in a square container with rigid boundaries. *Phys. Rev. Lett.*, 80:5129, 1998.
6. G.H. Keetels, H.J.H. Clercx, and G.J.F. van Heijst. Spontaneous angular momentum generation of 2d flows in an elliptical geometry. *Phys. Rev. E*, 78:036301, 2008.
7. J.B. Taylor, M. Borchardt, and P. Helander. Interacting vortices and spin-up in two-dimensional turbulence. *Phys. Rev. Lett.*, 102:124505, 2009.
8. W.J.T. Bos, S. Neffaa, and K. Schneider. Rapid generation of angular momentum in bounded magnetized plasma. *Phys. Rev. Lett.*, 101:235003, 2008.
9. S. Neffaa, W.J.T. Bos, and K. Schneider. The decay of magnetohydrodynamic turbulence in a confined domain. *Phys. Plasmas*, 15:092304, 2008.

Influence of helicities on statistical properties of MHD turbulence

P. Frick, I. Mizeva and R. Stepanov

Institute of Continuous Media Mechanics, Perm, Russia
frick@icmm.ru

In the ideal 3D magnetohydrodynamical (MHD) turbulence there are three integrals of motion: the total energy $E^T = E^v + E^b$ where $E^v = \langle |\mathbf{v}|^2/2 \rangle$, $E^b = \langle |\mathbf{b}|^2/2 \rangle$, the cross helicity $H_c = \langle \mathbf{v} \cdot \mathbf{b} \rangle$ and the magnetic helicity $H_b = \langle \mathbf{A} \cdot \mathbf{b} \rangle$, $\mathbf{b} = \nabla \times \mathbf{A}$. Cross helicity characterizes the correlation between the velocity and magnetic field pulsations, and magnetic helicity characterizes the correlation between the magnetic field and its vector potential.

The idea to consider the developed turbulence as a random process allows us to assume that the fully developed isotropic turbulence of a conducting fluid is usually characterized by low level of cross helicity. It is precisely the situation which has been commonly the focus of researchers' attention. Interest in cross-helicity was aroused by discovery of highly correlated pulsations of the velocity and magnetic field in solar wind [1]. Energy evolution analysis of freely decaying turbulence shows that helicity decays slower than energy, therefore correlation of \mathbf{v} and \mathbf{b} , defined by correlation coefficient $C = H_c/E^T$ can rise in time [2].

The magnetic helicity can play a particular role in the dynamo processes as it has been recognized by [3, 4]. The arguments are based implicitly on local conservation of magnetic helicity: since magnetic helicity is a conserved quantity, it can change only if there is a flux of magnetic helicity through the boundaries, or through resistive effects which, however, are very slow, otherwise magnetic helicity will suppress the α -effect. Loss of the magnetic field confinement is believed to be the cause of coronal mass ejections, a major form of solar activity in the corona. It was pointed out that the accumulation of magnetic helicity in the corona plays a significant role in storing magnetic energy (for review, see [5]).

In this paper we study the role of helicities in the fully-developed MHD turbulence using a shell model of turbulence. Shell models describe the spectral transport by a moderate number of variables and are an effective instrument for studying statistical properties of the developed small-scale turbulence. Every variable is a collective characteristic of the amplitudes of the velocity U_n and the magnetic field B_n pulsations in the wave number range

$k_n < |\mathbf{k}| < k_{n+1}$, where $k_n = \lambda^n$, and λ , - interval width. The shell equations for collective variables are constructed in such a way as to keep "basic" properties of the motion equations, namely they should have the same motion integrals and the same nonlinearity. The MHD shell models reproduce quite well known properties of MHD turbulence and small-scale dynamo [6]. We use below the generalized Melander's model [7] in the form:

$$d_t U_n = ik_n(\Lambda_n(U, U) - \Lambda_n(B, B)) - \frac{k_n^2 U_n}{Ru} + f_n, \quad (1)$$

$$d_t B_n = ik_n(\Lambda_n(U, B) - \Lambda_n(B, U)) - \frac{k_n^2 B_n}{Rm} + g_n, \quad (2)$$

where the nonlinear terms are written as

$$\begin{aligned} \Lambda_n(X, Y) = & \lambda^2(X_{n+1}Y_{n+1} + X_{n+1}^*Y_{n+1}^*) - X_{n-1}^r Y_n \\ & - X_n Y_{n-1}^r + i\lambda(2X_n^* Y_{n-1}^i + X_{n+1}^r Y_{n+1}^i - X_{n+1}^i Y_{n+1}^r) \\ & + X_{n-1} Y_{n-1} + X_{n-1}^* Y_{n-1}^* - \lambda^2(X_{n+1}^r Y_n + X_n Y_{n+1}^r) \\ & + i\lambda(2X_n^* Y_{n+1}^i + X_{n-1}^r Y_{n-1}^i - X_{n-1}^i Y_{n-1}^r), \end{aligned}$$

where star means complex conjugation, and superscripts r, i are real and imaginary parts. Ru and Rm are the kinetic and magnetic Reynolds numbers. f_n and g_n are the external forcing which is generally used to support turbulence. These equations conserve three values which are written in terms of the shell model variables: $E^T = \sum(|U_n|^2 + |B_n|^2)/2$ - energy, $H_c = \sum(U_n B_n^* + B_n U_n^*)/2$ - cross helicity, $H_m = \sum k_n^{-1}((B_n^*)^2 - B_n^2)/2$ - magnetic helicity. And the difference of our shell model from previous one [6] is a definition of magnetic helicity.

First, we have studied numerically the free decay. Initially kinetic and magnetic energies are concentrated in one shell at $k = 1$. Four cases have been considered in order to determine the role of helicities: a) $H_c = H_m = 0$; b) $H_c = 0, H_m = 1$; c) $H_c = 1, H_m = 0$; d) $H_c = 1, H_m = 1$. The corresponding spectra are shown in fig. 1 after 1000 units of time evolution for $Ru = Rm = 10^5$. In the case (a) most of the energy decays and helicities have alternating sign along the scales. The scenario of evolution changes in the presence of magnetic helicity (case b). Now magnetic energy can cascade to the dissipation scale only with a simultaneous inverse cascade of magnetic helicity to a larger scale. This leads to partial accumulation of the energy at the largest scale and to a decrease of a dissipation rate. Cross helicity (case c) completely blocks the energy transfer from the scale of initial energy location. The presence of both helicities in the initial distribution (case d) provides the combined effect: magnetic helicity forces the inverse magnetic energy cascade to larger scale and cross helicity suppresses the efficiency of energy transfers.

Stationary turbulence implies external forcing. We use forces f_n and g_n , which operate in two neighbor shells, providing constant injection rates of kinetic energy $\epsilon = 1$, cross helicity χ and magnetic helicity ξ .

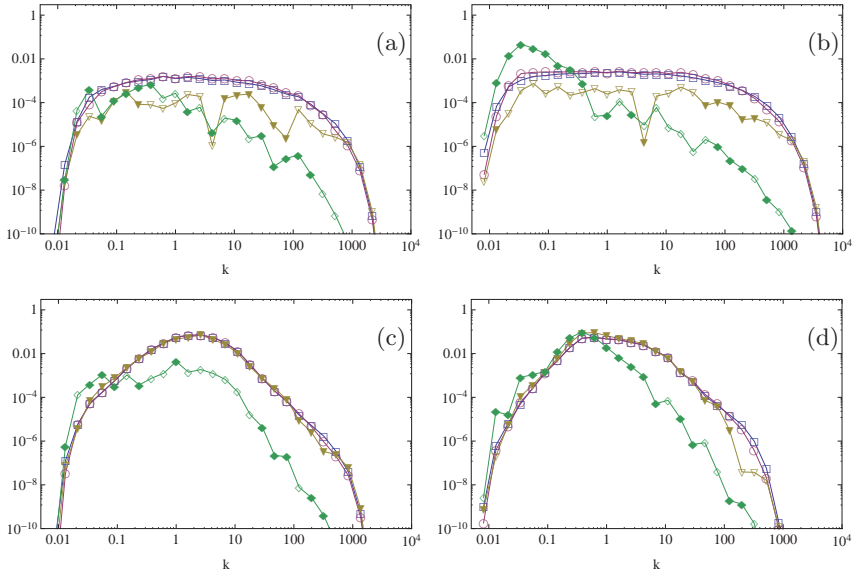


Fig. 1. Free decay for 4 initial conditions (a-d). Compensated spectra (by factor $k^{2/3}$) for kinetic energy (boxes), magnetic energy (circles), cross-helicity (triangles), magnetic helicity (diamonds) at the time moment $t=1000$. Filled symbols correspond to positive value of helicities at the given scale.

We have shown, that injection of cross helicity changes the spectral slope. The energy spectrum slope changes from Kolmogorov’s ”-5/3” to ”-2” (2). Cross helicity injection leads to energy accumulation in the turbulent flow (2 right panel). In the case of $\chi/\epsilon \rightarrow 1$ the velocity field and the magnetic field pulsations are correlated, the nonlinear terms in MHD equations are canceled and the energy cascade transfer is blocked. These numerical results are in good agreement with phenomenology suggested in [8]

Fig. 3 demonstrates a possible inverse cascade of magnetic helicity (see corresponding flux on the right). The injected magnetic helicity at the scale $k = 1$ can not go to smaller scale and provides acceleration of inverse energy cascade.

This work was supported by ISTC (project 3726) and RFBR-Ural grant No. 07-01-96007.

References

1. Belcher J.W., Davis L. // J.Geophys. Res, 1971. V.76. P.3534-3545.
2. Dobrowolny M., Mangeny A., Veltri P. // Phys. Rev. Lett., 1980. V.45. P.144-147.

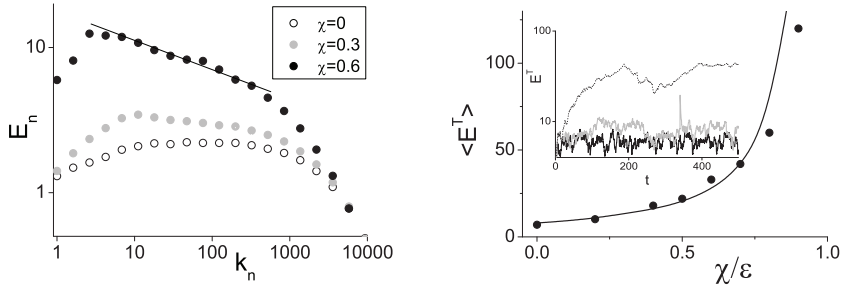


Fig. 2. Left: compensated by a factor $k_n^{2/3}$ energy spectra for different injection rate of cross helicity. Right: mean energy of stationary forced turbulence versus relative cross-helicity injection rate χ/ϵ . The energy evolution is shown in the inset : $\chi = 0$ – thick line, $\chi = 0.3$ – grey line, $\chi = 0.6$ – thin line.

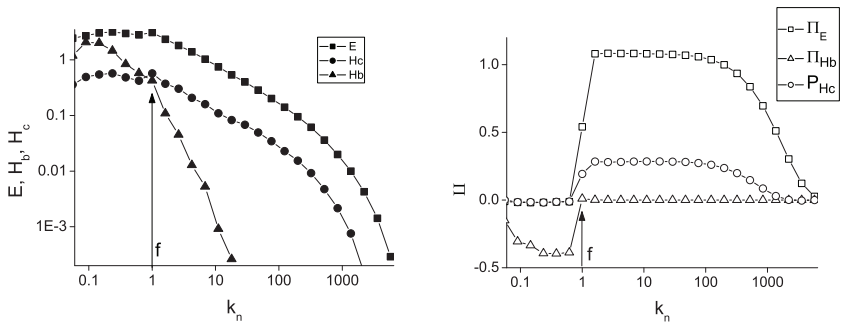


Fig. 3. Energy, cross helicity, magnetic helicity spectra (left) and fluxes (right) of forced MHD turbulence with defined helicities injection ($\epsilon = 1$, $\chi = 0.3$, $\xi = 0.4$).

3. Kleeorin, N., Moss, D., Rogachevskii, I., & Sokoloff, D. // A&A, 2000, V.361, L5
4. Blackman, E., & Field, G. // ApJ, 2000, V.534, P.984
5. Zhang, M., Flyer, N., & Low, B. C. // ApJ, 2006, V.644, P.575
6. Frick P., Sokoloff D. Cascade and dynamo action in a shell model of magneto-hydrodynamic turbulence// Phys. Rev. E, 1998, V.57, N.4, P.4155-4164.
7. Melander M.V. Helicity causes chaos in a shell model of turbulence// Phys. Rev. Lett. 1997, V.78 N.8 P.1456-1459.
8. I.A. Mizeva, R.A. Stepanov, P.G. Frik, // Doklady Akademii Nauk, 2009, V.424, N.4, pp.479483.

Transient growth in MHD duct flow

Thomas Boeck^a, Dmitry Krasnov^a, Maurice Rossi^b, and Oleg Zikanov^c

^aInstitute of Thermodynamics and Fluid Mechanics, TU Ilmenau, GERMANY

^bInstitut Jean Le Rond D'Alembert, CNRS Université Paris VI, FRANCE

^cDept. of Mech. Engineering, University of Michigan-Dearborn, Dearborn, USA

thomas.boeck@tu-ilmenau.de

The onset of turbulence in shear flows cannot be explained by classical hydrodynamic stability theory. The linear instability threshold is usually far above the practically observed one. An example in liquid-metal MHD is plane channel flow with wall-normal magnetic field B_0 (the Hartmann flow). Indeed, the critical Reynolds number for linear instability is about two orders of magnitude larger than the experimentally observed values [1]. Numerically, two problems were studied: the periodic Hartmann channel flow [2] and the complementary case of plane channel flow under spanwise magnetic field [3]. In the first case the basic Poiseuille flow is modified by the magnetic field (Hartmann profile) while it remains unaffected for the second one. Both studies were performed in the framework of a scenario based on transient growth and subsequent breakdown of optimal perturbations. In case of Hartmann flow, the optimal modes are purely streamwise rolls, while in the second case the optimal modes become rolls oriented at an oblique angle to the flow. In the present work we extend the previous studies to the case of a rectangular duct with insulating walls. The field B_0 is parallel to the sidewalls located at $y = \pm a$, so that the Hartmann layers are present at $z = \pm d$. On the side walls, the so-called Shercliff layers develop. In this geometry, transition mechanisms found in channel flow with either spanwise or wall-normal magnetic field can then be both relevant. The relative importance of these mechanisms is studied here by changing the aspect ratio $r = a/d$ of the duct (see Fig. 1): when $r \ll 1$ the case of channel flow under spanwise magnetic field is approached, on the contrary, when $r \gg 1$ the geometry would get close to the Hartmann channel flow case.

The mathematical model comprises the incompressible Navier-Stokes equations with the Lorentz force obtained with the quasistatic approximation. The optimal perturbations are Fourier modes of streamwise wavenumber α computed by the fixed-point iteration method based on the direct and adjoint equations (Ref.[3].) The numerical implementation is based on a projection-type method and second-order finite differences. The non-dimensionalization is based on the characteristic length $L \equiv \min(a/2, d/2)$ and the center-

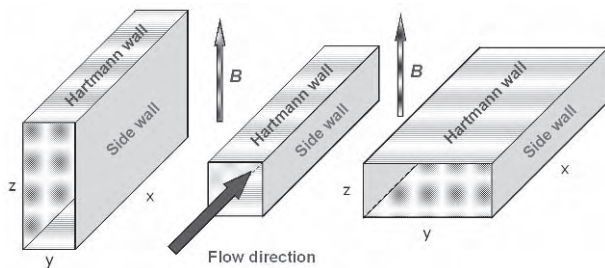


Fig. 1. Geometry of the duct flow under magnetic field B_0 . (left) $r \ll 1$ approaching the case of channel flow under spanwise field, (middle) $r \sim 1$ the general case of an almost square duct and (right) $r \gg 1$ approaching the Hartmann channel geometry.

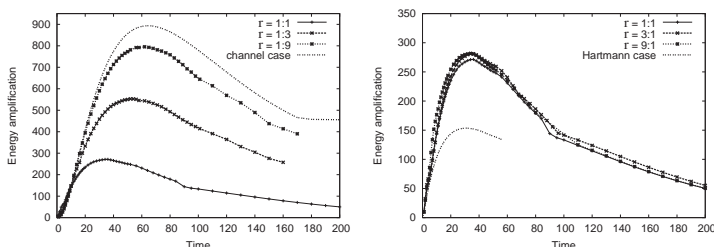


Fig. 2. Energy amplification for $Re = 5000$ and $Ha = 10$: $r < 1$ (left), $r > 1$ (right).

line velocity U . Two dimensionless numbers appear, the Reynolds number $Re = UL/\nu$ and the Hartmann number $Ha = L/\delta$, where $\delta = \frac{1}{B_0} \sqrt{\frac{\rho\nu}{\sigma}}$ with σ being electrical conductivity.

We focus on relatively weak magnetic fields, at which the transition can be expected. Fig. 2 shows the amplification factor G (maximized over wavenumbers α) as a function of the time T for $Re = 5000$ and $Ha = 10$. The results of a periodic channel with either wall-normal or spanwise magnetic field are shown for comparison in dots.

For small r the results for the amplification factor G approach the case of a channel with spanwise magnetic field. This effect is well seen in Fig. 2 as r is reduced. The maximum amplification increases significantly when r is reduced to $r \ll 1$. In this case, the long side walls parallel to the magnetic field should ultimately dominate, which is exactly what we observe (Fig. 4).

On the contrary, for large r (long Hartmann walls) the amplification factor G is significantly higher than for periodic Hartmann channel (Fig. 2). In fact, r has little effect on the amplification. This observation suggests that the Shercliff layers, which do not depend on r when $r \gg 1$, provide the dominant contribution to the amplification. This interpretation is confirmed by visualization of the optimal modes shown in Fig. 3. The pattern, visualized by the streamwise velocity perturbations, corresponds to the global optimal modes at initial and optimal time. It is clearly seen that the structures are largely

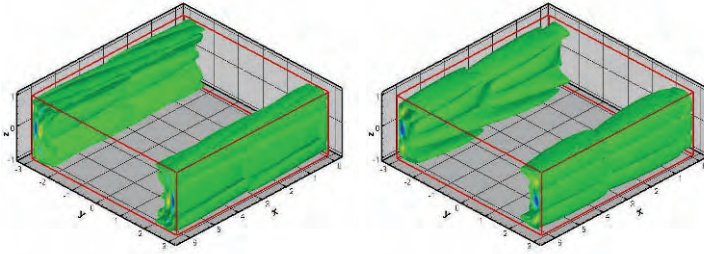


Fig. 3. Structure of optimal modes at $Re = 5000$ & $Ha = 10$ and $r = 3$. Streamwise velocity perturbations at initial time $T = 0$ (left) and at optimal time $T = T_{opt}$ (right).

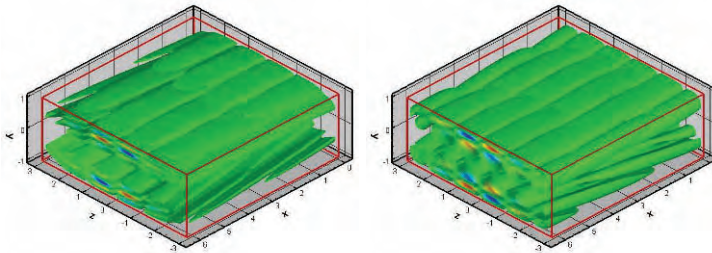


Fig. 4. Structure of optimal modes at $Re = 5000$ & $Ha = 10$ and $r = 1/3$. Streamwise velocity perturbations at initial time $T = 0$ (left) and at optimal time $T = T_{opt}$ (right).

confined to the short side walls parallel to the magnetic field. Remarkably, the optimal wavenumber α is nonzero in this case, which also separates MHD duct flow from the channel counterpart. Higher values of the Hartmann number ($Ha = 30$ and $Ha = 50$) were also tried for the same values of r . The level of amplification was reduced upon increasing Ha , but the same observations regarding the trends with r apply.

Further insight into the role of Shercliff (side) layers at large aspect ratio r can be obtained from fully non-linear simulations. We have developed a finite difference method for this purpose. Direct numerical simulations (DNS) with this code are currently performed in order to study transition in MHD duct flow systematically. First results for $Re = 5000$ and $Ha = 10$ concern the effect of the aspect ratio r , which has been varied in the limits from 1 to 6. The transition was triggered by random 3D noise imposed at the initially laminar flow state. Fig. 5 shows the results of DNS for the aspect ratio $r = 6$, the snapshots of the mean velocity profile correspond to various phases of transition. It is clearly seen that the basic conclusion of the linear analysis

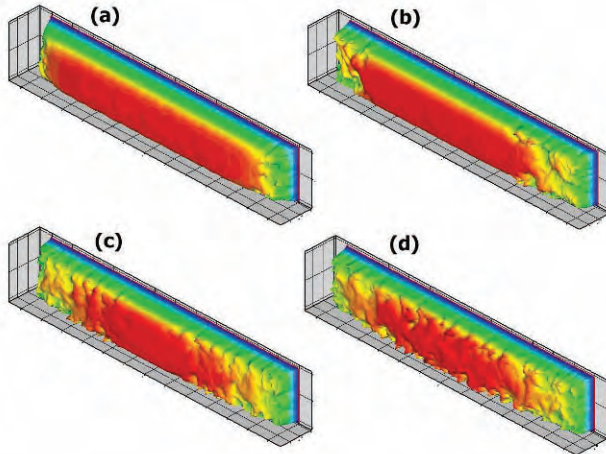


Fig. 5. Mean velocity profile in (y,z) -cross section at different stages of transition for $Re = 5000$, $Ha = 10$, $r = 6$.

is confirmed: the nuclei of instability are located in the region of side walls. Similar behavior was also observed at smaller $r = 3$ and also $r = 1$.

We remark that the appearance of transition in the side layers does not contradict the experimental transition results for the annular MHD duct [1]. These experiments can be interpreted as transition in the Hartmann boundary layers, and the transition range of Reynolds numbers matches fairly well with numerical results for periodic Hartmann channel flow [2]. However, transition in [1] could only be identified by qualitative changes in the dependence of the total friction drag on the Reynolds number. For the experimental values $Ha > 100$ the friction drag in the laminar case is mainly produced by the Hartmann layers. Transition might therefore remain unnoticed when the turbulence remains confined to the Shercliff layers. Numerical evidence for such behavior is a major objective of our ongoing transition simulations.

We conclude that the investigation of the optimal perturbations as sources of secondary instability proves very interesting because of the strong influence of the Shercliff layers.

TB, DK and MR acknowledge financial support from the Deutsche Forschungsgemeinschaft (Emmy-Noether grant Bo 1668/2-4).

References

1. Moresco, P., Alboussière, T., *J. Fluid Mech.* **504**, 167 (2004).
2. Krasnov, D., Zienicke, E., Zikanov, O., Boeck, T., Thess, A., *J. Fluid Mech.* **504**, 183 (2004).
3. Krasnov, D., Rossi, M., Zikanov, O., Boeck, T., *J. Fluid Mech.* **596** 73, (2008).

Optical visualisation of the flow around a cylinder in electrolyte under strong axial magnetic field.

O. Andreev, A. Kobzev, Yu. Kolesnikov, A. Thess

*TU Ilmenau, Faculty of Mechanical Engineering, Institute of Thermodynamics and Fluid Mechanics, P.O. 100565, 98684 Ilmenau, Germany,
olegs.andrejews@tu-ilmenau.de*

Introduction

Flows around obstacles are among the most common problems encountered in the fluid mechanics literature, and cylindrical obstacles definitely received the most extensive attention. The reason for this is that this relatively simple geometry already encompasses most of the important physical effects likely to play a role in flow around more complicated obstacles. This means that understanding the cylinder problem provides relevant insight on a wide variety of problem ranging from aerodynamics, with the flow around a wing or a vehicle, to pollutant dispersion around building, flows in turbines ... When the working fluid conducts electricity additional effects are involved. In particular, the presence of a magnetic field tends to homogenise the flow in the direction of the magnetic field lines which leads to strong alterations of the flow patterns known from the classical non-conducting case. This configuration is also a very generic one as Magnetohydrodynamic flows around obstacle also occur in a wide variety of applications: for instance, the space vehicle re-entry problem features the flow of a conducting plasma around an obstacle: [1] and [2] have shown that it could be influenced by a strong magnetic field in order to reduce heat transfer. The cooling blanket of the future nuclear fusion reactor ITER soon to be built in France, features a complex flow of liquid metal in a very high magnetic field (typically 10 T), in which the occurrence of obstacles cannot be avoided.

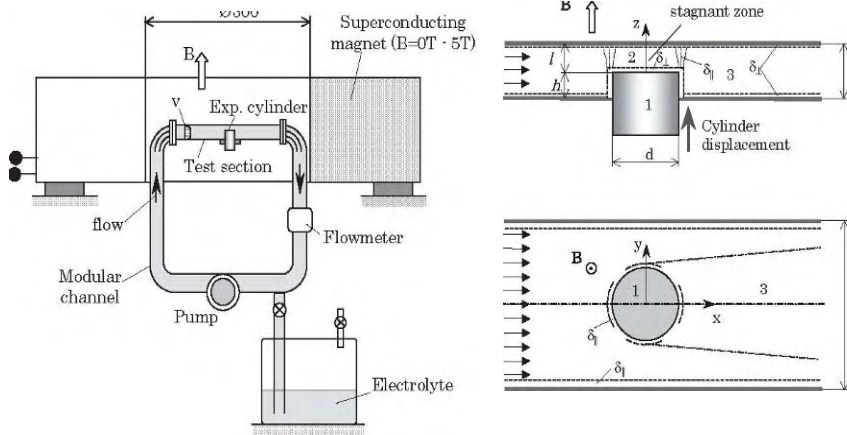


Figure 1. Schematic of flow facility showing modular channel and the test-section with cylinder, installed inside the superconducting magnet.

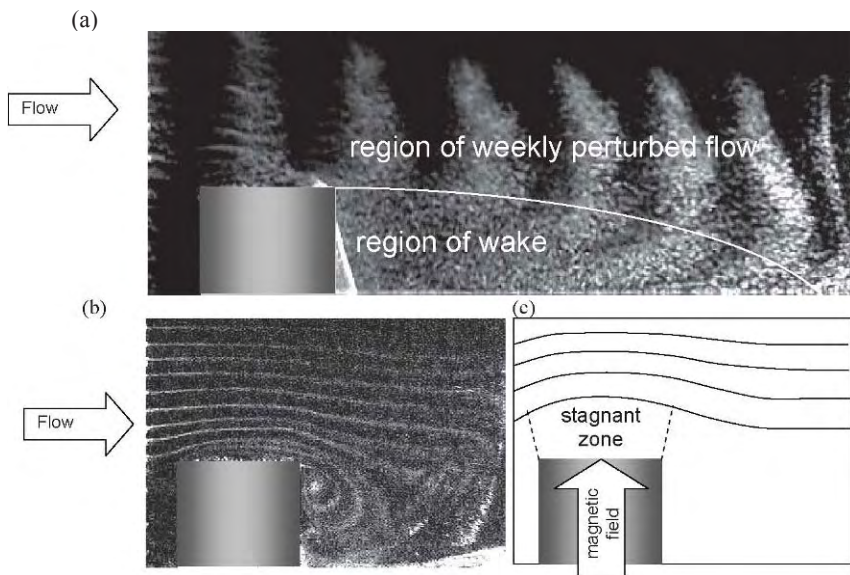


Figure 2. Flow around a truncated cylinder in its midplane ($Re = 500$, diameter and length of cylinder are $d=h=20$ mm). The flow without magnetic field is visualised by the (a) pulsed and (b) continuous electrical current. (c) Illustration of expected flow under axial magnetic field.

Experimental device

Since liquid metals are opaque, their interior cannot be visualized, which severely hampers our understanding of magnetohydrodynamic (MHD) flows. The purpose of the present work is to demonstrate that this fundamental limitation of experimental MHD can be overcome preliminary thanks to a superconducting 5-Tesla magnet at Ilmenau University of Technology. This facility permits us to perform MHD experiments with transparent electrolytes instead of opaque liquid metals. The test-section used is a rectangular channel made of Plexiglas. The channel cross-section is 50mm×60mm (see Figure 1). Diameter of the fully and truncated cylinder is varied within the range of $d = 5\text{--}25\text{mm}$. The cylinder is made movable with the aim to control a distance between the cylinder end the top wall. The experimental procedure includes velocity visualizations using tracer particles and dye as well as velocity measurements using PIV velocimetry for variable Reynolds number in the range of $30 < \text{Re} < 900$ and with variable Hartmann numbers in the range of $0 < \text{Ha} < 30$. For the first time the experiments provided a direct optical access to MHD-columns above the cylinders which have never before been directly observed.

Results

The results of preliminary experiments without magnetic field are shown in Figure 2. The flow is visualised in its midplane parallel by the axis of the cylinder. The gas bubbles generated by electrolyse on a regular grid of thin tungsten wires were used as the tracers illuminated by a light sheet. In Figure 2(a) the bubbles created by a pulse electrical current originate the regular vertical strips in the inlet flow. In the region above the cylinder the flow is not influenced by the obstacle. In the wake past the cylinder the bubbles strips are destroyed by the vortex street. It is visible that the wake of a truncated cylinder decays on the distance of three diameters for the given Reynolds number $\text{Re} = 500$. The experiment shown in Figure 2(b), the bounded vortex is visualised by continuous bubbles lines. At the absence of magnetic field the vorticity slightly diffuses from the cylinder on the distance, which does not exceed 3–4 mm. This diffusion of vorticity is defined by the balance of inertia and viscosity. An expected scenario of MHD flow around is shown in Figure 2(c). A stagnant zone directly above the cylinder should be generated because of electromagnetic diffusion of vorticity along the magnetic field in the so-called parallel MHD boundary layers δ_{\parallel} (see Figure 1). An MHD flow around of a virtual obstacle is well known from the studies of liquid metal flows at the presence of magnetic field [3]. Optical visualisation of this effect is one of the main task of the presented project.

In the framework of the experiments, which are performed in the TU Ilmenau we study the complex development of the MHD instability behind the fully and semi-immersed cylinder in dependence on the parameters Re and Ha and compare to the non-magnetic behavior. We transferred the results to MHD flows in practical applications with liquids of other physical properties.

Acknowledgments

The authors are grateful to the Deutsche Forschungsgemeinschaft for financial support in the framework of grant TH 497/27-1 at Ilmenau University of Technology.

References

- [1] Takizawa Y, A. Matsuda, S. Sato, T. Abe, and D. Konigorski. Experimental investigation of the electromagnetic effect on a shock layer around a blunt body in a weakly ionized flow. *Phys. Fluids*, 18:117105, 2006.
- [2] Andreev, O., Haberstroh, Ch., Thess, A., Visualization of Magnetoconvection, *Physics of Fluids* vol.15, 12, 2003.
- [3] Kolesnikov Yu.; Andreev O.: Heat transfer intensification promoted by vortical structures in a closed channel under magnetic field. *J. Exp. Thermal Fluid Sci.* (1997) vol.15(2), pp. 82-90.

Synthetic turbulence model and DNS for magnetohydrodynamics with rotation

B. Favier, F.S. Godeferd, and C. Cambon

Université de Lyon, Laboratoire de Mécanique des Fluides et d'Acoustique, École Centrale de Lyon, 69134 Ecully, France
benjamin.favier at ec-lyon.fr

1 Introduction

Many conducting fluids are subject to the combined Coriolis and Lorentz forces at the same time. On the one hand, interactions between a turbulent velocity field of an electrically conducting fluid and a magnetic field occur in many astrophysical and geophysical (geodynamo) systems. However, the full nonlinear coupling between Navier-Stokes and Maxwell equations remains difficult to solve numerically in many cases. On the other hand, the effect of solid-body rotation on homogeneous turbulence has also been extensively studied independently.

We consider here both effects, and we present the results of numerical simulations of incompressible homogeneous magnetohydrodynamic (MHD) turbulence submitted to a uniform magnetic field and to solid-body rotation. The magnetic field \mathbf{B}_0 is vertical and is given in Alfvén-speed units. The rotation rate $\boldsymbol{\Omega}$ is in a first approach aligned with \mathbf{B}_0 . The fluid is characterized by its magnetic diffusivity η and molecular viscosity ν . The magnetic Reynolds number R_M varies from 10^{-1} to 10^2 whereas the Reynolds number is 10^2 . The Elsasser number $\Lambda = B_0^2/2\Omega\eta$, characterizing the relative importance of the Lorentz force to the Coriolis force, varies from 10^{-1} to 10.

2 Numerical method

In addition to classical pseudo-spectral Direct Numerical Simulations (DNS), we propose a synthetic model of magnetohydrodynamic turbulence based on the kinematics of superimposed random modes. Kinematic simulations (KS) have already been used in many contexts from particle dispersion to aeroacoustics [1], as well as for small scale dynamo [2]. A complete description of the KS model can be found in the paper by Fung et al. [3]. The turbulent velocity field is synthesized as a random superposition of incompressible Fourier modes

$$u_j(\mathbf{x}, t) = \Re \sum_{n=1}^N \left(\hat{u}^{(1)}(\mathbf{k}_n) e_j^{(1)}(\mathbf{k}_n) + \hat{u}^{(2)}(\mathbf{k}_n) e_j^{(2)}(\mathbf{k}_n) \right) e^{i(\mathbf{k}_n \cdot \mathbf{x} + \omega_n t)} \quad (1)$$

where the orthonormal frame of reference $(\mathbf{e}^{(1)}(\mathbf{k}), \mathbf{e}^{(2)}(\mathbf{k}), \mathbf{k}/|\mathbf{k}|)$ ensures the divergence-free property of the fluctuating velocity field \mathbf{u} . In the general KS model, the characteristic frequency ω_n is introduced to model the unsteadiness of the flow (not considered in this first version for MHD). The amplitudes $\hat{u}^{(1)}$ and $\hat{u}^{(2)}$ are derived from a prescribed isotropic kinetic energy spectrum $E(k)$.

We consider an incompressible initially isotropic turbulent velocity field submitted to a large scale uniform magnetic field \mathbf{B}_0 and to solid-body rotation. The governing equations are linearized (low magnetic Reynolds number and low Rossby number limit) leading to the following linear system

$$\frac{\partial}{\partial t} \begin{pmatrix} \hat{u}^{(1)} \\ \hat{u}^{(2)} \\ \hat{b}^{(1)} \\ \hat{b}^{(2)} \end{pmatrix} + \begin{pmatrix} \nu k^2 & -\sigma_R & -i\sigma_B & 0 \\ \sigma_R & \nu k^2 & 0 & -i\sigma_B \\ -i\sigma_B & 0 & \eta k^2 & 0 \\ 0 & -i\sigma_B & 0 & \eta k^2 \end{pmatrix} \begin{pmatrix} \hat{u}^{(1)} \\ \hat{u}^{(2)} \\ \hat{b}^{(1)} \\ \hat{b}^{(2)} \end{pmatrix} = 0 \quad (2)$$

where $\sigma_R = 2\Omega k_3/k$ is the dispersion relation of inertial waves (k_3 is the vertical component of the wave vector, aligned with $\boldsymbol{\Omega}$) and $\sigma_B = \mathbf{B}_0 \cdot \mathbf{k}$ is the dispersion relation of Alfvén waves.

The main originality of the present work is to compute both the velocity field and the magnetic field using equation (1). The toroidal and poloidal amplitudes $\hat{u}^{(1)}(\mathbf{k}_n)$ (resp. $\hat{b}^{(1)}(\mathbf{k}_n)$) and $\hat{u}^{(2)}(\mathbf{k}_n)$ (resp. $\hat{b}^{(2)}(\mathbf{k}_n)$) in eq. (1) are derived from analytical linear solutions obtained in Fourier space by solving the linear system (2) and are thus time-dependent. Starting with given initial conditions, we are thus able to compute the equilibrium fields $\mathbf{u}(\mathbf{x}, t)$ and $\mathbf{b}(\mathbf{x}, t)$.

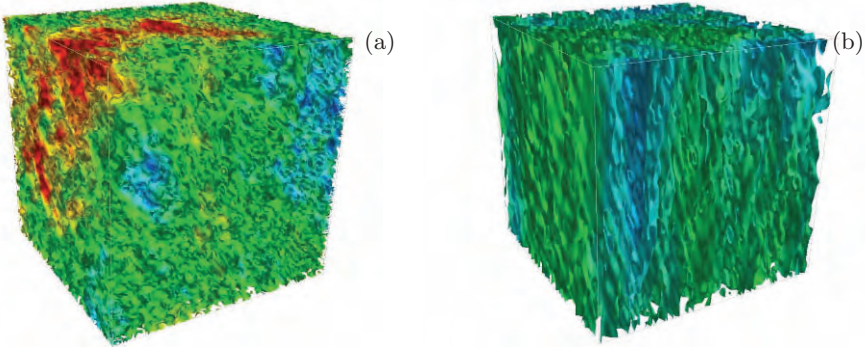


Fig. 1. Isovalues of kinetic energy in KS. Red color corresponds to high values whereas blue color corresponds to low values of the kinetic energy. (a) Initial isotropic condition. (b) After several dissipative times. The imposed magnetic field is vertical.

3 Results

In the following, we present different results obtained with the enhanced version of KS including linear dynamics, in comparison with DNS.

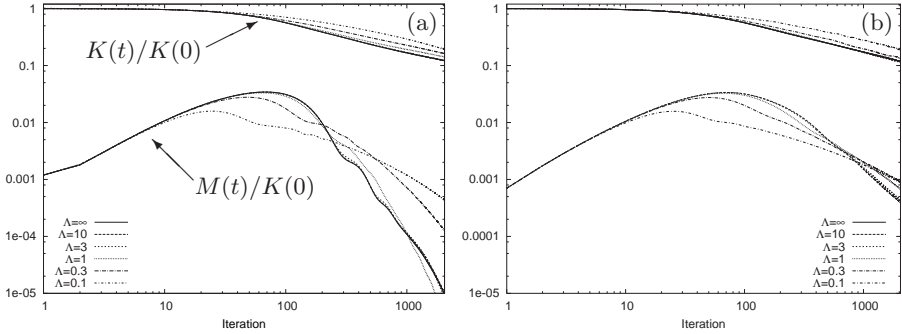


Fig. 2. Evolution of kinetic energy $K(t)$ and magnetic energy $M(t)$ versus time. $R_M \approx 10^{-1}$. $\Lambda = \infty$ corresponds to the non-rotating case. (a) DNS. (b) KS.

In the low R_M regime and without rotation, the Alfvén waves are damped in a particular domain in k space [4] and the turbulence tends to a two-dimensional state due to the anisotropy of ohmic dissipation (see Fig. 1 for KS results as well as [8, 7]).

The effect of the rotation on the decay of kinetic $K(t)$ and magnetic $M(t)$ energies is presented in Fig. 2. The KS model is less dissipative because of the absence of non-linear energy transfers. However, in both models, the decay of the magnetic energy is less pronounced in rotating cases.

For a magnetic Prandtl number $P_M = \nu/\eta \approx 1$ hence at higher R_M , an equipartition state of energy is observed due to the presence of Alfvén waves. Fig. 3 presents the evolution of the kinetic and magnetic energies with time. Rotation mainly damps the magnetic energy and this effect is very well reproduced by a simple linear model. Without rotation, the poloidal components of both velocity and magnetic fields are independent of their toroidal counterparts. But the linear system (2) shows an enhancement of the coupling existing between the poloidal and the toroidal velocity components

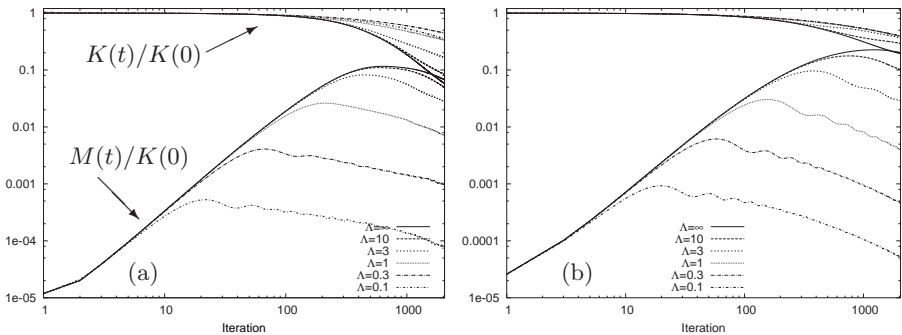


Fig. 3. Same as Fig. 2. $R_M \approx 10^2$. (a) DNS. (b) KS.

in the rotating case. If rotation is dominant, the energy is trapped in inertial waves so that the equipartition state due to Alfvén waves is no longer observed.

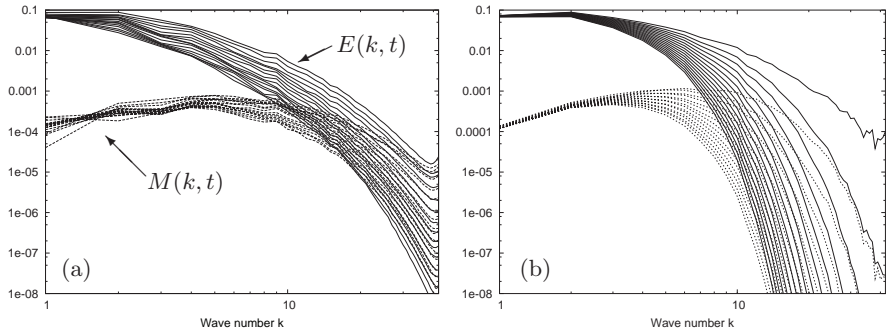


Fig. 4. Kinetic and magnetic energy spectra at different times. $\Lambda \approx 1$ and $P_M \approx 1$. (a) DNS. (b) KS.

Moreover, looking at Eulerian energy spectra on Fig. 4, one observes that the competition between Coriolis and Lorentz forces is a scale-dependent problem. The inertial waves are dispersive whereas the Alfvén waves are not. At large scale, the inertial waves are dominant, leading to dominant transfer of energy between poloidal and toroidal components of the velocity. At small scales, the Alfvén waves lead to an equipartition state. Note that, looking at Fig. 4(b), the linearity of the KS model is well observed: without any energy transfer terms, the small scales are rapidly dissipated.

4 Perspectives

In addition to more details about energy spectra, we will focus on the anisotropy of such flow (Shebalin angles [6], angular energy spectra [5]). The Lagrangian properties of rotating MHD turbulence will also be investigated using DNS as well as the KS model presented in this paper.

References

1. B. Favier, F.S. Godeferd and C. Cambon *J. of Turb.*, **9**, (2008)
2. S.L. Wilkin, C.F. Barenghi and A. Shukurov *Phys. Rev. L.*, **99**, 134501 (2007)
3. J. Fung, J. Hunt, N. Malik and R. Perkins *J. Fluid Mech.*, **236**, (1992).
4. H.K. Moffatt *J. Fluid Mech.*, **28**, (1967).
5. L. Liechtenstein, F.S. Godeferd and C. Cambon *J. of Turb.*, **6**, (2005)
6. J.V. Shebalin, W.H. Matthaeus and D. Montgomery *J. Plasma Phys.*, **29**, (1983)
7. S. Oughton, E.R. Priest and W.H. Matthaeus *J. Fluid Mech.*, **280**, (1994)
8. O. Zikanov and A. Thess *J. Fluid Mech.*, **358**, (1998)

Spectral analysis of energy transfers in anisotropic MHD turbulence

B. Teaca^{1,2}, D. Carati¹, B. Knaepen¹, and M. K. Verma³

¹ Statistical and Plasma Physics, Université Libre de Bruxelles, Campus Plaine, CP 231, B-1050 Brussels, Belgium

² Faculty of Physics, University of Craiova, A.I. Cuza 13, 200585 Craiova, Romania

³ Department of Physics, Indian Institute of Technology, 208016 Kanpur, India
bteaca@ulb.ac.be

Summary. We investigate anisotropic magnetohydrodynamic turbulence, in presence of a constant magnetic field, using direct numerical simulations. A method of decomposing the spectral space into ring structures is presented and the energy transfers between such rings are studied. For large values of the constant magnetic field, the total energy transfer appears to be dominant in the direction perpendicular to the mean magnetic field. The linear transfer due to the constant magnetic field also appears to be important in redistributing the energy between the velocity and the magnetic fields.

The study of energy transfers in anisotropic systems is useful for better understanding the dynamics of anisotropic turbulence, that in turn will help in developing LES models for MHD turbulence. The energy transfers in both fluid and MHD turbulence are usually presented in spectral space by computing the energy exchanges between the Fourier modes. Since the majority of modes have similar properties as their wave-number neighbors and bring similar contribution to the energy exchange between scales, the analysis of energy transfers is usually simplified by partitioning the spectral space into sub-domains and by considering the averaged energy transfers between these sub-domains [1, 2]. The partitioning of the spectral domain is arbitrary but several convenient geometrical structures are preferred. The spectral spherical symmetry observed in the case of isotropic turbulence naturally suggests a decomposition of the spectral domain into wave-number shells. For this case, the shell-to-shell energy transfer functions and spherical energy fluxes have been studied in detail [3, 4, 5, 6]. In the presence of a mean magnetic field, the flow develops a preferred direction and exhibits anisotropy [7, 8]. The degree of anisotropy depends on the strength of the mean magnetic field. The angular dependence with respect to the preferred direction then becomes as relevant as the wave vector amplitude in the spectral space partition, and a simple shell decomposition may not be appropriate any more. Coaxial cylindrical domains

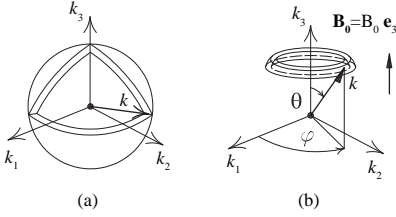


Fig. 1. a) Shell decomposition; b) Ring decomposition.

aligned with the preferred direction and planar domains transverse to each direction have both been used in the past to partition the spectral space [9].

In this work, we propose another partition, indexed $\{m, \alpha\}$, that is based on a ring decomposition of shells. This decomposition method takes into account the angular dependency of energy transfers in anisotropic systems, while it allows to recover easily the known shell-to-shell energy transfers in the limit of isotropic turbulence. The first index m corresponds to the spherical shell decomposition. A shell s_m contains all the wave-vectors \mathbf{k} with the property $k_m \leq |\mathbf{k}| < k_{m+1}$ (Fig. 1.a). The second index α corresponds to the angular dependency. For simplicity, the mean magnetic field is assumed to be aligned with \mathbf{e}_3 . The wave-vector \mathbf{k} forms an angle θ with respect to the \mathbf{B}_0 , with $\theta \in [0, \pi]$. The spectral domain is split into angular sections a_α so that each section contains the wave-vectors that have the angle θ bounded by $\theta_{\alpha-1} \leq \theta < \theta_\alpha$. The intersection between the spherical shells and the angular sections defines the ring structures $r_{m\alpha} = s_m \cap a_\alpha$ (Fig. 1.b).

From the incompressible MHD equations, in presence of a constant magnetic field \mathbf{B}_0 , we obtain the evolution equations for the energy contained by a ring:

$$\frac{\partial}{\partial t} E^{u\{m,\alpha\}} = N_u^{u\{m,\alpha\}} + N_b^{u\{m,\alpha\}} + L_{ub}^{\{m,\alpha\}} - D^{u\{m,\alpha\}} + I^f\{m,\alpha\}, \quad (1)$$

$$\frac{\partial}{\partial t} E^{b\{m,\alpha\}} = N_b^{b\{m,\alpha\}} + N_u^{b\{m,\alpha\}} - L_{ub}^{\{m,\alpha\}} - D^{b\{m,\alpha\}}, \quad (2)$$

where the terms $N_Y^X\{m,\alpha\}$ represent the energy transfer to ring $\{m,\alpha\}$ of field X from the field Y . The terms $N_Y^X\{m,\alpha\}$ are obtained from the *ring-to-ring* energy transfer functions $T_Y^X\{m,\alpha\}$ (which naturally satisfy the antisymmetry property $T_Y^X\{m,\alpha\} = -T_X^Y\{n,\beta\}$) as:

$$N_Y^X\{m,\alpha\} = \sum_{\{n,\beta\}} T_Y^X\{m,\alpha\}. \quad (3)$$

The linear transfer due to the constant magnetic field \mathbf{B}_0 is represented by $L_{ub}^{\{m,\alpha\}}$. The dissipation of energy for field X is labeled $D^X\{m,\alpha\}$ and the energy injection due to the external forcing used to bring the turbulent system to a stationary state is denoted by $I^f\{m,\alpha\}$.

We have performed DNS of 512^3 modes in a 2π length box, with periodic boundary conditions. The energy transfers are studied using a ring decompo-

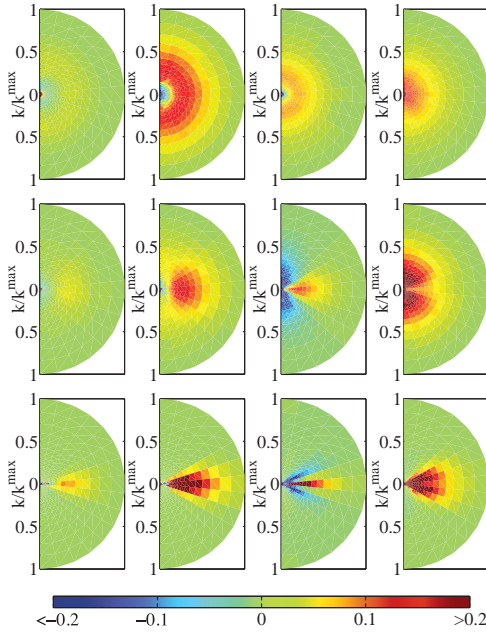


Fig. 2. The total nonlinear energy transfer to each ring. Left to right columns indicate: $N_u^{u\{m,\alpha\}}$, $N_b^{b\{m,\alpha\}}$, $N_b^{u\{m,\alpha\}}$ and $N_u^{b\{m,\alpha\}}$. Top to bottom represent the isotropic, *weak anisotropic* and *strong anisotropic* runs. **Note:** the rings are projected onto a plane and the intensity of the variables are color coded. The values displayed are normalized to the forcing energy injection rate. The plots take into account the width of each shell for which the boundaries have been normalized to the largest wave-number considered by our simulations, $k^{\max} = 256$.

sition of the spectral space, using 23 spherical shells with the boundaries for $m > 3$ given by the law $k_m = 2^{(m+8)/4}$ and 15 angular sections, with an angular separation of 12° . The forcing used is isotropic and acts only in the shell s_2 . Three runs have been compared. One run corresponds to the isotropic system ($\mathbf{B}_0 = 0$), and the other two cases are nonzero \mathbf{B}_0 that have been referred to as the *weakly anisotropic* and *strongly anisotropic* runs. The energy and energy dissipation (not shown) have been observed to depend on the angular section. The anisotropy becomes more pronounced for when the strength of the mean magnetic field is increased. We will resume to the presentation of the linear and nonlinear energy transfers, named after the terms in the MHD equations that generates them.

We present the total energy transferred to a ring from all the other rings ($N_Y^{X\{m,\alpha\}}$) in Fig. 2. The angular dependency of the transfer functions is evident. It is interesting to observe that the cross-field transfer (between the velocity and the magnetic fields) changes sign depending on the direction to \mathbf{B}_0 for the anisotropic cases. With the increase of \mathbf{B}_0 , the rings near the equator have stronger energy transfer compared to the ones near the poles.

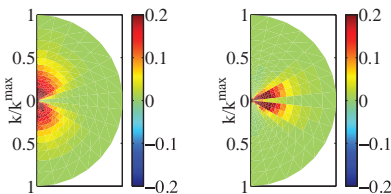


Fig. 3. Ring representation of the linear transfer $L_{ub}^{m,\alpha}$ for weak anisotropy (left) and strong anisotropy (right). Same note as in Fig. 2 applies.

The linear energy exchange rate $L_{ub}^{\{m,\alpha\}}$ is shown in Fig. 3. Because this term is proportional to \mathbf{B}_0 , it has to vanish in the direction perpendicular to the constant magnetic field. Interestingly, the transfer is also suppressed in the parallel direction for larger degrees of anisotropy and tends to concentrate towards the equatorial rings with the increase of \mathbf{B}_0 value.

These features can be largely explained by the global phenomenology of energy transfers. Indeed, the energy is injected into the system in kinetic form only and in the forcing range which is very close to the smallest shells. It is dissipated in the large wave-number shells, both by viscous and Joule effects. Since the analysis is performed in a statistically stationary regime, energy has to flow from u to b and from small to large shells. Also, outside the forcing range, the dissipation in a shell has to be exactly balanced by the total nonlinear transfer to this shell. Indeed, when summing the energy transferred to u and b , the linear transfers cancel exactly. In the anisotropic cases, energy is preferentially transferred towards the equatorial plane. In the *strong anisotropic* case, almost no energy is left close to the poles and the absolute transfers from the pole region are very small.

Clearly, these observations might have consequence in MHD turbulence modelling. There is a reasonable chance that models used in LES of isotropic turbulence would be also suitable for anisotropic MHD turbulence. Indeed, the information lost when removing the smallest scales in a LES does not affect the linear terms but only the nonlinear terms through mode-to-mode couplings. Anisotropy effects generated by the linear terms would be perfectly captured in an LES. The constant magnetic field explicitly affect the linear transfer terms but not the nonlinear terms. The nonlinear transfers only become anisotropic because they redistribute kinetic and magnetic energies that have been affected by the presence of \mathbf{B}_0 in the linear terms. There is thus no clear reason to design new models for anisotropic MHD turbulence. The same conclusion was reached in [10], for the low magnetic Reynolds number limit.

References

1. J.A. Domaradzki and R.S. Rogallo, Phys. Fluids A **2**, 413 (1990).
2. M.K. Verma, Phys. Report **401**, 229 (2004).
3. A. Alexakis, P.D. Mininni, and A. Pouquet, Phys. Rev. E **72**, 046301 (2005).
4. P.D. Mininni, A. Alexakis, and A. Pouquet, Phys. Rev. E **72**, 046302 (2005).
5. O. Debligny, M.K. Verma, and D. Carati, Phys. Plasmas **12**, 042309 (2005).
6. D. Carati, O. Debligny, B. Knaepen, B. Teaca, and M.K. Verma, J. of Turbulence **7** N51, 1 (2006).
7. W. H. Matthaeus, S. Ghosh, S. Oughton, and D. A. Roberts, J. Geophys. Res. **101**, 7619 (1996).
8. J. Cho and E.T. Vishniac, ApJ **539**, 273 (2000).
9. A. Alexakis, B. Bigot, H. Politano, and S. Galtier, Phys. Rev. E **76**, 056313 (2007).
10. B. Knaepen and P. Moin, Phys. Fluids **16**, 1255 (2004).

Part XIII Acoustics of turbulence flows

Boundary layer influence on cavity noise generation

V. Koschätzky, R. Delfos, B. J. Boersma and J. Westerweel

Laboratory for Aero & Hydrodynamics, Leegwaterstraat 21, TUDelft, 2628CA Delft, The Netherlands
v.koschätzky@tudelft.nl

Introduction

The generation of noise by flow over a rectangular cavity is an important benchmark problem for aeroacoustics and has been investigated both experimentally and numerically in the last decades [5]. Studies showed how the flow that generates past cavities depends on multiple factors such as the cavity geometry, the free stream velocity and the incoming boundary layer properties. In this paper we investigate the relationships between the incoming boundary layer, the development of the shear layer instabilities and the aeroacoustic emission. It has been previously suggested [1, 6, 3], that the character of the turbulent flow can change drastically depending on the ratio between the length of the cavity and the boundary layer momentum thickness, L/θ . It has been found that when this ratio is smaller than a certain value (between 80 and 100, depending on the study), self sustained oscillations of the shear layer do not occur. We demonstrate here how also the acoustic emissions change under the different conditions investigating flow and acoustic characteristics for laminar and turbulent upstream boundary layers.

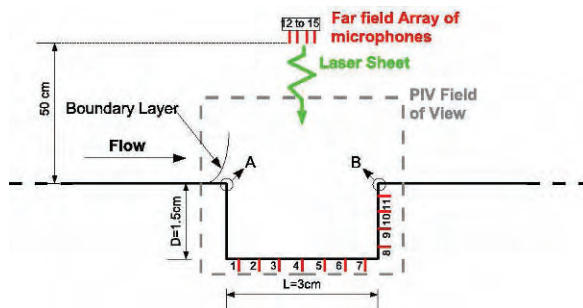


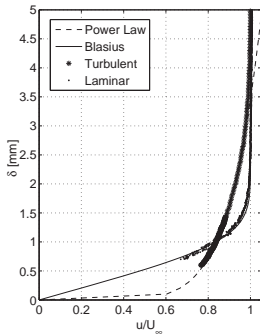
Fig. 1. Schematic representation of the experimental setup. The microphones are marked in red with a reference number aside.

Experimental setup

The study was carried out combining high resolution two dimensional PIV imaging, wall pressure measurements and far field noise records. The boundary layer was measured at the leading edge of the cavity with a hot wire anemometer. We performed experiments at both laminar and a turbulent boundary layer conditions with free-stream velocities of 10 m/s, 12 m/s and 15 m/s, giving a Reynolds number based on the cavity length L , between 20,000 and 30,000. The boundary layer is naturally laminar, turbulence is induced by means of a cylindrical tripping wire positioned upstream [4]. Experiments were conducted in a open jet wind tunnel facility. The cavity took place in a flat plate positioned in the test section aligned with the flow. The wall pressure fluctuations were measured with 11 microphones mounted flush with the cavity walls. The microphones were used here as high-sensitivity and high-frequency pressure transducers. The far field noise was recorded with 4 microphones positioned approximately one wavelength away.

Results

Boundary layer



Vel [m/s]		δ	L/θ
10	Lam.	2.60	92
	Turb.	4.74	63
12	Lam.	2.30	104
	Turb.	4.30	70
15	Lam.	2.14	112
	Turb.	3.90	77

Fig. 2. Left: Boundary layer profiles at 15 m/s. Right: Boundary layer thickness and momentum thickness for the different testing velocities and incoming boundary layers

The main objective of this experiment was to investigate the influence of the boundary layer on the acoustic emission of a cavity. To characterize the boundary layer approaching the cavity a hot wire was translated normally to the wall just before the cavity leading edge (Point A in figure 1). In figure are shown the measured boundary layer profiles at one speed together with the theoretical curves for boundary layers on a flat plate and the results for all the tested cases. The measurements show how, with a laminar boundary layer, the L/θ ratio is always above the threshold for self sustained oscillations while is not with a turbulent boundary layer.

Wall pressure, far field noise and PIV data

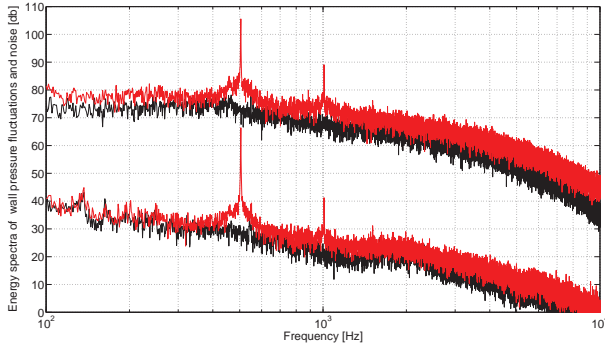


Fig. 3. Power spectra. Red: laminar b.l., Black: turbulent b.l., On top, microphone n.10, on the bottom, far field. For the position of the microphones refer to figure 1

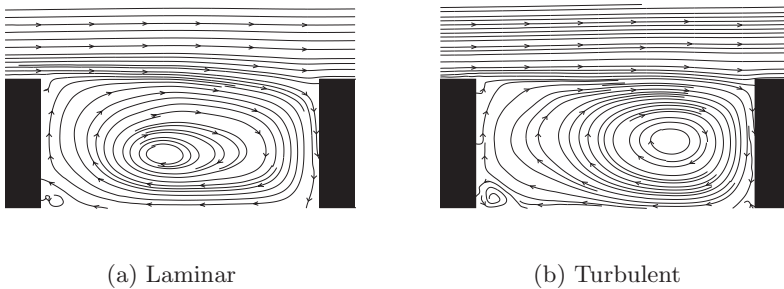


Fig. 4. Streamlines of the mean flow at 15 m/s

In the experiments with the laminar boundary layer both the wall pressure fluctuations and the far field noise measurements show a strong periodicity. The tones occur at the same frequency 3. This means that the noise generated by the cavity is principally due to the pressure fluctuations on the walls. As shown by Curle [2], dipole noise radiate with the same frequency of the velocity fluctuation while quadrupole noise with double that frequency. A dipole sound source is what to expect at these velocities since the ratio between the intensity of a quadrupole source and the intensity of a dipole one is proportional to the second power of the Mach number: $\frac{I_Q}{I_D} \sim Ma^2$. With a turbulent boundary layer, the broadband spectrum is comparable but without the tonal component. This can be explained looking at the flow in the two different cases. The PIV measurements show a completely different behavior. In the laminar boundary layer case the shear layer develops in a periodic shedding of eddies enhanced by a standing vortex inside the cavity reaching

Instability waves as a source of subsonic jet noise

V. Suponitsky and N.D. Sandham

School of Engineering Sciences, University of Southampton, SO17 1BJ
Southampton, UK
v.suponitsky@soton.ac.uk

The current work aims to get a further insight into the role of large scale structures/instability waves in noise generation in subsonic jets by carrying out direct numerical simulations. It is a continuation of earlier works [1, 2] in which a non-linear mechanism of subsonic jet noise generation was proposed and studied using the parabolized stability equations. The mechanism proposes an explanation of the experimental results (e.g. [3]) which show that a peak in sound radiation occurs at frequencies lower ($St \approx 0.2$) than those of the most energetic hydrodynamic modes ($St \approx 0.45$). The key point of this mechanism is that the ‘difference frequency’ modes arising from a nonlinear interaction between two primary instability waves make major contributions to far-field sound radiation from a subsonic jet. These modes are characterized by relatively low frequency, high amplitude and by a compact shape of the wave packet, and therefore can be efficient sound radiators in subsonic jets [4].

Simulations were performed for a round jet with $M = 0.9$ and $Re = 3600$ using an in-house code that has been extensively validated. A base flow was prescribed using the experimental data [3] and maintained during the simulations. By maintaining the base flow field we mean that if no disturbances are added to the flow, the prescribed flow field remains unchanged. This is achieved by adding a corresponding source term to the right hand of the Navier-Stokes equations. Maintaining the base flow allows us to isolate linear, weakly nonlinear and highly nonlinear (turbulent) mechanisms. The jet was perturbed at the inflow boundary over a range of frequencies and azimuthal

modes: $\tilde{u} = \sum_{i=1}^N \sum_{j=1}^M Re\{A_{ij}\hat{u}_{ij}(r)e^{i(n_j\theta - \omega_i t + \phi_{ij})}\}$, where A_{ij} is an amplitude

of a particular mode, $\hat{u}_{ij}(r)$ is an eigenfunction, n_j is the azimuthal mode number, ω_i is a real frequency and ϕ_{ij} is a randomized phase. In all simulations the flow is perturbed for frequencies of $\omega_k = 0.2k$, $k = 1, 35$ and each mode has the same amplitude of $A_{ij} = A$ (the jet exit velocity U and diameter D are used for normalization).

The power spectral density of pressure fluctuations calculated at $r = 30D$ and $\theta = 30^\circ$ (angle θ is measured from the jet downstream axis) is shown in Fig. 1(a) for the jet perturbed with different combinations of the azimuthal modes. It can be seen that in all cases the peak radiation occurs in the vicinity of $St \approx 0.2$. However, the shape of the peak and the amount of acoustic power contained at higher frequencies depends on the combination of azimuthal modes by which the jet was perturbed. When the jet is perturbed by the axisymmetric ($n = 0$) or first azimuthal modes ($n = 1$) the peak is narrower and less acoustic power can be found at higher frequencies in comparison with the cases in which the jet was perturbed by more than one azimuthal mode. The effect of the amplitude A of the inflow disturbance on the acoustic spectra is shown in Fig. 1(b) for the jet perturbed by modes $n = 0, \pm 1, \pm 2$. One can see that the amplitude of the inflow disturbance has little effect on the shape of the low frequency part of the spectra. Moreover, the acoustic power at these frequencies scales approximately with the square of the amplitude of the inflow disturbance, further indicating that sound at these frequencies is generated by a nonlinear mechanism. On the other hand, the amplitude of the inflow disturbance affects the shape of the high frequency part of the spectra. For small amplitude inflow disturbances the high frequency part of the spectra is characterized by more rapid decay in comparison to that obtained for the large amplitude (non-linear) inflow disturbances. The instantaneous sound field is shown by dilatation rate contours in Fig. 2 for a jet perturbed by the axisymmetric mode ($n = 0$) with $A = 5 \times 10^{-4}$ (part a), for a jet perturbed by modes $n = 0, \pm 1, \pm 2$ with $A = 5 \times 10^{-4}$ (part b) and for a jet perturbed by modes $n = 0, \pm 1, \pm 2$ with $A = 1 \times 10^{-4}$ (part c). One can see that a common feature of the sound fields obtained for the different cases is a highly directional low frequency sound that is confined to small angles from the jet downstream axis. The sound fields obtained when the jet was perturbed with mode $n = 0$ and $A = 5 \times 10^{-4}$ and with modes $n = 0, \pm 1, \pm 2$ and $A = 1 \times 10^{-4}$ resemble each other, although an additional peak at angles $\theta = 45^\circ - 50^\circ$ can be observed in Fig. 2(c). It can be shown that this noise at higher angles comes from the interaction between instability waves with azimuthal numbers $n = \pm 1$. The sound field obtained for the jet perturbed by $n = 0, \pm 1, \pm 2$ and $A = 5 \times 10^{-4}$ differs from the others as it contains a broader range of frequencies and more upstream sound. Instantaneous contours of the vorticity magnitude, corresponding to the sound fields shown in Fig. 2(a) and (b), are presented in Fig. 3(a) and (b), respectively. Comparing these vorticity fields, the main difference is that for the case shown in part (a) the jet does not break down into smaller structures near the end of the potential core, whereas in the case shown in part (b) breakdown of the jet column into finer structures and ultimately a transition to turbulence can be clearly observed. From the results presented in Figs. 1, 2 and 3 we can conclude that the low frequency sound confined to small angles from the jet downstream axis comes from non-linear interactions between primary instability waves, further supporting the non-linear mechanism of sound generation proposed in [1, 2]. On

the other hand, high frequency sound observed at low angles comes from the breakdown of the jet into finer structures near the end of the potential core. A significant portion of the sound at high angles also comes from the breakdown of the potential core. However, the low frequency part of the sound occurring at higher angles is likely to come from interactions of primary instability waves with azimuthal numbers $n = \pm 1$ (see also [5]). Finally to estimate the effect of maintaining the base flow we present results in Fig. 4 that were obtained from DNS without maintaining the base flow. One can see that we can get reasonably good approximations of the sound field and acoustic spectra by the simulations in which we maintain the base flow.

Acknowledgment: This work was funded by EPSRC Grant EP/E032028/1. Computer time was provided by EPSRC via the UK Turbulence Consortium (Grant EP/D044073/1).

References

1. N. D. Sandham, C. L. Morfey and Z. W. Hu, Nonlinear mechanisms of sound generation in a perturbed parallel jet flow, *J. Fluid Mech.*, **565**, 1 (2006).
2. N. D. Sandham, A. M. Salgado, Nonlinear interaction model of subsonic jet noise, *Phil. Trans. R. Soc. A* **363**, 2745, August 13 (2008).
3. J. L. Stromberg, D. K. McLaughlin and T. R. Troutt, Flow field and acoustic properties of a Mach number 0.9 jet at a low Reynolds number, *J. Sound Vib.* **72(2)**, 159 (1980).
4. N. D. Sandham, C. L. Morfey and Z. W. Hu, Sound radiation from exponentially growing and decaying surface waves, *J. Sound Vib.* **294**, 355 (2006).
5. Wu X., Huerre P., Low-frequency sound radiated by a nonlinearly modulated wavepacket of helical modes in a subsonic circular jet, *J. Fluid Mech.*, (in press).

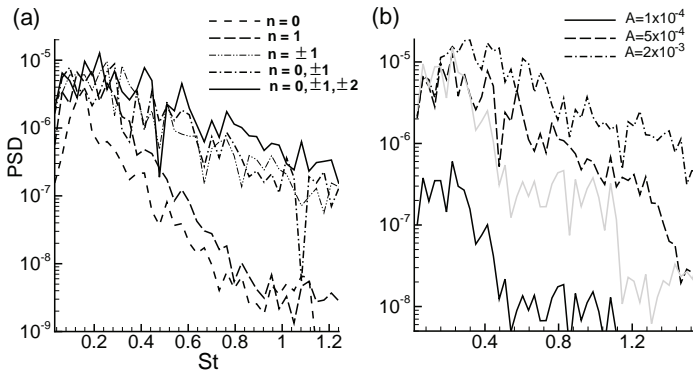


Fig. 1. Power spectral density of the pressure fluctuations calculated at $r = 30D$ and $\theta = 30^\circ$ ($M = 0.9, Re = 3600$). (a) effect of perturbing the jet with different combinations of azimuthal modes; (b) effect of the inflow disturbance amplitude on the jet perturbed by modes $n = 0, \pm 1, \pm 2$. The light grey line corresponds to the case with amplitude $A = 1 \times 10^{-4}$ multiplied by factor of 25.

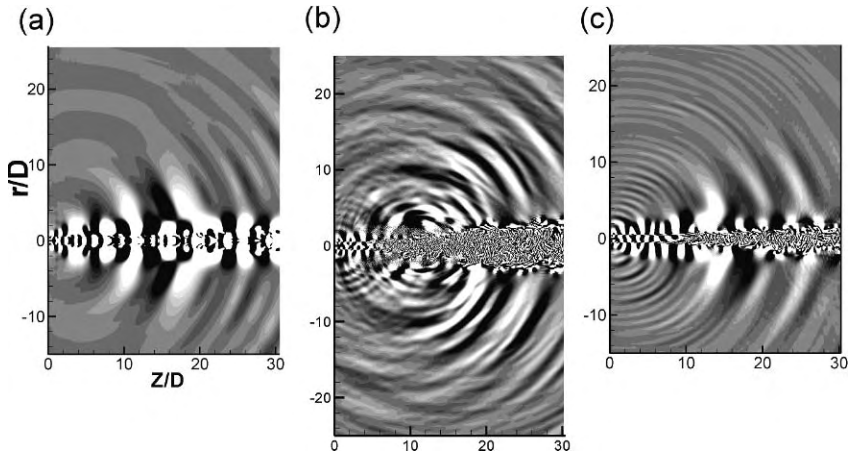


Fig. 2. Instantaneous sound field shown by dilatation rate contours ($M = 0.9$, $Re = 3600$). (a) jet perturbed only by the $n = 0$ mode with $A_{ij} = 5 \times 10^{-4}$; (b) jet perturbed by $n = 0, \pm 1, \pm 2$ modes with $A_{ij} = 5 \times 10^{-4}$; (c) jet perturbed by $n = 0, \pm 1, \pm 2$ modes with $A_{ij} = 1 \times 10^{-4}$.

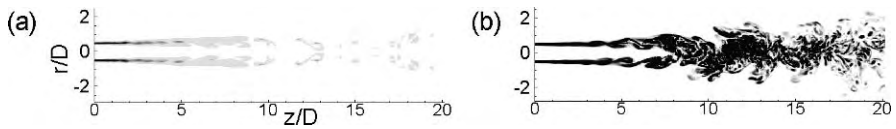


Fig. 3. Snapshots of the vorticity magnitude ($M = 0.9$, $Re = 3600$, $A_{ij} = 5 \times 10^{-4}$). (a) jet perturbed only by mode $n = 0$; (b) jet perturbed by modes $n = 0, \pm 1, \pm 2$.

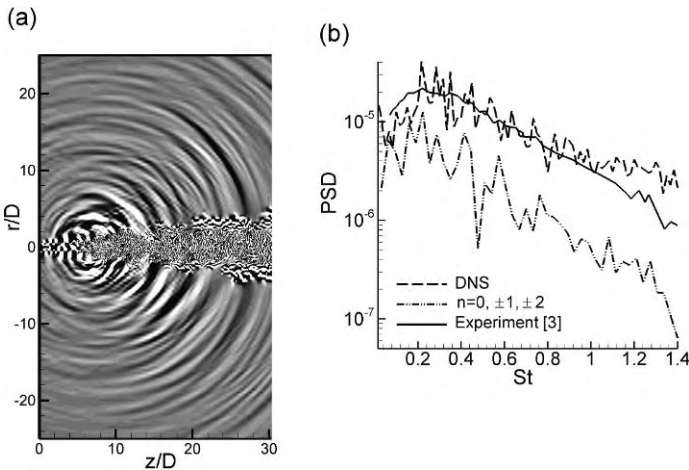


Fig. 4. (a) Instantaneous dilatation rate contours obtained from DNS calculations in which the base flow is not artificially maintained during the simulation; (b) Power spectral density of pressure fluctuations: effect of maintaining the base flow and comparison with experimental data ($r = 30D$ and $\theta = 30^\circ$).

Experimental study of sound production for constricted channels: application to simplified vocal tract geometries

O. Estienne¹, A. van Hirtum^{1*}, H. Bailliet² and X. Pelorson¹

¹Gipsa-Lab, UMR CNRS 5216, Grenoble Universités, ENSE3 - France

²Laboratoire d'Etudes Aérodynamiques (LEA), UMR CNRS 6609, Université de Poitiers, ENSMA, 40 Av. du Recteur Pineau - Poitiers - France

*E-mail: annemie.vanhirtum@gipsa-lab.inpg.fr

1 Introduction

Previous experiments on vocal tract mechanical models for fricatives consonants production – like /s/, /f/, /ch/ for unvoiced ones – has shown the importance of the geometrical configuration on the complex aeroacoustical noise signal produced [3]: the shape of the constriction, the shape and area function of the vocal tract downstream of the constriction, the presence of obstacles like teeth and upstream flow conditions are key points of the friction. From these results, and other observations made on human subjects by Narayanan *et al.* [2] by means of Magnetic Resonance Imaging (MRI), Howe and McGowan [1] established an aeroacoustical model for the pronunciation of the sibilant /s/ based on the assumption of a jet passing in the gap formed between lower and upper teeth. Predicted spectrum and SPL agreed reasonably well with measurements made previously by different authors, but Howe and McGowan noted that further experimental work is necessary to validate their assumption on turbulent jet interaction with teeth.

Indeed, most of observations and models of fricatives were only considering the acoustical aspect of the aeroacoustical phenomenon that consists in the interaction of air flow with vocal tract. This is why we propose to study the relation between acoustics and aerodynamics involved in friction. Measurements on a simplified mechanical replica of the vocal tract, with varying geometry and flow parameters, are presented. First results, concerning acoustical and dynamic pressure measurements are then confronted with regard to the evolution of these parameters.

2 From “in-vivo” observations to “in-vitro” experiments

The vocal tract replica, represented in the lower part of Fig. 1, is mainly composed of an aluminium alloy rectangular duct 18 cm long which corresponds

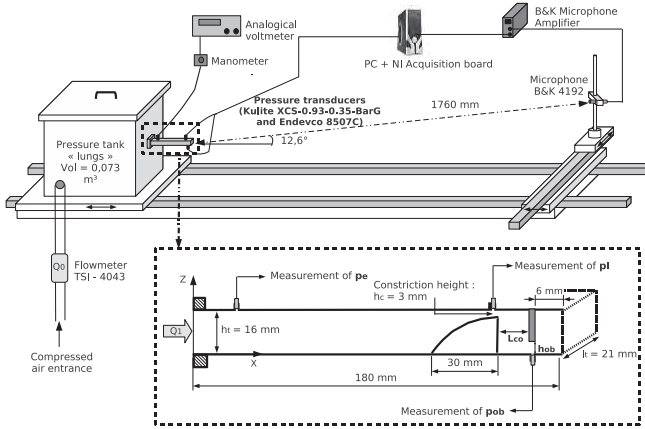


Fig. 1. Experimental setup mounted on a moving support and detailed mechanical replica of the vocal tract (in the dotted line box)

to an adult vocal tract length. The cross area of the duct is $A_t = 3.36 \text{ cm}^2$ which is an average of area functions found in literature [2].

A tongue model is set in the duct, which consists in a progressive section reduction over 30 mm ended by a rectangular constriction of height $h_c = 3 \text{ mm}$. The cross area of the constriction is $A_c = 0.63 \text{ cm}^2$, which is large in comparison with real fricatives constrictions. The height ratio relatively to the duct is $R_c = \frac{h_t}{h_c} = 5.3$. As in the case of friction, the turbulent jet formed at the constriction interacts with a rectangular “tooth” obstacle with length $l_{ob} = 3 \text{ mm}$ - see Fig. 1. Five different obstacle apertures h_{ob} , *i.e.* 0.6, 2.6, 5.5, 6.8 and 16 mm, are assessed including the no-obstacle case, corresponding to ratios relatively to the duct height $R_{ob} = \frac{h_t}{h_{ob}}$ of 26.70, 6.15, 2.91, 2.35 and 1; or an inverse ratio of approximately 4, 16, 34, 42 and 100%. The tongue can be switched between two positions, giving a constriction-obstacle distance L_{co} of 10 and 24 mm, respectively referred to as “front” and “back” cases. The duct axis contains three pressure taps: 1) at $x = 20 \text{ mm}$ for entrance pressure measurement p_e , 2) at $x = 160 \text{ mm}$ to have pressure recordings p_l in the constriction or jet zone regarding to tongue placement and 3) at $x = 172.5 \text{ mm}$ for measurements of p_{ob} in the reduced section formed by the obstacle.

Airflow is supplied by an Atlas Copco GA5 compressor and downstream of the main valve, a pressure regulator (Norgren 11-818-987) allows to modify the entrance flow rate Q_0 , measured by a TSI-4043 mass flowmeter, from 50 to 130 l/min with an interval of 20 l/min. A pressure tank is set before the entrance of the vocal tract replica in order to make the airflow homogeneous. Moreover, the tank is designed to significantly reduce the noise induced by airflow entrance. Flow rate measurements were made at the exit of the pressure tank in order to have an estimation of the replica entrance flow rate Q_1 .

3 Results

Spectral analysis was applied to acoustical data (B&K 4192) sampled at 44kHz in the far field. Resulting sound spectra for different tongue positions are shown in Fig. 2(a) for the no-obstacle case. A peak near 2.5 kHz is observed for all flowrates for the back position. The peak shifts to 3.5 kHz - with more energy - when the tongue is moved to the front position. The same is observed for all obstacles, except for $h_{ob} = 0.6\text{ mm}$. For $h_{ob} = 0.6\text{ mm}$ the spectra do not exhibit a peak shift and are independent on tongue position.

Sound spectra for different h_{ob} and front tongue position are presented in Fig. 3. Again, it is observed that the evolution of the noise measured for $h_{ob} = 0.6\text{ mm}$ differs from the other cases for which $h_{ob} > 0.6\text{ mm}$. Indeed, all other cases - as the no-obstacle one - present a spectral peak at 720 Hz and other peaks between 2 and 4 kHz for front tongue, that are shifted in a 1-2 kHz band for back tongue position. For all these cases, most of the energy is contained within the 0-6 kHz bandwidth; moreover the level of radiated noise increases with the flow rate as seen by comparing Fig. 3(a) and 3(b). Conversely, energy is distributed in a broad frequency band for $h_{ob} = 0.6\text{ mm}$ and it remains at a steady level with frequency when the flow rate is increased. Therefore, the spectrum for $h_{ob} = 0.6\text{ mm}$ in Fig. 3(b) fall at a lower level than for the case $h_{ob} = 2.6\text{ mm}$, that is, less noise is produced for a larger obstacle.

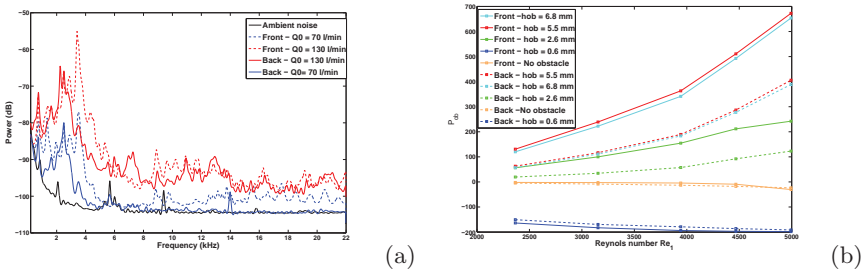


Fig. 2. (a) Sound spectra for the no-obstacle case and two different L_{co} values at flowrates Q_0 70 l/min and 130 l/min. (b) averaged pressures p_{ob} at “obstacle” spot. Front tongue curves are in full line and back tongue ones in dotted lines.

The entrance pressure p_e , increases 1) as the cross section at the obstacle level reduces and 2) as the Reynolds number $Re_1 = \frac{Q_1}{L_t \nu}$ increases. Again the $h_{ob} = 0.6\text{ mm}$ differs from the general trend observed for $h_{ob} > 0.6\text{ mm}$ since the pressure, about 300Pa, does not increase much as Re_1 increases. Comparison for different tongue positions reveals a pressure drop depending on the obstacle for the back case, except for $h_{ob} = 0.6\text{ mm}$ for which the drop

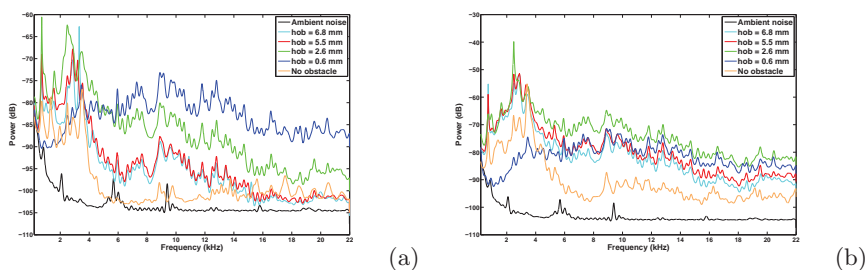


Fig. 3. Sound spectra for different values of h_{ob} , for the front tongue position: (a) flowrate Q_0 of 70 l/min. (b) flowrate Q_0 of 130 l/min.

is lower than 1%. The same loss is observed for p_{ob} , illustrated in Fig. 2(b). Contrary to $h_{ob} > 0.6$ mm, a pressure loss was observed for $h_{ob} = 0.6$ mm, meaning that the air flow which passes in the constriction at the obstacle has a very different behavior when the cross section became very low. This may be coupled with a largest obstacle surface interaction for the turbulent jet exiting from the tongue constriction.

4 Conclusion and perspectives

Sound and pressure measurements on an ‘in-vitro’ vocal tract mechanical replica representing frication configurations reflected the influence of tongue-obstacle distance and obstacle aperture. A different tendency is observed h_{ob} equal or superior to 0.6 mm. More investigation in pressure dynamics, spectra and velocity field characterisation will quantify more precisely the observed difference in behavior.

Acknowledgements: ANR-07-JCJC-0055 for financial support. The authors are grateful to D. Blanc and D. Rey from DA/Gipsa-lab for technical support.

References

1. M. Howe and R. McGowan. Aeroacoustics of [s]. *Proc. R. Soc. A*, 461:1005–1028, 2005.
2. S. Narayanan, A. Alwan, and K. Haker. An articulatory study of fricative consonants using magnetic resonance imaging. *Journal of the Acoustical Society of America*, 98 (3):1325–1347, 1995.
3. C.H. Shadle. The effect of geometry on source mechanisms of fricative consonants. *Journal of Phonetics*, 19(3-4):409–424, 1991.

Turbulent Pressure Statistics in an Underwater Boundary-Layer Experiment

J. Abshagen

WTD71 – Research Department for Underwater Acoustics and Marine Geophysics
Berliner Strasse 115, 24340 Eckernförde, Germany, JanAbshagen@bwb.org

Introduction

Pressure fluctuations of high-Reynolds-number turbulent boundary layers are of fundamental scientific interest with a large relevance for many applications. In an incompressible flow pressure couples non-locally different regions of a boundary layer and pressure fluctuations play an important role for the mechanisms underlying turbulence. In applications compressibility often cannot be neglected as pressure fluctuations can give rise to sound productions in a turbulent boundary-layer, generated e.g. at a wall of a moving vehicle. On the other hand compressibility can even be of crucial importance, such as in underwater applications. Properties of pressure fluctuations beneath a turbulent boundary layer are reviewed e.g. in [1, 2, 3, 4].

Sound is by far the least attenuated type of wave in the sea and therefore preferably used for signal transmission (e.g. for SONAR) in underwater applications. Measurements of turbulent boundary layers in a Reynolds number regime relevant to underwater applications have to be performed at sea (or partly in water or cavitation tunnels). The sea is a noisy environment and the mean sound level can exceed by far the level of turbulent pressure fluctuations, or vice versa, depending predominantly on the Reynolds number and the ambient noise level at sea.

Wavenumber-frequency decomposition

A typical example for the first situation can be seen in Fig. 1 (a). The power spectra result from a measurement of pressure fluctuations performed with an underwater towed system at relatively low towing speed corresponding to a Reynolds number of the momentum thickness of about $Re_\theta \approx 2000$. It can be seen from this measurement that the mean sound level at a hydrophone is much higher than the level of pressure fluctuations of the boundary layer. It is therefore crucial to discriminate both processes in order to separate the

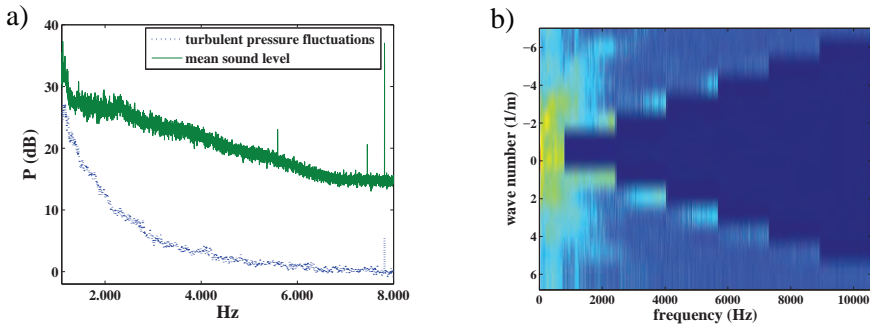


Fig. 1. (a) Comparison of mean sound level with estimated level of pressure fluctuations beneath a turbulent boundary layer of an underwater towed system at relatively low towing speed corresponding to $Re_{\theta} \approx 2000$, (b) Corresponding wave number-frequency spectrum (acoustic regime is filtered out).

turbulent pressure fluctuations from sound. Pressure was measured in this experiments with an equally-spaced array of hydrophones and the turbulent pressure fluctuations are estimated with the use of a wavenumber-frequency filter. This filter enables a separation of sound from turbulent pressure fluctuations in certain regions of the kf -space. The wave number-frequency spectrum corresponding to the power spectra shown in Fig.1 (a) is depicted in (b). Due to the dispersion relation of sound waves projected onto a linear array only the (dark blue colored triangular) acoustic region in the kf -spectrum can physically be attributed to sound. Spectral components of other noise sources, such as e.g. flow noise, do not necessarily underlie such restrictions and can therefore contribute to the low wave speed non-acoustic region in the kf -spectrum.

It can be seen from Fig. 1 (b) that in the low-frequency regime the non-acoustic region appears structured. Those structures result from mechanical (mainly bending) waves which are excited by turbulent pressure fluctuations. Above a certain frequency those structures are well separated from the acoustic region in the kf -spectrum (here above $f \approx 1500$ Hz). Flow noise can be considered as wave number white above such high frequencies and therefore the level can be estimated. The result of an estimation procedure applied to the kf -spectrum is shown in Fig. 1 (a).

Flow noise

Wavenumber - frequency filtering allows (partly) to separate flow noise from underwater sound and therefore enables an investigation of flow noise properties independent of environmental conditions (at least in a certain frequency regime).

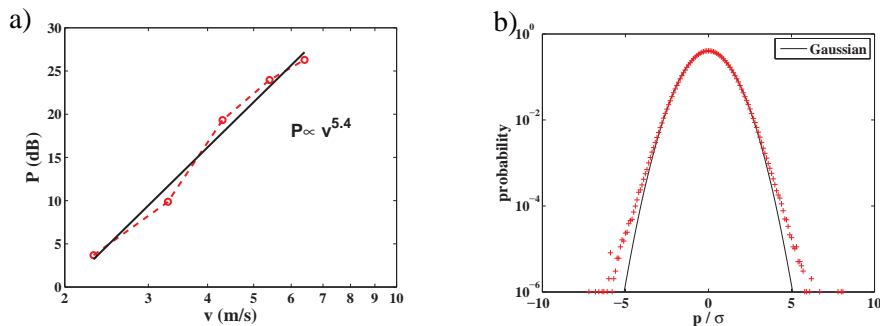


Fig. 2. (a) Scaling behavior of flow noise at $f = 1500\text{Hz}$, (b) probability distribution function of pressure fluctuations normalized by σ at $Re_\theta \approx 3000$ (Gaussian PDF is included for comparison).

A characteristic property of flow noise is the spectral scaling behavior. Typically, a scaling law of about $P \approx 1/f^4$ to $1/f^5$ has been suggested from previous measurements and theory in the high frequency regime (see e.g. [3] and ref. therein). Our experiments confirm those results, within the investigated frequency regime the flow noise spectrum decays with $1/f^4$ which is within the range of previous results. Most relevant for underwater applications is the strong increase of flow noise level with speed. Our results confirm the theoretically known $P \propto v^6$ law reasonably well (see e.g.[4] for a recent overview and ref. therein), as may be seen from Fig. 2 (a). Here, the dependence of flow noise level with towing speed is depicted for $f = 1500\text{ Hz}$.

Recent experiments on statistics of pressure fluctuations in a high Reynolds number turbulent boundary layer have revealed a non-gaussian probability distribution function which displays a relatively independence on Re_θ in the investigated high Reynolds number regime [5]. Non-gaussian statistics have been studied in high Reynolds number turbulence also for Lagrangian acceleration of fluid particles [6], velocity differences [7], and pressure gradient [8], and have been addressed theoretically by a 'superstatistic' approach [9].

Wavenumber-frequency filtering does not only allow an investigation of spectral but also statistical properties of flow noise even though the total spectral level at a single hydrophone is dominated by structure borne sound sources and underwater sound in the low and high frequency regime, respectively. Those sound sources have been found to have a Gaussian probability distribution function but they can be filtered out in the wavenumber-frequency regime in order to investigate the statistical behavior of flow noise. At lowest towing speed corresponding to $Re_\theta \approx 2000$ flow noise is also found to be close to a Gaussian behavior. Increasing the Reynolds number leads to a more pronounced non-Gaussian pdf. This may be seen, e.g., from Fig. 2 (b) where the pdf of flow noise (normalized with σ) for $Re_\theta \approx 3000$ is depicted.

Summary

Results on pressure fluctuations of turbulent boundary layers are presented which are obtained from underwater towing experiments. With the help of wavenumber - frequency filtering properties of flow noise have been investigated independently from the environmental conditions. In our experiments we have revealed a transition between Gaussian and non-Gaussian behavior. It is found that the transition occurs within a Reynolds number regime $Re_\theta \approx 2000 - 3500$. In this regime the boundary layer is turbulent and, as shown in Fig.2 (a), the level of turbulent pressure fluctuations significantly increases by a scaling law. Our results experimentally confirm scaling behavior of flow noise but also provide evidence for the relevance of non-Gaussian behaviour in underwater applications.

References

1. W. W. Willmarth, *Annu. Rev. Fluid Mech.* **7**, 13, (1975)
2. M. Bull, *J. Sound Vib.* **190**, 299, (1996)
3. W. R. Graham, *J. Sound Vib.* **206**, 541, (1997); Y. F. Hwang, W. K. Bonnes, and S.A.Hambric, *J. Sound Vib.* **319**, 199, (2009)
4. M.S. Howe, *J. Sound. Vibr.* **314**, 113 (2008)
5. Y. Tsuji, J. H. M. Fransson, P. H. Alfredsson and A. V. Johansson, *J. Fluid Mech.* **585**, 1, (2007).
6. F. Toschi and E. Bodenschatz, *Annu. Rev. Fluid Mech.* **41**, 375, (2009).
7. Zhen-Su Sche, Kui Ren, G. S. Lewis, and H. L. Swinney, *Phys. Rev. E* **64**, 016308, (2001).
8. T. Gotoh and R. H. Kraichnan, *Physica D* **193**, 231, (2004).
9. E. G. D. Cohen, *Physica D* **193**, 35, (2004); C. Beck, *ibid.*, **193**, 195 (2004).

Spectral reconstruction of sound radiated by an organ pipe

M. Abel and K. Ahnert

Institute für Physics and Astrophysics, University of Potsdam, 14476 Potsdam, Germany

markus.abel@physik.uni-potsdam.de

The sound radiated by a turbulent jet is not only interesting as a research topic by itself, but also highly relevant for many applications in nature and engineering. In this contribution, we outline a procedure to find a dynamical system from acoustical data. This approach should be considered in the context of reduced order modeling. Basically, we use a differential embedding to find a system of ODEs which recover the basic phase space dynamics of the measured system. Our investigations focus on the radiated sound and thus the spectral properties of the reduced order model are the quantity to be optimized.

Our experiment concerns a wind-driven musical instrument, where the basic functioning is understood; details of the sound production, however, are still not adequately modeled. We measured the sound signal $x(t)$ emitted by an organ pipe with a conventional microphone, differentiate the signal using a spectral method [1], and use the resulting vector $x, \dot{x}, \ddot{x}, \dots$ for embedding. The dynamical system in embedding space is found by nonparametric regression [1, 2, 3]. First, the dimension of the embedding space has to be determined. To find it we use the oscillatory character of the organ pipe and systematically take into account more and more harmonics (and consequently frequencies) in Fourier space. This way we tune the complexity of the embedded signal. For the reconstruction of the musical properties a two dimensional model is reasonable. Of course, if a more complete representation is wanted higher embedding dimension have to be taken into account.

The sound of an organ pipe is produced as follows: a jet (the „air sheet”) is emitted at the outlet of the pipe foot and hits the so called labium, a sharp edge at some distance where a weakly turbulent vortex street is formed. Without the pipe resonator, only the typical „whistling” of a turbulent vortex street is produced. Each time a vortex detaches, a pressure fluctuation enters the resonator inside which viscous damping and the geometry lead to the selection of characteristic waves to be radiated at the pipe mouth by an

oscillating air-sheet. This leads to a harmonic spectrum with strong coupling of the modes due to nonlinearity.

The experiment. We determined the emitted sound experimentally [4]. The organ pipe was wooden and closed at the upper end, tuned at $\nu_0 = 168.3\text{Hz}$. It was driven by an especially fabricated miniature organ with a blower connected to the wind-chest where the pipe was mounted. The wind supply pressure determines the stability of the signal; high pressures can render the signal unstable, and even chaotic. Measurements took place inside an anechoic box. The emitted signal was registered at a distance of 16mm. Noise in the signal comes from imperfections in the driving mechanism and from the background wind in the jet. The correct treating of noise is crucial for a correct differential embedding, as explained in detail below.

Numerical differentiation. Mathematically, the derivative of a function is obtained by infinitesimal calculus. Real data are afflicted with measurement noise and with machine accuracy. An estimate has to cope with these two restrictions and should be optimized with respect to some chosen criteria. For our problem, we want to have smooth but high accuracy estimates in order to find good functional representation of our system. We use a global approximation by Fourier-transforming the whole measured data and multiplying with powers of $i\omega$. At the start and end of the record, we throw away a well-chosen number of data for the reconstruction. This technique limits the loss of accuracy by addition [5] and we can use low-pass filtering to suppress experimental noise systematically [1]. To do so, we used an 8th order Butterworth-filter with a variable cutoff. A low cutoff results in little noise, but at the same time one must be aware that one possibly loses informations about signal; this way higher harmonics could be filtered away.

Let us consider a cutoff of some value slightly higher than the 1st harmonic. Of course, if we have to find the phase space of a harmonic oscillator this sufficient. If then the cutoff frequency is increased higher harmonics enter the game and mode coupling and nonlinearities play a bigger role. The phase space will become more and more complicated until the full dynamics is found in a low-order model. Now, the art is to determine the right cutoff such that the dynamics is complex enough to reveal the features we want to model, but not as complex as to impede a reconstruction. This is illustrated in Fig. 1 by plotting the signal $x(t)$ vs. the first derivative $\dot{x}(t)$. In this example, we set the pipe to an unstable regime with intermittent chaos with a wind supply pressure of 337 mBar.

Reconstruction of the dynamical system. The equations of motion in this reconstructed phase space read

$$\dot{x} = g_1(x, \dot{x}, \ddot{x}, \dots), \quad \ddot{x} = g_2(x, \dot{x}, \ddot{x}, \dots), \quad \dots \quad (1)$$

The task of finding the unknown functions g_1, g_2 from data is not trivial [6, 3]. Here, we focus on an autonomous oscillator model:

$$\dot{x} = y, \quad \dot{y} = -\omega_0^2 x - f(x, y). \quad (2)$$

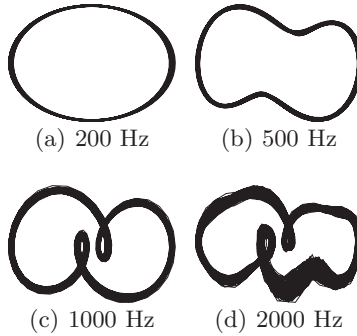


Fig. 1. Embedding of the time series of the organ pipe with different cut-offs k_0 . The wind pressure is 337 mBar such that the pipe showed signature of chaotic behavior. The axes, x and \dot{x} are omitted. With increasing cut-off nonlinearities play a bigger role. Of course for the first harmonic alone, a harmonic oscillation is found, cf. the top figure. So, one has to be careful to get rid of noise, but not to kill at the same time the nonlinear information hidden in the signal. Of course, a two-dimensional model cannot represent the trajectories for cut-off larger than 1000 Hz.

with only one function f to be determined. To get an estimate, basically we minimize the functional $\chi^2 = \sum_n \left[y(\dot{t}_n) + \omega_0^2 x(t_n) + f(x(t_n), y(t_n)) \right]^2$. Indeed, the minimization is a bit more complicated, involving side conditions, but these are rather technical points, reported elsewhere. We applied the minimization to a periodic signal (wind-supply at 140 mBar) with a cutoff of 1000 Hz, see Figure 2. To find f , one can choose from many models. Most appealing because of their nice properties are additive models, $f = f_1(x) + f_2(\dot{x})$ to be fitted nonparametrically. The reconstruction is shown in Figure 2(a); both parts, f_1 and f_2 are nonlinear, accounting for the existence of a limit cycle. The functions are represented in terms of polynomials and the model is investigated for its dynamical properties, especially the stability and the frequency of the limit cycle are used. The stability of the limit cycle is evaluated by integrating the equations (2) with the numerically given function f . We find a repeller at zero and a limit cycle to be attracting as is necessary for a stable autonomous oscillation.

How good is this model in terms of musical quality? Of course the true organ sound is not yet recovered. However, if one compares not only the phase space reconstruction (Fig. 2(b)) but as well the spectra of the system, a very good coincidence is found (Fig. 2(c)). Remarkably, not only the position of the harmonics is found quite nicely, but also the ratio of the amplitude of the harmonics coincide very well. This is an indication that the coupling between the modes is recovered, since it depends on the type of nonlinearity.

The reconstruction of a three-dimensional (or higher) phase space is much more involved in the technical realization. These results are still currently

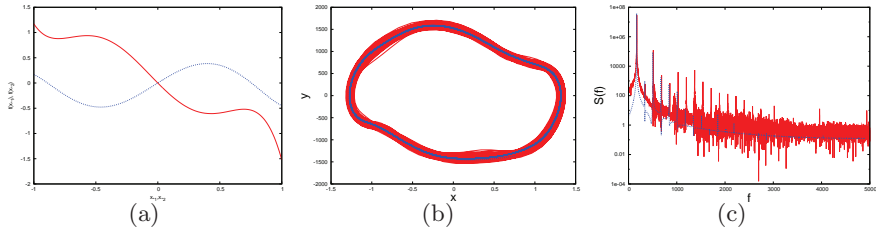


Fig. 2. (a): The function f is modeled additively by two functions $f_1(x)$ and $f_2(x)$. Both functions are nonlinear and allow for the existence of a limit cycle. The stability properties of the equations are confirmed numerically. (b): Two-dimensional phase space of the embedded signal. The red curve corresponds to the measured signal with $y = \dot{x}$ from numerical differentiation, the blue line results from the integration of an additive model for the nonlinearity f . (c): Power spectrum $S(f)$ to the time signal. The harmonics are precisely hit by our nonlinear model, and, even more important, the ratio of the amplitudes is very well recovered. The ref line the spectra of the original signal whereas the blue line is the reconstructed spectra.

checked and methods are developed further. It is clear that the use of the presented method lies mainly in low dimensional representations. However, as well a high dimensional system might be reproduced in terms of its dominant contribution, less important terms might be modeled stochastically. We are confident that these methods can assist modeling in the reduced order modeling of turbulent flows at least at moderate Reynolds numbers.

References

1. K. Ahnert and M. Abel. Numerical differentiation: global versus local methods. *Comput. Phys. Commun.*, 177(10):764–774, 2007. doi:10.1016/j.cpc.2007.03.009.
2. M. Abel. Nonparametric modeling and spatiotemporal dynamical systems. *Int. J. Bif. Chaos*, 14(6):2027–2039, 2004.
3. M. Coppejans. On kolmogorov’s representation of functions of several variables by functions of one variable. *Journal of Econometrics*, 123:1–31, 2004.
4. M. Abel, S. Bergweiler, and R. Gerhard-Multhaupt. Synchronization of organ pipes by means of air flow coupling: experimental observations and modeling. *J. Acoust. Soc. Am.*, 119(4):2467 – 2475, 2006.
5. D. Goldberg. What every computer scientist should know about floating point arithmetic. *ACM Computing Surveys (CSUR)*, 23(1):5–48, 1991.
6. A. N. Kolmogorov. On the representation of continuous functions of many variables by superposition of continuous functions of one variable and addition. *AMS Transl.*, 2(28):55, 1963.

Aerodynamic sound generation by turbulence in shear flows

G. Khujadze^{1,3}, G. Chagelishvili^{2,3}, M. Oberlack¹, A. Tevzadze³ and G. Bodo⁴

¹ Chair of Fluid Dynamics, Technische Universität Darmstadt, Germany
khujadze@fdy.tu-darmstadt.de

² M. Nodia institute of Geophysics, Tbilisi, Georgia,

³ E. Kharadze Georgian National Astrophysical Observatory, Tbilisi, Georgia

⁴ Osservatorio Astronomico di Torino, Pino Torinese, Italy

The nonlinear aerodynamic sound generation by turbulence has been long analyzed since the foundation of the theory of aerodynamic sound in pioneering paper by Lighthill [1]. Also, it was Lighthill [2] who noted that velocity shear can increase the acoustic wave emission in the aerodynamic situation due to the existence of linear terms in the inhomogeneous part of the analogy equations (second derivative of the Reynolds stress). In [3] it was disclosed and described a linear aerodynamic sound generation mechanism. Specifically, it was shown that the flow non-normality induced linear phenomenon of the conversion of vortex mode into the acoustic wave mode is the only contributor to the acoustic wave production of the unbounded shear flows in the linear regime. From the physical point of view the *potential vorticity* was identified as the linear source of acoustic waves in shear flows.

We perform comparative analysis of linear and nonlinear aerodynamic sound generation by turbulent perturbations in constant shear flows and study numerically the generation of acoustic waves by stochastic/turbulent perturbations embedded in 2D planar unbounded inviscid constant shear flow with uniform background density and pressure ($U_0(Ay, 0)$; $A, \rho_0, P_0 = const$). The governing hydrodynamic equations of the considered 2D compressible flow are:

$$\frac{\partial \rho}{\partial t} + \frac{\partial(\rho U_x)}{\partial x} + \frac{\partial(\rho U_y)}{\partial y} = 0, \quad (1)$$

$$\frac{\partial U_x}{\partial t} + U_x \frac{\partial U_x}{\partial x} + U_y \frac{\partial U_x}{\partial y} = -\frac{1}{\rho} \frac{\partial P}{\partial x}, \quad \frac{\partial U_y}{\partial t} + U_x \frac{\partial U_y}{\partial x} + U_y \frac{\partial U_y}{\partial y} = -\frac{1}{\rho} \frac{\partial P}{\partial y}, \quad (2)$$

$$\left(\frac{\partial}{\partial t} + U_x \frac{\partial}{\partial x} + U_y \frac{\partial}{\partial y} \right) P = -\frac{\gamma P}{\rho} \left(\frac{\partial}{\partial t} + U_x \frac{\partial}{\partial x} + U_y \frac{\partial}{\partial y} \right) \rho, \quad (3)$$

where γ – adiabatic index, $c_s^2 \equiv \gamma P_0 / \rho_0$ – sound speed. The potential vorticity is defined as: $\mathcal{W} = [\text{curl} \mathbf{U}]_z / \rho$.

Only stochastic streamwise and crossstream perturbation velocities are embedded in the flow at $t = 0$:

$$u_x(x, y, 0) \neq 0; \quad u_y(x, y, 0) \neq 0; \quad \rho'(x, y, 0) = 0; \quad P'(x, y, 0) = 0. \quad (4)$$

The embedded perturbation is localized in the crossstream direction and it is homogeneous in the streamwise direction. $u_x(x, y, 0)$ and $u_y(x, y, 0)$ are defined by the following stream function:

$$\psi(x, y, 0) = B \exp\left(-\frac{y^2}{L_l^2}\right) \int_{-\infty}^{+\infty} dk_x dk_y \left(\frac{k_x k_y}{k_0^2}\right)^4 \exp\left(-\frac{k_x^4 + k_y^4}{k_0^4}\right) \times \exp(ik_x x + ik_y y) \zeta(k_x, k_y), \quad (5)$$

$$u_x(x, y, 0) = \frac{\partial}{\partial y} \psi(x, y, 0), \quad u_y(x, y, 0) = -\frac{\partial}{\partial x} \psi(x, y, 0),$$

where $\zeta(k_x, k_y)$ is random number in the range $[0, 1]$ different for different k_x and k_y ; L_l – the localization scale in the crossstream direction; k_0 – the peak center in the streamwise wavenumber K_x axis. The half-width of the spectrum of the inserted perturbation meets the condition $\Delta k_0 \ll k_0$, that allows to discriminate linearly and nonlinearly generated acoustic waves and, thus, to carry out comparative analysis of linear and nonlinear aerodynamic sound generation by turbulent perturbation. The perturbations are inserted in the flow in the physical plane at the parameters $B = 0.5 \times 10^4$; $L_l = 3$; $k_0 = 10$; $c_s = 1$; $A = 4$ at $t = 0$. Simulations were performed using the hydrodynamics module of the PLUTO code [4]. The domain and the grid were $-10 \leq x, y \leq 10$ and 1024×1024 respectively. Finer grid (2048×2048) was used to test the results of the simulations. Dissipative effects are only those related to the use of a mesh of finite width Euler equations are solved using the PLUTO code.

A fault of acoustic analogy treatment in the identification of the true linear sources of aerodynamic sound

The specificity of the acoustic analogy approach is that results strongly depend on the form of the analogy equation as well as on the aero-acoustic variable chosen to analyze the process. This is more essential when the convective terms are important and the model should take into account the background flow. Hence, the acoustic analogy equation have been the subject to various approximations in order to take into account the effect of the background inhomogeneous flow correctly. However, identification of the true sources of aerodynamic sound remains relevant [5]. Discussing the true linear sources of aerodynamic sound, we compare the linear acoustic wave production in the unbounded shear flows induced by the non-normality of the flow (described in the paper [3]) with the linear part of the acoustic analogy source. The linear part of the acoustic analogy source may be defined as:

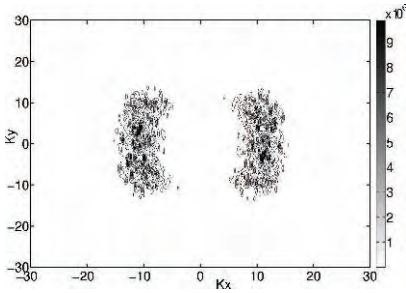


Fig. 1. The linear source of the acoustic analogy equation at $t = 0$ in the wavenumber plane ($S^{(l)}(k_x, k_y, 0)$).

$$S^{(l)} = 2 \frac{\partial^2}{\partial x^2} (\rho_0 A y u_x) + 2 \frac{\partial^2}{\partial x \partial y} (\rho_0 A y u_y) . \tag{6}$$

The spectrum of the source ($S^{(l)}(k_x, k_y)$) in our case at $t = 0$ is presented in Fig. 1. It shows that the acoustic analogy linear source is distributed in all quadrants of the wavenumber plane. I.e. the linear source generates acoustic field with $k_x k_y < 0$ too. However, according to [3] density perturbation is generated at $k_y \leq k_x$ and the linear generation of acoustic wave Spatial Fourier Harmonics (SFH) by the related vortex mode SFH takes place just at the moment of the crossing of the K_x axis by the last one. Consequently, the acoustic analogy linear source located in the quadrants II and IV (and having $k_x k_y < 0$) is the fault of acoustic analogy treatment. In our opinion, this is a very important conclusion of our research.

Comparative analysis of linear and nonlinear aerodynamic sound generation by turbulent perturbations

The energy of the linearly generated acoustic waves is defined by the mean flow shear parameter and the potential vorticity of the turbulent perturbations and the spectrum, by the k_x spectrum of the potential vorticity at $k_y = 0$. The nonlinear source we define by the nonlinear part of the acoustic analogy source:

$$S^{(nl)} = \frac{\partial^2}{\partial x^2} (\rho u_x^2) + 2 \frac{\partial^2}{\partial x \partial y} (\rho u_x u_y) + \frac{\partial^2}{\partial y^2} (\rho u_y^2) . \tag{7}$$

The spectrum of these sources at $t = 0$ are presented in Figs. 2 and 3. Fig. 2 shows that the potential vorticity of the perturbations along K_x axis is located in a streamwise wavenumber range $[k_0 - \Delta k_0, k_0 + \Delta k_0]$. Consequently, the linear aerodynamic sound should be located in the same range of k_x . At the same time Fig. 3 shows that $S^{(nl)}(k_x, k_y, 0)$ is located in a range $[2k_0 - 2\Delta k_0, 2k_0 + 2\Delta k_0]$, i.e. about twice farther than the potential vorticity from the center of the plane.

The density field in the wavenumber plane for parameters $B = 0.5 \times 10^4$; $L_l = 3$; $k_0 = 10$; $c_s = 1$; $A = 4$ at $t = 0.1$ is presented in Fig. 4. The density field in the physical plane for the same parameters at $t = 2$ (in basic unites [m] and [sec]) is presented on Fig. 5. Fig. 4 shows that the

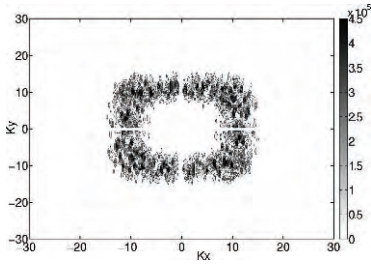


Fig. 2. The potential vorticity field at $t = 0$ in the wavenumber plane.

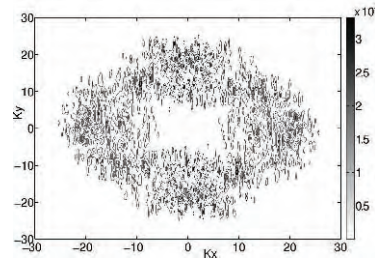


Fig. 3. The acoustic analogy nonlinear source at $t = 0$ in the wavenumber plane ($S^{(nl)}(k_x, k_y, 0)$).

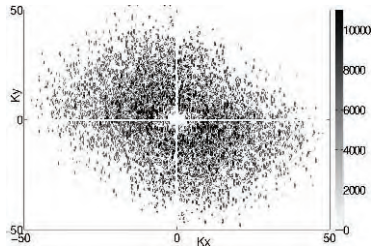


Fig. 4. The density field in the wavenumber plane at $t = 0.1$.

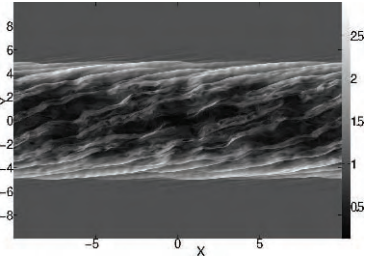


Fig. 5. The density field in the physical plane at $t = 2$.

density field of the perturbations along K_x axis is mainly located around k_0 with an extension to $2k_0$. The density field around k_0 relates to the linear mechanism of the wave generation. The density field close to $2k_0$ relates to the nonlinear mechanism. The figure shows that in the considered case the linear aerodynamic sound is stronger than the nonlinear one. According to Fig. 2, for the considered parameters, the mean flow vorticity is larger than the perturbation potential vorticity – the case when Rapid Distortion Theory (RDT) of turbulence is at work. According to our study the linear aerodynamic sound dominates over nonlinear one at moderate and high shear rates: $R \equiv A/k_0 c_s \geq 0.3$. The dominance of the linear aerodynamic sound occurs up to quite large amplitudes of the turbulent perturbations for which RDT is at work.

References

1. Lighthill M. J.: Proc. R. Soc. London, Ser. A **211**, 564 (1952).
2. Lighthill M. J.: Proc. R. Soc. London, Ser. A **222**, 1 (1954).
3. Chagelishvili G., Tevzadze A., Bodo G. et al.: Phys.Rev.Lett. **79**, 3178 (1997).
4. Mignone A., Bodo G., Massaglia S. et al.: Astroph. JS, **170**, 228, (2007).
5. Goldstein M. E.: J. Fluid Mech. **526**, 337, (2005).

Part XIV Reacting and compressible turbulence

On implicit turbulence modeling for LES of compressible flows

Stefan Hickel¹ and Johan Larsson²

¹ Institute for Aerodynamics, Technische Universität München, sh@tum.de

² Center for Turbulence Research, Stanford University, jola@stanford.edu

The subgrid-scale (SGS) model in a large-eddy simulation (LES) generally operates on a range of scales that is marginally resolved by discretization schemes. Consequently, the discretization scheme's truncation error and the subgrid-scale model are linked, which raises the question of how accurate the computational results are. On the other hand, the link between the SGS model and truncation error can be beneficially exploited by developing discretization methods for subgrid-scale modeling, or vice versa. Approaches where the SGS model and the numerical discretization scheme are fully merged are called implicit LES (ILES) methods.

Implicit SGS modeling requires procedures for design, analysis, and optimization of nonlinear discretization schemes. In order to improve on the aforementioned modeling uncertainties, we have proposed a systematic framework for implicit LES. The resulting adaptive local deconvolution method (ALDM) for implicit LES is based on a nonlinear deconvolution operator and a numerical flux function [1, 4]. Free parameters inherent to the discretization allow to control the truncation error. They are calibrated in such a way that the truncation error acts as a physically motivated SGS model. ALDM has shown the potential for providing a reliable, accurate, and efficient method for LES. Various applications, such as three-dimensional homogeneous isotropic turbulence, transitional and turbulent plane channel flow, and turbulent boundary-layer separation, demonstrate the good performance of the implicit model. Computational results show that a carefully designed implicit SGS model can perform at least as well as established explicit models, for most considered applications the performance is actually even better. This is possible because physical reasoning is incorporated into the design of the discretization scheme and discretization effects are fully taken into account within the SGS model formulation. The method is established for LES of turbulent flows governed by the incompressible Navier-Stokes equations and for passive-scalar mixing [3, 5]. The subject of this paper is the extension of the methodology to ILES of compressible turbulence.

Discretizations the compressible Navier-Stokes equations can be designed and analyzed along the lines of Refs. [4, 5]. A key element in finding suitable discretization parameters is a modified-differential equation (MDE) analysis in spectral space. The MDE of the discretization method is analyzed by measuring the effective spectral mass diffusivity, thermal diffusivity, and eddy viscosity in real numerical simulations. This *a posteriori* analysis followed from the hypothesis that the primary purpose of an SGS model is to provide the correct spectral distribution of the diffusion and dissipation of resolved scales by interactions with modeled SGS stresses.

For model calibration we essentially focus on the asymptotic regime of freely decaying three-dimensional homogeneous isotropic turbulence, which is a critical test case for predicting the proper SGS dissipation and SGS diffusion. A robust automatic optimization procedure based on an evolutionary approach was then used for minimizing a functional that measures the difference between the spectral numerical viscosity and diffusivity of ALDM and semi-analytical expressions for the eddy-viscosity and eddy-diffusivity spectra.

Simulations of forced and decaying isotropic turbulence at turbulent Mach numbers $M_t = 0.3$ and $M_t = 0.6$ are performed for *a posteriori* validation. The model predicts the correct time development of the r.m.s. temperature, density and pressure fluctuations (Fig. 1), as well as the proper inertial-range scaling of the energy and variance spectra (Fig. 2).

For final validation, compressibility effects on the Reynolds stresses and the turbulent transport in supersonic flow in a channel with cooled isothermal walls are presently being studied. It is planned to perform LES according to available DNS data of Foyi *et al.* [2] for reference at Mach number $M = 0.3, 1.5, 3.0, 3.5$, where the mean mass flow rate is increased between the cases, corresponding to friction Reynolds number $Re_\tau = 181, 221, 556, 1030$, respectively.

In the presentation, we will discuss in detail the theoretical and numerical background of the new method. Computational results will be shown for isotropic turbulence and turbulent channel flow.

References

1. N. A. Adams, S. Hickel, and S. Franz. Implicit subgrid-scale modeling by adaptive deconvolution. *J. Comp. Phys.*, 200:412–431, 2004.
2. H. Foyi, S. Sarkar, and R. Friedrich. Compressibility effects and turbulence scalings in supersonic channel flow. *J. Fluid Mech.*, 509:207–216, 2004.
3. S. Hickel and N. A. Adams. On implicit subgrid-scale modeling in wall-bounded flows. *Phys. Fluids*, 19:105106, 2007.
4. S. Hickel, N. A. Adams, and J. A. Domaradzki. An adaptive local deconvolution method for implicit LES. *J. Comp. Phys.*, 213:413–436, 2006.
5. S. Hickel, N. A. Adams, and N. N. Mansour. Implicit subgrid-scale modeling for large-eddy simulation of passive-scalar mixing. *Phys. Fluids*, 19:095102, 2007.

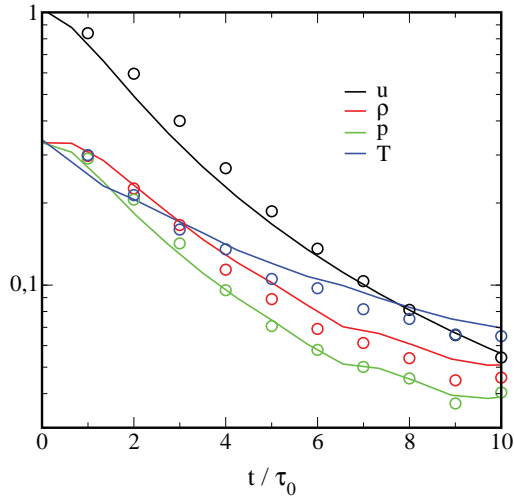


Fig. 1. Evolution of velocity, density, pressure, and temperature fluctuations for decaying homogeneous isotropic turbulence at $M_t = 0.3$; lines denote LES, \circ DNS.

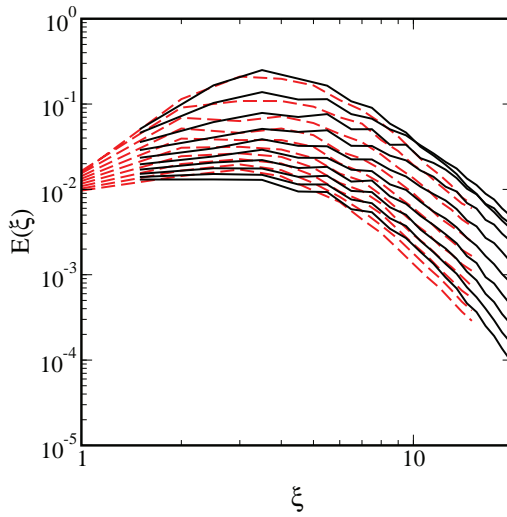


Fig. 2. Instantaneous spectra of turbulent kinetic energy at $t = 1, 2, \dots, 10$ eddy turnover times; - - - LES, ——— DNS.

Injection of a plane reacting jet into a supersonic turbulent channel flow

Christoph Schaupp and Rainer Friedrich

Lehrstuhl für Aerodynamik, TU München, 85748 Garching, Germany
r.friedrich@lrz.tu-muenchen.de

1 Introduction

The transverse injection of fuel into supersonic turbulent flow is a key feature of scramjet technology. In most combustion chamber designs, gaseous fuel is injected into the air stream at angles smaller than 90° to the wall, from ports in the duct wall or from pylons extending into the duct. The resulting flow and especially the mixing and reaction processes are very complex and not completely understood. While measurement of compressible turbulent and reacting flows is very difficult, numerical simulation promises to provide details of flow mechanisms which are presently not amenable to measurement. Previous work on incompressible inert and reacting jets in crossflow is extensive. Margason [7] provides an overview of numerical and experimental investigations from 1932–1993. More recent DNS and LES studies are due to Muppidi and Mahesh [9], Jones and Wille [4], Wegner et al. [11] and Denev et al. [2]. Work on supersonic inert jets in crossflow has been presented by Chenault et al. [1] and Sriram [10] using statistical turbulence models. Kawai and Lele [5] have recently performed LES of an under-expanded inert sonic jet injection into a supersonic turbulent crossflow in order to obtain detailed insight into the complex 3D flow physics and mixing phenomena.

2 Numerical details

The present study is a first step towards scramjet combustion. Its aim is to investigate a simplified geometrical and physical configuration using large-eddy simulation. A mixture of H_2 and N_2 , with mass fractions of 0.0169 and 0.9831, respectively, is injected transversely at sonic speed from a spanwise slot into a supersonic turbulent air flow in a channel (with mass fractions of 0.23 and 0.77 for O_2 and N_2), where infinitely fast reaction and heat release take place. The ratio of slot width to channel height is $1/32$. Sixth-order compact numerical schemes are used on Cartesian grids with proper refinement

towards walls and in the neighbourhood of the plane jet and its mixing layers. The spatially discretized low-pass filtered compressible Navier–Stokes and mixture fraction equations are integrated in time with a 4th-order Runge–Kutta scheme. In the LES approach used, closure of subgrid terms due to square non-linearities is obtained via approximate deconvolution [8], while the filtered heat release term is closed in analogy to RANS concepts, using a model for the conditionally filtered scalar dissipation rate. The approximate deconvolution approach alone allows to capture shocks, but leads to spurious oscillations. They are damped without affecting the turbulence fluctuations using localized grid-dependent artificial viscosities and diffusivities (cf. Kawai and Lele [5]). Specific heats and molecular transport coefficients depend on temperature and species concentration. Fully-developed turbulent channel flow is used as inflow condition — an LES of fully developed channel flow at a global Mach number of $M = 3.1$ and a global Reynolds number based on channel half width of $Re \approx 5000$ runs parallel (on a $168 \times 96 \times 192$ grid) with the LES of the injection case ($768 \times 96 \times 192$ grid). Walls are kept at constant temperature of $T_w = 700$ K. Coupling between inflow generator and injection simulation is achieved via MPI. Suitable initial conditions for the injection case are obtained from a separate statistical simulation which provides a steady state solution. Our LES approach has been validated by comparison with DNS data for temporal mixing layers [6].

3 Results

The reacting jet in crossflow causes strong modifications of the incoming supersonic turbulent channel flow. It leads to flow separation on the lower wall and to a separation shock. The shock reflects at the upper wall, generating an upper separation zone and in turn a separation shock. A snapshot of velocity vectors projected onto the yz -plane perpendicular to the main flow (containing the midplane of the slot) clearly shows, how the shock front is distorted by the incoming turbulence, figure 1. It also shows the laminar jet leaving the injection channel and rapidly mixing and reacting with the airstream of the channel. Occasionally and locally the injection process creates a Mach disk, to be seen in figure 2, where several quantities are demonstrated simultaneously, e.g. the sonic line (heavy line), contours of the reaction product (water vapor), contour lines of the density gradient and velocity vectors. Flow passing through the Mach disk (quasi-horizontal contour lines of the density gradient) changes direction abruptly. The contour lines of density gradients which are inclined at about 45 degrees separate hot reaction product from cold injected fluid. They are, in contrast to the shocked area, intersected by continuous velocity vectors.

More globally speaking, the mean flow in the channel not only passes through zones of deceleration and acceleration, but also through regions of compression and expansion with dramatic effects on turbulence production

and energy redistribution. Vertical profiles of the mean density (not shown) clearly indicate these zones. While the incoming flow has low mean density in the core region and high density at the wall due to the 'low' wall temperature, the separation shock increases the density downstream. A further increase is observed in the midplane of the jet, as a result of low temperature.

Profiles of the pressure-strain correlation $PS_{11} = \overline{p' \partial u_1' / \partial x_1}$, appearing in the transport equation of the axial Reynolds stress, reveal some correlation with the mean density. Compared to the incoming flow, PS_{11} has locally remarkable negative amplitudes, because the mean density there is increased compared to its values at the inflow plane. This is a strong indication of the fact that mean density variations control the redistribution of fluctuating kinetic energy among the three Reynolds stress components, as demonstrated by Foysi et al. [3] for fully-developed compressible turbulent channel flow and by Mahle et al. [6] for compressible reacting turbulent mixing layers.

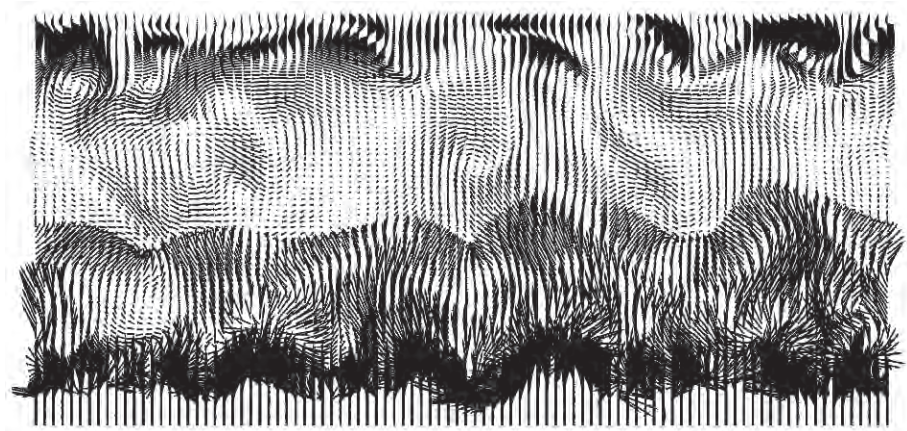


Fig. 1. A snapshot of the projection of velocity vectors onto a yz -plane through the slot midplane.

References

1. C. F. Chenault, P. S. Beran, and R. D. W. Bowersox. Numerical investigation of supersonic injection using a Reynolds-stress turbulence model. *AIAA Journal*, 37(10):1257–1269, 1999.
2. J. A. Denev, J. Fröhlich, and H. Bockhorn. Direct numerical simulation of a transitional jet in crossflow with mixing and chemical reactions. In *Fifth International Symposium on Turbulence and Shear Flow Phenomena*, pages 1243–1248, Garching, Germany, 2007.

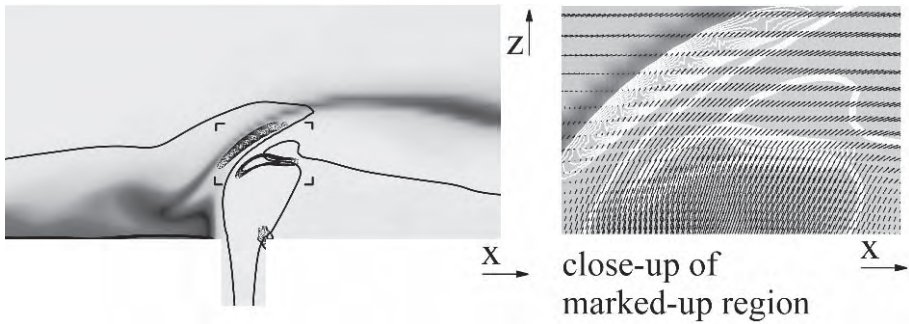


Fig. 2. Snapshots of contours of Y_{H_2O} , isolines of density gradient magnitude and sonic line in an xz -plane are shown. On right, an enlarged view of the Mach disk region, as marked-up on left, is depicted, including velocity vectors.

3. H. Foysi, S. Sarkar and R. Friedrich. Compressibility effects and turbulence scaling in supersonic channel flow. *Journal of Fluid Mechanics*, 509:207–216, 2004.
4. W. P. Jones and M. Wille. Large-eddy simulation of a plane jet in a crossflow. *International Journal of Heat and Fluid Flow*, 17(3):296–306, 1996.
5. S. Kawai and S. K. Lele. Large-Eddy Simulation of jet mixing in a supersonic turbulent crossflow. In *Annual Research Briefs*, pages 139–151, Center for Turbulence Research, Stanford University, 2008.
6. I. Mahle, H. Foysi, S. Sarkar and R. Friedrich. On the turbulence structure in inert and reacting compressible mixing layers. *Journal of Fluid Mechanics*, 593:171–180, 2007.
7. R. J. Margason. Fifty years of jet in crossflow research. Number 534 in AGARD Conference Proceedings, pages 1–1 to 1–41, Neuilly sur Seine, 1993. North Atlantic Treaty Organization.
8. J. Mathew, R. Lechner, H. Foysi, J. Sesterhenn, and R. Friedrich. An explicit filtering method for LES of compressible flows. *Physics of Fluids*, 15(8):2279–2289, 2003.
9. S. Muppidi and K. Mahesh. Direct numerical simulation of round turbulent jets in crossflow. *Journal of Fluid Mechanics*, 574:59–84, 2007.
10. A. T. Sriram. *Numerical simulations of transverse injection of plane and circular sonic jets into turbulent supersonic crossflows*. PhD thesis, Department of Aerospace Engineering, Indian Institute of Science, Bangalore, 2003.
11. B. Wegner, Y. Huai, and A. Sadiki. Comparative study of turbulent mixing in jet in cross-flow configurations using LES. *International Journal of Heat and Fluid Flow*, 25:767–775, 2004.

Turbulent premixed flame fronts: fractal scaling and implications for LES modeling

G. Troiani, F. Picano, C. M. Casciola

Dipartimento di Meccanica e Aeronautica, Università di Roma *La Sapienza*, Via Eudossiana 18, 00184 Roma, Italy
guido.troiani@uniroma1.it

1 Introduction

Large Eddy Simulation in turbulent combustion is a promising approach for simulation of high Reynolds number flows, typical of industrial combustion appliances. Self-similarity of reactive turbulent fronts emerges from their fractal properties, which can be suitably exploited to model the unresolved sub-grid contribution of combustion, see [1] and ref. therein. Following those authors, with appropriate hypotheses, the filtered progress variable equation reads

$$\frac{\partial \bar{\rho} \tilde{c}}{\partial t} + \nabla \cdot (\bar{\rho} \tilde{u} \tilde{c}) + \nabla \cdot (\bar{\rho} \tilde{u} \tilde{c} - \bar{\rho} \tilde{u} \tilde{c}) = \nabla \cdot (\overline{\rho D \nabla c}) + \bar{\omega} = \rho_u S_L \Xi |\nabla \bar{c}|, \quad (1)$$

where $\Xi = \overline{|\nabla c|} / |\nabla \bar{c}|$ is the wrinkling factor, strictly related to the flame surface density concept $\Sigma = \overline{|\nabla c|}$. The model can be closed using the fractal behavior of flames, i.e. $\Xi(\Delta) = (\Delta/\epsilon_i)^{D-2}$, where D is the fractal dimension of the flame front and ϵ_i is the scale below which the fractal scaling is lost (Δ is the mesh spacing). A crucial issue of this model is the determination of the fractal dimension D and of the inner cut-off ϵ_i and their dependence on turbulence/chemistry conditions.

Purpose of this work is twofold, first the evaluation of both D and ϵ_i by OH-LIF –Laser Induced Fluorescence– (see [2] for details) and DNS of pre-mixed methane/air jet flames in round and annular configurations. Second, on the ground of the fractal characteristics found, LES computations have been performed reproducing the experiments of *Chen and Mansour* at $Re = U_0 D / \nu = 16000$ (M3), $Re = 24000$ (M2) [3].

2 Methodology: experiments and numerics

Methane/air premixed flames have been realized in two different jet-burners. A cylindrical bunsen burner and an annular inlet bluff-body stabilized burner,

both fed with a mixture of CH_4 and air at different equivalence ratios. Reynolds numbers and equivalence ratios (Φ) ranges between 4000 and 10000 and from stoichiometric mixtures down to $\Phi = 0.6$. Velocity data have been acquired by both LDA and PIV systems by seeding the flow with $5 \mu\text{m}$ alumina particles, and OH-LIF allowed to extract flame front position. A thorough discussion of the two set-up can be found in [4, 5].

The numerical code discretizes the cylindrical formulation of the Low-Mach number asymptotic Navier-Stokes equations with or without sub-grid models in order to perform DNS or LES, respectively. Second order finite differences on staggered grid and a third order low storage Runge-Kutta numerical schemes are employed. Details and tests for incompressible jets can be found in [6]. All the adopted parameters simulate approximatively the experimental reactive annular jet with the same Reynolds number and with the ratio between laminar unstretched flame speed and the flow bulk velocity: $S_L/U_0 \simeq 0.05$. An Arrhenius one-step irreversible reaction $\omega = \omega_\infty(\rho Y_R)e^{-T_a/T}$, reproduces the combustion of a lean premixed methane/air mixture.

Dealing with LES, the major differences in the code are given by the sub-grid extra terms and the use of the concept of the progress variable that follows equation 1. The closure of the velocity sub-grid stresses are given Smagorinsky model with the shear-improved formulation [7] rearranged to take into account the variations of density. The sub-grid extra diffusivity of scalars is assumed proportional to the Smagorinsky eddy-viscosity: $D_T = 0.7\nu_T$. The simulations concern premixed round jets and reproduce the experimental configurations of *Chen and Mansour* [3].

3 Results and analysis

The instantaneous configuration of the flame front has a complex geometry, and recent evidence suggests its possible prefractal structure. The consequent multiscale nature of the surface implies the application of geometrical concepts from fractal theory to describe the amount of wrinkling. In fractal theory, a power law relationship exists between the number of boxes needed to cover a fractal object and the box size L , i.e.:

$$N(L) \propto L^{-D_2} , \quad (2)$$

where D_2 is the fractal dimension of an object embedded in a two dimensional space. In our case the object is given by a two dimensional cut of the flame fractal surface. Hence the dimension of the whole flame front is: $D = D_2 + 1$. The flamelet surface is represented by the fractal of dimension D in a range of scales confined between an inner (ϵ_i) and an outer (ϵ_o) cut-off. A number of experiments and DNS have been carried out by varying the nondimensional turbulence intensity u'/S_L . As anticipated, fractal characteristics have been evaluated by the box-counting technique, which consists in enumerating the

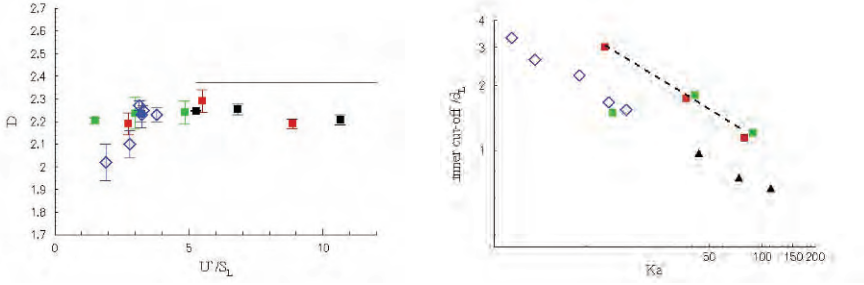


Fig. 1. Left: Fractal dimension *vs* normalized turbulent fluctuations U'/S_L . Error bars report the fitting error. In this panel it has been represented the value $D_2 + 1$ to be congruent with the fractal dimension of iso-surfaces. Thick line, fractal dimension for non-reacting scalar turbulent iso-surfaces, i.e. $D = 2.37$. Open symbols, DNS; closed symbols, experiments. Right: Inner cut-off normalized with thermal thickness (ϵ_i/d_L) *vs* Karlovitz number. Karlovitz number defined as $(d_L/\eta)^2$. Dotted line represents the scaling $\epsilon_i/d_L \propto Ka^{-0.5}$.

squared boxes of size L necessary to entirely cover the whole object that, in this case, is the contour of the flame front. If this number scales with equation 2, then the measured object is a fractal with dimension D_2 . Data at different u'/S_L have been fitted with a power law whose exponents are reported in figure 1. Increasing u'/S_L , the fractal dimension D reaches the value of $D = 2.23 \pm 0.03$ lower than $D = 2.37$, corresponding to perfectly passive scalar iso-surface fractal dimension.

The typical length scales at which the fractal scaling is lost denote outer and inner cut-offs. Supposing the latter to scale with Kolmogorov dissipative length η , we have:

$$\epsilon_i/d_L \propto Ka^{-1/2} . \tag{3}$$

A prediction well confirmed by data of figure 1.

In the following we show the results concerning LES with fractal closure for the progress variable. In particular the wrinkling factor $\Xi(\Delta) = \alpha(\Delta/\epsilon_i)^{D-2}$ ($\alpha = 1.0$ is assumed) is determined using the fractal characteristics extracted from experiments and DNS and presented in the previous paragraph: $D \simeq 2.23$ and $\epsilon_i \simeq \eta = (\nu^3/\varepsilon)^{1/4}$ with ε the turbulent kinetic energy dissipation. The Kolmogorov scale η is obtained assuming K41 theory. If the LES filter length Δ falls inside the inertial range, the dissipation can be estimated as $\varepsilon \simeq \tilde{u}_\Delta^3/\Delta$, where the characteristic velocity at scale Δ is $\tilde{u}_\Delta = \tilde{S}\Delta$ with \tilde{S} the filtered strain rate. Two premixed turbulent jet flames are used as test cases. These data are taken from the experiments M2 and M3 of *Chen and Mansour* [3] at Reynolds numbers of $Re = 24000$ and $Re = 16000$, respectively. The ratio between the laminar unstretched flame speed and the bulk jet velocity is: $S_L/U_0 = 0.01267$ and $S_L/U_0 = 0.019$ for the two flames respectively. In figure 2 the mean temperature field normalized by the adiabatic flame

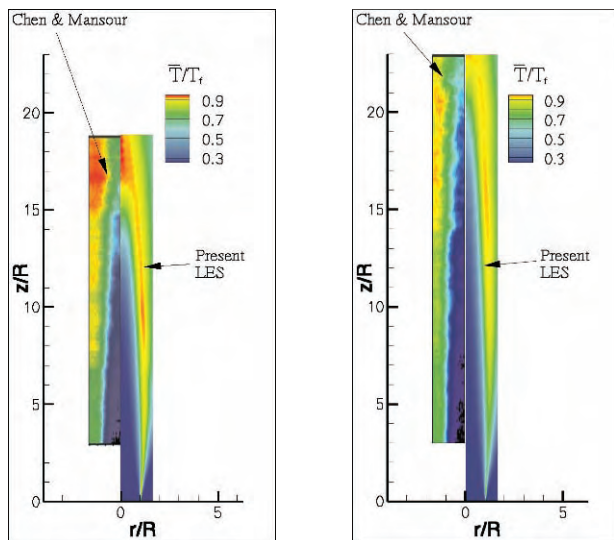


Fig. 2. Mean temperature field normalized with the adiabatic flame temperature. Left: experiments of *Chen and Mansour* [3]. Right: present LES computations. Upper panel, $Re = 16000$, $S_L/U_0 = 0.019$; lower panel, $Re = 24000$, $S_L/U_0 = 0.01267$.

temperature T_f is presented for both cases. Concerning the flame length, the correspondence is remarkable considering that model constants and mesh size are kept fixed in the two cases. In particular the mesh is about 60 and about 150 times smaller than needed in DNS for $Re = 16000$ and $Re = 24000$ respectively. The major differences between experiments and LES lie in the lower part of the shear layer and at the flame tip where the temperature found in experiments is smaller compared to that of LES. These phenomena can be due to local quenching effects that are frequent in regions with high shear rate, an issue that is currently under investigation.

References

1. R. Knikker, D. Veynante, C. Meneveau, *Physics of Fluids* 16 (11) (2004) L91–L94.
2. G. Troiani, M. Marrocco, III European Combustion Meeting -ECM2007- Chania, Crete.
3. Y. C. Chen, M. S. Mansour, *Experiments in Fluids* 26 (1-4) (1999) 277–287.
4. G. Troiani, *Combust. Flame* 156 (2) (2009) 539–542.
5. G. Troiani, M. Marrocco, S. Giammartini, C. M. Casciola, *Combust. Flame* 156 (3) (2009) 608–620.
6. F. Picano, C. M. Casciola, *Physics of Fluids* 19 (11) (2007) 118106.
7. E. Leveque, F. Toschi, L. Shao, J. P. Bertoglio, *J. Fluid Mech.* 570 (2007) 491–502.

Large eddy simulation of a lean premixed swirl flame in complex geometry - comparison of two turbulent combustion models

P. Wang¹, J. Fröhlich², U. Maas¹

¹Institute for Technical Thermodynamics, Karlsruhe University, 76128 Karlsruhe, Germany

²Institute of Fluid Mechanics, Technical University of Dresden, 01062 Dresden, Germany

ping.wang at mailbox.tu-dresden.de

Lean premixed combustion is employed to reduce emission, but can exhibit undesired effects such as lean blow-off and thermo-acoustic resonance. To cope with these, burners with strong swirl are utilized for flame stabilization. In the resulting complex flow system, flow instabilities are observed in both experiments and simulations. To date, large eddy simulation (LES) is becoming a widely used approach for understanding the properties of turbulent flow phenomena. However, LES of lean premixed combustion still constitutes an open challenge. Many turbulent combustion modeling methods have been developed for LES of such flows [1, 2]. Two types of them are the thickened flame (TF) model [3] and the flame surface density (FSD) model [4]. However, none of these models is ideal and suitable for all kinds of flame configurations. A detailed comparison was made between the TF and FSD by Lin et al. [5] for freely propagating premixed flames in homogeneous isotropic decaying turbulent fields, and qualitative agreement between them was found. In the present work, the performances of the two cited turbulent combustion models, TF and FSD, in simulating the lean premixed swirl flames in an industrial gas turbine model combustor is compared against the well-documented experiment data obtained by Meier et al. [6].

The simulated burner is sketched in Fig. 1a. It is constituted of a plenum, a swirl-injector and a combustion chamber. Methane is injected into the swirler and mixes rapidly with the incoming air, so that premixed gas enters into the combustion chamber with a square section of $85 \times 85\text{mm}$ and a height of 114mm . There, a V-shaped flame develops. This flame configuration has already been simulated with different methods using unstructured grids [7, 8, 9], and the results are generally in good agreement with the experimental data. In these simulations as well as the present ones, perfect premixing is assumed. The whole domain is divided into 257 blocks and consists of 4.7 million cells.

The Reynolds number based on the nozzle exit diameter $D = 27.85\text{mm}$, bulk velocity at the exit $U_b = 17.4\text{m/s}$ and the cold flow is about 30,000. The flame simulated has power 27kW and equivalence ratio 0.75, and it is estimated to be located in the thin reaction zones in the Borghi diagram [10]. A uniform velocity profile was imposed at the inlet and a convective outflow condition was used at the exit. The Werner-Wengle wall function was employed at all solid walls.

In this work, numerical simulations are performed with the in-house code LESOCC2C, in which both TF model and FSD model are implemented. It solves the Low-Mach-number version of the compressible Navier-Stokes equations on body-fitted curvilinear block-structured grids using second-order central schemes in space and a second order R-K method in time. Substantial experience has been gained with this code for similar flame configurations [11, 12].

In the TF model, pre-exponential constants and transport coefficients are both modified by a thickening-factor F to yield a thicker reaction zone which can then be resolved with LES mesh. The subgrid-scale (SGS) wrinkling is accounted for by an efficiency function E related to the subgrid-turbulent velocity and the filter width. The equation for the resolved mass fraction of the k -th species then reads

$$\frac{\partial \rho Y_k^{th}}{\partial t} + \frac{\partial \rho u_j Y_k^{th}}{\partial x_j} = \frac{\partial}{\partial x_j} (\rho D_k E F \frac{\partial Y_k^{th}}{\partial x_j}) + \frac{E}{F} \dot{\omega}_k(Y_j^{th}, T^{th}). \quad (1)$$

where D , $\dot{\omega}$, Y and T are the diffusion coefficient, production rate, species concentration and temperature, respectively. The superscript th represents thickened quantities. The equation for the Favre filtered progress variable has the form

$$\frac{\bar{\rho} \tilde{c}}{\partial t} + \frac{\bar{\rho} \tilde{u}_j \tilde{c}}{\partial x_j} + \frac{\partial}{\partial x_j} \bar{\rho} (\tilde{u}_j \tilde{c} - \tilde{u}_j \tilde{c}) = \frac{\partial}{\partial x_j} \left(\rho D \frac{\partial c}{\partial x_j} \right) + \bar{\omega} \quad (2)$$

The two RHS terms are then modeled with the algebraic model of [4],

$$\frac{\partial}{\partial x_j} \left(\rho D \frac{\partial c}{\partial x_j} \right) + \bar{\omega} = \langle \rho w \rangle_s \bar{\Sigma} \approx \rho_u s_L 4 \beta \frac{\bar{c}(1 - \bar{c})}{\Delta} \quad (3)$$

where β , Δ , ρ_u and s_L are the model constant, filter size, density of fresh mixture and laminar flame speed, respectively. Σ is the so-called flame surface density. In the present work, ρ_u and s_L are obtained from a separate one-dimensional simulation.

A dominant precessing vortex core (PVC) is found in the corresponding iso-thermal swirling flow as in [7]. A PVC also exists in both reactive simulations. A big spiral-type vortex attached to the center body is found entirely located in the unburnt region. Its movement is similar to the PVC in the iso-thermal case but is different from those in [8], where the Q criterion was used

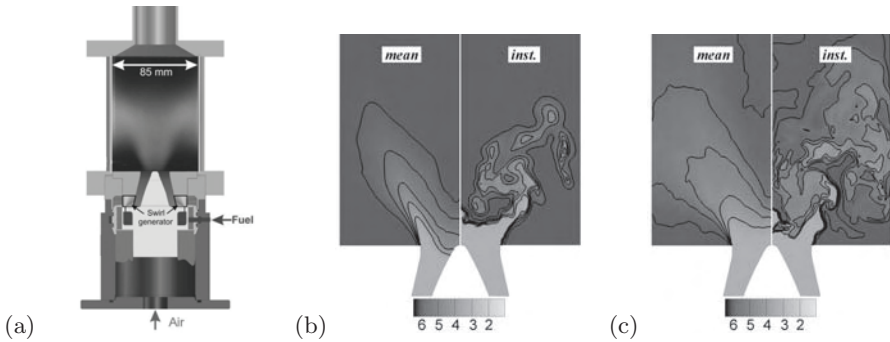


Fig. 1. (a) Schematic of the combustion chamber. (b) Temperature field for mean (left) and for instantaneous (right), obtained with the DTF model. (c) As (b) but obtained with the FSD model. Note: the temperature is normalized with 298.15K.

for visualization. Fig. 1b and 1c show the temperature field obtained with the two models, providing the mean field and a snapshot of the instantaneous field. The FSD model is seen to yield a larger reaction zone partly reaching the walls which is unrealistic, while the reaction is more vigorous with the DTF model. The different location of the flame has an impact on the velocity field shown in Fig. 2.

Profiles of velocity statistics in the $x - y$ centre plane are shown in Fig. 2. The origin of the coordinate system is located at the center of the jet exit, x - direction is to the downstream, y - and z - are normal to the surfaces of chamber. Overall, the agreement between the experimental data and the LES results is good. Profiles obtained with the TF model are closer to the experimental data than those obtained with the FSD model. The discrepancy at the position ($x = 1.5\text{mm}$) is not negligible, where sharp peaks of the rms fluctuations at the edge of jet nozzle are under-predicted. It demonstrates that the outer shear layer should be better resolved. Further calculations with finer grid resolution at the shear layer are under way.

Acknowledgements: The support of the German Research Foundation (DFG) through CRC606 project is gratefully acknowledged. The computations were performed on both the HP-XC clusters of SSCK Karlsruhe and the SGI Altix 4700 cluster of ZIH Dresden. The authors thank Dr. W. Meier (DLR, Stuttgart) for providing the experimental data in electronic form.

References

1. R.W. Bilger, S.B. Pope, K.N.C. Bray, et al., Proc. of Combust. Inst., **30**, 21 (2005).
2. H. Pitsch, Annu. Rev. Fluid Mech., **38**, 453 (2006).
3. O. Colin, F. Ducros, D. Veynante, T. Poinso, Phys. Fluids, **12**, 1843 (2000).

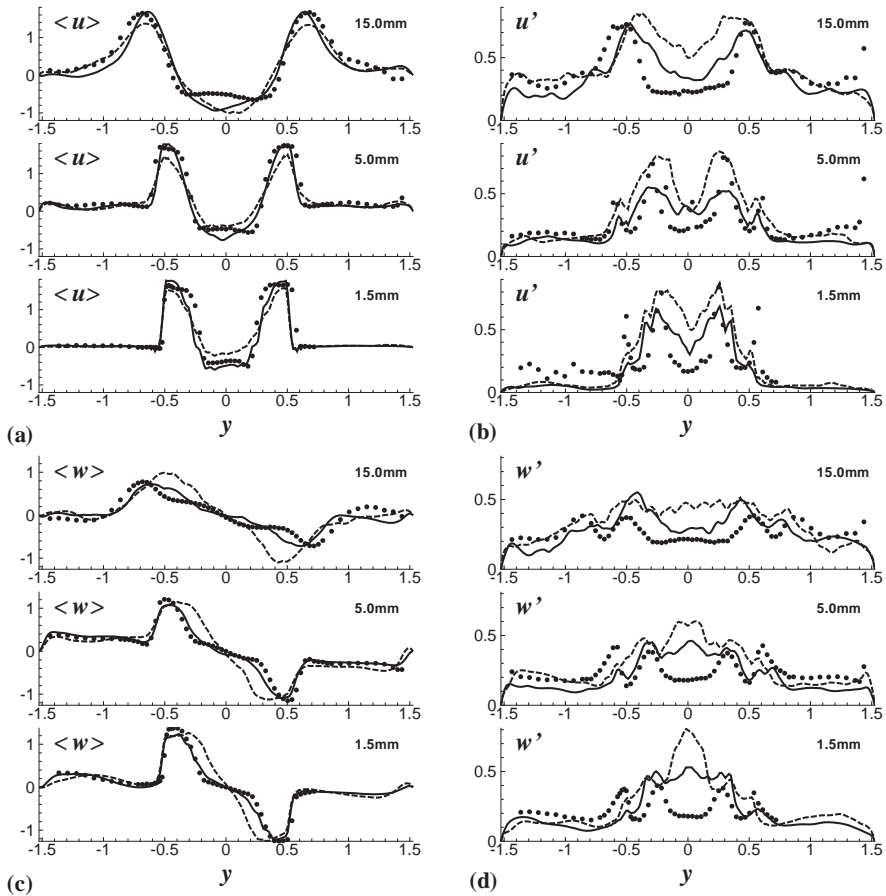


Fig. 2. Profiles of velocity statistics in the $x - y$ center plane. (a) mean streamwise velocity; (b) rms fluctuation of streamwise velocity; (c) mean velocity in z -direction; (d) rms fluctuations in z -direction. Symbols: experiment; solid lines: TF model; dashed lines: FSD model.

4. M. Boger, D. Veynante, H. Boughanem, et al., Proc. of Combust. Inst., **27**, 917 (1998).
5. W. Lin, F.E. Hernández-Pérez, C.P.T. Groth, et al., AIAA, 2008-1048 (2008).
6. W. Meier, P. Weigand, X.R. Duan, et al., Combust. Flame, **150**, 2 (2007).
7. S. Roux, G. Lartigue, T. Poinso, et al., Combust. Flame, **141**, 40 (2005).
8. V. Moureau, P. Minot, H. Pitsch, et al., J. Comp. Physics, **221**, 600 (2007).
9. J. Galpin, A. Naudin, L. Vervisch et al., Combust. Flame, **155**, 247 (2008).
10. N. Peters, Turbulent Combustion, Cambridge University Press (2000).
11. P. Wang, J. Fröhlich, ECM-4, Vienna, Austria, April (2009).
12. P. Wang, J. Fröhlich, TSFP-6, Seoul, South Korea, June (2009).

Part XV Posters

KS inertial range and validity of Richardson's law

F. C. G. A. Nicolleau

University of Sheffield, Sheffield Fluid Mechanics Group, Department of Mechanical Engineering, S1 3JD Sheffield, UK
F.Nicolleau@Sheffield.ac.uk

1 Kinematic Simulation

Kinematic Simulation (KS) is a Lagrangian model where a synthetic Eulerian velocity field $u(x, t)$ is assumed. It is then possible to track one, two or many particles and study their trajectories by integrating this velocity field. We use the KS code developed in [6] based on [3] for incompressible isotropic turbulence. The three-dimensional KS turbulent velocity field used in this paper is kinematically presented by a truncated Fourier series, sum of N_k random Fourier modes:

$$\mathbf{u}(\mathbf{x}, t) = \sum_{n=0}^{N_k} \mathbf{a}_n \cos(\mathbf{k}_n \cdot \mathbf{x} + \omega_n t) + \mathbf{b}_n \sin(\mathbf{k}_n \cdot \mathbf{x} + \omega_n t) \quad (1)$$

where N_k is the total number of modes included, \mathbf{a}_n and \mathbf{b}_n are decomposition coefficients corresponding to the wave vector \mathbf{k}_n , and ω_n is the unsteadiness frequency.

2 Kinematic Simulation and t^3 law

According to [8] and [1] two-particle separation variance $\langle \Delta^2(t) \rangle$ should obey the famous t^3 law for diffusion in isotropic turbulence

$$\langle \Delta^2(t) \rangle = G_\Delta \epsilon t^3 \quad (2)$$

where G_Δ is the Richardson universal dimensionless constant, ϵ the turbulent energy dissipation rate and t time.

There have been some contradictory conclusions as to the ability of KS to predict a t^3 law. According to [4, 5, 2, 7] KS predict (2), according to [10] they do not. It has been argued in [10] that owing to the lack of sweeping of small scales by large scales in kinematic simulation, the validity of the Richardson's power law might be affected.

3 Present study

In the present work, we revisit the t^3 law (2) starting from Richardson's locality-in-scale hypothesis [9] based on the diffusivity rather than the particles' separation. We generalise the argument in [10] to any power law spectra and conclude that

- the discrepancy between KS and Richardson's locality-in-scale hypothesis only appears for inertial range L/η larger than 10^4 , where L is the integral length scale and η the Kolmogorov length scale, which corresponds to significant Reynolds numbers. In other words, we argue that the discrepancies between the different authors on the ability of kinematic simulation to predict Richardson power law may be linked to the inertial subrange they have used. For small inertial subrange, KS is efficient and the significance of the sweeping can be ignored, as a result we limit the KS agreement with the Richardson scaling law t^3 for inertial subranges $L/\eta \leq 10000$.
- In any case, we show that the discrepancy observed for larger inertial range cannot be attributed to a lack of sweeping of small scales by large scales.
- We propose other explanations for the discrepancy, in particular we discuss the role of the Fourier modes distribution.

References

1. G. K. Batchelor, *Quart. J. R. Met. Soc.* **76**, 133, 1950.
2. J. Davila and J. C. Vassilicos, *Phys. Rev. Lett.* **91**, 144501, 2003.
3. J. C. H. Fung, J. C. R. Hunt, N. A. Malik and R. J. Perkins, *J. Fluid Mech.* **236**, 281, 1992.
4. J. C. H. Fung and J. C. Vassilicos, *Phys. Rev. E* **57**(2), 1677, 1998.
5. N. A. Malik and J. C. Vassilicos, *Phys. Fluids* **11**(6), 1572, 1999.
6. F. Nicolleau and A. ElMaihy, *J. Fluid Mech.* **517**, 229, 2004.
7. F. Nicolleau and G. Yu *Phys. Fluids* **16**(4), 2309, 2004.
8. A. M. Obukhov, *Bull. Acad. Sci. U.S.S.R., Géog. & Géophys., Moscow* **5**, 453, 1941.
9. L. F. Richardson, *Beitr. Phys. Frei. Atmos.*, **15**, 24-29, 1926.
10. D. J. Thomson and B. J. Devenish, *J. Fluid Mech.* **526**, 277, 2005.

Lagrangian Vortex Methods in Turbulent Channel Flows

R. Yokota, K. Fukagata, and S. Obi

Dept. Mechanical Engineering, Keio University, 3-14-1 Hiyoshi, Yokohama, Japan
rioyokota@mac.com

In our present study, we compare the turbulent statistics obtained from a vortex method calculation with a finite difference calculation for the turbulent channel flow.

The present vortex method is a standard vortex particle method, which uses the core spreading method with spatial adaptation [1] as the diffusion scheme. The Reynolds number was $Re_b = 5600$ and the calculation domain was $3\delta \times 2\delta \times 3\delta$, where δ is the channel half width.

The mean velocity profile after one wash-out time is shown in Fig. 1(a), while the mean velocity gradient and Reynolds stress after one wash-out time are shown in Fig. 1(b). The results of the vortex method show an excessive production of Reynolds stress in the viscous layer.

References

1. R. Yokota, T. K. Sheel, & S. Obi, Calculation of Isotropic Turbulence Using a Pure Lagrangian Vortex Method, *J. Comput. Phys.* **226** 1589 (2007).

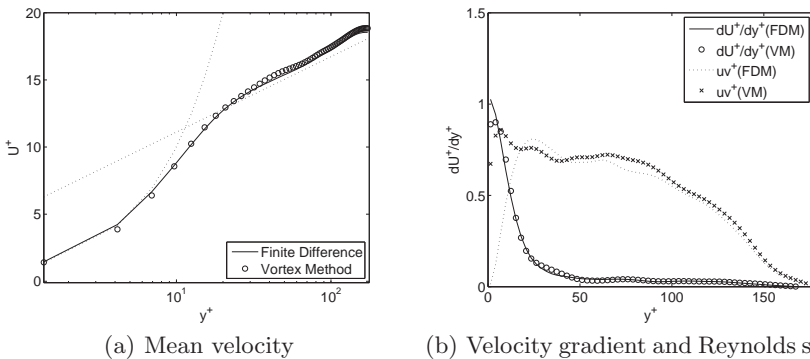


Fig. 1. Results of the finite difference method and vortex method after one wash-out

Unstable and turbulent flows simulated by means of the Boltzmann kinetic equation

V.V.Aristov, A.A.Frolova, O.I.Rovenskaya, and S.A.Zabelok

Dorodnicyn Computing Centre of Russian Academy of Sciences, Ul. Vavilova - 40,
119333, Moscow, Russia
aristov@ccas.ru

For description of unstable and turbulent compressible gas flows with nonequilibrium regions we apply direct methods of solving the Boltzmann kinetic equation [1, 2]. Solutions by the Boltzmann equation tend to the solutions of the Navier-Stokes equations according to the Chapman-Enskog expansion for stable flows. For unstable cases, especially for strong turbulent compressible flows the issue of the validity should be investigated. Free supersonic underexpanded jet flows has been simulated and the system of Taylor-Goertler streamwise vortices as the factor of instability has been observed. The comparisons of the frequencies and the magnitude of the amplitude of the turbulent oscillations in the shear layer with the experimental data have been satisfactory (and for turbulence there exist zones with non-Navier-Stokes transport according to the kinetic description). Numerical solutions are obtained with the Unified Flow Solver (UFS) [2] having the following features: adaptive mesh refinement, hybrid methods with automatic definition of continuum and kinetic domains, direct solver of kinetic equations, kinetic schemes approximating continuum equations. Attention is paid to the transition to the turbulence in the wake, e.g. turbulent instability in the wake behind a prism for the supersonic flow is observed (for this 2D simulation the kinetic Navier Stokes solver of the UFS is applied). The detailed energy processes of the turbulent flows are also considered. The spectral density of the kinetic energy for the unstable 2D flow in the square is obtained by the Boltzmann equation in [3]. Our results are compared with the known solutions by the BGK equation [4].

References

1. V. V. Aristov, *Methods of direct solving the Boltzmann equation and study of nonequilibrium flows*, Kluwer Academic Publishers, Dordrecht 2001.
2. V. I. Kolobov, R. R. Arslanbekov, V. V. Aristov, A. A. Frolova and S. A. Zabelok, *J. Comp. Math.*, **233**, 589 (2007).
3. O. I. Rovenskaia, *Comp. Math. Math. Phys.*, **47**, 1544 (2007).
4. A. Sakurai, and F. Takayama, *Phys. Fluids*, **15**, 1282 (2003).

Natural Transition in Plane Poiseuille Flow

H. G. Silva¹, R. A. C. Germanos², and M. A. F. Medeiros²

¹ Faculdade de Ciencias Integradas do Pontal-Universidade Federal de Uberlandia, Brazil

² Escola de Engenharia de Sao Carlos - Universidade de Sao Paulo, Brazil
ghioti@dem.feis.unesp.br

We present numerical and theoretical results on the natural transition in a plane Poiseuille flow. The natural transition is often studied in boundary layers, but the analysis in a parallel flow allows the use of the Reynolds number as a control parameter. The results indicated that the classical scenarios described in the literature play a role in natural transition and can lead to turbulent spots. In natural transition the wave systems are modulated in streamwise and spanwise directions and cause premature nonlinearity [1]. Spikes and turbulent spots are often present in natural transition, but the classical routes, namely, K-type and H-type instabilities and the oblique transition, have not been linked to these phenomena. Therefore, many questions remain regarding the relevance of these studies to natural transition. For instance, it is unknown whether such classical routes actually occur in natural transition, whether they occur simultaneously or interact, whether there is a dominant mechanism under some circumstances, etc. Such questions motivated the present work. Numerical simulation of the incompressible three-dimensional Navier-Stokes equations in a vorticity-velocity formulation was performed using high accurate numerical schemes. Owing to the complexity of the natural transition, the streamwise modulation was initially not considered. Therefore, only the three-dimensionality was studied yielding spanwise modulated wavetrains. Two cases were judiciously selected at $Re = 8000$. One case was located near the first branch of the two-dimensional stability diagram where the linear process is dominated by three-dimensional Tollmien-Schlichting (TS) waves. The other case was located far from the first branch where the linear process is dominated by a two-dimensional TS waves. Preliminary results can be found in [2]. Similar studies, but for boundary layers, can be found in [3].

The results shed light on some the questions posed in the introduction. In fact, all the nonlinear activity observed could be attributed to one of the classical nonlinear regimes. Each regime was active in a different parameter set. Indeed, when three-dimensional waves were the linearly most unstable, the observed scenario was linked to oblique transition, but, otherwise, K-type transition set in. These does not mean, however, that transition predictions

can be made directly from simulations that involve only a limited number of waves. In any case, the localized and explosive character of the interaction resembled a turbulent spot. The results also suggest that, for high subsonic flows, oblique transition should be the most likely scenario. Studies are currently under way to verify this conjecture. Also simulations of spanwise and streamwise modulated wavepackets are currently being performed. It is expected that these results will be available for presentation at the conference.

The authors acknowledge the financial support from the AFOSR, CNPq and FAPESP.

References

1. M. Gaster. The Physical Process Causing Breakdown to Turbulence. 12th Naval Hydrodynamics Symposium, Washington, 1978.
2. H. G. Silva, M. A. F. Medeiros. Nonlinear Regime of a Spanwise Modulated Wavetrain in a Plane Poiseuille flow. 6th School of Spring of Transition and Turbulence, in CD, San Carlos, Brazil, 2008.
3. M. A. F. Medeiros. The Nonlinear Evolution of a Wavetrain emanating from a point source in a boundary layer. *J. Fluid. Mech.*, 508:287317, 2004.

Stabilization of the turbulent flows in anisotropic viscoelastic tubes

N. Kizilova, and M. Hamadiche

Department of Theoretical Mechanics, Kharkov National University, Svobody sq.,
4, 61077 Kharkov, Ukraine

Laboratoire de Mécanique des Fluides et d'Acoustique, École Centrale de Lyon, 36
Av. Guy de Collongue, 69134 Ecully, France

`nknk@bk.ru`

`mahmoud.hamadiche@ec-lyon.fr`

Flow around the aircrafts and marine vehicles is turbulized that increases the skin-friction drag and fuel consumption. Here stability of the fully developed turbulent flow of an incompressible fluid in the viscoelastic tube is considered. The eddy viscosity concept is considered to be adequate and the flow velocity, wall displacement and pressures in the fluid and solid wall are time-averaged quantities. Continuity conditions for the components of the velocity and stress tensor at the fluid-wall interface and no displacement condition at the outer wall of the tube are considered. Solution of the coupled system has been found in the form of the normal mode and the obtained system has been studied using the numerical technique described in [1,2]. The temporal and spatial eigenvalues and the dependencies of the temporal and spatial amplification rates on the rheological parameters of the wall have been computed. It was shown stability of the modes can be increased by a proper choice of the wall parameters. Successful combinations of the wall thickness, elasticity and viscosity have been found for a large variety of materials. It was shown a substantial reduction in the viscous wall shear stress accompanied by a decrease in the turbulence production or Reynolds stress can be reached via using the viscoelastic coating on the rigid surface. The obtained results are in a good agreement with recent direct numerical computations [3].

References

1. M. Hamadiche and N. Kizilova, *Int. J. Dyn. Fluids*, **1**, 1 (2005).
2. M. Hamadiche, N. Kizilova and M. Gad-el-Hak, *Comm. Numer. Meth. Engin. Suppl.*, (2008).
3. T. Endo and R. Himeno, *J. Turbulence* **3**, 7 (2002).

Simulation of induced transition in hypersonic regime: Validation of foot print of the vortical structures

F. Pinna, S. Tirtey, O. Chazot and P. Rambaud

von Karman Institute for Fluid Dynamics, Chaussee de Waterloo, B-1640
Rhode-Saint-Genese, Belgium
fabio.pinna at vki.ac.be

The main goal of this research is to propose a numerical methodology able to predict the flow before the onset of transition occurring in a hypersonic flow. Presently CFD computations are carried out and compared with a huge database of wall experimental results obtained at VKI [4]. The numerical results are expected to provide a 3D definition of the structures letting their footprint at the wall and to support understanding of future hypersonic experiments at VKI. The study focuses on an isolated roughness immersed in the wall boundary layer with a flow at Mach 6 and a Reynolds number based on the ramp height of 20806. The used solver is a VKI in-house code named COOLfluid [2]. This object oriented framework for fluid dynamic is suited for multiphysics computation and allows the use of different numerical techniques. Presently, the use of perfect gas thermodynamics is adopted. Two different numerical techniques both in a steady and laminar configuration will be compared (Finite Volume Method versus Residual Distribution Method). A critical comparison/validation of the two type of calculations is done in front of the qualitative wall measurements (time averaged Heat flux and oil visualizations) . The tridimensional topology of the flow will be then revealed using vortical surfaces extracted thanks to the Q-criterion but also wall streamlines and streamlines extracted from the symmetry plane. The computations carried on so far with a 2nd order FVM does not allow to match completely the flow features, even if behind the ramp the Q criterion shows the appearance of a couple of streamwise vortices. The solution with other numerical techniques and possibly with a finer mesh will bring more insight in the flow physics. A further step will be achieved by using transition modeling as PSE [1] and bi-global stability analysis [3]. The steady laminar flow, obtained by CFD computations, will be used as mean flow to compute the flow stability downstream of the roughness.

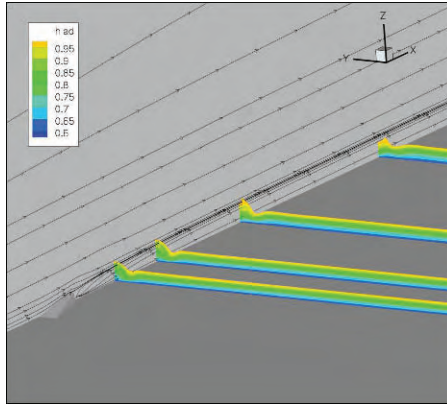


Fig. 1. (normalized)total enthalpy in planes perpendicular to the flow direction

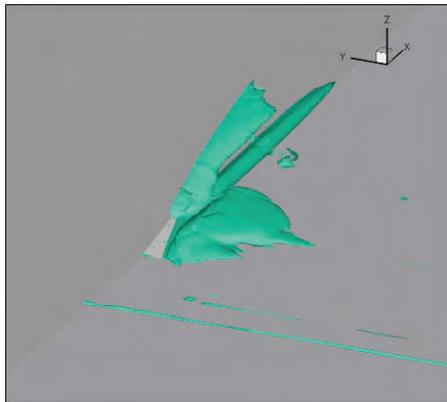


Fig. 2. Q criterion: isosurface for the value $2 \cdot 10^8$

References

1. T.Herbert, Parabolized stability equations, Special Course on Progress in Transition Modelling - Agard Report, 793 (1994).
2. A.Lani, T.Quintino, D.Kimpe, H.Deconinck, S.Vandewalle, and S. Poedts, Reusable object-oriented solutions for numerical simulation of PDEs in a high performance environment, Scientific Programming, 14 (2006), pp. 111–139.
3. W.Theofilis, Advances in global linear instability analysis of nonparallel and three-dimensional flows, Progress in Aerospace Sciences, 39 , (2003), pp. 249–315.
4. S.Tirtey, Characterization of a Transitional Hypersonic Boundary Layer in Wind Tunnel and Flight Conditions, PhD thesis, VKI, Rhode Saint Genese, 2008.

Active grid generated turbulence

P. Knebel, and J. Peinke

ForWind & Institute of Physics, Carl von Ossietzky Universität Oldenburg, 26129 Oldenburg, Germany
pascal.knebel at physik.uni-oldenburg.de

The traditional method of generating turbulence in a wind tunnel is by the insertion of mechanical grids into the air flow. The major drawback are the rather small achievable Reynolds numbers caused by low turbulence intensities of typically less than 5%. Another rather new approach to generate turbulence is to use a so called active grid, first developed and realized by Makita in 1991¹. In contrast to conventional grids it consists of several horizontal and vertical axes with surmounted flaps, that can separately and independently be moved by electrical drives. Based on his pioneering work and subsequent developments we developed a similar active grid for our wind tunnel. In our work we focus on the influence of different driving signals on the generated turbulence.

The wind tunnel is a closed loop section tunnel with a cross section of 1.10 by 0.80 m², that can be operated with a closed or an open (Goettingen style) test section. At open section, the test section length is 1.80 m and 2.70 m at closed section. The maximum wind speed of the free flow is 50 m/s.

By the choice of an adequate static or stochastic dynamic excitation of the axes of the grid, the turbulence intensity and thus the Reynolds number of the turbulent flow can be influenced. In particular we have investigated the features of generated turbulence by the static grid (zero driving signals), by periodically excited grid and by an excitation of the active grid by numerical signals which have the intermittent structure of measured turbulent signals. It seems that if we use a turbulent-like signal as a driving force for the grid, even a turbulent flow with larger inertial range can be generated. With further methods of data analysis, structure functions and multiscale statistics grasped by reconstructed Fokker-Planck equation we investigate if an other class of turbulence, like the one of the fractal grid, can be generated by special driving signals.

¹ H. Makita: Realization of a large-scale turbulence field in a small wind tunnel, Fluid Dyn. Res. 8, 53-64 (1991)

Velocity characterisation of axisymmetric jets from human-sized channels

X. Grandchamp, A. van Hirtum and X. Pelorson

GIPSA-lab, UMR CNRS 5216, Grenoble Universities, France
annemie.vanhirtum@gipsa-lab.inpg.fr

Objectives: Howe and McGowan (Proc. R. Soc. A, 461, 2005) pointed out the lack of low velocity flow measurements issuing from upper airway configurations. Therefore, influence of moderate bulk Reynolds number ($1130 < Re = U_b d / \nu < 11320$) for low length-to-tube diameter ratios, *i.e.* $L/d = \{4.4\ 7.2\ 20\ 53.2\}$, relevant for the human airways are investigated.

Methodology: The transversal velocity field is sampled by single sensor anemometry at a distance $x/d < 0.04$ from the outlet. Evolution of the measured mean velocity exit profile compared with Poiseuille and power law profile for $L/d = 7.2$, corresponding to a typical length-to-tube diameter ratio of human adult upper airways, is shown in Fig. 1(a). As expected, low L/d leads to intermediate exit profiles for $Re < 4530$. For higher Re , a power law gives a good approximation. Fig 1(b) shows that rescaling with the inner variable leads to a good approximation of the mean-velocity exit profile by a linear and logarithmic profile law: $U^+ = y^+$ and $U^+ = A \ln y^+ + B$.

Conclusion: Despite the low L/D ratios, the mean-velocity exit profiles non-dimensionalized with the wall variable, can still be approximated by linear and logarithmic distribution laws. Moreover, a Re dependency on the centre exit turbulence intensity is observed.

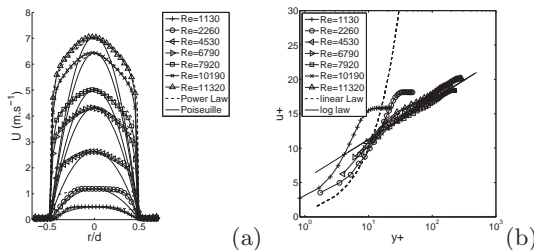


Fig. 1. For $L/d = 7.2$: (a) mean-velocity exit profile, (b) scaled with inner variable

The role of nonlocality in unsteady turbulence

W.J.T. Bos¹ and R. Rubinstein²

¹LMFA-CNRS Ecole Centrale de Lyon, Université de Lyon, Ecully, France

²NASA Langley Research Center, Hampton, Virginia, USA

One point closures such as the $k - \epsilon$ or Reynolds stress model are widely used to predict unsteady flows, even though their time response has been given relatively little attention. An elementary model problem consists of isotropic incompressible turbulence, kept steady by a time-periodic large-scale forcing. This case has been studied theoretically in a recent work [1], and frequency response functions for the turbulent kinetic energy and dissipation were obtained.

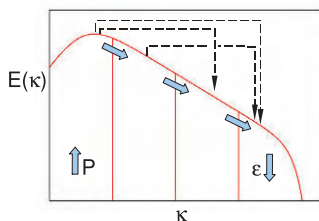


Fig. 1. Cartoon of the energy cascade, including both local and nonlocal interactions.

In the present communication, we discuss the influence of nonlocal interactions (illustrated in Figure 1 by dashed lines) on the time-response of turbulence models. A new multi-scale turbulence model is proposed, which includes the effect of these nonlocal interactions. Details can be found in [2].

References

1. W.J.T. Bos, T.T. Clarke, and R. Rubinstein. Small scale response and modeling of periodically forced turbulence. *Phys. Fluids*, 19, 055107, 2007.
2. R. Rubinstein and W.J.T. Bos On the unsteady behavior of turbulence models *Phys. Fluids*, in press, 2009

Coherent enstrophy production and dissipation in 2D turbulence with and without walls

Romain Nguyen van yen, Marie Farge and Kai Schneider

LMD-CNRS, École normale supérieure, Paris, France
M2P2, Université d'Aix-Marseille, Marseille, France
rnguyen@lmd.ens.fr

We study numerically the behaviour of coherent enstrophy for decaying flows in periodic and circular domains, when the initial Reynolds number Re tends to infinity. The computation is done using a Fourier pseudo-spectral scheme with volume penalization [2]. Wavelet filtering [1] is applied to split enstrophy into coherent and incoherent contributions. In both cases, we find that coherent enstrophy dissipation does not vanish when $Re \rightarrow \infty$. In the circular case, coherent enstrophy diverges when $Re \rightarrow \infty$ due to the boundary layer, but after a certain time its derivative seems to remain bounded independently of Re , indicating that a balance has established between production at the wall and dissipation in the bulk.

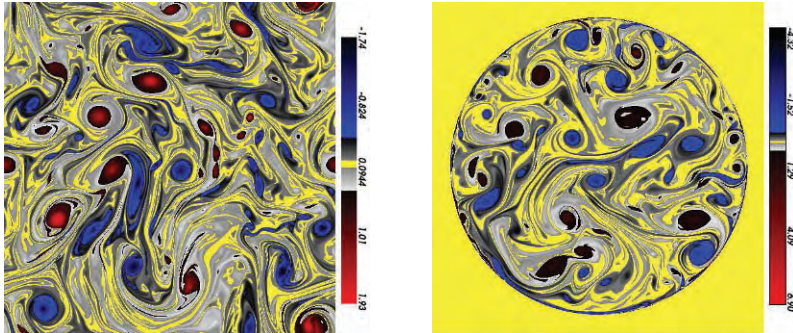


Fig. 1. Vorticity at $Re = 10^4$, $t \simeq 60$ turnover times. Left: periodic. Right : circular.

References

1. R. Nguyen van yen et al., *Physica D*, **237**, 2151-2157 (2008).
2. K. Schneider and M. Farge, *PRL*, **95**, 244502 (2005).

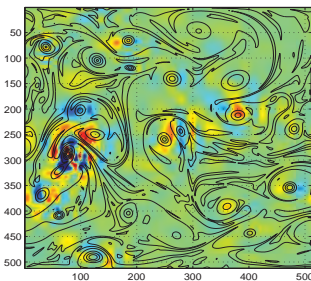
Space-scale analysis of enstrophy transfers in two-dimensional turbulence

P. Fischer, and Ch.H. Bruneau

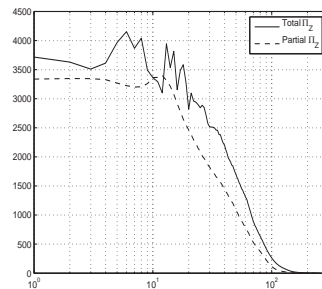
IMB Université Bordeaux 1, INRIA Team MC^2 , CNRS UMR 5251
351, cours de la Libération, 33405 Talence, France
`Patrick.Fischer@math.u-bordeaux1.fr`

We propose here a new mathematical tool for the analysis of the enstrophy flux in two-dimensional turbulence. We call this mathematical object the interaction function since it describes the interactions responsible for the enstrophy transfers in the flow. It is based on two-dimensional orthogonal wavelet decompositions of the two parts in the transport term of the Navier-Stokes equations. The interaction function for the enstrophy transfer is obtained through a very simple process in which the interactions are computed in the wavelet space and then reconstructed in the physical space.

The interaction function can accurately detect the area where the enstrophy transfers take place in a turbulent flow. This can be observed in Figure (a) where contour lines of the vorticity field are superimposed onto the interaction function representation. In this snapshot, a region with strong values around the point of coordinates (90, 285) can be detected. This zone corresponds to the interactions between two vortices of opposite signs and where most of the enstrophy cascade occur. We can verify that the enstrophy flux corresponding to this area is the main contribution to the total enstrophy flux of the global vorticity field (Figure (b)).



(a) *Enstrophy interaction function*



(b) *Enstrophy fluxes*

Hydrodynamic stability of a stratified suspension flow in a plane channel

S.A. Boronin

Institute of Mechanics, Lomonosov Moscow State University, 119192 Michurinskii pr. 1, Moscow, Russia. boroninsa@imec.msu.ru

Hydrodynamic stability of particle-laden flows was studied earlier within the two-fluid approach mostly under the assumptions that [1]: in the main flow, the concentration of the inclusions is uniform, the phase velocity slip is zero, and the particle volume fraction is negligibly small. In the case of suspension flows, where the particle-to-fluid substance density ratio is of order unity, the formulation described above has to be modified to take into account the finite volume fraction of the inclusions as well as non-uniform distribution of the particles in the main flow.

We consider the stability of a suspension plane-channel flow in the presence of viscosity gradients in the main flow induced by a particle concentration nonuniformity. The dispersed flow is described by a modified two-fluid model, which extends the standard dusty-gas model [1, 2] to the case of finite particle volume fraction [3]. The nonuniform profile of the main-flow particle volume fraction, specified analytically, reproduces the effect of particle migration from rigid walls.

The system of linearized governing equations coupled with the no-slip boundary conditions on the walls is reduced to the eigenvalue problem for a 4-th order ordinary differential equation, which is solved by the orthogonalization method.

A parametric study of unstable modes is performed. It is found that the stratified suspension flow is unstable even at very low Reynolds numbers for a wide range of governing non-dimensional parameters in contrast to the case of the uniform particle distribution [3]. In the latter case, the instability is triggered only by Tollmien-Schlichting (T-S) waves and the critical Reynolds number is of order 10^4 and higher. For stratified suspension flows, the instability due to viscosity gradients, typical of core-annular flows, was found earlier only within the framework of a simplified single-fluid approach.

The work is supported by RFBR (grant No. 08-01-00195).

References

1. P.G. Saffman, *J. Fluid Mech.*, **13**, 120–128 (1962).
2. F.E. Marble, *Ann. Rev. Fluid Mech.*, **2**, 397–446 (1970).
3. S.A. Boronin, *Fluid Dynamics*, **43**, 873–884 (2008).

Localization of compact invariant sets of the Lorenz' 1984 model

K.E. Starkov

CITEDI, IPN, Tijuana, 22510, Mexico

In 1984 E. Lorenz published a paper [1] in which he proposed "the simplest possible general circulation model": $\dot{x} = -y^2 - z^2 - ax + aF$, $\dot{y} = xy - bxz - y + G$, $\dot{z} = bxy + xz - z$, which is referred to as the Lorenz'1984 model. The existence of chaos was shown in [1, 2] for different values of parameters. Dynamical studies of this system were realized in papers [1, 2]; [3], [4]. This paper is devoted to study of a localization problem of compact invariant sets of the Lorenz'1984 model with help of one approach elaborated in papers of Krishchenko and Starkov, see e.g. [5]. This problem is an important topic in studies of dynamics of a chaotic system because of the interest to a long-time behavior of a system. In this work we establish that all compact invariant sets of the Lorenz' 1984 model are contained in the set $\{x \leq F; x^2 + y^2 + z^2 \leq \eta^2 = \frac{2(a+2)F^2 + 3G^2 + 2G\sqrt{aF^2 + G^2}}{4}\}$. Further, we improve this localization with help of refining bound η ; using additional localizations sets. By applying cylindrical coordinates to the Lorenz' 1984 model we derive yet another localization set of the form $\{y^2 + z^2 \leq G^2(1 + b^{-2}) \exp(4\pi b^{-1})\}$. Finally, we discuss how to improve the final localization set and consider one example.

Acknowledgment. This paper is partially supported by CONACYT (MEXICO), project N. 000000000078890.

References

1. E.N. Lorenz, *Tellus*, **36A**, 98 (1984).
2. E.N. Lorenz, *Tellus*, **42A**, 378 (1990).
3. C. Mazoller, A.C. Sicardi Schifino and L.Romanelli, *Physics Letters A*, **167**, 185 (1992).
4. A. Shil'nikov, G. Nicolis and C. Nicolis, *International Journal of Bifurcations and Chaos*, **5**, 1701 (1995).
5. A.P. Krishchenko and K.E. Starkov, *Physics Letters A*, **353**, 383 (2006).

Large-scale energy dissipation and equatorial superrotation in shallow water turbulence

R. K. Scott

School of Mathematics, University of St Andrews, St Andrews, Scotland
rks@mcs.st-and.ac.uk

Equilibration of two-dimensional shallow water turbulence is examined in the presence of small-scale, isotropic forcing, and two forms of large-scale energy dissipation representative of different geophysical situations: (i) linear friction, as a model of flow over a solid ground; and (ii) thermal damping, as a model of energy loss through long-wave cooling. The simplest case of constant background planetary rotation allows an immediate comparison of the two dissipation mechanisms in purely isotropic, homogeneous turbulence. In each case a population of coherent vortices, containing most of the total kinetic energy of the flow, forms at scales larger than the forcing scale. A simple vortex identification criterion reveals that the number density of vortices as a function of vortex size is independent of dissipation mechanism, but that the intensity of vortices grows with scale more strongly in the case of thermal dissipation than in the case of frictional dissipation. The scaling of the vortex population in physical space is shown to be consistent with the distribution of energy in spectral space, and can be understood in terms of the scale-selectivity of the two dissipation mechanisms.

Differences between frictional and thermal damping become striking in simulations of forced shallow water turbulence on the sphere. While shallow-water models have been successful in reproducing the formation of robust, and fully turbulent, latitudinal jets similar to those observed on the giant planets, they have consistently failed to reproduce prograde (superrotating) equatorial winds. Here, however, it is shown that shallow water models not only can give rise to superrotating winds, but do so very robustly, when the large-scale energy dissipation is the physically relevant thermal damping. With appropriate choice of thermal damping rate, equatorial superrotation can be achieved at apparently any deformation radius. The direction of the equatorial flow is influenced by the effect of dissipation on equatorial Rossby-gravity waves and by a cyclone-anticyclone asymmetry in the damping of coherent vortices.

The effects of rain on wind-driven turbulent flow

N. Takagaki, K. Iwano, and S. Komori

Department of Mechanical Engineering and Science, Kyoto University, 606-8501 Kyoto, Japan
 komori@mech.kyoto-u.ac.jp

It is of great interest to investigate the effects of rain on mass transfer across the wavy-sheared air-water interface in precisely estimating the mass transfer rate across the air-sea interface. The mass transfer rate across the air-water interface changes depending on the conditions of the free surface and water flow near the free surface. The purpose of this study is, therefore, to investigate the effects of rain on wind-driven turbulence through laboratory experiments in a wind-wave tank with a rain simulator. The values of the wave height and the velocity in the liquid side were measured for both no rain case and rain case ($R=133\text{mm/h}$), and we compared the values in no rain case with that in the rain case. Figure 1 shows the significant wave height (H_s) against the free stream wind speed (U_∞). It is found that H_s decreases due to rain at low wind speeds, because of the damping effect noted by Tsimplis and Thorpe[1]. However there is no rain effect on H_s at high wind speeds. Figure 2 shows the vertical distributions of the streamwise and vertical mean velocities (U_w, V_w), the streamwise and vertical turbulence intensities (u'_w, v'_w) and the Reynolds stress ($\overline{u_w v_w}$) in the liquid side. These values are increased by rain near the free surface. This suggests that the turbulence near the free surface in the liquid side is promoted by the impingement of raindrops.

References

1. M. Tsimplis, and S. A. Thorpe, Nature, **342**, pp. 893 – 895 (1989)

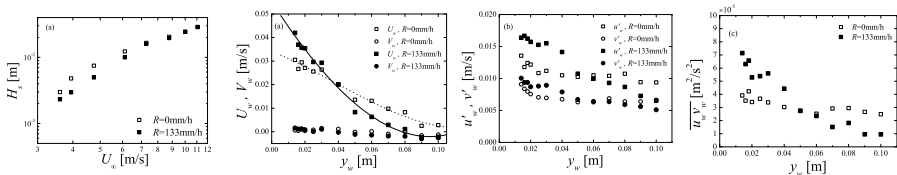


Fig. 1. H_s versus U_∞ .

Fig. 2. Vertical distributions of (a) U_w and V_w , (b) u'_w and v'_w and (c) $\overline{u_w v_w}$.

New results on grid-generated turbulence

Thomas Kurian and Jens H.M. Fransson

Linné Flow Centre, KTH Mechanics,
SE-10044 Stockholm, Sweden
mthomas@mech.kth.se

To experimentally study the receptivity of laminar boundary layers to free stream turbulence, the use of grids is the simplest and most effective way to generate turbulence. To investigate the receptivity it is essential to be able to vary the parameters of the free stream turbulence such as turbulence level and length scales. By altering the distance of different grids from the receptivity region, these parameters can be adjusted independently.

In the current experimental setup seven grids with mesh widths (M) in the range of 0.95 – 50 mm were studied with two X-probes. The grids were characterized in terms of kinetic energy decay, integral turbulent length scale (both streamwise and transverse), Kolmogorov and Taylor scales, power spectra, dissipation and level of anisotropy.

The downstream evolution of turbulent length scales and kinetic energy will be presented and compared with relations based on the assumption of isotropic turbulence. A new method for evaluating the coefficients in the power-law decay will be introduced. It will be shown that the levels of anisotropy (fig 1) and the power-law coefficients asymptotically approach the theoretical values based on the assumption of isotropy for large Re_M [1].

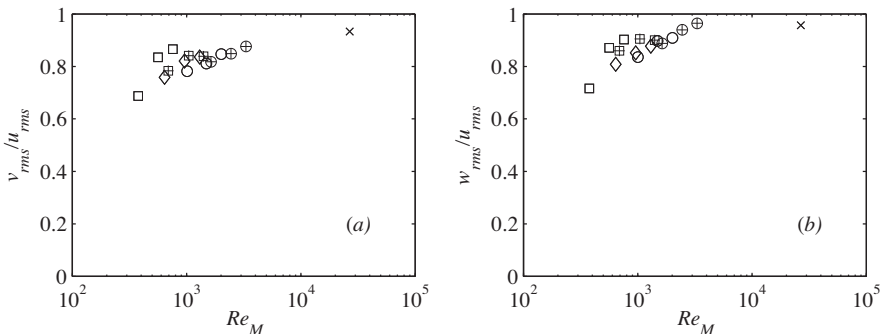


Fig. 1. Isotropy levels for for v and w component, (a) and (b) respectively.

- [1]. T. Kurian & J. H. M. Fransson, Grid generated turbulence revisited. *Fluid Dyn. Res.* **41** (2), pp. 021403 (2009).

Gas-liquid interaction under vibration field effect

V. Kholmer and L. Grinis

Civil Engineering Department, Sami Shamoon College of Engineering, 84100 Beer Sheva, Israel kholmer@sce.ac.il

Many fields of chemical technology require the uniform distribution of gas bubbles as well as increase of their residence time accompanied by decrease of their size and coalescence in liquid bulk. The common conclusion of studies that have been performed in the field is a plausible effect of vibration field employment on the reduction of the bubble size and decrease of the bubble rise velocity. The main benefits of the phenomenon are increase of the bubble residence time and the interfacial area which result in gas-liquid mass transfer enhancement.

In the present study we performed three sets of experiments. In the first set of experiments we used the plate vibrating in the rectangular vessel. In the second and the third sets we used the plate vibrating in the cylindrical bubble column. The first set of experiments dealt mainly with the effect of vibration parameters upon the gas bubbles mean diameter and residence time in the liquid. We tried also to determine the effect of the distance between the vibrating plate and the outlet gas orifice on the above mentioned bubble parameters. In the second and the third sets of experiments we tested the effect of the vibrating plate design and its location upon the bubble residence time in the liquid and the gas holdup. In the second set of experiments the gas was injected into the column (similar to the technique which was used in the first set) while in the third set the gas was entrained into the liquid bulk from its surface. It should be noticed that the experimental apparatus for all sets was almost the same. The best results (the longest residence time) were obtained for the smaller values of the pulsation amplitude. It seems that for bigger amplitude values (more than 0.5 mm) occurring liquid downward streams enforce the bubble movement out of the region of effective vibration field action thus weakening its effect. As a result of this phenomenon the bubble residence time in the liquid bulk decreases with the vibration amplitude increase. For the investigated amplitude range the vibration frequency increase results in the bubble residence time increase up to its maximum value for the frequency of about 30 Hz. The further increase of the vibration frequency results in the bubble residence time decrease.

An Invariant Nonlinear Eddy Viscosity Model based on a 4D Modelling Approach

M. Frewer

Institute of Fluid Dynamics, Technische Universität Darmstadt, Germany
frewer@fdy.tu-darmstadt.de

Without changing the physical content the averaged Navier-Stokes equations are geometrically reformulated on a true 4D non-Riemannian space-time manifold. Its clear superiority over the usual (3+1)D Euclidean approach can be fully summarized as follows:

i) *The variables of space and time are fully independent.* This implies that in any closure strategy not only space but also time derivatives have to be considered, hence not only allowing for a universal and consistent treatment of curvature effects but also for a universal and consistent treatment of non-stationary effects.

ii) *Physical quantities as velocities or stresses always transform as tensors, irrespective of whether they are objective (frame-independent) or not.* This is important when to model unclosed terms with non-objective quantities.

iii) *Frame accelerations or inertial forces of any kind can be interpreted as a pure geometrical effect.* This implies that inertial and non-inertial turbulence need not to be modelled separately anymore. A 4D turbulence model will describe non-inertial turbulence as rotation, swirling or curved surfaces equally well or equally bad as the corresponding inertial case.

iv) *The special space-time structure of the 4D manifold allows for additional modelling constraints, which are absent in the usual (3+1)D geometrical formulation.* For example, within the 4D manifold averaged and fluctuating velocities evolve differently, in the sense that the averaged 4-velocities evolve as pure time-like vectors, while the fluctuating 4-velocities as pure space-like vectors.

All these aspects will be demonstrated by proposing a 4D invariant nonlinear eddy viscosity model for high turbulent Reynolds numbers.

References

1. M. Frewer, More clarity on the concept of material frame-indifference in classical continuum mechanics, *Acta Mech.* **202**, 213 (2009).

Projection of the turbulence closure problem on the invariant triangle as the basis for improved predictions of complex flows

J. Jovanović, B. Frohnafel, and M. Breuer

Lehrstuhl für Strömungsmechanik, Friedrich-Alexander-Universität Erlangen, Germany

present addresses:

BF: Center of Smart Interfaces, TU Darmstadt, Germany

MB: Professur für Strömungsmechanik, Helmut-Schmidt-Universität Hamburg, Germany

jovan@1stm.uni-erlangen.de

A novel, anisotropy-invariant Reynolds stress model (AIRSM) of turbulence based on the application of the two-point correlation technique and invariant theory has been developed and tested [1, 2]. The model can be summarized as follows:

$$\begin{aligned} \frac{\partial \overline{u_i u_j}}{\partial t} + \overline{U}_k \frac{\partial \overline{u_i u_j}}{\partial x_k} &\simeq P_{ij} + a_{ij} P_{ij} + \mathcal{F} \left(\frac{1}{3} P_{ss} \delta_{ij} - P_{ij} \right) + (\mathcal{C} - 2\mathcal{A}) \epsilon_h a_{ij} - \frac{2}{3} \epsilon_h \delta_{ij} \\ &\quad + c_q \frac{\partial}{\partial x_k} \frac{\overline{u_i u_j} k^2}{q^2} \frac{J}{\epsilon_h} \frac{\partial k}{\partial x_k} + \frac{1}{2} \frac{\partial^2 \overline{u_i u_j}}{\partial x_k \partial x_k}, \\ \frac{\partial \epsilon_h}{\partial t} + \overline{U}_k \frac{\partial \epsilon_h}{\partial x_k} &\simeq -2\mathcal{A} \frac{\epsilon_h \overline{u_i u_k}}{k} \frac{\partial \overline{U}_i}{\partial x_k} - \psi \frac{\epsilon_h^2}{k} + c_\epsilon \frac{\partial}{\partial x_k} \frac{k^2}{\epsilon_h} J \frac{\partial \epsilon_h}{\partial x_k} + \frac{1}{2} \nu \frac{\partial^2 \epsilon_h}{\partial x_k \partial x_k}. \end{aligned}$$

Here \mathcal{F} , \mathcal{C} , \mathcal{A} , J and ψ are functions that depend on the invariants $\Pi_a = a_{ij} a_{ji}$ and $\text{III}_a = a_{ij} a_{jk} a_{ki}$ of the anisotropy tensor $a_{ij} = \overline{u_i u_j} / q^2 - 1/3 \delta_{ij}$ and the turbulent Reynolds number. The above model of turbulence takes full account on the influence of the anisotropy of turbulence and provides all of the coefficients analytically without appeal to experiment or numerical databases.

The AIRSM has been implemented into the numerical code COMET. Validation test cases are presented in which computations are carried out with $k - \epsilon$, SSG and AIRSM models.

References

1. J. Jovanović, *The Statistical Dynamics of Turbulence*. Springer, 2004.
2. V. Kumar, B. Frohnafel, J. Jovanović, M. Breuer, W. Zuo, I. Hadzić, R. Lechner, *Flow Turbulence Combustion*, DOI 10.1007/s10494-008-9190-y (2008).

A computational study of the hydrodynamic forces on a rough wall

C. Braun, M. García-Villalba and M. Uhlmann

Institute for Hydromechanics, Karlsruhe Institute of Technology, 76131 Karlsruhe, Germany

braun at ifh.uni-karlsruhe.de

The hydrodynamic interaction of a fluid with a rough wall results in a net force on the roughness elements. This can cause erosion of the roughness elements – an important aspect for sediment transport in rivers or the transport of solid media by fluids in mechanical applications. In order to deepen the understanding of the processes that lead to erosion, a direct numerical simulation of a turbulent open channel flow over a fixed rough bed was carried out. In the simulation spherical roughness elements were discretized by means of the immersed boundary method developed by [1].

The flow field statistics of the simulation compare well to data of previous studies with respect to the mean flow field as well as the turbulence statistics [2]. Furthermore, the instantaneous flow field exhibits the expected formations of streaks and of large structures that extend over the entire water depth as well as the formation of smaller coherent structures.

As a first step to deepen the understanding of the erosion mechanism, the particle forces are analyzed systematically by means of a statistical approach. The obtained results are compared with the experimental data of [3]. Agreement of the force statistics is obtained when the results of each case are normalized with the bulk velocity and the particle diameter. Nevertheless, the experimental and numerical setups differ with respect to Reynolds number, particle size, water depth to particle size ratio, particle shape and particle arrangement. The agreement between the obtained particle force statistics therefore indicates that the average force generating mechanism is persistent over a wide range of flow parameters.

References

1. M. Uhlmann, *J. Comp. Physics*, **209**(2), 448-476, (2005).
2. O. Flores and J. Jiménez, *J. Fluid Mech.*, **566**, 357-376 (2006).
3. B. Hofland, PhD-Thesis, TU Delft, (2005).

Turbulent flow structure investigation within target fluidic flowmeter

F.H. Hannemann, A.F. Nowakowski, F.C.G.A Nicolleau and H. Zheng

Sheffield Fluid Mechanics Group, Department of Mechanical Engineering
The University of Sheffield, Mappin Street, Sheffield S1 3JD, UK
a.f.nowakowski@sheffield.ac.uk

This contribution presents the development of computational capabilities to investigate the flow structure, design and performance of a new target fluidic flowmeter. The reference data for a wide range of Reynolds numbers were obtained experimentally. These data are used in this study for simulation validation purposes. When fluid passes the bluff body complicated phenomena like separation, reattachment and unsteady vortex shedding occur. The performance characteristics depend on jet properties and therefore are Reynolds number dependent.

The recently developed Detached Eddy Simulation (DES) hybrid technique for unsteady flows has been used in numerical simulations of the problem. The method combines Reynolds-averaged Navier-Stokes (RANS) method with Large-Eddy Simulation (LES) method. The entire boundary layer is treated by RANS and the separated region by LES (direct resolution of the dominant unsteady structures). The transition between RANS and LES is seamless with no explicit declaration of RANS versus LES zones.

The appropriate signal analysis of the obtained results have been conducted for a range of Reynolds numbers up to 4000. The DES approach has been reliable for both low and higher Reynolds numbers. The results show that a number of factors such as meter geometry and aspect ratio influence the performance of the flowmeter. This is observed in the quality of the signal manifested by the velocity oscillations. The Strouhal number should be high enough to eliminate any counting errors which may occur during transient flows. A minimum Reynolds number constraint for the measurements to be accurate has been evaluated for various design parameters. The significance of using knife edges which influence boundary layer separation has been established. The flow visualisation has revealed the recirculating flow downstream and its direct dependence on knife edges location.

The Wake of a Single 2D Roughness Element Immersed in a Turbulent Boundary Layer

B.T. Tee, L.K.B. Li, and T.B. Nickels

Department of Engineering, University of Cambridge, Trumpington Street, Cambridge, CB2 1PZ, United Kingdom

btt24@cam.ac.uk

Measurements are presented of a fully-developed zero-pressure-gradient turbulent boundary layer interacting with a single 2D roughness element. Mean velocity profiles were measured using 2D PIV over a smooth surface and a single roughness element. The roughness element was a square bar with cross-sectional dimensions of 10 mm x 10 mm and a length of 0.9 m. The experiments were conducted in the turbulence research water tunnel at Cambridge University, and at Reynolds numbers (based on the momentum thickness) ranging from 3016 to 4670. Velocity defect profiles were analyzed using three different outer velocity scales: friction velocity (u_τ), freestream velocity (U_∞)¹(Fig. 1) and, mixed outer scale ($\frac{U_\infty \delta^*}{\delta}$)². A discussion is presented of the wall-normal extent of the wake and of how it evolves with streamwise distance and different Reynolds numbers.

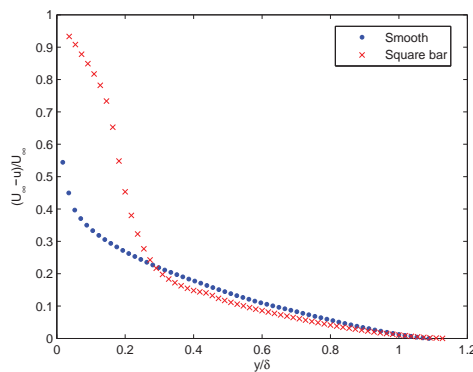


Fig. 1. Mean velocity defect profiles scaled with freestream velocity at $Re_\theta = 3290$.

References

1. W.K. George and L. Castillo, *Appl. Mech. Rev.*, **50**, 689-729 (1997).
2. M.V. Zagarola and A.J. Smits, *J. Fluid Mechanics*, **373**, 33-79 (1998).
3. M.P. Schultz and K.A. Flack, *J. Fluid Mechanics*, **580**, 381-405 (2007).

High spanwise wall-shear stress events in turbulent duct flow

S. Große¹ and W. Schröder²

¹ current address: Laboratory of Aero and Hydrodynamics, TU Delft University, 2628 CA Delft, The Netherlands, s.grosse@iaa.rwth-aachen.de

² Institute of Aerodynamics, RWTH Aachen University, 52062 Aachen, Germany

The wall-shear stress distribution in turbulent duct flow at a bulk Reynolds number of $Re_b = 15\,400$ has been assessed with the micro-pillar shear-stress sensor MPS³. The flow facility and the sensor are further described in [1, 2]. 12 sensors are used to detect the one-dimensional wall-shear stress distribution. The sensor is mounted at the center plane of the duct. The spatial resolution of the sensor line is $10.8\,l^+$ (viscous units) and the total field of view of $120\,l^+$ along the spanwise direction allows to capture characteristic dimensions of the wall-shear stress distribution at sufficiently high resolution. By applying Taylor's hypothesis along the streamwise direction, it is possible to determine the spatial wall-shear stress distribution.

Figure 1(a) shows a representative wall-shear stress distribution over $2\,000 \times 120\,l^+$. The vectors indicate the instantaneous wall-shear stress fluctuations $\tau'/\bar{\tau}_x$, the contours represent the streamwise wall-shear stress $\tau_x'/\bar{\tau}_x$. It is evident that regions of lower and higher wall-shear stress coexist. The low-shear regions represent elongated meandering zones of streamwise extensions in the order of $1\,000\,l^+$ or more being locally interrupted by high-shear regions. It is natural to identify these shear-stress distributions as 'footprints' of very near-wall turbulent coherent structures, i.e., low-speed and high-speed streaks aligned in the viscous sublayer of wall-bounded shear flows.

Two traces of the spanwise wall-shear stress fluctuations are given in figure 1(b). The position of the time traces have been chosen such that they are aligned symmetrically at spanwise positions of approximately $\pm 25\,z^+$ off these 'centered' events. Comparing the positions of the strong anti-correlating peaks with the distribution in figure 1(a) evidences these high spanwise wall-shear stress events to be related to the occurrence of high streamwise shear regions, which we relate to sweep events pushing higher-speed fluid towards the wall. Similar to the procedure applied by [3] a rough estimate of the wall-normal velocity (figure 1(c)) has been calculated from continuity considerations assuming the wall-normal velocity to possess a monotonic behavior within the viscous sublayer. This allows to derive the wall-normal velocity $u_{y(L)}$, where $y(L)$ is the wall-distance of the recorded pillar-tips. Furthermore, $-\partial u_y/\partial y = \partial u_x/\partial x + \partial u_z/\partial z$, the latter two terms are derived from the pillar-tip deflection assuming a linear velocity distribution within the sublayer

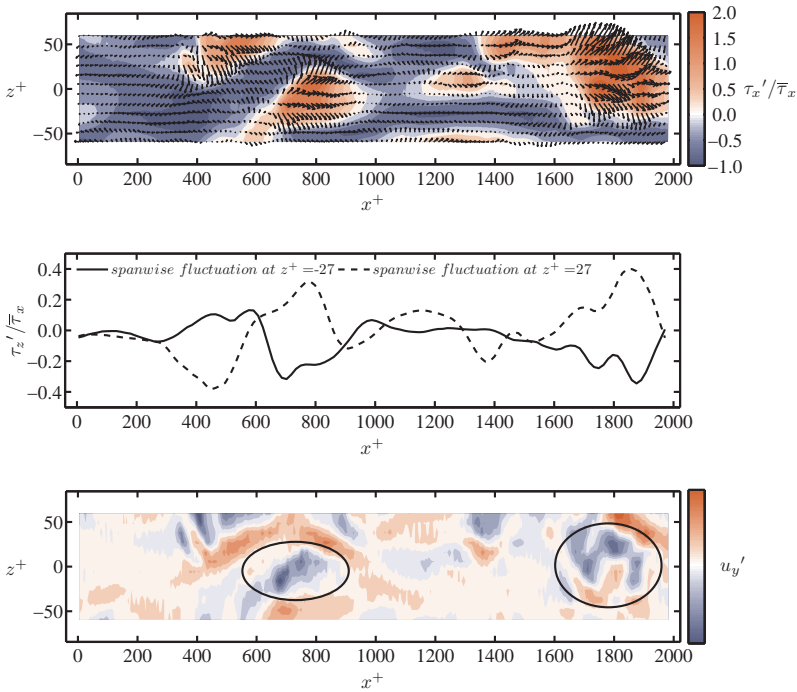


Fig. 1. (a) Wall-shear stress distribution, (b) spanwise wall-shear stress fluctuations at $\pm 27 z^+$, (c) wall-normal velocity fluctuations u_y' calculated from continuity considerations.

region. Note, a further assumption is that of a constant convection velocity. A comparison of figure 1(c) with 1(a) indicates regions of high streamwise shear to possess negative values of the wall-normal velocity (encircled region), which confirms the idea of sweep fluid approaching the wall. A conditional average of the streamwise fluctuation field associated with the existence of large spanwise fluctuations ($|\tau_z' / \bar{\tau}_x| \geq 0.20$) shows the spanwise fluctuations to coincide with strong streamwise fluctuations.

The above discussion indicates the large spanwise wall-shear stress fluctuations to be related to sweep motions of high-speed fluid originating from higher shear layer regions. The additional flux towards the near-wall region is compensated by a spanwise fluid distribution causing the high lateral fluctuation levels. The elongated low-shear regions are laterally shifted due to the occurrence of the high-speed fluid resulting in a strong meandering tendency of the streaks.

References

1. S. Große, PhD Thesis, RWTH Aachen University, 2008.
2. S. Große and W. Schröder, accepted for AIAA Journal, 2009.
3. J. Jiménez and P. Moin, Journal of Fluid Mechanics **225**, 213240, 1991

A POD-based reconstruction method for the flow in the near-wall region

B. Podvin, Y. Fraigneau, J. Jouanguy, J.P. Laval

LIMSI-CNRS, Orsay, France and LML, Lille, France
podvin@limsi.fr

We present a reconstruction method to estimate the instantaneous flow close to the wall of a turbulent channel. The motivation for the procedure is to come up with suitable wall models for large-eddy simulations. The idea is to apply the Proper Orthogonal Decomposition to the velocity field \underline{u} over a zone extending over the lower wall region to be modelled $\Omega_1 : 0 \leq y^+ \leq y_1$ and the LES numerical domain, $\Omega_2 : y_1 \leq y^+ \leq y_2$. The reconstruction method is a straightforward extension of the procedure described in Podvin et al. [Podvin et al., *Journal of Fluids Engineering* 2006]. The POD modes $a^n(t)$ are estimated by solving a linear system where the right-hand side contains information about the flow in the upper region, and the operator is the inner product of the empirical eigenfunctions restricted to the lower region.

The procedure is first applied to a DNS at $R_\tau = 180$. We have $y_1 = 50$ and $y_2 = 70$. We use both the snapshot method (no symmetries enforced) and the direct method (with symmetries). The energy of the POD modes was found to be well predicted with the method. The correlation coefficient between the true and estimated modes was found to be superior to 0.9 for all modes. We found that the energy content is also satisfactory when the direct method is used to compute the spatial eigenfunctions. Due to the enforcing of symmetries, the decomposition is then carried out in spectral space (Holmes et al. [*Turbulence, Coherent structures, Dynamical systems and Symmetry*, Cambridge University Press]). The temporal correlation between the true and the estimated modes was found to decrease with the spanwise wavenumber and to increase with the streamwise wavenumber.

We then considered a LES of a channel flow with transverse sliding walls at $R_\tau = 550$. The direct method was used to compute the POD eigenfunctions. We chose $y_1 = 100$ and $y_2 = 200$. The correlation coefficient exhibited similar features to that of the case $R_\tau = 180$. Further analysis is in progress.

This work has been performed under the WALLTURB project, funded by the EC under the 6th framework program (CONTRACT N:AST4-CT-2005-516008)

Near-wall velocity and wall shear stress correlations in a separating boundary layer

P. Nathan and P. E. Hancock

University of Surrey, Guildford, Surrey, GU2 7XH, UK
 p.hancock@surrey.ac.uk

Measurements have been made of time-synchronised instantaneous velocity, u , v , and instantaneous wall shear stress, τ , in the near wall layer of a turbulent boundary layer approaching and passing through (mean) separation, using a two-component LDA and a pulsed-wire shear stress probe.

Figure 1 shows $\overline{u(t, y)\tau(t)}/u'_\tau\tau'$. The velocity scale, u'_τ on the abscissa is based on the r.m.s of the wall shear stress fluctuation [1]. Mean separation was at $x = 140\text{mm}$. Particularly noticeable here is a) the curves fall very close to each other (except first two stations), b) the correlation decreases dramatically inside yu'_τ/ν of 6. One of the full lines corresponds to an oscillating viscous layer showing a qualitatively similar behaviour. The other shows the first two terms in the oscillating layer expansion. Figure 2 shows $\overline{u(t, y)\tau(t - \Delta t)}/u'_\tau\tau'$, at the mean separation position. A striking feature here is the nearly vertical contour lines. A similar pattern is seen at the other stations.

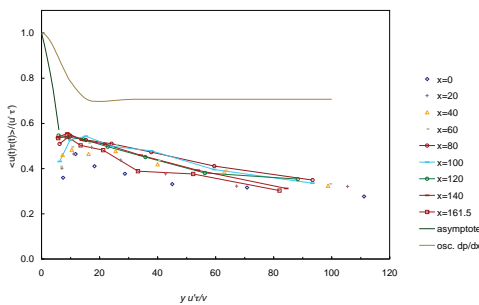


Fig. 1. Correlation coefficient.

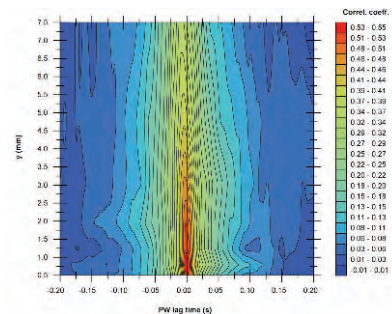


Fig. 2. Time-lag coefficient.

This work has been performed under the WALLTURB project. WALLTURB (A European synergy for the assessment of wall turbulence) is funded by the EC under the 6th framework program (CONTRACT N: AST4-CT-2005-516008)

[1] Hancock, P. E. 2007 Euro. J. Mech. B/Fluids, 26 (2007).

Lifetimes of flow topology in a turbulent boundary layer

G.E. Elsinga and I. Marusic

Department of Mechanical Engineering, The University of Melbourne, VIC 3010, Australia; Laboratory for Aero and Hydrodynamics, Delft University of Technology, The Netherlands
g.e.elsinga@tudelft.nl

This study involves an experimental investigation of the local flow topology dynamics in the logarithmic and outer region of a turbulent boundary layer. In particular, we wish to establish characteristic life-times for the energy containing eddies and possibly relate those to the coherent structures commonly observed in boundary layers. So far the instantaneous spatial organization of these eddies has received important attention, leaving, however, open questions regarding the dynamics and time-scales of these eddies.

The topology dynamics are investigated here using the experimental dataset of Schröder et al. (2008), who applied time resolved Tomographic PIV to obtain all three velocity components as well as their spatial and temporal derivatives. From this measurement the the second and third invariants Q and R of the velocity gradient tensor are determined uniquely defining the generalized local topology in each point at each time instant (Chong et al. 1990). Then the average rate of change of the invariants are calculated using a binning and conditional averaging approach (Ooi et al. 1999) given by:

$$\left\langle \frac{D(Q, R)}{Dt} \right\rangle (Q_0, R_0) = \left\langle \frac{D(Q, R)}{Dt} \middle| -\frac{1}{2} \leq \frac{Q - Q_0}{\Delta Q} < \frac{1}{2}; -\frac{1}{2} \leq \frac{R - R_0}{\Delta R} < \frac{1}{2} \right\rangle (1)$$

This results in a dynamical system where the average rates of change have become functions of the invariants themselves. Subsequent integration yields trajectories in the QR -plane describing the average evolution of the local flow topology following a fluid particle. These trajectories are found to orbit, very nearly periodically, and spiral inwards to the origin. We define a characteristic lifetime of the energy-containing eddies as the period of the orbit, which is found to be $14.3 \delta/U_\infty$ corresponding well with estimates of the advected lengths of very-large-scale motions or superstructures recently described in literature. Additionally, a second time scale may be defined representative of the invariants average decay rate over the cycles. It is associated to viscous diffusion and is at least and order magnitude larger than the orbit's period.

RDT or low wavenumber modes' dynamics?

S.R. Bogdanov

Karelian State Pedagogical University, Petrozavodsk, Russia
fmf at kspu.karelia.ru

Rapid Distortion Theory proved to be the excellent tool for studying the flows with $\alpha \ll 0$, where α is the ratio of distortion and "turn-over" time scales. Moreover it has long been recognized that this theory is also applicable to some kinds of slowly changing turbulence. The success of RDT remains the challenge and induce some basic questions, in particular - to what extent the linear effects are responsible for a fundamental aspects of turbulence?

This paper is the attempt to work out the alternative view of the mentioned challenge based on the consideration of the most general properties of the spectral tensors. Within such approach the suppression of nonlinear interactions is the result of analytical properties of the tensors in the low wavenumber limit rather than "rapidity" of distortion.

The procedure is based on the presentation $F_{ij}(\mathbf{x}, \mathbf{k}) = f_{ij}(\mathbf{x}, \boldsymbol{\theta})\varphi(kr_c)$ and similar ones for higher - order correlations. Following the "tensorial volume" concept it's supposed that in the low-wavenumber limit $kl \rightarrow 0$ the components of F_{ij} possess non-zero limits. Following Bogolubov's strategy one can treat "orientational amplitudes" $f_{ij}(\mathbf{x}, \boldsymbol{\theta})$ and $l(\mathbf{x}, \boldsymbol{\theta})$ as a set of "governing parameters" of turbulence. The one-point parameters of practical interest are easily derived with the help of the these functions after integration over spherical shell of unit radius in \mathbf{k} - space.

The linear subset of equations for f_{ij} is derived from the exact spectral equations. Together with equation for $l(\mathbf{x}, \boldsymbol{\theta})$ and turbulence energy balance they form the closed set. Some types of simple flows were considered for preliminary checking of the validity of this approach. The results coincides with RDT predictions when $\alpha \rightarrow 0$. The alternative limit $\alpha \rightarrow \infty$ leads to the well-known decay laws for grid turbulence. For general homogeneous distortion simple analytical solution is also available. In particular for axisymmetric contraction flow f_{ij} has the asymptotic form which don't depend on the initial form of the spectra. At that only 0.1 of the energy of most large eddies is concentrated in streamwise direction. The evolution of one-point characteristics strongly depend on the value of α . In particular, for moderate values of this parameter turbulent energy evolves through minimum.

Intermittency in high resolution direct numerical simulation of turbulence in a periodic box: a wavelet viewpoint

K. Yoshimatsu¹, N. Okamoto², K. Schneider³, Y. Kaneda¹, and M. Farge⁴

¹ Department of Computational Science and Engineering, Nagoya University, Nagoya, 464-8603, Japan yosimatu@fluid.cse.nagoya-u.ac.jp

² Center for Computational Science, Graduate School of Engineering, Nagoya University, Nagoya, 464-8603, Japan

³ M2P2-CNRS & CMI, Université de Provence, 39 rue Frédéric Joliot-Curie, 13453 Marseille Cedex 13, France

⁴ LMD-IPSL-CNRS, Ecole Normale Supérieure, 24 rue Lhomond, 75231 Paris Cedex 05, France

Fully developed turbulence exhibits an inhomogeneous distribution of the small scale activity in space and time, which is generally called flow intermittency. To characterize the intermittency, we compared data of a homogeneous isotropic turbulent flow, obtained by direct numerical simulation with 2048^3 grid points and a Taylor microscale Reynolds number $732[1]$, with two divergence-free random fields having the same energy spectrum and either the same helicity spectrum as that of the turbulent data, or vanishing helicity, using wavelet based scale-dependent statistics.

Scale-dependent helicity, which quantifies the geometrical statistics of the flow, shows strongly varies with scale only for the turbulent field, while this is not the case for the two random fields. To get insight into the dynamics of Navier-Stokes turbulence, we analyze Eulerian and Lagrangian accelerations. The scale-dependent flatness of the Lagrangian acceleration is one order of magnitude larger than the flatness of the Eulerian acceleration. The flatness of the Lagrangian and Eulerian accelerations increase with scale for the turbulent flow. In contrast, for both of the random fields the scale-dependent flatness remains almost constant. These results confirm that scale-dependent statistics are necessary to characterize the intermittency of fully developed turbulent flows. For further details we refer to [2].

References

1. Y. Kaneda *et al.*, Phys. Fluids **15**, L21 (2003).
2. K. Yoshimatsu *et al.*, Phys. Rev. E **79** 026303, (2009).

Detached Eddy Simulation of Turbulence Flows in a Pipe with Fractal Shape Orifices

H. W. Zheng, F. C. G. A. Nicolleau, and N. Qin

Department of Mechanical Engineering, University of Sheffield, Mappin Street, Sheffield S1 3JD, U.K.

H.Zheng at `sheffield.ac.uk`

Turbulence flows are very interesting topics in both academia and industry community. Although the physics of turbulent flows is still not well understood, one property we can be sure of is the multi-scale nature of turbulent flows. This inspired us to investigate turbulence flows in a pipe with multi-scale fractal-shape orifices. It is a challenging problem as it contains scales distributed in a fractal manner and more importantly we can control the fractal interaction and monitor the numerical performance as a function of the problem complexity. Although there are some works [1, 2, 3, 4] on this kind of problem, the numerical simulations on this topic are rare. Most of the numerical results of fractal generated turbulence flow employ the direct numerical simulation [5]. However, the results could only be compared qualitatively with the experiment results [5]. Thus, in this work, we would like to assess the feasibility of studying the turbulence flows after a fractal shape orifice by the detached eddy simulation.

The simulation is based on an existing parallelized density-based finite volume solver (DG-DES) which has been developed by Prof. Qin's group [6, 7]. It has been ported to HECToR and HPCx system recently.

To validate the performance of the present solver for fractal generated turbulence flow, the case with the snow flake fractal shape with two iterations (Fig. 1) is used as a test example. The mean velocity profiles at hole 2 and 8 are plotted in Fig. 2 and Fig. 3. It is clear that the results agree well with the experiment results done by A. C. H. Chong and F. C. G. A. Nicolleau [4].

References

1. C. Meneveau and K. R. Sreenivasan, The multi-fractal nature of the turbulent energy dissipation, *J. Fluid Mech.*, 224, 429-484, 1991.
2. D. Hurst and J. C. Vassilicos, Scalings and decay of fractal-generated turbulence, *Phys. Fluids*, 19:035103, 2007.

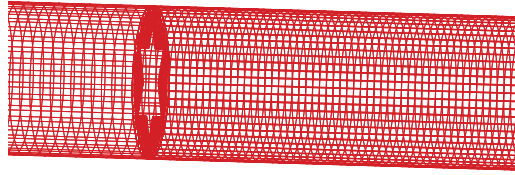


Fig. 1. Mesh

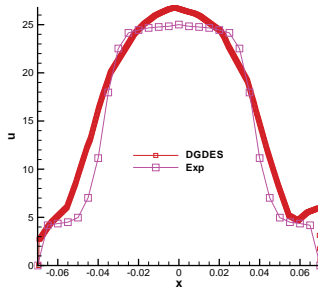


Fig. 2. Mean velocity profile at hole 2.

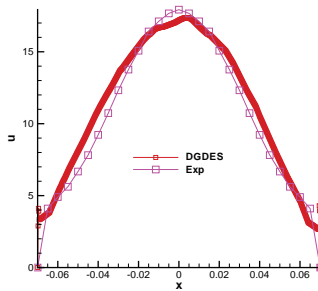


Fig. 3. Mean velocity profile at hole 8.

3. Laizet, S. and Vassilicos, J.C.: Multiscale of turbulence. *Journal of Multiscale Modelling* **1**(1), 177196 (2009)
4. A. C. H. Chong, *Turbulence flow generated by a fractal grid*, PhD Thesis, The University of Sheffield, 2008.
5. S. Laizet, E. Lamballais, J. C. Vassilicos, *A numerical strategy to combine high-order schemes, complex geometry and massively parallel computing for the DNS of fractal generated turbulence*, preprint, submitted to *Computers and Fluids*, 2008.
6. H. Xia, *Dynamic Grid Detached-Eddy Simulations for Synthetic Jet Flows*, PhD thesis, The University of Sheffield, 2005.
7. H. Xia and N. Qin, *Dynamic Grid and Unsteady Boundary Conditions for Synthetic Jet Flow*, AIAA 2005-106, 2005.

Recovery of subgrid-scale turbulence kinetic energy in LES of channel flow

Y. Tang and R. Akhavan†

Dept. of Mechanical Engineering, University of Michigan,
Ann Arbor, MI, 48109-2125, U.S.A

†Corresponding Author, E-mail: raa@umich.edu

A methodology is presented for recovery of the subgrid-scale (SGS) turbulence kinetic energy in large-eddy simulations (LES) of turbulent channel flow. The formulation is based on extending the one-dimensional energy spectra computed in LES at each wall-normal location using a filtered form of one-dimensional energy spectra derived from the theoretical formulations of Pao [1] or Kraichnan [2]. The extended spectra are integrated to recover the SGS turbulence kinetic energy as a function of the wall-normal direction, from which the individual components of turbulence intensities are recovered using the formulation of Winckelmans *et al.* [3]. To account for the anisotropy of turbulence in the near-wall region, a transformation is introduced to map the ellipsoidal iso-surfaces of turbulence kinetic energy density in the spectral-space to a spherical surface, where the filtering operations can be applied to the theoretical spectra. The transformation parameters are determined from the dissipative scale in each direction, while the constants in the theoretical spectra are determined by minimizing the errors between the theoretical and LES spectra. The turbulence kinetic energy recovery procedure is applied at a post-processing stage and is independent of the SGS model employed. Validation studies performed using a DNS database of a turbulent channel flow at $Re_\tau \approx 570$ show that the method can recover the total turbulence kinetic energy with errors of less than 1% and the SGS turbulence kinetic energy with errors of less than 10%. In application to LES data, the components of full turbulence intensities are recovered with an accuracy comparable to the accuracy with which the filtered statistics were predicted in LES.

References

1. Y. H. Pao, *Phys. Fluids*, **8**, 1063 (1965).
2. R. H. Kraichnan, *J. Fluid Mech.*, **5**, 497 (1959).
3. G. S. Winckelman, H. Jeanmart, D. Carati, *Phys. Fluids*, **14(5)**, 1809 (2002).

Beyond Reynolds stress analysis of quasilaminar flows

J. Araya,¹ R. B. Cal,² C. Meneveau,³ and L. Castillo⁴

¹ Swansea University, Swansea, SA2 8PP, UK j.g.araya@swansea.ac.uk

² Portland State University, Portland, OR, 97201, USA

³ The Johns Hopkins University, Baltimore, MD, 212180, USA

⁴ Rensselaer Polytechnic Institute, Troy, NY, 12180, USA

On Cal and Castillo, similarity analysis was performed for boundary layer flows approaching quasilaminarization. It was found amongst other results, that there is a redistribution of the Reynolds stress in all components for the boundary layer. It was also found that the redistribution of the stresses prevents the flows from fully achieving a laminar state as observed in Fig. 1 (*left*) using experimental data from Warnack and Fernholz. This is further explored by carrying direct numerical simulations of a strong sink flow using a dynamic approach. A rescaling-recycling plane is employed dynamically by involving an additional plane, a test plane, which is located between the inlet and recycle stations. This improvement and the use of multiple velocity scales permits the simulations of turbulent boundary layers subject to an arbitrary pressure gradient as shown in Fig. 1 (*right*). This yields the energy budget which provides information about the mechanism causing quasilaminarization.

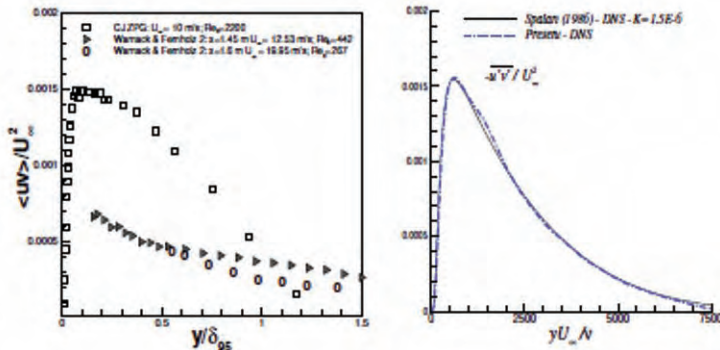


Fig. 1. Experimental (*left*) and computational (*right*) Reynolds shear stress normalized with the free-stream velocity.

Anisotropic Organised Eddy Simulation for statistical and hybrid modelling of turbulent flows around bodies

R. Bourguet, M. Braza, R. El Akoury and G. Harran

Institut de Mécanique des Fluides de Toulouse, Allée du Pr. Soula, 31400
Toulouse, France

Remi.Bourguet@imft.fr

To improve near-wall and near-wake behaviour of statistical and hybrid turbulence modelling approaches in non-equilibrium flows, the Organised Eddy Simulation (OES) methodology can be considered [1, 2]. OES distinguishes the structures to be resolved from those to be modelled on the basis of their organised (resolved part) or chaotic character (modelled part). The modelling of the chaotic processes can be achieved by reconsidering the Unsteady Reynolds Average Navier-Stokes (URANS) approach in respect of the modified shape of the energy spectrum, due to non-linear interaction of the coherent and random turbulence processes in the inertial range. The present communication focuses on the recent development of a *tensorial eddy-viscosity concept* within OES framework. On the basis of experimental measurements in the near wake of a circular cylinder at Reynolds number 1.4×10^5 [3], the structural properties of non-equilibrium turbulence have been investigated and especially the relationship between the phase-averaged strain rate and turbulent stress anisotropy tensors. As illustrated in Fig. 1, the first principal directions of these two ten-

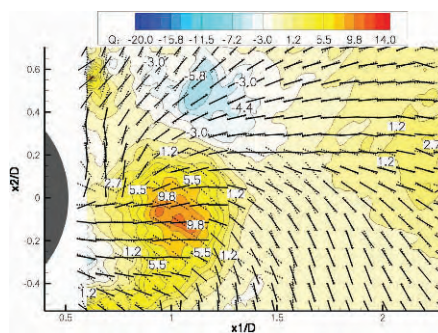


Fig. 1. First principal directions of turbulent stress anisotropy (dashed lines) and mean strain rate tensor (plain lines). Iso-contours of Q criterion.

sors can exhibit strong misalignments, especially in coherent structures [4]. This emphasises in particular that Boussinesq's hypothesis is not valid in these regions. To capture these non-linearities, an alternative to Non-Linear Eddy-Viscosity Models or Explicit Algebraic Reynolds Stress Models is developed. The anisotropy tensor is modelled by its projection onto the strain principal matrices. This allows an individual weighting of each principal matrix contribution. A generalisation of the linear eddy-viscosity model that involves a tensorial eddy-viscosity can be deduced [5]. This tensorial eddy-viscosity is estimated owing to new transport equations derived from the Differential Reynolds Stress Modelling by [6]. This Anisotropic OES turbulence modelling has been implemented in Navier-Stokes Multi-Block software and leads to promising results concerning the prediction of the flow past a NACA0012 airfoil at 20° of incidence, $Re = 10^5$ and $Ma = 0.18$. Moreover, this approach is considered to improved the statistical part of the hybrid Detached Eddy Simulation. An efficient prediction of the three-dimensional flow past a circular cylinder at $Re = 1.4 \times 10^5$ is achieved by the DES-OES approach based, at first, on a scalar eddy-viscosity (Fig. 2).

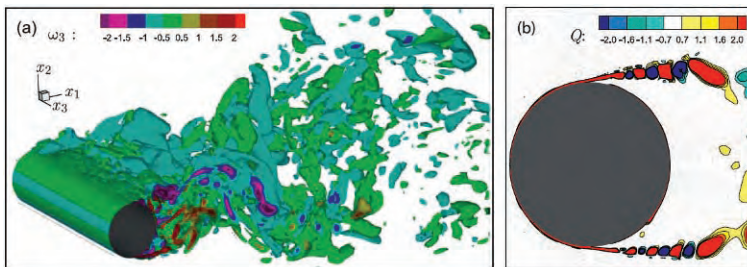


Fig. 2. DES-OES simulation: instantaneous (a) iso-surfaces of the transverse vorticity and (b) iso-contours of Q criterion, identification of KelvinHelmholtz instability.

References

1. Bouhadji, A., Bourdet, S., Braza, M., Hoarau, Y., Rodes, P. and Tzabiras, G., Notes on Num. Fluid Mech. and Mult. Design, **81**, 87 (2002).
2. Braza, M., Perrin, R. and Hoarau, Y., J. Fluids Struct., **22**, 755 (2006).
3. Perrin, R., Cid, E., Cazin, S., Svrain, A., Braza, M., Moradei, F. and Harran, G., Exp. Fluids, **42**, 93 (2007).
4. Bourguet, R., Braza, M., Perrin, R. and Harran, G., AIAA J., **45**(5), 1145 (2007).
5. Bourguet, R., Braza, M., Harran, G. and El Akoury, R., J. Fluids Struct., **24**(8), 1240 (2008).
6. Speziale, C.G., Sarkar, S. and Gatski, T.B., J. Fluid Mech., **227**, 245 (1991).

Experimental vortex generation and instabilities at flow around a magnetic obstacle

Yu. Kolesnikov, A. Thess

Institute of Thermodynamics and Fluidynamics, Ilmenau University of
Technolgy, 98684 Ilmenau, Germany
yuri.kolesnikov at tu-ilmenau.de

The flow structures around the magnetic obstacle (localized magnetic field) [1] in dependence on interaction parameter N were studied experimentally. We used horizontal open rectangular cell ($130 \times 10 \times 2$ cm) filled up by liquid metal alloy GaInSn and a permanent magnet ($3 \times 4 \times 2$ cm) moving under cell bottom. At visualization we fixed tracers of gas bubbles generated by weak acid solution, which moved on fluid free surface along stream-lines. At small N and large Re the flow is noneddying as in Fig. 1a. Vortex circulations in area of magnetic field action appears as in Fig. 1b when N reaches critical value N_{c1} [1]. At $N = N_{c2}$ ($N_{c2} > N_{c1}$) a six-vortex structure ("magnetic", attached, and connecting vortices) shown in Fig. 1c is generated.

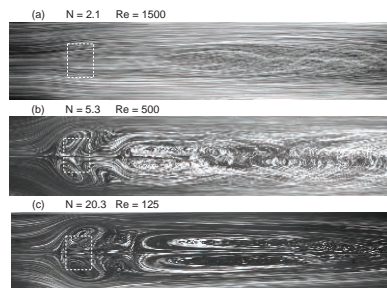


Fig. 1. The sequence of vortex structures at flow around a magnetic obstacle. White dash line is a magnet projection on free surface

References

1. E. V. Votyakov, Y. Kolesnikov, O. Andreev, E. Zienicke and A. Thess, *Phys. Rev. Lett.* **98** (14), 144504 (2007).

A dynamic multiscale subgrid model for MHD turbulence based on Kolmogorov's equation

L. Fang, W.J.T. Bos, L. Shao and J.P. Bertoglio

Laboratoire de Mécanique des Fluides et d'Acoustique, Université de Lyon, École centrale de Lyon, CNRS, Ecully, France. `le.fang at ec-lyon.fr`

Based on Kolmogorov's equation of filtered quantities [1,2], a new dynamic subgrid model for magnetohydrodynamic (MHD) turbulence is obtained. Similar to Politano's derivation [3], when the two-point distance ξ is much larger than the filter size, and is located in the inertial subrange, the simplified formulation of Kolmogorov's equation for filtered quantities reads:

$$-4\varepsilon_f^T \xi/5 = A^T, \quad -4\varepsilon_f^C \xi/5 = A^C, \quad (1)$$

in which ε_f^T and ε_f^C are the total dissipation and cross dissipation, respectively. The terms on the right hand sides are $A^T = \langle \delta u_l^{\leq 3}(\xi) \rangle - 6\langle b_l^{\leq 2}(x)u_l^{\leq}(x + \xi) \rangle$, $A^C = -\langle \delta b_l^{\leq 3}(\xi) \rangle + 6\langle u_l^{\leq 2}(x)b_l^{\leq}(x + \xi) \rangle$.

Following Agullo *et al.* [4] and introducing eddy-viscosity assumptions lead to

$$\varepsilon_f^T = 2\nu_t \langle S_{ij}^{\leq} S_{ij}^{\leq} \rangle + 2\eta_t \langle J_{ij}^{\leq} J_{ij}^{\leq} \rangle, \quad \varepsilon_f^C = 2(\nu_t + \eta_t) \langle S_{ij}^{\leq} J_{ij}^{\leq} \rangle. \quad (2)$$

Considering $E^C \approx 0$, *i.e.* assuming that the magnetic field does not directly affect the subgrid velocity stress, and ignoring the cross-helicity in (2) allow the simplified formulation

$$\nu_t = \frac{-5 \langle \delta u_l^{\leq 3}(\xi) \rangle}{8\xi \langle S_{ij}^{\leq} S_{ij}^{\leq} \rangle}, \quad \eta_t = \frac{15 \langle b_l^{\leq 2}(x)u_l^{\leq}(x + \xi) \rangle}{4\xi \langle J_{ij}^{\leq} J_{ij}^{\leq} \rangle}. \quad (3)$$

This new subgrid model is an extension of the CZZS model [1] for MHD turbulence. It has been tested in *A Posteriori* tests.

References

1. G. Cui, H. Zhou, Z. Zhang, and L. Shao, *Phys. Fluids* 16:2835, 2004.
2. L. Shao, Z. Zhang, G. Cui, and C.Xu, *Phys. Fluids* 17:115106.1, 2005.
3. H. Politano and A. Pouquet, *Physical Review E* 57:R21, 1998.
4. O. Agullo, W.C. Muller, B. Knaepen, and D. Carati, *Phys. Plasmas* 8: 3502, 2001.

Low-Prandtl number MHD cooling in a vertical cylindrical container

I.E. Sarris, A.I. Iatridis, C.D. Dritselis and N.S. Vlachos

Lab. of Fluid Mechanics & Turbomachines, Dept. of Mechanical Engineering,
University of Thessaly, 38334 Volos, Greece
sarris at uth.gr

Results of direct numerical simulations are presented for the strongly transient and turbulent natural convection cooling of an initially isothermal quiescent liquid metal placed in a cylinder under the effect of an external vertical uniform and constant magnetic field. The electrically conductive low Prandtl number fluid is put to motion when the vertical sidewall is suddenly cooled to a uniform lower temperature. See Sarris et al. [1] for further details.

Several simulations of the natural convection cooling of the liquid metal were performed in the range $1 \times 10^7 \leq Ra \leq 2 \times 10^9$ of Rayleigh numbers and Hartmann numbers between 0 and 300. Numerical results show that imposing the magnetic field, no observable effect is encountered at the initial stage of the vertical boundary layer development, while in the next stages, decelerates significantly the fluid motion. Imposing the magnetic field, conduction heat transfer is favored and the duration of the stratification and cooling stages are longer as shown in Fig. 1.

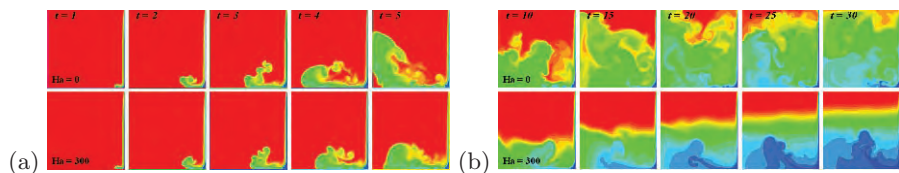


Fig. 1. Isotherms for $Ra = 10^9$, $Ha = 0$ (upper), and 300 (lower) for times (a) $1 \leq t \leq 5$ and (b) $10 \leq t \leq 30$.

References

1. I.E. Sarris, A.I. Iatridis, C.D. Dritselis and N.S. Vlachos, submitted (2009).

Anomalous scaling of passively advected magnetic field in the kinematic MHD Kazantsev-Kraichnan model

E. Jurčišinová, M. Jurčišin, and R. Remecky

Institute of Experimental Physics, Slovak Academy of Sciences, Watsonova 47,
04001 Košice, Slovakia
remecky at saske.sk

The problem of anomalous scaling of the equal-time correlation functions of the fluctuating part of a weak magnetic field \mathbf{B} deep inside the inertial interval is studied in the framework of the MHD Kazantsev-Kraichnan model in the presence of a strong large-scale magnetic field \mathbf{B}^0 . The model is described by the stochastic equation

$$\partial_t \mathbf{B} = \kappa_0 \Delta \mathbf{B} - (\mathbf{v} \cdot \partial) \mathbf{B} + (\mathbf{B} \cdot \partial) \mathbf{v} + (\mathbf{B}^0 \cdot \partial) \mathbf{v}, \quad (1)$$

where $\mathbf{v} = \mathbf{v}(\mathbf{x})$ is the incompressible velocity field and κ_0 is magnetic diffusivity. The term with \mathbf{B}^0 is a source of the anisotropy and plays the role of an external force.

The statistics of the velocity field \mathbf{v} is supposed in the following Gaussian form

$$\langle v_i(\mathbf{x}_1, t_1) v_j(\mathbf{x}_2, t_2) \rangle = \delta(t_1 - t_2) \int \frac{d^d \mathbf{k}}{(2\pi)^d} D_0 k^{-d-\varepsilon} P_{ij}(\mathbf{k}) \exp[i\mathbf{k} \cdot (\mathbf{x}_1 - \mathbf{x}_2)], \quad (2)$$

where D_0 is an amplitude and $P_{ij} = \delta_{ij} - k_i k_j / k^2$ is the transverse projector.

The influence of large-scale anisotropy on the anomalous scaling behavior is demonstrated. It is shown that the anomalous behavior is driven by the operators from the isotropic shell. The final asymptotic form of the correlation functions $B_{N-m,m}$ has the form $B_{N-m,m}(r) \sim r^{\gamma_N^* - \gamma_{N-m}^* - \gamma_m^*}$, where γ_y^* , $y = N, N-m, m$ are anomalous dimensions of the corresponding set of composite operators $F[y, p] = B_{i_1} \cdots B_{i_p} (\mathbf{B} \cdot \mathbf{B})^{(y-p)/2}$. The corresponding anomalous dimensions are calculated to the second order in the perturbation expansion in ε , i.e., in the two-loop approximation. The results are compared to the results obtained within the one-loop approximation and also to the two-loop results for the anomalous scaling of the Kraichnan rapid-change model of a passively advected scalar field. The corresponding discussion is done.

A new compressible turbulence model for free and wall-bounded shear layers

J.Y. Kim, and S.O. Park

Department of Aerospace Engineering, KAIST, Daejeon, Korea
sopark@kaist.ac.kr

Recent DNS (Direct Numerical Simulation) results indicate that the main compressibility effect in turbulence comes from the reduced pressure-strain term due to reduced pressure fluctuations. In our previous work, using the concept of moving equilibrium in compressible homogeneous shear flow, we developed a compressible pressure-strain model by modifying an incompressible linear pressure-strain model. The model is characterized by a decrease in the primary redistribution term but an increase in the secondary redistribution term. However, this model is not suitable for wall-bounded compressible flows since the compressible parameter is expressed as a function of turbulent Mach number only. It is well known that compressible effects vanish or become weak in compressible boundary layers, but the turbulent Mach number alone is not sufficient to mimic this nature. It is also widely known that the existing compressibility correction models deteriorate the prediction performance of the incompressible turbulence models in the calculation of supersonic wall-bounded flows.

It has widely been recognized that gradient Mach number is also an important parameter in addition to turbulent Mach number for compressible turbulence. Gradient Mach number is more adequately defined by using two-point correlation as indicated in DNS studies. Thus it is difficult to employ gradient Mach number in single-point closure models. Ristorcelli's model for dilatational terms includes gradient Mach number effect but important model coefficients are left undetermined. Yoshizawa *et al.* modified a linear eddy-viscosity model using the result of Two-Scale Direct-Interaction Approximation. Compressible effect was considered as a combination of non-equilibrium parameter and the turbulent Mach number.

In this work, we adopt the relationship between the normalized pressure variance and the compressible parameter in the model of Yoshizawa *et al.* to propose a modified compressible function of our earlier work which takes into account gradient Mach number effect. The proposed model is then applied to supersonic free shear and boundary layers for validation.

Modelling of turbulent flow in a gas burner.

K. Kwiatkowski and K. Bajer

Faculty of Physics, University of Warsaw, Poland
kamil@igf.fuw.edu.pl

When multi-species, non-premixed flows combine with chemical reactions, common situation in industrial devices, the mixing or diffusive phenomena become the key factors to understand the whole process. Turbulence is conducive to mixing of species and consequently may increase the reaction efficiency [1]. That motivates us to study in details the mixing of fuel with air, in a complex geometry industrial gas burner, without ignition and chemical reactions.

We create a 3D model of a real industrial syngas burner with additional air-inlet structures, which enhance the swirl and promote the generation of vortices.

The aim of simulations is to improve the performance of the burner by creating additional, controlled, vortex-driven mixing zones, where the partly burnt exhaust gases can again react with fuel. To design those vortex generators two fundamental theoretical problems seem to be immediately important and interesting [2]:

- mixing and reacting of two species in the velocity field *outside* a concentrated vortex. On that spatial scale the species concentrations, far away from the vortex axis, are constant.

- mixing and reacting of two species with constant concentrations *inside* a large vortex, assuming that the reaction is much faster than diffusion and therefore takes place only in a relatively thin layer.

References

- [1] K. Bajer, A. P. Bassom, and A. D. Gilbert. Accelerated diffusion in the centre of a vortex. *J. Fluid Mech.*, 437:395–411, 2001.
- [2] J. P. Crimaldi, J. R. Cadwell, and J. B. Weiss. Reaction enhancement of isolated scalars by vortex stirring. *Physics of Fluids*, 20(7):073605, 2008.

Contributors

- Abel, M., 863
Abshagen, J., 107
Adams, N.A., 743
Agostini, L., 427
Ahlers, G., 167
Ahnert, K., 863
Aider, J.L., 213
Akhavan, R., 359
Akkermans, R., 289
Alain, A., 31
Alamri, S., 265
Alexandrov, K., 163
Alfredsson, P.H., 603
Alizard, F., 67
Amili, O., 611
Amir, M., 667
Anand, G., 497
Andersson, H.I., 221, 335, 347, 623
663
Andreev, O., 833
Angot, P., 525
Araya, J., 951
Archer, P.J., 261
Aristov, V.V., 895
Armenio, V., 453
Arneodo, A., 719
Arratia, C., 183
Asmolov, E.S., 375
Atis, S., 59
Augier, P., 397
Auteri, F., 657
Avila, M., 107, 115, 125
Azhari, F., 179
Bai, H.L., 201
Bailliet, H., 855
Bailon-Cuba, J., 517
Bajer, K., 817, 965
Balarac, G., 779
Barenghi, C.F., 265, 281, 255
Barkley, D., 89
Baron, A., 657
Barri, M., 623, 301
Baudet, C., 31, 701
Bec, J., 485
Belan, M., 657
Belier, B., 701
Bendicks, C., 43
Bertoglio, J.P., 957
Bertolucci, A., 657
Biferale, L., 3, 325, 485
Billant, P., 397
Birch, D.M., 661
Bodenschatz, E., 167
Bodo, G., 867
Boeck, T., 633, 829
Boersma, B.J., 335, 347, 689, 847
Boffetta, G., 173, 549, 721
Bogdanov, S.R., 943
Boiko, A.V., 205
Bordás, R., 43
Borgnat, P., 755
Borodulin, V.I., 313
Boronin, S.A., 913
Bos, W.J.T., 35, 423, 525
Bosbach, J., 533
Bottaro, A., 141

- Boudet, J., 755
Bourgeois, O., 159
Bourgoin, M., 11, 31
Bourguet, R., 953
Bourouiba, L., 419
Bowman, J.C., 685, 791
Brandt, L., 85
Braun, C., 929
Braza, M., 953
Brethouwer, G., 51
Breuer, K., 233
Breuer, M., 927
Bruneau, Ch. H., 911
Brzek, B., 581
- Cadot, O., 217
Cahuzac, A., 755
Cal, R.B., 951
Calzavarini, E., 3, 11, 479
Cambon, C., 837
Cambonie, T., 213
Campana, E.F., 367
Carati, D., 813, 841
Carlotti, P., 389
Cartellier, A., 31
Casciola, C.M., 339, 351, 371, 729, 881
Castaing, B., 63, 701, 719
Castillo, L., 951
Castro, I.P., 667
Cekli, H.E., 237
Celani, A., 27, 169, 173, 505
Cencini, M., 485
Cenedese, A., 537
Chabaud, B., 159
Chagelishvili, G., 867
Chazot, O., 901
Chernov, V.V., 297
Chernyshenko, S.I., 601
Chernyshov, A.A., 465
Chevallard, L., 701, 719
Chiffaudel, A., 59
Chilla, F., 63
Chomaz, J.-M., 183, 273, 397
Cieslik, A.R., 293
Claus, J.M., 409
Clerc, H.J.H., 257, 289, 293, 415,
431, 453, 501, 529
Coleman, G.N., 261
- Collins, L., 343
Constantinescu, G., 439
Coquerelle, M., 779
Cortet, P.-P., 59
Cossu, 573, 645
Cottet, G.-H., 779
Creysse, M., 63
Criminale, W.O., 155
Cvitanovic, P., 75
- da Silva, C.B., 317, 561, 751
Dadashi, M., 277
Dam, N.J., 493
Dauchot, O., 89
Daviaud, F., 59, 701
David, S., 701
Davidson, P.A., 435, 557
de Angelis, E., 371
de Lange, R., 151
de Lillo, F., 549
de Lozar, A., 123, 129, 135
Deguchi, K., 79
Del Castello, L., 431
Delfos, R., 513, 629, 847
Delgado, A., 617
Denisov, S., 809
Depardon, S., 573
Dianat, M., 775
Diribarne, P., 281, 701
Doering, C.R., 483
Donnadieu, C., 273
Dormy, E., 801
Dritschel, D.G., 461
Dritselis, C., 959
du Puits, R., 159, 589
Dubrulle, B., 59, 701
Ducasse, L., 23
Duguet, Y., 85, 93
Duriez, T., 213
Durst, F., 131, 553
Duwig, C., 321
- Eckhardt, B., 83, 137, 791
Egbers, C., 97, 163
El Akoury, R., 953
El Khoury, G.K., 625
Elsinga, G.E., 941
Emran, M.S., 15, 517

- Ertunc, Ö., 131, 553, 617
 Estienne, O., 855
 Ezersky, A.B., 297
- Fabiani, F., 103
 Fang, L., 957
 Farge, M., 253, 423, 759, 909, 945
 Faulwetter, R., 163
 Fauve, S., 801
 Favier, B., 837
 Fischer, P., 911
 Fischer, P.F., 641
 Fletcher, J.P., 649
 Fröhlich, J., 783
 Fraigneau, Y., 937
 Fransson, J.H.M., 149, 603, 605, 609, 921
 Frewer, M., 925
 Frick, P., 809, 825
 Friedrich, R., 877
 Froehlich, J., 783
 Frohnäpfel, B., 209, 927
 Frolova, A.A., 895
 Fukagata, K., 189
 Funfschilling, D., 167
 Futterer, B., 97
- Gülker, G., 39
 Gagne, Y., 331, 701
 Gampert, M., 565
 Garcia-Villalba, M., 929
 Garden, J.-L., 159
 Gasteuil, Y., 19
 Gauthier, F., 159, 521
 Genc, B.Z., 617
 Generalis, S.C., 649
 Gerashchenko, S., 343
 Germanos, R.A.C., 897
 Geurts, B.J., 415
 Ghaffari, S.A., 277
 Gibert, M., 63
 Gibson, J.F., 75
 Gillissen, J.J.J., 335, 347
 Giorgilli, M., 537
 Girard, A., 701
 Godeferd, F.S., 837
 Gonzalez-Juez, E., 439
 Gorokhovski, M., 637, 693
- Goto, S., 269
 Gottwald, G.A., 461
 Grandchamp, X., 905
 Grinis, L., 923
 Grissinger, C., 801
 Gromov, P.R., 297
 Grosse, S., 2
 Grossmann, S., 479
 Grundestam, O., 177
 Gualtieri, P., 339, 729
 Gurka, R., 733
- Haddad, K., 131
 Hamadiche, M., 899
 Hanazaki, H., 447
 Hancock, P.E., 939
 Hannemann, F.H., 931
 Harlander, U., 163
 Harran, G., 953
 Hasegawa, Y., 189, 209
 Hattori, H., 593
 Henningson, D.S., 93, 641
 Herring, J.R., 449
 Hickel, S., 743, 783, 873
 Hochstrate, K., 107
 Hof, B., 123, 125, 129, 135, 145
 Hoffmann, N.P., 111
 Holzner, M., 119
 Homeyer, T., 39
 Horiuti, K., 705
 Hwang, Y., 645
- Iatridis, A.I., 959
 Iovieno, M., 677
 Ishigami, T., 363
 Itano, T., 649
 Iwano, I., 919
- Jacobitz, F., 23
 Jenny, P., 497
 Jiménez, J., 597
 Johansson, A.V., 177
 Johnston, H., 483
 Jouanguy, J., 937
- Kachanov, Y.S., 313
 Kadoch, B., 35, 525, 737

- Kalda, J., 541
Kamp, L.P.J., 289, 293
Kaneda, Y., 759, 945
Kang, H.S., 581
Karelsky, K.V., 465
Kasagi, N., 189, 209
Kawaguchi, Y., 71, 363
Kawahara, G., 329, 585
Kawamura, H., 71
Keetels, G.H., 257
Kempf, A., 763
Khaledi, H.A., 301
Khapaev, A.A., 443
Kholmer, V., 923
Kholmyansky, M., 715
Khujadze, G., 675
Kida, S., 249
Kim, J.Y., 963
Kimura, Y., 449
Kinzel, M., 119
Kizilova, N., 899
Kluwick, A., 577
Knaepen, B., 795
Knebel, P., 903
Kobzev, A., 833
Kolesnikov, Yu., 833, 955
Kolomensky, D., 525
Komori, S., 919
Kopp, G., 733
Kornilov, V.I., 205
Koschatzky, V., 847
Kostykin, S.V., 443
Kramer, W., 453
Krasnov, D., 633, 829
Krogstad, P.-A., 557
Kronenburg, A., 763
Kuik, D.J., 145
Kunnen, R.P.J., 415
Kurbatskaya, L.I., 405
Kurbatskiy, A.F., 405
Kurian, T., 609, 921
Kwiatkowski, K., 965
- Laddhari, F., 389
Lanotte, A.S., 485
Larsson, J., 873
Larsson, R., 85
Laval, J.P., 937
- Lavezzo, V., 343
Lebron, J., 581
Lee, D.H., 359
Leonardi, S., 103
Lessinnes, T., 813
Lévêque, E., 3, 11
Liberzon, A., 119, 733
Lienhart, H., 553
Lindborg, E., 51
Livescu, D., 545, 767
Lohse, D., 355, 479, 529
Luchini, P., 241
Lüthi, B., 119
Luzzatto-Fegiz, P., 305
- Müller, B., 179
Maas, U., 885
Macaskill, C., 461
Malinowski, S., 787
Marinc, D., 83
Marques, F., 115
Martinelli, F., 241
Martins Afonso, M., 505
Marusic, I., 941
Matsumoto, T., 47
Mazzino, A., 27, 169, 505, 549, 721
McGuirk, J.J., 775
Medeiros, M.A.F., 897
Mehdizadeh, A., 393
Meiburg, E., 439
Mellado, J.P., 401
Mellibovsky, F., 115, 137
Meneguz, E., 489
Meneveau, C., 581, 951
Meseguer, A., 115, 137
Michaelis, B., 43
Miozzi, M., 367
Mirzaei, M., 493
Miyao, T., 447
Mizerski, K.A., 817
Mizeva, I., 825
Mizuno, Y., 597
Mizuta, A., 47
Moisy, F., 427
Monti, P., 537
Moroni, M., 537
Morozenko, A., 541
Morrison, J.F., 225, 661

- Mortensen, P.H., 335
 Moxey, D., 89
 Muratore-Ginnaneschi, P., 169
 Musacchio, S., 173, 721
- Nagano, Y., 593
 Nagata, M., 79
 Narasimhamurthy, V.D., 665
 Naso, A., 509, 697
 Nathan, P., 939
 Neffaa, S., 737
 Negretti, E., 397
 Nguyen van yen, R., 909
 Nickels, T.B., 933
 Nicollean, F.C.G.A., 891, 931, 947
 Nikitin, N., 653
 Nikitin, N.V., 601
 Noskov, V., 809
 Nowakowski, A.F., 931
 Nygård, F., 221
- Oberlack, M., 393, 675, 681, 867
 Obi, S., 893
 Örlü, R., 605
 Özyilmaz, N., 553
 Ohlsson, J., 641
 Okamoto, N., 759, 945
 Okamura, T., 447
 Olivieri, A., 367
 Olla, P., 505
 Ooms, G., 689
 Oresta, P., 335
 Orlandi, P., 103
 Ortiz, S., 183, 273
- Pétrélis, F., 801
 Paranthoen, P., 297
 Parezanović, V., 217
 Park, S.O., 963
 Peguero, C., 233
 Peinke, J., 39
 Pelorson, X., 855
 Pereira, J.C.F., 317
 Peters, N., 401, 565
 Petitjeans, P., 253
 Petrosyan, A.S., 465
 Pettersen, B., 625
 Pfister, G., 107
- Picano, F., 339, 351, 881
 Pinelli, A., 329, 585
 Pinna, F., 901
 Pinton, J.-F., 11, 19
 Piotrowski, Z., 787
 Piva, R., 367, 371
 Plunian, F., 813
 Podvin, B., 937
 Poelma, C., 145
 Prosperetti, A., 355
 Pujals, G., 573
 Pumir, A., 23, 697
 Punzmann, H., 709, 725
- Qin, N., 947
 Quadrio, M., 241, 657
 Qubain, A., 225
 Qureshi, M.N., 31
- Rambaud, P., 901
 Ravelet, F., 629
 Reeks, M.W., 489
 Reis, R.J.N., 317
 Remetsky, R., 961
 Resagk, C., 589
 Revstedt, J., 321
 Rind, E., 309
 Rist, U., 67
 Ristorcelli, J.R., 545
 Roberts, M., 791
 Robinet, J.-C., 67
 Roche, P.-E., 159, 281, 521, 701
 Roschektayev, A.P., 313
 Rossi, M., 829
 Rousset, B., 701
 Rovenskaya, O.I., 895
 Rubinstein, R., 767, 907
 Ruppert-Felsot, J., 253
- Sabetghadam, F., 277
 Saitou, K., 705
 Salort, J., 159, 701
 Samanta, D., 135
 Sandham, N.D., 851
 Sarathi, P., 733
 Sardina, G., 339, 351, 729
 Sarris, I.E., 959
 Saveliev, V., 693

- Scagliarini, A., 3, 325, 485
 Scarsoglio, S., 155
 Schäfer, P., 565
 Schaupp, C., 877
 Scheichl, B., 577
 Schlatter, P., 93, 151, 641
 Schmeling, D., 533
 Schmidt, H., 401
 Schneider, K., 35, 423, 525, 737, 759, 821, 909, 945
 Schneider, T.M., 83, 137
 Schumacher, J., 15, 517, 633
 Scott, R.K., 461, 917
 Segalini, A., 609
 Sekimoto, A., 329
 Seoud, R.E., 711
 Sergeev, Y., 285
 Shao, L., 957
 Shats, M.G., 709, 725
 Shimizu, M., 249
 Shishkina, O., 229
 Silva, H.G., 897
 Smith, F.T., 577
 Smolarkiewicz, P.K., 787
 Soldati, A., 343, 489
 Soria, J., 613
 Soustov, P.L., 297
 Staplehurst, P.J., 435
 Starkov, K.E., 915
 Stepanov, R., 809, 825
 Stevens, B., 401
 Stevens, R.J.A.M., 529
 Straub, D., 419
 Stresing, R., 711
 Sugiyama, K., 479
 Suponitsky, V., 851
 Suramlshvili, N., 285

 Tabeling, P., 701
 Takagaki, N., 919
 Talamelli, A., 609
 Tan, G., 427
 Tang, Y., 949
 Tarlet, D., 43
 Tatsumi, T., 771
 Taveira, R.M.R., 561
 Teaca, B., 841
 Tee, B.T., 933

 ter Meulen, J.J., 493
 Tevzadze, A., 867
 Thévenin, D., 43
 Thess, A., 159, 589, 833
 Thibault, P., 701
 Thiria, B., 213
 Thomas, T.G., 261, 457
 Tirtsey, S., 901
 Tisserand, J.-C., 63
 Tizzi, M., 27
 Toh, S., 47, 649
 Tokyay, T., 439
 Tordella, D., 155, 657
 Torres-Nieves, S., 581
 Toschi, F., 3, 11, 325, 485, 755
 Tran, C.V., 461
 Trieling, R.R., 431
 Troiani, G., 881
 Tsinober, A., 119, 431, 715, 733
 Tsuji, Y., 705
 Tsukahara, T., 71, 363
 Tuckerman, L.S., 89

 Uhlmann, M., 329, 585, 929

 van Aartrijk, M., 501
 van de Water, W., 237, 493
 van Heijst, G.J.F., 257, 289, 293
 van Hirtum, A., 855, 905
 Vasanta Ram, V.I., 179
 Vassilicos, J.C., 711
 Verma, M.K., 813, 841
 Verzicco, R., 355, 529
 Vinkovic, I., 637
 Viré, A., 795
 Vlachos, N., 959
 Volk, R., 11
 von Terzi, D., 783
 Vozella, L., 169, 721

 Wagner, C., 229, 533
 Wallin, S., 177
 Wang, H.L., 601
 Wang, L., 565
 Wang, P., 885
 Warhaft, Z., 343
 Warncke, N., 513
 Wedin, H., 141

Wesfreid, J.E., 213
Westerweel, J., 145, 513, 621, 629,
847
Westhoff, A., 533
Willaime, H., 701
Williamson, C.H.K., 305
Withalm, M., 111
Woodruff, S.L., 767
Wunderlich, B., 43
Wyszogrodzki, A.A., 787

Xia, H., 725
Xia, K.-Q., 471
Xie, Z.-T., 409

Yakovenko, S.N., 457
Yamazaki, S., 593

Yang, Z., 775
Yokota, R., 893
Yoshimatsu, K., 759, 945
Youd, A.J., 265

Zabelok, S.A., 895
Zamansky, R., 637
Zhao, L.H., 335, 347
Zheng, H., 931
Zheng, H.W., 947
Zhong, J.-Q., 529
Zhou, Y., 201
Zikanov, O., 829

